Solid Freeform Fabrication Proceedings

August 2003

Solid Freeform Fabrication as an important and totally integrated approach to design, materials processing and manufacturing research results related to it is contained in this proceedings of the SFF Symposium held in Austin, Texas on August 4-6, 2003

SFF Topics covered in the Symposium include:

Process Development
Modeling
Applications
Materials

David L. Bourell , Richard H. Crawford,
Joseph J. Beaman, Kristin L. Wood,
and Harris L. Marcus, Editors

Library of Congress ISSN 1053-2153

REPORT DOCUMENTATION PAGE

Form Approved
OMB No. 0704-0188

1. REPORT DATE (DD-MM-YYYY)	2. REPORT DATE	3. DATES COVERED (From - To)
		8/1/2003 to 5/1/2004

4. TITLE AND SUBTITLE
Solid Freeform Fabrication Symposium - 2003
Report and Proceedings

5a. CONTRACT NUMBER
N00014 - 03-1-0913

5b. GRANT NUMBER
N00014- 03-1-0913

5c. PROGRAM ELEMENT NUMBER

6. AUTHOR(S)
D. L. Bourell and Kristin L. Wood

5d. PROJECT NUMBER

5e. TASK NUMBER

5f. WORK UNIT NUMBER

7. PERFORMING ORGANIZATION NAME(S) AND ADDRESS(ES)
The University of Texas at Austin
Solid Freeform Fabrication Symposium
1 University Station, C2200
Austin, TX 78712-0292

8. PERFORMING ORGANIZATION REPORT NUMBER

9. SPONSORING/MONITORING AGENCY NAME(S) AND ADDRESS(ES)
Ralph F. Wachter ONR 361
Ballston Centre Tower One
800 North Quincy Street
Arlington, VA 22217-5660

10. SPONSOR/MONITOR'S ACRONYM(S)

11. SPONSORING/MONITORING AGENCY REPORT NUMBER

12. DISTRIBUTION AVAILABILITY STATEMENT
approved for public release

13. SUPPLEMENTARY NOTES

14. ABSTRACT

Significant Research or Development Results During the Past Year: The Fourteenth Solid Freeform Fabrication Symposium, held at The University of Texas in Austin on August 4-6, 2003, was attended by 100 national and international researchers. Papers addressed SFF issues in computer software, machine design, materials synthesis and processing, and integrated manufacturing. A total of 66 presentations were made, 57 oral presentations and 9 poster presentations. Of these, 63 are included in the proceedings volume. The diverse domestic and foreign attendees represented industrial users, SFF machine manufacturers, universities, and government. The attendance was up this year from previous years. The Symposium organizers look forward to its being a continuing forum for technical exchange among the expanding body of researchers involved in SFF.

15. SUBJECT TERMS
Freeform Fabrication, Symposium, Proceedings

16. SECURITY CLASSIFICATION OF:			17. LIMITATION OF ABSTRACT	18. NUMBER OF PAGES	19a. NAME OF RESPONSIBLE PERSON
a. REPORT	b. ABSTRACT	c. THIS PAGE			David L. Bourell
unclass-ified	unclass-ified	unclass-ified	UL		19b. TELEPONE NUMBER (*Include area code*) (512) 471-3170

End of Fiscal Year Letter - ONR Grant **N00014-03-1-0913**
Solid Freeform Fabrication Symposium -2003
David L. Bourell, PI

A. Description of the Technical Research or Development Goals: This grant helped to underwrite the publication expenses associated with the Fourteenth Solid Freeform Fabrication (SFF) Symposium. The symposium took place on August 4-6, 2003 in Austin, Texas at the University of Texas.

It included papers on computer interfaces with SFF, materials processing and properties associated with SFF and machine design and requirements for SFF.

B. Significant Research or Development Results During the Past Year: The Fourteenth Solid Freeform Fabrication Symposium, held at The University of Texas in Austin on August 4-6, 2003, was attended by 100 national and international researchers. Papers addressed SFF issues in computer software, machine design, materials synthesis and processing, and integrated manufacturing. A total of 66 presentations were made, 57 oral presentations and 9 poster presentations. Of these, 63 are included in the proceedings volume. The diverse domestic and foreign attendees represented industrial users, SFF machine manufacturers, universities, and government. The attendance was up this year from previous years. The Symposium organizers look forward to its being a continuing forum for technical exchange among the expanding body of researchers involved in SFF.

The Symposium was again organized in a manner to allow the multi-disciplinary nature of the SFF research to be presented coherently, with various sessions emphasizing computer issues, machine topics, and the variety of materials aspects of SFF. The three-day event was completely composed of individual oral presentations (no panel discussions/presentations) to accommodate the demand for this dissemination format. The afternoon parallel sessions were split into two sessions, and the poster session was reduced to give preference to presenters desiring to give oral presentations at the meeting. We believe that documenting the constantly changing state of SFF art as represented by these Proceedings will serve both the people presently involved in this fruitful technical area as well as the large flux of new researchers and users entering the field. This year is the fourth year of production of a CD proceedings. Available in November 2003, this medium allows enhancements such as higher resolution photos and figures, color presentation and whole-document searching in place of a keyword index. The attendee list is included, and the table of contents has hyperlinks to the articles. Page numbering is sequential to facilitate citation. A hard-copy print-out of the entire document is also available to those desiring that format.

Several improvements were incorporated into the 2003 meeting. First, we provided an option for authors to submit a manuscript with refereed status. A refereed conference publication is important to some participants, primarily academicians, and we still accepted manuscripts for inclusion without review, as we have in the past. Of the 66 papers published in the proceedings, 32 were reviewed and noted in the publication. A second innovation for the meeting was awarding of best paper awards for the oral presentation and poster categories. The award consisted of a certificate to the authors. The best oral presentation and poster were chosen by the presentation being reviewed by at least 2 independent reviewers at the meeting. The criteria included clarity of presentation as well as quality, significance and soundness of the research. The 2003 winners were "Comparisons between Thermal Modeling and Experiments in Laser-Densified Dental Powder Bodies" by Kun Dai, Xiaoxuan Li, and Leon L. Shaw of the University of Connecticut-Storrs (poster) and "Rapid Manufacturing with Electron Beam Melting (EBM) – A Manufacturing Revolution?" by Morgan Larsson, Ulf Lindhe, and Ola Harryson of Arcam AB, Arcam AB and North Carolina State University, respectively.

We are pleased to report that the SFF Symposium attracted a large number of young scientists this year. We had 44 students attend this year, 44% of the entire meeting. Participants represented 38 universities (14 international universities), 11 industries (5 international) and 2

national labs and government agencies. The Organizing Committee has always valued the role of technical meetings as a venue for graduate students in research. We strive to make the conference affordable and therefore accessible to students. The 2003 meeting registration cost of $125 for students reflected this. Non-student cost was $350.

Information on the SFF Symposium was made available through the worldwide web at http://lff.me.utexas.edu/. On-line registration forms, hotel information, general information brochure, proceedings order forms, and maps are all available. The 2004 tentative program will be available on our website in early June. The symposium email address is sffsymp@uts.cc.utexas.edu.

C. Plans for Next Year's Research or Development: Plans are currently underway for organization of the Fifteenth Solid Freeform Fabrication Symposium. The dates are August 2-4, 2004.

Table of Contents

Modeling

Applications

Materials

PREFACE

The Fourteenth Solid Freeform Fabrication (SFF) Symposium, held at The University of Texas in Austin on August 4-6, 2003, was attended by over 100 national and international researchers from fourteen countries. Papers addressed SFF issues in computer software, machine design, materials synthesis and processing, and integrated manufacturing. The diverse domestic and foreign attendees included industrial users, SFF machine manufacturers, university researchers and representatives from the government. The Symposium organizers look forward to its being a continuing forum for technical exchange among the expanding body of researchers involved in SFF.

The Symposium was again organized in a manner to allow the multi-disciplinary nature of the SFF research to be presented coherently, with various sessions emphasizing process development, design tools, modeling and control, process parameter optimization, applications and materials. We believe that documenting the changing state of SFF art as represented by these Proceedings will serve both those presently involved in this fruitful technical area as well as new researchers and users entering the field.

This year is the first year for authors to elect to have their manuscript submissions rigorously reviewed as refereed submissions. At least two external reviewers assessed these manuscripts. Rejected manuscripts and manuscripts with mandatory revisions that were not revised have been included in the proceedings as unreviewed. There are a number of excellent manuscripts in the Proceedings for which the authors opted not to be reviewed. Reviewed manuscripts are noted as such before the paper abstract along with the date of acceptance.

The Organizing Committee held a best paper competition for the first time this year. Both oral presentations and the poster presentations were judged by at least two independent reviewers. The criteria included clarity of presentation as well as quality, significance and soundness of the research. The best oral presentation was awarded to Morgan Larsson from Arcam AB (Germany) who gave the paper "Rapid Manufacturing with Electron Beam Melting (EBM) – A Manufacturing Revolution?" The best poster presentation was awarded to Kun Dai, Xiaoxuan Li and Leon L. Shaw from the University of Connecticut-Storrs for the presentation entitled, "Comparisons Between Thermal Modeling and Experiments in Laser-Densified Dental Powder Bodies".

The proceedings papers are stored individually on the CD in pdf format by primary author last name, and Adobe® Acrobat® Reader™ installers for the Macintosh (OS 10.2.2-10.2.6) and PC (Windows XP) are included which may be used to view and search the pdf files. The Table of Contents file has links to all the papers. We have sequentially numbered the pages of the papers to facilitate citation. Some versions of Reader™ do not have search capabilities which are necessary to keyword search the SFF Symposium Proceedings. If you have problems with searching, you might consider installing the version of Reader™ from the CD. The Adobe website (http://www.adobe.com/) also has versions of Acrobat Reader which may be downloaded free of charge.

The editors would like to extend a warm "Thank You" to Rosalie Foster for her detailed handling of the logistics of the meeting and the Proceedings, as well as her excellent performance as registrar and problem solver during the meeting. We are grateful to Cindy Pflughoft who helped with Proceedings production. We would like to thank the Organizing Committee, the session chairs, the attendees for their enthusiastic contributions, and the speakers both for their significant contribution to the meeting and for the relatively prompt delivery of the manuscripts comprising this volume. We look forward to the continued close cooperation of the SFF community in organizing the Symposium. We also want to thank Ralph Wachter and the Office of Naval Research (N00014-03-1-0913) for supporting this meeting financially. The meeting was co-organized by the University of Connecticut at Storrs, and the Mechanical Engineering Department, Laboratory for Freeform Fabrication and the Texas Materials Institute at The University of Texas at Austin.

The editors.

this page intentionally blank

Organizing Committee

Joseph Beaman	University of Texas at Austin
David Bourell	University of Texas at Austin
Richard Crawford	University of Texas at Austin
Harris Marcus	University of Connecticut at Storrs
Kris Wood	University of Texas at Austin

Advisory Committee

David Alexander	Pratt & Whitney
Amit Bandyopadhyay	Washington State University
Ian Campbell	Loughborough University
Joe Cesarano	Sandia National Labs-NM
Richard Chartoff	University of Arizona
Stephen Danforth	Rutgers-The State University of New Jersey
Phill Dickens	Loughborough University
Steve Fishman	Office of Naval Research
Kesh Narayanan	National Science Foundation
Fritz Prinz	Stanford University
Eli Sachs	Massachusetts Institute of Technology
Brent Stucker	Utah State University
Ralph Wachter	Office of Naval Research

this page intentionally blank

Process Planning for Solid Freeform Fabrication Based on Laser-Additive Multi-Axis Deposition

Rajeev Dwivedi, Radovan Kovacevic
Research Center for advanced Manufacturing
Southern Methodist University, 1500 International Parkway Suite # 100,
Richardson, TX, 75081
Reviewed, accepted August 19, 2003

Abstract

This paper describes a new approach for rapid prototyping based on volumetric skeletonization. Contrary to most of the popular techniques for Solid Freeform Fabrication (SSF) based on 2-1/2 -axis layering as planar slices, this approach suggests the growth of the component along all three coordinate axes. While this approach offers many advantages in terms of the elimination of the support structures for the reduction of the staircase effects and the elimination of various post processes for the functional parts, this approach also offers challenges towards process planning. For various complicated shapes it may not be possible to generate the required shape using this approach; however, a hybrid approach which also incorporates the deposition by layers, may offer an optimum solution. Preliminary results are based on the successful laser-based additive deposition along multiple g-vectors. The material properties and the problems of possible porosities are still to be investigated. Advantages, process planning, applications, experimental results, and the challenges of this new method are the subject of this paper.

Introduction

Recent approaches for rapid prototyping assisted by flexible machines like a CNC, [1,2] robot [3-8] and promising results of the laser-based metal powder deposition, which allow material deposition from any direction [11] have inspired researchers to look forward to the multi-directional deposition for Rapid Prototyping. Another advantage inherent to the laser-based metal powder deposition is that the volume of material deposited can be controlled using different parameters, primarily the laser head speed, the laser power, the size of laser focal point, and the metal powder flow rate. Contrary to most of the Rapid Prototyping techniques that are based exclusively on the 2-1/2-axis planar layer deposition approach, the multi-direction material deposition approach offers many advantages.

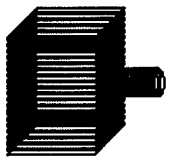

Figure 1. Multi-directional Slicing

In a traditional 2-1/2-axis planar layered deposition, the slicing of a branching structure may yield disconnected islands. The islands usually require supporting structures. A large

number of disconnected path elements for different islands render more turning points and path elements; therefore the total time and process complexity are increased. Different methods such as growth from the skeleton, progressive decomposition, and a hybrid approach can be used to exploit multi-directional material addition for part fabrication. Similar to the phenomenon of crystal growth that can be visualized as the growth of a solid from its tree-like dendritic skeleton, the slender parts can be fabricated by growing a part from its skeleton. An approach suggested by Singh et al. [9,10] which is based on the progressive decomposition of the part into sub-volumes, can be used such that each of the sub-volumes can be completely built along a certain direction in layers (Figure1). A hybrid approach that involves skeleton generation for support and the bulk of material added by 2-1/2-axis planar layered deposition process provides an alternate approach to optimize the part fabrication.

(a)Skeleton of the part

(b)Part after deposition of first layer

(c)Part grown from skeleton

Figure 2. Part grown from its skeleton

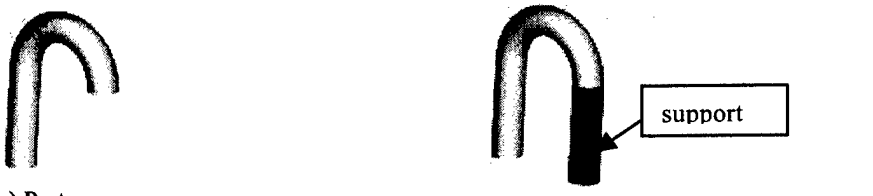

(a) Part

(b) Support required when 2-1/2 Rapid Prototyping method is used.

Figure 3: A part fabricated using 2-1/2-axis approach that requires support

This paper describes the approach for building a slender part from its skeleton. The approach is based on the thinning of a solid model to generate the skeleton of the component followed by regeneration of the solid from the skeleton (Figure 2). Various disadvantages of the traditional solid freeform fabrication techniques based on layered deposition that the proposed new method seeks to address are:

1. Staircase effect.
2. Requirement for support structure (Figure 3).
3. For various geometries, the trade-off between the material deposition rate and the mimimization of the support structures that govern the choice of part-build orientation.
4. The complexity of the process due to the treatment of rapid prototyping and the corresponding solid model of the component as a uni-directional layered structure.

5. Requirement for various post processing steps of the part.

Other advantages of fabricating a part form its skeleton include the ability to fabricate two loosely fitting components simultaneously. Multi-directional material deposition allows repairing a part without the need for relocation or reorientation. The use of freeform curves in space to deposit the material and the control of the material volume during deposition reduces the staircase effects.

The limitations that can be attributed to the Multi-directional material deposition approach include:

1. The geometry of the part may not allow the material deposition head to access all of the points.
2. A layer-by-layer technique is usually more suitable for the parts that have simple geometry and /or have an aspect ratio close to unity and have many branching structures.

The limitations, while governed by the geometry and material deposition technique employed, also depend on the orientation of the part. Different methods are investigated for the part fabrication by multi-directional material addition. The initial part of the paper discusses the different methods used for volume skeletonization. Also discussed is how the skeletonization algorithm is used for the process planning for material deposition. In the later part of the paper, the experimental results are discussed.

Volume skeletonization and process planning

A technique selected for the volume skeletonization should be able to address the following issues:

1. The skeleton must maintain the fundamental topology and geometry of the part.
2. The process planning should allow re-growth of the part from its skeleton.

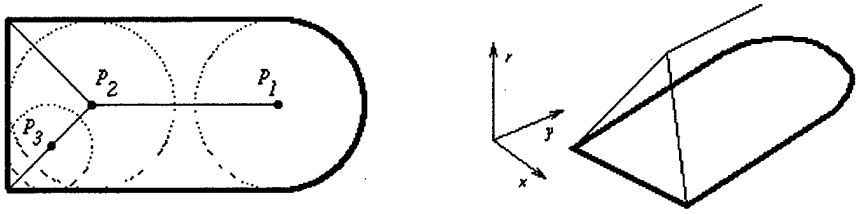

Figure 4 : Maximal inscribed sphere.[13]

The medial axis transform (MAT) is a shape representation method that describes an object by a lower-dimensional skeleton together with a local thickness [14]. MAT is defined by associating to each axis point $\boldsymbol{p}$ along the skeleton the radius $r(\boldsymbol{p})$ of the maximal inscribed sphere (Figure 4). The Voronoi diagram is a similar fundamental construction in computational geometry[14]. The Voronoi diagram captures the proximity structure of a collection of elements in space. Consider a fixed, finite set of points $\{s_i\}$ in Euclidean space. The points $\{s_i\}$ are called *sites*. An arbitrary point $\boldsymbol{p}$ is said

to lie in the Voronoi region of $\{s_i\}$ if $\boldsymbol{p}$ is closer to s_i than to any other site s_j. The Voronoi diagram divides space into regions according to the closest site. Attali et al. have [15] suggested the use of polyballs to approximate shapes and skeletons. The method suggested by Eric et al. [16] suggests an approach to the reconstruction of branching shapes that exploits the relationships between the skeleton of an object and the Voronoi graph of its boundary points. Their method is based on the division of space based on a set of points. The Voronoi graph and the skeleton may be approximated as the subset of the Voronoi elements that are completely included in the object. Gagvani et al. [17] have reported a technique for skeleton computation for articulation that can be used in an animation program. They (Gagvani et al.) suggested a method for voxel arrangement to generate a skeleton-tree from the volume. The method is based upon the distance transform, and the distance transform values are stored and used for regrowing the object from its skeleton.

For a solid X, which is a closed subset of R^3, its interior is defined as $p \in X$ and its exterior is the complement $p \notin X$ .The boundary of the solid is defined as $p \in \partial X \subset X$ that is the subset of solid where any neighborhood contains non-members. The distance transform maps the solid to its equivalent distance field. The corresponding distance field [18] is the scalar field associated with solid X, $F : R^3 \rightarrow R$ that maps a point in space to the distance from that point to the closest on ∂X.

$$F(p) = \begin{cases} -\min_{\forall q \in \partial x} (|p-q|) & p \in X \\ 0 & p \in \partial X \\ \min_{\forall q \in \partial x} (|p-q|) & p \notin X \end{cases}$$

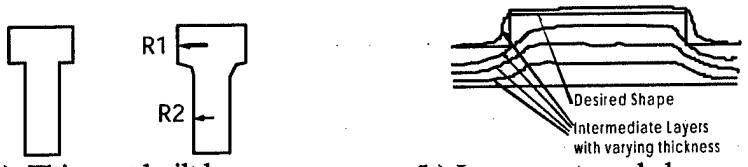

(a) Thin part built by one sweep

(b) Large part made by multi layer deposition.

Figure 5: Part fabrication by varying material volume

During the material deposition, the distance transform value of the skeleton is converted to the amount of material deposition at the location. The speed of laser head, the powder flow rate, the laser power, and the size of the focal point are the primary parameters that control the rate of material volume deposition. By controlling these parameters, the desired shape of the object is generated. For small or thin components, the part is generated by a single sweep of the laser head [Figure 5 (a)]; however, the larger

components need a multilayer deposition [Figure 5(b)]. For every layer, the thickness of the deposited layer is manipulated such that the final shape is obtained as the linear sum of intermediate layers [Figure 5(b)]. Process planning converts the distance transform values to the linear constant multipliers for the process parameters.

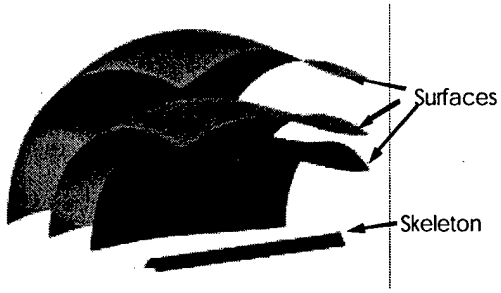

Figure 6. Tool path surfaces

The solid to be built is defined by the boundary $F(p)=0$ such that $p \in \partial X$. The trajectory for the m^{th} layer $g_i(p)$ of the process function is defined as:

$$F(p) = \sum_{i=1}^{m} (c_i + v_i + l_i) g_i(p)$$

c_i, v_i and l_i are the process parameter constants that correspond to the powder feed rate, laser head traverse speed, and the laser power feed rate. The process parameter-constant values are determined experimentally. Movement of the tool takes place along the surfaces described by the process function (Figure 6).

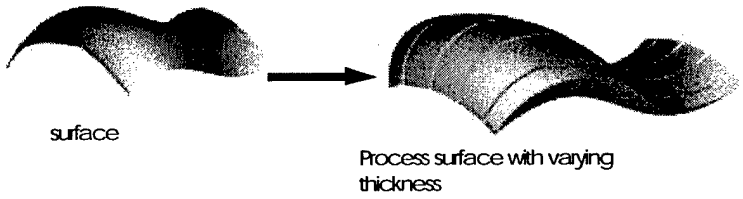

Figure 7. Mapping surface to process surface

The surfaces are homotopes of the intermediate material layers such that the variation in thickness of each layer is stored. The intermediate layers manufactured by material deposition are referred as process surfaces. Each surface, in turn, is comprised of closely spaced curves in the space. The thicknesses of the surfaces correspond to the material volume controlled by process parameters, and the space curves represent the deposition head path trajectory. As shown in the Figure 7, the geometric surface provides the trajectory for the deposition head; whereas, the process surface is obtained by attributing the material thickness to the trajectories. The process planning allows the varying volume of material to be deposited along the trajectories to obtain the final component.

Another approach for multi-directional material deposition is based on ellipsoid fitting. The ellipsoid fitting method can be used to approximate the shape of an object by

providing important and useful attribute sets. However, it does not provide an accurate description of the shape. The ellipsoid fit provides global measures for geometry. However, this attribute is a crude (first order) approximation of the shape [19].

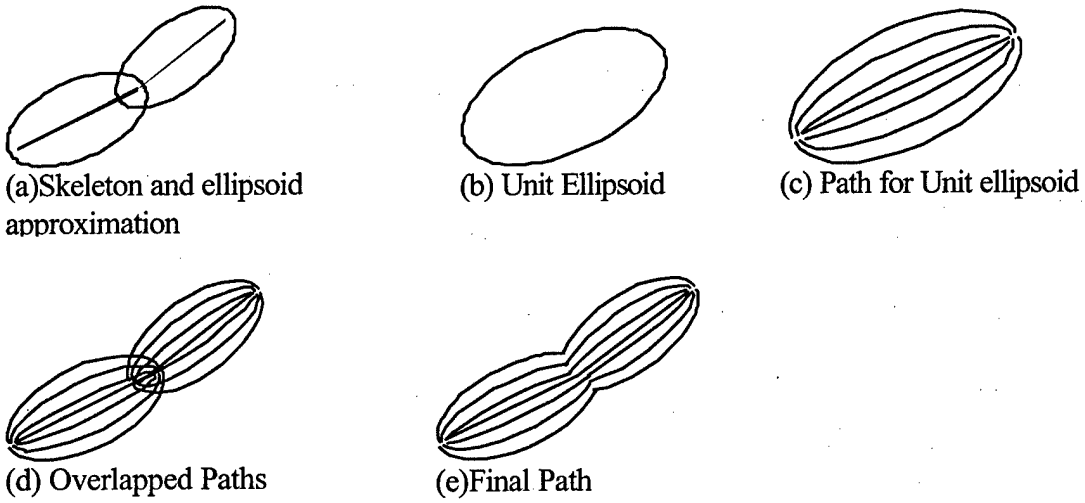

(a)Skeleton and ellipsoid approximation (b) Unit Ellipsoid (c) Path for Unit ellipsoid

(d) Overlapped Paths (e)Final Path

Figure 8. Path generation for part based on ellipsoid approximation.

In the case of machining after the material is deposited, in order to remove extra material, the shape approximation by ellipsoids can be used for process planning. The task of material deposition for a complex component is subdivided into the subtasks, where material deposition is performed for individual ellipsoids. A Boolean equivalent union of all the sub-paths of the ellipsoids renders the final path. Figure 8(a) depicts the skeleton of an object and its ellipsoid approximation. Figures 8(b) and 8(c) show a unit ellipsoid and the corresponding path for material deposition, and Figure 8(d) shows the overlapped paths for the ellipsoids used to approximate the solid. Figure 8(e) represents the equivalent of a Boolean union of the paths for individual ellipsoids to generate the final path.

Anne et al. [20] have suggested an algorithm for the construction of skeletal curves from an unorganized collection of scattered data points lying on a surface. A neighborhood graph is constructed over the set of points to compute geodesic distances between the root point and the other points. Connected level sets of the distance map are then extracted and organized in a tree structure. The root of the tree is an input to the algorithm. The centers of these levels sets constitute the skeletal curves.

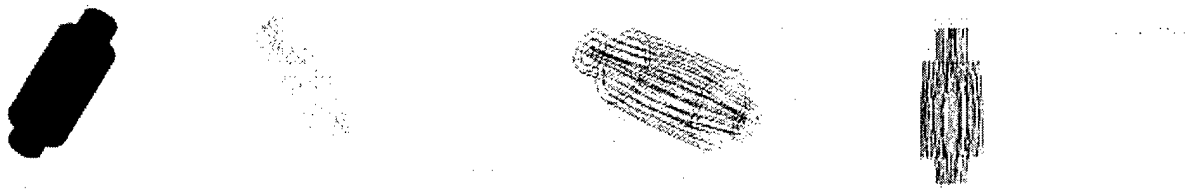

(a) Part (b) Surface points (c) Tool Path curves (d) Path curve, top view

Figure 9 Path generation from the scattered data points along the surface

To use the method based on skeletal curves for rapid prototyping, a solid model is represented as coaxial layers of surfaces. Since the part geometry is known *a priori*, the coaxial surfaces and the surface points are generated (Figure 9). The surface points are joined to build the skeletal curves. The skeletal curves should be built close enough to allow continuous surfaces. Simple and unbranched curves provide the path for the material deposition head; therefore, the steps for branching and center-extraction for the skeletal curves are eliminated. The points on each surface are connected to get unbranched skeletons to generate the path for the material deposition head. The component is fabricated by depositing the material from the innermost surface to the outer surfaces.

The Process Planning:

The process planning for part fabrication should be able to address the requirements and limits of the material deposition process. The method used for skeleton generation must capture the topology of the part and store enough information for the process planning. Other issues include the determination of a suitable orientation of the skeleton such that the growth of the part should not only allow the accessibility to all the points while the part is being built, but should also maintain the stability of the part during the growth such that the requirement of the support structures is eliminated or minimized. The selection of orientation must minimize the requirements for the support structures. The number of turning points and path segments increases the heat accumulation and the process complexity due to the frequent direction changes of the material deposition head. Therefore, a reduction in the total number of turning points and the path segments should be another criterion for path planning.

The material deposition for the thin structures is accomplished by a single sweep of the material deposition head. Variations in part thickness regulated by changing various process parameters. For the thicker structures, however, material is deposited as coaxial surfaces with varying thicknesses around the skeleton.

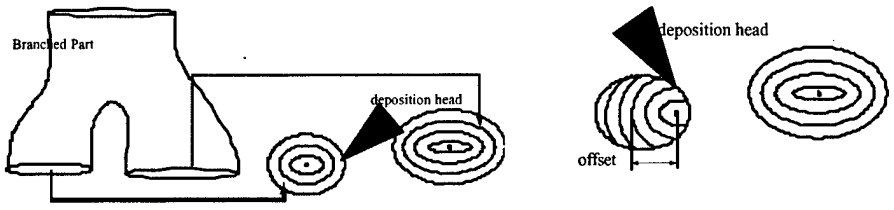

(a) Branched Part and deposition head inaccessibility

(b) Deposition head accessibility due to skeleton offset

Figure 10. Skeleton offset for accessibility

For branched and intricate geometries, the accessibility of the part by tool might be limited [Figure 10(a)]. A modification in the skeletonization approach such that the

skeleton is offset is suggested [Figure 10(a)]. The offset distance of the skeleton depends on the dimensions of the material deposition head.

Experimental Results:

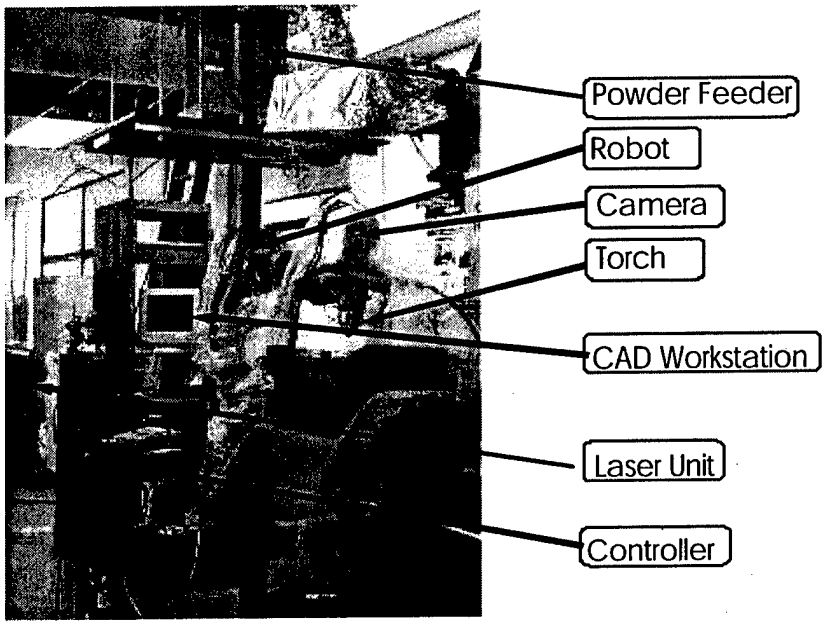

Figure 11. Experimental Setup

The experimental setup is a 6-axis robot with a laser deposition head mounted at its end effector (Figure 11). Nd-YAG laser unit is used for the laser power source. The controller unit controls the shutter on/off position, the laser power, and the powder feeder in real time. The CAD workstation generates the model file of component and the job instruction file for the robot. The material deposition head has four powder delivery nozzles arranged coaxially. The quantity of the powder delivery can be controlled by the powder feeder. Experiments are performed with H13 metal powder.

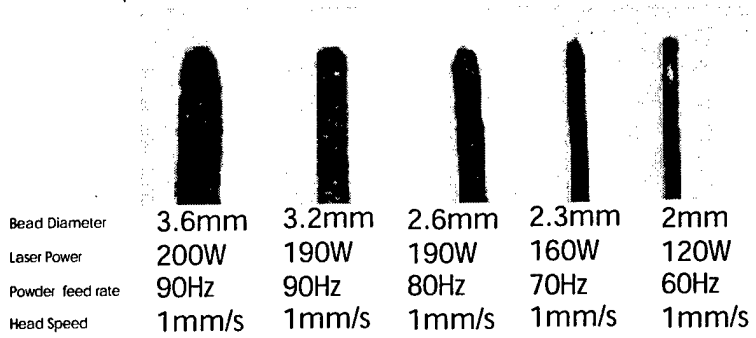

Figure 12. Variation in cross-section thickness with respect to the power and powder feed rate (Note: The rate of powder deposit is 0.05g/Hz of the powder feeder motor frequency)

A code was developed in (Visual Basic for Application) VBA for AutoCAD for simple cylindrical components. Different experiments were performed to study the influence of the process parameters on the material volume. This influence includes the variation in laser power, the powder feed rate, and the deposition head speed. The material is deposited by vertical movement of the material deposition head such that the laser head moves away from the just deposited material, and the molten pool is formed at the focal point of the laser.

It is observed that there is an increase in the material volume deposited with the increase in the powder feed rate, the speed of torch movement. However, the volume is further limited by the size of the molten pool, which in turn depends on the laser power. Figure 12 shows the variation of part thickness that corresponds to the material deposition rate for different parameters.

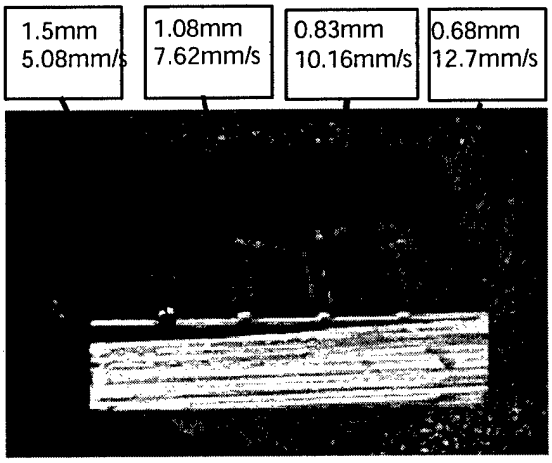

Figure 13. Variation in cross-section size with respect to the head speed (laser power = 380W, powder feed rate at 200Hz)

Figure 13 shows the dependency of the part thickness on the head speed. A single bead of the material is deposited at different speeds for the same rate of the powder feeding, and the laser power. The material deposition is done along the horizontal direction.

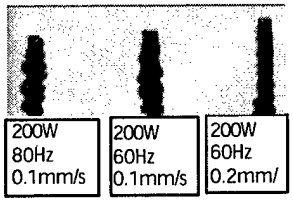

Figure 14. Irregular bead formation due to surface tension

The combination of laser power, torch speed, and powder feed rate determines the surfaces smoothness. The surface tension of the molten metal and the formation of spherical droplets can cause the formation of a rough surface. Figure 14 shows three

columns with rough surfaces. An increase in the speed of the torch and the corresponding lowering of the heat accumulation improves the surface quality. One of the most important factors that must be taken into account is the possible melting of the skeleton at any instant due to excessive heating. The determination of the optimum power is extremely important because excessive heat may melt the structure, and insufficient heat does not allow the formation of a proper of molten pool for the material welding.

By controlling the process parameters, various three-dimensional structures can be built. Experiments were performed to build slander parts and surfaces. The material addition is done for different g-vectors.

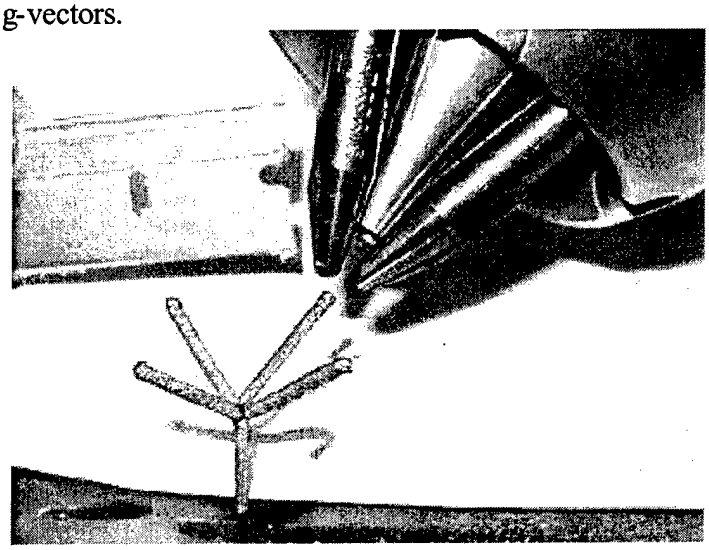

Figure 15. A branched structure made by laser cladding

Figure 15. shows a branched structure that is generated by laser cladding. The branched structure includes a vertical segment onto which four other segments each at an angle of 45 with respect to the x,y and z axes are added.

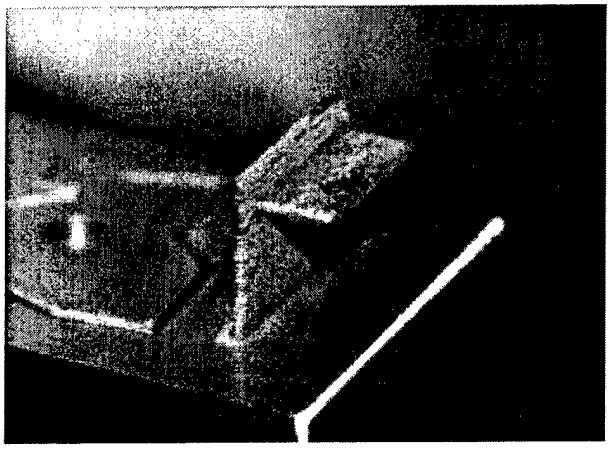

Figure 16. Surfaces created in space by laser cladding

Figure 16 shows surfaces made in the space by laser cladding. The surface thickness is equal to a single bead width. The surfaces are generated by depositing material, perpendicular and horizontal with respect to the gravity.

Conclusions

The variation in the material deposition rate by changing various process parameters: the powder feed rate, the laser power, and the laser head speed in laser-based metal powder deposition allows the fabrication of complex geometric skeletons. Different algorithms can be used for the process planning to fabricate a solid part based on the reconstruction of a solid from its skeleton. The process can be optimized and controlled by obtaining various process parameters experimentally. The experimental results have demonstrated the ability to manufacture complex and branched structure without the support structures inherent to the traditional techniques.

A hybrid technique that involves incorporation of the 2-1/2-axis deposition technique along with the fabrication of a part from its skeleton needs to be developed to create a more efficient process that combines the best of both of the methods.

A mathematical model for dependence of the material volume and the properties of the laser cladding on different parameters like the speed of laser head, the laser power, and the powder feed rate, is required.

Acknowledgements

This work was financially supported by THECB (Texas Higher Education Coordinating Board) Grants 003613-0022-1999 and 003613-0016-2001, NSF (National Science Foundation) Grants DMI-9732848 and DMI-9809198 and by the US Department of Education Grant P200A80806-98. Authors would like to acknowledge the help from Mr. Michael Valant Research Engineer, Research Centre for Advanced Manufacturing and Mr. Jhigang Liu for helping with the experiments.

References:

1. http://www.aerometcorp.com/theMachine.htm
2. Kovacevic, R., Will We Use Welding Technology to Make RPs, SME's Manufacturing Engineering Magazine, No. 4, 2001, pp. 26-27
3. K. Hartmann, R. Krishnan, R. Merz, G. Neplotnik, F.B. Prinz, L. Schultz, M. Terk and L.E. Weiss, Robot-Assisted Shape Deposition Manufacturing, Proceedings of the 1994 IEEE International Conference on Robotics and Automation, San Diego, May 1994.
4. K. Hartmann, R. Krishnan, R. Merz, G.Neplotnik, F.B. Prinz, L. Schultz, M. Terk and L.E. Weiss, "Robot-Assisted Shape Deposition Manufacturing", Proceedings of the 1994 International IEEE Conference on Robotics and Automation, San Diego, pp. 2890-2896, May 1994.

5. Shi, D. Gibson, I.,Improving surface quality of selective laser sintered rapid prototype parts using robotic finishing,Proceedings of the Institution of Mechanical Engineers Part B-Journal of Engineering Manufacture. vol 214 n 3 2000. p 197-203.
6. http://www.me.psu.edu/lamancusa/rapidpro/primer/chapter2.htm
7. http://www.sandia.gov/LabNews/LN01-29-99/lens_story.htm
8. Kovacevic, R., Jandric, Z., and Wang, H., Development of Welding-Based Layered Manufacturing/ Repair Processes, presented at the IIW Int. Conf. in connection with the Annual Assembly 2002 on Advanced Processes and Technologies in Welding and Allied Processes, Copenhagen, Denmark, June 24-25, 2002.
9. Singh, P. and Dutta, D., Multi-Direction Slicing for Layered Manufacturing, June, 2001, P. Singh and D. Dutta, Journal of Computing and Information Science in Engineering, Vol. 1, pp.129-142, June 2001.
10. Singh, P. and Dutta, D., Offset Slices for Layered Manufacturing, September, 2002, ASME DETC, Montreal, Canada
11. http://www.huffmancorp.com/Downloads/ProdSheets/Laser/HW-185.pdf
12. Boddu, M.R., Landers, R.G., and Liou, F.W., 2001, Control of Laser Cladding Processes for Rapid Prototyping – A Review, Twelfth Annual Solid Freeform Fabrication Symposium, Austin, Texas, August 6–8, pp. 460–467
13. Medial Axis Transform Definitions, http://www.lems.brown.edu/vision/people/leymarie/Refs/CompGeom/VermeerPJ/MATtoBrep/Ch1_defs.html
14. Tim Culver, Computing the Medial Axis of a Polyhedron Reliably and Efficiently, Ph D thesis, Department of Computer Science, University of North Carolina-Chapel Hill, October 2000.
15. D. Attali and P. Bertolino and A. Montanvert,Using Polyballs to Approximate Shapes and Skeletons,Pattern Recognition, Proc. 12th IAPR Jerusalem, October 1994, 626-628.
16. Eric Ferley, Marie-Paule Cani, Dominique Attali, Skeletal Reconstruction of Branching Shapes, Computer Graphics Forum number 5 volume 16 pages 283-293 , December 1997.
17. N. Gagvani, D. Kenchammana-Hosekote, and D. Silver, Volume Animation using the Skeleton Tree, Proceedings of Visualization 1998, pages 47-53, 1998.
18. Baerentzen,J.A.,Šrámek,M., Christensen,N.J, A Morphological Approach to Voxelization of Solids, Proceedings of The 8-th International Conference in Central Europe on Computer Graphics, Visualization and Digital Interactive Media 2000, pp44-51".
19. K. Reinders, Feature-Based Visualization of Time-Dependent Data, PhD thesis, Delft University of Technology, March 2001.
20. A Verroust, F. Lazarus, Extracting Skeletal Curves from 3D Scattered Data, International Conference on Shape Modeling and Applications March 01 - 04, 1999 , Aizu-Wakamatsu, Japan.

Digital Micromirror Device Based Microstereolithography for Micro Structures of Transparent Photopolymer and Nanocomposites

George W. Hadipoespito, Yong Yang, Hongseok Choi, Guoqing Ning, and Xiaochun Li
Department of Mechanical Engineering
University of Wisconsin-Madison
Madison, WI 53706
Reviewed, accepted August 19, 2003

Abstract: This paper describes a Digital Micromirror Device (DMD) based ultraviolet (UV) microstereolithography (μ-SL) system developed for rapid prototyping and manufacturing of micro 3D structures. Characterization experiments show that the developed the DMD-based imaging system irradiates an entire photopolymer layer at once, providing reasonable curing speed and good resolution at a low cost. 2D and 3D micro parts were fabricated. High frequency ultrasonic vibration (above 20 kHz) was experimented and verified that it can be used to significantly decrease the leveling time of viscous photopolymer. Furthermore, micro parts were also fabricated in nanocomposites, which were obtained by ultrasonic mixing of the transparent photopolymer and nano-sized ceramic particles. High quality micro models fabricated by this novel process could be used for micro scale investment casting, tooling, devices, and medical applications.

1. Introduction

Miniaturization is important in fabrication and commercialization of new industrial products that encompass complex geometries, high aspect ratios and complex microstructures. These miniature products can deliver a new generation of functionality and performance in a smaller volume. Smaller-size cellular phones and notebook computers, hearing aids, nozzles for ink-jet printers, and accelerometers for car air-bag system are some samples of products made possible by rapid development in micro fabrication. Beside the commercial/consumer products and applications, 3D microparts are also of great interest from research fields in microrobotics, micromechanics, and microfluidics.

Silicon-based microelectromechanical system (MEMS) techniques are very popular for the manufacture of micro sensors, electronics, actuators and other components in integrated microsystems. However, these MEMS techniques are two-dimensional (2D) processes involving multiple steps and requiring complicated processing procedures in a cleanroom environment. These 2D techniques are normally difficult, if not impossible, to fabricate arbitrary shape and composition without the use of microassembly. The investment costs of these processes are expensive, and the choice of material is somewhat limited. To name a few of those processes are surface and bulk micromachining, LIGA (X-Ray Lithography, Electroplating, and Molding), and RIE (Reactive Ion Etching) [Madou 2002].

Recently, microstereolithography (μ-SL) process emerged as a freeform process capable of creating 3D structures with complex geometries. Microstereolithography has its root from the stereolithography process rather than integrated circuit (IC) technology. Stereolithography is a process of creating 3D solid models in a layer-by-layer fashion from a 3D CAD model using

photopolymer as a based material. A focused ultraviolet (UV) laser, coupled with a galvano-mirror, is used to cure photopolymer in a vector-by-vector manner [Jacobs 1996, Beaman 1997, and Prinz 1997].

The core idea of microstereolithography processes is similar. A solid 3D model from any modeling software (Pro/E, Unigraphics, SolidWorks, etc) is tessellated into array of triangles, and output in STL (SteroLithography) file format. Using slicing software, this tessellated model is then sliced into layers according to the predetermined thickness. The software then creates some output files that will be read and used directly to build the part. The output build files are then used to build the part on the microstereolithography apparatus. The microstereolithography processes can be classified into two main categories, based on how each layer is build [Bertsch 1999 and 2000]:

1. Vector-by-vector process: a layer is formed by raster scan of a laser beam. The laser beam is stationary and focused precisely to a very fine spot on the surface of the photopolymer. The container and the material are moved horizontally in order to build the layer.
2. Integral process: each layer is cured by one irradiation only. A dynamic mask/spatial light modulator is used. For this type of process, the slicing software gives output in image files (usually monochrome bitmap files); each file contain the cross sectional image of one single layer. These files are then used to drive the dynamic mask.

After a layer is formed, a microstage holding the part is dipped into the photopolymer vat, allowing fresh layer of resin to coat the cured layer. Then the microstage is raised again, leaving only a thin layer of liquid photopolymer (usually in the order of several microns) between the cured layer and the surface of the polymer vat. The fresh layer is then cured, and then the recoating process repeats. Once building process is done, the part is washed with the appropriate solvent to remove the uncured polymer.

The integral stereolithography process is much faster than the vector-by-vector process. By employing a dynamic mask, e.g. Liquid Crystal Device (LCD), this process presents a technical breakthrough in the field of rapid prototyping. As an emerging dynamic mask, the performance of Digital Micromirror Device (DMD) is better than that of the LCD since DMD's fill factor of each pixel (85%) and its reflectivity (71%) are much better than those of the LCD (64% fill factor and 21% light transmission) [CRL Opto, DLP Technology]. In other words, when a pixel is in "active" or "on" state, the DMD can pass light more efficiently than the LCD. LCD-based μ-SL technology has been extensively studied [Bertsch 1999 and 2000]. EPFL (Swiss Federal Institute of Technology) at Lausanne, Switzerland, University of Sussex in United Kingdom, INPL (Lorraine National Polytechnic Institute) in France, and Saitama University in Japan are to name a few. Long layer settling time remains a difficult issue. Research team from Saitama University in Japan used DMD-based μ-SL to build 3D parts [Kaneko 2001]. A vibration generator working at frequency of 50 Hz was sued to reduce the leveling time and enhance the z-resolution by reducing layer thickness [Akahane 2001]. However, its layer thickness was still at approximately 100 μm. It should also be noted that Stanford Research Institute (SRI) has developed a projector-based imager system for ceramic-polymer prototyping [SRI 1999]. However, the system uses visible light, which is prone to interference and the system developed is suitable only for macroscale applications.

2. Experiment Apparatus

A microstereolithography (μ-SL) apparatus has been developed, as shown in Figure 1. The system employs a Digital Micromirror Device™ (DMD) as a dynamic mask/spatial light modulator, which eliminates the need to produce multiple masks to cure different layers of polymer. This apparatus uses an economical broadband UV light source to initialize polymerization of the molecules of the liquid polymer and thus form a solid layer. Detailed information of important elements of the system is described as follows.

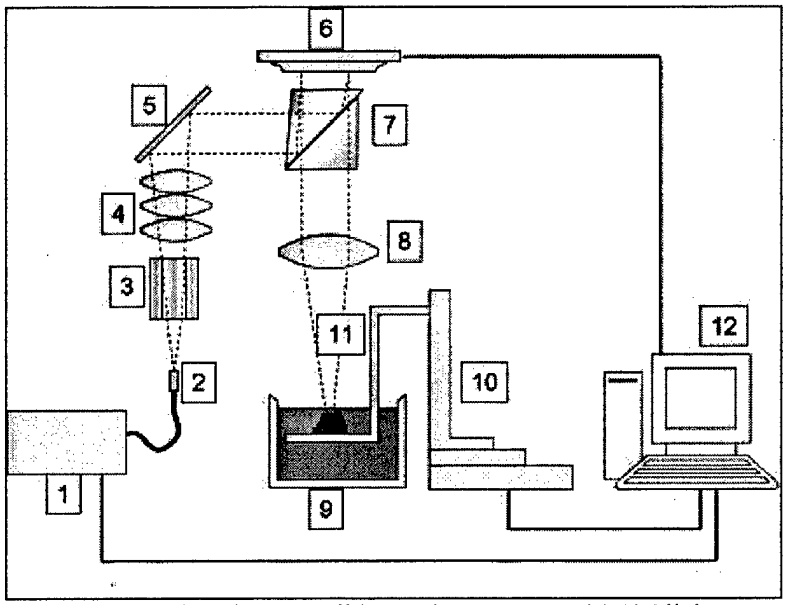

Fig. 1. Diagram of the microstereolithography apparatus: (1) UV light source; (2) light guide; (3) light pipe; (4) condenser lens system; (5) fold mirror; (6) DMD™; (7) TIR prism pair; (8) focusing lens system; (9) photopolymer bath; (10) x-y-z movable stage; (11) building platform; and (12) computer controller.

2.1. Optical System

The light path on the apparatus begins from the UV light source, identified by number 1 in Figure 1. The light is then transmitted using a UV light guide (number 2 in Figure 1) into a modified DMD-based multimedia projector (BenQ DX550). The light path starts at the light pipe (number 3 in Figure 1) and ends at the TIR (total internal reflection) prism pair (number 7 in Figure 1). A set of focusing lenses, identified by number 8 on Figure 1, is placed outside of projector to focus the reflected image from DMD onto the surface of polymer bath in a suitable size.

To supply UV light, a broadband GreenSpot™ UV Spot Curing System from UV Source, Inc. was used. The UV Spot Curing System consists of a high-pressure mercury lamp, a 100W power supply and ballast system, and a programmable shutter. The shutter is electronically controlled, and can be adjusted in increments of 0.01 second up to 99.99 seconds. The spectrum of the broadband UV light ranges from 300 and 470 nm, and has a peak at 365 nm. This external UV light source was selected to avoid difficult modifications required to integrate the stand-alone high-pressure mercury bulb into the projector. The light guide assembly was also supplied by UV Source, Inc. The light guide is liquid-filled, and provides good UV transmission between 300 and 500 nm.

The DMD has a resolution of 1024x768. It provides rapid change of image patterns (up to 10,000 paterns/s). It consists of thousands of micro mirrors, each with a size of 13.7 μm x 13.7 μm. Each individual mirror element can be rapidly electronically switched (up to 10,000 Hz) between "on" and "off" state. The light is thus selectively reflected, according to a designed image pattern, out of the projector into the focusing lens. For this study, the lens system was designed to provide approximately 1:1 ratio between the DMD pattern and the focused image. Silica lens was used since silica has good transmission in the UV region.

2.2. Photopolymer

Suitable photopolymers are critical for the μ-SL process. Important characteristics, such as viscosity, sensitivity, and wavelength response need to be considered. After UV curing, polymers will also exhibit different thermal, mechanical, and optical properties.

Several photopolymers from companies that specialize on stereolithography were evaluated. The DSM Somos 10120 WaterClear™ was selected because of its low viscosity (~130 cps @ 30° C), its relatively low critical exposure (E_c = 9.7 mJ/cm^2), and its transparency in both liquid and cured state. The transparency in the cured parts is of interest since transparent micro molds could be used for a visual monitoring of mold filling in micro-casting or channel filling in electroplating. Other properties of the polymer are presented on Table 1.

DSM Somos 10120 WaterClear 10120 Specification			
Physical Properties - Liquid		**Mechanical Properties**	
Appearance	Optically clear	Tensile Strength	3736 psi
Viscosity	~130 cps at 30° C	Elongation at Break	32%
Density	~1.12g/cm^2 at 25° C	Elongation at Yield	4.20%
Optical Properties at 355nm		Modulus of Elasticity	248 ksi
E_c (Critical Exposure)	9.7 mJ/cm^2	Index of Refraction, n	1.51
D_p (Slope of cure-depth vs. ln(E) curve)	0.16 mm (0.0063 in.)	Hardness (Shore D)	81
E_{10} (Exposure that gives 0.254 mm (.010 in.) thickness)	48 mJ/cm^2		

Table 1. Properties of DSM Somos WaterClear™ 10120 photopolymer. [Data from DSM Somos]

2.3. Motion Control

To provide an accurate linear movement of the building platform (number 11 on Figure 1), a PC-controlled three-axis micro-stage (number 10 on Figure 1) from Anorad Inc. was implemented. Two perpendicularly stacked LW-7 stages provide lateral (x and y directions) movements, while an Anoride 7-4 stage enables the platform to move vertically (in z direction). The stage system has a resolution of 30 nm and can travel in speed up to 200 mm/s.

2.4. Software

Two different types of software were used for the apparatus: CNC-2000, and Microsoft PowerPoint. The CNC-2000 controls the motion of the stages; manual input of a single command line is possible, as well as automatic input of a series of commands in G-code format.

Microsoft PowerPoint was used to create monochromatic patterns and images and transferring those to the DMD. Further software development is needed to automate the solid model slicing and image generating.

3. Experiment procedure

The experiments were performed to characterize the apparatus and evaluate its capability for fabrication of meso and micro-sized 3D objects. The results will be used in selecting important variables and optimizing the fabrication process.

3.1. Experiment on curing depth and exposure time experiment

This series of experiments was carried out to better understand the relationship between the exposure time and cured layer thickness. The experiment was conducted by fully curing a support polymer layer on top of a silicon wafer, as shown in part 2 in Figure 2. A circular part on this layer was intentionally left uncured for top layer measurement purpose. Then a fresh layer of liquid polymer was recoated above the cured layer by dipping and raising the building platform. Finally, this top layer was exposed to a focused UV light within a predetermined period of time (part 3 in Figure 2). The cured thickness was then measured by use of a microscope, as illustrated in part 4 in Figure 2. The relationship between exposure time and cured layer thickness can be determined.

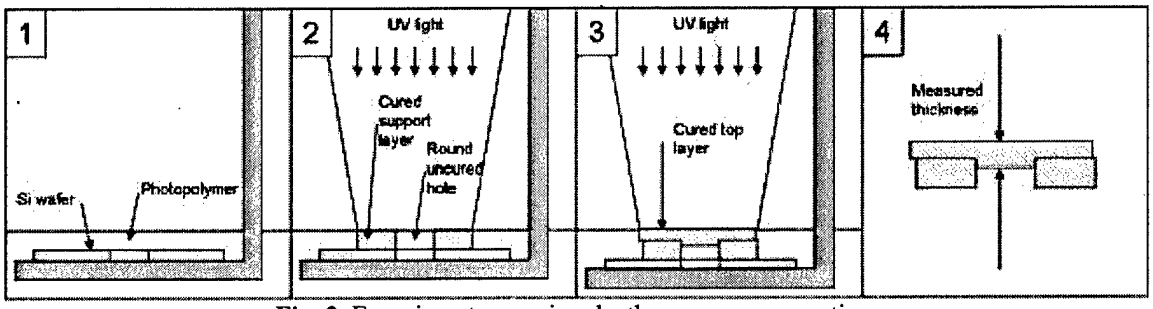

Fig. 2. Experiment on curing depth versus exposure time

3.2. Experiment on settling time

The apparatus builds microparts by stacking thin layers of photopolymers, preferably 5-micron thick for each layer. Conventional stereolithography apparatus normally utilizes a blade to achieve a desired layer thickness, normally 50~100 μm. However, this technique can not be applied on a μ-SL apparatus since the blade will destroy the micro part being built. A μ-SL apparatus usually relies on gravity to settle the polymer layer into a thin layer.

The experiment was conducted by lowering the building platform, and then raising it within the polymer bath up to height that is 10.0 μm below the surface of the photopolymer. Once the platform is raised, UV light was turned on periodically to cure a different small part of the settling polymer. The cured layer thicknesses were measured by a Tencor Alpha-Step 200 profilometer.

3.3. Experiment on resolution

There are two different resolutions on a μ-SL apparatus: lateral resolution, and vertical resolution. Lateral resolution is decided by the size of the individual mirror on the DMD as well as the focusing lens system. Vertical resolution is simply determined by the layer thickness; the smaller the layer thickness, the better the vertical resolution. However, thinner layer thickness demands more layers to build a 3D part.

The experiment was carried out to quantify the lateral resolution of the system. The experiment was conducted by curing a pattern of lines with different widths. After the sample was developed, the narrowest line width indicated the resolution of the apparatus.

3.4. Fabrication of Micro Parts

2D and 3D patterns/parts were fabricated to assess the capability of the apparatus. A microgear was of interest because it is a mechanical component containing small features. A microgear with 1.5mm lateral diameter was designed to be built using the apparatus, as shown in Figure 3a. To increase the complexity of the micropart, a cylinder and a second, smaller gear with fewer teeth (Figure 3b) were to be built on top of the base microgear.

A micropart with overhanging feature was also of particular interest. One attractive capability of the μ-SL process is that it is able to build overhanging features without the need of supporting structures. Hence, a micropillar with 1mm x 1mm lateral dimension with an overhanging section was designed, as shown in Figure 3c.

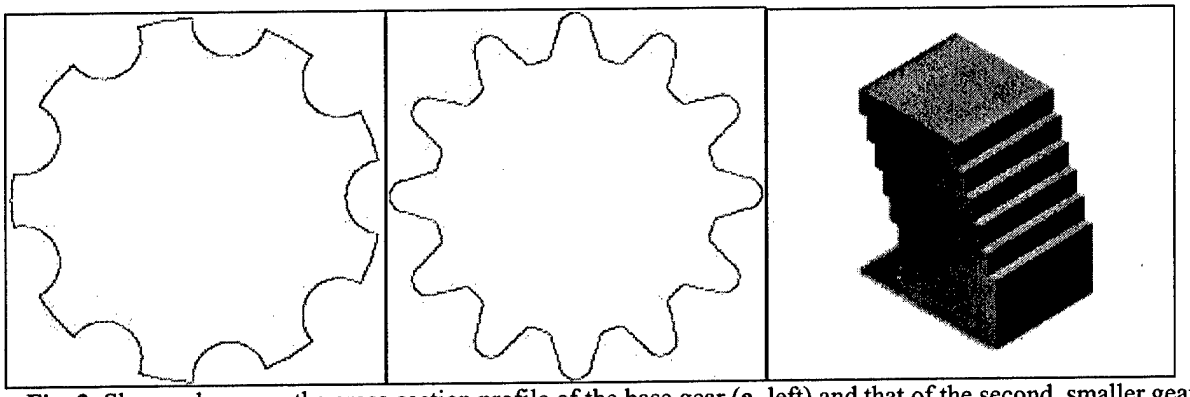

Fig. 3. Shown above are the cross-section profile of the base gear (**a**, left) and that of the second, smaller gear (**b**, middle) (the pictures are not in the correct scale). A CAD model of a micropillar with overhanging section was to be built using the apparatus (**c**, right).

3.5. Experiment on ultrasonic-assisted layer settling

High frequency ultrasonic vibration (above 20 kHz) was experimented in order to significantly decrease the leveling time of photopolymer. As shown in Figure 4, the experiment setup includes a 20 KHz ultrasonic ultrasonic transducer, a vibration table, and a silicon wafer. The thickness of the droplet of photopolymer on top of the silicon wafer was measured against time. A droplet of photopolymer of 14.6 μl was placed on top the silicon wafer under ultrasonic vibration. By measuring the diameters of settling droplets, the average thicknesses of the settling droplet layers were determined.

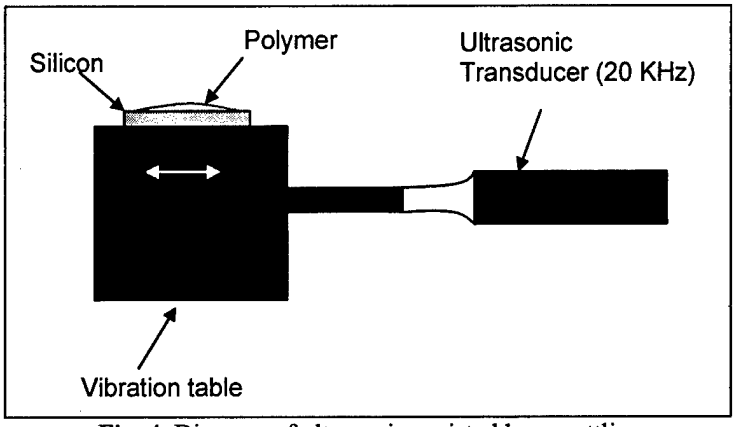

Fig. 4. Diagram of ultrasonic-assisted layer settling

3.6. Nano-composites preparation

The experiment was carried out to determine the feasibility of mixing polymer with nano-sized ceramic particle. Polymer-nano-composite material was of interest because it had the potential of improving mechanical properties of the fabricated parts.

High intensity ultrasonic waves were used to mix nano-sized Si_3N_4 (30 nm) with the photopolymer. A viscometer was used to measure the viscosity of the resulting polymer-nano-composite mixtures. The measurement result was plotted and used to determine the suitable nano-composite content in the mixture.

4. Results & Discussions

4.1. Curing depth and exposure time

Figure 5 shows the result of the curing depth versus exposure time. The linear fit of the data points on the plot suggests the cured layer thickness is proportional to the exposure time. The plot suggests that the polymer would not start to cure if the exposure time is less than 1.67 seconds in this μ-SL system. Other experiments verified this behavior. It might be attributed to the use of broadband UV light source and the fact that the photopolymer used is optimized for curing at 355nm wavelength. It might be better to use low power UV laser at 355nm to obtain optimized performance for this particular polymer. However, currently these UV lasers are expensive. One possible solution would be to find or develop photopolymers that have better response curve with respect to the spectrum of the broadband UV light.

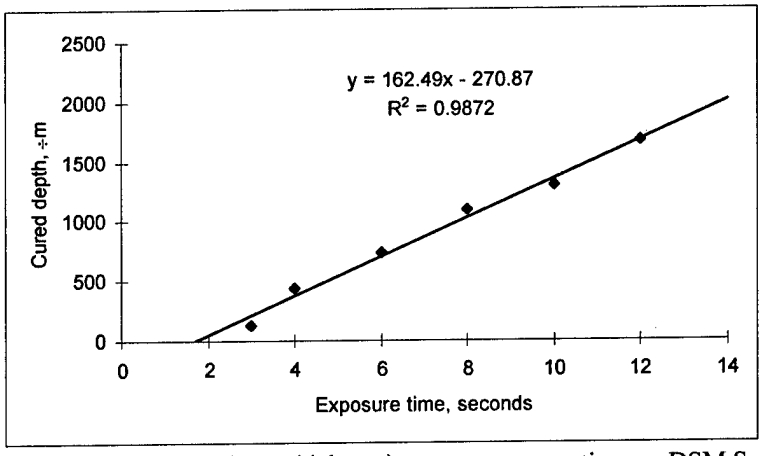

Fig. 5. Cured depth (cured layer thickness) versus exposure time on DSM Somos WaterClear 10120.

4.2. Settling time

Figured 6 shows how the polymer surface settled naturally (decreased in thickness with respect to the building platform) on top of silicon wafer as time elapsed. The plot suggests that the settling polymer layer thickness is proportional to the elapsed time. However, the settling time of the polymer was surprisingly long to reach 100 μm. The result suggests that 895.36 seconds would be necessary to obtain a polymer layer of 10 μm thick. Such a long settling time is not satisfactory for a rapid prototyping system. Further study is needed to find a more suitable photopolymer or to develop other means to spread thin polymer layer in this μ-SL system.

To overcome this settling problem, ultrasonic vibrations could help to achieve a significantly shorter layer settling time. Preliminary settling time experiments with ultrasonic vibrations were conducted, and results are presented in the subsection 4.5.

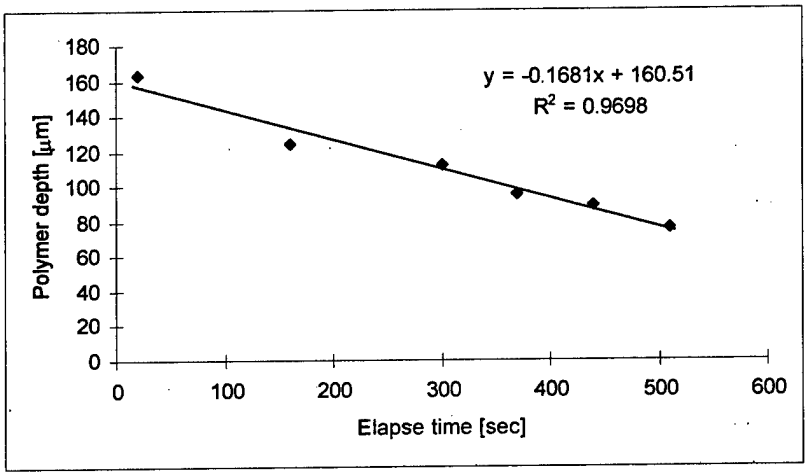

Fig. 6. The height of the polymer surface measured from the building platform versus elapsed time.

4.3. Resolution

By comparing the line widths on the computer screen to the cured line widths, the image ratio can be determined. A ratio of 1:20.3 can be achieved between the line width on the screen and the actual cured line width.

By use of microscope and SEM, the lateral resolution of the apparatus is determined to be approximately 20 μm. It dictates the smallest feature possible in X-Y plane to be built.

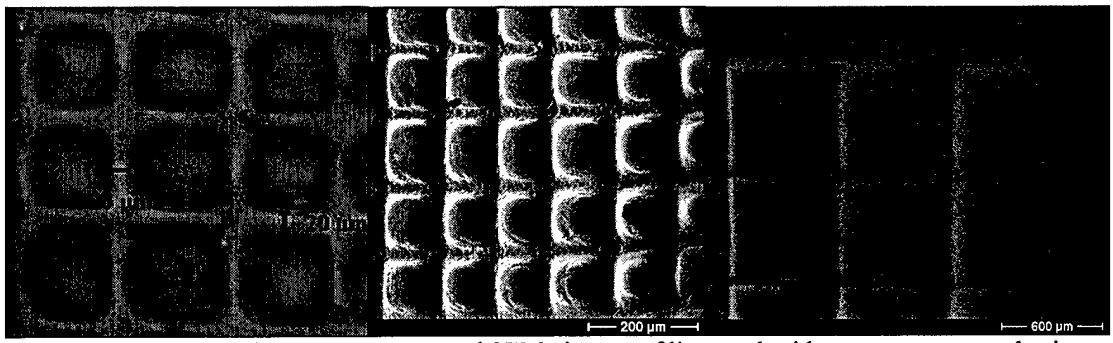

Fig. 7. Shown above are a microscope capture and SEM pictures of lines and grids patterns generated using μ-SL apparatus.

4.4. Fabrication of 3D Micro Parts

Figure 8 shows SEM pictures of 3D microparts fabricated with the μ-SL apparatus. Individual tooth can be distinguished on both micro-gears; however it seems some features were over cured. It is believed that optimization of process parameters will be necessary to solve this problem.

The last image in Figure 8 shows the micro-pillar. It seems no obvious overhanging feature appears. It is likely that the overhanging feature was washed out, possibly due to the recoating process. Further experimental study and process optimization are being carried out to obtain more sophisticated parts.

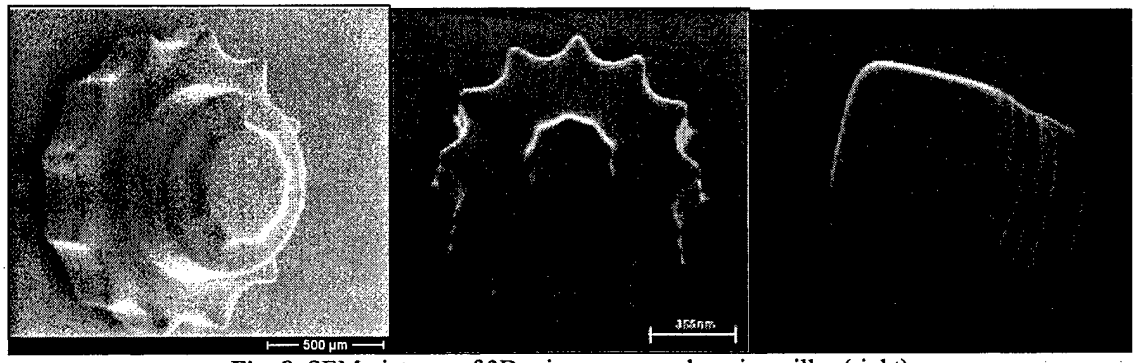

Fig. 8. SEM pictures of 3D microgears, and a micropillar (right)

4.5. Ultrasonic-assisted Layer Settling

Comparison between the results with and without ultrasonic vibration indicates that ultrasonic-assisted settling is very effective. It shines light for the future implementation of ultrasonic-assisted layer settling mechanism in the developed DMD-based μ-SL system.

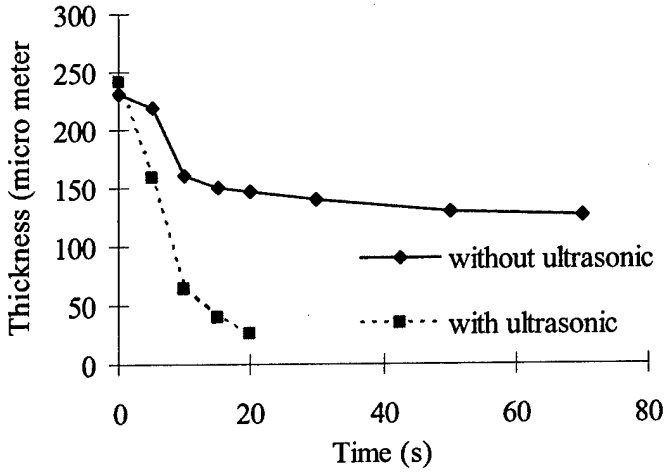

Fig.9. Polymer settling time on top of silicon wafer

4.6. Polymer Nanocomposite Parts

Figure 10 shows the viscosity trend of the photopolymer matrix nanocomposite as the nanoparticles content is increased. Based on the result, the nanocomposites having 1.0 weight % nanoparticles might have the combination of good strength improvement and their viscosity still remains low enough for recoating process. Thus photopolymer was mixed with 1.0 weight % by use of ultrasonic mixing. The resulting mixture was then used to fabricate a micro-gear shown in Figure 11. Visual observation under a microscope suggests that the nanoparticles within the microgear were dispersed quite uniform.

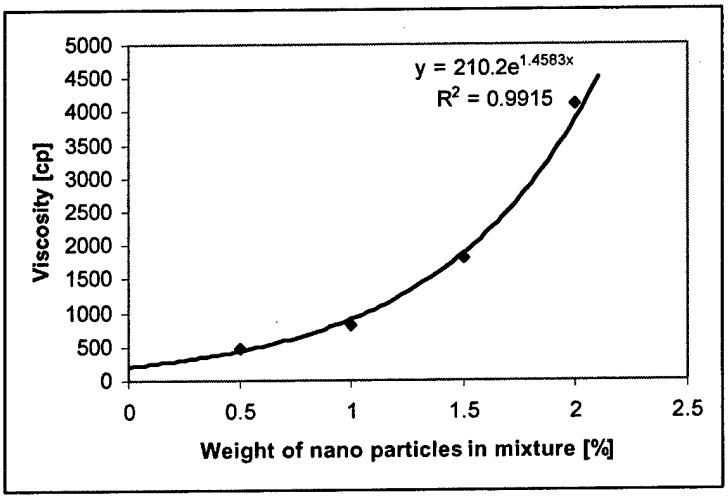

Fig. 10. Viscosity of photopolymer-nanoparticle mixture (measured at 1.0 rpm)

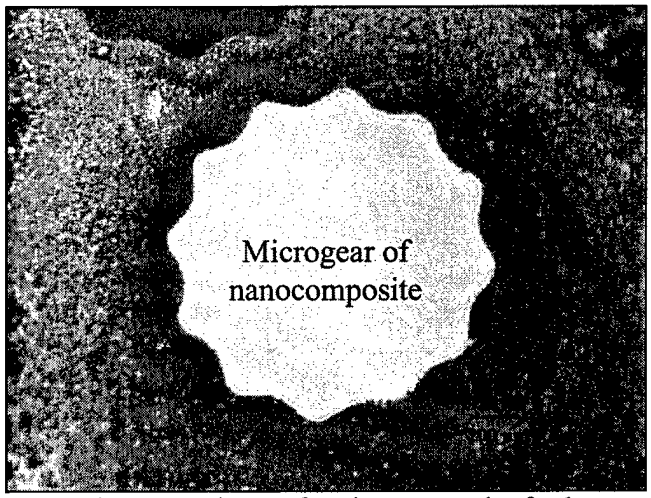

Fig. 11. A microscope picture of a microgear made of polymer-nano-composite.

5. Conclusion

A DMD-based microstereolithography apparatus has been realized. The apparatus attempts to combine the versatility of rapid prototyping, and the capability of fabricating high resolution micro structures. 2D and 3D microparts with 20 μm lateral resolution are realizable. Characterization experiments show that the developed the DMD-based imaging system irradiates an entire photopolymer layer at once, providing reasonable curing speed and good resolution at a low cost. Further study and process optimization will be needed to improve the quality of the micro parts.

High frequency ultrasonic vibration was experimented and verified that it can be used to significantly decrease the leveling time of viscous photopolymer. Uniform photopolymer matrix nanocomposites were obtained by ultrasonic mixing. The nanocomposites promise to improve properties of fabricated parts. Micro parts were also fabricated in nanocomposites.

6. Acknowledgements

The authors would like to thank Mr. Zhiwei Li for his assistance in the SEM pictures. We are grateful for the financial support from the Wisconsin Alumni Research Foundation (WARF).

7. References

Akahane, T., and Takahashi, K., "Non-Scanning Rapid Prototyping System", The Transactions of The Institute of Electrical Engineers of Japan Volume 121-E Number 5, MAY 2001

Beaman, J. J., Barlow, J. W., Bourell, D. L., Crawford, R. H., Marcus, H. L., and McAlea, K. P., "Solid Freeform Fabrication - A New Direction in Manufacturing", Kluwer Academic Publishers, 1997.

Bertsch, A., Bernhard, P., Vogt, C., and Renaud, P., "Rapid Prototyping of Small Size Objects," Rapid Prototyping Journal, 6, n4, pp. 259-266, 2000.

Bertsch, A., Lorenz, H., and Renaud, P., "3D Microfabrication by Combining Microstereolithography and Thick Resist UV Lithography," Sensors and Actuators, 73, pp.14-23, (1999).

Charwin, C. R., Farsari, M., Huang, S., Heywood, M. I., Young, R. C. D., Birch, P. M., Claret-Tournier. F., and Richardson, J. D., "Characterization of Epoxy Resins for Microstereolithographic Rapid Prototyping," International Journal of Advance Manufacturing Technologies, 15, pp. 281-286, 1999.

CRL Opto (http://www.crlopto.com/technology/twitedn.htm)

DLP Technology (http://www.dlp.com)

DSM Somos (http://www.dsmsomos.com)

Jacobs, P. F., "Stereolithography and other RP&M Technologies," ASME Press: 1996.

Kaneko, Y. and Takahashi, K., "UV exposure system for lithography and rapid prototyping using DMD projector", SID conference Record of International Display Research Conference, 2001, pp.1339-1342

Madou, M. J., "Fundamentals of Microfabrication," CRC Press: 2002.

Monneret, S., Provin, C., and LeGall, H., "Micro-scale Rapid Prototyping by Stereolithography," Proceedings of the IEEE, 2, pp. 299-304, 2001.

Prinz, F. B., chair, "Process Overviews" in "Rapid Prototyping in Europe and Japan", Vol. I, Analytical Chapters, International Technology Research Institute, Loyola College in Maryland, March 1997.

Provin, C., and Monneret, S., "Complex Ceramic-Polymer Composite Microparts Made by Microstereolithography," IEEE Transactions on Electronics Packaging Manufacturing, Vol. 25, n1, pp. 59-63, January 2002.

"SRI's Direct Photo Shaping (DPS)", Rapid Prototyping Report, pp.6-7, July 1999.

UV Source, Inc. (http://www.uvsource.com/home.html)

Advancements in the SIS process

Bahram Asiabanpour[1], Behrokh Khoshnevis[2], Kurt Palmer[2], Mehdi Mojdeh[2]

[1]Texas State University-San Marcos, TX 78666

[2]University of Southern California, Los Angeles, CA 90089-0193

Reviewed, accepted August 13, 2003

Abstract

Selective Inhibition of Sintering (SIS) is a new layer-based rapid prototyping process. This paper reports the progress in research and development of the SIS process. Specific printer path generation method, experimentation with various powder and inhibitor materials, and systematic models leading to optimum performance given various factors affecting part strength, surface quality, and dimensional accuracy are presented.

1- Introduction

Selective Inhibition of Sintering (SIS) is a new rapid prototyping process that like other RP processes, builds parts in a layer by layer fabrication basis (Khoshnevis, B., et al, 2003). The SIS developers hope that by successfully completing this process, they can present a very precise and inexpensive system to be used at the work tables of designers, modelers, and innovators to fabricate their product designs and ideas. The SIS process works by joining powder particles through sintering in the part's body, and by sintering inhibition of some selected powder bed areas. The selected areas of the powder bed for sintering inhibition are wetted by a printer. The printer nozzle moves in the XY plane and prints the inhibitor liquid on the model slice pattern. The print pattern includes the part boundary and hatch pattern for each layer of the sliced CAD model. The Selective Inhibition of Sintering process includes the following major steps (see Figure 1):

0- The inhibitor tank is filled with the inhibitor liquid and the powder feed tank is filled with polymer powder, the inhibitor tank pressure and printer voltage are set, and the printer home is found.
1- The powder feed tank pushes the powder level upward in the amount of desired step(s). The build tank moves the powder level downward in the amount of desired step(s). The amount of lowering movement sets the layer thickness in the final part.
2- The cylindrical roller from the source tank spreads the powder over the build tank. The roller rotates clockwise and moves in the X direction.
3- An X-Y printhead moves the print nozzle over the desired layer profiles. The input file for the print pattern is the machine path file which is generated by the machine path generator system.
4- The heat source attached to the moving part of the machine (including the printhead and roller) moves in the X direction and its temperature and movement create a sintered layer with an unsintered pattern in the selected area of the powder bed.

Repeat from step 1 unless the part is finished.

5- The model is removed from the sintered block and the post processing including cleaning, and adding wax or adhesive to the fabricated part, completes the SIS process.

An Alpha machine was built for initial research studies. Following figure shows the SIS machine performance in detail:

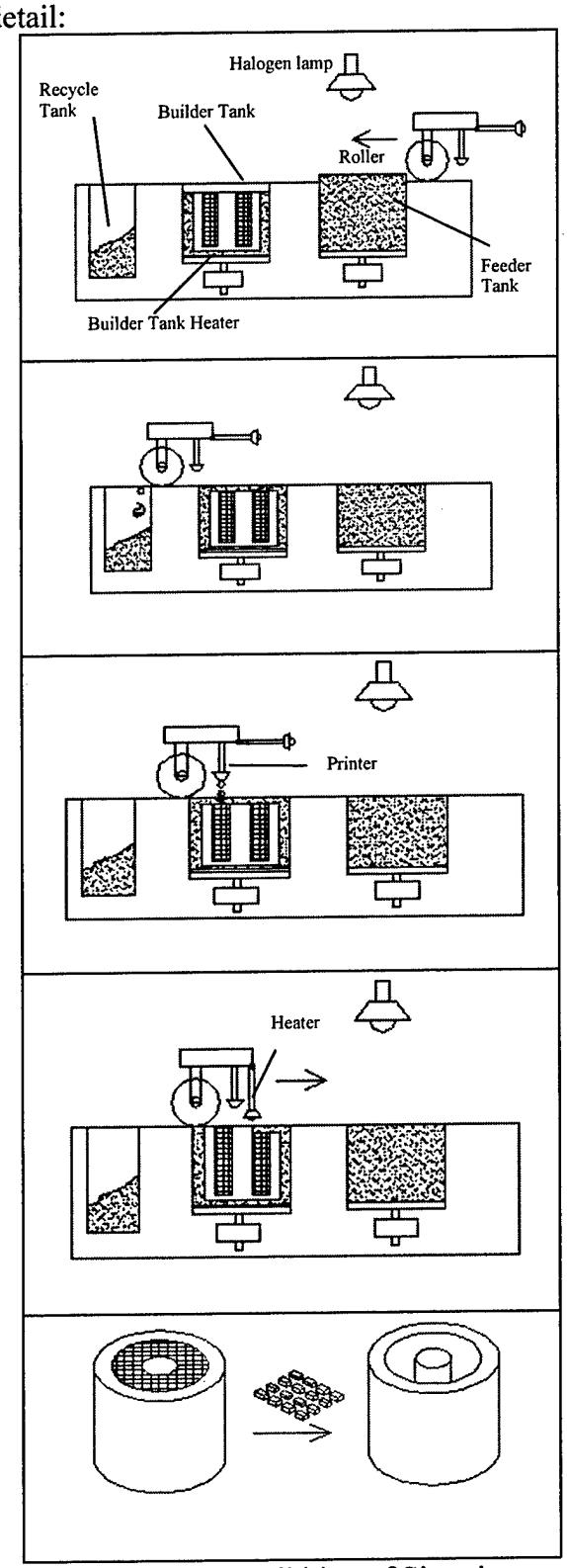

Figure 1. Selective Inhibition of Sintering process steps

2- Motivation

Because of different motivations, research on the SIS process was pursued in different directions. The first motivation for this research is due to the fact that without a machine path generation system, the SIS process will be limited to fabricating parts with very simple geometry. Also in many cases, lack of hatch path printing will make part separation from surrounding material impossible. The necessity for having such a system was the primary motivation for this research. Desirable properties for the new system include:

An appropriate machine path (i.e., boundary path and hatch path) printing pattern that enables the SIS machine user to easily remove the fabricated part from the surrounding material.

Machine path verification before sending the file into the SIS machine.

System capability to work in a wide variety of PCs with minimum computer memory.

Ability to process CAD models with any size and complexity.

Ability to fix or report the STL files errors.

The second motivation is due to the fact that to reach an acceptable level of accuracy, strength, and surface quality in the fabricated parts, all effective factors in the SIS process should be identified and controlled. A study for applying appropriate materials (powder and inhibitor) and identifying and optimizing effective factors on the quality (e.g., surface quality, part dimensional accuracy, and part strength) of the parts fabricated by the SIS process was necessary.

3- Machine path generation

The newly developed machine path generator system (Asiabanpour, B. Khoshnevis, B., 2003) uses STL files with the ASCII format as input and works in two steps. The first step generates slices at each increment of Z by intersecting the XY plane with the facets within the part. The second step uses all individual unsorted intersection lines in each Z increment to form the contour. This step includes sorting the intersection lines, recognizing the closed loops and disconnections (STL file error), and generating the machine path (i.e. boundary path and hatch path) and simulation files (Figure 2).

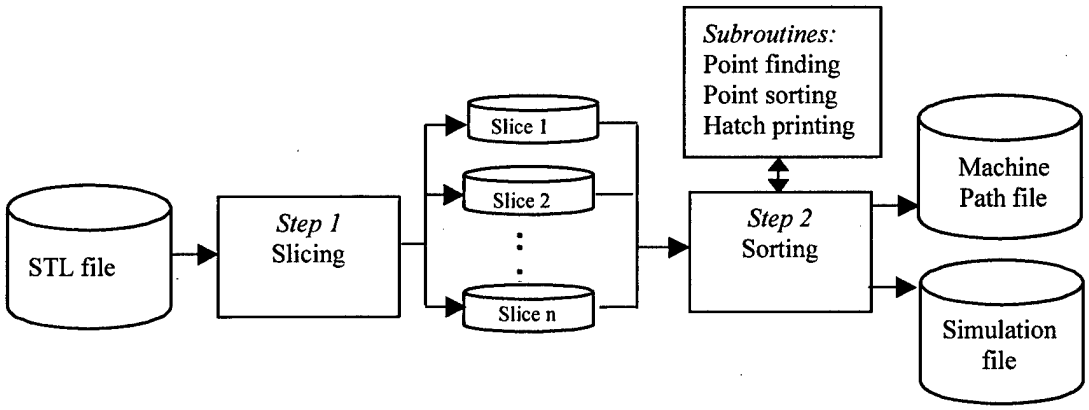

Figure 2.The two steps of slicing and machine path generation

In the first step the STL file is read as input. Slice files are then generated by executing the slicing algorithm. Only the intersection of those facets that intersect current Z=z are

calculated and saved. In this step, one facet is read at a time from the STL file. Then the intersection lines of this facet with all XY planes for $Z_{\min} \le z \le Min\{Z_{\max}, Max\{z_A, z_B, z_C\}\}$ are calculated. The intersection lines are stored in the specified file for the associated z increment. This results in one intersection line on each XY plane. By repeating this process for all facets, a set of slices is generated. This algorithm only saves the data of one facet in the computer memory, therefore only a small amount of computer memory is needed, and there is no practical limitation on the model size. In this step each slice is saved in a separate file on the disk. This guarantees that step 2 is run much faster as compared with the case where all slices are saved in a single file. After the completion of the slicing process, a set of vectors becomes available in each z increment. These vectors are not connected and are not in sequence.

In the machine path generation process, the software starts from one vector and tries to find the next connected vector to this vector. Then it does the same for the newly found vector until it reaches the start point of the first vector (in the closed loop cases) or finds a vector with no leading attachment (in faulty STL files containing disconnections). To sort the vectors, the algorithm reads one vector at a time from a slice file and writes it to another file. This file is either path file, when vector is connected to previous vector, or temp file, when the vector is not connected to the previous vector. Therefore, the sorting process does not need a large amount of memory to sort the data, and there is no limitation on the number of vectors in a slice and on input file size. In addition, unlike many other slicing algorithms that cannot handle disconnections caused by faulty facets (Leong et al. 1996), this algorithm can generate a machine path even with disconnection errors in the STL file. At disconnection instances the system sends a message to a log file and turns the printer off and starts from a new vector. Also for each selected vector the possibility of hatch intersection points are investigated.

At the end of the path generation process for one slice, the hatch intersection points are sorted and written into a machine path file. After the arrangement of all vectors in one slice (z increment), the process starts the arrangement of the vectors of the next slice. This process is continued until all vectors in all slices are sorted.

Three subroutines are called in the machine path generation algorithm. The first subroutine is for finding the intersection points of every line and horizontal and vertical hatch lines. According to the algorithm, every line which is written to the output file is called in the following subroutine to find and save the intersection point(s) of the line with the hatch lines. At the end of formation of the boundary path, all intersection points are sorted in ascending and descending orders for every other line. The last step of the algorithm is setting the print/no print command for the hatch lines.

Slicing and machine path generation algorithms have been implemented in the C programming language. The software has been successfully tested for several medium and large STL files up to 200 MB on different PCs and laptops.

Figures 3 and 4 show the algorithm implementation as presented by the path simulation module of the system.

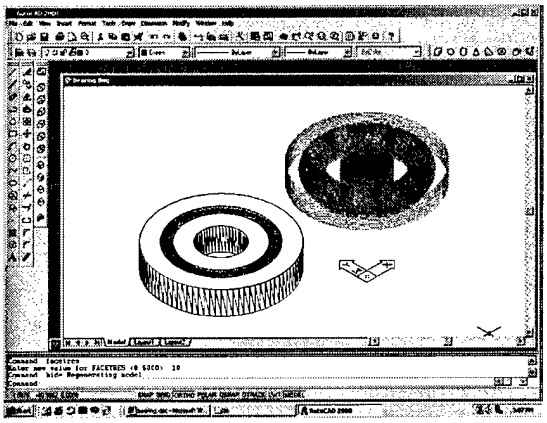

Figure 3.Visualization of the CAD model and the machine path in the AutoCAD environment

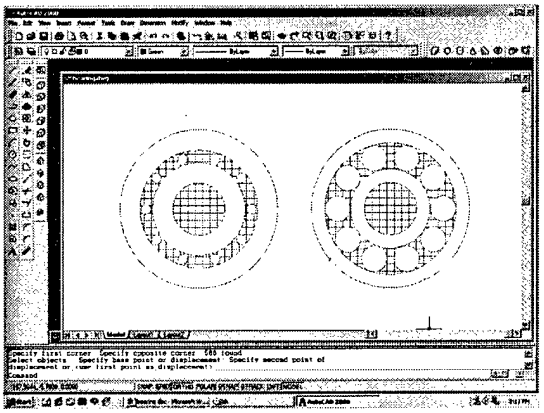

Figure 4.Visualization of two slices of the machine path in the AutoCAD environment

4- Material selection

Two types of materials are used in the SIS process: Powder and Inhibitor. Several affecting factors in the SIS process will remain constant by determining and using a specific powder and inhibitor for this process. In addition to the technological requirements for the selected materials, these materials should also be non-toxic, easily accessible, and relatively inexpensive.

4-1- Polymer selection

Conducted experiments showed that many polymers (e.g., polystyrene, polycarbonate, polyester), depending on the desired properties of the final part, can be used in the SIS process. The only exception was polyamide (DTM), where the glass transition point is very close to the melting point. However, each polymer requires the appropriate setting. Based on conducted experiments polystyrene polymer was the most appropriate polymer for making high quality parts (e.g., sharp edges, good attachment between layers, and low deformation). Also, according to a discussion with a Degussa researcher, Degussa is able to make customized polymers (e.g., with specific melting point, shrinkage, deformation, and strength) based on customers' needs. Therefore, many of the experimental limitations (e.g., part deformation) can be solved through material customization.

4-2- Inhibitor liquid selection

As the name implies, inhibitors are used to prevent the selected powder particles from sintering. Inhibition of sintering can be achieved through different phenomena. Regardless of the type of liquid, impact cutting and cooling phenomena are observed. Denser (heavier) liquids have more effective impact cutting. Liquids with high specific heat and evaporation energy constants have a more effective cooling phenomenon. Several liquids including water, isopropyl alcohol, commercial cleaning agents, organic solvents, light lubricating oils, mold release agents, and various silicone liquids were tested as candidates for the sintering inhibitor. They demonstrated no obvious inhibition phenomena other than impact cutting and cooling.

In addition, depending on the specific inhibitor chemical and physical properties, some other inhibition effects may be added to the list of inhibition phenomena. Inhibitor reaction with the polymer and separation phenomenon are two such effects.

There are several materials that can dissolve polymers. Dichlorobenzene ($C_6H_4Cl_2$) and butylbenzene ($C_6H_5(CH_2)_3CH_3$) are two examples. However, because of the toxic nature of the former and the destructive role of both in the printer head system, their application for the fabricated Alpha machine was impossible. In addition, polystyrene reacts with oxygen at high temperatures and in the presence of hydrogen peroxide, and hence inhibition occurs in the treated areas. However, it could not be demonstrated in the SIS process. Applying hydrogen peroxide as the inhibitor was successful for the low temperature sintering process (brittle or semi powdery parts), but for highly sintered parts the inhibition was not working at an acceptable level and removing parts from the surrounding materials was impossible.

Another phenomenon for the inhibitor can be separation between polymer particles to prevent them from joining to each other. Applying this idea has had the most successful results. In this phenomenon a soluble salt is printed as the inhibitor. After layer sintering and liquid evaporating, a thin layer of salt will remain in the selected area (Figure 5). At the end of the SIS process, this wall can be dissolved and washed away by water (Figure 6). A little alcohol is added to water to reduce the surface tension of the water. This enables water penetration into the solid block. Because of the weak powdery bounding between polymer particles in the selected area, the final part can be easily extracted from surrounding material. Potassium iodide (KI) has high solubility (135 gr/ 100 gr water) and a high melting point (635 o C). A saturated aqueous KI solution has been successfully used for many part fabrication experiments.

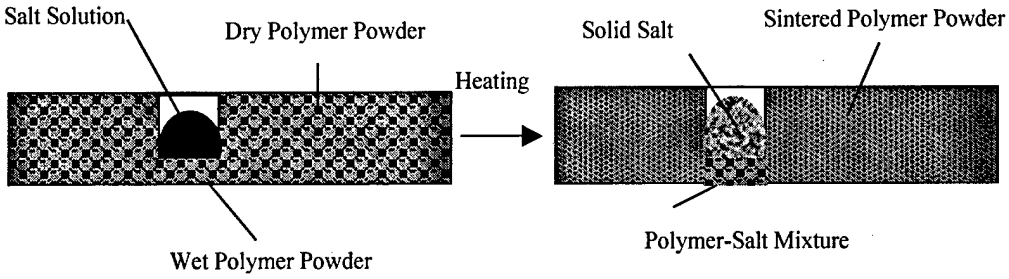

Figure 5. Water evaporation in the selected area

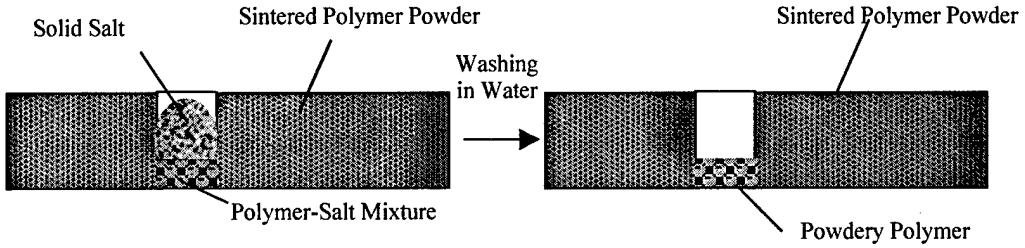

Figure 6. Washing the salt to extract the part

5- Physical and mechanical part quality improvement

Several properties (i.e., strength, surface quality, and dimensional accuracy) are important for the parts fabricated by the SIS process. Also, many different process operating conditions (factors) influence these properties. Statistical tools have been applied to improve the desirable properties of the parts fabricated by the SIS process. Initial attempts to simultaneously optimize all the responses for the SIS process produced several runs with missing data (immeasurable parts that were very brittle), and hence difficulties in applying statistical analysis tools. Consequently, it was decided that a region of operating conditions that provide acceptable part strength should be identified prior to investigation of conditions that improve surface quality and dimensional accuracy. Part properties improvement started with an investigation of part strength using Response Surface Methodology (RSM) and a region of acceptable operating conditions for the part strength was found. Then, by using RSM, the impact of the factors on the final part surface quality and dimensional accuracy (for x,y, and z directions) is modeled. After developing a desirability function model, process operating conditions for maximum desirability are identified. Finally, the desirability model is validated. Figure 7 illustrates the roadmap for this research.

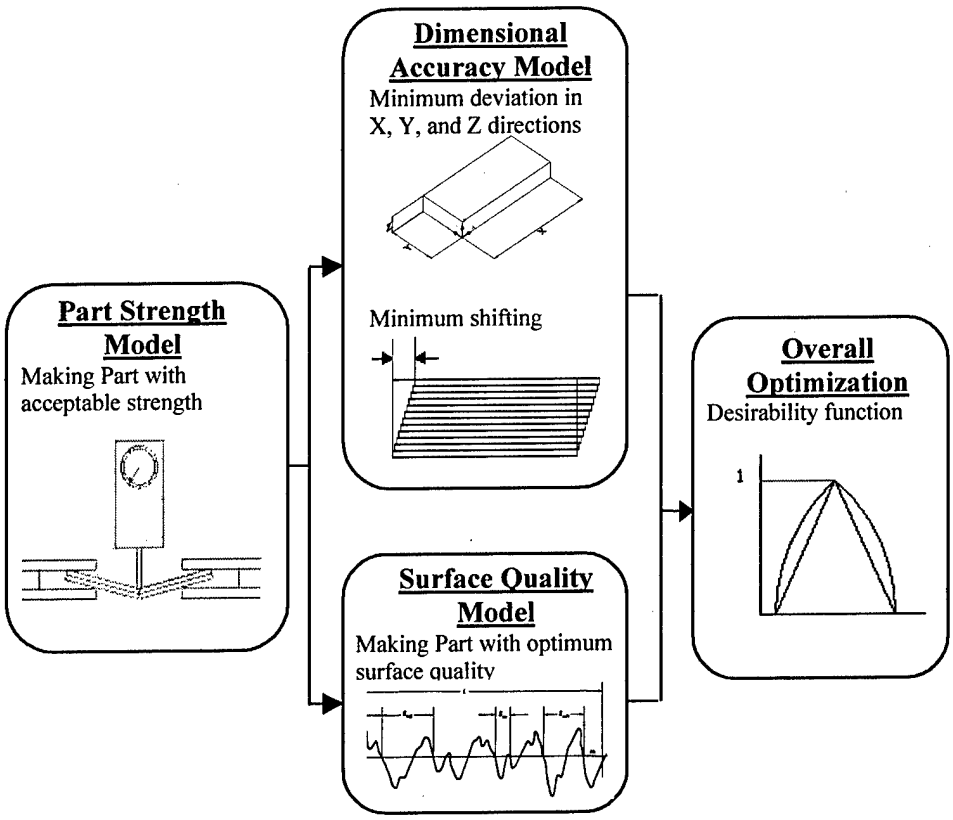

Figure 7. Roadmap for the SIS process properties optimization

5-1- Part geometry

A sample block with dimensions 45×20×6 mm was selected as the base part geometry for the experiments. Settings of the layer thickness factor produced specimen parts with differing numbers of layers; therefore, different machine path files were generated.

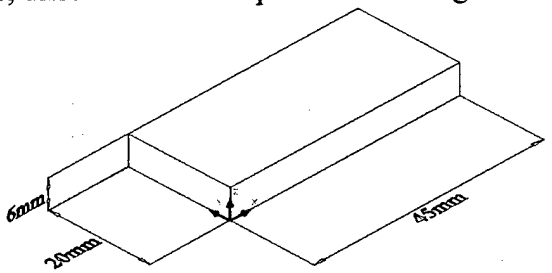

Figure 8. Base part

5-2- Part strength test

In the previous research (Asiabanpour, B., Palmer, K., Khoshnevis, B., 2003) the transverse rupture strength test, the standard basis for measuring the strength of the low ductility powder metallurgy materials (ASTM B528), was used as the response measure for the experiments (Figure 9).

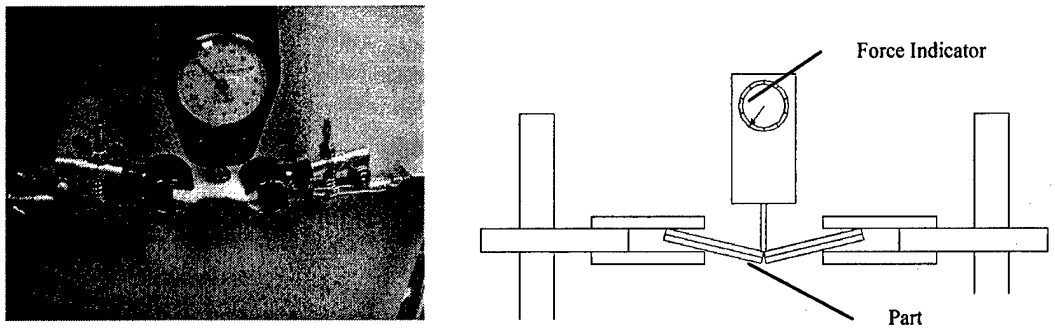

Figure 9. Part breaking mechanism

Then, a mathematical model of part strength versus effective factors was developed and region of acceptable operating conditions for the part strength (part strength > 50 oz) was found.

5-3- Part accuracy responses

Minimum deviation between fabricated part dimension and CAD model dimension was selected as one of the part accuracy criteria. To measure the deviation, each axis (X, Y, and Z) was studied separately. For finding deviation of each axis, length (X), width (Y), and height (Z) values of the fabricated parts were measured using a caliper. Then, deviations from CAD model dimension were calculated as the error percentage. For example, deviation in the X axis was calculated through $E_X = \frac{X - 45}{45} \times 100$, where X is the measured length of the fabricated part.

By observation of the fabricated parts from the previous experiments it was noticed that some of the parts had been made with noticeable shift in the X axis direction. To minimize such a defective property, layer shifting in the X axis direction was selected as another part accuracy response (named shift_X). Shift_X (total shift in X axis direction between first and last layer) was measured by a caliper in mm (Figure 10).

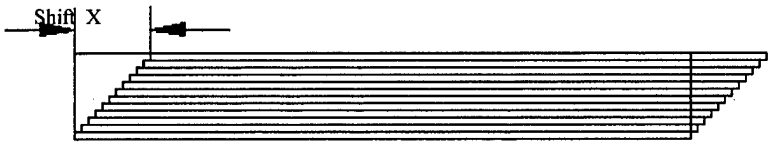

Figure 10. Shift_X

5-4- Surface quality response

Laser scanning systems are used to produce high precision surface quality evaluation. Mike Shellabear (1999) performed an extensive surface quality comparison between many commercial rapid prototyping systems. For surface quality measurement, he used a Zeiss Laser Scanning Microscope (LSM), which has a quoted accuracy of 0.2μm in X and Y directions and 0.6μm in Z direction.

In this research, a rating system was used as a low cost alternative to evaluate the part surface quality. For this purpose, ten sample parts with different surface qualities were selected

and assigned a rating between 1 and 10 to indicate the worst to the best surface quality. Then, all fabricated parts were rated by comparison to the selected sample parts.

For precise rating, four boundary sides of each part are studied individually (Figure 11). Each side is rated based on three major properties: holes made of the accumulated salt (due to over printing), sharpness of the edges, and smoothness of the surfaces. At the end, an average value resulting from the 12 ratings (4 sides × 3 properties for each side) is assigned as the part surface quality rating (Table 1).

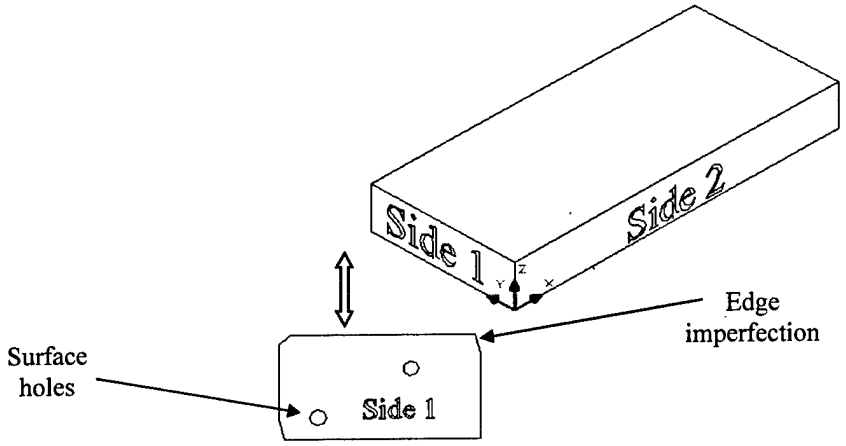

Figure 11. Part breakdown for surface quality rating

Table 1. Part surface quality rating system

Part	**Side 1**			**Side 2**			**Side 3**			**Side 4**			**Part grade**
No.	*Edge*	*Smoothness*	*Holes*	*E*	*S*	*H*	*E*	*S*	*H*	*E*	*S*	*H*	*Sum/12*
K	6	8	5	4	5	6	5	5	5	9	2	6	5.5
K+1	…	…	…	⋮	⋮	⋮						…	⋮

5-5- Factor identification & classification

Because of the similarity between factors that were expected to be effective on surface quality and factors that were expected to be effective on dimensional accuracy, a common list of eight factors was selected to be used in the new experiment. Based on previous experiences and preliminary experiments, eight factors are considered for statistically designed experiments. The list of factors includes two factors related to powder compaction, three factors related to inhibitor printing, and three factors related to sintering. Figure 12 illustrates the selected factors in the IDEF0 graph.

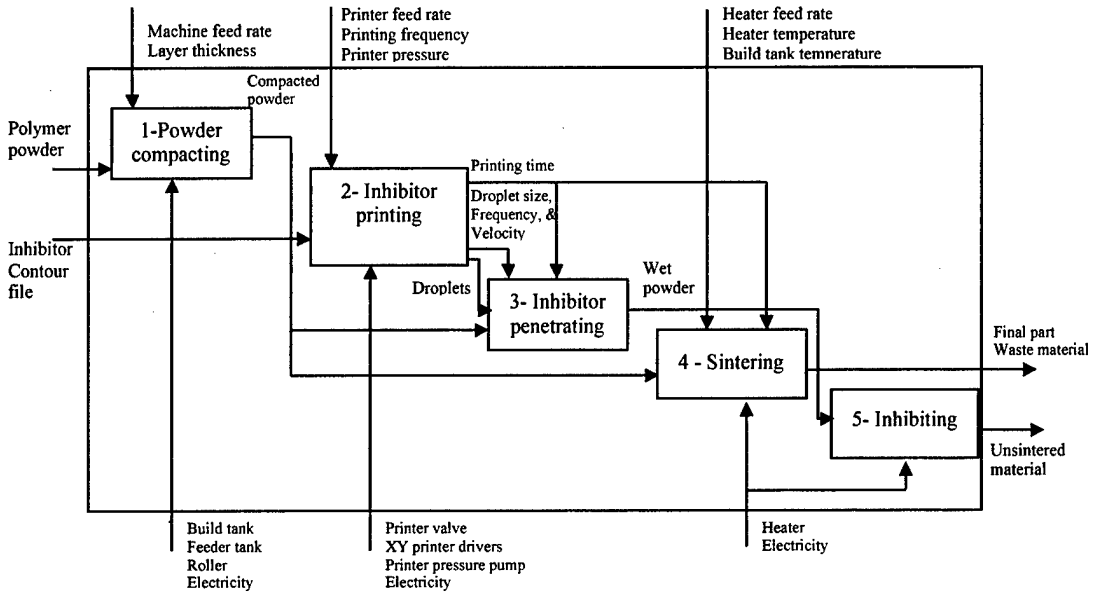

Figure 12. IDEF0 hierarchy for the SIS process and selected factors for statistically designed experiments

5-6- Design of experiments and analysis of result

Experimental design was implemented to characterize the SIS process in terms of how input parameters affect the part surface quality and dimensional accuracy. The data set of designed experiments was used to develop mathematical models to show the responses behaviors versus the factors. Five mathematical models were developed for part accuracy (Ex, Ey, Ez, Shift_x) and surface finish measurement.

5-7- Desirability function

Review of the developed regression models revealed the need for compromise in selection of factor settings. Each of the factors is involved in at least three of the models. Performance trends with respect to the factors are difficult to identify because of the inclusion of several two-factor interaction effects. Obviously, it is plausible that an increase in the value of one factor might produce a more favorable result for one response but would produce a less favorable result for another response. It is necessary to balance the responses to achieve overall desirable performance. A multi-response optimization technique is needed. We use a desirability function for this purpose. The general form of the component desirability function for each response is shown in Figure 13. The response value labeled *b* in Figure 13 represents the target quality. This response value corresponds to the maximum desirability (d=1). In theory, the response values labeled *a* and *c* represent the limits of acceptability. For each response a desirability function was defined. The goal, of course, is to improve desirability for all of the responses. Then, a composite desirability function is generated by use of a geometric mean. To develop a mathematical model for the relationship between the factors and the composite desirability function, the individual response models were used to predict the response values over a grid of locations in the factor space. Finally, the composite desirabilty was calculated and a regression model is built for this new response.

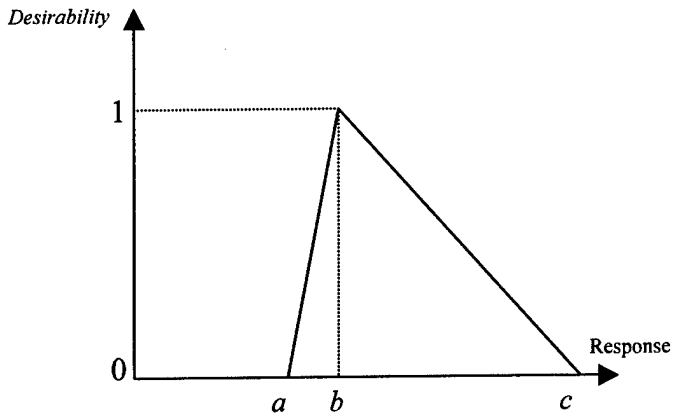

Figure 13. General form of the component desirability function

Canonical analysis and ridge analysis (Myers, R., and Montgomery, D., 2002) were used to find the optimum point for the mathematical model of desirability function.

Finally, the developed model was validated. To validate the model, 3 additional sample parts were fabricated. All five responses were measured for each part and average results were calculated for set of three parts. For each response, the individual response models were used to calculate 95% prediction intervals for the average of three values. All five of the actual averages fall within their respective prediction interval. These results indicate that the models are valid.

6- Physical part fabrication

Several 2.5 and 3D parts have been successfully fabricated by the SIS process using the machine and hatch path generation system. Figures 14 and 15 illustrate some of the fabricated parts.

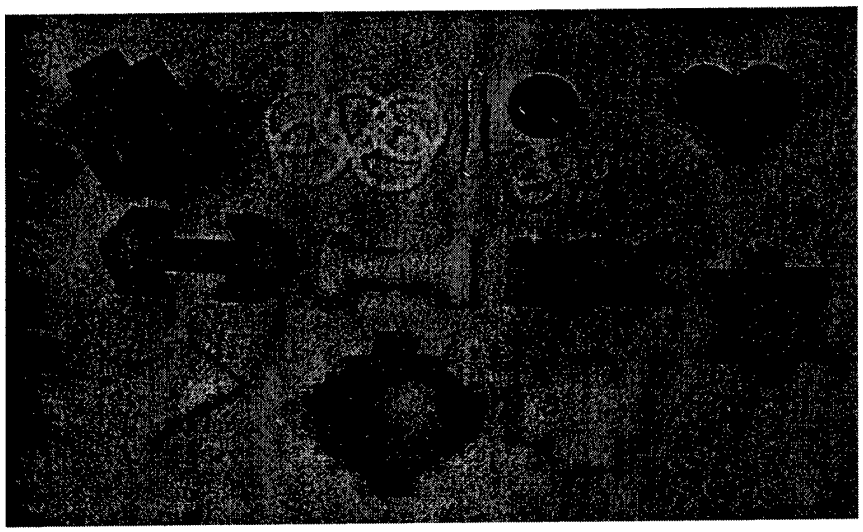
Figure 14.*2.5D* Parts fabricated by the SIS process

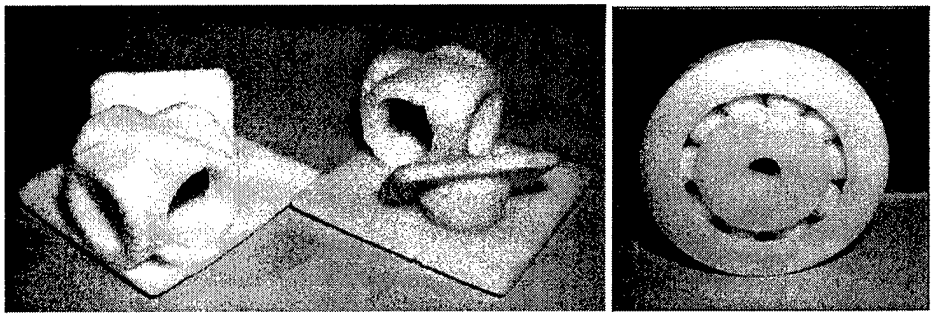

Figure 15.*3D* Parts fabricated by the SIS machine

7- Vision for future research

Results from research indicate a very promising future for the SIS process. SIS will be a strong competitive process against current RP commercial processes because of its ability to apply a variety of materials, as well as its accuracy, cost, speed, and ability to build functional part. However, many issues related to the SIS process should be studied and investigated. The multidisciplinary nature of the SIS process development opens a wide variety of areas for future work.

Hardware issues

Several changes in the original SIS machine structure could result in process improvement. Applying inkjet printer instead of a single nozzle printer makes the system much faster and more precise. Also, a larger build tank provides the ability to fabricate larger parts. In addition, improvement in heater system can cause more uniform layer thickness and consequently result in more accurate parts.

CAD/CAM issues

Current machine path development is specialized for the single nozzle printer. In case of applying inkjet printer, a CAD/CAM system is required to produce raster image, which includes boundary path and hatch pattern. Raster images can also provide data for multi-color printing to make multi-color parts.

Material issues

This research has focused on a limited number of polymer powders. Based on required part properties, many other polymers should be usable. The SIS process is also expected to be applicable to metallic powders. We are currently investigating the use of iron and aluminum powders. These powders may require the use of inhibitors that capitalize on inhibition phenomena other than particle separation at the microscopic level. For example, inhibitors that produce chemical reactions with the powder, or those that produce particle separation at the macroscopic level. Finding appropriate inhibitors to allow use of powders that produce a variety of part properties is a broad area of research.

Powder compaction issues

The fabrication of uniformly dense parts can be facilitated by compaction of the powder prior to sintering. This is especially true for metallic powders. However, the presence of the inhibitor in the powder layer complicates the description of compaction, specifically in terms of the dimensional stability of the layer. The extension of existing powder compaction models (ABAQUS 1997; Tran, et. al. 1993; Chenot, et. al. 1990) to the case of compaction for powder layers containing 'interior walls' of inhibitor material remains an open area for future work.

Powder waste reduction issues

Various means should be devised and studied for powder waste minimization. A combination of hardware and software approaches can significantly reduce powder waste in SIS and hence these approaches provide promising future research directions.

Process optimization issue

A systematic approach was explained in this thesis to optimize the process settings. However, all related factors were not considered in the statistically designed experiments. Consideration of other factors (e.g., material related factors) as well as application of other optimization methods (e.g., Taguchi) may lead to more realistic models.

References:

1- ABAQUS/Standard User's Manual, Version 5.7, vol. 1-3, Hibbitt, Karlsson, & Sorensen, Inc., Providence, RI, 1997.

2- Asiabanpour, B., "An experimental study of factors affecting the Selective Inhibition of Sintering process", Ph.D. Thesis, University of Southern California, Los Angeles, CA, 2003.

3- Asiabanpour, B., Khoshnevis, B., "A new memory efficient tool path generation method for applying very large STL files in vector-by-vector rapid prototyping processes", Computers and Industrial Engineering Conference, San Francisco, CA., 2003.

4- Asiabanpour, B., Palmer, K.,, Khoshnevis, B., "Performance Factors in the Selective Inhibition of Sintering Process", Industrial Engineering Research Conference, Portland, OR 2003.

5- Chenot JL, Bay F, Fourment L. Finite element siumulation of metal powder forming. International Journal of Numerical Methods Engineering ; 30: 1649-1674, 1990.

6- Khoshnevis, B., Asiabanpour, B., Mojdeh, M., and Palmer, K.,"SIS – A New SFF Method Based on Powder Sintering", Rapid Prototyping Journal, V. 1, N. 1, PP. 30-36, 2003.

7- Leong, K.F., Chan, C.K., and Ng, Y.M. "A study of stereolithography File Errors and Repair", The International Journal of Advanced Manufacturing Technology, PP. 407-414, 1996.

8- Myers, R. Montgomery, D., "Response Surface Methodology", John Wiley & sons, Inc., 2002.

9- Palmer, K., Design of experiments class handout (personal communication), University of Southern California, Los Angeles, CA, 2003.

10- Shellabear, M. "Benchmark Study of Accuracy and Surface Quality in RP Models", Rover, Project No. BE-2051, 1997, http://129.69.86.144/raptec/Reports/deliverables/Deli2_t42_all.PDF.

11- Tran, DV, Lewis RW, Gethin DT, Ariffin AK. Numerical modeling of powder compaction processes: displacement based finite element method. Powder Metallurgy, 36: 257-266, 1993.

Solid freeform fabrication by electrophotographic printing

Ashok V. Kumar, Anirban Dutta and James E. Fay
Department of Mechanical and Aerospace Engineering
University of Florida, Gainesville, FL 32611-6300

Abstract

A solid freeform fabrication technique is described where powder is deposited layer by layer using electrophotographic printing. In this process, powder is picked up and deposited using a charged photoconducting surface and deposited on a build platform. The paper describes a test bed that was designed and constructed to study the application of electrophotography to solid freeform fabrication. It can precisely deposit powder in the desired shape on each layer. The electric field required to transfer the powder on to the platform (or onto previously printed layers) was studied. A polymer toner powder was used to build small components by fusing each layer of printer powder using a hot compaction plate.

1. Introduction

Solid Freeform Fabrication (SFF) technologies are manufacturing / prototyping technologies that are characterized by layer-by-layer addition of material to fabricate components. These techniques are also known as layered manufacturing and rapid prototyping [1]. The layer-by-layer building approach allows significantly more complex parts to be built in one fabrication step than was previously possible thus simplifying process planning. SFF technology therefore can automate the process planning and fabrication of a part under computer control so that the only input needed is a solid model of the part.

Over the last decade many different technologies for Solid Freeform Fabrication have evolved. Broadly, the SFF techniques available currently can be classified as stereolithography, solid fusion and solidification, laminated object manufacturing, and powder based techniques. The stereolithography technique [2] selectively solidifies a liquid photopolymer while solid fusion and solidification [3], [4] fuses/melts the material and deposits it layer by layer. The laminated object manufacturing technology [5] cuts out laminates from sheets of part material and glues or fuses them together. In all these methods of SFF, special support structures are needed to support overhanging features of

the part. The two main powder-based techniques that have been commercialized are Selective Laser Sintering and 3D printing. For powder based methods no support structures are typically required to create complex shapes. Powder is selectively consolidated into a part and the remaining powder can be removed. In the SLS process [6], a thin layer of powder is deposited in a workspace container and the powder is then fused together using a laser beam that traces the shape of the desired cross-section. The process is repeated by depositing layers of powder thus building the part layer by layer. In the 3D printing process [7], a binder material selectively binds powder deposited in layers. Ink-jet printing technology is used to print the binder in the shape of the cross-section of the part on each layer of powder.

Electrophotographic Solid Freeform Fabrication (ESFF) [8], [9], [10] is also a powder based freeform fabrication technology that builds parts by printing powder layer-by-layer using electrophotography process [11]. The electrophotography process is used in photocopiers and printers to print toner powder on paper. This technology is capable of printing powder with high accuracy and resolution. Each layer of powder is printed in the shape of the cross-section. Two different processes for using electrophotography for SFF are described in this paper. In the first approach the part powder is printed layer by layer in the shape of the cross-sections of the part and thermally fused to previous layers. In the second approach, a part powder is first deposited uniformly by spreading a thin layer of powder using a roller and then a binder powder is electrophotographically printed in the cross-sectional image. This process is similar to 3D printing except that the binder is in powder form and printed using electrophotography. The binder is then thermal fused so that it diffuses into and binds the part powder. The challenges associated with printing powder for these two approaches were studied experimentally on a test bed. This test bed was designed as a flexible experimental platform to study layer by layer electrophotographic printing.

The design and working principle of the ESFF testbed is described in section 2. Using this test bed powder, parts can be built directly by printing part powder layer by layer as described in section 3. A technique for printing binder powder on a bed of part powder is described in section 4.

2. Description of the test-bed

An ESFF test bed was built that enables layer-by-layer deposition of powder using electrophotography technology. This test bed consists of an electrophotographic printing system, an automated two axes deposition/build platform and control system as well as a

thermal fusing and compacting system, all mounted on a structural frame. A model of the system is shown below in Fig. 1.

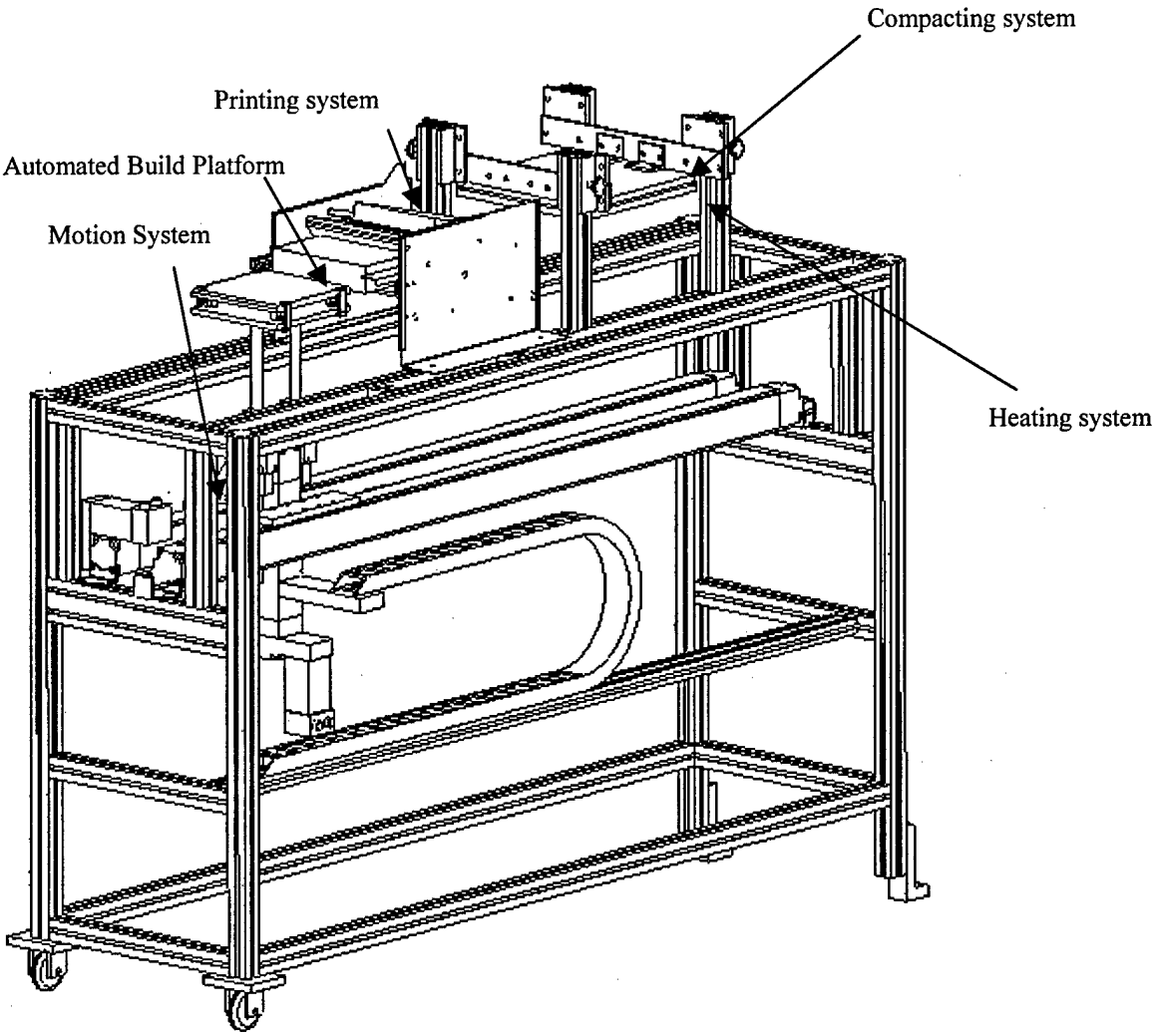

Figure 1: Model of the ESFF machine

A belt driven linear actuator moves the build platform in the horizontal (or x-) direction while a lead screw driven linear actuator moves the platform vertically (z-direction). Both the actuators are driven by servo-motors controlled by a digital control system. The printing system prints powder on the build platform as it passes below the printer. The cross-sectional images to be printed are computed by software that runs on a PC and can read in the solid model of the part to be fabricated in the STL format. The powder that is printed on the build platform is compacted and fused by the compacting system which is a heated non-stick plate mounted on a rigid frame.

The most important sub-system of the test bed is the electrophotographic printing system. Figure 2 shows the schematic diagram of the electrophotography engine used in a desktop laser printer from which components were taken to build the printing system for the test bed. The photoconducting drum is an aluminum drum that has a coating of photoreceptive material which is non-conductive in the dark and conductive when exposed to certain wavelength of light. When the drum rotates its surface is cleaned by the cleaner blade and then charged by the charging roller that is made of a conducting polyurethane on which a DC biased AC voltage is applied. The uniformly charged surface of the drum is selectively discharged by the laser image scanner that projects a UV laser on the drum surface. The region on the surface of the drum that is exposed to the laser beam becomes conductive and therefore gets discharged. A latent image is thus formed on the surface of the drum consisting of the discharged areas.

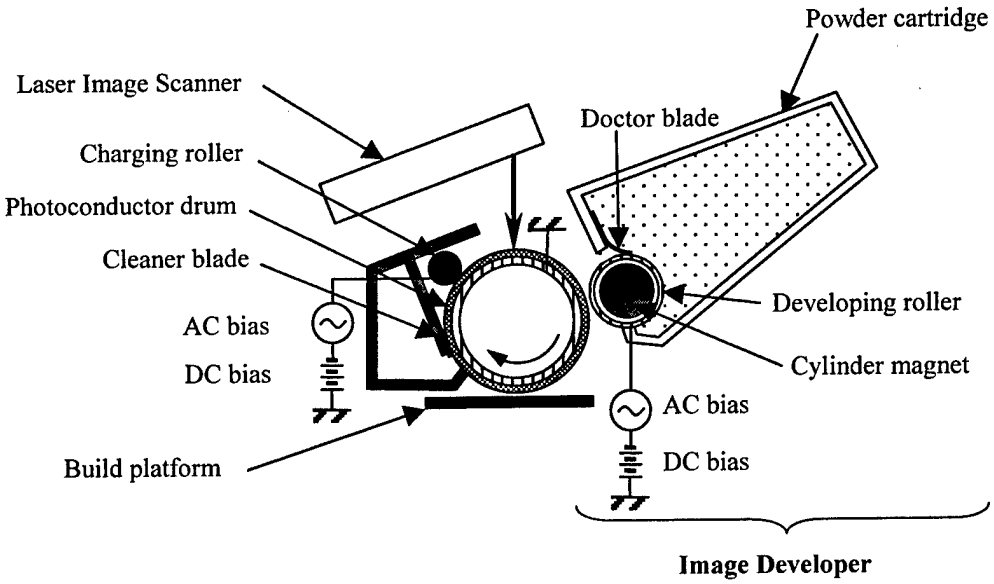

Figure 2: Schematic of the electrophotographic printing system

The latent image is converted into a real image when powder is electrostatically attracted (or developed) on to the discharged regions of the drum from the image developer. The image developer consists of the powder cartridge and the developing roller shown in Fig. 2. The developing roller is a hollow metallic roller which encases a cylinder magnet. The powder is magnetized so that it sticks to the developing roller. As this roller rotates a thin layer of powder squeezes out between the doctor blade and the roller. A DC biased AC voltage is applied to the roller to print this powder on to the

photoconductor drum. The powder is electrically charged to the same polarity (negatively) as the surface of the drum so that the powder is only printed on to the discharged areas due the electric field between the developing roller and the photoconductor drum.

The image developed on to the photoconductor surface is transferred to the printing surface or the build platform of the test bed. A positive charge is applied to the surface of the platform. The field generated by this charge attracts the negatively charged powder on the surface of the drum to the surface of platform, and thus the real image on the drum surface is transferred to the platform surface. The control system synchronizes the printing with the platform motion. The platform is moved at a velocity equal to the tangential velocity of the drum so that there is no relative velocity between the two surfaces as the image is transferred from the drum to the platform.

3. Direct part printing

The test bed described above has shown the feasibility of printing powder layer by layer using the electrophotography method. As mentioned earlier, one method for implementing solid freeform fabrication is to print part powder layer by layer in the shape of the cross-section and then fusing the printed powder to previous layers. This approach has been referred to here as direct part printing. A polymer powder consisting of styrene with various additives, including ferrous oxide to magnetize the powder, was used for printing. The particles in the powder were approximately 5 microns in size. The surface to be printed on was charged using a corona charging device and a constant DC voltage of 1000V was applied to the aluminum build platform to enable transfer of the image from the photoconductor drum to the build platform. The layer thickness is dependent on particle size as well as parameters such as charge per unit mass of powder, speed ratio between photoconductor drum and developer roller etc.

The electric field between the photoconductor drum and the print surface was computed using Gauss's law as follows [12]:

$$E(p,\sigma_s)=\frac{V_{DC}+\rho_1\frac{p^2}{2K_1\varepsilon_0}+\rho_2\frac{d_2^2}{2K_2\varepsilon_0}-\rho_3\frac{d_3^2}{2K_3\varepsilon_0}+\frac{p}{K_1\varepsilon_0}(\sigma_s+\rho_2 d_2)}{K_2\left(\frac{p}{K_1}+\frac{d_2}{K_2}+\frac{d_3}{K_3}\right)} \quad (1)$$

In the above equation, V_{DC} is the potential applied to the build platform, p is the height of the part (or previously printed layers), d_2 is the thickness of the fresh powder layer, d_3

is the thickness of the photo-conducting layer. K_1, K_2 and K_3 are the relative permittivity of the fused powder layer, fresh powder layer and photoconductor material respectively. ρ_1, ρ_2 and ρ_3 are charge per unit volume in the fused powder, fresh powder layer and the photoconductor layer respectively and ε_0 is the permittivity of the air. σ_s is the charge per unit area deposited on the print surface. The equation shows that the field strength decreases with part height p, if the surface is not charged (σ_s=0). Residual negative charge on the fused layers of powder (ρ_1<0) also can significantly decrease the electric field strength available for image transfer.

Figure 3 shows small parts built using the test bed. The parts were built simultaneously by printing powder over a thin layer of polymer sheet covering the aluminum platform. The parts are approximately 1 mm tall and took about 200 prints of polystyrene based powder. The print thickness is larger for the first few prints and then decreases to an average rate of approximately 5 microns per print. This low rate of printing can be improved by more efficient removal of residual charge from the previously printed layers and by increasing the charge density deposited by the corona charging device.

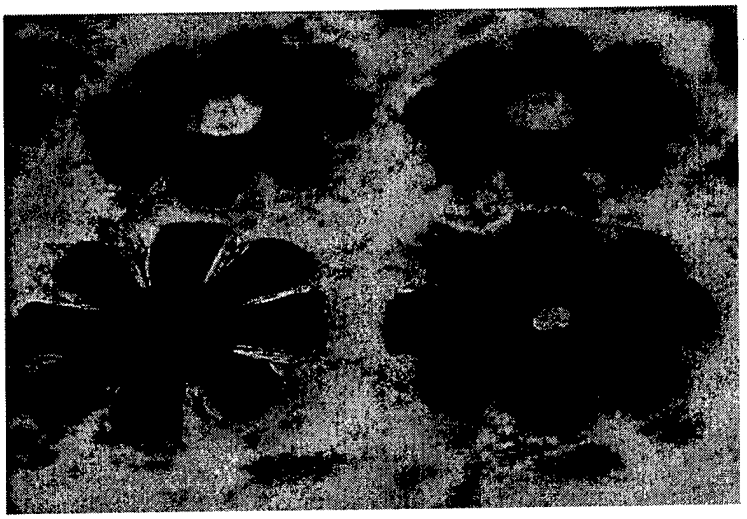

Figure 3: Parts made by the test bed

The printing system used in the test bed is capable of achieving up to 600 dpi. However, the accuracy and finish of the parts made using the process also depends up on the accuracy with which subsequent layers can be aligned over each other. Another factor that affects the part accuracy is the distortion that occurs during the fusing and compaction after each layer is printed.

4. Binder printing on part powder

An alternative way to build parts using electrophotography is to print a binder powder on uniformly deposited part powder as is done for 3D printing. The binder powder can then be fused thermally so that it diffuses into the part powder and binds the part powder together up on subsequent cooling and solidification. The success of this concept depends on the ability to deposit thin uniform layers of part powder and the efficiency with which the binder powder can be transferred on to the part powder bed. It is not feasible to transfer powder directly from the photoconducting drum on to previously deposited part powder bed because the charged regions of the drum will pick up some part powder. In other words, during the transfer process the part powder will get picked up by the photoconductor drum instead of the binder powder being printed from the drum to the powder bed. This can quickly damage the photoconductor especially if the part powder is abrasive. To protect the photoconductor drum and to minimize part powder reverse printing it is necessary to use either a transfer roller or a transfer belt. The ideas is that the binder can be first printed on to an intermediate transfer device and then subsequently transferred from this device to the part powder bed. Figure 4 shows the concept schematically where a transfer roller is shown between the photoconductor and the build platform. On the right an equivalent parallel plate model for the interface between photoconductor drum and transfer roller as well as the interface between the transfer roller and the print surface.

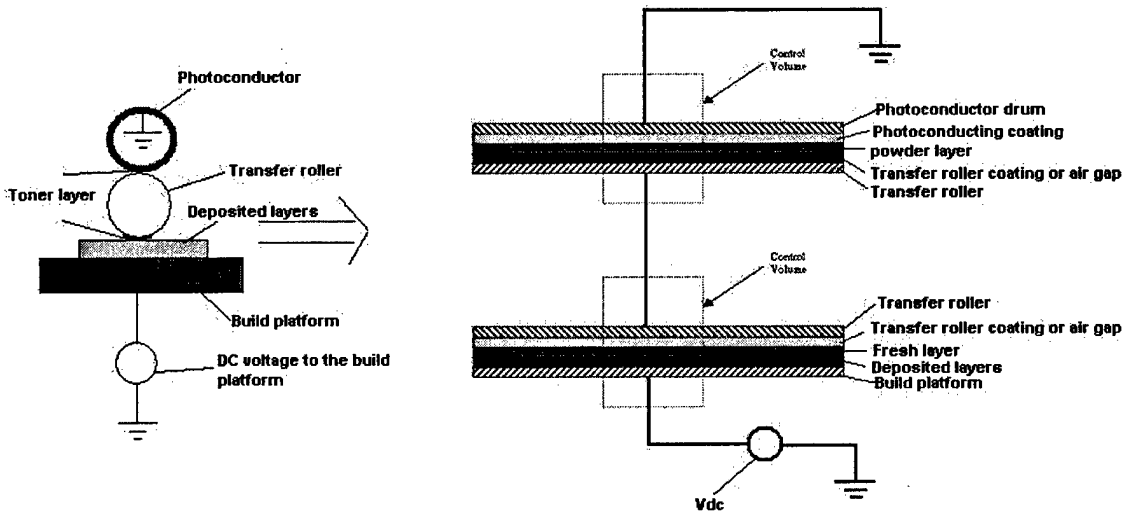

Figure 4: Parallel plate analogy for transfer device arrangement

Electric field is required at both interfaces to enable transfer of powder. A conductive (aluminum) drum was used as the transfer roller. The electric field for transfer can be created by applying a voltage to the build platform or by charging the top layer of the powder bed. Since the transfer roller is conductive its voltage is constant and the electric field created at one interface is transmitted to the other interface. The transfer roller rotates such that it has the same tangential velocity as the photoconductor drum so that the image can transfer from the photoconductor to the transfer roller. Similarly the build platform moves at the same velocity as the tangential velocity of the transfer roller to enable undistorted transfer of the image from the transfer roller to the platform.

If the part powder is metallic (conductive), it tends to get charged by the electric field and jumps back and forth between the transfer roller and the powder bed creating a powder cloud as shown in Fig. 5. The reason for this powder oscillation is that the powder particles are conductive and therefore loose their charge and get reversely charged due to the field as soon as they contact the transfer roller or the drum. This oscillation causes many problems including poor transfer of binder powder as well as distortion of the image. If the drum is covered with a thin insulator layer then the particles cannot loose charge to this layer and sticks to it resulting in reverse printing. Therefore this approach appears to be infeasible for conductive part powders unless some other means is used to hold down the part powder, such magnetic force if the part powder is magnetic.

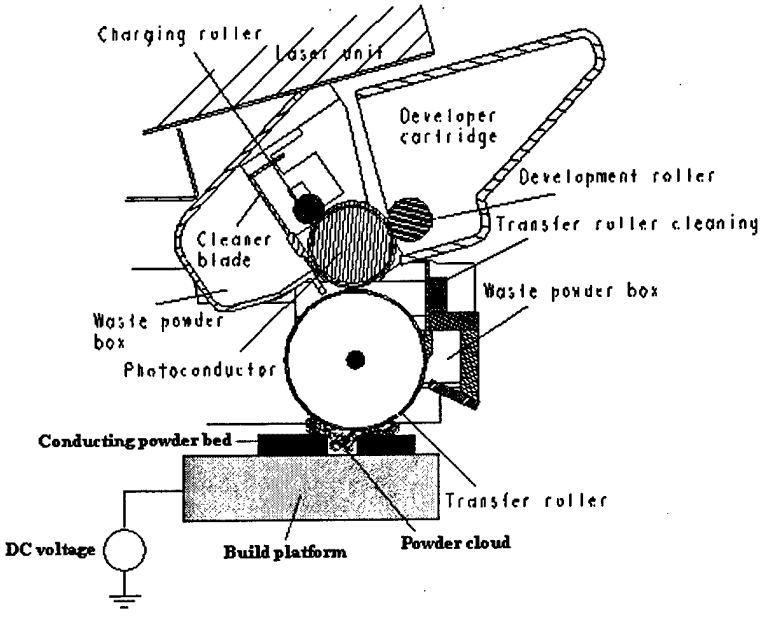

Figure 5: Transfer roller system with conducting part powder bed

For non-conductive part powders, the top surface of the powder bed must be charged to facilitate (or create the necessary field for) transfer of the binder powder. The charged particles on the surface need to be held down so that they do not get picked up by the transfer roller. Figure 6 shows a polystyrene binder powder printed on a ceramic (alumina) powder bed. The powder bed was created by spreading a layer of the ceramic powder uniformly and then it was compacted to impart green strength in order to minimize reverse printing. A thin polymer (insulator) cover was glued over the transfer roller to minimize chances of sparking between the photoconductor drum and the roller.

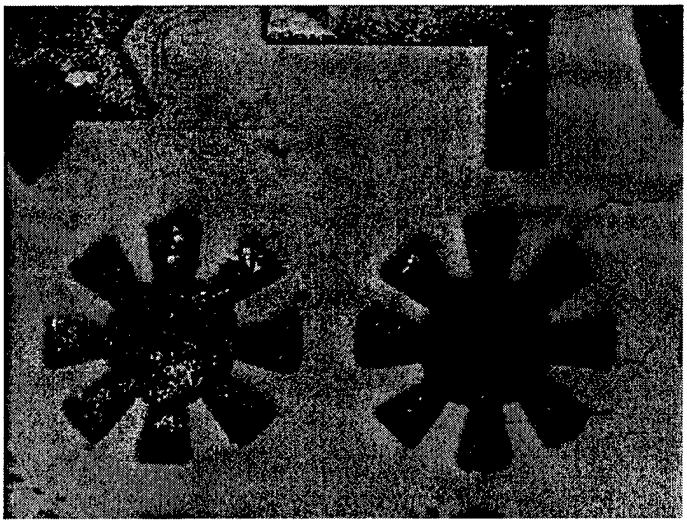

Figure 6: Toner powder on insulating alumina powder bed

In Fig. 6, the black binder powder is printed on alumina (white) powder bed. The white spots within the printed image were caused by reverse printing where the alumina powder was picked up by the transfer roller instead of the binder getting printed on the alumina powder bed. Another problem with this approach is that if the binder is too viscous after melting it may not diffuse into the part powder deep enough to ensure proper bonding between layers.

5. Conclusions

A test bed for studying electrophotographic solid freeform fabrication was built and used to show the feasibility of printing powder layer by layer in the shape of the cross-sectional images of a part to be fabricated. The test bed was fully automated and controlled from a program that reads in a solid model of the part, computes the cross-sectional images and prints them layer by layer on to a build platform. This approach

appears to be a feasible method for rapid prototyping small polymer components. 3D printing was also attempted by printing polymer binder electrophotographically on a ceramic powder bed. It was necessary to use a transfer roller to print the binder powder. The transfer roller can not prevent reverse printing but it protects the photoconductor drum from damage. Printing binder powder for 3D printing has other disadvantages that traditional 3D printing does not have including the need for melting the binder and poor bonding between layers. Direct part printing on the other hand appears to be a promising approach for building tiny components as well as for constructing heterogeneous parts if multiple powders can be printed layer by layer. However, further research is required to develop technology for reliably charging and printing a variety of powders including ceramic and metallic powders. This work is currently in progress and initial results have been encouraging.

6. Acknowledgement

Funding for this research from NSF grant number DMI-9875445 and ONR grant N00014-98-1-0694 is gratefully acknowledged.

7. References

[1] Kochan, D., 1993, Solid Freeform Manufacturing: Advanced Rapid Prototyping, Manufacturing research and technology, vol. 19, Elsevier.

[2] Kodama, 1981, "Display 3 dimensional information to a physical formed model", Trans. of Electronics and Communications Society, vol. 17, no. 6, pp. 237-241.

[3] Crump, S., 1992, "The extrusion process of Fused Deposition Modeling", in the Proceedings of the 3rd International conference on Rapid Prototyping, Dayton, OH.

[4] Amon, C.H., Beuth, J.L., Weiss, L.E., Merz, R. and Prinz, F.B., 1998, "Shape deposition manufacturing with microcasting: Processing, thermal and mechanical issues", Journal of Manufacturing Science and Engineering, Transactions of the ASME v 120 n 3 pp. 656-665.

[5] Feygin, M. and Hsieh, B., 1991, "Laminated Object Manufacturing: A simpler process" in Proceedings of Solid Freeform Fabrication Symposium, Austin, Texas.

[6] Bourell, D.L., Marcus, H.L., Barlow, J.W. and Beaman, J.J., 1992, "Selective laser sintering of metals and ceramics", International Journal of Powder Metallurgy (Princeton, New Jersey) v 28 n 4. pp. 369-381.

[7] Sachs E., Cima M., Williams P., Brancazio D., and Cornie J., 1992, "Three Dimensional Printing: Rapid Tooling and Prototypes Directly from a CAD Model," Journal of Engineering for Industry, vol. 114, pp. 481-488.

[8] Kumar, Ashok. V., 1998, Patent Number: 6,066,285; "Solid freeform fabrication using powder deposition", Assignee: University of Florida, Gainesville, FL; Date filed: December 11, 1998.

[9] Kumar Ashok V. and Zhang Hongxin, 1999, "Electrophotographic powder deposition for freeform fabrication", 10th Solid Freeform Fabrication symposium, 1999.

[10] Kumar Ashok V. and Dutta Anirban, 2003, "Investigation of an electrophotography based rapid prototyping technology", *Journal of Rapid Prototyping*, vol. 9, no. 2, pp. 95-103.

[11] Schien L., B., "Electrophotography and Development Physics", Springer-Verlag, NY, 1988.

[12] Kumar Ashok V. and Dutta Anirban, 2003, "Layered Manufacturing by Electrophotographic Printing", DETC2003/DAC-48724, Proceedings of the Design Automation Conference, Design Engineering Technical Conference.

MICROFABRICATION WITH FEMTOSECOND LASER PROCESSING

Michelle Griffith, Pin Yang, George Burns, and Marc Harris

Sandia National Laboratories
Albuquerque, NM 87815

Abstract

Our research investigates the special characteristics of femtosecond laser processing for microfabrication. The ultrashort pulse significantly reduces the thermal diffusion length. As a result, material is removed more efficiently with little damage to the surrounding feature volume. Currently, we are exploring the basic mechanisms that control femtosecond laser processing, to determine the process parameter space for laser processing of metals to address manufacturing requirements for feature definition, precision and reproducibility. One of the unique aspects to femtosecond radiation is the creation of localized structural changes. By scanning the focal point within a transparent material, we can create three-dimensional waveguides.

This paper will describe our results to explore femtosecond laser ablation for laser processing of metals and glasses. We will discuss the effect of laser parameters on removal rate, feature size/definition, aspect ratio, material structure, and performance. Examples of component fabrication in metals and glasses will be shown.

Introduction

At Sandia National Laboratories, miniaturization dominates future hardware designs, and technologies that address the manufacture of micro-scale to nano-scale features are in demand. Currently, Sandia is developing technologies such as photolithography/etching (e.g. silicon MEMS)[1], LIGA[2], micro-electro-discharge machining (micro-EDM)[3], and focused ion beam (FIB) machining[4] to fulfill some of the component design requirements. As in the macro world, no one micro- or nano-scale process can do it all. Some processes are more encompassing than others, but each process has its niche, where all performance characteristics cannot be met by one technology. For example, micro-EDM creates highly accurate micro-scale features but the choice of materials is limited to conductive materials. With silicon-based MEMS technology, highly accurate nano-scale integrated devices are fabricated but the mechanical performance may not meet the requirements. Femtosecond laser processing has the potential to fulfill a broad range of design demands, both in terms of feature resolution and material choices, thereby improving fabrication of micro-components. One of the unique features of a femtosecond laser is the ability to ablate nearly all materials with little heat transfer[5], and therefore melting or damage, to the surrounding material, resulting in highly accurate micro-scale features.

For many years, Sandia has been involved in the development of laser-based rapid prototyping (RP)[6] and direct fabrication technologies[7-9] to build prototype parts, as well as small lot production components. The significant aspect of these technologies is the utilization of a computer model, sliced into two-dimensional cross-sections, to drive the fabrication process,

where a part is fabricated layer by layer to create the three-dimensional shape. For example, we use these models to routinely fabricate polymeric three-dimensional representations for design verification and, in some instances, fabricate patterns for investment casting to obtain a metal component. Instead of using secondary processes, such as investment casting, to fabricate the final metal part, Sandia has developed a laser-based metal fabrication technology, known as Laser Engineered Net Shaping (LENS®)[7], to directly fabricate the metallic component. These technologies have greatly enhanced our ability to quickly fabricate parts but the size regime is typically on the macro-scale. The RP polymeric-based technologies are now scaled to the micro level but their properties do not typically meet the performance requirements of components that are of interest to Sandia. The LENS® process can produce parts down to the mm-scale but no smaller due to processing constraints.

At present, Sandia is developing a femtosecond laser micro-fabrication capability to expand into the micro-scale size regime for metals and glasses. We hope to produce accurate, reliable micro-components. To facilitate adoption of this technology in the manufacturing environment, further understanding is required to ensure routine fabrication of robust components with desired material properties. This requires understanding and control of the material behavior during part fabrication. This paper describes our initial research to understand the ablation process of stainless steel to determine the correct path sequencing to drive the process in order to fabricate components with clean surfaces and accurate features. The paper will also describe our work to understand the modification of glass structures and control of this phenomenon to fabricate waveguides and other photonic device based features.

Experimental Setup

Figure 1 is a photo of our femtosecond laser micro-fabrication system. We are using a Hurricane femtosecond laser from Spectra-Physics. This laser provides a small footprint which is more amenable for the manufacturing environment with the following characteristics: 800 nm wavelength, 120 fs pulse width, 1 KHz frequency, up to 1 mJ energy, and approximately 4 mm output beam. This beam is transferred to the working envelope by a series of mirrors and is focused with a microscope objective. The beam is focused onto the working surface and X-Y stages manipulate the geometry in the plane, whereas the microscope objective is mounted to a Z stage to manipulate the beam position.

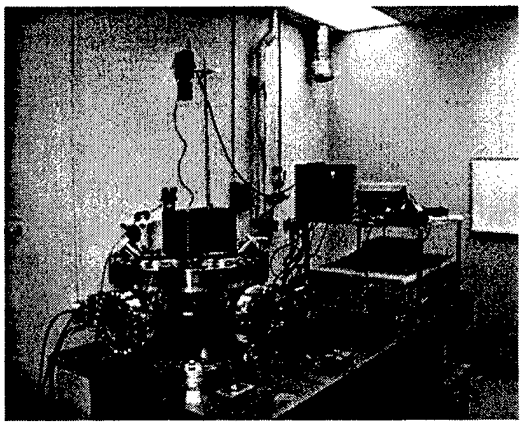

Figure 1. Sandia's femtosecond laser micro-fabrication system.

Stainless steel 304L foils were used for the metal work. Typically, 50-200 micron thick foils were used. The foils were mounted into a picture frame holder, where features ablated through thickness easily fall out of the foil for analysis. A 20X objective was used resulting in a minimum spot size of 60 microns at 975 mW. Smaller spot sizes are easily obtainable, but for this work a larger spot size was used to aid in understanding the ablation process. Full power (975 mW) was used for most studies. Since this work involves the utilization of traditional RP techniques, effects of travel velocity, layer decrement, and geometric features were studied. Sandia-developed software was used to define the path sequence for part fabrication. Simple machine language (M and G codes) was used for initial parameter studies. Ablated features were analyzed by optical and scanning electron microscopy. Width and depth of features were measured by interferometry techniques.

When our femtosecond laser was used to modify the local glass structure, the power of laser beam had to be reduced to prevent optical damages to the glass. The energy of the beam was first reduced by rotating a half wave plate together with a thin film polarizer along the beam path. Further energy reduction was accomplished by the use of neutral density filters. The glass used in this evaluation was a thermally treated chemical vapor deposited (CVD) amorphous quartz (Quartz International, Albuquerque, NM). The laser beam was directed through a long-working-distance microscope objective (Mitutoyo, NIR 20X, NA = 0.40) and focused into the polished glass approximately 500 to 750 μm below the surface. Typical laser energy per pulse used in this investigation was controlled between 0.45 to 0.9 μJ. The samples were scanned perpendicular to the focused fs laser pluses at a rate of 20μm/s to create micron-sized lines inside the bulk glass. The optical properties of these scanned lines were studied using near-field and far-field techniques. Light scattering in these modified regions (waveguides) was determined by image analysis of light intensity decay along the beam direction, using a digital camera. Laser-induced birefringence was characterized by using a Dalsa CA-D1-0128T camera attached to an Olympus transmitted light microscope (BH-2) with samples between crossed polars on a rotation stage. Digital signals from these images were processed using a National Instruments PCI-1424 digital image capture card and software written in LabVIEW G code.

Results in Metals

A. Ablation Properties

For complex part fabrication, we will need to process parts in a layered manufacturing approach. Much of our understanding of ablation with respect to velocity and layer decrement for stainless steel can be found in the following reference[10]. By utilizing a layered manufacturing approach, a three-dimensional shape is represented by two-dimensional cross-sections where each cross-section is represented by a raster pattern. There are two choices for volumetric material removal: 1) fast travel velocity and smaller layer decrement or 2) slow travel velocity and larger layer decrement. Processing speed is of great importance in the manufacturing environment, but so is final part resolution and cleanliness. For this work, all studies were done in air, where it is generally more difficult for the species to ablate away from the surface resulting in redeposition onto the sidewalls or top surfaces. It is beneficial to process

in air for a variety of factors from simpler equipment (no vacuum/gas handling equipment) to easy sample exchange. Other researchers have found techniques[11] to provide good feature definition without species redeposition while processing in air. Appropriate techniques will be incorporated into our system in the future.

In order to correctly choose the layer thickness and raster width (known as hatch) we need to understand the effect of velocity on feature width and depth. Initially, single lines, 10 mm long, were drawn at various velocities and their width and depth measured using interferometry. A foil thickness of 50 microns was used for this study. Figures 2a and 2b show the measured ablated depth and channel width. As expect, the depth decreases as the velocity increases from 46 microns to 5 microns for a change in velocity from 0.4 mm/s to 3.4 mm/s. At slower velocities, one would expect the channel width to match closely to the minimum spot size, 60 microns, and decrease in width as the velocity increases. In Figure 2b, the data shows this general trend within error. Inconsistencies are most likely due to species redeposition thereby adding measurement error depending on the efficiency or inefficiency of removal.

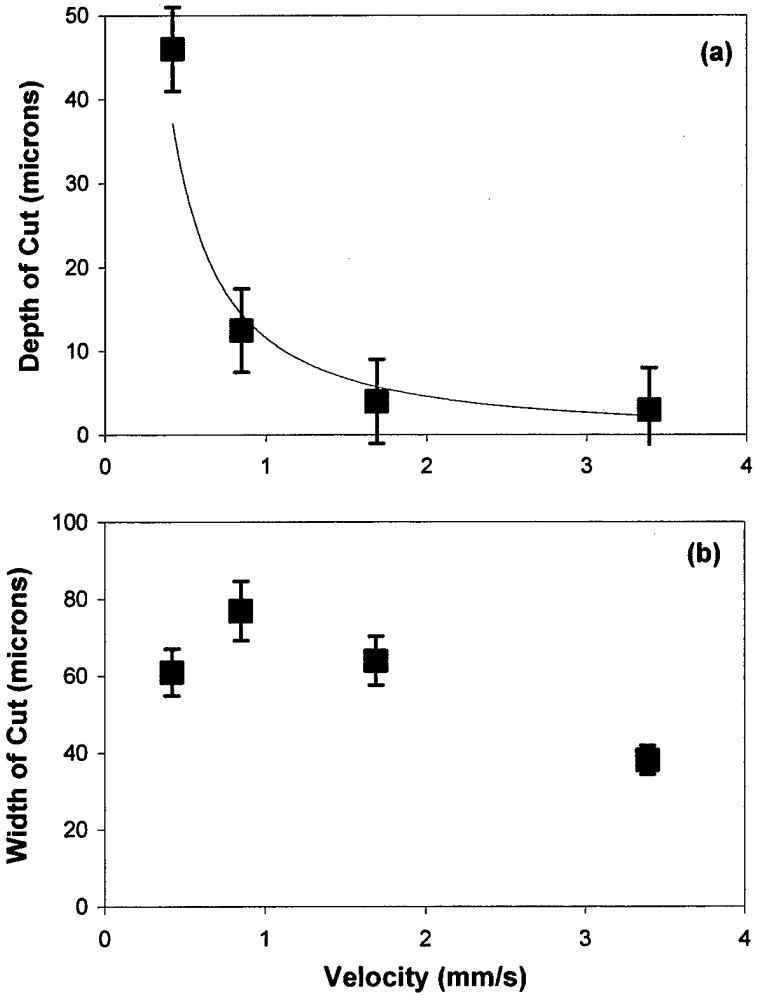

Figure 2. Ablated depth (a) and channel width (b) for lines processed at four travel velocities at 975 mW. A 50 μm foil thickness was used in this study.

B. Components

With the knowledge of depth and width at various velocities, complex shapes were tried. For manufacturing speed, it would be best to utilize the greatest decrement possible, or try to match the 46 micron cut shown in the previous section. Since Figure 2A shows a dramatic change in depth for a small change in velocity at low travel speeds, a decrement value of 25 microns was chosen at a speed of 0.4 mm/s. Figure 3 shows the results for a comb-like geometry that was cut into a 200 micron think SS304 foil. Comb arms are 200 microns wide with 250 micron spacing. The comb geometry is reasonably accurate dimensionally, but as the figure shows, there is a large amount of recast material along the sidewalls. Furthermore, it took twelve passes to ablate through the thickness or a discrepancy of 100 microns. This discrepancy can be explained by the ablation energy being utilized to remove old material that has recast within the channel.

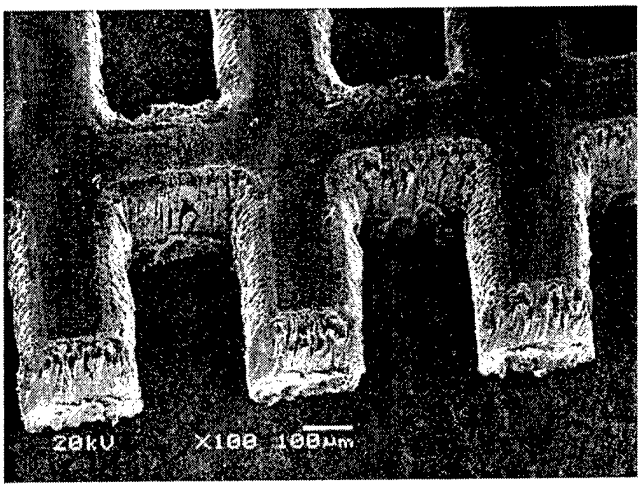

Figure 3. Comb geometry fabricated at 0.42 mm/s with 25 micron layer decrements.

In contrast, Figure 4 shows clean and accurate features for a ratchet gear fabricated with 5 micron decrements using a travel velocity of 1.7 mm/s. The gear was cut through a 100 micron thick foil in 18 passes, or 90 microns, resulting in a more efficient process where energy is directly utilized to cut features. Even though the gear was cut from a 100 micron foil, it is apparent that the small layer increment is better for part fabrication. For this parameter set, the particles can volatize away from the channel without heavy plasma shielding or increased particle-particle collisions.

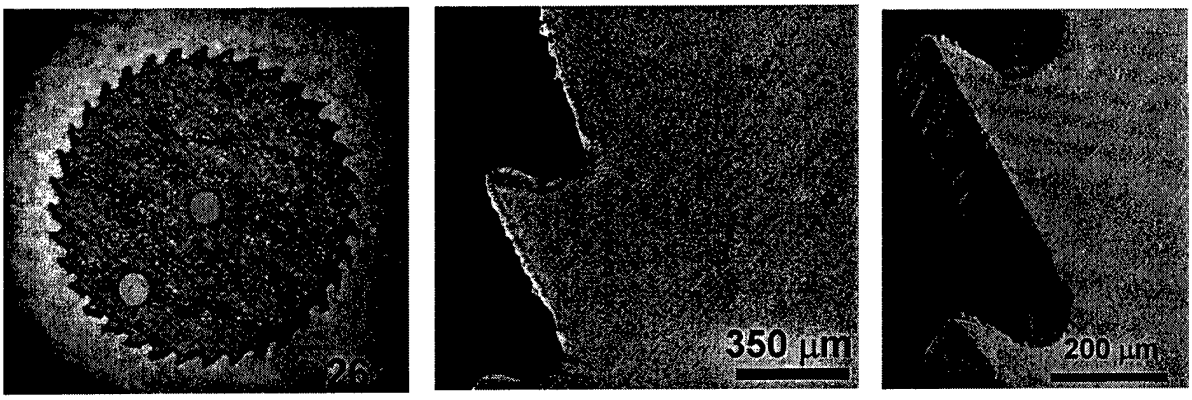

Figure 4. Ratchet gear fabricated in 100 micron thick SS304 foil using the following parameters: 1.69 mm/s travel velocity and 5 micron layer decrement.

Results in Glasses

A. Structure Modification

When an intense femtosecond laser pulse is focused inside bulk glass, the intensity in the local volume can become high enough to cause absorption through nonlinear processes, leading to optical breakdown or photo-damage. Slightly below the optical breakdown threshold, this nonlinear, multi-photon absorption can locally alter the glass structure and cause refractive index changes.[12-16] If the intensity of the laser is below the threshold level of multi-photon absorption, glass becomes almost transparent to the laser beam. Therefore, it is important to identify the proper processing space that can effectively increase the refractive index without creating photo-damage in the bulk glass. Figure 5 shows the micro-Raman spectrum of bulk silica glass and normalized spectrum of a laser-damaged region (0.1 mJ). Under cross-polarized light condition, the damaged regions exhibit stress birefringence and are occasionally associated with microcracks. Without the normalization procedure, the intensity of the Raman bands from the laser-damaged region is consistently less than that from the bulk glass. This reduction in intensity indicates that the modified regions have structures of lower density where some glass has been partially replaced by voids. However, this reduction in intensity becomes significantly less for laser-modified regions (0.9 µJ) that produce refractive index change without creating stress birefringence. Furthermore, the normalized Raman spectra show an increase in the 490 and 605 cm^{-1} peaks in the damaged region, indicating an increase in the number of 4- and 3-membered ring structures in the silica network. The formation of these 4- and 3- ring structures are sometimes associated with the creation of new quasi-surfaces at small voids in the silica-rich matrices.[18] In addition, the Raman band peaking between 400 and 500 cm^{-1} is significantly narrower in the spectra from laser modified regions compared to the bulk glass. The relative narrowness of the bands in the spectra indicates that the silica networks in these areas have a smaller distribution of ring sizes, with fewer large rings. This type of modification of the silica network is typically achieved by quick melting followed by fast re-solidification during the laser process.

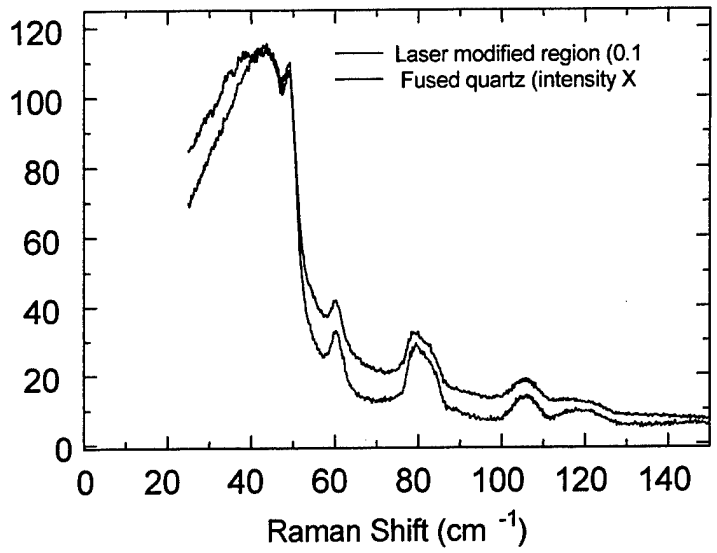

Figure 5. Micro-Raman spectra for bulk glass and laser modified regions.

B. *Components*

With the knowledge of the effect of average laser power on structure modification of glass, direct writing waveguides inside amorphous quartz was explored. Figure 6 shows the top view, near-field and far-field patterns of laser-modified lines above (0.1 mJ) and below photo-damage threshold (0.9 μJ). The near-field and far-field patterns were obtained from the transmitted beams at 650 nm through 2 mm length of laser-modified regions. The near-field pattern of waveguides created below damage threshold illustrates the propagation of a single LP_{01} mode through the waveguide inside of a bulk glass. The far-field pattern indicates that this transmitted mode possesses a nearly Gaussian profile. Above the photo-damage threshold (> 2.2 μJ), extensive light scattering is observed, which is consistent with the Raman analysis results where some glass has been partially replaced by voids. Experimental results suggest that these laser-modified regions have a unique biaxial optical birefringence, where the maximum birefringence is in the range of 0.002 to 0.004. Figure 7 (a) illustrates the variation in transmitted light intensity through the laser-modified regions under cross-polarized light. The polarization direction of the laser beam was systematically rotated 10° from spot to spot. The observation of an optical extinction for every 90° suggests that the laser-modified regions possess an optical birefringence property. Furthermore, the sinusoidal variation of the transmitted light intensity (see Fig. 7 (b)) is consistent with the theoretical prediction of a birefringent material. Results indicate that the laser-induced birefringence property in the bulk glass can be controlled by laser power level, accumulated exposure, and polarization direction of the writing laser.[19] Details of the creation of birefringence by the femtosecond laser pulse will be reported elsewhere.[19]

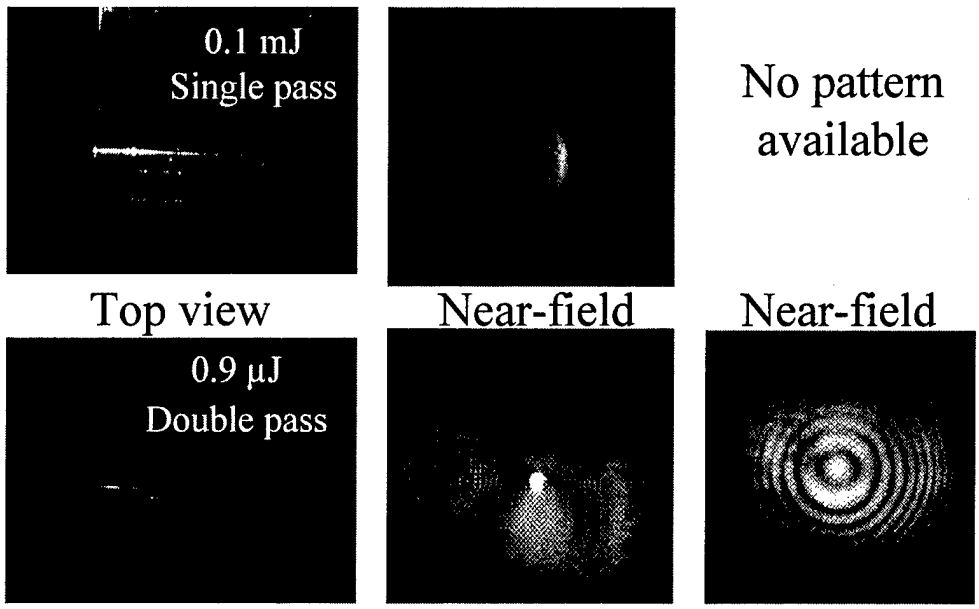

Figure 6. Direct-write buried waveguides in glass by femtosecond pulse laser. The top and bottom images are regions modified above and below the photo-damage threshold, respectively.

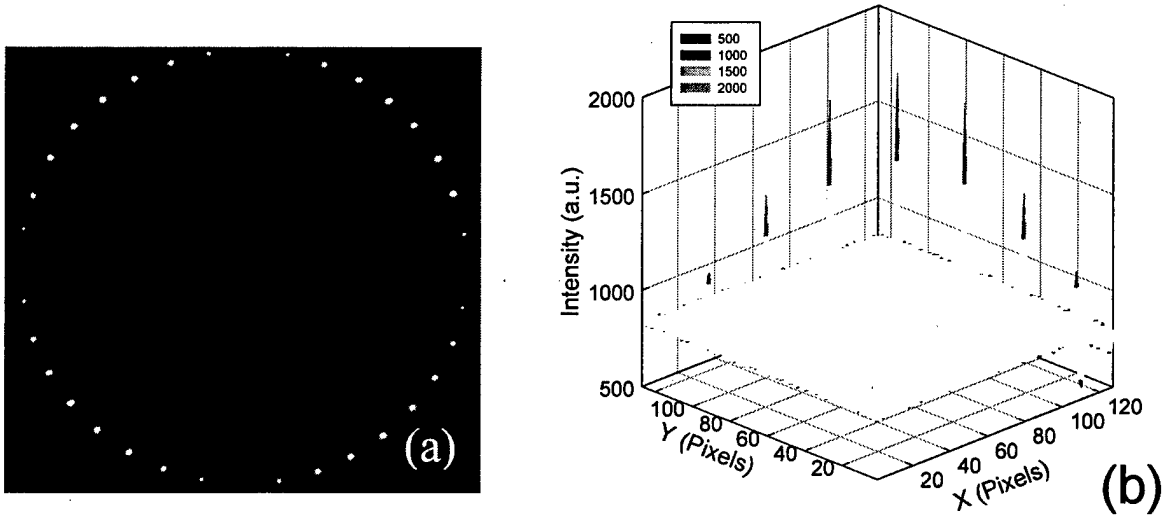

Fig. 7 (a) Transmission image of laser modified regions under a cross polarized light, the polarization direction of the laser beam is rotated 10° for each modification, (b) the change of transmitted light intensity in the first quarter.

Conclusions

Initial studies show that femtosecond laser processing is a promising manufacturing technology to fabricate micro-components. We have demonstrated with a basic understanding of travel velocity and layer decrement on resulting channel morphology, complex shapes can be fabricated in stainless steel. A key factor in producing clean features is choosing the correct layer decrement that allows the ionized species to escape the channel. Using a unique non-linear absorption behavior, we have demonstrated that femtosecond laser pulses, when properly adjusted, can locally modify the glass structure and directly fabricate waveguides in bulk glass. Results show these laser-modified regions possess an optical birefringence property which can be controlled by the polarization direction of the laser beam. The capability of creating and controlling birefringence properties in glass by laser processing could have significant implications for the development of novel optical devices.

Acknowledgments

This work supported by the U. S. Department of Energy under contract DE-AC04-94AL85000. Sandia is a multiprogram laboratory operated by Sandia Corporation, a Lockheed Martin Company, for the United States Department of Energy.

References

1. J. J. Sniegowski, "Moving the World with Surface Micromachining," *Solid State Technology*, February Issue, pp. 83-90. 1996.

2. J. Hruby, "LIGA Technology and Applications", *MRS Bulletin, Vol. 26, No. 4*, p. 337, 2001.

3. G. L. Benavides, L. F. Bieg, M. P. Saavedra, E. A. Bryce, "High Aspect Ration Meso-scale Parts Enabled by Wire Micro-EDM", *Journal of Microsystems Technologies, Vol. 8, No.6*, p. 395, 2002.

4. D.P. Adams, G.L. Benavides, "Micrometer-scale Machining of Metals and Polymers Enabled by Focused Ion Beam Sputtering", *Materials Research Society, V546, Symposium O Proceedings, April 1999*, pp. 201-205, 1999.

5. B. N. Chichkkov, C. Momma, S. Nolte, F. von Alvensleben, A. Tunnermann, "Femtosecond, Picosecond, and Nanosecond Laser Ablation of Solids", *Appl. Phys. A 63*, pp. 109-115, 1996.

6. C. L. Atwood, M. C. Maguire, M. D. Baldwin, "RP&M Applications at Sandia National Laboratories", *Stereolithography and Other RP&M Technologies*, Society of Manufacturing Engineers, Dearborn, Michigan, pp. 253-272, 1996.

7. M. L. Griffith, M. T. Ensz, J. D. Puskar, C. V. Robino, J. A. Brooks, J. A. Philliber, J. E. Smugeresky, W. H. Hofmeister, "Understanding the Microstructure and Properties of Components Fabricated by Laser Engineered Net Shaping (LENS)", *Materials Research Society, V625, Symposium Y Proceedings, April 2000*, pp. 9-20. 2000.

8. M. L. Griffith, M. T. Ensz, D. L. Greene, D. E. Reckaway, J. A. Romero, T. B. Crenshaw, L. D. Harwell, T. E. Buchheit, and V. Tikare, "Solid Freeform Fabrication using the WireFeed Process", *Proceedings of the Solid Freeform Fabrication Symposium, August, 1999*, University of Texas, Austin, TX, pp.529-536, 1999.

9. J. Cesarano, R. Seglaman III, P. D. Calvert, "Robocasting Provides Moldless Fabrication from Slurry Deposition", *Ceramic Industry 148*, pp. 94-102, 1998.

10. M. L. Griffith, M. T. Ensz, D. E Reckaway, *Femtosecond Laser Machining of Steel*, Proceedings of SPIE Photonics West 2003: Laser Applications in Microelectronics and Optoelectronic Manufacturing VIII, to be published by SPIE, Bellingham, WA, 2003.

11. S. Nolte, C. Momma, G. Kamlage, A. Ostendorf, C. Fallnich, F. von Alvensleben, H. Welling, "Polarization Effects in Ultrashort-pulse Laser Drilling", *App. Phys. A 68*, pp.563-567, 1999.

12. K. Miura, J. Oiu, H. Inouye, and T. Mitsuyu, "Photowritten Optical Waveguides in Various Glasses with Ultrashort Pulse Laser", *Appl. Phys. Lett. 71*, pp.3329-3331, 1997.

13. D. Homoelle, S. Wielandy, A. L. Gaeta, N. F. Borelli, and C. Smith, "Infrared Photosensitivity in Silica Glasses Exposed to Femtosecond Laser Pulses", *Opt. Lett. 24*, pp. 1311-1313, 1999.

14. S. Cho, H. Kumagai, K. Midorikawa, and M. Obara, "Time-Resolved Dynamics of Plasma Self-Channeling and Bulk Modification in Silica Glasses Induced by a High-Intensity Femtosecond Laser", *First International Symposium on on Laser Precision Microfabrication, V4088, Proceedings of SPIE, June 2000*, pp. 40-43, 2000.

15. C. B. Schaffer, J. F. Garcia, and E. Mazur, "Bulk Heating of Transparent Materials Using a High-Repetition-Rate Femtosecond Laser", *Appl.P hys. A 76*, pp.351-354, 2003.

16. J. W. Chan, T. R. Huser, S. H. Risbud, and D. M. Krol, "Modification of the Fused Silica Glass Network Associated with Waveguide Fabrication Using Femtosecond Laser Pulses', *Appl. Phys. A 76*, pp.367-371, 2003.

17. K. Miura, J. Qiu, T. Mitsuyu, and K . Hirao, "Preparation and Optical Properties of Fluoride Glass Waveguides Induced by Laser Pulses", *J. Non-Cryst. Solids 256&257*, pp. 212-219, 1999.

18. D. R. Tallant, B. C. Bunker, C. J. Brinker, and C. A. Balfe, "Raman Spectra of Rings in Silicate Materials", *Materials Research Society, V73, Symposium Y Proceedings, November 1986*, pp. 261-267. 1986.

19. P. Yang, G. R. Burns, J. Guo, T. S. Luk, and A. G. Vawter, "Femtosecond Laser Pulse Induced Birefringence in Optically Isotropic Glass", submitted to Appl. Phys. Lett., 2003.

ALGINATE-BASED RAPID PROTOTYPING SYSTEM

P.J. BARTOLO, R. LAGOA, A. MENDES

Department of Mechanical Engineering, School of Technology and Management
Polytechnic Institute of Leiria
Morro do Lena, Alto do Vieiro, Leiria, Portugal

Reviewed, accepted August 13, 2003

Abstract

Alginate hydrogels are an import class of ionic biopolymers for medical and biotechnological applications, produced by the combination of alginate with a proper cross-linking agent. During the gel formation, cross-links can be formed between the alginate chains and cationic species, changing the elastic behaviour of the material that controls the volume change phenomena of the gels.
This paper proposes a new rapid prototyping system to produce three-dimensional alginate structures by extruding, layer-by-layer, a previously prepared solution of sodium alginate in water mixed with a solution of calcium chloride, both of known concentration. The building process to obtain these gel structures is described, from a chemical point of view, and some obtained structures are shown. The alginate concentration over both the kinetics and accuracy effects of the process is investigated. The preliminary findings of this research work promise to open an exciting new area for medical applications.

Keywords: Alginate, Hydrogels, Biomimetics, Medical Applications, Rapid prototyping.

Introduction

The engineering activity, a *design by human* process, is usually portrayed as a unique human process, relying on the intuition, experience and judgment of engineers and designers, to create a representation of objects meeting a set of requirements. However, there is also a *design by nature* (Bartolo and Bartolo, 2003) process, the process through which all the organisms dynamically adapt to its environment, performing its different functions, such as respiration, reproduction, sensing, movement, etc. This *design by nature* is an evolutionary transformation process with a unique goal, the survival of each population of organisms through the correct adjustment to the environment. This kind of design process has been optimised throughout years and years of natural evolution.

Just as an ecosystem incorporates change and adapts towards self-sustaining processes, lessons from nature can be used to support and optimise the *design by human* activity. The philosophy under this research project is the belief that engineers can learn with nature. This process of borrowing the best from nature is called biomimetics (Jeronimidis and Atkins, 1995) and this research study focuses on this new concept, investigating a new route to produce three-dimensional patterns in alginate hydrogels for medical applications, through a biomimetic free form manufacturing system. This system intends to replicate natural procedures used by some marine brown algae, namely *Laminaria Hyperborea*, to produce alginate, a structural component of the algae.

Hydrogels have been receiving much attention due to their potential use in a wide variety of biomedical applications, including tissue engineering scaffolds, drug delivery, contact lenses, corneal implants and wound dressing (Griffith and Naughton, 2002; Garcia and Ghaly, 1996;

Kim et al., 1998). Most hydrogels are usually synthesized using reactive monomers and cross-linkers. However, they do consume non-renewable resources, employ hazardous manufacturing steps and are not biodegradable, apart from not always being biocompatible so their use in medical applications is limited. Consequently, research attention has been centred on generating hydrogels from natural and biocompatible polymeric materials, such as collagen, gelatin, chitosan and alginate. Biomaterials present properties, such as biocompatibility, biodegradability, sensitivity to pH, electrical or temperature stimuli, that enables its use in biotechnology and medical applications.

Biologic manufacturing system

The alginate-based rapid prototyping system, which is in a preliminary research stage, intends to produce alginate solid structures by extruding a previously prepared solution of sodium alginate in water mixed with a solution of calcium chloride, both of known concentration. Understanding the reaction kinetics of the gelation process of alginate-based systems is the first step for the development of an intelligent system leading to the design, optimisation and control of an alginate-based rapid prototyping system.

Alginate is a natural linear polysaccharide that contains 1,4-linked β-D-mannuronic (M) and α-L-guluronic (G) acid residues (Figure 1), arranged in a non-regular and block-wise fashion along the chain (Kang *et al*, 2002). The biological properties of this biopolymer have been exploited in numerous medical and surgical applications, such as drug delivery, cell encapsulation, etc (Gombotz and Wee, 1998; Bucke, 1987).

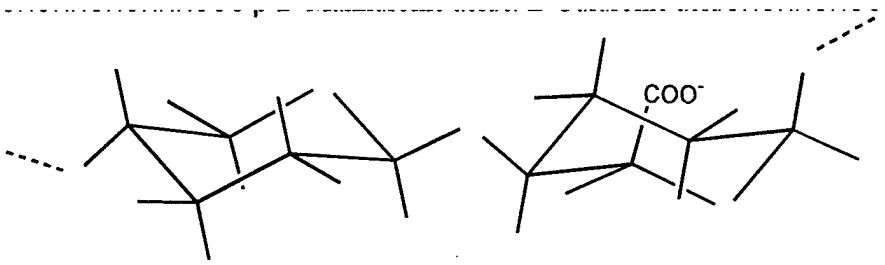

Figure 1: Structure of an alginate showing a linkage between the mannuronic and guluronic acid.

Gelling occurs when divalent ions (Ca^{2+}, Ba^{2+}, Fe^{2+}, Sr^{2+}, etc.) or trivalent ions (Al, etc.) take part in the interchain ionic binding between G-blocks in the polymer chain giving rise to a three dimensional network. Such binding zones between the G-blocks are often referred to as "egg boxes" (Figure 2). This ions act as cross-linkers that stabilise alginate chains forming a gel structure, which contains cross-linked chains interspersed with more freely movable chains that binds and entraps large quantities of water. The gelling process is characterised by a re-organisation of the gel network accompanied by the expulsion of water (Serp *et al.*, 2002).

Its reactivity with calcium and the subsequent gel formation capacity is a direct function of the average chain length of the G blocks, showing a great affinity for Ca^{2+} ions (Gombotz and Wee, 1998). Gels made of M-rich alginate are softer and more fragile, and may also have lower porosity. This is due to the lower binding strength between the polymer chains and to

the higher flexibilities of the molecules. The gelling process is highly dependent upon diffusion of gelling ions into the polymer network.

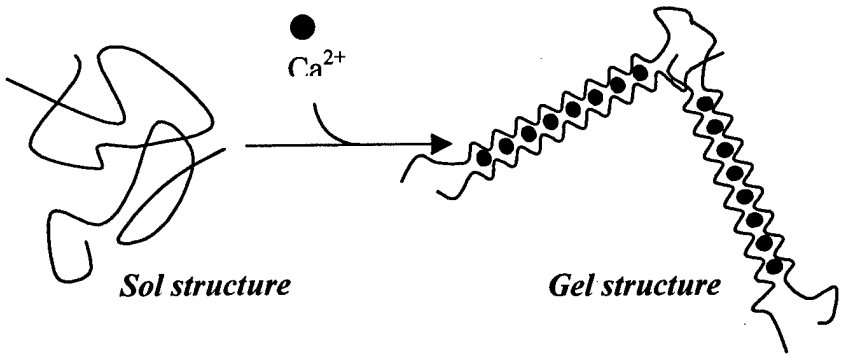

Figure 2: Alginate gelling results from reticulation of the chains by calcium ions.

Material

Sodium alginate was purchased at Panreac (Barcelona, Spain). Calcium chloride was supplied by Carlo Erba (Milano, Italy). All solutions were prepared with pure water, with conductivity of 0.054 μS/cm. Alginate solutions were prepared by addition of weighted portions of sodium alginate to measured volumes of water. Due to their high viscosity, these solutions were agitated by orbital shaking for three hours at 50 °C to ensure good homogeneity. Calcium chloride solution 5% (w/v) was obtained dissolving the salt in water. This solution was diluted to obtain solutions containing different concentrations of calcium chloride.

Results

To evaluate the kinetics of the gelling process solutions, containing different concentrations of alginate and different concentrations of calcium chloride ($CaCl_2$), they were prepared and mixed at room temperature. The effect of the alginate concentration is shown in Figure 3, which describes the weight loss as a function of time for solutions containing different amounts of alginate (1% and 2%) mixed with a solution of 5% $CaCl_2$. Figure 4 illustrates the variation of weight loss as a function of time, for a solution containing 2% of alginate mixed with solutions containing different amounts of $CaCl_2$. The experimental data (discrete values), was fitted using a sigmoidal equation. Fitting the experimental data enables us to have a continuous range of values to better evaluate the gelation process. To correlate the experimental data and the values obtained from the sigmoidal equation, a numerical routine using the Marquardt-Levenberg (Press *et al.*, 1986) multivariable non-linear regression method was employed. A good correlation was achieved by controlling the number of steps, the increment and a small tolerance parameter, corresponding to the difference of values at the step n+1 and values at the step n, which is used for convergence purposes.

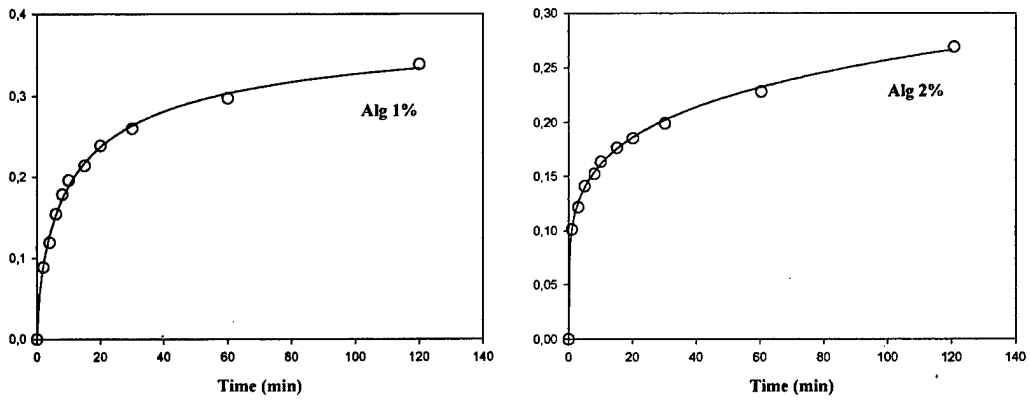

Figure 3: Weight loss *vs* gelation time for two solutions containing different concentrations of alginate mixed with a solution of of 5% $CaCl_2$

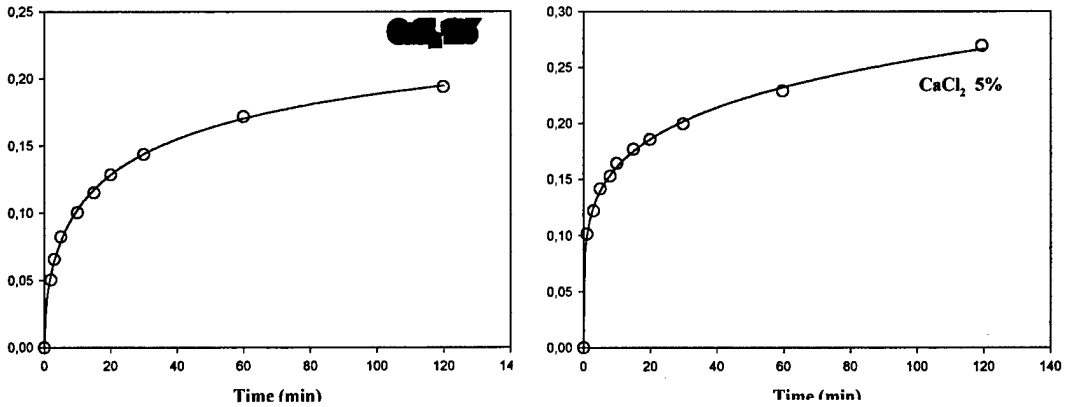

Figure 4: Weight loss *vs* gelation time for a solution containing 2% of alginate mixed with solution containing different concentrations $CaCl_2$.

The weight loss increases with time and is more significant for samples produced by solutions containing low contents of alginate and high contents of calcium chloride is shown in Figures 3 and 4. This is due to two main reasons:

the amount of water present in the initial alginate solution, which is higher in more dilute solutions

the kinetics of the gelation process, which is higher whenever solutions containing higher concentrations of $CaCl_2$ are used.

The calcium divalent ions act as cross-linkers that stabilise alginate chains forming a gel structure. Therefore, increasing the concentration of calcium chloride present in the solution increases the cross-linking of polymeric chains and the expulsion of water. During the gel formation, calcium ions diffuse from the liquid solution to the forming gel and its complexation by the carboxylic groups of G blocks increases the gel stiffness. This phenomenon is accompanied by a significant loss in water at counter-current of the flux of calcium ions (Figure 5). Ahmad and Huglin (1994) and Hu and Lin (1994) claim that the water contained in alginate gels can been found in two states: free-water and non-free-water.

Therefore, it is expected that the water leaving the gel during the gelation process is the one which interacts less with the polymer (free-water).

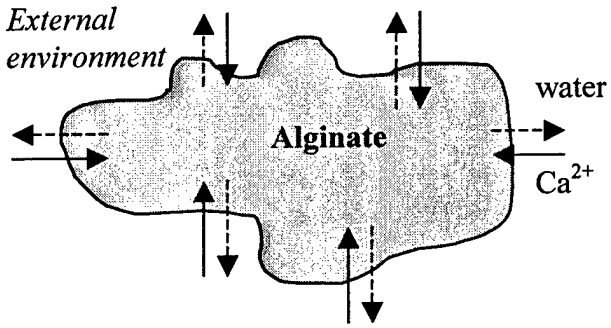

Figure 5: The diffusion of chemical elements during the gelation process of alginate structures.

Figure 6 compares the variation of the rate of weight loss with time as a function of both alginate and $CaCl_2$ concentration. This Figure shows that maximum value of the rate of weight loss is almost independent of the concentration of alginate or calcium chloride and occurs very fast, in less than one minute. However, the rate of weight loss is higher for samples produced with solutions containing higher concentrations of alginate or solutions containing higher concentrations of $CaCl_2$.

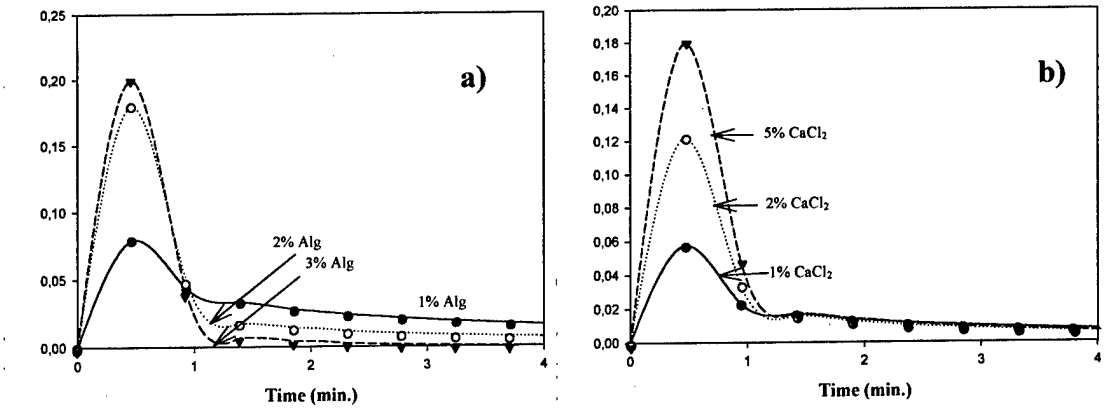

Figure 6: Variation of the rate of weight loss *vs* time as a function of a) alginate concentration for samples produced through a solution containing 5% of $CaCl_2$; and b) calcium chloride concentration for samples produced through a solution containing 2% of alginate.

The variation of the maximum value of the rate of weight loss with the concentration of calcium chloride for samples produced using a solution of 2% of alginate was fitted using a sigmoidal equation (r^2=1) as shown in Figure 7. This variation reveals two main regions. The first region corresponds to the gelation processes performed with solutions containing concentrations of $CaCl_2$ lower than 3%. In this region, the concentration of $CaCl_2$ has great impact on the rate of weight loss and consequently on the gelation kinetics. The second region appears at high values of CaCl2. This can be attributed to diffusion limitations of the divalent ions of Ca^{2+} as the gel structure is formed. Analogous behaviour is observed in Figure 8 for

the variation of the maximum value of the rate of weight loss with the concentration of alginate produced through a solution of 5% of calcium chloride.

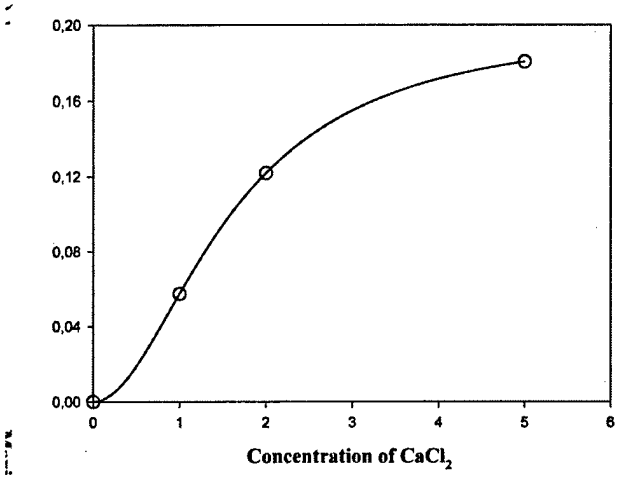

Figure 7: Variation of the maximum value of the rate weight loss *vs.* concentration of $CaCl_2$ for samples produced through a solution containing 2% of alginate.

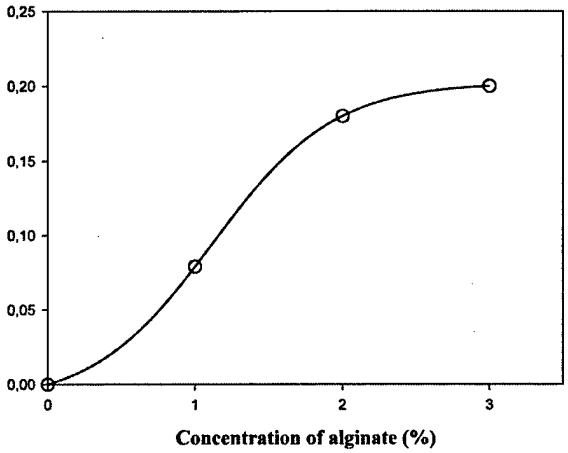

Figure 8: Variation of the maximum value of the rate weight loss *vs.* concentration of alginate for samples produced through a solution containing 5% of $CaCl_2$.

Due to the loss of water during the gelation process, high shrinkage values are observed compromising the accuracy of the process in terms of the dimensional generation of three-dimensional structures. The shrinkage is a function of the kinetics of the gelation process and, consequently, is a function of the concentration of alginate and calcium chloride. Figure 9 shows the variation of the linear shrinkage as a function of time and weight loss of a disc produced through a solution with 2 wt% of alginate combined with a solution containing 5% of $CaCl_2$.

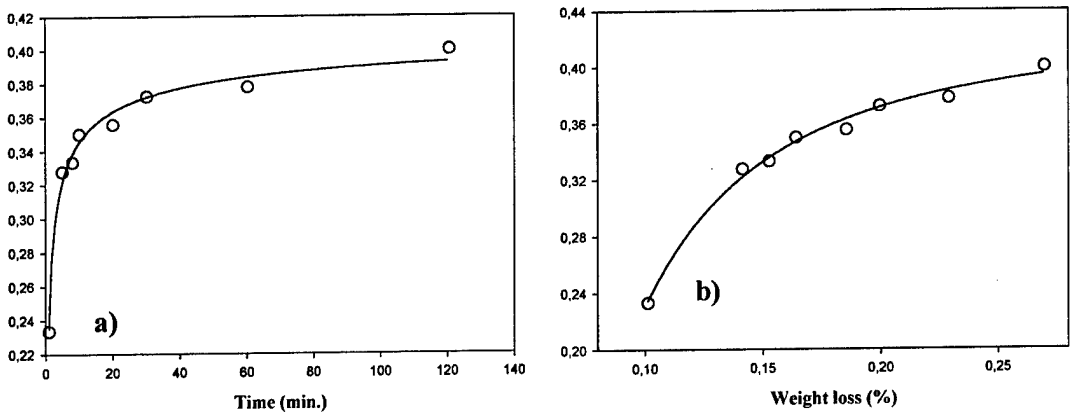

Figure 9: Variation of the shrinkage as a function of a) time and b) weight loss of a disc produced through a solution with 2% of alginate mixed with a solution containing 5% of $CaCl_2$.

The accuracy in the definition of the geometric shape of alginate structures is also strongly dependent on both the concentrations of alginate and calcium chloride. Figure 10 displays the shapes of different circular structures produced by mixing a solution with 2% of alginate with solutions containing different concentrations of $CaCl_2$. A better definition is obtained using high contents of alginate and $CaCl_2$. The gelation process of alginate structures will enable to retain the shape of structures during a large period of time (see Figure 11), owing to the fast process of he gelation rate during the first 5 minutes, that slows down afterwards slowing down the rate of weight loss.

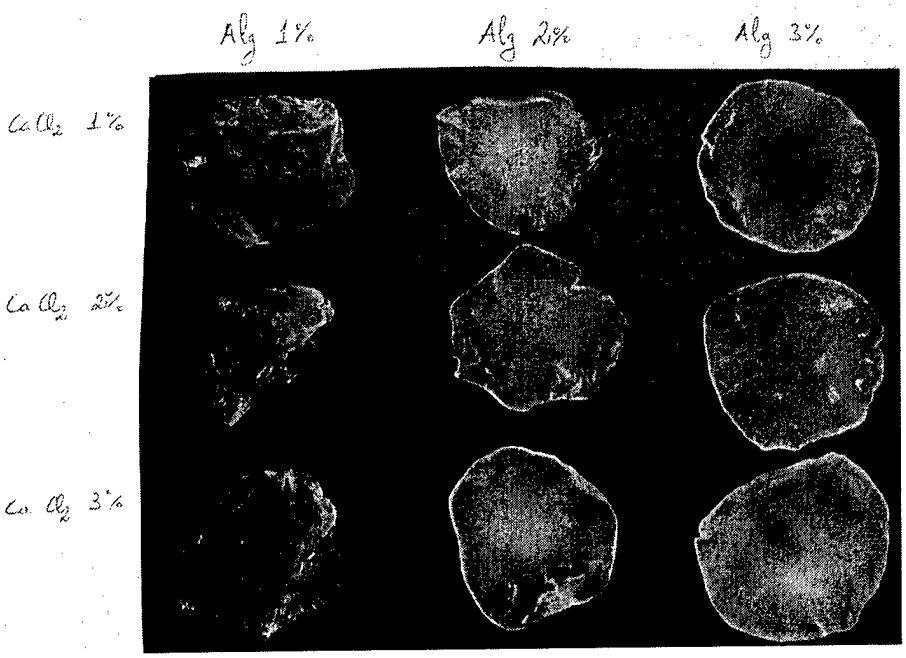

Figure 10: Circular structures produced by mixing solutions containing different concentrations of alginate with solutions containing different concentrations of $CaCl_2$.

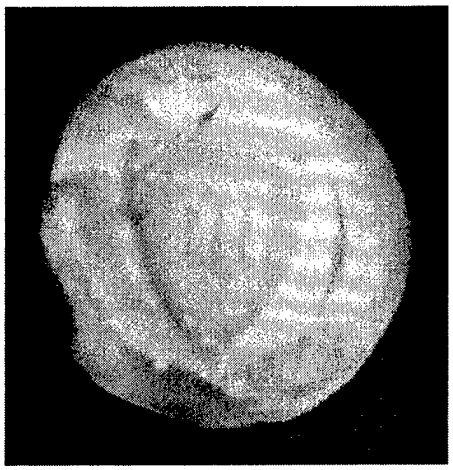

Figure 11: An alginate structure three weeks after its generation.

A phenomenological model previously developed for stereo-thermo-lithographic processes (Bartolo and Mitchell, 2003; Bartolo and Mitchell, 2001) was adopted to evaluate the kinetics of the gelation process of alginate systems. According to this model, the rate of weigh loss, dW/dt, is given by the following equation:

$$\frac{dW}{dt} = \Gamma \cdot W^m (1 - W)^n$$

where Γ is the gelation rate constant, W is the fractional value of weight loss, and m and n are the exponential coefficients of the kinetic model. All the kinetic parameters have been found to be dependent on both the alginate and calcium chloride concentration.

The rate constant is given by the following equation:

$$\Gamma = \xi \cdot \exp\left(\frac{\gamma}{[CaCl_2]}\right) \cdot \exp\left(\frac{\varphi}{[Alg]}\right)$$

where ξ, γ and φ are constants, $[CaCl_2]$ is the concentration of calcium chloride and [Alg] is the concentration of alginate. The rate constant was found to be dependent on the alginate and calcium chloride concentrations in an Arrhenius way as shown in Figure 12.

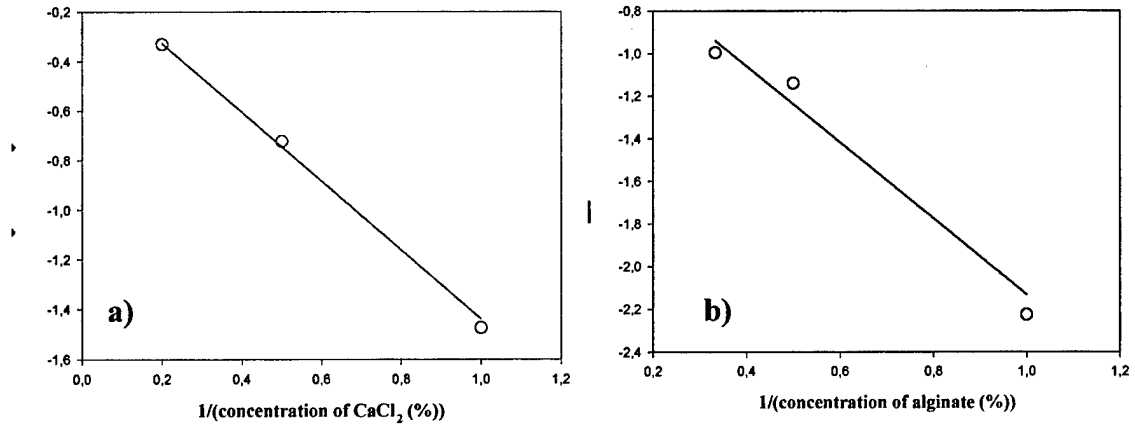

Figure 12: a) Variation of ln (k) *vs.* (1/concentration of $CaCl_2$) for samples produced using a solution containing 2% of alginate. b) Variation of ln (k) *vs.* (1/concentration of alginate) for samples produced using a solution containing 5% of $CaCl_2$.

The exponential coefficients' dependencies with the $CaCl_2$ concentration are determined through an exponential regression (r^2=1 for the exponential coefficient **n** and r^2=0.98 for the coefficient **m**), and are shown in Figure 13. This Figure reveals that the exponential coefficient **m** increases with the concentration of calcium chloride, while the coefficient **n** decreases. Similar behaviour is observed for exponential coefficients' dependencies with the alginate concentration.

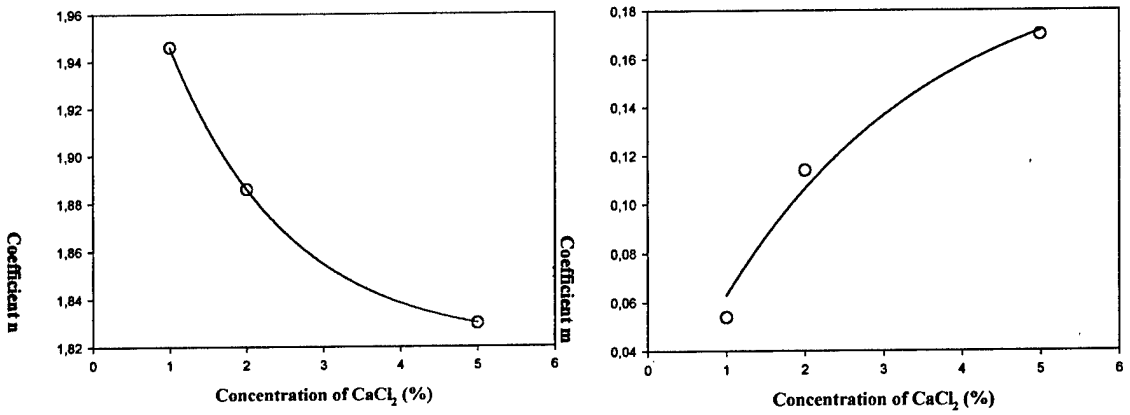

Figure 13: Variation of the exponential coefficients *vs.* concentration of $CaCl_2$ for samples produced using a solution containing 2% of alginate.

The model intends to provide:

a better understanding of the gelation process;

a more accurate estimation of build times and weight loss profiles;

a platform for testing new alginate structures or other bio-polymeric systems and process improvements;

the development of a standard set of parameters and gels for some pre-determined three-dimensional model characteristics.

Conclusions

A new rapid prototyping system to produce three-dimensional alginate structures has been described from a chemical point of view. The gelation process is strongly dependent on both the alginate and calcium chloride concentrations. During the gelation process a significant water loss is observed influencing the shrinkage of the produced structures. Stable alginate structures are obtained after 20 minutes and the shape of these structures is retained for a long period of time.

A kinetic model, describing the gelation process, is also proposed. This computational model will support the development and optimisation of this alginate-based rapid prototyping system, avoiding a great amount of experimental work.

Future work will focus on the relationship between morphology/mechanical properties and gelation kinetics in order to better understand the generation process of gel structures. This will help to produce appropriated porous structures for tissue engineering.

References

Ahmad, M.B. and Huglin, M.B., DSC studies on states of water in cross-linked poly(methyl methacrylate-co-N-vinyl-2-pyrrolidine) hydrogels, *Polymer Int.*, 1994, **33**, 273-277.

Bartolo, H.M and Bartolo, P.J., Learning from biological systems, in Innovative *Developments in Architecture, Engineering and Construction*, Edited by C.J. Anumba, Millpress, Rotterdam, 2003.

Bartolo, P.J. and Mitchel, G., Modelling the curing kinetics of thermosetting resins in stereolithographic applications, *Proceedings of the 7th European Conference on Advanced Materials and Processes*, Published by Associazione Italiana di Metallurgia, 2001.

Bartolo, P.J. and Mitchell, G., Stereo-thermal-lithography: a new principle for rapid prototyping, *Rapid Prototyping Journal*, 2003, **9**, 150-157.

Bucke, C., Cell immobilization in Ca-alginate, *Methods Enzymol.*, 1987, **135**, 175-188.
Garcia, A.M. and Ghaly, E.S., Preliminary spherical agglomerates of water soluble drug using natural polymer and cross-linked technique, *J. Control Rel.*, 1996, **40**, 179-186.

Gombotz, W.R. and Wee, S.W., Protein release from alginate matrices, *Adv. Drug Deliv. Rev.*, 1998, **31**, 267-285.

Griffith, L.G. and Naughton, G., Tissue engineering – current challenges and expanding opportunities, *Science*, 2002, **295**, 1009-1014.

Hu, D.S.G. and Lin, M.T.S., Water-polymer interactions and critical phenomena of swelling in inhomogeneous poly(acrylonitrile-acrylamide-acrylic acids) gels, *Polymer*, 1994, **33**, 4416-4422.

Kang, H., Jeon, G., Lee, M., Yang, J., Effectiveness test of alginate-derived polymeric surfactants, *J Chem Technol Biotechnol*, 2002, **77**, 205-210.

Kim, S.S., Utsunomiya, H., Koski, J.A., Wu, B.M., Cima, M.J., Sohn, J., Mukai, K., Griffith, L.G., Vacanti, J.P., Survival and function of hepatocytes on a novel three-dimensional synthetic biodegradable polymer scaffold with an intrinsic network of channels, *Ann. Surg.*, 1998, **228**, 8-13

Press, H., Flannery, B.P., and Teukolsky, S.A., *Numerical recipes*, Cambridge University Press, Cambridge, 1986.

Serp, D., Mueller, M., Stockar, U. and Marison, I.W., Low-temperature electron microscopy for the study of polysaccharide ultrastructures in hydrogels. II. Effect of temperature on the structure of Ca^{2+}-alginate beads, *Biotechnology and Bioengineering*, 2002, **79**, 253-259.

EXPERIMENTAL STUDIES IN STEREOLITHOGRAPHY RESOLUTION

Benay Sager, David W. Rosen, Meghan Shilling and Thomas R. Kurfess
The Woodruff School of Mechanical Engineering
Georgia Institute of Technology
Atlanta, GA 30332-0405

ABSTRACT

As we move towards micron-scale rapid manufacturing, it is critical to understand build resolution of Stereolithography technology. In order to determine the resolution limitations, positive and negative features on Stereolithography parts were built and analyzed. Results from several experiments were compared to an analytical model and important resolution issues are highlighted. Based on these experimental results, parameters that will maximize build resolution for a number of well-understood shapes are suggested in the paper. Build resolution experimental results, analysis, and measurement techniques are discussed. Conclusions are drawn related to feature shape as resolution limits are approached.

1. INTRODUCTION

Stereolithography (SLA) is a layered rapid prototyping process in which an UltraViolet (UV) laser is used to selectively cure a vat of liquid photopolymer resin in order to physically make a part from the generated CAD model. Even though the technology has been commercially available for over 15 years, no real attempt has been made to apply it to micro manufacturing until recently. With the interest in applying this technology to the micro manufacturing area comes the need to study the resolution of Stereolithography. More specifically, the limits of the resolution, both theoretical and empirical, need to be established.

It is important to make the distinction between resolution and accuracy before moving any further. Accuracy is defined as the measure of closeness to the nominal dimensions and geometry of the intended SLA part (Davis 2001). On the other hand, resolution refers to the fineness of the technology, quantifying the absolute limit of the technology.

2. STEREOLITHOGRAPHY RESOLUTION

Stereolithography resolution is affected by pre-build and build software (Software Imposed Parameters or SIP) and parameters that are inherent in the process (Process Parameters or PP). More information about the classification of resolution-affecting parameters could be found in (Sager and Rosen 2002). SLA resolution can be separated into horizontal (x-y plane) and vertical (z plane) resolution issues, and this paper will focus on the effect of horizontal resolution issues. The resolution limiting factors in horizontal domain are:

- Linewidth compensation (SIP)
- Laser beam spot diameter (PP)
- Stereolithography grid (PP)
- Resolution of the .stl file (SIP)

The laser beam spot diameter and the linewidth compensation parameter are the two parameters that have the most influence on horizontal resolution of the process on mesoscale manufacturing. Simply put, the laser beam spot diameter on the build surface is the smallest feasible feature size that can be scanned. Linewidth compensation determines how the laser beam should be offset when scanning a feature so that a cross-section would not be too small or too large. A brief description of these two parameters will be given. However, it is important to keep in mind that all four parameters would have significant influence when micron-size manufacturing is concerned.

2.1 Laser Beam Spot Diameter

The laser beam diameter is fixed at 200 μm on the build surface for most 3D Systems' SLA systems. In theory, this is the absolute limiting size of a feature that can be built. However, because of the scanning patterns, the smallest feature that can be built is around one-and-a-half times the laser beam diameter, around 300 μm. In high resolution systems such as the 3D Systems' Viper Si2 machine, the laser beam spot diameter is 75 ± 15 μm, and features as thin as 80 μm have been built using this spot size.

2.2 Linewidth Compensation

The linewidth compensation parameter ensures that the cross section of thin parts is scanned correctly by shifting over the center of the laser beam spot. In other words, linewidth compensation compensates for the width of the cured linewidth.

The default value for linewidth compensation is 125 μm, which is ½ of the laser beam diameter. When a rib that is 250 μm is to be built, if the default value of linewidth compensation is applied, the outline of the rib is shifted towards the inside of the profile and a line is created rather than a closed profile. Since a line is not interpreted by the SLA system as part of a cross-section, it would not be scanned. On the other hand, if a smaller linewidth compensation value such as 25 μm is used, the rib feature will be scanned. This would result in a thicker-than-desired rib that is 400 μm thick; however, the feature would not be altogether omitted. However, as aforementioned, it could also result in very inaccurate thin features.

3. ANALYTICAL BACKGROUND

Stereolithography is a complex process that is enabled by a number of mechanisms working together. Because of this, it is important to identify the main components that have a bearing on the theoretical resolution for the process.

As the laser beam is scanning along the vat surface, a cured line is formed. The shape of this line is a parabola (Jacobs 1992), and its cure depth is given as:

$$C_d = D_p \ln(E_{\max} / E_c) \qquad \text{(Equation 1)}$$

where C_d is the cure depth, D_p is the penetration depth for a resin, E_{max} is the maximum centerline laser exposure on the build surface, and E_c is the critical exposure for a resin. Equation (1) is known as the working curve for SLA, where D_p and E_c are resin constants. In the horizontal platform, the width of the cured line depends on the laser beam spot radius as well as a resin constant:

$$L_w = W_o \sqrt{2C_d / D_p} \qquad \text{(Equation 2)}$$

where L_w is the cured linewidth and W_o is the laser beam spot radius. For the linear portion of the working curve, the range of values for the cure depth can be estimated as $D_p < C_d < 4D_p$, which is equivalent to the range $1 < C_d / D_p < 4$ (Jacobs 1992). Therefore, it is possible to speak of a meaningful range of theoretical cured linewidth values for the SLA process. This is shown in Table 1 for different SLA machines.

The width of a wall formed by a stack of scanned lines can be computed using Equation (3) (Rosen 2002), where n is the number of layers.

$$width = 2\left[\frac{W_o^2}{2}\ln\left(\sqrt{\frac{2}{\pi}}\frac{P_L}{W_o V_s E_c}\sum_{k=0}^{n-1} e^{-kl/D_p}\right)\right]^{\frac{1}{2}} \qquad \text{(Equation 3)}$$

Table 1. Typical Stereolithography cured linewidth values

Machine		Resin		L_w (mm)			
Name	W_o (mm)	Name	D_p (mm)	Low ← Typical →			High
				$C_d/D_p=1$	$C_d/D_p=2$	$C_d/D_p=3$	$C_d/D_p=4$
SLA 250	0.12	DSM 7110	0.14	0.170	0.240	0.294	0.339
SLA 3500	0.125	SL 7510	0.145	0.177	0.250	0.306	0.354
Viper si2	0.125	SL 5510	0.12	0.177	0.250	0.306	0.354
Viper si2	0.125	DSM 10120	0.158	0.177	0.250	0.306	0.354
Viper si2 HR	0.0375	SL 5510	0.12	0.053	0.075	0.092	0.106
Viper si2 HR	0.0375	DSM 10120	0.158	0.053	0.075	0.092	0.106

From Table 1, it can be seen that the Viper si2 machine, when operated in the high-resolution mode, has a smaller laser beam spot radius. This means that thinner cured linewidth values of between 0.053 and 0.075 mm (53 to 75 microns) can be expected when using this machine. These values are important to keep in mind when the limits of resolution are considered.

4. EMPIRICAL STUDY

To quantify the effects of laser beam spot diameter and linewidth compensation on horizontal build resolution, a number of experiments were performed with different part cross-sections. Of particular interest was the predictability of negative and positive features. After building these cross-sections in Stereolithography machines, they were measured using a number of measurement techniques. The description of each cross-section, its outline, what it was intended to test, and how it was measured are shown in Table 2.

Table 2. Shapes used for empirical testing

Shape	Ribs	Grids	Gears	Holes
Outline	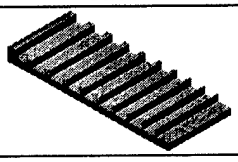	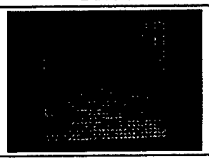	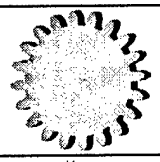	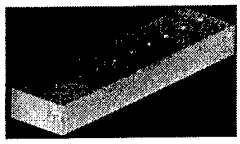
Detail	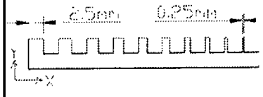	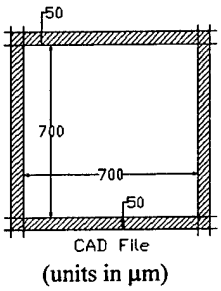	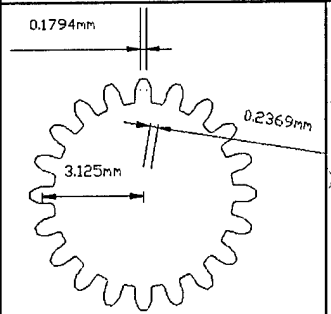	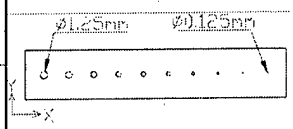
What it is testing	Resolution for positive features	Resolution variation with build location	Resolution variation with curved surfaces/features	Resolution for negative features
How it is measured	Micrometer	White light Interferometer	Optical microscope	White light interferometer

The detail drawings show the horizontal cross-section for each shape as seen from the top view. The ribs were built using a number of different machine/resin combinations in order to quantify the resolution of different machines. The thickness of the ribs varied from 2.5 mm to 0.25 mm with 0.25 mm increments.

The rectangular grids were built in order to quantify how the thickness of a wall varies with respect to changing location on the build platform. The grids were built at the center of the vat and at the corners. The intended wall thickness for each grid was 50 μm.

A spur gear with 20 teeth was selected as a suitable profile for resolution study; not only because gears are very important in engineering, but also they have curved positive and negative profiles. The spur gear had 6.25 mm pitch diameter with an intended gap of 0.237 mm between teeth and tooth thickness of 0.179 mm.

In order to test the building ability of negative features, a part with holes was designed. This part had vertical holes that ranged from 1.25 mm to 0.125 mm in diameter with 0.125 mm increments. In all the parts built, the effect of the linewidth compensation parameter was also studied.

4.1 Data Collection and Analysis

Depending on the outline of the cross-section measured and the level of measurement detail required, different measurement techniques were used in this study. For measuring the thickness of the rib parts, using a micrometer was sufficient. For the gear cross-sections, the outline of the gears as well as the measurements were desirable. Therefore, an optical microscope with a 5x zooming lens was sufficient.

Interferometers, in particular white light interferometers, are currently being used to inspect mesoscale parts. Georgia Tech has a Zygo NewView 200 white light interferometer, which was used for collecting much of the grid and hole data. The interferometer uses the principle of interference to create a 3-dimensional surface profile of the parts. This data, however, is limited to a single view due to the slope limitations on measurement. Because the white light interferometer was initially created to measure surface characteristics such as surface roughness, it was designed to have very good resolution in the z-direction (out of plane). This resolution is more than adequate for mesoscale parts. The resolution in the lateral (x and y) directions, however, is not quite as good but will be sufficient for initial measurements. The lateral resolution is dependent on the objective being used. For the objectives in the Precision Machining Laboratory the lateral resolutions are 2.2 μm and 8.8 μm (for the 10x and 2.5x objectives, respectively) at regular camera resolution.

Conventional coordinate metrology is not appropriate for the type of data that are gathered using a white light interferometer. A single surface does not hold enough information for comparison to a CAD model or to an analytic surface (other than a plane). Because a CAD model is a series of surfaces that intersect, data from other surfaces are needed to properly orient the model or surface to the data. Due to this limitation, two-dimensional curves such as lines and circles are of interest.

For two-dimensional analysis, the data on a single surface are not what need to be analyzed. The edges of the data hold the important information. Therefore, it is necessary to extract edge data points from the original point cloud before any dimensional analysis can be performed. The edge point extraction takes several steps. First, a plane is fit to the surface data and an "image" is created. The pixel size of the image is set to the distance between the evenly spaced data points and the intensity, or color, of the pixel is directly related to the height of the pixel above the fit plane. After the "image" is created, a median filter is applied to remove noise.

After being filtered, edge points are either located by binarization and a simple row and column sweeping algorithm or an edge detector and contour tracking algorithm based on the idea of finding the center of mass in combination with a contour tracking technique. The edge points can then be analyzed by being fit to two-dimensional shapes such as lines, circles, and ellipses. This entire process is illustrated in Figure 1.

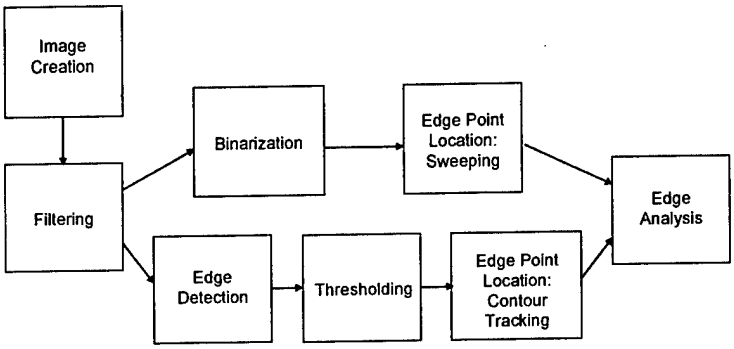

Figure 1: Analysis Flowchart

The methods described above have been validated using generated test data of circles and bars. Perfect circles and perfect bars yielded perfect results. When known noise was added, both sets yielded expected results. This procedure is fully outlined in (Shilling 2003).

4.2 Rib Parts

The outline of the rib parts and their detail cross-section were presented in Table 2. The rib parts were built using a number of machine/resin combinations, linewidth compensation, and layer thickness values, which are shown in Table 3. The goal was to quantify the resolution for each machine, along with the effect of different linewidth compensation values. In short, four comparative studies were done with the rib parts:

1. Thickness at tip of rib versus thickness at base of rib
2. Thickness of rib on top surface of build versus thickness of rib on bottom surface of build
3. Resolution of Stereolithography machine used
4. Resolution with respect to linewidth compensation value used

The thickness values at the tip of ribs were very similar to those at the base of ribs. It should be kept in mind that the distance between the tip and base of each rib is very short, about 2.5 mm. Therefore, such a small change in location of the laser beam as it was scanning the parts would not cause a significant change in the resolution of the final parts.

It is known that upfacing and downfacing surfaces in SLA have different resolution. This is partly due to the curing effects, and partly due to the fact that at the bottom of each build support

structures are anchored to the build platform (Jacobs 1996). For all six rib parts built, the thickness for a particular rib (rib 5) at the top and bottom surfaces is shown in Figure 2. There is a consistent thickness difference between bottom and top surfaces. This thickness difference is quantified in Table 4.

Table 3. Build parameters for rib parts 1-6

Part	Machine	Resin	Linewidth Comp. (mm)	Layer Thickness (mm)
1	SLA 3500	SL 7510	0.125	0.004
2	SLA 250	DSM 7110	0.125	0.004
3	SLA 250	DSM 7110	0.025	0.004
4	Viper Si2	SL 5510	0.0375	0.002
5	Viper Si2	SL 5510	0.01875	0.002
6	Viper Si2	SL 5510	Off	0.002

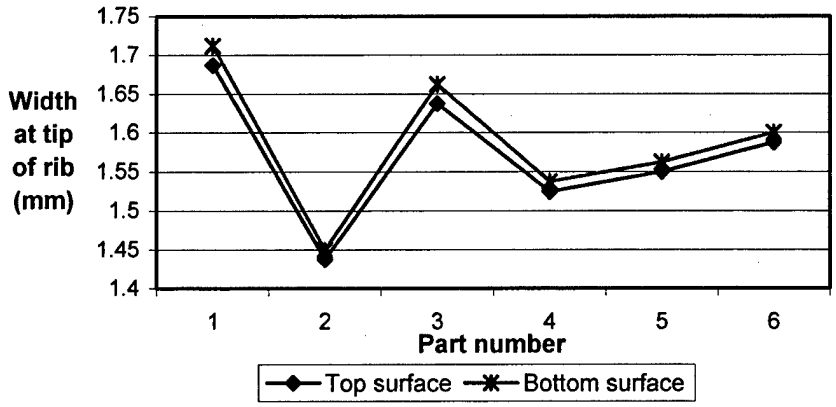

Figure 2. Top versus bottom surface for rib 5 width

Table 4. Difference in thickness between top and bottom surfaces for rib 5

Part number	Bottom surface thickness for rib part number (mm)	Top surface thickness for rib part number (mm)	Difference (μm) [Bottom – Top]
1	1.7125	1.6875	25
2	1.45	1.4375	12.5
3	1.6625	1.6375	25
4	1.5375	1.525	12.5
5	1.5625	1.55	12.5
6	1.6	1.5875	12.5

In Table 4, it can be seen that the thickness difference varies between 12.5 and 25 microns. This is an expected result, since the bottom surface of SLA builds typically have poorer resolution. When a SLA layer is scanned, in order to make sure it would anchor to the previous layer, it is "overcured" by a specified thickness into the previous layer. Additional overcuring of a number of layers causes the bottom surface of a SLA build to have thicker cross-sections than intended; hence a poorer resolution than top build surface. Therefore, it can be concluded that the top surface has features that are on average between 10-20 microns thinner than the bottom surface.

Another aspect of this study is quantifying the resolution of different SLA machines used. For each rib, the difference between the intended and measured thickness for different machines

is shown in Figure 3. It can be seen that when the default value for the SLA 250 machine was used, a part whose ribs were thinner than intended was obtained. On the other hand, as expected, the Viper si2 machine high-resolution build style produced parts with highest resolution.

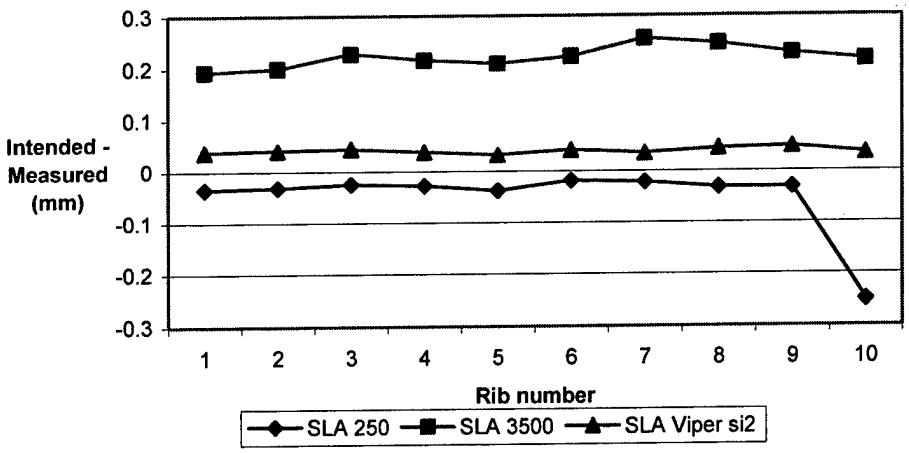

Figure 3. Average dimensional error for different SLA machines

A comparison of rib width values based on the different linewidth compensation values that can be used when preparing a build for the Viper si2 machine was made. Three different linewidth compensation values were used: the default value of 0.0375 mm, 0.01875 mm, and 0 mm. These different values and their resulting measurements are shown in Table 5.

Table 5. Comparison between expected and measured error

Linewidth compensation value used (μm)	Analytical expected error (μm)	Average measured error (μm)	Error discrepancy (μm)
37.5	0	39	**39**
18.75	37.5	57	**20**
0	75	104	**29**

As shown in Table 5, the lowest average error of 39 microns was obtained when the default linewidth compensation value of 37.5 microns was used. When the same default linewidth compensation value is used, the expected error is zero because the thickness of the laser beam is adequately compensated for. There seems to be a consistent error between the measurements and expected results when different linewidth compensation parameter values are used. It can be argued that by accounting for the error based on linewidth compensation value used, the error between the intended and measured thickness could be reduced. Table 5 presents expected error discrepancy within the range of 20-40 microns based on empirical results. It is clear that the parts built will be thicker than intended, and this value can be quantified as between 20 and 40 μm.

4.3 Grid Parts

The grid parts were built for a number of studies, including build location, orientation, and effect of linewidth compensation parameter on build resolution (Sager 2003). However, in this paper, only the effect of build location on build resolution will be presented. Four identical test parts were built simultaneously at the four corners of the build platform of the Viper si2 machine. The labeling for the locations of these parts is presented in Figure 4. Each grid part had

the dimensions of 25 mm by 25 mm in x and y directions respectively. The distance between the center of the vat and the center of the grid parts was 112.5 mm.

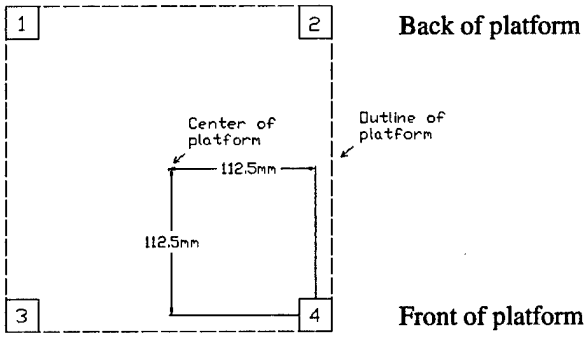

Figure 4. Location of grid parts on build platform

Measurements of the vertical cross-section of the parts taken by researchers at Siemens AG yielded results that suggest a heavy dependence of wall thickness on build location, as shown in Table 6. These measurements were taken from the grids around the center of each grid part and represent the average thickness of the walls. For each wall, the thickness was measured at three locations. These locations were towards the top of the wall, around the center of the wall, and towards the bottom of the wall.

Table 6. Grid average wall thickness with respect to build platform location

Position on platform	Thickness at location (μm)			Representative thickness (μm)
	1	2	3	
Center	126	133	121	127
1	226	265	253	248
2	210	246	274	243
3	250	263	275	263
4	171	217	184	191

Ignoring the smallest and largest values that were obtained at corners 4 and 3 respectively, the representative thickness at the corners can be taken as 243-248 μm. When compared to the wall thickness at the center of the build platform of 127 μm, this value is almost doubled. Such a difference between wall thickness values at center and corner of the build platform suggests that location on the build platform plays a major role in determining how thick a wall will become. This could be attributed to the change in laser beam characteristics as the laser beam moves away from the center of the build platform. For example, in order to adequately calculate the shape of cured line, the changes in the shape and size of the laser beam radius must be taken into account. Moreover, as we move away from the center of the build platform, the laser beam becomes out of focus, causing the wall thickness to become larger.

In addition to change in wall thickness with respect to build location, change in wall thickness with respect to vertical location was observed. This phenomenon is a direct result of overcuring each layer and is shown in Figure 5. In Figure 5, the bottom of the wall is the right side. As shown, the thickness at the bottom of the wall is around 130-145 μm. The left side of Figure 5, which corresponds to the top of the grid wall, was measured to be around 100 μm under the microscope.

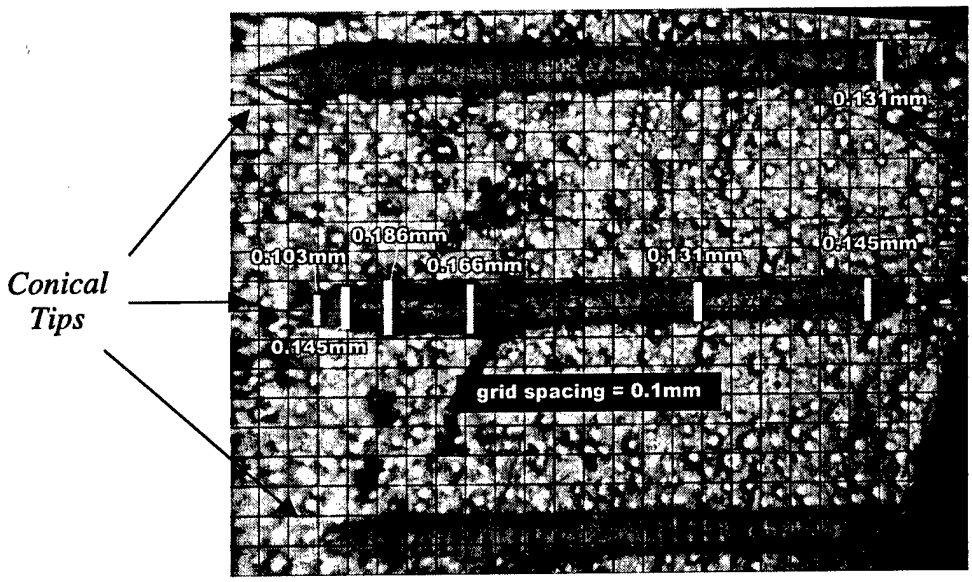

Figure 5. Vertical cross-section of grid walls

As aforementioned, the walls are thinner at the top due to the lack of overcure and print through for the latest-built layers. Print-through is a Stereolithography error that accumulates on a lower layer when an upper layer is scanned. The analytical model expressed by Equation (3) enables an explanation of this cone-tip effect (Rosen 2002; Sager 2003). This model suggests that the wall thickness of the build surface is 78 μm and the representative wall thickness is 95 μm (Sager 2003) for the Viper si2 high-resolution build style. This 17 μm discrepancy is in the middle of the measured overcure related error range of 10 - 25 μm. A representative wall thickness can be computed by adding the analytical thickness estimate to the linewidth compensation error range (20 - 40 μm). This yields an expected wall thickness range of 115 - 135 μm, which is smaller than the observed thicknesses. Additional research is needed to investigate this difference.

Table 7. Analytical, empirical, and expected empirical values for grid part walls

Measurement	Wall thickness on build surface (μm)	Representative wall thickness (μm)
Analytical	78	95
Empirical	100	130~145
Expected range	78 + (20~40) = **98~118**	95 + (20~40) = **115~135**

4.4 Holes

A hole study was performed to determine both the resolution of negative features as well as the changes in hole diameter from the top surface of the part to several layers into the part. In addition to comparing feature sizes in the top and lower layers, the purpose of this test was to determine the smallest hole that could be built.

After initial measurement, the part was ground using a small sample grinder to get a surface finish sufficient for measurement by the interferometer, so that the size of holes beneath the top surface can also be measured. From visual inspection, this was determined to be the 0.375 mm-diameter hole. After x-y-z data sets were collected using the interferometer, the data was

analyzed according to the steps outlined earlier in this paper. The results from measurement of the holes, as well as expected results are presented in Table 8.

Table 8. Radii from Hole Test Parts (in μm)

	PART LOCATION		
Circle	Expected (1)	Center (2)	Center ground (3)
A (1)	635.00	559.67	614.19
B (2)	571.50	500.80	623.16
C (3)	508.00	569.12	496.11
D (4)	444.50	462.41	446.43
E (5)	381.00	386.75	384.09
F (6)	317.50	319.17	312.55
G (7)	254.00	251.93	247.38
H (8)	190.50	193.63	190.50
I (9)	127.00	122.59	110.56
J (10)	63.50	46.09	-

The parts were measured using the Zygo New View 200 white light interferometer with the 10X objective (2.2.μm lateral resolution). There were problems with the Zygo stage, so the largest area that could be analyzed was approximately 700 by 500 μm. This caused some problems with the circles of larger diameters, but was sufficient for circles of smaller diameters.

Not enough data from the largest three holes in the hole test parts was collected to allow for reliable measurement. Although the results are presented, the values given might not represent the actual values of the radii of the holes. Additionally, the smallest hole was not present after the specimen was ground. The difference between the intended and measured hole radii is presented in Figure 6.

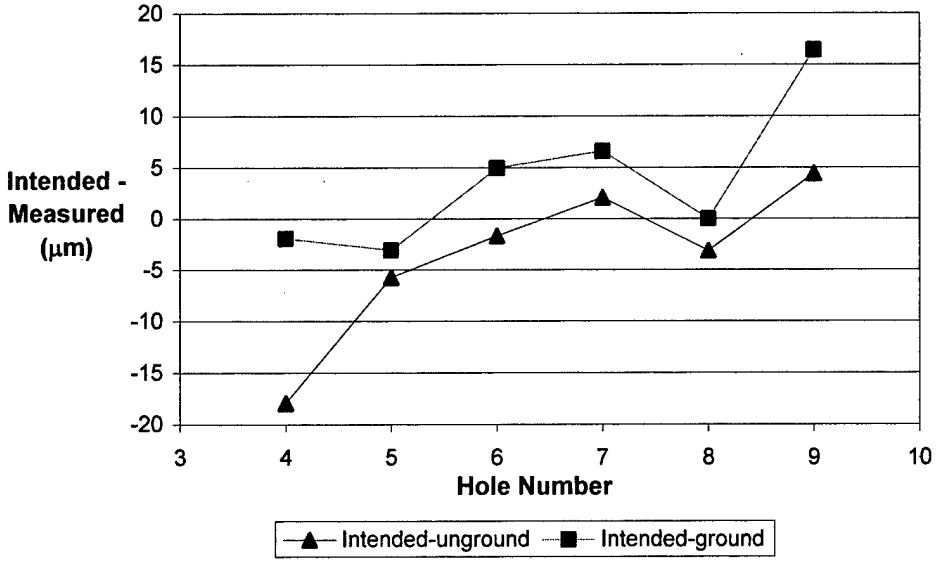

Figure 6: Comparison of ground and unground part

The results from comparing the ground part to the same unground part are presented in Figure 6, ignoring the largest three holes because of problems with the interferometer and the smallest hole because of its disappearance. It is seen that the diameters of the holes for the ground part are slightly smaller than that of the unground part in all cases, reflected by the larger difference between intended and measured hole diameters. This is consistent with the idea that the lower layers are exposed to more UV light; thus have a chance to cure more thoroughly.

4.5 Gears

A number of 6.25 mm-diameter spur gears were built in order to study resolution of curved cross-sections. The gear had teeth width of 179 μm and gap between teeth of 237 μm. The average thickness of gear teeth was 186 μm on top and 198 μm on bottom surface when small feature compensation parameter (SFP) was used. The gap between gear teeth, a negative feature, was 312 μm on top and 280 μm on bottom surface when SFP was used.

It can be said that SFP enabled generation of thin positive features that are more dimensionally accurate on the top surface of a build. In addition, the profile of the gear teeth was much sharper with the use of SFP. It was noticed on the SLA parts that some of the gear teeth lost their curved involute profile accuracy because they were too thin, which shows the limits of SLA resolution were reached with this spur gear profile.

5. CONCLUSIONS AND FUTURE WORK

With the rib parts built, it can be concluded that the bottom surface of SLA parts are thicker than the top surface. For the SLA Viper si2 system, the thickness discrepancy has been measured to be 20-40 μm, which is consistent with the analytical model of the curing process. The grid part experiments suggest that as we move away from the center of build platform, the resolution of SLA machines changes dramatically. Based on the empirical results and comparison with analytical models, a range of expected thickness values can be specified for high aspect ratio walls. Even though the Viper si2 system has a laser beam spot diameter of 75 μm, the realistic range for representative wall thickness is 115-135 μm. The ability to build small negative features using SLA technology has been demonstrated. However, more work is needed in quantifying the smallest negative feature that can be built. For certain shapes that are well understood, values for certain software parameters that would maximize build resolution are presented in Table 9.

Table 9. Use of build parameter values to obtain maximum build resolution

Build/ Recoat Parameter	**Geometry / Part**			
	Grids/ Thin walls and/or features	*Ribs*	*Gears*	*Lenses/ curved surfaces*
Linewidth compensation	Off	Default	Default	Default
Small feature preservation compensation (*Viper si2 only*)	On			
High resolution spatial tolerance (*Viper si2 only*)	On if highly tessellated area			On
Stl file deviation	Lowest allowable surface deviation			$\delta = C_{res} * R$, C_{res}=3.4E-05
Build orientation	45-degree	Vertical	Normal	Vertical
Build location	Center of build platform			
Sweeping	On			

The linewidth compensation parameter's default value should be used for builds other than thin walls. For parts that have thin walls or small features, turning the linewidth compensation off will ensure that the small feature is not omitted by the laser. This is critical for all the SLA machines that do not have small feature preservation compensation parameter.

The laser beam spot diameter is the biggest contributor to the limitation of SLA resolution. The spot diameter determines the size of the smallest feature that could be built on the horizontal platform. Since SLA is a stacking of a number of two-dimensional layers, it can be said that the resolution in the horizontal direction dictates the resolution in the vertical direction. Therefore, being able to control the laser beam spot diameter would improve the process resolution greatly.

For maximum x-y resolution, parts should be built in the center of the build platform if possible. In addition, using the sweeper blade ensures that the resin on the top surface of the SLA build is evenly distributed after each layer is scanned. Ribs or any other high aspect ratio features should be built in the vertical orientation to reduce stair steps.

Although white light interferometry was originally developed for surface measurements, it can be a useful tool in mesoscale part characterization when combined with several image-processing techniques. This method, however, is quite limited in its lateral resolution, speed, and three-dimensional measuring capabilities. In order to increase the speed and completeness of the measurement, new systems need to be developed.

In order to truly quantify the resolution of SLA technology, a study of three-dimensional resolution is needed. In the future, more experiments should be performed with negative features, including shapes that are rectangular such as a square-shaped hole. In addition, a comprehensive cure model that will take into account the effect of focus depth, change of laser beam angle, and resin properties is under study.

ACKNOWLEDGEMENTS

We gratefully acknowledge the support from the RPMI member companies and the George W. Woodruff School of Mechanical Engineering at Georgia Tech. This work was partially funded by the National Science Foundation under Grant Number DMI-9988664.

REFERENCES

Davis, B. E. 2001. "Characterization and Calibration of Stereolithography Products and Processes", *Master's Thesis*, Georgia Institute of Technology, Atlanta, GA.

Jacobs, P. F. (1992). Rapid Prototyping & Manufacturing: Fundamentals of Stereolithography, Society of Manufacturing Engineers.

Jacobs, P. F. (1996). Stereolithography and other RP&M Technologies: from Rapid Prototyping to Rapid Tooling, Society of Manufacturing Engineers.

Rosen, D. W. (2002). ME 7227 Rapid Prototyping in Engineering Class Notes. Atlanta, GA, Georgia Institute of Technology.

Sager, B. 2003. "A Method for Understanding and Predicting Stereolithography Resolution", *Master's Thesis*, Georgia Institute of Technology, Atlanta, GA.

Sager, B. and D. Rosen (2002). Stereolithography Process Resolution. Solid Freeform Fabrication Symposium, Austin, TX.

Shilling, K. M. 2003. "Two Dimensional Analysis of Mesoscale Parts Using Image Processing Techniques", *Master's Thesis*, Georgia Institute of Technology, Atlanta, GA.

Vantico Incorporated (2002). Vantico web page: http://www.vantico.com.

PRELIMINARY INVESTIGATIONS ON THE DEPOSITION OF FINE POWDERS THROUGH MINIATURE HOPPER-NOZZLES APPLIED TO MULTI-MATERIAL SOLID FREEFORM FABRICATION

Pranav Kumar, Elizabeth Beck and Suman Das
Department of Mechanical Engineering
The University of Michigan, Ann Arbor

Abstract

A concept for multi-material solid freeform fabrication is proposed to enable the fabrication of heterogeneous components. This concept features nozzles designed for depositing thin layers of multiple patterned materials followed by selective laser sintering for consolidation to desired densities. Although prior work on the design of small-scale nozzles for powder delivery is lacking, our design is guided by background theory for particle flow through hoppers. Experimental guidelines for the delivery of powders with particle sizes in the 10-125μm range through hopper-nozzle orifices with diameters in the 0.5-2mm range are presented. This is a preliminary investigation of particle flow behavior necessary for continuous mass flow rates under gravity, low gas pressure-assisted flow, and vibration-assisted flow conditions. As proof of concept, several patterned beds of single and multiple materials were deposited on an X-Y table. A simple model to predict the linewidth of lines deposited by gravity flow is presented.

1. INTRODUCTION

The development of SFF techniques for producing a new class of artifacts with spatially-varying structure and multi-functional characteristics is in part dependent upon the ability to deposit and consolidate multiple materials. In particular, the selective laser sintering (SLS) process is well-suited to the incorporation of multiple powdered materials [11]. The SLS process presently uses a roller device to sweep thin layers of a single powdered material across the build area. It has been proposed to replace this roller device by an array of hopper-nozzles that can directly write lines, dots and patterned regions of multiple powdered materials [12].

The designated name "hopper-nozzle" refers to the design of experimental nozzles based on existing hopper theory. In the chemical and process industries, hoppers have been inexpensively designed to store, discharge bulk solids, and eliminate undesirable flow instabilities (i.e. arching, rat-holing, and oscillatory flow). Unfortunately, difficult hopper and powder sizes are avoided due to the lack of fundamental understanding of flow phenomena. This can be attributed to the complex interaction of granular solid and interstitial fluid that plays a large role in delivery through small orifice diameters.

2. BACKGROUND

Granular bulk solids exhibit characteristics unique from any other state. The granular mass is generally an amorphous, random-packing of particles influenced by the interstitial fluid occupying its voids. Unlike a fluid, the pressure under a vertical column of granular material is independent of its height, which makes a constant flow rate of material possible irrespective of the column height.

Many researchers have investigated the flow of a powder through orifices under gravity and have established empirical correlations to predict the mass flow rate [1,7,8,9]. Among all these

correlations, Beverloo's correlation [1] is the most widely used to predict the discharge rate. It is given by

$$G_s = C\rho_B\sqrt{g}\left(D_0 - kd\right)^{2.5} \quad \text{g/s} \qquad (1)$$

where G_s is mass flow rate of particles(g/s), C is empirical constant, ρ_B is bulk density of powder(g/mm^3), g is acceleration due to gravity(mm/s^2), D_0 is hopper orifice diameter(mm), k is empirical constant for particle shape, and d is mean particle diameter. C and k are dimensionless constants and they take the values 0.583 and 1.4 respectively as reported by Beverloo et al. [1].

Spink and Nedderman [2] found that Beverloo's correlation is valid only for powders of particle size greater than 500 μm. Eq. (1) indicates that particle flow rate increases slowly as particle size decreases (curve-1 in Fig. 1). Significant deviations from this equation occur at small particle sizes, where it is found that the discharge rate passes through a maximum and then progressively and rapidly decreases as particle size decreases below 500μm (curve-2 in Fig.1). The reduction in flow rate of fine powders has been attributed to retarding influence of interstitial fluid by various researchers [2, 3, 4]. Spink et al. [2] developed an iterative numerical method based on stress distribution, voidage distribution and air pressure gradient distribution in the powder column to predict the discharge rate. However, their theoretical model did not match their experimental results. Moreover, their theoretical model is cumbersome to implement.

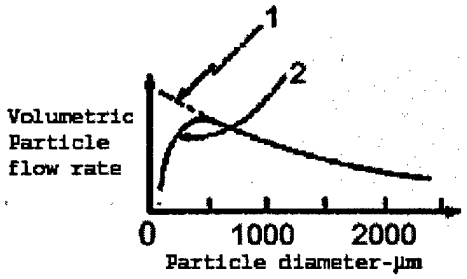

Fig. 1 Volumetric discharge rate vs. particle size [2]

The orifice size used in experiments by various past researchers was very large and on the order of 2-100mm [1,2,7,8,9], because their research was mostly concerned with industrial processing systems, such as feeding of catalyst pallets to a cracking plant. The smallest orifice size found in previous studies was 2mm used in the work of Beverloo et al. [1].

For development of a SLS hopper-nozzle powder delivery system we intend to use orifice sizes in the range 10μm-2mm. The powders used for SLS are typically 0.1-150μm in diameter. Flow behavior for this range of particle size and nozzle size combinations has not been investigated previously. The intent of this study is to determine whether a simple correlation for SLS powder sizes and intended orifice sizes can be extended from Beverloo's correlation. Research on granular flow is still in the exploratory phase, and the time-dependent behavior of a bulk powder material may not yet be based on characteristics of the constituent particles [5]. Progress in this area must depend upon uncovering new correlations between the observed behavior and measured particle characteristics [6]. With this in mind, the study aims to provide experimental results on the use of hoppers with fine powders, the design of the test apparatus, and results of preliminary mass flow rate experiments conducted on a number of particle sizes and hopper-nozzles.

3. EXPERIMENTS

3.1. Hopper-Nozzle Design

Pipette tips, typically used for repetitive liquid dispensing, were an inexpensive and practical choice for producing multiple, nozzles with various opening diameters. The 1-200μL Uni-Tip© from BioPlas Inc., Fig. 2(a), is a siliconized polypropylene pipette tip with polished internal surfaces to help eliminate sample residue. The orifices of pipette tips are of nominal diameter 0.75mm with a half-angle of 6.575° (Fig. 3). They are designed for precise volumetric delivery; however there is no guarantee on the uniformity of the orifice diameters. A pack of 48 tips may have deviation up to 0.1mm.

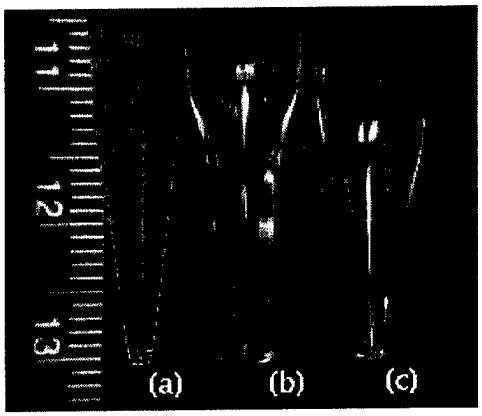

Fig. 2 Pipette tips, pipettes and drawn pipettes are used as test hopper-nozzles

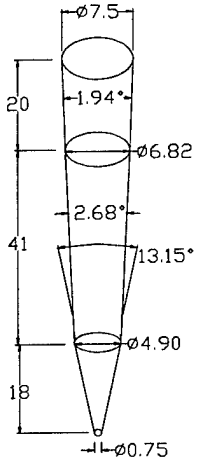

Fig. 3 Pipette tip dimensions

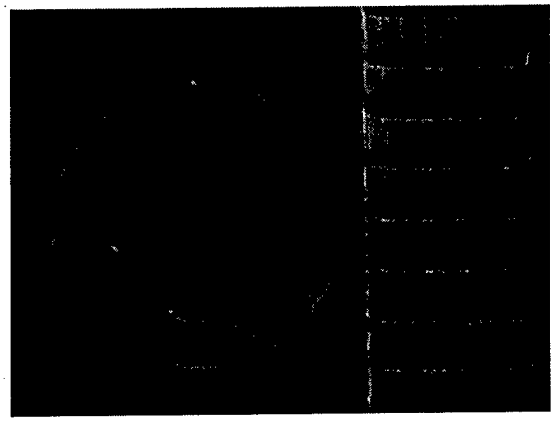

Fig. 4 A high resolution image of the cut orifice at approximately 40 X magnification

Because the tips are made of polypropylene, they were fairly easy to trim with a utility knife under a magnifying glass. Images taken with a high-resolution digital camera (Fig. 4) were used to make diameter adjustments and verify the quality of the cut surface [12]. Eleven orifice diameters from 0.75mm to 2.5mm in steps of 0.125mm were created for testing. As an alternative to the polypropylene tips, Pyrex 5mL glass pipettes, Fig. 2(b), were diamond-ground to diameters 1.0-2.0mm in steps of 0.1mm. In addition, by heating and drawing the glass pipettes, smaller diameters in the 0.1 to 1.0mm range were produced, Fig. 2(c).

3.2. Powder Delivery Apparatus

An extended column for powder above the pipette tip is needed, and additional height was achieved with 30mm long, 8mm O.D., 5mm I.D Pyrex glass tubing. The tube was held vertically by a standard laboratory support stand and clamps (Fig. 6). The end of the Pyrex glass tube was ground down, tapering to 7mm so that pipette tips could be conveniently attached and removed during experiments (Fig. 5).

Gravity and pressure-assisted flow conditions were achieved by modifying the conditions at the upper free surface of the powder column. When the top of the powder column is open to atmosphere, gravity flow condition is achieved. Pressure assisted experiments were designed to achieve continuous flow for powder/nozzle combinations for which there was no flow under gravity. A 250 psi compressed air supply, regulated by two Bellofram© type 70 precision air regulators, was fed through 1/4" O.D., 3/16" I.D. nylon tubing to the powder column (Fig. 6). Both air regulators are capable of reducing the 250 psi line supply; however the 0-2 psi regulator

has a much larger number of turns than the 0-30psi. regulator, providing fine tuning in the low pressure range. Two Omega© digital pressure gauges with 0.01 psi resolution were joined to the regulators for pressure readings. A stopcock was used above the powder column to stop/start air-pressure assistance. Vibration assisted experiments were designed as an alternative to pressure assisted flow to get a continuous flow when there was no flow under gravity and to overcome some problems encountered with pressure assisted flow, as will be discussed later in this paper. For vibration assisted flow experiments, a piezoelectric (PZT) actuator strip was placed near the tip of nozzle (Fig. 7). The PZT actuator has a resonance frequency of 29 kHz, free deflection of 3.4 μm and could be actuated at any frequency in the range 0-25 kHz using a sinusoidal signal of different frequencies generated using a LabView program and National Instruments PCI-MIO-16E-1 input/output card.

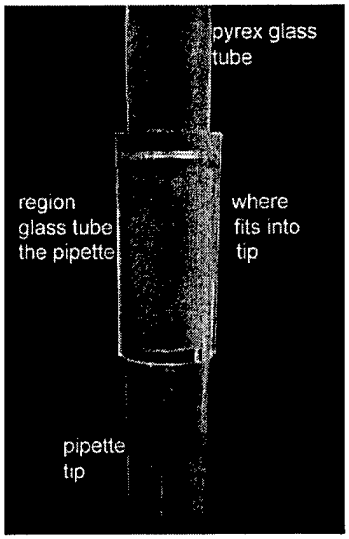

Fig. 5 Glass tube attached to pipette tip to get extended column of powder

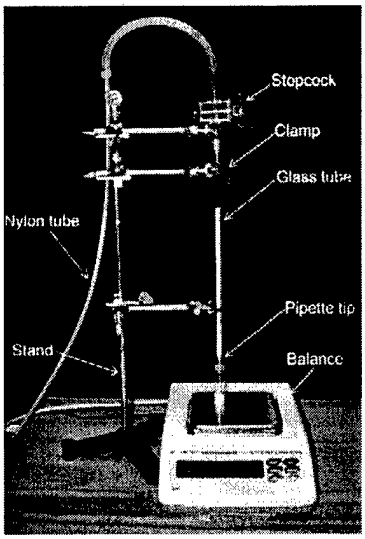

Fig. 6 Test setup; data acquisition with 1-mg resolution balance, 10Hz sampling with PC interface

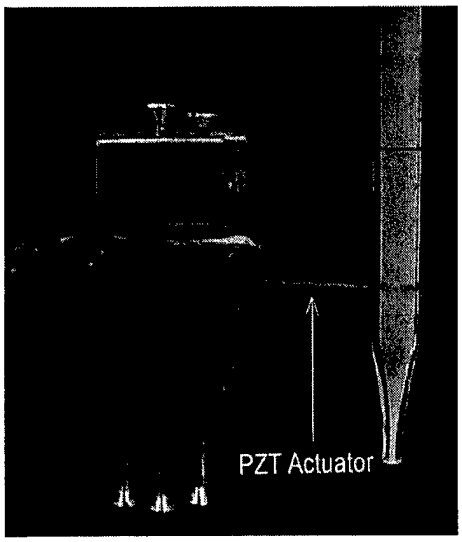

Fig. 7 Use of a PZT actuator strip for vibration assisted flow

3.3. Mass Flow Rate Experiments

The test particles were high-quality soda-lime glass beads, verified by a distribution histogram as 90% within the specified U.S. sieve mesh sizes and 90% spherical. The particle sizes used were 325-400mesh (38-45μm), 270-325mesh (45-53μm), 230-270 mesh (53-63μm), 200-230mesh (63-75μm), 170-200mesh (75-90μm), 140-170mesh (90-105μm), and 120-140mesh (105-125μm). All the powders had bulk density of 1.3 g/cc.

The A&D GF-200 Precision Balance, a 0-200g, 0.001g resolution digital balance with RS-232C serial interface was used for sampling. The balance has Windows Communications Tools© software for easy data transfer. In its most rapid response mode, the balance has a 10Hz sampling frequency. Data can be imported into Microsoft Excel© or stored as unformatted data for other applications.

Experiments began with the calibration of the balance with an ASTM standard 100g mass. The powder delivery apparatus was positioned over the scale, and powders were deposited into an 8mL narrow-mouth glass bottle. Four samples were taken under each test condition, and mass

data from the balance was transferred directly to a PC and stored as generic data files. The files were then processed using a program written in Matlab© for generating plots of the mass accumulation and mass flow rate versus time.

3.4. Angle of Repose Experiments

The angle of repose is defined as the angle of the free surface of a pile of powder to the horizontal plane. It is a measure of flowability and cohesiveness of a powder. A modified Angle of Repose of a Heap test (British Std. 4140) [10] was used to characterize the flow of each of the test particles. Some of the modifications include:

a) A substrate of identical powdered material as that of deposited powder was used.

b) A polyethylene funnel with inner diameter of 4mm was used.

c) The height of the polyethylene funnel above the substrate was lowered from 5.2cm to 5mm to save powder used in each test (only 0.5 grams of powder was needed).

d) Concentric circles used to measure the angle of repose were drawn for every 5°.

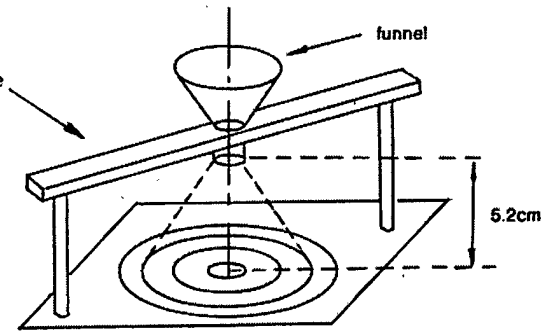

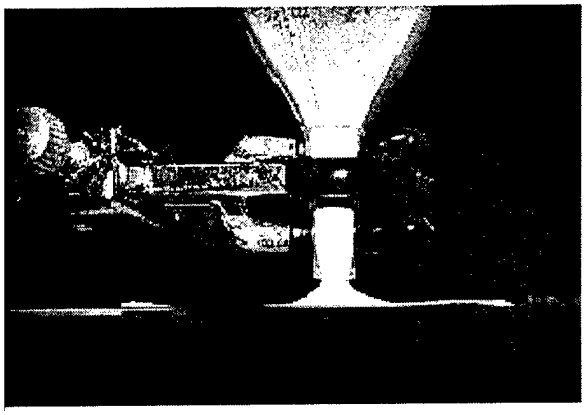

Fig.9. Modified setup to measure angle of repose

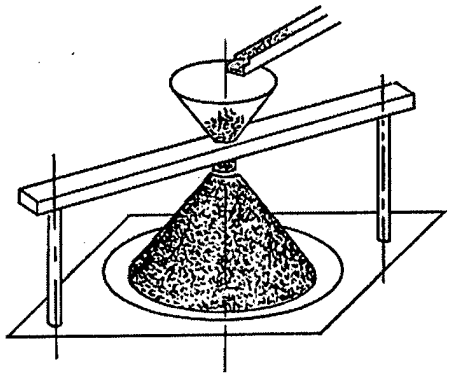

Fig.8. Setup for measuring angle of repose, British Std. 4140 [10]

3.5 Pattern Deposition Experiments

Deposition experiments were conducted on a servo motor-driven X-Y table, with optical encoder feedback. This table is controlled by an SB214PC multi-axis controller from ACS-Tech80 Inc. The maximum resolution of the table is 0.0005in. (0.0127mm). Patterned bed designs were programmed using ACS-programming language.

4. RESULTS AND DISCUSSION

4.1. Gravity Flow

Table 1 shows the average mass flow rate for the range of nozzle sizes and particle sizes tested under gravity flow. Under gravity, there was no flow for particle sizes below 63μm through the entire range of nozzle openings (orifice diameters) tested. Fig. 10 shows the plot of mass flow rate vs. nozzle opening for the four particle sizes that flowed under gravity. It is observed that there is very little variation in the mass flow rate with particle size in the range tested and flow

rate for all particle sizes, in the range(63-125μm) can be described by a single power law curve fit with $R^2 = 0.9823$

Orifice diameter D_0 (mm)	Average mass flow rate(g/s) for various powder particle sizes (mesh)						
	120-140 (105-125 μm)	140-170 (90-105 μm)	170-200 (75-90 μm)	200-230 (63-75 μm)	230-270 (53-63 μm)	270-325 (45-53 μm)	325-400 (38-45 μm)
0.75	0.0173	0.0173	0.0210	0.0168			
0.875	0.0259	0.0285	0.0245	0.0260			
1.00	0.0315	0.0275	0.0346	0.0423		NO	
1.125	0.0484	0.0467	0.0474	0.0536			
1.25	0.0542	0.0650	0.0752	0.0692			
1.375	0.0947	0.1014	0.1048	0.1151		FLOW	
1.5	0.1063	0.1064	0.1560	0.1493			
1.625	0.1745	0.1585	0.1976	0.1925			
1.75	0.2255	0.2237	0.2154	0.2072			
1.875	0.2758	0.2615	0.2700	0.2765			
2.00	0.3073	0.2991	0.2972	0.2901			

Table 1. Gravity mass flow results

From Beverloo's correlation, eq. (1), we get

$$G_s = C\rho_B\sqrt{g}\left(D_0 - kd\right)^{2.5} \Rightarrow D_0 = \left(\frac{1}{C\rho_B\sqrt{g}}\right)^{0.4} G_s^{0.4} + kd \qquad (2)$$

There is a linear relationship between D_0 and $G_s^{0.4}$. Therefore, if Beverloo's correlation, for some values of C and k, holds for this experiment, a linear relationship would be expected between D_0 and $G_s^{0.4}$ obtained from the experimental data. Fig. 11 shows a plot of D_0 vs. $G_s^{0.4}$ for the experiment. It is observed that experimental data can be described by a straight line with a fit of $R^2 = 0.9828$. Using a mean particle size of 91μm, from the slope and intercept on D_0-axis of this line and using eq. (2) we get

$$C = 0.604, \; k = 2.86 \qquad (3)$$

The values of C and k were also calculated for each of the four particle size distributions individually in a similar manner and are listed in tab. 2. The mean values of C and k obtained from these calculations are 0.0602 and 2.855 respectively, which are very close to those obtained above from a single line fit through all the experimental data. This shows that the value of C and k given by relation (3) can be used with eq. (1) with a mean particle size $\bar{d}$ =91μm to predict the mass flow rate for the particle sizes in the range 63-125μm. Thus, for the particle sizes in the range 63-125μm, flow rate under gravity can be predicted by a single expression

$$G_s = 0.604\rho_B\sqrt{g}\left(D_0 - 2.86\bar{d}\right)^{2.5} \text{ g/s}, \; 0.75mm \le D_0 \le 2.00mm, \quad \bar{d} = 91\mu m \qquad (4)$$

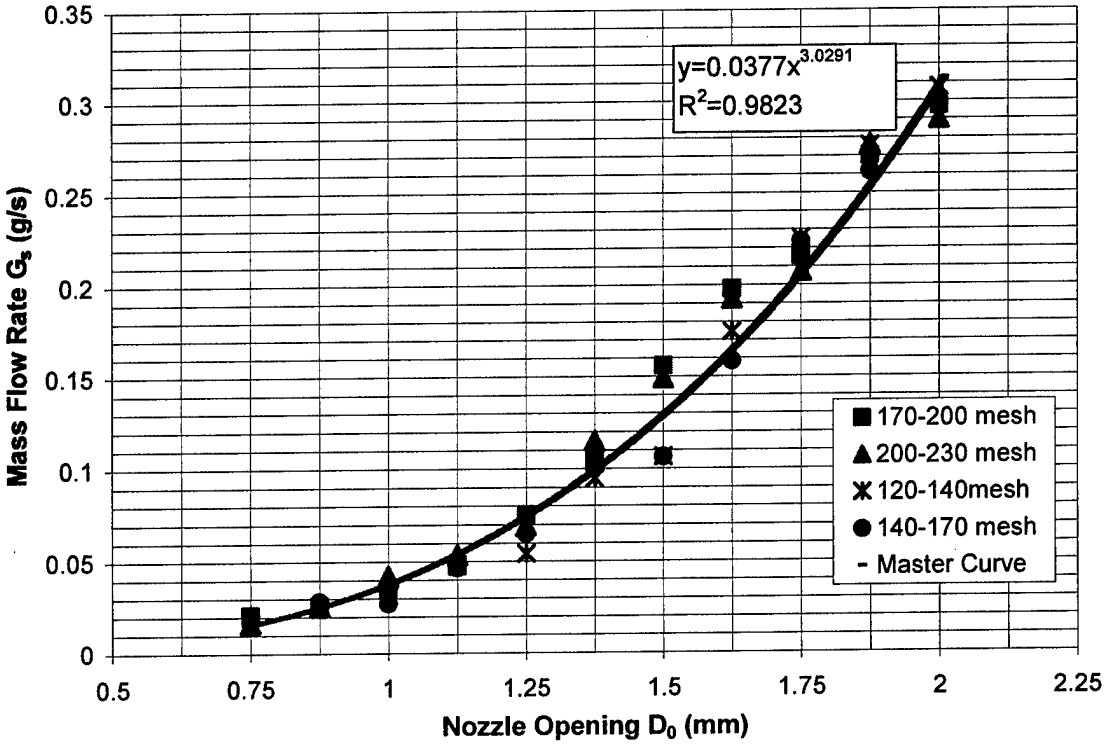

Fig. 10 Mass flow rate as a function of nozzle opening with particle size as a parameter

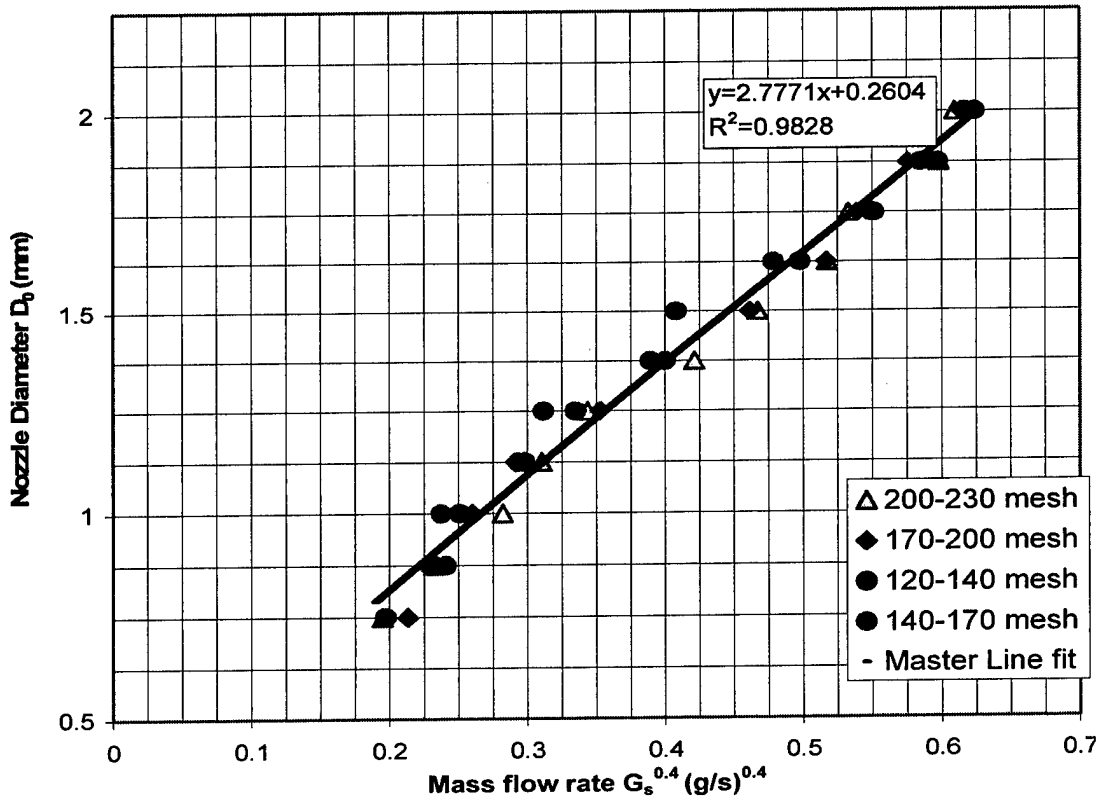

Fig. 11 Master linear plot of D_0 vs. $G_s^{0.4}$ for the experimental data of all the particle sizes tested

It should be noted that the value of C =0.604 obtained from our experiment is nearly the same as that (0.583) obtained by Beverloo et al. [1], while the value of k is almost double (2.86 vs. 1.4). The differenece in the values of k might be due to the fact that the particle size used in our experiments (10-125μm) is one order of magnitude smaller than that(1.6-3.0mm) used by Beverloo et al. It is possible that the value of k depends on the particle size, d. However due to lack of experimental data for the particles in the range 125μm-1.6mm the exact dependence of k on d could not be deduced.

Particle Size	C	k
120-140 mesh	0.650	2.665
140-170 mesh	0.601	2.828
170-200 mesh	0.576	2.774
200-230 mesh	0.580	3.154
Average	0.602	2.855

Table 2. Values of C and k obtained from individual plots of D_0 vs. $G_s^{0.4}$ for each particle size

4.2. Pressure-assisted flow

As mentioned earlier, particles below 63μm do not flow under gravity through the nozzle sizes tested. To fluidize these powders gas pressure assistance was used. However, some problems were encountered. When the column height was low, the powder spurted out with very high velocity, an undesirable effect. Minimum possible kinetic energy of powder particles is desired so that powder spreading on a substrate is minimized when a pattern is deposited. For the fine powders (e.g., 10-25μm), constant flow rate was not achieved; the flow was sporadic and unpredictable as shown in fig.12. Hence, an alternate approach to depositing fine powders consistently was sought.

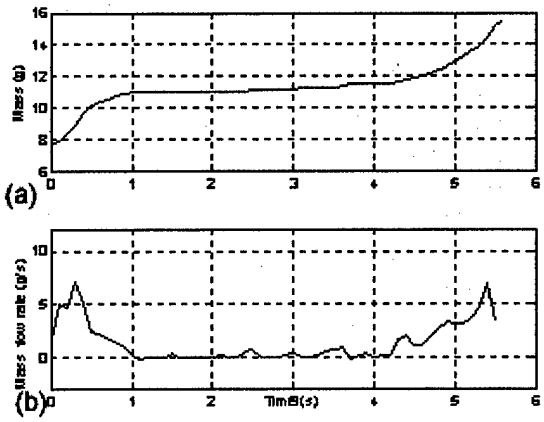

Fig. 12 (a) mass vs. time plot, (b) mass flow rate vs. time plot for 10-25μm powder from 1.5mm nozzle under 0.75 psi pressure

4.3. Vibration-assisted flow

To overcome the problems presented by pressure-assisted flow, vibration assistance was used. A PZT actuator strip, as shown in fig. 7 and discussed earlier, was placed near the tip of nozzle to vibrate the powder column with low amplitude and high frequency. The plot of flow rate vs. vibration frequency for two powders that did not flow under gravity is shown in fig.13. It is observed that there is a peak at 13 kHz for the particular position of PZT with respect to the nozzle opening that was used in the experiment.

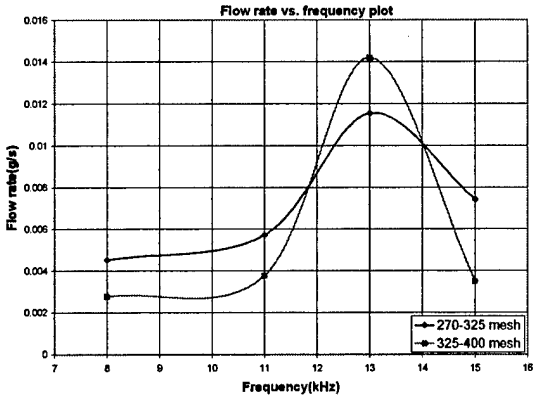

Fig. 13 Plot of mass flow rate vs. frequency for flow through 0.5mm glass nozzle

Continuous flow was obtained even for very fine powder (10-25μm) through a 200 μm nozzle opening. An additional benefit of vibration assisted flow is that automatic valving to start and stop the flow was achieved without any additional mechanism. Further investigation on vibration assisted flow is under way.

4.4. Angle of Repose and Linespread

The angle of repose for various powders as measured by powder piling experiment is shown in tab. 3.

Particle size μm (mesh)	250-300	90-106 (140-170)	63-75 (200-230)	45-53 (270-325)	38-45 (325-400)	10-25
Angle of repose (degrees)	30	35	40	45	50	50

Table 3. Angle of repose

The angle of repose is a measure of cohesiveness of a powder; the larger the angle the more cohesive is the powder. When a line of powder is deposited, the width of line depends on the nozzle diameter and the cohesiveness of the powder. The spread of a deposited line is more for less cohesive (free flowing) powder than for more cohesive powder. Therefore, for the same nozzle diameter, the width of a deposited line is more when angle of repose is less and vice versa.

A simple model to predict the linewidth deposited under gravity flow was developed based on angle of repose and principle of mass conservation which translates to the fact that the volume of the powder exiting the nozzle per unit time should be same as volume deposited if we assume the bulk density of the powder to be the same in the nozzle and the deposited line. For the powders in the 63-125μm size range, the linewidth is given by the following relations:

Let θ be the angle of repose and $h = \dfrac{0.604\sqrt{g}\left(D_0 - k\bar{d}\right)^{1.5}}{v}$ (5)

Where v = velocity at which nozzle is moving (mm/s)

Case-1:For $\theta > \tan^{-1}\left(\dfrac{h}{D_0 - k\bar{d}}\right)$ Linewidth, $B = \left(D_0 - k\bar{d}\right)\left[1 + \dfrac{0.604\sqrt{g}\left(D_0 - k\bar{d}\right)^{0.5}}{v\tan\theta}\right]$ mm (6)

Case-2:For $\theta \le \tan^{-1}\left(\dfrac{h}{D_0 - k\bar{d}}\right)$ Linewidth, $B = \dfrac{1.55\sqrt[4]{g}\left(D_0 - k\bar{d}\right)^{1.25}}{\sqrt{v\tan\theta}}$ mm (7)

Fig. 14 shows pictures of lines of 140-170 mesh powder (θ = 35°) deposited at three different speeds from 0.75mm nozzle. Table 4 compares the calculated linewidths with actual linewidths obtained from experiments. It is observed that the predicted linewidths matches experimentally measured values closely (within approximately two particle diameters).

V(mm/s)	Calculated Linewidth	Experimental Linewidth
68	0.58 mm	0.8 mm
56	1.00 mm	1.2 mm
25	1.51 mm	1.5 mm

Table 4. Comparison of predicted linewidth with experimentally measured linewidth

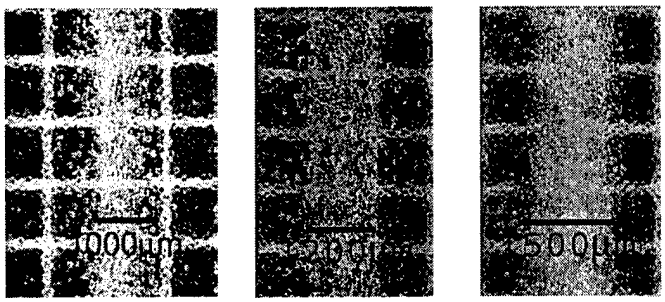

Fig. 14 Lines of 140-170 mesh powder deposited from 0.75 mm nozzle at nozzle speeds 68, 56, 25mm/s respectively (left to right)

4.5. Pattern Deposition

The following illustrations are proof-of-concept for various types of single and multi-material patterned beds that are envisaged for the construction of various heterogeneous devices.

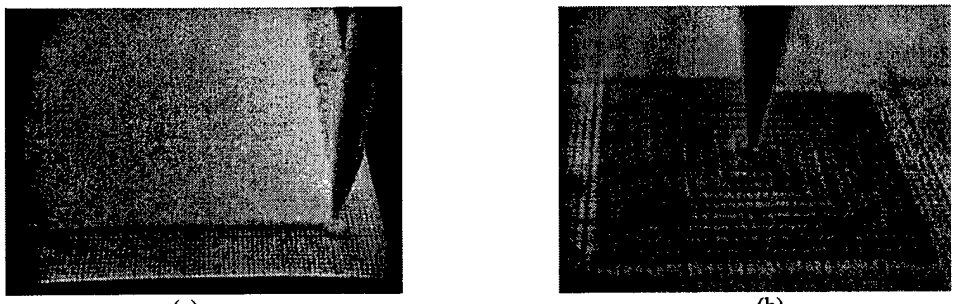

(a) (b)

Fig. 15 (a) Rastered bed of 90-106μm glass beads deposited under gravity flow; Area deposited: 60mm X 60mm, Total deposition time: ~120 seconds, Nozzle opening: 0.75mm **(b)** Single layer of a "Swiss Roll" microcombustor device deposited under gravity flow; Material: dyed red 90-106μm soda-lime, Nozzle openings: 0.75mm, Line Spacing: 2mm, Typical deposited linewidth: 0.8 mm, Deposition Speed: 25.4 mm/s, Deposition time: 30 seconds

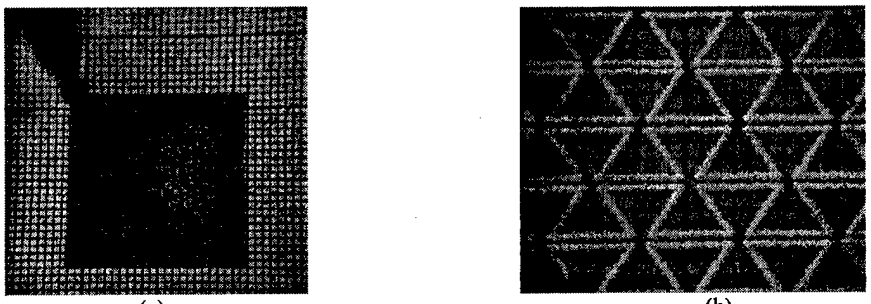

(a) (b)

Fig. 16 (a) A single layer of a radial graded composition deposited under gravity flow; Material: soda-lime glass beads (90-106 μm) transitioning to Ti-6Al-4V (75-125μm), Nozzle opening: 0.75 mm, Line spacing: 0.75mm, Typical deposited linewidth: 0.8 mm **(b)** negative Poisson's ratio "bowtie structure" deposited with vibration assistance; Material: Nylon-6 (10-100 μm), Nozzle opening: 0.5 mm, Line spacing: 2.5mmX5mm(each half bowtie), Typical deposited linewidth: 0.2mm

CONCLUSIONS

A preliminary study of the flow of fine powders from small scale hoppers demonstrates that highly spherical particles in the size range 63-125μm may be delivered at continuous mass flow rate under gravity and the mass flow rates can be predicted by Beverloo's correlation with C=0.604 and k=2.86. The value of k might have a dependence on particle size, d, however this

dependence could not be deduced due to lack of necessary experimental data. For delivering powders below 63μm, alternate techniques need to be adopted. Gas pressure assistance can be used, but some problems are associated with it, e.g., powder spurting out with high velocity, and sporadic and unpredictable flow in the case of fine powders. Vibration assistance seems to have potential of delivering fine powders through small nozzle openings. This method also has an advantage of achieving automatic valving without any additional mechanism.

The linewidth model can be used to predict the widths of lines for powders with particle sizes in the 63-125μm range deposited under gravity through a nozzle opening in the range of 0.75mm-2mm.

The results of this study are useful for development of a hopper-nozzle array for incorporating multiple powders in the SLS process. Future work will include further investigation of vibration assisted flow, developing a numerical model for granular flow processes, and developing more sophisticated model to predict linewidth.

REFERENCES

[1] Beverloo W.A., Leniger H.A., and Velde J. van de, *Chem. Eng. Sci.*, **15** (1961) 260
[2] Spink C.D. and Nedderman R.M., *Powder Technol.*, **21** (1978) 245
[3] Keneman F.E., *Izv. Akad. Nauk SSSR, Otd. Tekhn. Nauk, Mekh. Mashinostr.*, **2** (1960) 70
[4] Schofield C., Holland J., Miles J.E.P., and Shook C.A., *Trans. Inst. Chem. Eng.*, **47** (1969) 154
[5] Jaeger H.M. and Nagel S.R., *Science*, **255** (1992) 1523
[6] Woodcock C.R. and Mason J.S., *Chapman and Hall. New York* (1978)
[7] Newton R.H., Dunham G.S., and Simpson T.P., *Trans. Amer. Inst. Chem. Eng.* **41** (1945) 215
[8] Franklin F.C. and Johanson L.N., *Chem. Eng. Sci.*, **4** (1955) 119
[9] Fowler R.T. and Glastonbury J.R., *Chem. Eng. Sci.*, **10** (1959) 150
[10] Svarovsky L., *Elsevier Applied Science. London and New York* (1987) 73
[11] Das S., *Proceedings of the 2003 NSF Design, Service and Manufacturing Grantees and Research Conference,* Birmingham, Alabama, Jan 6-9, 2003
[12] Santosa J., Jing D., and Das S., *Solid Freeform Fabrication Symposium Proceedings,* University of Texas, Austin (2002) 620

Discrete Multiple Material Selective Laser Sintering (M^2SLS): Nozzle Design for Powder Delivery

K. Lappo, K. Wood, D. Bourell, J.J. Beaman
Mechanical Engineering Department
Laboratory for Freeform Fabrication
The University of Texas at Austin, Austin, TX 78712

Abstract

Previous research focused on the advancement of the Selective Laser sintering (SLS) technology to incorporate discrete multiple material processing. The powder delivery subsystem rolled each material sequentially into selectively removed voids in the part bed, produced by vacuum suction, to form a single horizontal layer. This method, although it minimized changes to the traditional SLS technology, produced components with significant material cross contamination between discrete regions. A new powder delivery method was designed to alleviate this problem in which alternatively a nozzle precisely deposits material into vacuum suctioned. Micro-powders, such as those used in SLS, do not readily flow through openings due to the adverse cohesive and drag forces. A uniform powder flow rate for micro-sized particles is achieved by the introduction of pressurized air through the nozzle wall near the outlet. Experiments were performed to determine the optimal hopper back pressure and nozzle injected air pressure to obtain uniform flow rate for the commonly used Duraform PA bulk material.

Introduction

Students at The University of Texas at Austin have pursued Multiple-Material Selective Laser Sintering (M^2SLS) research efforts. M^2SLS is separated into two distinct categories, functionally graded material for FGM (material composition is varied over a distance) and discrete (material regions are separated by discrete boundaries). Perez performed experimental investigations of powder mixing and delivery devices for FGM [1]. WC-Co one dimensional FGM SLS components were built by Jepson [2]. Selective powder delivery methods for M^2SLS were investigated by Jackson and simple discrete M^2SLS components were built using a DTM Sinterstation 2000 [3, 4]. Although simple geometry parts were built successfully using vacuum suction as a selective powder removal method, several process issues arose during the investigation of discrete M^2SLS selective powder delivery subsystems. The focus of this research is to design a powder delivery subsystem for discrete M^2SLS building on previous research results. Design methodology is applied to generate concepts for alternative delivery methods. Figure 1 is a schematic of the material delivery method utilized in preliminary experiments.

Powder Classification

Typically, SLS powders are plastic and polymer coated metal or ceramic in the size range of 40 nm – 150 μm. During processing powder is transported to the build platform by a roller, doctor blade or nozzle. It is necessary to understand the transport behavior of powders in this

size range. Fluidized solids behavior is classified into four groups, characterized by density differences $(\rho_s - \rho_f)$ and mean particle size [5]. Powders are grouped by broadly similar properties when fluidized by a gas. Behavioral predictions should be limited to individual groups, for many characteristics of fluidized powders are dissimilar even though few are common to all fluidized powders.

Group A consists of materials having a small mean particle size and/or a low particle density (less than 1.4 g/cm^3). Powders in this group are characterized by an appreciable bed expansion before bubbling commences and slow (0.3-0.6 cm/s) collapse upon sudden gas supply cut off. Group B contains powders in the mean size and density ranges 40 μm < d_{sv} < 500 μm and 4 g/cm^3 > ρ_s > 1.4 g/cm^3. In contrast to group A powders, naturally occurring bubbles start to form at or slightly above minimum fluidization velocity. Powders that are cohesive belong in group C. "Normal" fluidization is extremely difficult; the powder lifts as a plug in small diameter tubes or channels (rat-holes) badly. These behaviors are seen because the interparticle forces are greater than those the fluid can exert on the particle. This is generally the result of very small particle size, strong electrostatic charge or high water content. The last classification, group D, is for large and or very dense particles. Figure 1 shows the classification diagram.

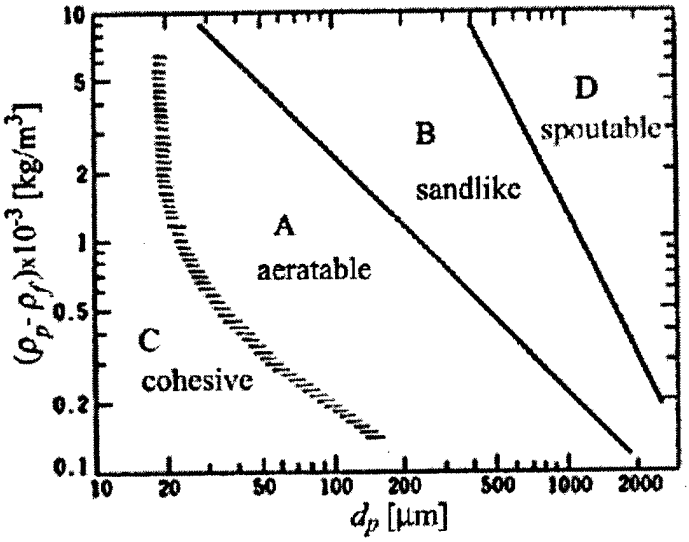

Figure 1: Geldart powder classification diagram for fluidization by air (ambient conditions) [6].

Discrete M^2SLS

Building on fundamental knowledge of powder classification discussed above, research focus is turned to a precision powder delivery subsystem. A precision delivery method alleviates process issues encountered with the selective delivery method used in simple geometry part build. A proposed method removes and replaces secondary and possibly primary material roller delivery with nozzle delivery. This will eliminate part shifting and powder cross-contamination issues which arose during preliminary experiments for electrostatic and vacuum powder removal

methods. A schematic of a process where the primary powder is roller delivered and the secondary powder is nozzle delivered is shown in Figure 2.

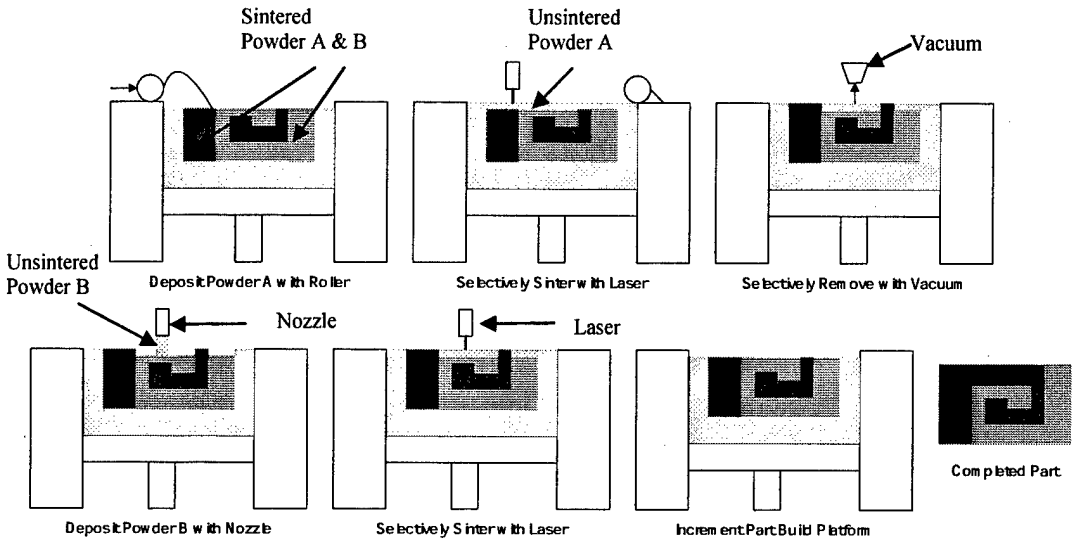

Figure 2: Schematic of precision discrete M^2SLS powder delivery method.

To develop this concept uniform powder delivery must be accomplished. Powder must be taken from storage bins and delivered to the build chamber. The delivery rate, line width and height must be controlled to ensure accurate part geometry. The first step is to investigate the effect of design variables on the rate of powder discharge. A Design of Experiments (DOE) is discussed in the next section.

Nozzle Powder Delivery

A simple nozzle powder delivery experiment is designed to determine the effect of several design variables on the flow rate of two powders, DuraForm PA and CastForm PS. Preliminary trials are performed to determine where control variables will be set for experimentation and bounds for performance variables. Das reports uniform mass flow is achieved for decreased particle size with an increase in back pressure [7]. The delivery back pressure is set at a constant 1.5 psi for experimentation. Nozzle aeration pressures are tested in 0.1 psi increments between 0 psi and 1.0 psi. Trials reveal a high cohesive arching sensitivity to slight decreases in nozzle air pressure. It is found that above 0.1 psi nozzle air pressure tends to disperse the powder turbulently (discharge a large radial spray) or cause cohesive arching after the powder in the nozzle is discharged. Figure 3 displays both the desired and undesired discharge patterns. This second effect is seen when the nozzle pressure exceeded the amount of air required to separate the particles and acts as an upward force on the powder column. Below 0.1 psi the powder intermittently arches cohesively at the beginning of the trial or mid trial. The nozzle aeration pressure is set at 0.1 psi for all trials of the DOE. The design parameters used for the DuraForm PA and CastForm PS experiments are discussed in the next sections.

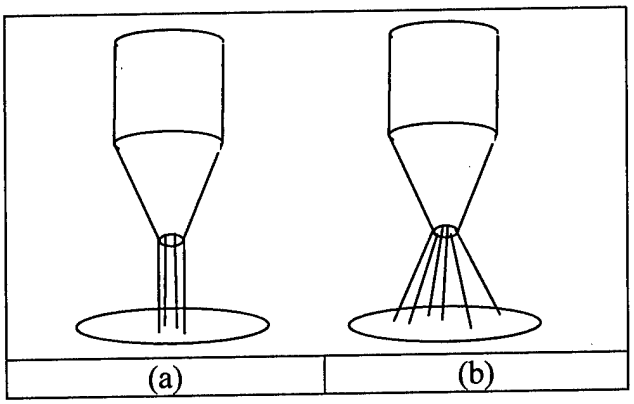

Figure 3: Powder discharge from conical nozzle (a) desired discharge with minimal spray and (b) turbulent discharge with excessive spray.

Nozzle Design

The nozzles were built by traditional SLS out of DuraForm PA. Two sets of four nozzles pictured in Figure 4 were fabricated. The center shaft of one set of nozzles is coated with silver paint which is connected to conductive tape and wired to ground. This allows a pathway for residual charge to travel from the powder. SLS was chosen as the nozzle fabrication method due to the ease of building complex shapes with internal cavities and small channels.

The inner shaft of each nozzle has a 25.0 mm vertical wall with an inlet diameter of 5.0 mm, a half angle of 10.5° and an outlet diameter of 2.5 mm. Each nozzle contains an air inlet and an internal chamber allowing air to pass through the inner wall into the powder pathway. The shape of the nozzle air configuration is varied to determine the effect on powder flow. The spiral configuration is chosen from an analogy design methodology technique and a radial configuration is chosen to investigate a uniform distribution of aeration near the nozzle orifice. A list of the nozzles used in the DOE is given in Table 1.

Nozzle #	Shape	Coating	Standpipe
1	R	N	N
2	S	N	N
3	R	N	Y
4	S	N	Y
5	R	Y	N
6	S	Y	N
7	R	Y	Y
8	S	Y	Y

Table 1: Design nozzles used where R is radial, S is spiral, Y is yes and N is no.

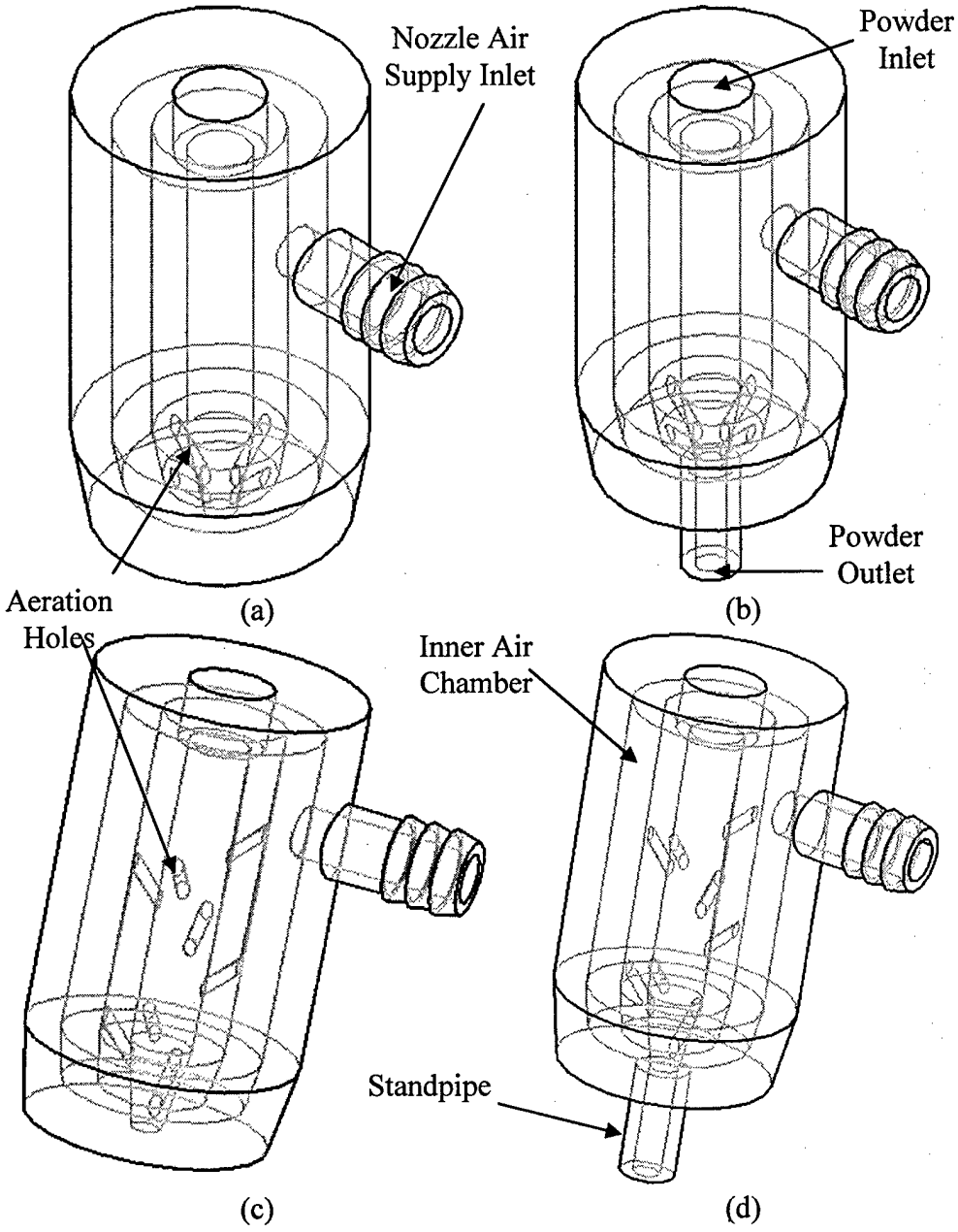

Figure 4: Nozzles used for DuraForm PA and CastForm PS powder delivery DOE (a) radial air configuration, (b) radial air configuration with standpipe, (c) spiral air configuration, and (d) spiral air configuration with standpipe.

Experimental Setup

The mass of powder discharged from interchanged nozzles is measured at timed intervals. Powder is contained in a 52 cm glass tube with a 5.0 mm inner diameter. Individual nozzles are attached to the bottom of the glass tube for the respective trial. A Fisher Scientific A-160 Balance (0.0001 resolution) collects mass measurements at 10 Hz. Two Bellofram regulators (0-5 psi) and Wika pressure gauges (0-3 psi) are used to regulate and monitor the back

and nozzle pressures respectively. Hyperterminal is used to acquire data directly from the balance. Figure 5 is an image of the experimental powder delivery setup.

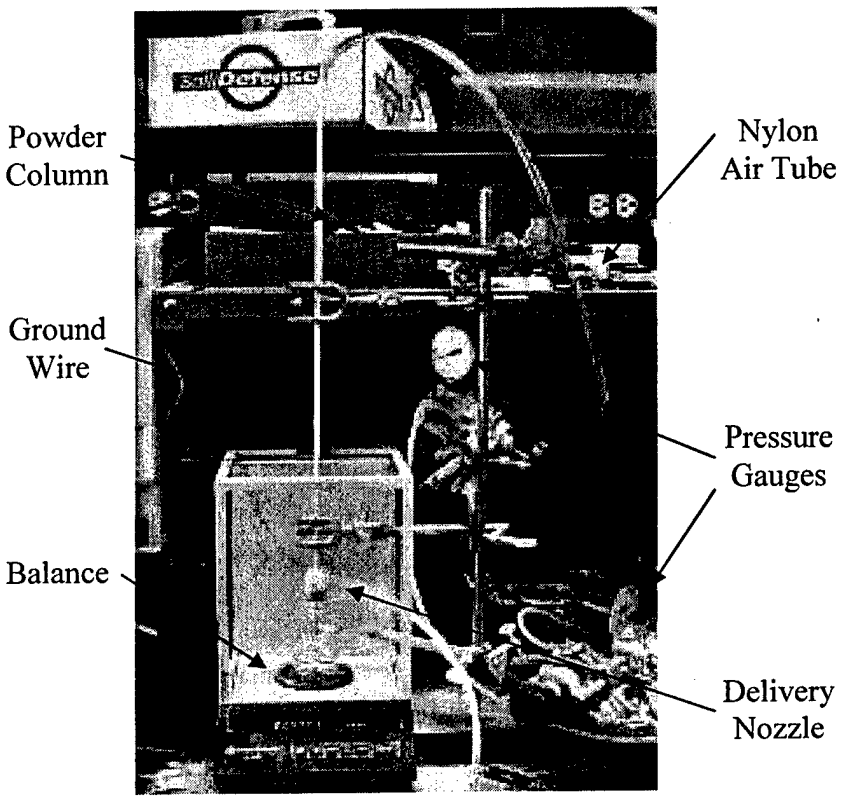

Figure 5: Experimental setup for nozzle powder delivery.

The maximum tube powder capacity is measure before each trial, 4.5 g for DuraForm PA and 4.0 g for CastForm PS. Since a critical height must be maintained for mass flow in a hopper, up to thirteen times the hopper diameter [31], this is critical for data analysis. Pressures are adjusted and the powder is allowed to discharge from the nozzle.

Design of Experiments

A DOE evaluates the individual and coupled effects of design variables on a performance metric [8] of which two are considered, the deviation of mass flow rate from uniform (y_1) and the correlation factor of mass flow rate to a linear trend line (y_2). Both of these metrics are measured as deviations from target values where the targets. Uniform flow is represented by a zero slope mass flow rate curve with a correlation factor of one. The number of trials (N) is set at 2^n, where n is the number of design variables. The number of experiments performed (X) is double the number of trials and they are randomized to prevent in accuracy due to noise. Separate experiments are performed for two materials, DuraForm PA and CastForm PS. Discharge of powder is seen with all nozzle geometry variations for DuraForm PA but not for CastForm PS, therefore the design variables are not the same. During initial investigation of CastForm PS delivery, initial and intermittent cohesive arching is encountered with nozzles with a standpipe,

therefore the nozzles containing a standpipe are remove from the experiment. Experimental design variables for both experiments are given in Tables 2 and 3.

d_1	: Air Inlet Shape	d_2	: Coating (Silver Paint)	d_3	: Standpipe
+	4 x radial		Yes		Yes
-	8 x helix		No		No

Table 2: Design variables for DuraForm PA delivery experiment.

d_1	: Air Inlet Shape	d_2	: Coating (Silver Paint)
+	4 x radial		Yes
-	8 x helix		No

Table 3: Design variables for CastForm PS nozzle powder delivery experiment.

In addition to both control and design variables, noise variables must be taken into account. Several test conditions contribute to inconsistent mass flow patterns and tendencies toward cohesive arching. Environmental humidity can have an effect of powder behavior due to polymer susceptibility to water absorption. Also, the test temperatures for these experiments are well below the build temperature, 180° C and 86° C for DuraForm PA and CastForm PS respectively. Interparticle and particle-wall friction contribute to uniform flow resistance. SLS parts, regardless of the material system used, present a grainy surface finish due to the powder particle size, the layer-wise building sequence and to the vibration of the roller mechanisms during powder delivery [9]. Extensive noise can cause performance metric sensitivity to design variables to be statistically insignificant if prominent.

Collected Data

The mass flow rate is derived from the interval mass measurements and the measurement rate. Both the cumulative mass and flow rate are plotted. Figure 6 is a plot representative of the data collected during most trials. This plot is data from DuraForm PA experiment nine (trial 3) corresponding to a radial aeration configuration, no conductive inner wall coating and a standpipe. The flow rate starts off fairly uniform and increases as the powder level reaches the critical height required to maintain mass flow. As the remaining powder is pushed from the glass tube there is a sharp peak in the mass due to the force on the balance due to the back and nozzle air flows and a recoil as the air pressure is relieved. Performance metric analysis is performed on mass measurements before the critical height is reached.

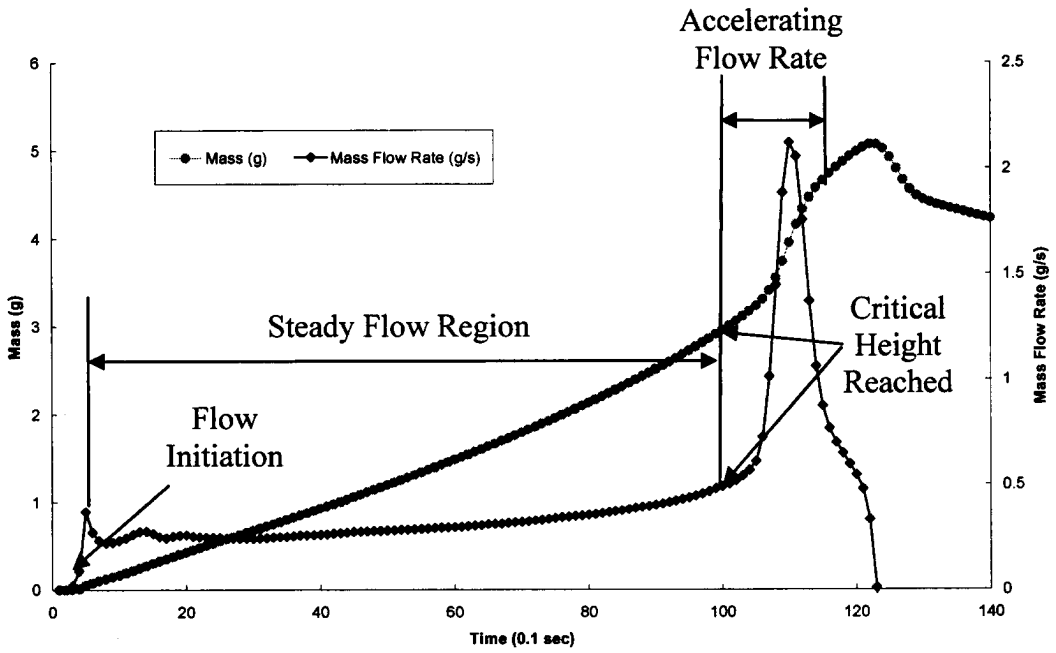

Figure 6: DuraForm PA experiment 9 trial 3 data plot (radial air configuration, no conductive coating and with standpipe).

The effect of change in design variables on powder flow in the steady flow region of the data plot is of interest. The mass flow curve from the flow initiation point to the critical height point is fit to a linear curve. The mass flow rate uniformity is measured as the absolute value of the deviation in the slope of the curve from zero, which is represented in Equation 5.1. The correlation factor is calculated as the least squared sum of a linear trend line deviated from one.

$$y_1 = \left| 0 - \dot{m} \right| \quad (1)$$

Sixteen experiments, two replicates (r) of eight trials, are performed for the DuraForm PA DOE. The data is represented in two matrices (each with size X by 1) for the uniformity of mass flow rate and correlation factor measurements respectively. The normalized values for DuraForm PA design variable and coupled term high and low bounds are represented by "1" and "-1", presented in Tables 4. Similarly, eight experiments are performed for CastForm PS powder delivery investigation. Table 5 represents the collected data from this DOE.

Experiment	Trial #	Mean	d1	d2	d3	d1d2	d1d3	d2d3	d1d2d3	y1	y2
2	8	1	-1	-1	-1	1	1	1	-1	0.5639	0.0374
5	8	1	-1	-1	-1	1	1	1	-1	0.2674	0.0135
1	7	1	-1	-1	1	1	-1	-1	1	0.0215	0.8800
13	7	1	-1	-1	1	1	-1	-1	1	0.0690	0.6030
4	6	1	-1	1	-1	-1	1	-1	1	0.0416	0.4680
16	6	1	-1	1	-1	-1	1	-1	1	0.2790	0.1929
11	5	1	-1	1	1	-1	-1	1	-1	0.1420	0.1318
14	5	1	-1	1	1	-1	-1	1	-1	0.1170	0.1949
3	4	1	1	-1	-1	-1	-1	1	1	0.0237	0.0420
7	4	1	1	-1	-1	-1	-1	1	1	0.0460	0.0216
9	3	1	1	-1	1	-1	1	-1	-1	0.0210	0.2311
12	3	1	1	-1	1	-1	1	-1	-1	0.0210	0.3823
10	2	1	1	1	-1	1	-1	-1	-1	0.0270	0.0910
15	2	1	1	1	-1	1	-1	-1	-1	0.0900	0.1713
6	1	1	1	1	1	1	1	1	1	0.0210	0.1932
8	1	1	1	1	1	1	1	1	1	0.0260	0.0812

Table 4: Collected data from DuraForm PA DOE.

Exp #	Trial #	Mean	d1	d2	d1d2	y1	y2
1	4	1	-1	-1	1	0.0229	0.1061
4	4	1	-1	-1	1	0.0095	0.1081
5	3	1	-1	1	-1	0.0199	0.1174
6	3	1	-1	1	-1	0.0019	0.3880
2	2	1	1	-1	-1	0.0015	0.3492
7	2	1	1	-1	-1	0.0015	0.3258
3	1	1	1	1	1	0.0011	0.3047
8	1	1	1	1	1	0.0021	0.2052

Table 5: Collected data from CastForm PS DOE.

Results and Discussion

Nozzle powder delivery of DuraForm PA and CastForm PS shows promise due to the majority of data collected that show seemingly uniform mass flow rates with little pulsing. Three trials between both DOEs resulted in repeatable results for both y_1 and y_2 for repeat experiments. The powder flow behavior is consistent and the total powder discharge time for replicate experiments in all cases is +/- 0.5 sec. Figures 7 and 8 are data plots of mass flow rate for the DuraForm PA and CastForm PS repeatable trial results. In addition to these promising results, several trials resulted in repeatability of either y_1 or y_2 but not both. These plots are presented in the Appendix with the full set of plots and data tables.

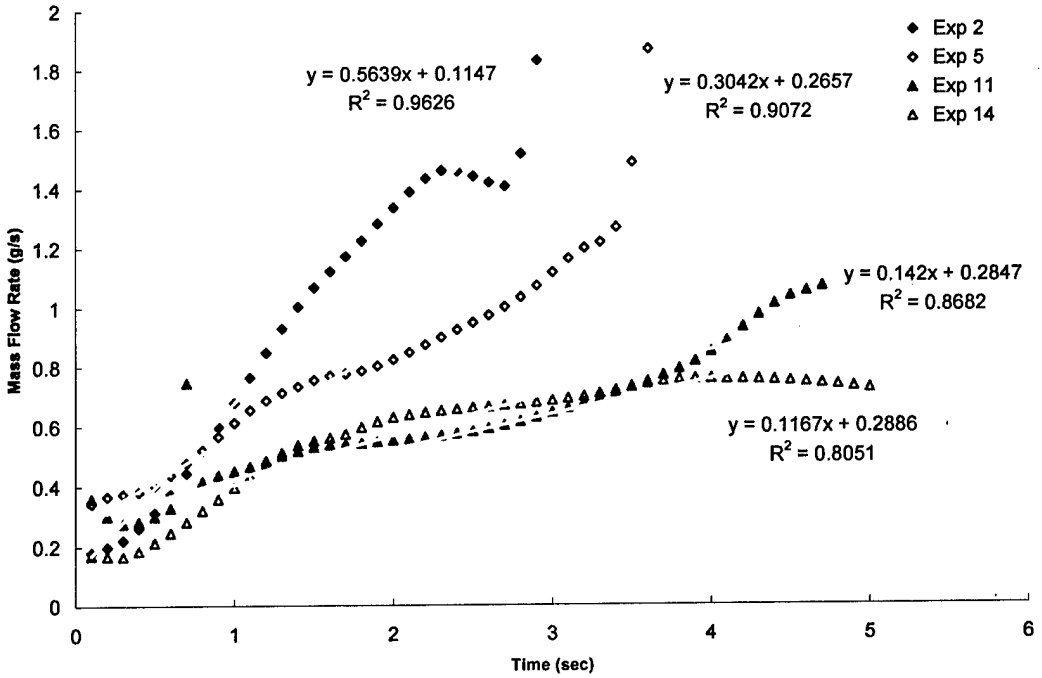

Figure 7: Repeatable trial results from DuraForm PA DOE for both y_1 and y_2, experiments 2 and 5 from trial 8 and experiments 11 and 14 from trial 5.

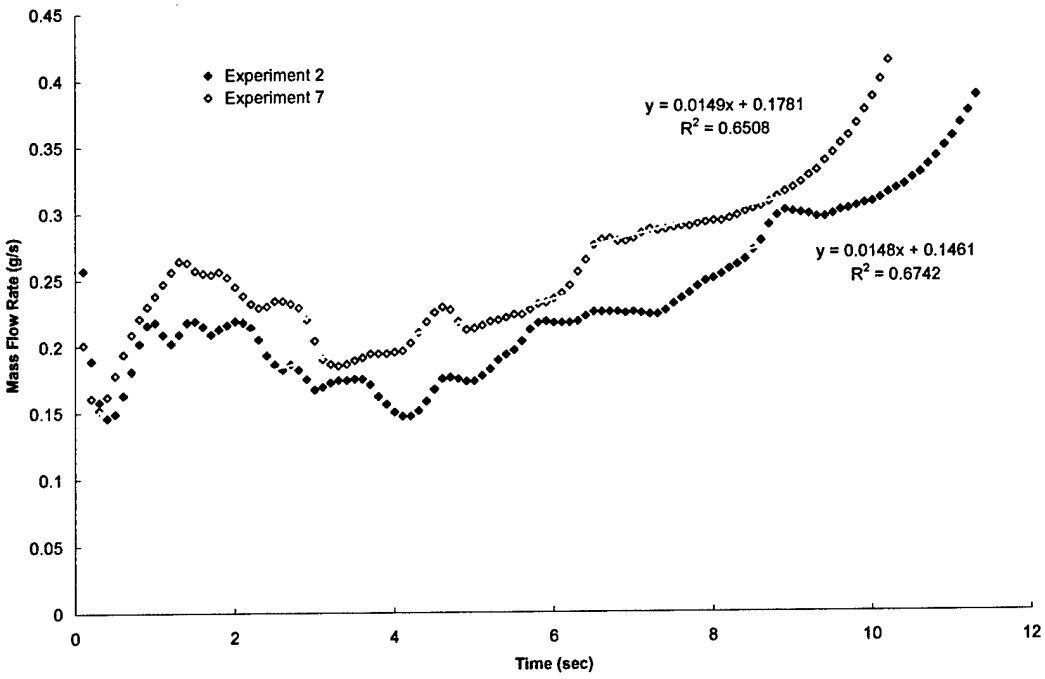

Figure 8: Repeatable trial results from CastForm PS DOE for both y_1 and y_2, experiments 2 and 7 from trial 2.

Unfortunately, results were not consistent during testing due to excessive noise. For example, only one data set was collected for attempts with all nozzle geometries with no nozzle

aeration pressure, shown in Figure 9. Fortunately, this plot shows a fairly uniform mass flow rate with an average powder acceleration of 0.0011 g/s^2 and minimal deviation from this trend line near the onset of discharge. This result shows promise for the investigation of nozzle parameters not studied in these experiments in coordination with aeration configuration. Replicate data sets with these parameters were unable to be collected due to cohesive arching.

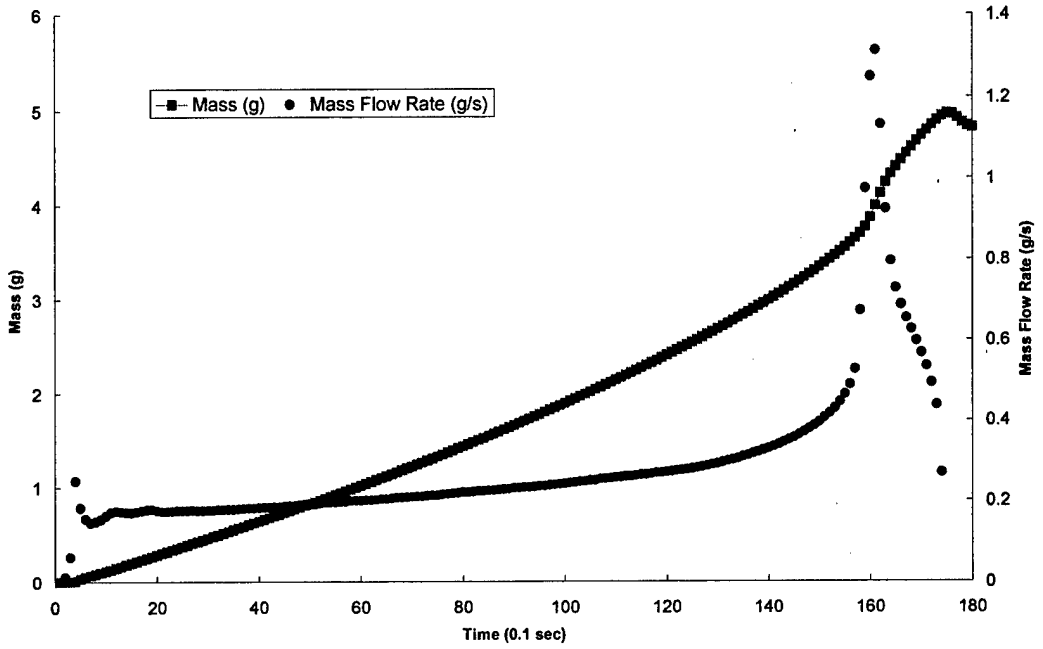

Figure 9: DuraForm PA powder delivery with no nozzle aeration pressure, radial aeration configuration, no conductive inner wall coating and no standpipe.

A trend observed in the mass flow rate of a few data sets is a linear increase to a uniform rate before reaching the critical powder height. Figure 10 is from DuraForm PA experiment 15 (trial 2) corresponding to a radial aeration configuration with a conductive coating and no standpipe. A significant deviation from zero slope and correlation factor of one is seen in these plots of mass flow rate. This flow behavior is not duplicated in the replicate experiment of trial 2, which caused significant noise in the data set.

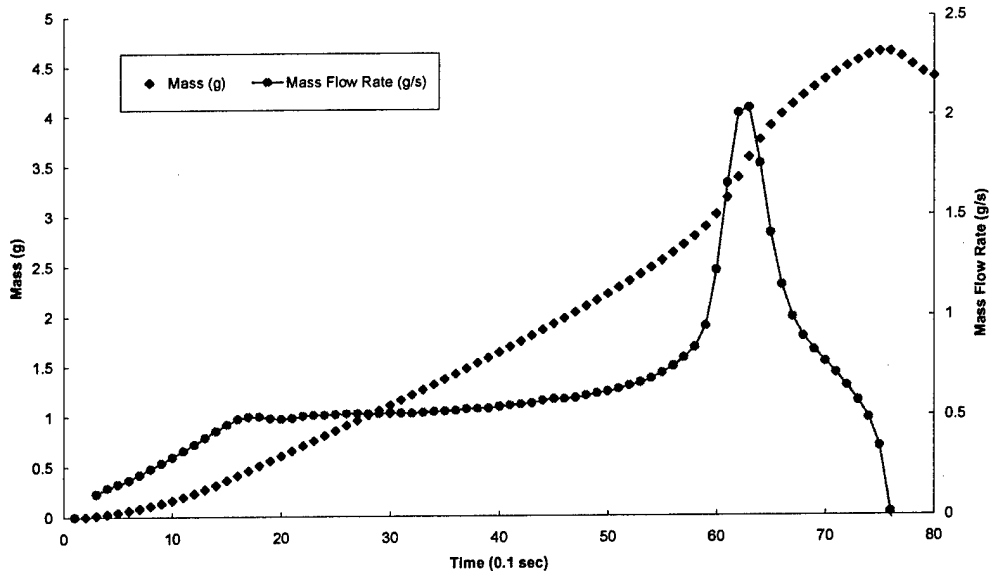

Figure 10: DuraForm PA experiment 15 (trial 2) corresponding to a radial aeration configuration with a conductive coating and no standpipe.

Inconsistent flow is seen in two DuraForm PA experiments. The powder in the glass tube does not steadily fall into the nozzle, but the nozzle aeration steadily clears the pathway. An unsteady mass flow rate is observed in these instances as shown in Figure 5.10 representing data from experiment one (trial 7) having a spiral aeration configuration and a conductive wall coating but no standpipe. The mass flow rate of this experiment is clearly not uniform. The resulting correlation factor is the minimum seen for all experiments at 0.12 with a deviation from 1.0 of 0.82. These two plots significantly contributed to the noise in the DuraForm PA DOE.

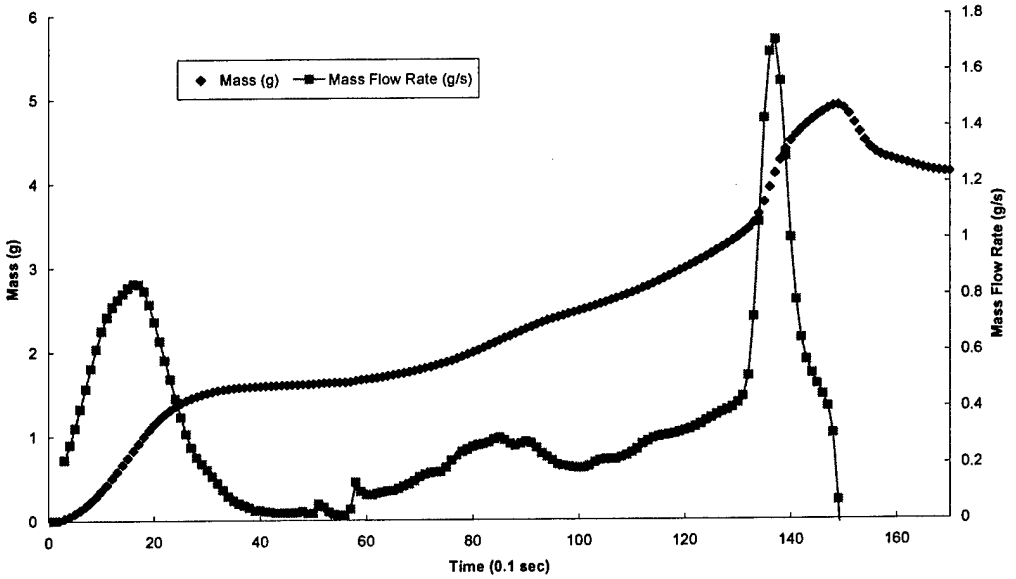

Figure 11: DuraForm PA experiment one (trial 7) having a spiral aeration configuration and a conductive wall coating but no standpipe.

Analysis of Variance (ANOVA)

ANOVA is used to test the significance of performance metric sensitivity to individual design variables and couples effects. These research efforts focused on two performance metrics of deviation of mass flow rate from uniform and flow rate data correlation factor as discussed above. The collected data is utilized to form two matrices, [X] and [y]. The [X] matrix is comprised of the mean, individual and coupled normalized terms, having the same number of rows as experiments performed and the same number of columns as trials. The [y] matrix is a column vector with the number of rows equal to the number of experiments performed. The sensitivity coefficients are found using the matrix operation of Equation 2, which form the general formulas for two and three variable linear models given in Equations 3 and 4 respectively:

$$[\beta]=\left([\mathrm{X}]^T[\mathrm{X}]\right)^{-1}[\mathrm{X}]^T[y] \quad (2)$$

$$P=\beta_0+\beta_1 d_1+\beta_2 d_2+\beta_{12} d_1 d_2+error \quad (3)$$

$$P=\beta_0+\beta_1 d_1+\beta_2 d_2+\beta_3 d_3+\beta_{12} d_1 d_2+\beta_{13} d_1 d_3+\beta_{23} d_2 d_3+\beta_{123} d_1 d_2 d_3+error \quad (4)$$

The probability of significance of each sensitivity coefficient is determined using ANOVA. The terms associated with coefficients deemed significant with a 90% confidence remain in the model. Other terms are considered to be part of the noise and are dropped from the model equation.

Another method for determining statistical noise is to calculate the standard deviation (σ) of [y] data. The statistical noise is considered to be three times the standard deviation. If a sensitivity factor, $E=2\beta$, is less than the statistical noise, it can be considered insignificant to the performance.

DuraForm PA

Collected data in Table 4 is used to calculate the performance metric sensitivity coefficients for the DuraForm PA DOE. The statistical noise is 0.0185 and 0.2660 for the y_1 and y_2 data respectively. Performance metric sensitivity coefficients for both sets of DuraForm PA data are summarized in Table 6. Only the sensitivity coefficient β_0 is significant in comparison to the statistical noise for y_1. Two coefficients are significant in the correlation factor data, β_0 and β_{23}. ANOVA is performed to compare statistical significance confidence using the F-test.

Trial	Mean	d_1	d_2	d_3	d_1d_2	d_1d_3	d_2d_3	$d_1d_2d_3$
$Beta_1$	**0.0111**	-0.0077	-0.0018	-0.0056	0.0025	0.0044	0.0040	-0.0045
$Beta_2$	**0.2333**	-0.0816	-0.0427	0.1039	0.0252	-0.0337	**-0.1442**	0.077

Table 6: Average powder acceleration DuraForm PA experimental results.

No sensitivity coefficients are significant within a 90% confidence using ANOVA for the average powder acceleration data. The coefficients β_1 and β_{12} have the highest level of confidence. β_1 corresponds to the individual performance sensitivity to aeration configuration in the nozzle. The notably higher significance to change in performance metric shows a stronger

effect on aeration configuration as a design variable. All coupled coefficients have confidence levels <90% for the y_2 data set, which only compares with the β_{23} significance from earlier findings. These values are highlighted in Table 7.

Term	Variable	DOF	SS_1	SS_2	MS_1	MS_2	$F0_1$	$F0_2$	P_1	P_2
B0	mean	1	0.0326	0.1084	0.0326	0.1084	1.00	1.00	0.65	0.65
B1	d1	1	0.0939	0.1069	0.0939	0.1069	2.88	0.99	0.87	0.65
B2	d2	1	0.0053	0.0295	0.0053	0.0295	0.16	0.27	0.30	0.38
B3	d3	1	0.0506	0.1722	0.0506	0.1722	1.55	1.59	0.75	0.76
B12	d1d2	1	-0.0774	-0.3481	0.0774	0.3481	2.37	3.21	0.84	0.89
B13	d1d3	1	-0.0082	-0.8274	0.0082	0.8274	0.25	7.63	0.37	0.98
B23	d2d3	1	-0.0269	-0.9800	0.0269	0.9800	0.83	9.04	0.61	0.98
B123	d1d2d3	1	-0.0613	1.0139	0.0613	1.0139	1.88	9.35	0.79	0.98
Total	n/a	15	0.3243	0.8625	0.0216	0.0575				
Error	n/a	8	0.2608	0.8673	0.0326	0.1084				

Table 7: ANOVA results for DuraForm PA delivery data.

The slopes and correlation factors analyzed are on a small scale (0 – 1). Deviation in a sample causes a large standard deviation in the set. It is consistent that the statistical analysis reveals sensitivity factors to have low confidence levels. The average deviation from uniform mass flow rate slope is 0.0111 g/s^2 for the DuraForm PA experiments with a low of 0.0021 g/s^2 and high of 0.0564 g/s^2.

CastForm PS

Similar results are seen in the CastForm PS data. Table 8 lists the sensitivity coefficients for the y_1 and y_2 performance metrics respectively. The statistical noise for these data sets are 0.0172 and 0.2098. Comparing these coefficients to the noise, only the mean sensitivity coefficient for the deviation from uniform flow rate data is greater than the noise. ANOVA is used to test if any coefficients have significance with confidence <90%.

Trial	Mean	d_1	d_2	d_1d_2
$Beta_1$	0.0075	-0.006	-0.0013	0.0013
$Beta_2$	0.2381	0.0582	0.0158	-0.057

Table 8: Average powder acceleration CastForm PS experimental results.

As seen with DuraForm PA, no coefficients reach a 90% confidence significance level. The β_1 and β_{12} coefficients have the highest level of confidence as seen in the DuraForm PA data. DuraForm PA and CastForm PS have similar material properties and particle size distributions. The average particle diameters are 58 μm and 62 μm for DuraForm PA and CastForm PS respectively with particle size range of 25-106 μm [10-11]. The densities of the two powders are also comparable at 0.97 g/cm^3 and 0.86 g/cm^3 (ASTM D792). The ANOVA for the deviation from uniform mass flow rate showed no significant coefficients also.

Term	Variable	DOF	SS_1	SS_2	MS_1	MS_2	$F0_1$	$F0_2$	P_1	P_2
B0	mean	1	0.0001	0.0688	0.0001	0.0688	1.00	1.00	0.63	0.63
B1	d1	1	0.0003	0.0271	0.0003	0.0271	2.25	0.39	0.79	0.44
B2	d2	1	0.0000	0.0020	0.0000	0.0020	0.11	0.03	0.24	0.13
B12	d1d2	1	-0.0002	-0.3295	0.0002	0.3295	1.78	4.79	0.75	0.91
Total	n/a	7	0.0006	0.0969	0.0001	0.0138				
Error	n/a	4	0.0005	0.2752	0.0001	0.0688				

Table 9: ANOVA for average powder acceleration CastForm PS results.

The presence of desired data trends shows promise in powder delivery by nozzle with aeration through the wall. Further investigation of alternative design parameters such as nozzle material (wall friction coefficient), half angle, inlet diameter, outlet diameter and nozzle shape in coordination with the design variables evaluated in these DOEs will aid in understanding powder behavior. Several factors are considered for improvement of powder delivery by nozzles.

Two materials were investigated in this research effort, which are readily available, but very similar in size, distribution and properties. The goal of powder delivery for multiple materials is to have the ability to deliver any material desired dependent on application. DuraForm PA and CastForm PS are two polymer powders currently used commercially with small particle sizes (25-106 μm). These materials were chosen because delivery of smaller powders is difficult. Cohesive attraction between particles causes unpredictable powder behavior. Experimental improvements will be seen when a broad base of materials are investigated.

DuraForm PA nozzles built with traditional SLS, which proved to be a large source of statistical noise. The surface roughness of SLS parts is typically in the range of the bulk powder size. Powder delivery through a nozzle is complicated by additional friction factors. The wall friction contributes to undesired flow behavior. The use of a polymer contributes to the build up of residual electrostatic charge along the wall and powder. The use of an alternative nozzle material for powder delivery will reduce the noise due to particle-wall interaction. A polished inner channel wall will reduce friction and a grounded metallic nozzle material will provide a pathway for charge removal.

Experimental environmental conditions for data collection are far from normal operating conditions for DuraForm PA and CastForm PS. Both powders are processed at elevated temperatures, in excess of 80°C, and additional environmental controls. These experiments were performed at room temperature with no humidity control or monitoring. Additional equipment would be required to provide these parameters. Nozzle powder delivery will be more accurate when investigation is performed as close to realistic operating conditions as possible.

One nozzle geometry and two aeration configurations were investigated in these experiments. The aeration holes are 1.0 mm diameter (smallest SLS feature size), which should be reduced for optimal performance. Both the nozzle geometry parameters; diameters, half angle and shape and aeration configuration should be varied to determine the optimal performance for powder delivery of a given material. A simple radial arrangement with four holes was used, where the number of holes could be varied along with the placement of the holes. A straight vertical line could be used similar to the spiral configuration.

A 52 cm glass tube was used as the powder hopper for powder discharge. The amount of data observed to have a relatively uniform mass flow rate comprises a small fraction of the column height. The use of a larger powder column will allow the collection of larger data sets per experiment. In addition, the implementation of controls in the future to eliminate any fluctuation in back and nozzle pressures will prevent the fluctuation of mass flow rate from uniformity.

There is promise for delivery of powder with nozzles. Success was observed with other gravity powder discharge experiments at The University of Michigan [7]. Positive data was observed in these research efforts. With the incorporation of the noted improvements discrete multiple material powder delivery has the potential of success.

References

[1] Perez, J. (1999). *Powder Delivery for a Multiple Material Selective Laser Sintering Machine*, Masters Thesis, University of Texas at Austin.

[2] Jepson, L. (2002). Multiple Material Selective Laser Sintering, PhD Dissertation, University of Texas as Austin.

[3] Jackson, B., Wood, K., Beaman, J. (2000). "Discrete Multi-Material Selective Laser Sintering (M^2SLS): Development for an Application in Complex Sand Casting Core Arrays", *Proceedings of the Solid Freeform Fabrication Symposium*, University of Texas at Austin, pp 176-182.

[4] K. Lappo, B. Jackson, K. Wood, D. Bourell, J.J. Beaman (2003). "Discrete Multiple Material Selective Laser Sintering (M^2SLS): Experimental Study of Part Processing," *Proceedings of the Solid Freeform Fabrication Symposium*, University of Texas at Austin, submitted.

[5] Geldart, D. "Types of Gas Fluidization", Powder Technology, 7 (1973) 285-292.

[6] Kobayashi, T., Kawaguchi, T., Tanaka, T. and Tsuji, Y., "DEM Analysis on Flow Patterns of Geldart's Group A Particles in Fluidized Bed," Proc. of World Congress on Particle Technology 4 (CD-ROM), July 21-25, Sydney, Australia, (2002), Paper No. 178.

[7] Santosa, J. "Expterimental and Numerical Study on the Flow of Fine Powders from Small-scale Hoppers Applied to SLS Multi-Material Deposition", Proceedings of the Solid Freeform Fabrication Symposium, 2002, pp 620-627.

[8] Otto, K., Wood, K. (2001). Product Design: Techniques in Reverse Engineering and New Product Development, Prentice Hall, NJ.

[9] I.Y. Tumer; D.C.Thompson, K.L.Wood and R.H. Crawford, "Characterization of Surface Fault Patterns with Application to a Layered Manufacturing Process", Journal of Manufacturing Systems, Vol. 17, No.1, 1998.

[10] DTM Corporation (1997). "The Sinterstation® System Guide to Materials: DuraForm™ Polyamide," Dec 1997, DCN: 8001-10014.

[11] DTM Corporation (1999). "The Sinterstation® System Guide to Materials: CastForm Polystyrene," April 1999, DCN: 8002-10006.

Discrete Multiple Material Selective Laser Sintering (M^2SLS): Experimental Study of Part Processing

K. Lappo, B. Jackson, K. Wood, D. Bourell, J.J. Beaman
Mechanical Engineering Department
Laboratory for Freeform Fabrication
The University of Texas at Austin, Austin, TX 78712
Reviewed, accepted August 19, 2003

Abstract

Since the introduction of Solid Freeform Fabrication technologies, processing capabilities have evolved to include simultaneous processing of multiple materials in a single component. Selective Laser Sintering (SLS) technology advancement research is being conducted at The University of Texas at Austin to incorporate discrete multiple material processing. Multiple material freeform components are manufactured with material regions separated by discrete or blended (functionally graded) interfaces. An application for discrete M^2SLS processing is found in the production of complex sand core geometries for hollow features in casting. Materials research was performed to identify a support material which burns out during the core firing with little or no residue. A Design of Experiments was performed to determine the effectiveness of electrostatics as a selective powder removal process. Feasibility of producing components by means of discrete M^2SLS was proven through the fabrication of simple geometry tubes.

Introduction

Now that single material processing is thoroughly understood for most solid freeform technologies, the push is toward advancement of these processes to include the processing of multiple materials simultaneously. Multiple material freeform components can be classified as discrete, where material regions are separated by discrete boundaries, or functionally gradient materials (FGM), where the material composition is varied over a distance. Technologies such as Shape Deposition Manufacturing (SDM) and Laser Engineered Net Shaping (LENS) have been successful in producing discrete and FGM multiple material freeform components respectively [1-2]. Processing multiple material components by means of SLS is advantageous over other freeform techniques due to the wide material pool available [3]. Any material that can be obtained in a powder form and is heat-fusible with or without a binder is a potential SLS process material. Materials used in traditional manufacturing processes, such as sand and polystyrene in casting operations for example, are also SLS bulk materials providing the capability to produce fully functional components by indirect or direct methods.

Sand Casting

The traditional process of creating sand casting cores is complex and time consuming. Each internal core is created separately and then assembled by precise gauging. DTM Corporation (now 3D Systems) created a material, Sandform (polymer coated sand particles), which allows the preassembled manufacturing of complex geometry sand casting molds by indirect-SLS manufacturing. A green part is produced by traditional SLS and the green mold is

cleared of any support powder from the SLS build. The polymer binder is burned out and the sand particles are sintered during a furnace post fire process.

Unfortunately, a process problem is introduced when cleaning the green part of support powder after SLS processing. Removal of powder from small vent holes (1/4" diameter) often requires excessive handling which can result in fracture of the green mold. One solution to this problem is modification of the current SLS process to incorporate the simultaneous processing of multiple materials in a single build. A secondary material can be utilized as part support during the build which will burn out leaving little to no residue on the mold during furnace firing stage, eliminating the need to handle the part to remove excess Sandform from the green part. Freeform multiple material components can be classified as discrete (material regions are separated by discrete interfaces) or functionally gradient (material blend composition is varied over a distance). A proposed powder delivery method for discrete M^2SLS is discussed below.

Discrete M^2SLS Process

Traditional SLS employs a counter-rotating roller to deliver a uniform layer of a single powder to the part bed. The complication arises in the deposition of multiple powder regions in a single horizontal layer during the automated part build process. There are three general methods to perform the deposition; (1) by depositing a complete layer followed by iterative selective removal and blind deposition of secondary materials, (2) precisely placement of each material in the desired location, or (3) a combination of these two. Our research focuses on the first powder delivery method and is displayed in Figure 1.

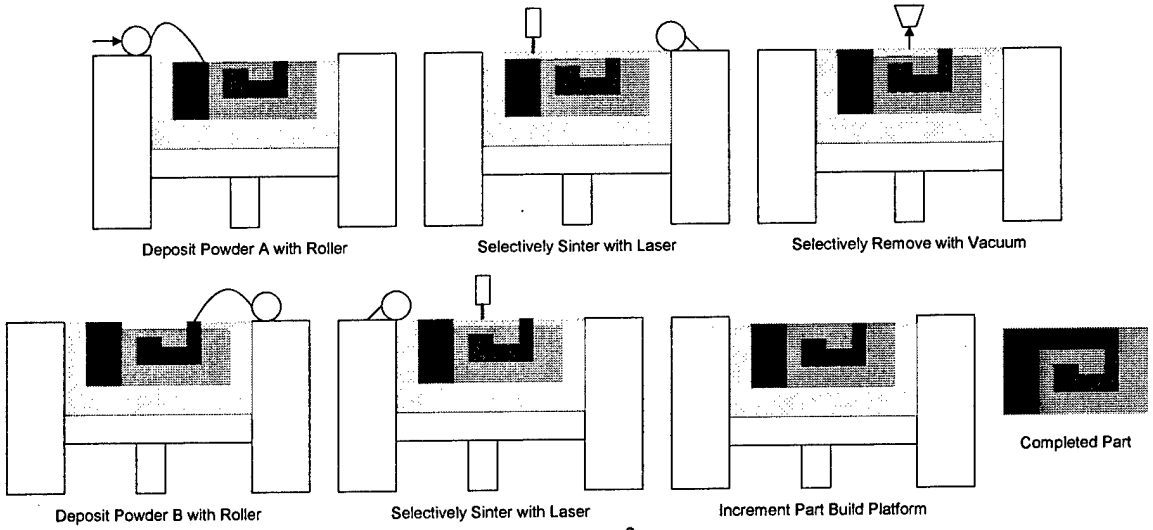

Figure 1: Process schematic for the M^2SLS powder delivery method.

First, a uniform layer of the first desired powder (Sandform in our case) is delivered by a counter-rotating roller as in traditional SLS and the CO_2 laser sinters the powder where desired in the cross-section. The second step is the selective removal of Sandform by vacuum suction to create a void where a region of CastForm PS is desired. Finally, a small amount of powder is placed on the build platform and swept in to place by the roller and sintered where desired. The part bed is lowered and this process is repeated until a complete complex geometry multiple

material component is produced. Electrostatic powder removal is investigated as an alternative powder removal method experimentally.

Experimental Setup

Two selective powder removal processes were chosen for comparison during concept selection for the design of a powder delivery subsystem. Both electrostatic and vacuum suction powder removal processes are studied as means of selectively removing powder from the part bed to create a void where a secondary material can be deposited. Electrostatic forces can lift small particles as used in alternate applications such as forensics and laser printers [4-6]. A simple three variable experiment is designed to investigate the volume of powder that can be removed from a powder bed using electrostatic attraction. Similarly, vacuum suction can lift powder to create a void for secondary powder deposition. Simple geometry multi-material components are fabricated in a DTM Sinterstation 2000 using suction to selectively create voids during part build.

Electrostatic Powder Removal

An experiment is performed to determine the effects of three variables on the layer thickness removed from a scaled powder bed using electrostatic attractive force. Figure 2 is a schematic of the experimental setup cross-section. The setup is similar to a parallel plate capacitor with a vertical air gap and loose powder resting on the bottom plate. The upper plate (charge plate) is supplied with an alternating current, while bottom plate was grounded. During a brief charging time (1-5 sec) the loose powder jumps from the bed and adheres to the charge plate. The charge plate is weighed before and after each trial with a Fisher Scientific A-160 balance (0.0001 resolution) to obtain an accurate change in mass. A simple Design of Experiments (DOE), which is discussed below, is used to evaluate the sensitivity of mass removed to each variable.

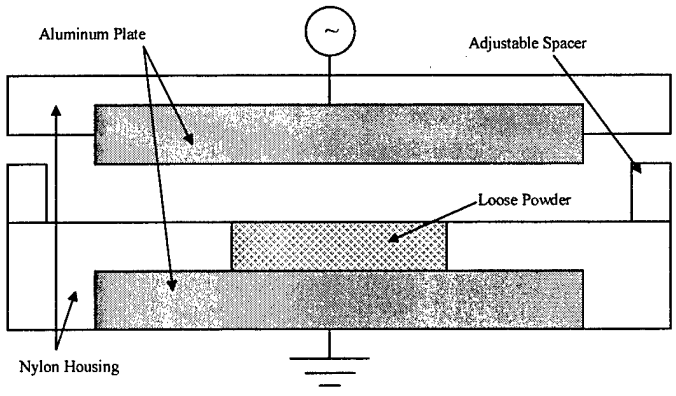

Figure 2: Electrostatic experimental setup cross-section schematic.

Simple Geometry Component Build

Simple geometry components were built in a DTM Sinterstation 2000, pictured in Figure 3. The process steps described in the schematic of Figure 1 were used to build these parts. A

separate part build is set up for each material region within a cross section. The process chamber door is opened after each material region is built to manually remove residual powder with vacuum suction and place powder on the build platform to be delivered by the roller. As many as ten layers were built sequentially in each part. Part quality and process issues will be discussed below.

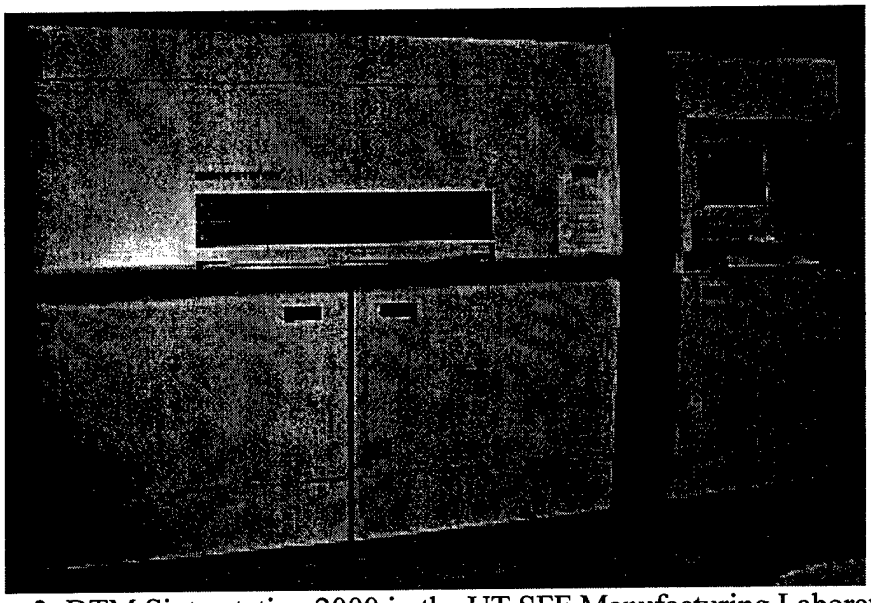

Figure 3: DTM Sinterstation 2000 in the UT SFF Manufacturing Laboratory.

Design of Experiments

The Design of Experiments evaluates the effects of three main electrostatic control variables on the ability to attract loose powder from a particle bed. The performance metric chosen is mass lifted from the powder bed. The three process parameters or design variables investigated were powder removal height, charge voltage and powder material. The design variables and levels used are listed below in Table 1. The control variables, which are kept constant throughout the experimental trials, are the test bed dimensions and testing environment (pressure and temperature). The significant noise variables are the test environment humidity, powder moisture content, residual charge on powder between trials and the particle size distribution. Experimental data and results are presented below.

d_1 : Powder Removal Height (mm)	**d_2 : Charge Voltage (V)**	**d_3 : Powder Material**
$d_1^+ = 4.826$	$d_2^+ = 6750$	d_3^+ = Duraform
$d_1^- = 0.762$	$d_2^- = 2700$	d_3^- = Castform
$\Delta d_1 = 4.064$	$\Delta d_2 = 4050$	

Table 1: Design variables and levels.

Table 2 shown below illustrates the DOE matrix used for the experiments. The trials were randomized to eliminate any bias that could be introduced due to the order in which the

experiments were conducted. In addition, the trials were completed in one day to minimize environmental variation noise. The numbers "–1" and "1" indicate the normalized value of the design variable used for that trial, which represent the low and high values respectively. For example, trial number six pertains to a set of d1 = "-1", d2 = "1" and d3 = "-1", therefore the experiment was performed with a powder removal height of 0.762 mm, a charge voltage of 6750 V with Castform powder. Table 2 includes the measured values of mass (g) of powder removed from the powder bed in each trial. An initial inspection of the data shows moderate variations between replicates indicating the presence of noise. The results will be discussed in more detail below.

Experiment	Trial #	Mean	d1	d2	d3	d1d2	d1d3	d2d3	d1d2d3	y
3	8	1	-1	-1	-1	1	1	1	-1	0.0204
12	8	1	-1	-1	-1	1	1	1	-1	0.0210
2	7	1	1	-1	-1	-1	-1	1	1	0.0114
4	7	1	1	-1	-1	-1	-1	1	1	0.0106
14	6	1	-1	1	-1	-1	1	-1	1	0.0336
16	6	1	-1	1	-1	-1	1	-1	1	0.0457
6	5	1	1	1	-1	1	-1	-1	-1	0.0789
7	5	1	1	1	-1	1	-1	-1	-1	0.0766
9	4	1	-1	-1	1	1	-1	-1	1	0.0393
15	4	1	-1	-1	1	1	-1	-1	1	0.0395
1	3	1	1	-1	1	-1	1	-1	-1	0.0102
13	3	1	1	-1	1	-1	1	-1	-1	0.0055
5	2	1	-1	1	1	-1	-1	1	-1	0.1121
10	2	1	-1	1	1	-1	-1	1	-1	0.1190
8	1	1	1	1	1	1	1	1	1	0.2510
11	1	1	1	1	1	1	1	1	1	0.1966

Table 2: Design of experiments collected data

An Analysis of Variance (ANOVA) was performed on the collected data. The ANOVA is used to determine sensitivity factors and test their feasibility. This is done by decomposing the total variation observed across experiments into sources of variation [7]. From the feasible coefficients a three-factor linear regression model can be obtained. The general form of the full three-factor linear regression model is:

$$P = \beta_0 + \beta_1 d_1 + \beta_2 d_2 + \beta_3 d_3 + \beta_{12} d_1 d_2 + \beta_{13} d_1 d_3 + \beta_{23} d_2 d_3 + \beta_{123} d_1 d_2 d_3 + error \quad (1)$$

where the β's are the regression fitting coefficients for each variable and combined effect [8]. Table 3 is a summary of the experimental result from which the regression coefficients are derived.

Trial	Mean	d_1	d_2	d_3	d_1d_2	d_1d_3	d_2d_3	$d_1d_2d_3$	$P_{i,1}$	$P_{i,2}$	$P_{i,avg}$
1	1	1	1	1	1	1	1	1	0.2510	0.1966	0.2238
2	1	-1	1	1	-1	-1	1	-1	0.1121	0.119	0.1156
3	1	1	-1	1	-1	1	-1	-1	0.0102	0.0055	0.0079
4	1	-1	-1	1	1	-1	-1	1	0.0393	0.0395	0.0394
5	1	1	1	-1	1	-1	-1	-1	0.0789	0.0766	0.0778
6	1	-1	1	-1	-1	1	-1	1	0.0336	0.0457	0.0397
7	1	1	-1	-1	-1	-1	1	1	0.0114	0.0106	0.0110
8	1	-1	-1	-1	1	1	1	-1	0.0204	0.021	0.0207
Beta	0.067	0.0131	0.0472	0.0297	0.0234	0.006	0.0258	0.0115			

Table 3: Design of experiments results

Results

ANOVA is also used to test for significance of the mean and each regression coefficient in the general model using the F-test [8]. If the amount of variation of each variable and/or combined effect is high ($> 3\sigma$) compared to its effect on powder mass removal, the coefficient will be insignificant and can be eliminated from the general model resulting in a reduced order model. Table 4 gives the ANOVA calculations including the Probability of the F-Test. The terms with F-Test probability values approaching 1.00 are values of high confidence. With 90% confidence a reduced order model is established.

Term	Variable	DOF	SS	MS	F0	P
B_0	mean	1	0.0093	0.0093	46.52	1.00
B_1	d_1	1	0.0028	0.0028	13.89	0.99
B_2	d_2	1	0.0357	0.0357	179.44	1.00
B_3	d_3	1	0.0141	0.0141	70.91	1.00
B_4	d_1d_2	1	0.0088	0.0088	44.24	1.00
B_5	d_1d_3	1	0.0006	0.0006	2.93	0.87
B_6	d_2d_3	1	0.0107	0.0107	53.56	1.00
B_7	$d_1d_2d_3$	1	0.0021	0.0021	10.64	0.99
Total	n/a	16	0.0763	0.0048		
Error	n/a	8	0.0016	0.0002		

Table 4: ANOVA table of statistical results and Probability of F-Test.

The terms associated with the linear regression coefficients determined to be insignificant are eliminated from the general form of the model. These terms do not effect the experimental variation and will have little to no effect on the experimental results [7]. The reduced order terms with high coefficient values are the most sensitive to small variations in the corresponding experimental terms. The performance of the electrostatic removal of loose powder from the test

bed is affected most dramatically by change in applied charge voltage. Only the coupled coefficient β_{13} was deemed insignificant, therefore the remaining terms are included in the reduced order model, shown below.

$$P = 0.067 + 0.0131d_1 + 0.0472d_2 + 0.0297d_3 + 0.0234d_1d_2 + 0.0258d_2d_3 + 0.0115d_1d_2d_3 \quad (2)$$

Figure 4 illustrates two simple geometry components manufactured by M^2SLS with vacuum suction used for the selective powder removal method. The components each consist of a solid Sandform base built in a traditional SLS automated build topped with several multi-material (Sandform and Castform) layers built manually as discussed above. These parts were successfully produced after several manufacturing attempts and process parameter variations. Several process issues arose due to the inconsistent environment while opening and closing the chamber door during the manual build of the multiple material layers. These process and additional materials research issues are discussed below.

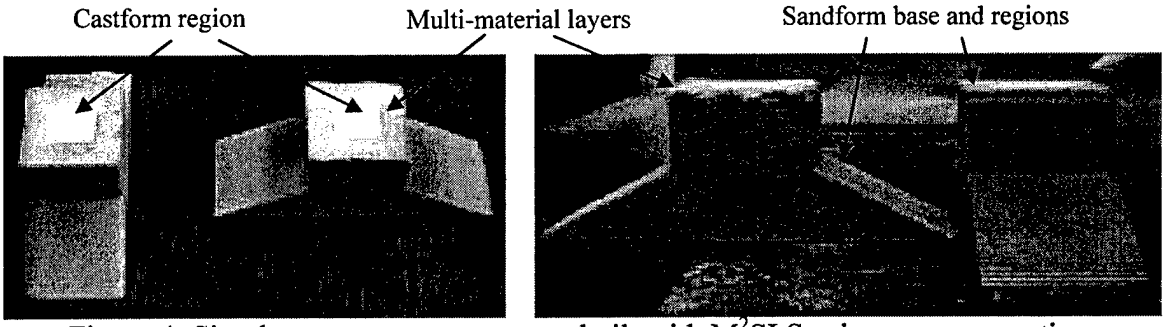

Figure 4: Simple geometry components built with M^2SLS using vacuum suction.

Discussion

The result of the DOE produced several important insights into the removal of loose powder from a particle bed by means of electrostatic attraction. Results showed that although significant amounts of powder were removed by electrostatic force, the removal patterns were inconsistent between trials. The objective of the experiment was to determine if the depth of the powder removed from the test bed can be controlled within the window of deposited layer thickness of traditional SLS, 0.004"-0.015". When accounting for the density and loose packed volume of the powders removed, minimum and maximum depths removed were 0.0008" and 0.0239" respectively. One combination of test parameters gave a promising result. The trial five parameter combination ("1", "1", "-1") resulted in the most uniform powder removal from the test bed. Figure 5 demonstrates this pattern. These results in conjunction with a successful part build show promise for the potential to build discrete multi-material freeform powders from a wide range of material with SLS. Unexpected experimental results were observed during electrostatic removal of powders and manual build of simple geometry components.

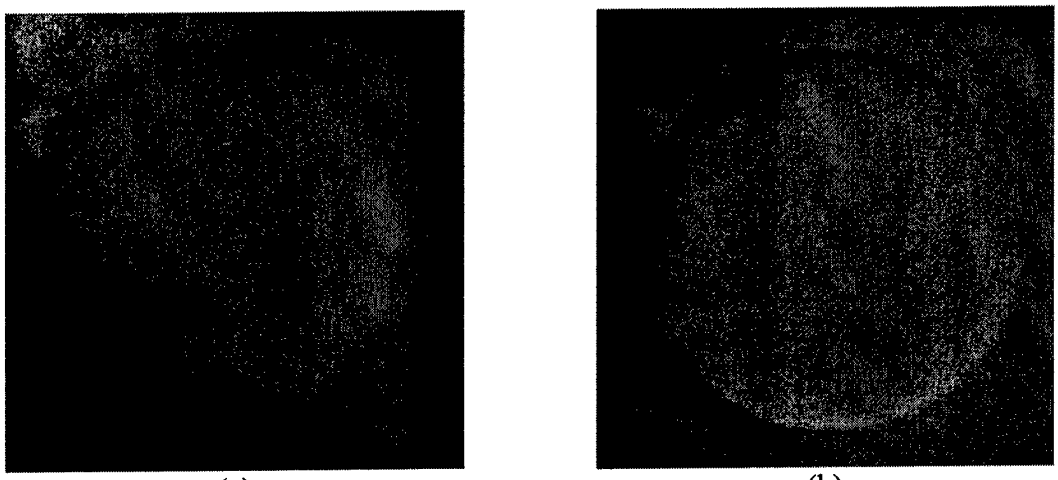

(a) (b)

Figure 5: Trial 5 powder removal pattern (a) powder collected on the charge plate and (b) remaining powder in test bed.

Several trial parameter configurations result in inconsistent powder removal. The parameter combination of Trial 6 ("-1", "1", "-1") causes the powder to build in isolated locations, which in time build bridges between the powder bed and charge plate. This creates a connective path, preventing the charge from distributing uniformly on the plate. This can be caused by imperfections on the surfaces of the charge plate or the powder bed. A halo formed around the perimeter of the powder bed opening signifying a build up of charge around the rim of the bed. Another interesting effect is the appearance of a snake-like pattern in the attracted powder and bed as produced by the Trial 2 ("-1", "1", "1") parameter combination. During experimental testing under these conditions discharge sparks were seen between the charge plate and powder surface. The attracted and remaining powder patterns are pictured in Figure 6. While the mass of the powder removed under these parameter combinations is significant, the patterns are nonuniform. This leads to excessive powder removal in regions while insufficient powder removal in the remaining regions. Considering the goal is to remove a uniform layer of powder from a bulk powder bed, these results are undesirable.

While the experimental results show promise for the use of electrostatic attraction as a selective powder removal method, there is the presence of inconsistent performance. The ANOVA revealed all but one regression coefficient to be significant to the mass of powder removed from the powder test bed. This implies that the error in the model is low. Although this is desired, the inconsistent powder removal patterns prove the complexity of a system using this technology. The challenge of using electrostatics is only expected to increase when incorporating process parameters as seen in SLS. Other powder removal methods will be evaluated before the further investigation of electrostatics as the primary means.

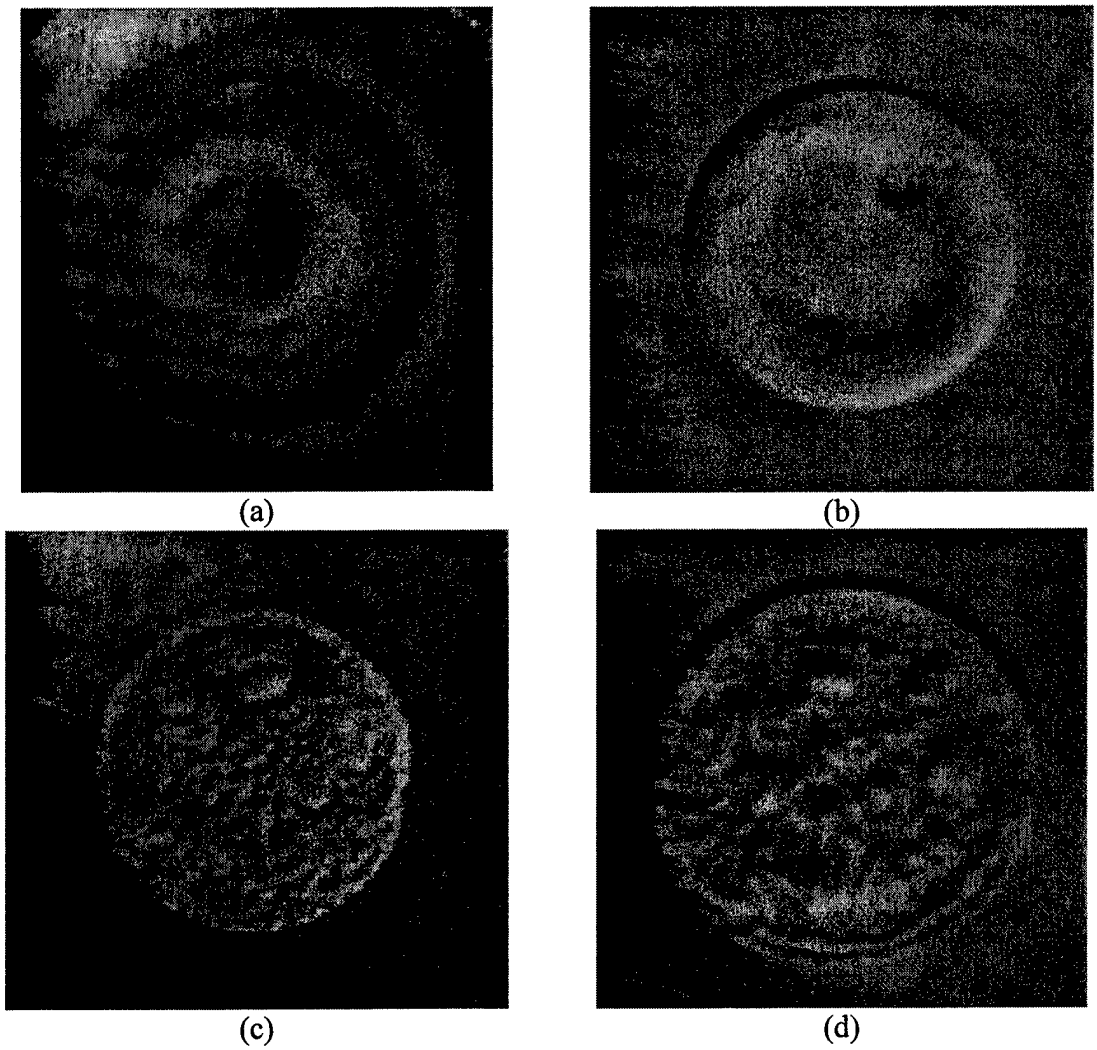

Figure 6: Undesired powder removal pattern (a) trial 6 attracted powder pattern, (b) trial 6 powder remaining in test bed, (c) trial 2 attracted powder pattern, and (d) trial 2 powder remaining in test bed.

Process Issues

During the simple geometry part fabrications several process issues arose. SLS powders require elevated build chamber temperatures for optimal sintering. Optimal powder sintering is achieved during SLS by elevating the temperature of the powder to just below the powder (direct SLS) or binder (indirect-SLS) and supplying energy to surpass the melt threshold with a laser [9]. Some powders require additional build environmental controls such as an inert atmosphere to prevent oxidation. The manual multi-material powder delivery requires the chamber to be opened between material regions. Disrupting the chamber environmental equilibrium, especially process temperatures, inhibits the part build. Incomplete interlayer fusion was seen in the layers built manually. Figure 7(a) displays layers flaking away around the edges of a multi-material cross-section.

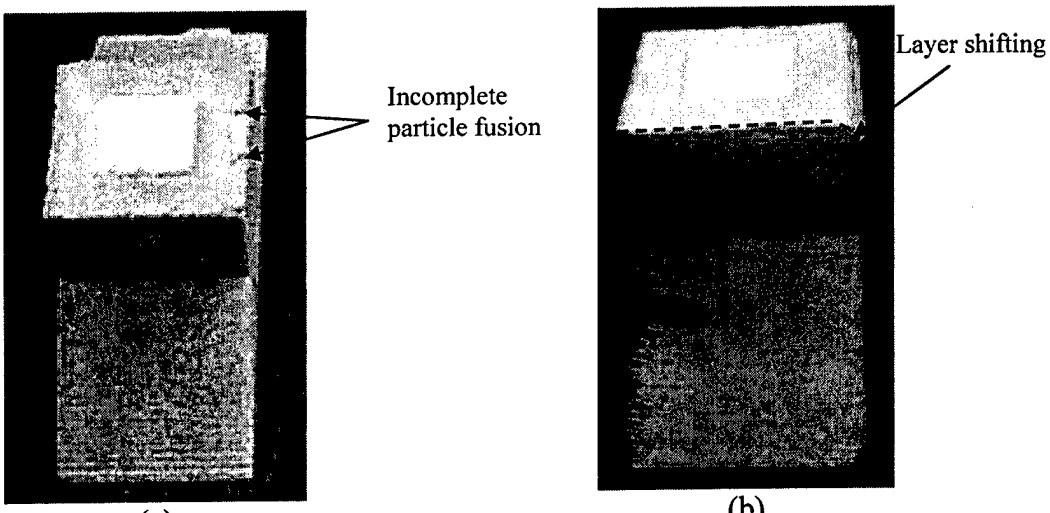

Figure 7: M^2SLS process issues; (a) interlayer delamination or incomplete powder adhesion and (b) layer shifting of multiple material layers.

The mechanical delivery of the second powder by a roller caused two problems. Initially the part bed piston was left even with the build platform for delivery of the Castform. As the roller delivers the Castform to fill the void region layer shifting occurs when the roller collided with the part. This was compensated by lowering the piston below the level height to allow sufficient clearance between the part surface and the roller. Misalignment of the two material regions within the cross-section results, which causes part dimension in accuracy. The second problem is material cross-contamination. As the roller delivers the Castform it is rolled over the entire exposed part surface and part bed. Residual Castform is left on the surface outside the desired deposition area and intermixes with the unsintered Sandform in the bed. The Castform can add to the problem of incomplete fusion between consecutive Sandform layers and possibly contribute to delamination. Figure 8 displays the desired Castform deposition area and the evidence of powder outside this region. The upper layers of this part delaminated at the interlayer boundary.

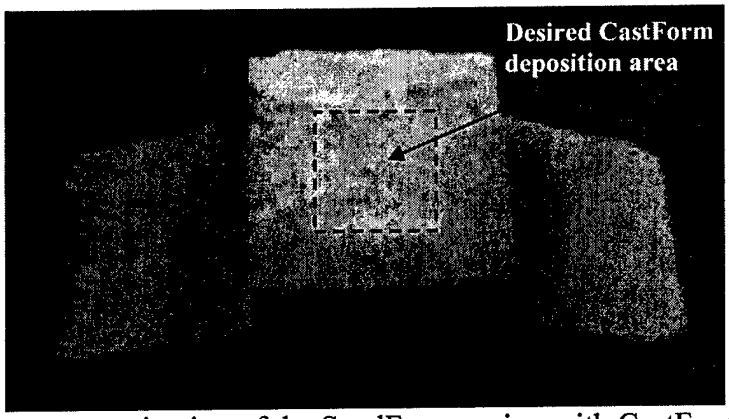

Figure 8: Cross-contamination of the SandForm region with CastForm outside the desired deposition region.

Future Work

The successful simple geometry discrete M^2SLS component part build encourages the research effort for SLS technology advancement here at The University of Texas at Austin. The induced process issues encountered during investigation of electrostatics and vacuum selective powder removal techniques reveals the need for further design efforts. The delivery method used in this experiment, although traditional SLS process and machine changes are minimized, induced further process issues that must be alleviated for Discrete M^2SLS to be commercially successful. Design methodology will be applied to investigate design alternatives. Further experimentation will be performed to test the feasibility of precision rather than selective powder delivery subsystems.

References

[1] Griffith, M., et al. (1997). "Multi-Material Processing By LENSTM," *Solid Freeform Fabrication Symposium Proceeding*, University of Texas at Austin, pp. 387-394.

[2] Feng, J., and Hays, D. (2000). "Theory of Electric Field Detachment of Charged Toner Particles in Electrophotography," *Journal of Imaging Science and Technology*, 44, No. 1, Jan/Feb, pp. 19-25.

[3] Perez, J. (1999). *Powder Delivery for a Multiple Material Selective Laser Sintering Machine*, Masters Thesis, University of Texas at Austin.

[4] Tantec: Static Control Solutions (1996). "Charging Applications Guidebook," Schaumburg, IL.

[5] ESD Journal (2003). "Electrostatics in Forensics," *The ESD &Electrostatics Magazine,* www.esdjournal.com/articles/indent/indented.htm, May 12.

[6] Kimura, M., Wamou, M., and Mou, H. (1990). "The Electrostatic Transfer of Toner Images," Fujitsue Science Technology Journal, 25, No. 4 pp. 262-271.

[7] Otto, K., Wood, K. (2001). Product Design: Techniques in Reverse Engineering and New Product Development, Prentice Hall, NJ.

[8] R.E. Walpole (1998): Probability and Statistics for Engineers and Scientists, 6th Edition, Prentice-Hall.

[9] Beaman, J.J., Barlow, J.W., Bourell, D.L., Crawford, R.H., Marcus, H.L., McAlea, K.P. (1997). Solid Freeform Fabrication: A New Direction in Manufacturing, Kluwer Academic Publishers, MA.

A Motion Planning Approach for Fabrication of Complex 3-D Shapes in a LENS™ Process

By

Musa Jouaneh
Professor
Dept. of Mechanical Engineering
& Applied Mechanics
University of Rhode Island
Kingston, RI 02881
Tel: 401-874-2349
Email: jouaneh@egr.uri.edu

and

Brent Stucker
Assistant Professor
Mechanical & Aerospace Engineering
Utah State University
Logan, UT 84322-4130
Tel: 435-797-8173
Email: stucker@mae.usu.edu

Abstract

This paper discusses an approach for planning the motion of the laser deposition head relative to the part for fabrication of complex 3-D shapes such as parts with overhangs, branches, and internal cavities in direct metal deposition processes such as the LENS™ process. The proposed approach is based on slicing the solid model of the part into equal-thickness slices perpendicular to the normal build direction and formulating a motion planning strategy based on the properties of these slices. The paper discusses the four sub-approaches that are proposed to handle a variety of complex 3-D shapes parts.

Introduction

The Laser Engineered Net Shaping (LENS™) process developed at Sandia National Laboratories and commercialized by Optomec Design Company of Albuquerque, New Mexico, is one of the first successful techniques for direct metal deposition. A LENS™ machine delivers powder directly to the beam/powder interaction region on the substrate. A high-powered Nd:YAG laser melts the powder, solidifying it to the substrate. The LENS™ machine scans the entire x-y cross-sectional slice from the CAD model, steps in the z-axis, and then repeats the process over again until the part is fabricated.

An important problem in the LENS™ process is the development of general motion planning algorithms that plan the motion of the laser deposition head relative to the part for fabrication of complex 3-D shapes such as parts with overhangs, branches, and internal cavities and passages. Current methodology uses a computer model of the part to produce a tool path that guides the laser deposition system to form successive layers, building the part from bottom to top. The parts are built using a three-axis positioning system that moves the laser head relative to the part. As the part is formed, the powder delivery nozzle moves upward. This approach does not work for parts with complex features such as branches. For these parts, the parts need to be rotated to enable the laser head to be perpendicular to the part section while being fused.

This paper addresses the development of a general motion planning methodology that can work for arbitrary-shaped parts. The goal is to start with a solid model of the part to be manufactured as an input and to generate multi-axis laser scanning paths as an output. The proposed method assumes the LENS™ fabrication machine will be equipped with at least two additional axes to allow for two axes of part rotation. These axes can be either added to the laser deposition head, to the holder that the part is mounted to, or as a combination of the two. Any developed methodology need to be general enough to work with multi-axis configurations for both part manipulation or deposition head manipulation setups.

Very little work has been reported in the literature on motion planning of multi-axis LENS™ machines. In addition, no work has been reported yet to automatically control, based on the solid model alone, deposition for more than 3 axes of motion. Researchers at Sandia [1] have reported on the use of a six-axis robot to hold and manipulate a part during deposition. Optomec, the commercializer of the LENS™ technology, has sold machines which are equipped with 5-axes of motion. But, no software has yet been formulated which takes advantage of these axes in a generic and automatic way. The use of more than 3 axes of motion has always required significant operator intervention and programming to enable fabrication of complex geometries. Lockheed Martin, which owns an Optomec LENS™ machine, has reported on the use of a six-axis articulated robot [2] that carries the deposition head, but they too have been unable to successfully develop a methodology for using these additional axes without significant operator intervention.

Classification Procedure

In developing a methodology for conversion of a solid model CAD file into a motion file that drives the multi-axis LENS™ machine, our approach is based on slicing the solid model into equal-thickness slices perpendicular to the normal build direction. The first step in this approach is to develop a classification procedure that can classify the different types of parts based on the properties of these slices. We have categorized all solid parts into the following four categories:

Normal Build Parts: Are those parts that none of their slices has an overhang. Examples of such parts are shown in Figure 1.

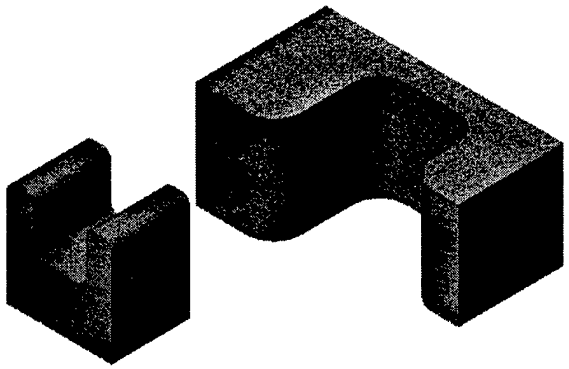

Fig. 1 Normal Build parts

Rotationally Symmetric Overhang Parts: Are those parts that are rotationally symmetric and also some of their slices have an overhang. Examples of such parts are shown in Figure 2.

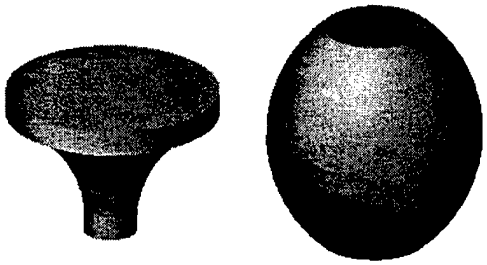

Fig. 2 Rotationally Symmetric Overhang parts

Regular Overhang parts: Are those parts that are non-rotationally symmetric, some of their slices have overhangs, and there are no closed branches or internal cavities. An example of such parts is shown in Figure 3.

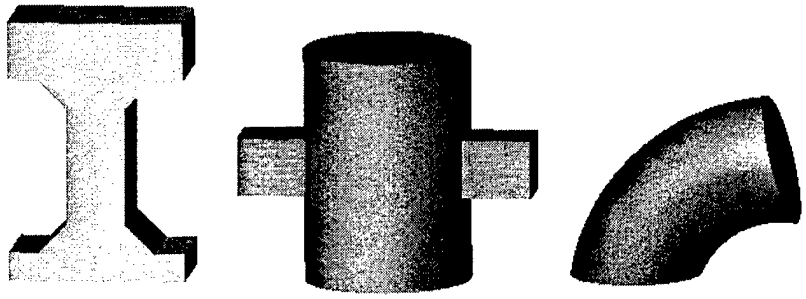

Fig. 3 Regular Overhang parts

Complex Overhang Parts: Are those parts that have either closed branches or internal cavities. Examples of such parts are shown in Figure 4.

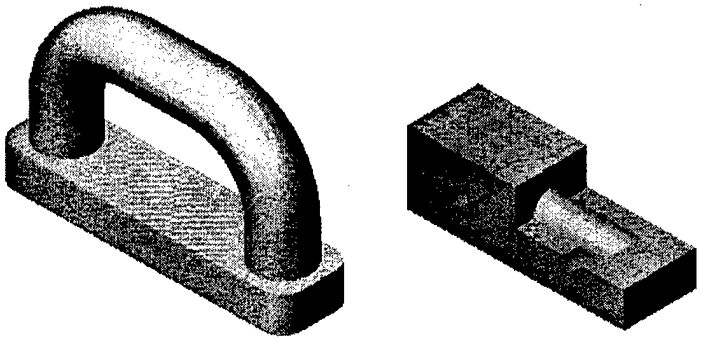

Fig. 4 Complex Overhang Parts

To aid in the classification procedure, we need to develop several algorithms. These include ones to compute if the current slice has an overhang relative to the lower slice, to compute if a slice has more than one closed contour, and to compute if the slices are rotationally symmetric.

Planning Approach

The second step in this approach is to develop a fabrication strategy for each of these categories. Parts of the first category can be fabricated with three axis machines and automatic approaches for their fabrication already exist. All parts in the remaining categories require more than three axes of motion to be fabricated, and will be discussed in this paper.

For Rotationally Symmetric Overhang parts, our approach is to fabricate the part in two stages. In the first stage, the no-overhang core of the part will be made. In the second stage, the core will be rotated 90 degrees and the reminder of the part fabricated similarly to a standard cylindrical cladding operation.

For the third category of parts, Regular Overhang parts, our approach is to start fabricating the part slice- by-slice starting from the lowermost slice until we reach a slice that has an overhang. At this point, the non-overhanging portion of the slice will be fabricated first, then the part will be rotated (typically 90 degrees) and the overhang portion will be fabricated as if it was a normal part. The approach will then be repeated for the remaining slices.

As an illustration of this approach, Figure 5 shows a simplified 2-D sequence for fabricating a part that has an overhang. The bottom two slices ("a" and "b") have no overhang so they are built using standard procedures. The third slice has an overhang, so it is split into two portions. Portion "c" is fabricated first on the top of the two previous slices. The part is then rotated 90 degrees, and then portion “d” is fabricated. The part is rotated back to its original orientation before fabricating the fourth slice. The fourth slice has an overhang relative to the third slice, so it is fabricated in two portions ("e" and "f") similar to the third slice. The last slice ("g") is fabricated last in the normal build orientation. In actual implementation, the slices will be thin (0.01" typically), so several slices will be combined together so that the overhanging portions will have sufficient strength.

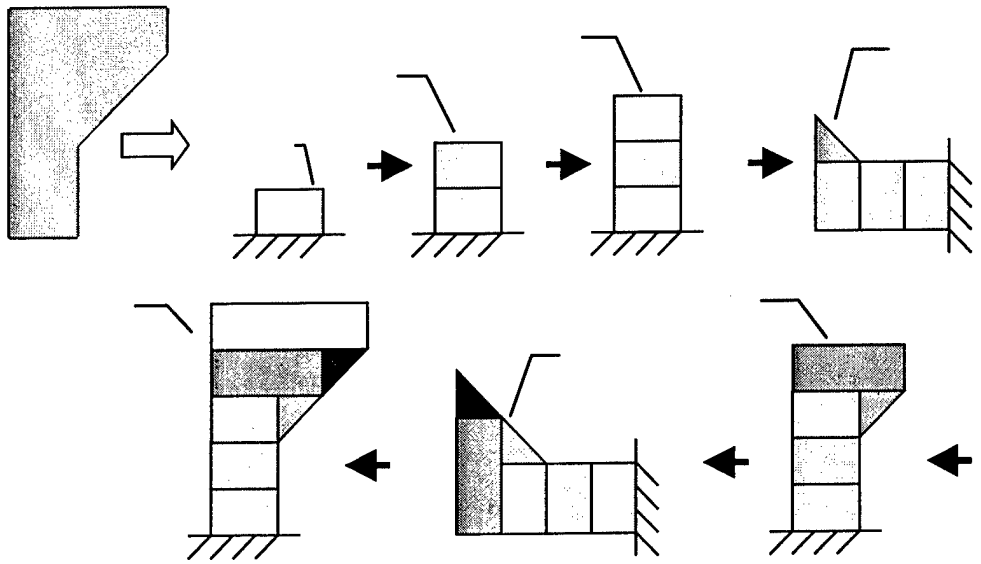

Fig. 5 Illustration of the build strategy

For the fourth category of parts, Complex Overhang parts, our approach will be similar to that of the third category with the exception that it may not be possible to fabricate the whole part using the above strategy alone due to limitations arising from interference between the laser head and the part or due to lack of powder support for certain portions of the parts. For these cases, a modified strategy is suggested which involves re-positioning of the part to enable part fabrication and building at angles that are not perpendicular to the build surface. Build angles ranging from 60-120 degrees are easily achievable using LENS™, and in some cases build angles from 45-135 degrees are achievable, thus there remains some flexibility for building parts whose geometry makes it impossible for the head to be exactly perpendicular to the deposition surface. For certain geometries it may be necessary to build "sacrificial" supports, which must be removed later. The removal of these supports will be greatly simplified by utilizing a sacrificial material that can either be chemically removed or simply melted out after fabrication. This is possible due to the multi-material deposition capabilities of LENS™.

Discussion

For the proposed approach, the following issues need to be addressed:

1. Sequencing of the fabrication procedure for parts with several branches, including identification of the initial build orientation.
2. Checking for interference between the part and the machine head
3. Generation of the needed geometrical information for fabrication when the part axis is rotated away from the normal build direction.

We believe that the proposed fabrication strategy is novel and has the following advantages:

1. Slicing is a standard feature available on most CAD packages that interface with rapid prototyping systems.
2. All the part characteristics are determined based on evaluating the properties of the slices, which are mathematically not difficult to evaluate.
3. The planning procedure is local and does not require decomposition of the part into different sub-volumes.

Currently work is underway to implement the above presented method. The successful implementation of such a 5-axis deposition control scheme will greatly enhance the ability of direct metal deposition processes to produce and repair real components with substantial geometric complexity.

References

1. D. Hensinger, A. Ames, and J. Kuhlmann. "Motion Planning for a Direct Metal Deposition Rapid Prototyping System". In *Proceedings of the 2000 IEEE International Conference on Robotics & Automation*, San Francisco, CA, pp. 3095-3100, April 2000.
2. "Rapid Manufacturing Technologies". *Materials & Processes*, Vol. 159, Issue 5, May 2001.

THE IMPACT OF IN-HOUSE RP UPON FINAL YEAR INDUSTRIAL DESIGN STUDENT PROJECTS

R. I. Campbell and A. R. Hodgson
Department of Design and Technology, Loughborough University, LE11 3TU, UK
Reviewed, accepted August 13, 2003

Abstract

A vital part of the Industrial Design and Technology degree course at Loughborough University is the development of appearance and functional prototypes. Previously, the use of rapid prototyping (RP) has been fairly limited because of the high cost and problematic timing issues of using external facilities. However, during 2003, the availability of an in-house FDM 2000 machine has greatly increased the use of RP models. This paper identifies the impact this has had upon a) the design approach, b) the characteristics of the models produced and c) the use of the models with user evaluation trials. Conclusions drawn show that RP has brought major benefits but that there are some pitfalls that must be avoided.

Introduction

The Industrial Design and Technology degree course at Loughborough University is characterised by an integrated treatment of the aesthetic, ergonomic and functional aspects of product design. Final year students are encouraged to incorporate all three into their major design project and to validate their product design through user evaluation. This necessitates the use of appearance models and functional prototypes within user evaluation trials. Conventionally, appearance models will be used to convey aesthetics and some ergonomic aspects to the user while functional prototypes are used to convey the remaining, more technical features. In industry, rapid prototyping (RP) has been used to help produce both appearance models and functional prototypes, often yielding significant time and cost savings. However, recent research at Loughborough [Evans, 2003] has shown that the greatest benefit of RP to industrial design is the ability to create an integrated appearance model/functional prototype, often called an appearance prototype. When used in this manner, it can not only reduce time and costs but also improve the designer's confidence in the results of user trials because of the increased realism of the prototypes used. Therefore, it has become an aim of the Department of Design and Technology (DDT) at Loughborough to encourage the use of RP whenever possible and beneficial.

If rapid prototyping (RP) is to become a widely used tool within the field of industrial design, it is necessary for students of the subject to be completely familiar with its capabilities and limitations. To this end, DDT set up close relationships with local RP service providers, initially in a nearby RP bureau, and more recently, in another department at Loughborough. However, the uptake of RP remained rather low, with less than 10% of final year students making use of it during their major design project. This was partly due to the relatively high cost of using the RP bureau and some scheduling problems with the other university department. However, it was also believed that there may have been a lack of willingness to use RP techniques because they were seen as "engineering only" tools. At the beginning of the 2002/03 academic year, DDT acquired FDM 2000 and ThermoJet RP machines for its own use. Although quite old, the FDM

machine worked well, once a new deposition head had been fitted. It was hoped that the addition of an in-house facility would promote greater student familiarity with RP techniques in general and break down any perceived barriers. This paper describes the effect that in-house RP has had within DDT and the impact it has had upon the students' design process. The overall aim of the paper is to present results and draw conclusions that will help industrial design departments in other universities who find themselves in a similar situation.

Background

The Industrial Design and Technology course at Loughborough is a three year undergraduate programme that can lead to a BSc or BA, depending on which optional modules are taken. It is one of only a few university courses in the UK which place major emphasis on both the outward, aesthetic properties of a product together with the internal technology required to provide the product's function. Therefore, the students cover a wide range of subjects including sketching, manual model making, product semantics, multi-media presentation, engineering drawing, electronics, mechanics, materials, computer-aided design (CAD) and design for manufacture. Great importance is attached to a hands-on approach to design. Students undertake project work in all three years aimed at assimilating and applying the knowledge they have gained from other modules. Graduates from the programme have been known to embarque on careers in engineering design as well as industrial design.

The major design project undertaken by all final year students is the culmination of all their practical activities. It runs across both semesters and has a nominal student time input of 500 hours, in total. The first semester concentrates on finding a potential market for a product, developing a product design specification, generating several concept designs and selecting one for further development. During semester two the students are expected to convert the chosen concept design into a fully detailed design, produce a functional prototype, have it evaluated by potential users and consider design for manufacture issues. If the functional prototype does not reflect the actual appearance of the final product then a student will be expected to produce an appearance model also. It is during this "prototype manufacture" stage of the project that students will employ their model making skills. Traditionally, this has involved manual modelling in blue foam, medium density fibreboard (MDF), various plastics, aluminium, steel and occasionally, textiles. The techniques used include machining, forming, welding, filling, sanding and painting. Computer numerical control (CNC) milling and routing is sometimes used for both component and tool manufacture, and more recently, vacuum casting has been used to replicate models in more representative materials. In the past, the predominant use of manual techniques has often made it difficult for students to combine both an organic form and intricate internal details within a single appearance prototype.

Throughout the duration of the project, students are expected to attend weekly seminars that cover both organisational aspects of the module and various skills and knowledge they will need to apply. RP is introduced to the students during one of these seminars. They are given an overview of how it works, the techniques available, its pros and cons, and the importance of having a high quality CAD model to drive the RP process is stressed. All of the students will have covered 3D CAD in both their first and second year but mostly this is confined to solid modelling techniques. It should be noted that around half of the students will already have had a

more detailed introduction to RP during an optional final year module entitled "Computer-aided Modelling and Manufacture" (CAMM). This module also exposes them to more advanced CAD/CAM techniques such as freeform surface modelling and three axis CNC machining. Therefore, the CAMM students tend to have acquired more skills and knowledge in regard to the "digital" design process. It is interesting to note that 85% of the students who used RP during their project had attended the CAMM module.

Data Collection

The aim of this research was to determine the effect that the introduction of in-house RP has had within DDT and, in particular, the impact it has had upon the students' design process. To do this it was necessary to gain an insight into how and why students had used RP. This was undertaken in two ways. Firstly, a questionnaire was given to all the final year students asking specific questions about their use (or non-use) of RP. The aim of the questionnaire was to obtain some quantitative data regarding the use of RP. The questionnaire generally followed the same format as one that had been used with industry-based designers in a previous research project [Campbell, 1998]. However, it had to be tailored to the different circumstances faced by students. The questions are listed in the Appendix. Secondly, to gain more qualitative data on the impact that RP had had upon students' design process, several student projects were treated as case studies. Their use of RP was tracked throughout their projects and the resulting prototypes analysed to see what benefits RP had yielded. The results obtained from both strands of the research are now presented together with some preliminary analysis.

Questionnaire Results and Analysis

The questionnaire was issued to all 90 final year Industrial Design students who had just completed their major individual design project. 35 students completed the questionnaire, equivalent to a response rate of 39%. Of these 35 students, 20 had used RP during their project whereas 15 had not. It is known that a large majority of those who did not respond had not used RP. Therefore, it can be estimated that approximately 25% of the final year had used RP this year, a big increase over the previous year when only around 10% had used it. A range of reasons where given for not using RP with just under half of the responses being "not appropriate to project". This is a fairly vague phrase but other students were more specific. Virtually equal numbers cited "lack of know-how", "unsuitable materials", "product too large", "RP too expensive" and "simpler to use conventional techniques" as reasons for not using RP. In regard to RP being too expensive, the students were charged at a rate of 25 pence (40 US cents) per gramme for FDM models. This was much less than a commercial rate but could still result in larger models having a significant cost. The "lack of know-how" most likely refers to a deficiency in CAD skills rather than a lack of knowledge about RP techniques. This can be assumed because only half of the students took the optional final year CAMM module.

Of the 20 students who did use RP, the predominant reason given (cited by 14 students) was "the ability to create more complex or more organic product forms". Other reasons were "improved accuracy", "better surface finish", "faster process", "more convenient" and "to gain experience". None of these was cited by more than four students. It should be understood that

the majority of the students were comparing RP to conventional, manual techniques for model making rather than to CNC machining or other final production processes.

Half of the students required only a small number of RP models (five or less) and the distribution for the remainder can be seen in Figure 1. The largest number of models made for any one student was 26. 11 of the students made use of the in-house FDM machine, whereas the numbers who used SLA, ThermoJet and SLS were 8, 4 and 2 respectively (7 students used more than one machine). Although the cost of using FDM was greater (SLA, ThermoJet and SLS models were provided for free), the convenience of using locally located facilities seemed to be more important to many. Other reasons given for usage of particular techniques were accuracy, strength, surface finish and suitability for investment casting. Indeed the fact that several students used more than one technique showed that they had gained an understanding of the relative merits of the various systems available.

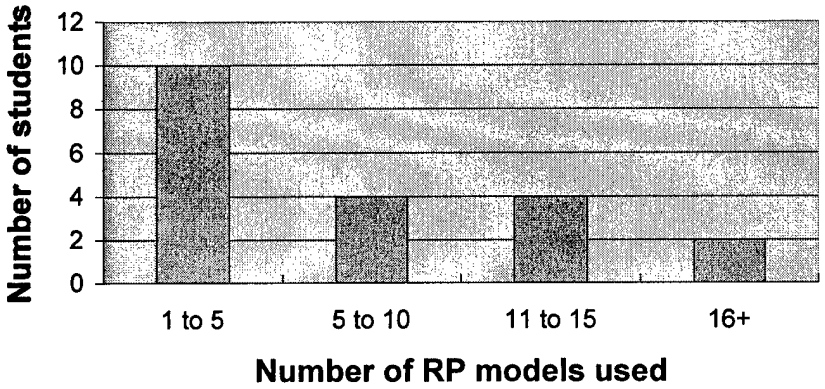

Figure 1: Number of students against numbers of models used.

75% of the students used their RP models as functional components within their prototype whereas only 20% used models for purely visualisation purposes. This shows that the majority of students had recognised the ability of RP to create models that have similar characteristics to final production components. 25% of students used their RP models for vacuum casting, again the aim being to arrive at functional components. Other uses for the models where investment casting (1 student), assembly checking (2 students) and ergonomic testing (1 student). Several students used different models for different purposes, again showing a good understanding of RP system capabilities.

In an attempt to determine if RP had opened up new design possibilities for the students, they were asked if they would still have made the same models if RP had not been available. Unfortunately, nine of students answered "not sure" which does not give much indication of their thought processes. However, four students said they would have made do without a physical model, perhaps using 2D images or a CAD animation instead of an appearance model. Obviously, for these students, RP had enabled them to produce a more tangible output from their design process. For the seven students who said they would definitely have made the same models, all of them said they would have used manual modelling techniques with three saying they would also have used CNC machining. Following on from this, the students were asked if they had used conventional modelling techniques alongside RP. 85% of them had done so and

the number of students using each of a wide range of techniques is shown in Figure 2. This shows that the traditional skills of industrial designers compliment well the capabilities of RP. The students were entirely at ease with creating a high quality prototype from an RP model with stair-stepping and supports. Furthermore, the technological capabilities of the students enabled them to combine this model with others created using plastic and metal-forming techniques.

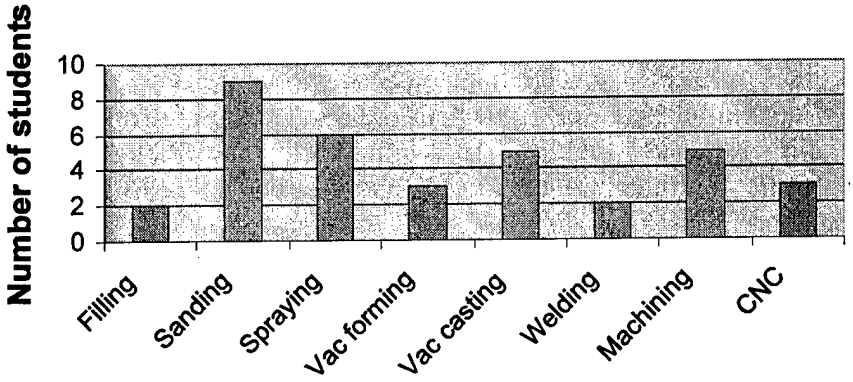

Figure 2: Conventional modelling techniques used alongside RP

The students reported a variable degree of success with using RP. The proportion of RP models that were deemed "satisfactory" by each student varied from 100% to zero. Figure 3 shows the wide distribution of satisfaction levels. Most students have had a reasonably favourable experience in using RP but one student was dissatisfied with all the models produced. This was partly due to different expectations from the models and partly from the different RP techniques used. 70% of the students judged the quality of their RP models by the level of accuracy, 50% by appearance and 40% by surface finish (Most students listed more than one criteria). However, the strength, functionality and surface texture of the RP models were also considered important by some students. RP models produced by some techniques do not measure up well against all of these criteria. The two predominant reasons given for lack of satisfaction were "poor surface finish" (cited by eight students) and "poor accuracy" (cited by seven students. Considering that some students had used RP specifically to improve upon these two factors, it is possible they held some rather unrealistic expectations that have not been met.

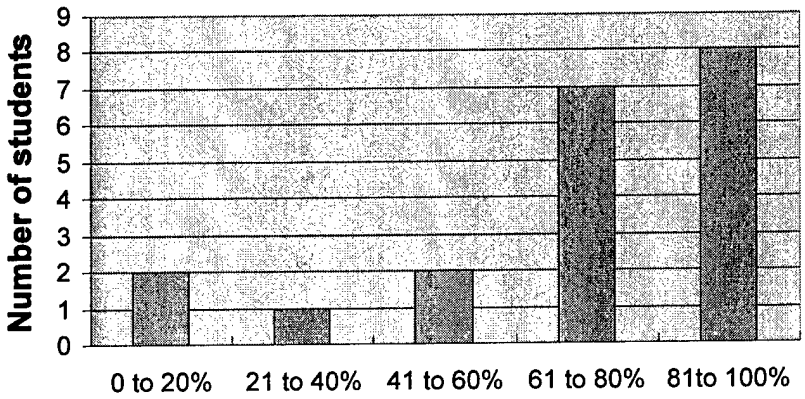

Figure 3: Proportion of RP models judged satisfactory by students.

The last question tried to gauge what impact RP had had upon the design process employed by the students. They were asked how RP had changed their approach to design. 25% of students said that RP had enabled them to produce a more realistic prototype. A further 10% stated that they had been able to produce a single appearance prototype. When taken with the 15% who cited "more complex shape possible" the result is that half of the students had been able to change their physical modelling strategy because of RP. The only other change in design process that was cited by more than one student was that model making had been quicker. This may also refer to the fact that only one set of models was required rather than both an appearance model and a functional prototype.

The results of the questionnaire demonstrated that RP had been used intelligently by many students and had proved beneficial to their design project. However, little indication was given as to the extent that RP can change the way students work. To determine this, three of the highest ranked student projects were taken as case studies and analysed in more detail.

Case Studies

Three student projects used as case studies to probe further into issues that had been raised by the questionnaire. These were a) changes in the design approach followed, b) changes in the characteristics of the models produced and c) the enhanced use of the models within user evaluation trials. Each of the three case studies is now discussed in turn.

Case study 1 – Michael's Glue Gun

Michael's product was a re-design of a glue gun that was aimed at the 'hobbyist' and 'craftsman' who wanted more sophisticated control of the glue as it is dispensed. His final design integrated mechanical, electronic and visual elements in order to meet his intended design specification (see Figure 4).

Figure 4: Final design of glue gun

Early design development raised major problems concerning his aim to incorporate a motorised glue delivery system into a small pen-like product. Instead, it was decided that a separate motor housing should be coupled to the pen via a drive cable, since the required purpose-built motors and mechanical components were outside the scope of his project work. He also decided that his product would be evaluated using two different prototypes. Firstly, an appearance model that would represent the aesthetics and "feel" of the final design, and secondly, a functional prototype that would represent the functional operation of the product – a key part of the 'added value' for this new product.

Towards the later stages of the design project, Michael developed two parallel designs using CAD modelling to create a detailed assembly of parts. One design was to represent the new glue gun as it would be commercially manufactured, with custom designed electrical and mechanical parts. The model for this design was to be made using SLA parts. The other design included a similar (though slightly different) dispenser, a simple drive unit that would house a prototype motor drive (from a cordless screwdriver) and prototype electronics circuit. His intention was to deliver the glue with varying speed, to sense when the user has finished and retract the glue stick to prevent it dripping, and also to vary the heating element power depending on the intended gluing operation. The system required significant development and so a large drive unit, with substantial space for further development, was built in the stronger FDM 2000 material. Figure 5 shows the two different prototypes side by side, and their differences are quite apparent.

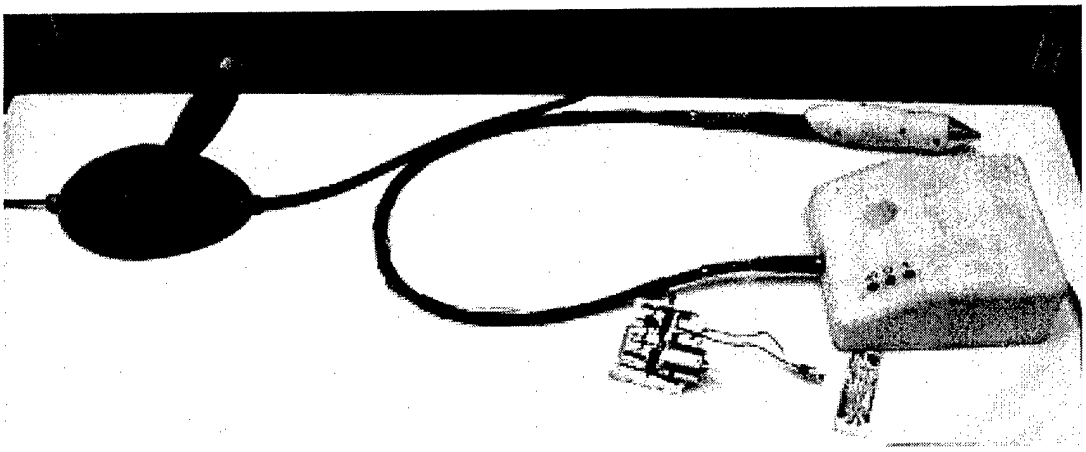

Figure 5: Appearance model (on left) and functional prototype (on right).

Michael made no attempt to finish the surface of the FDM parts used to make the functional prototype. However, the SLA parts for the appearance model of the final design were hand finished and painted. Although not as robust as the FDM model, the purpose of this prototype served only to illustrate form and appearance, and it complemented the functional prototype well. The main conclusion to be drawn here was:

that RP processes can be carefully selected to produce different prototype outcomes.

Case study 2 - Jon's CD Player

Jon used a variety of different RP processes at different phases of his design development work, all linked to his significant CAD modelling capability with Pro/ENGINEER software. He designed a domestic CD player, which included speakers that could be separately located, and also allowed remote control of the CD player volume and track (see Figure 6). The product comprised a main body (that included the CD player itself and the speaker battery chargers) and two symmetrical speaker 'pods' (that included audio receivers and control transmitters, together with batteries and NXT sound exciters so that the speaker cases acted as sound boards). This allowed the CD player to be used in wet environments, like showers, since the speaker 'pods' could be completely sealed.

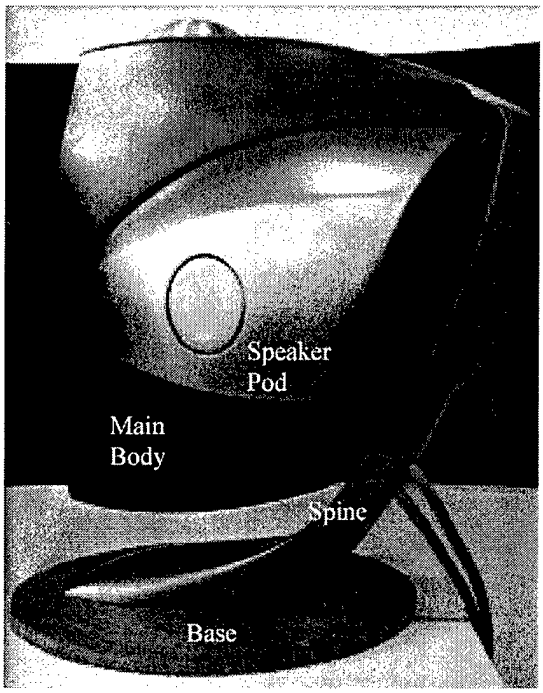

Figure 6: CD Player with various features indicated.

Jon made use of ThermoJet wax models for proving the fit of the pods to the main body, and went through a number of design iterations to prove the initial concepts as the shape and form of the product developed. The product functionality took longer than anticipated to complete, so instead of using SLA models and vacuum casting to produce prototype polymer shells, he chose to use FDM models and then finish/paint their surfaces. He considered that the extra time needed to finish the FDM surface would be less than the time required to make silicone moulds and cast resin parts.

The two plastic mouldings that formed the main body were attached to a cast aluminium 'spine'. Although Jon considered modelling the spine by hand (which would have sufficed for such an early prototype), he decided to use a ThermoJet wax model of the part to make an investment casting in aluminium alloy, made as a one-off part. This provided a rigid framework

onto which the less substantial RP parts could be fastened, and so the CD player could be effectively evaluated as a fully working, appearance prototype.

that the faster, less functional RP techniques enable rapid and copious design iterations,

that the need for separate appearance model and functional prototype can be eliminated via the combined use of RP and secondary processes.

Case study 3 – Kelly's Food Preparation Device

Like Jon, Kelly made use of a several RP techniques at different phases of her design project. She was developing a food preparation product that exploited a new textured plastic within what was aimed to be a "cooking is fun" context. As with all students of the Industrial Design and Technology course, she started by analysing the potential market and considering the needs of users, helping her to generate initial ideas, concepts and design specifications. During this time, some mechanical parts were modelled in CAD, and evaluated through mechanical simulation, but she still felt the need to physically model the mechanism.

The shape and form of the different parts were developed using a combination of sketch work and CAD modelling, and then built in wax using the ThermoJet process (an example part is shown in Figure 7). These helped Kelly to evaluate the overall appearance of her design together with the comfort and other related ergonomic factors of the hand-held parts in particular. These parts could have been modelled in foam, either by using 3-axis CNC routing, or by hand. However, the wax RP model was an accurately formed prototype part that very closely followed the CAD model and Kelly's intended design. It required minimal finishing and was quickly achieved using an STL file generated from Pro/ENGINEER. The ability of the model to build internal features in the casing parts was particularly beneficial, since it allowed Kelly to check for fit and location of mechanical parts. Several versions of wax-modelled prototypes were produced during the concept development phase of the project, alongside continuing sketch and CAD modelling work. It is thought that the use of quick and easy RP output enabled a more effective design to be developed through a number of early design iterations.

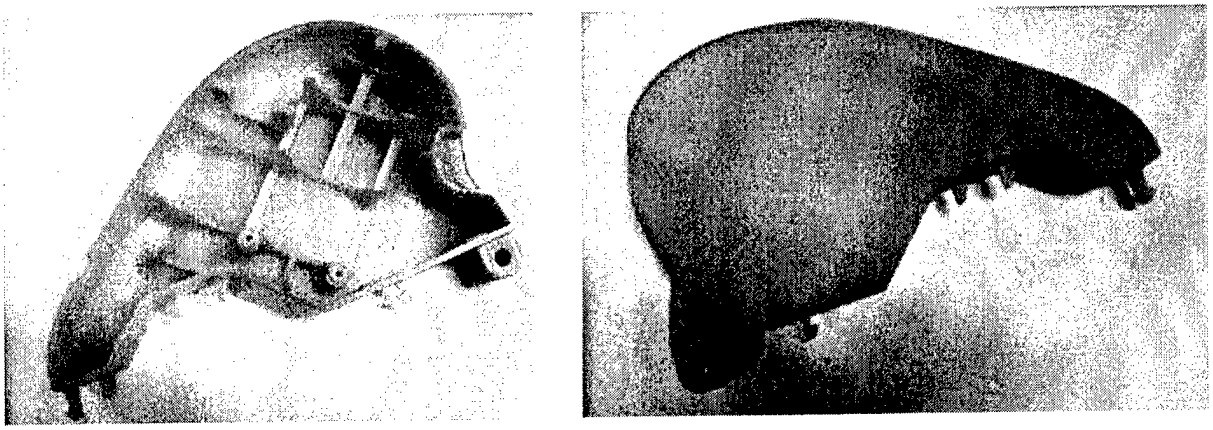

Figure 7: One of the ThermoJet models used for aesthetic, ergonomic and assembly evaluation.

As the project progressed, more robust components became necessary for full assembly and testing purposes and so FDM was used. Kelly decided to hand-finish these parts to in order to present her progress to her external "client company" (see Figure 8).

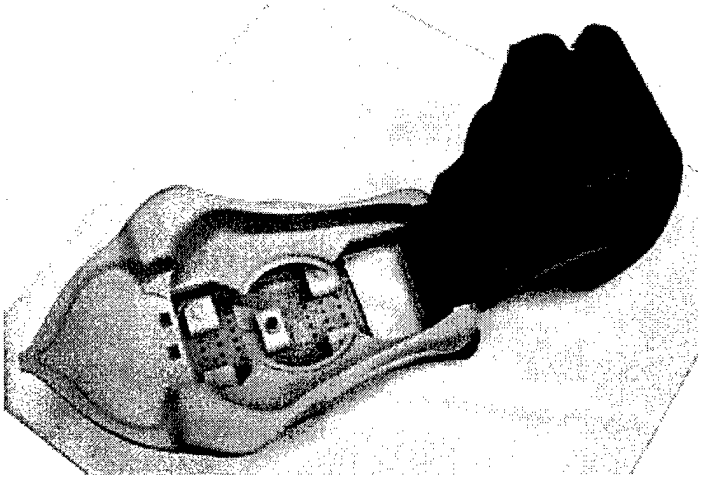

Figure 8: Hand-finished FDM parts

However, the quality of surface finish and detail was not considered to be sufficient for a final appearance prototype. Following some minor re-design after evaluation of the FDM models, Kelly used SLA models with subsequent vacuum casting for this purpose. Figure 9a shows a combination of SLA and vacuum casting parts prior to final finishing.

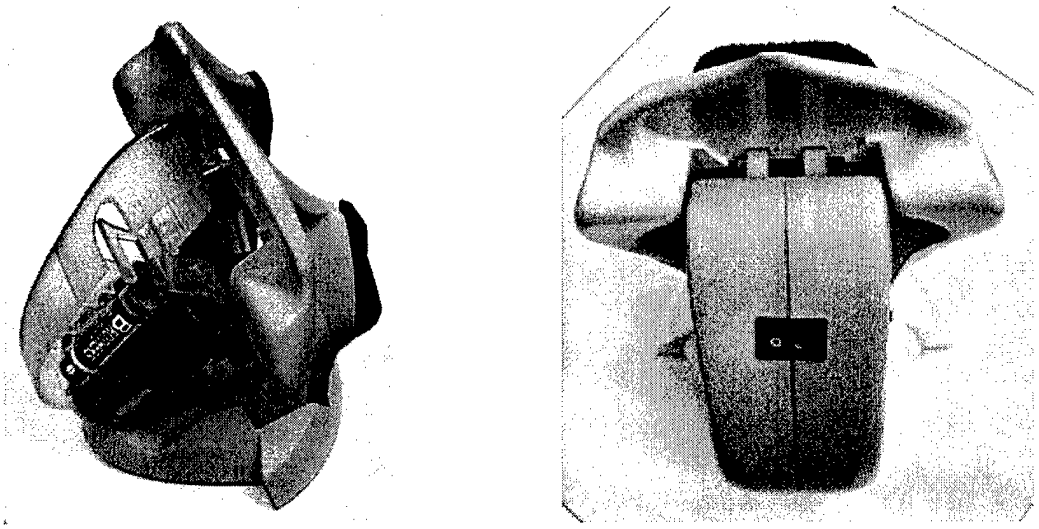

(a) (b)

Figure 9: Appearance prototype before and after finishing.

The SLA models required less finishing than FDM would have needed, and were vacuum cast in an ABS-replicating resin with appropriate colouring pigment to minimise finishing requirements. This resulted in an appearance prototype that was robust enough to be used by a

number of people in a typical food preparation context (see Figure 9b). The resulting evaluation provided very effective feedback on the user acceptance and operation of the product. The main conclusions to be drawn from this project were:

that the use of RP at different stages in the design process enabled more design iteration and resulted in a higher quality product,

that the combination of RP with conventional modelling techniques provided a high quality appearance prototype that was suitable for extensive user trials in a realistic environment.

Conclusions

The availability of an in-house FDM machine served to raise the general profile of RP within the department. As a result, the student use of other RP techniques increased over previous years. Aligned to the increased availability of RP modelling was the development of increased CAD modelling capability. Students were able to capture their design intent in Pro/ENGINEER through a combination of solid modelling, surface modelling and freeform surface modelling (using ISDX). This was a pre-requisite for their RP work, and vital to the successful implementation of RP in both appearance models and functional prototypes.

The questionnaire captured data from most of the students who had used RP for their design project. RP was primarily adopted to achieve more complex and more organic forms that would otherwise be difficult and time consuming. This was only beneficial because the traditional model making skills of industrial designers were used to produce high quality model finishes. Different RP systems were used for different outputs and it was highly desirable that a range of complimentary techniques were available. Some students had unrealistic expectations of what RP could achieve. It is therefore essential that students are well informed about various system capabilities. Most significantly, half of the students stated that RP had changed their strategy for creating physical models.

These results were supported by the case studies, which showed that RP processes had been carefully selected to achieve different outcomes. They also showed that the rapid and copious design iterations facilitated by RP result in more optimised designs. The most important change in modelling strategy was the combination of aesthetics and functionality within a single prototype. This led to more realistic user trials, which in turn, should give more reliable feedback on the product design.

References

Evans, M.A. and Campbell, R.I. (2003), "A Comparative Evaluation of Industrial Design Models Produced Using Rapid Prototyping and Workshop-Based Fabrication Techniques", accepted for publication in Rapid Prototyping Journal.

Campbell, R.I. (1998), "Using Feature-based Product Modelling to Integrate Design and Rapid Prototyping ", PhD thesis, Manufacturing Engineering and Operations Management, University of Nottingham, UK.

Appendix: Questions asked in the questionnaire

1. Did you use one or more rapid prototyping (RP) models for your design project?

(If yes, please go to question 5.)

2. Did you consider using RP during your design project?

(If no, please go to question 4.)

3. Why did you decide not to use RP? Thank you for completing the questionnaire.

4. Why did you not consider using RP? Thank you for completing the questionnaire.

5. Why did you decide to make use of RP models?

6. How many RP models did you have made for your design project?

7. Which RP system(s) were used and why did you select them?

8. What design or prototyping purpose did you use your RP models for?

9. Would you still have made these models if RP had not been available?

10. If yes to question 9, how would you have made your models?

11. Besides using RP, did you still make use of other model-making techniques (e.g. to make other parts or to finish your RP models)?

12. If yes to question 11, which technique(s) did you use?

13. What criteria did you use when evaluating the quality of your RP models?

14. What proportion of the RP models you had built were of satisfactory quality for your purpose?

15. What were the reasons for any of your models not being satisfactory?

16. How has the availability of RP changed your approach to your design project?

Thank you for completing the questionnaire.

A MULTI-MATERIAL VIRTUAL PROTOTYPING SYSTEM

S. H. Choi and H.H. Cheung
Department of Industrial and Manufacturing Systems Engineering
The University of Hong Kong,
Pokfulam Road,
Hong Kong.

Reviewed, accepted August 13, 2003

Abstract

This paper proposes a virtual prototyping system for digital fabrication of multi-material prototypes. It consists mainly of a topological hierarchy-sorting algorithm for processing slice contours, and a virtual simulation system for visualisation and optimisation of multi-material layered manufacturing (MMLM) processes. The topological hierarchy-sorting algorithm processes the hierarchy relationship of complex slice contours. It builds a parent-and-son list that defines the containment relationship of the slice contours, and subsequently arranges the contours in an appropriate sequence which facilitates optimisation of toolpath for MMLM by avoiding redundant movements. The virtual simulation system simulates MMLM processes and provides vivid visualisation of the resulting multi-material prototypes for quality analysis and optimisation of the processes.

1. Introduction

Layered Manufacturing (LM) is an additive manufacturing process that produces a physical prototype from a CAD model layer-by-layer. The CAD model can be generated from many sources, including CAD designs and conversion data from a 3D scanner. LM systems are widely adopted in manufacturing and medical applications to save cost and time. Manufacturers use LM technology to produce prototypes of products for design evaluation, and as master patterns for production tools. Surgeons use it to plan and explain complex surgical operations, especially craniofacial and maxillofacial surgeries. LM technology has also been explored for direct manufacture of biologically active implants. Currently, commercial LM machines can only produce single-material prototypes (Qiu et al., 2001; Zhu and Yu, 2002). However, there is an increasing demand for multi-material prototypes. This is because high value-added products tend to involve advanced and complex design, while medical operations are becoming more complicated and delicate. Indeed, a multi-material prototype that can clearly differentiate one part from another of a product, or tissues from blood vessels or bone structure of a human organ, will be particularly useful for designers or surgeons, respectively. Therefore, it would be very desirable and useful to develop multi-material layered manufacturing (MMLM) technology.

In general, a multi-material object may compose of either several materials with varying composition or a collection of discrete materials (Kumar etc al., 1998; Qiu and Langrana, 2002). Effective representation of multi-material objects is a vital step in the development of MMLM technology. However, a critical problem is that current CAD models do not contain any material information. Consequently, most LM systems treat a model as homogeneous models during down-line process planning (Cheng and Langrana, 2001; Patil et al., 2002).

Although MMLM technology has attracted much research interest and some pioneering work has started, practical and viable MMLM machines have yet to be developed.

A MMLM machine may include mainly two sub-systems, namely a hardware material-depositing mechanism and a computer control software system that is able to process multi-material slice contours to control the material-depositing mechanism, as shown in Fig. 1.

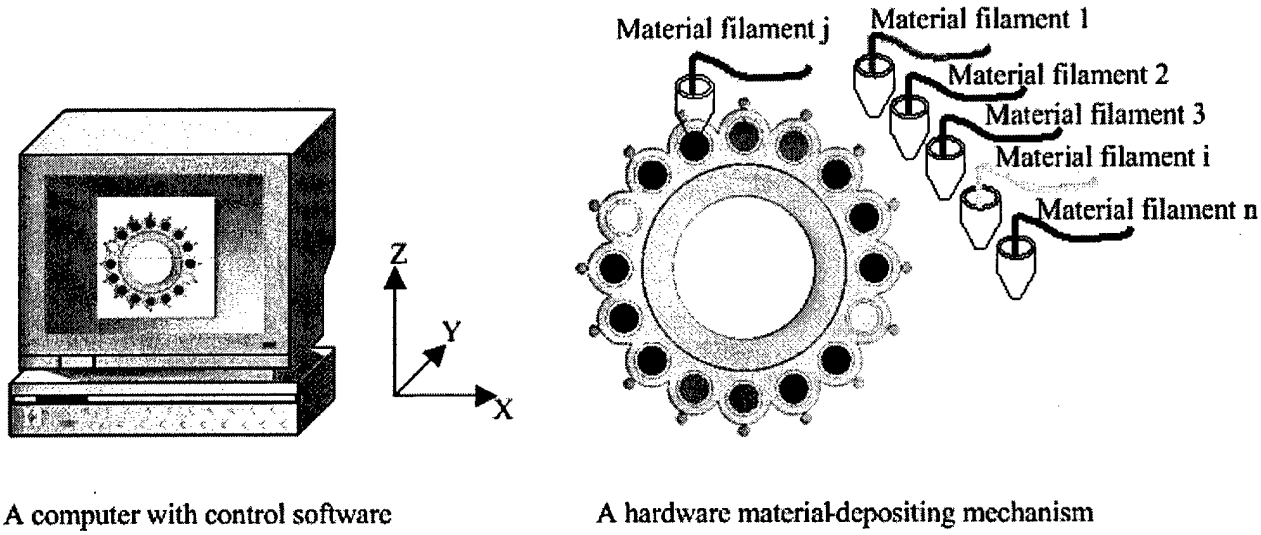

Fig. 1. A layer of a multi-material part being fabricated

The development of MMLM technology is largely a software issue. The material-depositing mechanism may consist of an array of nozzles or tools, each of which deposits a type of material on specific areas of a layer. The tools may be bundled together or may be controlled to move independently. They may be adapted from those used in the existing single-material LM machines. However, a viable computer software system for MMLM processes has yet to be developed. The system should be able to generate multi-material slice contours, which are subsequently sorted and intra-connected to relate specific slice contours to a particular tool, such that the area is appropriately deposited with the desired material. Hence, the processing of complex multi-material slice contours and the planning of multi-toolpath are particularly important. They facilitate the system to control tools depositing selected material at the appropriate contours and simultaneously avoid redundant movements and possible collisions of the tools which move otherwise independently to increase efficiency.

This is, however, a daunting task because slice contours are generally random in nature with no explicit topological hierarchy relationship. As a result, it is very difficult to identify one contour from another within a slice as required for generating toolpath for MMLM fabrication. Therefore, it can be seen that the difficulty of processing slice contours, and the required software system, largely hinders the development of MMLM technology.

In this paper, a multi-material virtual prototyping system for digital fabrication of multi-material prototypes is proposed. The software system may be subsequently adapted and integrated with a material deposition mechanism to form a practical MMLM machine. It consists mainly of (1) a topological hierarchy-sorting algorithm for processing slice contours and arranging the contours in an appropriate sequence which will facilitate optimisation of toolpath for MMLM by avoiding redundant movements; and (2) a dexel-based virtual simulator for visualisation and optimisation of MMLM processes.

2. Review of the related works

MMLM technology provides a powerful way to fabricate multi-material parts, such as micro electronic parts, bone replacement products, innovative cellular and cell-containing tissue scaffolds. Its benefits and needs have been widely recognised. Some researchers have recently started working on MMLM and they have made important contributions. Their work has been categorically focused on a few areas, such as CAD representation of heterogeneous objects for MMLM, optimisation of multi-toolpath for MMLM, development of experimental systems for simple objects, and virtual simulation of MMLM processes.

2.1. CAD representation of heterogeneous objects for MMLM

In order to fabricate multi-material prototypes with MMLM technology, both material and geometrical information of the objects must be made available. Although STL is now a de facto standard file format for LM industry, it only contains geometrical information. Therefore, some researchers have recently proposed CAD formats for heterogeneous objects to facilitate general CADCAM applications, including MRPII (Kumar et al., 1998 and Morvan and Fadel, 1999). Chiu and Tan (2000) proposed a modified STL file format in which a material structure is used to represent materials. Patil et al. (2002) proposed an R-function and a standard file format to model and represent heterogeneous solids using the concepts of ISO 10303.

Such proposed formats, when fully developed and widely adopted, will be useful for MMLM. However, there are still some major problems to solve. Indeed, a significant proportion of complex objects, particularly human organs and bone structures are not designed using CAD systems. Instead, they are captured by laser digitisers, or Computed Tomography (CT) and Magnetic Resonance Imaging (MRI) scanners. The digitised images are normally processed to form a model in STL format or to extract the slice contours, which are random in nature without any explicit topological hierarchy relationship. Hence, processing such slice contours for mutli-toolpath generation remains a challenging obstacle that has yet to be surmounted for the development of MMLM.

2.2. Optimisation of multi-toolpath for MMLM

Toolpath generation plays an important role in automated fabrication of multi-material prototypes. The main purpose of toolpath planning is to find a solution that requires the shortest processing time possible. Park (2003) suggested a toolpath generation procedure for the Z-constant contour machining. It involved the generation of slice contours and the subsequent toolpath by linking the contours. In MMLM, the slice contours are random in nature without any explicit topological hierarchy relationship. There may be redundant movements and collisions when the nozzles move to extrude the specific material at the related contours in a slice. Zhu and Yu (2002) described that two holders would collide with each other if their distance was shorter than the diameter of the tool holders when they attempted to fill two very close contours. They proposed a dexel-based spatio-temporal modelling approach for detecting collisions. Such pioneering works are useful for optimisation of mutli-toolpath for MMLM, although they could only be used to process simple objects.

2.3. Development of experimental multi-material LM machines for simple objects

A few researchers have recently attempted to develop experimental MMLM machines for simple objects. Weiss et al. (1997) described building multi-material structures with pre-fabricated parts, such as advanced tooling and embedded electronic devices. Qiu and Langrana (2002) reported the development of a MMLM machine for fabrication of multi-

phase electromechanical components for naval and other military applications. These systems are among the pioneering work, despite that they could only handle very simple parts.

2.4. Virtual simulation of MMLM process

Cheng and Langrana (2001) and Qiu et al. (2001) described a virtual simulator used to simulate the fabrication of multi-material prototypes. Using computer graphics technology, the simulator was able to detect and remove errors of MMLM process easily and quickly. Generating a virtual multi-material part by the simulator is much faster than the time to generate a physical part. Virtual reality technology has been used for medical applications (Zajtchuk and Satava, 1997). Although their systems have focused more on relatively simple objects, they have highlighted the uselessness of virtual simulation for MMLM.

3. The Proposed multi-material virtual prototyping system

The above pioneering work has made much contributions to the development of MMLM technology. However, there is a lack of integrated effort to tackle the core software problem of processing and planning multi-toolpath for fabrication of complex objects. Therefore, a multi-material virtual prototyping system is proposed to fabricate digital multi-material prototypes. The system consists mainly of a topological hierarchy-sorting algorithm for processing slice contours, and a virtual simulation system for visualisation and optimisation MMLM processes. The topological hierarchy-sorting algorithm constructs the hierarchy relationship of complex slice contours for subsequent fabrication of multi-material prototypes (Choi and Kwok, 2002). In particular, slice contours with established hierarchy relationship facilitate collision detection, as well as the optimisation of toolpath by avoiding redundant back-and-forth movements. The virtual simulation system uses a dexel-based approach for digital fabrication of physical prototypes (Choi and Chan, 2002; Choi and Samavedam, 2001). The workflow of the proposed system includes multi-colour STL model design, slicing multi-material objects, sorting complex slice contours, generation of multi-toolpath, and digital fabrication of multi-material prototypes.

3.1. Representation of multi-material objects by multi-colour STL models

For building multi-material prototypes, both geometry and material information should be provided. In the proposed system, multi-colour STL models are used to represent multi-material objects. Each colour represents a particular type of material. Thus, a multi-colour STL model contains both geometry and material information. A software for processing multi-colour STL models has been developed as an integral part of the proposed system and is used to assign colours into STL models. Some commercial available software such Magics RP (Materialise, 2003) and FlashTL (TNO, 2003) are also able to assign colours into STL models. A tolerant slicing algorithm (Choi and Kwok, 2002) is used to generate multi-material slice contours that are outputted in a modified common layered interface (CLI) file format. Each colour that represents a particular type of material is assigned to each point of the related contours in a layer.

3.2. Optimisation of multi-toolpath with the topological hierarchy-sorting algorithm

In general, complex slice contours are random in nature without any explicit topological hierarchy relationship. This may result in redundant movements, and possibly collisions, when the nozzles move independently to extrude specific materials at the related contours. The topological hierarchy-sorting algorithm simplifies the relational complexity of slice contours, especially with respect to multiple-inclusion contours, by constructing the hierarchy relationship between the contours and the internal cavities. It first builds a parent-and-son list that defines the containment relationship of the slice contours, and subsequently

arranges the contours in an appropriate sequence. With the hierarchy relationship, a complex slice with multiple-inclusion contours can be treated as a family of contours, which can be conveniently processed for toolpath planning. Referring to Fig. 2, the slice contours are grouped into ten families to be made of five discrete materials. The materials are represented by five different colours, namely green, yellow, purple, red and blue. Therefore, five nozzles should be used to extrude five discrete materials in the slice. The contour families with the same material are grouped together, and are subsequently processed to generate hatching vectors that define the toolpath. Hence, the contour families are grouped into five sets of contour families, namely [family1, family 2, family3, family 4], [family5], [family 6, family 10], [family 7, family9] and [family 8]. Based on the grouping of contour families, sequential toolpath without any redundant back-and-forth movements is easily generated. Therefore, the topological hierarchy-sorting algorithm helps optimise the toolpath planning and hence the efficiency of MMLM.

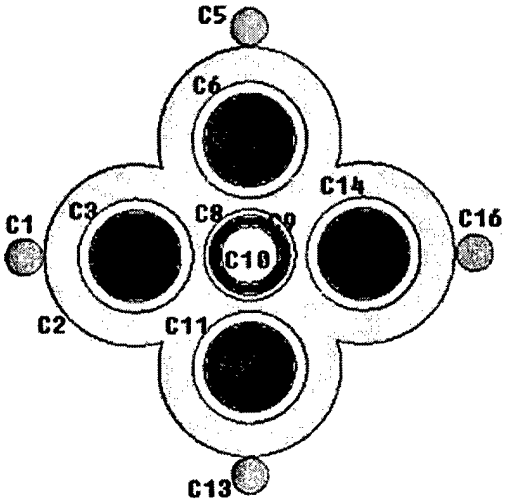

Topological relationship of contours

Level 0 | C1 C5 C13 C16 | C2

m0 m4

Level 1 C3 C6 C8 C11 C14

Level 2 C4 C7 C9 C12 C15

m1 m2 m2 m1

Level 3 C10

m3

Contour families	Colour	Material
1. C1	Green	m0
2. C5	Green	m0
3. C13	Green	m0
4. C16	Green	m0
5. C2, C3, C6, C8, C11, C14	Yellow	m4
6. C4	Purple	m1
7. C7	Blue	m2
8. C9, C10	Red	m3
9. C12	Blue	m2
10. C15	Purple	m1

mi represents material number. (i = 0,1,2.....,n)

Fig. 2. Illustration of topological hierarchy relationship multi-material slice contours

3.3 Digital fabrication of multi-material prototypes

After processing the slice contours and generation of multi-toolpath, the proposed system simulates a MMLM process to fabricate digital multi-material prototypes. Subsequently, it provides vivid visualisation of the resultant prototypes for quality analysis and optimisation of the MMLM process. The designer can manipulate the prototype using the utilities provided to visualise the quality of the product prototype that a MMLM machine will

subsequently deliver. The designer can also navigate around the internal and opaque structures of the prototype to investigate the product design. Furthermore, the digital multi-material prototype may be superimposed on its STL model to highlight dimensional deviations. The system also calculates the maximum and the average cusp heights that indicate the overall accuracy of the prototype. To study the dimensional errors, a tolerance limit may be set and any locations with deviations beyond the limit will be clearly highlighted. The designer may thus identify and focus on the parts that need modifications. To improve the accuracy and the surface quality of specific features of the prototype, the process parameters, such as orientation of the model, the layer thickness or the hatch space, may be changed accordingly.

4. A case study – a ring

Hong Kong is the leading exporter of imitation jewellery and the second largest exporter of precious jewellery in the world. It has also evolved into a trading and distribution centre for pearls in recent years. Jewellery products are getting more fashion-oriented. As a result, innovative designs are becoming more important. Some jewellery manufacturers realise that they should not only rely on individual skills. They have recently adopted LM technology to develop high value-added jewellery items. Hence, the proposed multi-material virtual prototyping system will be particularly useful for building digital multi-material prototypes to help improve designs and shorten development cycles of jewellery products at competitive costs. Designers can view and evaluate their designs with digital prototypes instead of physical ones, at minimal costs and time possible. Furthermore, digital prototypes may be conveniently transmitted over the Internet to facilitate global manufacturing.

A ring in Fig. 3 was therefore chosen as an example to illustrate how the proposed system fabricates digital multi-material prototypes of jewellery products. The ring is made of thirteen kinds of materials and its shape is complex. To produce such multi-material prototypes, an array of nozzles may be used to extrude materials on relevant slice contours in a layer. The topological hierarchy-sorting algorithm constructs the hierarchy relationship of complex slice contours which facilitates the optimisation of multi-toolpath in MMLM by avoiding redundant movements. The case study illustrates how the system generates efficient sequential toolpath of each nozzle, and subsequently how it facilitates quality analysis and optimisation of MMLM processes.

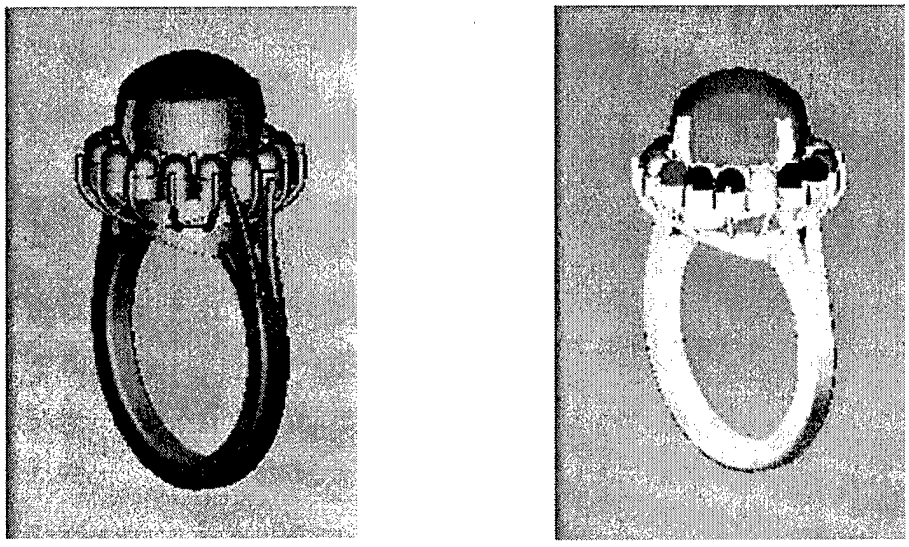

(a) Monochrome STL exported from CAD model

(b) Multi-colour STL model modified from monochrome STL model

Fig. 3. Monchrome and multi-colour STL models of the ring

Based on a monochrome STL model of the ring in Fig. 3a, a multi-colour STL model in Fig. 3b is created by assigning colours to represent appropriate materials of the ring. The multi-colour STL model is sliced to generate slice contours that contain both geometry and material information. A layer of the ring is shown in Fig. 4. In this layer, there are totally 52 contours that are sorted into three hierarchy levels and are grouped into 34 contour families. Each family has its own material property. The layer consists of 11 discrete materials. The contour families with the same material property are grouped into a set. The 34 contour families are grouped into 11 sets because the layer is made of 11 kinds of materials. For each set of contour families, hatching vectors are generated and then arranged in an appropriate sequence. Each set of hatching vectors is used to control a specific nozzle or tool that extrudes a material on the related set of contour families. Fig. 5 shows a layer of the digital fabrication process of the ring prototype. Each nozzle moves sequentially and deposits a material on the related set of contour families in the layer by avoiding redundant movements. More details of the digital fabrication process of the ring is shown in Fig. 6.

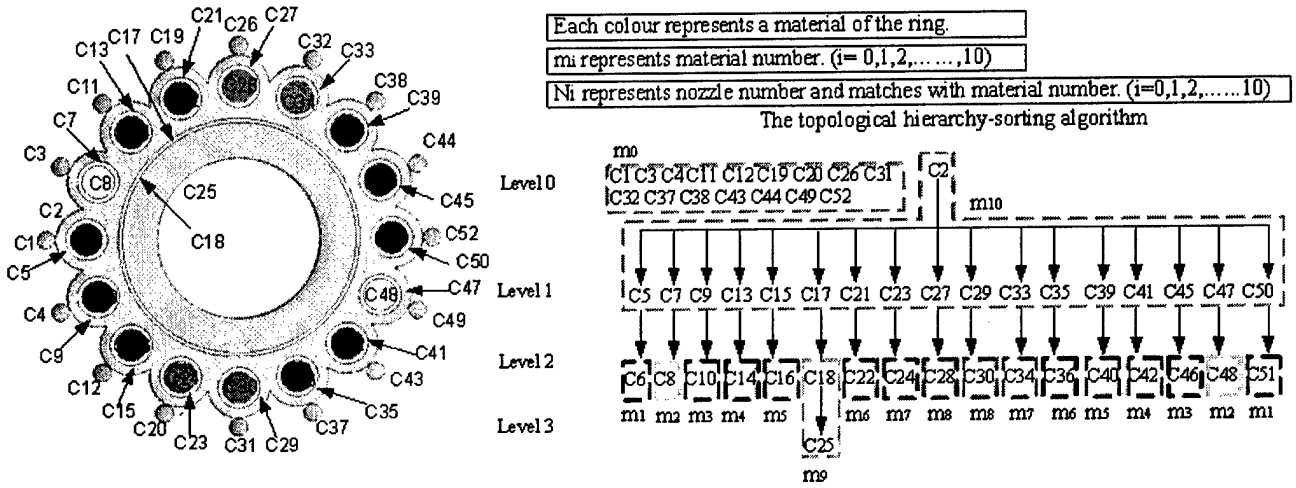

Fig. 4. A layer of complex slice contours with hierarchy relationship

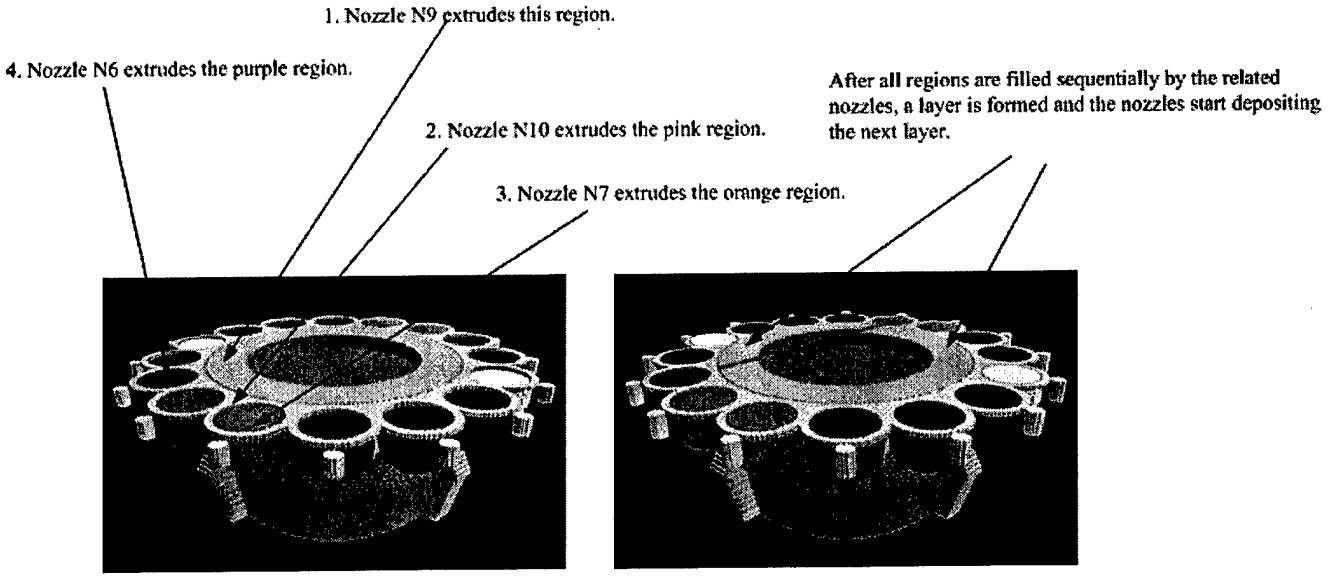

Fig. 5. Nozzles move sequentially to deposit materials on related contours

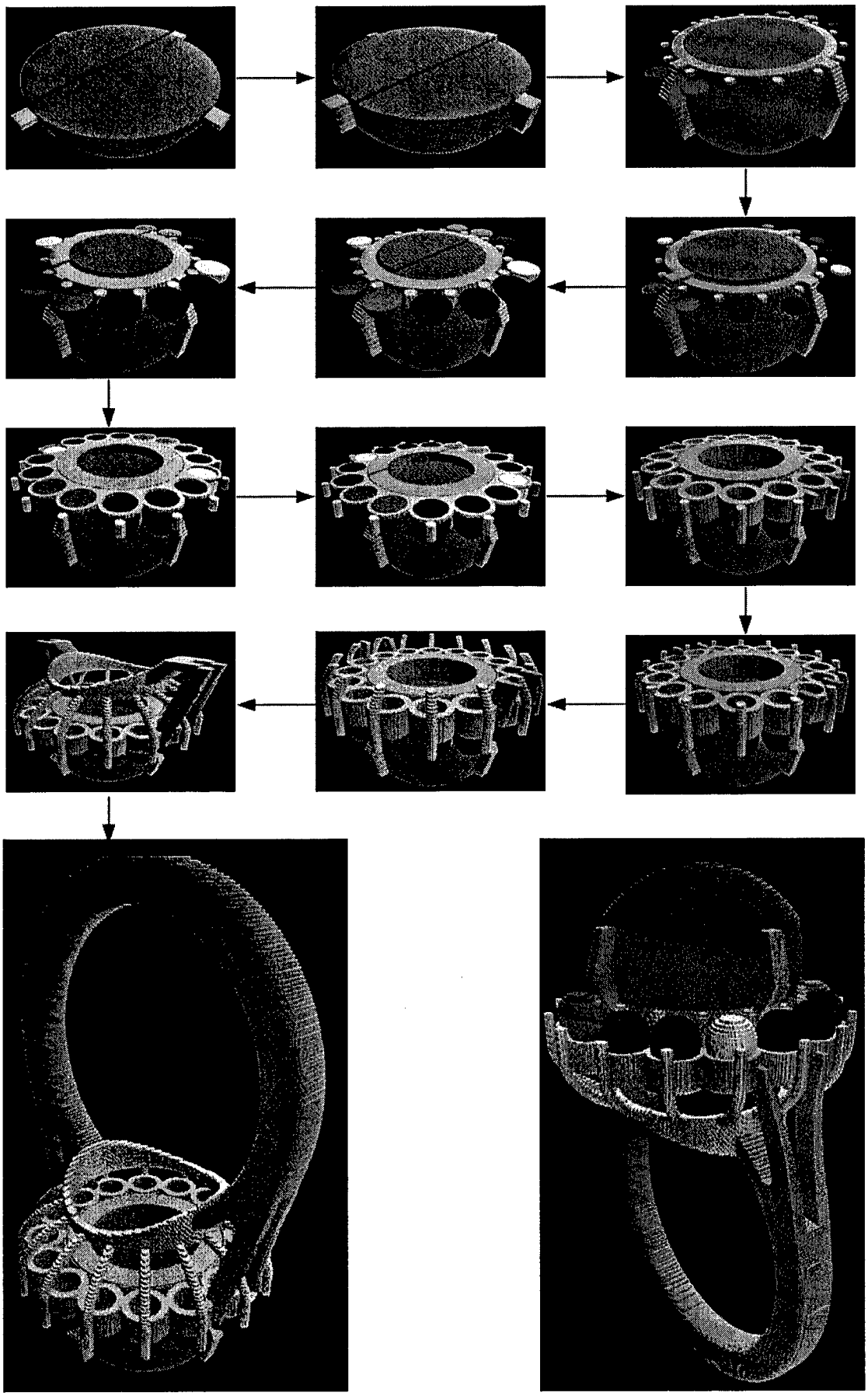

Top view

A complete multi-material virtual prototype of the ring.

Bottom view

Fig. 6. Digital fabrication process of a multi-material prototype of the ring

The system also provides vivid visualisation of the resultant prototypes for quality analysis and optimisation of the MMLM process. Fig.7 shows the ring prototype being superimposed on its STL model. The surface texture and the dimensional deviation are clearly illustrated. In addition, the system calculates the cusp heights to evaluate the overall dimensional deviations. In this case, the average and the maximum cusp heights are 0.097mm and 0.176mm, respectively. Suppose that any deviations more than 0.175mm are considered not acceptable, the designer may choose to highlight the areas which are out of the design limit for subsequent investigation of these important features. Fig. 8 shows the same ring with some pins on them. The pins indicate the facets of the STL model with cusp heights more than 0.175mm. The colour of the pins may be red or green. The red ones points to the maximum deviations whereas the green ones pointed to the unacceptable deviations. If unsatisfactory deviations are located at important parts of the model, the designer may choose either to change the model orientation to shift the deviations or to reduce the layer thickness and the hatch space to improve the accuracy.

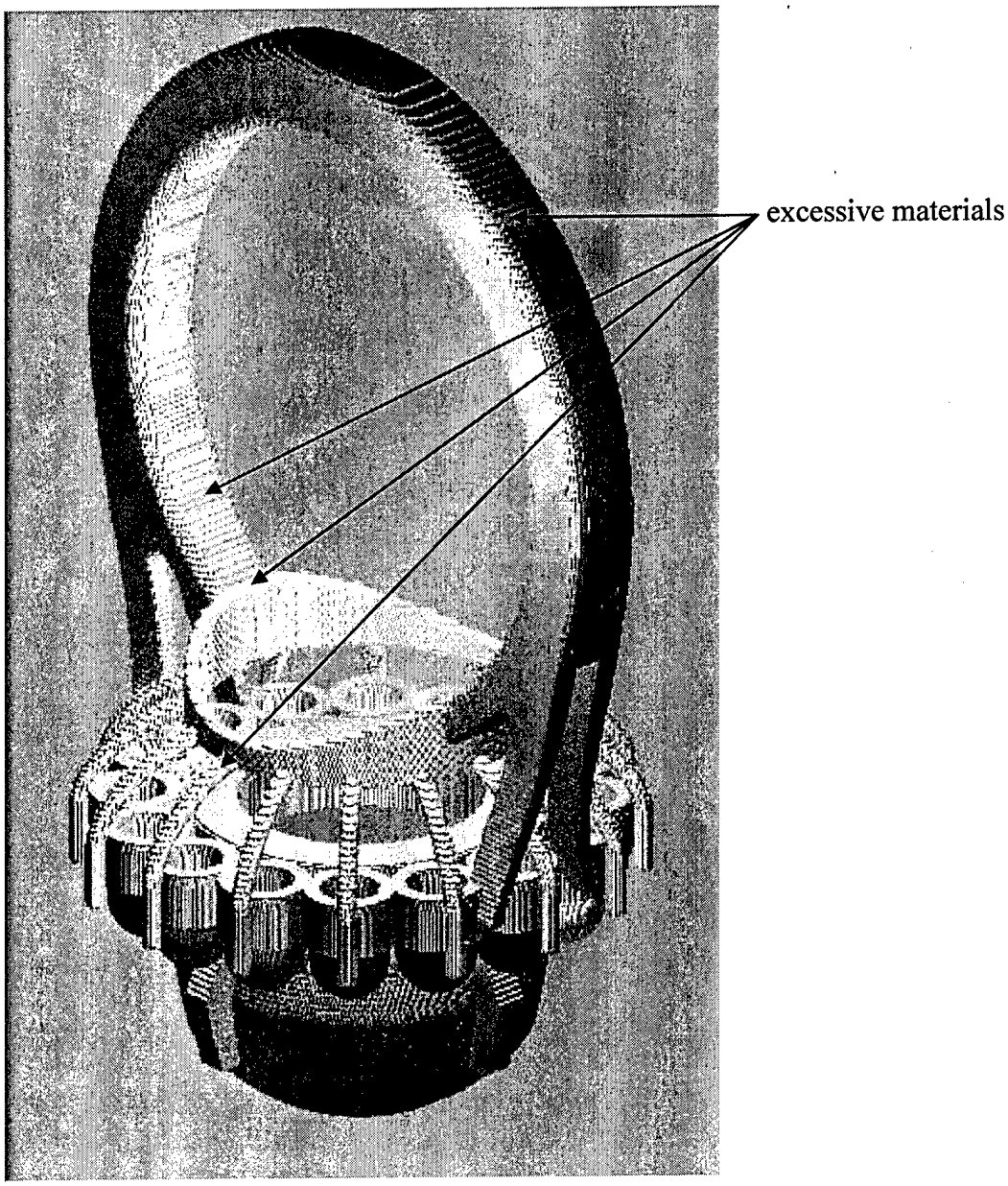

Fig.7. Superimposition of the ring prototype on its STL model

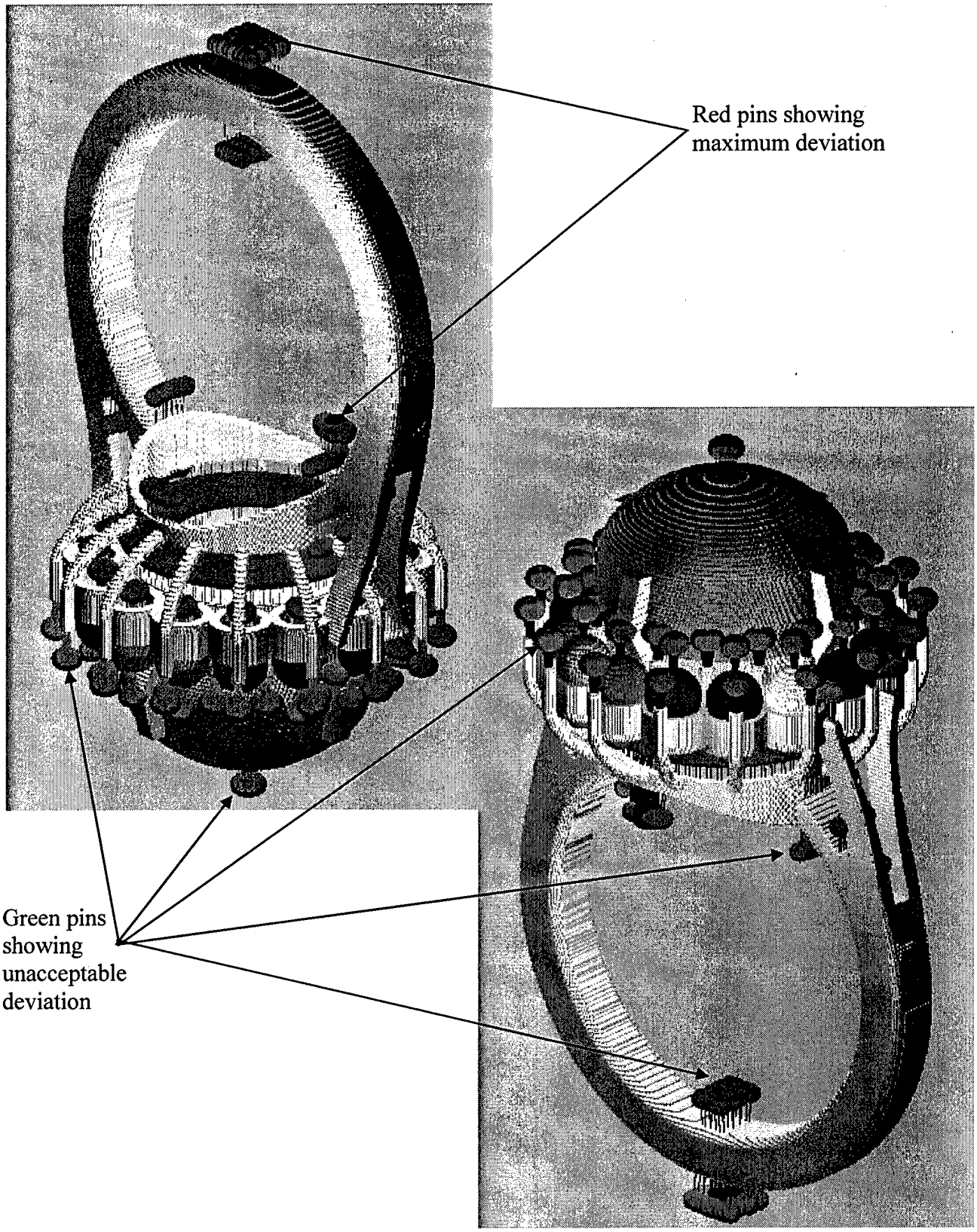

Fig. 8. Areas of the ring with dimensional deviations beyond design limits

5. Conclusion

This paper proposes a multi-material virtual prototyping system that processes complex multi-material slice contours for planning and validation of toolpath for subsequent control of nozzles or tools to fabricate multi-material prototypes. Indeed, multi-toolpath planning plays a significant role of in the development of practical MMLM machines. The proposed system uses a topological hierarchy-sorting algorithm to process the hierarchy relationship of complex slice contours. It builds a parent-and-son list, and subsequently arranges the contours in an appropriate sequence. With the hierarchy relationship of the contours, sequential toolpath are generated and used to control the nozzles or tools to sequentially move and deposit the selected materials at the appropriate contours by avoiding redundant back-and-forth movements. Besides, the proposed system simulates a MMLM process to fabriacte digital multi-material prototypes. Subsequently, it provides vivid visualisation of the resultant prototypes for quality analysis and optimisation of the MMLM process as a way of minimal costs and time possible. The system can be subsequently adapted and integrated with a material deposition mechanism to form a practical MMLM machine.

Acknowledgements

The authors would like to acknowledge the Research Grant Council of the Hong Kong SAR Government and the CRCG of the University of Hong Kong for their financial support for this project.

References

Cheng, T.H. and Langrana, N. 2001. A system approach in extrusion-based multi-material CAD. Proceedings of the Solid Freeform Fabrication Symposium, The University of Texas at Austin, TX. 313-321.

Chiu, W.K. and Tan, S.T. 2000. Multiple material objects: from CAD representation to data format for rapid prototyping. Computer-Aided Design, 32(12):707-717.

Choi, S.H. and Chan, A.M.M. 2002. A dexel-based virtual prototyping system for product development. Rapid Prototyping Journal, 8(5):300-314.

Choi, S.H. and Kwok, K.T. 2002. Hierarchical slice contours for layered-manufacturing. Computers in Industry, 48(3):219-239.

Choi, S.H. and Samavedam, S. 2001. Visualisation of rapid prototyping. Rapid Prototyping Journal, 7(2):99-114.

Kumar, V., Rajagopalan, S., Cutkosky, M. and Dutta, D. 1998. Representation and processing heterogeneous objects for solid freeform fabrication. IFIP WG5.2 Geometric Modelling Workshop, Dec.7-9, Tokyo.

Materialise. http://www.materialise.com/magics-rp/main_ENG.html 2003.

Morvan, S.M. and Fadel, G.M. 1999. Heterogeneous solids: possible representation schemes. Proceedings of the Solid Freeform Fabrication Symposium. The University of Texas at Austin, TX. 187-197.

Park, S.C. 2003. Tool-path generation for Z-constant contour machining. Computer-Aided Design, 35(1):27-36.

Patil, L., Dutta, D., Bhatt, A.D., Furrens, K., Lyons, K., Pratt, M.F. and Sriram, R.D. 2002. A proposed standard-based approach for representing heterogeneous objects for layered manufacturing. Rapid Prototyping Journal, 8(3):134-146.

Qiu, D., Langrana, N., Danforth, S., Safari, A. and Fafari, M. 2001. Intelligent toolpath for extrusion-based LM process. Rapid Prototyping Journal, 7(1):18-23.

Qiu, D. and Langrana, N. 2002. Void eliminating toolpath for extrusion-based multi-material layered manufacturing. Rapid Prototyping Journal, 8(1): 38-45.
TNO. http://www.ind.tno.nl 2003.
Weiss, L., Merz, R., Prinz, F.B., Neplotnik, G., Padmanabhan, P., Schultz, L. and Ramaswami, K. 1997. Shape deposition manufacturing of heterogeneous structures. Journal of Manufacturing Systems, 16(4):239-248.
Zajtchuk, R. and Satava, R. 1997. Medical applications of virtual reality. Communications of the ACM, 40(9):63-64.
Zhu, W.M. and Yu, K.M. 2002. Tool path generation of multi-material assembly for rapid manufacture. Rapid Prototyping Journal, 8(5):277-283.

IMPLEMENTATION OF A FUNCTIONALLY GRADIENT MATERIAL MODELING AND DESIGN SYSTEM

Aparajit Pratap, Richard H. Crawford
Laboratory for Freeform Fabrication, Department of Mechanical Engineering
The University of Texas at Austin, Austin, TX 78712
Reviewed, accepted August 13, 2003

Abstract

New advancements in Solid Freeform Fabrication (SFF) processes promise the capability to produce Functionally Gradient Material (FGM) parts, in which the material compositions vary spatially. To realize this potential there is a need for CAD methods and design software to model, design, represent and exchange material information and instructions to the manufacturing process. However, currently available commercial CAD systems are limited to representing and storing only geometric information, which is not adequate for material design purposes. This work presents an extension of a theoretical approach based on Volumetric Multi-Texturing (VMT) and hypertexturing schemes to make the material design process intuitive and user controllable. Inverse distance weighted interpolation is used in conjunction with procedural material functions to accomplish axial or linear material gradient directions from surface to surface across a solid. This offers the capability of specifying fixed material composition values to the faces in the solid and blending them across the interior of the solid. The extension of the proposed approach to the modeling of discrete material domains is also discussed. These material regions can be combined using special sets of operators depending on the form of the material functions. Finally, a design environment has been developed, which allows users to systematically apply material information to geometry and captures design intent.

1 Introduction

Solid Freeform Fabrication encompasses emerging rapid prototyping technologies used in making components with complex geometries without human intervention or part-specific tooling. SFF processes involve the use of a computer-generated model to provide the geometric information required in the fabrication process. In general SFF is based upon layered manufacturing techniques, in which the parts are produced layer by layer in an additive fashion. SFF thus has access to the interiors of solids and provides the most suitable means of building parts with highly accurate local material composition control, which cannot be achieved by conventional fabrication processes. These capabilities enable the use of the technology in the manufacture of parts composed of functionally gradient materials. Functionally gradient material components have smoothly varying material composition. They possess large variations in the volume fractions of their constituents and variations in microstructure because of which they exhibit some useful properties such as reduced thermal and residual stresses at joints, improved thermal and mechanical properties and high specific strength and oxidation properties [4].

The current state of solid and geometric modeling is at an advanced stage of development however existing commercially available CAD modelers do not support material design information. Thus there is a need for new modeling systems that can design and represent heterogeneous material parts. The problem addressed in this work is the implementation of a

design environment for multi-material part modeling and representation. The methodologies used are largely based on implicit procedural and Volumetric Multi-Texturing (VMT) schemes [9]. Issues such as combining and blending the effects due to multiple material constituents at a point, extensibility of smoothly varying material gradients to modeling of discrete material interfaces and achieving multiple directionality of material variation within a part have been addressed. Appropriate data structures for geometry and material attributes have been constructed for material data storage and retrieval and user interface design issues have been discussed, with emphasis on user interaction and input methods to make the design process more intuitive and predictable for users.

1.1 Previous Work

Several researchers have been working to develop heterogeneous material modeling systems. Kumar and Dutta [7] proposed a set-based approach for spatial discretization of the solid interior by associating material density functions with material subsets called r_m sets. Pegna and Safi [12], Kumar and Wood [6] and König and Fadel [5] have used finite element based methods to model and optimize material density distributions given a particular design objective and constraints. Marsan and Dutta [8] and Jackson and Petrikalakis [3] have applied volumetric mesh schemes to describe material data.

Several mesh free methods have also been applied to FGM design, which do not rely on any form of spatial decomposition of the geometry. Hu and Jiang [2], Siu and Tan [15] and Wahlborg and Ganter [16] are some researchers who have adopted heterogeneous solid modeling techniques to material modeling. Wahlborg and Ganter [16] have introduced a heterogeneous implicit solid modeling scheme that makes use of the Boolean operators union, intersection and difference on heterogeneous objects to model both solid as well as material spaces defined as implicit primitives. Biswas and Shapiro [1] discuss the parameterization of the interior of a shape using functions of normalized distance fields from material features with known material properties. The material functions are continuous and constructed using known design and manufacturing constraints and are interpolated using transfinite interpolation, with inverse distance weights to obtain overall material functions.

Representations in the form of spatial discretizations are inefficient due to large data sizes and errors due to approximations. This adds to the cost of computation and to the difficulty in modifying material models. The schemes implemented in this work are based on a mesh free implicit procedural approach and are therefore devoid of the errors that arise from spatial decomposition.

2 Implicit Procedural Approach

The material modeling scheme used in the implementation of the design interface is largely based on implicit procedural and Volumetric Multi-Texturing techniques that were first introduced by Park et al [9].

2.1 Hypertexture

Hypertexture is a technique in computer graphics that makes use of 3D volume density functions to create effects such as explosions, furry objects and eroded surfaces or objects that have variations in density. The functions that control the density distribution in the fuzzy region are called density modulation functions (DMF) and are chosen to be higher order procedural functions built upon *bias* and *gain* functions as described by Perlin [13]. The *bias* function can be used to control the magnitude of the density value and is defined over a unit interval by a power function as:

$$bias_b(t) = t^{\frac{\ln(b)}{\ln(0.5)}} \tag{1}$$

where $bias_b(0.0) = 0.0, bias_b(0.5) = b$, and $bias_b(1.0) = 1.0$. The *gain* function is used to set the density gradient. It is also defined over a unit interval and is constructed by splining two bias curves:

$$gain_g(t) = \begin{cases} \frac{1}{2} bias_{1-g}(2t), \text{ for t} < 0.5 \\ 1 - \frac{1}{2} bias_{1-g}(2-2t) \text{ otherwise} \end{cases} \tag{2}$$

The function used in this work is simply a product of the *bias* and *gain* functions. It is a monotonically increasing function that lies in the interval [0,1].

$$dmf = bias_b(t) \cdot gain_g(t) \tag{3}$$

2.2 Blending Functions

These are smoothing functions used to approximate Boolean operations on density modulation functions. Ricci [14] introduced smoothing functions to approximate unions and intersections on surfaces describing 3D solids. The functions chosen for intersection, I and union, U are respectively:

$$\begin{aligned} I_p(f_1,....,f_n) &= \left(f_1^{\,p} + ... + f_n^{\,p}\right)^{1/p} \\ U_p(f_1,...,f_n) &= \left(f_1^{-p} + ... + f_n^{-p}\right)^{-1/p} \end{aligned} \tag{4}$$

where p is a positive number and is the blending factor that controls the degree of smoothness and $(f_1,...,f_n)$ are the n individual functions to be blended. Park [10] has used Ricci's functions with implicit surfaces to construct complex 3D solids for global material spaces. He derives a general form for a union operation from Ricci's intersect function to perform a blending on density modulation functions, which can be generalized for n functions $(f_1,...,f_n)$ as:

$$f_{blend}(\vec{P}_{\text{int}}, a) = \left[1+(-1)^{n-1} \begin{vmatrix} f_1^a & f_2^a & \cdots & f_{n-1}^a & f_n^a & 1 \\ 1 & f_2^a & \cdots & 1 & f_n^a & 1 \\ . & . & .... & . & . & \\ . & . & .... & . & . & \\ . & . & .... & . & . & \\ 1 & 1 & \cdots & 1 & f_n^a & 1 \\ 1 & 1 & \cdots & 1 & 1 & 1 \end{vmatrix} \right]^{1/a} = \left(1+(-1)^{n-1} \prod_{i=1}^{n} \left(f_i^a - 1\right)\right)^{1/a} \tag{5}$$

where a is a positive real number [11]. Increasing the value of the blending factor a, has the effect of sharpening the texture of the blend.

2.3 Volumetric Multi-Texturing

Volumetric Multi-Texturing (VMT) is a popular computer graphics technique to represent fuzzy features like clouds, smoke and flames and is extended by Park [11] to the modeling of material clouds. Using the VMT approach any point $\vec{p}_{\text{int}}$ interior to an object in geometric space G^3 can be interrogated to return the material density d_p^i at that point using a set of procedural functions F_m such that for each material i:

$$F_m^i(\vec{p}_{\text{int}}) = d_p^i, \vec{p}_{\text{int}} \in G^3,$$
$$\sum_{i=1}^{n} F_m^i(\vec{p}_{\text{int}}) = \sum_{i=1}^{n} d_p^i = 1 \quad (6)$$

The densities d_p physically represent volume fractions of each material and sum to one at each point for all n materials that compose the part. Therefore only $n-1$ functions, F_m's are needed to fully constrain the model. Each function, F_m is a procedure consisting of several contributing functions, f_{m_i} that are attached to surfaces (faces or group of faces) in the part geometry. These contributing functions are combined together using the blending function described in equation (5) and are functions of the distances of the sample point from the part surfaces and reference geometry such that the closer the sample point is to an entity the greater is the influence of the contributing function associated with that entity in determining the density at that point.

Park [11] introduces two classes of gradient functions, namely, global and local (surface) gradients. Global gradients are one-dimensional scalar functions (either density modulation functions or user-defined functions) defined over material spaces called blobs that are mapped onto 3D geometry. The shape of the global material space determines the overall pattern of the material distribution. In this work a B-rep representation of the material space geometry has been added to the existing implicit surface description by Park [10]. If the material function is a function of an independent parameter t, in the case of B-reps, t varies linearly with distance from the boundary surfaces whereas in the case of an implicit surface, t evaluates to the implicit function value and is therefore proportional to the distance from the surface. Material gradient functions similar to those used with global gradients when assigned to the surfaces of the part geometry serve as surface gradients. The global gradient function, when multiplied with the surface gradient, is trimmed to force the net gradient to conform to the boundary surface of the part geometry.

3 Multi-Directional Material Variation

The existing material modeling method focuses on improving surface coatings on components that are exposed to severe thermal and mechanical stress environments. The current approach therefore places importance on material variation from the surfaces of components into the interior and does not support general material distributions in the interior. Further, user-

prescribed boundary material compositions on surface features are not satisfied. Modeling a linear material gradient pattern that starts with one material fraction on one face and blends into another material fraction on another can be achieved by using multiple surface gradient functions for each face, one material function for each material. Consider an object with different material functions assigned to each face in a pair of adjacent faces. A simple blend of the two functions in the overlapping region where each face has an influence on the material properties at points on the adjacent face, would not yield the exact material compositions specified on the faces. For this reason the functions for each material for each face need to be trimmed to the boundary values on the neighboring face using a different approach, as described below.

3.1 Inverse Distance Weighting Function

Consider n faces or surface features and let the material composition of a material k be C_i on the face F_i, such that $0 \le C_i \le 1$. The net material composition of material k at a given point p due to the influence of all n faces is:

$$f_k(p) = f_{blend,k}(p)\left(\sum_{i=1}^{n} C_i W_i(p)\right) \tag{7}$$

where W_i is a weight function controlling the influence of the blended material function, $f_{blend,k}(p)$ with the face F_i. The weight function has the following properties:

- In order for $f_k(p) = C_i$ for points on the face F_i,

$$W_i(p) = \begin{cases} 1, \forall p \in F_i \\ 0, \forall p \in F_j, j = 1,..,n, j \neq i \end{cases} \tag{8}$$

- $W_i(p)$ must form a partition of unity to restrict the sum of the terms on the right hand side of equation 3.12 to one.

$$\sum_{i=1}^{n} W_i(p) = 1, 0 \le W_i(p) \le 1 \tag{9}$$

- The weight functions should be as smooth as the blended function, $f_{blend,k}$.

The weight function is chosen based on distances u_i of points p from the reference surfaces for the material functions (surface gradient functions) such that it is inversely proportional to some power of u. Normalizing the weight function by the sum of all weights yields a function that varies between 0 and 1:

$$W_i(p) = \frac{u_i^{-k}}{\sum_{j=1}^{n} u_j^{-k}} = \frac{\prod_{j=1; j\neq i}^{n} u_j^k}{\sum_{i=1}^{n} \prod_{j=1; j\neq i}^{n} u_j^k} \tag{10}$$

where u_i is the distance of p from the face F_i and the exponent k controls the smoothness of the weight function. These functions are called the inverse distance weighting functions or Shepard's method of data interpolation, as discussed by Biswas and Shapiro [1].

The limitation of this approach is that it does not ensure that the sum of the material densities at a point p for all materials $\sum_{j=1}^{m} f_j(p)$ equals 1, where m is the total number of materials. One way to treat this inadequacy is to consider the remaining quantity $\left(1-\sum_{j=1}^{m} f_j(p)\right)$ to constitute porosity in the part or to constitute the volume fraction of the $(m+1)^{th}$ material. Another way is to normalize the volume fraction due to an individual material k to obtain:

$$f_{k,N}(p)=\frac{f_k(p)}{\sum_{j=1}^{m} f_j(p)} \tag{11}$$

such that

$$\sum_{k=1}^{m} f_{k,N}(p)=1 \tag{12}$$

As a result of this addition, it is now possible to model multiple material gradient patterns, namely linear as well as concentric or radial material gradations so as to achieve any direction of material variation. Figure 1 shows concentric contours of material gradation between two materials for a cross-section of a bottle mold. It is modeled by assigning a single density function for the primary material to each of the four faces forming the boundary, which blends into the secondary material in the interior. In Figure 2, three faces have been assigned 100% composition of one material each. Using the proposed method, it is now possible to clamp each material composition to be exactly 100% on its respective face and achieve a gradual blend of the three into each other. Here the depth of material influence for each face is set to be greater or equal to the length of a side of the square cross-section.

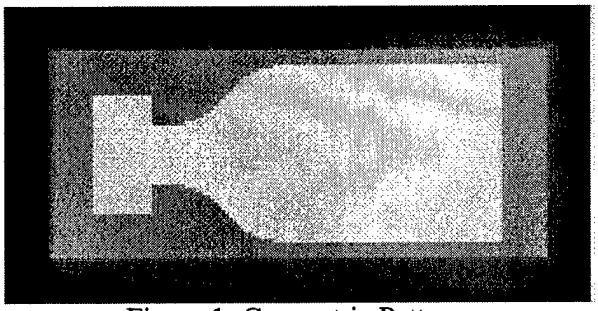

Figure 1: Concentric Pattern

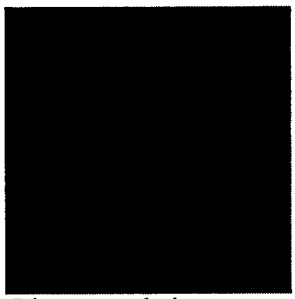

Figure 2: Linear gradation pattern with 3 materials

4 Modeling Discrete Material Domains

The current approach does not account for discrete heterogeneity of materials and hence offers only a restricted case of material modeling. Modeling discrete material regions can be considered as a special case of FGM modeling. The same approach can be applied to discrete material modeling by using constant functions or step functions with the reference geometry. The global material spaces can be used to define discrete material domains confined within the B-rep by assigning constant material fractions to individual blobs. Since assigning a value of 1 to the

bias and gain functions makes the density modulation function in equation 3 a step function at the midpoint of the [0, 1] interval, material compositions could be made to change discretely at these points (see Figure 3). The blobs can then be combined using regularized Boolean operations for B-rep geometry and *min* and *max* functions [16] or equivalent Ricci's functions for implicit solids. Modifications to Boolean operations or equivalent rules must be formulated to combine the corresponding material regions.

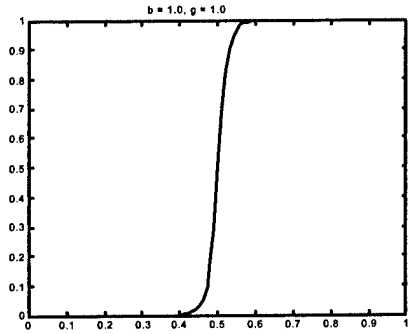

Figure 3: DMF curve for bias = 1.0, gain □ 1.0

In this work generalized Boolean operations are applied to scalar material functions f and g as in hypertexturing [13]:

$$\begin{aligned} &\text{Intersection: } f(x)\cdot g(x) \\ &\text{Union: } f(x)+g(x)-f(x)\cdot g(x) \\ &\text{Complement: } 1.0-f(x) \\ &\text{Difference: } f(x)-f(x)\cdot g(x) \end{aligned} \tag{13}$$

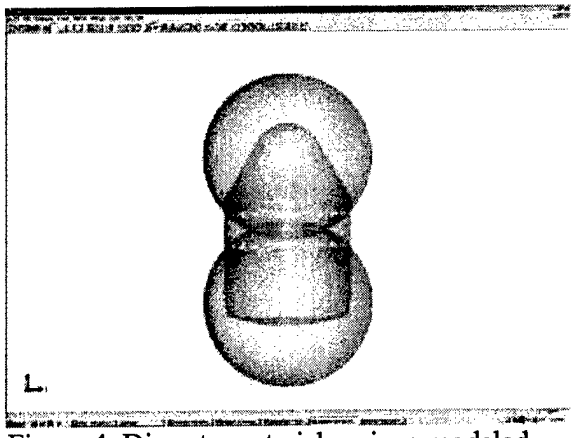

Figure 4: Discrete material regions modeled using global gradient

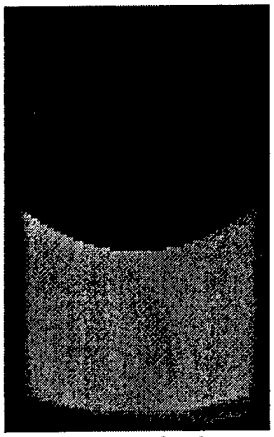

Figure 5: Difference of spheres

Using the above operators on material functions, material regions of arbitrary complexity can be constructed from primitive shapes. Consider the drill insert shown in Figure 4. The two spheres illustrate the use of blobs as global density gradients to define discrete material regions. Figure 5 is obtained after performing a difference of the upper sphere from the bottom one. The net gradient takes the shape expected if a Boolean subtraction were performed on the spheres.

The smooth gradient near the boundary is the result of using smooth functions for the surface gradient.

5 Implementation and Results

The material modeler has been developed and implemented using the 3D ACIS® Modeler and the HOOPS 3D Application Framework. ACIS is a geometric modeling kernel written in C++ that supports modeling of wireframe, surface and solid geometry in a unified data structure. It defines geometric shapes as B-reps and saves model information in the "SAT" format, a format that is slowly becoming a *de facto* standard for the exchange of CAD data. ACIS has been used to build the data structures for the geometry and material information and to perform the required modeling operations. A skeletal application based on HOOPS 3D, a graphics toolkit, has been used to design the user interface for the application.

5.1 Attribute Architecture for Material Information

ACIS supports user-defined attributes that can be attached to geometric and topological entities and can be saved along with them in an SAT file. In this research, user defined attribute classes constructed in ACIS have been used to store the material data associated with the part for use by procedures that generate material distributions. Figure 6 shows the data structure used for modeling the overall density gradient in a part. The blocks in blue represent the user defined attribute classes and the arrows, their associations with each other.

The blob attribute (ATTRIB_BLB) consists of either an ACIS BODY (B-rep) or a user defined implicit function describing an implicit solid primitive since the global density gradient can be modeled in either one of these two ways. This attribute also consists of the *bias* and *gain* parameters for the density modulation function or a user defined material function associated with the blob surface. Finally it specifies the depth of influence of the blob surface over the material composition at an interior point.

The blend attribute (ATTRIB_BND) located one level higher in the hierarchy stores information on how to combine the blob functions using union, intersect or difference operators as described in section 4. It also contains a blending factor, a, which is used to blend the blob functions in the case of a union operation using equation 5. The blend attribute is assigned to the part to be modeled. The blob attributes are stacked together in a doubly linked list such that at all times the blob at the top of the stack is pointed to by the owning entity, which is the blend attribute in this case. The remaining blobs can be accessed using the "next" pointer of the previous one in the list. The blend attribute in turn is owned by the ACIS BODY and can be accessed by it.

The surface gradient data is stored in two separate attribute classes, map and join. The map attribute (ATTRIB_MAP) contains an array of material compositions assigned to a face on the part and arrays of dmf parameters of bias and gain for each material function attached to the face. The owning entity in this case is an ACIS FACE (see Figure 7). There is also a provision for user defined material functions for each material and an array for the depths of influence of the face for the contributing material functions for each material.

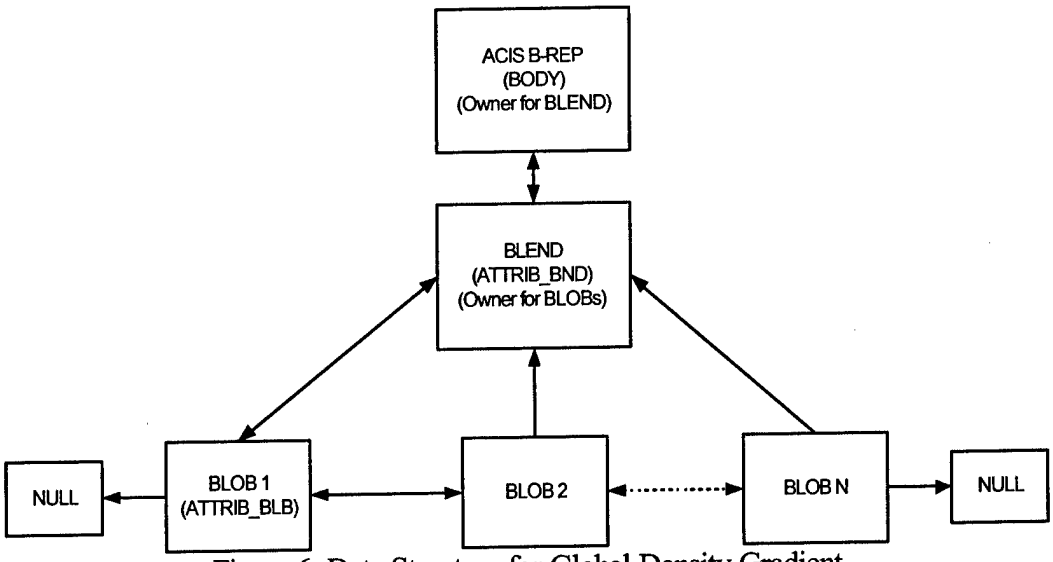

Figure 6: Data Structure for Global Density Gradient

One of the features of the material modeler implementation is the automatic selection of faces to be used to blend associated material functions in the part. The approach used here is that of blending faces that are adjacent to an edge or vertex, using a blending factor unique to that edge or vertex. For this purpose a join attribute class (ATTRIB_JON) containing the value for the blending factor is created and attached to an EDGE or VERTEX owning entity (see Figure 7).

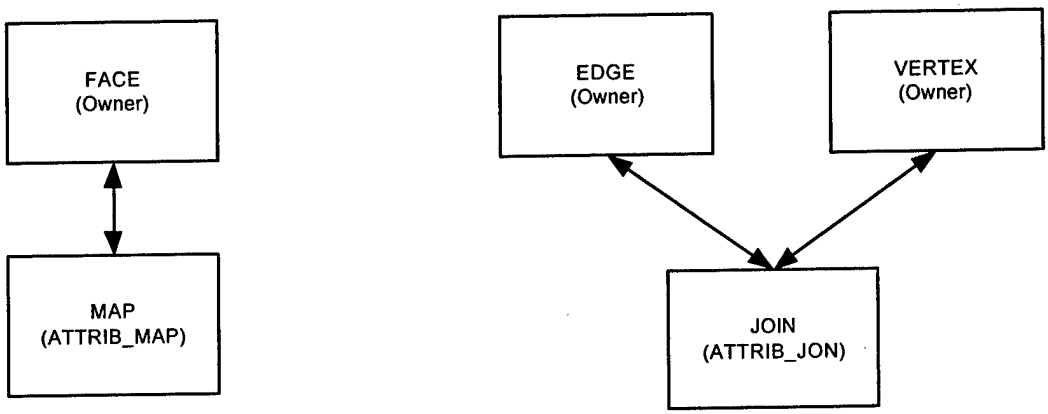

Figure 7: Data Structures for Surface Density Gradients

The user interface (GUI) for the material modeling application has been built using the HOOPS 3D Application Framework (HOOPS/3dAF). It supports the implementation of the material modeling features that have been described above. B-rep models in the ACIS SAT format can be imported in the viewer. The interface has the provision for creating solid primitives and performing Boolean operations on them to serve as complex geometry for the blobs. Implicit functions for the definition of blob geometries and material density functions for both global and surface gradients can then be assigned to the part geometry. Finally geometry and material attributes can be saved and retrieved to and from SAT files. The computed material distribution is displayed as an image.

5.2 Results

The following example is the FGM design of a pulley shown in Figure 8. Here the design intent is to make the part more wear resistant in areas subject to maximum wear. For example the pulley can be built from stainless steel while having a greater concentration of a wear resistant material like carbide in areas near the hub and the rim [3].

The part is modeled using a surface gradient approach. The material information for only one material (primary material) is entered (carbide in this case) and the secondary material density (stainless steel) is the complement of the first. The faces that compose the surfaces of the rim and hub of the pulley respectively, are selected and assigned a material function (see Figure 8 (a) and 8 (b)). Since these surfaces are composed of the same material (carbide) they are all assigned a 100% material fraction for the same material. Figure 8 (c) displays the resulting material gradient distribution on a cross-section of the pulley passing through its center laterally.

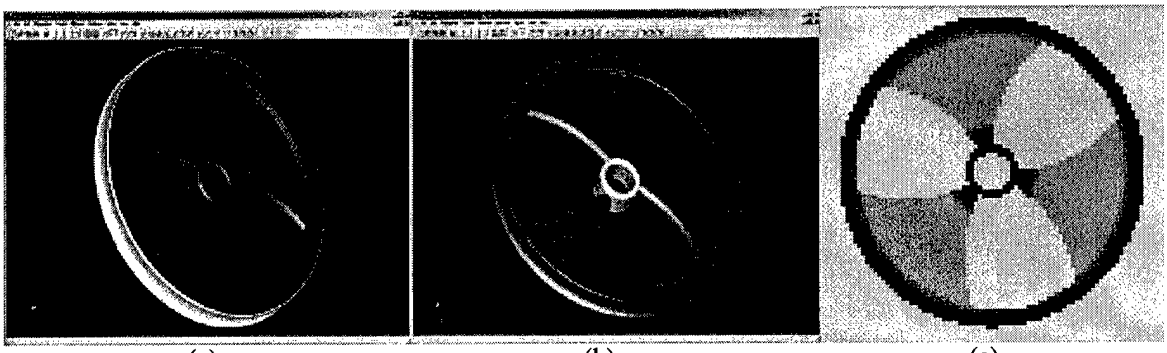

(a) (b) (c)

Figure 8: FGM Design of a pulley

This example illustrates the ease with which the model of the pulley can be designed for FGM variation. The design is shown to be completed in four steps using the material modeling interface. It can also be seen that the material variation conforms to the original design intent of having greater concentration of carbide at the hub and the rim, indicated by the region colored in magenta and a gradually increasing concentration of stainless steel with increasing distance away from the hub and the rim on the spokes.

6 Conclusions and Future Work

New developments in SFF processes promise the capability of fabricating functionally gradient material parts. To realize this potential new CAD methods and design software must be developed to enable designers to model, design, and transmit FGM objects and instructions to the manufacturing process. FGM's are expected to show clear advantages over homogeneous materials in terms of mechanical and thermal properties. The goals of the work presented were to take existing research [9] based on implicit procedural methods and extend it in order to build a tool to design volumetric material information accurately and intuitively. The advantages of the procedural approach are accurate description of three-dimensional material data and compactness in data storage by having to store only the instructions for the procedures and their arguments.

Volume discretization methods are discarded, leading to increased accuracy, concise representation and resolution independence.

Inverse distance weighted functions have been used in conjunction with the procedural material functions to accomplish axial or linear material gradient directions and offers the user the capability of specifying fixed material composition values to the faces in the solid and blending them across the interior of the solid. The definition of global density gradients can be expanded by representing them as both implicit surfaces as well as boundary representations (B-reps). This permits the user to draw or import more complex geometry to define global material spaces. However the use of B-reps to define global gradients significantly increases the amount of data that must be stored compared to a single compact implicit function expression that could define an entire implicit solid. It has been proposed that one-dimensional density functions can be step functions or constant material fractions in order to represent homogeneous material regions. These material regions can be combined using special sets of operators depending on the form of the material functions. Finally, a usable material modeling interface has been designed by which designers can systematically apply material information to B-rep geometry and observe the resulting material distributions in cross-sections of the solid. The user interface captures design intent and is an intuitive tool for designers to use.

6.1 Future Work

Apart from material volume fractions in a component, the macro-structures are equally significant in determining the physical properties of the part. Therefore designing and optimizing the structure variation of materials, e.g. composites, is a valid area of further research. This therefore presents the possibility of designing and optimizing smooth spatial (3D) variations in a structure between two materials by grading reinforcement orientations. Another prospective area for exploration is the formulation of a design methodology for FGM objects that must be placed in the context of an overall design process. Creating such a design methodology would involve investigating how a designer interacts with the model. For FGM modeling, the specification of graded material information is closely related to the geometric design. Ideally, a design system would allow the user to interactively modify the geometry and the composition in any order. Methods for achieving this goal depend on the underlying representation as well as the chosen design methods.

Though geometric data can be exchanged to a limited extent between data formats there is still a need for a new standard data exchange format that is universally supported by most CAD systems to efficiently and accurately translate non-geometric data and attributes from one format to another. In addition to this there would also be the need for new data translators to translate data back and forth between native formats and the new standard format. The next step in multi-material manufacturing is to use the material model and convert it into machine instructions by developing an SFF process-specific process-planning algorithm. The research can only be validated when results in the form of physical products can be produced. Therefore the development of the necessary hardware and the compatible software for tool-path generation is a vital research area that needs to be investigated in the future.

References

1. Biswas, A., Shapiro, V., Tsukanov, I., "Heterogeneous Material Modeling with Distance Fields", *Technical Report SAL 2002-4*, Spatial Automation Laboratory, University of Wisconsin-Madison, 1513 University Avenue, Madison, WI 53706, June 2002.
2. Hu, X., Jiang, T., Lin, F., Sun, W., "Reasoning Boolean Operation for Modeling, Simulation and Fabrication of Heterogeneous Objects", *Proceedings of the 2000 Solid Freeform Fabrication Symposium*, Austin, TX, August, 2000, pp. 417-427.
3. Jackson, T. R., Patrikalakis, N. M., Sachs, E. M., Cima, M. J., "Modeling and Designing Components with Locally Controlled Composition", *Proceeding of the1998 Solid Freeform Fabrication Symposium*, Austin, TX, August, 1998, pp. 259-266.
4. Jepson, L., Beaman, J. J., Bourell, D. L., Wood, K. L., "SLS Processing of Functionally Gradient Materials", *Proceeding of the 1997 Solid Freeform Fabrication Symposium*, Austin, TX, August 9-11, 1997, pp. 67-80.
5. König, O., Fadel, G., "Application of Genetic Algorithms in the Design of Multi-Material Structures Manufactured in Rapid Prototyping", *Proceeding of the 1999 Solid Freeform Fabrication Symposium*, Austin, TX, August 9-11, 1999, pp. 209-217
6. Kumar, A. V., Wood, A., "Representation and Design of Heterogeneous Components", *Proceeding of the 1999 Solid Freeform Fabrication Symposium*, Austin, TX, August 9-11, 1999, pp. 179-186.
7. Kumar, V., Dutta, D., "An Approach to Modeling and Representation of Heterogeneous Objects", *Journal of Mechanical Design*, ASME, No. 120, December, 1998, pp. 657-667.
8. Marsan, A., Dutta, D., "On the Application of Tensor Product Solids in Heterogeneous Solid Modeling", *ASME Design Engineering Technical Conference*, Atlanta, Georgia, September, 1998.
9. Park, S. M., "Advanced Data Exchange for Solid Freeform Fabrication", *PhD Dissertation*, The University of Texas at Austin, December 2000
10. Park, S. M., Crawford, R. H., Beaman, J. J., "Functionally Gradient Material Design and Modeling using Hypertexture for Solid Freeform Fabrication", *Proceeding of the 1999 Solid Freeform Fabrication Symposium*, Austin, TX, August, 1999, pp. 199-207.
11. Park, S. M., Crawford, R. H., Beaman, J. J., "Volumetric Multi-Texturing for Functionally Gradient Material Representation", *Proceedings of the 6th ACM Symposium on Solid Modeling and Applications*, Ann Arbor, MI, June 6-8, 2001, pp. 216-224.
12. Pegna J., Safi, A., "CAD Modeling of Multi-Modal Structures for Freeform Fabrication", *Proceedings of the 1998 Solid Freeform Fabrication Symposium*, Austin, TX, August 10-12, 1998.
13. Perlin, Ken, Hoffert, E. M., "Hypertexture", *Computer Graphics*, Vol. 23, No. 3, July 1989.
14. Ricci, A., "A Constructive Geometry for Computer Graphics", *The Computer Journal*, Vol. 16, No. 2, pp. 157-160, 1973.
15. Siu, Y. K., Tan, S. T., "Modeling the Material Grading and Structures of Heterogeneous Objects for Layered Manufacturing", *Computer Aided Design*, Vol. 34, Issue 10, September 2002, pp. 705-716.
16. Wahlborg, J., Ganter M. A., Schwartz, D. T., Storti, D., "H-ISM: An Implementation of Heterogeneous Implicit Solid Modeling", *ASME Design Engineering Technical Conference*, Montreal, Canada, September, 2002.

Direct Slicing of STEP Based NURBS Models for Solid Freeform Fabrication

B. Starly, A. Lau, W. Sun
Dept of Mechanical Engineering and Mechanics, Drexel University
Philadelphia, PA 19104

and

W. Lau, T. Bradbury, A. Youssef, C. Gaylo
Therics, Inc. 115 Campus Drive
Princeton, NJ 08540
Reviewed, accepted August 13, 2003

Abstract
Direct slicing of CAD models to generate process planning instructions for solid freeform fabrication may overcome inherent disadvantages of using STL format in terms of the process accuracy, ease of file management, and incorporation of multiple materials. This paper will present the results of our development of a direct slicing algorithm for layered freeform fabrication. The direct slicing algorithm was based on a neutral, international standard (ISO 10303) STEP-formatted NURBS geometric representation and is intended to be independent of any commercial CAD software. The following aspects of the development effort will be presented: 1) Determination of optimal build direction based upon STEP-based NURBS models; 2) Adaptive subdivision of NURBS data for geometric refinement; and 3) Ray-casting slice generation into sets of raster patterns. Feasibility studies applying the direct slicing algorithm to example models and the generation of fabrication planning instructions involving multi-material structures will also be presented.

Keywords: Direct slicing, STEP, NURBS, free form shapes, adaptive subdivision.

---

1. Introduction

Layered **M**anufacturing (LM) or **S**olid **F**reeform **F**abrication (SFF), a new class of manufacturing techniques introduced during the mid 1980s have grown rapidly over the past decade because of its proven ability to reduce product development cycle time. In the current industrial **R**apid **P**rototyping (RP) practice, the 3D CAD data are first converted to an intermediate **STereoLithography** (STL) format, a tessellation procedure where the model is approximated by triangles, sliced and then fabricated by the machine. But with the rapid growth of the RP industry, particularly RP towards rapid manufacturing, rapid tooling and biomedical applications, there has been a growing dissatisfaction with this format among the RP community due to the limitations inherent within the format. The geometric description used to represent solid CAD objects significantly affects the accuracy and quality of the final parts produced with this technology especially in the case of freeform shapes. The limitation of the current STL format generated through a tessellation procedure of the CAD model can be summarized as follows [1]:

Tessellation involves approximation of surfaces with triangular facets which is undesirable in general, particularly when we are dealing with models that contain freeform shapes.
As model precision demands become more stringent, the number of facets required to adequately approximate these freeform shapes will increase. This would account for huge STL file sizes, and thus increasing the chances of errors.
Many CAD systems fail to generate valid model tessellations and often involve manual fixation of errors raising the need to improve tessellation procedures. However, this calls for implementing robust and efficient procedures which may be difficult and would be computationally expensive to implement.
STL format fails to include other design content within the model such as topology, internal material variations, multi-material regions.

Manufacturers of free form surface models are in need of something other than the currently available STL format. Direct Slicing of CAD models without the intermediate STL format seem to be a promising approach in this direction. Direct slicing of the solid model keeps the geometric and topological robustness from the original data. Its advantages include greater model accuracy, pre-processing time reduction, elimination of checking and repairing routines, and file size reduction [2]. Since the direct mathematical formulation of the surface is used, the full data of the original solid modeler is therefore available and the loss that occurs during tessellation is avoided. Both direct slicing and adaptive direct slicing improve the accuracy and surface quality of the final RP parts. The approach also eliminates the verification and repairing processes, decreases human intervention, increases the robustness of data transfer, slicing and other preprocessing parameters. With this approach of direct input from computer aided design models, CAD and RP vendors would be able to sell their software/machines as a fully integrated CAD/CAM RP system.

Accuracy was not an issue that was addressed upon in the early days of RP simply because the parts could only be used for prototyping and design verification purposes. A wealth of research is available in published literature [3-5] regarding STL slicing and the different methods through which it can be achieved. However, improving the accuracy of an RP part has become the focus of the RP community under the increasing need for prototyping functional parts with engineering properties and dimensional tolerances comparable to conventionally produced parts. One among the first to try out direct slicing was Rajagopalan et al [6], where they have directly sliced the Non-Uniform Rational B-spline Surfaces (NURBS) in an I-DEAS based CAD system. The process relied on I-DEAS to perform the slicing which made it package-specific. With regards to improving surface finish, variable thickness slicing methods (adaptive slicing) for handling peaks, flat areas and staircase effect have also been proposed by Dolenc and Makela [7]. Jamieson and Hacker [2] developed a direct slicing algorithm based on the Unigraphics slice modules which directly sliced the model using first constant layer thickness. Consecutive contours were compared and if the difference was small, they were accepted. If not, a middle slice is created and the process of comparison performed again. The procedure is repeated until the difference between any two consecutive slice contours is either small or the minimum layer thickness has been reached. It has been recognized that in order to improve the surface quality of a part built by an LM technique, it is necessary to minimize the staircase effect which is inherent in all LM techniques. In a more recent study, Weiyin et al [8] developed an adaptive direct slicing algorithm that operates directly on NURBS based models to generate skin contours and then uses a selective hatching strategy to reduce the build time of the model. Almost all of the papers published above in some way depend on external modeling packages to

perform the slicing which in turn limits the capability on the level of control and variety that can be achieved. A STEP-based transfer of model data to a process planning system has been made use of by Gilman et al [9] using commercially available software. A Boundary Representation (B-rep) solid model of a part is translated into STEP format for transfer of design data to the process planning software. LM data is generated using faceted boundary representation and then transferred to the RP machine for prototyping. It has been recommended that the development of STEP specifically for the purpose of LM process planning due to its flexibility in terms of representing 3D CAD data as well as 2D contour slices thereby simplifying the standardization procedure with one common platform [1].

The objective of this paper is to present a method on a direct slicing approach that is independent of any CAD modeling package and will make use of STEP as the starting input file of the model to be prototyped. We have currently focused on NURBS based freeform shapes to demonstrate the capability of the algorithm and the proposed methodology with regards to raster line pattern layout. The following section will briefly detail our proposed methodology and some of the key steps in the process of direct slicing. This is followed by a review of the NURBS equations that need to be numerically solved to obtain the slice ray patterns during the slicing operation. The key steps of optimal orientation, adaptive refinement, root finding and evaluation of points are detailed. Section 5 gives several case studies example models that have been sliced to showcase the proposed method. The paper concludes with a summary and future research initiatives.

2. Direct Slicing of NURBS using Ray Casting

Non-Uniform Rational B-Spline (NURBS) are the industry standard tools for the representation and computer aided-design of freeform models [10] in the field of automotive design, ship design etc. Central to the problem of slicing NURBS surfaces is the determination of intersection points between the slicing plane and the model. This is also a problem that is researched upon by the computer graphics community with regards to Ray-tracing of NURBS surfaces [11-14]. Ray tracing of free form surfaces determines the visible parts by constructing rays from the viewpoint through the pixels of the image plane into the scene. The rays are intersected with the surfaces of the scene and the first surface hit determines the color of the pixel. If the ray misses all objects, the corresponding pixel is shaded with the background color. Ray tracing handles shadows, multiple specular reflections, and texture mapping in a very easy straight-forward manner. This is important to the designer since it would help him assess the surface quality and texture and hence help in a better design process. The basic approaches in most ray-tracing algorithms with regard to determination of the intersection points remain the same and only vary with regards to efficiency in terms of memory usage and the speed taken to ray trace a particular scene. Most ray tracing algorithms have performed while tessellating freeform shapes to gain speed and reduce complexity. However direct intersection using the exact mathematical equations has also been performed [14]. In our proposed methodology, we have used the same basic approach using the exact mathematical equations to deal with finding the intersection points which will be detailed in the following sections. We have however extended it to the slicing domain for use in the LM manufacturing scenario. The difference lies in the fact that in LM, intersection points both in the form of entry and exit points need to be determined along with the vector layout pattern of the rays within the model. Rather than a tracing operation, a ray casting method is performed in order to perform the slicing procedure.

Within STEP files, solid and surface models may be represented as rational or non-uniform rational B-spline surfaces. Unlike STL files where the facet information of the triangle is used to obtain the slice contour, direct slicing works on using the exact mathematic representation of the freeform shapes in computing the slice contours or tool patterns. A rational B-spline surface (10) is expressed parametrically in the form,

$$S(u,v) = \frac{\sum_{i=1}^{n+1}\sum_{j=1}^{m+1} W_{ij} P_{ij} b_{ik}(u) b_{jl}(v)}{\sum_{i=1}^{n+1}\sum_{j=1}^{m+1} W_{ij} b_{ik}(u) b_{jl}(v)} \tag{1}$$

where parameters u and v range from zero to one, n and m the degree of the surface in u and v direction. The P_{ij} terms are 3D net control points of the control polygon and W_{ij} terms their corresponding weights, b_{ik} and b_{jl} are B-spline basis functions of order k and l respectively. The B-spline basis functions are defined by the Cox-deBoor recursion formulas as given by:

$$b_{jl}(s) = \begin{cases} 1 & \text{if } ku_j \le u \le ku_{j+1} \\ 0 & \text{otherwise} \end{cases} \qquad b_{jl}(s) = \begin{cases} 1 & \text{if } kv_l \le v \le kv_{l+1} \\ 0 & \text{otherwise} \end{cases}$$

and

$$b_{jk}(u) = \frac{(u - ku_j) b_{(j)(k-1)}(u)}{ku_{j+k-1} - ku_j} + \frac{(ku_{j+k+1} - u) b_{(j+1)(k-1)}(u)}{ku_{j+k+1} - ku_{j+1}}$$

$$b_{lk}(v) = \frac{(v - kv_l) b_{(l)(k-1)}(v)}{kv_{l+k-1} - kv_l} + \frac{(kv_{l+k+1} - v) b_{(l+1)(k-1)}(v)}{kv_{l+k+1} - kv_{l+1}} \tag{2}$$

where the values of ku_j and kv_l are defined by the knot vector associated with the NURBS surface in the u and v direction respectively. The STEP file contains all information that is required to define the NURBS uniquely and a STEP reader may be employed to extract the relevant information. For further discussion on B-splines and their properties, the author refers them to [12].

The core aspect of our approach is outlined in Figure 1. The NURBS surface is geometrically refined using an adaptive subdivision procedure to break them down into smaller domains of parametric values. Bounding boxes are then used to cover up the entire surface based on these smaller domains. The rays shoot out intersecting the model at several boxes. For a box that is hit, a root finding procedure is initiated to converge at the intersection point. The procedure is repeated for all rays that are cast onto the slice plane and for every slice plane that intersects the NURBS model.

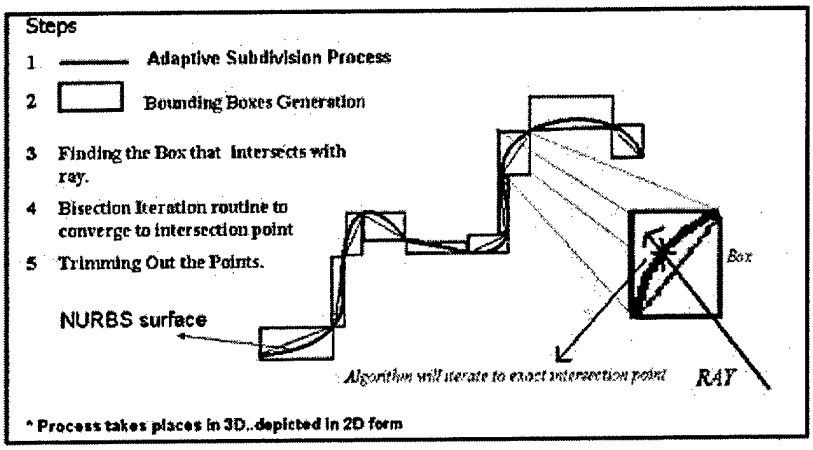

Figure 1: Step by Step procedure on calculation of NURBS intersection points

3. Ray Casting of NURBS surfaces

In the ray casting approach, the bounding box of the model is first determined allowing the start position of the ray to be defined from any predefined corner of the box which then shoots out across intersecting the model. A ray is defined as having an origin 'o' and a unit direction vector 'd' and can be defined as:

$$r(s) = \bar{o} + s * \bar{d} \tag{3}$$

Using the method followed by Kajiya [11], the ray r(s) can be rewritten as an intersection between 2 planes given by $\{p|\ P_1.(p,1) = 0\}$ and $\{p|\ P_2.(p,1) = 0\}$ where $P_1=(N_1,d_1)$ and $P_2=(N_2,d_2)$. The normal to the first plane is defined as

$$N_1 = \begin{cases} (d_y, -d_x, 0) & \text{if } |d_x| > |d_y| \text{ and } |d_x| > |d_z| \\ (0, d_z, -d_y) & \text{otherwise} \end{cases} \tag{4}$$

N_2 will always be perpendicular to the ray direction and the plane N_1, hence

$$\overline{N_2} = \overline{N_1} x \overline{d} \tag{5}$$

Since both planes contain the origin '$\bar{o}$', it can be deduced that P1.(o,1) = P2.(o,1) = 0. Thus,

$$\begin{aligned} d_1 &= -\ \overline{N_1} \cdot \bar{o} \\ d_2 &= -\ \overline{N_2} \cdot \bar{o} \end{aligned} \tag{6}$$

An intersection point that needs to be calculated should satisfy the following two conditions,

$$\begin{aligned} \overline{P} \ .(S(u,v),1) &= 0 \\ \overline{P_2} \ .(S(u,v),1) &= 0 \end{aligned} \tag{7}$$

The above equation needs to be solved using numerical means and we have employed the Bisection Iteration routine to determine the values of u and v that will satisfy (7). However before the root finding operation begins, a number of pre-processing steps are performed. In the steps that follow,

we explain the details regarding optimal orientation, refinement using adaptive subdivision, generation of the bounding volumes, root finding, evaluation and identification of output points.

Step 1: Orientation

The model orientation within the fabrication bed affects the build time, part strength and surface finish. Thus before the part is sliced, a minimization of certain objective criteria specified by the designer will be done to find the optimal orientation for slicing the model. A number of orientation schemes have been devised. Some base their orientation with the largest convex hull of the object as the base [15], while some others orient the part based on certain critical features of the model [16]. We have used a scheme in which the model is incrementally oriented about user specified axes to obtain the least possible build height dimension. Given a set of n NURBS surfaces S(u,v) that is enclosed in a bounding box of height H (a function of orientation angle "_"), the objective function can be mathematically expressed as:

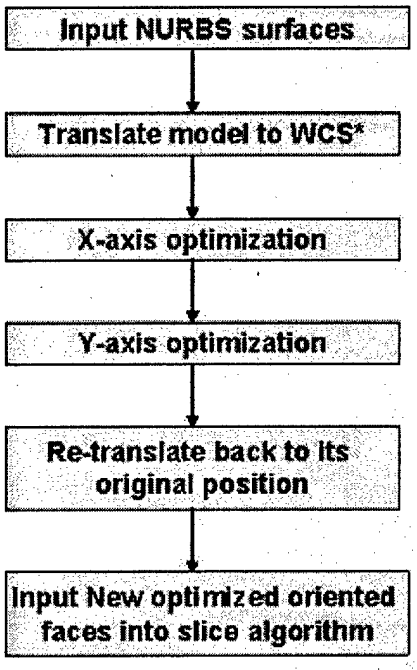

Min Z = H(_) subject to 0 < _ < 360 (8)

where Z is the build height of the model and _ is the orientation of the model with respect to the object coordinate axes. The optimally oriented NURBS faces then act as the input to the second phase. The algorithm steps are as shown in Figure2.

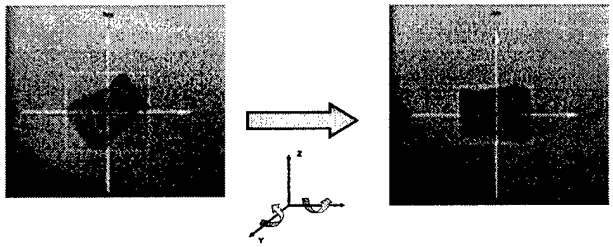

Figure 2: Optimization Algorithm

Step 2: Refinement

Refinement or subdivision of the NURBS surface is the addition of more control points to a surface without changing its process. This process is implemented using the Oslo Algorithm [17]. The basic idea would be to take in the original set of knot vectors that make up the surface and add new knot values into them creating more number of control points corresponding to the new knot vectors. If the addition of the new knot values at the same parametric value where the number added is equal to the order of the curve, then the two new surfaces created will have the same shape as the original unrefined surface. They would each

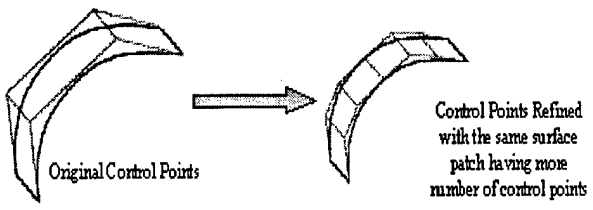

Figure 3: Refined Process of NURBS using the Oslo Algorithm

have a set of control points at the region where they join. The procedure is illustrated in Fig 3. This is done for the following two reasons. Numerical methods work better and faster when the parametric domain is smaller and no multiple value roots exists within the patch. Secondly, by refining the mesh, the various sub-patches which are essentially NURBS by themselves can be enclosed using bounding volumes thereby enabling the slice algorithm to determine which sub-patch contains the actual root. This stems from the fact that it is easier to determine the collision of rays with primitive bounding volumes than NURBS surfaces. Hence by identifying the sub-patch in which the solution exists, the domain in which the numeric solver has to work is limited and hence results in better chances of finding the roots.

The adaptive subdivision of the NURBS surface continues as long as a subdivision or flatness criteria is met. Regions that have more curvature are subdivided more than regions that are more or less flat and hence the name adaptive subdivision. Each new sub-patch contains all information that defines the NURBS and an appropriate ID is given to it. The refinement procedure is extensively used in the tessellation of parametric surfaces and has been studied extensively by a number of researchers. However, our main criteria in refinement of the mesh opposed to the tessellation procedure is not to ensure accuracy in representation but more in guaranteeing that the convergence occurs within the refined sub-patch. In this regard, selection of the subdivision factor is an important step, and an appropriate value controls to a great extent the success of accurate slicing.

Step 3: Boundary Volume Data structure Generation

As the refinement procedure of NURBS progresses, the boundary volume data structure gets filled up; sub-patches are stored in the data structure along with a unique id. The main idea

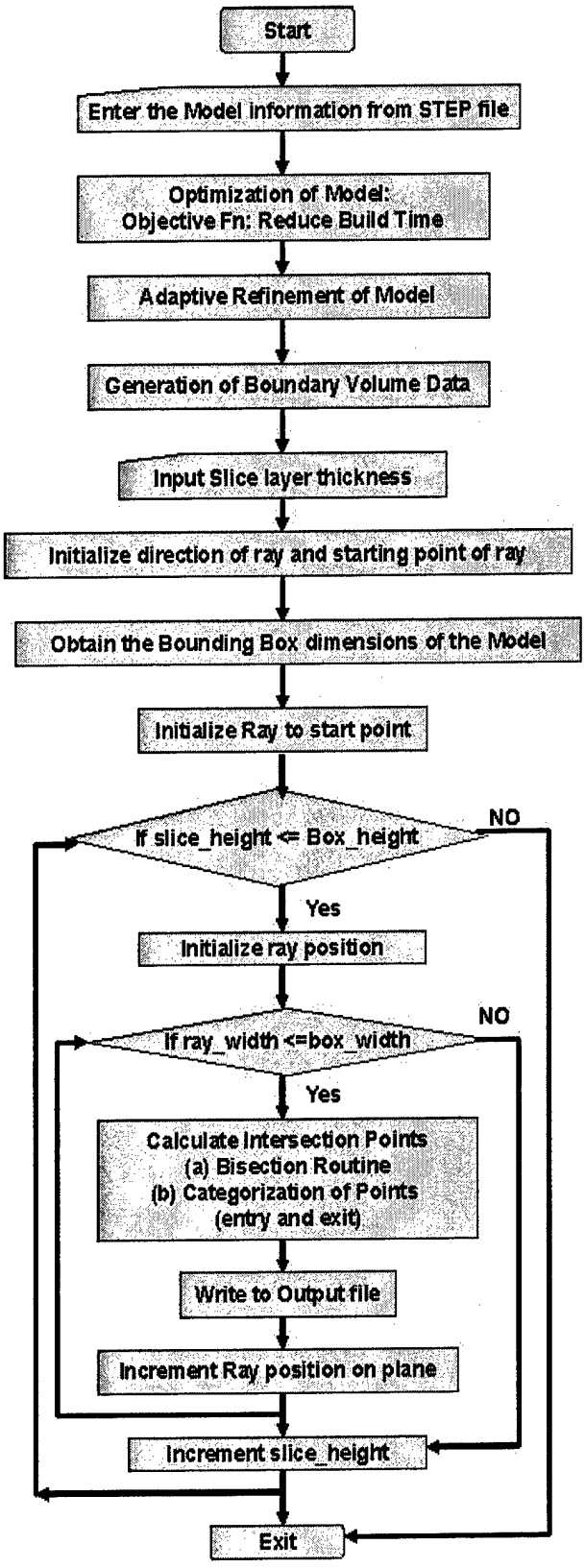

Figure 4: General Slicing Algorithm

behind the storage of these sub-patches is the generation of the boundary volume. Boundary volumes are usually primitives that enclose the sub-patch completely. Some of the candidate primitives that can be used are oriented boxes, spheres and parallelepipeds. The selection of a primitive depends on the tightness of fit and speed of intersection calculation with the ray. We have used in our approach axis aligned boxes that are oriented with the main coordinate axis of the model. Once they are axis aligned, the process of creating the boundary volumes is easier, and a ray-box intersection will involve less computation and hence speed up the process.

The bounding box is created using the control net points created from the refinement stage of the process. An important aspect to note is that the control mesh of a NURBS patch will always enclose the surface and therefore any convex shape surrounding the control net would also enclose the surface. Figure 1 gives an illustration in 2D on how the boxes get generated. Failure to enclose the sub-patch surface completely results in ray hits being missed and hence gaps in the sliced model.

Step 4: Numerical Solution - Bisection Iteration Routine

There are a variety of numerical methods that are available to solve for the intersection points. Among them include bisection algorithm, linear interpolation, Newton Iteration, and fixed point iteration [18]. Although the latter two methods are fast, in some cases they do result in solution divergence rather than convergence. Our problem reduces to finding the value (u*, v*) that corresponds to the intersection point of the ray and the NURBS surface. Though ray-tracing methods in model rendering employ Newton's iteration since it proves to be a faster process, we have used the bisection iteration routine mainly due to its simplicity and robustness. Time is not a critical factor in slicing as opposed to obtaining the roots of the equation.

The surface sub-patch contained within the boxes that were hit by the ray are retrieved from the boundary volume data structure and passed onto the solver method. The routine works with iterating towards the solution of one variable. However, we need to solve for 2 variables (u, v) that satisfy the equation. This is achieved by keeping one variable constant and iterating towards the best value of the second variable that satisfies the equation. If the error in the points generated does not satisfy a tolerance, _, the first variable is incremented by a pre-defined amount and the procedure repeated. The process continues until either a solution is found or the limit of the first variable is achieved.

We use two criteria to decide when to terminate the Bisection iteration routine. The first condition is our success criteria: if we are closer to the desired point by some determined tolerance, _, given by:

$$| F (u , v)| < \_ \qquad (9)$$

we then report a successful hit. The value of _ determines two aspects, first, the accuracy of our results and second, success in reporting a hit. A tight value might result in the routine reporting a miss and on the other hand a bigger tolerance will result in intersection point offset errors. The second condition is the failure criterion, meaning that if this condition is met, the routine exits reporting a miss. If during the routine, the error calculated is approximately same as the error in the previous iteration, the iteration exits reporting a miss provided the success criteria has not been met. This is mathematically written as

$$F_n(u,v) = F_{n-1}(u,v) \quad \text{subject to } F_n(u,v) > \_ \tag{10}$$

where n is the n^{th} step of iteration

Step 5: Categorization of Intersection Points (Entry or Exit)

Once the intersection points are found out for every ray that is cast onto the slice planes, these points need to be classified as an entry or an exit point. We have done this by calculating the normal of the surface at the point under consideration. The normal vector can be calculated by the cross product of the tangent vectors in the u and v direction evaluated at the point given respectively by equations (11) and (12) as

$$T_u = \frac{\delta}{\delta u} S(u,v) \tag{11}$$

$$T_v = \frac{\delta}{\delta v} S(u,v) \tag{12}$$

The normal vector at this point is then given by $\overline{N} = T_u \times T_v$ (13)

If it is assumed that the ray shoots across in the y direction, then a point is classified to be as: an entry point If $N_y < 0$; an exit point if $N_y > 0$; and an edge point if $N_y=0$. The points once classified are stored in a predefined format to be displayed on screen and for conversion to machine instructions.

4. Implementation and Case Study examples

The algorithms were implemented in C++ and tested for a variety of model shapes that included simple NURBS surfaces as well as complex curved ones. Figure 4 gives the generalized algorithm for ray-casting of NURBS surfaces that includes all of the steps outlined above. Three of the test example cases are as shown below in Figures 6 to 8.

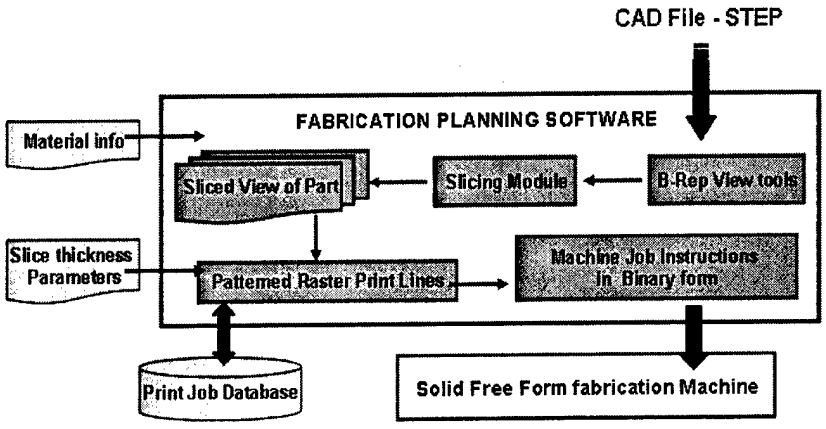

Figure 5: Process Flow during Fabrication

All the models were sliced at a constant layer thickness and ray offsets on the slice plane. Figure 5 details the data process planning steps right from the CAD file input stage to that of the final fabrication stage. For heterogeneous models, intersections of a ray to each geometric body are

calculated in sequence. Thus the material associated with the geometric body being sliced can be captured and stored in the slicing data structure.

Model 1: This model is relatively small with about 16 NURBS surface definitions and was extracted from the STEP input CAD file using a STEP reader. A subdivision factor of 0.01 and a tolerance value of 0.01 were used for adaptive refinement and root finding respectively. Figure 6(a)

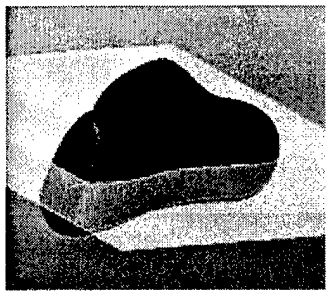

(a)

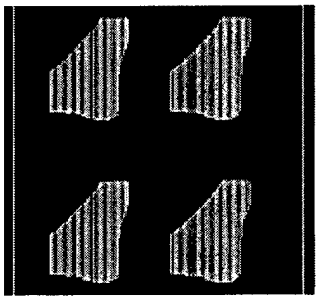

(b)

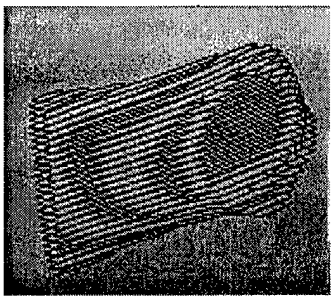

(c)

Figure 6(a): Case Study Example Model 1 with 16 NURBS surfaces.
Figure 6(b): Slice Raster Lines at a slice layer.
Figure 6(c) : Entry and Exit Points displayed

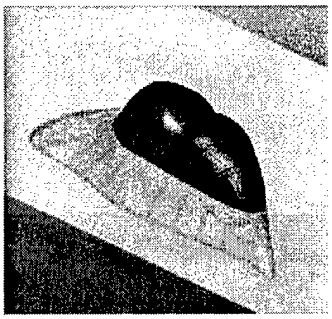

(a)

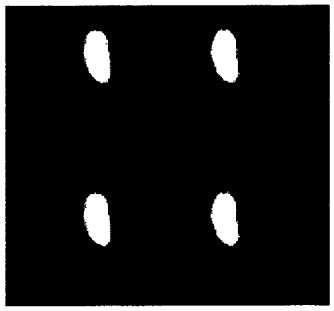

(b)

(c)

Figure 7(a): Case Study Example Model 2 with 102 NURBS surfaces.
Figure 7(b): Slice Raster Lines at a slice layer.
Figure 7(c): Entry and Exit Points displayed.

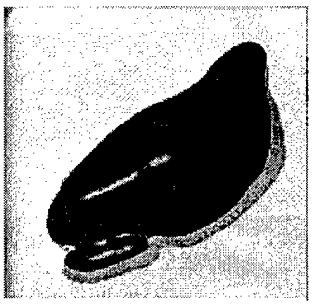

(a)

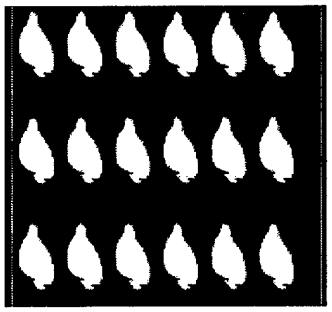

(b)

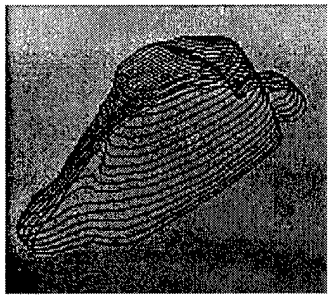

(c)

Figure 8(a): Model 3 Layout – 135 NURBS surfaces.
Figure 8(b): Sliced View layout
Figure 8(c) : Sliced entry and exit points displayed

shows the model optimally oriented with the least height in the z-direction. Figure 6(b) shows a slice layout on the fabrication bed at the slice position defined by the slice plane as shown in Figure 6(a).

Model 2: The second model contained 102 NURBS surface definitions, extracted through the same method using the reader and the data transferred to the algorithm. In this case a subdivision factor of 0.1 was sufficient for appropriate slicing with no perceivable slice errors during part layout. The same tolerance value of 0.01 was used for the root finding routine. Figure 7(a) shows the model optimally oriented and Figure 7(b) illustrating the sliced model part layout.

Model 3: The third model is more complex not only in terms of having more number of NURBS surface but also in terms of its overall shape. This model depicts the capability of the algorithm to handle multiple exit, entry points as well as accurate slicing at edges of the model. A subdivision factor of 0.1 and a tolerance value of 0.01 was used for the process. Figure 8(a) illustrates the model and Figure 8(b) the corresponding slice layout on the fabrication bed. It can be seen that the model was sliced appropriately with key features detected at the slice plane shown.

5. Conclusion

Direct Slicing of CAD model promises to offset the disadvantages posed by the STL format. It does not involve any file repair routines and file sizes are much smaller to handle. It also facilitates the possibility of slicing multi-material volumes or heterogeneous models, a definite advantage over STL files. Since the exact representation is used, complete design information is carried over to the fabrication stage with no loss in information. Although direct slicing does take longer to slice, this problem can be offset by efficient algorithms in terms of reducing memory usage and faster computing power. A point to note is also a careful selection of the subdivision factor and the tolerance value. We have found that under continued trials, an intuition is developed on the selection of the right parameters which works best for the models. Future research would involve the development of an adaptive direct slicing method on heterogeneous models and an appropriate slice layer format in terms of STEP that would be able to transfer slice information across different RP platforms. Effort would also be put into quantifying the exact accuracy obtained by direct slicing rather than using the STL format.

6. References

1. Anne L. Marsan, Vinod Kumar, Debasish Dutta, and Michael J. Pratt, *"An Assessment of Data Requirements and Data Transfer Formats for Layered Manufacturing"*, Technical Report NISTIR 6216, National Institute of Standards and Technology, Gaithersburg, MD.
2. Jamieson, R., Hacker, H. "Direct slicing of CAD models for rapid prototyping" Rapid Prototyping Journal, Vol 1(2), 1995.
3. Luo R C.; and Y. W. Ma, "A Slicing Algorithm for Rapid Pototyping and Manufacturing", 1995 IEEE International Conf. on Robotics and Automation, Nagoya, Japan, May 1995,Vol (3); pp 2841 -2846,
4. Suh, Yong Seok and Wozny, Michael J. "Adaptive Slicing for Solid Freeform Fabrication Processes," Solid Freeform Fabrication Symposium 1993, H. L. Marcus et al., eds. University of Texas, Austin, August 1993, pp. 404-410.
5. Tait S, Smith., Rida T. Farouki , Mohammed Al- Khandari, "Optimal Slicing of free form surfaces", Computer Aided Geometric Design(19), 2002, 43-64
6. Rajagopalan, M., Aziz, N.M., Huey, C.O. "A model for interfacing geometric modeling data with rapid prototyping systems", Advances in Engineering Software, Vol 23, 1995; pp 89-96.

7. Dolenc and I. Mäkelä, "Slicing procedures for layered manufacturing techniques," *Computer-Aided Design*, Vol. 26(2), 1994; pp. 119-126.
8. Weiyin M , Peiren M," An adaptive slicing and selective hatching strategy for layered manufacturing ", Journal of Materials Processing Technology; Vol 89, 1999; pp 191-197
9. Gilman, Charles R. and Rock, Stephen J. "The Use of STEP to Integrate Design and Solid Freeform Fabrication," Solid Freeform Fabrication Symposium, University of Texas, Austin, August 1995.
10. Rogers D F, "Introduction to NURBS: with Historical Perspective", Morgan Kaufmann Press, 2000, ISBN 1558606696
11. Kajiya J T, "Ray tracing parametric patches", Computer Graphics SIGGRAPH '82 Proceedings, Vol 16(3), 1982; pp 245-254.
12. Daniel L, Jacob Gonczarowski, "Improved techniques for ray tracing parametric surfaces", The visual computer, Vol 6(3),1990; pp 134-152.
13. Michael AJ Sweeney, Richard Bartels, " Ray tracing free form B-spline surfaces", IEEE Computer Graphics & Applications, Vol 6(2),1986;
14. William M, Elaine C, Russell F, Peter S, "Practical Ray tracing of Trimmed NURBS surfaces", Journal of Graphics Tools, Vol 5(1), 2000; pp 27-52.
15. Sreeram, Puduhai N. and Dutta, D. "Determination of Optimal Orientation Based on Variable Slicing Thickness in Layered Manufacturing," Proceedings of the ASME Winter Annual Conference, San Francisco, CA; Nov. 1995.
16. Frank, Dietmar and Fadel, Georges. "Preferred Direction of Build for Rapid Prototyping Processes," Proceedings of the Fifth International Conference on Rapid Prototyping, R. P. Chartoff, A. J. Lightman, and J. A. Schenk, eds. University of Dayton, June 1994; pp. 191-200.
17. Bartels R, John B and Brian B, " An introduction to splines for Use in computer graphics and geometric modeling", Morgan Kaufmann Press, Los Altos, CA, 1987; ISBN 1558604006
18. William H P, Saul A, Wm T, Brian P, "Numerical recipes in C : the art of scientific computing", Cambridge University Press; 2nd edition,1993, ISBN 0-521-43108-5

INTEGRATED DECISION SUPPORT SYSTEM FOR SELECTION OF RP PROCESSES

M. Mahesh, H.T. Loh*, Y.S. Wong and J.Y.H. Fuh
Department of Mechanical Engineering,
National University of Singapore, Singapore
*Correspondence: mpelht@nus.edu.sg

Reviewed, accepted August 13, 2003

Abstract

This paper describes an 'Integrated Decision Support System for the Selection of RP Processes (IDSSSRP)'. The basic methodology proposed in the IDSSSRP is a Sigma approach towards benchmarking of the Rapid Prototyping (RP) processes. It characterizes a RP process by using benchmarking and the sigma approach to assess its capability compared to its potential. Although the six-sigma approach has basically been a management concept and the success of its implementation has been on process time reduction and quality improvement, this paper adopts the use of six-sigma tools and benchmarking in the characterization of RP processes. Apart from geometrical benchmarks, other benchmarks include mechanical benchmarks and process benchmarks. Benchmarking individual RP processes facilitates standardization and reduces variability in the prototypes produced by the processes. Following standardizations of geometrical, mechanical and process benchmarks, a saturated database can then become very useful in providing decision support to the end user on a particular process as well as a source of information for benchmarking new RP machines. A case study of the benchmarking process developed on the Direct Metal Laser Sintering-Selective Laser Sintering (DMLS-SLS) RP process is presented using the proposed approach. This paper also outlines the working and implementation of a web-based decision support system based on the IDSSSRP.

Key Words: Benchmarking, Six-sigma, Decision support, Process optimization, Process characterization, Saturated database

Introduction

Rapid Prototyping is currently a popular technique in the manufacturing industry. It is based on a material additive process for the fabrication of prototypes and is different from the conventional manufacturing techniques, which are material removal processes. The proposed IDSSSRP offers advice on various RP processes/ systems based on the benchmarking exercise. Although an old concept, benchmarking is recently gaining much attention in manufacturing when a particular process or a system based on that process needs to be evaluated. A benchmark also becomes crucial in its ability to recognize a particular process or a system to meet up with a certain set of requirements that are established to be the industry set standards. In the RP industry however, a generic benchmark that establishes standards in terms of evolving prototypes with the desired dimensional accuracy, form, fit and surface accuracy is yet to be established. The main

purpose of the paper is to highlight the overall procedure involved in evolving generic RP benchmarks (i.e. geometrical, mechanical benchmark parts and process benchmarks), and using the benchmarked results for decision support. A generalised integrated decision support system for the selection of RP processes is proposed for evaluating RP processes and the systems based on those processes. The basic methodology proposed is a sigma approach towards benchmarking of the RP processes. It is important to mention here that the proposed idea is yet to be fully realised, however case studies done on the DMLS-SLS process/machine are a proof for the validity of the proposed approach.

Methodology

The proposed methodology in the IDSSSRP is a six-sigma approach in benchmarking the RP processes. The combination of the benchmarking in setting standards and six-sigma to minimize the redundancies in a given process has been proven successful and feasible by a study on the DMLS process.

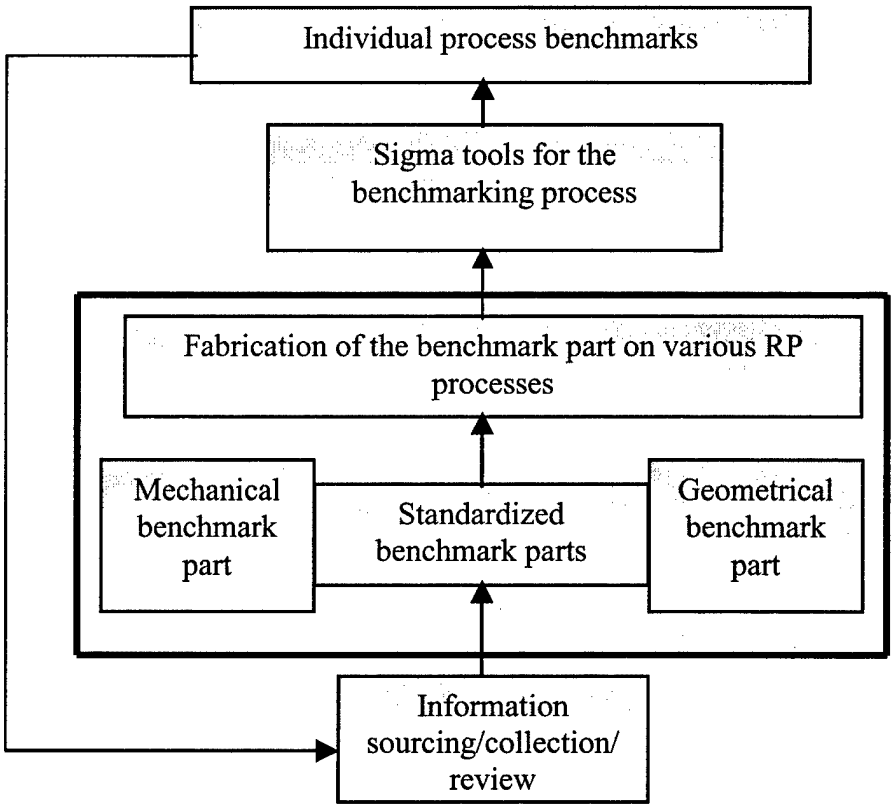

Fig 1. Flow chart for an integrated benchmarking process plan

Figure 1 gives an overall view of the integrated benchmarking process plan. It first starts with the information sourcing of various RP processes, system capabilities, etc from the RP industry. A good understanding of current standards, if available could initially help to visualize the importance of a particular process. Although several benchmarks (benchmark parts) are available in the RP industry, the aim here is to highlight the importance of standardized benchmarks. We suggest that there just should not be just a geometrical benchmark part or a mechanical benchmark part but also standardized benchmarks for the various processes and the

measurement techniques as well. It implies that after standardized geometrical and mechanical benchmark parts are finalised, they will have to be built on various RP systems to establish related RP process benchmarks. A standardised measurement procedure should also be practised so as to reduce the inconsistency and variability when determining the results of fabrication on an RP system or process.

The proposed approach can provide standardized benchmark parts for evaluating the geometrical and dimensional accuracy and mechanical properties of prototypes produced via standardized benchmarked processes and verified from benchmarked measurement techniques. As mentioned earlier, the standardized benchmarked process could be established by fabricating the benchmark part on the RP systems to identify the process that could lead to the benchmark part being fabricated with the best accuracy and surface finish.

The benchmark part is subjected to recalibration when there are changes and improvements in the technology associated with the specific process. The benchmarking exercise is therefore a continuous process and is important to update the developments in the technology.

RP Benchmarking Exercise

A generalised benchmarking approach consists of ten steps in five phases according to Camp R.C [1]. The basic five phases are adopted with modification to meet the requirements in benchmarking for rapid prototyping.

Planning

The first step is to identify what is to be benchmarked and which RP practices are to be studied and its source of comparison, if any. For comparisons some sort of a performance measurement of the various RP processes and systems has to be identified to ultimately decide on employing a particular RP process, machine or material in the realization of the final prototype. To aid this performance evaluation in general, standardized benchmarks are considered important, and for purposes of rigorous investigation of a particular RP process/ system, there can be an individual standardized geometrical, mechanical and process benchmarks. Details on the benchmarks can be referred from Wong [2].

Identifying comparative processes: A source for comparison has always been an important aspect in the benchmarking exercise of a particular industry, technique or method. In the RP industry the idea is to compare across the various RP processes/systems in the order of their performance exhibited in building benchmark parts. Comparisons have to be done on the various RP techniques available in the industry, to mention a few like the SLA, SLS, FDM and the LOM with respect to a process that could lead to a prototype with the best geometrical accuracy and mechanical properties. To ensure consistency for comparison purposes benchmark parts have to be fabricated on each RP process including systems based on the process.

RP data collection and validation: A careful investigation had to be made to collect and analyse the different processes/systems with current procedures in the fabrication of a prototype. The information can be obtained from RP companies or alternatively from various RP bureau services, including the very important hands-on experience of RP operators. The best process that could lead to a better prototype (benchmark part) can ultimately be reiterated to establish it

as a standardized procedure for particular processes in delivering a good prototype. The idea is to rate and rank the processes in some order of performance. Standardised individual benchmark parts for the geometric accuracy and mechanical strength could further assist in measuring the efficiency and performance of a particular RP process. After the data has been collected some sort of validation has to be made to ensure the consistency of the data for comparison and verification purposes

Analysis

Determining current performance gap: Take for example two prototypes of the benchmark part are fabricated from two different machines, but similar configuration, one prototype can turn out to be better than the other. In such case, the performance of both systems and more importantly the processes based on those systems, have to be analysed carefully to determine the performance gap and obviously adopt the best practice that could realize a better prototype. The basic aim is to identify the gap between the new approach and that of the other practices.

Integration

A database can be created to document the findings from the benchmarking exercise and integrated to a web-enabled decision support system that can offer the end user support and suggestions based on the benchmarked procedures. This could also serve the purpose of communicating the findings to gain acceptance, thereby establishing the level of future performance to the organizations using RP technology.

Action

This is one of the most important phases to establish the credibility of the proposed approach where an experimental verification is important to identify the best process in realising a prototype. By careful implementation of specific actions and monitoring progress vital data could be obtained on best practices that could be later established as standards. Development, implementation and monitoring of action plans could be suggested to maturity with the success expected in the proposed approach of IDSSSRP.

Maturity

This is the final stage when the expected result through benchmarking will be communicated for practice by the RP users. In other words this is the final phase in which the best practices are fully integrated into processes.

RP Benchmarking and performance measurement

Benchmarking is not a measurement by itself but also a process of establishing the gaps in performance and as such ensuring that an action plan is put in place to close identified gaps [3]. In Fig 2, the ladder model emphasises on the generalised actions that are to be taken in process benchmarking to close the gaps in performance. It starts with the actual planning, which is an important step to understand the currents standards if any or setting an initial standard for comparison purposes. A rigorous information sourcing is crucial at this point. After the standards are being set, the performance of the various RP processes or systems based on those processes for example can be compared across so that corrective actions can be taken accordingly based on comparisons with the standards. If the performance is better than the existing standards set, the

standards should be replaced accordingly. The benchmarking is always a never-ending improvement. As mentioned earlier initial benchmarks need to be set as a standoff for more generic comparisons in the case of the RP industry.

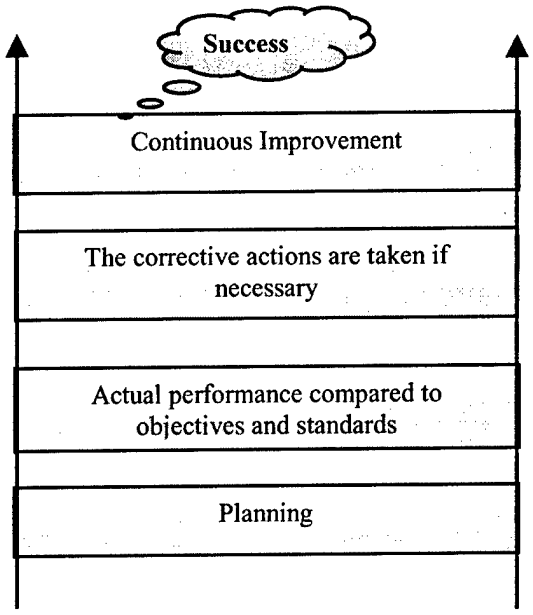

Fig 2. Action Ladder model in Benchmarking

A Sigma Approach to RP Benchmarking

Six-sigma is basically a process quality goal that comes out of statistical probability measurement and process capability techniques. There are numerous six-sigma tools, both experimental and statistical, to analyse a process [4]. We propose the use of six-sigma tools in the benchmarking exercise to identify standardised processes in delivering prototypes. Since experiments form the core of the RP benchmarking process, it is important to validate the approach proposed and also to measure and verify the results acquired from systems based on a particular processes. In our approach the geometrical benchmark part designed will have to be fabricated on different RP systems and a best process is to be identified. That could lead to the benchmark part being fabricated with the best geometrical accuracy and surface finish. In parallel, however, a mechanical benchmark part can also be fabricated as well, to identify the best process that could lead to the benchmark part to have the best set of mechanical properties. Note that there can be several factors that need to be optimised and controlled in order to get to a so-called best prototype, so it is best to use the six-sigma process analysis to optimise the critical factors. The RP benchmarking could be a time consuming and tedious task but once the benchmark is established then the subsequent work can get simpler. A case study on our DMLS-SLS process is highlightened to demonstrate the feasibility of the proposed approach. This study serves to demonstrate the feasibility of the proposed approach on optimising new processes and systems based on the benchmarking exercise.

Case Study on the DMLS-SLS Process

The case study was done on a specially developed DMLS-SLS machine to demonstrate the proposed approach. The DMLS system is mainly a metal sintering machine and has not been successful in building prototypes with a specific plastic powder. This was evident when an attempt was made to build the geometrical benchmark part on the DMLS system. The process was far away from with the limits of a sigma process. The solution to this problem was to initially study the process thoroughly and then identify the key factors that directly influence the quality of the resultant prototype. Apart from identifying the factors, it was also important to identify procedures for a smooth process as a whole. Screening experiments helped us to resolve some of the problems associated with the use of the plastic powder sintering, such as choice of base plates, necessity of powder pre-heating, reshuffling the operation sequence of the powder feeder cylinder, part bed cylinder and scraper movements in order to reduce excess friction causing the parts to fail.

Considering the whole process, our objectives (target) could be summarised as follows:

- To reduce the number of failed parts (good benchmarks parts to be fabricated)
- To identify a smooth process of fabrication.
- To optimise the process for the best or optimised results.

Table 1: Breakdown of the Control factors

List of factors	**Important factors**	**Experimental Control factors**	**Levels**		
Temperature	Laser power	Laser power	**20**	25	30
Scaling	Scanning speed	Scanning speed	**1200**	1400	1600
Offset	Scrapper Speed	Layer thickness	0.2	**0.1**	0.15
Material	Layer thickness	Part bed temperature	35	40	45
Slicing	Part bed temperature				
Scanning speed	Scanning pattern	**Taguchi's L 9(3^4) Orthogonal Array** ↓			
Laser power	Hatch size				
Inert gas					
Layer thickness					
Part bed temperature					
Scrapper speed					
Scanning pattern					
Hatch size					
Part placement parameters					
Build package settings					

Exp. No	Control Factors			
	Temperature	Laser power	Layer thickness	Scanning speed
1	1	1	1	1
2	1	2	2	2
3	1	3	3	3
4	2	1	2	3
5	2	2	3	1
6	2	3	1	2
7	3	1	3	2
8	3	2	1	3
9	3	3	2	1

→

Factor levels	**Values**
1	- Default
2	Default
3	+ Default

In the designed experiments two quality characteristics such as *geometrical accuracy* in terms of (% deviation) in mm from the nominal dimensions and *surface finish* (Ra, least value desirable) in μm were used as response factors during the experiments. If the critical factors (and their interactions if applicable) are identified, then these factors can be tuned accordingly to make the noise factors insensitive. Apart from identifying an optimized set of parameters, the aim was also to identify a tuned process (benchmarked process) that would help the RP users to follow a standardized procedure accordingly based on their part to be prototyped.

The screening and selection of factors were done using six-sigma tools. The purpose of using six-sigma tools was to deduce and reduce flaws in the process. Table 1 lists the various factors and the reduction to a crucial few that can be used to control the DMLS-SLS process as a whole. The identification of the critical factors allows the DOE to get an optimised scaling of factors that will give the best output with least or negligible influence of noise. In our case study the initial choice of factors was done using tools like Ishikawa "fish bone" diagram and quality function deployment (QFD). Ishikawa "fish bone" diagram was useful to initially identify some of the many potential causes of the variability in the DMLS-SLS process. A QFD was later performed based on the general understanding of the probable factors that could be responsible directly or indirectly in shaping the final prototype in the DMLS-SLS process. A DOE was performed based on the orthogonal array and experiments were done by fabricating the benchmark part, to identify the best setting of control factors with desirable response in terms of geometrical accuracy and surface finish. On implementing the proposed approach on the DMLS-SLS process for plastic powder, the part failures were considerably reduced and the performance was within the limits from the target.

Results and Discussions

On the completion of the experiments measurements were made on the fabricated benchmark parts using a co-ordinate measuring machine (CMM). CMM part programming was used to ensure accuracy, consistency and an efficient comparison. Minitab was used in the statistical analysis of the raw data from the measurements. In our experiments since we were interested on the influence of the control factors on the responses, namely geometrical accuracy and surface finish, it was important to analyze the levels of those factors from the experiments.

The graph in Fig 3 shows the main effects for surface roughness. The main effects plot is most useful when several factors are involved. By comparing the changes in the means level, we can identify those factors that influence the response the most. A main effect is present when different levels of a factor affect the response differently. Also for a factor with different levels, we can find which level increases the mean compared to the other levels. This difference is a main effect.

Since our objective is to reduce the surface roughness, or in other words to have a good surface finish, it can be interpreted from the graph on main plots that the optimised setting (reducing Ra) for prototyping parts from this particular plastic material will include a layer thickness of 0.15mm or higher, medium laser power of about 25-30W, medium scan speed of about 1400 mm/s and a low to medium temperature setting.

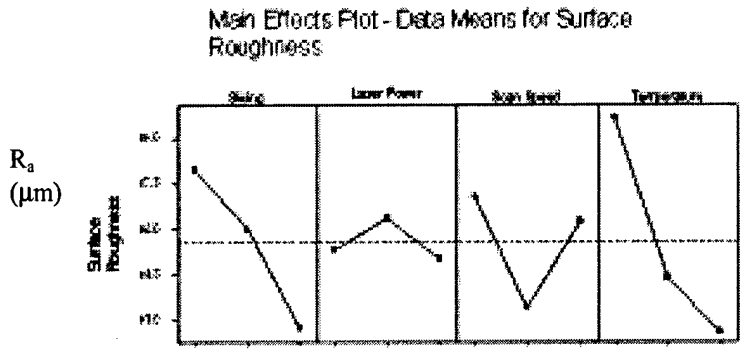

Fig 3. Main plots-data means for surface roughness

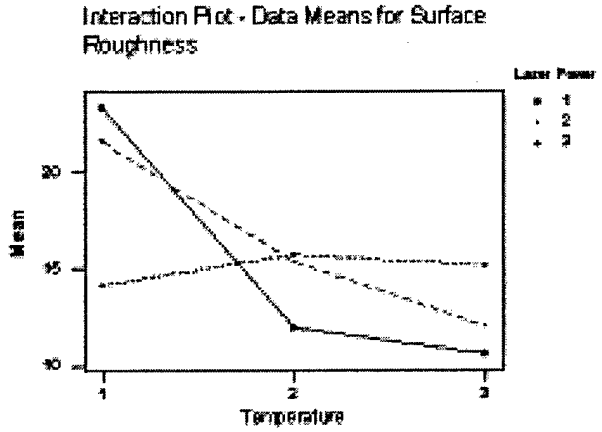

Fig 4. Interaction plots for laser power and temperature

The interaction plots for Laser power and temperature in term of data means of surface roughness are as shown in the Fig 4.

The following figures show the pictures of the benchmark parts before (Fig 5) and after (Fig 6) the application of the proposed approach on the DMLS-SLS process.

Fig 5. Failed benchmark parts

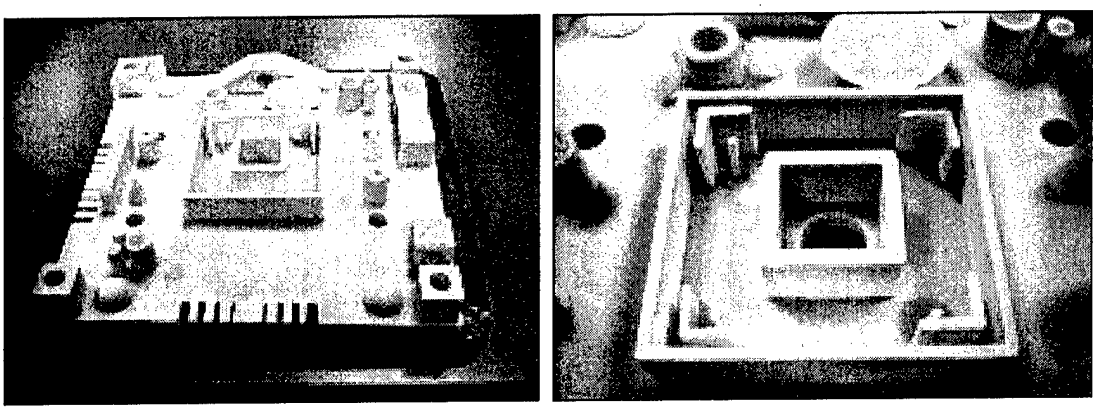

Fig 6. Benchmark part built with a clear profile showing some of the pass/fail features

The failure of the parts was mainly due to improper setting of the control factors, which was later overcome from the identification of their proper setting from the designed experiments. Based on the measured data, optimizations were incorporated in the software in terms of scaling factors and laser beam compensations to arrive at the desired dimensional accuracy. It is evident from Fig 6, the optimized DMLS-SLS process to fabricate benchmark parts with a good surface finish, also improves the clarity and dimensional accuracy of the features being built.

Implementation of IDSSSRP

At the end of the day the findings have to communicated to the users so that iterations can be done to finalize the benchmarks and offer support to the end users. The following Fig 7 presents a framework of the main modules in the implementation of the IDSSSRP.

RP knowledge database:

The RP knowledge database is the central repository that contains general information of the RP industry. It contains information about the different RP processes, systems based on those processes and also the various materials that are used in the various process/systems for the realization of the prototypes. In addition it also includes information on service bureau for various prototyping tasks.

RP benchmarking /standardizations:

This is the core part of the proposed approach which comprises of a search for the industry standards and evolving generic benchmarks for standardized evaluation of the various RP processes/systems. Additional information on benchmarking for performance evaluation of RP systems could be referred to in [2].

Experimentation:

A series of experiments have to be done by fabricating the standardized benchmark parts to identify the best process in realizing the prototype. To accomplish this, action plans have to be developed. Six-sigma tools can aid in the development of action plans. By the implementation of specific actions and monitoring progress, vital data could be obtained on a best process that could be established as a standard.

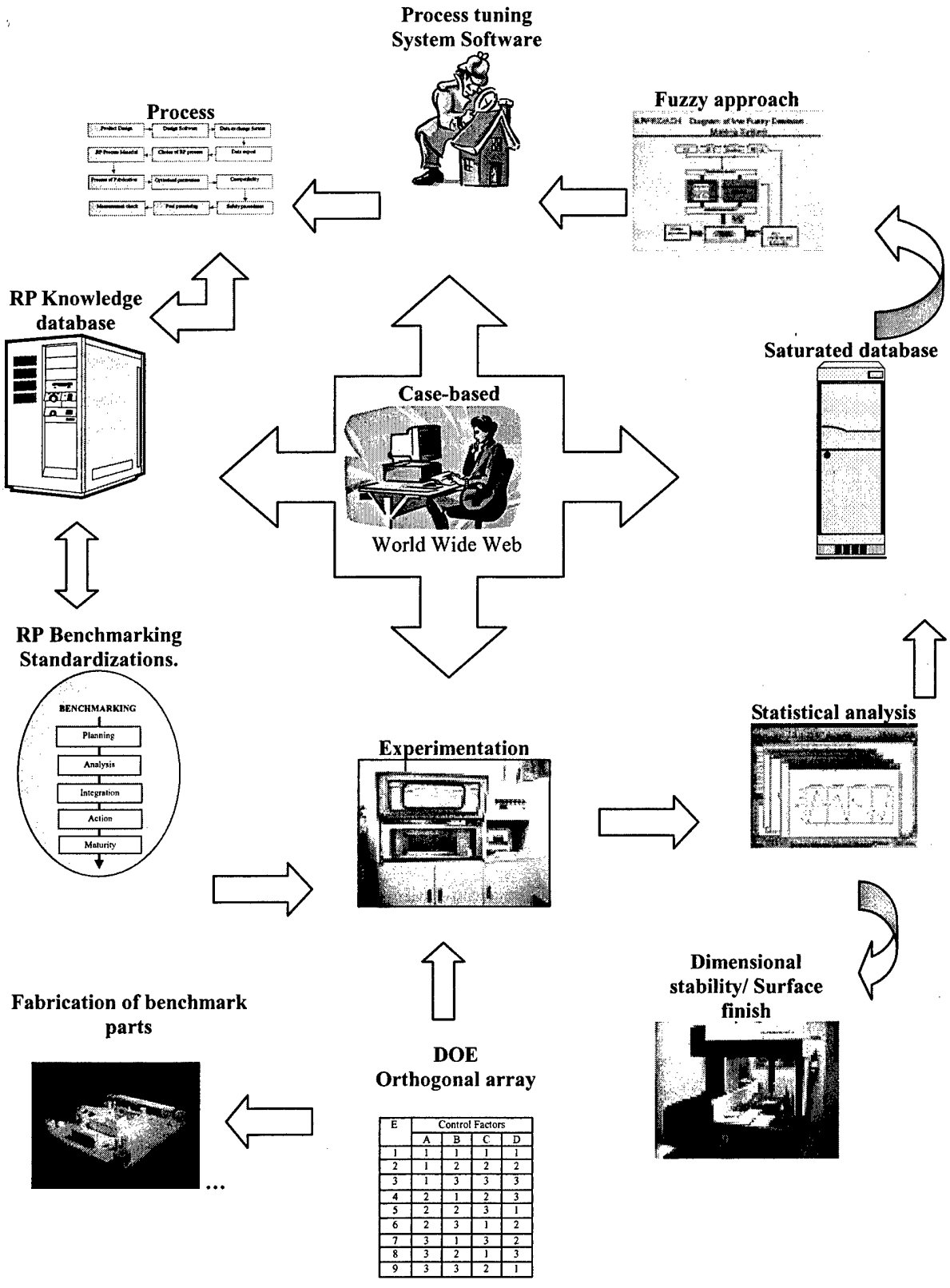

Fig 7. System Architecture for a web based IDSSSRP

Statistical analysis:

The results in terms of quantitative measurements that are obtained by the fabrication of the standardized benchmark parts should be statistically examined and recorded. As in the case of the geometrical benchmark part, the quality characterization will be in terms of the dimensional accuracy and surface finish. Apart from parametric optimizations of particular RP processes to evolve optimized process benchmarks, a dictated statistical analysis procedure will additionally aid comparisons across capabilities of various RP techniques.

Saturated database:

This is the collection of vital and assorted information that is obtained by the act of the benchmarking exercise. This module can be an independent one or can alternatively form a core part of the Central Knowledge database. The saturated database is basically to offer decision support with information that is obtained by benchmarking and standardizations.

Intelligent analysis:

The purpose of benchmarking and standardizations are to offer more consistent and rigorous operating conditions in the RP industry. As an essential part of the benchmarking exercise is to offer decision support, the saturated database and the central knowledge database work to complement each other in offering intelligent decision in terms of choosing a particular RP process and associated materials depending upon the necessity and the requirements of the end user.

Process tuning/ benchmarked process:

This concerns the iterative process of the benchmarking exercise for standardizing particular processes. A simple DOE and additional case studies can be useful in the parametric optimizations and process tuning of particular processes to evolve with benchmarked procedures. Vital information obtained for particular processes will be updated in a saturated database as process benchmarks.

Part of the proposed approach begins with the design of benchmark parts that will be used in testing the capabilities of processes/systems and simultaneously identifying the process benchmarks. Details on the proposed benchmark part, and details of its fabrication on the various RP processes like the SLA, SLS, FDM and LOM can be referred from Wong [2]. Some of the problems encountered during the fabrication of the benchmark part are also discussed.

Conclusion

A generalized approach for an integrated benchmarking process plan is highlighted so that efficient standardizations can be done for the entire RP processing. The proposed approach could be time consuming but yield more meaningful results. Once the standardizations are set right, a web accessible intelligent decision support system would be able to suggest to a RP user about the information on a system based on a particular process and provide him with relevant

information of the most suitable system and process that could help him realize his prototype in the best possible outcome. The benchmarked processes and the measured data that can be obtained by fabricating the standardized benchmark part, and later stored in a saturated database [5] could provide even more useful solutions for the user's needs, in terms of geometric accuracy, surface finish, size, geometrical features, etc.

References

1 **Camp R.C**, 'Benchmarking: The search for industry best practices that lead to superior performance'. ASQC Quality press, 1989.

2 **Wong Y.S, Fuh J.Y.H, Loh H.T, Mahesh M,** 'Rapid prototyping and manufacturing (RP&M) benchmarking', Chapter 3, Software Solutions for RP, PEP Ltd, UK, 2002.

3 **Mohamed Z, Paul L**, 'Practical benchmarking: the complete guide' Chapman & Hall publications, Chapter 9,p 75-80, 1994.

4 **Stamatis D.H,** 'Six Sigma and Beyond Problem Solving and Basic Mathematics' St. Lucie Press, 2002.

5 **Fuh J.Y.H, Loh H.T, Wong Y.S, Shi D.P, Mahesh M, and Chong T.S,** 'A Web-based database system for RP machines, processes and materials selection', Chapter 2, Software Solutions for RP, PEP Ltd, UK, 2002.

Modeling for the Control of the Laser Aided Manufacturing Process (LAMP)

Mallikharjuna R. Boddu, Vishnu P. Thayalan, and Robert G. Landers

1870 Miner Circle, 211 Mechanical Engineering Building
Department of Mechanical and Aerospace Engineering and Engineering Mechanics
University of Missouri – Rolla, Missouri 65409
Phone: 573–341–4586
Email: {mallik,vishnu,landersr}@umr.edu

Reviewed, accepted August 19, 2003

ABSTRACT

Many state–of–the–art Rapid Prototyping (RP) technologies adopt lasers to fabricate 3–D solid parts by material deposition in layers. The ability of these RP technologies to control the process requires a thorough understanding of the process mechanics. This paper presents the analysis of an analytical, dynamic model explaining the complex phenomenon of Laser Aided Manufacturing Process (LAMP). The equilibrium of the dynamic model is analyzed and dynamic simulations are performed to determine its stability characteristics. This model forms the basis for the real–time control of the LAMP.

INTRODUCTION

Rapid prototyping (RP) is a valuable tool for the fabrication of 3D models. RP decreases the product development cycle by enabling the part to be built in hours instead of weeks directly from the CAD model by eliminating the intermediate step of die preparation. There are a variety of RP processes currently available. RP processes can be divided into those that are formative, subtractive, or additive. Additive–based RP is gaining importance due to its capability to build functional–gradient parts. Laser based RP is one such technology experiencing striding growth in the manufacturing industry since its introduction in the early 1980s. There are around 25 different laser based RP technologies practiced under different names such as stereolithography, Fused Deposition Modeling (FDM), Direct Metal Deposition (DMD), Laser Engineered Net Shaping (LENS), etc. [Steen, 1998]. All of these methods concentrate on building 3D functional parts with minimum cost and in the least amount of time with required tolerance and surface finish.

Laser Aided Manufacturing Process (LAMP) is a technology that is being developed at the University of Missouri–Rolla to fabricate high–resolution 3D parts of arbitrary shapes directly from CAD models with the ability for the user to define material composition throughout the building process. LAMP is based on the simple technique of adding layers until a 3D metal prototype is obtained by selective cladding point–by–point and layer–by–layer [Boddu *et al.*, 2001]. The dimensional accuracy of the part is maintained from the initial stages by allowing the deposition and milling operations to be performed in shifts throughout the part building process, but the scientific challenge lies in the ability of the LAMP system to precisely fabricate the part by minimizing the post deposition operation. This depends on the capability of the system to control the LAMP process in real–time. Previous efforts have been made by many authors in designing a control system to regulate the laser metal deposition process. But these efforts have been limited to regulating few of the process parameters due to the complexities and limitations

involved in understanding the dynamics of the process. Modeling has always been a complex task due to the complex mechanical flow, thermal transfer and material transformation mechanisms involved in the description of the process [Doumanidis and Kwak, 2001]. Therefore, some authors have restricted themselves to empirical modeling to relate the clad characteristics to the process parameters.

Weerasinghe *et al.* (1983) performed the initial efforts to empirically model the laser cladding process. They concentrated on producing uniform clad layers by overlapping single clad tracks. This work explored the effect of laser power, beam diameter and mode structure, traverse speed, powder flowrate and powder shape and size on cladding rate, clad thickness and width, surface finish, powder utilization, substrate dilution, segregation, porosity, residual stress, cracking, microstructure, and adhesion. The empirical relations based on the experimental results showed the variation of clad width and clad height to the variation in cladding speed, coverage rate, and overlap factor.

Blake *et al.* (1985) explained the effect of irregular powder flowrates on dilution of laser cladding processes. For constant laser power and traverse speed, the amount of powder flowing into the melt pool determines the energy available at the substrate and hence the amount of dilution. Therefore, the less powder fed into the melt zone, the greater the dilution. However, more powder fed into the melt zone results in a significant reduction of specific energy into the substrate, creating a possible lack of fusion. They used a dynamic powder feeder with an in–process feedback control system to determine the affect of powder feeder variables (flowrate, flow orientation, etc.), laser associated variables (power, beam configuration, etc.), and traverse speed of the positioning system on surface finish, dilution, cracking, porosity, homogeneity, adhesion, and distortion.

Hu *et al.* (2001) discussed the instabilities and irreparability problem suffered by SFF methods for metal part building due to the presence of a large number of parameters governing the process. The authors used infrared imaging of the melt pool as an imaging technique for controlling the 3D laser melt pool. Relationships have been established based on the variations of the characteristics of images with variations in the process parameters. A PID controller was designed with feedback from infrared image sensing to control the area of the thermal field. The area of the thermal field represents the laser energy absorbed by the part per unit length in the processing zone. Hence, the control of the area of the thermal field, by regulating laser power and traverse speed, brings an even heat input rate in 3D laser cladding. The authors also demonstrated that, by controlling the heat input during the laser deposition process, the geometrical accuracy, uniformity of deposits, and microstructure can be improved.

Koomsap *et al.* (2001) developed a simulation–based design of a laser–based free–forming process controller. The difficulty in designing a process for the models is the nonlinear effect of individual process parameters in the temperature field (Koomsap *et al.*, 2001). The authors developed a metamodel, which is an estimation of the physical model that relates the surface temperature to laser power, table velocity, and powder flowrate. The surface temperature was represented as a function of laser power, table velocity, and powder flowrate. Based on the simulations obtained for different settings of the laser power, table velocity, and powder flowrate, a steady state metamodel was developed using the polynomial regression models from

the steady state results. This was used to form a dynamic metamodel based on the criteria that the surface temperature during the transient periods was non oscillatory, implying the process was either a critically damped or overdamped process.

A novel method of rapid layered manufacturing for building fully–dense metal parts by preplaced powder technique was investigated by Yevko *et al.* (2001). They considered pulsed–laser mode, continuous laser mode, power level, laser beam, and scanning speed as parameters that influenced the clad properties: namely, height and width. A process model was developed and simulated to determine qualitative relationships between process parameters and clad properties by calculating the global temperature field within the powder and baseplate. The nonlinear heat transfer problem was solved by a numerical finite–difference method.

A two–dimensional finite element model for laser cladding by powder injection was developed by Hoadley *et al.* (1992) to study the effect of laser power and processing velocity on the thickness of the deposited clad. This model determines the steady state temperature field, the shape of the melt pool and the position of the melt surface relative to the laser beam. An emperical model for laser cladding was developed by Toyserkani *et al.* (2002) for realtime process control. A Hammerstein–Wiener nonlinear model and a Elman recurrent neural network were implemented to identify the dynamic laser cladding model. The Hammesteine–Wiener approach proved more useful in accurately describing the transient response of the process. Laser intensity, table velocity, and powder feedrate were the inputs, and clad height and melt pool temperature were the process output parameters.

Selective Laser Sintering (SLS) is one of the leading commercial RP technologies that build solid objects by selectively fusing powder at each successive layer according to a numerically–defined cross–sectional geometry. Williams *et al.* (1998) modeled the effects of selected parameters on the SLS process by determining the amount of energy delivered at the substrate surface. A three–dimensional heat diffusion problem was formed to describe the thermal energy transferred in the SLS process.

PROCESS MODELING

A more general dynamic process model for the laser metal deposition process was presented in Doumanidis and Kwak (2001). This model has the capability to form the basis for a process controller. This paper will perform an analysis of this model. First, the model is briefly presented. Performing a mass balance of the melt pool

$$\rho \dot{V}(t) = -\rho A(t) v(t) + \mu_m m(t) \tag{1}$$

where ρ is the material density (kg/m^3) and is assumed to be constant, V is the bead volume (m^3), A is the cross sectional area in the direction of deposition (m^2), v is the table velocity in the direction of deposition (m/s), μ_m is the powder catchment efficiency, and m is the powder flow rate (kg/s). Assuming an elliptical bead, the volume and cross sectional area in the direction of deposition, respectively, are given by

$$V(t) = \frac{\pi}{6} w(t) h(t) l(t) \tag{2}$$

$$A(t)=\frac{\pi}{4}w(t)h(t) \tag{3}$$

where w is the bead width (m), h is the bead height (m), and l is the bead length (m). Performing a momentum balance of the melt pool in the direction of deposition

$$\rho\dot{V}(t)v(t)+\rho V(t)\dot{v}(t)=\rho\frac{\pi}{4}w(t)h(t)v^2(t)+\left[1-\cos(\theta)\right]\left[\gamma_{GL}-\gamma_{SL}\right]w(t) \tag{4}$$

where θ is the wetting angle (rad), γ_{GL} is the gas to liquid surface tension parameter, and γ_{SL} is the solid to liquid surface tension parameter. Performing an energy balance of the melt pool

$$\begin{aligned}\rho c_l\dot{T}(t)V(t)+\rho\dot{V}(t)\left[c_s(T_m-T_0)+h_{SL}+c_l(T(t)-T_m)\right]=-\rho\frac{\pi}{4}w(t)h(t)v(t)c_s(T_m-T_0)+\\ \mu_Q Q(t)-\frac{\pi}{4}w(t)l(t)\alpha_s(T(t)-T_m)-\left[\frac{\pi}{\sqrt[3]{2}}\left[w(t)h(t)l(t)\right]^{\frac{2}{3}}\right]\left[\alpha_G(T(t)-T_0)+\varepsilon\sigma\left(T^4(t)-T_0^4\right)\right]\end{aligned} \tag{5}$$

where T is the average melt pool temperature (K), c_s is the solid material specific heat ($J/(kgK)$), T_m is the melting temperature (K), T_0 is the ambient temperature (K), h_{SL} is the specific latent heat of fusion–solidification (J/kg), c_l is the molten material specific heat ($J/(kgK)$), μ_Q is the laser efficiency, Q is the laser power (W), α_s is the convection coefficient (W/m^2K), α_G is the heat transfer coefficient (W/m^2K), ε is the surface emissivity, and σ is the Stefan–Boltzmann constant (W/m^2K^4). Using the steady–state solution for the conductive temperature distribution in a material subjected to an energy source moving at a constant velocity, the bead width–length relationship at the average temperature is given by the following elliptical relationship

$$l(t)=X(t)+0.25\frac{w^2(t)}{X(t)} \quad with \quad X(t)=\max\left[\frac{w(t)}{2} \quad \frac{\mu_Q Q(t)}{2\pi k(T(t)-T_0)}\right] \tag{6}$$

where k is the thermal conductivity constant ($W/(mK)$).

EQUILIBRIUM ANALYSIS

It is often of interest to determine the steady–state solution of equations (1)–(6). Two situations will be considered: one where the process variables are known and the process parameters must be determined and one where the process parameters are known and the process variables must be determine. Often, the designer knows the desired melt pool temperature, bead width, and bead height. Typically the bead length is not of interest. In this case, the designer would like to determine the process parameters that produce the desired melt pool temperature, bead width, and bead height. Setting the left hand side of equation (4) to zero, the equilibrium table velocity is

$$\bar{v} = \sqrt{\frac{-4\left[1-\cos(\theta)\right]\left[\gamma_{GL}-\gamma_{SL}\right]}{\rho\pi\bar{h}}} \tag{7}$$

where the bar denotes equilibrium value. Note that γ_{GL} must be less than γ_{SL} for the equilibrium table velocity to be positive. Setting the left hand side of equation (1) equal to zero, the equilibrium powder flow rate is

$$\bar{m} = \frac{\rho\pi\bar{w}\bar{h}\bar{v}}{4\mu_m} \tag{8}$$

To solve for the equilibrium laser power and the equilibrium bead length, the left hand side of equation (5) is set equal to zero and the bisection routine is applied to the resulting equation and equation (6). Note that if the bead length is equal to the bead width, equation (5) may be directly solved for the equilibrium laser power; however, for many situations this is not the case. Finally, the equilibrium bead volume is solved using equation (2).

The following parameters are taken from Doumanidis and Kwak (2001): $\rho = 7200\ kg/m^3$, $\mu_m = 0.92$, $\mu_Q = 0.58$, $T_0 = 292\ K$, $\theta = 90^0$, $c_l = 780\ J/(kgK)$, $h_{SL} = 2.45*10^5\ J/kg$, $T_m = 1673\ K$, $\alpha_s = 183\ W/(m^2K)$, $\sigma = 5.67*10^{-8}\ W/(m^2K^4)$, $\alpha_G = 24\ W/(m^2K)$, and $\varepsilon = 0.53$. To achieve the same simulation results presented in Doumanidis and Kwak (2001), the following parameters were found by trial and error: $k = 6.5\ W/(mK)$, $\gamma_{GL}-\gamma_{SL} = -0.00036$, and $c_s = 1250\ J/(kgK)$. For a desired melt pool temperature of 2000 K, bead width of 5 mm, and bead height of 2 mm, the powder flow rate, table velocity, and laser power should be 20.8 g/min, 5.64 mm/s, and 999 W, respectively. Also, the bead length and volume, respectively, are 9.06 mm and 47.4 mm^3.

Sometimes a designer would like to predict the melt pool temperature and bead morphology for a set of process parameters. Given, the powder flow rate, laser power, and table velocity, equations (1)–(6) are solved for the melt pool temperature and bead morphology. Setting the left hand side of equation (4) to zero, the equilibrium bead height is

$$\bar{h} = \frac{-4\left[1-\cos(\theta)\right]\left[\gamma_{GL}-\gamma_{SL}\right]}{\rho\pi\bar{v}^2} \tag{9}$$

Again, note that γ_{GL} must be less than γ_{SL} for the equilibrium bead height to be positive. Setting the left hand side of equation (1) equal to zero, the equilibrium bead width is

$$\bar{w} = \frac{4\mu_m\bar{m}}{\rho\pi\bar{h}\bar{v}} \tag{10}$$

To solve for the equilibrium melt pool temperature and the equilibrium bead length, the left hand side of equation (5) is set equal to zero and the bisection routine is applied to the resulting equation and equation (6). Finally, the equilibrium bead volume is solved using equation (2). For a powder flow rate, table velocity, and laser power of 25 g/min, 5 mm/s, and 1200 W,

respectively, the melt pool temperature is 1928 *K*, the bead width is 5.32 *mm*, the bead height is 2.55 *mm*, the bead length is 11.1 *mm*, and the bead volume is 78.8 mm^3.

The equilibrium bead height is inversely proportional to the square of the table velocity and is independent of the other process parameters. The equilibrium bead width is proportional to the powder flow rate, proportional to the table velocity, and is independent of the laser power. The melt pool temperature and bead length depend on all of the process parameters. The sensitivities of melt pool temperature and bead length with respect to laser power, table velocity, and powder flow rate are shown in Figure 1 for the numerical parameters given above. For sensitivities with respect to laser power, the powder flow rate and table velocity are 25 *g/min* and 5 *mm/s*, respectively. For sensitivities with respect to powder flow rate, laser power and table velocity are 1200 *W* and 5 *mm/s*, respectively. For sensitivities with respect to table velocity, the laser power and powder flow rate are 1200 *W* and 25 *g/min*, respectively. The melt pool temperature is relatively constant for low laser powers, increases quickly for laser powers around 1100–1200 *W*, and increases slowly for high laser powers. For the laser metal deposition process, it is desirable to keep the melt pool temperature just above the melting temperature; in this example, 1750–1850 *K*. If the melt pool temperature is too low, the substrate and powder will not melt and, if the melt pool temperature is too high, plasma will result and the part microstructure will not form properly. The bead length is minimum around 1100–1200 *W*, increases quickly for low laser powers, and increases slowly for high laser powers. For a very low laser power, approximately 200 *W*, both the melt pool temperature and bead length suddenly become small. This is due to the discontinuity in equation (6). The laser power becomes so small that the bead length is equal to the bead width. The melt pool temperature is a maximum for a table velocity of approximately 10 *mm/s*, decreases sharply for lower table velocities, and decreases slowly for higher table velocities, eventually becoming constant. The bead length is a minimum for a table velocity of approximately 5 *mm/s* and increases sharply for lower and higher table velocities. The melt pool temperature is relatively constant for high powder flow rates and increases steadily as the powder flow rate decreases. The bead length increases slowly as the powder flow rate increases until approximately 25 *g/min* where the bead length increases sharply. From a controls perspective, it appears that table velocity, powder flow rate, and laser power should be used to regulate bead height, bead width, and melt pool temperature, respectively.

SIMULATION STUDIES

A series of simulations are now conducted to analyze the laser metal deposition system. To simulate the differential–algebraic equations, a 4^{th} order Runge–Kutta routine is used. An initial bead volume and an initial melt pool temperature are specified. Given initial conditions for the process parameters, equations (2), (4), and (6) are solved iteratively to determine consistent conditions for the bead dimensions (i.e., width, height, and length). The differential equations (1) and (5) are solved at each time step using the 4^{th} order Runge–Kutta routine and equations (2), (4), and (6) are solved iteratively to determine the bead dimensions. Note that the 4^{th} order Runge–Kutta routine requires intermediate derivative calculations that, in turn, require intermediate values of the state and algebraic variables. Thus, for every intermediate bead volume and melt pool temperature values, the bead dimensions are solved iteratively using equations (2), (4), and (6).

Simulations for step changes in the process parameters are shown in Figure 2. The system operates under steady conditions for 5 seconds and then the step changes in the process parameters are applied. The laser power changes from 1200 *W* to 1440 *W*, the table velocity changes from 5 *mm/s* to 6 *mm/s*, and the powder flow rate changes from 25 *g/min* to 30 *g/min*. The time responses were first–order and second–order type responses. It is interesting to note that the melt pool temperature had a smooth response while the bead dimensions, which are governed by the algebraic equations, had sharp responses to step changes in the process variables. Also, a step change in powder flow rate alone caused a very slow response in the bead dimensions as compared to the other simulations. To understand the stability characteristics, a multitude of simulations are conducted and the phase plots, i.e., plots of a state variable versus another state variable, are graphed. The phase plots are shown in Figure 3 for a variety of process parameter combinations. The phase plots include bead volume versus melt pool temperature, bead width versus bead height, bead width versus bead length, and bead height versus bead length. In all of the phase plots, the trajectories go to the equilibrium parameter values demonstrating the system is stable in the given region. It is interesting to note that the bead width and bead height have an inverse relationship.

SUMMARY, CONCLUSIONS, AND FUTURE WORK

This paper analyzed the equilibrium and stability properties of a dynamic model of the laser metal deposition process. The equilibrium bead height is inversely proportional to the table velocity and the equilibrium bead width is proportional to the powder flow rate and table velocity. The equilibrium bead length and melt pool temperature have a complex relationship to all of the process parameters. The dynamic analysis showed that the equilibrium is a stable equilibrium with a large region of attraction. Also, the bead width and bead height dynamically have an inverse relationship. In future work, analytically approximations of the sensitivity of the equilibrium bead length and equilibrium melt pool temperature to the process parameters and the region of attraction will be determined.

ACKNOWLEDGEMENTS

The authors gratefully acknowledge the financial support of the National Science Foundation (DMI–9871185), Society of Manufacturing Engineers (#02022–A), Missouri Research Board, and UMR's Intelligent Systems Center.

REFERENCES

Blake, A.G. and Eboo, G.M., 1985, "State of the Art Laser Hardfacing Using Dynamic Powder Feed Technology," *Conference on the Laser vs. the Electron Beam in Welding, Cutting and Surface Treatment*, Reno, Nevada, pp. 196–214.

Boddu, M.R., Landers, R.G., and Liou, F.W., 2001, "Control of Laser Cladding for Rapid Prototyping–A Review," *Twelfth Annual Solid Freeform Fabrication Symposium*, Austin, Texas, August 7–9, pp. 460–467.

Doumanidis, C. and Kwak, Y.M., 2001, "Geometry Modeling and Control by Infrared and Laser Sensing in Thermal Manufacturing with Material Deposition," *ASME Journal of Manufacturing Science and Engineering*, Vol. 123, pp. 45–52.

Hu, D., and Wu, Y., 2001 "Heat Input Control in 3D Laser Cladding Based on Infrared Sensing," *ASME International Mechanical Engineering Congress and Exposition*, November, pp. 333–341.

Hoadley, A.F.A. and Rappaz, M., 1992, "A Thermal Model of Laser Cladding by Powder Injection," *Metallurgical Transactions Part B*, Vol. 23B, pp. 631–642.

Eager, T.W., and Tsai, N.S., 1983, "Temperature Fields Produced by Traveling Distributed Heat Sources," *Welding Journal*, Vol. 62, No. 12, pp. 346s–355s.

Koomsap, P., Prabhu, V.V., Schriempf, J.T., and Reutzel, E.W., 2001, "Simulation–Based Design of Laser–Based Free Forming Process Control," *Journal of Laser Applications*, Vol. 13, No. 2, pp. 47–59.

Steen, W.M., 1998, *Laser Material Processing*, 2nd Edition, Springer Verlag.

Toyserkani, E., Khajepour, A., and Corbin, S., 2002, "Application of Experimental–Based Modeling to Laser Cladding," *Journal of Laser Applications*, Vol. 14, No. 3, pp. 165–173.

Weerasinghe, V.M. and Steen, W.M., 1983, "Laser Cladding with Pneumatic Powder Delivery," *Lasers in Materials Processing*, pp. 166–174.

Williams, J.D. and Deckard, C.R., 1998, "Advances in Modeling the Effects of Selected Parameters on the SLS Process," *Rapid Prototyping Journal*, Vol. 4, No. 2, pp. 90–100.

Yevko, V., Park, C.B., Zak, G., Coyle, T.W., and Behabib, B., 1998, "Cladding Formation in Laser Beam Fusion of Metal Powder," *Rapid Prototyping Journal*, Vol. 4, No. 4, pp. 168–184.

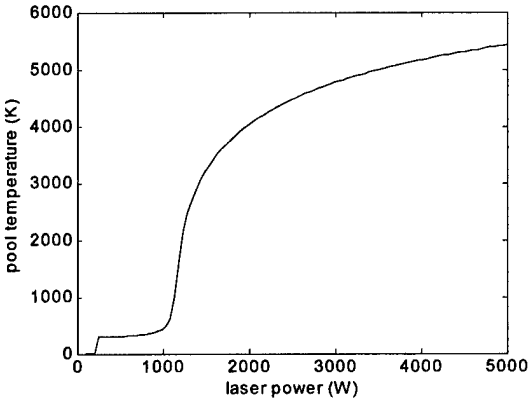

(a) melt pool temperature vs. laser power

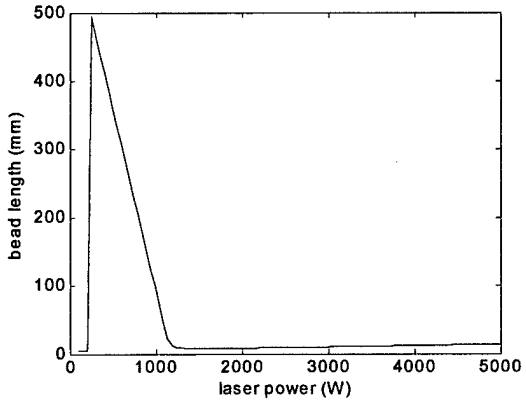

(b) bead length vs. laser power

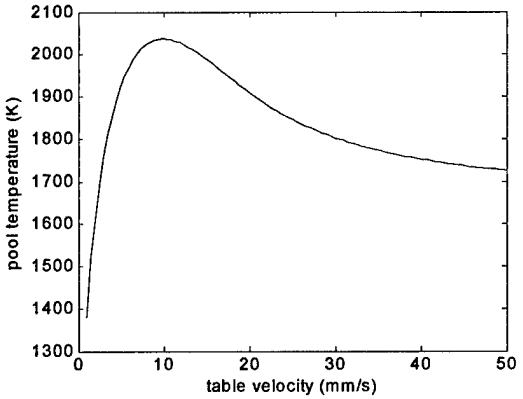

(c) melt pool temperature vs. table velocity

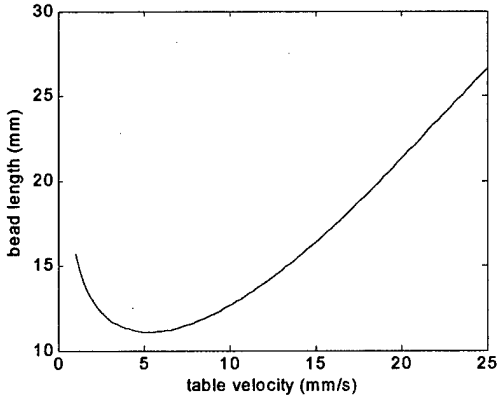

(d) bead length vs. table velocity

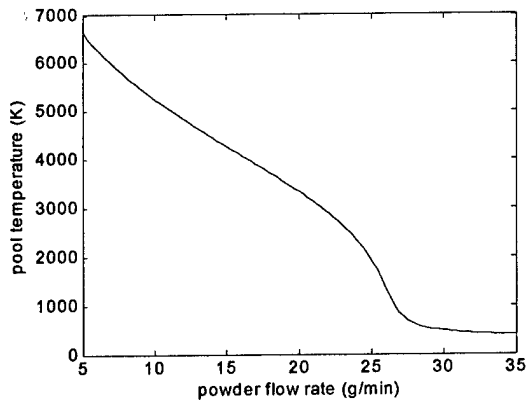

(e) melt pool temperature vs. powder flow rate

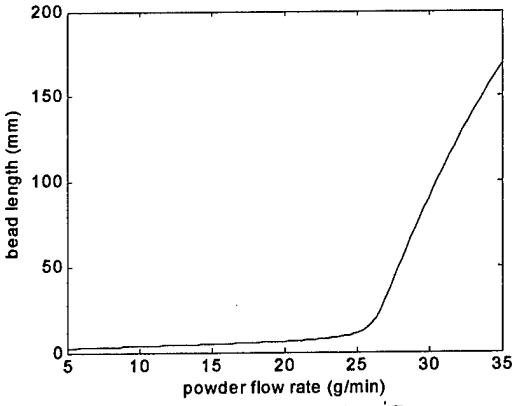

(f) bead length vs. powder flow rate

Figure 1: Equilibrium Melt Pool Temperature and Bead Length as a function of Process Parameters.

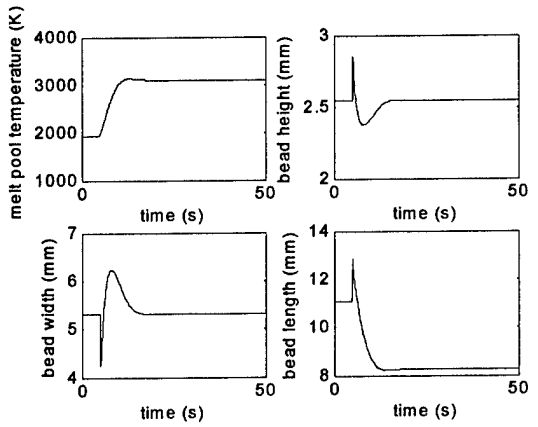

(a) step change in laser power

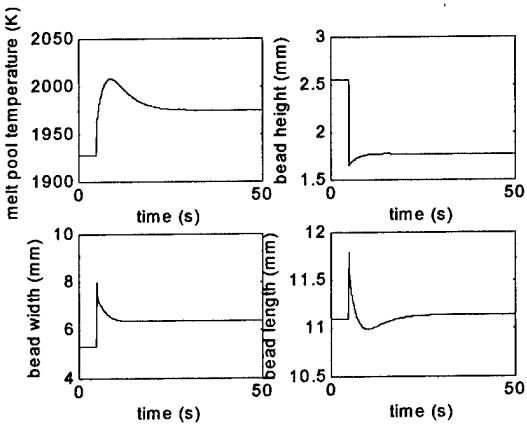

(b) step change in table velocity

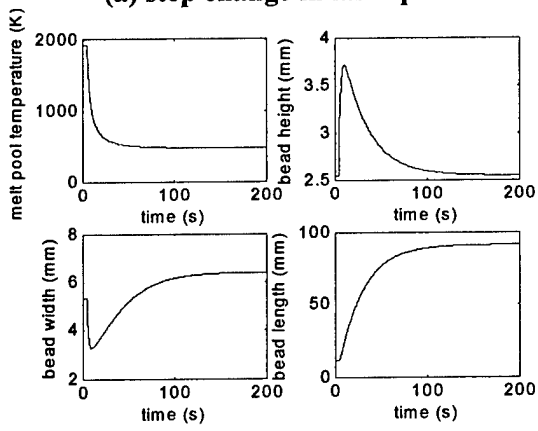

(c) step change in powder flow rate

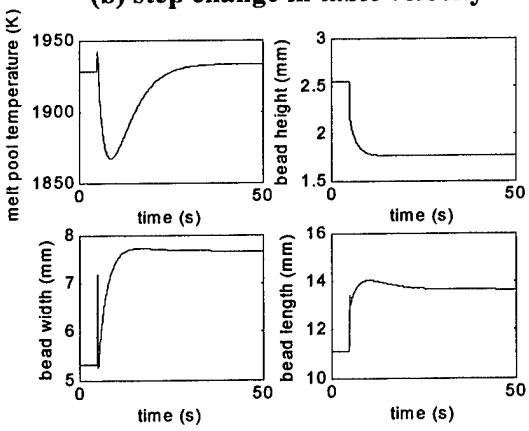

(d) step change in all process parameters

Figure 2: Dynamic Simulation with $Q(0) = 1200\ W$, $v(0) = 5\ mm/s$, $m(0) = 25\ g/min$, $V(0) = 78.8\ mm^3$, $T(0) = 1930\ K$, $w(0) = 5.32\ mm$, $h(0) = 2.55\ mm$, and $l(0) = 11.1\ mm$.

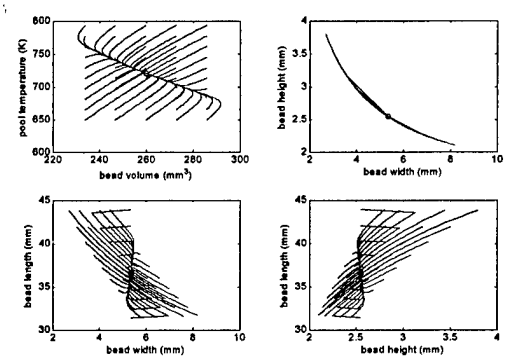

(a) $Q = 1100\ W$, $m = 25\ g/min$, and $v = 5\ mm/s$

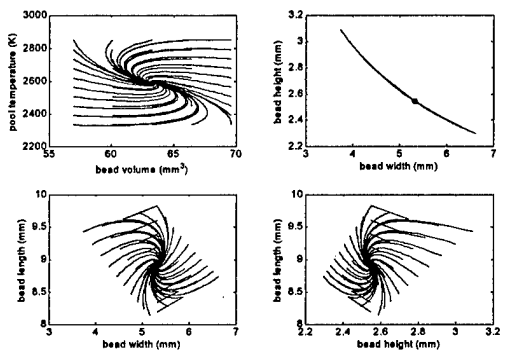

(b) $Q = 1300\ W$, $m = 25\ g/min$, and $v = 5\ mm/s$

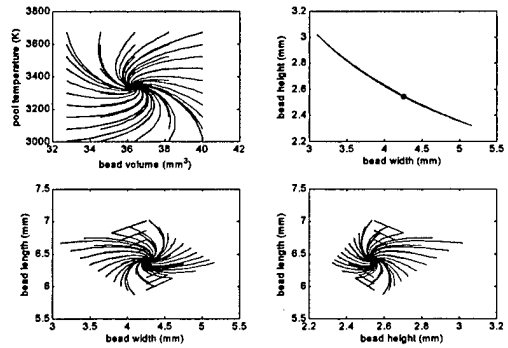

(c) $Q = 1200\ W$, $m = 20\ g/min$, and $v = 5\ mm/s$

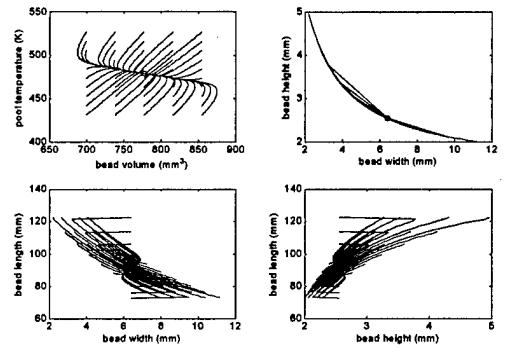

(d) $Q = 1200\ W$, $m = 30\ g/min$, and $v = 5\ mm/s$

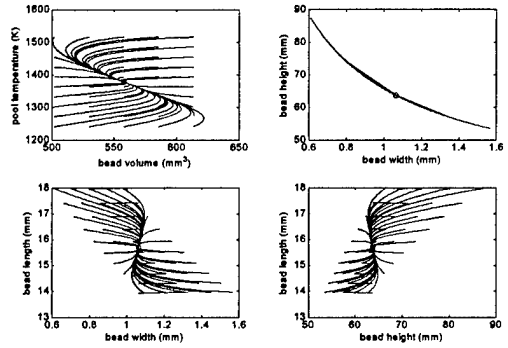

(e) $Q = 1200\ W$, $m = 25\ g/min$, and $v = 1\ mm/s$

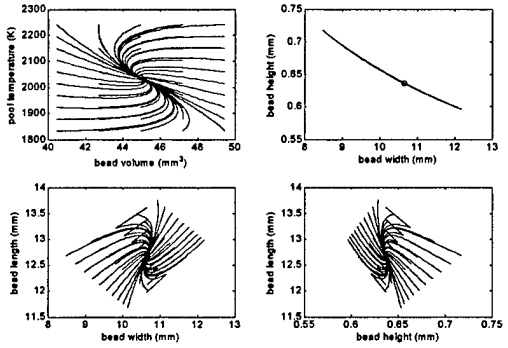

(f) $Q = 1200\ W$, $m = 25\ g/min$, and $v = 10\ mm/s$

Figure 3: Phase Plots. Equilibrium Point Denoted by Circle.

Melt Pool Size and Stress Control for Laser-Based Deposition Near a Free Edge

Pruk Aggarangsi and Jack L. Beuth
Department of Mechanical Engineering
Carnegie Mellon University
Pittsburgh, PA

Michelle Griffith
Sandia National Laboratories
Albuquerque, NM

Abstract

Thermomechanical models developed in this research address two experimental observations made during the deposition of thin-walled structures by the LENS™ process. The first observation (via thermal imaging) is of substantial increases in melt pool size as a vertical free edge is approached under conditions of constant laser power and velocity. The second observation (via neutron diffraction) is of large tensile stresses in the vertical direction at vertical free edges, after deposition is completed and the wall is allowed to cool to room temperature. At issue is how to best control melt pool size as a free edge is approached and whether such control will also reduce observed free edge stresses. Thermomechanical model results are presented which demonstrate that power reduction curves suggested by process maps for melt pool size under steady-state conditions can be effective in controlling melt pool size as a free edge is approached. However, to achieve optimal results it is important that power reductions be initiated before increases in melt pool size are observed. Stress simulations indicate that control of melt pool size can reduce free-edge stresses; however, the primary cause of these stresses is a constraint effect which is independent of melt pool size.

Introduction

The LENS™ Process: The primary application of this work is to the Laser Engineered Net Shaping (LENS™) process developed at Sandia National Laboratories (Griffith et al., 1996). The LENS™ process is one of a number of competing processes developed with the goal of automatically fabricating complex shapes or features directly out of metal, based on a 3-D computer-aided-design model of the part. In the LENS™ process, parts are constructed by focusing a high-power laser beam onto a metal substrate, where it intersects streams of metallic powder. The laser locally melts the powder to form a molten pool on the top surface of the growing part. By moving the substrate under the laser beam, a part is built up, line by line and layer by layer. Parts are deposited onto a large metal base plate, which conducts heat away from the part, and acts to constrain the part from deformation during deposition. As shown in Fig. 1, the process is particularly well-suited for the construction of fine features such as thin-walled structures. The models developed in this research directly address the construction of thin-walled features. Work is underway to not only optimize LENS™ process parameters manually, but to use real-time thermal images of melt pool size as part of a feedback mechanism controlling the process (Griffith et al., 1999).

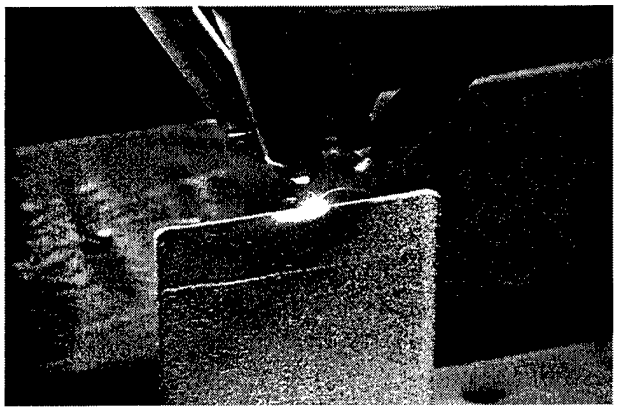

Figure 1 Image of the LENS™ process fabricating a thin-walled structure.

Problem Considered: The research described herein is motivated by two observations made during the construction of thin-walled features. The first observation comes from direct thermal imaging of the melt pool during metal deposition (Rangaswamy et al., 2003). Figure 2 shows experimentally obtained thermal contours as seen from the side of a stainless steel wall from such experiments. As the laser moves across the top of the wall with a constant laser power and velocity, the thermal contours reach a steady-state configuration (as viewed by an observer moving at the velocity of the laser). As a free surface is approached, however, the melt pool size becomes significantly larger, due to the decreased ability of the substrate to conduct heat away from the melt pool.

Precise control of melt pool size is essential for accurate deposition of thin-walled structures and a key issue is how laser power and/or velocity might be altered to maintain a constant melt pool size as a free edge is approached. The problem is exacerbated by the fact that a reduction in laser velocity (and thus an increase in thermal energy imparted to the wall per distance moved in the deposition direction) may be needed to accurately deposit material near free edges, where a velocity reversal is needed to continue with deposition of the next layer of material. Although critical for thin-walled structures, analogous problems exist as free edges are approached in the deposition of bulky structures.

A second observation serving as motivation for this research comes from neutron diffraction measurements of stress in thin-walled structures at a fixed depth from the deposition surface (Rangaswamy et al., 2003). Figure 3 shows a plot of measured stresses as a function of distance across the width of a deposited thin wall (where the width is measured in the deposition direction). Measurements are taken at a depth of 45 mm from the top surface of a wall that is 90 mm tall, 25.4 mm wide and 1.5 mm thick. The y coordinate is defined as being the horizontal coordinate along the direction of deposition (along the width), the x direction is defined as being the horizontal coordinate normal to the direction of deposition (through the thickness) and the z coordinate is in the vertical (height) direction. In contrast to stresses near the top of the wall, which consist of large stresses in the y (deposition) direction and essentially zero stress in the x and z directions, at a depth into the substrate there are large stresses in the z (vertical) direction and relatively small stresses in the other two directions. The z stress is tensile near the left and right free edges and compressive in the middle of the wall. Because there is no net force applied to the wall in the z direction, the area under the σ_{zz} vs. y curve is zero.

The stresses plotted in Fig. 3 were measured on a thin wall that was still attached to the large base plate it was built upon. One possible source of the tensile σ_{zz} stresses in the plot of Fig. 3 is constraint from the comparatively stiff base plate keeping the wall from experiencing a bending-type deformation. In this case, the base plate would induce tensile stresses on the outside edges of the plate and compressive stresses in its middle, as is seen in the stresses plotted

in Fig. 3. However, in this particular case, the wall has a large height relative to its width. This would tend to limit the effect of the base plate on the stresses at the wall's mid-height. An analogous source of the tensile σ_{zz} stresses plotted in Fig. 3 could be constraint from the portion of the wall below the location where the stresses are measured. If a wall is tall compared to its width, the wall can constrain its own bending-type deformation, setting up stresses that have a distribution like that seen in Fig. 3. A final possible cause of the σ_{zz} stresses is the increase in melt pool size near the free edge. Elevated temperatures along the vertical edge could result in the build-up of tensile stress in the vertical direction as the free-edge region cools. In this scenario, smaller contractions in the z direction in the bulk of the wall would constrain larger contractions in the z direction near the free edge, inducing tensile stresses in the free edge region. As a thin wall is constructed, this sequence of events would occur with the deposition of each wall layer.

The primary motivation of this work is to understand increases in melt pool size near free edges in the LENS™ and other similar processes, and how such increases can be controlled via dynamic decreases in laser power. A secondary issue to be considered is the existence of measured tensile stresses near the free edge in thin-walled structures and whether control of melt pool size could reduce or eliminate them.

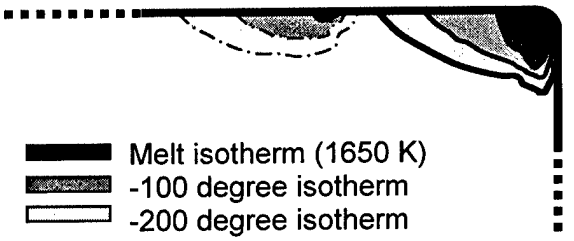

Figure 2 Temperature contour plot from thermal imaging experiments on a thin wall, showing significant melt pool size increase near a free edge (from Rangaswamy et al, 2003).

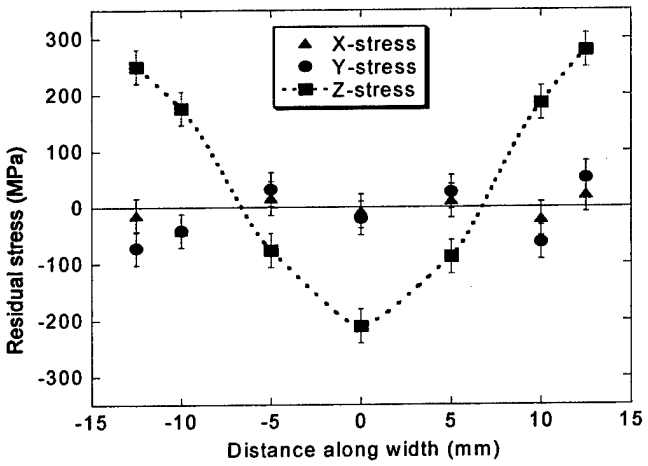

Figure 3 Plot of residual stress measured in a LENS™-deposited thin wall as a function of distance along the wall width (from Rangaswamy et al, 2003).

Existing Work: Most experimental and modeling research on automated laser-based fabrication processes has addressed the manipulation of process parameters for process control under steady build conditions. Over the past eight years, an extensive research effort to develop the LENS™ process at Sandia Laboratories has resulted in an understanding of what process parameters are needed to build a number of standard shapes out of stainless steel, titanium and a few other alloys. Despite this success, gaining a fundamental understanding of the inter-related effects of process variables such as laser power and velocity on critical process parameters such as melt pool size and residual stress remains a challenge. Such an understanding is needed to further develop LENS™ and other related laser-based freeform fabrication processes.

Modeling work by Vasinonta et al. (1999, 2001a, 2001b) has begun to address this need by developing easy-to-use "process maps" allowing the prediction of steady-state melt pool size in thin-walled and bulky features for any practical combination of LENS™ process variables. The simultaneous control of residual stress and melt pool size has been addressed by Vasinonta et al. (2000). A brief overview of the process map approach to understanding laser-based freeform fabrication processes is given by Beuth and Klingbeil (2001) and a complete presentation of the process map approach for controlling steady-state melt pool size and residual stress in thin-walled and bulky parts is given by Vasinonta (2002). Most of the numerical approaches used in the research described in this paper are based on this earlier work. A new application of the process map approach involves developing process maps of cooling rates and thermal gradients at the melt pool boundary with the goal of predicting microstructure (Bontha and Klingbeil, 2003) (also in this symposium proceedings). The ultimate goal of this body of research is to understand in a fundamental way the control of melt pool size, stress and material properties in laser-based deposition processes and to present results in a form that process engineers can readily use. Portions of this research also make use of results presented in insightful internal reports from Sandia Laboratories by Dobranich and Dykhuizen (1998a, 1998b) and Dykhuizen and Dobranich, (1998). Their steady-state analytical and numerical simulations address the importance of a number of simplifying assumptions used in modeling the LENS™ process.

Although an understanding of steady-state process control is important, ultimately an understanding of dynamic process control is needed to advance laser-based freeform fabrication processes. Experimental studies of the LENS™ process by Griffith el at. (1999) and Hofmeister et al. (2001) have addressed this issue by considering transient control of melt pool size via a thermal imaging feedback control system. Their control system has the ability to alter process parameters as needed to maintain a consistent melt pool size. The research described in this paper represents an initial effort to model transient changes in melt pool size for a commonly encountered event (the approach of a free edge). Conclusions from this paper have served as the basis for developing process maps for transient melt pool size control, which is addressed in another paper in this symposium (Birnbaum et al., 2003).

Modeling Approach

The ABAQUS finite element software package was used for calculating temperatures and stresses in a thin wall. The 2-D model consists of a concentrated heat source moving across a tall thin wall 25.4 mm in length with a thickness of 1.5 mm and a height of 90 mm. These dimensions match those of the thin wall used to develop the neutron diffraction results plotted in Fig. 3. In all simulations presented in this paper, the heat source begins at the left edge of the wall, travels left to right across the wall to the right free edge, and then traverses the top of the wall again, traveling from right to left. As such, only the final pass of the laser over the wall is modeled (where the thin wall studied by Rangaswamy et al. (2003) was built up via multiple laser passes).

A moving heat source is simulated by applying a concentrated heat flux at a node on the model surface for a time equal to the distance between model nodes divided by the laser velocity. Nodal temperature results of the current step are then used as initial conditions for the next step, where a new concentrated heat flux is applied to the next node. A mechanical model of the same

mesh density and dimensions is used to simulate residual stresses caused by time-dependent temperatures from the thermal model. Meshes used for the thermal and mechanical simulations contained 32218 nodes and 31860 elements and an image of the region near the melt pool in the middle of the wall is included as part of Fig. 4. Although meshes are sufficiently dense to capture melt pool size and shape in all regions of the model, a higher density mesh is used near the right free edge, where explicit values of melt pool depth are extracted. In all simulations presented herein, deposition of 316 stainless steel is modeled (matching the experiments in Rangaswamy et al., 2003).

Figure 4 gives the boundary conditions used in the thermal and mechanical simulations. Thermal simulations model all free edges as insulated boundaries, neglecting convection and radiation at these locations, as suggested in the work by Dobranich and Dykhuizen (1998a). A fixed temperature condition is enforced at the base of the wall, modeling the base plate the wall is deposited onto as an ideal heat sink (the base plate itself is not modeled). Mechanical simulations model the free edges as traction-free, with displacements constrained to be zero at the base of the wall, modeling the mechanical constraint of the base plate.

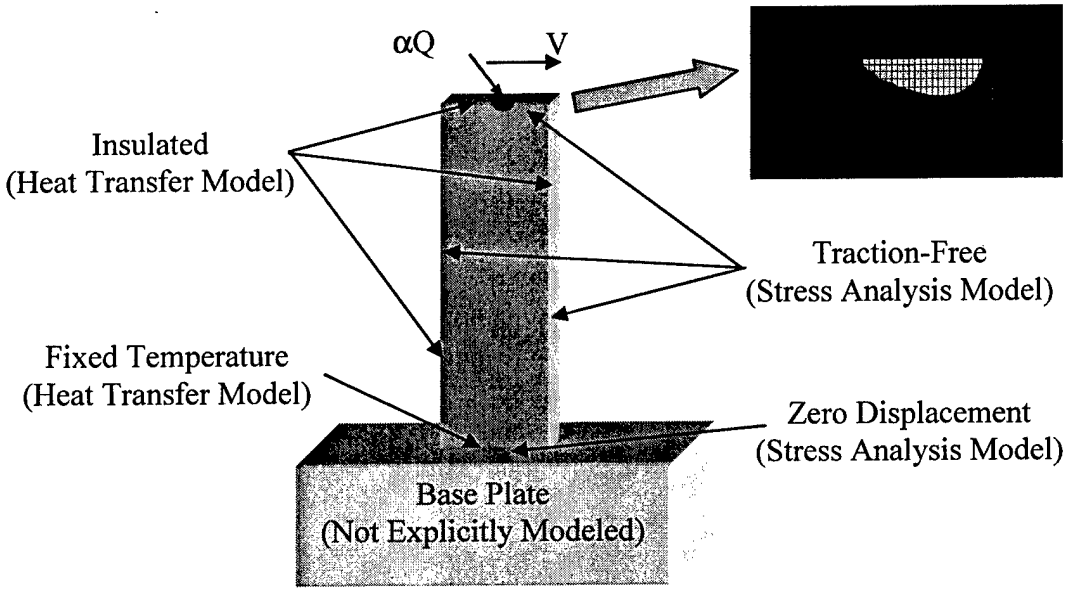

Figure 4 Schematic of the thin wall thermal and mechanical models, simulating heat transfer from a point heat source moving across the top edge and resulting thermal stresses.

Thermal properties of AISI 316 stainless steel used in the simulations include a solidus temperature of 1644 K, a liquidus temperature at 1672 K and constant density of 7652 kg/m^3 (Peckner and Bernstein, 1977). Based on data plotted by Peckner and Bernstein (1977) the variation of thermal conductivity and specific heat with temperature is approximated up to the solidus temperature by the following linear relations:

$$k = 11.82 + 0.0106\,T \quad (W/mK) \tag{1}$$

$$c = 389.66 + 0.230\,T \quad (J/kgK)\,.$$

Above the solidus temperature, k and c are held constant. A latent heat of fusion of 2.65×10^5 J/kg is also used.

Mechanical properties used in the simulations are also taken from Peckner and Bernstein (1977). The Young's modulus and coefficient of thermal expansion are approximately linear functions of temperature and are represented by the following equations:

$$E = 200 - 0.094(T\text{-}300) \text{ GPa} \qquad (2)$$

$$\alpha = 14.55 + 0.0037T \quad 10^{-6}/\text{K}$$

Above the solidus temperature, the Young's modulus and coefficient of thermal expansion are held constant at 1 GPa and 20.6×10^{-6}/K, respectively. The temperature dependence of yield stress is taken from tabulated data of yield stress divided by room temperature yield stress. A room temperature yield stress of 441 MPa was used, as measured for LENS™-deposited SS 316 (Griffith et al., 1996).

Process Maps for Melt Pool Size

As shown by Vasinonta et al. (1999, 2001a), the solution of Rosenthal (1946) for a point heat source moving across a (2-D) half-space can be used as the basis for developing "process maps" that rigorously quantify the relationship between melt pool size and laser power, laser speed, part height and part preheat temperature. Although the process maps are strictly applicable to steady-state thermal conditions, in this paper they are used as a guide for determining power reductions needed to maintain a constant melt pool size under transient conditions as a free edge is approached. As suggested by the Rosenthal (1946) solution, a process map for melt pool length in thin-walled structures is represented through three dimensionless variables: the normalized melt pool length, $\bar{l}$, the normalized substrate height, $\bar{h}$, and the normalized melting temperature, $\bar{T}_m$, which are defined as follows:

$$\bar{l} = \frac{l}{2k/\rho cV}, \quad \bar{h} = \frac{h}{2k/\rho cV} \text{ and } \bar{T}_m = \frac{T_m - T_{base}}{\alpha Q/\pi kt}. \qquad (3)$$

In eq. (3), l is the melt pool length, t is the wall thickness and h is the wall height. ρ, c, k and T_m are the density, specific heat, thermal conductivity and melting temperature of the deposited material, respectively. αQ is the absorbed laser power, V is the laser velocity, and T_{base} is the wall and base plate preheat temperature.

If thermal properties are temperature-independent, results from the analysis of a concentrated heat source moving over a thin-walled structure of finite height, h, can be represented as a single surface plotted on three coordinate axes of $\bar{l}$, $\bar{h}$ and $\bar{T}_m$. Vasinonta et al. (1999, 2001a) demonstrate that even for analyses including temperature-dependent properties and latent heat, results can be graphically represented in terms of these dimensionless variables with acceptable accuracy, valid of over the full range of process variables used in the deposition of stainless steel in the LENS™ process. Coupled with rules developed for its effective use, the resulting "process map" allows the presentation of melt pool length results for all combinations of process variables in a compact and useable form.

Modeling Results

Melt Pool Depth Control: The plots of model results in Figs. 5 and 6 demonstrate how melt pool depth can be controlled through reductions in laser power as a free edge is approached. In both figures, the term heat flux power refers to absorbed laser power, αQ, where α is taken as equal to 0.35. In this paper, melt pool depth is considered instead of melt pool length because it is potentially related to the development of tensile stresses at the free edge. Control of melt pool depth is also critical in ensuring bonding between deposited layers. As indicated by the solid red line in Fig. 5, for the case of a heat source moving toward a free edge with constant laser velocity and power (designated by the dashed red line), melt pool depth is increased by a factor of roughly 2.5. This behavior is caused by the proximity of the free edge reducing conductive heat transfer from the melt pool area.

The melt pool depth increases seen under constant power conditions (the data designated by the solid red line) have been used to estimate power reductions needed to control melt pool depth as the free edge is approached. This data has been combined with results from the process map research by Vasinonta et al., 1999, 2001a. In that work, it is shown that the Rosenthal analytical solution can be used to effectively predict melt pool length in tall walls of SS304 if properties of SS304 at 1000 K are used in calculating dimensionless variables. Based on this result, the Rosenthal solution with properties of SS304 at 1000 K (which are similar to SS316) was used to calculate the percent reduction in laser power needed to return to the ambient steady-state value of melt pool depth as a function of laser travel distance. The resulting power vs. travel distance curve is given as the black dashed line in Fig. 6. This power vs. distance curve yields a substantially smaller increase in melt pool size as the free edge is approached (the black solid line).

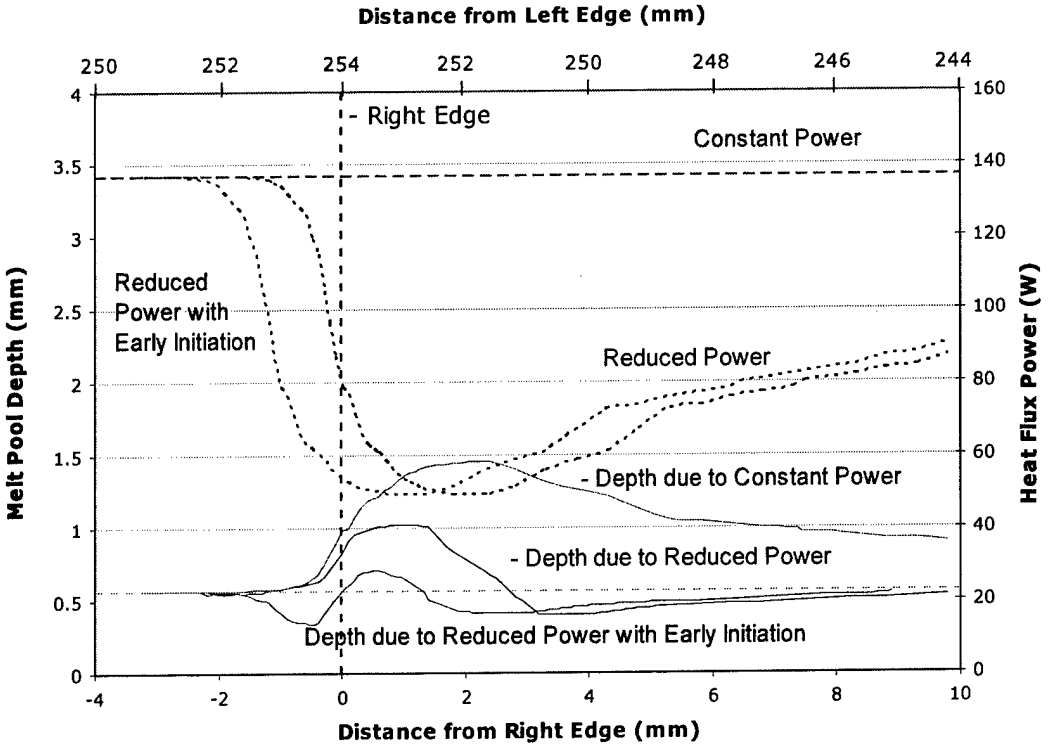

Figure 5 Melt pool depth vs. horizontal distance traveled near a free edge, for constant and varying laser powers with and without early initiation in laser power reduction.

Although it is an improvement, the melt pool size changes designated by the solid black line of Fig. 5 are still not optimal. A roughly 75% increase in melt pool depth is seen. A critical issue is the time delay between a power change at the melt pool and resulting changes in the melt pool size. The results designated by the blue dashed and solid lines illustrate an attempt to remedy this. In this case, the power reduction vs. travel distance curve, designated by the blue dashed line, is identical to the black dashed line, but the reduction in power is initiated before the melt pool size begins to increase. The resulting plot of melt pool size vs. travel distance shows an initial decrease in melt pool size, followed by a much smaller melt pool size increase. Overall, the melt pool size is near the free edge is effectively controlled.

It is important to reiterate that the power reduction curve used in this case (the blue dashed line in Fig. 5) is based on melt pool size increases under constant power conditions. Because those melt pool size increases now do not occur, the power reduction magnitudes as the laser moves away from the free edge are larger than they need to be. This is clearly seen in the melt pool size data for values of distance from the right edge greater than 2 mm. The melt pool depth does not approach its steady-state value because the power (which is based on the red solid line data) has not been increased to its steady-state value. To consider this issue, another simulation has been performed that includes not only the early initiation of power reductions, but also a sudden increase to 60% of the ambient power at the time when the melt pool depth reaches its steady-state value as it moves away from the free edge, followed by an increase to 80% of the ambient power. Figure 6 shows the results of this case, which is meant to simulate some type of feedback control of melt pool size. The resulting plot of melt pool depth shows good control of melt pool size as the laser leaves the free edge region.

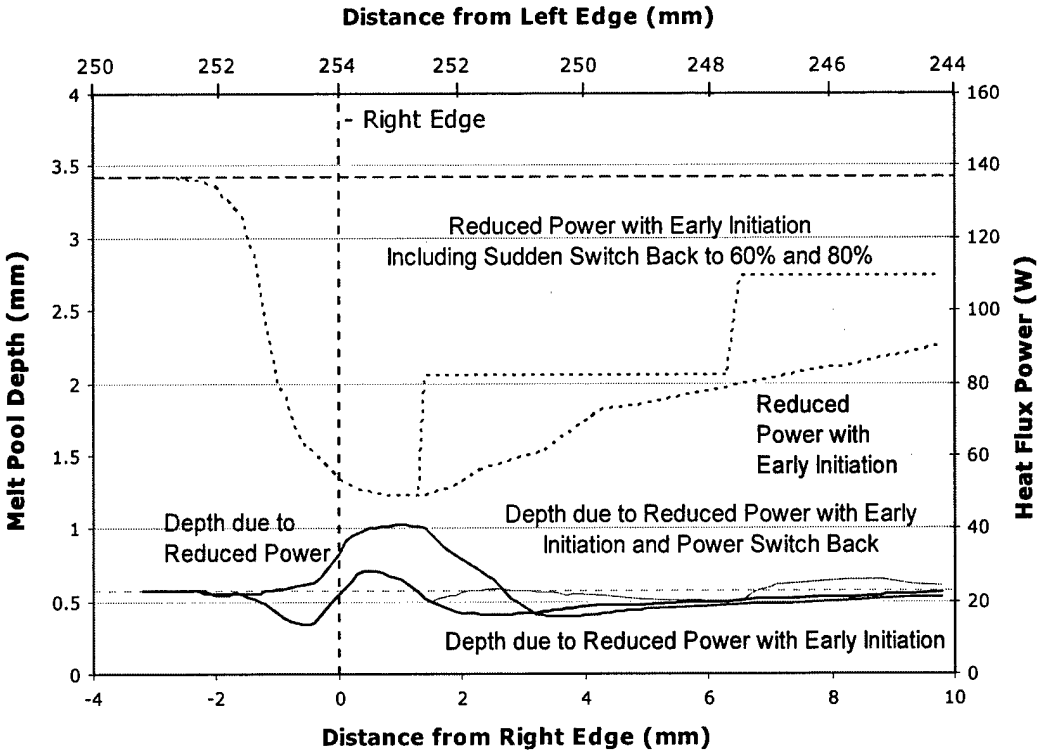

Figure 6 Melt pool depth vs. horizontal distance traveled near a free edge, for varying laser powers including one case with early initiation of power reduction and a sudden switch to 60% and then 80% of the ambient laser power.

Collectively, the results of Figs. 5 and 6 show that power reductions suggested by steady-state model results (e.g. the process maps of Vasinonta et al., 1999, 2001a) can be a useful guide for maintaining a consistent melt pool size as a free edge is approached. However, if power reductions are initiated at the time when the melt pool size begins to increase (as would be done in a feedback control system) the benefit is limited. Instead, power reductions should be initiated in advance of observed increases in melt pool size. Finally, at some point feedback control must be used to effectively return the melt pool to steady state conditions. Thus effective control of melt pool size requires a combination of accurate tracking of heat source location, accurate modeling to determine the initiation time and magnitude of power reductions, and feedback control of power based on observed melt pool sizes.

Stress Control: Figures 7 and 8 show stress contour plots in thin-walled structures after cool-down to room temperature, resulting from a heat source traveling across the top of the wall from left to right and then from right to left. The contour plot of Fig. 7, which is for the case of constant laser power, shows a significant amount of tensile residual stress in the vertical direction near the left and right edges. Although the model is for a single back and forth pass of the heat source, the resulting stresses are qualitatively similar to the experimental results plotted in Fig. 3. The contour plot of Fig. 8 is for the same case as that for Fig. 7; however, the melt pool size has been controlled near the free edges via the power reduction curve designated by the blue dashed line of Fig. 6. It is clear that the tensile stresses near the free edge are not significantly changed by controlling melt pool size (though they are reduced slightly).

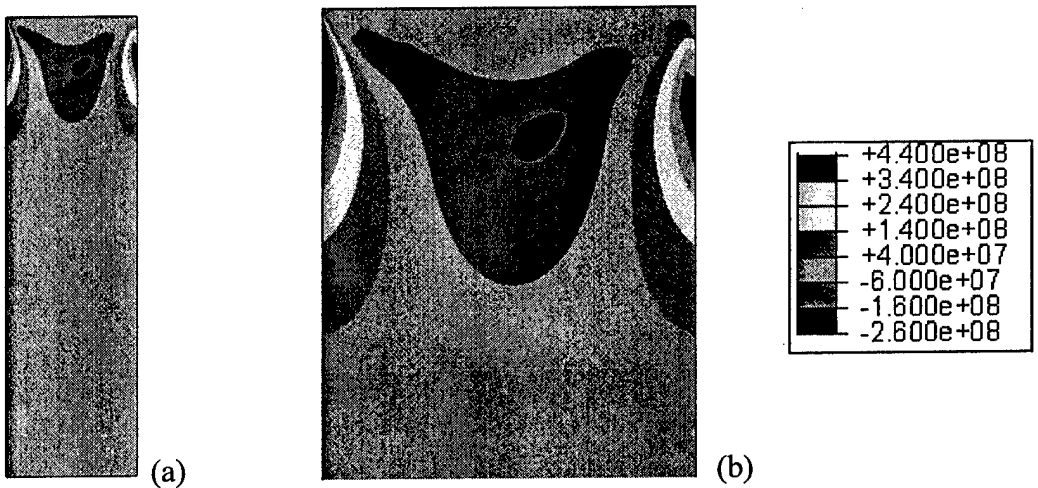

Figure 7 (a) Vertical stress contours after cool-down to room temperature obtained from a model with constant laser power and (b) magnification of the top portion of the contour plot.

Finally, Fig. 9 provides a stress contour plot from an elastic thermal simulation designed to replicate the types of stresses induced in the tall wall by the laser. That simulation consists of a thermal mismatch problem, where a layer on top of the wall is subjected to a uniform free thermal contraction relative to the rest of the wall. The thickness of the layer was chosen to roughly match the thickness of the region in the top of the heat source simulation experiencing tensile stresses in the horizontal direction. The magnitude of the thermal mismatch strain was chosen to give an average stress in the layer roughly equal to the tensile stress in the horizontal direction in the top region of the heat source model. As shown in Fig. 9, the elastic simulation

clearly produces stress contours analogous to those from the heat source simulation of the thermal deposition process.

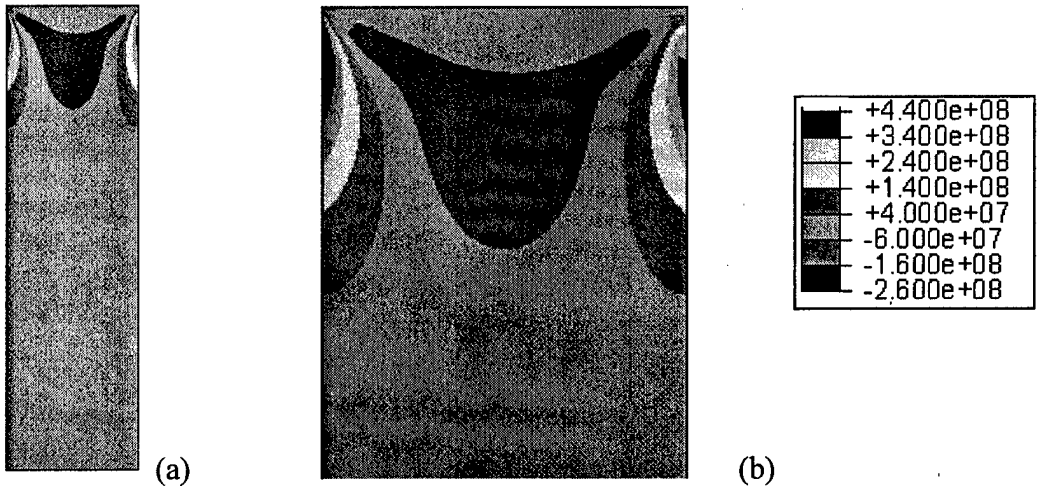

Figure 8 (a) Vertical stress contours after cool-down to room temperature obtained from a model with reduced laser power near the left and right edges (controlled melt pool depth) and (b) magnification of the top portion of the contour plot.

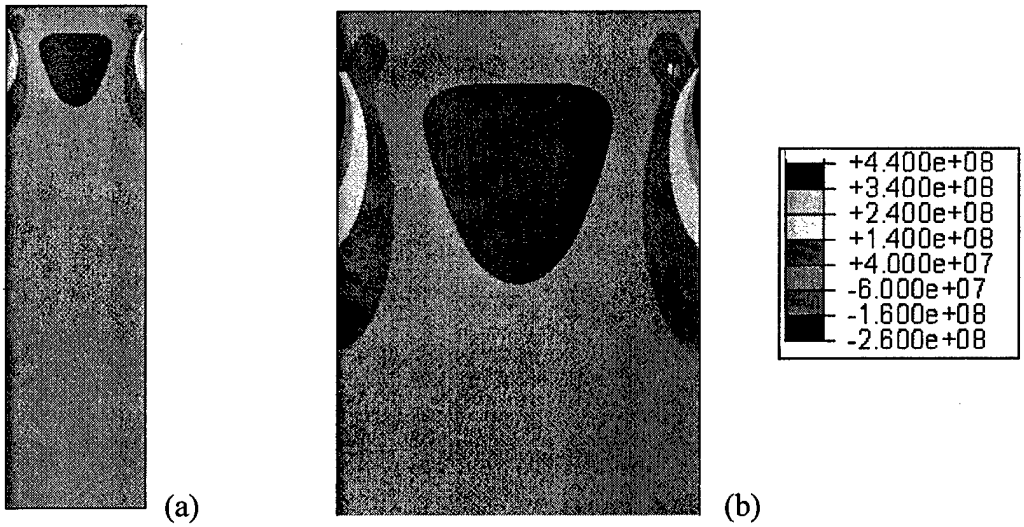

Figure 9 (a) Vertical stress contours from an elastic simulation reproducing the model cool down process and (b) magnification of the top portion of the contour plot.

The conclusion from the stress results of Figs. 7-9 is that the primary cause for measured and modeled tensile stresses in the vertical direction near the free edges of deposited thin walls is not melt pool size increases. Substantial reductions in melt pool size near the free edges yield only a minor reduction in free edge stresses. Also, the same types of stresses are seen in the elastic simulation of a thermal mismatch strain, where no melt pool exists at all. For the simulations performed in this study, constraint of the base plate is also not an issue. The walls are so tall relative to their width that the stresses at the base of the wall due to constraint of the base plate are not significant. If the constraint at the base plate were removed, the effect on the free edge stresses would be minimal. There may be some role of base plate constraint for the stresses plotted in Fig. 3, however, which were measured at a location halfway up the wall

height. The main cause for the tensile stresses in the vertical direction near the free edge appears to be constraint from bending-type deformation by the bulk of the wall below the top surface. In a tall wall built up by successive deposition of layers, one would expect tensile stresses at the free edges (and compressive stresses in the middle of the wall) along nearly the entire wall height, falling rapidly to zero as the top free edge is approached. Removal of the base plate would relax these stresses near the base of the wall only.

Conclusions

The primary goal of this research was to gain insight into how increases in melt pool size seen at free edges in the LENS™ and other similar processes can be controlled. A second goal was to understand the development of tensile residual stresses measured near the free edges of thin-walled structures, determining whether control of melt pool size in that region could in turn help reduce these stresses. The modeling work performed in this research demonstrates that power vs. melt pool size relationships developed from steady-state models can be used as a guide in determining power reductions needed to maintain a consistent melt pool size as a free edge is approached. However, if one waits until an increase in melt pool size begins to occur before initiating power reductions (as is done in feedback control systems) melt pool size cannot be effectively controlled. Instead, power reductions should be initiated in advance of melt pool size changes to compensate for the time required for system response to laser power changes. Thus, a key component of melt pool size control is effective process modeling to determine appropriate power changes and distances from the free edge to initiate them. As the laser leaves the free edge, feedback control becomes important to achieve a rapid return to steady-state conditions.

Mechanical models have determined that localized increases in melt pool size are not the primary cause for large magnitude tensile stresses measured in the vertical direction near free edges. Instead, these stresses are primarily caused by constraint of the wall from a bending type of deformation. If a wall is short compared to its width, or at the base of a tall wall, the constraint will come from the large base plate the wall is deposited onto. Away from the base of tall walls, tensile stresses near the free edges are induced by constraint of the wall itself. These stresses will remain even after the wall is machined from the base plate.

Acknowledgements

This research was supported by the National Science Foundation Division of Design, Manufacture and Industrial Innovation, through the Materials Processing and Manufacturing Program, award number DMI-0200270. The authors would like to thank Dave Alexander and Ralph Anderson of Pratt & Whitney for their insights and effort in guiding the industrial applications of this research.

References

1. Beuth, J.L. and Klingbeil, N.W., 2001, "The Role of Process Variables in Laser-Based Direct Metal Solid Freeform Fabrication," *JOM,* September 2001, pp. 36-39.
2. Birnbaum, A., Aggarangsi, P. and Beuth, J.L., 2003, "Process Scaling and Transient Melt Pool Size Control in Laser-Based Additive Manufacturing Processes, " *Solid Freeform Fabrication Proceedings* (D.L. Bourell, J.J. Beaman, H.L. Marcus, R.H. Crawford and J.W. Barlow, eds.), Proc. 2003 Solid Freeform Fabrication Symposium, Austin, August 2003 (this symposium).

3. Bontha, S. and Klingbeil, N.W., 2003, "Thermal Process Maps for Controlling Microstructure in Laser-Based Solid Freeform Fabrication," *Solid Freeform Fabrication Proceedings* (D.L. Bourell, J.J. Beaman, H.L. Marcus, R.H. Crawford and J.W. Barlow, eds.), Proc. 2003 Solid Freeform Fabrication Symposium, Austin, August 2003 (this symposium).
4. Dobranich, D. and Dykhuizen, R. C., 1998a, "Scoping Thermal Calculation of the LENS™ Process," Sandia National Laboratories Internal Report, 1998.
5. Dobranich, D. and Dykhuizen, R. C., 1998b, "Analytical Thermal Models for the LENS™ Process," Sandia National Laboratories Internal Report.
6. Dykhuizen, R. C., and Dobranich, D. 1998, "Cooling Rates in the LENS™ Process," Sandia National Laboratories Internal Report.
7. Griffith, M.L., Keicher, D.M., Atwood, C.L., Romero, J.A., Smugeresky, J.E., Harwell, L.D. and Greene, D.L., 1996, "Freeform Fabrication of Metallic Components Using Laser Engineered Net Shaping (LENS)," *Solid Freeform Fabrication Proceedings* (D.L. Bourell, J.J. Beaman, H.L. Marcus, R.H. Crawford and J.W. Barlow, eds.), Proc. 1996 Solid Freeform Fabrication Symposium, Austin, August 1996, pp. 125-132.
8. Griffith, M. L., Schlienger, M. E., Harwell, L. D., Oliver, M. S., Baldwin, M. D., Ensz, M. T., Smugeresky, J. E., Essien, M., Brooks, J., Robino, C. V., Hofmeister, W. H., Wert, M. J. and Nelson, D. V., 1999, "Understanding Thermal Behavior in the LENS™ Process," *Journal of Materials Design,* Vol. 20, No. 2/3 pp. 107-114.
9. Hofmeister, W.H., Griffith, M.L., Ensz, M.T. and Smugeresky, J.E., 2001, "Solidification in Direct Metal Deposition by LENS Processing," *JOM*, Vol. 53, No. 9, 2001, pp. 30-34.
10. Peckner, D. and Bernstein, I. M.,1977, *Handbook of Stainless Steels,* McGraw-Hill, 1977.
11. Rangaswamy, P., Holden, T.M., Rogge, R.B. and Griffith, M.L., 2003, "Residual Stresses in Components Formed by the Laser-Engineered Net Shaping (LENS™) Process," submitted to *J. Strain Analysis.*
12. Rosenthal, D., 1946,"The Theory of Moving Sources of Heat and Its Application to Metal Treatments," *Transactions of ASME,* Vol. 68, 1946, pp. 849-866.
13. Vasinonta, A., Beuth, J. L. and Griffith, M. L., 1999, "Process Maps for Laser Deposition of Thin-Walled Structures," *Solid Freeform Fabrication Proceedings,* (D.L. Bourell, J.J. Beaman, R. H. Crawford, H. L. Marcus and J. W. Barlow, eds.), Proc. 1999 Solid Freeform Fabrication Symposium, Austin, August 1999, pp. 383-391.
14. Vasinonta, A., Beuth, J.L. and Griffith, M.L., 2000, "Process Maps for Controlling Residual Stress and Melt Pool Size in Laser-Based SFF Processes," *Solid Freeform Fabrication Proceedings* (D.L. Bourell, J.J. Beaman, R.H. Crawford, H.L. Marcus and J.W. Barlow, eds.), Proc. 2000 Solid Freeform Fabrication Symposium, Austin, August 2000, pp. 200-208.
15. Vasinonta, A., Beuth, J. L. and Griffith, M. L., 2001a, "A Process Map for Consistent Build Conditions in the Solid Freeform Fabrication of Thin-Walled Structures," *Journal of Manufacturing Science and Engineering.* Vol. 123, pp. 615-622.
16. Vasinonta, A., Beuth, J.L., and Ong, R., 2001b, "Melt Pool Size Control in Thin-Walled and Bulky Parts via Process Maps," *Solid Freeform Fabrication Proceedings* (D.L. Bourell, J.J. Beaman, R.H. Crawford, H.L. Marcus, K.L. Wood and J.W. Barlow, eds.), Proc. 2001 Solid Freeform Fabrication Symposium, Austin, August 2001, pp. 432-440.
17. Vasinonta, A., 2002, "Process Maps for Melt Pool Size and Residual Stress in Laser-Based Solid Freeform Fabrication," Ph.D. Thesis, Carnegie Mellon University, May 2002.

TWO-DIMENSIONAL MODELING OF SINTERING OF A TWO-COMPONENT METAL POWDER LAYER ON TOP Of MULTIPLE SINTERED LAYERS WITH A MOVING GAUSSIAN HEAT SOURCE

Tiebing Chen and Yuwen Zhang
Department of Mechanical Engineering
New Mexico State University
Las Cruces, NM 88003
Reviewed, accepted August 19, 2003

Abstract

Selective Laser Sintering (SLS) of metal powder is modeled as a two-dimensional melting and resolidification of a loose powder layer on top of the sintered metal layers with a moving heat source. The shrinkage induced by melting is accounted for and the problem is modeled using a temperature-transforming model. The results indicate that both the moving heat source intensity and scanning velocity have significant effects on the sintering process. Since the thermal conductivity of the sintered layer is relatively high compared with that of the loose powder, higher heat source intensity and lower scanning velocity are needed to achieve complete melting of the loose powder and bond the current layer to the existing sintered layers. A parametric study is performed and the best combinations of the processing parameters are recommended.

Introduction

Selective Laser Sintering (SLS) is a process that the three-dimensional part is fabricated layer-by-layer from a CAD design [1]. Fabrication of near full density parts from metal powder in the SLS is achieved by melting and resolidification induced by a moving laser beam. A liquid pool is formed when laser beam scans over the top surface of loose powder and then resolidified after the laser beam moves away. Multiple sintered layers, which are fabricated layer by layer due to the reciprocated movement of laser beam, are formed to fabricate three-dimensional part.

Melting and resolidification are the mechanisms to bond powder particles to form a layer of part and they are also the mechanisms to bond different layers together to form a functional part. Fundamentals of melting and solidification have been investigated extensively and detailed reviews are available in the literatures [2, 3]. It should be noted that melting in SLS of metal powder significantly differs from the normal melting process since the significant density change due to the shrinkage accompanies melting. For a single-component powder system, balling phenomenon, which is the formation of small spheres with the approximate diameter of laser beam, occurs since the molten metal is contained by fully loose powder rather than fully dense material. The tensile force on the surface of molten metal is not enough to keep it to a layer-wise geometry. The balling phenomenon can be avoided by using a two-component powder system that contains two types of metal powders possessing significantly different melting points [4, 5]. During the SLS process, only low melting point metal powder goes though melting and resolidification while the high melting point metal powder remains solid in the process. Since the high melting point metal powder alone cannot sustain the powder layer structure, the powder layer collapse upon melting of low melting point metal powder particles. Solidification of low melting point metal bonds the high melting point metal powder particles together to form fully

densified part. The liquid-solid phase change during melting of a two-component packed bed was investigated by Mughal and Plumb numerically [6] and a constant porosity model is developed. Zhang and Faghri [7] analytically solved a one-dimensional melting problem in a semi-infinite powder bed containing a two-component powder mixture subjected to a constant heat flux heating. Chen and Zhang [8] obtained an analytical solution of one-dimensional melting of the two-component metal powder layer with finite thickness.

Since the laser beam is moving over the powder layer and it has a very small diameter compared with the dimension of powder layer, SLS of metal powder is a three-dimensional transient melting and resolidification problem. It is economical to simulate melting and resolidification in a two-dimensional mixed metal powder layer before the real complex three-dimensional model of SLS is developed. A two-dimensional transient model of laser-melting problem with a moving laser beam, of which the interface energy balance was neglect, was developed by Chan et al. [9]. Basu and Srinivasan [10] solved a two-dimensional steady–state laser-melting problem using an alternative direction implicit scheme with a false transient formulation. Melting and resolidification of a subcooled semi-infinite two-component metal powder bed with a moving Gaussian heat source was simulated by Zhang and Faghri [11]. The two-dimensional melting and resolidification problem of a two-component metal powder layer with finite thickness was investigated numerically by Chen and Zhang [12], who demonstrated that the powder layer thickness, moving heat source intensity and scanning velocity have significant effects on the sintering depth. SLS is a process that functional part is fabricated by sintering of powder layer by layer. Except for the first layer, the consecutive layers are always fabricated by sintering of a loose powder layer on top of existing sintered layers. The present paper focuses on the effects of the combination of laser beam intensity and scanning velocity on the sintering process in the loose powder layer when the number of existing sintered layers increases. With prescribed numbers of existing sintered layers, the optimized moving laser beam intensity associated with specified scanning velocity was obtained. A through parametric study will be conducted and an empirical correlation will be proposed.

Physical model and problem statement

A loose powder layer containing two-component metal powders possessing significantly different melting point sits on the top of multiple sintered layers, as shown in Fig. 1. Each existing sintered layer is produced by sintering of two-component metal powder and is considered to be infinite horizontally but finite vertically. A moving Gaussian laser beam interacts with the top surface of the loose powder and then melting is induced. It should be noted that only the low-melting-point-temperature powder melts during the laser sintering process. It is assumed that the sintered layer is fully densified so that the thickness of each sintered layer can be determined by using the thickness and porosity of the loose powder layer. It is very important to identify the best combination of processing parameters that allow complete sintering of the loose powder and secure bonding of the newly sintered layer to existing sintered layer. During the simulation, the sintering depth is permitted to slightly exceed the interface of the loose powder layer and the next existing sintered layer so that each layer can be bonded together tightly.

The following assumptions are made for the physical model:

(1) Melting and resolidification in SLS is a conduction controlled phase-change problem.

(2) The thermal properties of the low melting point powder are the same for both liquid and solid phases.

(3) Two kinds of metal powders are fully mixed and the initial porosity is uniform. The porosity of the sintered layer is zero, which means all of the gas is driven out by shrinkage after the loose powder layer is sintered.

(4) The bottom of the computational domain is adiabatic.

(5) The horizontal dimension of the powder layer is sufficiently large compared with the size of the heat source so that the problem is quasi-steady-state.

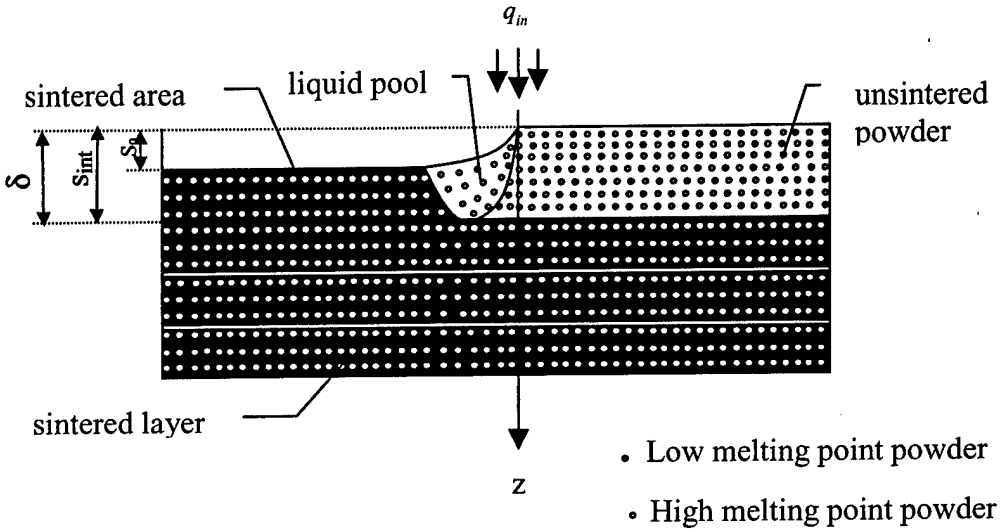

Fig. 1 Physical model

The physical model is formulated using a temperature transforming model, which converts the enthalpy-based energy equation into a nonlinear equation with a single dependent variable - temperature. In this methodology, the solid-liquid phase change is assumed to occur in a very small range of phase-change temperatures from $(T_m^0 - \delta T^0)$ to $(T_m^0 + \delta T^0)$ [13]. The beauty of temperature transforming model is that the converged solution can always be obtained without the limitation on grid size and time step when it deals with the conduction-controlled phase-change problem. It can also successfully model convection controlled solid-liquid phase change problem. A moving coordinate system, of which the origin is fixed at the center of the heat source and moved together with it at the speed, u, is employed. If one observes from the origin, the powder layers travel at a velocity, $-u$, in the opposite moving direction of the laser beam. Therefore, a nonlinear convection term is introduced into the governing equation. Since the horizontal dimension of powder layer is much larger than the size of the heat source, the physical model is a steady-sate melting and resolidification problem in a moving coordinate system. The dimensionless governing equation in the moving coordinate system is

$$-U\frac{\partial(CT)}{\partial X}+W\frac{\partial(CT)}{\partial Z}=\frac{\partial}{\partial X}(K\frac{\partial T}{\partial X})+\frac{\partial}{\partial Z}(K\frac{\partial T}{\partial Z})-(-U\frac{\partial S}{\partial X}+W\frac{\partial S}{\partial Z}) \quad (1)$$

where the dimensionless variables are defined in the nomenclature. The dimensionless shrinkage velocity, W, heat capacity, C, source term, S, and thermal conductivity, K, in eq. (1) in the

loose powder layer are different from those in existing sintered layers below, which have been fully densitified. In the loose powder layer,

$$W=\begin{cases}-\varepsilon_s U\dfrac{\partial \eta_{st}}{\partial X} & Z\le\eta_{st}\le\Delta\\ 0 & Z>\eta_{st}\le\Delta\end{cases} \tag{2}$$

$$C=\begin{cases}(1-\varepsilon)(\phi C_L+1-\phi) & T<-\Delta T\\ (1-\varepsilon)(\phi C_L+1-\phi)+(1-\varepsilon)\phi\dfrac{C_L}{2Sc\Delta T} & -\Delta T<T<\Delta T\\ (1-\varepsilon)(\phi C_L+1-\phi) & T>\Delta T\end{cases} \tag{3}$$

$$S=\begin{cases}0 & T<-\Delta T\\ \dfrac{(1-\varepsilon)\phi C_L}{2Sc} & -\Delta T<T<\Delta T\\ \dfrac{(1-\varepsilon)\phi C_L}{Sc} & T>\Delta T\end{cases} \tag{4}$$

$$K=\begin{cases}K_{eff} & T<-\Delta T\\ K_{eff}+\dfrac{K_p-K_{eff}}{2\Delta T}(T+\Delta T) & -\Delta T<T<\Delta T\\ K_p & T>\Delta T\end{cases} \tag{5}$$

In the resolidified region at the left side of liquid pool and below the loose powder layer,

$$W=0 \tag{6}$$

$$C=(1-\varepsilon)(\phi C_L+1-\phi) \tag{7}$$

$$S=\frac{(1-\varepsilon)\phi C_L}{Sc} \tag{8}$$

$$K=K_p \tag{9}$$

where K_{eff} is the dimensionless effective thermal conductivity of the loose powder region and K_p is dimensionless thermal conductivity in the sintered region. The mathematical descriptions of K_{eff} and K_p are given in Zhang and Faghri [11]. The corresponding boundary conditions of eq. (1) are as following

$$-K\frac{\partial T}{\partial Z}=N_i\exp(-X^2)-N_R[(T+N_t)^4-(T_\infty+N_t)^4]-Bi(T-T_\infty)\quad Z=\eta_0(X) \tag{10}$$

$$\frac{\partial T}{\partial Z}=0,\quad Z=\Delta_s+N\Delta_p,-\infty\le X\le\infty,\quad \tau>0 \tag{11}$$

$$T=-1,\qquad |X|\to\infty,\qquad 0\le Z\le\Delta,\qquad \tau>0 \tag{12}$$

The location of liquid surface is related to the sintered depth with the assumption that the sintered layers are fully densitified, i.e.,

$$\eta_0(X)=\varepsilon_s\eta_{st}(X) \tag{13}$$

Numerical Solution

A false transient method is employed to solve eq. (1) numerically since a steady-state problem is difficult to deal with. In this methodology, a false transient term, $\frac{\partial(CT)}{\partial\tau}$, is included in eq. (1) and then the converged steady-state solution is obtained when the temperature distribution and sintering depth do not vary with the false time. Equation (1) with false transient term can be discretisied by the finite volume method [14]. A block-off technique recommended by Patankar [14] is employed to deal with the irregular geometry of liquid pool caused by the downward movement of top liquid surface due to shrinkage. Therefore, the computational domain is the regular rectangle and the density and thermal conductivity in the empty space created by the shrinkage are set to zero. The power-law scheme [14] is employed to discretize the convection-diffusion terms. The iteration and underrelaxation are needed in order to obtain the converged solution. A very small dimensionless phase-change temperature range, $\Delta T = 0.001$, is used in the numerical computation.

The dimensionless horizontal length of computational domain is much greater than the magnitude of moving heat source in order to obtain the quasi-steady-state solution. The dimensionless thickness of each existing sintered layer can be determined using the porosity and thickness of loose powder layer as indicated in previous section. The total dimensionless thickness of the whole computational domain in Z direction increases with added numbers of sintered layers. The origin of coordinate system ($X=0$, $Z=0$) is located at the center of top surface of computational domain in X direction. The non-uniform grids are employed in both of X and Z directions. The numerical solution is carried out for non-uniform grids in X direction of which the fine grids are distributed around the origin symmetrically. The fine grids zone is greater than the width of moving heat source. For the non-uniform grids in Z direction, the fine grids are distributed uniformly in the loose powder layer and the consecutive coarse grids in multiple sintered layers are set up in arithmetic progression with variable grid size according to different numbers of sintered layers. The gird number used in the present paper is 122×32 to 122×47 depending on the number of existing sintered layers. Finer grid sizes were also used but their results did not provide a noticeable difference with the present grid size. It should be noted that finer grids in existing sintered layers is needed in order to obtain the converged solution when too large numbers of sintered layers are concerned, for example, 50 in the present paper.

The optimized combination of heat source intensity and scanning velocity is obtained when the sintering depth penetrates the bottom surface of loose powder layer. In order to trace the sintering depth, a small value of heat source intensity associated with a specific scanning velocity is assigned at first. The dimensionless false time step is assumed to be a value that can not be too large since the convection term is appeared in the governing equation because of the introduced moving coordinate system. The false time step used in the present paper is $\Delta\tau = 0.01$ for $N \leq 10$ and $\Delta\tau = 0.001$ for $N = 50$. The value of heat source intensity is grown with a small increment if the sintering depth is determined not to move further at the previous value of heat source intensity. When the sintering depth approaches the bottom surface of the loose powder layer very closely, the dimensionless false time step and increment of heat source intensity is shifted to a smaller value in order to obtain more accurate solution. The computing procedure is finished when the sintering depth penetrates the bottom surface of loose powder layer.

Results and discussion

The sintering process in a loose powder layer was simulated when the numbers of sintered layers below are 1, 2, 3, 5, 10 and 50 respectively. The effects of dimensionless moving heat source intensity, dimensionless scanning velocity and numbers of sintered layers, which are dominant parameters for a two-dimensional sintering process, were investigated numerically. The effect of subcooling parameter on the sintering process is also investigated.

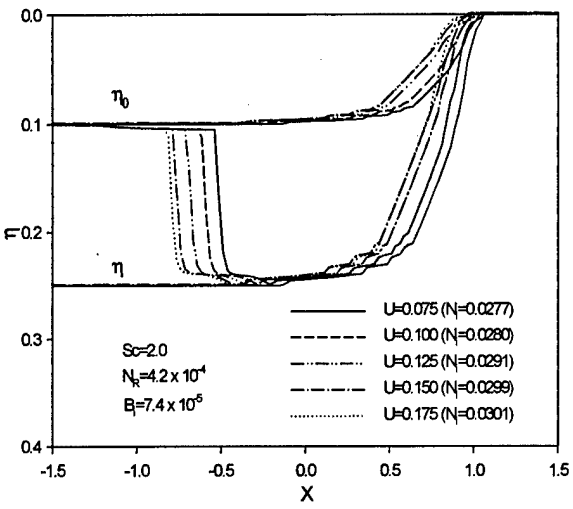

Fig. 2 Combined effects of dimensionless moving heat source intensity and scanning velocity on the sintering process ($N = 1$)

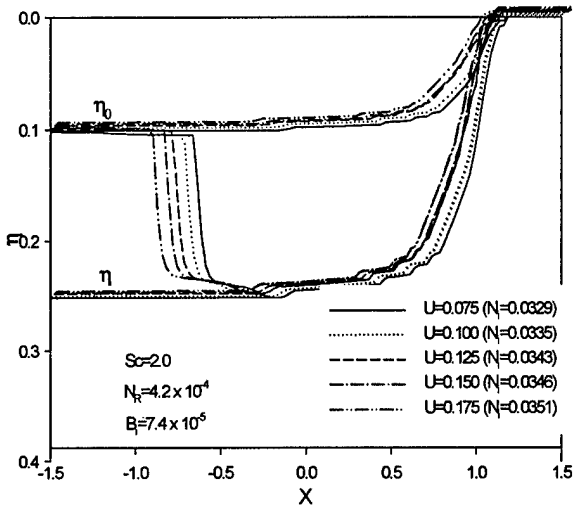

Fig. 3 Combined effects of dimensionless moving heat source intensity and scanning velocity on the sintering process ($N = 2$)

Figure 2 shows the combined effects of dimensionless moving heat source intensity and scanning velocity on the sintering process when there is one sintered layer below. The optimized laser beam intensities is shown in parentheses. The sintering depth penetrates the loose powder layer slightly in order to bond the newly sintered layer to the existing sintered layer. It can be seen that the shape of liquid pools is similar when the scanning velocity increases. The upper part of the liquid pool stretches in the opposite direction of the moving heat source like a tail. The entire liquid pool shifts slightly toward the negative X direction when the scanning velocity increases. The increment of optimized dimensionless heat source intensity is small compared with the increase of scanning velocity from 0.075 to 0.175. It is necessary to let the sintering depth overpass the bottom surface of loose powder layer slightly in order to bond layers together.

The combined effects of dimensionless moving heat source intensity and scanning velocity on the sintering process when there are two sintered layers below are shown in Fig. 3. The shape of the liquid pool at each scanning velocity is similar to those in Fig. 2 When one more sintered layer is added, the heat source intensity at each scanning velocity increases significantly in order to obtain the same sintering depth in the loose powder layer. More heat is conducted away from the loose powder layer since the dimensionless thermal conductivity of sintered part is larger than that of loose powder layer. The numerical simulations are then performed for more sintered layers below and the results are shown in Fig. 4-7. The similar trend of moving heat source intensity at different scanning velocities compared with the corresponding case in Fig. 2 and Fig. 3 can be found. With increasing numbers of sintered layers, the moving heat source intensity at

each scanning velocity is significantly increased. The increment of heat source intensity is similar when the added sintered layer has the same thickness. The liquid pool in the sintering process still keeps the similar shape but its volume is growing because of greater heat source intensity needed. The fluctuation in the front part of liquid pool is growing apparently with increasing numbers of sintered layers below.

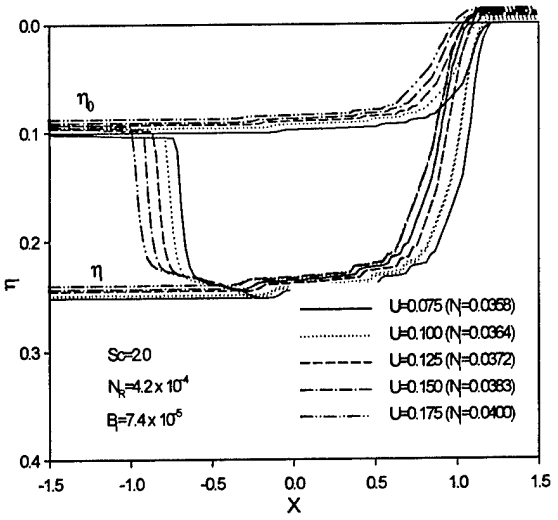

Fig. 4 Combined effects of dimensionless moving heat source intensity and scanning velocity on the sintering process ($N = 3$)

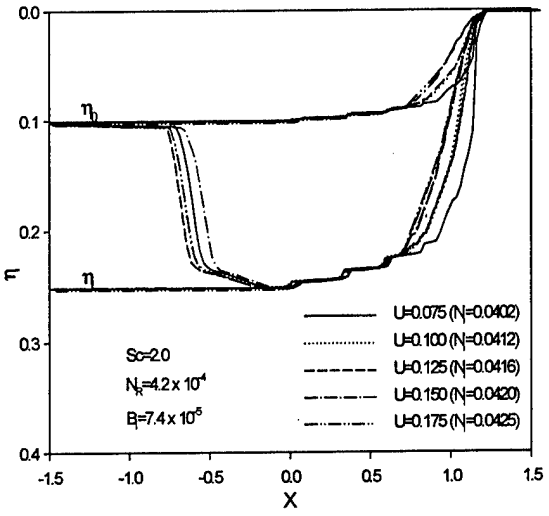

Fig.5 Combined effects of dimensionless moving heat source intensity and scanning velocity on the sintering process ($N = 5$)

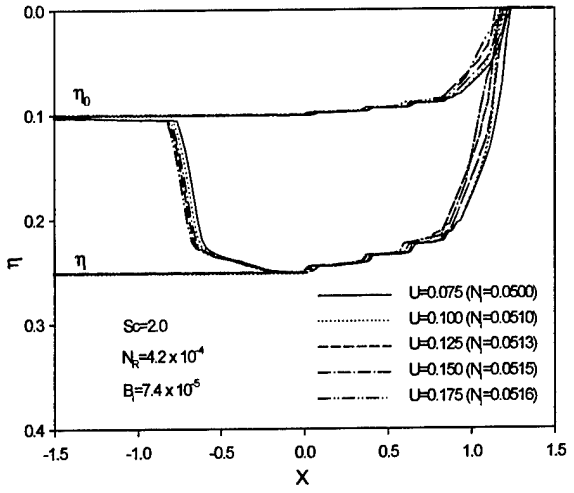

Fig. 6 Combined effects of dimensionless moving heat source intensity and scanning velocity on the sintering process ($N = 10$)

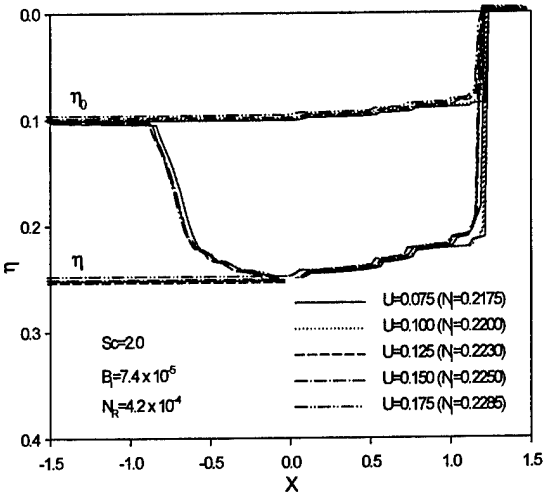

Fig. 7 Combined effects of dimensionless moving heat source intensity and scanning velocity on the sintering process ($N=50$)

In order to obtain the empirical correlation for the optimized dimensionless moving heat source intensity, a parametric study is performed and the results are shown in Fig. 8. The parameters used to in the simulation are shown in Table 1. The optimized dimensionless moving

heat source intensity is plotted as a function of scanning velocity, U, according to different numbers of sintered layers of which each layer has the same thickness. It can be seen that the optimized dimensionless moving heat source intensity increases with increasing scanning velocity at prescribed numbers of sintered layers and increases significantly when the numbers of sintered layers are added. The optimized dimensionless moving heat source intensity shown in Fig. 8 can be correlated into the following expression,

$$N_i = AU^{-0.0045} + N^{-0.0072} \tag{14}$$

where $A = -0.9627 + 4.3930\times10^{-3} N$ and $U > 0$. The error of eq. (14) is within 9.9%.

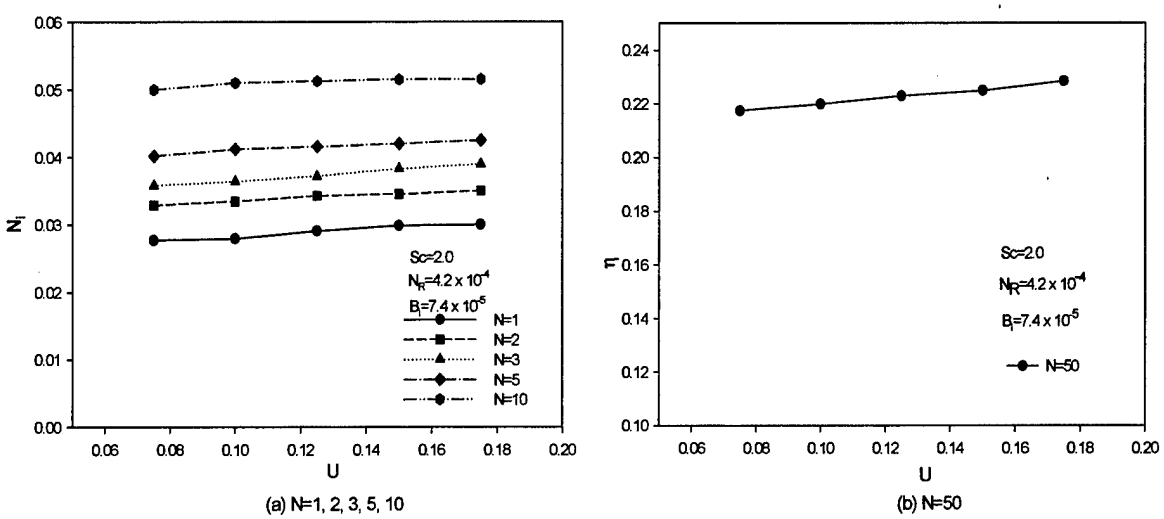

Fig. 8 Optimized dimensionless moving heat source intensity vs. scanning velocity

Table 1 Parameters used in parametric study

ε_s	0.4	N_t	1.5	Sc	2.0	N_i	$0.2 \sim 0.4$
N_R	4.2×10^{-4}	T_∞	1.0	B_i	7.4×10^{-5}	U	$0.075 \sim 0.175$
Δ_s	0.25	ϕ	0.4	K_{LH}	2.9	C_{LH}	0.7
N	1,2,3,5,10,50						

In order to investigate the effect of preheating on the sintering process, effect of subcooling parameter on the sintering process is studied and the results are shown in Fig 9, in which the number of existing sintered layers below is fixed at one. The optimized dimensionless moving heat source intensity to achieve the same sintering depth decreases when the lower subcooling parameter is employed. The shape of liquid pool keeps similar when the lower subcooling parameter is used. At lower subcooling parameter, the initial temperature is closing to the melting point of the low-melting-point metal powder. The lower subcooling parameter is

beneficent to the sintering process since not only the moving heat source intensity needed is reduced but also the pre-heating time is shortened.

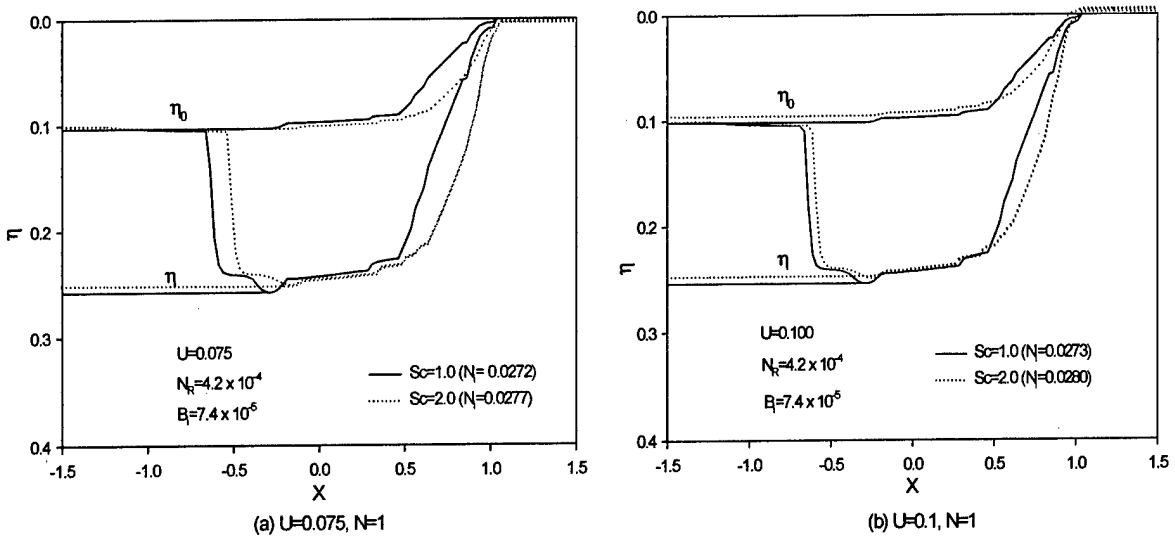

Fig. 9 Effect of subcooling number on the sintering process

Conclusions

A parametric study of a two-dimensional SLS process in a loose powder layer on top of multiple sintered metal powder layers is presented. The results showed that the optimized dimensionless moving heat source intensity increases with increasing scanning velocity in order to achieve the desired sintering depth to bond the newly sintered layer to the existing sintered layer. With increasing numbers of existing sintered layers below, the optimized dimensionless moving heat source intensity at a specific scanning velocity increases significantly. An empirical correlation on the dimensionless moving heat source intensity is obtained. The optimized dimensionless moving heat source intensity decreases when the lower subcooling parameter is used.

Acknowledgement

Support for this work by the Office of Naval Research under grant number N00014-02-1-0356 is greatly acknowledged.

Nomenclature

b moving heat source half width (m)

Bi Biot number, hb/k_H

C dimensionless heat capacity, C^0/C_H^0

C^0 heat capacity, ρc_p

c_p specific heat, ($W/kg\,K$)

h convective heat transfer coefficient, ($W/m^2\,K$)

h_m latent heat of melting or solidification, J/kg

I_0 heat source intensity at the center of the heat source, (W/m^2)

k thermal conductivity, (W/mK)

K dimensionless thermal conductivity, k/k_H

N numbers of sintered layers under the loose powder layer

N_i dimensionless moving heat source intensity, $\alpha_a I_0 b/[k_H(T_m^0 - T_i^0)]$

N_R Radiation number, $\varepsilon\sigma(T_m^0 - T_i^0)^3 b/k_H$

N_t temperature ratio for radiation, $T_m^0/(T_m^0 - T_i^0)$

s solid-liquid interface location (m)

s_0 location of surface (m)

s_{st} sintered depth (m)

Sc subcooling parameter, $C_H^0(T_m^0 - T_i^0)/(\rho_L h_{sl})$

T dimensionless temperature, $(T^0 - T_m^0)/(T_m^0 - T_i^0)$

t false time (s)

T^0 temperature (K)

u heat source moving velocity (m/s)

U dimensionless heat source moving velocity, ub/α_H

V volume (m^3)

w velocity of liquid phase (m/s)

W dimensionless velocity of the liquid phase, wb/α_H

x moving horizontal coordinate

X dimensionless moving horizontal coordinate, x/b

z vertical coordinate (m)

Z dimensionless vertical coordinate, z/b

Greek symbol

α thermal diffusivity $(m^2 s^{-1})$

δ powder layer thickness, m

Δ dimensionless powder layer thickness, δ/b

ΔT^0 one-half of phase-change temperature range (K)

ΔT one-half of dimensionless phase change temperature range

ε volume fraction of gas (porosity for unsintered powder), $V_g/(V_g + V_L + V_H)$

ε_e emissivity of surface

η dimensionless solid-liquid interface location, s/b

η_0 dimensionless location of the surface, s_0/b

η_{st} dimensionless sintered depth, s_{st}/b

ρ density (kg/m^3)

σ Stefan-Boltzman constant, $5.67\times10^{-8} W/(m^2 K^4)$

τ false dimensionless time, $\alpha_H t/b^2$

ϕ volume percentage of low melting point powder, $V_L/(V_L + V_H)$

Subscripts

eff	effective
H	high melting point powder
L	low melting point powder
m	melting point
p	sintered parts
s	solid

References

[1] Conley, J., and Marcus, H., 1997, "Rapid Prototyping and Solid Freeform Fabrication," *Journal of Manufacturing Science and Engineering*, Vol. 119, pp. 811-816.

[2] Viskanta, R., 1983, Phase Change Heat Transfer, in: G.A. Lane (Ed.), *Solar Heat Storage: Latent Heat Materials*, CRC Press, Boca Raton, FL.

[3] Yao, L., and Prusa, J., 1989 "Melting and freezing," *Advances in Heat Transfer,* Vol. 25, pp. 1-96.

[4] Manzur, T., DeMaria, T., Chen, W., and Roychoudhuri, C., 1996, "Potential Role of High Powder Laser Diode in Manufacturing," presented at SPIE Photonics West Conference, San Jose, CA

[5] Bunnell, D., 1995, *Fundamentals of Selective Laser Sintering of Metals*, Ph.D. Thesis, University of Texas at Austin.

[6] Mughal, M., and Plumb, O. A., 1993, "Thermal Densification of Metal-Ceramic Composites," *Scripta Metallurgica et Materialia,* Vol. 29, pp. 383-388.

[7] Zhang, Y., and Faghri, A., 1999, "Melting of a Subcooled Mixed powder Bed with Constant Heat Flux Heating," *International Journal of Heat and Mass Transfer,* Vol. 42, pp. 775-788.

[8] Chen, T., and Zhang, Y., 2003, "Analysis of Melting in a Mixed Powder Bed with Finite Thickness Subjected to Constant Heat Flux Heating," *Proceeding of ASME Summer Heat Transfer Conference*, Las Vegas, NV.

[9] Chan, C., Mazumder, J., and Chen, M., 1984, "A Two Dimensional Transient Model for Convection in Laser Melted Pool," *Metall. Trans.,* Vol. 15A, pp. 2175-2184.

[10]Basu, B., and Srinivasan, J., 1988, "Numerical Study of Steady-State Laser Melting Problem," *Int. J Heat Mass Transfer*, Vol. 31, No.11, pp. 2331-2338.

[11]Zhang, Y., and Faghri, A., 1998, "Melting and Resolidification of a Subcooled Mixed Powder Bed with Moving Gaussian Heat Source," ASME *Journal of Heat Transfer* Vol. 120, pp. 883-891.

[12]Chen, T. and Zhang, Y., 2003,"Melting and Resolidification of a Two-Component Metal powder Layer Heated by a Moving Gaussian Heat Source," IMECE2003, Washington, DC.

[13]Cao, Y. and Faghri, A., 1990, "A Numerical Analysis of Phase Change Problems Including Natural Convection," *Journal of Heat Transfer,* Vol. 112, pp. 812-816.

[14] Patankar, S. V., 1980, *Numerical Heat Transfer and Fluid Flow*, McGraw-Hill, New York.

Thermal Process Maps for Controlling Microstructure in Laser-Based Solid Freeform Fabrication

S. Bontha and N.W. Klingbeil
Department of Mechanical and Materials Engineering
Wright State University
Dayton, OH, 45435

Abstract

The ability to predict and control microstructure in laser deposited materials requires an understanding of the thermal conditions at the onset of solidification. The focus of this work is the development of thermal process maps relating solidification cooling rate and thermal gradient (the key parameters controlling microstructure) to laser deposition process variables (laser power and velocity). The approach employs the well-known Rosenthal solution for a moving point heat source traversing an infinite substrate. Cooling rates and thermal gradients at the onset of solidification are numerically extracted from the Rosenthal solution throughout the depth of the melt pool, and dimensionless process maps are presented for both thin-wall (2-D) and bulky (3-D) geometries. In addition, results for both small-scale (LENS™) and large-scale (higher power) processes are plotted on solidification maps for predicting grain morphology in Ti-6Al-4V. Although the Rosenthal results neglect temperature-dependent properties and latent heat effects, a comparison with 2-D FEM results over a range of LENS™ process variables suggests that they can provide reasonable estimates of trends in solidification microstructure. The results of this work suggest that changes in process variables could potentially result in a grading of the microstructure (both grain size and morphology) throughout the depth of the deposit, and that the size-scale of the laser deposition process is important.

Introduction

Laser deposition of titanium alloys and other metallic materials is currently under consideration for application to aerospace components, and offers significant increases in efficiency and flexibility compared to conventional manufacturing methods [1]. However, the widespread use of this promising technology will ultimately depend on the ability to predict and control the microstructure and resulting mechanical properties of the deposit [2]. To date, only limited experimental data exists to link deposition process variables (e.g., laser power and velocity) to resulting microstructure (e.g., grain size and morphology) in laser deposited titanium alloys [3-5], and suitable microstructures have typically been obtained only by trial and error. The ability to predict and control microstructure in laser deposition processes requires an understanding of the thermal conditions at the onset of solidification, which is the focus of this work.

Recent studies in the literature [6-10] have employed the Rosenthal solution [11] for a moving point heat source on an infinite substrate to identify the dimensionless process variables governing thermal conditions in laser deposition processes. In conjunction with thermal finite element modeling, this has enabled the development of "process maps" relating deposition process variables to melt pool size and residual stress in both thin-wall (2-D) and bulky (3-D) geometries. In the current study, a similar approach is used to investigate solidification cooling rates and thermal gradients (the key parameters controlling microstructure) in laser deposition processes. Cooling rates and thermal gradients at the onset of solidification are numerically

extracted from the Rosenthal solution throughout the depth of the melt pool, and dimensionless process maps are developed for both thin-wall and bulky deposits. The results are plotted on solidification maps for Ti-6Al-4V, which provide insight into the effects of process variables on grain morphology. Finally, a comparison is made between small-scale processes (e.g., LENS™) and large-scale (higher power) processes, several of which are under development for laser additive manufacturing applications. This comparison is particularly relevant in light of other recent investigations into the effects of size-scale on melt pool size and residual stress [12].

Geometries Considered

This study considers both the thin-wall (2-D) and bulky (3-D) geometries of Fig. 1, in which the process variables of interest are the absorbed laser power αQ and velocity V. In each case, it is assumed that the height h and length L are sufficiently large such that the steady-state Rosenthal solution for a point heat source traversing an infinite half-space applies [11].

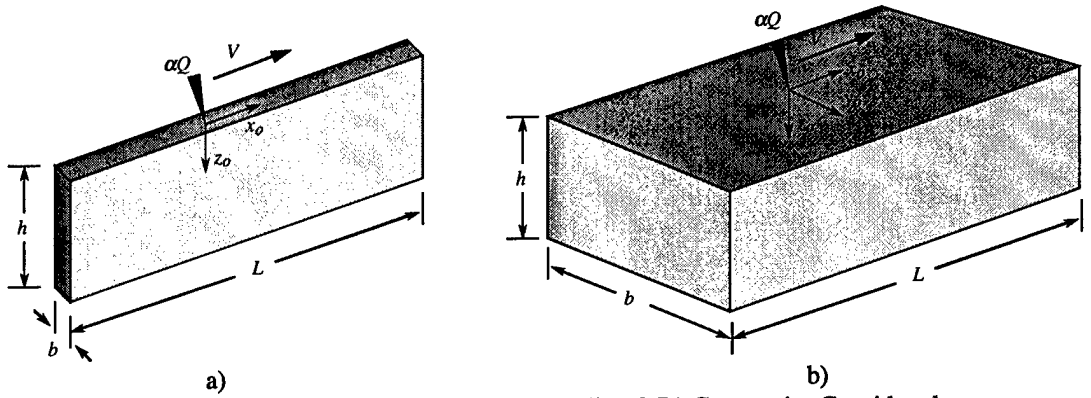

Figure 1. a) Thin-Wall (2-D) and b) Bulky (3-D) Geometries Considered

Thermal Process Maps for Thin-Wall Geometries

The results of this section are limited to the thin-wall geometry of Fig. 1a. Such structures are commonly manufactured using LENS™ and other small-scale metal deposition processes. As discussed by Vasinonta *et al.* [8], the 2-D Rosenthal point source solution for the geometry of Fig. 1a can be expressed in dimensionless form as

$$\bar{T} = e^{-\bar{x}_o} K_o\left(\sqrt{\bar{x}_o^2 + \bar{z}_o^2}\right), \tag{1}$$

where K_o is the modified Bessel function of the second kind, order zero. The dimensionless variables in eq. (1) are defined in terms of the absorbed laser power αQ and velocity V as

$$\bar{T} = \frac{T - T_o}{\alpha Q / \pi k b}, \quad \bar{x}_o = \frac{x_o}{2k / \rho c V} \quad \text{and} \quad \bar{z}_o = \frac{z_o}{2k / \rho c V}, \tag{2}$$

where T is the temperature at a location (x_o,z_o) relative to the moving point source (see Fig. 1a), T_o is the initial temperature of the wall, b is the wall thickness, and ρ, c and k are the density, specific heat and thermal conductivity of the material, respectively.

As previously discussed, the parameters of interest in controlling microstructure are the solidification cooling rate and thermal gradient. Noting that the relative coordinates (x_o,z_o) at any time t are related to any fixed spatial coordinates (x,z) as $(x_o,z_o) = (x\text{-}Vt,z)$, expressions for the

dimensionless cooling rate and thermal gradient can be obtained through differentiation of eq. (1). In so doing, the dimensionless cooling rate and thermal gradient are defined as

$$\frac{\partial \bar{T}}{\partial \bar{t}} = \left(\frac{2\pi k^2 b}{\alpha Q \rho c V^2}\right)\frac{\partial T}{\partial t}, \quad \left|\overline{\nabla T}\right| = \left(\frac{2\pi k^2 b}{\alpha Q \rho c V}\right)|\nabla T|. \tag{3}$$

Values of the dimensionless cooling rate and thermal gradient at the onset of solidification are obtained by evaluating the corresponding derivatives of eq. (1) along the boundary of the melt pool. The coordinates (x_o, z_o) which lie on the boundary of the melt pool are obtained by replacing T with the melting point T_m and finding the roots of eq. (1) numerically. The numerical root finding was conducted using the software package MATLAB, and results for melt pool length were verified against those previously published in the literature [6-10].

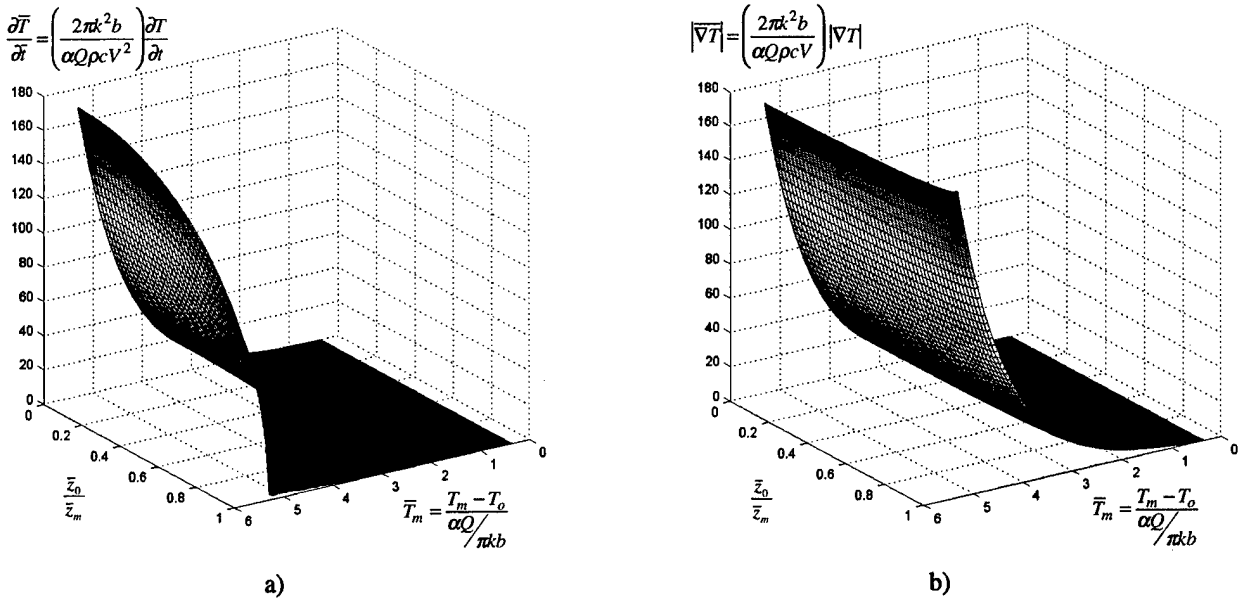

Figure 2. Process Maps for Solidification a) Cooling Rate and b) Thermal Gradient for Thin-Wall Geometries

In conjunction with the dimensionless variables defined in eqs. (2) and (3), the Rosenthal solution enables the development of process maps for solidification cooling rate and thermal gradient throughout the depth of the melt pool. Such results are shown in Fig. 2, where the dimensionless cooling rate and thermal gradient are plotted as a function of normalized melting temperature $\bar{T}_m$ and relative depth within the melt pool $\bar{z}_o / \bar{z}_m$. The normalized melting temperature varies with laser power, and is defined in terms of the melting temperature T_m as

$$\bar{T}_m = \frac{T_m - T_o}{\alpha Q / \pi k b}. \tag{4}$$

The normalized depth varies in the range $0 \le \bar{z}_o / \bar{z}_m \le 1$, where $\bar{z}_m$ signifies the deepest extent of the melt pool for a given value of $\bar{T}_m$.

The results of Fig. 2 indicate that for fixed material properties, changes in laser power (or changes in $\bar{T}_m$) can have a significant effect on the solidification cooling rate and thermal

gradient. When plotted on a log scale (not shown here), the results indicate that changes in laser power can change both the dimensionless cooling rate and thermal gradient by several orders of magnitude. Furthermore, for fixed values of $\overline{T}_m$ (or fixed laser power), the normalizations of eq. (3) indicate that the actual thermal gradient scales linearly with the laser velocity, while the actual cooling rate scales with the square of the velocity. Hence, changes in laser velocity can also have a significant effect on solidification cooling rate and thermal gradient. Finally, the results of Fig. 2 suggest that for fixed laser power and velocity, the cooling rate can vary significantly throughout the depth of the melt pool, particularly for high values of $\overline{T}_m$. On the other hand, the thermal gradient is more sensitive to depth within the melt pool for low values of $\overline{T}_m$. These results suggest that depending on the material system considered, changes in laser power might allow grading of the microstructure as a function of depth within the deposit.

Thermal Process Maps for Bulky 3-D Geometries

As discussed by Vasinonta *et al.* [9], the Rosenthal solution for a point heat source traversing the top of a bulky 3-D geometry (Fig. 1b) can be expressed in dimensionless form as

$$\overline{T} = \frac{e^{-\left(\bar{x}_0+\sqrt{\bar{x}_0^2+\bar{y}_0^2+\bar{z}_0^2}\right)}}{2\sqrt{\bar{x}_0^2+\bar{y}_0^2+\bar{z}_0^2}}, \tag{5}$$

where

$$\overline{T} = \frac{T-T_0}{\left(\alpha Q/\pi k\right)\left(\rho cV/2k\right)}, \quad \bar{x}_o = \frac{x_o}{2k/\rho cV}, \quad \bar{y}_o = \frac{y_o}{2k/\rho cV} \text{ and } \bar{z}_o = \frac{z_o}{2k/\rho cV}. \tag{6}$$

Comparison of eqs. (6) and (2) reveals that in terms of laser deposition process variables, the temperature normalization for bulky 3-D geometries is different from that for thin-wall geometries. The 2-D normalization is a function only of laser power, while the 3-D normalization depends on both laser power and velocity. The dimensionless cooling rate and thermal gradient for bulky 3-D geometries are defined as

$$\frac{\partial \overline{T}}{\partial \bar{t}} = \left(\frac{2k}{\rho cV}\right)^2\left(\frac{\pi k}{\alpha QV}\right)\frac{\partial T}{\partial t}, \quad \left|\overline{\nabla T}\right| = \left(\frac{2k}{\rho cV}\right)^2\left(\frac{\pi k}{\alpha Q}\right)|\nabla T|. \tag{7}$$

The above definitions have a higher order velocity dependence compared to the 2-D normalizations of eq. (3), which is a direct result of the temperature normalization of eq. (6).

For bulky 3-D geometries, values of the dimensionless cooling rate and thermal gradient at the onset of solidification are obtained by evaluating the corresponding derivates of eq. (5) along the boundary of the melt pool cross section in the (x,z) plane (i.e., along $y_o = 0$). The resulting process maps for solidification cooling rate and thermal gradient are plotted in Fig. 3 as a function of normalized melting temperature $\overline{T}_m$ and relative depth within the melt pool $\bar{z}_o/\bar{z}_m$. Note that according to eq. (6), the dimensionless melting temperature for bulky 3-D geometries is defined in terms of both laser power and velocity as

$$\overline{T}_m = \frac{T_m - T_o}{\left(\alpha Q/\pi k\right)\left(\rho c V/2k\right)}. \tag{8}$$

The results of Fig. 3 indicate that for fixed material properties, changes in laser power or velocity (or changes in $\overline{T}_m$) can have a significant effect on cooling rate and thermal gradient, and hence the resulting microstructure. In general, the trends are similar to those for thin-wall geometries (Fig. 2). However, owing to the different temperature normalizations in 2-D and 3-D, comparing the magnitudes of the dimensionless results in Figs. 2 and 3 can be misleading. For example, although the magnitudes of the *dimensionless* cooling rates are larger in Fig. 2a than in Fig. 3a, the *actual* cooling rate for a given laser power and velocity is greater in 3-D than in 2-D.

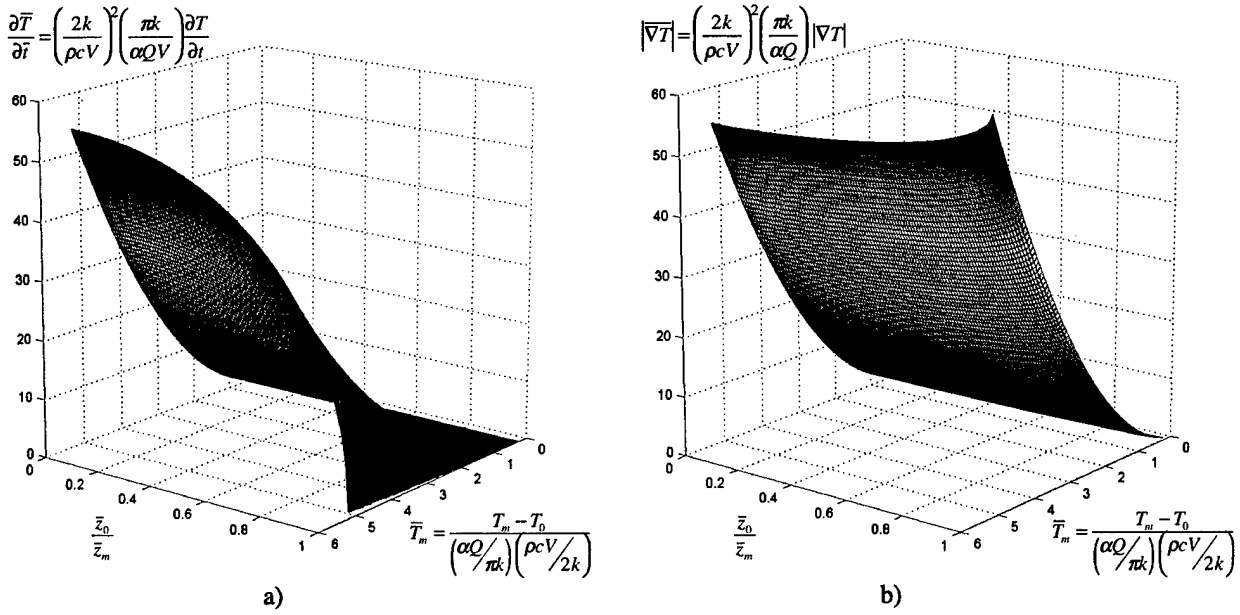

Figure 3. Process Maps for Solidification a) Cooling Rate and b) Thermal Gradient for Bulky (3-D) Geometries

Solidification Maps for Ti-6Al-4V

As discussed in [2,3], results for solidification thermal gradient and cooling rate can be interpreted in the context of a solidification map to provide predictions of grain morphology in laser-deposited Ti-6Al-4V. Given the solidification cooling rate $\partial T/\partial t$ and thermal gradient $G = |\nabla T|$, the solidification velocity R is determined as

$$R = \frac{1}{G}\frac{\partial T}{\partial t}. \tag{9}$$

The expected grain morphology can be predicted as either equiaxed, columnar or mixed by plotting points in G vs. R space (i.e., on the "solidification map"), which has been previously calibrated for Ti-6Al-4V [3].

Solidification maps showing the effects of laser power and velocity over a range of typical LENS™ process variables for thin-wall Ti-6Al-4V deposits are shown in Figures 4 and 5. The results of Figs. 4a and 5a have been extracted from 2-D thermal FEM analyses of a

particular thin-wall geometry (b=2.26 *mm*, h=8.69 *mm*, L=50.4 *mm*), as described by Klingbeil *et al.* [2]. The FEM results include temperature-dependent properties and latent heat effects for Ti-6Al-4V. The results of Figs. 4b and 5b are extracted directly from the Rosenthal results of Fig. 2, with thermophysical properties for Ti-6Al-4V assumed constant at the melting temperature T_m=1654°C. Both the FEM and Rosenthal results assume the fraction of absorbed laser power to be α=0.35.

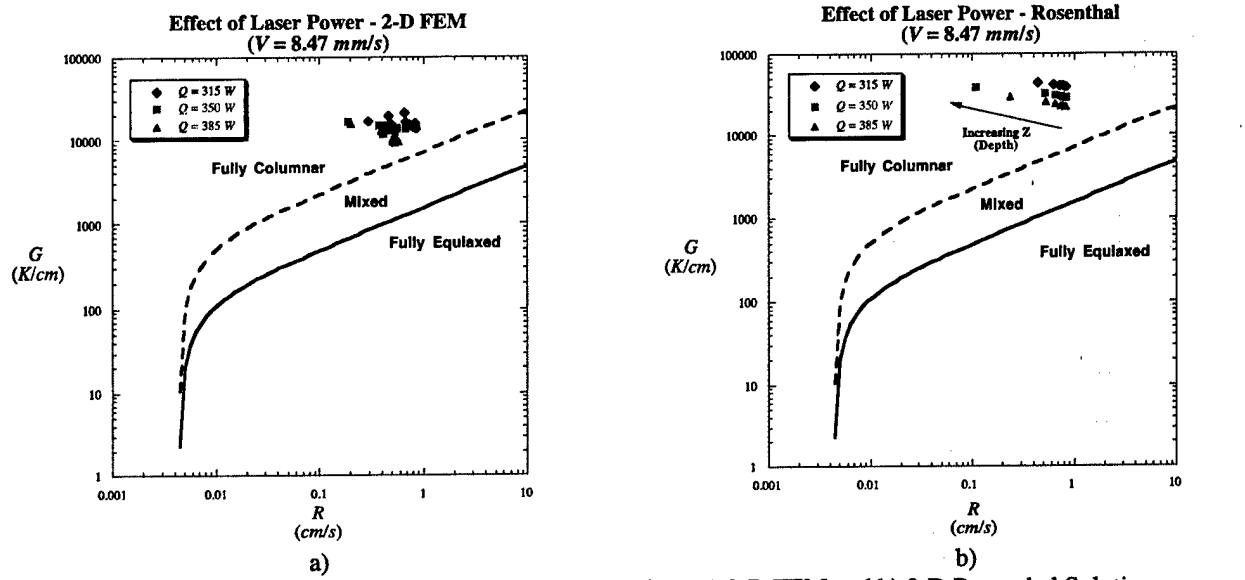

Figure 4. Effect of Laser Power on Grain Morphology from a) 2-D FEM and b) 2-D Rosenthal Solution

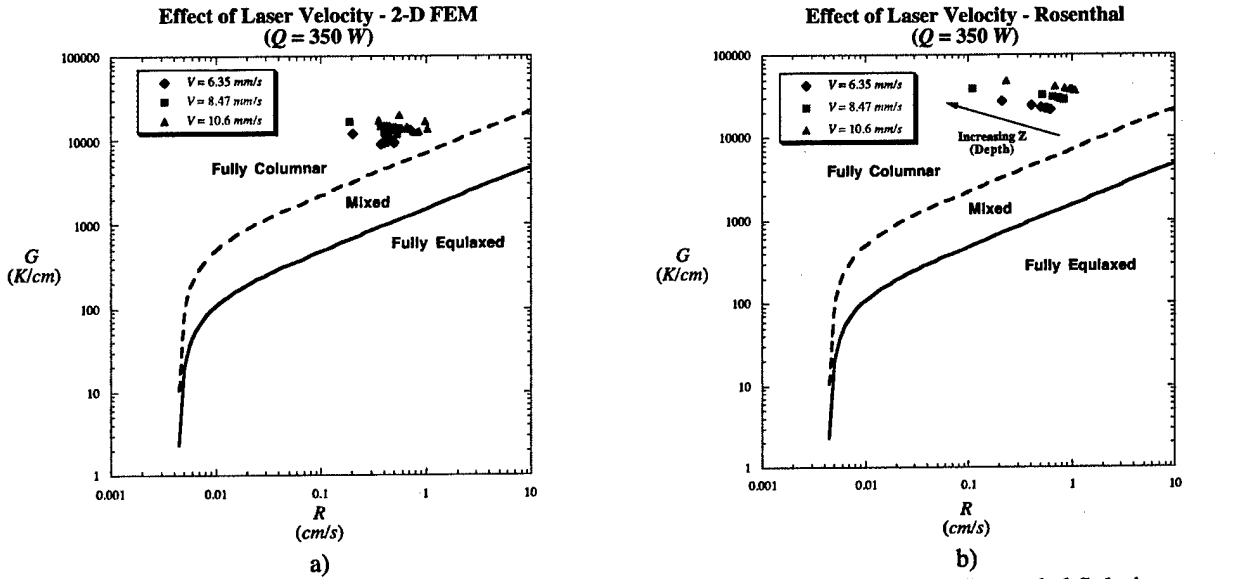

Figure 5. Effect of Laser Velocity on Grain Morphology from a) 2-D FEM and b) 2-D Rosenthal Solution

Although the Rosenthal results neglect the nonlinear effects of temperature-dependent properties and latent heat of transformation, trends in G vs. R data are in reasonably good agreement with the FEM results. In particular, both the Rosenthal and FEM results predict a fully columnar morphology, which is in keeping with experimental observations of LENS™ deposited Ti-6Al-4V [3-5]. However, results also suggest that increasing laser incident energy

(increasing power or decreasing velocity) tends to shift the data closer to the boundary for a mixed columnar/equiaxed grain morphology.

Given the utility of the Rosenthal results for thin-wall LENS™ deposits, the approach can be extended to provide insight into large-scale (higher power) processes. Since wall thickness is an unknown function of laser power, a comparison between LENS™ and large-scale processes is best made for bulky 3-D geometries. Solidification maps obtained from the 3-D Rosenthal results throughout the depth of the melt pool are plotted in Fig. 6 for both small-scale (LENS™) and large-scale processes. The range of LENS™ powers is restricted to 350-850 *W*, while large-scale processes are considered in the range 5000-30000 *W*. In each case, the laser velocity is held constant at $V = 8.47$ *mm/s*, and the fraction of absorbed laser power is taken to be α=0.35.

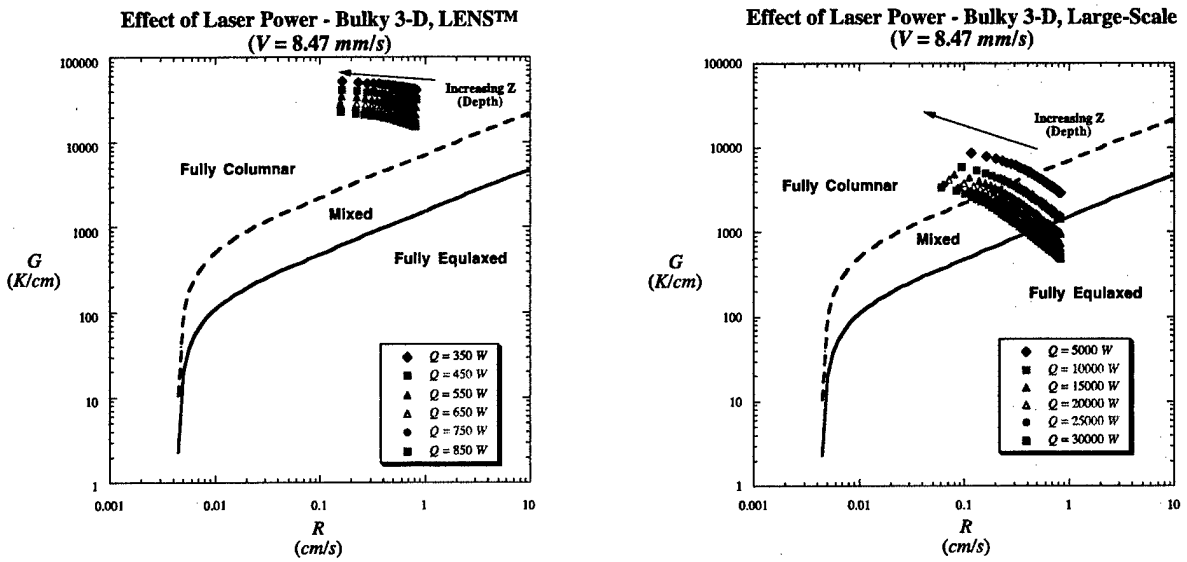

Figure 6. Predicted Grain Morphology in Bulky 3-D Deposits for a) Small-Scale (LENS™) and b) Large-Scale Processes

The results of Fig. 6 reveal that size-scale can have a significant effect on predicted grain morphology in laser deposited Ti-6Al-4V. The results of Fig. 6a predict a fully columnar morphology over the full range of LENS™ powers, which is in keeping with experimental observations [3]. However, the results of Fig. 6b reveal that large-scale processes can result in a grading of the microstructure throughout the depth of the deposit, with a mixed or even fully-equiaxed microstructure at the surface. As observed for thin-wall deposits, the trend toward mixed or equiaxed microstructure increases with laser incident energy.

Conclusions

The ability to predict and control microstructure in laser deposited materials requires an understanding of the thermal conditions at the onset of solidification, which is the focus of this work. Based on the Rosenthal solution for a moving point heat source, process maps for solidification cooling rate and thermal gradient are presented as a function of deposition process variables and depth within the deposit. The results of this work suggest that variations in laser power and velocity can change solidification cooling rates and thermal gradients by several orders of magnitude, which depending on the material system could have a significant effect on resulting microstructure and mechanical properties. Results specifically for Ti-6Al-4V suggest

that increases in laser incident energy could potentially yield a mixed or even fully-equiaxed microstructure near the surface of the deposit, and that the size-scale of the process is important.

Acknowledgments

This work has been supported by the National Science Foundation, grant number DMI-0224517, as well as by the Joint AFRL/DAGSI Research Program, project number ML-WSU-01-11. The authors would also like to thank J.L. Beuth, P.A. Kobryn and H.L. Fraser for their thoughts and insights regarding this collaborative research effort.

References

1. Kobryn, P.A. and Semiatin, S.L., 2001, "The Laser Additive Manufacture of Ti-6Al-4V," *JOM*, Vol. 53, No. 9, pp. 40-42.

2. Klingbeil, N.W., Brown, C.J., Bontha, S., Kobryn, P.A. and Fraser, H.L., 2002, "Prediction of Microstructure in Laser Deposition of Titanium Alloys," *Solid Freeform Fabrication Proceedings*, (D.L. Bourell, R. H. Crawford, J.J. Beaman, K.L. Wood, H.L. Marcus, eds.), Austin, August 2002, pp. 142-149.

3. Kobryn, P.A., Moore, E.H. and Semiatin, S.L., 2000, "The Effect of Laser Power and Traverse Speed on Microstructure, Porosity and Build Height in Laser-Deposited Ti-6Al-4V," *Scripta Materiala*, Vol. 43, pp. 299-305.

4. Kobryn, P.A. and Semiatin, S.L., 2001, "Mechanical Properties of Laser-Deposited Ti-6Al-4V," *Solid Freeform Fabrication Proceedings*, (D.L. Bourell, J.J. Beaman, R.H. Crawford, H.L. Marcus and J.W. Barlow, eds.), Austin, August 2001.

5. C. A. Brice, K. I. Schwendner, D. W. Mahaffey, E. H. Moore, and H. L. Fraser, 1999, "Process Variable Effects On Laser Deposited Ti-6Al-4V," *Solid Freeform Fabrication Proceedings*, (D.L. Bourell, J.J. Beaman, R.H. Crawford, H.L. Marcus and J.W. Barlow, eds.), Austin, August 1999.

6. Vasinonta, A., Beuth, J.L. and Griffith, M.L.,1999, "Process Maps for Laser Deposition of Thin-Walled Structures," *Solid Freeform Fabrication Proceedings*, (D.L. Bourell, J.J. Beaman, R.H. Crawford, H.L. Marcus and J.W. Barlow, eds.), Austin, August 1999, pp. 383-391.

7. Vasinonta, A., Beuth, J.L. and Griffith, M.L., 2000, "Process Maps for Controlling Residual Stress and Melt Pool Size in Laser-Based SFF Processes," *Solid Freeform Fabrication Proceedings*, (D.L. Bourell, J.J. Beaman, R.H. Crawford, H.L. Marcus and J.W. Barlow, eds.), Austin, August 2000, pp. 200-208.

8. Vasinonta, A., Beuth, J.L. and Griffith, M.L., 2001, "A Process Map for Consistent Build Conditions in the Solid Freeform Fabrication of Thin-Walled Structures," *Journal of Manufacturing Science and Engineering*, Vol. 123, No. 4, pp. 615-622.

9. Vasinonta, A., Beuth, J.L., and Ong, R., 2001, "Melt Pool Size Control in Thin-Walled and Bulky Parts via Process Maps," Solid Freeform Fabrication Proceedings (D.L. Bourell, J.J. Beaman, R.H. Crawford, H.L. Marcus, K.L. Wood and J.W. Barlow, eds.), Proc. 2001 Solid Freeform Fabrication Symposium, Austin, August 2001, pp. 432-440.

10. Beuth, J.L. and Klingbeil, N.W., 2001, "The Role of Process Variables in Laser-Based Direct Metal Solid Freeform Fabrication," *JOM*, Vol. 53, No. 9, pp. 36-39.

11. Rosenthal, D., 1946, "The Theory of Moving Sources of Heat and its Application to Metal Treatments," *Transactions of ASME*, Vol. 68, pp. 849-866.

12. Birnbaum, A., Aggarangsi, P. and Beuth, J., 2003, "Process Scaling and Transient Melt Pool Size Control in Laser-Based Additive Manufacturing Processes," *Solid Freeform Fabrication Proceedings*, Austin, August 2003.

Level Set Methods for Modeling Laser Melting of Metals

Haseung Chung and Suman Das
Department of Mechanical Engineering
University of Michigan
Ann Arbor, MI 48109-2125

Abstract

The physical model describing heat transfer and melting taking place during and after the interaction of a laser beam with a semi-infinite metal surface is based on the classical Stefan problem with appropriately chosen boundary conditions to reflect direct selective laser sintering of metals. A level set method for solving this problem is presented in this paper. From the results of these computations, we obtain time evolution of solid-liquid interface and temperature distribution.

INTRODUCTION

Direct selective laser sintering of metals [1] is a process in which a high-energy laser beam directly consolidates a metal powder or powder mixture to full density. Direct selective laser sintering of metals is a complex process exhibiting multiple modes of heat, mass and momentum transfer, and chemical reaction mechanisms. Among them, melting and resolidification processes in direct SLS can have significant effect on the temperature distribution, residual stress, and final microstructure quality of the parts. The inherent complexity of this process imposes serious constraints on the complexity of the models that can be constructed to enable a fundamental understanding of the important physical mechanisms in SLS. This understanding is essential to implement effective process control [2].

There are numerous previous studies for understanding this kind of phase change problem involving moving boundaries. Above all, tracking the motion of a moving front has been of great interest for many researchers. In this paper, a convenient scheme to track moving interfaces using level set theory is extended to the analysis of the Stefan problem. This level set formulation is based on front capturing. In this formulation, the boundary of solid-liquid interface is modeled as the zero set of a smooth function ϕ defined on the entire physical domain. The boundary is then updated by solving a nonlinear equation of the Hamilton-Jacobi type on the whole domain. This level set formulation of the moving interface was introduced by Osher and Sethian [3] and was capable of computing geometric properties of highly complicated boundaries without explicitly tracking the interface [4]. Equation 1 is the level set equation given by Osher and Sethian. For certain forms of the speed function F, one obtains a standard Hamilton-Jacobi equation. Equation 1 describes the time evolution of the level set function ϕ in such a way that the zero level set of this evolving function is always identified with the propagating interface shown in Fig. 1 [5].

$$\phi_t + F|\nabla\phi| = 0 \qquad (1)$$
$$\text{given } \phi(x, t=0)$$

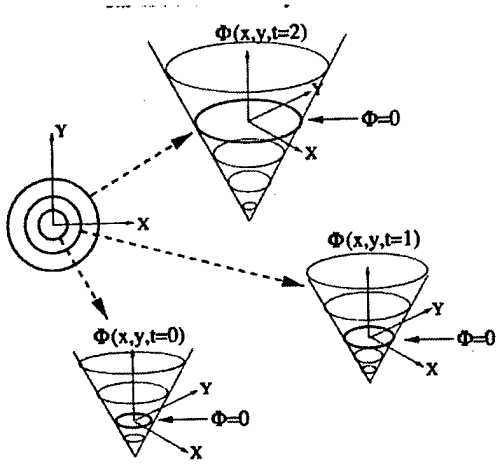

Fig. 1 Transformation of front motion into initial value problem

PHYSICAL MODEL

In this paper, an axisymmertic heat conduction model with phase change in a 5 mm^3 solid is considered. Heat flux from a laser flows in through the top surface during heat up while the other sides are assumed insulated. If heating continues long enough, melting commences and the melt interface moves inward. On the other hand, heat is lost from the top surface only by radiation. The following assumptions are made for developing the model.

- Powder is treated as a solid and no sintering densification occurs during the process.
- Laser beam intensity distribution is uniform across the beam diameter.
- Material properties are independent of temperature in both solid and liquid state.
- No convective heat transfer at top surface (process occurs in a vacuum).
- No melt pool convection, no convective heat transfer at melt interface.
- No evaporative heat loss and no evaporative mass transfer at top surface.
- Top surface is diffuse and gray.

The governing equations are

$$\frac{\partial}{\partial x}\left(k\frac{\partial T}{\partial x}\right)+\frac{\partial}{\partial y}\left(k\frac{\partial T}{\partial y}\right)+\frac{\partial}{\partial z}\left(k\frac{\partial T}{\partial z}\right)+\dot{q}=\rho c_p\frac{\partial T}{\partial t} \tag{2}$$

with boundary conditions on the top surface

$$-k\frac{\partial T}{\partial n}=\alpha_a q''+\varepsilon\sigma(T_\infty^4-T^4) \tag{3}$$

and Stefan condition

$$k_s\frac{\partial T}{\partial n}\bigg|_s-k_l\frac{\partial T}{\partial n}\bigg|_l=\rho V\lambda \tag{4}$$

NUMERICAL SCHEME AND EXPERIMENTAL PARAMETERS

There are a few widely used methods for phase change problems such as enthalpy methods, temperature based equivalent heat capacity methods and front tracking schemes. Each method has some disadvantages as well as some advantages. In this paper, level set method based on the finite elements method was developed. For solving this problem, commercial

software, FEMLAB (by COMSOL) was used. FEMLAB can model virtually any physical phenomena described by partial differential equations (PDEs) including heat transfer, fluid flow, electromagnetics and structural mechanics. FEMLAB also allows users to couple these various transport processes and reactions running simulations on all of them simultaneously [6].

To deal with the discontinuity of material properties from solid to liquid, we introduced the Heaviside (step) function in our model [7].

$$H = \begin{cases} 0 & if\ \phi \le -\delta \\ \dfrac{\phi+\delta}{2\delta} + \dfrac{\sin(\pi\phi/\delta)}{2\pi} & if\ |\phi| < \delta \\ 1 & if\ \phi \ge \delta \end{cases} \quad (5)$$

Using this function, material properties are defined as following.

$$\rho = \rho_l + (\rho_s - \rho_l)H(\phi) \quad (6)$$

$$C_p = C_{pl} + (C_{ps} - C_{pl})H(\phi) \quad (7)$$

$$k = k_l + (k_s - k_l)H(\phi) \quad (8)$$

Other parameters values used for the computations are shown in table1.

Domain size	Number of Elements	Time step	Laser beam diameter	Laser beam power
5 x5x5 mm^3	3048	1 x 10^{-4} sec	200 μm	1 kW.

Table1: Parameters used for numerical computations

Figure 2 shows mesh structure used for the computations.

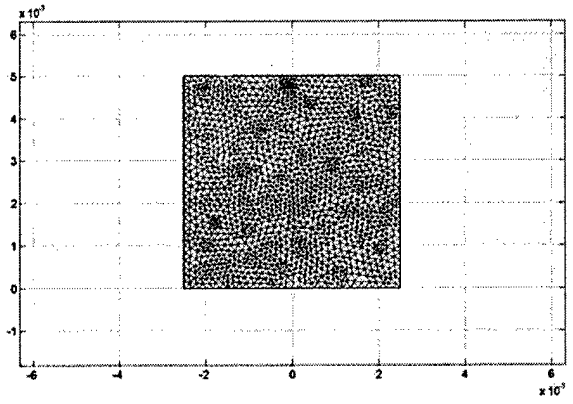

Fig. 2 Mesh structure

RESULTS AND DISCUSSION

Figure 3 and 4 show initial location of solid-liquid interface and temperature distribution. As shown in Fig. 3, zero level set of function which indicates solid-liquid interface is assigned initially as top surface.

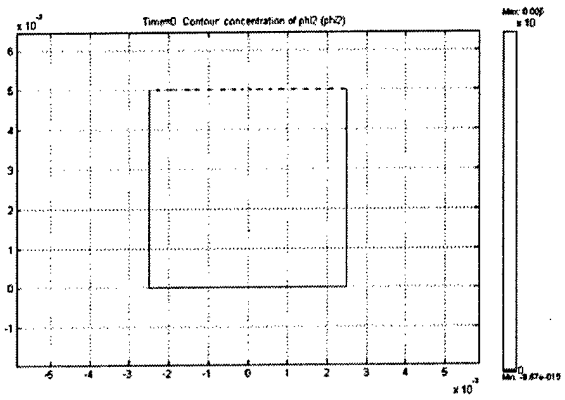

Fig. 3 Location of solid-liquid interface at t = 0 sec

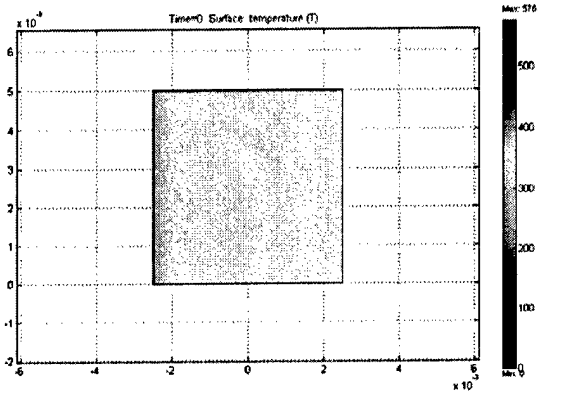

Fig. 4 Temperature distribution at t = 0 sec

As time goes on and heat flux continues to be supplied, the location of solid-liquid interface penetrates deeper and diffuses out axially. Figure 5 and 6 show this phenomenon which can be expected.

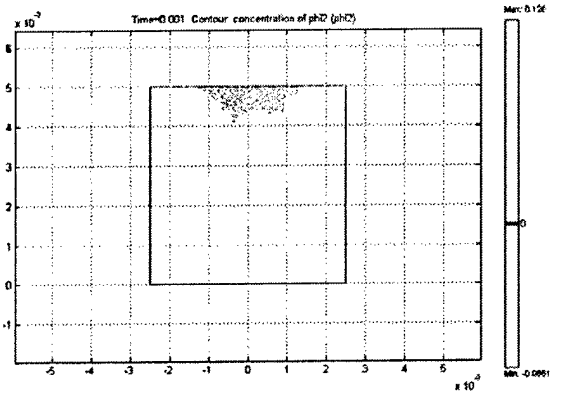

Fig. 5 Location of solid-liquid interface at t = 0.001 sec

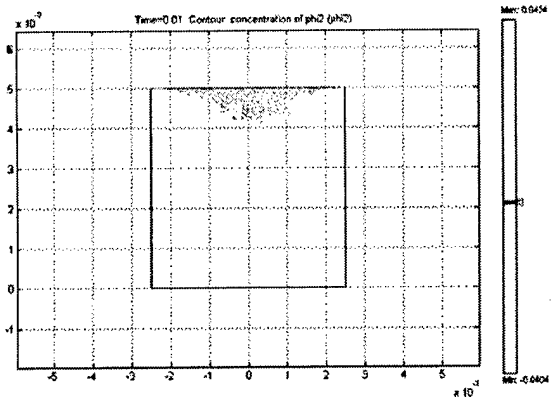

Fig. 6 Location of solid-liquid interface at t = 0.01 sec

Figure 7 and 8 show temperature distribution at corresponding time respectively. Here the peak temperature is far in excess of melting temperature. This is likely a result of not including the effect of latent heat of vaporization.

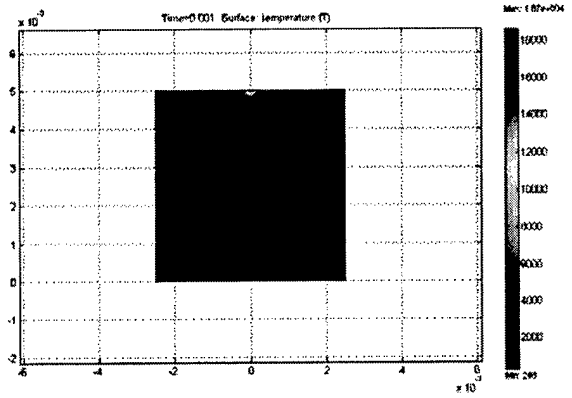

Fig. 7 Temperature distribution at t = 0.001 sec

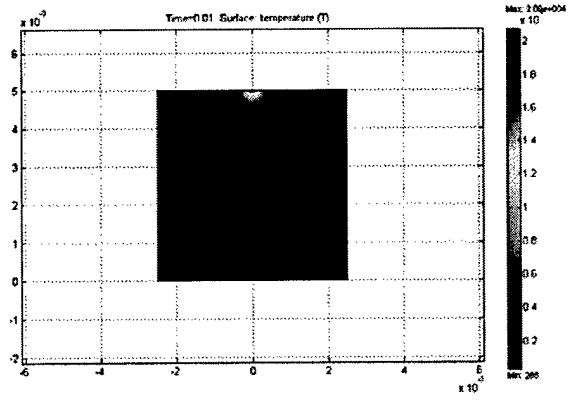

Fig. 8 Temperature distribution at t = 0.01 sec

From this simulation, we proved that the level set method is a useful method for phase change problems. The model presented in this paper will be extended to solidification process for tracking the solid-liquid interface location. Further, we can use an additional level set function to simulate surface deformation due to fluid flow from surface tension gradients simultaneously. Future work will include level set re-initialization process to get more accurate results. Re-initialization is a preferable method to avoid steep or flat gradients developed in the level set function ϕ. The level set function has to keep the exact signed distance from the evolving interfaces. By adding this process, we can acquire more accurate and smoother deformed surface as well as solid-liquid interface.

REFERENCES

1. Suman Das, *Direct Selective Laser Sintering of High Performance Metals-Machine Design, Process Development and Process Control*, Ph.D. dissertation, The University of Texas at Austin, 1998
2. Suman Das and Haseung Chung, "A Model of Laser-Powder Interaction in Direct Selective Laser Sintering of Metals", Solid Freeform Fabrication Symposium Proceedings, The University of Texas at Austin, 2001.
3. Osher, S., and Sethian, J.A., "Fronts Propagating with Curvature-Dependent Speed: Algorithms Based on Hamilton-Jacobi Formulations", Journal of Computational Physics, Vol. 79, 1988, pp. 12-49.
4. Y. C. Chang, T. Y. Hou, B. Merriman, and S. Osher, "A Level Set Formulation of Eulerian Interface Capturing Methods for Incompressible Fluid Flows", Journal of Computational Physics, Vol. 124, 1996, pp. 449-464.
5. J. A. Sethian, *Level Set Methods and Fast Marching Methods*, 2000, Cambridge University press.
6. FEMLAB Model Library, 2000, COMSOL AB.
7. L. L. Zheng and H. Zhang, "An adaptive level set method for moving-boundary problems: application to droplet spreading and solidification", Numerical heat Transfer, Part B, Vol. 37, 2000, pp. 437-454.

NOMENCLATURE

Symbols

c_p = specific heat (J/kgK)
t = time (sec)
k = thermal conductivity (W/mK)
q'' = heat flux (W/m^2)
H = Heaviside function
T = temperature (K)
x = Cartesian coordinate (m)
y = Cartesian coordinate (m)
z = Cartesian coordinate (m)

Greek Letters

α_a = absorptivity of surface
α = thermal diffusivity (m^2/s)
ε = emissivity of surface
δ = small value
λ = latent heat of fusion (kJ/kg)
ρ = density (kg/m^3)
σ = Stefan-Boltzmann constant
ϕ = level set function

Comparisons between Thermal Modeling and Experiments in Laser-Densified Dental Powder Bodies

Kun Dai, Xiaoxuan Li, Leon L. Shaw
Department of Metallurgy and Materials Engineering
Institute of Materials Science
University of Connecticut
Storrs, CT 06269, USA

Abstract

A three-dimensional thermal finite element model including the effect of the powder-to-solid transition has been developed to investigate the transient temperature distribution during laser densification of dental powder bed for the layer-by-layer fabrication. The model encompasses the effects of the temperature- and porosity-dependent thermal conduction and radiation as well as the temperature-dependent natural convection. The simulation result is compared with the experiments which establish the temperature dependence of the dental porcelain microstructure and utilize this dependence to construct the temperature distribution profile. It is found that the trend of the simulation result matches the experiments very well.

Keywords: Dental restoration, Laser processing, Finite element modeling, Thermal analyses, Powder melting and solidification.

I. Introduction

Solid freeform fabrication (SFF) is an automated manufacturing process that builds three-dimensional complex-shaped structures layer-by-layer directly from CAD data [1]. The recent advancement of SFF has led to a multi-material laser densification (MMLD) process for dental restoration [2-4]. Through this approach artificial teeth are expected to be fabricated from a computer model without part-specific tooling and human intervention, thereby offering the potential to reduce the labor cost and increase the restoration rate. However, as the densification of the dental porcelain powder is accomplished via a laser beam, an understanding of the temperature distribution in the laser-assisted densification process is necessary in order to understand the phase transformation and microstructural evolution of the dental porcelain powder during laser densification. The understanding developed will provide the guideline to optimize the laser processing condition so that the microstructure and thus the mechanical properties of the laser-densified bodies are similar to those obtained via traditional furnace annealing process. The approach of finite element modeling (FEM) has been taken in this study to investigate the temperature distribution during laser densification. The FEM approach is necessary because the relative density of the workpiece changes continuously with time during

laser densification until it reaches near full density. As a result, the thermal conductivity of the workpiece also changes continuously. Thus, the transient temperature field of the workpiece is too complex to calculate using analytical methods, and numerical simulation becomes necessary.

Many numerical modeling efforts have been carried out to investigate the temperature field in various SFF processes [5-22]. However, they are not suitable for the laser-assisted dental restoration process which requires the numerical models to encompass at least the effects of the powder-to-solid transition, laser power density, closed-loop temperature control, temperature-dependent thermal convection, and temperature- and porosity-dependent thermal conduction and radiation. Most of the existing SFF models (e.g., Refs. 5 – 22) are not so sophisticated. Therefore, in this study we have developed a model that includes (i) a coupled-filed analysis between temperature and porosity fields, (ii) the incoming laser beam power with Gaussian distribution, (iii) the optical pyrometer simulation in addition to the closed-loop temperature control, (iv) powder-to-solid transition, (v) temperature-dependent thermal convection, and (vi) temperature- and porosity-dependent thermal conduction and radiation. The results from the numerical simulation have been compared with experiments and found to match the experimental measurements quite well.

II. Model Description

The model developed is shown in Figure 1 and consists of a dental porcelain powder compact with a dimension of 10mm length, 6mm width and 2mm height before laser densification. In simulation the laser beam is modeled as a heat flux, Q, with a Gaussian power distribution as an incoming heat source, which moves at a constant rate (240 μm/s) along the X-axis as shown in Figure 1. The heat losses from the six surfaces of the model are assumed to result from thermal natural convection and the radiation. The dental porcelain powder is composed of 63.40% SiO_2, 16.70% Al_2O_3, 1.50% CaO, 0.80% MgO, 3.41% Na_2O, and 14.19% K_2O (wt%). The material thermal properties for the dense solid porcelain used in the model are summarized in Table 1. The dental porcelain is assumed to be at a molten state above 1073K (100K higher than the lower temperature of the forming temperature range of the porcelain) and no volume shrinkage is considered when powder porcelain converts to dense porcelain.

The modeling is carried out using the ANSYS commercial finite element package. The thermal element (Solid70), which has eight nodes with a single degree of freedom (*i.e.*, temperature) at each node and has a 3D thermal-conduction capability, is used to simulate the temperature field [23]. Each element near the surface has a size of 0.25 mm length, 0.25 mm width and 0.2 mm height. The model is first used to calculate the temperature distribution in the powder bed within a small time step resulting from the heating of a laser beam moving at a constant rate along the X-axis. The powder elements convert to dense molten elements if their temperatures are higher than 1073K according to the calculated temperature field, and the temperature distribution in the powder bed within the next small time step is calculated using the updated material properties. This simulation loop continues until the total amount of the small time steps, which is decided by the laser scanning rate, is reached, and then the laser beam moves stepwise by one element to carry out the next simulation loop. The substrate preheating is

achieved in the simulation by assigning an elevated temperature (460^0C) as the nodal temperature of the bottom surface.

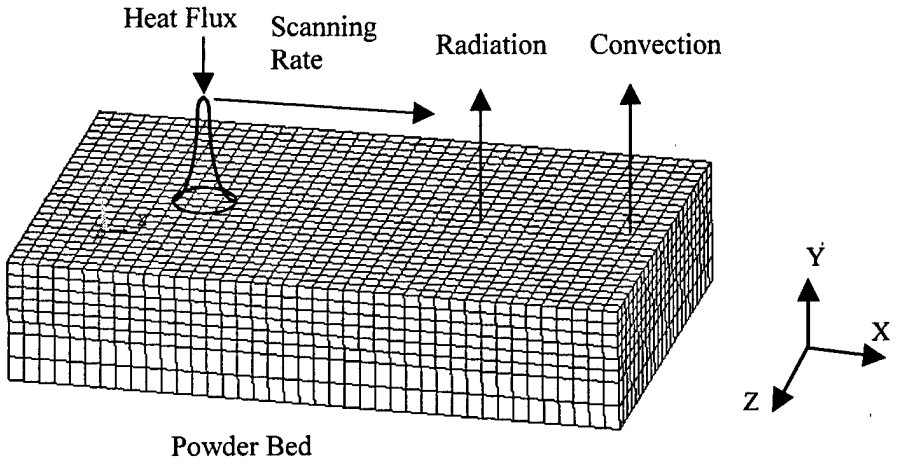

Figure 1. Finite element model developed to simulate the temperature field during laser densification of the dental porcelain body.

Table 1. Summary of Thermal Properties of Dental Porcelain [24 – 28]

T (K)	300	520	631	700	830	960	1173	1373	1540	1726	1730	1800
k (W/m-K)	1.11	1.37	1.55	1.67	1.93	2.23	2.82	2.82	2.82	2.82	2.82	2.82
C_p (J/kg-K)	742	1025	1125	1178	1266	1341	1444	1474	1474	1474	1474	1474
α (10^{-6}/K)	2.80	3.36	3.87	4.27	5.25	6.54	9.43	9.43	9.43	9.43	9.43	9.43
E (GPa)	70	55.6	48.4	43.9	35.4	26.9	—	—	—	—	—	—
ε	0.7											
ρ (kg/m^3)	2520											
T_m (K)	1573											
T_f (K)	973 to1273											
ν	0.2											

*T–Temperature, k–Thermal Conductivity, C_p–Specific Heat, α–Thermal Expansion Coefficient, E – Elastic Modulus, ε –Emissivity, ρ –Density, T_m – Melting Temperature, T_f – Forming temperature, ν –Poisson's Ratio.

The thermal properties of the powder bed are a strong function of the porosity of the powder bed. It is assumed that the porosity of the powder bed is temperature independent before the powder becomes liquid. This is a reasonable assumption because the reduction in porosity due to solid-state sintering is minimal under the present laser densification condition which brings the local temperature of the area irradiated by the laser beam to above the forming temperature of the porcelain in less than 6 seconds. For the region outside the irradiated area, the time for the region to expose to high temperatures is also relatively short (less than 100 seconds) because of the scanning rate used. Furthermore, the temperature at the region outside the irradiated area is also relatively low because of the low thermal conductivity of the powder compact. As such, the porosity of material has been simplified in two levels, that is, the initial porosity φ_0 before the powder converts to liquid, and zero porosity (fully dense) after the powder

has converted to liquid. The thermal properties of the powder bed, therefore, are treated as a function of temperature and the initial porosity φ_0. The details of these functions and thermal boundary conditions can be found in a recent paper [21] and described briefly as follows.

A. Thermal Conductivity of the Powder Bed

Effective thermal conductivity of the powder bed, k, is estimated by Equation (1) with the assumption that the particles are spheres and there is no flattening of contact surfaces [29].

$$\frac{k}{k_f} = (1-\sqrt{1-\varphi_0})(1+\frac{\varphi_0 k_r}{k_f}) + \sqrt{1-\varphi_0}\left(\frac{2}{1-\frac{k_f}{k_s}}\left(\frac{1}{1-\frac{k_f}{k_s}}\ln\left(\frac{k_s}{k_f}\right)-1\right)+\frac{k_r}{k_f}\right) \quad (1)$$

Where, k_f and k_s are the thermal conductivities of the ambient air and solid particle, respectively; k_r is the thermal conductivity portion of the powder bed due to radiation among particles and equals to [29,30]

$$k_r = 4F\sigma T^3 x_r \quad (2)$$

where σ is the Stefan-Boltzmann constant, x_r is the average diameter of the powder particles, T is the temperature of powder particles, and F is a view factor which is approximately taken as 1/3 [30].

B. Thermal Radiation of the Powder Bed

The emissivity of the powder bed, ε, is obtained by

$$\varepsilon = A_H \varepsilon_H + (1-A_H)\varepsilon_S \quad (3)$$

where, A_H is the area fraction of the surface that is occupied by the radiation-emitting holes, ε_S and ε_H are the emissivities of solid particle and hole, respectively. For a powder bed composed of randomly packed, single-sized spheres, A_H and ε_H are given by [31]

$$A_H = \frac{0.908\varphi_0^{\,2}}{1.908\varphi_0^{\,2} - 2\varphi_0 + 1} \quad (4)$$

and

$$\varepsilon_H = \frac{\varepsilon_S\left[2+3.082(\frac{1-\varphi_0}{\varphi_0})^2\right]}{\varepsilon_S\left[1+3.082(\frac{1-\varphi_0}{\varphi_0})^2\right]+1} \quad (5)$$

C. Thermal Convection around the Powder Bed

The heat transfer coefficient, h_c, is temperature and size dependent [32]

$$h_c = \frac{N_u k_f}{L} \tag{6}$$

where L is the characteristic length of the specimen, N_u is the Nusselt number, and k_f is the thermal conductivity of the fluid as defined before. N_u is given by [33]

$$\sqrt{N_u} = \sqrt{N_{u0}} + \left[\frac{G_r P_r / 300}{(1+(0.5/P_r)^{9/16})^{16/9}}\right]^{1/6} \tag{7}$$

when $10^{-4} \leq G_r P_r \leq 4\times10^{14}$, $0.022 \leq P_r \leq 7640$, and $N_{u0} = 0.67$ for a plate [33]. G_r and P_r in Equation (7) are Grashof and Prandtl numbers, respectively [32].

$$G_r = g\frac{L^3 \rho_f{}^2 \beta_f (T - T_{amb})}{\eta_f{}^2} \tag{8}$$

and

$$P_r = \frac{C_p \eta_f}{k_f} \tag{9}$$

where g is the gravitational acceleration, ρ_f is the density of the ambient air, β_f is the thermal volumetric expansivity and $\beta_f = 1/T_f$ for idea gases, η_f is the viscosity of the air, C_p is the specific heat of the air. The effect of the variation of air properties with temperature is evaluated at $T_f = 0.5(T + T_{amb})$, where T is the surface temperature of the powder bed, T_{amb} is the ambient temperature [32].

D. Thermal Boundary Conditions for Powder, Liquid and Solid

The part being built is assumed to be in contact with air and the heat loss through air is approximated through the natural thermal convection and thermal radiation between the part and the ambient air. Since the model includes three kinds of material status (i.e., powder, liquid and solid), the thermal boundary conditions are very complicated and vary with porosity, phase status and surface temperature which is the function of incident laser power and laser scanning rate. Under the assumption of little convection of liquid within the molten pool due to its small size (~ 2 mm), liquid and solid have been assumed to have the same thermal convection boundary as the powder bed, i.e., thermal convection around the surface of liquid pool and solid is determined by the temperatures of the ambient air and the liquid and solid under consideration [see eqs. (6-9)]. Heat loss q_r due to radiation of solid and liquid is described by [32]

$$q_r = \sigma\varepsilon_s\left(T^4 - T_{amb}{}^4\right) \tag{10}$$

where T is the surface temperature of solid and liquid, and ε_s is the emissivity of the dense porcelain, T_{amb} is the ambient temperature, and σ is the Stefan-Boltzmann constant.

The model of a moving Gaussian distribution laser beam, pyrometer temperature simulation, closed-loop temperature control of the laser power are described in detail in the paper [20] and is described as follows.

E. Heat Input

The heat flux of the laser beam, Q, is related to the power of the laser beam, P, through the following relation [34]:

$$Q = \frac{2P\alpha_a}{\pi r_0^2} e^{-\frac{2r^2}{r_0^2}} \tag{11}$$

where α_a is the absorptivity of the workpiece, r_0 is the radius of the laser beam at which the heat flux value is e^{-2} times of that of the laser beam center, and r is the distance of a point on the surface of the powder bed measured from the laser beam center. When the center of the laser beam scans the surface of the powder bed from the starting point (X_0, Y_0, Z_0) to (X, Y_0, Z_0) point along the positive X-direction with a constant velocity V for a period time t, r is given by

$$r^2 = (X - X_0 - Vt)^2 + (Z - Z_0)^2 \tag{12}$$

In the present study, the radius of the incident laser beam, r_0, is 0.5 mm, the laser scanning velocity, V, is 0.24 mm/s. The absorptivity of the dental porcelain workpiece, α_a, was varied in the simulation, and a value of 0.41 was needed for the simulated laser input power to match the experimental values. This absorptivity value is comparable with experimental scatter for measured values of α_a for sintered SiC near the processing temperatures used here [35].

F. Pyrometer Simulation

In laser-densification experiments, an optical pyrometer continually monitors the temperature distribution at the surface of the powder bed during laser densification. This pyrometer temperature is used as the feedback signal in a closed-loop control program to adjust the incident laser power as needed to achieve a desired constant laser spot temperature. In the simulation, the pyrometer temperature measurement and the closed-loop control process are modeled as follows.

The power, E, of the thermal radiation emitted by the laser-heated workpiece that reaches the pyrometer can be expressed by [35]

$$E = \int I(\lambda, T)\Delta\lambda dA \tag{13}$$

where λ is the wavelength of the emitted radiation , $\Delta\lambda$ is the wavelength band of the emitted radiation that is sampled by the pyrometer, T is the temperature at a very small area dA through which the radiation passes to reach the pyrometer, termed the pyrometer sampling area hereafter, $I(\lambda, T)$ is the spectral distribution of blackbody emissive power and given by Planck's radiation law [36]:

$$I(\lambda,T)=\frac{2\pi hc^2}{\lambda^5\left(e^{\frac{hc}{\lambda\sigma T}}-1\right)} \tag{14}$$

where h is Planck's constant, c is the speed of light, and σ is Stefan-Boltzmann constant. Because of the Gaussian heat input and movement of the laser beam, the surface temperature, T, within the pyrometer sampling area is not uniform, and neither is $I(\lambda,T)$. Thus, to carry out the integration of equation (13), approximations are made by dividing the sampling area into n small areas and assuming that T and I are constant within each small area. With these assumptions, equation (13) is reduced to

$$E=\sum_{i=1}^{n} I(\lambda,T_i)\Delta\lambda\Delta A_i \tag{15}$$

where T_i is the surface temperature of the area ΔA_i and n is the number of the small areas within the pyrometer sampling area, A_p. To further simplify the computation, it is assumed that every ΔA_i has the same area, and thus

$$A_p=n\Delta A_i \tag{16}$$

and equation (15) becomes

$$E=\Delta\lambda\Delta A_i\sum_{i=1}^{n} I(\lambda,T_i) \tag{17}$$

To relate the thermal radiation power collected by the pyrometer to the pyrometer temperature reading, an effective temperature, T_{eff}, is introduced as

$$E=\Delta\lambda\Delta A_i\, n\, I(\lambda,T_{eff}) \tag{18}$$

Combining equations (14), (17) and (18), it has

$$T_{eff}=\frac{hc}{\lambda\sigma\ln\left(1+n\Big/\sum_{i=1}^{n}\left(e^{\frac{hc}{\lambda\sigma T_i}}-1\right)^{-1}\right)} \tag{19}$$

G. Closed-Loop Temperature Control

T_{eff} in Equation (13) is the effective (nominal) surface temperature of the workpiece as measured by the pyrometer for a given incident laser power. If T_{eff} differs from the desired laser spot temperature, T_p, then the incident laser power is adjusted accordingly to simulate the closed-loop temperature control in the experiment. This is achieved in the simulation by adjusting the laser power from one simulation step to the next using the following equation

$$P_{i+1} = P_i \frac{T_p}{T_{eff}} \tag{20}$$

where P_i and P_{i+1} are the incident laser power in the simulation steps i and i+1, respectively. It can be found that this equation allows the surface temperature of the workpiece, T_{eff}, to quickly approach the desired laser spot temperature, reproducing in the simulation the closed-loop temperature control process used in the experiments.

III. Comparison between Simulation and Experimental Results

One of the key criteria for validating the model is to check whether the model can achieve a constant pyrometer temperature (i.e., a constant temperature on the surface of the powder bed) by continuously adjusting the laser input power. Figures 2 and 3 show the comparison between the experimental and simulated pyrometer temperature as a function of the location of the scanning laser beam with a nominal surface temperature of 900 and 1050^{0}C, respectively. It can be seen that the variations in temperature are less than 4% of the desired pyrometer temperatures for all four nominal surface temperatures modeled, which indicates that the closed-loop temperature control in experiments can be simulated with the present model. Furthermore, the pyrometer temperatures achieved by simulations and experiments match quite well.

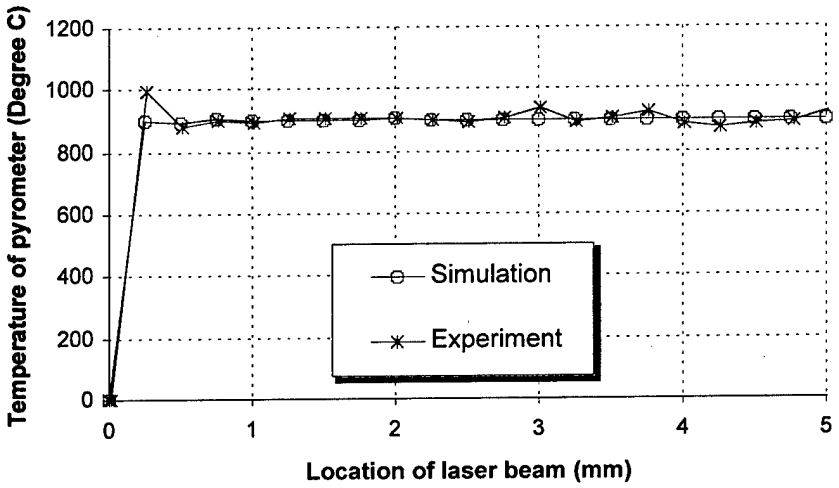

Figure 2. Comparison between the experimental and simulated values of the pyrometer temperature as a function of the location of the scanning laser beam with a nominal surface temperature of 900^{0}C and substrate preheating to 460^{0}C.

The model established is utilized to predict the temperature distribution in the porcelain body during laser densification. Figure 4 show the simulation result with a nominal surface temperature of 1050^{0}C and substrate preheating of 460^{0}C. It is quite clear that the temperature distribution obtained is consistent with the expectation that the highest temperature is located at

the center of the scanning laser beam and the temperature gradually decreases as the location moves away from the center in all directions within the porcelain body. More importantly, when compared with the experimental result (Figure 5), it is found that the predicted temperature distribution pattern matches the measurement quite well. Furthermore, the temperature range predicted also matches the measurement reasonably well. However, a direct comparison of the temperature value between the simulation and experiment is not possible at this stage because of the different laser densification conditions used in Figures 4 and 5. The work on simulations with the identical laser densification condition as the experiment is currently under way and will be published in a forthcoming paper [37].

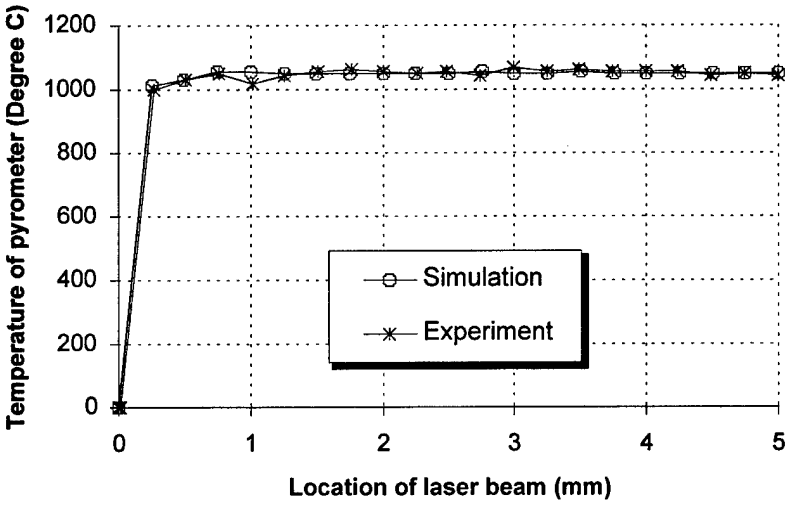

Figure 3. Comparison between the experimental and simulated values of the pyrometer temperature as a function of the location of the scanning laser beam with a nominal surface temperature of 1050^0C and substrate preheating to 460^0C.

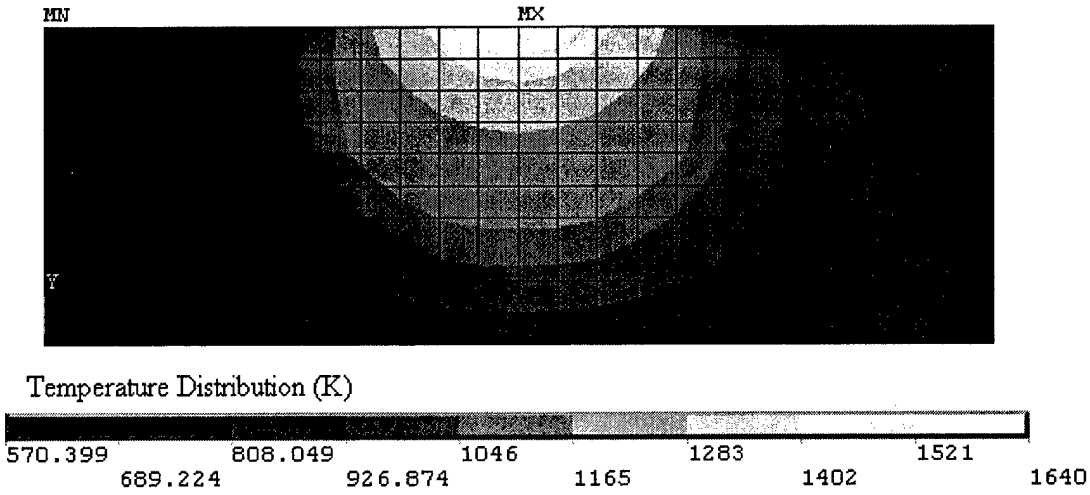

Figure 4. Temperature distribution in the powder bed at the cross section of x = 6.75mm when the laser beam scans to this location with a nominal surface temperature of 1050^0C and substrate preheating to 460^0C.

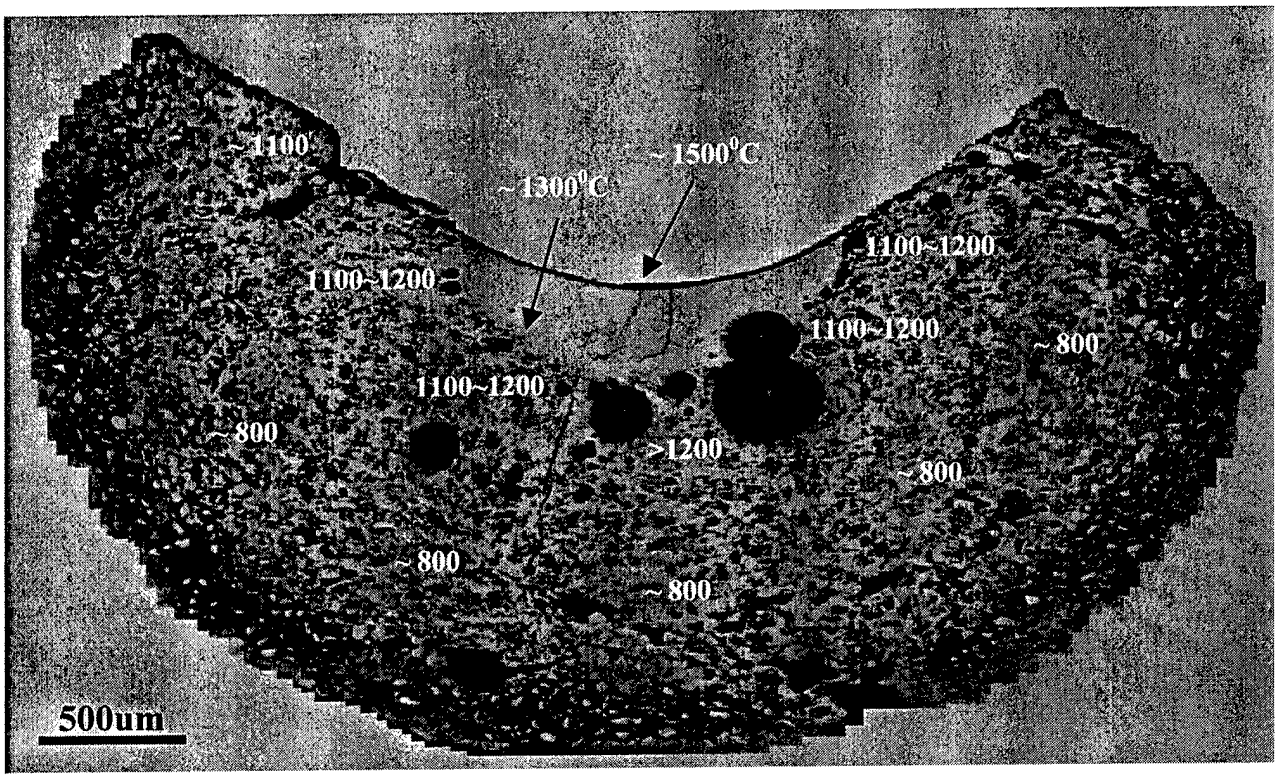

Figure 5. Temperature distribution at the cross section of a porcelain body perpendicular to the laser scan direction during laser densification with a nominal surface temperature of 1100°C and substrate preheating of 400°C [37].

IV. Conclusions and Remarks

A 3D finite element model that encompasses the effects of the powder-to-solid transition, laser power density, closed-loop temperature control, temperature- and porosity-dependent thermal conduction and radiation as well as the temperature-dependent natural thermal convection has been developed to carry out the thermal analysis of laser-densified dental porcelain bodies. The temperature distribution in the porcelain body during laser densification has been simulated using this model and is compared with the experiment. The results predicted by the model matches the experiment well, and the model will be used in the future to provide guidance for selecting laser processing conditions to obtain the desired microstructure and geometry of the dense body. This is the first comprehensive model that includes all key parameters in laser densification of powder lines. The model can be extended to simulate many other laser materials processing methods that require consideration of phase transformations, closed loop temperature control, and heat transfer.

Acknowledgements – The authors gratefully acknowledge financial support provided by the National Science Foundation under Grant Nos: DMI-9908249 and DMI-0218169.

References

1. Beaman, J.J., Barlow, J.W., Bourell, D.L., Crawford, R.H., Marcus, H.L. and McAlea, K.P., *Solid Freeform Fabrication: A New Direction in Manufacturing*, Kluwer Academic Publishers, MA, 1997.
2. L. Shaw, X.-X. Li, J.-W. Wang, H. L. Marcus, T. B. Cameron, and C. Kennedy, "Dental Restoration through Laser Densification of Dental Porcelain Powder," in *Rapid Prototyping of Materials* (F.D.S. Marquis and D.L. Bourell, Eds.), TMS, Warrendale, PA, 2002, pp. 107-118.
3. J.-W. Wang, X.-X. Li, L. Shaw, H. L. Marcus, T. B. Cameron, and C. Kennedy, "Studies on Slurry Extrusion for Dental Restoration," in the *Proceedings of the 13th Annual SFF Symposium* (D. L. Bourell, J. J. Beaman, R. H. Crawford, H. L. Marcus and J. W. Barlow, Eds.), The University of Texas at Austin, 2002, pp. 83-91.
4. X.X. Li, J.W. Wang, A. Augustine, L.L. Shaw, H. L. Marcus and T. B. Cameron, "Microstructure Evaluation for Multi-Materials Laser Densification of Dental Porcelains", in Proc. of the 12th Annual SFF Symposium, D. L. Bourell, J. J. Beaman, R. H. Crawford, H. L. Marcus and J. W. Barlow, Eds., the University of Texas at Austin, 2001, pp. 195-202.
5. R.K. Chin, J.L. Beuth and C.H. Amon, "Thermomechanical Modeling of Molten Metal Droplet Solidification Applied to Layered Manufacturing", Mech. Mater., 1996, Vol. 24, pp.257-271.
6. C.H. Amon, J.L. Beuth, R. Merz, F.B. Prinz and L.E. Weiss, "Shape Deposition Manufacturing with Microcasting: Processing, Thermal and Mechanical Issues", J. Manufact. Sci. Eng., 1998, 120 [3], pp. 656-665.
7. R.K. Chin, J.L. Beuth and C.H. Amon, "Successive Deposition of Metals in Solid Freeform Fabrication Processes Part 1: Thermomechanical Models of Layers and Droplet Columns", Journal of Manufacturing Science and Engineering, 2001, Vol. 123, No. 4, pp. 623-631.
8. R.K. Chin, J.L. Beuth and C.H. Amon, "Successive Deposition of Metals in Solid Freeform Fabrication Processes Part 2: Thermomechanical Models of Adjacent Droplets", Journal of Manufacturing Science and Engineering, 2001, Vol. 123, No. 4, pp. 632-638.
9. R. Ong, J.L. Beuth and L.E. Weiss, "Residual Stress Control Issues for Thermal Deposition of Polymers in SFF Processes", in Proc. of the 11th Annual SFF Symposium, D. L. Bourell, J. J. Beaman, R. H. Crawford, H. L. Marcus and J. W. Barlow, Eds., The University of Texas at Austin, 2000, pp. 209-218.
10. A. Vasinonta, J.L. Beuth and M.L. Griffith, "A Process Map for Consistent Build Conditions in the Solid Freeform Fabrication of Thin-Walled Structures", Journal of Manufacturing Science and Engineering, 2001, Vol. 123, No. 4, pp. 615-622.
11. A. Vasinonta, J.L. Beuth and R. Ong, "Melt Pool Size Control in Thin-Walled and Bulky Parts via Process Maps", in Proc. of the 12th Annual SFF Symposium, D. L. Bourell, J. J. Beaman, R. H. Crawford, H. L. Marcus and J. W. Barlow, Eds., The University of Texas at Austin, 2001, pp. 432-440.
12. A.H. Nickel, D.M. Barnett, F.B. Prinz, "Thermal Stresses and Deposition Patterns in Layered Manufacturing", Materials Science and Engineering A, 2001, Vol. 317, pp. 59-64.
13. M. Shiomi, M. Matsumoto, K. Osakada, F. Abe, "Two-Dimensional Finite Element Simulation of Laser Rapid Prototyping, Simulation of Materials Processing: Theory, Methods and Applications", in Proc. NUMIFORM 2001 (K. Mori ed.), Toyohashi, Japan, 2001, A.A. Balkema Publishers, pp. 1059-1064.

14. M. Matsumoto, M. Shiomi, K. Osakada and F. Abe, "Finite Element Analysis of Single Layer Forming on Metallic Powder Bed in Rapid Prototyping by Selective Laser Processing", Int. J. Machine Tools & Manufacture, 2002, Vol. 42, pp. 61-67.
15. F. Niebling, A. Otto, "FE-Simulation of the Selective Laser Sintering Process of Metallic Powders", Proceedings of 3rd International Conference on Laser Assisted Net Shaping (LANE2001), Erlangen, Germany, August 2001, pp.371-382.
16. K. Dai and L. Shaw, "Thermal and Stress Modeling of Multi-Material Laser Processing", Acta Mater., 2001, Vol. 49, pp. 4171-4181.
17. K. Dai and L. Shaw, "The Size Effect on Stresses and Distortion of Laser Processed Multi-Material Components", Metall. Mater. Trans. A, Vol. 34A, 2003, pp.1133-1145.
18. K. Dai and L. Shaw, "Distortion Minimization of Laser-Processed Components through Control of Laser Scanning Patterns", Rapid Prototyping Journal, 2002, Vol. 8, No. 5, pp. 270-276.
19. K. Dai and L. Shaw, "Finite Element Modeling for Laser-Assisted Dental Restoration Process," in *Proc. of the 2003 NSF Design, Service and Manufacturing Grantees and Research Conference* (R. G. Reddy, Eds.), Birmingham, AL, 2003, pp. 2292-2300.
20. K. Dai, J. Crocker, L. Shaw and H. Marcus, "Modeling of Selective Area Laser Deposition (SALD) and SALD Vapor Infiltration of Silicon Carbide," *Rapid Prototyping Journal*, in press.
21. K. Dai and L. Shaw, "Thermal and Mechanical Finite Element Modeling of Laser Forming from Metal and Ceramic Powders," *Acta Mater.*, in press.
22. K. Dai and L. Shaw, "Preheating Effects on Multiple Materials Laser Densification," in the *Proceedings of the 13th Annual SFF Symposium* (D. L. Bourell, J. J. Beaman, R. H. Crawford, H. L. Marcus and J. W. Barlow, Eds.), The University of Texas at Austin, 2002, pp. 392-399.
23. ANSYS Inc., *ANSYS On-Line Reference Manuals: The ANSYS Elements Reference*, Release 6.1, ANSYS Inc., Canonsburg, PA, 2002.
24. Y. S. Touloukian and D.P. DeWitt, *Thermophysical Properties of Matter, Volume 8, THERMAL RADIATIVE PROPERTIES: Nonmetallic Solids*, IFI/Plenum, New York, NY, 1972.
25. Y. S. Touloukian, R.W. Powell, C.Y. Ho, and P.G. Klemens, *Thermophysical Properties of Matter, Volume 2, THERMAL CONDUCTIVITY: Nonmetallic Solids*, IFI/Plenum, New York, NY, 1970.
26. Y.S. Touloukian and E. H. Buyco, *Thermophysical Properties of Matter, Volume 5, SPECIFIC HEAT: Nonmetallic Solids*, IFI/Plenum, New York, NY, 1970.
27. S.J. Schneider, *Engineered Materials Handbook, Volume 4: Ceramics and Glasses*, ASM International, Metals Park, OH, 1991.
28. J. R. Mackert, M. B. Butts, R. Morena and C. W. Fairhurst, "Phase Changes in a Leucite-Containing Dental Porcelain Frit", *J. Am. Ceram. Soc.*, 1986, 69[4], C-69 - C-72.
29. S. S. Sih and J. W. Barlow, "The Prediction of the Thermal Conductivity of Powders", in the *Proc. of 1995 Solid Freeform Fabrication Symposium* (H. Marcus, J. Beaman, D. Bourell, J. Barlow, and R. Crawford, eds.), The University of Texas at Austin, 1995, pp. 397-401.
30. S. S. Sih and J. W. Barlow, "Measurement and Prediction of the Thermal Conductivity of Powders at High Temperature", in the *Proc. of 1994 Solid Freeform Fabrication Symposium* (H. Marcus, J. Beaman, J.Barlow, D. Bourell and R. Crawford, eds.), The University of Texas at Austin, 1994, pp. 321-329.

31. S. S. Sih and J. W. Barlow, "Emissivity of Powder Beds", in the *Proc. of 1995 Solid Freeform Fabrication Symposium* (H. Marcus, J. Beaman, D. Bourell, J. Barlow, and R. Crawford, eds.), The University of Texas at Austin, 1995, pp. 402-408.
32. D.R. Poirier and G.H. Geiger, *Transport Phenomena in Materials Processing*, The Minerals, Metals and Materials Society, Warrendale, PA, 1994.
33. E.U. Schlunder (Editor-in-Chief), *Heat Exchanger Design Handbook*, Hemisphere Publishing Corporation, New York, NY, 1983.
34. J. Mazumder and A. Kar, *Theory and Application of Laser Chemical Vapor Deposition*, Plenum Publishing Co., New York, NY, 1995.
35. Y.W. Zhang, *Thermal Modeling of Advanced Manufacturing Technologies: Grinding, Laser Drilling, and Solid Freeform Fabrication*, Ph.D. thesis of the University of Connecticut, 1998.
36. E.U. Schlunder (Editor-in-Chief), *Heat Exchanger Design Handbook*, Hemisphere Publishing Corporation, New York, NY, 1983.
37. X.-X. Li and L. Shaw, "Phase Transformation and Microstructure of Dental Porcelain Powder in Laser-Assisted Rapid Prototyping Processes," to be submitted to Dental Mater.

Process Control of Laser Metal Deposition Manufacturing – A Simulation Study

Robert G. Landers

1870 Miner Circle, 211 Mechanical Engineering Building
Department of Mechanical and Aerospace Engineering and Engineering Mechanics
University of Missouri – Rolla, Missouri 65409
Phone: 573–341–4586
Email: landersr@umr.edu

Reviewed, accepted August 13, 2003

ABSTRACT

The laser metal deposition process is a rapid manufacturing operation capable of producing functional prototypes with complex geometries and thin sections. This process inherently contains significant uncertainties and, therefore, extensive experimentation must be performed to determine suitable process parameters. An alternative is to directly control the process on–line using feedback control methodologies. In this paper, a nonlinear control strategy based on feedback linearization is created to automatically regulate the bead morphology and melt pool temperature. Extensive simulation studies are conducted to validate the control strategy.

INTRODUCTION

Laser Metal Deposition (LMD) is a novel layered manufacturing process. A laser melts metal powder (or a wire) to form a molten pool, which quickly solidifies and forms a track. This layered manufacturing process may be used to create functional prototypes and functional gradient material (FGM) metal parts. Also, parts may be repaired using the LMD process, thus, reducing scrap and extending product service life. Extensive experimentation is required to determine suitable process parameters and only near–net shape parts may be produced. Subsequent processing is required if dimensional accuracy is critical. Further, due to the variability in the LMD process, constant process parameters will often not guarantee the part will meet quality specifications in terms of mechanical properties (e.g., hardness, porosity). This variability is due to uncertainties in the process itself (e.g., changes in conduction as the part geometry changes) and from inherent disturbances (e.g., acceleration/deceleration of the table axes). This paper investigates the viability of nonlinear process controllers to regulate the melt pool temperature and track morphology.

Mazumder *et al.* (1999) described the application of multiple sensors for closed–loop feedback control of the bead height. The height controller shuts off the laser until it passes the excess built up region, thus preventing the powder from melting. Doumanidis and Skoredli (2000) established a dynamic distributed parameter model with in–process parameter identification to generate a three–dimensional surface geometry. Geometric predictions were made by a real–time model. A controller was designed to regulate the part geometry taking advantage of these predictions. Morgan *et al.* (1997) controlled the laser focal point and melt pool temperature and Li *et al.* (1987a) developed an in–process laser control loop, which is based on an algorithm involving tune currents. The later system used a microprocessor based in–process beam control

unit using beam sensing via a Laser Beam Analyzer (LBA). Koomsap *et al.* (2001) presented a simulation–based design of a laser based, free–forming process controller. A simplified model called a metamodel was introduced to express the relationship between process characteristics and three process parameters: laser power, traverse speed, and powder feedrate. A dynamic metamodel was obtained and a temperature feedback controller was used to regulate the process. Derouet *et al.* (1997) measured the melt pool profile and maximum temperature and correlated this data with the melt pool depth. Using laser power and traverse speed, the melt pool depth was regulated at a constant value with a proportional plus integral plus derivative (PID) controller. Li *et al.* (1987b) developed a real time expert system and a laser cladding control system to determine the optimal operating conditions for a given requirement and for online fault diagnosis and correction. Fang *et al.* (1999) adjusted process parameters from layer–to–layer to compensate for defects using statistical process control techniques. Munjuluri *et al.* (2000) conducted simulation studies to regulate the bead profile and dilution.

These studies indicate that the quality of the laser metal deposition process may be regulated with process control technologies; however, comprehensive, systematic control strategies that account for the inherent process nonlinearities are still lacking.

PROCESS MODELING

The process model used in this paper is based on the model given by Doumanidis and Kwak (2001). Performing a mass balance of the melt pool

$$\rho\dot{V}(t) = -\rho A(t)v(t) + \mu_m m(t) \tag{1}$$

where ρ is the material density (kg/m^3) and is assumed to be constant, V is the bead volume (m^3), A is the cross sectional area in the direction of deposition (m^2), v is the table velocity in the direction of deposition (m/s), μ_m is the powder catchment efficiency, and m is the powder flow rate (kg/s). The volume and cross sectional area in the direction of deposition, respectively, are given by

$$V(t) = \frac{\pi}{6} w(t)h(t)l(t) \tag{2}$$

$$A(t) = \frac{\pi}{4} w(t)h(t) \tag{3}$$

where w is the bead width (m), h is the bead height (m), and l is the bead length (m). Performing a momentum balance of the melt pool in the direction of deposition

$$\rho\dot{V}(t)v(t) + \rho V(t)\dot{v}(t) = \rho\frac{\pi}{4} w(t)h(t)v^2(t) + \left[1-\cos(\theta)\right]\left[\gamma_{GL} - \gamma_{SL}\right]w(t) \tag{4}$$

where θ is the wetting angle (rad), γ_{GL} is the gas to liquid surface tension parameter, and γ_{SL} is the solid to liquid surface tension parameter. Performing an energy balance of the melt pool

$$\begin{aligned}\rho c_l\dot{T}(t)V(t) + \rho\dot{V}(t)\left[c_s(T_m - T_0) + h_{SL} + c_l(T(t) - T_m)\right] = -\rho\frac{\pi}{4} w(t)h(t)v(t)c_s(T_m - T_0) + \\ \mu_Q Q(t) - \frac{\pi}{4} w(t)l(t)\alpha_s(T(t) - T_m) - \frac{\pi}{\sqrt[3]{2}}\left[w(t)h(t)l(t)\right]^{\frac{2}{3}}\left[\alpha_G(T(t) - T_0) + \varepsilon\sigma\left(T^4(t) - T_0^4\right)\right]\end{aligned} \tag{5}$$

where T is the average melt pool temperature (K), c_s is the solid material specific heat ($J/(kgK)$), T_m is the melting temperature (K), T_0 is the ambient temperature (K), h_{SL} is the specific latent heat of fusion–solidification (J/kg), c_l is the molten material specific heat ($J/(kgK)$), μ_Q is the

laser efficiency, Q is the laser power (W), α_s is the convection coefficient (W/m^2K), α_G is the heat transfer coefficient (W/m^2K), ε is the surface emissivity, and σ is the Stefan–Boltzmann constant (W/m^2K^4). Using the steady–state solution for the conductive temperature distribution in a material subjected to an energy source moving at a constant velocity, the bead width–length relationship at the average temperature is given by the following elliptical relationship

$$l(t) = X(t) + 0.25\frac{w^2(t)}{X(t)} \quad with \quad X(t) = \max\left[\frac{w(t)}{2} \quad \frac{\mu_Q Q(t)}{2\pi k\left(T(t) - T_0\right)}\right] \tag{6}$$

where k is the thermal conductivity constant ($W/(mK)$). The steady–state and dynamic numerical solution to equations (1), (2), and (4)–(6) is addressed in Boddu *et al.* (2003).

Design of Feedback Linearization Controllers

Two LMD process controllers, based on feedback linearization, are presented in this section. The first controller is utilized to regulate the track width. Combining equations (1)–(3)

$$\dot{V}(t) = -\frac{1.5v(t)}{l(t)}V(t) + \frac{\mu_m}{\rho}m(t) = f_1 + g_1 m(t) \tag{7}$$

The state variable is track volume and the input variable is powder mass flow rate. The output equation is

$$y_1(t) = w(t) = \frac{6}{\pi h(t) l(t)}V(t) \tag{8}$$

While the state equation is linear in the state variable, the system has time–varying parameters that are known and, thus, may be canceled. Therefore, a feedback linearization control scheme is utilized. Since $\frac{\partial y_1}{\partial w} g_1 \neq 0$, the system has a relative degree of one and the following control law may be used

$$m(t) = \frac{a\left[w_r - w(t)\right] - f_1}{g_1} \tag{9}$$

where w_r is the reference track width (m) and a_1 is the controller parameter (s^{-1}). The control law in equation (9) cancels the time–varying dynamics and replaces them with first–order, time–invariant linear dynamics. The closed–loop system now has a time constant of a^{-1}, which may be selected by the designer.

The second LMD process controller is utilized to regulate the melt pool temperature. Combining equations (1) and (5), the temperature nonlinear state equation is

$$\begin{aligned}\dot{T}(t) = &-\frac{1}{\rho c_l V(t)}\left[\mu_m m(t) - \rho A(t) v(t)\right]\left[c_s\left(T_m - T_0\right) + h_{SL} + c_l\left(T(t) - T_m\right)\right] \\ &-\frac{\pi}{4c_l V(t)} w(t) h(t) v(t) c_s\left(T_m - T_0\right) - \frac{\pi}{4\rho c_l V(t)} w(t) l(t) \alpha_s\left(T(t) - T_m\right) \\ &-\frac{\pi}{\sqrt[3]{2}}\frac{1}{\rho c_l V(t)}\left[w(t) h(t) l(t)\right]^{\frac{2}{3}}\left[\alpha_G\left(T(t) - T_0\right) + \varepsilon\sigma\left(T^4(t) - T_0^4\right)\right] + \frac{1}{\rho c_l V(t)}\mu_Q Q(t) = f_2 + g_2 Q(t)\end{aligned} \tag{10}$$

The state variable is melt pool temperature and the input variable is laser power. The output equation is

$$y_2(t) = T(t) \tag{11}$$

The state equation is highly nonlinear and has time–varying parameters that are known and, thus, may be canceled. A feedback linearization control scheme is again utilized. Since $\frac{\partial y_2}{\partial T} g_2 \neq 0$, the system has a relative degree of one and the following control law may be used

$$Q(t) = \frac{b\left[T_r - T(t)\right] - f_2}{g_2} \tag{12}$$

where T_r is the reference melt pool temperature (K) and b is the controller parameter (s^{-1}). Again, the control law in equation (12) has canceled the time–varying dynamics and replaced them with first–order, time–invariant linear dynamics and the closed–loop system has a time constant given by b^{-1}, which may be selected by the designer.

SIMULATION STUDIES

A series of simulations are now conducted to analyze the feedback linearization controllers. The following parameters are taken from Doumanidis and Kwak (2001): $\rho = 7200\ kg/m^3$, $\mu_m = 0.92$, $\mu_Q = 0.58$, $T_0 = 292\ K$, $\theta = 90^0$, $c_l = 780\ J/(kgK)$, $h_{SL} = 2.45*10^5\ J/kg$, $T_m = 1673\ K$, $\alpha_s = 183\ W/(m^2K)$, $\sigma = 5.67*10^{-8}\ W/(m^2K^4)$, $\alpha_G = 24\ W/(m^2K)$, and $\varepsilon = 0.53$. To achieve the same simulation results presented in Doumanidis and Kwak (2001), the following parameters were found by trial and error: $k = 6.5\ W/(mK)$, $\gamma_{GL}–\gamma_{SL} = –0.00036$, $c_s = 1250\ J/(kgK)$,

The reference bead width is 4.5 *mm* and the reference melt pool temperature is 1773 *K* for all the simulations. In the first three simulations, the bead width controller given by equation (9) is implemented for three different values of the parameter a, the laser power is 1200 *W*, and the table velocity is 5 *mm/s*. The results are shown in Figures 1–3. For $a = 0.2$ and 0.5, the powder flow rate was decreased to perfectly track the reference bead width. As expected, the speed of response was smaller for the larger controller gain. However, for $a = 1$, the controller was unstable. The powder mass flow rate increased exponentially, the bead width went towards zero, and the bead height became unreasonably large. In the simulation, the minimum melt pool temperature is the ambient temperature since the LMD system cannot take energy out of the melt pool. The results demonstrate that the speed of response cannot be arbitrarily small. Also, it is interesting to note that the reference temperature was not tracked. This is to be expected since an arbitrary value of laser power was selected.

The next set of simulations are shown in Figures 4–6 where the melt pool temperature controller, given by equation (12), is implemented for $b = 0.2$, 0.5, and 24, respectively. The powder flow rate and the table velocity are constant values of 25 *g/min* and 5 *mm/s*, respectively. Again, the reference melt pool temperature was tracked in the steady–state and the speed of response decreased as the controller gain increased. However, the speed of response is limited as the system went unstable for $b = 25$ (not shown). Again, the reference bead width is not tracked since the powder flow rate was an arbitrary value.

In the next set of simulations, shown in Figures 7 and 8, the bead width controller and the melt pool temperature controller are implemented simultaneously. In the first simulation, $a = b = 0.5$ and the table velocity is a constant 5 *mm/s*. In the next simulation, $a = b = 0.2$, the table is

accelerated for part of the period, and the table is decelerated for part of the period. The exact table velocity and acceleration profiles are shown in Figure 8. Note that in implementation, the powder flow rate is calculated first since the laser power needs this value in its calculation. The controllers, when utilized together, are able to simultaneously regulate the bead width and melt pool temperature. The entire effect of the table acceleration does not appear in the differential equations and, thus, is not completely taken into account by either controller. However, the controllers are able to maintain the desired references after the table reaches a new constant velocity. Also, the table acceleration is seen to have much more impact on the bead dimensions than on the melt pool temperature.

SUMMARY, CONCLUSIONS, AND FUTURE WORK

This paper presented a nonlinear, multivariable control method to regulate the bead width and melt pool temperature in an LMD process. The controllers were applied to a simulation of the LMD process. The results demonstrate that the bead width and melt pool temperature can be regulated simultaneously, but there is a limitation on the closed–loop system's speed of response. If the controller gain is too large, instability will occur. Also, it was shown that table acceleration had a dramatic effect on the bead dimensions but not the melt pool temperature. Future work will be to validate the controllers experimentally and analytically determine their stability limits.

ACKNOWLEDGEMENTS

The author gratefully acknowledges the financial support of the National Science Foundation (DMI–9871185), Society of Manufacturing Engineers (#02022–A), Missouri Research Board, and UMR's Intelligent Systems Center.

REFERENCES

Boddu, M.R., Thayalan, V., and Landers, R.G., 2003, "Modeling for the Control of the Laser Aided Manufacturing Process (LAMP)," in *Fourteenth Annual Solid Freeform Fabrication Symposium*, Austin, Texas, August 4–6.

Derouet, H., Sabatier, L., Coste, F., and Fabbro, R., 1997, "Process Control Applied to Laser Surface Remelting," *Proceedings of ICALEO*, Sec. C, pp. 85–92.

Doumanidis, C. and Kwak Y–M., 2001, "Geometry Modeling and Control by Infrared and Laser Sensing in Thermal Manufacturing with Material Deposition," *ASME Journal of Manufacturing Science and Engineering*, Vol. 123, No. 1, pp. 45–52.

Doumanidis, C. and Skoredli, E., 2000, "Distributed–Parameter Modeling for Geometry Control of Manufacturing Processes with Material Deposition," *ASME Journal of Dynamic Systems, Measurement, and Control*, Vol. 122, No. 1, pp. 71–77.

Fang, T. and Jafari, M.A., 1999, "Statistical Feedback Control Architecture for Layered Manufacturing," *Journal of Materials Processing and Manufacturing Science*, Vol. 7, pp. 391–404.

Koomsap, P., Prabhu, V.V., Schriempf, J.T., Reutzel, E.W., 2001, "Simulation–Based Design of Laser–Based Free Forming Process Control," *Journal of Laser Applications*, Vol. 13, No. 2, pp. 47–59.

Li, L., Hibberd, R.H., and Steen, W.M, 1987a, "In–Process Laser Power Monitoring and Feedback Control," *4th International Conference of Lasers in Manufacturing*," pp. 165–176.

Li, L., Steen, W.M., Hibberd, R.H., and Weerasinghe, V.M., 1987b, "Real–Time Expert Systems for Supervisory Control of Laser Cladding," *Proceedings of ICALEO*, pp. 9–15.

Mazumder, J., Schifferer, A., and Choi, J., 1999, "Direct Materials Deposition: Designed Macro and Microstructure," *Materials Research Innovation*, Vol. 3, pp. 118–131.

Morgan, S.A., Fox, M.D.T., McLean, M.A., Hand, D.P., Haran, F.M., Su, D., Steen, W.M., and Jones, J.C., 1997, "Real–Time Process Control In CO_2 Laser Welding and Direct Casting: Focus and Temperature," *International Congress on Applications of Lasers and Electro–Optics*, Sec. F, pp. 290–299.

Munjuluri, N., Agarwal, S., and Liou, F.W., 2000, "Process Modeling, Monitoring and Control of Laser Metal Forming," *Eleventh Annual Solid Freeform Fabrication Symposium*, Austin, Texas.

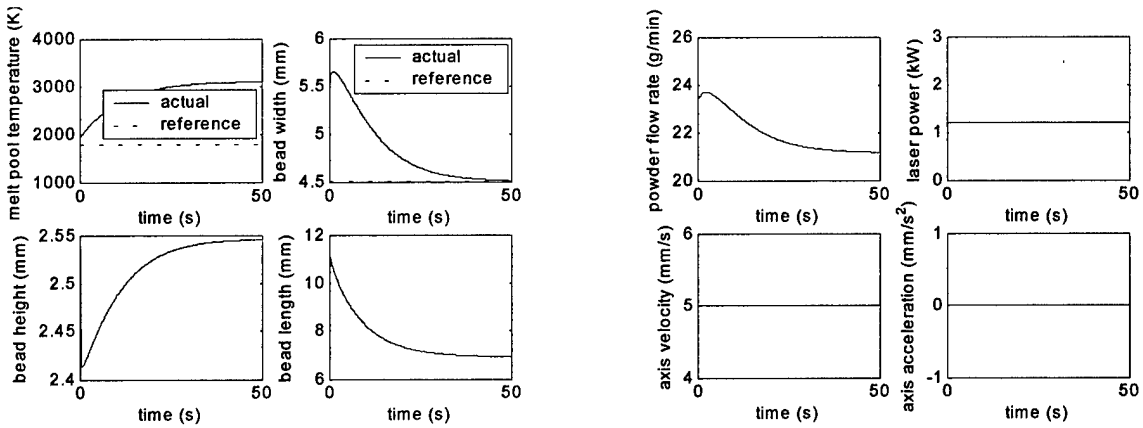

Figure 1: Bead Width Control with $a = 0.2$.

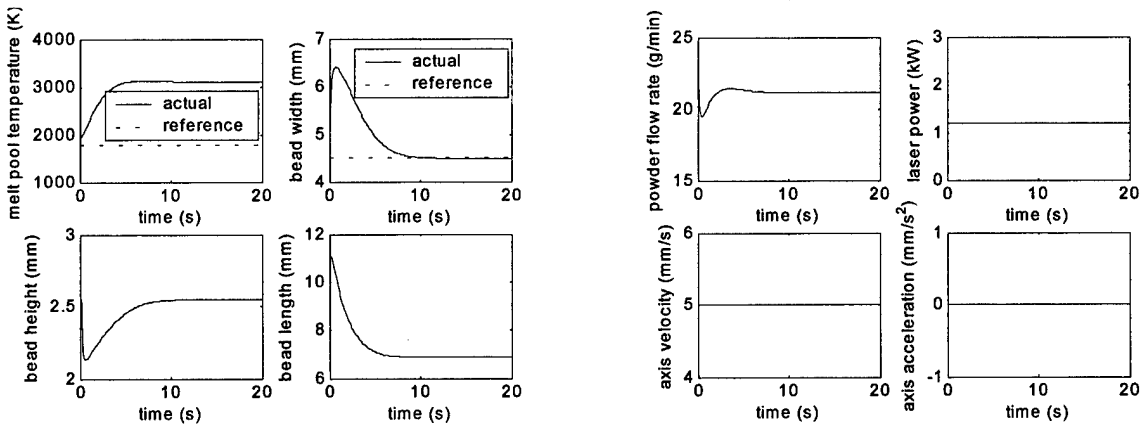

Figure 2: Bead Width Control with $a = 0.5$.

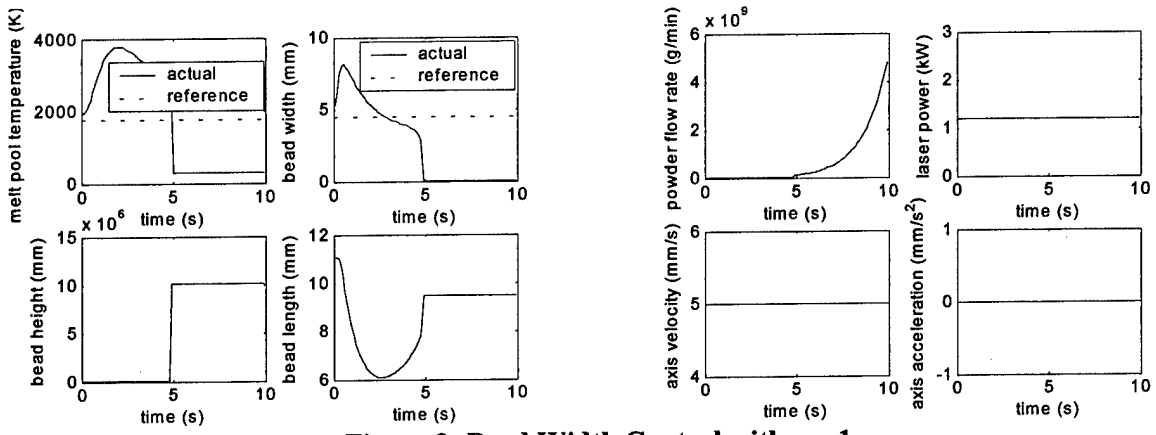

Figure 3: Bead Width Control with $a = 1$.

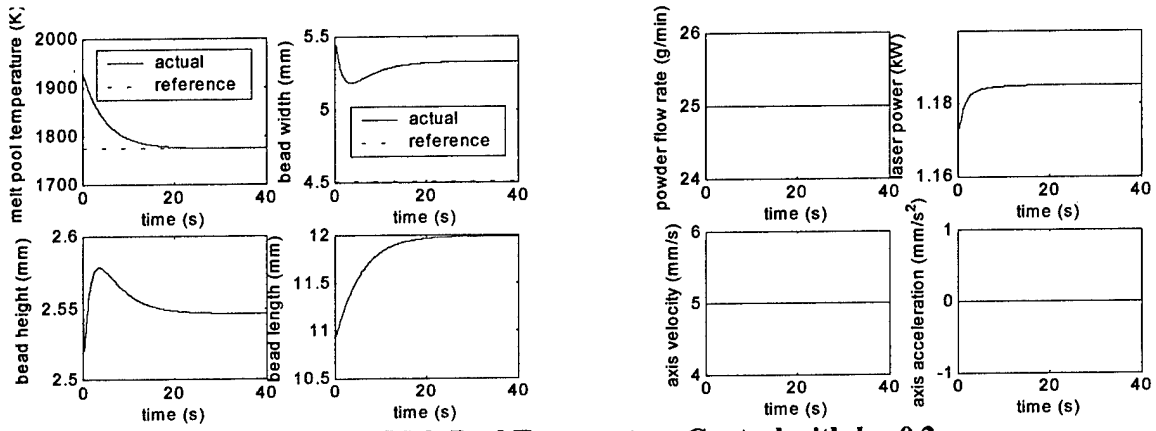

Figure 4: Melt Pool Temperature Control with $b = 0.2$.

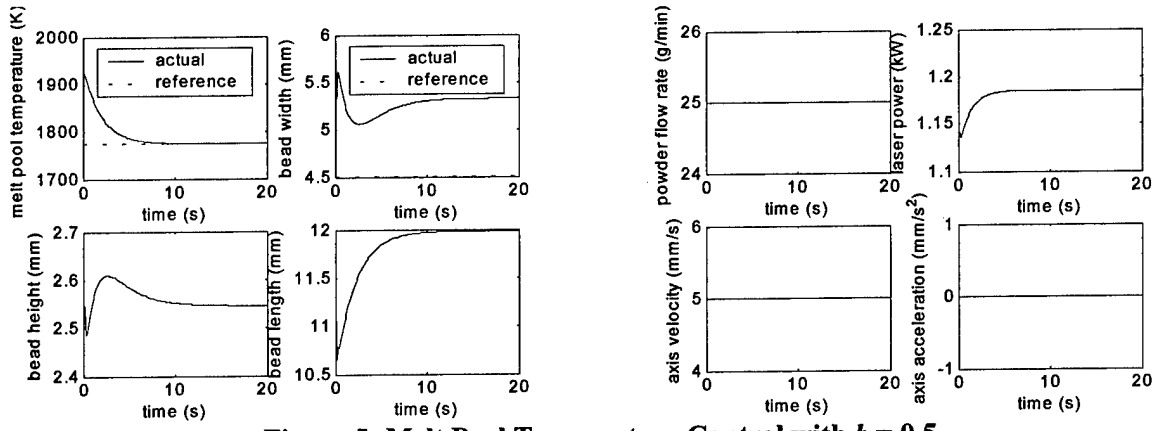

Figure 5: Melt Pool Temperature Control with $b = 0.5$.

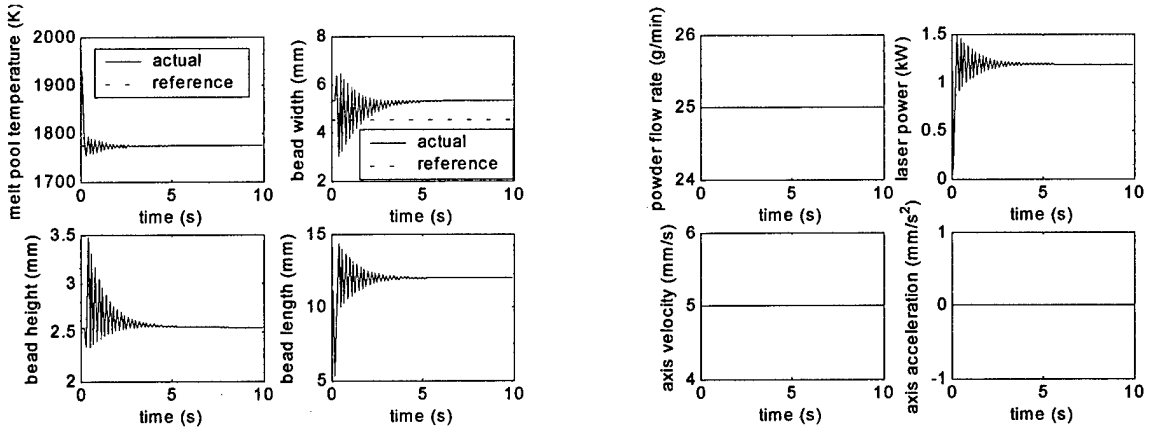

Figure 6: Melt Pool Temperature Control with $b = 24$.

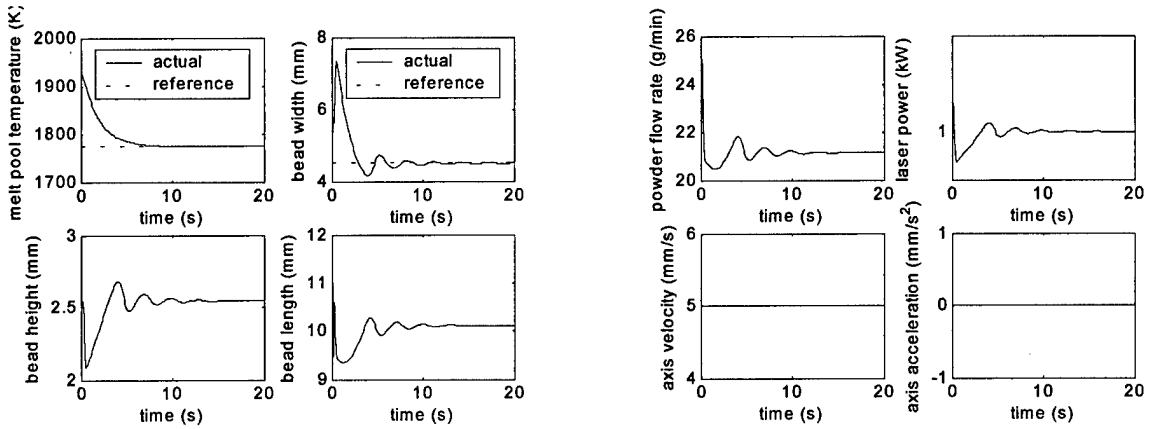

Figure 7: Temperature and Bead Width Control with Constant Table Velocity ($a = b = 0.5$).

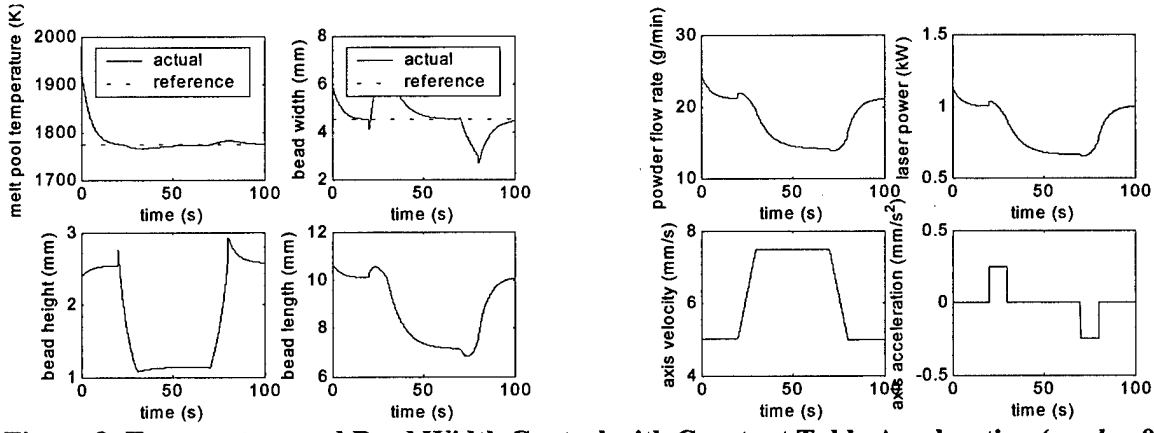

Figure 8: Temperature and Bead Width Control with Constant Table Acceleration ($a = b = 0.2$).

Application of a Diagnostic Tool in Laser Aided Manufacturing Processes

Sashikanth Prakash, Mallikharjuna Rao Boddu and Frank Liou
Department of Mechanical, Aerospace and Engineering Mechanics
University of Missouri - Rolla
Reviewed, accepted August 19, 2003

Abstract

Lasers play a vital role in producing parts with high dimensional accuracy, strength and quality in today's rapid prototyping industry. In the process of Laser Metal Deposition, many problems are encountered where the part quality does not meet the required standards. This could be due to the nonconformity of control parameters or unnecessary interactions between the control factors. This paper discusses the implementation of Dr. Genichi Taguchi's optimization techniques using Design of Experiments (DOE) where a series of fractional factorial experiments are performed on the laser deposition process. The results from these experiments are evaluated with respect to the rate of deposition alongside the part quality and the optimized level setting of control parameters are determined efficiently. This tool can be used to detect and diagnose flaws and discrepancies in the Laser Metal Deposition process and optimize it accordingly.

Introduction

Laser Metal Deposition (LMD) is a process where metal powder is focused on a substrate and a laser beam melts the powder and deposits it. It is possible to convert any part into a series of slices and each slice can be deposited by the above method accurately (layered deposition) and the whole part can be fabricated. The advantage of this process is that complex geometries can be constructed with high degrees of accuracy to achieve near net shape with a solid model of the part. The Laser Aided Material Processing system (LAMP, shown in figure 1) at the University of Missouri Rolla is primarily comprised of a 2.5 KW Nd: YAG Rofin Sinar laser (at TEM_{00}) with integrated 5-Axis FADAL CNC with a maximum spindle speed of 7500 RPM.

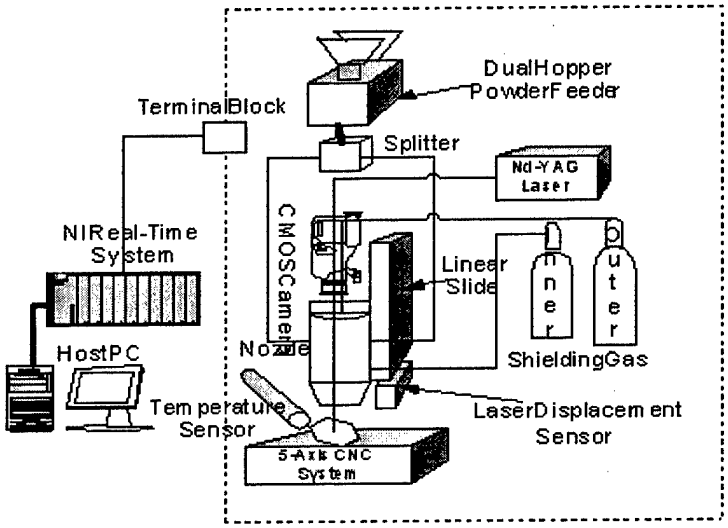

Figure 1. A Schematic of the Laser Aided Material Processing system (LAMP).

There is a coaxial screw feed dual powder delivery system that is capable of delivering two types of powder for Functionally Gradient Material parts. The 5-axis CNC ensures high part finish quality and can be used to remove any unwanted deposit. A schematic of the factor interrelationship is shown in figure 2.

This process has the capability of producing overhang parts and does not use support material because additional use of support increases the build time of the part and requires a time consuming post-processing. With a five-axis deposition integrated with five-axis machining, these obstacles are removed [1]. This paper deals with the testing of H13 powder deposited on H13 substrates and optimized for maximum build rate and at the same time, for having a good part quality. The hardness and the porosity will be used to evaluate part quality in this case study. There is a large range of layer thickness as well as deposition rates that can be achieved using laser deposition. The deposit rate can be increased by increasing the laser power, powder flowrate and the traverse speed. However, the requirement of a good part quality puts a limit on optimal deposition speeds. Both the layer thickness and the volume deposition rates are affected predominately by the specific energy and powder mass flow rate.
Here, specific energy (SE) is defined as:

$$SE = P/(Dv), \quad (1)$$

Where "P" is the laser beam power, "D" is the laser beam diameter and "v" is the process traverse speed. Also it is well known that actual laser power absorbed in the melt pool is not the same as nominal laser power measured from a laser power monitor due to absorptivity and other plasma related factors depending on the materials [2]. The use of adjusted specific energy is thus preferable. Considering the factors, it has been reported that there is a positive linear relationship between the layer thickness and adjusted specific energy for each powder mass flow rate [3].

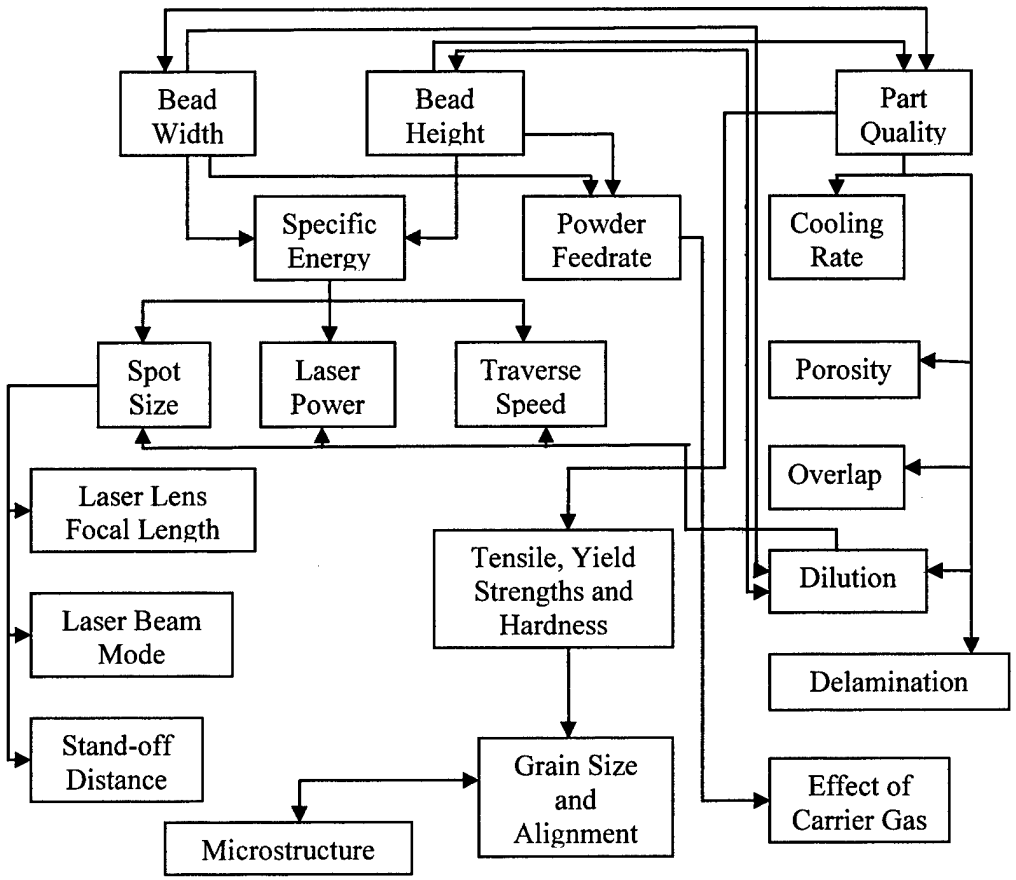

Figure 2. Schematic showing the basic laser deposition factor interrelations.

Design of Experiments - Taguchi Methods of Optimization

The Taguchi system of quality engineering is aimed at improving the robustness of a product and reducing the sensitivity to external variation. In other words, the part or product should perform as per customer expectations in the presence of various operational conditions. A special set of arrays called Orthogonal Arrays (also known as fractional factorial experiments) is used to optimize the processes. Not all the combinations of parameter levels are used to find out the best setting for a particular result, but a well defined combination that spans the whole set evenly is used. The main advantage is that an optimized result can be achieved in the least possible time.

Experimental Approach

The steps that were used in the implementation of the Taguchi methods are:

- Identifying the factors and interactions: A total of 7 factors were chosen in this process as shown in table 1.
- Identifying the levels of each factor: It was found that 3 factors were necessary to check the linearity in the variation. Moreover, there is a good chance of getting closer to the best values more quickly.
- Selecting an appropriate orthogonal array (OA): An orthogonal array "A" is defined as an "N * k" array with entries from the set "S" with a number of levels "s", strength "t" and index "λ"[4]. The arrays must be chosen according to the number of control parameters, their respective levels and the factors which interact with each other. The L18 was chosen for this experiment.
- Assigning the factors and interactions to columns of the OA: One column was allocated to measure the factor interactions and any other factors and errors that were not taken into consideration.
- Conducting the experiments: Three samples were used for each experiment for repeatability. Analyzing the data and determining the optimal levels – this is an important part of the whole process and helps in obtaining the optimized values depending on the output we choose to measure. In the analysis of data, Signal to Noise ratios (S/N) are used in controlling the target as well as reducing the variation about the target. The three types of Signal to Noise Ratio approaches are Nominal the Best, Smaller the Better and Larger the Better. Analysis of Variance (ANOVA) is used in this process is to calculate the percentage contribution of the control factors associated with the conclusions.
- Conducting the confirmation experiment: This is done to validate the accuracy of the experiment. If the predicted values that we obtain after optimization match the results from the confirmation experiment, then the experiment is valid.

Factor Level Selection

	Control Factors	Levels		
		1	2	3
1	Laser Power (P)	500	750	1000
2	Spot Size (D)	0.71	0.74	0.81
3	Inner gas pressure (IG)	3	4	-
4	Outer gas pressure (OG)	8	10	12
5	Feedrate (F)	20	25	30
6	Powder Flowrate (PF)	7.5	12.5	17.5
7	Percentage Overlap (O)	25	35	45

Table 1. Control factor levels and their values chosen for this experiment.

In order to determine the levels of the factors in the experiment, a series of experiments was conducted and it was ensured that there was a deposition and good bonding with the substrate. It can be noted that the inner gas pressure has only 2 levels and the other factors have 3 levels (table 1). The Degrees of Freedom (DOF) that we need to conduct for this experiment is 13. So it is appropriate to use the L18 orthogonal array for the experiment as shown in figure 4. Three samples were made for each experiment for repeatability hence the overall DOF for the control factors changes to 39. The main goal is to improve the deposit build rate and also maximize hardness (maximum of 120 in the Rockwell B scale) and minimize the porosity. These characteristics are combined into a single yardstick known as an Overall Evaluation Criterion (OEC) which is to be used to weight the output of the various combinations of the factors. The different values are first normalized and a weight is allotted to each characteristic to ensure a single standard is followed throughout the experiment. It is important to note that the deposits were four layers and had a square area with zigzag deposition pattern for subsequent layers.

Inner Gas pressure PSI	Laser Power Watt	Feedrate IPM	Powder Flow rate g/min	Outer gas pressure PSI	Spot Size mm	Overlap Factor %	Error
1	1	1	1	1	1	1	1
1	1	2	2	2	2	2	2
1	1	3	3	3	3	3	3
1	2	1	1	2	2	3	3
1	2	2	2	3	3	1	1
1	2	3	3	1	1	2	2
1	3	1	2	1	3	2	3
1	3	2	3	2	1	3	1
1	3	3	1	3	2	1	2
2	1	1	3	3	2	2	1
2	1	2	1	1	3	3	2
2	1	3	2	2	1	1	3
2	2	1	2	3	1	3	2
2	2	2	3	1	2	1	3
2	2	3	1	2	3	2	1
2	3	1	3	2	3	1	2
2	3	2	1	3	1	2	3
2	3	3	2	1	2	3	1

Table 2. The actual experimental layout of the L18 array.

The above setup (table 2) is a typical L18 array. It should be noted that there is a separate column attributed to the errors. This error column was added mainly to take into account the interactions and unaccountable noise factor effects that would affect the performance of the system. The main emphasis was to reduce the effect of the errors or variations and make the system more robust to these error variations and produce the expected result even in the presence of these errors. The array was set up and quality characteristics for the various combinations of control factors and their various levels were calculated and then the mean, standard deviation, and signal to noise ratios for the noise as well as the control factors were computed. The signal to noise ratio for the "Larger the Better" case was considered for the build rate and the hardness. The three quality characteristics were then combined to form a single Overall Evaluation Criterion (OEC) and used for comparison and further calculations.

Formulation of the Overall Evaluation Criterion

It is quite common to encounter a situation where there is more than one Quality Characteristic (QC). It is possible to analyze the QCs separately, but it cannot be guaranteed that a single common optimized result will be achieved. It would more often be different and contradicting. This emphasizes the use of what is called an Overall Evaluation Criterion. In this case a certain relative weight percentage must be allocated to each QC subjectively during the experiment planning session. The different QCs are adjusted in such a way that they give rise to a QC that is either Smaller the Better (STB) or Larger the Better (LTB). To combine the different QCs into a single OEC, they must be normalized first and then weighted. The Nominal the Best (NTB) QC must be modified to represent the deviation from the nominal value which would become STB [5]. In this case the build rate, hardness and the porosity were given a weight percentage of 40, 40 and 20 respectively. To simplify the experimental array, the individual sample readings have not been shown in the experiment table (table 3). There were three readings taken for each quality characteristic on each sample. Only their mean values are shown in the table. The OEC is formulated as a LTB case for all three characteristics. The hardness was measured in the Rockwell B scale, the build height and width were measured in an optical microscope and the time was calculated from the NC code for the deposition. The build rate was calculated as build volume per unit time in mm^3/s. The porosity was viewed at 500X resolution and measured by a ranking system from a scale of 1 to 10.

Here the OEC was formulated as follows [5]:

$$OEC = \left\{ \frac{QC_a - QC_{\min(a)}}{QC_{\max(a)} - QC_{\min(a)}} * W_a\% \right\} + \left\{ \frac{QC_b - QC_{\min(b)}}{QC_{\max(b)} - QC_{\min(b)}} * W_b\% \right\} \ldots\ldots \quad (2)$$

The above equation is for a larger the better case where QC_a is the performance value of "a", QC_b is the performance value of "b", QC_{max} & QC_{min} are the best and the worst performance values of the respective QCs and W_x is the weight percentage allotted to the QC "x". For a smaller the better case, we can modify the above equation to suit a larger the better case as shown below [5]:

$$OEC = \left\{ \frac{QC_a - QC_{\min(a)}}{QC_{\max(a)} - QC_{\min(a)}} * W_a\% \right\} + \left\{ \left(1 - \frac{QC_{\max(b)} - QC_{(b)}}{QC_{\max(b)} - QC_{\min(b)}} \right) * W_b\% \right\} + \ldots \quad (3)$$

In equation 3, characteristic "b" is smaller the better whereas the OEC is formulated for larger the better approach. For NTB approaches, it must be noted that the OEC will be evaluated based on the magnitude of deviation from the nominal value. This magnitude must be made to be smaller the better. This can be easily reformulated to fit larger the better as shown above [5].

Experiment

Trial	IG	P	F	PF	OG	D	O	INT	Avg.	Avg.	Avg.	OEC 1 - 40:40:20		OEC 2 - 33:34:33	
No.	PSI	Watt	IPM	g/min	PSI	mm	%		Build rate	Hardness	Porosity	Mean	S/N Ratio	Mean	S/N Ratio
1	3	500	20	7.5	8	0.71	25	1	2.99	95.80	6.33	12.58	26.76	16.03	28.87
2	3	500	25	12.5	10	0.74	35	2	5.21	99.30	7.33	38.15	36.40	45.60	37.95
3	3	500	30	17.5	12	0.81	45	3	6.73	117.70	5.67	60.30	40.38	50.29	38.80
4	3	750	20	7.5	10	0.74	45	3	3.39	116.40	6.67	53.90	39.40	52.91	39.24
5	3	750	25	12.5	12	0.81	25	1	5.98	106.80	7.33	54.61	39.52	59.27	40.23
6	3	750	30	17.5	8	0.71	35	2	11.05	116.00	6.67	85.59	43.42	79.87	42.82
7	3	1000	20	12.5	8	0.81	35	3	7.80	111.20	7.67	73.38	42.08	77.69	42.58
8	3	1000	25	17.5	10	0.71	45	1	9.68	118.40	7.67	94.03	44.24	94.93	44.32
9	3	1000	30	7.5	12	0.74	25	2	3.49	116.40	6.00	47.67	38.34	42.27	37.29
10	4	500	20	17.5	12	0.74	35	1	4.21	115.20	7.33	61.93	40.61	65.12	41.05
11	4	500	25	7.5	8	0.81	45	2	1.59	111.30	6.67	37.32	36.21	39.04	36.60
12	4	500	30	12.5	10	0.71	25	3	5.04	108.40	6.67	46.76	38.17	47.19	38.25
13	4	750	20	12.5	12	0.71	45	2	3.10	115.80	7.33	58.28	40.08	61.99	40.62
14	4	750	25	17.5	8	0.74	25	3	6.69	117.80	6.67	70.32	41.71	66.80	41.27
15	4	750	30	7.5	10	0.81	35	1	1.59	111.70	6.67	38.02	36.37	39.61	36.73
16	4	1000	20	17.5	10	0.81	25	2	7.30	106.20	7.00	55.80	39.70	57.64	39.99
17	4	1000	25	7.5	12	0.71	35	3	2.45	115.70	7.33	55.38	39.64	59.53	40.27
18	4	1000	30	12.5	8	0.74	45	1	7.26	118.50	6.33	70.66	41.75	64.39	40.95
											Total	**1014.7**	**704.79**	**1020.2**	**707.80**
											Mean	**56.37**	**39.15**	**56.68**	**39.32**

Table 3. The experimental array with the measured performance statistics and S/N ratio.

From table 3, we can see that there is an attempt made to evaluate another OEC with 33:34:33 weightage. This was done to study the change in the optimal values when all QCs are given equal importance. The OEC 2 can be used only if the part quality is of primary importance. It is also important to note that the optimal level settings may not be the same for different QCs. The optimal combination for hardness may differ from that of porosity. When both are used, there would be a trade-off in the result obtained.

Analysis of the Means (ANOM)

The Analysis of the Means (ANOM) is conducted basically to do a two step optimization. This is done by first reducing the variation in the process (using the S/N ratio and maximizing the slope) and then shifting the mean or target performance to get the best output. The ANOM was conducted next and the factor level plots were constructed. The levels of the control factors with the highest S/N ratio were used in verification of the predicted values for the confirmation experiment [6]. The ANOM tables for the mean and the Signal to Noise ratio are shown below (tables 4 and 5).

	Inner Gas pressure	Laser Power	Feedrate	Powder Flow rate	Outer gas pressure	Spot Diameter	Overlap Factor
Mean	PSI	Watt	IPM	g/min	PSI	mm	%
1	**57.80**	42.84	52.64	40.81	**58.31**	**58.77**	47.96
2	54.94	60.12	**58.30**	56.97	54.44	57.10	58.74
3	-	**66.15**	58.17	**71.33**	56.36	53.24	**62.41**

Table 4. ANOM for the Means.

	Inner Gas pressure	Laser Power	Feedrate	Powder Flow rate	Outer gas pressure	Spot Diameter	Overlap Factor
S/N	PSI	Watt	IPM	g/min	PSI	mm	%
1	38.95	36.42	38.11	36.12	38.66	38.72	37.37
2	**39.36**	40.08	39.62	39.67	39.05	**39.70**	39.75
3	-	**40.96**	**39.74**	**41.68**	**39.76**	39.04	**40.34**

Table 5. ANOM for the Signal to Noise Ratios.

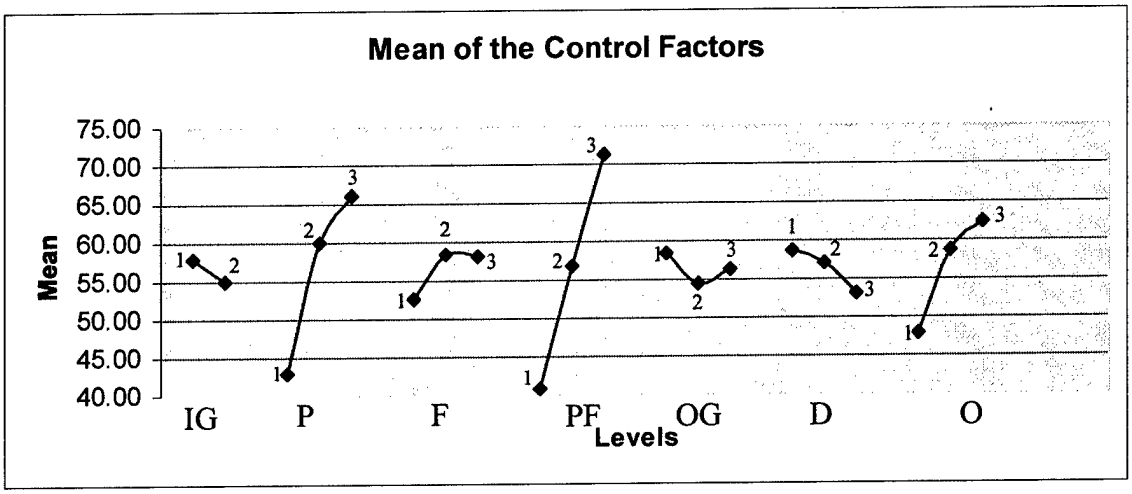

Figure 3. Factor Effect Plots for the Means.

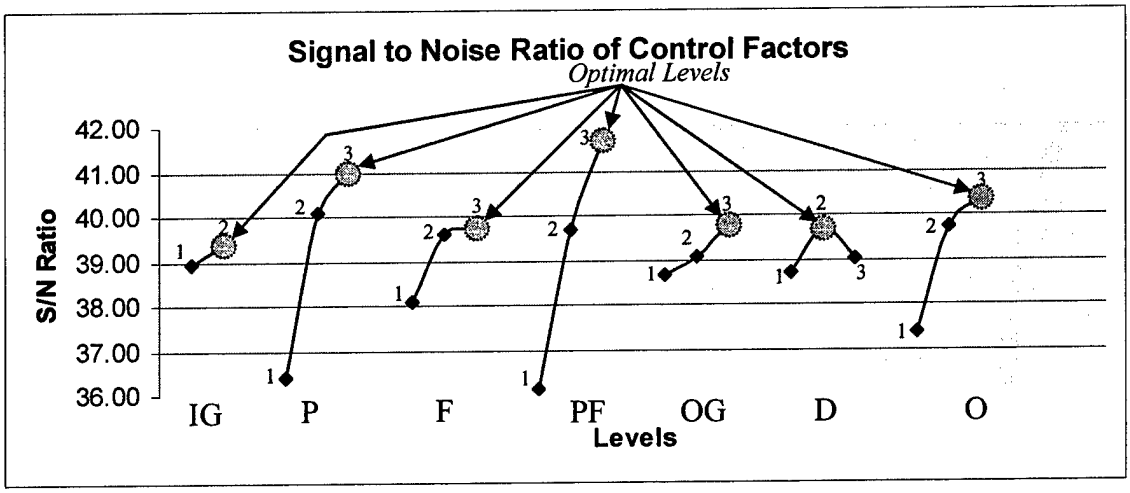

Figure 4. Factor effect Plots for the Signal to Noise Ratios.

In the above figures (3 and 4), IG / OG are Inner Gas / Outer Gas (PSI), P is Laser Power (W), F is the Feedrate (IPM), PF is the Powder Flowrate (g/min), D is the Spot Diameter (mm), O is the Overlap (%) and INT denotes the Interactions and Noises (their effects and percentage contributions would be calculated for further evaluation).

Optimal Levels

From the plots and the Analysis of the Means, it was found that the optimal levels that are required to produce the given OEC 1 are IG_2= **4 PSI**, P_3 = **1000W**, F_3 = **30 IPM**, PF_3 = **17.5 g/min**, OG_3 = **12 PSI**, D_2 = **0.74mm** and O_3 = **45%**. With these optimal levels the expected performance should be predicted and the confirmation experiment should be carried out to verify the validity of the results.

From OEC 2, the study of the ANOM shows that the optimal levels remain the same except for the Feed rate and the Overlap factor. It must also be noted that there are only slight differences in the S/N ratio values of those control factors.

Predictive Model

The predictive model is constructed from the ANOM results and is formed by considering the optimum level contribution of each factor to the deviation from the overall mean value for the experiment. The general formula for a predictive value is given below: [6]

$$y(A,B,C,D) = \overline{y} + (\overline{y_A} - \overline{y}) + (\overline{y_B} - \overline{y}) + (\overline{y_C} - \overline{y}) + \ldots \quad (4)$$

Where, y is a Quality Characteristic and A, B, C, etc. are the control factors.

In this experiment the predicted value for the S/N ratio was calculated to be **45.6** and the results of the confirmation experiment showed an S/N ratio of **45.2** which showed that the experiment was valid.

Analysis of Variance (ANOVA)

ANOVA is a statistically based decision making tool used for detecting any discrepancies in the average performances of the groups of data tested. ANOVA breaks down total variation into comprehendible sources. In other words it enables us to quantitatively estimate the relative contribution each control factor makes to the overall performance. This contribution is expressed as a percentage. The importance of each control factor is measured by comparing the variance between the control factor effects with that of the experimental data. Here a mathematical technique known as the Sum of Squares (SS) is used to measure the deviation of the control factor effects on the average response quantitatively, from the overall experimental mean response. The effects of random experimental error can also be determined in this process. The basic steps involved in ANOVA are firstly determining the Grand Total Sum of Squares (GTSS). The GTSS is comprised of the overall experimental mean (or) the Sum of Squares due to the mean which is given by [6]:

$$GTSS = \sum_{i=1}^{N} (S/N)_i^2 \quad (5)$$

And the Sum of Squares due to the variation about the mean (or) the total Sum of Squares is given by [6]:

$$Total\ SS = \sum_{i=1}^{N} (S/N_i - \overline{S/N})^2 \quad (6)$$

It is important to note that GTSS = Total SS + SS due to the mean (See table 6).

	$(dB)^2$
Grand Total Sum of Squares	27845.98
Total Sum of Squares	250.27
Sum of Squares due to the Mean	27595.71

Table 6. The Sum of Square values obtained from the experiment.

The Sum of Squares due to variation about the mean for a Factor A can be given as [6]:

$$SS_A = \begin{pmatrix} (\text{Number of experiments at } A_{\text{Level 1}}) * (\overline{S/N}_{\text{Level 1}} - \overline{S/N})^2 + \\ (\text{Number of experiments at } A_{\text{Level 2}}) * (\overline{S/N}_{\text{Level 2}} - \overline{S/N})^2 + \\ \ldots + (\text{Number of experiments at } A_{\text{Level N}}) * (\overline{S/N}_{\text{Level N}} - \overline{S/N})^2 \end{pmatrix} \quad (7)$$

Percentage Contribution of Parameters

The percentage contribution is the portion of the total variation that was observed in an experiment and is attributed to each significant factor and/or interaction. It is a function of the sums of squares of each factor. If the factor and/or interaction levels were controlled precisely, then the total variation would reduce by the amount indicated by the percentage contribution. The percentage contribution due to error provides an estimate of the adequacy of the experiment. It is given by [6]:

$$Percentage\ Contribution = (SS_{factor} / Total\ SS) * 100 \quad (8)$$

SS for Factors		Percentage Contribution
SS_{IG}	0.77	0.31
SS_P	69.52	27.78
SS_F	9.92	3.96
SS_{PF}	95.00	37.96
SS_{OG}	3.75	1.50
SS_D	3.02	1.21
SS_O	29.81	11.91
SS_{INT}	12.42	4.96
SS_{Error}	26.08	10.42

Table 7. Sum of Squares due to each factor and their Percentage Contribution.

From the Percentage Contributions (table 7 and figure 5) we may note that there are more unaccountable errors contributing around 10.4% to the overall variation along with the 4.96% of assumed interactions and uncontrolled noises. This is attributed to three main causes:

- Uncontrollable noise factors.
- Factors which are not included in the experiment and
- Experimental error [5] [7].

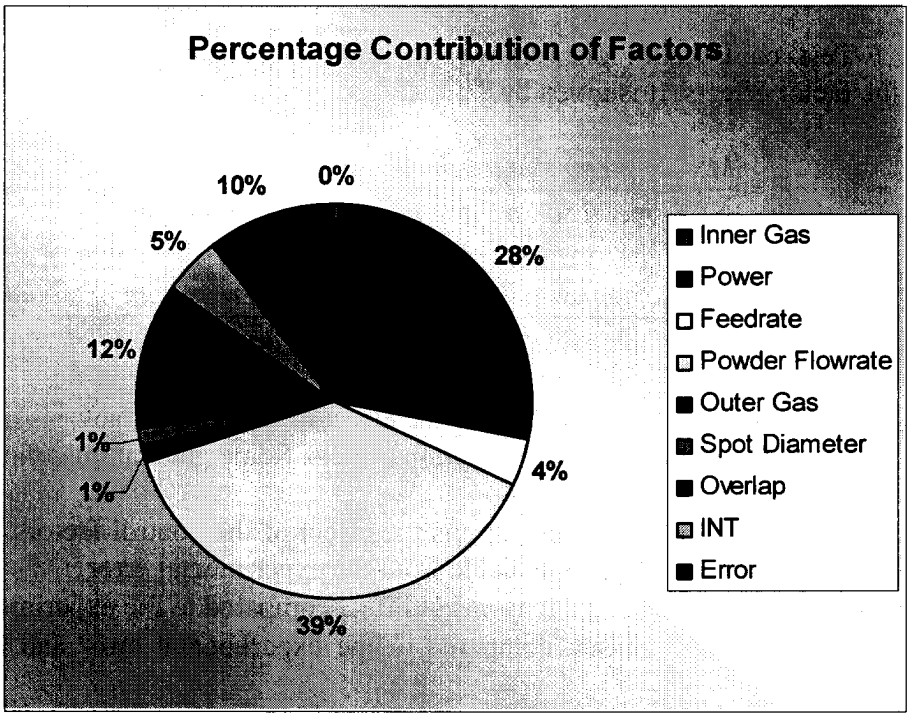

Figure 5. Pie chart showing the Percentage Contributions.

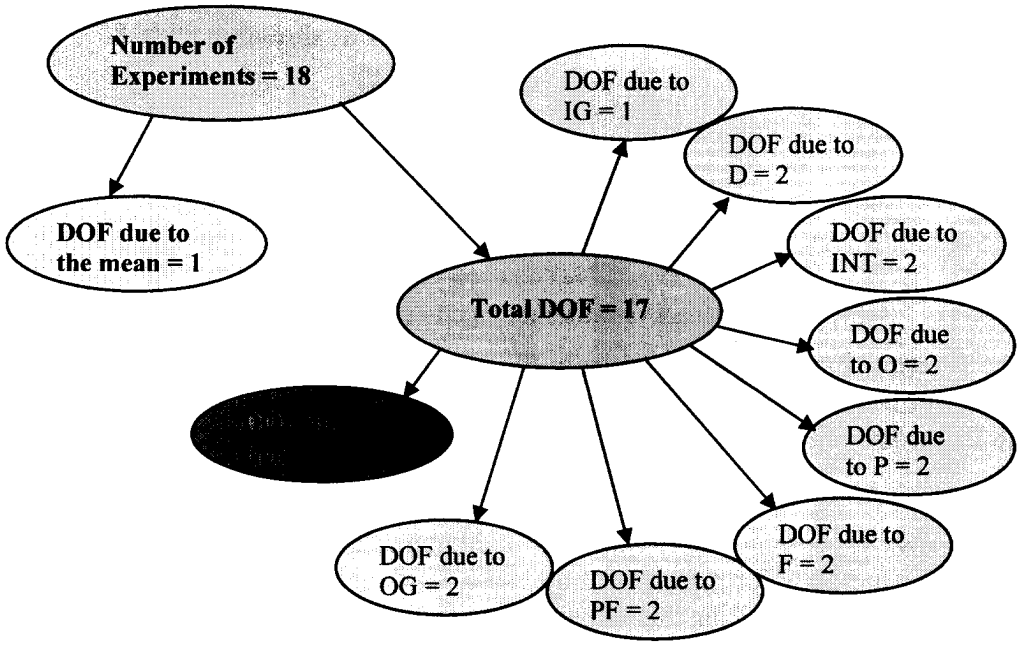

Figure 6. Schematic of the Degree of Freedom decomposition [6].

From figure 6, it is found that the DOFs due to all the factors taken into consideration are two less than the total DOF. This means that there are experimental errors and unknown or uncontrollable factor contributions worth two DOFs [7]. In this situation, it is necessary to do an F-Test to validate the importance of the control factors and prove that they can still control the process in the presence of these errors and variations.

F- Test

The F-Test or F-Ratio, also known as the variance ratio, is used to test the significance of the factor effects. It is given by [6]:

$$F = \frac{MS}{S_e^2} = \frac{mean\ square\ due\ to\ a\ control\ factor}{mean\ square\ due\ to\ experimental\ error} \tag{9}$$

$$\text{Where, } MS = \frac{factor\ effect\ sum\ of\ squares}{factor\ degrees\ of\ freedom} \quad (9.1) \quad \& \quad S_e^2 = \frac{error\ sum\ of\ squares}{error\ degrees\ of\ freedom} \quad (9.2)$$

When the value of F is more than 1, then the effect of the control factor is more than the variance due to experimental error and the interaction effects. Some general guidelines for the F-Ratio are [6]:

- F<1, then the experimental error outweighs the effect of the control factors. The control factors will be trivial and indistinguishable from the experimental error.
- F≈2, the control factor only has a reasonable effect compared to the experimental error.
- F>4, the control factor is strong compared to the experimental error and is obviously significant.

It is recommended to pool the insignificant control factors with the error. This makes it possible to calculate the contribution of the significant control factors more effectively [6] [7]. In this experiment, laser power, powder flow rate and overlap will be counted as significant factors and the remaining factors will be pooled together as the error as shown in table 8.

Factors	Mean Square
S_e^2	5.08609
MS_P	34.75926
MS_{PF}	47.49824
MS_O	14.90408

Table 8. Mean Square values for the significant factors and the error.

The F ratios that are calculated from the above values (F_P = 6.8, F_{PF} = 9.3& F_O = 2.9) show that Laser Power and Powder Flowrate are clearly significant when compared to the errors and Overlap factor has only a reasonably significant effect on the errors.

Conclusion

The LAMP process at UMR was optimized using the Design of Experiments approach based on Taguchi's methods for maximum build rate, hardness and minimum porosity within the level settings that were decided for this experiment. The control factor interactions were studied and it was shown that the contribution of some control factors namely the laser power, the overlap factor and the powder flowrate are significant and the optimal levels for this experiment were determined. The contribution of the errors which include the experimental error, error due to interactions between factors and error due to uncontrollable noises were also studied and the system was made robust to these variations. A comparative study was also done with equal weightage for all the Quality Characteristics and the optimal values were not found to vary by much.

It is required that this process be further improved. This can be done by using the results of this experiment and conducting iterative experiments to hone in on the best possible level values of the control parameters that are least sensitive to the variations and are more improved and repeatable.

References

1. Liou, F. W., Choi, J., Landers. R. G., *et al.,* "Research and Development of a Hybrid Rapid Manufacturing Process", *Twelfth Annual Solid Freeform Fabrication Symposium*, Austin, Texas, August 6–8, 2001, pp. 138–145.
2. Duley W. W., "Laser Processing and Analysis of Materials", Plenum Press, New York, 1983, pp. 69-78.
3. Mazumder J., Choi J., Nagarathnam K., Koch J., and Hetzner D., "The Direct Metal Deposition of H13 Tool Steel for 3-D Components", JOM, 49(5), 1997, pp. 55-60.
4. Hedayat, A. S.; Sloane, N. J. A.; and Stufken, J. "Orthogonal Arrays: Theory and Applications". New York: Springer-Verlag, 1999.
5. Ranjit, K. Roy, "Design of Experiments using the Taguchi Approach – 16 Steps to Product and Process Improvement", John Wiley & Sons, Inc., 2001.
6. William Y. Fowlkes, Clyde M. Creveling, "Engineering Methods for Robust Product Design Using Taguchi Methods in Technology and Product Development", Addison Wesley Publishing Company, Massachussets, 1998.
7. Ross, R. J. "Taguchi Techniques for Quality Engineering", McGraw-Hill, New York, 1989.

Acknowledgments

This research was supported by the National Science Foundation Grant Number DMI-9871185, Missouri Research Board, and Army Research Office. Their support is gratefully appreciated.

The authors would also like to thank Gail Richards for proofreading the paper and enhancing its overall quality.

Design of a customized multi-directional layered deposition system based on part geometry.

Prabhjot Singh, Yong-Mo Moon, Debasish Dutta, Sridhar Kota

Abstract

Multi-Direction Layered Deposition (MDLD) reduces the need for supports by depositing on a part along multiple directions. This requires the design of a new mechanism to re-orient the part, such that the deposition head can approach from different orientations. We present a customized compliant parallel kinematic machine design configured to deposit a set of part geometries. Relationships between the process planning for the MDLD of a part geometry and considerations in the design of the customized machine mechanism are illustrated. MDLD process planning is based on progressive part decomposition and kinematic machine design uses dual number algebra and screw theory.

1. Introduction

The past decade has seen the development of numerous Layered Manufacturing (LM) techniques. The main advantage afforded by LM is its ability to produce geometrically complex parts without specialized tooling in a relatively short period of time. LM processes are characterized by the need for sacrificial structures to support overhanging regions of the part. This necessitates time consuming post-processing and degrades part quality.

Multi-Direction Layered Deposition (MDLD) Systems such as [3][4][5][7] build parts without supports by depositing a part along multiple directions. Depending on the process, either the deposition nozzle or the base table has multi-axis kinematics (refer Figure 1).

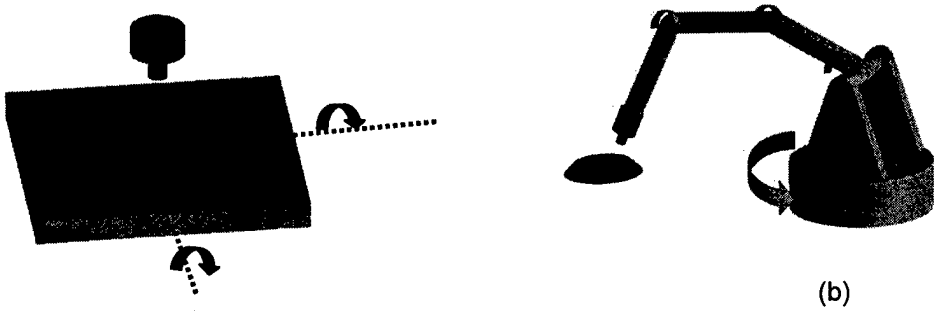

Figure 1: (a) Deposition Table with rotational and translational actuation (b) Deposition nozzle mounted on a multi-axis robotic arm.

This necessitates a mechanism with more than 3 degrees of freedom. A full 6 degree of freedom mechanism is expensive and is very often redundant for customers engaged in the design and fabrication of specific geometries. Recognizing this, recent research efforts such as [8][15] have proposed simplified kinematics for multi-direction deposition systems. While they have a distinct advantage over 2.5D LM systems, the fixed configuration of the nozzles/deposition table restricts support-less deposition to a few part geometries.

In this research we propose a cost effective method to achieve multi-direction deposition by using kinematics which are customized to fabricate a specific family of parts.

For a given geometric part family, our approach comprises of two tasks. The first task is the process planning underlying multi-direction layered deposition of a given member of the part family. The input part geometry is converted into sets of uniform parallel slices aligned along a set of vectors called the *build directions*. In the second task, slice geometry and build directions are used to derive the machine kinematics. Traditionally mechanism design has been a mixture of art and science. Researchers in the past have tried to classify, compile and codify basic elements of mechanisms in order to systematize the creative design process. In this research, we propose a compliant parallel kinematic machine (CPKM) design methodology [9][10]. The CPKM methodology synthesizes the mechanism using dual number algebra and screw theory. The synthesized mechanism has high accuracy because it uses compliant joints which are clearance and friction free mechanical component. A typical CPKM mechanism is shown in Figure 2.

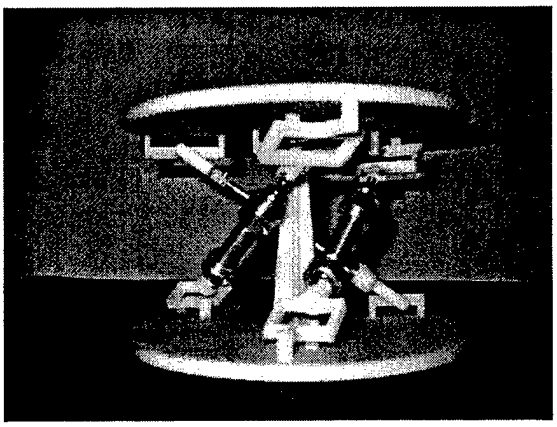

Figure 2: A deposition table constructed using the Compliant Parallel Machine Design Methodology

The remainder of the paper is organized as follows: Section 2 details the process planning methodology underlying the MDLD of a part. Section 3 presents a brief summary of the theory underlying CPKM and its relevance in the context of MDLD. In Section 4 we define an illustrative parametric part family along with its MDLD process planning. The output of the process planning information is used in

Section 5 to construct the kinematics of a CPKM. Section 6 concludes the paper with a summary of the research and directions for future research.

2. Process Planning Methodology for MDLD

A process planning framework for MDLD was proposed in an earlier publication [11]. It was assumed that the deposition nozzle is mounted on a multi-degree of freedom robotic arm. No other assumptions were made about the kinematics of the MDLD system. In [11] we addressed the core question in the analysis of multi-direction deposition systems, which is: how much of the part should be built in one direction and why? A brief overview of the process planning tasks is covered in this section. The reader is referred to [11] and [12] for further details.

Assuming that the initial orientation of the part is user defined, the following MDLD process planning tasks were identified:

1. Decomposition of the part volume.
2. Establishing the Build Directions.
3. Sequencing the Decomposed sub-volumes.

The overall strategy for multi-direction slicing involves the progressive decomposition of the part (P) into sub-volumes each of which can be completely built along a certain direction. The input to each stage of this progressive decomposition is an unprocessed sub-volume (V_{unproc}) of the part which is processed using two operations:

1. Find a build direction, $\overline{B}$.
2. Using $\overline{B}$ to decompose V_{unproc} into buildable and unbuildable sub-volumes.

The buildable part of V_{unproc} is classified as a processed sub-volume (V_{proc}) with $\overline{B}$ as its assigned build direction. The unbuildable sub-volume (V_{unproc}) forms the input to the next stage of the decomposition process. This stage-wise decomposition stops when:

$$\bigcup_i V_{proc_i} = Vol(P)$$

Where $Vol(P)$ is the volume of the part P.

2.1. Part Volume Decomposition

The overhang angle constraint as defined by Allen and Dutta [2] restricts the deposition of overhanging regions in LM. For a given build direction ($\overline{B}$), the part volume decomposition algorithm is concerned with the identification and disjunction of part volumes which can be built and those which cannot. The algorithm defines surface regions to be unbuildable when the angle between the surface normals and the build direction is greater than 90 degrees. Such unbuildable surface regions are

bounded by *silhouette edges* of the surface [6] when viewed from $-\overline{B}$, the opposite of the assigned build direction. Unbuildable part volumes are then identified by sweeping the unbuildable surface regions along $\overline{B}$ and subtracting the resulting swept volume from the part P. This is shown through an illustrative CAD model below (ref. Figure 3).

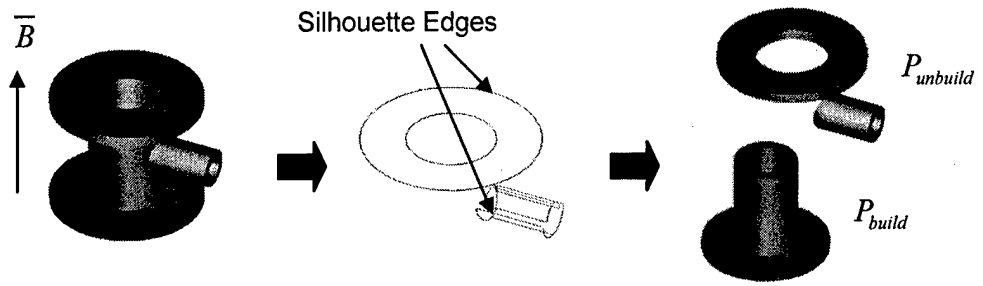

(a) Part Volume Decomposition

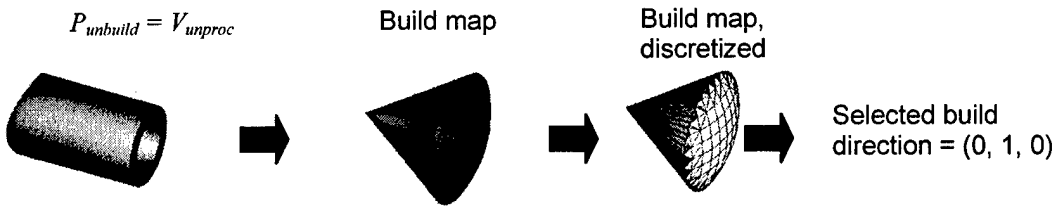

(b) Build Direction Determination

Figure 3: Part volume decomposition and build direction determination for MDLD.

2.2. Build Direction Determination

In this task a build direction is assigned to an unprocessed sub-volume. It involves both the identification of all feasible build directions and the selection of the best build direction. Any vector which makes an angle of 90 degrees or lesser with all surface normals of the part boundary is considered to be a feasible build direction. The set of all feasible build directions is called the *build map*. The best build direction (a member of the build map) minimizes the average weighted cusp height as defined by Alexander and Dutta in [1]. An illustrative build map of a part volume and the selected build direction for a CAD model is shown in Figure 3b.

2.3. Volume Sequencing

Layered deposition requires the presence of a base substrate. Using Figure 3a as a reference, P_{build} must be deposited before $P_{unbuild}$ since the base or the common face between the two sub-volumes lies on P_{build}. Consequently the deposition of $P_{unbuild}$ cannot

start till its base has been created, establishing P_{build}'s precedence in the deposition sequence.

The overall process planning algorithm for MDLD is summed up in the following flowchart (ref. Figure 4). As mentioned, the orientation of the part relative to the deposition table, i.e. the initial build direction ($\overline{B}$) is user defined. The build direction determination module and volume decomposition are applied recursively till the entire part is decomposed. These are succeeded by Part volume sequencing and slicing along assigned build directions ($\overline{B}$).

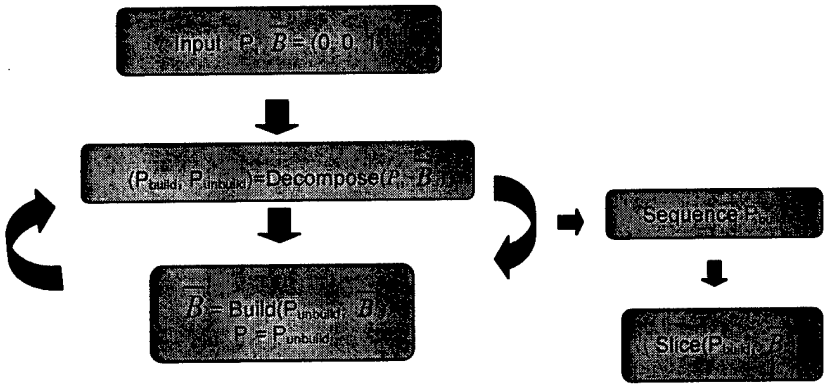

Figure 4: Overall algorithm for MDLD process planning

An illustrative CAD model with its volume decomposition is shown in Figure 4a. The model is consequently sliced as shown in Figure 4b. The initial build direction is chosen along the Z^+ axis.

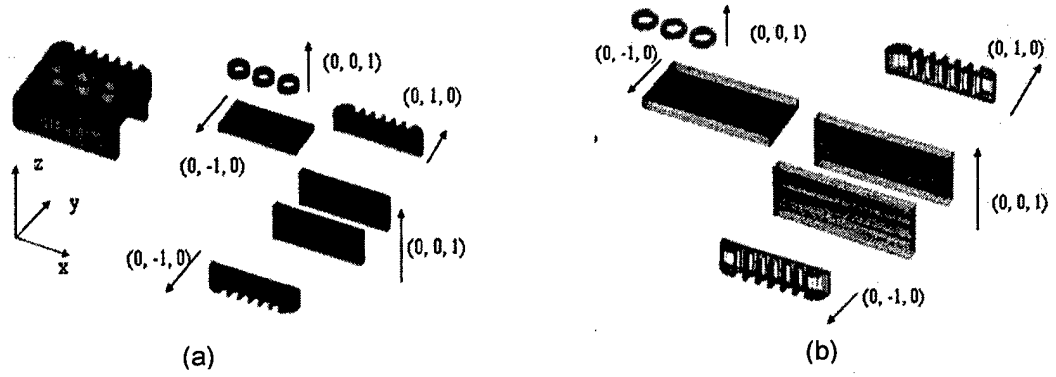

Figure 3: (a) A CAD model with its MDS decomposition and associated build directions (b) Slices of MDS subvolumes along selected build directions.

3. Mechanism Synthesis

A machine for MDLD is comprised of two parts; 1) X-Y printing overhang head unit, and 2) the workpiece orientation unit. Generic LM machines have an X-Y printing unit that has coordinated control in the X-Y direction and a separate control for the Z direction. To design the MDLM machine, we need to add the workpiece orientation unit that aligns the building direction to the Z axis of the head unit. This paper presents the design of the workpiece support unit that is using the compliant mechanisms.

Traditional mechanisms attain motion through the use of rigid links and discrete joints. They are ubiquitous in the world of machines and have been studied for centuries. Within the last several decades, there has been a growing interest in what have been termed compliant mechanisms. Unlike their rigid body counterparts, compliant mechanisms utilize the flexibility of their members to transmit or transform motion and forces. While traditional mechanisms are designed to be stiff and strong, compliant mechanisms are designed to be flexible and strong.

Not every problem is best solved with compliant mechanisms, but for applications better suited for compliant mechanisms, there are a number of significant benefits. They can be summarized as follows:

- *Assembly*: Compliant mechanisms are designed to be monolithic. Thus, there is a reduced need for mechanism assembly. In most cases, compliant mechanisms are designed to be coupled with actuators. This typically requires some assembly, but the number of parts is far less in comparison to traditional mechanisms.
- *No wear*: Compliant mechanisms attain mobility through deformation, and therefore do not experience wear. As such, there is a reduced need for maintenance such as lubrication. Also, failure occurs either from static or fatigue failure. These types of failure are more predictable than wear phenomena.
- *No backlash*: Due to the absence of discrete joints, compliant mechanisms do not suffer from backlash. As a result, high precision may be attained.
- *Energy storage*: Compliant mechanisms store elastic energy as they deform. This energy may be used to assist in applications requiring a return stage. There is a reduced need for springs and possible actuation.

The design of multi-degrees of freedom mechanism is not always been a simple task while maintaining the accuracy and stiffness of the mechanisms. One of the most popular design of spatial multi degrees of freedom mechanisms is parallel kinematic machines (PKM) which is know to have high stiffness. However, PKM has poor accuracy compare to the serial mechanisms and planar mechanisms since it needs more mechanical joints than the other mechanisms. In this paper, we are using the compliant joint [9] based parallel kinematic machines; CPKM (Compliant Parallel Kinematic Machines) so the mechanism has high stiffness without the accuracy problems.

The mechanism does not need the full six degrees of freedom since CPKM is customized around a parametric part family. In this paper, we take the building block approach to design a CPKM with less than six degrees of freedom [10].

CPKM is comprised of a top plate (end effector or work holding), a bottom plate, a constraining leg and active legs. The top plate holds the workpiece and the bottom plate is attached to the MDLM machine. The constraining leg is a one serial kinematic chain that connects those two plates and defines the total degrees of freedom of the workpiece supporting unit. The active legs are attached after the constraining leg is configured so that the machine can be activated.

To design CPKM, its requirements should be clarified first. The requirements for a CPKM are the required motions. To capture the characteristics of the motions, screw theory based dual vector representation and its algebra has been used in this research. When we think of a motion, it includes many aspects of the motion such as range of motion, type of motion, direction of motion and location of motion. The dual vector representation is one of the most suitable methods to represent these in explicit form. The algebraic operations and modeling methods used in this research is following reference [9].

The format of the dual number representation of a motion (or screw) has four parts; 1) magnitude, 2) dual pitch, 3) direction vector and 4) coupled vector. The magnitude and dual pitch capture the required range and the types of the motions respectively. The direction vector and the coupled vector is a line represented in dual vector form, thus it contains the orientation and location of the motion axis.

$$\begin{aligned} \hat{\$} &= M\hat{P}\hat{\mathbf{L}} \\ &= \left[M_{\max}, M_{current}, M_{\min}\right]\left\{P_A + \varepsilon P_L\right\}\left\{\mathbf{D} + \varepsilon\mathbf{C}\right\} \end{aligned} \tag{1}$$

Where M_{max}, $M_{current}$, and M_{min} represent the maximum, current and minimum value of the magnitude respectively. P_A and P_L represent the angular and linear pitches respectively. And **D** and **C** represents the direction and couple vector of the lines.

The range of motion is calculated as the $M_{max} - M_{min}$. If the magnitude is a single number then the motion is considered as the displacement from 0 to the magnitude. The dual pitch has two numbers; P_A and P_L. For a pure rotational motion and a pure translational motion, the dual pitches are $(1 + \varepsilon\ 0)$ and $(0 + \varepsilon\ 1)$ respectively. For a generic screw motion, the dual pitch is $(1 + \varepsilon\ h)$ and the unit of the magnitude is angle. The direction vector (**D**) indicates the direction of the motion axis. The couple vector is the cross product of the location of the line and the direction vector ($\mathbf{C} = \mathbf{R} \times \mathbf{D}$). Therefore, the dual vector satisfies the following conditions.

$$\begin{aligned} |\mathbf{D}| &= 1 \\ \mathbf{D}\cdot\mathbf{C} &= 0 \end{aligned} \tag{2}$$

For the multi-DoF motions, the dual vector itself contains variables that capture the DoF. However, it is not desirable to have more than one DoF for a motion. Therefore,

we will use multi-DoF dual vectors only for the intermediate motions and they will be decomposed into single DoF in the end.

The decomposition of the motion is required to match the required motions to the kinematic structure of the constraining leg. The decomposed motions can be directly used to synthesize the constraining leg since the order of screws also determines the dependency between the motions as in a serial kinematic chain.

The second step toward the design of CPKM is to configure the constraining leg for the required motions.

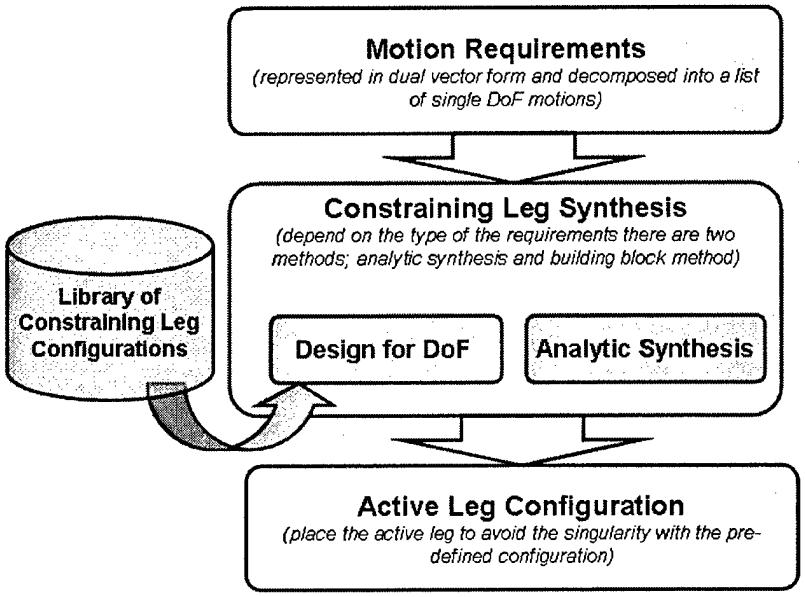

Figure 6. CPKM Design process

After configuring the constraining leg, the active legs should be added to complete the CPKM design. The generic design of the active legs is designed so that it has six DoF. However, the actual DoF of the active leg is five since the actuator constraints one DoF from the configuration. Now the active legs have five DoF, in other words each of them constraints one DoF, the active legs control the DoF of the CPKM with those constrained DoF and hence causes the singularity. In adding active legs, the arrangement should be carefully done otherwise it will cause redundancy or singularity.

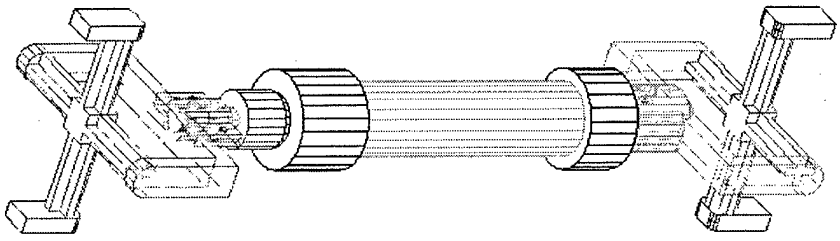

Figure 7. active leg design

4. Illustrative Part Family (PF) Definition and MDLD Process Planning

According to Shah and Mantyla [13] a solid model in which the main model entities, such as faces, edges etc., are related by geometric constraints defines a parametric solid model. The geometric constraints specify mathematical relationships between the numerical variables of the model entities. For the purposes of this research we shall define a part family to be the set of parametric solid models which share the same topology and geometric constraints. A member of the part family is instanced by assigning a value to each of the geometric constraints. We do not concern ourselves with constraint satisfaction or constraint propagation as addressed in [13] and [14]. Instead, our objective is to show the relationship between MDLD process planning and CPKM synthesis in the context of geometrically varying solid models.

An illustrative part family is shown in the following figure (ref. Figure 4).

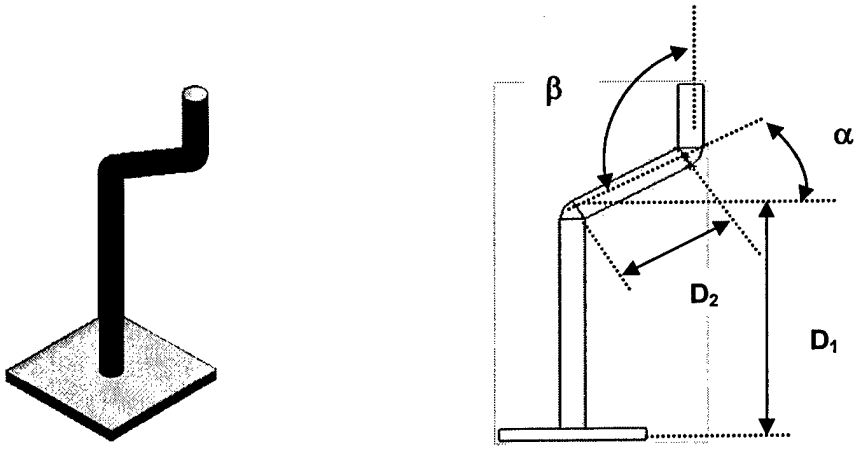

(a) An instance of the Illustrative part family

(b) Geometric Constraints

Figure 4: Illustrative Part Family

In Figure 4, the geometry of the part varies as the parameters, α, β, D_1 and D_2 are changed. The following constraints are placed on the part family parameters:

Parameter	Minimum Value	Maximum Value
α	-30°	30°
β	90°	180°
D_1	50 mm	150 mm
D_2	20 mm	60 mm

The diameter of the tubular section is fixed at 10 mm and the base dimensions are 50x50 mm.

In the following sections, we will present the MDLD process planning for the part families. The output from the process planning will be used to design a customized CPKM mechanism.

4.1. MDLD Process Planning for PF

MDLD process planning tasks for the part family are derived from those discussed in Section 2.0. The build directions for the part family vary with the geometric constraints which effects the resultant part volume decomposition. The process planning tasks for an illustrative part family member are shown in Figure 5. These include part volume decomposition and slicing. Uniform slice thickness is assumed throughout. Note that the sequence of deposition is $V_1 - V_2 - V_3$, based on the existence of the base surface (as discussed in Section 2.0). The deposition nozzle is assumed to be oriented along the build direction.

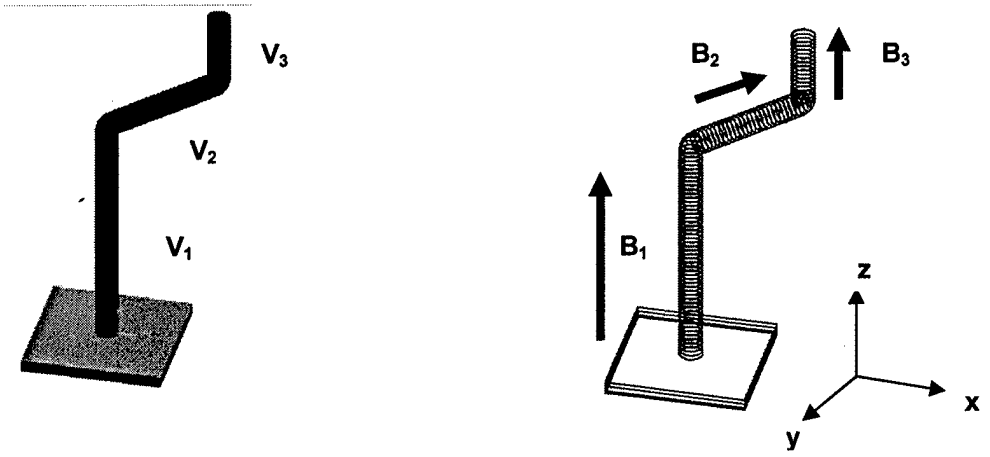

(a) MDLD decomposition

(b) Multi-Directional Slicing

Figure 5: MDLD Process Planning for an illustrative PF member

B_1 ,(refer Figure 5b) the initial build direction is along the Z axis. The following table summarizes the variation in the build directions, B_2 and B_3 with the variation in α and β.

Build Direction	Dependence (x, y, z)
B_1	$(\cos\alpha, 0, \sin\alpha)$
B_2	$(-\cos(\beta - \alpha), 0, \sin(\beta - \alpha))$

5. Compliant Mechanism for fabricating the PF

The example has two build directions, B_1 and B_2. The task of the workpiece orientation unit is to orient the workpiece from the up-right to the oriented angle of B_2.

Therefore one can assume that the mechanism requires one degree of freedom which is: rotation about the Z axis in the global coordinates.

Table 1. Library of constraining legs for DoF requirements

Rotation \ Translation	0	1	2	3
0				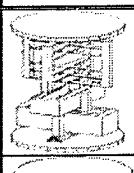
1	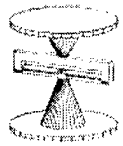	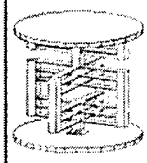	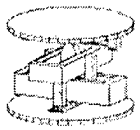	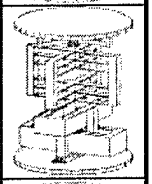
2	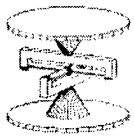	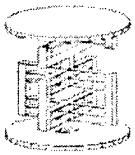	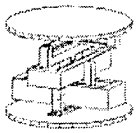	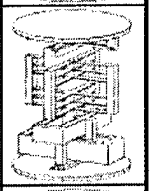
3	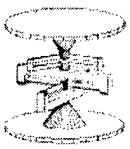		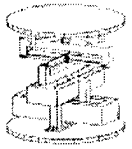	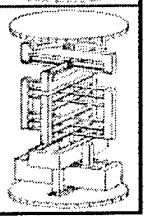

From Table 1, the one rotation and no translation configuration is selected as the candidate configuration of the constraining leg. Since the mechanism need to orient the workpiece by angle α, the sizing of the compliant joint is determined to satisfy the motion range requirement [9].

After having the constraining leg configured, the active leg is placed. Since the mechanism needs only one degree of freedom, it needs one active leg. To balance the active leg layout, we put two active legs as in the figure 6.

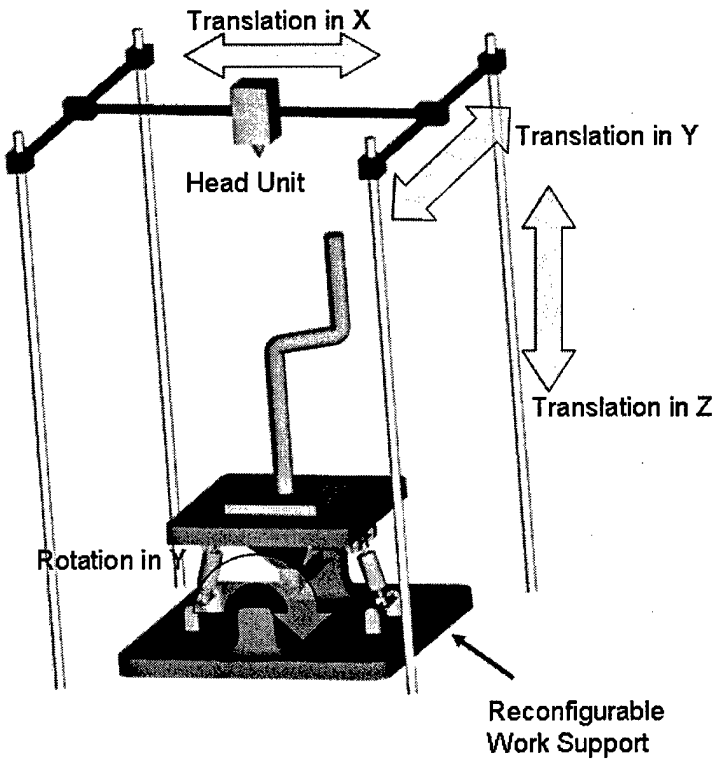

Figure 6: MDLD machine for PF member

As the part family changes, the reconfigurable work support unit could be replaced for the new requirements.

6. Conclusions and Future Work

In this research we have presented a synergistic framework in which the kinematics of an LM machine are designed using the output from the MDLD process planning for a parametric part family. The presented approach has the potential to be more cost effective when compared to MDLD systems which employ 5-6 axis kinematics. Our assumptions regarding the mode of material deposition are generic. Future research will be directed at interfacing with a specific deposition technique (such as Direct Metal Deposition (DMD) [7]). We will also focus on complex application specific part families. This will entail the inclusion of collision detection techniques resulting in the possible requirement for support structures and changes in the orientation of the deposition nozzle orientation.

References

[1] Alexander, P. and Dutta, D., "Part Orientation and Build Cost Determination for Layered Manufacturing", Computer-Aided Design, 30, 1998, pp 343-358.

[2] Allen, S. and Dutta, D., "Wall Thickness Control in Layered Manufacturing for Surfaces with Closed Slices", Computational Geometry: Theory and Applications, Vol. 10, 1998, pp 223-238.

[3] Arcella, F., Albott, D., House, M., "Rapid Laser Forming of Titanium Structures", http://www.aerometcorp.com/rapid_laser_paper.htm.

[4] Dickens, P. et al., "Rapid Prototyping using 3D Welding", Solid Freeform Fabrication Symposium, 1992.

[5] Griffith, M. et al., "Laser Engineered Net Shaping (LENS) for Fabrication of Metallic Components", ASME International Mechanical Engineering Congress and Exposition, 1996.

[6] Hoschek, J. and Lasser, D., Computer-Aided Geometric Design, A.K. Peters, 1993.

[7] Mazumder, J., Choi, J., Nagarathnam, K., Koch, J. and Hetzner, D., "Direct Deposition of H13 Tool Steel for 3-D Components", JOM, 49, No. 5, pp. 55-60.

[8] McMains, S., "Double Sided Layered Manufacturing", Japan-USA Symposium on Flexible Automation, , Hiroshima, Japan , July 2002, pp.269-272.

[9] Moon, Y. and Kota, S., "Design of Compliant Parallel Kinematic Machines", AMSE DETC, Montreal, Canada, 2002.

[10] Moon, Y. and Kota, S., "Automated Synthesis of Mechanisms using Dual-Vector Algebra", Mechanism and Machine Theory, 37, 2002, pp 143-166.

[11] Singh, P. and Dutta, D., "Multi-Direction Slicing for Layered Manufacturing", Journal of Computing and Information Science in Engineering, June 2001.

[12] Singh, P. and Dutta, D., "Offset Slices for Layered Manufacturing", ASME DETC, Montreal, Canada, September, 2002.

[13] Shah, J. and Mantyla, M., Parametric and Feature-Based CAD/CAM, John Wiley and Sons, Inc., 1995.

[14] Shapiro, V. and Vossler, D., "What is a Parametric Family of Solid?", Third ACM/IEEE Symposium on Solid Modeling and Applications, Salt Lake City, 1995.

[15] Yang, Y., Fuh, J., Loh, H. and Wong, Y., "Multi-orientation Deposition for Support-less Layered Manufacturing Process", preprint.

Multi-Direction Layered Deposition – An Overview of Process Planning Methodologies

Prabhjot Singh and Debasish Dutta
Department of Mechanical Engineering
University of Michigan, Ann Arbor, MI 48109

Abstract

Layered Manufacturing (LM) techniques build a part by adding thin layers of material. In many LM processes overhangs require the deposition of sacrificial supports resulting in an increase in the build time, wastage of material and costly post-processing. This has led to the development of LM systems which can deposit material along multiple directions and eliminate the need for supports. We survey the configurations of available multi-direction deposition systems. An overview of the process planning challenges is presented. Literature on process planning methodologies is reviewed.

1.0 Introduction

Layered Manufacturing (LM) processes have developed the ability to deposit a variety of materials with an increased emphasis on the fabrication of functional prototypes. There is a vast body of literature covering various aspects of Layered Manufacturing processes. The interested reader is directed towards [8] for a survey of LM processes and the Proceedings of the annual Solid Freeform Fabrication Proceedings hosted by the University of Texas, Austin.

In this paper we will concern ourselves with a specific set of LM processes which can deposit material along multiple directions. The development of these processes has been motivated by two salient characteristics of LM processes, namely the need for support structures to deposit overhanging features (refer Figure 1a) and the so called *staircase effect*. The staircase effect concerns the approximate construction of surfaces which are not aligned along the build (deposition) direction and is qualified by the cusp height (Ref. Figure 1b). The cumulative effect of these is a longer build time, material wastage, deterioration of surface quality and time consuming post processing.

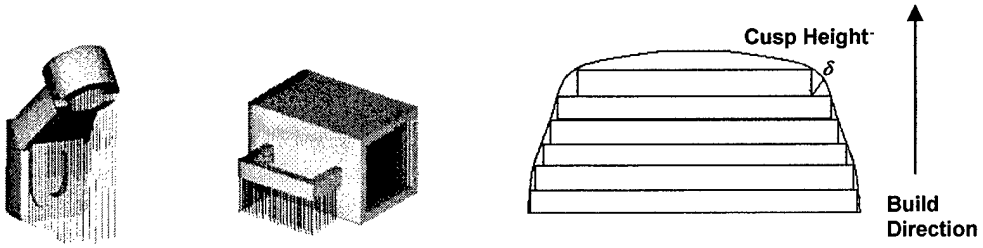

(a) Supports required

(b) Approximate Surface – Staircase effect

Figure 1: The need for multi-direction layered deposition

Multi-Direction Layered Deposition Systems (MDLD) systems have the ability to deposit material along multiple directions. A part is decomposed into smaller sub-volumes which are built along multiple build directions. This enables support-less layered deposition and a better control over the cusp height. The focus of this paper is the survey of research into process planning for MDLD. Process planning refers to the generation of tool paths and selection of process parameters to build an object using a manufacturing process. The reader is referred to [7][8] for a survey of process planning tasks for LM. The use of multiple deposition directions necessitates additional process planning for MDLD. To better understand the tasks involved, we begin by briefly summarizing the capabilities of the available MDLD techniques and their process characteristics. The physics of the deposition processes is not discussed in detail; instead the focus is on deriving the process characteristics which have a bearing on the associated process planning. This survey also motivates the categorization of the process planning tasks.

2.0 Multi-Direction Layered Deposition Techniques

Multi-direction Layered Deposition processes have developed independently and employ a variety of deposition modes for part fabrication. The degree of freedom in choosing a deposition direction varies from one process to another.

Some of the MDLD processes use 2.5D LM machines retrofitted with specialized kinematics permitting limited MDLD capabilities. Examples are the Double Sided Layered Manufacturing [11] and the Multi-Orientation Deposition (MOD) processes [17]. Double-Sided Layered Deposition uses a traditional Fused Deposition Modeling (FDM) machine with an additional fixturing mechanism which permits the deposition of the part along two directions. The part to be built is divided into two halves with a parting plane. The bottom half is deposited first. It is then flipped over and the remainder is deposited on its backside. The MOD process uses two deposition nozzles aligned perpendicular to each other in conjunction with a deposition table with x-y and a rotational degree of freedom. This permits the support-less deposition of annular regions using offsets of a base layer.

Processes specifically designed to have MDLD capabilities include Direct Metal Deposition (DMD) [10], Five Axis Rapid Metal Forming [19], Laser Chemical Vapor Deposition [15][16] (LCVD) and 3D Welding [4]. Both DMD and the Rapid Metal Forming process utilize a laser cladding process with CO_2 and Nd:YAG lasers respectively. A high power laser generates a small melt pool on the substrate while metal powder is injected through a concentric nozzle. MDLD is realized by the use of a deposition table with translational and rotational degrees of freedom. The Rapid Metal Forming process uses a 5-axis CNC milling machine in addition to the deposition process. This improves the surface quality while the part is being fabricated.

LCVD is an adaptation of the traditional Chemical Vapor Deposition (CVD) process. In this process the substrate is placed in a chamber with a supply of CVD reagent gases. The substrate is heated close to its melting point; thereafter a laser is used to locally heat a spot on the surface. This initiates a thermal decomposition of the reactant gases resulting in the deposition of material at the same spot. MDLD is realized by

moving the substrate relative to the laser beam. Since the mode of deposition is via a local chemical reaction, a variety of substrate shapes are possible.

The 3D welding process was one of the earliest attempts at creating an MDLD system using a welding torch mounted on a highly articulated robot arm. The weld electrode provides the deposition material.

3.0 Process Constraints affecting Process Planning

The objective of MDLD is support-less part fabrication. The overhang angle [2] between two contiguous layers is the most important process constraint in MDLD process planning. It determines the extents of a part volume that can be deposited without the need for sacrificial supports. The overhang angle is defined as the maximum of the minimum distance between a point on the *i-1* layer and the corresponding point on the *i*th layer. The angle, θ between the surface normal and the build direction, and the overhang, Δo (with Δl being the slice thickness) are related as: $\Delta o = \Delta l * \cot\theta$ [2]. The process specific maximum value of the angle θ is called the overhang angle. It is an inverse function of the slice thickness and also depends on the surface tension of the deposited material. Figure 2 shows the relationship between the layer thickness, the surface normal, the build direction and the overhang angle.

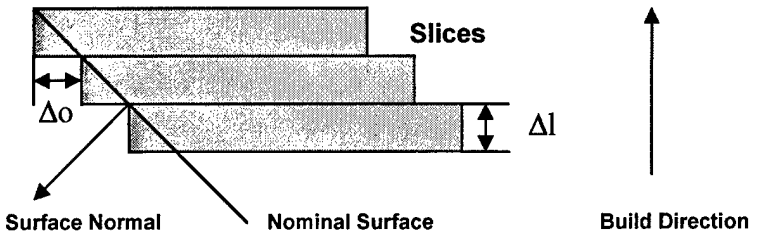

Figure 2: Relationship between the overhang angle, the slice thickness, the surface normal and the build direction.

Other constraints which restrict support-less part deposition are the machine kinematics and the bounding volume of the deposition mechanism. The effect of both these constraints is manifested by the need for support structures. This is discussed in greater detail in the next section.

4.0 Process Planning Challenges and Solutions

In MDLD, support-less fabrication of parts is facilitated by changing build directions so that the overhang angle between the layers is not exceeded. The discussion in the previous section explained the conditions under which an overhanging layer requires supports.

Figure 3 provides an overview of the process planning tasks in MDLD. The first task in MDLD is setting the orientation of the part relative to the deposition table. This is followed by two computational tasks which comprise the core of MDLD process planning. The first of these is determining the extents of the part volume which can be deposited along a certain build direction. The second task is the estimation of a new build direction in the event a part cannot be deposited completely along one direction. The change in build direction is realized by re-orienting the part using a multi-axis deposition table or by moving the nozzle mounted on a multi-axis robot arm. In either case the direction of deposition is perpendicular to the deposited layers. Together, these tasks are used to decompose the part into smaller volumes which are deposited along the associated build directions. These tasks are usually carried out recursively. In the ideal case part decomposition enables support-less fabrication. However, real world MDLD systems are constrained by limited freedom of motion and the likelihood of collisions during the deposition process. Depending on the part geometry, sacrificial supports may be required. The volume of sacrificial supports can be minimized by appropriately choosing an initial orientation of the part relative to the deposition table.

After part decomposition, build direction determination and support structure generation are completed the part is sliced. This is succeeded by the generation of deposition path patterns (path planning).

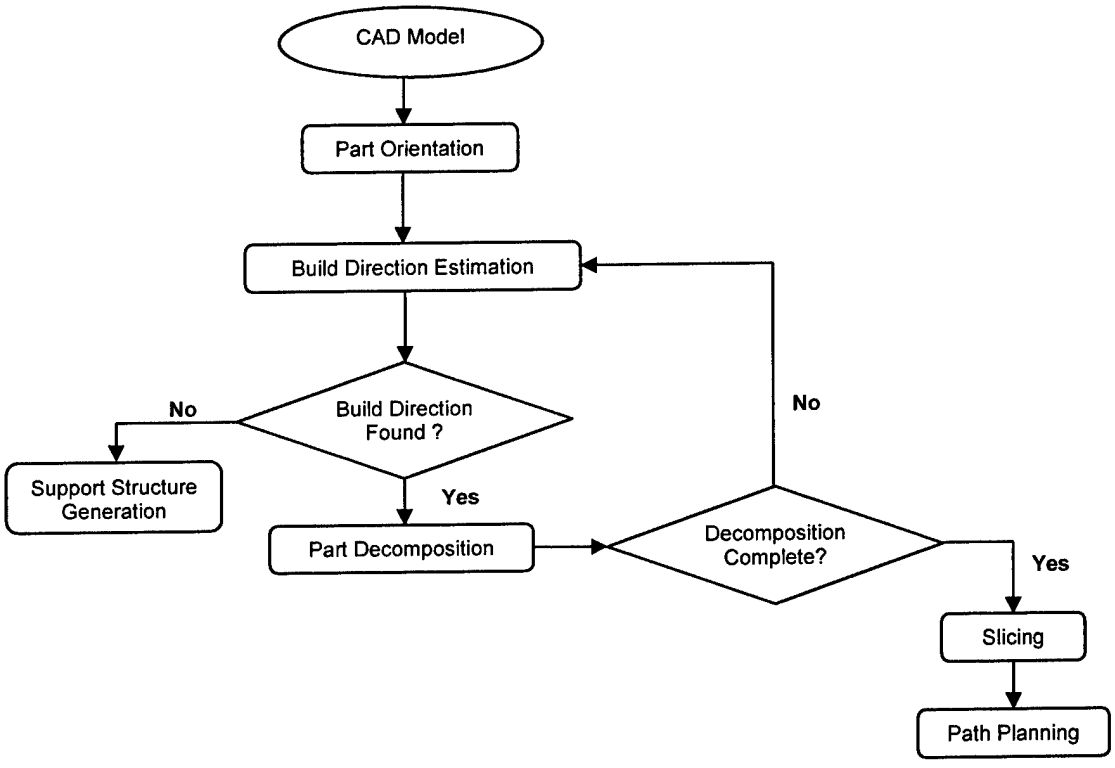

Figure 3: Sequence of Process Planning Operations for MDLD

In the following sections, we review the research in the development of algorithms for the following process planning tasks:

- Part Orientation
- Part Decomposition and Build Direction Determination
- Slicing
- Deposition Path Generation

Where literature is not available, we list the likely computational problems in the solution to the respective process planning task.

4.1 Part Orientation

Part orientation in LM literature refers to the orienting the part relative to the deposition table. The computational challenge in this process planning task is the search for a build direction along which either the build time is minimized or the part's surface quality is maximized. A summary of the literature concerning LM part orientation is provided in [7].

In the context of MDLD, this task is complex due to multiple build directions assigned to smaller part volumes. Setting up metrics such as improved part quality or reduction in build time must take into account the kind of part decomposition algorithms employed. Furthermore, the choice of initial orientation can also influence collisions between the deposited layers and the MDLD mechanism.

Literature concerning MDLD part orientation is scant. One of the efforts is due to Fekete and Mitchell [5] with the object of minimizing the number of build directions. This, according to the authors will improve surface quality at the interface of the part volumes. The computational problem is shown to be NP-hard for 3D parts of genus 0. Factors such as collisions are not considered.

4.2 Part Decomposition

As previously mentioned, in this process planning task the extent of a part volume which can be deposited along any given build direction is determined. The build direction itself is an input. We shall refer to a part volume that can be deposited without supports along a chosen build direction as a *buildable volume*. Various algorithms have been proposed to disjunction parts into buildable and unbuildable part volumes. These algorithms either use a CAD model or slices of a CAD model as input. Before reviewing the research on part volume decomposition, we discuss two relevant process characteristics of MDLD namely the deposition of non-planar slices and the effect of collisions on support-less part deposition.

MDLD processes have the ability to deposit non-planar slices. These are offsets of a base surface and are parallel to each other. Figure 4 shows the geometry of these slices. Figure 4a show the base surface in red. The part is deposited using offsets of this base surface (ref. Figure 4b). The build direction is along the surface normal. Such slices

are referred to as transitional walls [18], conformal layers [12] or offset slices [13][14] in literature.

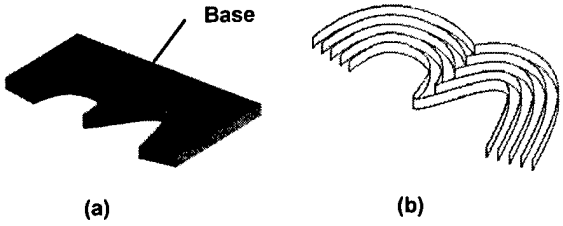

Figure 4: Non-planar slices – offsets of the base surface

The second process characteristic of MDLD is the effect of collisions during the deposition process. Collisions occur due to the finite volume of the MDLD apparatus and limitations in machine kinematics. To avoid collisions, especially for smaller part sub-volumes, support structures are deposited. Most research efforts employ concepts such as the visibility maps of surfaces [6] to detect collisions.

4.2.1 Review of Part Decomposition Algorithms

Part decomposition for 2.5D LM machines retrofitted for MDLD is discussed in [11] and [17]. In [11] the part is deposited in two opposite directions and consequently there are two part sub-volumes. The part is decomposed using a plane. The need for supports is determined using the castability analysis [3] for 2 mold parts. The MOD process [17] has two nozzles mounted perpendicular to each other. The part decomposition algorithm in MOD uses a sliced CAD model as input. The computation of unbuildable slice regions is accomplished by performing the Boolean difference operation between two successive layers. If the overhanging region (result of the Boolean difference) exceeds the process specific overhang angle it is termed as a macro-overhang and is deposited using offsets of the base surface. The process is shown in Figure 5. The authors do not account for collisions during the deposition process.

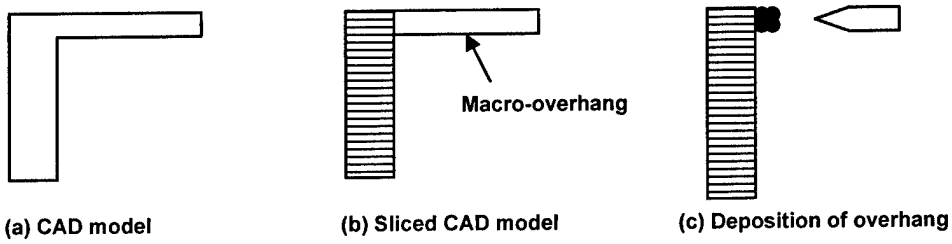

Figure 5: Deposition of Macro-overhangs in the MOD process [17].

Part decomposition algorithms and associated analysis for processes specifically designed for MDLD can be found in [5][13][14][18]. In [13] the authors assume a

deposition nozzle mounted on a generic 6-axis manipulator. The part decomposition algorithm uses the CAD model and the build direction (B) as inputs. The overhang is restricted to 90 degrees. Silhouette edges associated with the negative of the build direction (-B) on the faces of the CAD model bound regions which are unbuildable (based on the overhang criterion). The surface regions bounded by the silhouette edges are swept along the build direction to create a (swept) volume. The unbuildable volume is obtained by intersecting the swept volume with the input CAD model; the difference gives the buildable volume. Figure 6 demonstrates an example of the approach taken in [13]. The silhouette edges of the part along $-\overline{B}$ are identified (ref. Figure 6b) and the resultant buildable and unbuildable part volumes are shown in Figure 6c.

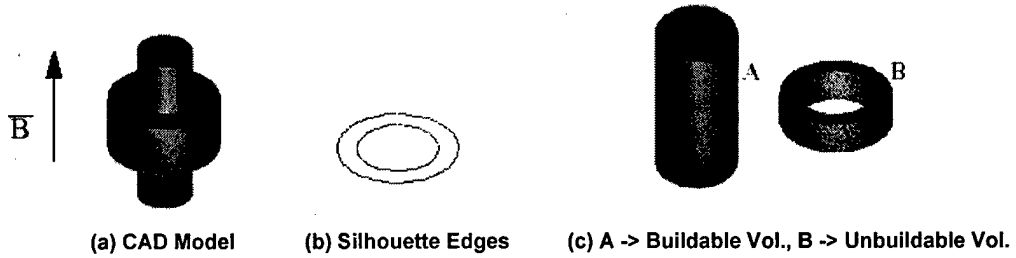

Figure 6: Part decomposition approach taken in [].

The analysis in [13] assumes planar slices. An extension to offset or conformal slices is presented in [14] which is restricted to extruded part geometries.

In [18] the authors present a process planning framework for the 5-axis Rapid Metal Forming process. This is an additive-subtractive MDLD process [19]. The authors use an adaptive slicing algorithm in which the slice planes are not parallel to each other. Consequently, the slices have non-uniform thicknesses (ref. Figure 7). The slice planes are chosen to conform to the geometric continuity of the part. Regions between two slice planes are the buildable part volumes. The associated build direction is the normal to the lower slice plane. The deposition of such slices is done in two stages. First, slice(s) of uniform thickness are deposited with extra material. These are then shaped using a 5-axis CNC machine. This ensures that the final part has increased accuracy as surfaces of the final part are a first order (tangent) approximation of the CAD model.

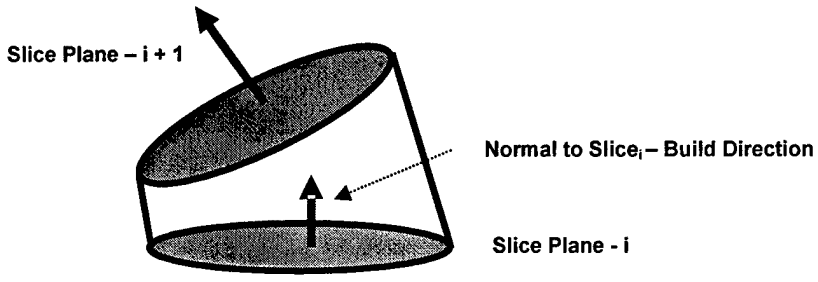

Figure 7: Deposition of Slices with non-uniform thickness [18]

In the case of large overhangs, such as shown in Figure 5, the authors deposit the part using transitional walls (offset slices).

4.3 Build Direction Determination

This process planning task assigns a build direction to an unbuildable part volume. Unbuildable part volumes result from part volume decomposition. In [11][17], where only a limited set of build directions is possible, this process planning task is trivial. In processes specifically designed with MDLD capabilities, all feasible build directions must be identified. If the angle between a vector and all surface normals of the (unbuildable) part boundary is less than the overhang angle it is considered to be a feasible build direction. In [13][18] the authors use spherical maps [6] to represent the set of all feasible build directions. The best build direction is chosen by minimizing metrics such as the average weighted cusp height [1].

4.4 Slicing and Deposition Path Generation

Multiple degrees of freedom in MDLD permit the deposition of both planar and non-planar slices. Planar slices are deposited along their respective build directions. The path planning for material deposition proceeds along the same lines as in 2.5D LM. The reader is referred to [9] for more details.

As mentioned in Section 4.2, non-planar slices are offsets of a base surface and are parallel to each other. The slice thickness is measured along the surface normal. [12][13][14][18] propose to use the deposition direction of the base substrate to generate the deposition patterns for offset slices. Figure 8 shows the approach using an example part. The build direction for the base surface (B_{base} in Figure 8a) is pre-assigned. The deposition paths for an offset slice (ref. Figure 8b) are generated by intersecting it with planes aligned along the build direction of the base surface. The distance between two contiguous planes is equal to the slice thickness. The number of the planes depends on the span of the base surface along its build direction.

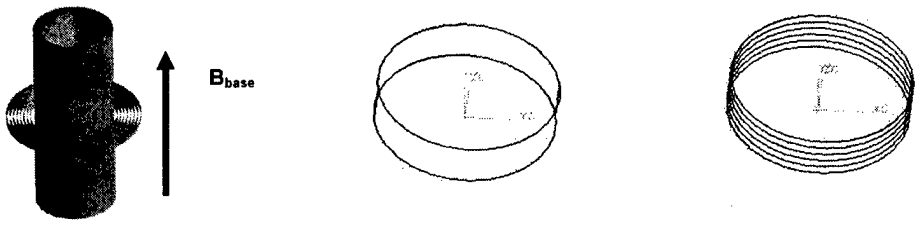

(a) Offset Slices of a CAD model

(b) Deposition Patterns for an offset slice

Figure 8: Deposition Path Planning for Offset Slices

5.0 Summary

In this paper we have reviewed literature on the process planning tasks involved in multi-direction layered deposition. Some of these processes are still being developed and the associated process planning methodologies are being actively researched. MDLD consolidates the advantages offered by layered manufacturing by limiting the need for supports. Further development is likely to be driven by the need for fully functional, custom manufactured metal parts.

References

[1] Alexander, P. and Dutta, D., "Part Orientation and Build Cost Determination for Layered Manufacturing", Computer-Aided Design, 30, pp 343-358, 1998.

[2] Allen, S. and Dutta, D., "Wall Thickness Control in Layered Manufacturing for Surfaces with Closed Slices", Computational Geometry: Theory and Applications, Vol. 10, pp 223-238, 1998.

[3] Bose, P., Bremmer, D. and van Kreveld, M., "Determining the Castability of Simple Polyhedra", Vol. 19, No 1-2, 1997.

[4] Dickens, P. et al., "Rapid Prototyping using 3D Welding", Solid Freeform Fabrication Symposium Proceedings, 1992.

[5] Fekete, S., Mitchell, J., "Terrain Decomposition and Layered Manufacturing", International Journal of Computational Geometry and Applications, Vol. 11, No. 6, 2001.

[6] Gan, J., Woo, T. and Tang, K., "Spherical Maps: their construction, properties and approximation", ASME Journal of Mechanical Design, Vol. 116, No. 2, 1994.

[7] Gibson, I., "Software Solutions for Rapid Prototyping", Professional Engineering Publishing Limited, 2002.

[8] Kulkarni, P., Marsan, A. and Dutta, D., "A Review of Process Planning Techniques in Layered Manufacturing", Rapid Prototyping Journal, Vol. 6, No. 1, 1999.

[9] Kulkarni, P. and Dutta, D., "Deposition Strategies and Resulting Part Stiffnesses in Layered Manufacturing ", ASME Journal of Manufacturing Science & Engineering, 1999.

[10] Mazumder, J., Choi, J., Nagarathnam, K., Koch, J. and Hetzner, D., "Direct Deposition of H13 Tool Steel for 3-D Components", JOM, Vol. 49, No. 5, pp. 55-60, 1997.

[11] McMains, S., "Double Sided Layered Manufacturing", Japan-USA Symposium on Flexible Automation, pp.269-272, 2002.

[12] Park, J. and Rosen, D., "Issues in Process Planning for Laser Chemical Vapor Deposition", Solid Freeform Fabrication Symposium Proceedings, 2002.

[13] Singh, P. and Dutta, D., "Multi-Direction Slicing for Layered Manufacturing", Journal of Computing and Information Science in Engineering, Vol. 1, No. 2, pp. 129-142, 2001.

[14] Singh, P. and Dutta, D., "Offset Slices for Layered Manufacturing", ASME Design Engineering Technical Conference, 2002.

[15] Westberg, H., Boman, M., Johansson, S., Schweitz, J.A., "Truly three dimensional structures microfabricated by laser chemical processing", International Conference on Solid-State Sensors and Actuators, 1991.

[16] Williams, K., Maxwell, J., Larsson, K., Boman, M., "Freeform fabrication of functional microsolenoids, electromagnets and helical springs using high-pressure laser chemical vapor deposition" Twelfth IEEE International Conference, 1999.

[17] Yang, Y., Fuh, J., Loh, H. and Wong, Y., "Multi-orientation Deposition for Support-less Layered Manufacturing Process", preprint.

[18] Zhang, J., Ruan, J. and Liou, F. "Process Planning for a Five-Axis Hybrid Rapid Manufacturing Process," Proceedings of the Eleventh Annual Solid Freeform Fabrication Symposium, 2000.

[19] Zhang, J. and Liou, F., "Adaptive Slicing for A Five-Axis Laser Aided Manufacturing Process," ASME Design Automation Conference, 2001.

The Effect of Layer Orientation on the Tensile Properties of Net Shape Parts Fabricated in Stereolithography

Andrew C. Layton and David W. Rosen
Manufacturing Research Center
Georgia Institute of Technology
Atlanta, Georgia 30332

Abstract

Stereolithographic technologies create parts in thermoset plastic polymeric mixtures of acrylates and epoxies. In order to predict the mechanical behavior of these parts, it is critical to understand the effects that build parameters have on the final properties of the polymer. Using a statistics based approach, the build parameters of layer orientation, layer thickness, and resin class are used as inputs. The response variables, peak stress, elongation at break and Young's modulus (modulus of elasticity), are examined using the methodology specified in ASTM D638-01 with modifications as noted. An initial test in Somos 8120 showed the surprising (and statistically significant) result that load bearing capability in the build direction was greater than in the in-layer direction. Additional tensile tests in Somos 8120 and Vantico SL-5510 were undertaken to verify this result, and determine if this effect is present across different classes of resin. This report details the rationale behind this experiment, presents the results to date, and outlines future efforts.

1.0 Introduction

It is reasonable to assume that material property anisotropies exist due to the nature of layer-based fabrication processes. A sizable body of published work shows material anisotropies in the Fused Deposition Modeling (FDM) [1], and Selective Laser Sintering (SLS) [2][3] technologies; however, there is not a corresponding sizable body of published work with respect to stereolithographic (SLA) processes and photopolymers. Some qualitative discussions of the stereolithography materials in the early 1990's recognized that material anisotropies were likely; however, the differences should not be statistically significant. There does not seem to be a quantitative work in the public record to verify this supposition, though there may be information in the proprietary domain.

As part of a larger effort to characterize SLA materials, a simple screening experiment was performed. The intent was to verify that the expected material anisotropy based on the relationship of build direction to tensile loading direction was small enough (i.e., statistically insignificant) that we could build tensile test coupons in any convenient orientation within the vat.

Stereolithography processes build parts by irradiating a homogeneous photopolymer resin in liquid form. The irradiating energy is provided by an ultra-violet laser. The photoinitiators in the resin system are formulated to react to the specific wavelength of the laser and initiate a polymer chain addition reaction when irradiated. An optic system focuses the laser energy to a discrete spot on the surface of the liquid resin. Laser spot location and motion are controlled

through the mirror and galvanometer set. By vector scanning the laser spot, a line of solidified material is formed. Successive overlapping vector scans create a series of bonded lines to form a layer. A second series of vector scans, moving the laser spot in a series of overlapping scans 90° from the previous direction, helps ensure complete reaction of the material, and formation of a good intra-layer bond.

A 3-dimensional object is created by bonding layers together. Subsequent layers are created by depositing additional resin on the surface of the previous layer, and repeating the hatching and filling processes. The laser energy solidifies the current layer as described above, but some energy is imparted to the previous layer. This energy causes a slight overcure of the previous layer, and causes the inter-layer bond to develop.

The solidified lines that form a single layer are irradiated in an overlapping pattern within a short time frame. This should have the effect of initiating very high levels of cross-linking between the individual scan lines within a layer. High levels of cross-linking would seem to indicate high strength. The inter-layer bonding is initiated by the 'left-over' energy not absorbed by intra-layer cross-link formation. The energy felt at the liquid / solid interface should be more variable than that felt in the liquid. Since the solidified layer has already developed a cross-link network, the number of potential cross-linking sites for inter-layer bond formation should be substantially less than the number available for intra-layer bonding. These two factors should lead to the intuitive conclusion that intra-layer strength is superior to inter-layer strength.

2.0 Experimental Method

Three sets of experiments were performed in this study: (1) a screening experiment in Somos 8120; (2) a more in-depth experiment in Somos 8120; and (3) a validation experiment in Vantico SL-5510. For the first two experiments, the test coupons were built in an SLA-3500 using the standard "Fast" build style. The test coupons for the validation experiment were built in an SLA Viper Si^2 using the standard "Exact" build style in the low-resolution mode. Both of these SLA machines use Nd:YVO_4 laser systems with output wavelengths of 355 nm, and all of the test coupons were built from the same series of .stl files. In all three experiments, testing was within 24 hours of fabrication.

2.1 Screening Experiment in Somos 8120. For the initial screening experiment in DSM 8120, three sets of thirty-six samples were tested. (1) Built flat in the XY plane – Flat group; (2) edgewise in the XY plane – Edge group; and (3) standing along the Z-axis – Standing group. We were not able to gather valid data with respect to the peak stress, elongation at break and modulus of elasticity of the Standing group; however, we were able to gather valid data with respect to ultimate load for all three groups. We chose to use ultimate load as a proxy value for the peak stress in comparing the three groups.

Given the use of the ultimate load as a proxy for peak stress, and the surprising result, we felt it prudent to replicate the experiment, gather valid data for peak stress, elongation at break and Young's modulus, and reexamine the result. Realizing that the Flat and Edge groups were simply variations on a theme, and recalling that maximum shearing stress occurs on a 45° offset plane [4], we redefined the sample orientation set to include in-plane, transverse, and shear loaded samples.

2.2 Second experiment in Somos 8120. For this experiment, we considered three orientations designated as Flat (in-plane), Standing (transverse), and Angled (shear). The three orientations are illustrated in Figure #1.

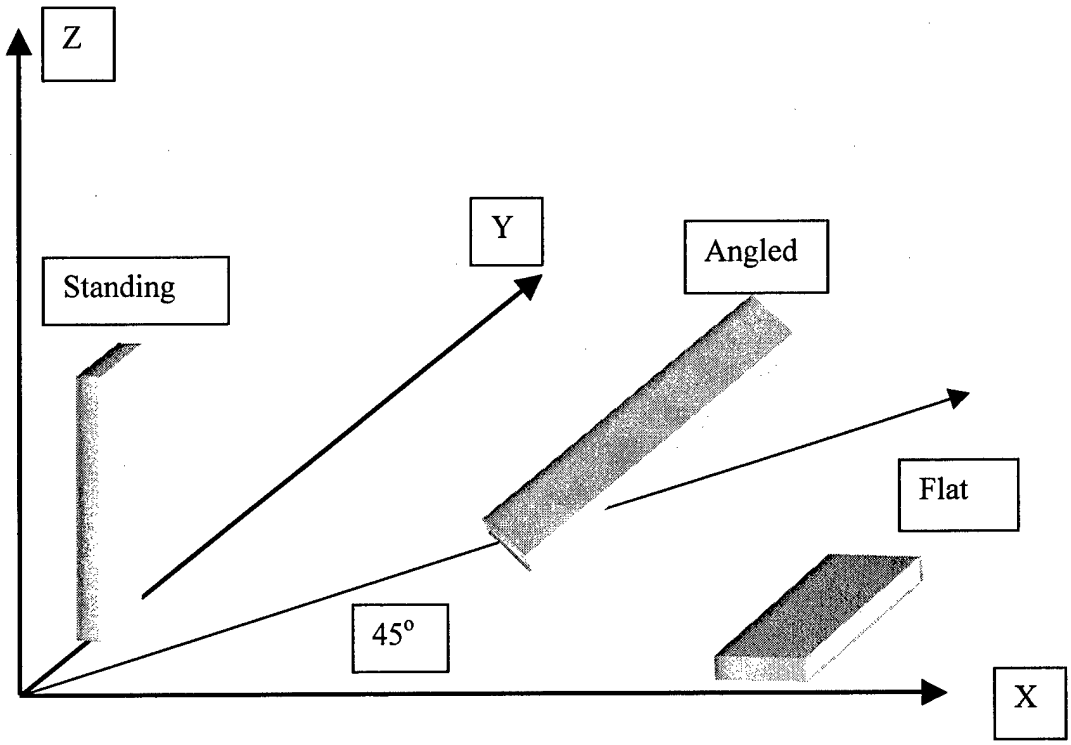

Figure 1. The three representative sample orientations with respect to the XYZ frame

We arrived at these three orientations by using the following rationale. The primary axes and 45° offsets from the primary axes combine to describe seven (7) unique orientation vectors. If we allow one degree of freedom, a 90° rotation around the vector axis, we create fifteen (15) unique sample orientations. We see that these fifteen sample groups represent five distinct inter-layer orientations with respect to the "longitudinal - long transverse - short transverse" frame of the individual samples. Each of these five inter-layer orientations is comprised of three sample groups.

Within these five orientation plane groups, there are three primary groups – "Long-LT" and "Long-ST" orientation planes are both "In-plane" with respect to the loading direction, both "A" and "B" orientation planes are "shear," and the "LT-ST" orientation plane is "transverse." Figure #2 provides a graphical representation of the five distinct inter-layer orientations and their subsequent grouping into the three primary groups denoted. Any single group within a particular primary group (In-plane, transverse, or shear) should provide a reasonable representation for all of the groups within the same primary group. This supposition is borne out by the result of the initial experiment that showed a consistent result within the two in-plane loaded groups (groups Flat and Edge). Based on this evidence and our convenience, we chose the Flat, Standing, and Angled groups for use in subsequent experiments.

Orientation Plane	Groups	Graphic
LT-ST (Transverse)	**STANDING** (Z-45) (ZXY)	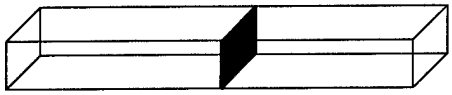
Long-LT (In-plane)	**FLAT** (XY-0) (XYZ)	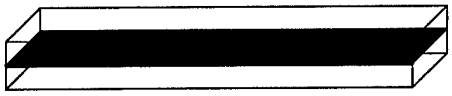
Long-ST (In-plane)	(XZY) (YZX) (XY-90)	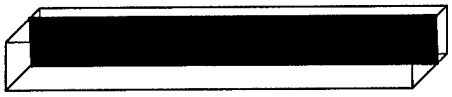
"A" (Shear)	**Angled** (XZ-90) (YZ-90)	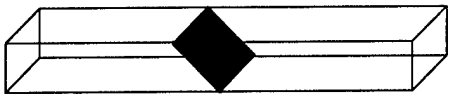
"B" (Shear)	(XZ-0) (Norm-90) (YZ-0)	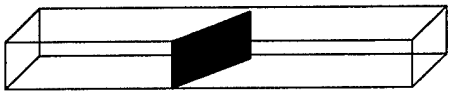

Figure 2: Inter-layer bonding plane relative to Long -LT- ST frame

2.3 Validation Experiment in Vantico SL-5510. For the validation experiment in Vantico SL-5510, we fabricated 12 test coupons for each of the same primary groups tested in the second Somos 8120 experiment. Post-processing, curing, and testing were consistent with the standard methods and uniform across each experiment.

2.4 Methods and Apparatus. While exposure to background UV, relative humidity and heat have been shown to affect the properties of parts fabricated in the stereolithography process, we have not sought to control them in this study. The broad spectrum of users neither actively nor consistently controls these factors. One of the purposes of this research is to examine what the user would see outside of the standard conditions. The ASTM standard is designed to provide an "apples-to-apples" comparison of materials – control as many factors as possible and allow the response variable to be driven overwhelmingly by the factor of interest. This is a valid scenario, but it does not necessarily represent what the user in the field will experience.

Similarly, the ASTM D638 standard prescribes fabrication of the test coupons by either die cutting or machining from flat material (e.g., sheet), or by molding. Neither of these matches the SLA process particularly well – generally, SLA parts are made to net shape and used. There may be some surface finishing or treatment, but mostly the surfaces are used as fabricated. By fabricating the test coupons to net shape, we leave the edge effects extant. So, we have chosen to examine those factors (layer orientation, layer thickness, and resin selection) that the user actively controls. For the purposes of this experiment, we do conform to the specifications found in the ASTM standard (coupon form and dimensions, strain rates, etc) not discussed above.

We have discussed layer orientation in the section above, the other parameters of interest are:

Layer thickness (Quantitative) – This is a discrete parameter that can be set at one of three values - .002 inches, .004 inches, or .006 inches.

Resin Class (Qualitative) – This refers to the general class of materials represented by each of the subject resins.

Layer thickness is a user selectable parameter based on the build style chosen. Advanced users have the capability to create and tailor custom build styles. Like vat orientations, the potential number of different styles that can be created is unlimited. For the purposes of approximating typical user results, we limit our build styles and, consequently, layer thickness to those provided by the resin manufacturers.

Resin Classes - There are three classes of material in the stereolithography process: polyethylene-like / polypropylene-like (PE/PP); general purpose; and ABS-like. Each has a different combination of rigidity and durability properties. Parts made from PE/PP - like resins have low rigidity and high durability while GP resins yield high rigidity and low durability. ABS-like materials are highly rigid and highly durable.

The chemical composition of the resins within classes is similar, so a commonly used resin should provide a good representation of its class; however, there are differences in chemistry between the classes. Differences in the cross-linking reaction are a potential cause for differences in the material properties. By using a representative resin from each class, we seek to gain data that will help us define this phenomenon as being process related, chemistry related, or an interaction of process and chemistry. For our purposes we will use these resins to represent the three classes.

General purpose (Epoxy Acrylate):	Vantico SL-5510
Polyethylene-like:	DSM Somos 8120
ABS-like:	Vantico SL-7560

The particular formulations and compositions of the resin systems are proprietary. A review of the constituents of the resin systems shows, even without a precise delineation of constituents, that the materials are dissimilar enough in nature to allow us to declare them to be different [5], [6]. This is borne out by an examination of the experimental data values. The differences in the measured loads, stresses and elongation are large enough to see by observation without need for comparison of the mean values by statistical methods.

After fabricating the test coupons and post-processing them according to standard practice, we subjected the coupons to tensile testing in an Instron Tensile Tester model 4466. The standard manufacturer provided software (Instron Series IX Automated Material Tester – version 8.11.00) was used for reporting of the pertinent data.

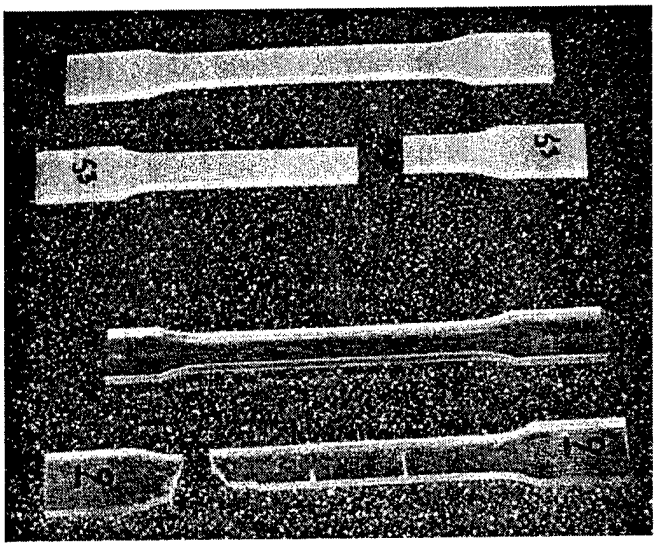

Figure 3:
Typical test coupons before and after

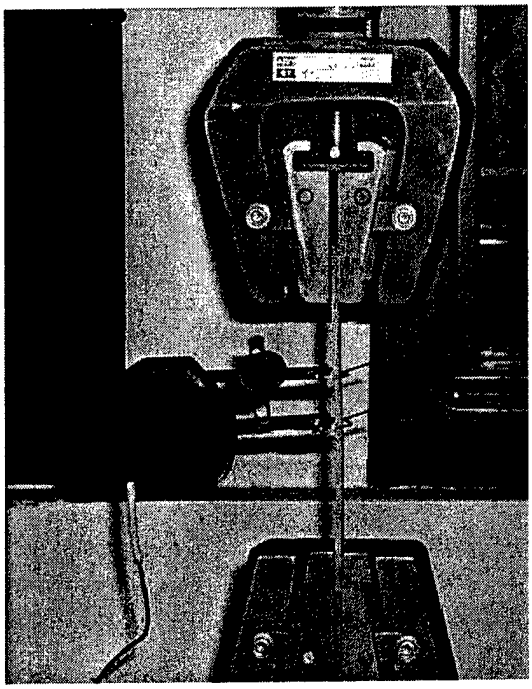

Figure 4: Instron tensile testing set-up

2.5 Statistical methods. The tensile testing data was subjected to Analysis of Variance (ANOVA) for a fixed effects model per standard and accepted methodologies [7]. As a short review - ANOVA allows us to partition the total variability of the data into its component parts. In our experiment, these components are: (1) the variability between groups due to differences in treatment, and (2) variability within a particular group due to random error. Dividing the components by the degrees of freedom, we have an estimated sample variance of each component. The estimate of the sample variance between treatment groups is denoted MS_t, and the estimate of the sample variance within groups due to random error is denoted MS_e.

Applying Cochran's theorem, we compare the two components. If the null hypothesis, (that the treatments are equal) is true, then the estimated sample variances should both be independently distributed Chi-square random variables. The ratio of the two components is distributed as an "F" statistic. Standard "F" test tables give a reject value based on the level of confidence, the degrees of freedom of the treatments, and the degrees of freedom of the random errors.

Our test statistic is derived by taking the ratio MS_t / MS_e. Any value of this test statistic greater than the standard table value allows us to reject the null hypothesis. If we cannot reject the null hypothesis, then performing a contrast gives us no additional information. We have chosen a 1% level of confidence - meaning that the probability of falsely rejecting the null hypothesis as a result of this comparison to the standard table values is less than 1%.

Since we are testing more than two distinct groups within each material property and class, a rejection of the null hypothesis would require further analysis contrasting each possible pair of treatment groups. This gives us additional information regarding the sources of the differences between the individual groups, and relationships between the groups.

3.0 Experimental Results

3.1 Screening Experiment. For the initial screening experiment, an analysis of variance of the ultimate load data associated to Figure #5 showed that we were able to reject the initial hypothesis - that build direction anisotropies were *not* significant in load carrying capability - with a much less than 1% chance of falsely rejecting. The test statistic value needed for the 1% chance of false rejection was 4.98 (or greater). Our analysis of experimental data yielded a test statistic of 57.81 - an order of magnitude greater than the "reject" value.

Contrasts of the Flat, Edge and Standing data groups showed a statistically significant difference between the Flat and Standing groups, and between the Edge and Standing groups. The Flat and Edge groups did not demonstrate a statistically significant difference. These contrasts make sense.

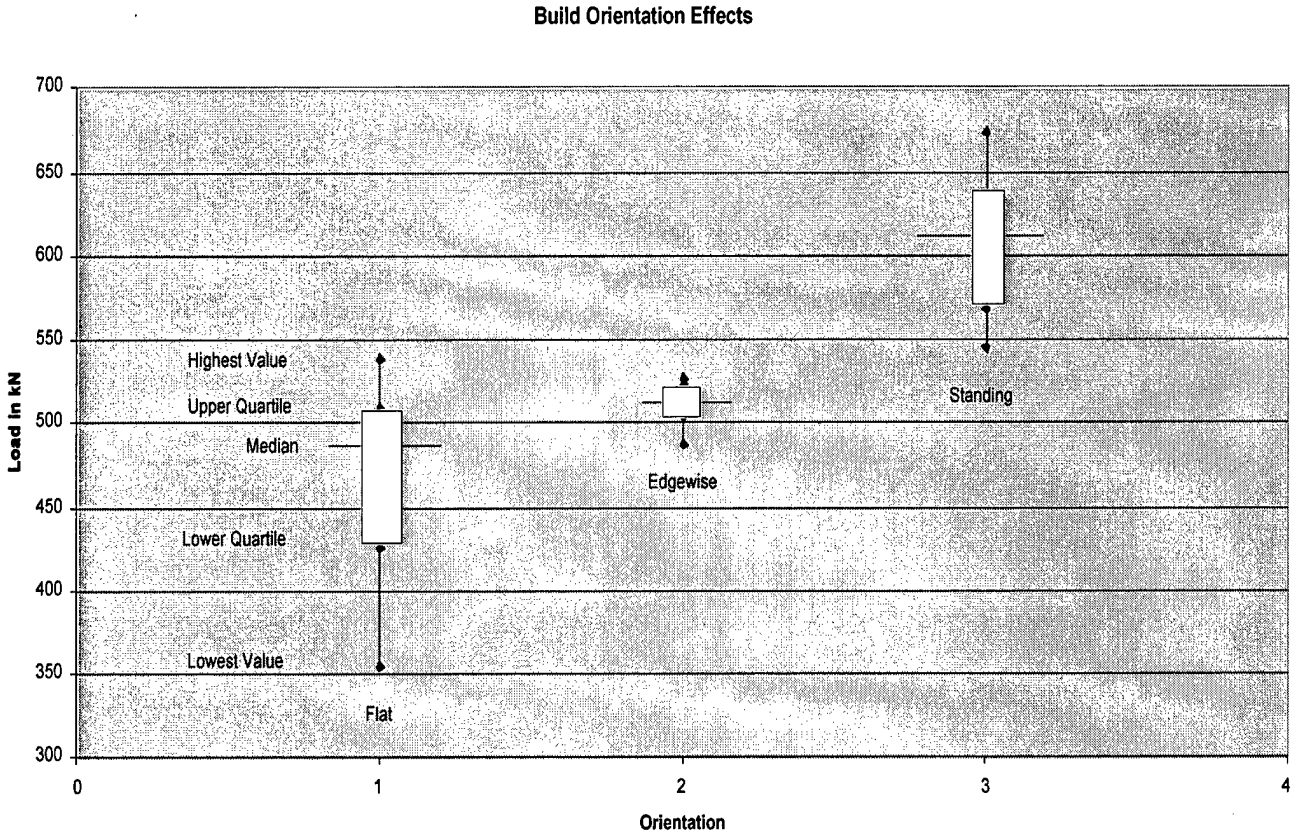

Figure 5: Load carrying capability data for the initial experiment

The difference in means between the Flat and Edge groups is less than 5%, and all of the data values of the Edge group fit between the high and low extremes of the Flat group. On further examination, one can see that both the Flat and Edge groups experience in-plane loading during tensile testing. This is not where one would anticipate the anisotropy to be evident. Rather this is an expected result of comparing two variations of in-plane loading samples.

The difference in mean of the Standing group with respect to the means of the Flat group and the Edge group is +25% and +20%. It is not surprising to see differences between the mean of the transverse loaded Standing group and the means of the in-plane loaded Flat and Edge groups. This is where one would expect to see evidence of an anisotropy; however, it is surprising that the mean of the Standing group exceeds the means of the Flat and Edge groups by fairly large, and statistically significant, percentages.

3.2 The Second Experiment in DSM 8120 material yielded a similar result with additional information. In this experiment, we examined three hypotheses based on the loading direction versus build layer orientation relationship, namely this relationship would not cause statistically significant anisotropies in Peak Stress, Young's Modulus, and Elongation at Break for test coupons aged less than 24 hours. Also, when an anisotropy was identified, a contrast of the data groups was undertaken. A summary of the test data and contrast results is provided in Figure #6.

Parameter	Group	Mean	Std Dev	Different from Flat	Different from Standing	Different from Angled
Peak Stress (psi)	Flat	2098.35	63.15	--	Yes	Yes
	Standing	2495.53	131.47	Yes	--	Yes
	Angled	2238.14	43.20	Yes	Yes	--
Young's modulus (ksi)	Flat	10.32	0.39	--	Yes	Yes
	Standing	12.90	0.52	Yes	--	Yes
	Angled	11.13	0.41	Yes	Yes	--
Elongation (%)	Flat	10.19	0.78	--	No	Yes
	Standing	9.05	1.57	No	--	No
	Angled	8.18	0.66	Yes	No	--

Figure 6: Summary of 8120 data for the second experiment

Peak Stress - The analysis of variance for the peak stress data showed that we were able to reject the initial hypothesis - that build direction anisotropies were *not* significant in peak stress - with a much less than 1% chance of falsely rejecting. The test statistic value needed for the 1% chance of false rejection was 5.39 (or greater). Our analysis yielded a test statistic of 24.96 - an order of magnitude greater than the "reject" value.

A statistical contrast of the two peak stress data groups with the least difference in means, the Flat and Angled groups, showed statistically significant differences between those groups. Contrast bears out a statistically significant difference between the Flat and Standing groups as well. The Angled and Standing groups were contrasted as well. These two also proved to have statistically significant differences. In all of the contrast cases, the test statistic values were an order of magnitude greater than the required rejection value, and each of the groups was different from the others with respect to the Peak Stress property.

Young's modulus - An analysis of variance for the Young's modulus data showed that we were able to reject the initial hypothesis - that build direction anisotropies were *not* significant in

Young's modulus - with a much less than 1% chance of falsely rejecting. The test statistic value needed for rejection was 5.39 (or greater). Our analysis of the experimental data yielded a test statistic of 38.78 – again, an order of magnitude greater than the "reject" value.

Contrasting the groups Flat and Angled, we see a statistically significant difference in the Young's modulus. Subsequent contrast of the remaining two possible comparisons shows that they are different as well with respect to the Young's modulus property.

Elongation at Break – The initial analysis of variance of the entire data set of three groups shows that we can reject the hypothesis - that build direction anisotropies were *not* significant in Elongation at Break – with a less than 1% chance of falsely rejecting that premise. The test statistic value needed for the 1% chance of false rejection was 5.39 (or greater). Our analysis of experimental data yielded a test statistic of 10.45.

In this case, the Flat and Angled groups showed the largest difference in the group means. The least difference in means was between the Standing and Angled groups. The test statistic for the Standing and Angled contrast was 3.09 versus a minimum reject value of 7.95 – we cannot reject the hypothesis based on differences in these two groups. A similar result occurs with the Standing and Flat groups – the test statistic is 5.14 versus a reject value of 7.95 or greater. Only in the contrast of the groups with the largest difference in means, groups Flat and Angled, do we have a test statistic sufficiently large (46.66) to reject the null hypothesis.

3.3 Validation Experiment in Vantico SL-5510 - As noted in the Experimental Method section, the suspected material property anisotropies may be related to the chemical composition of a particular class rather than being process related, or evident across all classes. A similar series of tests were run using net-shaped coupons fabricated from Vantico SL-5510 resin. A similar result in this material may give an indication that the effect is process related.

				Different from	Different from	Different from
Parameter	Group	Mean	Std Dev	Flat	Standing	Angled
Peak Stress (psi)	Flat	5762.32	152.26	--	Yes	Yes
	Standing	7755.67	972.35	Yes	--	No
	Angled	7837.70	838.50	Yes	No	--
Young's modulus (Ksi)	Flat	51.23	3.43	--	No	Yes
	Standing	55.76	9.70	No	--	No
	Angled	59.33	8.26	Yes	No	--
Elongation(%)	Flat	33.90	3.70	--	Yes	Yes
	Standing	21.70	6.40	Yes	--	No
	Angled	22.30	7.40	Yes	No	--

Figure 7: Summary of test data and contrast results in Vantico SL- 5510 resin

Peak Stress - The analysis of variance for the peak stress data showed that we were able to reject the initial hypothesis - that build direction anisotropies were *not* significant in peak stress - with a much less than 1% chance of falsely rejecting. The test statistic value needed for the 1% chance of false rejection was 5.39 (or greater). Our analysis of yielded a test statistic three orders of magnitude greater than the "reject" value.

A statistical contrast of the two peak stress data groups with the least difference in means, the Standing and Angled groups, showed no statistically significant differences between those groups. The test statistic for these two groups was .05 versus a reject value of 7.95 or greater, and the hypothesis that the two treatment means are different cannot be rejected. Contrasting the two remaining sets leads to the rejection of the hypotheses in both cases. The Standing and Flat contrast and the Angled and Flat contrast reject the hypothesis with test statistics of 49.22 and 71.17, respectively.

Young's modulus - Similarly, an analysis of variance for the Young's modulus data showed that we were able to reject the initial hypothesis - that build direction anisotropies were *not* significant in Young's modulus - with a much less than 1% chance of falsely rejecting. The test statistic value needed for the 1% chance of false rejection was 5.39 (or greater). Again, the analysis yielded a test statistic three orders of magnitude greater than the "reject" value.

Group contrast results are summarized in Figure #7. Even though the ANOVA of the full data set rejects the hypothesis with a test statistic much larger than the required reject value, we see that two of the contrasts do not show a statistically significant difference between treatment means of the groups under consideration. Neither the Angled and Standing contrast nor the Flat and Standing contrast is capable of rejecting the hypothesis. In these two contrasts, the test statistics were .94 and 2.33, respectively while the reject value was 7.95 or greater.

Elongation at Break – The initial analysis of variance of the entire data set of three groups shows that we can reject the hypothesis - that build direction anisotropies were *not* significant in Elongation at Break – with a less than 1% chance of falsely rejecting that premise. The test statistic value needed for the 1% chance of false rejection was 5.39 (or greater). Our analysis of experimental data yielded a test statistic of 15.75 – nearly a factor of 3 greater than the "reject" value.

In this case, both the Flat and Angled group contrast and the Flat and Standing group contrast generated test statistics sufficiently large to reject the hypothesis. The test statistics generated were 24.06 and 32.96, respectively, versus reject statistic of 7.95 or greater. The test statistic for the Standing and Angled contrast was .04 versus a minimum reject value of 7.95 – we cannot reject the hypothesis.

Summary of results – Statistically significant material anisotropies related to build orientation were shown for the Peak Stress, Young's modulus and Elongation at Break properties of net shaped test coupons fabricated using the Stereolithography process. This anisotropic effect was seen in two chemically different classes of material.

4.0 Conclusions

The initial screening experiment yielded two results: First, that there is a statistically significant anisotropy in the ultimate load carrying capability as a result of the relationship between build orientation and loading direction; and secondly, that the intuitive solution that the in-plane (Flat) property would be superior to the transverse plane (Standing) property was found not to hold in this case. The first result may be expected, but the second result is somewhat of a surprise.

The second experiment confirmed the finding of the first experiment and amplified the finding by yielding data on the Peak Stress, Young's modulus, and Elongation at Break properties. The in-plane loaded (Flat) coupons showed the lowest Peak Stress and Young's modulus and exhibited the greatest Elongation at Break. The transverse loaded (Standing) coupons showed the highest Peak Stress and Young's modulus while the least Elongation at break was found in the shear loaded (Angled) orientation.

The third experiment set had a similar finding – statistically significant anisotropies in Peak Stress, Young's modulus, and Elongation at Break – in a different class of material. Again the in-plane loaded (Flat) coupons showed the lowest Peak Stress and Young's modulus and exhibited the greatest Elongation at Break; however, in this trial, the transverse loaded (Standing) and shear loaded (Angled) coupons switched rankings. The shear loaded (Angled) coupons showed the highest Peak Stress and Young's modulus while the least Elongation at break was found in the transverse (Standing) loaded orientation.

The similar results with regard to the in-plane loaded coupons (Flat) across all three trials may be an indication of a process driven effect. The switching of ranks of the transverse loaded (Standing) and shear loaded (Angled) coupons in the results of the second and third experiments may be an indication of some process-chemistry interaction. The only two orientations that were found to be statistically different in every contrast, regardless of material, were the shear loaded (Angled) and in-plane loaded (Flat) orientations.

These results support the existence of a process driven effect with respect to tensile properties as a function of build orientation. Also, the data suggests that there may be a secondary process-chemistry interaction.

5.0 Future work

The next series of experiments will seek to verify the process driven effect by testing the third class of material. As noted, we will be using Vantico 7560 to represent the ABS-like class of materials. Other materials run on equipment other than our own, my yield additional information. In addition, to gain further information on the process driven effect, we will be testing coupons built in 7110 on a HeCd laser system. Given the proprietary nature of the materials, verification of a process-chemistry interaction could be quite difficult to verify.

Also, we will be checking this effect at various stages of material aging to determine if it is consistent across time, or simply transient.

6.0 Acknowledgments

The RPMI is supported by member companies. We would like to thank 3D Systems, Baxter International, DSM Somos, Pratt & Whitney, Siemens, and Vantico for their long-standing commitment and generous support.

7.0 References

[1] Montero, M; Roundy, S; Odell, D; Ahn, S-H; and Wright, P. K., "Material Characterization of Fused Deposition Modeling (FDM) ABS by Designed Experiments," Society of Manufacturing Engineers, 2001.

[2] Agarwala, M. K.; Bourell, D; Beaman, J. J., "Densification of Selective Laser Sintered Metal Parts by Hot Isostatic Pressing," Solid Freeform Fabrication Proceedings, 1994, pp 65-73. (Discusses ansiotropy of linear shrinkage.)

[3] Subramanian, P. K.; Vail, N. K.; Barlow, J. W.; and Marcus, H. L., "Anisotropy in Alumina processed by SLS," Solid Freeform Fabrication Proceedings, 1994, pp 330-338. (Discusses ansiotropy of green strength.)

[4] Popov, E.P., "Mechanics of Materials," 2nd edition, Prentice-Hall, Inc, Englewood Cliffs, NJ, 1976.

[5] Material Safety and Data Sheet (MSDS) for DSM 8120.

[6] Material Safety and Data Sheet (MSDS) for Vantico 5510.

[7] Montgomery, Douglas C., "Design and Analysis of Experiments," 4th edition, John Wiley & Sons, NY, NY, 1997.

American Society for Testing and Materials Specification D 638-01

Timoshenko, S. and Young, D. H., "Engineering Mechanics," 2nd edition, McGraw Hill Book Company, NY, NY, 1940.

Solid Freeform Fabrication Based on Micro-Plasma Powder Deposition

Huijun Wang, Wenhui Jiang, Michael Valant and Radovan Kovacevic
Research Center for Advanced Manufacturing, Southern Methodist University
Richardson, TX 75081
Reviewed, accepted August 25, 2003

Abstract

This paper presents a solid freeform fabrication (SFF) technique based on micro-plasma powder deposition (MPPD). The relationship between the geometric features of the deposited layers and the welding parameters is investigated. The arc length is controlled through the monitoring of the arc voltage. The result of building parts with functionally graded components by the MPPD process is shown as well. The microstructure and the properties of the deposited layers are analyzed. The experimental results show that the MPPD process is a promising welding-based solid freeform fabrication technology.

Introduction

Successfully responding to the ever changing and continually increasing high demands of today's global markets requires the rapid product development and manufacturing of new designs. Visualization tools often play a major role in taking an idea from the initial concept through the design phase, and into the final product development process. The following terms are often used interchangeably when referring to rapid prototyping technology: solid free-form fabrication, desktop manufacturing, layered manufacturing, and tool-less manufacturing. Solid freeform fabrication is one of the fastest growing automated manufacturing technologies that have significantly impacted the length of time between initial concept and actual part fabrication. However, to fully realize the potential cost and timesavings associated with rapid prototyping, the capacity to go from CAD models directly to metal components and tooling is crucial [1]. The use of arc welding to create freestanding shapes was established in Germany in the 1960's [2]. Companies such as Krupp, Thyssen, and Sulzer developed welding techniques for the fabrication of large components of simple geometry such as pressure vessels that can weigh up to 500 tons [3]. Other work in this area was undertaken by Babcock and Wilcox [4] who worked mainly on large components produced in an austenitic steel material. Also, work by Rolls-Royce has centered on investigating three-dimensional welding as a means of reducing the waste levels of expensive high-performance alloys that can occur in conventional processing. They have successfully produced various aircraft parts of nickel-based and titanium-based alloys. Research work on the welding-based rapid prototyping continues at universities and institutes such as the University of Nottingham, UK [5], the University of Minho, Portugal, the University of Wollongong, Australia [6-7], Southern Methodist University, USA [8-9], Korea Institute of Science and Technology and Hongik University [10], Indian Institute of Technology Bombay and Fraunhofer Institut Produktionstechnik und Automatisierung [11]. Most of the research work in this area is based on gas metal arc welding (GMAW) [3, 5, 6-8, 10] or gas tungsten arc welding (GTAW) [9].

The plasma arc technique is the only arc-welding process that is capable of achieving the energy density required for "keyhole" penetration - full penetration. However, high penetration keyhole welding is not the only capability of plasma arc welding. It can also be used as a low penetration weld surfacing technique. In this form it is commonly known as plasma transferred arc (PTA) surfacing or cladding. Being a modern advanced technology, PTA surfacing/cladding is widely used to coat details in high-risk functional areas with special materials that are resistant against intensive wear, corrosion, thermal, and percussive loading. Compared with conventional arc surfacing technologies, the PTA offers [12]:

1. A high deposition rate up to 10 kg/h;
2. A minimum losses of filler material;
3. A high quality of deposited metal;
4. A minimum penetration into the base metal (< 5%);
5. Deposits between 0,5 - 5,0 mm thickness and 3,0 - 50,0 mm width can be produced; rapidly in a single pass;
6. Fe-, Ni-, Co-, Cu- base alloys as well as composite materials can be clad.

In a competition with the laser surfacing/cladding, the PTA technology offers much higher productivity, a comparably higher quality of deposits and significantly lower costs. A PTA powder surfacing/cladding system (including power source, nozzle, and powder-feeding system) usually is about one-tenth the cost of a laser-based powder surfacing/cladding system.

In recent years, a number of researchers have paid more attention to the PTA surfacing/cladding technology. Matthes et al. [13-14] found that plasma-arc powder surfacing with the pulsed arc is a further development of shape welding that considerably reduces the thermal deformation of the component. The deformations and residual stresses caused on flat components by the intensive heat input during shape welding exert a negative influence on the component properties, particularly in the case of multi-pass weld surfacing. Dilthey et al. [15] developed a combined plasma-arc powder surfacing technique. It was a development from plasma-arc powder surfacing and plasma spraying. The advantages of the combined plasma-arc powder surfacing technique were less penetration depth and dilution, better mechanical properties of the surfacing weld, smaller heat-affect zone, and improvement in the possibility for isothermal heat input. Draugelates et al. [16-17] developed a plasma-arc powder nozzle and optimized the processing parameters with regard to heat input and powder delivery for the heavy-duty torch. It turned out that extensive coatings could be economically produced in one layer with dilution under 10%. They also implemented a two-powder plasma-arc surfacing process to manufacture anti-corrosion and anti-wear surfacing reinforced with oxide ceramics. So, plasma-arc-based deposition has been successfully used in cladding and surfacing. However, no literature has been found on the research topic – solid freeform fabrication based on plasma/micro-plasma powder deposition process. This paper investigates the feasibility of applying a micro-plasma powder deposition for solid freeform fabrication.

Experimental set-up

Micro-plasma arc welding is a kind of plasma arc welding (PAW) using low current and a specially designed welding torch. PAW usually works in two basic methods: transferred and

non-transferred arc modes. A flowing plasma gas is provided through the center of the torch and exits through a copper nozzle. When an arc is established between the tungsten electrode positioned within the body of the torch and the copper nozzle, the gas is ionized, forming high-temperature plasma. The arc can be transferred to the workpiece where the intense heat causes fusion, and a weld is produced. With compression of the copper nozzle, the energy density of the micro-plasma arc becomes much higher, and the arc diameter and the HAZ become much smaller than that in a conventional welding arc such as a GTAW arc. So, micro-plasma welding applications often overlap with laser welding applications. The working principle of micro-plasma metal powder deposition is shown in Figure 1. A transferred plasma arc exists between the torch nozzle and the substrate, and generates a molten pool on the surface of the substrate. The metal powder is fed into the molten pool by the carrier gas (argon) through the powder feed nozzle. Then, the fed powder is melted under the high temperature of the plasma arc. With the moving away of the plasma arc, the molten metal solidifies to form a deposited layer.

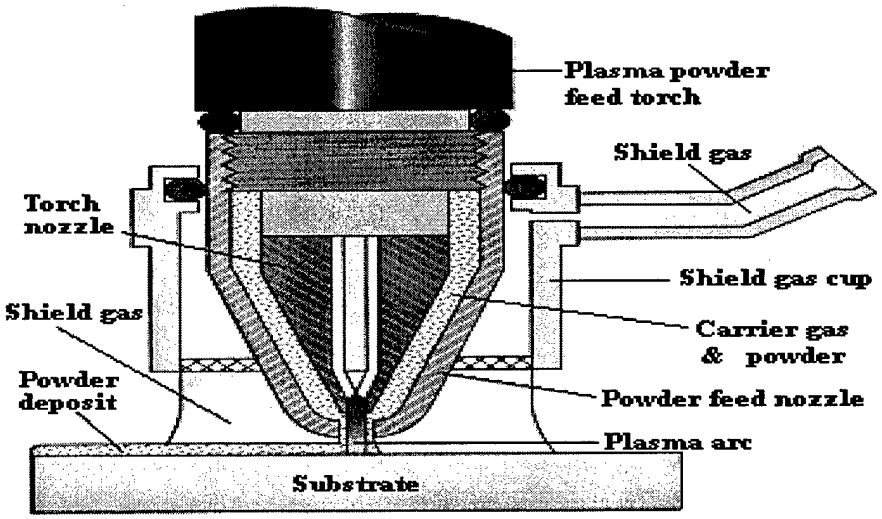

Fig. 1 Schematic diagram of micro-plasma powder deposition

The developed MPPD rapid prototyping system is shown in Figure 2. It consists of two axes in vertical position (Z axis and R axis), one axis in the horizontal position (X axis), two powder feeders, a powder feeder controller, a MPPD torch, a micro-plasma welding power source, a motion system controller, and a computer. The Z-axis is used to lift the welding torch up with the increase of the deposited wall during the deposition process. The three-dimensional part is built on a substrate that is fixed on a rotating axis, the R-axis. The R-axis is attached to the X-axis in the horizontal position. By controlling the movement of the X-axis in the depositing process, a part with a variable diameter can be obtained. The two powder feeders can be controlled at different powder feeding-rates, respectively. So, powders with different compositions can be deposited to build parts with functionally graded compositions.

Substrate Preheating

Compared with the subsequent deposited layers, the first deposited layer has unique deposition conditions: the deposition base is the surface of a substrate (in this paper the dimensions of the

substrate are: outer diameter, 25 mm; inner diameter, 14 mm; height, 10 mm) at room temperature (25 °C). The subsequent layers are deposited on the surface of a previously deposited layer that is heated up to around 1000 °C. When a temperature gradient exists in a body, the heat energy is transferred by conduction. The heat-transfer rate per unit area is proportional to the normal temperature gradient:

$$q/A \sim \partial T / \partial x \quad (1)$$

where q is the heat-transfer rate, A is the section area perpendicular to the direction of the heat flow, and $\partial T/\partial x$ is the temperature gradient in the direction of the heat flow. When depositing the first layer, the temperature gradient between the welding-arc-heated area and the rest of the substrate is very large. The heat from the welding arc quickly dissipates into the substrate. So, it is difficult to accumulate enough energy to generate a molten pool on the surface of the substrate that is at room temperature. The status of the molten pool has a significant effect on the quality of the deposited layer. A smooth and uniform molten pool is the key for obtaining a deposited layer of high quality. One solution to the problem is to increase the initial temperature of the substrate before the starting of the deposition process. In this paper, the micro-plasma welding arc is used as a heat source to preheat the substrate. According to experimental results, the preheating parameters are determined as follows: welding current, 15 A; welding speed, 1 mm/s; and preheating time, 180 seconds.

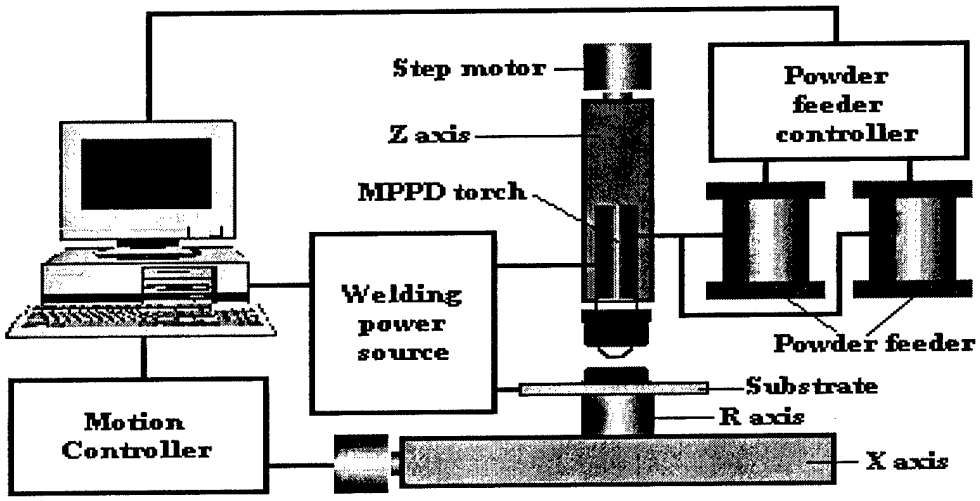

Fig. 2 Experimental Set-up for micro-plasma powder deposition

Arc length control

The arc length control is a key in the MPPD process. The reasons are as follows:

1. The heat input from the micro-plasma arc fluctuates with the variation of the arc length, and in turn, the molten pool size also fluctuates. The heat input from the welding arc Q is defined in Equation (2):

$$Q = \eta IV \quad (2)$$

where η is the coefficient of efficiency, I is the welding current, and V is the arc voltage. The welding power source has a constant-current characteristic. The heat input is directly proportional to the arc length. So, a variation of the arc length causes a fluctuation in the arc voltage (V), and consequently, the heat-input (Q) varies as well. As well known, the heat input has a determinant effect on the molten pool size. So, a fluctuation of the arc length usually leads to an undesired variation of the molten pool size and in turn results in non-uniform deposited layers.

2. The arc length has an effect on the height of the deposited layer. In Figure 3, L1 and L2 denote arc length respectively and L1 is larger than L2. Assuming that except for the arc length all other parameters such as welding current, pilot gas flow rate, shielding gas flow rate, carrier gas flow rate, powder feeding speed, and traveling speed are the same in the two different cases, therefore the micro-plasma arc and the flowing behaviors of the carrier gas and the powder are the same. The shape of the feeding powder stream is shown in Figure 4. Laser strips are projected to the powder stream, and the reflection of the laser strips is recorded. It is seen that the shape of the powder stream is a cone. The shorter the distance between the nozzle and the cross section along the axis of the nozzle, the smaller the cross-section area. To simplify the analysis, assume that the distribution density of the powder is uniform on each cross section that is vertical to the axis of the nozzle. According to the law of conservation of mass, the smaller the cross-sectional area of the carrier-gas and powder flow, the larger the distribution density of the powder. So per unit area of the molten pool, much more powder is received at arc length L2 than at arc length L1. Because the height of the deposited layer is directly proportional to the amount of the fed powder on the molten pool per unit area, a larger height of the deposited layer is generated when the arc length is short.

In order to monitor and control the arc length in the MPPD process, the relationship between the arc length and the arc voltage is investigated. For instance, when the current is 15 A, the relationship between the arc length and the arc voltage is shown in Figure 5. It is seen that the arc voltage has a linear relationship with the arc length when the current is constant. The arc voltage is directly proportional to the arc length. In addition according to the experimental results, it is also noted that the current has an effect on the relationship between the arc voltage, and the arc length and the effect of current is nonlinear and complicated. So, an arc length control strategy is developed based on the real-time measurement of the arc voltage and current:

1. The arc voltage is acquired at selected arc lengths and currents. The selected arc lengths are from 1 mm to 6 mm with an increment of 0.5 mm. The selected currents are from 10 A to 15 A with an increment of 1 A.
2. Five linear equations can be obtained by linear regression analyses of the data acquired at different currents. Each linear equation describes the relationship of the arc voltage and the arc length at a corresponding current.
3. In the MPPD process, the current is always set to be one of the selected current values (10 A, 11 A, 12 A, 13 A, 14 A, and 15 A). The current is constant after it is set because the power supply has a characteristic of constant-current output. So, the effect of current fluctuation on the relationship of the arc voltage and arc length can be neglected. The arc length control process consists of the following steps: acquiring arc voltage, low-pass filtering of the acquired signal, selecting a linear equation according to the current value, calculating the arc length, and moving the torch 0.05 mm up (down) if the calculating result is smaller (larger) than the given arc length. Repeat the process.

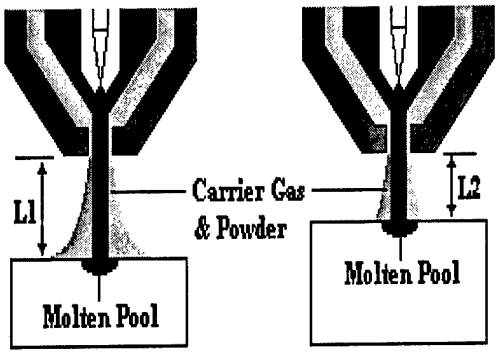

Fig. 3 Effect of arc length on powder feeding

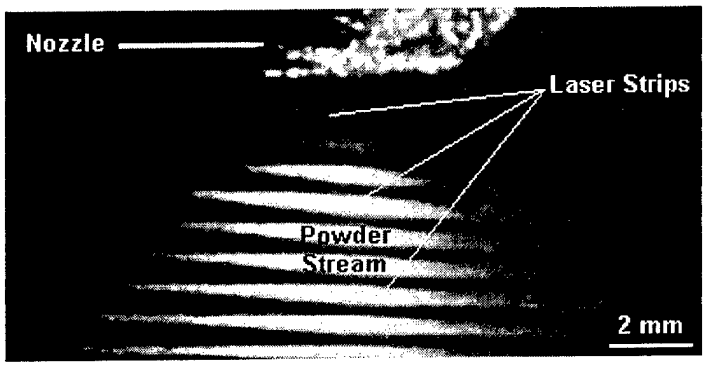

Fig. 4 Shape of the feeding powder stream

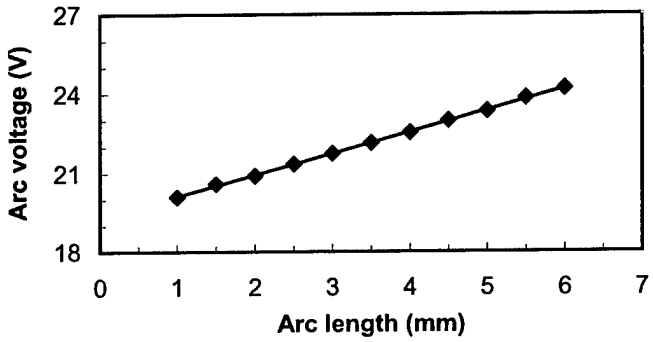

Fig. 5 Relationship between arc length and arc voltage at 15-A current

Relationship between welding parameters and deposited layer's geometry

The effect of the welding speed on the deposited layer's geometries is shown in Figure 6(a). The welding speed is 3.14 mm/s, 4.18 mm/s, and 6.28 mm/s, respectively. The welding current is 15 A, the arc length is 3.0 mm, the plasma gas flow rate is 0.4 l/min, the shielding gas flow rate is 10 l/min, and the powder-carrier gas flow rate is 3.5 l/min. The powder is H13 tool steel, and the powder-feeding rate is 2.3 g/min. It is seen that both of the deposited layer's width and height decrease with the increase in the welding speed. The effects of the welding speed on the width and height of the deposited layer are almost the same. The effect of the welding current on the deposited layer's geometry is shown in Figure 6(b). The welding current is 15 A, 13 A, and 11 A, respectively. The welding speed is 3.14 mm/s, the arc length is 3.0 mm, the plasma gas flow rate is 0.4 l/min, the shielding gas flow rate is 10 l/min, and the powder-carrier gas flow rate is 3.5 l/min. The powder is H13 tool steel and the powder-feeding rate is 2.3 g/min. It is seen that the width of the deposited layer increases with the increase in the welding current. The height of the deposited layer decreases slightly with the increase in the welding current. The effect of the powder-feeding rate on the deposited layer's geometries is shown in Figure 6(c). The powder is H13 tool steel, and the powder-feeding rate is 1.2 g/min, 2.3 g/min, and 3.6 g/min, respectively. The welding current is 15 A, the arc length is 3.0 mm, the plasma gas flow rate is 0.4 l/min, the shielding gas flow rate is 10 l/min, and the powder-carrier gas flow rate is 3.5 l/min. It is seen that the deposited layer's height increases with the increase in the powder-feeding rate. The deposited layer's width slightly decreases with the increase in the powder-feeding rate. It is also seen that the powder-feeding rate has a much larger influence on the height of the deposited layer than on the width of the deposited layer.

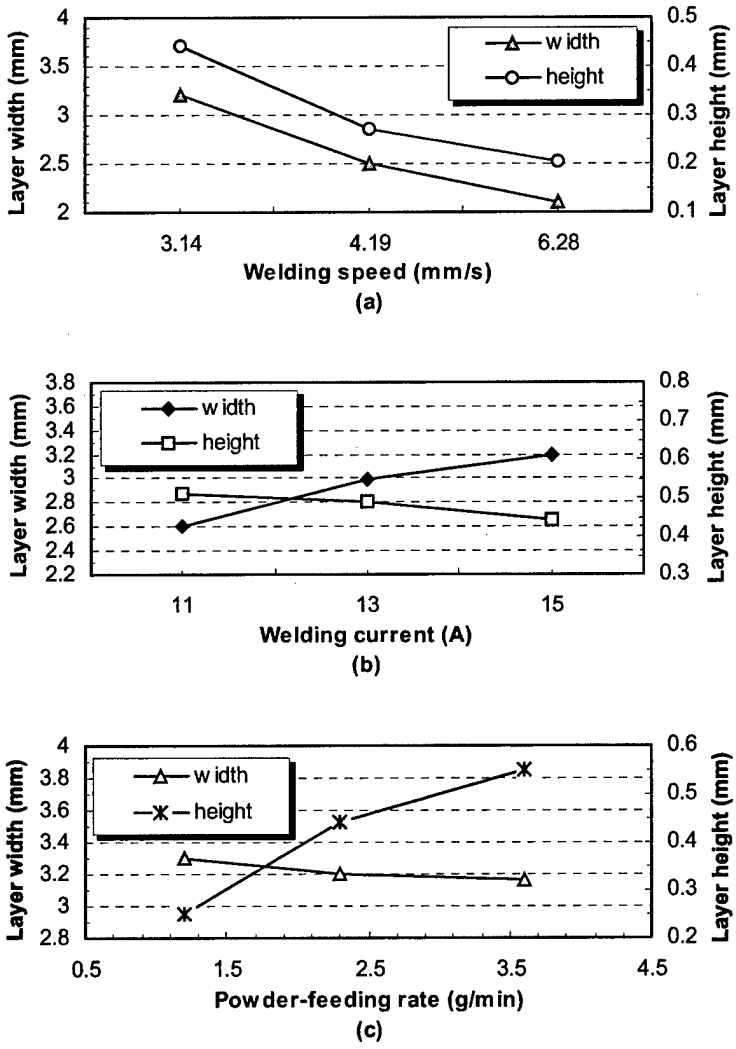

Fig. 6 Effects of welding parameters on the geometries of the deposited layer: (a) effect of welding speed; (b) effect of welding current; (c) effect of powder-feeding rate

Test parts

Several test parts are built with the developed MPPD process as shown in Figure 7. The geometrical parameters of the part in the form of a cylinder [Figure 7(a)] are as follows: number of layers is 80; the average layer of thickness is about 0.42 mm; the outer diameter is 22.4 mm; and the inner diameter is 17.2 mm. The geometrical parameters of the part in form of a cone [Figure 7(b)] are as follows: number of layers is 40; the average layer of thickness is about 0.35 mm; the outer diameter at the top is 30.0 mm; the inner diameter at the top is 26.2 mm; the outer diameter at the bottom is 21.5 mm; the inner diameter at the bottom is 16.5 mm; and the over-hang angle is 23 degree. The test part in the form of a cylinder, as shown in Figure 7(a), is deposited with 80 layers. The traveling speed is 3.14 mm/s. The diameter of the deposited part is 20 mm. The powder-feeding rate is 2.3 g/min. So, the amount of feeding powder in the deposition process is 61.3 g. The weight of the substrate is 28.9 g. After the deposition process,

the total weight of the substrate and the deposited cylinder part is 65.1 g. So, the powder utilization efficiency in this deposition process is about 59%.

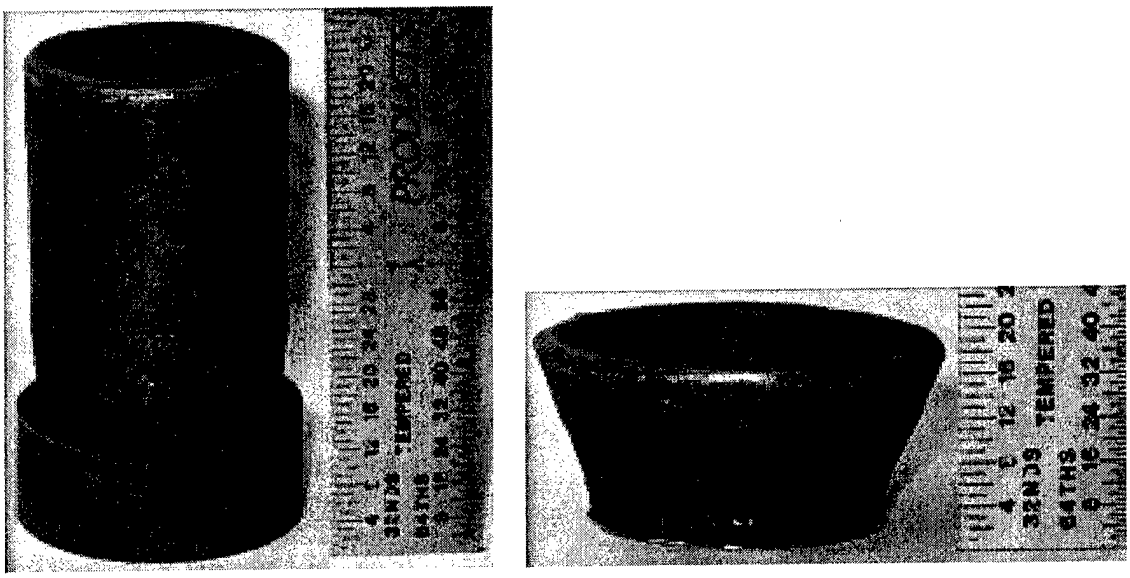

(a) (b)

Fig. 7 Test parts: (a) part in form of a cylinder; (b) part in form of a cone

The term functionally graded composition (FGC) is applied to components whose composition and structure vary progressively as a function of position. A FGC (along the z-axis) test part is produced by the successive deposition of the H13 tool steel powder and tungsten carbide powder. The part is in the form of a cylinder (the height, 6 mm; the outer diameter, 23.0 mm; and the inner diameter, 17.5 mm) and is built with 20 layers on a mild-steel substrate. The cross section of the FGC part is shown in Figure 8. In the first 12 layers, the feeding powder is 100% H13 tool steel powder. From layer 13, the tungsten carbide powder is blended with H13 tool steel. The percentage of volume of the tungsten carbide powder increases gradually from 0 to 20 %. Figure 9 shows the interface between the substrate and the deposited wall that corresponds to position A in Figure 8.

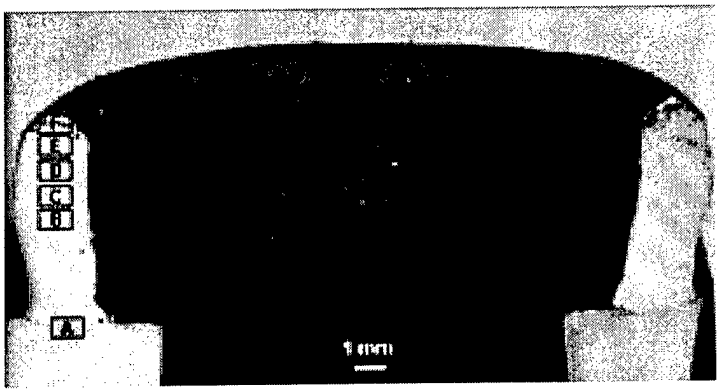

Fig. 8 Cross section of a FGM test part

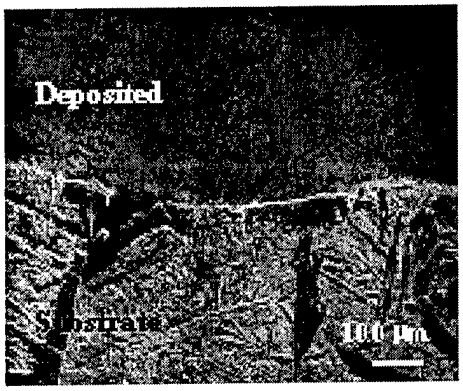

Fig. 9 Interface between the substrate and the deposited wall

Scanning electron microscopy (SEM) observation indicates that injected tungsten carbide dissolves and subsequently, fine carbides precipitate from supersaturated melt during cooling, as shown in Figure 10. The dissolution of tungsten carbide is rather aggressive during deposition. Only at the top of the part can injected coarse tungsten carbide be observed, as shown in Figure 11. The reprecipitation of fine carbide happens extensively. Its morphology, size, and amount are closely related to the amount of injected tungsten carbide. Figure 12 shows typical microstructures of reprecipitated carbide that correspond to the positions B, C, D, and E in Figure 8. In these back-scattered electron images, the precipitated carbide appears brighter than the matrix, indicating that it is rich in tungsten. At the lowest amount of injected tungsten carbide, the precipitated carbide is fewer, globular, and located at the grain boundary of the matrix [Figure 12(a)]. By increasing the injected tungsten carbides, the amount of precipitated carbide increases and its morphology evolves into an intergranular network [Figure 12(b)]. The higher amount of injected tungsten carbide results in the formation of herringbone [Figure 12(c) and (d)]. At a higher magnification, a significant amount of dark carbide can be seen [Figure 13]. It may be MC rich in titanium and chromium, whose contents in H13 are as high as 5.2 and 4.3 wt.%, respectively.

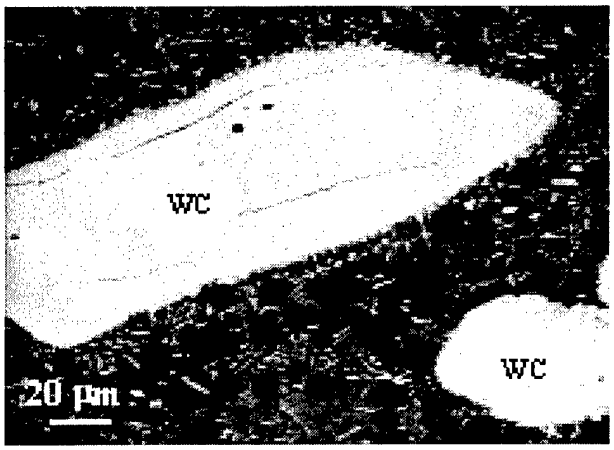

Fig. 10 Dissolution of tungsten carbide and Precipitation of fine carbides (WC – tungsten carbide)

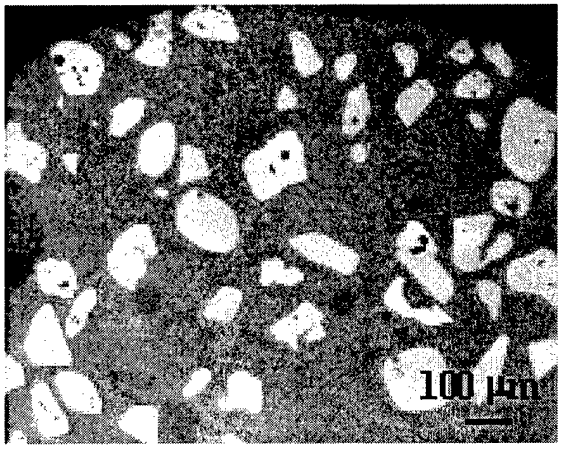

Fig. 11 Coarse tungsten carbide on top layers of the FGM part

Microstructural observation indicates that tungsten carbide is unstable and dissolves during deposition. Injected coarse tungsten carbide is observed only at the top of the deposited part. This result may be attributed to rapid cooling and a higher amount of injected tungsten carbide. Dissolution of injected tungsten carbide increases the contents of tungsten and carbon in the melt. During subsequent cooling, tungsten carbide precipitates from the supersaturated melt. From the present metallographical observation, it can be inferred that a eutectic reaction is predominant during solidification. When the amount of injected tungsten carbide is smaller, and consequently, fewer tungsten and carbon atoms are released into the melt, the melt is hypoeutectic and tungsten carbide precipitates as a final formed phase and is pushed to the grain boundary of the matrix. A higher amount of injected tungsten carbide increases the contents of tungsten and carbon in the melt. That increase results in a eutectic reaction during solidification, forming herringbone carbide.

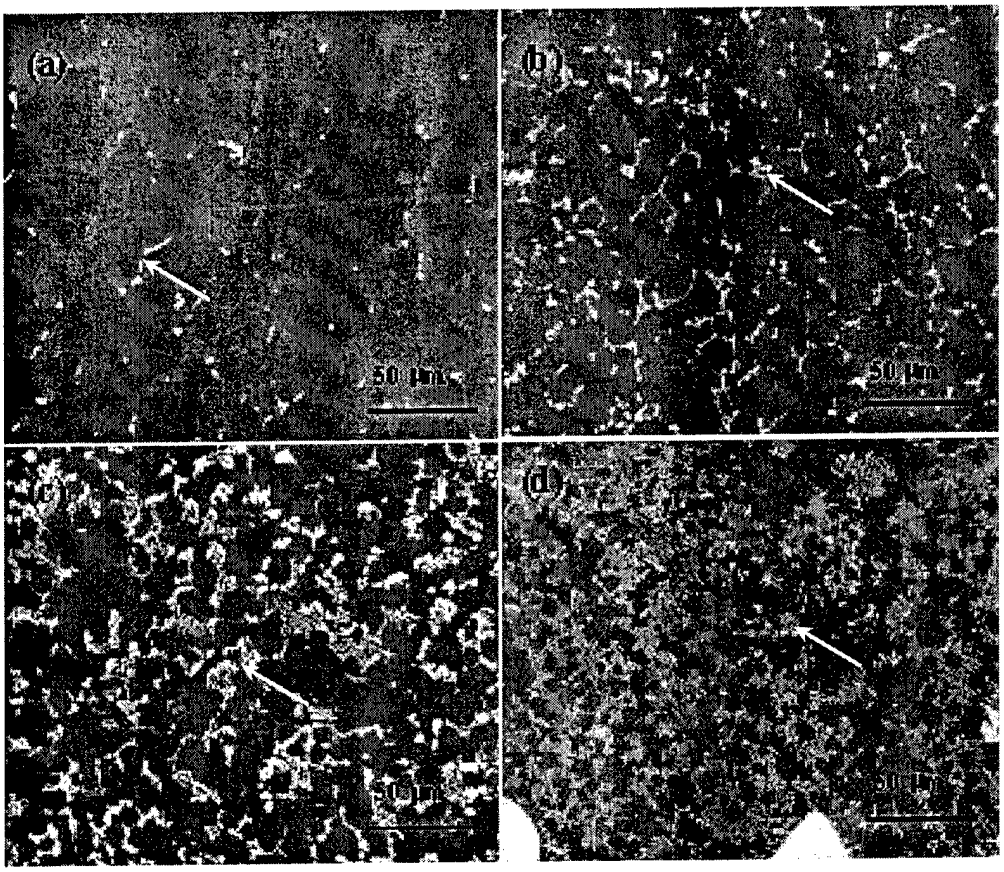

Fig. 12 Microstructures of re-precipitated carbide corresponding to the position in Fig.8: (a) position B; (b) position C; (c) position D; (d) position E. (the arrow indicates the phases

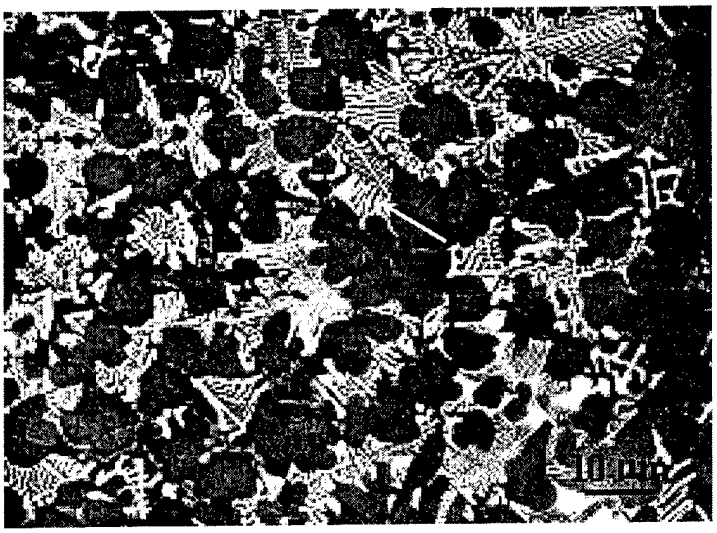

Fig. 13 Microstructures of re-precipitated carbide at a higher magnification (the arrow indicates the phases)

The Vickers hardness (HV) distribution along the cross section of the test FGC part is shown in Figure 14. It is seen that the hardness of the deposited wall continuously increases by increasing the amount of injected tungsten carbide. The hardness value is an average value at three different points in the same testing area. The hardness of the tungsten carbide is 1114 Hv.

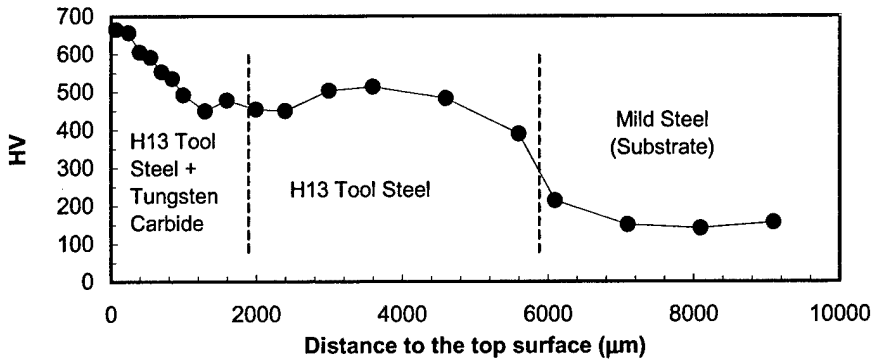

Fig. 14 Hardness (HV) distribution on the cross section of the test FGM part

Conclusions

The MPPD based SFF process allows the components to be directly built from the corresponding powder. Substrate preheating and arc length control are required in the developed deposition process. The arc voltage signal can be used to monitor and control the arc length according to the developed control strategy. The power of the micro-plasma arc applied in the deposition process is less than 375 W. A number test parts are made of H13 tool steel powder with acceptable surface quality and mechanical properties including parts with functionally graded composition. The powder utilization efficiency is about 59%. The microstructural observation on the FGC part shows that the dissolution of tungsten carbide is fast occurring during deposition. Injected coarse tungsten carbide can only be observed at the top of the part. The reprecipitation of fine carbide happens extensively. From the metallographical observations, it can be inferred that a eutectic reaction is predominant during solidification. Experimental result shows that the hardness of the built FGC part continuously increases with increase in the amount of injected tungsten carbide.

Acknowledgement

The work was financially supported by U.S. Department of Education Grant No. P200A80806-98 and THECB's Grant No. 003613-0016-2001.

Reference

1. J. J. Beaman, J. W. Barlow, R. H. Bourell, H. L. Craford, H. L. Marcus and K. P. McAlea, "Solid Freeform Fabrication: A New Development in Manufacturing," Kluwer Academic Publishers, Dordrecht/Boston/London, 1997.
2. K. Kassmaul, F. W. Schoch, and H. Lucknow, "High Quality Large Components "Shape Welded" by a SAW Process", September 1983, Welding Journal.

3. K-H. Piehl, "Formgebendes Schweißen von Schwekomponenten", January 1989, Company report: Thyssen Aktiengesellschaft, Duisburg.
4. T. E. Doyle, (Babcock & Wilcox), "Shape Melting Technology", October 1991, The Third International Conference on Desktop Manufacturing: Making Rapid Prototyping Pay Back, The Management Round Table.
5. P. M. Dickens, R. Cobb, I. Gibson, and M.S. Pridham, "Rapid Prototyping Using 3D Welding," Journal of Design and Manufacturing, No.3, 1993.
6. A. F. Ribeiro and J. Norrish, " Metal Based Rapid Prototyping for More Complex Shapes", 6th Biennial International Conference on "Computer Technology in Welding", TWI, Abington Publishing, 9-12 June 1996, Lanaken, Belgium.
7. A. F. Ribeiro and J. Norrish, " Rapid Prototyping Process Using Metal Directly", Proc. of the 7th Annual Solid Freeform Fabrication Symposium, Aug. 12-14, 1996, Austin, TX.
8. R. Kovacevic and H. E. Beardsley, "Process Control of 3D Welding as a Droplet-Based Rapid Prototyping Technique", Proc. of the 9th Annual Solid Freeform Fabrication Symposium, Aug. 10-12, 1998, Austin, TX
9. H. Wang and R. Kovacevic, "Rapid Prototyping Based on Variable Polarity Gas Tungsten Arc Welding for 5356 Aluminum Alloys", the Proceedings of the Institution of Mechanical Engineers, Part B, Journal of Engineering Manufacture, Vol. 215, November, 2001, pp. 1519-1527.
10. Y. Song, S. Park, K, Hwang, D. Choi and H. Jee, "3D Welding and Milling for Direct Prototyping of Metallic Parts", Proc. of the 9th Annual Solid Freeform Fabrication Symposium, Aug. 10-12, 1998, Austin, TX
11. K. Karunakaran, P. Shanmuganathan, S. Roth-Koch and U. Koch, "Direct Rapid Prototyping of Tools", Proc. of the 9th Annual Solid Freeform Fabrication Symposium, Aug. 10-12, 1998, Austin, TX
12. http://www.plasma-master.com.ua/eng/science/science_pta.htm
13. K.-J. Matthes, K. Alaluss and F. Khaled, "Utilisation of the Finite-element Method in Order to Optimize Shaping Plasma-arc Powder Weld Surfacing for the Manufacture of Forming Tools Suitable for High Stresses", Schweissen und Schneiden/Welding and Cutting, Vol. 54, No. 3, 2002, pp. 165-169.
14. K.-J. Matthes and K. Alaluss, "Plasma-arc Powder Surfacing with Pulsed Arc for Minimum Deformation Shaping", Schweissen und Schneiden/Welding & Cutting, Vol. 48, No. 9, Sep, 1996, pp. E170-E172.
15. U. Dilthey, J. Ellermeier, P. Gladkij and A. V. Pavlenko, "Combined plasma-arc powder surfacing", Schweissen und Schneiden/Welding and Cutting, Vol. 45, No. 5, May, 1993, pp. E75-E76.
16. U. Draugelates, B. Bouaifi and S. Giessler, "Two-powder Plasma-arc Surfacing of Nickel-base Alloys Containing Oxide Ceramics", Schweissen und Schneiden/Welding & Cutting, Vol. 50, No. 11, Nov, 1998, pp. 217-218.
17. U. Draugelates, B. Bouaifi and S. Schultze, "Heavy-duty Plasma-arc Powder Surfacing with Duplex Steels", Schweissen und Schneiden/Welding and Cutting, Vol. 51, No. 5, May, 1999, pp. E77-E81.

Experimental Study of the Cooling Characteristics of Polymer Filaments in FDM and Impact on the Mesostructures and Properties of Prototypes.

Q. Sun, G.M. Rizvi, C.T. Bellehumeur [1*] and P.Gu[2]
[1]Department of Chemical and Petroleum Engineering
[2]Department of Mechanical and Manufacturing Engineering
University of Calgary, Calgary, Alberta, T2N 1N4 Canada

Reviewed, accepted August 19, 2003

Abstract

The bonding quality among polymer filaments in the fused deposition modeling (FDM) process determines the integrity and mechanical properties of the resultant prototypes. This research investigates the bond formation among extruded acrylonitrile butadiene styrene (ABS) filaments in the FDM process. Experimental measurements of the temperature profiles were carried out for different specimens and their effects on mesostructures and mechanical properties were observed. Models describing the formation of bonds among polymer filaments during the FDM process are discussed. Predictions of the degree of bonding achieved during the filament deposition process were made based on thermal analysis of extruded polymer filaments. The bond quality was assessed based on the growth of the neck formed between adjacent filaments and their failure under flexural loading. Further experimental work is underway to assess the validity of the proposed models.

1. Introduction

Rapid prototyping (RP) is one of the fastest growing manufacturing technologies for fabrication of cost effective models, prototypes and one of a kind parts. It is being applied in a very large number of fields, such as aerospace, automotives, architecture, and medicine. RP technologies provide the ability to create almost completely finished products from CAD files. Moreover, it has been shown that some RP techniques have the potential to fabricate parts with locally controlled properties (porosity, density and mechanical properties) [1,2]. The FDM machine is basically a computer numerically controlled (CNC) gantry machine, carrying double miniature extruder head nozzles. In the FDM process, parts are fabricated by extruding a semi-molten filament through a heated nozzle in a prescribed pattern onto a platform. As the material is deposited, it cools, solidifies and bonds with the surrounding material. The fabrication of parts with locally controlled porous structure and mechanical properties can be achieved by varying the deposition strategy, deposition orientation and other process conditions. However, for directly producing functional parts, fundamental understanding of mechanical properties of FDM parts with respect to fabrication process parameters is essential.

* Corresponding Author: C.T. Bellehumeur, cbellehu@ucalgary.ca, tel.: (403) 220-8804, fax: (403) 282-3945

FDM prototypes are composites of partially bonded filaments and voids. The bonding quality among filaments in FDM parts is an important factor in determining the integrity and mechanical properties of resultant prototypes. The formation of bonds in FDM process is driven by the thermal energy of semi-molten material. The quality of bonds formed between individual filaments depends on the growth of the neck formed between adjacent filaments and on the molecular diffusion and randomization at the interface. The bond formation process can be viewed as a sintering process for which the wetting phenomenon is of importance. It can also be modeled following approaches similar to those used to describe polymer welding, where the issue of molecular diffusion dominates.

Studies in FDM have primarily been directed towards the development of new materials or techniques for material deposition [3-5]. The mechanical properties of filaments and FDM parts were also investigated by a number of researchers [6-8]. However, considerable research efforts are still needed to fully understand the mechanical properties and their relations to the fabrication processes. In particular there is a lack of literature on experimental determination of the thermal profiles of the parts built using FDM. This data is especially important, as it is indicative of the bond formation between adjacent filaments. This paper provides the results of experimental determination of the thermal profiles of some simple shapes produced using the FDM process and their effects on the bond formation in terms of neck growth between adjacent filaments and the intermolecular diffusion at the interface and their evaluation in regards to the mechanical properties of the parts.

2. Experimental Work

The FDM 2000 from Stratasys Inc was used in this study. A commercial acrylonitril butadiene styrene (ABS P400) was used. The material was heated to 270°C and extruded through a nozzle onto a platform. The envelope temperature was set to 70°C. All parts were built using tip 12 with zero air gap. In addition, parts produced in this study consisted of unidirectional specimens to enhance the effects of the parameters being studied. The parts produced for mesostructure characterization and for mechanical testing were built with the normal five layers of support material. As the support material may have different characteristics, the parts generated for the measurements of the filament's temperature profile were built without the support layers.

The temperature profiles of extruded filaments were monitored using 0.003" K type thermocouples. The thermocouples were imbedded in the foam of the base plate of the FDM machine. The measurements were recorded and analysed through a high-frequency analog-digital converter (1000 readings per second), amplifier, data acquisition card 6024E and software Labview 6.0 on a PC.

The samples collected from the parts were sectioned using a Leica RM2165 microtome. The samples' cross-sections were viewed under optical microscopy. Pictures of these cross-sections were taken with a CCD camera mounted on an Olympus BX60 microscope and features were analyzed using the image analysis software Image-Pro®.

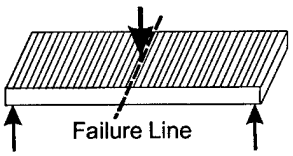

Figure 1: Flexural strength test sample

The flexural strength testing of the specimens was carried out on the ATM testing machine (Model TTS Series). The tests conformed to ASTM standard D 1184-98 for flexural strength of laminated sheets bonded with glue. The specimens were constructed so that the failure occurs in the bonds between adjacent filaments as shown in Figure 1. One deviation from the standard was that failure occurred between filament bonds in the same layer instead of the bonds between adjacent layers. The test also differed from the standard in that 12 layers of laminates were used instead of the stipulated eight layers, so that parts with reasonable dimensions could be tested.

3. Thermal Processes in FDM

The bonding between individual roads of the same layer and of neighboring layers of FDM parts is driven by the thermal energy of the semi-molten material that is extruded from the FDM head. The temperature history of interfaces plays an important role in determining the bonding quality. When the filament is deposited and is in contact with surrounding material, the interface's temperature is well above the material's glass transition (T_g). This condition favors molecular diffusion at the interface and the development of adhesive bonds.

Several heat transfer models describing the FDM process have been proposed in the literature. Yardimci [9] developed a family of numerical models for the fused deposition ceramic (FDC) processes. A similar analysis method is applicable to the FDM process that uses thermoplastic polymer as a raw material. Rodríguez-Matas [10] presented a two-dimensional heat transfer model in which the filament is laid on a stack of other filaments. The model assumes constant heat convection coefficient and perfect contact among stacked filaments. The results of the analysis show that the interface temperature rises above the glass transition temperature (T_g) immediately upon extrusion of the filament and stays above for a short period of time. In Rodríguez's analysis, the variations in the temperature across the filament thickness are taken into consideration, which allows for consideration of the boundary conditions at the interface. The model, however, neglects all contact resistances between the filaments. Based on this 2D model, the conduction heat transfer with the foundation is dominant over the convection heat transfer with the environment. Li and co-workers [11-12] used the lumped-capacity analysis for modeling the cooling process of the extruded filament, because the diameter of the extruded filament is fairly small and a uniform temperature distribution throughout the filament cross-section can be assumed.

3.1. Temperature Profile of a Single Filament

Experimental measurements performed on a single filament deposited on the base plate foam platform were used to assess the validity of the two models described above (Figure 2). The material properties were selected based on the work presented by Li et al. [12]. The measured data is in general agreement with these models, lying somewhere in between the two predicted values. It is interesting to note that at the higher temperatures prevailing in the initial

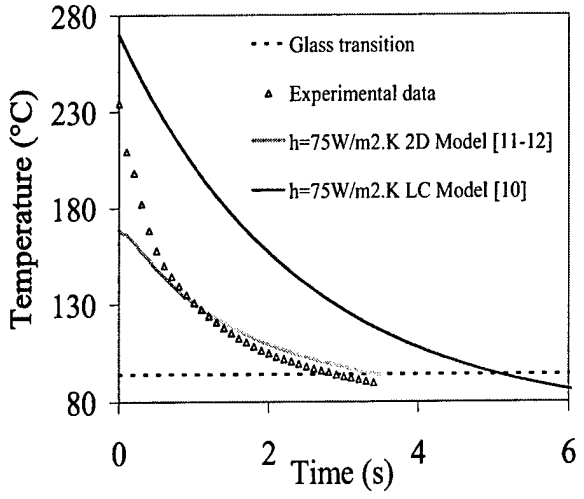

stage, the measured temperature profile exhibits more similarity to the lumped capacity model predictions, while at lower temperatures the measured data tends to follow the 2D model predictions [10]. The filament reached T_g in about three seconds, which is not very different from the predictions of both models.

Figure 2: Single filament cooling profile where *h* denotes the convective heat transfer coefficient.

3.2. Multi Layered Specimen: Temperature Profiles and Mechanical Tests

Two sets of specimens were constructed to carry out mechanical tests in order to assess the bond strength between the filaments. The dimensions of the test specimens were 3.1 mm x 19.1 mm x 31 mm, and all the filaments were oriented perpendicular to the longitudinal axis of the parts for the tests so that failure would occur in the bonds between the adjacent filaments of the lower layer as shown in Figure 1. In the first set, the specimens were built individually, whereas for the second set, three specimens were cut from one longer piece (Figure 3a). The temperature profiles at the base of each representative specimen were also recorded and are shown in Figure 3b.

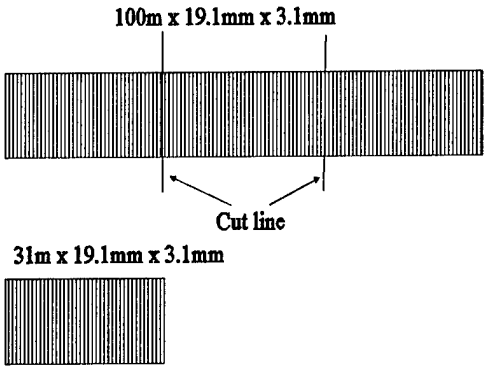

Figure 3a: Different specimens for flexural strength tests

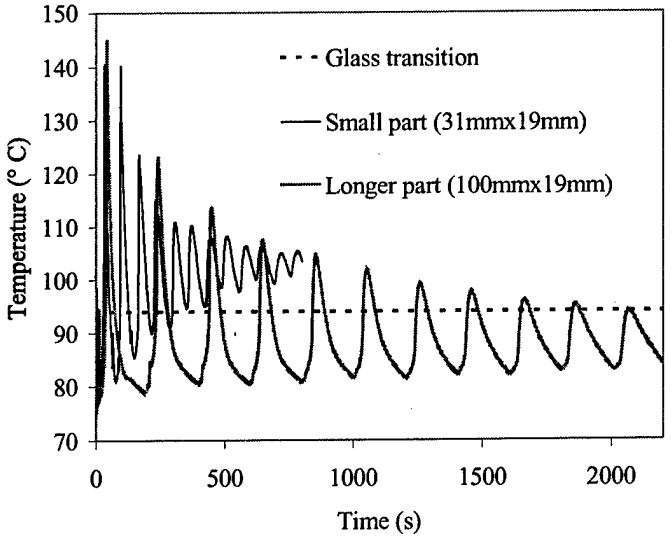

Figure 3b: Comparison of the temperature profiles for different specimens

One must note that the highest temperatures recorded in these profiles were lower than that measured for a single filament. This was due to the fact that a larger set of data (1000) was averaged to get one record per second, compared to 100 records per second for the previous case. Therefore, the higher values were averaged with lower values to give smaller peaks. Secondly, the models discussed in the previous section are only valid for single roads and cannot be applied to the situation represented in this case, where conduction is the dominant mode of heat transfer from the adjacent and upper layer filaments. It can be seen that for the specimens built individually (first set) the temperature at the base of the part remains above the glass transition temperature (T_g) after the 4th layer is built and continues to be high until the parts are completed. For the second set of specimens, the temperature reaches a level above T_g for only a short duration during the deposition of each layer of filaments. Therefore, it is to be expected that the individually made specimens will be stronger than the specimens cut from longer pieces. This expectation is indeed borne out by the mechanical testing and the results are shown in Table 1. The flexural strength of the individually made specimens was 2810 kPa, whereas, it was 2277 for the specimens cut from the larger part. The higher temperature profile, which gave rise to higher flexural strength, was the result of the shorter traverse of the FDM head for making one layer of the individually built specimen compared to the three times larger traverse to build the longer part from which three specimens were cut. This resulted in better bonding between the adjacent filaments and consequently the individually built parts exhibited higher failure loads.

The test data exhibited a much larger standard deviation in the results of the specimens cut from the longer parts (Table 1). This deviation could be the result of two possible factors. The first was that a number of larger parts exhibited miniature fault lines between adjacent filaments. One possible cause of these faults could be the wear in the mechanical system of the FDM machine. The obviously faulty samples were discarded on visual inspection, but if the fault was in the inner layers, or too small, it would escape visual inspection. Another factor was that the temperature profile was observed to change with variations in the location of the parts built. This would cause variation in exposure temperature/time of the parts being built. Further experimentation is required before drawing any definite conclusions.

Part type	Cut from longer piece	Individually built
Flexural strength (kPa)	2277.0	2810.0
Standard deviation (kPa)	105.9	87.2
Total samples used	8	4

Table 1: Comparison of the flexural strength for individual parts of different size

Layer undergoing failure	Bottom	Top
Flexural strength (kPa)	2277.2	2153.6
Standard deviation (kPa)	105.9	65.9
Total samples used	8	5

Table 2: Comparison of the flexural strength for failure in the top vs. bottom layers of the specimens cut from the longer part

The temperature profile of the longer part shown in Figure 3b also suggests that the top layers of the specimen are exposed to shorter durations of temperature above T_g compared to the lower layers. This would indicate that the lower layers of the specimen should have higher bond strengths than the upper layers. To verify this, a number of samples were prepared and tested so

that the failure would occur either in the top or in the bottom layer of the specimens, and the results are shown in Table 2. Indeed, the bottom layers did exhibit higher bonding strength between the adjacent filaments. The flexural strength of the specimen when the fracture was caused to occur in the bottom layer was 2277 kPa against a value of 2153 kPa when the fracture was caused to occur in the top layer. Again the standard deviation was quite large, since the specimens were cut from the longer parts as already discussed above.

3.3. Effects of Prolonged Exposure to Higher Temperatures on the Mesostructure

It was generally observed that the temperature profile of the bottom layers of the parts remains at temperatures higher than T_g for a longer period of time compared to the upper layers. Thus, different neck growth between adjacent filaments can be expected in the top and bottom regions. However, this phenomenon was not readily observable in a twelve-layer specimen. Consequently, thirty-layer specimens were prepared. Figure 4 shows a magnified picture and the temperature profile for these specimens. As can be seen, after the first few layers, the temperature was above T_g until the completion of the part. The voids in the lower region are clearly smaller than in the upper region indicating larger neck growth in the bottom of the part. The dimensionless neck growth in the top few layers is 0.187 compared to 0.310 in the bottom layers. One possible explanation for the larger neck growth could be the longer diffusion time as discussed in the later sections dealing with modeling. Other explanations could be the effect of gravity or the effect of continued downward pressure from the FDM head while the part is being built.

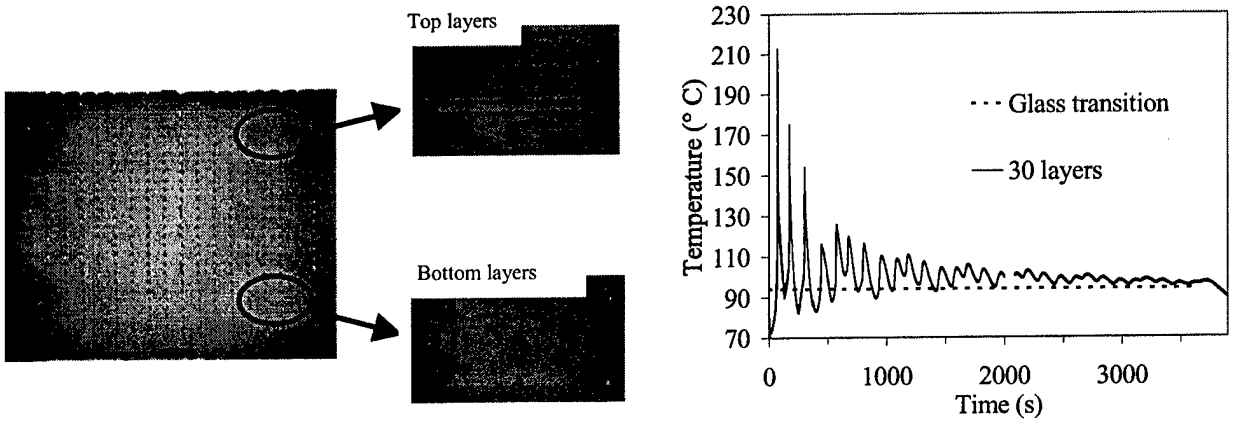

Figure 4: Mesostructure and temperature profile of a 1.5" x 1.5" x 30-layer part

3.4. Effects of Filament's Deposition Strategy on Temperature Profiles and Mesostructures

The impact of the deposition strategy on the parts' characteristics was examined in this work. Figure 5 shows the temperature profile at the base of a part with dimensions 200 mm x 12 mm x 2.8 mm in which the filaments were deposited in the longitudinal direction. After the second layer is formed, the temperature at the base remains above T_g for the duration of the build time. Figure 6 shows the temperature profile at the base of a part with dimensions 130 mm x 28 mm x 2.8 mm in which the filaments were deposited in the lateral direction. Due to the short path

length, the temperature reaches much higher values as the FDM head approaches the thermocouple, but later drops below the T_g limit as the head recedes. In this case the part is exposed to higher temperature for a longer time. Table 3 summarizes the results obtained for the dimensionless neck formed between adjacent filaments. The lateral specimen exhibits a higher dimensionless neck growth, and consequently has a lower void fraction due to longer exposure to higher temperatures.

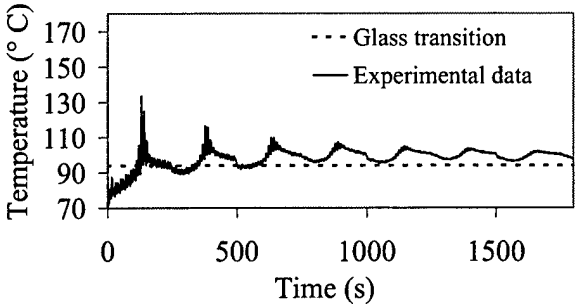

Figure 5: Temperature profile for a longitudinally built part

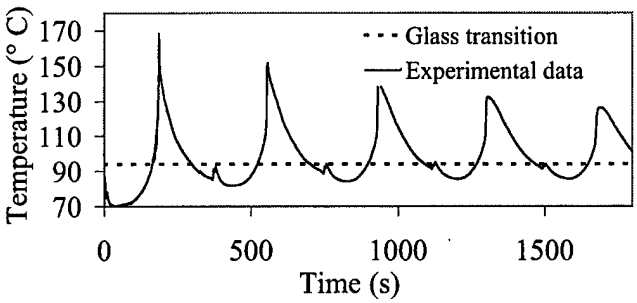

Figure 6: Temperature profile for a laterally built part

	Longitudinal parts	Lateral parts	Top layers (30-layer part)	Bottom layers (30-layer part)	Sintering model prediction
Dimensionless Neck growth	0.191	0.233	0.187	0.310	0.152
Void fraction (%)	0.091	0.081	--	--	--

Table 3 Dimensionless neck growth and void fraction for various parts

4. Prediction of Bond Formation

The formation of bonds between polymer filaments in the FDM process can be described as shown in Figure 7. The cross-sections of filaments are idealized as circles in the figure. The first step of the process is the establishment of interfacial molecular contact by wetting. The molecules then undergo motions toward preferred configurations to achieve the adsorptive equilibrium [9]. Molecules diffuse across the interface, forming an interfacial zone, and/or react to form primary chemical bonds across the interface. The randomization can be reached only after extensive inter-diffusion of chain segments under critical conditions. These processes can be interpreted either in terms of sintering of adjacent particles or inter-diffusion of molecules at the contact interface, both of which occur at elevated temperatures. Predictive models, for both sintering and diffusion, which utilize the measured temperature profiles, are discussed in the following sections.

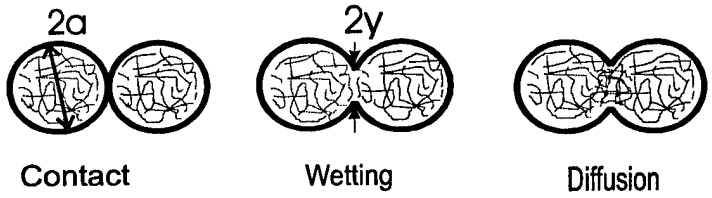

Figure 7: Schematic of bond formation between two filaments

4.1. Sintering Model

Analytical models describing the sintering rate that occur, due to Newtonian and viscoelastic flows, in various polymers have been proposed and assessed by Hornsby and Maxwell [13], Mazur and Plazek [14], and Bellehumeur et al. [15-16]. In this work, the model proposed by Pokluda and co-workers [17] has been used.

$$\frac{d\theta}{dt} = \frac{\Gamma}{a_o \mu} \frac{2^{-5/3} \cos\theta \sin\theta (2 - \cos\theta)^{1/3}}{(1 - \cos\theta)(1 + \cos\theta)^{1/3}} \qquad (1)$$

with $\theta = \sin^{-1} y/a$. The model is valid for the coalescence of two particles and predicts the neck growth between the particles as a non-linear function of time t, material viscosity μ, initial particle radius a_o, and surface tension Γ. Details on the mathematical development and assessment of the model have been discussed elsewhere [11-12].

The sintering model is used to determine the neck growth formation between the sintering particles, thus providing information about the degree of wetting achieved at the filaments' interface, which is an indication of the neck growth. Previous work [1] has shown that the neck growth becomes negligible at temperatures below 200°C for ABS P400. This temperature is to be referred to as the critical sintering temperature for ABS P400. Quantitative predictions about the degree of bonding achieved during the filament deposition process were made based on the lumped-capacity heat transfer and Newtonian sintering models. The selection of model parameters was based on criteria presented in reference [12]. These results were found to be only in general agreement with the experimental observations (Table 3). Quantitatively, the difference might due to simplifying the cross-section shape of the filament (circle versus ellipse), neglecting gravity force in the sintering model and neglecting elastic deformation that may occur at temperatures below the critical sintering temperature.

4.2 Diffusion Model

The theory of intermolecular diffusion across the interface under isothermal conditions is well established in literature. The isothermal models work quite well for quasi-isothermal processes such as autoclaving. However, for on-line consolidation type processes such as FDM, where thermal transients are present at multiple time scales, a non-isothermal model is needed. A

model put forwarded by Fang [18] for the healing process under non-isothermal conditions was used to predict bond strength. The model considers a temperature dependent welding time and describes the bond strength as a function of the temperature history. The non-isothermal degree of healing evolution with time is developed starting from a fundamental formulation of the reptation of polymer chains and is given by the following expression:

$$D_h(t) = \frac{\sigma}{\sigma_\infty} = \left[\int \frac{1}{t_w(T)} dt \right]^{1/4} \tag{2}$$

where $t_w(T)$ is the temperature dependent welding time, σ_∞ is the strength of the fully healed interface, and σ is the stress for the FDM part. For a given temperature history, and a given temperature dependence of the welding time, the degree of healing can be evaluated using equation 2. The respective temperature profiles in conjunction with the extruded ABS P400 welding time, as determined by Rodríguez [8], were used to quantitatively predict the bond strength of the parts produced for mechanical testing. The welding time used is only valid in a very narrow temperature range and needs to be re-examined at higher temperatures in future work.

$$t_w = C \exp(Q_d / RT) \tag{3}$$

where $Q_d = 388.7$ kJ/mol and $C = 1.080 \times 10^{-47}$ s.

The model described by equation 2, was implemented numerically to predict the degree of healing as a function of time. The numerical integration was carried out until the degree of healing reached a value of unity, or until the specified time was completed, whichever occurred first. Furthermore, for amorphous materials the healing mechanism is active only as long as the material temperature is above its glass transition point, hence only that time when the temperature was above the glass transition point was taken into consideration.

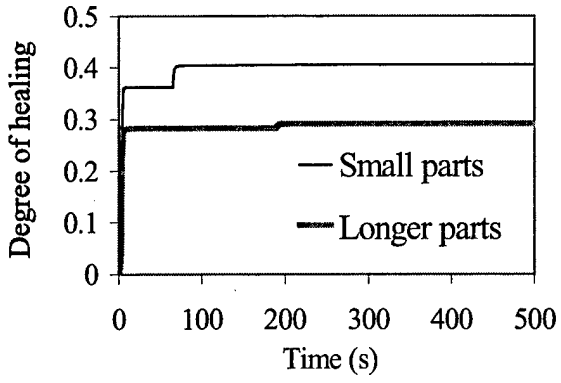

Figure 8: Degree of healing of FDM parts with different temperature histories

The modeling results are shown in Figure 8. From Figure 3b it can be seen that the individually produced parts stay above glass transition temperature longer and consequently have a higher degree of healing with the resultant higher bond strength. Figure 8 shows a drop of 28% in the degree of healing for the longer part from which the three specimens were cut. However, the drop in the load bearing capacity of these specimens was only about 10%. The difference can be attributed to the available welding time data, which covers only a narrow temperature range, but is extrapolated for a wider temperature range, causing errors. As an example, the extrapolated welding time for a temperature of 170°C was 0.01 seconds, which is obviously not correct. For the shorter part, the time spent at higher temperatures was greater, resulting in over estimation of the degree of healing.

4.3 Model Comparison

Under the conditions selected for the processing of ABS P400, sintering has a significant effect on bond formation, but only for the short duration of time that the temperature is higher than 200° C. Experimental observations showed that the filament temperature is below this temperature and above the glass transition point for a considerably longer period of time where the bonding is driven by the molecular diffusion at the interface. Therefore, the sintering model can be applied to the initial period when the filament temperature is above 200° C and the diffusion model is more appropriate for predicting subsequent bond strength development.

5. Conclusions

In this paper, on-line measurements of the cooling temperature profiles of extruded filaments in the FDM process were carried out. It was found that most theoretical models for the cooling profile of the extruded filaments fail to predict the temperature history of filaments embedded in a multi-layered part. Experimental measurements of the temperature profiles for different specimens and their effects on the mesostructures and mechanical properties were discussed. Based on the heat transfer analysis and the sintering experimental data, the prediction of the growth of the neck formed between adjacent filaments was evaluated using the sintering model. A non-isothermal diffusion model was used for the prediction of the bonding evolution at the interface between filaments due to molecular diffusion.

The future research will be focusing on obtaining accurate estimates for the non-isothermal diffusion model and generating predictions of bond strength development between filaments in FDM parts. Parametric studies will be conducted to investigate the effects of various process conditions on temperature histories and on the evolution of mechanical properties with time.

6. Acknowledgements

The financial support for this work was provided by the Natural Sciences and Engineering Research Council of Canada (NSERC) through Research Grants awarded to Drs. Bellehumeur and Gu.

7. References

1. Li, L., Sun, Q., Bellehumeur, C. and Gu, P., *Solid Freeform Fabriction Symposium*, Austin, TX, Aug., pp1-8 (2001).
2. Li, L., Sun, Q., Bellehumeur, C. and Gu, P., *J. Manuf. Process.* (in press, 2003).
3. M.K. Agarwala, A. Bandyopadhyay, R. van Weeren, N.A. Langrana, A. Safari, and S. C. Danforth, Solid Freeform Fabrication Symposium, Austin, TX (1996).
4. R. W. Gray, D. G. Baird and J. H. Bohn, *Rapid Prototyping Journal*, 4, 14-25 (1998).
5. M. Atif Yardimci, S.I. Guceri, S.C. Danforth, and M. Agarwala, *Proceedings of the Solid Freeform Fabrication Symposium*, Austin, TX, 539-548 (1996).
6. J.W. Comb, W.R. Priedeman and P.W. Turley, *Manufacturing Science and Engineering*, 68-2, 547-556 (1994).
7. P. Kulkarni and D. Dutta, *ASME Transactions: Journal of Manufacturing Science and Engineering*,

121, 93-103 (1999).
8. J.F.R. Matas, "Modeling the mechanical behavior of fused deposition acrylonitrile-butadiene styrene polymer components", Ph. D Dissertation, Department of Aerospace and Mechanical Engineering, Notre Dame, Indiana (1999).
9. M. A. Yardimci and S.I. Guceri, *Proceedings of the ASME Materials Division, ASME 1995*, MD-Vol. 69-2, pp1225-1235, IMECE (1995).
10. Thomas, J.P., Rodríguez, J.F., Modeling the fracture strength between fused deposition extruded roads, Solid Freeform Fabrication Symposium Proceeding, Austin, TX (2000)
11. L. Li, Q. Sun, C. Bellehumeur and P. Gu, *Solid Freeform Fabrication Symposium*, Austin, TX, Aug., pp. 1-8 (2002).
12. L. Li, P. Gu, Q. Sun and C. Bellehumeur, *Trans. NAMRI/SME*, Volume XXXI, pp. 613-620 (2003).
13. P. R. Hornsby P. R. and A. S. Maxwell, *J.Mater. Sci.*, 27, pp. 2525-2534 (1992).
14. S. Mazur S., and D. J. Plazek, *Prog. Org. Coat.*, 24, pp. 225-236 (1994).
15. C. T. Bellehumeur C. T., M. Bisaria and J. Vlachopoulos, *Polym. Eng. Sci.*, Vol 37, No. 3, pp. 270-278 (1997).
16. C. T. Bellehumeur C. T., M. Kontopoulou, and J. Vlachopoulos, *Rheol. Acta*, Vol. 37, pp. 270-278 (1998).
17. Pokluda, C. T. Bellehumeur, and J. Vlachopoulos, *AIChE J.*, Vol. 43, pp. 3253-3256 (1997).
18. F.Yang,R. Pitchumani, Vol.35, Macromolecules , pp. 3213-3224 (2002).

LENS Deposition of Complex Geometries

D.D. Gill, M.L. Griffith, D.E. Reckaway, C.F. Briner, D.G. Abrams
Manufacturing Science & Technology Center, Sandia National Laboratories
Albuquerque, NM 87185

Abstract

The Laser Engineered Net Shaping (LENS®) system at Sandia National Laboratories, a laser-based direct metal deposition process, was recently used for the fabrication of a complex prototype. The LENS process involved the challenges of adjacent areas of thick and thin cross section, overhanging unsupported features, high aspect ratios, and a hemispherical substrate. These challenges were overcome through the use of closed-loop weld pool control, height monitoring, a strong understanding of build parameters, and unique process planning strategies. The near-net shape LENS part was completed with annealing and conventional machining to produce the complex components in a reduced timeframe.

Introduction

Three prototype components were needed in a reduced timeframe recently for pre-production testing. These stainless steel components are approximately 280mm diameter with a hemispherical base and have features that include 2mm thick walls as tall as 110mm and solid blocks as large as 41cm^3. The conventional methods of fabrication have been conventional machining from a billet of material and investment casting followed by finish machining. It was proposed that the prototypes could be completed by the LENS process more quickly than either of the traditional methods of production. LENS is a laser metal deposition system that focuses a laser on a substrate creating a small weld pool, and then deposits powdered metal into the weld pool [1]. As the substrate is moved by a set of computer controlled axes, the deposited metal builds a part line by line and layer by layer. The conventional machining of the desired prototype components takes around 350 hours of machine time. These parts are very difficult to machine due to the high aspect ratio of 55 for the wall structure and the very narrow 4mm space between the walls. Equally difficult is the location of casting facilities interested in producing very small quantities of parts at reasonable costs. LENS is a perfect match for this need. The LENS system at Sandia has sophisticated process planning software to convert a triangulated version of a solid model file directly into modified M&G code for the LENS machine. Several challenges needed to be overcome for this project to be a success however. The process planning software required the addition of a secondary clearance plane due to the hemispherical shape of the substrate, and strategies developed for accurate building on surfaces that are not perpendicular to the incoming laser beam. Additionally, the system had to build thick blocks directly adjacent to thin wall structures maintaining accurate dimensions as both were constructed. This was accomplished utilizing a closed loop weld pool monitoring system [2] in conjunction with height monitoring and control. Finally, once the LENS deposition was completed, methods of stress relieving heat treatment were developed along with the utilization of conventional machining to complete the components.

Process Planning and LENS Metal Deposition

The deposition utilized hybrid building techniques in which the substrate becomes an integral part of the final component. In this case, the substrate was a 40mm tall dome of

approximately 280mm diameter. The substrate is shown in Figure 1(a) as it is ready to go into the LENS machine. Figure 1b shows a solid model of the features to be LENS deposited on the substrate.

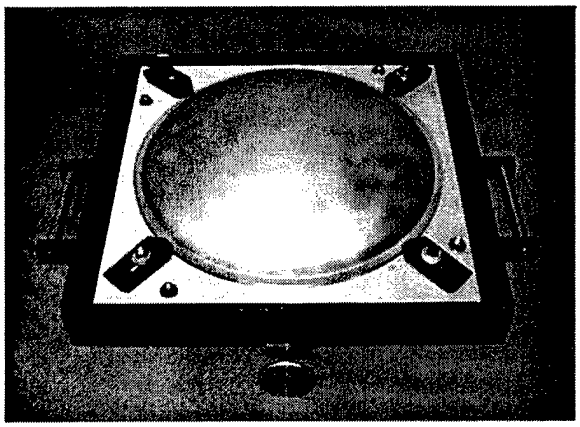

(a)

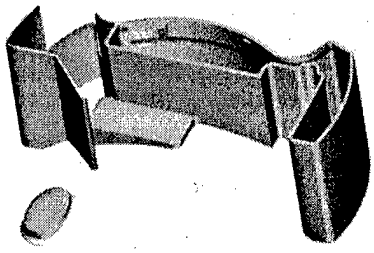

(b)

Figure 1. (a) Dome Substrate Ready for LENS Deposition and (b) Solid Model of Features to Be Deposited by LENS

Because the substrate is dome shaped, it was necessary to develop a secondary retract plane in the process planning software that represented a safe distance at which the LENS deposition head could retract to clear the center of the dome as it traversed from one side of the build to the other. A strategy for using the secondary retract plane was developed so that the head would only retract when traversing the dome, but not at other times when it would waste time. The process planning software also has optimization strategies for determining when to switch from one feature to another. All features were done with multiple passes in which the laser first traversed the borders of the geometry and then returned to fill in or hatch between the borders. Because the geometry contains discontinuities between the different features, the process planning software must choose when to switch from one feature to another. The software attempts to follow the longest continuous path possible while building and attempts to then build the closest remaining feature whenever it finishes building a previous geometry. This strategy causes the long traverses and use of the secondary retract plane to be minimized to help speed the building process.

The knitting of the LENS deposition to the substrate occurred on angled surfaces due to the dome substrate. Typically, this knitting is one of the most critical steps of the LENS building process determining the strength of the interfacial bond. In this case, tests of representative geometry on steeply angled substrates showed that it was important for the area of the weld pool to be increased during the deposition of the interfacial layers, especially due to the angled substrate. One of these test blocks is shown in Figures 2(a) and 2(b). Further testing, shown in Figure 2(c) was also required to determine the effects of the angled substrate on the incident powder cone which deposits the powdered metal in the weld pool. The process planning software was amended so that it gave a special notation to the interfacial geometry that notified the closed loop monitoring system of the need for a different set of weld pool parameters at these times.

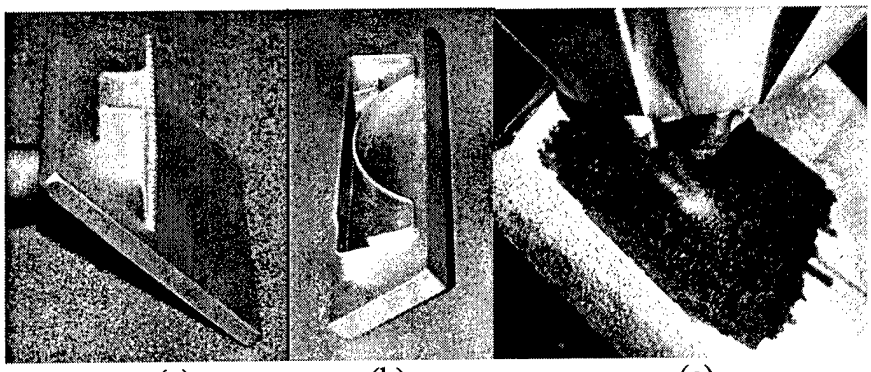

(a) (b) (c)

Figure 2. (a, b)Test LENS Features Deposited on a Substrate Positioned at a 45° Angle to the Incident Laser Beam and (c)Test of Powder Cone Geometry on Angled Substrate

As the component's metal features were being deposited, the weld pool monitoring system actively maintained the appropriate weld pool for the different conditions encountered in the part geometry. This was especially important as the build transferred from the very thin wall structures to the thick block sections due to differences in heat conduction pathways which severely influence the build parameters of the deposition and must be carefully controlled by the weld pool monitoring system to assure a fully dense build with uniform material properties in all features regardless of geometry.

A separate system monitored the height of the deposition throughout the building process and helped to maintain a uniform and accurate feature height. The greater heat retention of thin wall structures causes them to grow taller than the neighboring blocks if not controlled through the height monitoring system. This monitoring allowed all geometry to be built to 1.5mm taller than the height of the computer model, leaving plenty of material for the machining processes to remove.

During the deposition process, the waste powder that did not become entrained in the weld pool was removed from the build environment manually and was reintroduced into the material hoppers. This greatly reduced the overall quantity of powder required for the deposition process.

Deposition Results

The deposition of each component was completed at a rate of 13cm^3/hr with the entire build process requiring 33 hours. The final geometry had good accuracy with respect to the original model. The wall straightness was accurate and the wall thickness error was 0.13mm as compared to 2.5mm for typical castings. During the length of the build, a significant amount of heat was introduced into the deposition features and substrate. As is expected, this heat causes the final geometry to be somewhat smaller than the model due to shrinkage upon cooling. For this geometry, the outside walls were 0.5-1mm inboard of the model's walls. Also, the shrinkage caused some warp in the dome section. The dome was deflected 1mm at two points around the perimeter, well below typical casting errors. The warp in the dome was not a problem because the dome used for the substrate was significantly thicker than the final design thickness to impart strength in the substrate during the deposition process. This excess thickness was removed from the dome by machining the dome after LENS deposition was completed.

Post Deposition Annealing and Machining

Once LENS deposition was completed, the components required heat treatment and finish machining. Because of the heat induced during the LENS deposition process, it was necessary to anneal the parts to remove residual thermal stress before machining. The annealing process was difficult to predict due to the diverse features present on the components. Two small plates were tack welded to the top of the freestanding thin walls to prevent movement during the annealing process and the temperature of both the wall structures and the block features was monitored. The component is shown ready for heat treatment in Figure 3(a). Though the heat treatment cycles developed worked adequately, this is an area of research that needs to be pursued in the future.

Once the residual stress had been removed, the components were finish machined using traditional milling, turning, and die-sink EDM. The final test of the accuracy of the build was the fit of several concurrently produced components that were electron beam welded to the wall structure. The final part is shown in Figure 3(b).

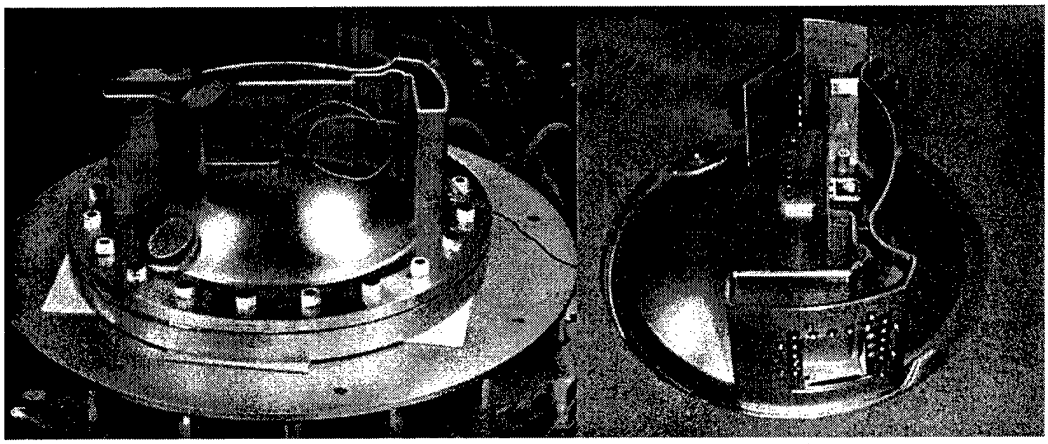

(a) (b)

Figure 3. (a)LENS Built Component Ready for Heat Treatment and (b)After Completion of Finish Machining

Conclusion

The use of LENS deposition for the manufacturing of 3 prototypes showed the ability of this process to produce complex, accurate, fully functional, components directly from CAD solid models in a reduced timeframe over the competing technologies. The process showed the capabilities of the Sandia National Laboratories' LENS system to deposit complex geometry while maintaining high accuracy in the features. The post deposition annealing and finish machining completed the prototyping process.

References

[1] Griffith et. al., *Understanding the Microstructure and Properties of Components Fabricated by Laser Engineered Net Shaping (LENS),* Materials Research Society, V625, Symposium Y Proceedings, April 2000.

[2] Hofmeister et. al., *Solidification in Direct Metal Deposition by LENS™ Processing*, JOM-Journal Of The Minerals Metals & Materials Society, v. 53(#9) pp. 30-34 Sep 2001.

Process Scaling and Transient Melt Pool Size Control in Laser-Based Additive Manufacturing Processes

Andrew Birnbaum, Pruk Aggarangsi and Jack Beuth
Department of Mechanical Engineering
Carnegie Mellon University
Pittsburgh, PA 15213

Abstract

This modeling research considers two issues related to the control of melt pool size in laser-based additive manufacturing processes. First, the problem of process size scale is considered, with the goal of applying knowledge developed at one processing size scale (e.g. the LENS™ process, using a 500 watt laser) to similar processes operating at larger scales (e.g. a 3 kilowatt system under development at South Dakota School of Mines and Technology). The second problem considered is the transient behavior of melt pool size due to a step change in laser power or velocity. Its primary application is to dynamic feedback control of melt pool size by thermal imaging techniques, where model results specify power or velocity changes needed to rapidly achieve a desired melt pool size. Both of these issues are addressed via a process map approach developed by the authors and co-workers. This approach collapses results from a large number of simulations over the full range of practical process variables into plots process engineers can easily use.

Introduction

Substantial progress has been made over the last decade in developing laser-based manufacturing processes for the purposes of solid freeform fabrication, cladding, component repair and additive manufacturing of features onto existing parts. In particular, over roughly the past eight years, an extensive research effort at Sandia National Laboratories to develop the LENS™ process (Griffith et al., 1996) has yielded an understanding of process parameters needed to build a number of standard shapes out of stainless steel, titanium and other alloys. Significant progress has also been made in developing real-time feedback control via thermal imaging of the melt pool (Griffith el at., 1999 and Hofmeister et al., 2001)

Recently, the use of laser-based processes for component repair and additive manufacturing applications has received significant attention in the aerospace industry. In the case of additive manufacturing, significant cost savings are possible in the manufacture of some components if laser-based deposition is used to add small features to larger parts manufactured by traditional processes. For example, the traditional approach for manufacturing aircraft engine casings is to forge them with a thickness roughly twice that of the final casing thickness. Machining is then used to remove large amounts of material, leaving small-scale features on the casing surface. Significant cost savings are possible by instead forging a near-net-thickness engine casing and adding external features via laser deposition.

With the developments described above, two key issues have emerged as critical for the advancement of laser-based additive manufacturing processes. The first is the need for a fundamental understanding of process scaling. Many industrial applications demand the use of large-scale deposition processes, yet significant process development has occurred on small-

scale processes. For instance, the LENS™ process uses a 500 W Nd:YAG laser. In contrast AeroMet, which manufactures components for the aerospace industry, uses an 18 kW CO_2 laser. There is currently no fundamental understanding of how to apply deposition knowledge acquired from small-scale systems to analogous large-scale systems. The result is that whenever a new laser-based manufacturing system is developed at a different size scale, processing engineers have to nearly start from scratch, performing large numbers of experiments to characterize their process.

The second critical issue for laser-based additive manufacturing processes is the need for a fundamental understanding of transient changes in process characteristics such as melt pool size with changes in process variables such as laser power and velocity. This understanding is needed to aid in the real-time feedback control of melt pool size. In particular, an understanding of thermal response times (the time for a step change in power or velocity to produce a desired change in melt pool size) is needed. For example, results presented for thin-walled structures by Aggarangsi et al. (2003) (also in this symposium proceedings) demonstrate that effective control of melt pool size during the approach of a free edge requires initiation of power reductions before melt pool size increases are observed. This is due to the fact that the time needed for the melt pool size to change due to a power reduction is comparable to the time over which the melt pool size increases as the free edge is approached.

The research described in this paper represents an initial attempt at addressing these two issues. Work described herein builds directly on modeling work by Vasinonta et al. (1999, 2001a, 2001b) developing easy-to-use "process maps" allowing the prediction of steady-state melt pool size in thin walled and bulky features for any practical combination of LENS™ process variables. The simultaneous control of residual stress and melt pool size has been addressed by Vasinonta et al. (2000). A brief overview of the process map approach to understanding laser-based freeform fabrication processes is given by Beuth and Klingbeil (2001) and a complete presentation of the process map approach for controlling steady-state melt pool size and residual stress in thin-walled and bulky parts is given by Vasinonta (2002). Most recently, process maps of cooling rates and thermal gradients at the melt pool boundary have been developed with the goal of predicting microstructure (Bontha and Klingbeil, 2003) (also in this symposium proceedings).

The approaches and results from this earlier work can be used by process engineers to determine, in general, how to modify process variables in order to obtain an ideal melt pool size, control maximum residual stresses and control microstructure. However, results from this earlier work are tailored for application to the LENS™ or other similarly sized processes. Also, only steady-state melt pool size control is addressed. In this paper, results are presented which show how a process map approach can be extended to understand melt pool size control over a range of process size scales and to understand the transient response of melt pool size to step changes in laser power or velocity.

Numerical Models and the Process Map Approach

Numerical Models: Both issues addressed in this paper are considered with reference to the 2D thin-walled geometry shown in Fig. 1. The geometry represents a thin-walled structure deposited onto a comparatively large base plate that acts as a heat sink. The models used in this

paper are analogous to models developed by Vasinonta (2002). Models are of a concentrated heat source moving across the top of the thin wall and do not model the effects of material addition. The absorbed laser power is designated as αQ, where α is the fraction of laser power from the source that is absorbed by the thin wall. In comparing with experiments and in determining ranges of absorbed laser powers a value of $\alpha = 0.35$ is used. Predictions from numerical models assuming a value of $\alpha = 0.35$ have shown good agreement with melt pool lengths in thin-walled structures measured via thermal imaging using the LENS^{TM} process (Vasinonta et al., 1999, 2002a). The successive deposition of layers is not modeled, but the preheating effects of the deposition of prior layers can be approximated via the specification of an elevated uniform temperature in the wall and base plate, designated as T_{base}, which exists before the laser begins its travel across the top of the wall. In all cases considered in this paper, the wall is tall enough that any increases in height will not change the results (results are independent of wall height). The issue of sufficient wall heights to achieve this condition is addressed by Vasinonta et al. (1999, 2001a). Similarly, in this study melt pool size results are taken when the heat source is sufficiently far from the vertical free edges that results are independent of the distance from the edges. In the process scaling simulations, processes using large values of laser power were performed with models having length and height dimensions scaled up to ensure that the conditions described above were satisfied. Numerical models for transient response simulations have larger length dimensions than analogous process scaling simulations because steady state conditions must be reached twice during the analyses.

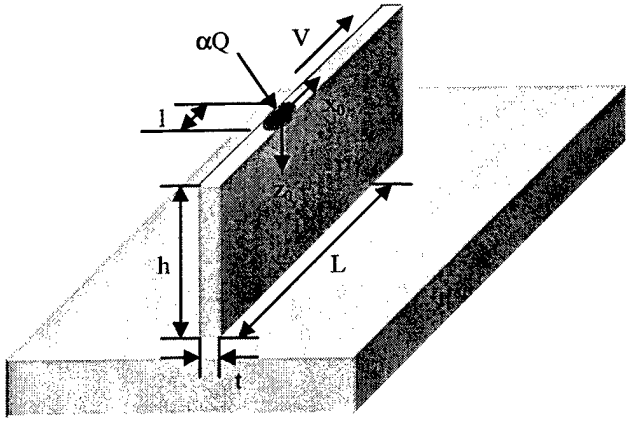

Figure 1 Thin-Walled Structure with Base Plate

Figure 2 shows a typical finite element mesh used for the scaling effects analysis. A similar (but longer) mesh was used for the transient response simulations. The boundary conditions for both types of analyses are thermal insulation on the vertical free edges, as well as the top edge, while a constant temperature is enforced at the bottom edge, simulating the effects of the base plate. Out of plane conduction is also restricted as this is a 2D model. The models use four-node quadrilateral bi-linear elements provided by the ABAQUS finite element package. In going from left to right, there are two separate mesh densities. The first third of the model has fairly coarse resolution while the remaining portion is of significantly finer resolution. This approach was taken to reduce analysis time with the caveat that fine resolution is only required away from the left vertical edge, where melt pool length values are extracted from the model. Mesh resolution also increases as the top edge of the model is approached. For the process scaling simulations, constant power is applied to nodes over pre-determined time steps. Time

steps are specified as equal to the element edge length divided by the heat source velocity. The transient melt pool analysis includes step changes in absorbed laser power and/or velocity.

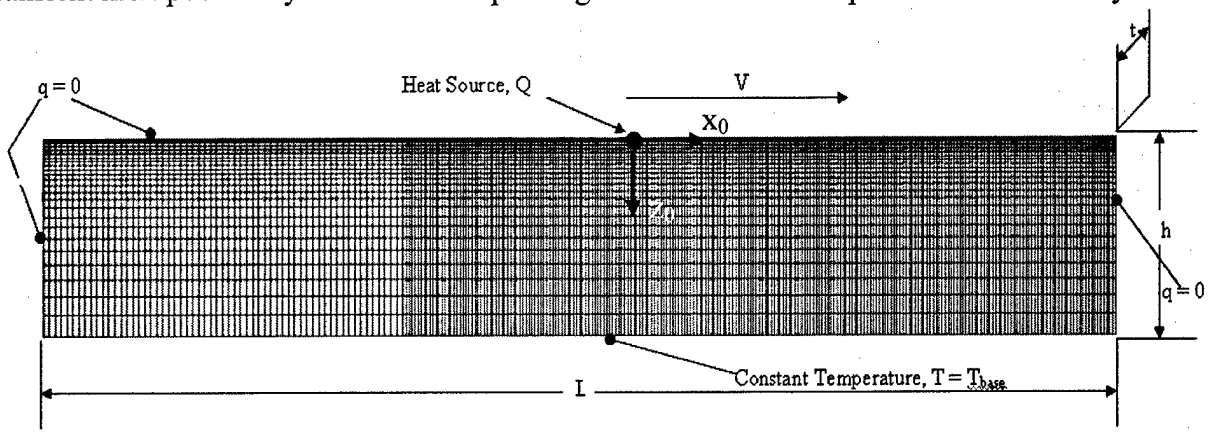

Figure 2 Finite Element Mesh with Boundary Conditions

Thermal properties of AISI 304 stainless steel are used as inputs to the models (Dobranich and Dykhuizen, 1998). A solidus temperature of 1672 K, a liquidus temperature of 1727 K, a latent heat of fusion of 2.65×10^5 J/kg, and a constant density of 7652 kg/m^3 are specified, while temperature dependent thermal conductivity, k and specific heat, c are given by the following linear equations:

$$k = 8.116 + 0.01618(T) \ (W/m) \qquad (1)$$
$$c = 465.4 + 0.1336(T) \ (J/kgK)$$

below a temperature of 1500 K. Above 1500 K, both thermal conductivity and specific heat are held constant at the 1500 K value.

Process Map Approach: Because the process scaling and transient analysis research described herein build upon previously developed process map concepts, a brief overview of the earlier research as applied to thin-walled structures is provided here. A process map for melt pool length for a thin-walled structure traversed by a concentrated laser heat source has been developed by Vasinonta et al. (1999, 2001a). As suggested by the Rosenthal (1946) solution for a point heat source moving across a (2-D) half-space, a process map for melt pool length is represented through three dimensionless variables: the normalized melt pool length ($\bar{l}$), the normalized substrate height ($\bar{h}$) and the normalized melting temperature ($\bar{T}_m$) which are defined as follows:

$$\bar{l} = \frac{l}{2k/\rho cV}, \ \bar{h} = \frac{h}{2k/\rho cV} \text{ and } \bar{T}_m = \frac{T_m - T_{base}}{\alpha Q/\pi kt}. \qquad (2)$$

In eq. (1), ρ, c and k are the density, specific heat and thermal conductivity, respectively. If thermal properties are temperature-independent, results from the analysis of a concentrated heat source moving over a thin-walled structure of finite height, h, can be represented as a single surface plotted on three coordinate axes of $\bar{l}$, $\bar{h}$ and $\bar{T}_m$. This forms the basis of a process map for laser deposition of thin-walled structures.

The process map for deposition of thin-walled structures of stainless steel 304 via the LENS™ process is shown in Fig. 3. It consists of three surfaces plotted on three coordinate axes. The middle surface was developed from finite element simulations with temperature-independent properties. The results from temperature-dependent property simulations are also presented in Fig. 3 as upper and lower error surfaces that bound the results. The space between these error surfaces reflects the range in results seen when process variables are varied over the range of interest in the LENS™ process.

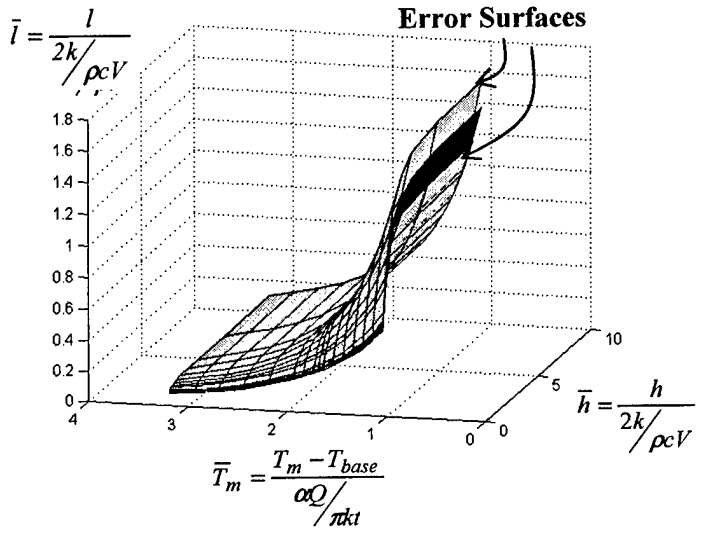

Figure 3 Process Map for Steady-State Melt Pool Length

The plot of Fig. 3 shows that the variability of results due to temperature-dependent properties can be confined to +/-6.5% if certain procedures for applying the process map are followed (Vasinonta et al., 2001a). In brief, these procedures are:

1. Properties at 1000 K are used in the normalizations.
2. For cases involving a change in preheat, a linear change in thermal conductivity with a preheat temperature (in deg. C) is assumed, given by $k = 24.3 + 0.013(T_{base}-30)$ W/(mK).
3. For predicting steady-state melt pool lengths resulting from a change in process variables, wall thickness is assumed to scale proportionally with melt pool length. It is also assumed that the melt pool length/wall thickness scaling is unaffected by velocity.

The third assumption is necessary because the wall thickness, t, is included in the normalized variable $\bar{T}_m$ used in the process map. This requires that some assumption be made regarding the relationship between melt pool length and wall thickness. It also means, however, that within the limits of assumption #3 and given a value of t from a single experiment, the process map can be used to predict not only melt pool lengths as a function of process variables, but also wall thicknesses.

In summary, the process map approach developed in previous work allows the representation of the dependence of melt pool length on absorbed laser power, αQ, laser velocity, V, and wall preheat temperature, T_{base}, in the form of a single, easy-to-use plot in terms of dimensionless variables. The variability of results due to the temperature dependence of material properties can be kept within practical limits. However, the process map of Fig. 3 is specifically developed for the deposition of 304 stainless steel over the range of process variables of interest in

the LENS™ process. Results in the next section of this paper will address methods for extending this approach to other process variable ranges. Also, the process map of Fig. 3 only allows prediction of steady-state melt pool lengths. It gives no information on the rate of change of melt pool length (from one steady-state value to another) if process variables are altered. This is the second major topic addressed in this paper.

Process Scaling

Targeted Manufacturing Process: A laser processing facility is currently under development within the Advanced Materials Processing Center at the South Dakota School of Mines and Technology for use in not only net shape manufacturing but also welding, micro-machining, surface treatment and other applications. The system consists of a 3 kW Nd:YAG laser with a robotic positioning system, dual powder feeders and geometric, temperature and position sensing and feedback control capabilities. It is currently being tested for net shape manufacturing applications through the building of a series of flat, thin-walled structures deposited using laser powers from 450 W to 900 W. These initial tests will be followed up by tests on thin walls and other shapes for powers up to 2700 W. Laser velocities of interest range from 10 to 20 mm/s (Sears et al., 2003).

Because the power range of the laser at the AMP Center is significantly larger than that for the 500 W LENS™ system, the development of this new facility offers a unique opportunity for testing the applicability of a process map approach on multiple process size scales. In the next section, methods are presented for using process map concepts to model melt pool size and wall thickness for processes at multiple scales. Wall thickness predictions from process maps are then compared to available data from the AMP Center in the 450 to 900 W power range. In addition, wall thicknesses are predicted beyond the range of available data, up to a power level of 2700 W, providing researchers at the AMP Center with predictions of wall thicknesses in advance of their experiments.

Process Maps for Multiple Process Scales: In this section, methods are described for extending the process map approach for predicting melt pool length and wall thickness to processes operating at multiple size scales. The earlier work by Vasinonta showed that melt pool length predictions from models of the LENS™ process could be collapsed into a single plot of nondimensional variables if thermal properties at 1000 K are used in the normalization. In this section, it will be shown that processes at larger size scales can be similarly represented if properties at lower temperatures are used in the normalization.

In order to analyze the effects of process scaling, laser powers of 125 W to 2700 W (αQ from 43.8 W to 945 W assuming a value of $\alpha = 0.35$) were divided into three power ranges. The upper range is from 1300 W to 2700 W (αQ from 455 W to 945 W). The middle range has powers from 429 W to 1286 W (αQ from 150 W to 450 W). The lower range is based on the LENS™ process and has powers ranging from 123 W to 471 W (αQ from 43.2 W to 165 W). These ranges were chosen with the goal of maximizing range size, while keeping maximum errors from use of the process map within practical limits.

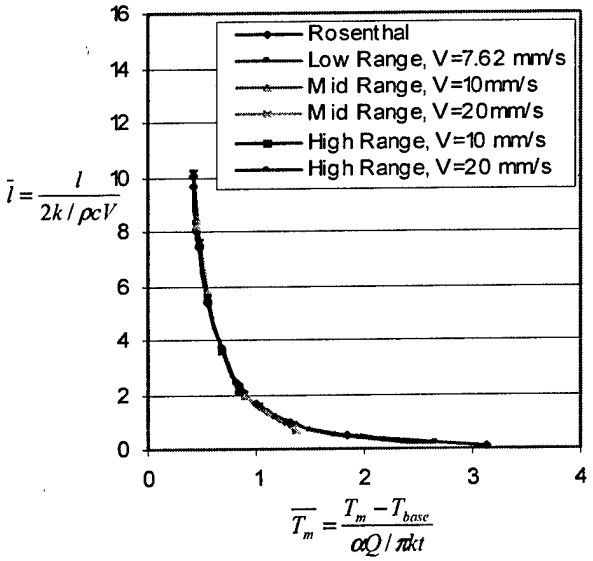

Figure 4 Comparison of Normalized Results with the Rosenthal Solution over Three Power Ranges, Using a Pre-Heat Temperature T_{base} = 303 K

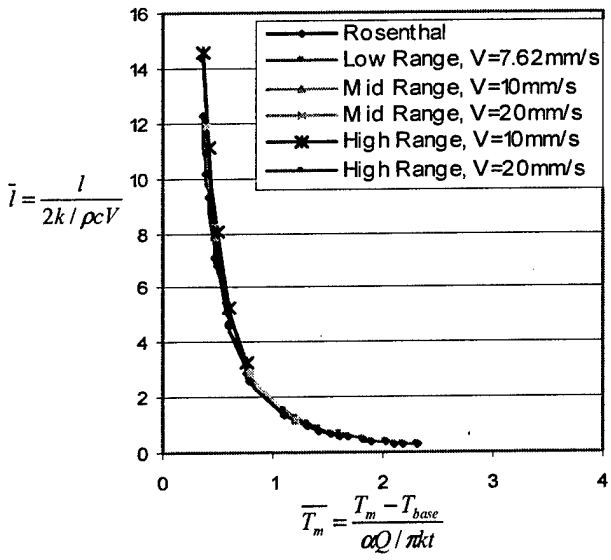

Figure 5 Comparison of Normalized Results with the Rosenthal Solution Over Three Power Ranges, Using a Pre-Heat Temperature T_{base} = 673 K

As in earlier process map work, a single experimental value of the wall thickness, t, is needed to predict values of l and t as a function of absorbed laser power, αQ, laser velocity, V, and wall and base plate preheat temperature, T_{base}. A prediction of melt pool length, l, for the experimental case yields a value of l/t that is used in all subsequent predictions. In the earlier work, because the velocity range of interest was confined to the relatively narrow range of 5.93 to 9.31 mm/s it was assumed that the ratio of l/t was independent of laser velocity. In this section it will be shown that this assumption can give less than satisfactory results over a larger velocity range. Also, as in earlier work, prediction of melt pool length and wall thickness using the process map must be done using an iterative scheme. For instance, a larger value of αQ results in a new (smaller) value of $\overline{T}_m$. That smaller value of $\overline{T}_m$ results in new (larger) values of l and t, but the larger value of t in turn results in a slightly larger value of $\overline{T}_m$. This again leads to new values of l and t. These calculation steps are repeated until $\overline{T}_m$, l and t no longer change significantly.

Figures 4 and 5 provide plots of $\bar{l}$ vs. $\overline{T}_m$ over the three ranges of $\overline{T}_m$ identified above, covering the full range of laser powers from 125 W to 2700 W (αQ from 43.8 W to 945 W) applicable to the LENS™ and AMP Center processes. Because they are for tall walls, the 2-D plots of Figs. 4 and 5 correspond to values from the process map of Fig. 3 for the limiting case of large values of $\bar{h}$. More specifically, data plotted in the low range of powers (large values of $\overline{T}_m$) reproduces the data of Fig. 3 for large $\bar{h}$. Data for smaller values of $\overline{T}_m$ is new and relates to power ranges and velocities appropriate for the AMP Center process. Figure 4 gives results for a value of T_{base} = 303 K and Fig. 5 gives results for an upper bound value of T_{base} = 673 K. In both cases, results are given for the upper and lower bounds of V = 10 mm/s and V = 20 mm/s for the middle and upper power ranges (applicable to the AMP Center process). Results at V = 15 mm/s were also obtained but are not shown because they fall between results for the upper and lower values of velocity.

The plots of Figs. 4 and 5 show that errors can be confined to +/-8% in the upper and middle power ranges if the following procedures for applying the process map are followed:

1. Properties at a normalization temperature $T_{norm} < 1000$ K are used in the normalizations.
2. For cases involving a change in preheat, a linear change in thermal conductivity with a preheat temperature (in deg. C) is assumed, given by $k = k_{Tnorm} + 0.013(T_{base}-30)$ W/(mK), where k_{Tnorm} is the conductivity at the chosen normalization temperature.
3. For predicting steady-state melt pool lengths resulting from a change in process variables, wall thickness is assumed to scale proportionally with melt pool length.

In other words, the process map approach can be applied over multiple process size scales by simply changing the normalization temperature with changes in power range.

Temperatures at which process parameters are normalized by are chosen to minimize errors in the process map (Figs 4 and 5) due to temperature-dependent properties. Figure 6 shows the functional dependence of normalization temperature on median $\overline{T}_m$ values for each power range. The plot can roughly be approximated as linear over the range of $\overline{T}_m$ values considered. It is not clear whether a linear extrapolation to higher powers (lower values of $\overline{T}_m$) would be accurate. However, a linear extrapolation of the curve toward $\overline{T}_m = 0$ (αQ approaching infinity) suggests a normalization temperature near 820 K. This change in normalization temperature would yield relatively small changes in k and c (see equation (1)). This suggests that the modeling of even larger scale processes via a process map approach may be straightforward. It also suggests that the effects of changes in process scale are reduced at higher power ranges and that experimental results from the AMP Center process may provide significant insight into processes operating at significantly larger laser powers.

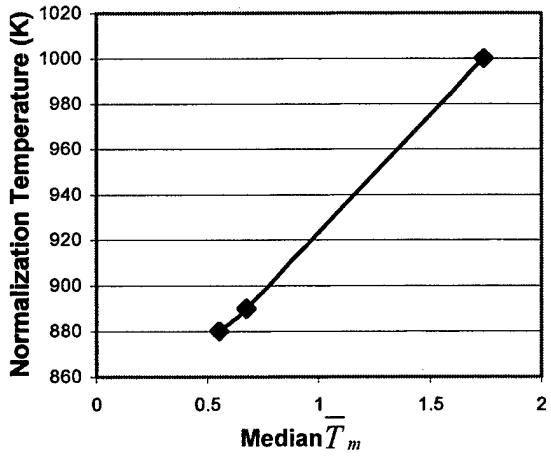

Figure 6 Normalization Temperature as a Function of Median $\overline{T}_m$

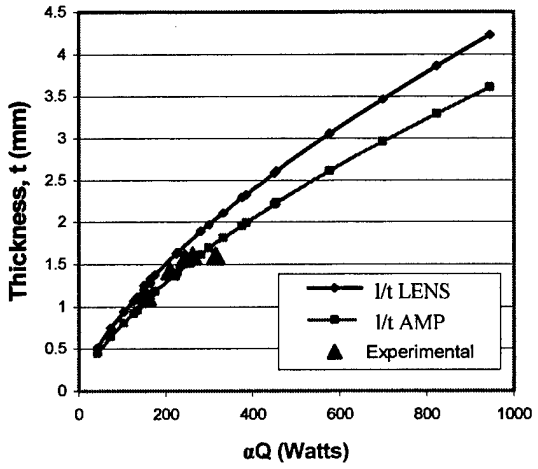

Figure 7 Comparison of Experimental and Predicted Thicknesses as a Function of αQ

Application of the Results: Figure 7 shows a plot of predicted and measured wall thicknesses vs. αQ. Measured values are from the AMP Center process (Sears et al. (2003)) for a laser velocity of 20 mm/s and are shown as large data points. Predictions as a function of αQ and for V = 20

mm/s are shown as plotted lines with small data points. Two sets of predictions are presented. The top line represents process map predictions using an experimental value of t from the LENS™ process for αQ = 105 W and V = 7.62 mm/s to determine l/t. Although the trends in the experiments are captured by these predictions, the predicted values are larger than the experimental values.

This difference can be explained by the use of a value of l/t determined from experiments at a significantly lower velocity than was used in the experiments. This ratio will, in fact, increase with an increase in velocity. The second set of predictions (the lower line) was generated from the same process map results (Figs. 4 and 5), but with a value of t from the AMP process for αQ = 210 W and V = 14 mm/s used to determine l/t. These predictions agree quite well with the available experimental data. Furthermore, the predictions for larger powers could be a useful tool in reducing the number of experiments AMP engineers need to perform while developing their process.

Transient Response of Melt Pool Size

In this section, numerical results are presented for transient changes in melt pool size due to a step change in laser power and/or velocity, for application to feedback control of melt pool size. Furthermore, results are presented in a non-dimensional process map format using the rules outlined in the Process Map Approach section, allowing the results from a large number of simulations to be presented in a compact form. In this section, simulations are for the LENS™ process; however, the same approach could be applied to other laser-based deposition processes.

Figure 8 provides a plot of normalized melt pool length as a function of normalized laser travel distance for multiple values of step changes in laser velocity and/or power. The "baseline" set of initial process variables are αQ = 105 W, V = 7.62 mm/s and T_{base} = 303 K. These variables result in a value of $\overline{T}_m$ = 1.29 and a value of $\bar{l}$ = 1.01. Increases in absorbed laser power per thickness of 10% and 50% and decreases of 10% and 50% have been identified as baseline changes in process variables of interest, resulting in values of $\overline{T}_m$ equal to 1.18, 0.86, 1.44 and 2.59, respectively.

Considering just the baseline set of initial variables and power changes, Fig. 8 shows how normalized melt pool length changes from the steady-state value of 1.01 to other steady-state values as a function of the normalized distance traveled by the laser. Actual values of melt pool length and laser travel distance can be calculated from the normalized values using the properties of SS304 at 1000 K. Furthermore, the distance needed to reach the new steady-state value of melt pool length can be converted to a time to reach steady state by dividing by the laser velocity.

Figure 8 is more than a plot of changes in melt pool length due to step changes in power, however. It is really a plot of normalized melt pool length vs. normalized laser travel distance for the changes in $\overline{T}_m$ shown for any practical combination of process variables. For each $\overline{T}_m$ value, two combinations of process variables αQ, V and T_{base} that give the highest and lowest values of $\bar{l}$ in the steady-state process map were selected, representing upper and lower bound

cases. For all values of $\overline{T}_m$ the upper bound case corresponds to values of T_{base} = 400 °C and the lower bound case corresponds to values of T_{base} = 30 °C. A series of transient simulations were then performed between upper bound cases and between lower bound cases (with T_{base} fixed) for each of the four step changes in $\overline{T}_m$. The results of all of these simulations are plotted in Fig. 8.

Overall, the process map approach developed for steady-state conditions has allowed a compact presentation of transient results over the full range of process variables of interest in LENS™. However, although the steady-state normalized results have an error of no more than +/- 6.5% (designated by the error bars in the figure), transient results are not necessarily confined to these limits. As shown in Fig. 8, distances (or times) needed to transition to a new steady-state melt pool size are greater for decreases in $\overline{T}_m$ (e.g. an increase in power) than for equivalent increases in $\overline{T}_m$. Using the properties of 304 stainless steel at 1000 K and a velocity V = 7.62 mm/s, the conversion between $\bar{x}$ and x is x (in mm) = 1.39 $\bar{x}$. For V = 7.62 mm/s, this gives thermal response times roughly in the range of 0.2 to 1.1 seconds, which is consistent with response times measured via thermal imaging of the LENS™ process.

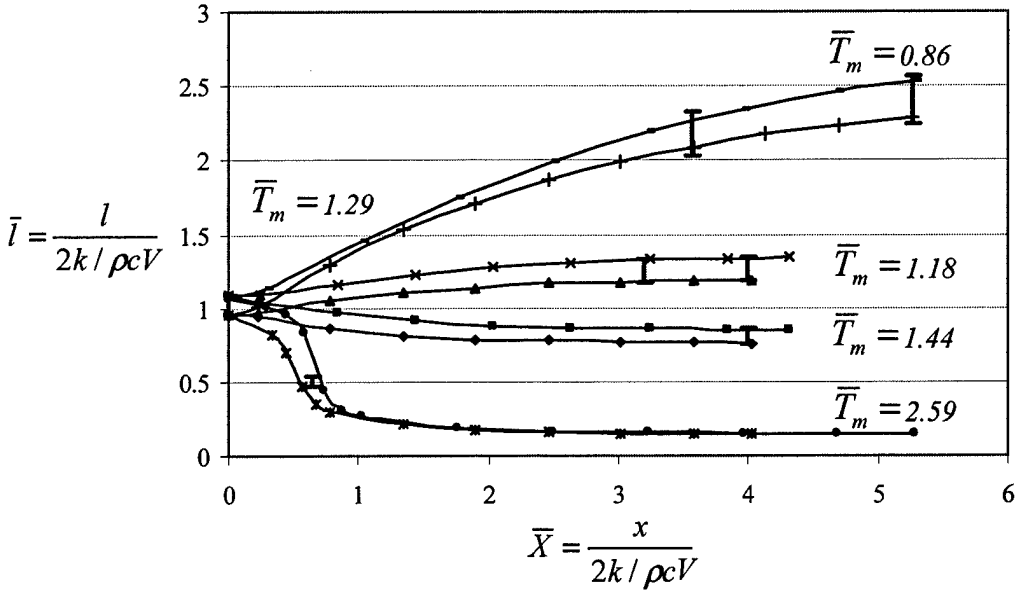

Figure 8 Melt Pool Size Transient Response Process Map with Error Bars Showing a Variation of ±6.5% from the Mean Values

Summary and Conclusions

In this study, process map approaches previously developed for application to the LENS™ process under steady state conditions have been extended to predict transient changes in melt pool length and wall thickness and to predict steady-state melt pool lengths and wall thicknesses for processes on multiple size scales. Results thus far have been limited to thin-walled structures; however, these concepts should be extendable to other common geometries. Process scaling predictions of wall thicknesses have been made for the full power range of a large-scale process currently under development and predictions have compared well to thicknesses measured to date. Predictions of transient changes in melt pool size for the LENS™

process are also consistent with observations of transient melt pool size via thermal imaging. Results have confirmed the applicability of a process map approach to understanding transient behavior; however, error limits under transient conditions may not match those observed in steady-state models. Melt pool size thermal response times for LENS™ range approximately from 0.2 to 1.1 seconds. This sets a lower bound on response times for melt pool size thermal feedback control systems.

Acknowledgements

This research was supported by the National Science Foundation Division of Design, Manufacture and Industrial Innovation, through the Materials Processing and Manufacturing Program, award number DMI-0200270. The authors would like to thank Dave Alexander and Ralph Anderson of Pratt & Whitney for their insights and effort in guiding the industrial applications of this research. The authors are also grateful for to Jim Sears of the South Dakota School of Mines and Technology and Michelle Griffith of Sandia National Laboratories for the important experimental data they have provided.

References

1. Aggarangsi, P., Beuth, J.L., and Griffith, M.L., 2003, "Melt Pool Size and Stress Control for Laser-Based Deposition Near a Free Edge, " *Solid Freeform Fabrication Proceedings* (D.L. Bourell, J.J. Beaman, H.L. Marcus, R.H. Crawford and J.W. Barlow, eds.), Proc. 2003 Solid Freeform Fabrication Symposium, Austin, August 2003 (this symposium).
2. Beuth, J.L. and Klingbeil, N.W., 2001, "The Role of Process Variables in Laser-Based Direct Metal Solid Freeform Fabrication," *JOM,* September 2001, pp. 36-39.
3. Bontha, S. and Klingbeil, N.W., 2003, "Thermal Process Maps for Controlling Microstructure in Laser-Based Solid Freeform Fabrication," *Solid Freeform Fabrication Proceedings* (D.L. Bourell, J.J. Beaman, H.L. Marcus, R.H. Crawford and J.W. Barlow, eds.), Proc. 2003 Solid Freeform Fabrication Symposium, Austin, August 2003 (this symposium).
4. Dobranich, D. and Dykhuizen, R.C., 1998, "Scoping Thermal Calculation of the LENS Process," Sandia National Laboratories Internal Report.
5. Griffith, M.L., Keicher, D.M., Atwood, C.L., Romero, J.A., Smugeresky, J.E., Harwell, L.D. and Greene, D.L., 1996, "Freeform Fabrication of Metallic Components Using Laser Engineered Net Shaping (LENS)," *Solid Freeform Fabrication Proceedings* (D.L. Bourell, J.J. Beaman, H.L. Marcus, R.H. Crawford and J.W. Barlow, eds.), Proc. 1996 Solid Freeform Fabrication Symposium, Austin, August 1996, pp. 125-132.
6. Griffith, M. L., Schlienger, M. E., Harwell, L. D., Oliver, M. S., Baldwin, M. D., Ensz, M. T., Smugeresky, J. E., Essien, M., Brooks, J., Robino, C. V., Hofmeister, W. H., Wert, M. J. and Nelson, D. V., 1999, "Understanding Thermal Behavior in the LENS™ Process," *Journal of Materials Design,* Vol. 20, No. 2/3 pp. 107-114.
7. Hofmeister, W.H., Griffith, M.L., Ensz, M.T. and Smugeresky, J.E., 2001, "Solidification in Direct Metal Deposition by LENS Processing," *JOM,* Vol. 53, No. 9, 2001, pp. 30-34.
8. Rosenthal, D., 1946,"The Theory of Moving Sources of Heat and Its Application to Metal Treatments," *Transactions of ASME,* Vol. 68, 1946, pp. 849-866.
9. Sears, J.W., Marquis, F., Arbegast, W. and Langerman, M., 2003, personal communication.
10. Vasinonta, A., Beuth, J. L. and Griffith, M. L., 1999, "Process Maps for Laser Deposition of Thin-Walled Structures," *Solid Freeform Fabrication Proceedings (*D.L. Bourell, J.J.

Beaman, R. H. Crawford, H. L. Marcus and J. W. Barlow, eds.), Proc. 1999 Solid Freeform Fabrication Symposium, Austin, August 1999, pp. 383-391.

11. Vasinonta, A., Beuth, J.L. and Griffith, M.L., 2000, "Process Maps for Controlling Residual Stress and Melt Pool Size in Laser-Based SFF Processes," *Solid Freeform Fabrication Proceedings* (D.L. Bourell, J.J. Beaman, R.H. Crawford, H.L. Marcus and J.W. Barlow, eds.), Proc. 2000 Solid Freeform Fabrication Symposium, Austin, August 2000, pp. 200-208.
12. Vasinonta, A., Beuth, J. L. and Griffith, M. L., 2001a, "A Process Map for Consistent Build Conditions in the Solid Freeform Fabrication of Thin-Walled Structures," *Journal of Manufacturing Science and Engineering.* Vol. 123, pp. 615-622.
13. Vasinonta, A., Beuth, J.L., and Ong, R., 2001b, "Melt Pool Size Control in Thin-Walled and Bulky Parts via Process Maps," *Solid Freeform Fabrication Proceedings* (D.L. Bourell, J.J. Beaman, R.H. Crawford, H.L. Marcus, K.L. Wood and J.W. Barlow, eds.), Proc. 2001 Solid Freeform Fabrication Symposium, Austin, August 2001, pp. 432-440.
14. Vasinonta, A., 2002, "Process Maps for Melt Pool Size and Residual Stress in Laser-Based Solid Freeform Fabrication," Ph.D. Thesis, Carnegie Mellon University, May 2002.

APPLICATON OF DESIGN OF EXPERIMENTS (DOE) ON THE PROCESSING OF RAPID PROTOTYPED SAMPLES

J.Weinmann, H. Ip, D. Prigozhin, E. Escobar, M. Mendelson, and R. Noorani

National Science Foundation
Research Experience for the Undergraduates Program
Loyola Marymount University
Los Angeles, CA

Abstract

The purpose of this experiment was to improve the Fused Deposition Modeling Process by examining the tensile strength of samples fabricated in a Stratasys FDM 1650 Machine utilizing the methods of Design of Experiments. A two-level, four-factor, full factorial experiment was conducted. The selected factors were temperature, air gap, slice thickness, and raster orientation. A regression equation determined the level each factor should be set in order to optimize the FDM machine settings. It was found that single factors - small air gap, small layer thickness and low raster orientation, as well as the interaction between high temperature and small layer thickness yielded the greatest effect the response.

1. Introduction

Fused deposition modeling (FDM) is a process that is used for fabricating solid prototypes from a computer-aided design (CAD) data file [1]. The process fabricates 3-D parts from a build-up of 2-D layers. In this process, an Acrylonitrile-Butadiene-Styrene (ABS) thermoplastic polymer is extruded through a heated nozzle to deposit the layers. In a previous paper, we showed that the orientation of the layers created anisotropic tensile properties [2]. Other investigators have also experienced similar results [3].

Previous investigators have used design of experiments (DOE) as a method to maximize strengths of the FDM-processed specimens of silicon nitride [4] and ABS polymer [3]. Many of the factors used for influencing the strength were entirely different in these studies. These investigators have not physically interpreted their selected factor levels in terms of the material properties and microstructure.

The purpose of this paper is to use quality engineering tools to design, analyze and physically interpret our selection of the FDM processing factors and their levels.

2. Experimental Methods

The 12-step design process was used for our experimental [5]. First, the problem of concern was the low strength of FDM-processed ABS test specimens; second, our objective was to maximize the tensile strength; third, the yield and ultimate strengths were selected as the quality characteristics, i.e., the response; fourth, the factors were determined by team brainstorming and were recorded on a cause-effect diagram [6]; fifth, four factors and no-noise factors were selected for our study; and sixth, a two-level experiment was selected.

Seventh, an L16 (2^4) full-factorial experiment was used for the DOE; eighth, all of the selected factors could potentially interact with each other; ninth, all of the interactions were listed; tenth, the trials were randomized and three replications per trial were used; eleventh, the column effects method and plots of the response vs. the effects of factors and interactions were used to analyze the data; and twelfth, the 95% statistically significant factors and interactions were identified. Our results were interpreted in terms of fracture behavior and microstructure to validate our results.

A Stratasys FDM-1650 modeling machine was used to fabricate the test specimens. The materials were ABS P400 build material and the support material [1]. Each material was in the form of a filament that was fed into a heated extrusion head to form a semi-liquid polymer. The polymer was deposited at locations on the X-Y plane according the part requirements in the STL file. The layer thickness was determined by the FDM Quickslice™ software. Then the head was moved vertically to deposit a new 2-D layer on top of the previous one. In this way, the 3-D solid model was built-up by multiple depositions of 2-D layers.

Each layer was formed by first depositing the perimeter (road width) around the X-Y plane of the test specimen design and then filled the inside of the perimeter with a raster pattern that had a preferred orientation. The layer bonded to the underlying structure. This process was similar to the 2-D lay-up of 90°/45° and 0°/45° laminate composites [7].

The design of the test specimens was in the shape of a dog-bone, similar to ASTM D638-97. However, the width of the gauge section in the test specimen was reduced to 8.13 mm (0.320 in.), because some specimens had failed outside the gauge length. The gauge length was 68.8 mm (2.71 in.) long and had a constant thickness of 3.18 mm (0.125 in.). The overall length of the specimens was 127 mm (5.0 in.). The 0° fibers were oriented along the length of the samples, parallel to the tensile direction.

The specimens were tested in tension by an Instron 4505 universal testing machine. The cross-head speed of the test machine was 0.0212 mm/s. Strain was measured with an extensometer, and the stress vs. strain curves were plotted. The yield stress was measured at 0.2% offset strain, and the ultimate strength was measured at the maximum tensile stress.

A microscopic analysis of the fracture surfaces in the tensile samples was conducted at magnifications ranging from 6.5X to 45X. Pair wise comparisons of the samples were conducted in such a way that only one factor level was varied between the pair.

3. Design of Experiment

A cause-effect diagram was used to list the possible causes affecting the tensile strength of the test specimens. Some of the possible causes were the build specifications (road width, air gap, layer thickness, raster orientation), machine environment (model temperature), and ABS material (density). Four factors were selected for this experiment: (A) model temperature, (B) air gap, (C) layer thickness, and (D) raster orientation at two levels, i.e., low (-1) and high (+1), as shown in **Table 1**. An L16 (2^4) experimental design was utilized as shown in **Table 2**. The mean tensile strength data, $\overline{Y}_{yield}$ and $\overline{Y}_{ultimate}$, are shown for the yield and ultimate strengths, respectively.

Parameter (Factor)	Description	Low Level (-1)	High Level (+1)
A	Temperature	268°C	277°C
B	Air Gap	-0.0254 mm	0 mm
C	Layer Thickness	0.254 mm	0.356 mm
D	Raster Orientation	0°/45°	90°/45°

Table 1. Factors and Levels

Trial	A	B	C	D	$\overline{Y}_{yield}$ (MPa)	$\overline{Y}_{ultimate}$ (MPa)
1	268°C	-0.0254 mm	0.254 mm	0°/45°	15.70	16.31
2	268°C	-0.0254 mm	0.254 mm	90°/45°	12.62	13.64
3	268°C	-0.0254 mm	0.356 mm	0°/45°	11.99	12.86
4	268°C	-0.0254 mm	0.356 mm	90°/45°	9.06	10.36
5	268°C	0 mm	0.254 mm	0°/45°	12.97	13.38
6	268°C	0 mm	0.254 mm	90°/45°	12.98	13.81
7	268°C	0 mm	0.356 mm	0°/45°	11.91	12.83
8	268°C	0 mm	0.356 mm	90°/45°	7.67	8.77
9	277°C	-0.0254 mm	0.254 mm	0°/45°	17.56	17.77
10	277°C	-0.0254 mm	0.254 mm	90°/45°	18.70	19.00
11	277°C	-0.0254 mm	0.356 mm	0°/45°	10.31	11.39
12	277°C	-0.0254 mm	0.356 mm	90°/45°	9.17	10.35
13	277°C	0 mm	0.254 mm	0°/45°	13.70	13.90
14	277°C	0 mm	0.254 mm	90°/45°	12.53	13.64
15	277°C	0 mm	0.356 mm	0°/45°	10.60	11.36
16	277°C	0 mm	0.356 mm	90°/45°	6.67	8.83

Table 2. L16 (2^4) Experimental Design Report

4. Analysis of Data

Based on the results in **Table 2**, the column effects for factors A, B, C, D and their interactions were determined for both yield and ultimate strengths. The analysis of the effects on the response was plotted in **Figs. 1 and 2**. The ~95% ($\pm 2\sigma$) confidence interval for the standard error of the effects [8] of each factor was calculated to be ± 0.73 MPa. When the response lies outside this interval, the effect is significant; and the converse is true when the effects are inside the interval.

In **Fig. 1,** factors B (air gap), C (layer thickness), D (raster orientation), and interaction AC lay outside the 95% confidence interval 12.13 ± 0.73 MPa, which indicates only these factors and interaction have significant effect on yield strength. **Fig. 2** shows the detailed analysis of the AC interaction. The conclusion from these figures is that to maximize the yield strength, the low-level of factors B, C and D, and the interaction of high-level A and low-level C should be selected.

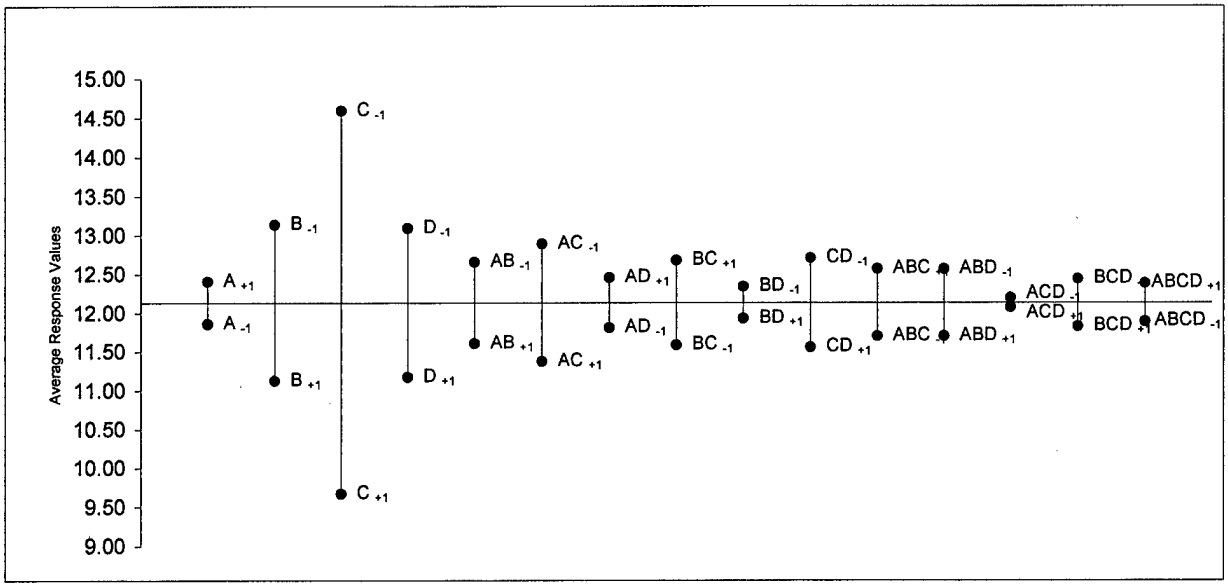

Fig. 1. Yield Strength Response (MPa) vs. Effects of Factors/Levels

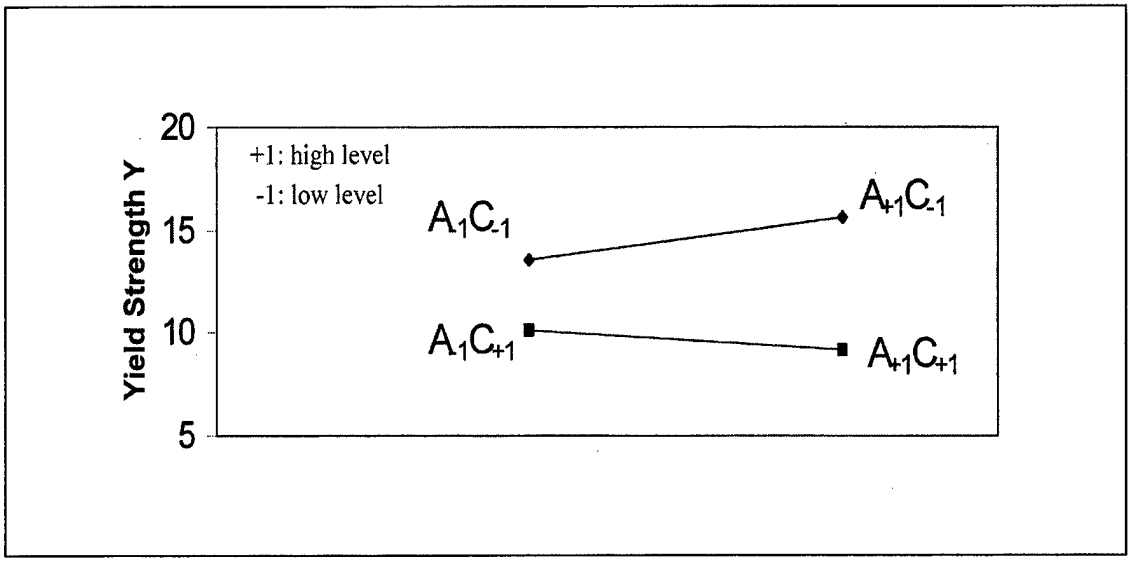

Fig. 2. Interaction between Temperature (A) and Layer Thickness (C) on Yield Strength

In **Fig. 3**, only factors B (air gap) and C (layer thickness) lay outside the 95% confidence interval 13.01 ± 0.73 MPa. Therefore, these are the only factors that have significant effects on ultimate strength. In order to achieve maximum ultimate strength, the low-level of factors B and C should be selected.

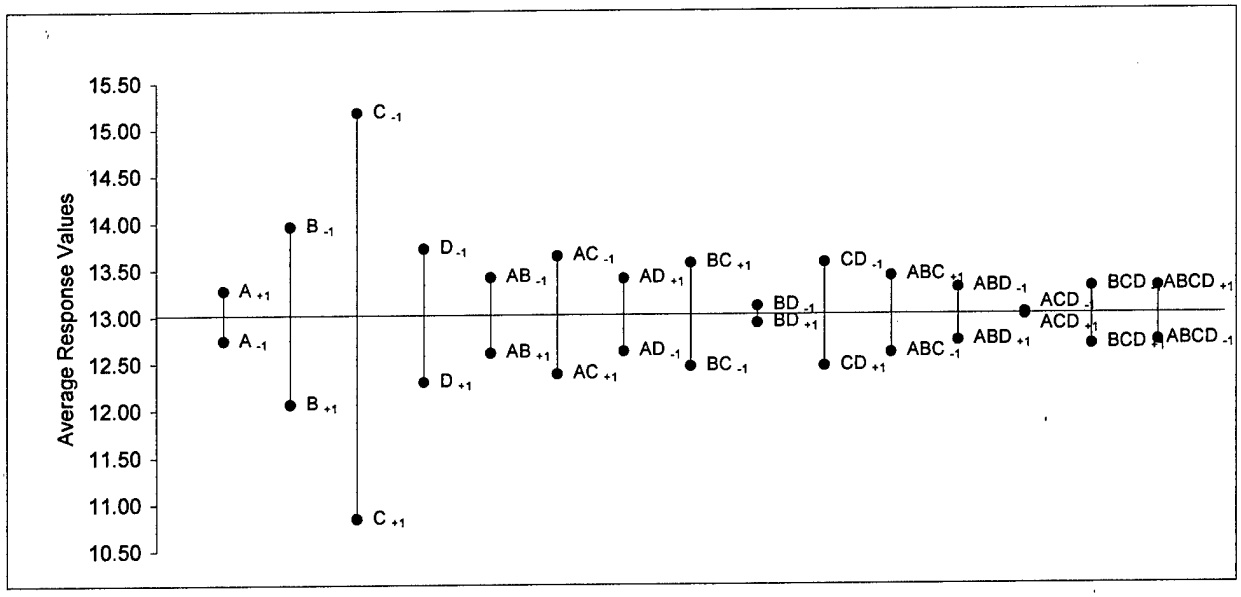

Fig. 3. Ultimate Strength Response (MPa) vs. Effects of Factors/Levels

In order to verify the above results, a regression equation was used to predict different factor levels and two-factor interactions that maximized the strength response, $\hat{y}$ [9]:

$$\hat{y} = \beta_o + \Sigma_i \beta_i x_i + \Sigma_i\Sigma_j \beta_{ij} x_i{*}x_j = \beta_o + \beta_B x_B + \beta_C x_C + \beta_D x_D + \beta_{AC} x_{A+1}{*}x_{c-1} \qquad (1)$$

Here x_i represents factors B, C and D which take on ±1 values for the low/high levels that will maximize tensile strength. Also, $x_i{*}x_j$ represents the interaction of $A_{+1}{*}C_{-1}$ that takes on ±1 values. The values of the β coefficients are shown in **Table 3**. Coefficient β_o represents the intercept (or mean value of Y). Coefficients β_i are the slope of multiple regression for factors B, C and D. β_{AC} represents the coefficient that is associated with the A*C interaction. Here the coefficients are one-half the effects of each factor and interaction in **Figs. 1** and **3.** The values of the coefficients are shown in **Table 3**.

Tensile Strength (MPa)	Coefficients				
	β_0	β_B	β_C	β_D	β_{AC}
Yield	12.13	-1.01	-2.46	-0.96	-0.76
Ultimate	13.01	-0.95	-2.17	--	--

Table 3. Calculated Coefficients for B, C, D Factors and Interaction AC in Eq. (1).

Eq. (1) verifies that for maximum yield strength, factor levels should be B_{-1}, C_{-1}, D_{-1}, and $A_{+1}C_{-1}$. For maximum ultimate strength, the factor levels should also be B_{-1} and C_{-1}.

When the interaction effects are moderate (see **Fig. 2**), errors can result in selecting the factor levels if the interactions are not taken into account. For example, in previous work [4], all of the columns in their 3-level experimental design were filled with main factors. This created a lower resolution experimental design, where the interactions and their aliases could not be analyzed. In this case, Eq. (1) would become an additive response of main factors, where $\Sigma_i\Sigma_j \beta_{ij} x_i{*}x_j = 0$. When our interactions were analyzed, $A_{+1}C_{-1}$ was preferred over $A_{-1}C_{-1}$.

5. Physical Interpretation

The selected process factor levels must physically make sense from the point of view of the structural properties and microstructure of ABS polymer. The yield strength was correlated with stretching the polymer chains and viscoelastic flow of ABS, and the ultimate strength was correlated with fracture initiation through the ABS structure [7]. Once a critical crack length was initiated, it propagated either at 45° or 90° to the tensile axis depending upon the raster orientation.

The FDM machine deposited the raster patterns at 0°/45° and 90°/45° oriented composite structures. The weak interfacial bonding between the oriented fibers can be caused by (1) weak interlaminar shear properties of the fibers, (2) the volume change during the ABS transformation from liquid to solid, or (3) formation of pores during FDM processing [2].

Factor B – Air Gap: When the air gap was set at a negative value, the adjacent fibers overlapped each other. This increased the bonding between the fibers and created a tighter structure, as the porosity between the fibers was reduced. The lower porosity composite is expected to translate into a higher tensile strength. Hence, it is reasonable that a lower air gap setting (B_{-1}) would maximize the composite strength.

Factor C – Layer Thickness: When the layer thickness was reduced, the fiber diameter was reduced, and the fiber shape became more oval as shown in **Fig. 5**. Also, the 0° fibers (light phase) overlapped each other to a greater extent when the layer thickness was low. The lower layer thickness reduced the porosity and increased the volume fraction of fibers (to a smaller extent), which strengthened the overall composite structure. This adequately explains why a low layer thickness (C_{-1}) is selected for increasing the tensile strength.

Factor D – Raster Orientation: When the two raster orientations were compared, the difference between them was in the 0° and 90° oriented fibers since the 45° layers acted similarly in both cases. Fibers oriented parallel to the tensile axis would exhibit maximum strength, while those oriented perpendicular to it would have their weakest strength. This is shown in **Fig. 4** where the 90°/45° structure fibers perpendicular to the tensile axis. However, the 0°/45° structure was strong along the 0° axis, and fracture was along the weaker 45° fiber interfaces, where the interlaminar sheer stress was high. Therefore, 0°/45° structures are expected to have a higher tensile strength than 90°/45° structures. It is logical to select D_{-1} factor level for maximizing the tensile stress.

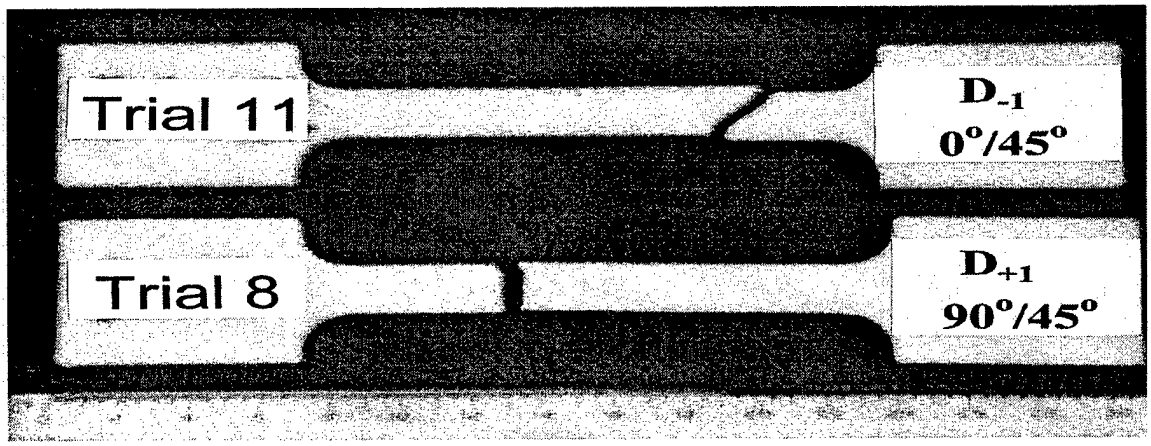

Fig. 4. Fracture of Tensile Specimens

AC Interaction: The high temperature allowed a longer time for viscous flow of the ABS material to fill the open porosity. It also contributed to a greater degree of bonding between the fibers. Hence, it would be expected that the higher temperature (A_{+1}) would increase the tensile strength. As previously explained, the low layer thickness (C_{-1}) setting was preferred for increasing the tensile strength. Therefore, it is not surprising that the high temperature and low layer thickness ($A_{+1}C_{-1}$) would interact to maximize the tensile strength.

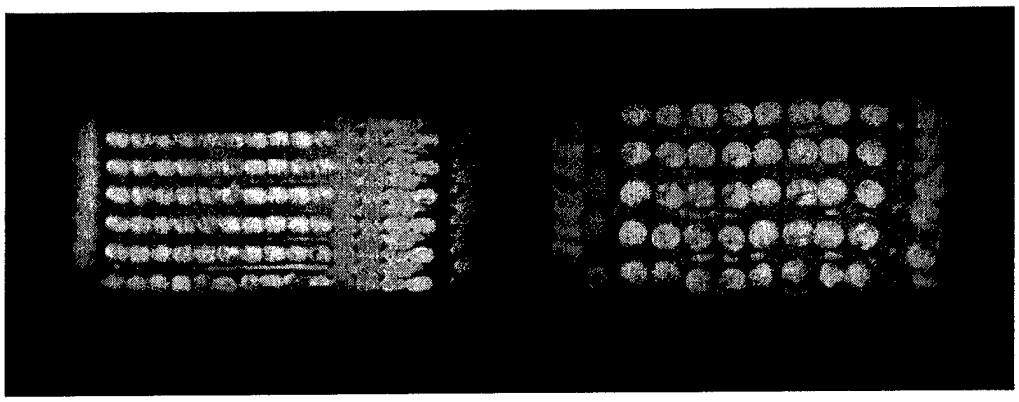

Fig. 5. Trial 9 (Left) and Trial 11 (Right)
Trial 9: Fracture surface of $0^{o}/45^{o}$ composite at low layer thickness.
Trial 11: Fracture surface of $0^{o}/45^{o}$ composite at high layer thickness.

6. Conclusions

Using an L16 (2^4) full factorial experimental design, the following conclusions resulted from our work:

1. The yield strength is maximized by low air gap, low layer thickness, low raster orientation and the interaction between high mold temperature and low layer thickness.
2. The ultimate strength is maximized by low air gap and low layer thickness.
3. The effects of the factor levels on tensile strength were explained in terms of their microstructure and processing.

Acknowledgment

The work was funded by a National Science Foundation (NSF) grant to Loyola Marymount University for the Research Experience for Undergraduates (REU) program.

References

[1] Stratasys, FDM-1650 modeling machine, system documentation, web site: http://www.stratasys.com.

[2] Es-Said, O., Noorani, R., Mendelson, M., Foyos, J., and Marloth, R. (2000), "Effect of Layer Orientation on Mechanical Properties of Rapid Prototyped Samples," *Materials and Manufacturing Processes*, 15 [1], 107-122.

[3] Montero, M., Roundy, S., Odell, D., Ahn, S-H, and Wright, P. (2001), "Material Characterization of Fused Deposition Modeling (FDM) ABS by Designed Experiments," *Society of Manufacturing Engineers, Annual Conference*, pp. 1-21, Cincinnati, OH, April .

[4] Walish, J., Sutaria, M., Dougherty, M., Vaidyanathan, R., Kasichainula, S., and Calvert, P. (1999), "Application of Design of Experiments to Extrusion Freeform Fabrication (EFF) of Functional Ceramic Prototypes," *Solid Freeform Fabrication Conference*, Proceedings, pp. 103-110, Univ. of Texas, Austin, August.

[5] Ross, P.J. (1996), *Taguchi Techniques for Quality Engineering*, 2nd Edition, McGraw-Hill.

[6] Summers, D.C. (1997), *Quality*, Prentice-Hall, Upper Saddle River, NJ.

[7] Gibson, R.F. (1994), *Principles of Composite Material Mechanics*, McGraw-Hill, Inc., New York.

[8] Montgomery,D.C., Runger, G.C., Hubele, N.F. (2000), *Engineering Statistics*, 2nd Ed., J. Wiley & Sons, NY.

[9] Montgomery, D.C. (2001), *Design and Analysis of Experiments*, 5th edition, John Wiley & Sons, Inc, New York.

Optimization of SLS Process Parameters using D-Optimality

Amol Ghanekar and Richard Crawford
Department of Mechanical Engineering
The University of Texas at Austin

Douglas Watson
National Instruments, Inc.
Austin, TX

Solid Freeform Fabrication (SFF) refers to a group of processes that manufacture parts of arbitrarily complex geometry without tooling. Currently, the operation of most SFF machines requires skilled operators with expertise in choosing process parameters in ordered to achieve the desired part quality. Thus, the "push-button 3D hardcopy" promise of SFF has yet to be realized. This paper presents a framework for selecting optimal process parameter values automatically for the selective laser sintering (SLS) process. The research described considered five process parameters that are important for the SLS process. To achieve quality measures from the five process parameters, optimization is inevitable. The method optimizes these process parameters of SLS with respect to a set of desired quality measures, based on user input of the relative importance of each of the quality measures. The basis for the framework is the so-called D-optimality criterion applied to a series of factorial experiments that capture empirically the relationships between the process parameters and part quality measures. The framework is implemented in MINITAB™ and a macro is used to perform the optimization

1 INTRODUCTION

Manufacturing processes that build parts by adding material on a layer-by-layer basis, in contrast to conventional methods that remove, reshape or add material are defined as Solid Freeform Fabrication (SFF) [1]. With such techniques, a prototype part is manufactured directly from a three-dimensional (3-D) CAD drawing source. Productivity in manufacturing is achieved by guiding a product from concept to market quickly and inexpensively. SFF technology aids this process as it automates the fabrication of a prototype part from a three-dimensional CAD drawing. This physical model conveys more complete information about the product earlier in the development cycle. The turnaround time for a typical rapid prototype part is a few days [1]. Conventional prototyping may take months, depending on the method used [2]. SFF is a quicker, more cost-effective means of building prototypes as opposed to conventional methods. The advent of SFF has changed mechanical design significantly [2].

While the technology involved in physically building a prototype is progressing, the process of reliably moving from a computer-generated model directly to a viable part is still in its infancy. Relatively little effort has been made to fully characterize the relationships between process parameters and part quality metrics [4]. A small percentage of users are aware of how these processes actually work, what types of results they will produce, and thus what process parameter choices will result in parts of the desired quality. This situation causes machine operators to make assumptions during the manufacturing stage as to what the designers' intentions are for the parts to be produced, and to select process parameter values accordingly. The research reported in this paper lays the groundwork for reaching the ultimate goal of "point

and click" SFF. We present an approach that allows the designer or the SFF part user to rank the final part quality measures that are important so that process parameters can be set accordingly. In particular, we describe an optimization technique for allowing the designer to know at the design stage whether a part manufactured by the given process parameters (i.e. the machine settings) can produce a part with the required quality.

1.1 Research Objectives

In all but the simplest design problems, engineers and manufacturers make decisions to optimize multiple criteria or objectives simultaneously. The problem at hand is an example of multicriteria optimization.

> **The purpose of this research is to develop a method to optimize the capabilities of a SFF machine so that, given particular part quality (output) measures and their relative importance, the optimal values of the process parameters (input) can be determined.**

Our approach to realizing this goal involved two main objectives. First, we conducted a series of experiments to characterize the SFF process. These were factorial experiments in which several process parameters were varied systematically, and the resulting part properties were measured. The second objective was developing a computer environment for optimizing the process parameters for a target part quality. Different multicriteria optimization techniques were reviewed and the so-called D-optimality technique was chosen. The chosen implementation environment for the optimization is a commercially available statistical analysis system, MINITAB™. A demonstration program was developed in the macro programming environment of MINITAB™. The implementation was then tested and evaluated. In the next section, our experimental results are summarized. Section 3 describes the optimization macro that was developed, and section 4 presents an example of its use. We summarize the research in section 5.

2 EXPERIMENTS

A concrete set of manufacturing rules and constraints for a Solid Freeform Fabrication process allows part manufacturers to account for the designer's intent as the part is produced. The designer can also determine if it is possible to manufacture the part satisfactorily. With information on the capabilities of a particular SFF machine, the part model can be altered as it is designed so that it will ultimately be feasible using SFF to fabricate a part with the desired quality. We have developed a standard procedure for evaluating a SFF process [4] and have applied the procedure to a SLS SinterStation 125. This section summarizes that work.

2.1 Selective Laser Sintering

Selective laser sintering is a layered manufacturing process in which powdered material is melted by laser heat into the desired shape through the repeated scanning of cross-sectional areas that will eventually form the 3D model (See Figure 1). The machine consists of two[1] pistons

[1] The most recent commercial systems have three cylinders, including two supply cylinders. The Sinterstation used for these experiments has only one supply cylinder.

within cylinders that contain, respectively, supply powder and the part being built, a roller to spread the powder evenly, radiant heaters, sensors and a controller to heat the powder, and a laser and its optics. An inert atmosphere is maintained inside the build chamber.

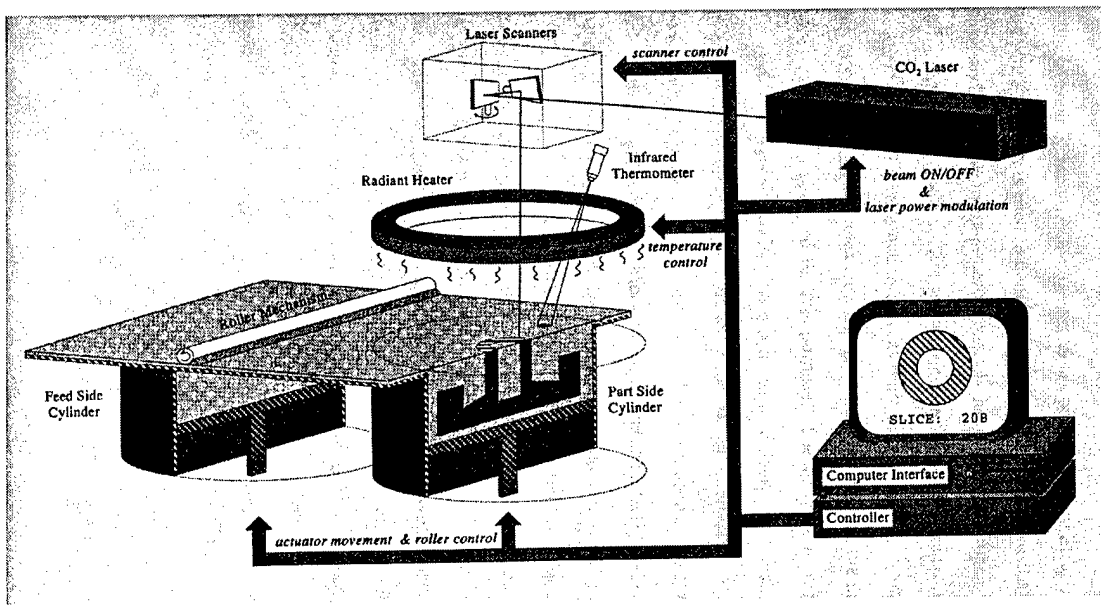

Figure 1. The selective laser sintering process [2].

The selective melting process is accomplished by a CO_2 laser. The path of the laser is controlled by galvanometers that are connected to the control computer. The computer has a sliced 3D model that dictates the path the laser takes. Various scanning techniques are used or under research [4, 5]. We used the simple X vector raster scan for our experiments.

Once the entire layer is scanned, a new layer of powder is deposited upon the previous layer. The part bed cylinder is lowered, causing the surface of the part bed to drop a prescribed amount. The powder bed cylinder is raised to provide powder for the next layer. The roller apparatus then traverses across the top of the powder bed, pushing the raised portion of the powder across the chamber to the lowered surface of the part bed. The powder covers the previously scanned areas with a thickness of powder that is determined by the amount the part cylinder has dropped. This value is the "layer thickness". The laser then scans the next layer. This process repeats until the 3D part is completed.

2.2 Process Parameters and Part Quality Attributes

In this research, the relationships between SLS process parameters and part quality attributes were determined experimentally. Full factorial experiments were used for data collection [4]. This type of experiment allows the minimal number of builds while still providing enough information to evaluate the main effects of each input parameter, as well as the interaction effects of the combined input parameters, with the same level of precision as "one-at-a-time" experiments [6]. In full factorial experiments, an experimental run is performed for every combination of factor levels. This is the most conservative of the experiment designs.

In these experiments, only one material, Duraform™, was explored. Duraform™ is a polyamide material used for fabricating functional prototypes. The process parameters below were identified as having significant relationships to part quality.

- **Laser power**. Laser energy density, quantified by the Andrew number [3], is a function of the laser power, scan speed, and scan spacing, and has the units of J/in^2. For our experiments, the scan speed and scan spacing were held constant. Thus, energy density was modified by varying the laser power between 4W and 8W.

- **Powder age**. In the experiments described here, both recycled and virgin Duraform™ powde rs were used. Recycled powder refers to unsintered powder from previous builds. The effects of powder age were tested using virgin powder and powder that had been recycle d at least 10 times.

- **Layer thickness**. Material choice severely constrains the allowable variation in this paramete Bounding limits for layer thickness were determined from the size of the particles and the ma ximum layer thickness at which inter-layer bonding occurs, based on preliminary tests.

- **Part orientation**. This parameter measures the deviation between a part-based coordinate sys tem and the build direction in the machine. The parts were oriented in the build cylinder such that the effects of scanning perpendicular to the long axis of the test part, as well as along its long axis, were tested. Additionally, orientations of 0°, 45°, and 90° around the parts' long axes were evaluated.

- **Scan vector length**. This parameter is related to part orientation in the build plane. The SLS workstation used for the experiments scans in a raster pattern. A long slender part will be sca nned differently, depending on the orientation of its long axis with respect to the scanning dir ection.

A series of specimens was fabricated on a DTM Corp. SinterStation 125, with the process parameters described above varied according to a full factorial design. The levels of the various process parameters are summarized in Table 1 below. The effects of part orientation and scan vector length were tested by fabricating multiple parts in the same build with different orientations (both in the build plane and with respect to the build direction).

Table 1. Process parameter levels.

Parameter	No. of Levels	Levels (Uncoded)
Laser Power	2	5 W and 6.5W
Age of powder	2	Old and new
Layer Thickness	2	0.004" and 0.005"
Scan Vector Length	2	Short and long
Orientation	4	-90, 0, 45 and 90 Deg

After fabricating the specimens, we measured the following part quality attributes:

- **Part strength.** Several different measures of strength were tested using the tensile,

compressive, and bending forms of loading, and the impact strength or toughness of the sample. The values were obtained using a MTS tensometer and Izod impact tester designed for plastics. Sample hardness was measured using a Rockwell Hardness tester.

- **Dimensional accuracy**. For functional prototypes dimensional accuracy is important. Dimensional accuracy includes large dimension accuracy, small dimension accuracy and minimum positive and negative feature sizes. The analysis for each was performed at different orientations since the accuracy in the z direction is different from accuracy in the x and y directions.

- **Thermal expansion.** This attribute was measured with a Perkin-Elmer 7 series Thermal Analysis System.

- **Surface roughness.** The surface roughness was measured with a contact profilometer to evaluate the effects the parameters have on surfaces that are parallel, perpendicular, and angled with respect to the build plane.

Table 2 below summarizes the measured part attributes.

Table 2. Property limits of DuraForm™ parts on the SS125.

Property	Upper Limit	Lower Limit
Tensile Strength [psi]	7922	7
Bending Strength [psi]	10657	35
Compressive Strength [psi]	17510	1303
Density [gm/cm^3]	94.15	64.19
Impact Toughness [J/cm]	153.42	17.07
% Dimensional Error		0.72
Thermal Expansion Coefficient [1/^{O}C]	1.69E-04	9.71E-05
Surface Roughness [μm]	33.5	7.7

3 OPTIMIZATION OF PROCESS PARAMETERS

In this section we describe our process parameter optimization tool. We chose to implement the optimization tool in an existing statistical analysis package after careful consideration of the desired functionality [12]. In particular we wanted an optimization method that would:

- Optimize the experimental design (combination of process parameter values) used to achieve the desired part quality measures.

- Use non-linear regression techniques to locate the optimal points.

- Obtain the output for the process parameters in coded/uncoded units. Coded means the values are normalized in the range of −1 to 1, while uncoded means the values are obtained in the actual parameter units.

- Associate importances and weights with part quality measures to reflect the designer's preferences.
- Find an optimal way to balance the customer needs (many part quality measures) that a designer must take into account before reaching a conclusion about the input parameters (process parameters) for the part.
- Provide a user interface that shows the initial condition and the optimized condition and be able to switch back and forth between them.
- Illustrate the interactions among various process parameters.

Clearly, these functional requirements call for a multicriteria optimization method that uses regression (non-linear) techniques to achieve global optimization. After studying several techniques [7], the so-called "D-optimality" technique (discussed in the next section) was selected. The MINITAB™ statistical package was chosen as the implementation environment, as it supports regression analysis and provides a macro programming facility for customizing the package. Also, the graphical interface generates plots and provides a dialog capability for user input. MINITAB™, being a statistics software package, also runs factorial designs and provides response surface analysis.

3.1 D-Optimality

Since the 1980's much work has been done in the field of experimental design, and considerable attention has been given to the use of the computer for constructing experimental designs for the user [8]. For a given computer design where the response variable, y, is a function of the design variables, $\mathbf{x}$, we usually do not know the nature of the functional relationship. We approximate the unknown relationship or function with an empirical model of the form [8]:

$$y = g(\mathbf{x}, \mathbf{ß}) + \varepsilon, \tag{1}$$

Where $g(\mathbf{x}, \mathbf{ß})$ is an interpolating function, $\mathbf{ß}$ is a vector of unknown coefficients in g, and ε is the random error (or bias from true physical relationships). For factorial experiments we usually assume that the interpolating function is a low order (*e.g.*, linear) polynomial:

$$y = \mathbf{f}^{\mathrm{T}}(\mathbf{x})\mathbf{ß} + \varepsilon = \beta_1 f_1(\mathbf{x}) + \beta_2 f_2(\mathbf{x}) + \mathrm{K} + \beta_n f_n(\mathbf{x}) + \varepsilon \tag{2}$$

Equation 2 is called the regression equation. Each of the terms $f_i(\mathbf{x})$ is a multiplicative combination of the design variables, raised to the appropriate power, that contribute to that term. For instance, for a linear model with two variables, there are four terms:

$$f_1(\mathbf{x}) = 1$$
$$f_2(\mathbf{x}) = x_1$$
$$f_3(\mathbf{x}) = x_2$$
$$f_4(\mathbf{x}) = x_1 x_2$$

To define the interpolating function g, we need to find values for the coefficients $\mathbf{ß}$ in equation (2). We can do this by rewriting equation (2) in terms of the known response values measured from the experiments. The n sample experiments are characterized by the design points $\mathbf{x}_1, \mathbf{x}_2, \mathbf{K}, \mathbf{x}_n$. Each design point $\mathbf{x}_i$ consists of a unique set of values for the k design variables. Let

$$\mathbf{y} = [y_1, y_2, \mathbf{K}, y_n]^T$$

be the measured response values for the n sample experiments, and

$$\mathbf{X} = [\mathbf{f}(\mathbf{x}_1), \mathbf{f}(\mathbf{x}_2), \mathbf{K}, \mathbf{f}(\mathbf{x}_n)]^T$$

be the $n \mathrm{X} k$ design matrix. Then equation (2) can be rewritten as the set of equations:

$$\mathbf{y} = \mathbf{X}\mathbf{ß} + \mathbf{e} \tag{3}$$

where $\mathbf{e}$ is now a vector of error terms, one for each of the n sample experiments.

Unbiased estimates of $\mathbf{ß}$ can be found if the expected error values are zero and the variances of the errors for all design points are the same:

$$\begin{aligned} \mathrm{E}(\mathbf{e}) &= \mathbf{0} \\ \mathrm{V}(\mathbf{e}) &= \sigma^2 \mathbf{I} \end{aligned} \tag{4}$$

where s is the standard deviation and $\mathbf{I}$ is the identity matrix.

With equation (3), the least squares technique can be used to compute $\hat{\mathbf{ß}}$, an estimate of $\mathbf{ß}$, assuming the number of design points in the experiment exceeds the number of parameters β_i:

$$\hat{\mathbf{ß}} = (\mathbf{X}^T\mathbf{X})^{-1}\mathbf{X}^T\mathbf{y} \tag{5}$$

Using these estimates and equation (2), the estimate the value of the response variable is:

$$\hat{y} = \mathbf{f}^T(\mathbf{x})\hat{\mathbf{ß}} \tag{6}$$

A measure of the accuracy of the estimates $\hat{\mathbf{ß}}$ is the variance-covariance matrix $\mathrm{V}(\hat{\mathbf{ß}})$, defined as:

$$\mathrm{V}(\hat{\mathbf{ß}}) = \sigma^2(\mathbf{X}^T\mathbf{X})^{-1} \tag{7}$$

The optimal design is one that minimizes the variance defined in equation (7). However, the minimum of a matrix is not a well-defined concept. A number of operational criteria have been developed. One criterion, D-optimality, seeks to minimize the determinant of the matrix $(\mathbf{X}^T\mathbf{X})^{-1}$. Of the available optimality criteria, D-optimality gives accurate parameter estimates

and takes the least time to compute [8, 9, and 10]. D-optimality is also appropriate when multiple responses are involved. Hence we have chosen the D-optimality criterion for our research.

3.2 Implementation

In this research, D optimality is applied to the 9 responses (part quality measures), the data for which was obtained from [4]. The implementation uses a D-optimality macro in MINITAB™. For each optimization run, the part quality measures to be optimized are first chosen. Then the goal for each response (maximize, minimize, or target) is chosen, and the user provides values for parameters (limits and targets) appropriate for each type of goal. Weights are then associated with the responses. The weights define the shape of the desirability function. The values of the weights vary from 0.1 to 10 to de-emphasize or emphasize the response. Finally, importances are assigned to the responses. Values of importance must be between 0.1 and 10 [11]. If all responses are equally important, the default value of one is used for each response. The composite desirability is then the geometric mean of the individual desirability [11]. However, if some responses are more important than others, the user can incorporate this information into the optimal solution by setting unequal importance values.

4 EXAMPLE: PROSTHESIS SOCKET OPTIMIZATION

In this section we present an example where different target values for the part quality measures are required for different regions of the part. The example focuses on determining the optimal process parameters for fabricating a patella tendon bearing (PTB) socket, part of prosthesis used by below-the-knee amputees. An image of a PTB socket is shown in Figure 2. This socket is designed such that the residual limb contacts all areas of the socket. However, the socket is designed with compliant areas in the regions where pressure sensitive tissue touches the socket. The patella tendon area is the weight bearing part in the socket while the pressure sensitive areas are the distal end and the fibula end (see Figure2). The bottom of the socket consists of a pylon fitting that is attached to an aluminum pylon and prosthetic foot assembly.

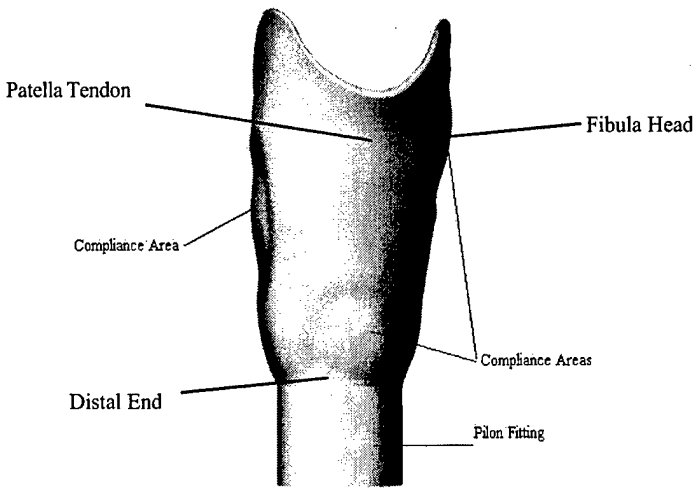

Figure 2. Patella tendon bearing socket.

For this example the compliant areas have different part quality targets than the other areas of the socket. The two part quality measures identified as the most important for the user in each area are tensile strength and 3 point bending strength, respectively. Goals, weights and importances were assigned to each of the nine quality measures and optimized. The macro begins by assuming a full factorial design and obtains data from the "responses.xls" file. The macro then performs sequential optimization, and the search improvement for optimization is done using one exchange point. The following were the goals, importances and weights for the compliant part of the socket.

Table 2. Properties of the compliant part of socket

Quality Measures	Goal	Lower	Target	Upper	Weight	Importance
Tensile	Maximum	19	7775	7775	1	1
3 Point	Minimum	29	1000	11090	1	10
Charpy	Maximum	17.95	153.4	153.4	1	8
Density	Target	64.19	94.2	94.2	1	6
Compress	Maximum	1302.5	16665.1	16665.1	1	0.5
Surface Roughness	Target	7.7	7.7	33.5	1	2
Thermal Exp	Minimum	0	90E-6	133E-6	1	0.1
Dimension Ave	Minimum	0.1	0.1	1.7	1	9
% Dimension	Minimum	0.3	0.3	43.8	1	9

As can be seen from the parameter settings the goal is to minimize the 3 point bending strength, with a maximum importance. This is because the areas where the socket needs to be compliant must have little bending resistance, *i.e.*, minimum 3 point bending strength. The composite desirability achieved for the given settings (goals, weights and importances) of the process parameters is 0.52613. The parameter settings for the five process parameters (uncoded) according to this optimization are:

Table 3. Parameter settings for the five process parameters for compliant areas of socket.

Parameter	Setting
Power	5.24
Thickness	0.005
Age	new
Vector Length	long
Orientation	-90

For load-bearing areas of the socket the goals, importances and weights are summarized below in Table 4. The goals include maximizing the tensile strength, with a maximum importance attached to this goal. As these parts of the socket must bear the weight of the patient, tensile strength becomes the controlling material property. The composite desirability achieved for the given settings (goals, weights and importances) of the process parameters is 0.50847. The parameter settings for the five process parameters (coded) according to this optimization are given in Table 5.

Table 4. Properties of the remaining part of socket

Quality Measures	Goal	Lower	Target	Upper	Weight	Importance
Tensile	Maximum	19	7775	7775	1	10
3 Point	Minimum	29	1000	11090	1	4
Charpy	Maximum	17.95	153.4	153.4	1	8
Density	Target	64.19	94.2	94.2	1	6
Compress	Maximum	1302.5	16665.1	16665.1	1	6
Surface Roughness	Target	7.7	7.7	33.5	1	2
Thermal Exp	Minimum	0	90E-6	133E-6	1	0.1
Dimension Ave	Minimum	0.1	0.1	1.7	1	9
% Dimension	Minimum	0.3	0.3	43.8	1	9

Table 5. Parameter settings for load-bearing areas of socket.

Parameter	Setting
Power	5.58W
Thickness	0.0046"
Age	Old
Vector Length	Long
Orientation	-70 degree

This example focuses on a part to be manufactured by SLS in response to different customer needs for different parts of the same socket. The optimization function shows that the power, thickness and vector length will have to be changed for the socket to work as intended.

In the compliant areas of the socket the power level should be lower than that in the load-bearing areas of the socket. Layer thickness, powder age, and orientation should also vary for the compliant areas and the load-bearing areas of the socket. See Table 6 below for a comparison of the values:

Table 6. Comparison of five process parameters for compliant and the load-bearing areas of socket.

	Compliant Part	Rest of the socket
Power	5.24 W	5.58W
Thickness	0.005"	0.0046"
Age	New	Old
Scan Vector Length	Long	Long
Orientation	-90 degree	-70 degree

4.1 Interpretation of Results

In this section we interpret the results of optimizing the process parameters for the application described above, beginning with laser power. An increase in the process parameter

laser power means the powder melts more thoroughly and forms better bonds between layers. This leads to increases in tensile, 3 point bending, and compression strengths. Better bonding in turn leads to better dimensional. For the load-bearing areas of the socket the tensile strength has importance 10 (most important) followed by average dimension, % dimension error and charpy impact strength. These areas of the socket must be structurally sound, *i.e.*, the tensile strength should be large enough to transfer the patient' s weight to the pylon fitting.

Increasing the layer thickness reduces the tensile, 3-point bending and compressive strengths [4]. This is because, with an increase in layer thickness for a given power, the powder does not melt as thoroughly as it would for thinner layers or higher power. For the compliant part the 3 point bending is the most important part quality measure followed by average dimension, % dimension error and charpy impact strength. Thus, a smaller 3 point bending strength is desired to allow more bending in compliant. Layer thickness affects several part quality measures, the most important being the build time. The surface roughness should decrease with decreased layer thickness because the stair step effect [4] between layers is reduced.

Powder age indicates either new powder or recycled powder. Watson [4] showed that accuracy decreases with an increase in the number of times the powder is recycled. Because compliance is increased by changing the local geometry (either thickness or by incorporating compliant features), accuracy is important in the compliant areas of the socket. Also, recycled powder requires more thermal energy, which can have the side effect of part growth or curl.

The scan vector length affects the density of the part produced. The part starts to cool immediately after the laser passes over the powder. The longer the laser takes to melt the adjacent powder the higher the thermal gradients. With long scan vectors the powder takes longer to cool than with short scan vectors [4]. Other part quality measures are also affected by the scan vector length due to the galvanometer motion. The motion of the galvanometers is such that, when the direction changes, they first decelerate, stop briefly and then accelerate in the other direction. This can result in high energy density over the scanned area. Also a part with complex geometry may require small scan vectors. Since this prosthesis does not have any complex geometric features, we decided to use large scan vector lengths. This speeds the build process up and reduces costs.

Orientation is a major factor in determining the final part quality. For taller parts, the machine processes more layers, and more time is required to complete the build. Laser scan time is dependent on volume and not on orientation. If the part can be oriented in such a way that the longest side is in the plane then the time and cost needed to produce the part are greatly reduced. Orientation also affects part strength. In the x-y direction the powder melts homogeneously, while in the z direction there is a possibility of improper bonding between layers. This can lead to relatively poor lamination and strength reduction in that direction. For compliant areas, where more strain is desired for a given stress value, Watson [4] shows that orienting the part with the longest dimension in the z direction results in more compliance and lower 3-point bending strength. Since our method does not account for the geometry and sizes of the parts in x, y and z direction we assume that the part is oriented to minimize the time of manufacture and ultimately the cost. For the prosthesis socket, this means the longest dimension is in the x-y. The parameter optimization results suggest that for the required part quality measures the orientation should be

such that the longest dimension is along the z direction for the compliant areas of the socket and slightly tilted (20 degrees to the earlier orientation) for the load-bearing areas of the socket. This, of course, is not possible, but serves to illustrate how our method accounts for orientation in process parameter selection.

4.2 Optimization Plots for Prosthetic Socket

The MINITAB™ user interface presents the optimization results in graphical form. Figures 3 and 4 show optimization plots obtained for the prosthetic socket example. There are six columns in each figure. The first column lists the parameters and gives the optimal value for the settings. The subsequent columns give the process parameters, high and low coded values, and the optimal value. For instance, the second column plots the variation of power from -1 to 1 in coded units. The vertical red line in each column shows the optimal process parameter settings for all the different part quality measures. The dotted blue line in each row gives the response for the set weights and importances.

The plots summarize the optimize results, allowing the user to effectively detect trends. For instance, in Figure 4 the tensile strength variation is linear (in blue) and hence shown by a straight line. In contrast, for the compressive strength, the variation for orientation process parameter is quadratic, indicated by the curve in the plot. A comparison of Figures 3 and 4 shows that the optimal points of operation are different (shown by red vertical lines). Also the responses for the part quality measures are different in both the figures for a given response, as the objectives, weights and importances are different in each case.

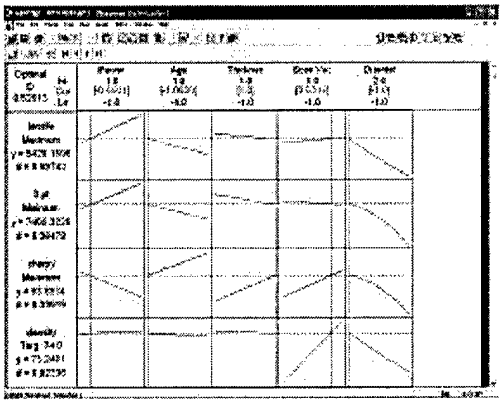

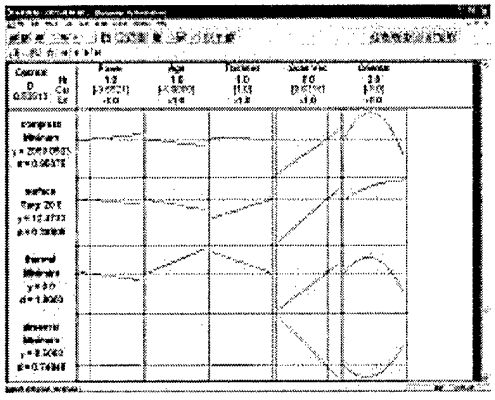

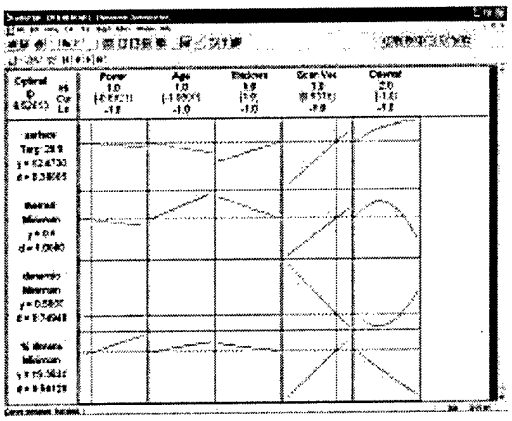

Figure 3. Optimization plots for compliant areas of the socket.

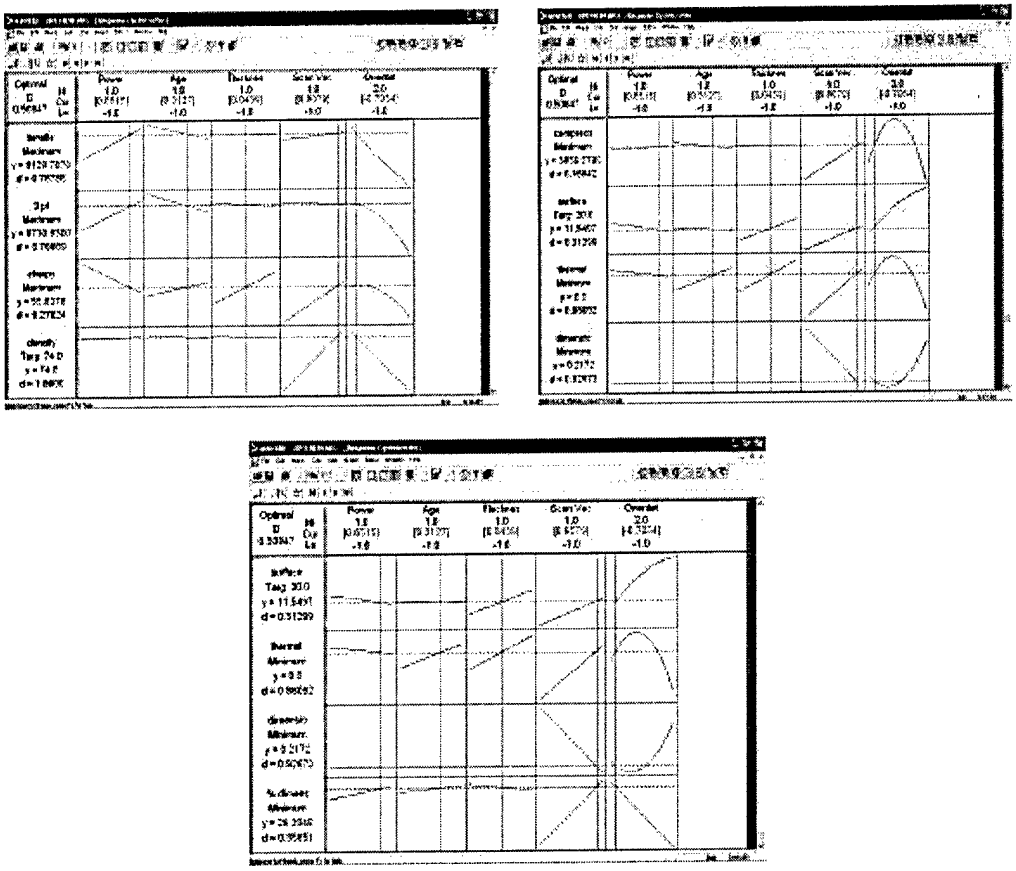

Figure 4: Optimization plot for load-bearing areas of the socket.

5 CONCLUSIONS

This paper describes a system for choosing optimal process parameter values for manufacturing a part using selective laser sintering. The system uses the D-optimality algorithm and nonlinear regression to determine the best values for process parameters based on experimental part quality data from a series of factorial experiments. Our approach allows the designer to prioritize the different part quality metrics and focus on those that are most important

to the customer. Using this system, the part designer can balance the various requirements of a customer to achieve the optimal part quality.

The research suggests several avenues of future work. The most obvious extension of the work is to apply the framework to other SFF machines and processes. Watson [4] describes a methodology for characterizing SFF processes. We believe the framework described in this paper is general enough to accommodate data from other processes and machines, but this must be shown with concrete examples

A second area of improvement is the optimization environment itself. The current implementation of the macro requires use of the MINITAB™ drop-down menus. This is a cumbersome artifact of the chosen implementation vehicle. Other implementation tools should be studied to determine if a more suitable environment is available.

A third, more general extension of this tool is extending to a true manufacturability evaluator. Currently the system only reports the optimal process parameters. It does not provide a measure of how manufacturable the design is, nor does it give suggestions on improving manufacturability. This goal is clearly necessary to realize the potential of SFF to be "push button" manufacturing technologies.

REFERENCES

1. Jacobs, P.F., 1992, *Rapid Prototyping and Manufacturing: Fundamentals of Stereolithography*, Society of Manufacturing Engineers.

2. Beaman, J. J., Barlow, J. W., Bourell, D. L., Crawford, R. H., Marcus, H. L., and McAlea, K. P., 1997, *Solid Freeform Fabrication: A New Direction in Manufacturing*, Kluwer Academic Publishers.

3. Nelson, J. C., 1993, *Selective Laser Sintering: A Definition of the Process and an Empirical Sintering Model*, Ph.D. dissertation, The University of Texas at Austin.

4. Watson, D., 1999, *Process Optimization of Selective Laser Sintering through the Use of Design Rules and Constraints*, Masters thesis, The University of Texas At Austin.

5. Bagchi, A., 1994, "Benchmarking of Rapid Prototyping systems- Beginning to Set Standards," *Proceedings of the 1994 Solid Freeform Fabrication Symposium*, Austin, TX, pp. 146-153.

6. Montgomery, D. C., 1976, *Design and Analysis of Experiments*, John Wiley & Sons, New York.

7. Das, I., 1997, *Nonlinear Multicriteria Optimization and Robust Opti*mality, PhD thesis, Rice University.

8. Eschenauer H., Koski J., Osyczka A., editors, 1990, *Multicriteria Design Optimization*, Springer Verlag.

9. Steuer, R. E., and Sun, M., 1995, "The Parameter Space Investigation Method of Multiple Objective Nonlinear Programming: A Computational Investigation," *Operations Research*, Vol. 43, no. 4, pp. 641-648, July-August 1995.

10. St. John, R. C., and Draper, N. R., 1975, "D-Optimality for Regression Designs: A Review," *Technometrics*, Vol. 17, no. 1, February 1975.

11. *MinitabHelp Manual*, Minitab™ Inc. State College, PA.

12. Ghanekar A. S., 2003, *The Optimization of SLS process parameters using D-optimality*, Masters thesis, The University of Texas At Austin.

FREEFORM FABRICATION OF 3D ZINC-AIR BATTERIES AND FUNCTIONAL ELECTROMECHANICAL ASSEMBLIES

Evan Malone, Kian Rasa, Daniel Cohen, Todd Isaacson, Hilary Lashley, Hod Lipson

Computational Synthesis Laboratory, Department of Mechanical and Aerospace Engineering, Cornell University, Ithaca NY 14853 USA

em224@cornell.edu

Reviewed, accepted August 19, 2003

Abstract

This paper reports on a fabrication platform and extensions to deposition-based processes that permit freeform fabrication of three-dimensional functional assemblies with embedded conductive wiring and power sources. Structure and joints are produced by fused deposition of thermoplastics and deposition of elastomers. Conductive wiring is achieved by deposition of various low-melting-point alloys and conductive pastes. Batteries based on zinc-air chemistry are produced by deposition of zinc, electrolyte, and catalysts, with separator media and electrodes. Details of the deposition processes are provided and several printed assemblies are demonstrated.

Introduction

In the last several years, there have been an increasing number of solid-freeform fabrication processes and materials being researched. It has not escaped the notice of some that this diversity is nearing the point at which almost any conventionally manufactured part could be made entirely via SFF processes, and that a synthesis of compatible processes may permit the fabrication of entire functional assemblies [Weiss and Prinz, 1998; Safari *et. al.*, 2000] and even complete functional systems [Lipson *et. al.*, 2000]. The Cornell Computational Synthesis Laboratory (CCSL) is investigating the freeform fabrication of functional, integrated, electromechanical systems, and an understanding of the interface between the design process and this new fabrication domain. A high-performance motion control platform and an initial set of tools have been designed and constructed that have enabled the exploration of layered fabrication processes in a wide variety of materials and material combinations. The materials experimented with thus far include thermoplastics, low-melting-point alloys, and a variety of gels and slurries. Here we report on freeform fabrication of a zinc-air battery which is capable of powering a small DC brush motor, thermoplastic and elastomer flexure joints, two approaches to embedded wiring, and structures with embedded wiring. These components are some of the basic building blocks necessary for freeform fabrication of three-dimensional, functional, electromechanical systems.

Fabrication Platform

In order to provide maximum freedom for experimentation with a wide variety of materials and processes, a custom robotic platform and two material deposition tools have been designed and constructed. The initial requirement employed in the design of these tools can be stated briefly as follows: the motion control platform should provide maximal parametric freedom to the deposition processes, and permit the sequential use of many deposition processes in the course of fabricating a given object. The most significant assumption informing the design is that materials will be deposited as streams or droplets in a layered manufacturing process. Positioning is therefore limited to three Cartesian axes, and an emphasis was placed on velocity

regulation, path-following and positioning accuracy, resolution, repeatability, and high acceleration to achieve fine features while printing at a constant material feed rate. Lower acceleration performance would require more complex deposition feedrate control. Table 1 describes the performance requirements employed in the design of the positioning system.

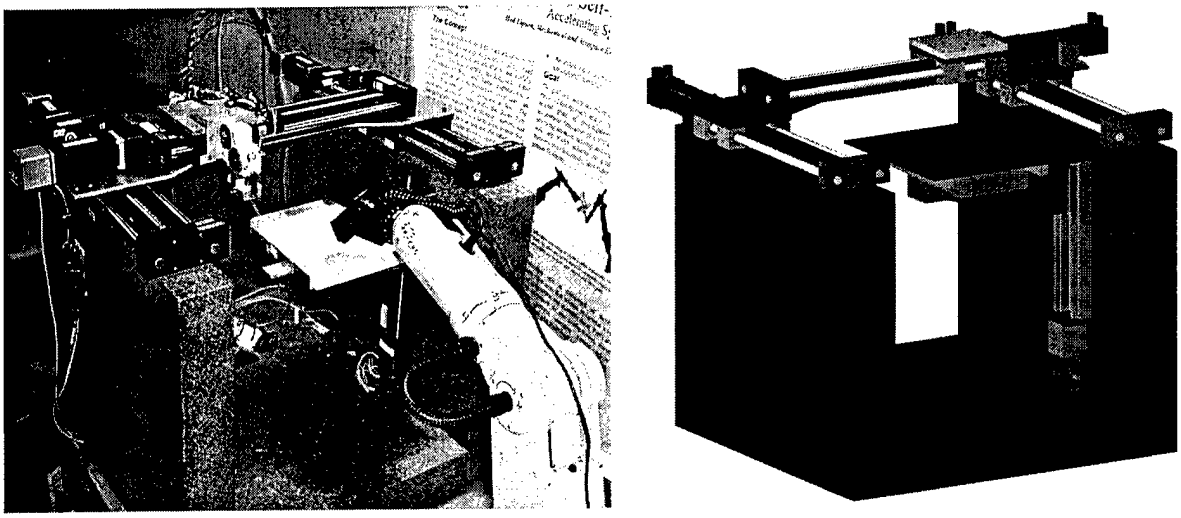

Figure 1: Gantry robot fabrication platform

A Cartesian gantry-configuration robot (Figure 1) has been selected for this application for its relatively simple control, large payload capacity relative to rigidity, and positioning/path-following performance. Linear motors, ballscrews, and cable-pulley systems were all considered for the drivetrain, and ballscrews were selected for simplicity. A cable-pulley system is an attractive alternative because the drive motors themselves do not need to be located on the moving components of the system.

Table 1: Fabrication System Performance Specifications

Minimum material stream/drop diameter	250	μm	0.010	in
Materials cross-section area	4.9×10^{-8}	m^2		
Build rate	2.5×10^{-9}	m^3/s	0.55	in^3/h
Nominal speed along path	0.05	m/s		
Min turn radius at nominal speed	125	μm	4.92×10^{-3}	in
Tool Position Accuracy (+/-)	25	μm	9.84×10^{-4}	in
Tool Position Repeatability (+/-)	25	μm	9.84×10^{-4}	in
Positioning Resolution	5	μm	1.97×10^{-4}	in
Build envelope x	0.3	m	11.8	in
Build envelope y	0.3	m	11.8	in
Build envelope z	0.3	m	11.8	in
Max XY acceleration	20.75	m/s^2	2.12	g

A software application has been created to manage path planning and control. Multi-material objects are defined using multiple STL (stereolithography) files, each describing a single material. Each material is associated with a deposition tool and material properties governing layer thickness, deposition width and deposition rates. Geometry slicing and path generation algorithms construct unique perimeter contour and fill raster paths based on the tools' and materials' parameters, and combine the layers into a fabrication sequence with increasing

height. Special care is needed to prioritize layers of similar heights according to interaction among materials.

Deposition Tools

A freeform fabrication system capable of producing complex, functional products requires a highly versatile deposition tool or set of deposition tools to address the need to deposit a broad range of materials with vastly different physical properties. The set of materials explored in the freeform fabrication of batteries can be organized into four basic categories: plastics, metals, liquid chemicals, and chemical pastes. For the initial experiments, two separate deposition tools were designed – one for plastics and metals, and another for liquid chemicals and pastes. The tools were designed to be compatible with both a Cartesian robot and a six-axis robotic arm in order to allow for experimentation with both types of positioning systems. Load restrictions and dimensional limitations of robotic arms require that tools be small and lightweight, a feature that also leads to lower systemic inertia and enhanced robotic performance.

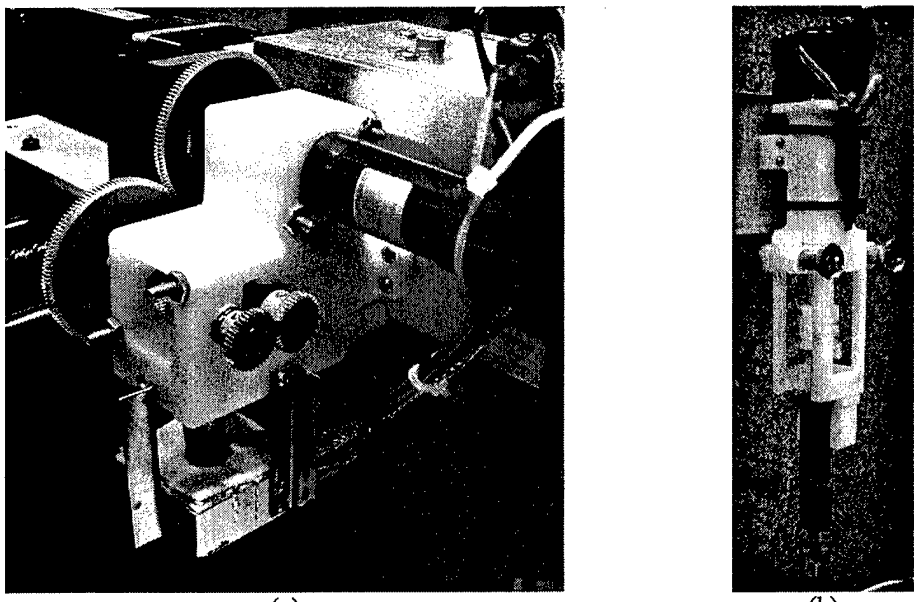

(a) (b)

Figure 2: Extrusion tools constructed: (a) wire-fed extruder, and (b) syringe tool

The deposition tool for metals and plastics (Figure 2a) is an extruder that feeds material in wire form (0.050" – 0.070" diameter) through an actively air-cooled metal guide tube and into a heated liquefier block containing a nozzle [Swanson *et. al.* 1999]. The tool has been successfully tested with solid core Pb-Sn solder wire, as well as ABS (acrylonitrile-butadiene-styrene) thermoplastic wire.

A separate tool was designed to deposit liquids and chemical pastes (Figure 2b). This tool accepts standard commercial 10cc Luer-lock syringe barrels and plungers. The plunger position is actuated by a linear stepper-motor capable of exerting 50 lbf. Prior experiments with a pneumatic dispensing system proved open-loop pressure control to be unsuitable for freeform deposition of slurries; instead, volumetric control provided by the current approach is more broadly applicable, and also allows for more precise reverse-flow control. The design of the tool simplifies experimentation with a broad range of materials. Materials may be easily changed by substituting a different syringe barrel and plunger in the plunger-driver component of the tool.

Freeform Fabrication of a Zinc-Air Battery

The freeform fabrication of a functional battery was selected as a comprehensive test of the multiple material capabilities of the previously described platform. There is little literature on the production of freeform, three-dimensional energy storage devices, though a planar thin-film cell has recently been demonstrated by Power Paper Ltd. (2003) for low-power applications. Freeform fabricated batteries are a major step toward freeform fabricated, active, functional, electromechanical systems. The size, shape, and performance of a cell become free design parameters, and can be customized for the specific geometry and functional requirements of a product. A cell can be placed at arbitrary locations within the product, rather than forcing the design of a product to be limited by the characteristics of commercially available energy sources. With this in mind, research and experiments were conducted in an effort to produce a freeform cell. For the purpose of these experiments, a cell is defined as a device that converts the chemical potential energy between its anode and cathode materials into electrical energy by means of redox reactions: reduction (electron gain) at the cathode, oxidation (electron loss) at the anode. A battery is comprised of one or more connected cells. The essential components of a Zn-air cell are the negative terminal, anode, separator, cathode catalyst, cathode, positive terminal, and electrolyte (Table 2, Figure 6).

Table 2: Key Battery Components / Materials Tested*

Cell Component	Materials Tested
Electrolyte	0.25 Molar -> 8 Molar solution of potassium hydroxide (KOH) and distilled water
Negative terminal	Paste of methylcellulose (MC) with copper (Cu, 99% purity 2-5 μm), or with silver (Ag, 99% purity 1 μm)
Anode	Slurry of electrolyte with zinc (Zn, 97.1% purity, dust) and surfactant
Separator	Paper, or Rescor 740 insulating ceramic foam (Cotronics Inc.)
Cathode catalyst	Slurry of carbon black, manganese dioxide (MnO_2, 80-85% purity), and electrolyte
Cathode	Air
Positive terminal	Paste of methylcellulose with nickel (Ni, 99% purity -325 mesh), or copper, or silver

* Many of these materials are hazardous, and should only be handled with proper training and protective equipment

Zinc-air cell chemistry was the first considered because of its simplicity and high energy density. The basic chemical reactions are:

At Air Cathode: $\frac{1}{2}\ O_2 + H_2O + 2e \rightarrow 2OH^-$

At Zn Anode: $Zn \rightarrow Zn^{2+} + 2e$

$Zn^{2+} + 2OH^- \rightarrow Zn(OH)_2$

$Zn(OH)_2 \rightarrow ZnO + H_2O$

Overall: $\mathbf{Zn + \frac{1}{2}O_2 \rightarrow ZnO : E_0 = 1.65\ V}$

The experiments outlined below investigate the effects on cell performance of electrolyte concentration, current collector composition and geometry, cell structure and construction, and cathode catalyst composition. After the initial tests were conducted and the fundamental characteristics understood, the research shifted to adapting a battery design to solid-freeform fabrication processes.

Zn-Air Electrolyte Experiments

Tests were conducted with the aim of understanding the basic anode and electrolyte chemical ratios and concentrations, and all other variables were held constant. The test procedure [Isaacson, 2003] included mixing the Zn with various concentrations of KOH (0.25M to 8M) and placing the mixtures in an ABS cell casing, using copper wire as both the negative and positive terminals (Figure 3a).

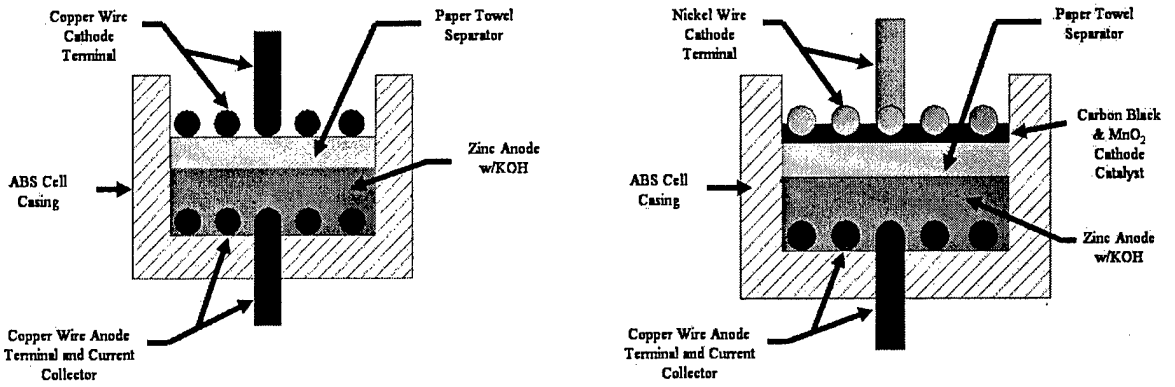

Figure 3: Experimental cells, in cross-section: (a) basic Zn-air cell and (b) Zn-air cell with MnO_2 and carbon black catalyst

Paper was initially used as a separator for simplicity and consistency. The cells were loaded with a 102 Ohm resistor and the voltage recorded. It was found that an electrolyte concentration of 7M to 8M gave the cell a more consistent voltage over its lifetime.

Catalyst Experiments

Manganese dioxide and carbon black were then added to the cell to improve cell performance [Tinker, 2002]. The ratio of MnO_2 to carbon was derived from manganese dioxide alkaline cells. These materials are also used as a catalyst in commercial Zn-air batteries [Linden *et. al.* 2002; Duracell, 2001]. By weight, the anode was comprised of 65% Zn and 35% 8M KOH, the catalyst was comprised of 50% MnO_2, 44% 8M KOH, and 6% carbon black, and the separator layer consisted of 8M KOH saturated paper. The cell was constructed in a similar way to the previous cell design with the addition of a catalyst layer (Figure 3b), and tested in the same manner. Important observations made from these tests were that the consistency of cell performance improved and the voltage doubled compared to previous tests. The most significant observation was that the power output increased by 500%. To reduce the potential energy barrier at the terminal junctions, nickel and copper wire were used for the cathode and anode current collectors respectively.

Surface Area and Current Collector Experiments

Tests were conducted to understand the effects of surface area and increase overall performance. Using the same cell chemistry and mass of material as in previous tests, the cell surface area was increased from a 1" diameter to a 3" diameter, and the current collectors/terminals were doubled in length (6" coiled wire to a 12" coiled wire). The cells were loaded with a 33 Ohm resistor to acquire data relevant to the goal of running a 30mW electric DC brush motor. The graphs (Figure 4) below demonstrate that cells of this simple design are

able to supply more than 30mW at 1V for more than ½ hour. The cells were able to turn the motor, and in doing so, validated the tested cell chemistry and structure.

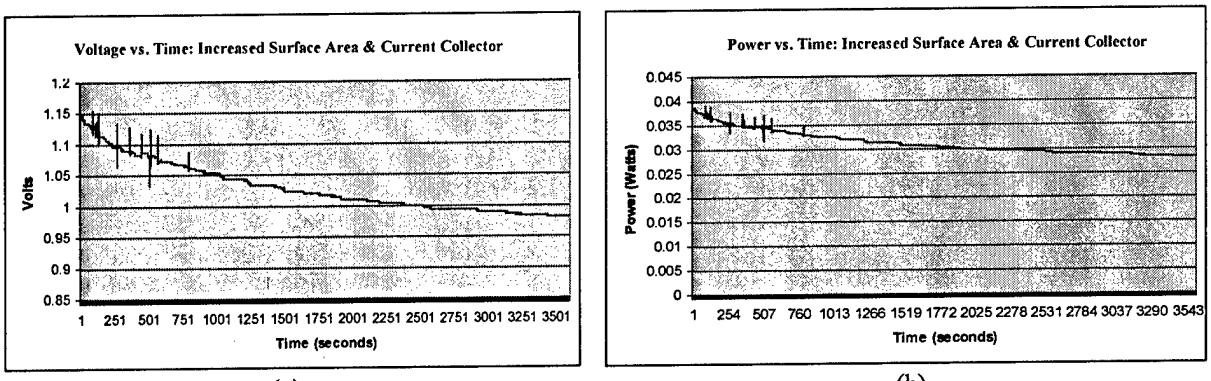

(a) (b)

Figure 4: (a) Voltage vs. time of cell with increased surface area and current collector area and (b) power vs. time of cell with increased surface area and current collector area

Separator Experiments

Methylcellulose (MC) gel and Rescor 740 insulating ceramic foam were both tested for their efficacy as separator layers, to replace the only remaining unprintable component in the cells – paper. Methylcellulose (3 grams of MC to 100mL of 100°C distilled water) does not interact well with 8M KOH electrolyte [Danko, 2003] - the gel deteriorates and allows shorting between cathode and anode. Rescor 740 (100 parts base to 64 parts activator) is a permeable ceramic foam which absorbs the electrolyte and allows for the migration of ions across the layer, making it a viable choice as separator.

Extrusion Experiments

Conductive Pastes

Various metallic pastes and solder alloy were tested as materials for current collectors. Pb-Sn solder proved to be incompatible with the cell chemistry and was ruled out as a terminal material. MC was mixed in 1:1 ratios by mass with Cu, Ni, and Ag powders, and each was extruded through a syringe creating extrudable wires. Silver paste proved to be the best material for the cell terminals for two reasons; the silver terminals did not react with the cell chemistry and had lowest electrical resistivity of the pastes. This paste was thus used for both the anode and cathode current collectors/terminals. The nozzles used for testing were 14Ga stainless steel needles, which produced a stream approximately 1.4mm in diameter.

Separator

Surfactant was added to the Rescor 740 ceramic foam material to enable extrusion and to delay the curing of the material while in the syringe. The foam slurry is highly viscous and prone to phase separation, and requires a large diameter nozzle for successful extrusion. Initial testing indicated that the addition of the surfactant in the separator material reduces power output slightly, and more testing is necessary to determine the optimum material and/or Rescor/surfactant ratio. The internal diameter of the nozzle used was 1.9mm, and the resulting stream of material was about 1.3mm in diameter.

Anode

The anode material (a slurry of Zn and KOH solution) was exceptionally difficult to extrude, as Zn settles out of the slurry and clogs the syringe. Surfactant was added to prevent clogging, but the resultant increase in ease of handling comes at the expense of some cell power output. Therefore, the slightest possible amount of surfactant was used. The anode consisted of 60% Zn, 30% KOH, and 10% surfactant by weight. The nozzle diameter was approximately 7mm, resulting in comparably-sized drops of deposited material.

Catalyst

The MnO_2 and carbon black powders are extrudable when pre-mixed with KOH solution. In order to achieve an homogeneous slurry, the catalyst material was forced through a syringe several times before use, using a pneumatic dispensing machine. 14Ga stainless steel syringe needles were used, and these produce a stream of about 1.4mm in diameter.

Freeform Fabricated Cell Design

The next round of experiments focused on the fabrication process. These tests were designed to demonstrate that 100% of the materials for a complete cell could be extruded, to verify that freeform fabricated cell performance would be adequate (i.e. sufficiently powerful to turn the motor and have comparable voltage/power output to previously tested cells), and to identify problems that might occur during production with the fabrication platform.

Table 3: Process for Constructing a Manually Extruded Cell

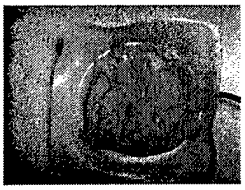	**Negative Terminal** The silver slurry was extruded into a container with a copper wire exposed to the silver for data collection purposes. It was then dried using a heat gun. The heat helps to evaporate the water from the MC solution and allows the material to be strong enough to receive the load of the next layer.
	**Anode** Here the Zn-KOH and surfactant slurry was added over the silver negative terminal.
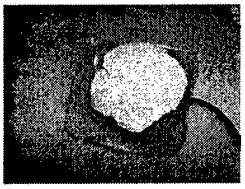	**Separator** For testing purposes, the Rescor separator layer was pre-cast. It was allowed to cure at room temperature for approximately five hours to ensure that the layer was solid and would not interfere with the other cell components and chemistry.
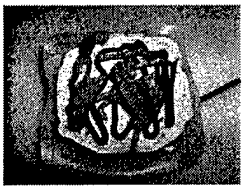	**Catalyst and Cathode Terminal** Finally, after the separator was placed over the Zn, the catalyst was extruded freely over the separator. The silver slurry was then liberally extruded over the catalyst and separator. A copper wire (not shown) was placed over the silver cathode terminal for data collection purposes.

Manually Extruded Cell and Results

Firstly, a cell was made by hand using only the extrudable materials and extrusion deposition. This process is detailed in Table 3 above. The graphs below (Figure 5) show the voltage and power output of the cell - loaded with a 100 Ohm resistor - over a one hour period. The all-extruded cells have satisfactory performance, delivering more than 10mW at more than 1V for the entire hour of data collection. The downward spike in the graphs occurred when the cell was connected to the motor for demonstration testing. Multiple tests conducted with this cell design and manufacturing technique show repeatable results over a sample size of approximately six cells, suggesting the feasibility of producing a functional cell on the freeform fabrication platform.

Voltage vs. Time: Manually Extruded Cell

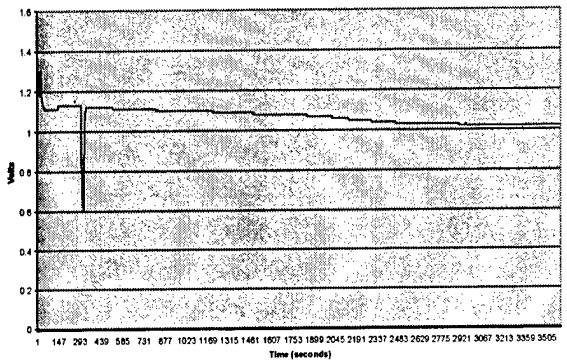

(a)

Power vs. Time: Manually Extruded Cell

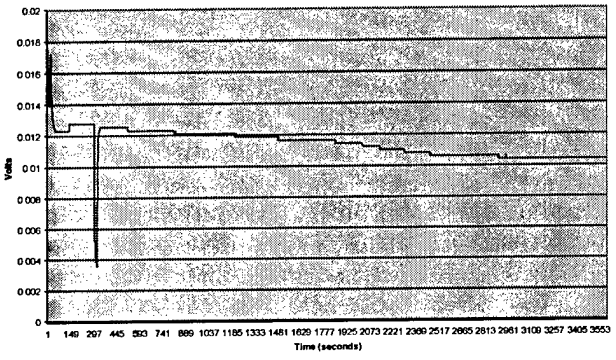

(b)

Figure 5: Performance of manually extruded cell; (a) voltage, and (b) power to 100 Ohm load.

Freeform Fabricated Cell

The freeform fabricated cell design is essentially identical to that of the manually fabricated test cells. Figure 6 shows a cross-section view of the cell design. The zinc anode is surrounded by silver paste to enclose the zinc and prevent KOH evaporation, and to increase the reaction surface area of the negative terminal.

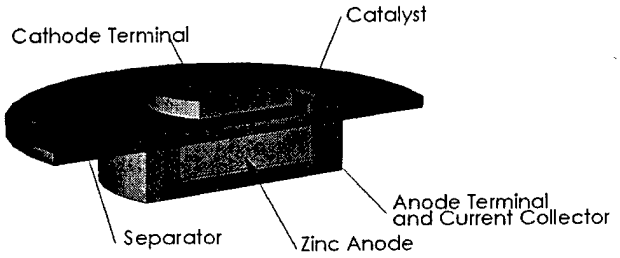

Figure 6: Cross-sectional view of freeform fabricated cell design

The separator layer is intentionally designed to be excessively large compared to the rest of the cell components to ensure that the cell does not short. The catalyst layer is extruded on top of the separator layer, and the cathode terminal, constructed of MC/silver paste, is printed directly

over the catalyst. Both the anode and the cathode terminals are connected to the motor or the data acquisition board via copper wires. Figure 7 highlights some key steps in the successful freeform fabrication of this cell design.

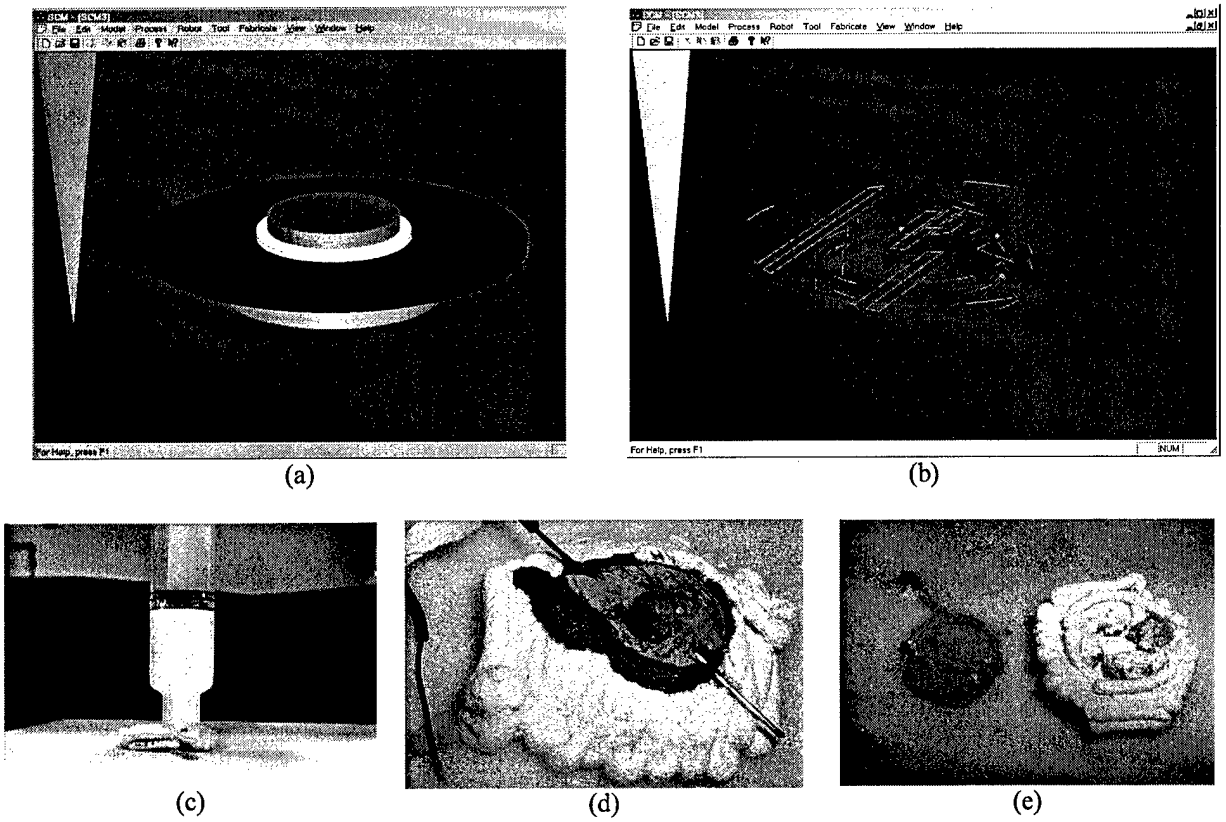

Figure 7: Sequence of operations in freeform fabrication of battery: (a) solid view of battery model in CCSL SCM software, (b) slicing of battery model in SCM application to generate tool paths, (c) deposition of Rescor separator layer, (d) close-up photograph of completed battery, and (e) dissection of battery (anode terminal on left and separator layer/zinc anode on right)

Results and Discussion

The performance benchmark test for the freeform-fabricated cell was the ability to power a small DC brush motor, which consumes about 30mW, unloaded. The cell was able to provide the starting current for the motor, and ran the motor for about 2 seconds. Figure 8 depicts the open circuit voltage of the cell after it ran the motor. When comparing this voltage to previous tests it is evident that the cell has excellent construction (no internal shorting) because the open circuit voltage is near the theoretical maximum potential for a cell of this chemistry (~1.6V). After having run the motor, however, the cell was no longer able to generate significant power, perhaps because of poor oxygen transport into the cell, electrolyte evaporation, or insufficient zinc quantity. A thinner separator layer, enclosing the cell in a thermoplastic case, and increasing the volume of deposited zinc anode will be examined as remedies for each of these problems, respectively. It is also apparent that the dimensions of the physical cell differ from those specified in the design. This is a result of the number of materials involved, material preparation variability, material property degradation, and high sensitivity of tool calibration to material properties. Further refinements in equipment calibration and material processing methods will improve output control.

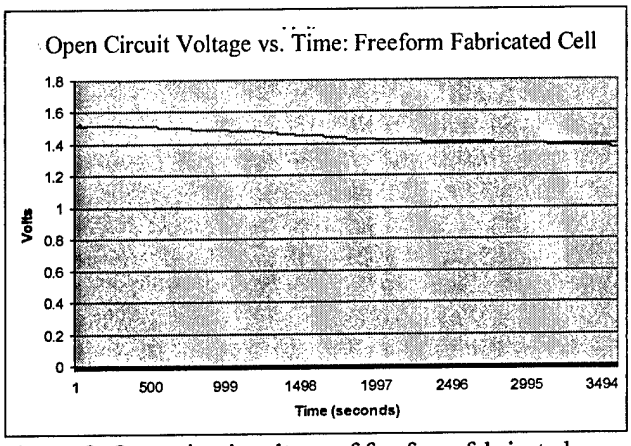

Figure 8: Open circuit voltage of freeform fabricated battery

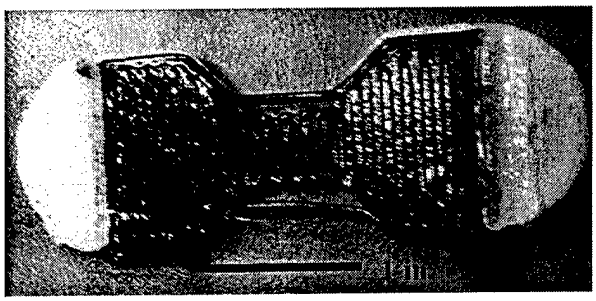

Figure 9: ABS and RTV silicone elastomer flexure joint

Other Material/Functionality Experiments

As a demonstration of a multi-material functional mechanical assembly, a flexure joint was fabricated using ABS as the rigid end members and a 1-part, room-temperature vulcanizing (RTV) silicone as the flexible connection (Figure 9). The silicone is filled with carbon black to make it freestanding upon extrusion. The combination of electrical and mechanical functionality within the same freeform fabricated part is highly desirable and a number of approaches have been investigated [Ting *et. al.* 2001; Safari *et. al.* 2000]. Some initial qualitative experiments with applications of MC / metal powder pastes as functional materials outside of batteries have revealed that dehydration of the MC gel can lead to shrinkage and cracking of a deposited road of MC paste, and that adhesion to substrates also suffers after dehydration. A rudimentary electromechanical assembly was freeform fabricated as lines of silver / MC paste embedded in an ABS and silicone flexure joint (Figure 10c). This device successfully carried sufficient current to light an LED (~10mA), but was too delicate to survive much mechanical use due to cracking and detachment of the conductive paste.

Solder alloys are being investigated as a means of depositing wiring into components, and fabricating metal parts [Priest *et. al.*, 1997], and at least one commercial process exists which is capable of depositing solder alloy wiring onto a wide variety of substrates [Hayes *et. al.*, 1998]. Our previous experiments revealed that a large reservoir of molten eutectic alloy, for instance in a syringe, has the tendency to drain uncontrollably from the reservoir or to freeze in a nozzle. As an alternative approach, a solid-core, Pb-Sn solder wire was used as the feedstock for the wire-fed extrusion tool, and solder deposits were made directly on a build surface. Figure 10a depicts the results of these tests. It was found that there are small, separate regions of the parameter space in which it is possible to form either lines of overlapping frozen droplets of approximately 1mm in diameter (Figure 10a, left), or a very thin but continuous wire of approximately 250μm in diameter (Figure 10a, right). As a test of compatibility between materials, several ABS and solder test coupons were freeform fabricated (Figure 10b). The deposited solder is electrically continuous for the entire "U" shape in the right-hand sample which was produced at a fast feed rate, but only continuous about 2/3 of the total length of the "U" for the left-hand sample, which was produced at a much slower solder feed rate. The lead-tin solder does not wet ABS well, so making a robust interface between the two materials

requires some surface preparation, or simply tightly embedding the solder within a channel in the ABS material. There is some indication that wetting may be improved by the use of indium-bearing alloys, although this has yet to be tested.

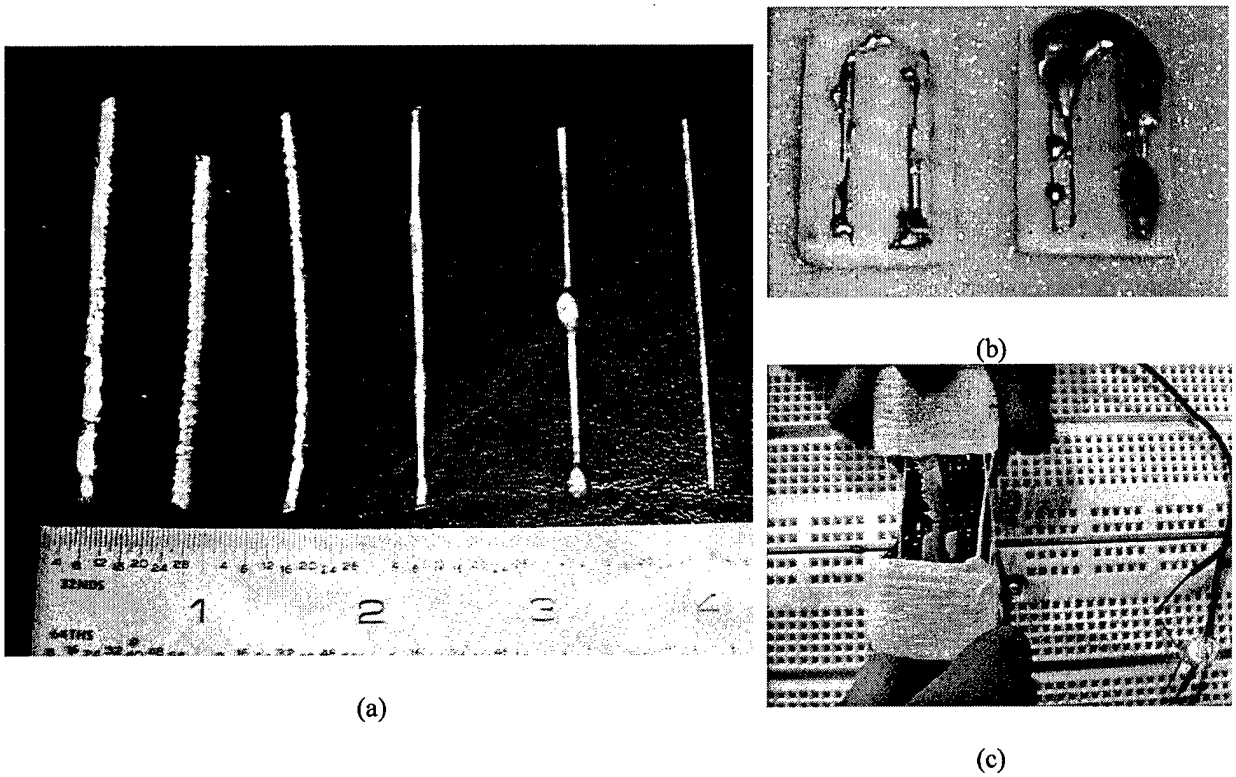

Figure 10: (a) Effect of deposition parameters on quality of solder alloy wiring, (b) partial success at embedding solder alloy wiring in thermoplastic part, and (c) flexure joint with silver/methylcellulose paste conductor

Conclusions

A zinc air cell has been successfully manufactured via freeform deposition techniques. The printed cell delivered at least 30mW for 2sec, from only 1gm of zinc slurry. Mechanical flexure joints have been freeform fabricated, as have a thermoplastic part with embedded metal wiring and a flexure joint with embedded silver/methylcellulose paste wiring which is capable of carrying more than 10mA of current. Obvious routes exist to improving the functionality and durability of all of these. The battery, flexure joints, and embedded wiring together demonstrate the feasibility of combining multiple materials into fully functional assemblies within a single freeform fabrication platform. Through further testing and optimization, higher performance cells are achievable, as are more sophisticated functional assemblies, leading the way to the production of immediately useable, freeform fabricated, electromechanical devices.

Acknowledgments

This work was supported in parts by the U.S. Department of Energy, grant DE-FG02-01ER45902. Thanks to Douglas Charles of Inco Technical Services for information on mixing ratios of methylcellulose and metal particles, and to Cordelia Rasa for information about methylcellulose products. D.C. thanks the NASA/NY space grant program for its support.

References

Danko, Thomas, Strength Properties of Separators in Alkaline Solutions, Viskase Corporation, Chicago, 2003

Duracell Incorporated, 2001, "Duracell zinc Air Batteries, Material Safety Data Sheet."

Fuller, S., Willhelm, E., Jacobson, J., "Ink-Jet Printed Nanoparticle Microelectromechanical Systems," *Journal of Microelectromechanical Systems*, 11, no. 1, (Feb 2002): 54-60

Harris, Frank, and Sieminski, Dennis, "Recent Advances Enable Primary zinc-Air for Portable Devices" Wireless Symposium Spring 1999 Conference, San Jose Ca, February 22-26 1999

Hayes, D.J., Cox, W.R., Grove, M.E., "Micro-jet printing of polymers and solder for electronics manufacturing," *J. Electron. Manuf. (Singapore)*, 8, no. 3-4, (Sept.-Dec. 1998): 209-16

Isaacson, Todd, 2003, "Printable Energy Source", Cornell University, Master of Engineering, Engineering Design Project Report

Linden, David and Reddy, Thomas, eds., 2002, *Handbook of Batteries*, 3rd Edition, (McGraw-Hill)

Lipson, H., Pollack J. B., 2000, "Automatic Design and Manufacture of Artificial Lifeforms", *Nature 406, pp. 974-978.*

Marcus H. L., Gas (SALD) and Gas/Powder (SALDVI) Solid Freeform Fabrication (SFF), (with J.E. Crocker, S. Harrison, L. Sun, and L.L. Shaw), Journal of Metals, 1998

Naimer, Neal, and Koretz, Binyamin, and Putt, Ronald, "Zinc-Air Batteries for UAVs and MAVs", Electric Fuel Corporation, Auburn Alabama, December 6, 2002

Olmsted, John, and Williams, Gregory, 1994, *Chemistry: The Molecular Science,* (Mosby-Year Book Inc.).

Priest, J., Smith, C., and DuBois, P., 1997, "Liquid Metal Jetting for Printing Metal Parts," Solid Freeform Fabrication Proceedings (D. L. Bourell, J. J. Beaman, H. L. Marcus, R. H. Crawford, and J. W. Barlow, eds.), The University of Texas at Austin, August 1997

Safari, A.; Danforth, S.C.; Jafari, M.; Allahverdi, M.; Jadidian, B.; Mohammadi, F., "Processing and properties of piezoelectric actuators developed by fused deposition technique" Applications of Ferroelectrics, 2000. ISAF 2000. Proceedings of the 2000 12th IEEE International Symposium on, Volume: 1 , 2001, Pages: 79 -82 vol. 1

Swanson, William J., and Hopkins, Paul E., U.S. Patent 6,004,124, 1999.

Tinker, Lawerence, 2002, "Air Electrode Performance in zinc-Air Batteries for Portable Products," Annual Battery Conference, January 2002.

Ting, F.P.Y., Gibson, I., and Cheung, W.L., 2001, "Study on selective laser sintering components with electrically conductive channels," Solid Freeform Fabrication Proceedings (D. L. Bourell, J. J. Beaman, H. L. Marcus, R. H. Crawford, and J. W. Barlow, eds.), The University of Texas at Austin, August 2001

Weiss, L. and Prinz, F., 1998, "Novel Applications and Implementations of Shape Deposition Manufacturing," Naval Research Reviews, Office of Naval Research, Three/1998, Vol. L

Rapid Prototyping for Aerospace Launch Vehicles

K. Siva Prasad*, E.Rathakrishnan+, Sanjay.G .Dhande*

*Department of Mechanical engineering, IIT-Kanpur, India
+Department of Aerospace Engineering, IIT-Kanpur, India

Reviewed, accepted August 28, 2003

Abstract

Initial studies of the aerodynamic characteristics of proposed launch vehicles can be made more accurately if lower cost, high-fidelity aerodynamic models are available for wind tunnel testing early in design phase. Rapid Prototyping (RP) is an emerging key technology for producing accurate parts directly from CAD models quickly, with little need of human intervention. Use of RP models was studied at the NASA Marshall Space Flight Center (MSFC). It was concluded that RP methods and materials can be used only for preliminary design studies and limited configurations because of the RP material properties that allow bending of models under higher loading conditions. The reported results and analysis were based on wind tunnel balances. These balances give total load on the body. Thus, there is a need for studying the pressure distribution, the wave pattern and the system behavior under high-speed conditions. In order to study the above goals, a blunt nose cone of a launch vehicle/ missile was tested which was made using the solid based RP method FDM, with a Mach number of 2.0. It is concluded that RP models can take the load at the Mach number 2.0 and also can capture the pressure distribution and wave pattern.

1. Introduction

Since ancient times, making and testing of prototype is a usual practice before going to the final production. Especially in aerospace industry, this is a crucial stage because one can get the aerodynamic characteristics of the proposed launch vehicle. The fabrication of these prototypes is experimented with many forms like material removal process, castings, injection molding etc. Before 1980, the techniques used making of prototypes were craft based and extremely labor intensive. In early 1980's the concept of prototyping had changed slightly called soft or virtual prototyping. The models can be made virtually and these can be stressed, tested, analyzed and modified as if they were physical prototypes. In addition, prototypes tend to become relatively more complex about twice the complexity as before 1980. Correspondingly, the time required to make physical models increased tremendously but the building of physical prototype still depended on craft based methods in spite of the introduction of better precision machines (like CNC machines). In mid 1980's the key prototyping technology called Rapid Prototyping (RP) evolved to speed up the prototype manufacturing process. RP is a term, which embraces a range of new technologies for producing accurate parts directly from CAD models with a little need of human intervention. RP of physical parts is also known as solid free form fabrication (SFF), desktop manufacturing or layer manufacturing technology. Till today, making

functional prototype from RP is one of the challenging tasks. In the present work, an attempt is made to make a functional prototype called wind tunnel models for aerospace applications. There are two important issues in RP to employ it for making wind tunnel models. They are structural integrity and surface roughness. To improve the structural strength of RP models one has to know the maximum loading distribution on the model. The present work demonstrates the measurement of the pressure distribution on the wind tunnel model so that one can understand the loading distribution on the model.

2. Literature Review

Preliminary aerodynamic assessment of future launch vehicle configurations through RP models was studied by NASA Marshall Space Flight center. It was shown to be feasible in limited direct application to wind-tunnel testing. There will be a tremendous advantage in cost savings, model design time and fabrication time; about factor four compared to standard model design and fabrication process. It was concluded that FDM and SLA produced satisfactory results for low speed conditions and diverging at higher loading conditions because RP material properties allow bending of model components under high loading conditions [1]. To improve bending resistance one has to concentrate on the pressure distribution on the body. The NASA results are based on the strain gauge balance. This balance gives total lift, drag and load on the body. There is no information regarding pressure distribution on the body. In this direction, Siva et. al. [2] made an attempt to find out the pressure distribution on RP circular cylinder at a supersonic speed. They studied pressure distribution both quantitatively and qualitatively. There was no permanent deformation in the shape and the experiments were found to be repeatable 100%. In the similar direction an attempt has been made to find out the pressure distribution over a blunt nose cone body both quantitatively and qualitatively, in the present study.

3. Model Construction

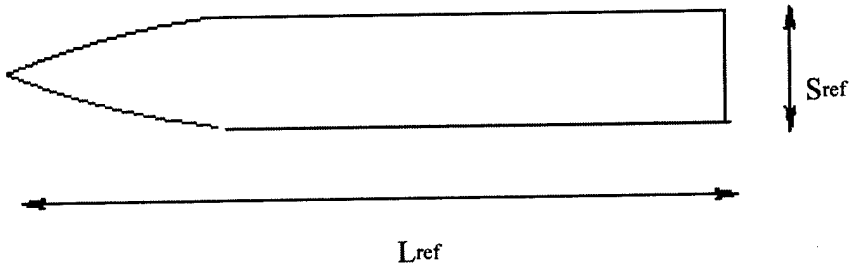

Fig. 1 Geometry of the Blunt Nose Cone Body.

A blunt nose cone body has been chosen for the present study. The model (shown in Fig. 1, L_{ref} = 60 mm, S_{ref} = 314 mm^2) is made out of a solid based RP method FDM (Fused Deposition Modeling). The 3D model is converted into STL (Stereolithography) format in the CAD systems and sent to the FDM slicing software, called Quick Slice. There the STL file is sliced into thin-cross sections of desired thickness, creating a .SLC file (Slice format file). Supports are created for overhanging parts and sliced as well. The sliced model and support are converted into a .SML file (Stratasys Machine Language) that contains actual instructions for the FDM machine. A tool path is generated which is followed by the numerically controlled extruder head. As the head moves in X and Y- directions following the tool path, the thermoplastic material is extruded out of a nozzle and then deposited in ultra thin layers, one layer at a time. Since the envelope surrounding the head is maintained at a temperature below the melting point of material, the extruded material quickly solidifies [3, 4]. The extruder head has two nozzles, one for the part material and the other for the support material. The support can be easily removed by breaking away. The part is built on a foam foundation attached on a Z-stage platen. The Z-stage platen moves downwards as the part is built progressively.

4. Test Facility

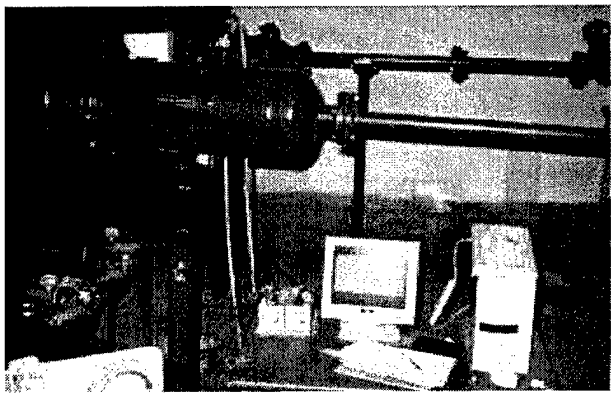

Fig. 2 Open Jet Facility at I.I.T-Kanpur, India

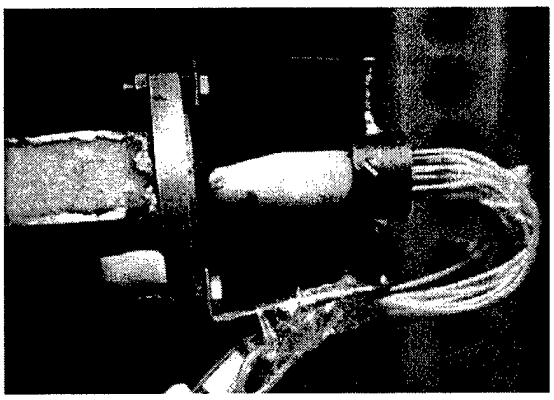

Fig. 3. Model Mounted on Wind tunnel

The experiments were conducted in the jet facility at High speed Aerodynamics Laboratory, Indian Institute of Technology Kanpur, India. The test facility consists of compressor, storage tanks and jet test facility as shown in Fig. 2. A two - stage reciprocating compressor capable of delivering 360 cfm of air at a pressure of 500 psi is used in this laboratory. The compressed air is then passed through a pre-filter consisting of porous stone candles to remove solid contaminates, like rust particles and oil droplets. An activated carbon filter is used for finer filtering. The compressed air is dried in a dual tower semi-automatic silica gel driver. While one tower is in use, a portion of the dried air is heated and used to reactivate the other. A diaphragm type back pressure valve operated by pressure relief pilot permits the dryer to operate at 500 psi, while the pressure in the storage tank builds up from atmospheric to storage pressure. The compressed air is stored in three tanks, having a total capacity of 300 ft^3 at 300 psi. The pitot pressure sensed by the probe was measured using a PSI model 9010, 16-channel

pressure transducer (interfaced with a PC386). The model 9010 transducer is capable of measuring pressure up to 300 psig, which is approximately 20 atm. The accuracy of the transducer (after rezero calibration) is specified to be ± 0.15% full scale.

5. Flow Structure

The kinetic theory says that flow consists of a large number of fluid molecules in unit volume and the transport of mass, momentum and energy takes place through the motion of these molecules. Also, the molecules carry the signals about the presence of the disturbance around the flow field at a speed equal to speed of sound. When the incoming stream is subsonic i.e. the flow speed is less than the speed of sound and the molecules far upstream of the cylinder get the information about the presence of the body through the signals which travel with speed, a_∞ well in advance before reaching the cylinder. Therefore, the molecules orient themselves in order to flow around the cylinder. But when the incoming stream is supersonic, the molecules travel faster than the signals, and there is no possibility that they will be informed of the presence of the body, before they reach the cylinder. Also, the reflected signals from the face of the cylinder tend to coalesce a short distance ahead of the body. Their coalescence forms a thin compression front called shock wave (as shown in Fig. 4).

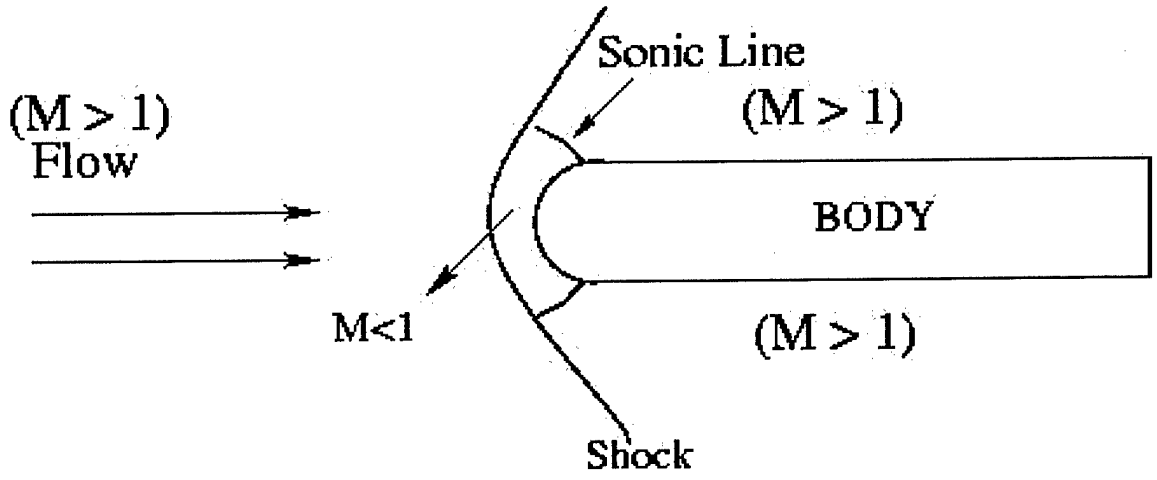

Fig. 4 Physical Significance of the Flow

In the flow process, across the front results in an abrupt change in fluid properties. The thickness of the shock is comparable to the mean free path of the gas molecules in the flow field. The formation of shock takes place after the fluid molecules impinge on the face of the cylinder and rebound. The shock formed normal to the flow direction is called normal shock. The compression wave inclined to at an angle to the flow is called oblique shock. So, the normal shock is a special case of oblique shock. Upstream of the shock, the flow has no information about the presence of the body. However, the streamlines behind the normal shock quickly

compensate for the obstruction, since the flow is subsonic after a normal shock [5]. Oblique shocks usually occur when a flow is turned into itself i.e. when a supersonic flow is turned away from itself, results in the formation of an expansion fan.

The flow is deflected into itself by the oblique shock. All the streamliners are deflected to the same angle at the shock, resulting in an uniform parallel flow downstream of shock. The angle is referred to as flow deflection angle. Across the shock wave, the Mach number decreases and the pressure, density and temperature increase. The corner which turns the flow into itself is called compression or concave corner. In contrast, in an expansion or convex corner, the flow is turned away from itself an expansion fan. All the streamlines are deflected to the same angle after the expansion fan, resulting in uniform parallel flow downstream of the fan. Across the expansion wave, the Mach number increases and the pressure, density and temperature decreases. The flow turns suddenly across the shock and the turning is gradual across the expansion fan, and hence the flow properties through the expansion fan change smoothly, with the exception of the wall streamline where change is sudden. Thus, a model exposed to a supersonic flow experiences a combination of impact, gradual and sudden changes in the loading distribution. Hence, a RP model sustains a supersonic flow can be viewed as appropriate for aerospace application demanding structures with this kind of capability.

6. Results and Discussion

A blunt cone followed by a cylindrical body (stem) is one of the typical shapes of high-speed vehicles like missiles/launchers. Therefore, in the present study, one such typical shape is fabricated out of RP as shown in Fig. 3 and tested at Mach 2.0. This offers a natural advantage to the present investigation which aims at studying RP models behavior under varying aerodynamic loading conditions. The flow field over this body is a complex one, involving detached shock, expansion fan and compression waves. The interaction of these waves causes a considerable impact and shear load. To understand the loading on the blunt nose-cone cylinder combination was tested at Mach 2.0, the model was provided surface pressure taps at X/D = 0.1, 0,25, 0.5 and 2.25 at NPRs 4 to 9, insteps of 1. These NPRs (Nozzle Pressure Ratio) were chosen in such a manner that the Mach 2.0 flow is coming with overexpanded state with adverse pressure gradient at NPR 4, 5, 6, nearly correctly expanded state at NPR7 and underexpanded state with favorable pressure gradient prevails at NPR 8, 9. The model will be experiencing all the three kinds of above expansion. Further, the nature of waves will be strongly influenced by the level of expansion. To investigate the behavior of RP model under the said complex situation was studied both qualitatively and quantitatively. The surface pressures were measured for quantitative analysis and flow field was visualized for qualitative analysis.

The measured pressures have been made non-dimensional with reference to the flow field downstream of the detached shock standing a head of the blunt nose. It is essential to note that the flow field downstream of bow/detached shock is a complex one since the Mach number in the field varies from subsonic at the centerline to supersonic as we move along the shock direction. Therefore, identifying a free stream reference dynamic pressure for entire flow field is impossible. So, the dynamic pressure along the axial line just downstream of bow shock has been taken as representative dynamic pressure since the flow is subsonic at the zone and hence at the

nose at C_P should be +1. This can be validation of the measured data and calculation procedure. It should be re iterated here that C_P values at other location should be considered as qualitative but they can serve as reasonable estimate of load on model understanding the load acting on the model.

In the present study, two planes chosen along the model from nose to the base. Along axis1 (shown in Fig 5) is seen that C_P at nose is +1, this clearly indicates that the validity of the present measurement, since it agrees exactly with the theory. At an axial location X/D = 0.25, the C_P becomes much larger than unity, indicating that the flow is accelerating from X/D = 0 to 0.25. This is because the region between the detached shock and nose faces a normal shock at the nose point in line with the axis of the model and oblique shock for the location away from the shock. The oblique shock progressively becomes weaker with increase of transverse distance from the axis. This results in continuous increase of Mach number at downstream of shock in the transverse direction. Due to this the pressures measured at locations away from X/D = 0.0 up to X/D = 0.25 are experiencing C_P which are considerable higher than one (reference dynamic pressure just downstream location). The C_P goes to close to zero at X/D = 0.5 indicating that the flow continuously accelerates downstream of the nose. For X/D = 2.25 location which is on the horizontal stem the C_P becomes negative. The NPR dictates the level of expansion at the nozzle exit influences the flow around the model significantly. From X/D = 0 to 0.5, the C_P increases at all locations compared to lower NPRs where as from X/D = 0.5 to 2.25, the C_P assumes considerable lower values compared to lower NPRs. This is because as the NPR increase, the shock at the nose moves closer to the body and also the curvature of the bow shock decreases. This makes the normal portion of the bow shock stronger and the oblique weaker as NPR increases. Due to this variation of the nature of the shock, the shock strength and the flow field at the downstream of the shock is strongly influenced by the NPR. For the present investigation, this can be regarded as welcome distribution since it is the primary objective here to study the RP model exposed to a supersonic stream which offers a varying pressure load on the model from nose to tail. The result on another axis is shown in Fig. 6. Here again the behavior is similar to axis1 and reveals that X/D is stronger in between 0.25 to 0.5 and is closer to zero and stays up to 0.5. But the pressure load from 0.5 to the end is not influenced by the axial location.

To have an understanding of the waves present around the RP model, the flow field was visualized in fig 7 to 13, for different NPRs. It is interesting to note that the NPR has strong influence on the wave pattern around the model. With increase of NPR, the wave moves closer to the model and also the interaction of the waves around the model is severe. The combined effect of the interaction causes varying pressure load on the model as seen from C_P plots.

7. Conclusions

A blunt nose cone body was tested at Mach 2.0 speed at different NPRs to demonstrate the feasibility of functional testing of RP models for high speed applications. The surface pressures were measured on the body both quantitatively and qualitatively. RP model is experiencing the severe drag due to differential loading on the model. The load patterns indicate that the skin friction action on the surface is considerable. The model has been exposed to the

complex field continuously during the order of tens of minutes for every NPR to ensure that the model does not suffer ay surface damage effect due to the aerodynamic load acting at Mach 2.0. A through inspection revealed that the model surface was intact free from any surface defect. Therefore, it can be stated that the RP is suitable for model to fly at supersonic speeds.

References

1. A. Springer, "Evaluating Aerodynamic Characteristics of Wind – Tunnel Models Produced by Rapid Prototyping", Journal of Spacecraft And Rockets, 1998, Nov – Dec, Vol 35, No. 6, November – December, pp 755 - 759.
2. K. Siva Prasad, E. Rathakrishnan and S. G. Dhande, " Rapid Prototyping for Supersonic Bluff Bodies", Proceedings of RPSI, An International Symposium.
3. Kai, Chua Chee and Fai, Leong Kah, 1997, Rapid prototyping Principles & Applications in Manufacturing, John Wiley & Sons, N Y, USA.
4. Pham, D. T., and Gault, R. S., 1998, "A Comparison of Rapid Prototyping Technologies", Int. J. Mach Tools and Manf. 38, pp. 1257-1287.
5. E. Rathakrishnan, " Gas Dynamics", Prentice – Hall of India Private Limited, New Delhi, 2001.

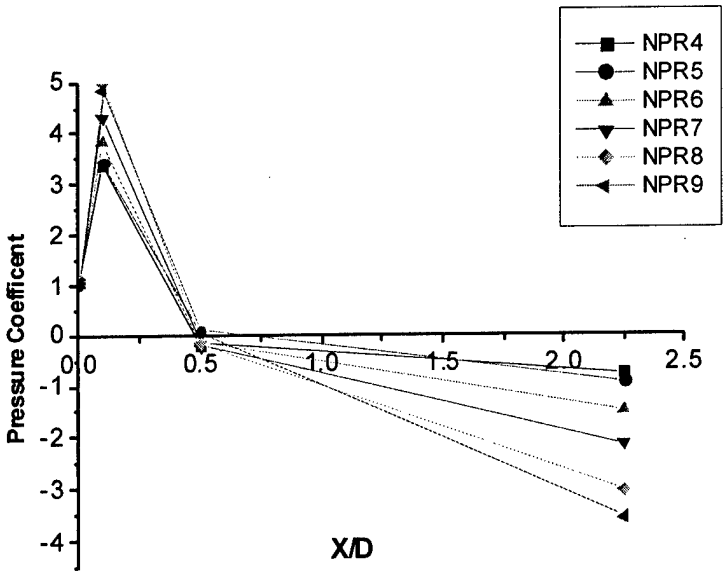

Fig. 5: Pressure Coefficient distribution along the axis 1

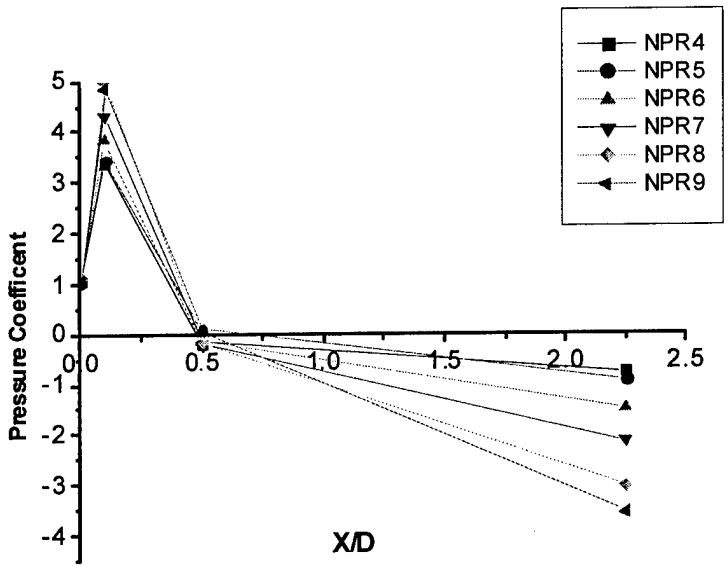

Fig. 6: Pressure Coefficient distribution along the axis 2

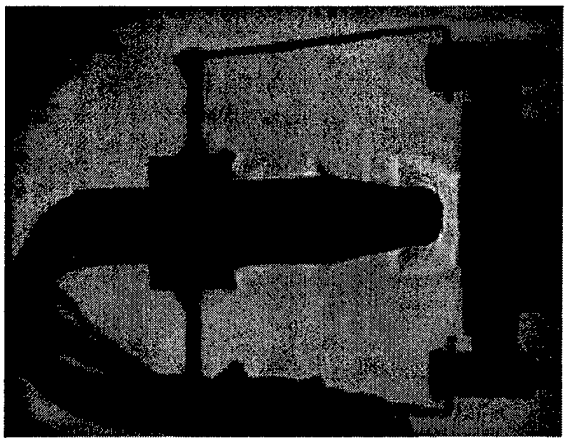

Fig. 7 Wave Pattern at NPR 4

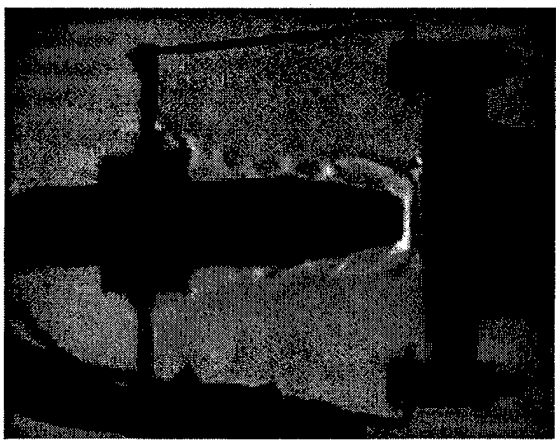

Fig. 8 Wave Pattern at NPR 5

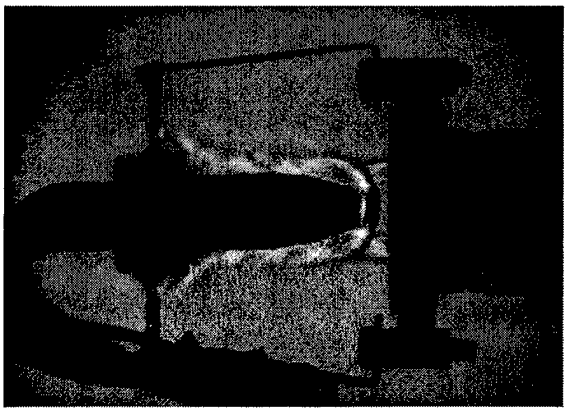

Fig. 9 Wave Pattern at NPR6

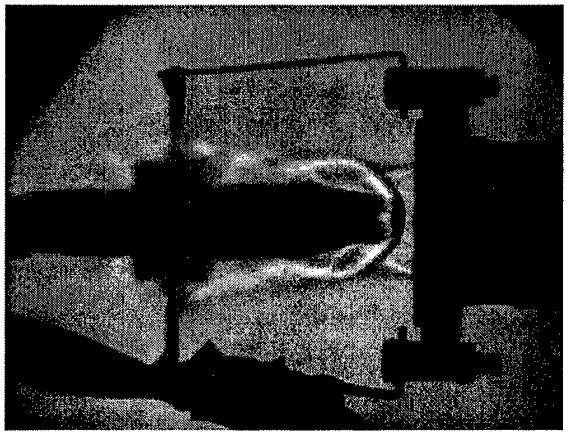

Fig. 10 Wave Pattern at NPR7

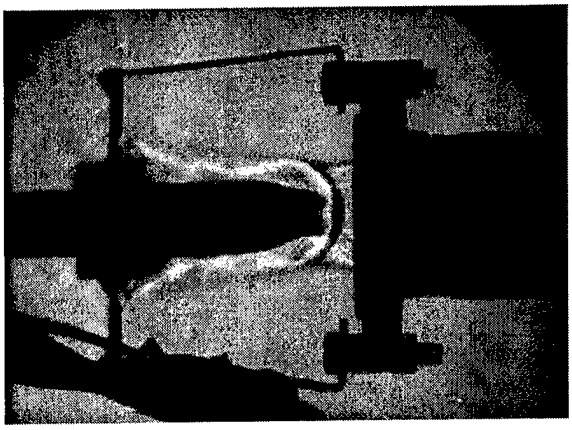

Fig. 11 Wave Pattern at NPR8

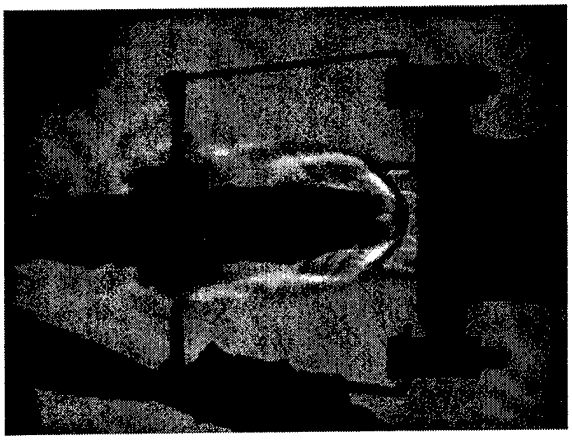

Fig. 12 Wave Pattern at NPR9

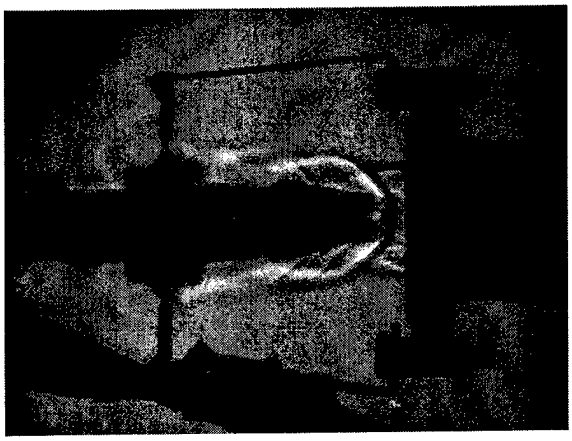

Fig. 13 Wave Pattern at NPR 10

Functionally Graded Polymer Matrix Nano-Composites by Solid Freeform Fabrication: A Preliminary Report

Richard Chartoff, Brian McMorrow, and Pierre Lucas
Department of Material Science and Engineering
University of Arizona; Arizona Materials Laboratory
Tucson, Arizona 85712, USA

ABSTRACT

A research program has been initiated to develop a Solid Freeform Fabrication (SFF) technology for combining nanosized particulate or fiber reinforcements with a photocurable thermoset matrix resin in order to produce functional graded composites. The composites that are being studied initially are optical components filled with nano-phase ceramic particles that form gradient refractive index lenses (GRIN). The Solid Freeform Fabrication (SFF) method employs an ink-jet deposition (IJD) process to form the composites. The IJD process has the advantage of incorporating nano-reinforcements into a low viscosity matrix resin that is relatively easy to process and rapidly photocures to produce functional polymeric parts. It also has the advantage that major modifications to the basic SFF processing methodology are not necessary.

The emphasis in the program is on demonstrating the feasibility of this approach for fabrication of gradient refractive index lenses (GRIN), which are flat instead of the traditional spherical lens geometry. As a result these lenses will be less costly to produce than conventional curved lenses. SFF is an ideal technique for meeting the needs of GRIN lens fabrication because changes in composition can be made from layer to layer and even within each layer, allowing for the introduction of compositional and structural gradients. Thus it has the potential for creating the spatial material distributions required for designing computer optimized, custom made GRIN lenses. Integral to the SFF process are computer design procedures that specify the exact material deposition patterns that need to be employed in order to optimize the performance of the GRIN lens.

The optical nano-composites will serve as a model system that we will use to work out the many challenges for implementing a viable SFF polymer composites technology. We then will make use of the information obtained and lessons learned from the work on optical composites and extend the development to structural composites that incorporate nano-particulate clays and carbon nanofibers.

POLYMER NANO-COMPOSITES FOR GRIN OPTICAL APPLICATIONS

Background

Optical lenses are traditionally created from blocks of uniform material by grinding curved (usually spherical) surfaces. The spatial contour of the index of refraction change provides optical power when the shape and orientation are appropriately chosen. The non-planar surfaces (Figure 1) of this type of lens are detrimental to many commercial and military applications. The curvature is the source of the glint signature used for detecting covert observation. The curvature also will generate turbulence if the lens forms the window of a detector viewing out from a moving body, such as an aircraft. This situation often necessitates the use of an additional window fitted to the surface curvature, which may adversely affect optical clarity or light transmission.

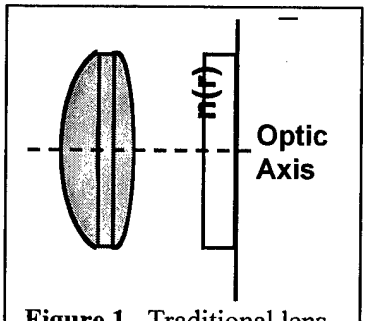

Figure 1 Traditional lens shape and refractive index profile.

Gradient index of refraction lenses (GRIN) present an alternative geometrical format. They provide the multi-dimensional spatial variation of refractive index required for optical power by implementing a non-uniform material distribution. (Figure 2) the use of GRIN techniques decouples the optical power generation from the curvature of the element. GRIN lenses can be fabricated with planar surfaces on either side or both sides. This should greatly simplify and reduce the cost of the fabrication of lenses by eliminating the need for grinding and polishing operations.

The common methods usually used for generating a radial variation in the material properties are chemical diffusion or ion-bombardment, which implant foreign materials into a uniform cylinder or plate of a host material. The implantation density can be varied as a function of radial position. However, with these methods there are technical difficulties in achieving the required axial concentrations of material species. Both of these methods also result in penetration-depth variations of the species introduced. This results in the optical properties changing as a function of distance along the optic axis. Thus independent control of the spatial variation of the material composition is not possible. As a result, the density profiles needed for optimal performance are difficult to achieve. So an SFF, layered manufacturing technique is an innovative, additive approach to the fabrication of GRIN lenses.

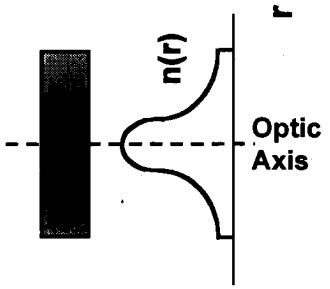

Figure 2 Radial gradient GRIN lens shape and refractive index profile.

Approach to Solving the Problem

In our research program we are exploring the feasibility of an SFF ink-jet deposition process that creates GRIN lenses from polymer/ceramic composites that have composition tunable optical properties. These composites are based on optically clear, photocurable thermoset resins containing various amounts of nanosized ceramic particles, to provide positionally controlled, tailored refractive indices. The utility of such composites in producing a wide refractive index tunability with little scattering has been demonstrated by Ho, et.al. [1]. The amount of light scattering in the composites is small, since the particles are much smaller than the wavelength of light.

There are four major elements of our GRIN research. These can be delineated as:

1. Polymer and composite development; this includes formulation or synthesis, ceramic particle dispersion, and polymer and composite processing
2. Ink-jet printing and processing of layers;
3. CAD GRIN design implementation;
4. Process feasibility demonstration; characterization of optical properties

Currently we are concentrating on elements 1 and 2 (encompassing the more basic materials processing related issues) in order to validate the viability of the concepts proposed. We are using a standard piezo ink-jet printer head for the initial exploratory work to demonstrate the basic concepts outlined here. The reservoirs in the ink-jet printer head contain a range of polymer/ceramic concentrations, so that the concentration of particles (and the index of refraction) at any location can be controlled by depositing appropriate amounts of material from the different writing heads. Following deposition, the layers are photocured by UV light. The UV light application mode is controlled so as to provide suitable optical and mechanical properties in the final product. Aspects of polymer cure control will include optimizing the cure advancement of each layer precisely so as to achieve a seamless interface and the application of radiation in specific patterns that will minimize the effects of cure shrinkage and residual stress buildup in the cured material.

Ink-jet Printheads

In order to achieve a sufficient refractive index gradient in a lens as large as several inches across, it will be necessary to both increase the material refractive index difference, Δn (as discussed below) by using a higher index ceramic filler and to implement a more sophisticated print system. Present day advanced commercial ink-jet capabilities include high-performance, multichannel printheads. For example, there are multi-nozzle piezo-driven printheads designed specifically for printing UV inks onto polymeric substrates at high deposition rates [2]. Nozzle diameters in these systems are of the order of 20μm or less. The printers also have gray-scale resolution capabilities with greater than 900dpi resolution. In order to work with higher viscosity formulations, the temperature can be controlled by a heating element integrated into the printhead mount that heats both the printhead and the ink supply. An example of the utility of printheads of this type in a related SFF application is micro devices made from a UV curable (cationic) epoxy resin [3].

Printability of Nanoparticle Loaded Polymers; Nozzle Clogging

The photocurable monomer that we have chosen to work with initially is hexanediol-diacrylate (HDODA). HDODA is a low viscosity liquid with viscosity of several cP. At the low solids contents that will be used for this application (<< 20% by volume), the relative viscosity of the loaded polymer systems will remain low [4, 5]. This will insure ease of printability at low temperatures and help to mitigate the potential ink-jet printer nozzle clogging issue. That nozzle clogging should not be an issue is further suggested by the work of Sharp and Adrian [6], who considered particle bridging in particle loaded fluids flowing through microchannels. Their experiments identified 'shear-induced arching' as a mechanism that causes microtube blockage. They found that this mechanism is most likely to occur only when $0.33D < dp < 0.46D$, where dp is the particle diameter and D is the microtube diameter. This was observed for flows of particle-laden fluids with concentrations as low as 0.5%. Since in our case the ink jet nozzle is of the order of 20μm in diameter, dp is around 10^{-3} less than D.

Ceramic Filler Selection

It has been demonstrated that appropriately large optical gradients can be achieved through the use of ceramic particles dispersed in a polymeric matrix [1]. Typical UV cured polymers have refractive indices in the 1.4 to 1.7 range. There are several ceramics that have a considerably higher refractive index than these organic polymer systems, as indicated in Table 1 [7].

Table 1: Average Refractive Index of Some Common Ceramic Systems [7]

Material	Average Refractive Index
Alumina (corundum)	1.75
Quartz (SiO2)	1.55
Zircon (ZrSiO4)	1.95
Spinel (MgAl2O4)	1.72
Rutile (TiO2)	2.71
Silicon Carbide (SiC)	2.68
Galena (PbS)	3.9
Barium Titanate (BaTiO3)	2.4
Zirconia (ZrO2)	2.3
Iron Oxide (Fe2O3)	3.0
Zinc Oxide	2.0

The use of a high refractive index ceramic (>2.0) in an organic matrix provides for a wide range of refractive index in the GRIN optics. The refractive index in the graded optics can be controlled by varying the concentration of the dispersed ceramic. (To avoid optical scattering from the dispersed particles, the ceramic powders used in the GRIN system should be nano-particulate (5nm – 40nm) and should be very well dispersed.) A greater difference in the refractive index between the ceramic particle and the organic matrix will allow a wide gradient to be achieved with a minimum amount of ceramic particles. In calculating the

necessary GRIN optical parameters it is found that the larger is Δn, the easier it becomes to fabricate GRIN lenses with shorter focal lengths as well as thinner cross-sections.

In summary, the polymer matrix will be of lower refractive index and the nano particulate ceramic will be of higher refractive index. The graded refractive index can be achieved by varying the ceramic loading in the matrix monomer as well as the deposition pattern and drop size for deposition. The initial matrix material chosen is HDODA, which, when polymerized, has a refractive index of ~1.6. Initial experiments will be performed using a ceramic such as zirconia due to its commercial availability and relatively high refractive index. After the feasibility of using nano-particulate zirconia has been demonstrated using the ink-jet printing method, the use of higher refractive index ceramics, for example, rutile, barium titanate, and iron oxide will be explored in order to increase the Δn window.

We noted above that ceramic loadings of 20% by volume will be a maximum limit. Assuming a linear rule of mixing to estimate refractive index of ceramic dispersed systems (worst case), the effective refractive index of a 20% zirconia loaded HDODA system will be approximately 1.74. Using appropriate optics design methods, the resultant Δn of 0.14 is found to be adequate for fabricating GRIN test optics of dimensions up to a few inches in size.
For Fe_2O_3 the Δn is 0.28, which provides much greater latitude in GRIN fabrication. The initial goal for proof of concept is to fabricate an optical wedge with a linear radial refractive index gradient.

Particle Stabilization and Dispersion

A key factor in the printed optics fabrication of GRIN elements with ceramic particle index modifiers is complete deagglomeration and dispersion of the nano-ceramic particles. Agglomeration and poor dispersion of ceramic particles in the organic matrix will result in scattering, degrading the GRIN optic's performance. Traditional deagglomeration and dispersion techniques are ultrasonication and surface treatment of the powder during synthesis [8]. Significant progress has been made in the synthesis of nano-particulate ceramic powders in recent years. Spherical nano-particulate ceramic powders with narrow particle size distributions are commercially available. Significantly, the same sources that synthesize the nano-particle ceramic powders have been able to develop surface treatments to keep the powders deagglomerated and with a high degree of dispersability. Such surface treatments are applied to the powder particles during the synthesis process. The treatments are of various types, which effectively functionalize the surface with an adsorbed monolayer, resulting in steric-stabilization that prevents agglomeration of the powder. These coatings are tailored so that appropriate wetting of the particles by an organic monomer is achieved. The surface functionalized ceramic particles are dispersed in the monomer by mixing using an ultrasonic vibration technique. Because of the small size of the particles and relatively large surface tension forces, settling of the particles is not expected.

Numerous references to steric stabilization of nanoparticles by surface functionalization by different approaches are available in the literature. Specific examples of this are contained in references [9-15]. These include grafting polymers such as silanes onto the particle surfaces [9-11, 15] or using adsorbed monolayers of a polymer or surfactant [13-15].

Polymer Matrix: Photocuring and Residual Stresses; Chemical Stability; Air Bubbles

A key issue in photocuring is that the effects of residual stresses must be minimal so as to effectively eliminate dimensional distortion and spurious stress-induced refractive index gradients. This can be addressed in two ways: 1) by implementing random segmented cure patterns [16], where UV radiation is applied to small areas separated from each other, in a sequential pattern until the entire layer is cured, and 2) applying radiation in incremental doses small enough such that cure is carried out slowly. By combining these two principles the

polymer will retain rubbery characteristics long enough so that much of the cure-induced residual stress can relax before full vitrification of the resin occurs [17]. The use of incremental curing methods has been shown to be quite effective in minimizing residual stresses by allowing each small area to undergo a high degree of stress relaxation before being joined to other cured areas.

The chemical stability of the proposed system is important because we wish to develop optical properties that are stable over long time periods. HDODA cures to produce transparent, water-white optical qualities. The presence of residual photoinitiator quantities could cause yellowing to develop during aging that occurs over a period of time after the GRIN lens is produced. In collaboration with a supplier of photoinitiators we have identified an effective non-yellowing photoinitiator that is stable in the cured resin.

In order to minimize dust contamination and reaction inhibition (due to presence of oxygen) of the samples, we are forming GRIN samples under a nitrogen blanket in a 'clean' environment. We do not anticipate problems with imperfections introduced through bubble formation. There are several reasons for this. First of all, previous SFF ink-jet deposition work [3] has shown that void free spherical micro -lenses can be formed with such printheads using a photocured cationic epoxy resin. Epoxy resins have higher viscosities than the HDODA formulations of interest here. If an epoxy can be processed without bubble formation, it is most likely this will not be a problem with HDODA. Further we will be working with very thin layers (<25μm in thickness) and very small droplets. Also, there will be substantial overlap of droplets as the material is being deposited. All of these are factors that will promote dissipation of air bubbles. However, if we do find that micro-bubbles are a problem, we will add small amounts of an organic soluble surfactant to the resin formulations. This method of bubble suppression is very effective and is used frequently in chemical systems to prohibit bubble formation.

Substrates

The type of substrate to be employed for the proposed application will affect the face of the lens and might compromise the quality of light transmission. Three types of substrates will be considered as working surfaces. In preliminary trial studies of the concepts proposed here, we formed thin films around .002" thick, using a conventional ink-jet printer with a mylar film as a substrate, (film similar to those used for overhead transparencies). The results indicated that both material deposition and the surface of the films produced were of good quality (by simple visual inspection). We have not yet looked at any quantitative measure of surface clarity, and roughness. Also, if mylar should not prove totally effective, we will work with silicon and sodium chloride single crystal substrates. Silicon has been used previously in RP fabrication of micro-ceramic components by other workers [18] and is commonly used for preparing AFM (Atomic Force Microscopy) specimens. We have used NaCl single crystals [19] as substrates for producing extremely smooth thermoset epoxy resin samples for AFM characterization. An advantage in using NaCl is that the substrate can be simply dissolved away from the deposited polymer after the polymer has been cured, leaving an ultra smooth surface behind.

Previous Research on Inkjet Printing of Ceramic Filled Polymers

Ink-jet deposition methods have been used previously for SFF of ceramic particle-filled resins and have proved useful because of their improved resolution relative to other SFF methods. Relevant prior work of other research groups on SFF of ceramics using drop-on-demand ink-jet deposition is reviewed here to provide additional background information for those who would care to explore the topic in more detail. All of the previous studies concern SFF and deposition of monomers (and resins) containing high loadings of ceramic particles of appreciably larger dimensions than the nanoparticles of interest here. The object in these former studies has been using the ceramic slurries to construct green-forms for making ceramic components. The resins in these compositions then serve as a binder for the ceramic powder, which is subsequently burned out prior to densification of the ceramic. Various references that concern ink-jet deposition of

monomers containing high- loadings of ceramic particles (greater than 40% by volume) are noted in the list of references [20-29]. These are representative of the work being done by three different research groups, those at the University of Michigan [20-22], University of Manchester (England) [21-23, 28,29], and UCLA [24-27].

Additional research of note that relates specifically to GRIN lenses is that being done by the Cima-Sachs 3-D Printing group at MIT. A recent publication of theirs [30] discusses the use of the slurry based 3-D Printing process for fabricating complex structured materials by printing organic binders in selected positions on each printing layer. This process was modified in an effort to fabricate GRIN lenses by depositing polymers containing different concentrations of an alumina dopant at various positions in a silica powder bed. Two different dopant concentration profiles, which had maximum alumina concentrations of 1.63 mol% and 2.50 mol%, were printed into the silica powder beds. The doped ceramic powders then were sintered at 1650°C into optical transparency, and the magnifying effects of GRIN lenses with gradient profiles of alumina were observed. This work is only in an exploratory state and the method requires extensive post-processing. It will be interesting to learn whether sufficient resolution and control of concentration gradients for producing effective GRIN lenses can be achieved in this method, even though there are problems with spreading of the droplets due to the porous nature of the substrate [31].

ACKNOWLEDGEMENTS

Preliminary work on this topic was initiated at the University of Dayton's Rapid Prototype Development Laboratory in collaboration with Dr. Allan Lightman. We are pleased to acknowledge that the current project at the University of Arizona is sponsored by the National Science Foundation, Division of Design, Manufacture and Industrial Innovation under Grant No. DMI–0341924.

REFERENCES

1. P.K.H Ho, D. S. Thomas, R.H. Friend and N. Tessler, ***Science*, 285**, 233-236 (1999)
2. Refer to URL: http://www. xaar.co.uk for a complete description
3. W. Voit, K.V. Rao, and W. Zapka, "Direct-Write Process for UV-Curable Epoxy Materials by Inkjet Technology", Mat. Res. Soc. Symposium. Proc., **758**, LL3.5.1, (2003)
4. L.E Nielsen and R.F. Landel, "Mechanical Properties of Polymers and Composites", 2nd Ed., Marcel Dekker, Inc., NewYork, NY, 378-384 (1994)
5. M.K. Agarwala, et. al., "Rheological Behavior of Powder Injection Molding Model Slurries," ***J. Rheol.*, 36(2)**, 319-333, (1992)
6. K. V. Sharp, R. J. Adrian, " Shear-Induced Arching of Particle-Laden Flows in Microtubes", Proc.of 2001 ASME International Mechanical Engineering Congress and Exposition, New York, NY, 1-5, (Nov. 11-16, 2001)
7. W. D. Kingery, et. al., "Introduction to Ceramics," 2nd Ed., Wiley, New York, 662, (1976)
8. Terry A. Ring, "Fundamentals of Ceramic Powder Processing and Synthesis," Academic Press, San Diego, Chapters 9 and 10, (1996)
9. M.-I. Baraton, " Surface Functionalization of Ceramic Nanoparticles: Application to Ion-Sensing and Gas-Sensing Devices", Mat. Res. Soc. Symp. Proc., **705**, Y6.1.1, (2002)
10. M. P. Stewart, E. G. Robins, T. W. Geders, M. J. Allen, H. Cheul Choi, and J. M. Buriak, " Three Methods for Stabilization and Functionalization of Porous Silicon Surfaces via Hydrosilylation and Electrografting Reactions, ***Phys. Stat. Sol:* (a) 182**, 109 (2000)
11. J-R Roan, " Attraction between Nanoparticles Induced by End-Grafted Homopolymers in a Good Solvent", ***Phys. Rev. Let.*, 86 (6)**, 1027-30, (2001)

12 C. Lourenco, Mteixeira, S. Simoes, and R. Gaspar, "Steric Stabilization of Nanoparticles: Size and Surface Properties", ***Int. J. Pharmacuetics***, **138**, 1-12, (1996)
13. A. K. Boal, K. Das, M. Gray, and V. M. Rotello, "Monolayer Exchange Chemistry of γ-Fe_2O_3 Nanoparticles," ***Chem. Mater.***, **14**, 2628-26 (2002)
14. Ivan Sondi, Dan V. Goia, and Egon Matijevi´c, "Preparation of Highly Concentrated Stable Dispersions of Uniform Silver Nanoparticles" ***Journal of Colloid and Interface Science,*** **260**, 75_81(2003)
15. M.-I. Baraton, ed., "Synthesis, Functionalization and Surface Treatment of Nanoparticles", American Scientific Publishers, Los Angeles, CA, 323pp., ISBN: 1-58883-009-8, (January, 2003); Provides a state of the art review of surface functionalization of nanoparticles for diverse applications
16 J.S. Ullett, R.P. Chartoff, A.J. Lightman, J.P. Murphy, and J.Li, "Reducing Warpage in Stereolithography Through Novel Draw Styles", Proc. Fifth International Conf. on Rapid Prototyping , University of Dayton, Dayton, OH, 109-125 (1994)
17. R.B. Prime, in "Thermal Characterization of Polymeric Materials", 2nd Edition, ed. Edith Turi, Academic Press, New York, NY, Ch. 6: 'Thermosets', (1997)
18. X.N. Jiang, C. Sun, X. Zhang, B. Xu , Y.H. Ye b, "Micro-Stereolithography of Lead-Zirconate-Titanate Thick Film on Silicon Substrates", ***Sensors and Actuators***, **87**, 72-77, (2000)
19. B.G. Russell, " A Study of the Influence of Micro and Nano-Phase Morphology on the Mechanical Properties of a Rubber-Modified Epoxy Resin", Doctorial Dissertation, University of Dayton, Dayton, Ohio, (August, 2002).
20. G. A. Brady and J.W. Halloran, "Differential Photo-Calorimetry of Photopolymerizable Ceramic Suspensions", ***J. Mat. Sci.***, **33**, 4551-60 (1998)
21. K.A.M. Seerden, N. Reis, B. Derby, P.S. Grant, J.W. Halloran and J.R.G. Evans, "Direct Inkjet Deposition of Ceramic Green Bodies; I: Formulation of Build Materials", MRS Symp. Proc., **542**, 141-46, (1999)
22. N. Reis, K.A.M. Seerden, B. Derby, J.W. Halloran and J.R.G. Evans, "Direct Inkjet Deposition of Ceramic Green Bodies: II: Jet Behaviour and Deposit Formation", MRS Symp. Proc., **542**, 147-52, (1999)
23. M. Mott, J.H. Song and J.R.G. Evans, "Microengineering of Ceramics by Direct Inkjet Printing", ***J. Amer. Ceram. Soc.***, **82**, 1653-58, (1999)
24. E. Maniasa, J. Chen, N. Fang, and X. Zhang, "Polymeric Micro-mechanical Components with Tunable Stiffness", ***Appl. Phys. Let.***, **79(11)**, 1700-03, (2001)
25. C. Sun and X. Zhang, "Experimental and Numerical Investigations on Micro-Stereolithography of Ceramics", ***J Appl. Phys.***, **92(8)**, 4796-5003, (2002)
26. C. Sun, X. Zhang, "The Infuences of the Material Properties on Ceramic Micro-stereolithography", ***Sensors and Actuators:*** **A**, **101**, 364-70 (2002)
27. D. Wu, N. Fang, C. Sun, and X. Zhang, " Adhesion Force of Polymeric Three-dimensional Microstructures Fabricated by Micro-stereolithography", ***Appl. Phys Let,*** **81(21)**, 3963-65, (2002)
28. C. Ainsley, N. Reis, and B. Derby, "Direct Ink Jet Printing of Alumina Components" Mat. Res. Soc. Symp. Proc., **698,** (2002)
29. D-Y. Shin, P. Grassia and B. Derby, "Analysis of Drop-On-Demand Ink Jet Print Head for Rapid Prototyping", Mat. Res. Soc. Symp. Proc., **698**, (2002)
30. H-R. Wang, M. J. Cima, and E. M. Sachs, "Alumina-Doped Silica Gradient Index (GRIN) Lenses by Slurry-Based Three-Dimensional Printing," Mat. Res. Soc. Symp. Proc., 758, LL1.5.1,(2003)
31. R. K. Holman, M. J. Cima, S A. Uhland, and E. Sachs, "Spreading and Infiltration of Inkjet-Printed Polymer Solution Droplets on a Porous Substrate", ***J. Colloid and Interface Sci.***, **249**, 432_440 (2002)

Control of the Cross Section Geometry of Extruded Dental Porcelain Slurries for Rapid Prototyping Applications

Jiwen Wang, Leon L. Shaw, Harris L. Marcus
Department of Metallurgy and Materials Engineering
Institute of Materials Science
University of Connecticut, Storrs, CT 06269

T. B. Cameron
Dentsply Ceramco
Burlington, NJ 08016

Abstract

This study investigates the dependence of the cross section geometry of extruded dental porcelain slurries on the rheological property of the slurry and the extrusion conditions. It is found that a pseudoplastic slurry is a basic requirement for obtaining extruded lines with rectangular cross sections. The cross section geometry of the extrudate is also strongly affected by extrusion parameters including the extrusion nozzle height, nozzle moving speed, and extrusion rate. Proper combinations of these extrusion parameters are necessary in order to obtain extrudates with near rectangular cross sections. The results obtained have been explained in terms of the interactions among the rheological properties of the slurry, the shear rate imposed on the slurry during extrusion, the wettability of the slurry on the substrate, and the forced flow of the slurry during extrusion.

Keywords: Slurry extrusion, dental porcelain, rheology of slurry, solid freeform fabrication

I. Introduction

3D objects fabricated through line-by-line and layer-by-layer approaches require that each line deposited has a rectangular cross section in ideal cases. Lines with such cross section geometry can prevent or minimize the formation of voids between lines and layers. This study investigates the dependence of the cross section geometry of extruded dental porcelain slurries on the rheological property of the slurry and the extrusion conditions for dental restorations via the multi-material laser densification (MMLD) process [1-3].

Currently, there are two general routes for preparing pastes and slurries for SFF. One requires the use of polymers or resins as the binder in order to maintain the shape of the extrudate [4,5]. These polymers and resins are burned out in the subsequent heat treatment while contamination may remain in the extrudate. The second route is to prepare aqueous pastes or

slurries without addition of binders and to control the cross section geometry of the extrudate by adjusting the pH value, salt concentration, and volume fraction of solid in the paste [6-11]. Using fine Al_2O_3 powder, Cesarano, et al [7] have shown that when a slurry is pseudoplastic and drying rates are appropriate, the lines extruded yield nearly rectangular cross sections with relatively straight walls and flattened tops. The paste formulation and particle size have also been shown by Du, et al [11] to have strong effects on the extrudability of thin wall thickness tubes and their thickness and uniformity.

Although the effects of rheological behavior of pastes and slurries on the cross section geometry of the extrudate have been studied by several researchers [6-11], the dependency of the cross section geometry on extrusion parameters has never been systematically investigated. To address this issue, the effects of extrusion parameters on the cross section geometry of the extrudate in conjunction with the effects of rheological behavior of dental porcelain slurries have been investigated in this study. The extrusion parameters investigated include the nozzle height of the extruder, nozzle moving speed, and extrusion rate, all of which are experimental variables and thus can be adjusted to achieve the desired cross section geometry. The results indicate that the effects of these extrusion parameters on the cross section geometry of the extrudate can be explained in terms of the interactions among the rheological properties of the slurry, the shear rate imposed on the slurry during extrusion, the wettability of the slurry on the substrate, and the forced flow of the slurry during extrusion.

II. Experimental

The dental porcelain powder was provided by Degussa-Ney Dental Inc., Bloomfield, CT. The chemical composition of the porcelain is confidential; however, it is within 5% of the nominal composition of the Weinstein patent [12], which has the following composition (wt%): 63.40% SiO_2, 16.70% Al_2O_3, 1.50% CaO, 0.80% MgO, 3.41% Na_2O, and 14.19% K_2O. The as-received powder has angular shapes and their equivalent particle sizes range from 1 to 50 micrometers. To reduce the particle size of the porcelain powder to sub-micrometers, ball-milling process was conducted using a single axis mixer machine loaded with Al_2O_3 balls. After milling, the powder was dispersed in de-ionized water and the submicron-sized particles were separated from coarse particles (> 1 μm) through sedimentation. Only the submicron-sized particles were used to prepare the slurries.

The porcelain slurries were prepared using de-ionized water as the solvent with a solid loading of 40 – 50 vol %. Uniform and stable slurries were obtained by gently mixing the slurry for 24 hours using the mixer machine loaded with Al_2O_3 balls. The porcelain slurry was extruded using a MMLD machine designed and constructed at the University of Connecticut. The machine consists of four major components: (i) the process chamber that can have a vacuum down to 10^{-2} torr, (ii) micro-extruders for powder slurry delivery of up to 3 different materials, (iii) a laser heating system for powder densification with temperature sensing and control system, and (iv) a X-Y-Z positioning system. The pressure exerted on the porcelain slurry within the micro-extruder was applied via an electric cylinder (model: NV-BN23-105B). The slurries were extruded onto SiC plates with a 700μm nozzle. The motion and position control was provided by a computer through a Galil DMC-1800 multi-axis motion control card. The extrusion variables

that could be controlled independently and investigated in this study were the nozzle height of the micro-extruder (i.e., the distance between the nozzle tip and the substrate), the nozzle moving speed (with respect to the substrate, mm/s), and the extrusion rate (i.e., the volume of the slurry extruded per unit time, ml/s).

The rheology of the porcelain slurries was measured using a Brookfield DV II digital viscometer. The zeta potential of the slurries was measured at the National Science Foundation Engineering Research Center for Particle Science and Technology in the University of Florida using a Zeta-Reader instrument. The pH value of the slurry was measured using a Denver basic pH meter. The cross section geometry was defined by the line width and height of the extrudate and its contact angle with the substrate. To measure these geometrical parameters, the porcelain lines extruded were encapsulated using epoxy before cutting and polishing after which these parameters were observed and measured using an optical microscope.

III. Results and Discussion

3.1 Rheological Behavior of Dental Porcelain Slurries

Figure 1 shows the zeta potential of the dental porcelain powder as a function of the pH value. It indicates that the iso-electric point (i.e.p.) of the dental porcelain powder is at about 5.0, which is between the i.e.p. of Al_2O_3 (8.7) and SiO_2 (2.0). Since Al_2O_3 and SiO_2 are the main components of the dental porcelain [12], the zeta-potential of the porcelain powder appears to be controlled by a combined interactive effect of these two compounds. It can be inferred from Figure 1 that slurries with pH < 3.0 or pH > 8.0 should be relatively stable. This is the case because the surfaces of powder particles with these pH values are mainly positively charged (for pH < 3.0) or negatively charged (for pH > 8.0) [13,14]; the same charges on their surfaces provide large repulsive forces between particles, thereby preventing coagulation and thus leading to stable slurries. In contrast, slurries with pH values between 3.0 and 6.5 would be unstable because coagulation of particles will happen quickly owing to the zero or near-zero net charge on the surfaces of these particles.

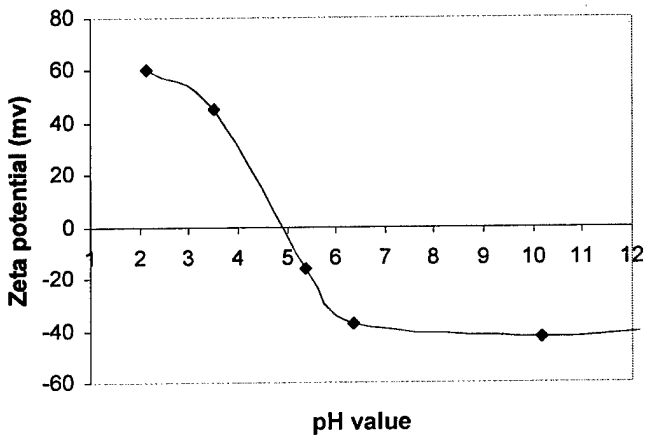

Figure 1. Zeta potential of the dental porcelain powder as a function of the pH value.

Based on Figure 1, clearly, a pseudoplastic slurry with moderate viscosity can be prepared with a pH value near 7.0 – 7.5 because at pH = 5.0 the slurry becomes unstable with high viscosity and at pH > 8.0 or < 3.0 the slurry is very stable. Slurries with pseudoplastic (shear thinning) behavior are highly desirable for controlling the cross section geometry of the extruded line because slurries with shear thinning properties can be extruded with a relatively low extrusion force and solidify in place once the slurry leaves the nozzle due to the removal of shear stresses. Thus, most of the extrusion studies presented below are carried out using dental porcelain slurries with pH = 7.0 – 7.5 unless otherwise mentioned.

Figure 2 compares the cross section geometry of the extrudates with pH values equal to 9.3, 8.0 and 7.0. At pH = 9.3, the slurry is very stable with a relative low viscosity. As a result, the slurry flows continuously after it leaves the nozzle and thus takes on an arch shape with a low contact angle of 40 degrees. At pH = 8.0, the viscosity of the slurry increases slightly and thus the slurry spreads out less on the surface of the substrate, resulting in an increased contact angle of 60 degrees. At pH = 7.0 (approaching the i.e.p.), the slurry becomes pseudoplastic because the low electrical charges of the same sign of the particles allows them to approach to each other, but at the same time prevents them to coagulate. As a result of its shear thinning behavior, the contact angle of the extrudate with the substrate increases to 95 degrees, clearly indicating nearly no spreading after the slurry leaves the nozzle of the extruder. With a contact angle near 90 degrees, the cross section of the extrudate is approaching a rectangular shape which is highly desirable as a "building block" for fabrication of 3-dimensional objects through layer-by-layer approaches.

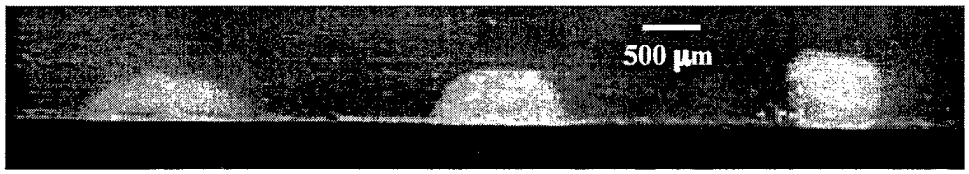

	pH = 9.3	pH = 8.0	pH = 7.0
Contact angle (degree)	40	60	95

Figure 2. Cross section photos of extrudates with different pH values.

3.2 Effects of Nozzle Height on the Cross Section Geometry of Extrudates

The distance between the nozzle tip of the extruder and the substrate, termed as the nozzle height hereafter, greatly influences the cross section geometry of the extrudate. The distance between the nozzle and the substrate will limit the space within which the slurry can flow. For a certain slurry extrusion rate and nozzle moving speed, there is a critical nozzle height (h_c) above which the cross section geometry of an extruded single line is mainly controlled by the rheological behavior of the slurry and the wettability of the slurry on the substrate. When the nozzle height is lower than h_c, the volume of the slurry extruded will be too large for the space between the nozzle and the substrate. As a result, the slurry is forced to spread in the directions perpendicular to the deposited line along the surface of the substrate, and the resultant shape of the extrudate is not only determined by the rheological properties and wettability of the slurry,

but also by the space between the nozzle and the substrate. In contrast, when the nozzle height is larger than h_c, there is enough space for the deposited slurry so that the rheological properties and wettability of the slurry will determine the cross section geometry of the extrudate.

Our experiments indicate that the critical nozzle height can be estimated using the following equation:

$$h_c = \frac{V_d}{v_n D_n} \qquad (1)$$

where V_d is the volume of the slurry extruded per unit time (called the extrusion rate hereafter), v_n the nozzle moving speed, and D_n the nozzle diameter. The physical meaning of eq. (1) is that the volume of the slurry extruded per unit time is equal to the volume available per unit time between the nozzle and the substrate. When the nozzle height is lower than h_c, the slurry is forced to take up the space beyond the volume defined by the product of the nozzle height, the nozzle diameter, and the distance traveled by the nozzle per unit time.

Nozzle height (μm):	200	330	670	1000
Contact angle (degree):	40	65	85	95

Figure 3. Cross section of the single lines extruded using a dental porcelain slurry of pH = 7.5 with V_d = 2.5 x 10^{-3} ml/s, D_n = 0.7 mm, v_n = 4.25 mm/s, and different nozzle heights as indicated.

Figure 3 shows the cross section of the extrudates deposited with different nozzle heights. The contact angles of these extrudates with the SiC substrate are measured and presented in Figure 4. When the nozzle height equals to 200 and 330 μm, the slurries spread widely along the substrate with low contact angles, which indicates that the nozzle height is lower than h_c because the slurry has been forced to flow beyond the space defined by the nozzle height, the nozzle diameter, and the distance traveled by the nozzle per unit time. When the nozzle height equals to 670 μm, the contact angle closes to 90 degrees and no spreading is observed. A further increase in the nozzle height (1000 μm) does not alter the shape of the extrudate much with only a small increase in the contact angle. The critical nozzle height calculated using eq. (1) for the extrusion condition shown in Figure 3 is 840 μm which is between 670 μm and 1000 μm tested in the experiment. These results indicate that when the nozzle height is near the critical nozzle height, the contact angle of the slurry on the SiC substrate used in this study is about 90 degrees.

However, when the nozzle height is substantially smaller than h_c (e.g., the cases of 200 and 330 μm in Figure 3), the forced flow is present and the contact angles will be smaller than 90 degrees.

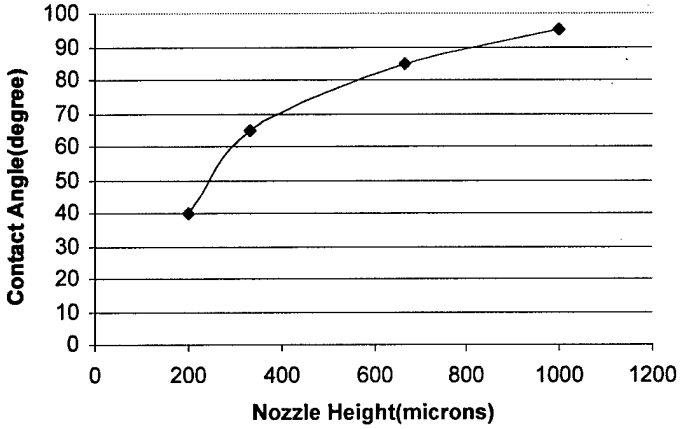

Figure 4. The contact angle as a function of the nozzle height for slurries with pH = 7.5.

3.3 Influence of the Shear Rate on the Cross Section Geometry of Extrudates

Because of the pseudoplastic behavior of the slurry, extrusion conducted with high shear rates will have relative low viscosity, whereas extrusion with low shear rates will have high viscosity. In order to investigate the true effects of the shear rate on the cross section geometry of the extrudate, a set of the experiments have been designed in which both the extrusion rate and the nozzle moving speed have been increased proportionally in order to keep the critical nozzle height [see eq. (1)] and the deposition density constant. The deposition density, D_d, is defined as the volume of the slurry extruded per unit time divided by the product of the nozzle diameter and the moving speed of the nozzle. When both the critical height and the deposition density are kept constant, the change in the extrusion rate provides a genuine evaluation of the effect of the shear rate.

The results from this special set of the experiments are shown in Figure 5. At high extrusion rates (0.01 ml/s and 0.005 ml/s), the contact angles are smaller than 90 degrees. In contrast, at low extrusion rates (0.0025 ml/s and 0.00125 ml/s), contact angles are greater than 90 degrees. This is so because high extrusion rates result in high shear rates which in turn leads to low viscosities. Thus, when high extrusion rates are used, the slurry flows fast after it leaves the nozzle tip. As a result of the fast flow, the slurry spreads out along the surface of the substrate before it freezes and a low contact angle results. In contrast, when low extrusion rates are used, the flow of the slurry after it leaves the nozzle tip is limited because of its high viscosity. As a consequence of this limited flow, a high contact angle results.

It is noted, however, that in spite of the dependency of the cross section geometry on the shear rate, the effect of the shear rate on the contact angle is relatively small in comparison with that of the pH value and the nozzle height. As seen from Figure 5, the variation of the contact

angle due to the different shear rates investigated is within 20%, which is much smaller than 100% changes achieved by altering the nozzle height (Figures 4 and 5).

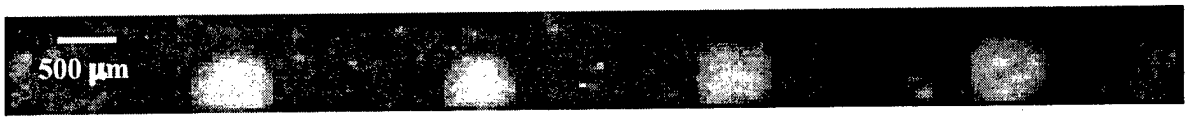

Extrusion rate (ml/s):	0.01	0.005	0.0025	0.00125
Nozzle moving speed (mm/s):	17.5	8.5	4.25	2.125
h_c (mm):	0.84	0.84	0.84	0.84
Deposition density (mm^3/mm^2):	0.84	0.84	0.84	0.84
Contact angle (degree):	85	90	95	105

Figure 5: Cross section of the single lines extruded with different extrusion rates and nozzle moving speeds as indicated, while keeping all other processing parameters constant.

IV. Concluding Remarks

The present extrusion study clearly shows that in order to get favorable cross section geometry of the porcelain powder line in SFF processes, extrusion parameters including the nozzle height, nozzle moving speed and the extrusion rate should be optimized. However, optimization can be achieved only when the slurry is pseudoplastic. The latter can be accomplished by adjusting the pH value of the slurry for the dental porcelain powder to between 7.0 and 7.5. Once the proper slurry is prepared, extrusion conditions can have strong impact on the cross section geometry of the extrudate. There is a critical nozzle height (h_c) for a given set of the extrusion rate, nozzle moving speed, and the nozzle diameter. When extrusion is carried out with the nozzle height above the critical nozzle height, the cross section geometry of the extrudate is mainly determined by the rheological behavior of the slurry and the wettability of the slurry on the substrate. When the nozzle height is lower than the critical nozzle height, the resultant shape of the extrudate is not only controlled by the rheological properties and the wettability of the slurry, but also by the forced flow of the slurry along the surface of the substrate. A rectangular cross section results when low extrusion rates are used. In contrast, an arch-shaped cross section with low contact angles is obtained if high extrusion rates are used.

Acknowledgements – The authors gratefully acknowledge financial support provided by the National Science Foundation under Grant Nos: DMI-9908249 and DMI-0218169.

References

1. X. Li, J. Crocker, E. Geiss, L. Shaw, H. Marcus, and T. Cameron, "Evaluation of Microstructure and Properties for Multi-Materials Laser Densification of Dental Restorations," in Proc. of the 11th SFF Symposium, D. L. Bourell, J. J. Beaman, R. H.

Crawford, H. L. Marcus and J. W. Barlow (eds.), University of Texas, Austin, TX, 2000, pp. 159 – 167.
2. L. Shaw, X. Li, J. Wang, H. L. Marcus, T. B. Cameron, and C. Kennedy, "Dental Restoration through Laser Densification of Dental Porcelain Powder," in Rapid Prototyping of Materials, F.D.S. Marquis and D.L. Bourell (eds.), TMS, Warrendale, PA, 2002, pp. 107-118.
3. J. Wang, X. Li, L. Shaw, H. L.Marcus, and T. B. Cameron, "Multi-Material Powder Delivery in Rapid Prototyping of Dental Restoration," in Proc. of the 12th SFF Symposium, D. L. Bourell, J. J. Beaman, R. H. Crawford, H. L. Marcus and J. W. Barlow (eds.), University of Texas, Austin, TX, 2001, pp. 546-552.
4. R. Clancy, V. Jamalabad, and P. Whalen, "Fused Deposition of Ceramics: Progress Towards a Robust and Conrolled Process for Commercialization," in Proc. of the 8th SFF Symposium, D. L. Bourell, J. J. Beaman, R. H. Crawford, H. L. Marcus and J. W. Barlow (eds.), University of Texas, Austin, TX, 1997, pp. 185-193.
5. M. Agarwala, A. Bandyopadhyay, R. van Weeren, A. Safari, S. C. Danforth, N. A. Langrana, V. Jamalabad, and P. J. Whalen, "FDC: Rapid Fabrication of Structural Components," Bull. Am. Ceram. Soc., 75 [11] 60-65 (1996).
6. D. Dimos, P. Yang, T. J. Garino, M. V. Raymond, and M. A. Rodriguez, "Direct-Write Fabrication of Integrated, Multilayer Ceramic Components," in Proc. of the 8th SFF Symposium, D. L. Bourell, J. J. Beaman, R. H. Crawford, H. L. Marcus and J. W. Barlow (eds.), University of Texas, Austin, TX, 1997, pp. 33-40.
7. J. Cesarano III, T. A. Baer, and P. Calvert, "Recent Developments in Freeform Fabrication of Dense Ceramics From Slurry Deposition," Proc. of the 8th SFF Symposium, D. L. Bourell, J. J. Beaman, R. H. Crawford, H. L. Marcus and J. W. Barlow (eds.), University of Texas, Austin, TX, 1997, pp. 25-32.
8. J. Davies and J. G. P. Binner, "Plastic Forming of Alumina from Coagulated Suspensions," J. Euro. Ceram. Soc., 20, 1569-1577 (2000).
9. Z. Chen, K. Ikeda, T. Murakami, and T. Takeda, "Effect of Particle Packing on Extrusion Behavior of Pastes," J. Mater. Sci., 35, 5301-5307 (2000).
10. J. Davies and J. G. P. Binner, "Coagulation of Electrosterically Dispersed Concentrated Alumina Suspensions for Paste Production," J. Euro. Ceram. Soc., 20, 1555-1567 (2000).
11. Y. Du, N. M. Sammes and G. A. Tompsett, "Optimisation Parameters for the Extrusion of Thin YSZ Tubes for SOFC Electrolytes," J. Euro. Ceram. Soc., 20, 959-965 (2000).
12. M. Weinstein, S. Katz, and A. B. Weinstein, "Fused Porcelain-to-Metal Teeth," U.S. Pat. No. 3 052 983, Sept. 11, 1962.
13. B. Derjaguin and L. Landau, "Theory of the Stability of Strongly Charged Lyphobic Sols of the Adhesion of Strongly Charged Particles in Solutions of Electrolytes," Acta Physicochim. URSS, 14, 633-662 (1941).
14. E. J. W. Verwey and J. Th. G. Overback, Theory of the Stability of Lyphobic Colloids, Elsevier, Amsterdam, Netherlands, 1948.

DESIGN AND ANALYSIS OF ORTHOGONALLY COMPLIANT FEATURES FOR DURAFORM/SLS MANUFACTURED PLATES

Mario Faustini*, Richard Crawford*, Richard R. Neptune*, William Rogers†, Andrew Gitter† and Gordon Bosker†

*The University of Texas at Austin
†The University of Texas Health Science Center in San Antonio

Abstract

In many applications of parts manufactured by Solid Freeform Fabrication (SFF), compliance is an important factor. In order to achieve given deformation goals with optimal shape, the design of compliant mechanisms and elements fabricated with SFF techniques must take into account the particular constraints and boundary conditions of the target application as well as the specific material properties of the part. The present work focuses on the design and evaluation of compliant features for a geometrically constrained thin-wall part subject to loads normal to its tangent plane. Such features would need to be embedded in the object. The manufacture of prosthetic sockets for lower-limb amputees is the specific application presented, where greater compliance is needed at sites in contact with pressure sensitive tissues. Sample parts were fabricated by selective laser sintering, and the material used was Duraform.

1 Introduction

Compliance is in many cases a fundamental and desired property of a mechanical structure. In many applications, compliance is very important for proper function of a part. In others it is a much more elegant and functional design solution that substitutes joints and links of mechanisms by incorporating controlled flexibility within the structure itself. In order to proceed with the design of compliant features, very strict constraints must be considered and evaluated [Howell, 2001]. The part material and its mechanical properties must be studied, boundary conditions for the structure must be well defined, the target deformation under specific loads must be set, and a thorough failure prevention study, using both static and fatigue theory, should be performed.

This article focuses on the primary design stages of orthogonally compliant features of plates and thin walls (where the load/displacement direction of the feature is normal to the plate or wall), and evaluating the design options that are more promising for a given set of design goals for an specific application. The design example to be considered is the incorporation of compliance features in sockets for below-the-knee prostheses, produced with selective laser sintering (SLS) using Duraform.

2 Fabrication of Sockets for Below-the-Knee Prostheses using SLS

The production of sockets for prostheses using SFF (Figure 1) has several potential advantages compared to common, more labor intensive and time-consuming fabrication methods [Walsh et al., 1989; Freeman et al., 1998]. One of the main advantages is that SFF directly creates sockets

from digital shape information, eliminating the need for molds, hand lamination and finishing procedures. Another advantage of SLS is the ability to create complex geometries with minimal cost penalty in manufacturing, which significantly expands the options for developing and exploring alternate socket designs.

Figure 1: On the left and center, a patient testing an SLS fabricated socket; on the right, the description of the parts of a prosthesis for below-the-knee amputees.

Our method, developed through collaboration of the Laboratory for Freeform Fabrication at The University of Texas at Austin and the Rehabilitation Engineering Laboratory of The University of Texas Health Science Center at San Antonio [Rogers et al., 2001], creates a computer model of the socket from digital source taken from the patient's residual limb. The shape of the socket is designed so that the load is supported by specific regions of the limb that can safely resist contact pressures generated when the patient walks. This design is called the Patellar-Tendon Bearing (PTB) socket, illustrated schematically in Figure 2.

Some areas of the residual limb are not suitable for high contact pressures, either because they are too sensitive to pain, are susceptible to developing sores, or other various health issues. Notwithstanding the reason, high pressures at these sites lead to discomfort for the patient during gait (thus affecting rehabilitation) and, sometimes, pose a health risk for the patient. Thus, it is necessary to incorporate means of relieving contact pressure over these areas. One way to achieve this is to make the socket orthogonally compliant at these high pressure contact sites.

Currently, local compliance is achieved by reducing the wall thickness of the socket at pressure sensitive areas, as seen in Figure 3. However, this approach provides limited compliance and pressure relief. A more effective design may be to take advantage of the ability of SLS to easily create geometric variants of traditional socket shapes that allows a controlled expansion of socket volume to adapt to limb change during gait.

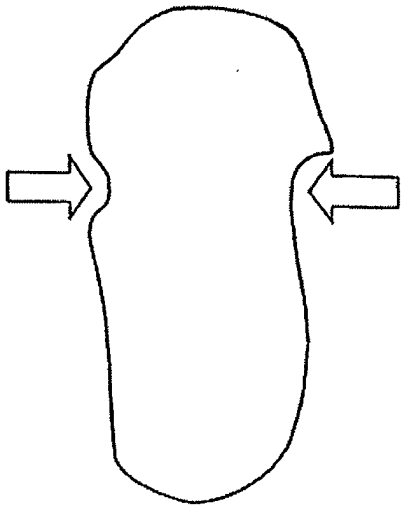

Figure 2: Schematic of a socket based on the PTB approach, with main force vectors shown.

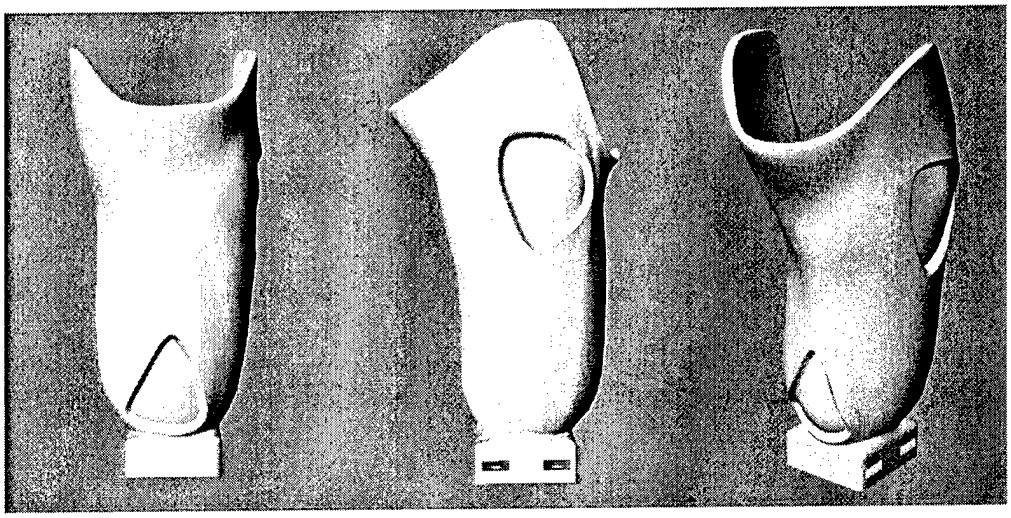

Figure 3: Example of a current SLS fabricated socket with locally thinned walls in areas where compliance is needed.

3 Design Goals and Constraints

In order to allow the effective and successful design of orthogonally compliant features to be incorporated into the socket structure, it is necessary to identify the design goals and constraints. First, a target deformation for the compliant region when subjected to the normal steady-load pressure must be specified. The optimum value of the desired displacement at the center of the compliant site is, however, difficult to set precisely, since it depends on several parameters that may vary from patient to patient and can be highly subjective. Our experience has shown that positive results occur when the target displacement should be between 2 and 4 mm.

Second, the incorporated compliant features on the wall of sockets should not compromise structural safety during gait. Moreover, such features should not affect the shape of the inside of the socket and should have minimal impact on its outer appearance. The latter condition, although very subjective, is nevertheless important for the patient to feel positive about using the prosthesis.

Third, areas with no material on the socket wall, such as slots and holes, should have minimal dimensions. Since the limb requires a constant minimal pressure to be applied to all areas, even on more sensitive areas, large holes on the wall should be avoided altogether. Features that lead to high localized contact pressure gradients and concentrations should also be avoided, since they can lead to circulatory problems for the patient.

Finally, compliant features should not produce spikes or sharp corners when deformed. Hence, slots on the socket wall should not self-intersect or cross each other. Figure 4 shows an example of a possible socket with compliant features that satisfy these design goals and constraints.

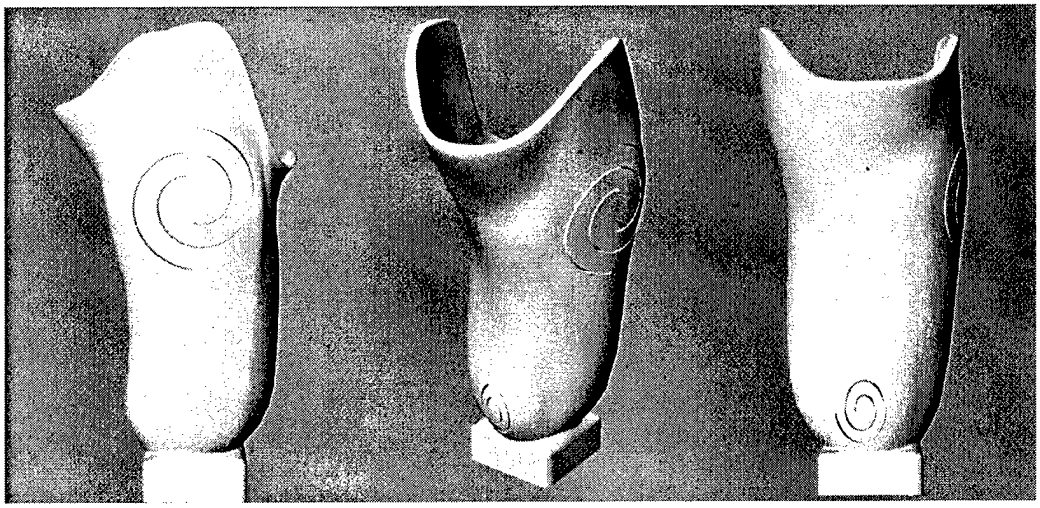

Figure 4: Example of orthogonally compliant features incorporated in a socket.

4 FEM Evaluation of Some Design Options

For the evaluation of various design options that satisfy the design constraints described in the previous section, computer modeled test discs were evaluated using finite element analysis (FEA) and prototypes were produced with SLS and Duraform material. These discs were dimensionally similar to compliant areas on the socket, as shown in Figure 5. Geometric features such as slots and holes will be added to each disc to assess their ability to provide compliance.

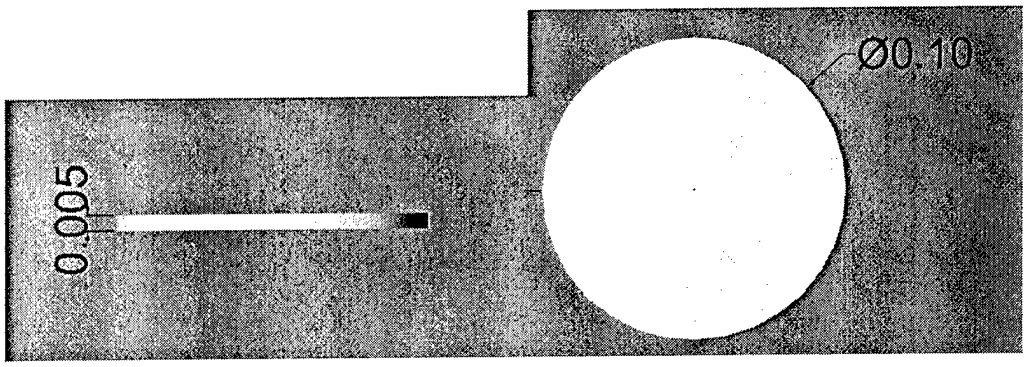

Figure 5: Test disc to evaluate compliance options (dimensions in meters)

The boundary conditions for the FEA analysis where defined as follows: the borders of the discs were fully restrained and a pressure of 10 kPa is applied at one of the free faces. SDRC I-DEAS 8 was used for the analysis and all elements were defined as 10-node parabolic tetrahedra. The material properties used for Duraform were those published by 3D Systems (Valencia, CA).

Figure 6 shows the deformation results for a solid control disc, with no compliant features. The displacement at the center due to the 10 kPa pressure was 5.54×10^{-5} m. Figures 7, 8 and 9 show the results for 4, 8 and 16 straight slots radially distributed on the discs, respectively. The central displacement achieved varied from 6.27×10^{-5} to 7.20×10^{-5}m as the number of straight slots was increased. However, a design with more than 16 slots would start to compromise structural integrity due to higher stress concentrations.

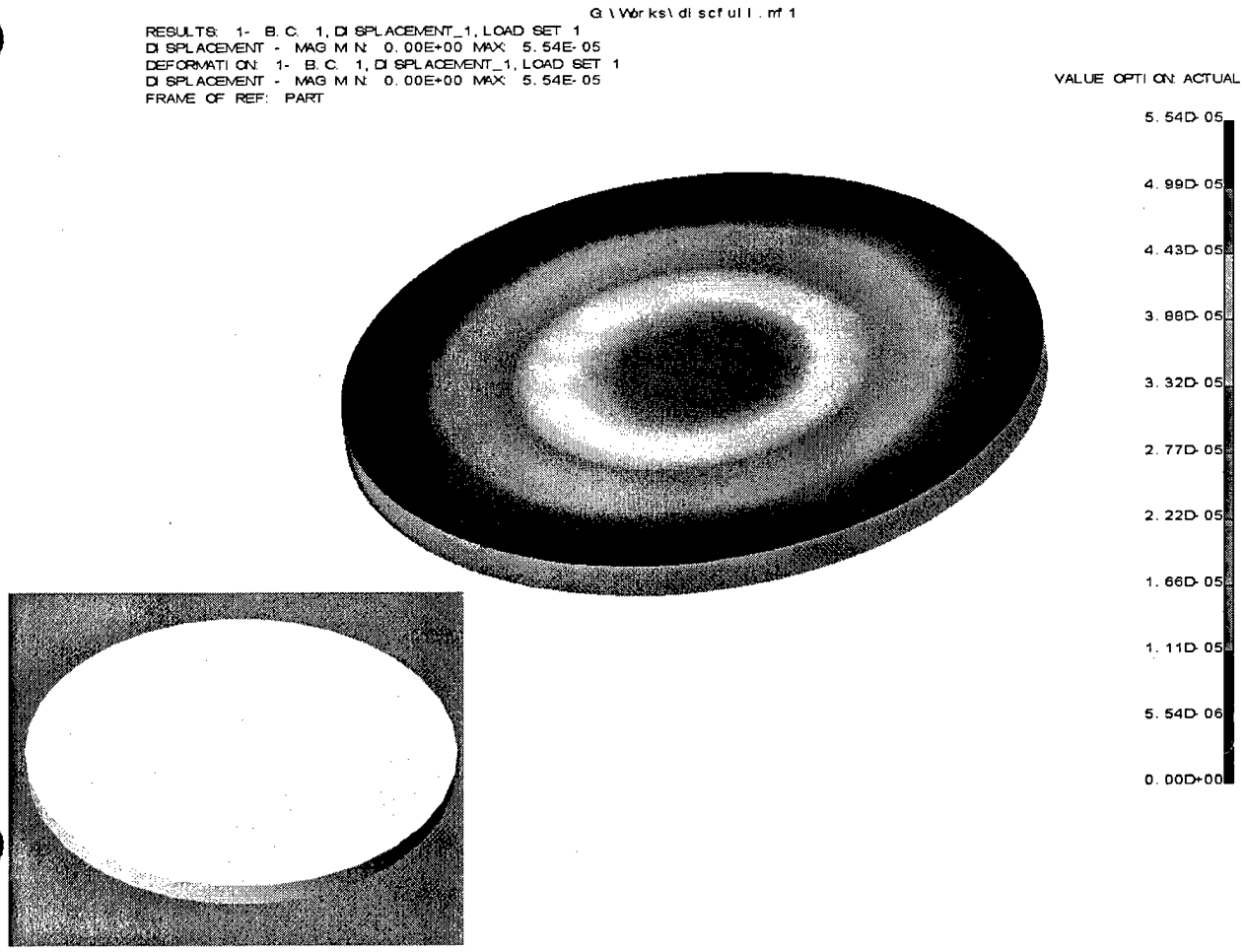

Figure 6: FEA deformation results for control disc with no special compliant features.

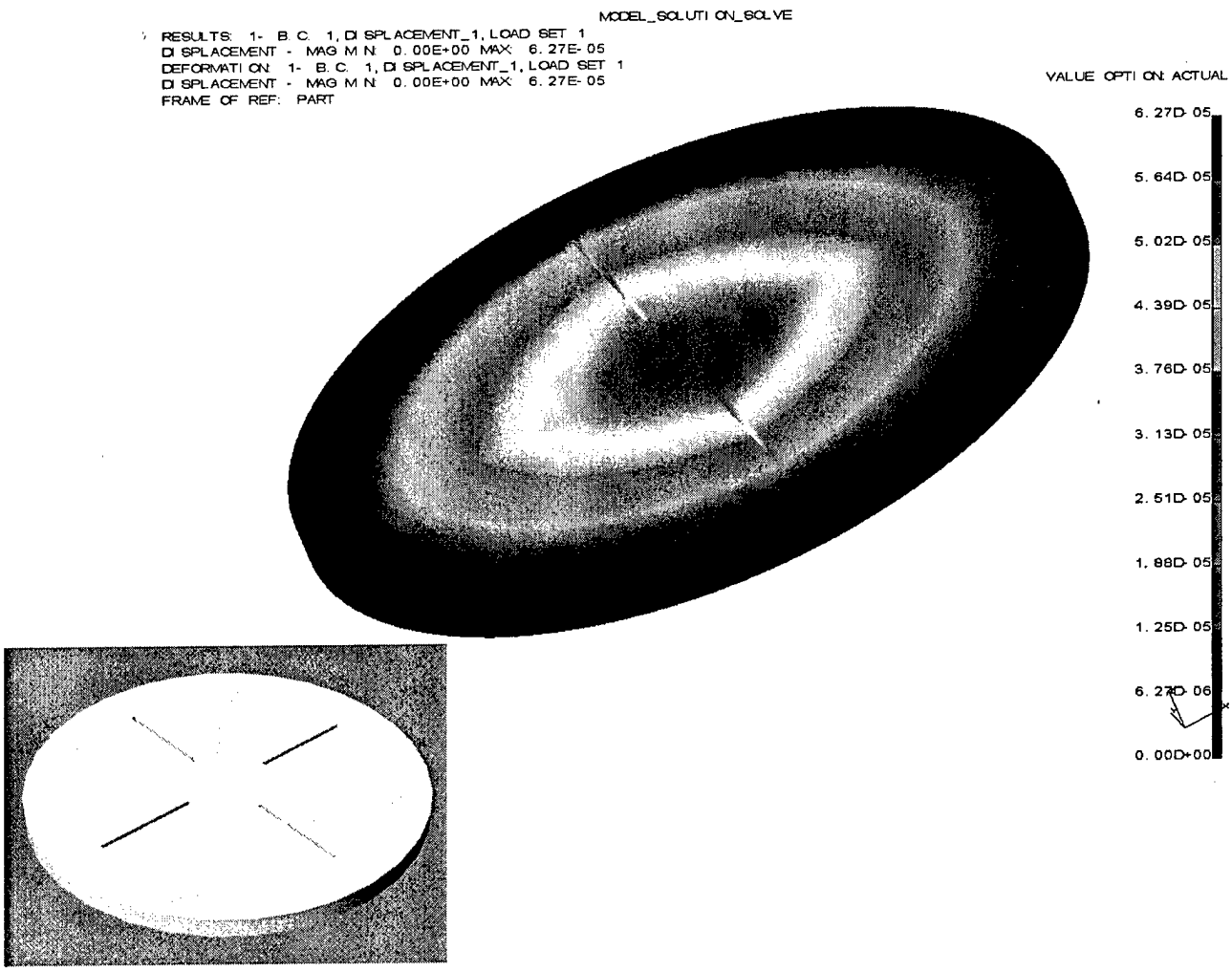

Figure 7: FEA deformation results for test disc with 4 radial slots.

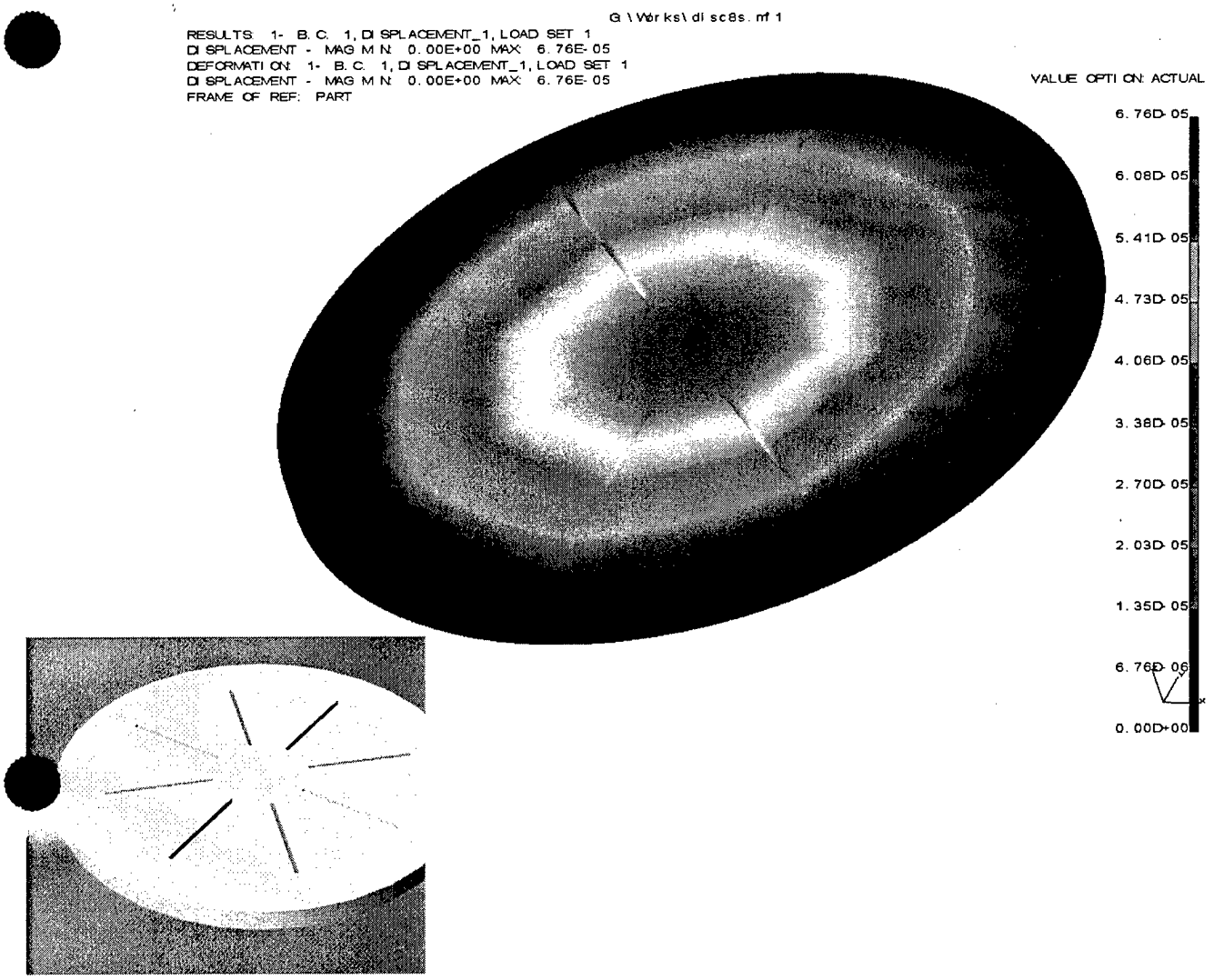

Figure 8: FEA deformation results for test disc with 8 radial slots.

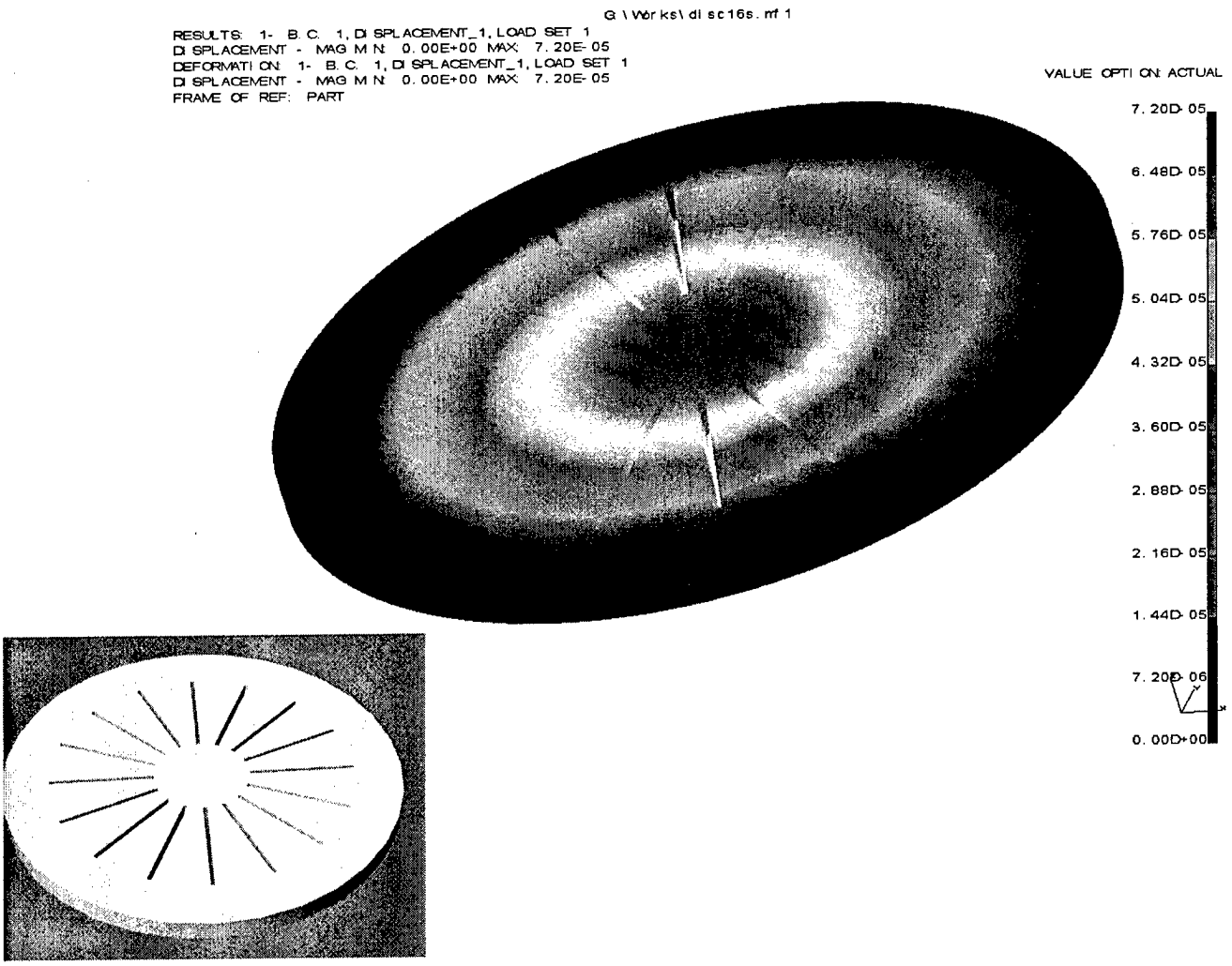

Figure 9: FEA deformation results for test disc with 16 radial slots.

Figure 10 presents an option with 4 larger void spaces, which is topologically similar to the solution given by optimization methods. For this design, the central displacement reaches a value of 8.52 x 10^{-5}m, which is still not as high as desired. In addition, there is a potential problem with localized pressure gradients (due to contact discontinuity) at the borders of the holes that may affect the peripheral circulation in the residual limb.

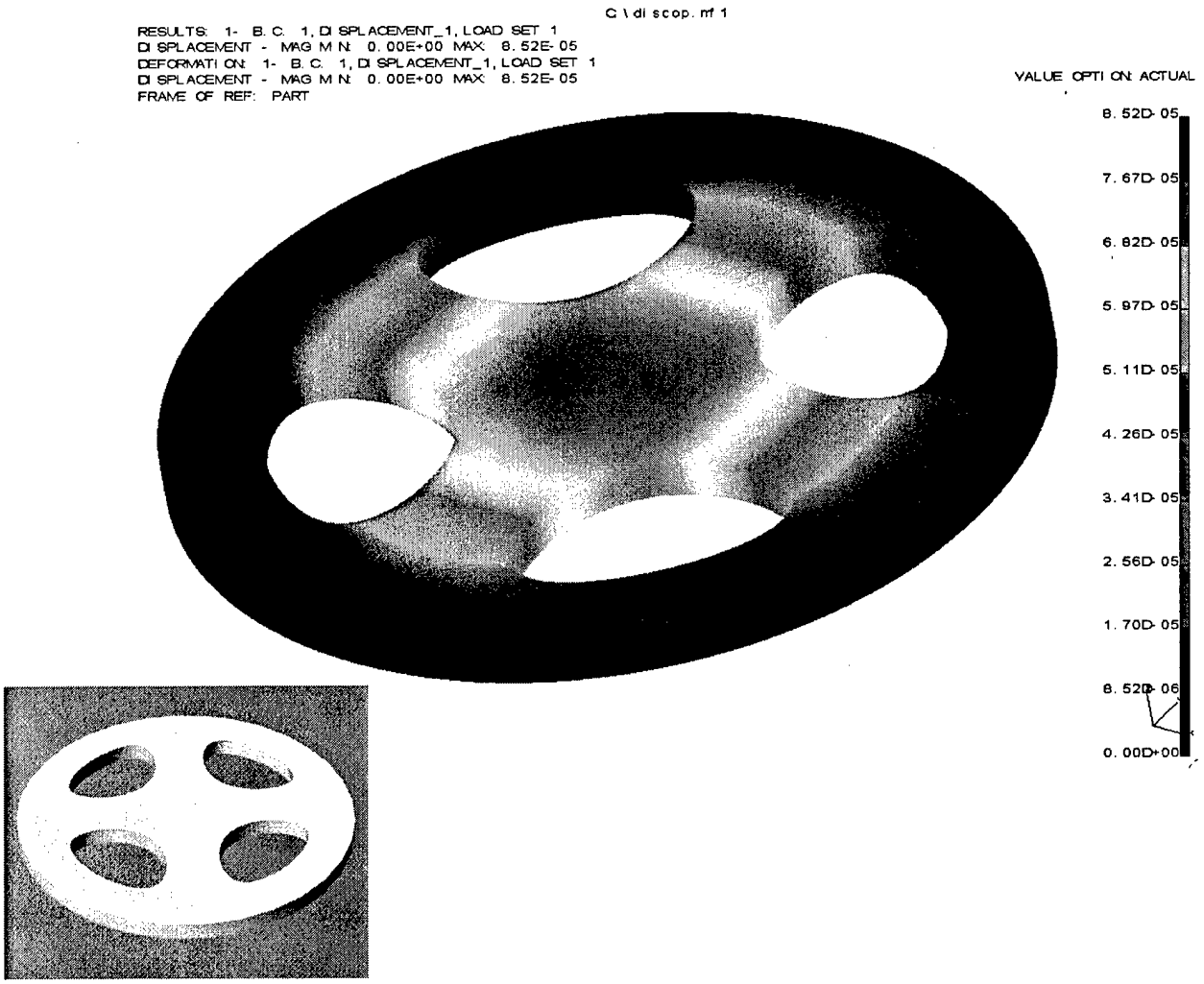

Figure 10: FEA deformation results for test disc with 4 void spaces.

Finally, Figures 11 and 12 display the results for designs with spiral slots (2 and 4 radially distributed spirals, respectively). For the case with 2 spirals, a central displacement of 4.38 x 10^{-3} m was achieved, which is very satisfactory. The case with 4 spirals, on the other hand, results in a central displacement of 8.88 x 10^{-3} m, which was considered to be too large.

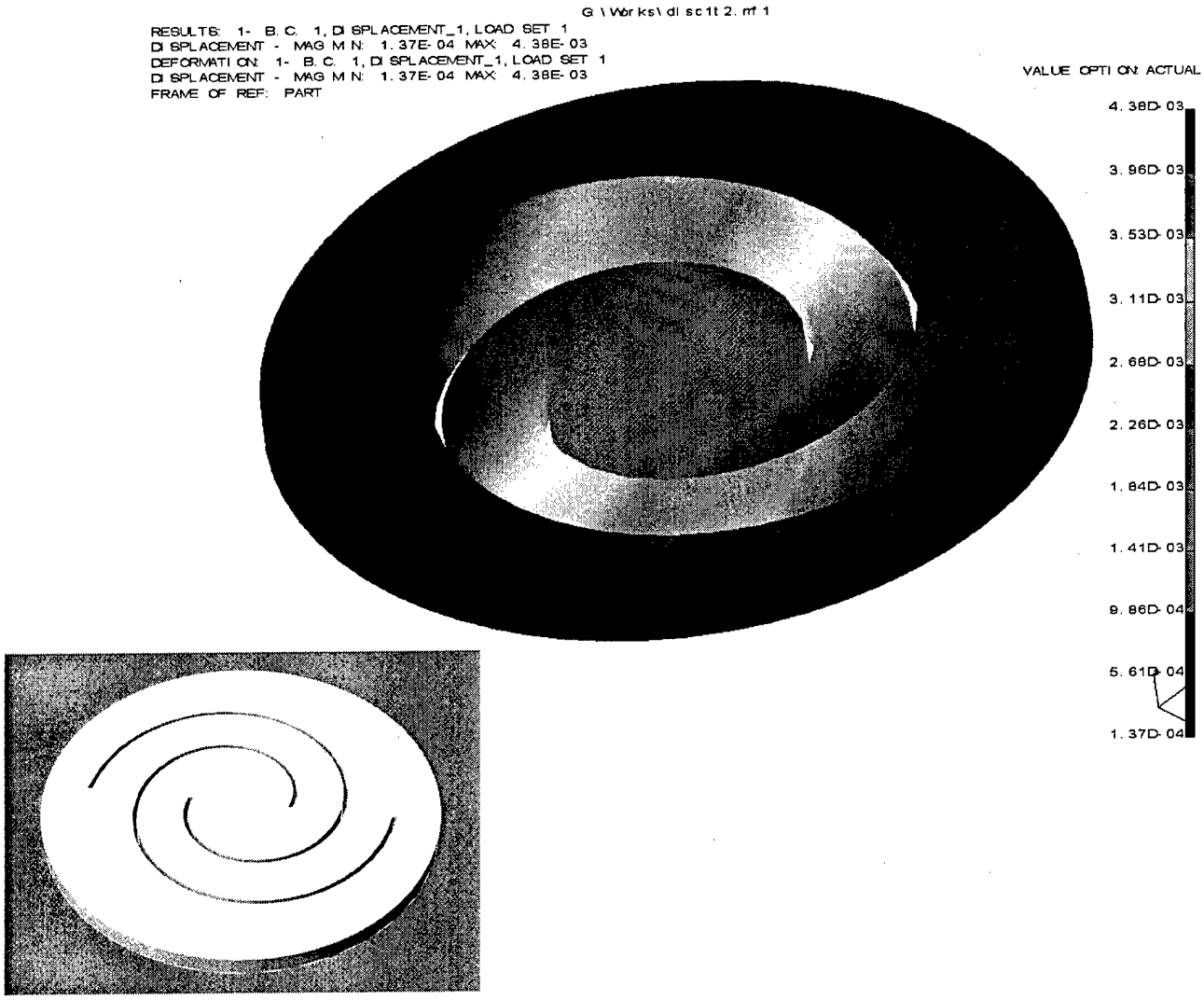

Figure 11: FEA deformation results for test disc with 2 spiral slots.

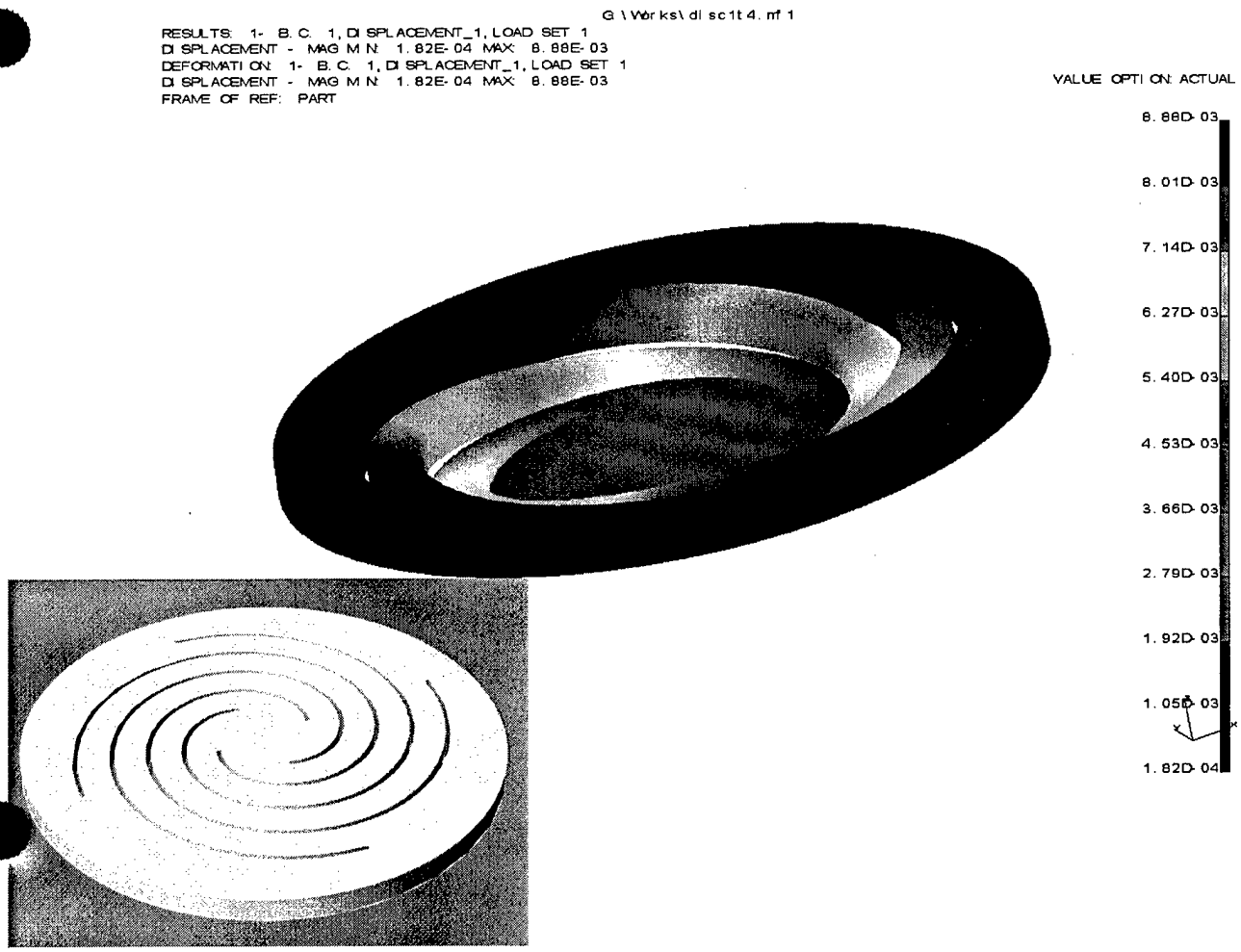

Figure 12: FEA deformation results for test disc with 4 spiral slots.

5 Conclusions and Future Work

This article presents a preliminary evaluation of design options for orthogonally compliant features to be used in sockets for below-knee prostheses using SLS. Of the options investigated, the most effective design incorporated two spiral slots, which balanced providing the needed displacement while avoiding high contact pressures.

This work is a preliminary study of specific topologies for compliant features using a trial and error approach. Future work will be directed at applying a modified version of topology optimization method to systematically optimize designs that satisfy the design constraints. One such technique is the Homogenization Method [Bendoe et al., 1993; Suziki and Kikuchi, 1991; Nishiwaki et al., 1998], which considers a design domain described by a 2D microstructure of unit cells, each one with void space (with sides defined by values **a** and **b**, which vary from 0 – no material – to 1) and orientation (defined by angle θ) (Figure 13). In general terms, the method consists of a recursive approach that calculates homogenized elasticity coefficients for the design domain, calculates sensitivities with FEM, optimizes for compliance with respect to **a** and **b**, filters results to eliminate checkboard patterns, updates angle θ and repeats all steps until convergence is achieved.

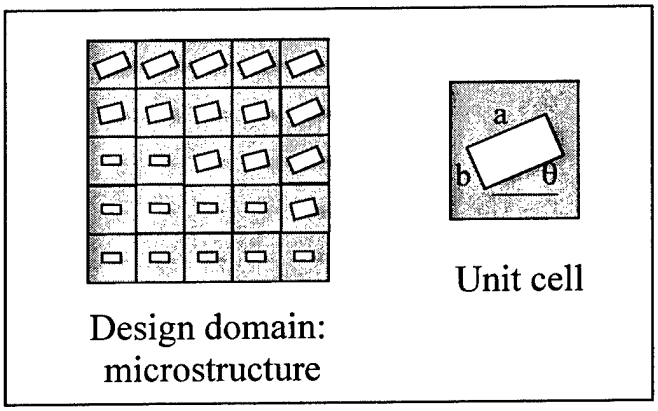

Figure 13: Design domain for the Homogenization Method.

However, some modifications must be applied to this method to allow its use with orthogonally compliant plates. First, a microstructure with orthogonal boundary conditions must be developed. Another fundamental modification is to filter solutions with large void areas, which violate design constraints for socket application. Finally, fatigue analysis should be performed on the compliant features.

Acknowledgements

The authors gratefully acknowledge financial support for this work from the VA Rehabilitation Research and Development Service.

References

Bendoe, M. P., Diaz, A., and Kikuchi, N., 1993, "Generating Optimal Topologies in Structural Design Using a Homogenization Method," *Computer Methods in Applied Mechanics and Engineering*, 71 (1988), pp. 197-224

Freeman, D., Wontorcik, L., 1998, "Stereolithography and Prosthetic Test Socket Manufacture: A Cost/Benefit Analysis", *Journal of Prosthetics and Orthotics*, Vol. 10, Num. 1, 1998.

Howell, L. L., 2001, *Compliant Mechanisms*, John Wiley & Sons, New York.

Nishiwaki, S., Frecker, M., Min, S. and Kikuchi, N., 1998, "Topology Optimization of Compliant Mechanisms Using the Homogenization Method," *Internation Journal for Numerical Methods in Engineering*, 42 (1998), pp. 535-559

Rogers, W., Gitter, A., Bosker, G., Faustini, M., Lockhande, M., Crawford, R., 2001, "Clinical Evaluation of Prosthetic Sockets Manufactured by Selective Laser Sintering", *2001 Solid Freeform Fabrication Symposium Proceedings*, Austin, TX.

Suzuki, K. and Kikuchi, N., 1991, "A Homogenization Method for Shape and Topology Optimization," *Computer Methods in Applied Mechanics and Engineering*, 93 (1991), pp. 291-318.

Walsh, N. E., Lancaster, J. L., Faulkner V. W., Rogers, W. E., 1989, "A Computerized System to Manufacture Prostheses for Amputees in Developing Countries", *Journal of Prosthetics and Orthotics*, Vol. 1, Num. 3, pp. 165-181, 1989.

REACTION BONDED SILICON CARBIDE:

SFF, PROCESS REFINEMENT AND APPLICATIONS

R. S. Evans, D. L. Bourell, J. J. Beaman and M. I. Campbell
Department of Mechanical Engineering, The University of Texas at Austin, Austin, TX 78712

Abstract

Reaction bonded silicon carbide (RBSiC) has a wide variety of industrial applications and a manufacturing process based on Selective Laser Sintering (SLS) has been demonstrated in previous research at the University of Texas. That study was directed toward semiconductor manufacturing applications and was based on prior indirect SLS methods. Several key research questions were addressed for three main manufacturing phases: preform SLS, binder burnout and reactive infiltration. The current research is focused on development of material systems and manufacturing capability and is directed toward a broader set of potential applications. Preform formation utilizes SiC powder of an appropriate average particle size mixed with a multi-component binder. The preform or green part is then placed in a vacuum furnace to carbonize the binder. The details of the binder chemistry must support accurate SFF shapes and acceptable surface roughness, a strong green part and maintenance of the part shape during the first furnace operation. Finally, the physics and chemistry of the infiltration process, based on the microstructure of the initial green preform, determine the viability of the manufacturing process and the characteristics of the final composite material.

The functionality of metal, polymer and ceramic matrix composites can support the growing SFF industry desire to move beyond functional prototyping and into manufacturing arenas. This project is being explored for more general application to matrix composite materials, especially highly functional systems tailored specifically for SLS. The goal is to establish the governing principles of binder function, carbonization and infiltration as well as to understand the interdependence of these phases in terms of manufacturing application. With this understanding new applications and special SLS composites can support the development of new products and a greater SFF manufacturing presence.

This paper provides an introduction to the material, a look at basic rapid manufacturing trends, an overview of the previous work, a review of relevant RBSiC material science issues, and an outline of the current study.

Why Silicon Carbide?

Material Properties

SiC is an extremely hard, heat resistant, abrasion resistant, chemical resistant, and thermally conductive material. However, it is very difficult to manufacture. Fully dense, sintered varieties of SiC can cost $400 per cubic inch just for raw material. The powdered variety, however, may be purchased by the boxcar for around $2.00/pound. Discovered over a century ago, SiC has been the subject of extensive materials research for many decades [Taylor and Laidler]. Over 140 microstructural variations of the material have been identified, each

associated with certain formation parameters and subtle property differences [Babula]. For this paper, two main variations are important; high temperature α-SiC, formed above 2000°C and relatively low temperature β-SiC with synthesis at temperatures as low as 1150°C, probably as a precipitate or gas-phase deposition. Table 1, compiled from several standard sources, illustrates several advantages of SiC material and puts it in context with aluminum and steel. As with all ceramics, SiC is brittle. However, some fiber-reinforced SiC composites have shown promising impact strength.

Material	Density	Tensile Modulus	Flexural Strength	Thermal Cond.	Melt/ Soft Temp.
Silicon Carbide	3.1 kg/m^3	>400 GPa	550 MPa	120 W/m/K	2800°C
RBSiC	2.9 kg/m^3	200-375 GPa	40-450 MPa	110 W/m/K	1375°C
Aluminum	2.7 kg/m^3	62-70 GPa	240 MPa	150-210 W/m/K	550-650°C
Steel	7.8 kg/m^3	~195 GPa	750-2500 MPa	15-35 W/m/K	300-650°C

Table 1 : Material Properties (for basic comparison only)

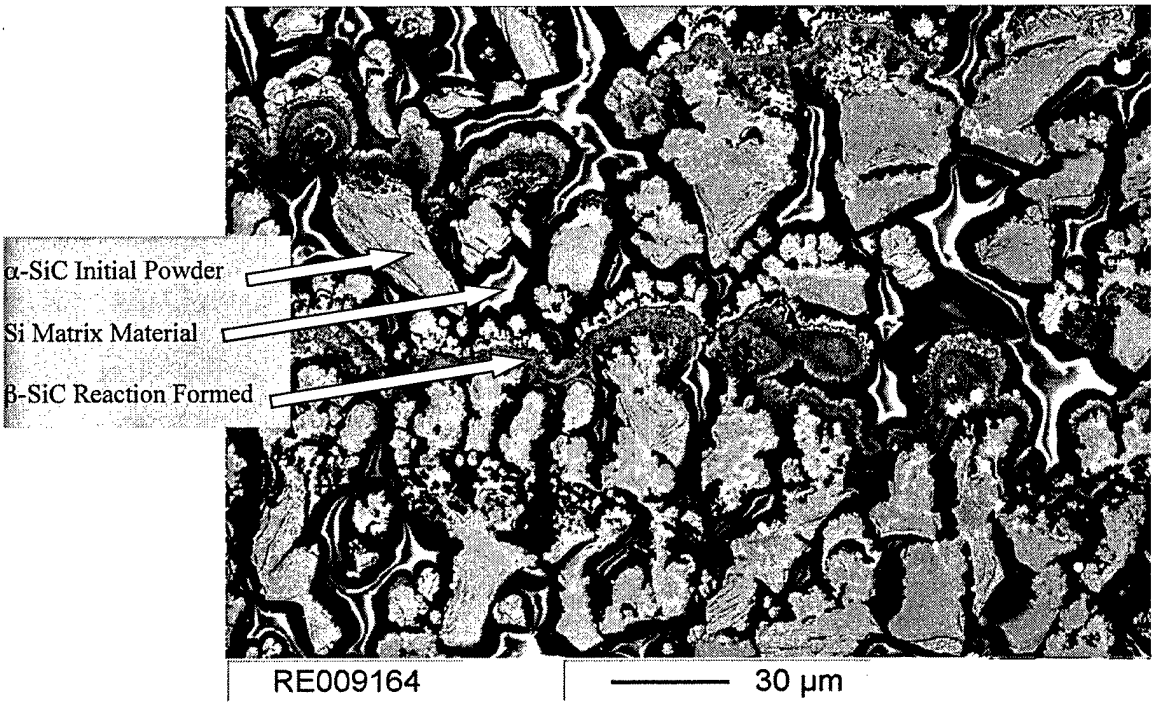

Figure 1 : RBSiC from Laser Sintered Preform
(http://www.fraunhofer.de/english/press/md-e/md1998/f_1298-f5e.html)

Typical manufacturing processes for SiC are pressureless sintering, gas pressure sintering, hot pressing, hot isostatic pressing, chemical vapor deposition, re-crystallization and reaction sintering

-Suyama et al., p.1201

The temperatures, pressures and material preparation of these processes make them costly and impractical for large scale operations. Reaction sintering (pursuing fully dense SiC) and its close relative, reaction bonding (creating a matrix composite) as seen in Figure 1, are considered

the most promising fabrication strategies for SiC materials due to their net-shape capabilities, speed and low cost [Suyama et al., Rajesh and Bhagat]. Suyama, et al., add that the process imparts almost negligible dimensional changes. Figure 1 shows the main elements of RBSiC; α-SiC from the starting powder, β-SiC formed during the infiltration process and remaining Si. Additional details about reactive infiltration are discussed below. Several variations on these processes are found in industry. The process employed by Poco Graphite (www.poco.com) involves machining graphite to final part dimensions and a chemical vapor infiltration process to convert the carbon structure to SiC. Rohm and Haas (www.cvdmaterials.com/silicon.htm) employs a chemical vapor deposition process directly into SiC. Other companies create SiC/carbon powder slurries which are molded into part shapes and directly sintered or reaction infiltrated.

Product Applications

A wide variety of SiC products exist today, as seen in Table 2, but not all of them represent potential for SLS manufacturing. Many have simple shapes due to the difficulty involved in making complex shapes with SiC. Others require fully dense SiC, rather than RBSiC. Finally, those made using certain molding operations are mass produced, which leaves SLS at a disadvantage. However, the ability of SLS to make nearly any shape could put SiC into service for entirely new applications.

Turbine components	Semiconductor	Beams
Automotive	Wear & Corrosion Resistant	Batts
Armor	Components	Posts and Rollers
Burner Nozzles	Heat Exchanger Tubing	Ball valve parts
Metal working equipment	Valve & Valve Trim	Wear plates
Bearings	Hydrocyclones	Kiln furniture
DC Magnetron Sputtering	High Temperature /	Brakes
Faucet Washers	Thermal Components	Foundry equipment
Mechanical Seal Faces	Thermocouple Tubes/Prices	Heat exchangers
Pulp and Paper	Kiln Systems	

Table 2 : Current Applications of SiC Components

Rapid Manufacturing

Rapid manufacturing (RM) may not soon replace mass production, but the economic model advanced by Hopkinson and Dickens, as an example, indicates SLS is a viable alternative to injection molding at product runs up to 14,000 units and with some lower cost RM materials that number would increase significantly. The fit with foundries has been one of integration into previously existing manufacturing standards [McDonald, et al., p.87]. The opportunity for parallel fabrication in SFF also tends to favor smaller parts. Yet, complex parts even now are more cost effectively produced via RM methods [Pham and Dimov]. As an example, the heat exchanger assembly for the Pratt and Whitney PW6000 engine is manufactured using SLS to create the shape of each part before casting in aluminum. The reduced costs of tooling, design freedom and flexibility have been addressed widely in SFF literature, but what may be more critical is the importance of materials research for realizing the anticipated impact of RM [Kai & Fai. p.201, Hague et al.].

Rapid manufacturing will become more of a reality when the properties of the materials that are produced become more acceptable and consistent. This materials research is one of the main stumbling blocks to (RM)...

-Hague, et al., p.30

Even though SLS has the largest material set among SFF techniques [Ryder, et al.] there is a long way to go before designers have the range of materials necessary to address a critical mass of manufacturing tasks [McDonald, et al., p.240]. During this material development a move from low-volume applications toward higher volumes could proceed with improved RM processes, increasing the design of products to be made specifically by SFF techniques.

Previous Project Overview

The previous work was driven by a desire to leverage the capabilities of SFF to develop a new fabrication scheme for RBSiC, particularly for the manufacture of wafer carrier boats. The resistance of SiC materials to thermal shock and corrosion fits well with the challenging constraints of high-temperature semiconductor processing. The coefficient of thermal expansion (CTE) matches well with Si, reducing the particulate contamination and wafer defects when compared to the more traditional quartz fixtures, and contributes to the estimated 20x service life over quartz. Wang's focus was on the physics and chemistry of pressureless liquid Si infiltration of the porous preforms. She established the basic indirect process used to make SiC from SLS performs; laser sintering a SiC powder mixed with binder compounds (green part), carbonization of the binder (brown part) and reactive infiltration of liquid silicon. The novelty of this research was the use of SLS for the creation of SiC performs for reaction bonding. The main developments during Wang's work were an examination of wicking mechanisms in porous media, an analysis of the SiC forming reactions present and ultimately a fabrication process that produced viable parts. Figure 2 shows a part made during the previous study.

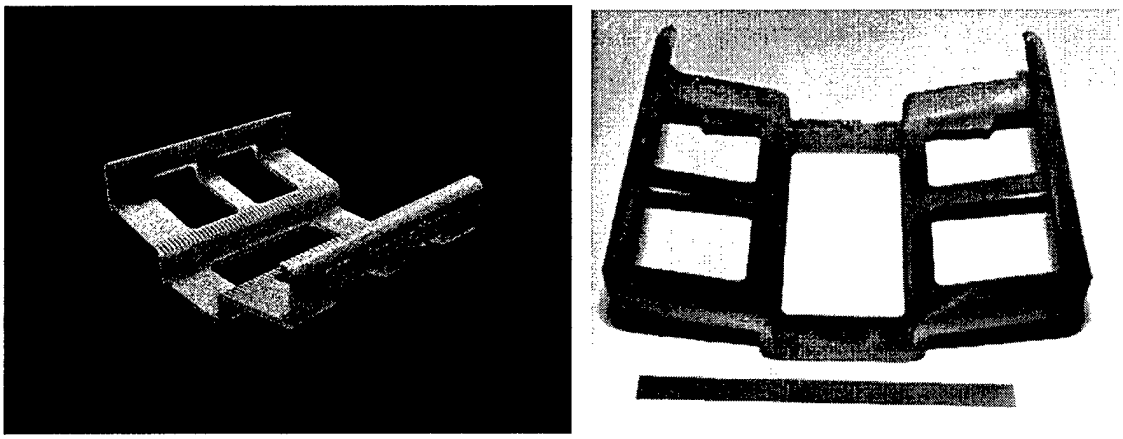

Figure 2 : (a) A Rendering of a Slotted Horizontal Boat. (b) A Silicon Carbide/Silicon Composite Boat Produced by Selective Laser Sintering and Silicon Infiltration. Also shown is a 6-Inch Scale.

Roughly concurrent to the UT work was a study conducted in Germany [http://ikpindy2.verfahrenstechnik.uni-stuttgart.de/RP_IKP/keramik/SiSiC.html]. The purpose of that work was to create a high-SiC content final part. Although SLS was used to form the

performs several differences existed especially in initial powder and additional resin infiltrations, presumably to enhance the carbon structure after carbonization. Figure 1 was taken from information published about that work.

Several key questions from this previous work provide avenues of exploration for the current research. First, the green strength of the preforms was barely adequate for handling the parts and preparing them for the furnace operations. A viable manufacturing operation would need a significant improvement in this area. The density of parts increased both with infiltration temperature (1450-1600°C) and with dwell time (0.1,1 and 5hrs). The flexural strength was at a maximum when infiltration was at 1500°C for 1hr and at 1600°C and 0.1hrs. Relatively low strengths were found at all temperatures for the 5 hr dwell time. The greater final density of parts that underwent longer infiltration dwell times suggests more SiC growth; however, this does not necessarily correlate with better final part performance. The differing strength versus temperature [Wang, p.134] indicates the likelihood that the shorter infiltration (0.1h) has not developed significant regions where the β-SiC has established a fragmented structure, a phenomenon discussed below. In other words, although the density of the parts increased, it is possible that the microstructure supports a weaker final part. Although changing the particle size is expected to improve surface roughness, as Wang suggests, it can have greater influence on other parameters such as part strength or infiltration success. Finally, the coefficient of thermal expansion (CTE) was found to be closer to silicon (~$3.5x10^{-6}$ @ 500°C) than pure SiC (~$4.75x10^{-6}$ @ 500°C). The lowest CTE was from samples formed with the 5 hr dwell which paradoxically suggests lower SiC content.

Successful development of the best composite materials will require deeper understanding of the formation of SiC during infiltration. The structure of the "green part" and the "brown part" after binder decomposition need to be improved and correlated to the structure of the final material. Ultimately, the characteristics of the initial binder and SiC powder mixture will need to be optimized for the best system of processing and final part characteristics.

Key Issues in New Research Effort

Binder Development

The polymer chemistry and function of each constituent in the previous binder system is being examined. A new formulation is being developed based on the knowledge from the previous work, a literature review of liquid infiltration and a focused research effort. The specific elements of the binder study, including constituent chemistry, rheology and green and brown part structures are expected to be published separately and are beyond the scope of this paper. It is anticipated that the uniformity and consistency of the finished parts will be greatly supported by this work. There is a correlation between surface conditions, particle sizes and the packing density achievable in the part bed as may be inferred from the work of Paik et al. The final strength of the material is related to this packing density as well as the dispersion of the constituent materials. Further, the microstructure of the green preform is intimately related to the final properties of the infiltrated part. In addition, this work will be a springboard for studying the mechanics of unsupported, pressureless, reactive infiltration as well as the microstructural elements that evolve through the entire SFF-based manufacturing process.

Material Formation

When liquid Si meets carbon it reacts to form SiC. When a porous (<200 μm pore size) SiC preform is placed in contact with liquid silicon, the silicon fills the preform to at least a height of 2m [Wang]. In the following paragraphs a few challenges are discussed that undermine the simplicity of the previous statements.

A rather significant ~116kJ/mol is released when this reaction occurs [Rajesh and Bhagat]. Wang observed a local temperature increase of 400°C. This heat of reaction, which changes based upon the structure of the carbon, influences the formation of SiC and the characteristics of the final parts. This combined with the significant changes in permeability observed by Rajesh and Bhagat indicate an influence on wicking kinetics and therefore final composite microstructure based on temperature at the onset of wicking. It may be possible to tailor preform characteristics for more rapid or more effective infiltration. Enhanced SiC formation from "solution reprecipitation" due to the increased exposure of C to Si melt which is likely due to carbon diffusing from higher temperature regions of the Si melt and supersaturating others. Favre et al., observed significant SiC growth at the liquid atmosphere boundary, away from the interface between carbon and silicon which they attributed mainly to the diffusion of $CO_{(g)}$ to the SiC grains within the Si melt. The effects of reaction heating, dissolved carbon and other transport phemomena need to be addressed.

A thorough understanding of the wetting characteristics and the driving capillary action from the previous work coupled with a newly available model of transient permeability within preforms for reaction-formed SiC materials [Rajesh and Bhagat] should provide insight into the infiltration mechanics. If the Si is introduced to the preform as a melt, the main SiC formation occurs within the first minute of contact and proceeds to a relatively final thickness of 10-12 μm at carbon surfaces [Favre, et al.]. After this thickness has been reached further growth is inhibited by the extremely low diffusion of carbon or Si through SiC. High compression forces at the grain boundaries cause crystals to break away, causing periodic growth and local breaks [Favre, et al.]. These breaks cause a sudden exposure of carbon to Si and also cracks in the carbon surface itself. In small capillary channels the growth of SiC can choke off the subsequent flow of Si. SiC growth can also occur in other regions where liquid saturation or gas-phase (specifically $Si_{(G)}$, $SiO_{(G)}$ CO and CO_2) transport supports growth. The quick initial boundary growth and the liquid surface growth are both promising SiC formation avenues, but must be understood in practice.

Residual silicon has a detrimental effect on the mechanical properties and reliability of the finished parts [Paik et al.] with fracture of RBSiC dominated by the failure of the Si matrix [Fernandez et al.]. This is especially apparent in maximum temperature, acid resistance and fracture toughness. The sintering study by Suyama et al. generated a remarkably strong sintered material by, "controlling the residual Si size under 100 nm." Fernandez, et al., also observed a significant strength when a continuous SiC structure (from carbonized wood) was a feature of the infiltrated material. This was corroborated by the work of Dyban where larger SiC particles (~100μ) maximized the connection of SiC to SiC within the structure of the infiltrated material. Again, it seems likely that a very capable material may be made, but what is possible within this manufacturing strategy is unclear.

Basic Research Tasks

It is known that the infiltration reaction occurs and that fully dense parts may be created. Yet, we need to explore the transient permeability, the local temperature effects, the reaction kinetics, the kinetics of various chemical reactions, and the evolution of the composite microstructure. These elements must be linked to the nature of the preforms that can be produced via SLS. We want to create a final material system with an interconnected microstructure of SiC that supersedes the limitations of a silicon matrix. One key to this may be in the tailoring of the carbonized brown part which may help to create an interstitial β-SiC structure similar to that formed in RBSiC created from charcoal as discussed by Fernandez et al. and others. This will be challenging due to the complexity of SiC formation coupled with the need for a binder material and initial powder to work within the constraints of SLS processing.

There is a desire to move from proof of concept to a far more refined process and better finished product. Based on this greater understanding of each manufacturing phase we seek methods of part design as well as a deeper understanding of this technology in terms of Rapid Manufacturing. In other words, we want to tie the potential of the microstructure to a system for understanding the tradeoffs across the manufacturing process and incorporating the design of finished parts. More generally, we see the development of new materials as a key driver to the future development of SFF technology in general and expect that this project will generate a template for the more rapid deployment of additional powder-based composite materials in SLS systems.

Conclusion

In this paper we have discussed SiC material, specifically in a reaction bonded form and its applications. The previous work conducted at UT has provided a good foundation for the current effort. The desire within the SFF industry to support more manufacturing presence will require more extensive research into highly functional materials that may be manipulated effectively into useful shapes. This particular material system is complicated but we are confident that it will yield a viable manufacturing alternative for a variety of applications and serve as a basis for additional SFF materials research.

References

Babula, A. J., "Silicon Carbide : Its Nonabrasive Electrical Properties and Applications," IEEE Potentials, Feb./Mar. 1997, p.27-30

Cooper, K. G., Rapid Prototyping Technology : Selection and Application, Marcel Dekker, New York (2001)

Dimla, D. E., Singh, H., Day, M., "Fabrication of Functional Metal Parts Using Laser Sintering – A Case Study," Third National Conference on Rapid Prototyping, Tooling, and Manufacturing Proceedings, 20-21 June 2002, Professional Engineering Publishing, London, p.115-122 (2002)

Dyban, Y., "Structuring of Multiphase Compacts in the SiC-Carbon System. I. Structuring in Green Blanks," Powder Metallurgy and Metal Ceramics, V. 40, No.1-2 (2001)

Dyban, Y., "Structuring of Multiphase Compacts in the SiC-Carbon System. II. Structuring During Sintering," Powder Metallurgy and Metal Ceramics, V. 40, No.5-6 (2001)

Dyban, Y., "Structuring of Multiphase Compacts in the SiC-Carbon System. III. Structuring in Green Blanks," Powder Metallurgy and Metal Ceramics, V. 41, No.3-4 (2002)

Favre, A., Fuzellier, H., Suptil, J., "An Original Way to Investigate the Siliconizing of Carbon Materials," Ceramics International, V. 29, p.235-243 (2003)

Fernandez, J. M., Muñoz, A., Lopez, A.R. D., Feria, F. M. V., Dominguez-Rodriguez, A., Singh M., "Microstructural-Mechanical Properties Correlation in Siliconized Silicon Carbide Ceramics," Acta Materialia, V. 51, p.3259-3275 (2003)

Fischer, P., Karapatis, N., Romano, V., Glardon, R., Weber, H. P., "A Model for the Interaction of Near-infrared Laser Pulses with Metal Powders in Selective Laser Sintering," Applied Physics A., V. 74, pp.467-474 (2002)

Groover, M. P., Fundamentals of Modern Manufacturing : Materials, Processes and Systems, John Wiley and Sons, New York (2002)

Hague, R., Campbell, I., Dickens, P., "Implications on Design of Rapid Manufacturing," Journal of Mechanical Engineering Science, V. 217, pp. 25-30, (2003)

Hopkinson, N., Dickens, P., "Analysis of Rapid Manufacturing – Using Layer Manufacturing Processes for Production," Journal of Engineering Science, V. 217, pp.31-39 (2003)

Kai, C. C., Fai, L. K., Rapid Prototyping : Principles & Applications in Manufacturing, John Wiley & Sons, Singapore (1997)

King, D., Tansey, T., "Rapid Tooling: Selective Laser Sintering Injection Tooling," Journal of Materials Processing Technology, V.132, pp.42-48 (2003)

Lind, J., Kotila, J., Syvänen, T., Nyrhilä, "Dimensionally Accurate Inserts and Metal Components by Direct Metal Laser Sintering," Materials Research Society Symposium Proceedings, V. 625, pp. 45-50 (2000)

McDonald, J. A., Ryall, C. J., Wimpenny, D. I.(editors), Rapid Prototyping Casebook, Professional Engineering Publishing Limited, London (2001)

Paik, U., Park, H. C., Choi, S. C., Ha, C. G., Kim, J. W., Jung, Y. G., "Effect of Particle Dispersion on Microstructure and Strength of Reaction-bonded Silicon Carbide," Materials Science and Engineering, A334, pp.267-274 (2002)

Pham, D. T., Dimov, S. S., "Rapid Prototyping and Rapid Tooling – The Key Enablers for Rapid Manufacturing," Journal of Mechanical Engineering Science, V. 217, pp.1-23 (2003)

Rajesh, G., Bhagat, R. B., "Infiltration of Liquid Metals in Porous Compacts: Modeling of Permeabilities During Reactive Melt Infiltration," Transport in Porous Media, V.36, p. 43-68 (1999)

Ryder, G. J., Harrison, D. K., Green, G., Ion, W. J., Wood, B. M., "Benchmarking the Rapid Design and Manufacture Process," Third National Conference on Rapid Prototyping, Tooling, and Manufacturing, 20-21 June 2002, High Wycombe, UK, p.97-104, Professional Engineering Publishing, London (2002)

Suyama, S., Kameda, T., Itoh, Y., "Development of High-strength Reaction-sintered Silicon Carbide," Diamond and Related Materials, V. 12, p.1201-1204 (2003)

Taylor, A., Laidler, D. S., "The Formation and Crystal Structure of Silicon Carbide," British Journal of Applied Physics, V.1, No. 7, p.174-181, (1950)

Wang, H.Y., "Advanced Processing Methods for Microelectronics Industry Silicon Wafer Handling Components," Dissertation, The University of Texas at Austin, December 1999

Rapid Prototyping of 3D Scaffolds for Tissue Engineering Using a Four-Axis Multiple-Dispenser Robotic System

L. Geng[a], Y.S. Wong[a]*, D.W. Hutmacher[b], W. Feng[a], H.T. Loh[a]. and J.Y.H. Fuh[a]

[a]*Laboratory for Concurrent Engineering and Logistics, Department of Mechanical Engineering, National University of Singapore, 10 Kent Ridge Crescent, Singapore 119260, Singapore*

[b]*Division of Bioengineering, Department of Orthopedic Surgery, National University of Singapore 10 Kent Ridge Crescent, Singapore 119260, Singapore*

Reviewed, accepted August 13, 2003

Abstract

A desktop rapid prototyping (RP) system has been developed to fabricate scaffolds for tissue engineering (TE) applications. The system is a computer-controlled four-axis machine with a multiple-dispenser head. This paper presents the scaffold fabrication process to build free-form scaffolds from relevant features extracted from given CT-scan images for TE applications. This involves obtaining the required geometric data for the scaffold in the form of a solid model from CT-scan images. The extracted scaffold model is then sliced into consecutive two-dimensional (2D) layers to generate appropriately formatted data for the desktop RP system to fabricate the scaffolds. The basic material processing involves the sequential dispensing of two or more materials to form a strand. The four-axis system enables strands to be laid in a different direction at each layer to form suitable interlacing 3D free-form scaffold structures. The multiple-dispenser head also allows the introduction of living cells and additional materials during the scaffold building. The building of the scaffolds with the desktop RP system is described based on the sequential dispensing of chitosan dissolved in acetic acid and sodium hydroxide solution. Neutralization of the acetic acid by the sodium hydroxide results in a precipitate to form a gel-like chitosan strand.

Keywords: Scaffold; Rapid prototyping; Tissue engineering

1. Introduction

In tissue engineering (TE), scaffolds built from synthetic or natural materials serve as temporary surrogates for the native cellular matrix. Rapid prototyping (RP) is suitable for tailoring individual patient-specific scaffold parts because of its flexibility to build complex structures. At present, several RP techniques have been exploited and adapted for generating individual TE scaffolds, such as fused deposition modeling (FDM) [1,2], laminated object manufacturing (LOM) [3], three-dimensional printing (3DP) [4], multiphase jet solidification (MJS) [5] and 3D plotting [6].

*Correspondence author: Dr. Y.S. Wong
Email: mpewys@nus.edu.sg

This paper presents the development of a four-axis multiple-dispenser robotic system to fabricate scaffolds. The process involves the sequential dispensing of materials that coagulate to form inter-lacing strands for the building of the scaffold. An additional property is that the basic structures can be achieved without high temperature, unlike FDM. This enables fabrication with materials or material additives that will otherwise decompose under the high-temperature fabrication condition. It also facilitates the incorporation of proteins and living cells into the scaffold via additional dispensers. This feature makes the process more suitable for tissue engineering applications.

The focus is on the scaffold fabrication technology for TE. The mechanical and structural requirements of TE scaffolds and the pre-requisites for scaffold fabrication techniques are described. Emphasis is on the fabrication process using the robotic dispensing system to build scaffolds. This includes obtaining individual geometrical data to form 3D CAD model and segmenting the model to two-dimensional (2D) layers to generate data for the four-axis multiple-dispensing RP system to fabricate scaffolds automatically.

2. Materials and requirement for fabricating scaffold

2.1 Materials

As the scaffolds for tissue engineering will be implanted in the human body, the scaffold materials should be non-antigenic, non-carcinogenic, non-toxic, non-teratogenic and possess high cell/tissue biocompatibility, so that they will not trigger any adverse cellular reactions after implantation.

In this research, chitosan was used as the scaffold material. Chitosan, which is a naturally occurring amino-polysaccharide, is biodegradable, biocompatible and nontoxic [7]. A high-purity chitosan powder ($C_{12}H_{24}N_2O_9$) is used. The material was prepared by dissolving chitosan in acetic acid to form a hydrogel. The gel was contained in the plastic syringe barrel and dispensed by pressurized air. NaOH solution was used as coagulation and dispensed via another syringe using a motorized plunger.

2.2 Requirement

Besides material issues, the macro- and micro-structural properties of the scaffold are also very important [8, 9]. In general, the scaffolds require individual external shape and well defined internal structure with interconnected porosity.

Ideally, a scaffold should have the following characteristics:

(a). be highly porous with an interconnected pore network for cell growth and flow transport of nutrients and metabolic waste; (b) have suitable surface chemistry for cell attachment, proliferation, and differentiation; (c) possess mechanical properties to match those of the tissues at the site of implantation; (d) be easily fabricated into a variety of shapes and sizes and (e) possess interconnecting porosity so as to favor tissue integration and vascularity. [10, 11]

3. The process

RP is suitable for tailoring individual parts for specific applications and this has a great impact for the biomedical industry. RP already has areas of applications in building prosthetics and mechanical implant structures [12]. These computer models were produced by computer-aided design (CAD) software from computer tomography (CT) or magnetic resonance imaging (MRI) data. Considering the time, flexibility and accuracy requirements, RP technologies are very suitable for application in tissue engineering to fabricate scaffolds.

A general framework for the application of rapid prototyping in the area of tissue engineering is shown in Fig. 1 [13]. A specific area of the patient is scanned by computer tomography or magnetic resonance and the data are imported into a CAD software. The scaffold is designed according to the individual requirements using the CAD software and postprocessed data for the fabrication of the scaffold is then transferred to a RP system to produce the scaffold with a biocompatible and biodegradable material. Living cells are seeded onto the surface of the scaffold after or during the RP process. When the cell number increases following cell culture treatment, the scaffold is implanted into the human body and eventually replaced by natural tissue.

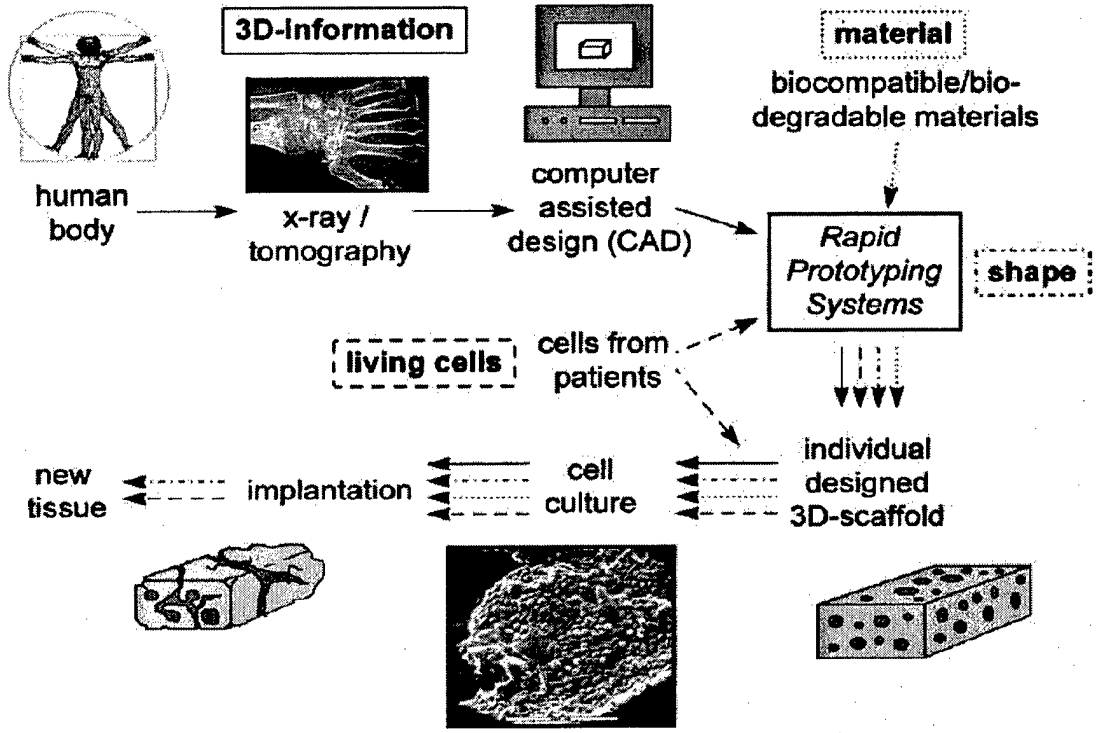

Figure 1. A framework of biomedical RP [13]

3.1 Input data

Computed Tomography (CT) and Magnetic Resonance Imaging (MRI) systems are the two most commonly used medical scanning systems. Through both the CT and MRI scan, a series of digitized gray-scale slice images of the scanned body is obtained. A suitable three-dimensional (3D) computer model is derived from the scanned images using the Materialise's

Interactive Medical Image Control System (Mimics) software [14]. The Mimics software is an interactive tool for the visualization and segmentation of CT / MRI images and 3D rendering of objects. The purpose of the data processing is to produce 3D reconstructions of objects directly from the digitized gray-scale image data and to convert the medical data to the data that can be processed by rapid prototyping systems. This involves separating the data of the tissue of interest from the scan data sets, or generating a certain part of the tissue from the available data. In some cases, the missing part of the tissue is extracted to create the implant for the scaffold building. Once the certain tissue part is separated or created, it can be converted into data formats that are compatible with RP systems, including Standard Triangulation Language (STL), Initial Graphic Exchange Specification (IGES), Standard for the Exchange of product Model Data (STEP), Common Layer Interface (CLI) and Virtual Reality Modeling Language (VRML), etc.

3.2 Robotic dispensing system

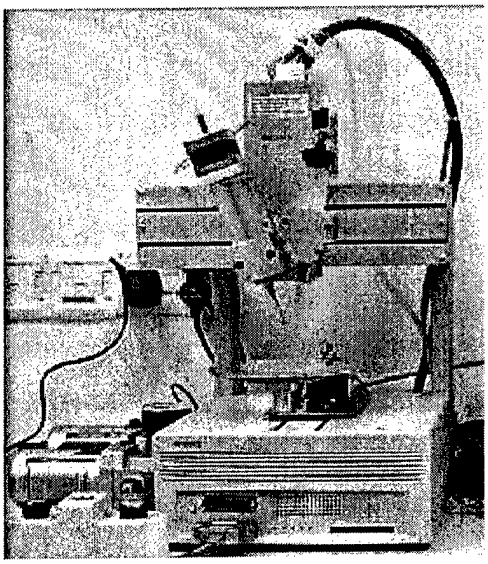

Figure 2. RPBOD system

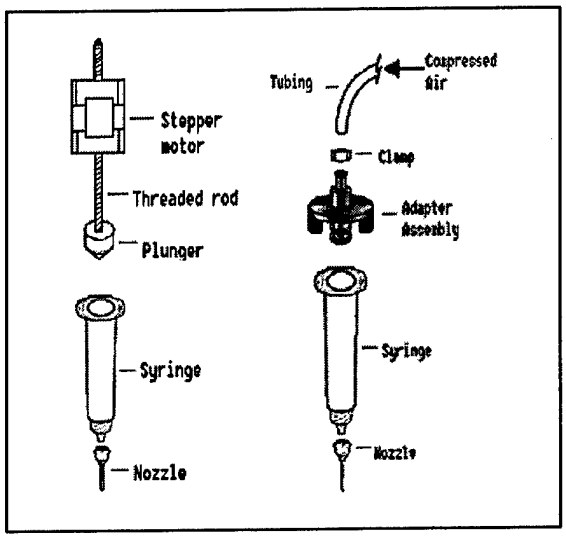

Figure 3. Mechanical & pneumatic dispenser

The rapid prototyping system shown in Figure 2 for the fabrication of scaffolds is a four-axis multiple-dispenser robotic system (RPBOD) based on the Sony Robokits. It is capable of three simultaneous translational movements along the X-, Y- and Z-axes with an added rotary motion about the Z-axis. The three translational movements have positioning accuracy of up to 0.05mm and a minimum step resolution of 0.014mm.

There are two kinds of dispensing mechanisms, pneumatic and mechanical (Figure 3). The pneumatically driven syringe dispenser is controlled by a solenoid-operated pneumatic valve. The mechanical dispenser is controlled by a plunger driven by a stepper motor. By controlling the displacement of the plunger, the dispensing rate can be precisely regulated, particularly at very low flow rate (such as 0.5 μl/sec).

The control software integrates the processes of slicing, which generates sliced layers in the +Z-direction, and dispensing, based on the slicing, to build suitable scaffold layer-by-layer.

3.3 Scaffold building

To generate a scaffold, the chitosan and NaOH are sequentially dispensed in each scan pass. The chitosan fluid was extruded and allowed to contact the base. The coagulation medium (NaOH) follows closely before the chitosan spreads out. The two materials react to precipitate into a strand. As shown in Figure 4, the tip on the right dispenses the chitosan and that on the left dispenses the NaOH solution, positioned approximately 5 mm apart. The dispense sequence is from left to right, and the nozzles are individually timed to dispense only when over the same section.

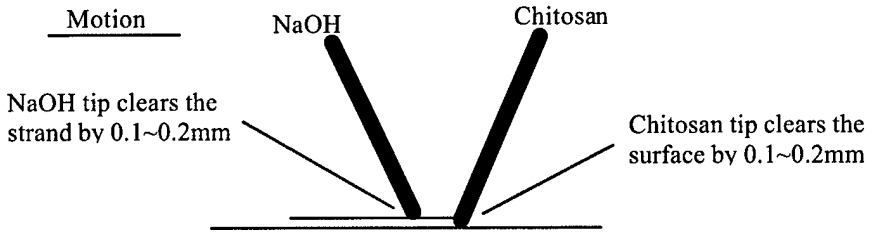

Figure 4. Nozzles position of twin dispensing

Figure 5 shows the process of scaffold fabrication by the dual dispensing method. During the dispensing process, the chitosan gel is dispensed as the dispenser moves (from left to right), leaving the chitosan gel on the base. Immediately following, the the mechanical dispenser drops the NaOH solution to precipitate the chitosan gel.

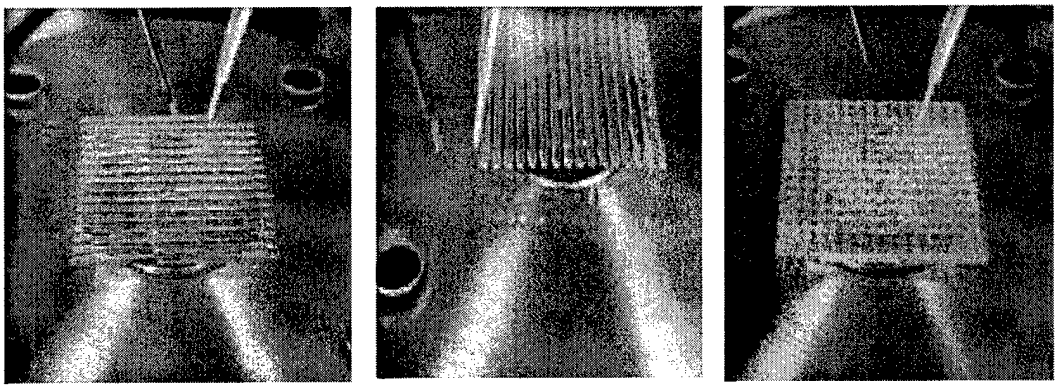

(a) **(b)** **(c)**

Figure 5. Scaffold fabrication process by dual dispensing

(a) Fabrication of first layer; (b) Start of dispensing for second layer;

(c) Scaffold building layer by layer.

After the first layer, the base is rotated by 90 degrees and the dispensers are lifted to a higher level that allows for the chitosan gel for the next layer to lay on the previous layer. The robot then generates the second layer similarly (Figure 5b) and the scaffold is progressively built as layers are sequentially generated in this manner (Figure 5c).

The chitosan scaffold built by this dual dispensing method exhibits excellent uniformity and strength. This has practically eliminated the occurrence of edge curling, the primary cause of strand dragging in chitosan scaffolding fabrication process. Edges of scaffolds are also better defined and good surface uniformity of the top layer is maintained (Figure 6). The process has good reproducibility, once properly calibrated [15].

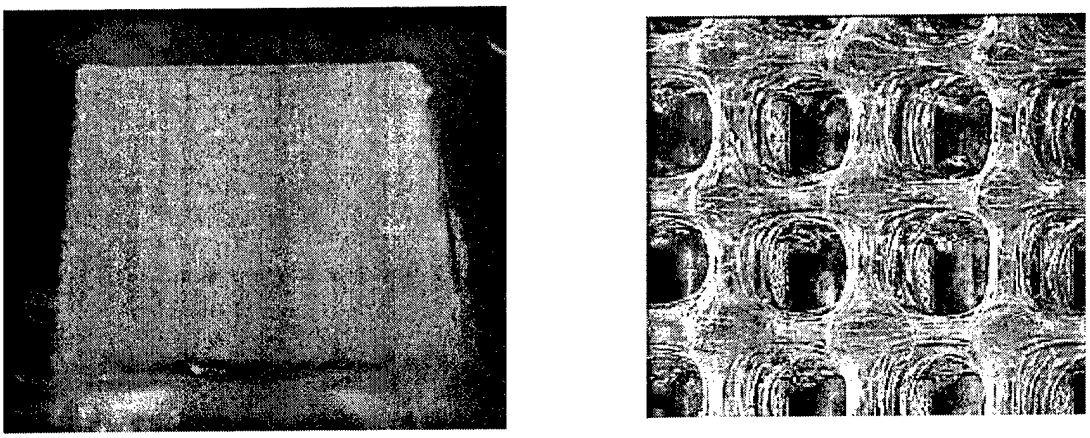

Figure 6. Freshly built chitosan scaffold and the air-dried scaffold under optical microscope (15X)

3.4 Generation of irregular shape scaffold

The advantage of RP technologies is their ability to produce complex 3D shape from a given computer model. As described earlier, the Mimics software enables scan data to be imported and the model of certain tissue part can be appropriately separated or generated, and subsequently converted into a data format that is compatible with the RP system. Figure 7 shows the model of a skull generated from its CT scan images. The bone has been separated from other soft tissues by setting a suitable threshold value. A 3D computer model of a patch has also been interactively created that can fill the hole by using editing and segmentation tools provided in Mimics. The model is then transferred in STL format to the RPBOD. Figure 8 shows the model displayed on the monitor of the RPBOD.

The model can be appropriately rotated before slicing in the Z-direction. The information of these layers is saved as CLI file, which is a simple, efficient and unambiguous format for data input to fabricate the model layer-by-layer. Figure 9 (a) and (b) show four consecutive scanned layers. The direction of the scan lines is set to intersect that of the preceding layer at 90 degrees. Hence, the built strands crossed at each layer to form the scaffold. The quality of built scaffold depends on the characteristics of the materials and experimental conditions, including the concentration, dispenser speed, and dispensing rate.

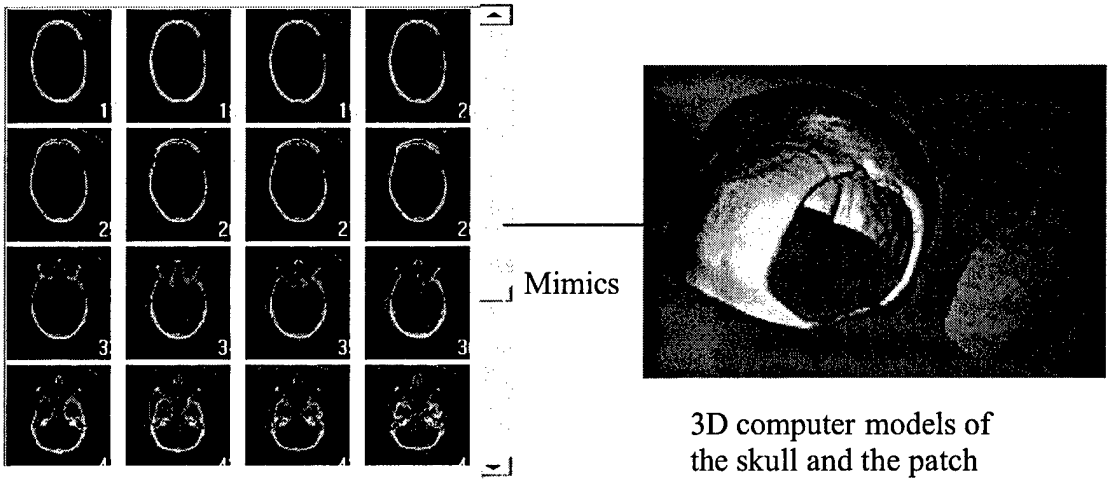

Figure 7. The conversion of CT images to 3D computer mode by Mimics.

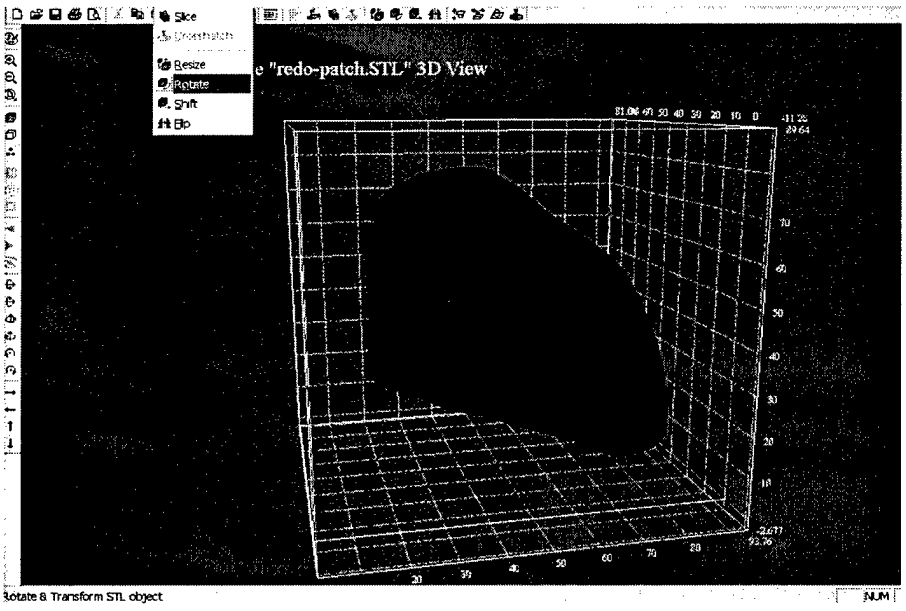

Figure 8 Model of skull defect patch shown on the RPBOD monitor

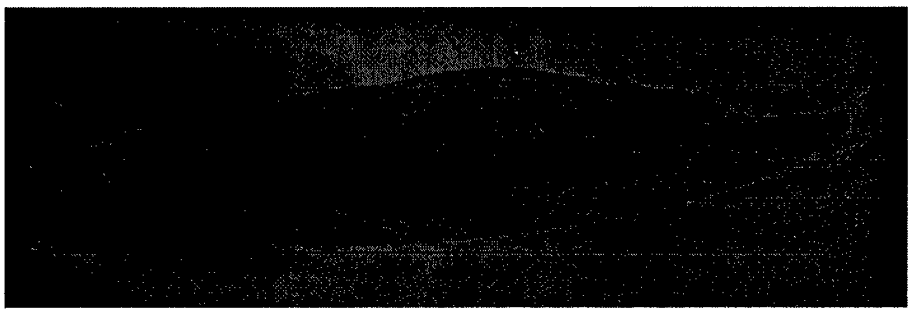

(a) Sliced model

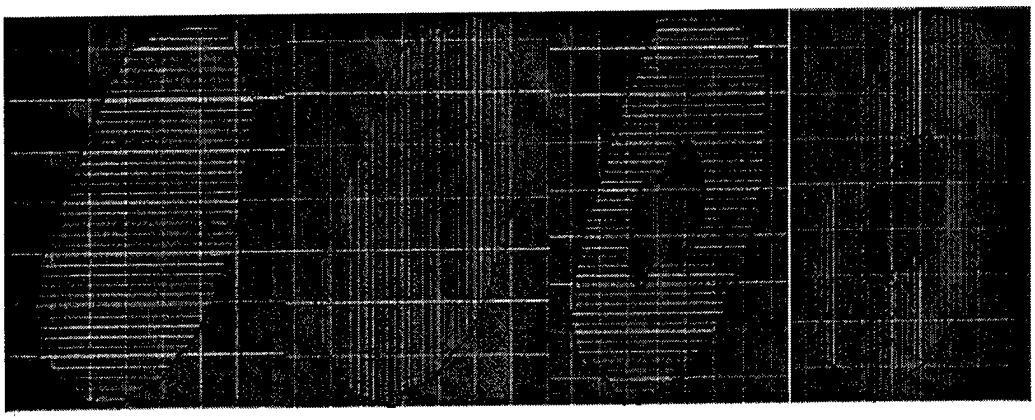

(b) Consecutive layers

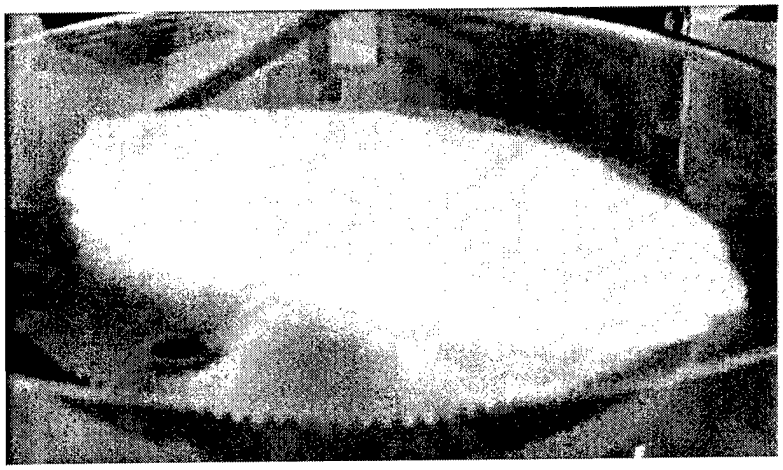

(c) Scaffold part built (15 layers)

Figure 9 Chitosan scaffold of the patch built by RPBOD system

The built part shown in Figure 9(c) is based on the model shown in Figure 9(a) and indicates the potential of the system to build free-form scaffold. Parameters, such as strand distance and layer height, have significant effect on the quality of the built part. Presently, hanging sections of the built part are not supported. Future function will consider providing appropriate support structures.

4. Results and Discussion

The pneumatic dispenser extrudes the viscous gel through a small diameter (0.1 ~ 0.2 mm) needle at a pressure from 2 to 4 bar, depending on the dispensing rate and the size of the needle. However, when the solution is of low viscosity, it flows in an uncontrollable way. Therefore the pneumatic dispenser is not suitable for the dispensing of low-viscosity solution, such as NaOH solution. On the other hand, the mechanical dispenser can achieve dispensing of low-viscosity fluids at low flow rate of 0.5 μl/sec.

Greater flexibility and advantage can be achieved with the method of dual dispensing with different dispensers to suit the nature of the fluid to be dispensed. In the case of single dispensing of one solution into a container of another solution, there is the problem of gradual lowering of concentration and agitation of the solution in the container. These problems are eliminated in the dual and sequential dispensing of the solutions. Additionally, improved adhesion is achieved. Moreover, the operating speed is also improved since agitation of the solution that is dispensed into is not a problem.

5. Conclusion

The RP robotic dispensing system (RPBOD), combining RP technology with tissue engineering, provides much potential for the design and desktop manufacturing of biomedical scaffolds. Rapid prototyping of scaffolds by the RPBOD is presented using a biocompatible chitosan gel for tissue engineering. During the scaffold fabrication, high temperature is not required and with the multiple-dispenser feature, it allows fabrication with materials or material additives, which otherwise decompose under heat, as well as the incorporation of proteins and living cells. The porosity of the resulting scaffolds can be controlled to facilitate good ventilation and cell growth Important challenges for further research are the incorporation of growth factors as well as cells seeding into the 3D dispensing plotting materials. Improvements regarding the mechanical properties and the growth of cells are also necessary.

References

[1] D.W. Hutmacher, "Scaffolds in tissue engineering bone and cartilage", Biomaterials 21 (2000) 2529–2543.
[2] D.W. Hutmacher, S.H. Teoh, I. Zein, K.W. Ng, J.-T. Schantz, J.C, Leahy, "Design and fabrication of a 3D scaffold for tissue engineering bone", in: C.M. Agrawal, J.E. Parr, S.T. Lin (Eds.), "Synthetic Bioabsorbable Polymers for Implants", STP 1396, American Society for Testing and Materials, West Conshohocken, PA, 2000, pp. 152–167.
[3] C. Steidle, D. Klosterman, R. Chartoff, G. Graves, N. Osborne, "Automated fabrication of custom bone implants using rapid prototyping", 44th Int'l SAMPE Symposium and Exhibition, Long Beach, CA, May1999.The Rapid Prototype Development Laboratory Online Technical Paper Library,
http://www.udri.udayton.edu/rpdl/papers.htm.
[4] S.S. Kim, H. Utsunomiya, J.A. Koski, B.M. Wu, M.J. Cima, J. Sohn, K. Mukai, L.G. Griffith, J.P. Vacanti, "Survival and function of hepatocytes on a novel 3D synthetic biodegradable polymer scaffold with intrinsic network of channels", Ann. Surg. 228 (1998) 8– 13.
[5] K.K. Uwe, B. Bernd, A. Carsten, J. Valk, "Creating of bio-compatible high stress resistant and resorbable implants using multiphase jet solidification technology", Time-Compression Technologies '98 Conference: Proceedings, 13– 14 October 1998, Nottingham, UK, Rapid News Publ., London, Great Britain, 1998, pp. 209–214.
[6] R. Landers, R. Mu¨lhaupt, "Desktop manufacturing of complex objects, prototypes and biomedical scaffolds by means of computer-assisted design combined with computer-guided 3D plotting of polymers and reactive oligomers", Macromol. Mater. Eng. 282 (2000) 17– 21.

[7] S. Miyazaki, K. Ishii, T. Nadai, "The use of chitin and chitosan as drug carriers", Chem. Pharm. Bull. 29 (1981) 3067.
[8] Cima LG, Vacanti JP, Vacanti C, Ingber DE, Mooney D, Langer R. "Tissue engineering by cell transplantation using degradable polymer substrates". J Biomech Eng 1991;113:143–51.
[9] Wake MC, Patrick Jr CW, Mikos AG. "Pore morphology effects on the .brovascular tissue growth in porous polymer substrates". Cell Transplant 1994; 3:339–43.
[10] Thomson RC, Wake MC, YaszemskiMJ, Mikos AG. "Biodegradable polymer scaffolds to regenerate organs". Adv Polym Sci 1995; 122:245–274.
[11] Hutmacher DW. "Scaffold design and fabrication technologies for engineering tissues: state of the art and future perspectives". J Biomater Sci Polym E 2001; 12: 107–24.
[12] Cheri Steidle, Don Klosterman, Richard Chartoff, George Graves and Nora Osborne, "Automated Fabrication of Custom Bone Implants Using RP", 44th Int'l SAMPE Symposium and Exhibition, Long Beach, CA, May 1999.
[13] R. Landers, A. Pfister, U. Hubner,H. John,R. Schmelzeisen, R. Mulhaupt, "Fabrication of soft tissue engineering scaffolds by means of rapid prototyping techniques", Journal of Materials Science 37 (2002) 3107 – 3116.
[14] The introduction of Mimics software, the webpage of Materialise (03, July, 2003) : http://www.materialise.com/mimics/main_ENG.html
[15] Tan. K.P. "Improvement of RPBOD system for multiple dispensing and application to tissue engineering" Thesis for Bachelor Degree, Department of Mechanical Engineering, National University of Singapore, 2002.

Rapid Manufacturing with Electron Beam Melting (EBM) – A manufacturing revolution?

Authors
Morgan Larsson, Technical Manager, Arcam AB
Ulf Lindhe, M.Sc., Manager of Marketing, Sales and Service, Arcam AB
Ola Harrysson, Ph.D., Assistant Professor, Industrial Engineering Department, North Carolina State University

ABSTRACT

The Electron Beam Melting technology is the result of intensive research and development and has a wide array of applications within areas such as Rapid Prototyping, Rapid Manufacturing, Tooling and Biomedical Engineering. The technology combines first-class material properties with high build speeds. The presentation will provide a basic understanding of the technology, technical status, applications and ongoing R&D.

Basic process & background

Arcam, founded 1997, has developed a unique Free Form Fabrication (FFF®) technology for Direct Manufacturing of fully dense parts from metal powder. The technology is based on Electron Beam Melting (EBM) and the parts are built up by melting the metal powder layer-by-layer.

The founders were prompted by a vision to revolutionize the art of manufacturing of complex parts. The technology is the result of intensive research and development and has a wide array of applications within areas such as Rapid Prototyping, Direct Manufacturing, Tools for Injection Molding and Die-Casting as well as Biomedical Engineering.

The technology offers a high level of geometric freedom together with first-class material properties. The CAD to Metal® technology provide fully dense metal with material properties identical with or close to the target metals used. Most conductive materials can be used although steel and titanium alloys the only materials available as per today. The strategy in the development is to combine excellent material properties with high build speeds.

With its ability to directly process complex geometries, the Electron Beam Melting process is ideal for direct manufacturing of complex parts in low volumes. The process enables customization of parts and parts optimized for the CAD to Metal process can feature geometries that cannot be achieved in other manufacturing technologies, thus providing superior performance in the part and value to the

customer. The process works directly from CAD data and is fast. The designer can have a fully functional detail within 24 hours from completion of the design. The process often requires significantly less lead-time than sand casting or investment casting.

The combination of Electron Beam Melting and vacuum provide high power and good environment for the process resulting in excellent material properties.

The major difference between the Electron Beam Melting process and methods such as Laser Sintering/Laser Melting is efficiency of the Electron Beam gun compared with a laser. The electron beam technology is several times more energy efficient than laser technology resulting in less power consumption and lower maintenance and manufacturing costs. Arcam is currently using a 4 kW EB gun on its standard machine. Reflection in the pool of melted metal is also a non-issue with electron beam technology.

The availability of sufficient power in the heat source in any fully melting freeform fabrication system is of key importance to achieve good material properties and high build speeds.

Electron Beam Melting (EBM)

The fundamental idea behind the CAD to Metal® technology is to build up metal details in layers of metal powder, each of which is melted by an electron beam to exactly the geometry defined by the computer model.

The part is first designed in a 3D CAD program. The file is transferred to pre-processing software where the model is sliced into thin layers. The parts are built up layer-by-layer by the Electron Beam Melting (EBM) process in a vacuum chamber. On completion of the CAD to Metal Process the net-shape part is cleaned and can be finished as necessary by conventional methods.

The electron beam is generated in an Electron Beam Gun situated on the top of a vacuum chamber. The Electron Beam Gun is fixed and the beam is deflected to reach the entire building area.

The electrons are emitted from a filament, which is heated to high temperature. The electrons are then accelerated to half the speed of light in an electric field. The beam of electrons is controlled with two magnetic fields. The first acts as a magnetic lens and is responsible for focusing the beam to the desired diameter. The second magnetic field deflects the focused beam to the desired point on the building table.

Advantages and disadvantages

Electron Beam Welding has become a vital technology in many industries. Some of its benefits include:

Ability to achieve a high energy level in a narrow beam.
Vacuum melt quality can yield high strength properties of the material.
Vacuum environment eliminates impurities such as oxides and nitrides.
Permits welding in refractory metals and combinations of dissimilar metals

Electron Beam Melting benefits from all of these factors in the same way. Compared with laser sintering/melting additional benefits include:

Higher efficiency in generating the beam of energy resulting in lower power consumption as well as lower maintenance and installation costs
High actual overall power resulting in high build speeds
Deflection of the beam can achieved without moving parts resulting in high scanning speed and low maintenance.

Some apparent disadvantages of electron beam technology are:

Requires vacuum which adds another system on the machine which cost money and must be maintained [Added benefit: Vacuum eliminates impurities and provide and good thermal environment for freeform fabrication]
Electron beam technology produces X-rays while in operation [Solution: The vacuum tank shields the rays perfectly if properly designed.]

Process availability and current use status

As per June 30th, 2003, 8 units have been built with a 9th system in production. Four of the systems are situated at Arcam while two beta-systems where installed at companies in Sweden during 2002. The present model was launched in December 2002 and during 2003 two of these systems have been installed. One system is in operation in Italy and one system at NC State University in Raleigh, North Carolina, USA.

The best applications, now and in the future

Present R & D is focusing on parts for high performance applications within automotive and aerospace industry as well as biomedical applications such as implants. Typical applications are complex parts manufactured in low volumes where casting and machining would require too much of lead-time, machine time or scrapping of material.

The technology can also be used to manufacture parts featuring geometries that cannot be achieved in other manufacturing technologies, thus providing superior

performance in the part and value to the customer. Examples of such applications are:

Complex lattice/framework structures for lightweight design
Internal cavities for lightweight design, weight distribution optimization and flow control
Optimization of material and stress distribution
Conformal cooling channels

The technology is used by teams within the car racing industry for fabrication of high performance parts and prototypes.

Fabrication of custom designed orthopedic implants can benefit from efficient freeform fabrication in metals such as commercially pure and alloyed titanium. There is a future for customized Knee- and Hip-implants that will provide better fitting and longer lasting prostheses and most areas of orthopedic implant surgery can benefit from customized implants.

North Carolina State University has several research projects related to customize implant technology. Areas of research include

Optimize the bone-implant interface for better performance
Reduce bone remodeling due to better stress distribution
Customize implant due to size and shape of Tibia and Femur.
Fabrication of implant components in titanium using the EBM-machine

Custom Implants

Each year over 500,000 Americans go through a hip or knee implant surgery to restore the function of a worn out joint. One of the main problems is that we are all different and the generic implants don't fit perfectly on most people, decreasing the longevity and the function of the implant. To improve the current generic implants, an effort has been made at North Carolina State University to design custom implants based on a Computed Tomography (CT) scan of the particular patient. The CT-scan is converted into a CAD-model of the patient's joint and a custom implant can be designed with optimal fit, shape and geometry.

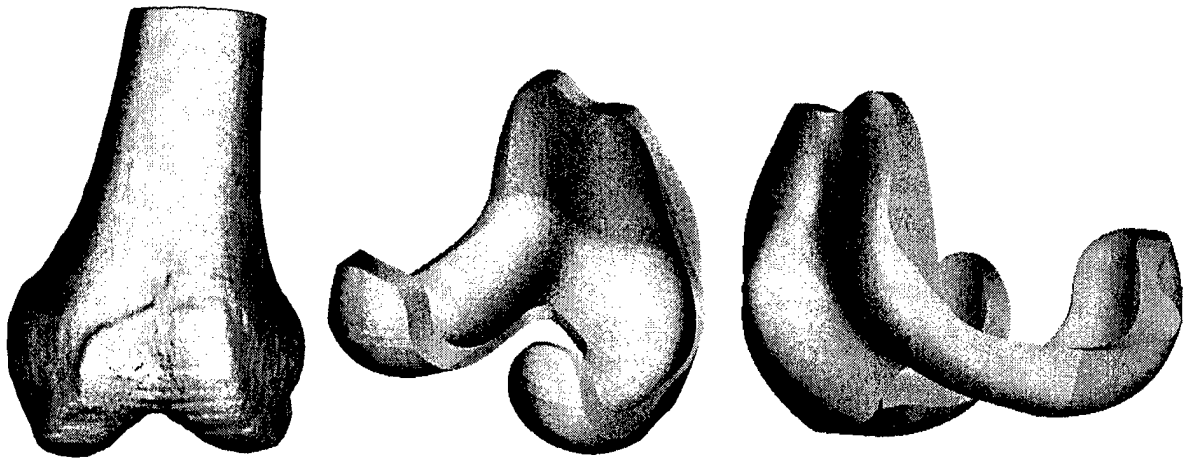

The custom designed implant component could be fabricated through investment casting using an RP-pattern as a master, but would take a considerable amount of time and would be labor intensive, making the implant prohibitively expensive. Using the EBM-technology and the newly developed titanium alloy, the implant component could be fabricated in a matter of hours with very little labor involved using the same manual finishing as with conventional implant fabrication.

Plates for repair of severe bone fractures

Titanium and stainless steel plates are often used to repair and secure severe bone fractures on both humans and animals. The standard bone plates come in different sizes and are normally flat with evenly distributed holes. The surgeon spends a considerable amount of time in surgery to shape the bone plate to conform to the patient's specific anatomy using hand tools. This is an iterative process that prolongs the surgery, increasing the risk of trauma and infection. In many cases it is difficult to align the evenly distributed holes with the bone to attach the screws. In a new project at NCSU, custom designed bone plates are being developed using patient specific CT-scans and the EBM-technology. The surgeon will decide where to place the holes for the screws to achieve the optimal result and the plate is designed to perfectly conform to the curvature of the bone.

Materials

In theory, most conductive metals can be used in the process. To convert theory into reality Arcam is devoting significant resources to R&D in materials sciences in order to constantly develop and refine the CAD to Metal process for an increasing number of metals and alloys. Partners in materials R&D include companies and organizations such as

Chalmers University of Technology, Göteborg, Sweden
Max Planck Institute, Düsseldorf, Germany
North Carolina State University, Raleigh, NC, USA
Volvo Aero Corporation, Sweden

The CAD to Metal® process fully melts the metal powder in order to provide fully-dense metal with material properties identical with or close to the target metals used. Parts are built up in vacuum under strict temperature control.

Initial development of the technology was carried out with iron-based metals and the process has been verified for the following materials:

Tool Steel
Low Alloy Steel
Alloyed Titanium
Commercially Pure Titanium

The current build volume that has been achieved is within a 200x200x160 mm envelope with massive parts in steel having a maximum size limitation of some 150x150x160 mm. The accuracy is within +/- 0.3 mm and is comparable to castings.

Mechanical Properties

	Ti6Al4V	**H13**
Hardness	30-35 HRc	48-52 HRc
Tensile Strength (Rm)	930 Mpa / 135 ksi	1300 Mpa / 190 ksi abt 1500 Mpa/ 220 ksi after heat treatment
Yield Strength (Rp0.2)	880 Mpa / 125 ksi	1000 Mpa /144 ksi
Modulus of elasticity	128 000 MPa	210 000 MPa
Elongation	> 10 %	N.A.
Microstructure	Lamellar alpha-phase with larger beta-grains. The material has a naturally aged condition directly from the process	Martensitic structure with a typical grain size between 10-30 mm due to fine uniform vanadium carbide dispersion.

DIRECT FABRICATION OF METAL ORTHOPEDIC IMPLANTS USING ELECTRON BEAM MELTING TECHNOLOGY

O. L. A. Harrysson[1], D. R. Cormier[1], D. J. Marcellin-Little[2], K. R. Jajal[1]

[1] Department Of Industrial Engineering, North Carolina State University, Raleigh NC 27695,

[2] Department of Clinical Sciences, North Carolina State University, Raleigh NC 27606

Reviewed, accepted August 13, 2003

Abstract

Metal orthopedic implants have been used for many decades with great success. Replacement joints and plates for bone fractures are usually made from titanium, cobalt-chromium or stainless steel. Through recent advancements in biomodeling, custom orthopedic implants can be designed. However, fabrication of these custom implants can be prohibitively expensive with traditional processes. With the introduction of Electron Beam Melting (EBM), direct fabrication of fully dense metal components is possible. In this paper, the development of titanium for the EBM-process will be discussed, and direct fabrication of custom designed orthopedic implants made out of steel and titanium will be demonstrated.

Introduction

Over 500,000 Americans undergo joint replacement surgery each year, with hip and knee implants being the most common. The number is predicted to exponentially increase over the next couple of decades[1]. Many different types of bone plates are used to fixate bones after a severe fracture or after an osteotomy. Joint implants and bone plates are usually made out of stainless steel, titanium or cobalt-chromium and come in standard sizes and generic shapes. Even though total joint replacements have been successfully used for several decades, the longevity of the implant components is not satisfactory in many cases, especially in younger patients [1, 2]. One of the most common causes for implant revision is loosening of the component, which is mostly caused by bone remodeling [3]. Bone is a living tissue that is constantly changing due to external forces to optimize its structure and minimize its weight [4]. Bone will increase in density when experiencing a dynamic load, and it will decrease in density when experiencing a static load or no load at all. This is a common problem for astronauts when spending an extended amount of time in microgravity. Older people experience the same problem when they become less active, and their condition is referred to as osteoporosis.

When implanting a joint replacement, the affected portion of the joint must be removed to provide healthy bone to interact with the implant [5]. Modern implants are coated with a porous titanium coating on the bone-implant interface surface to enhance and promote bone ingrowth. These implants do not use any type of adhesive to secure the implant component to the bone and solely depend on the bone ingrowth to provide a secure and stable attachment. This is the preferred approach to be used on all healthy patients with sufficient bone growth. Due to the current manual surgical tools available to the surgeon, the bone-implant interface on a standard knee implant is designed with straight, flat surfaces (see figure 1.) [6].

[1] Data provided by American Academy of Orthopaedic Surgeons, Dept. of Research and Scientific Affairs

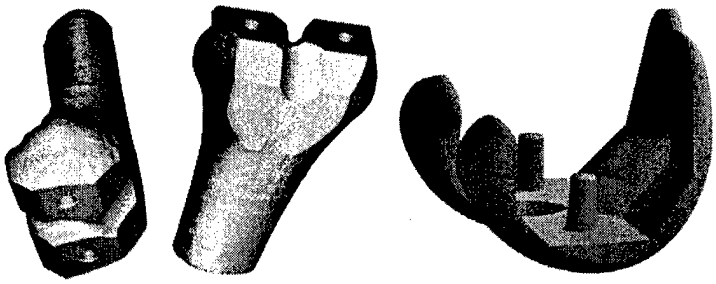

Figure 1. Computer models of a human distal femur prepared for implantation and a generic femoral implant component.

The geometry limitations cause areas with increased pressure and areas with decreased pressure, which causes bone remodeling and finally loosening of the implant components. To further increase the problems, all humans are different, and standard implants only come in 5-7 sizes with generic shapes. The longevity of the implant is highly dependent on the initial fit and how well it resembles the natural shape of the joint [7]. Hip and knee implants have had the same basic design for several decades, which have been limited by the hand tools available to the surgeons. The manual saws and drills can only produce straight cuts and holes, and the precision is highly dependent on the surgeon's skill. Recently, two robotic surgical systems have been commercialized that can perform the cutting and drilling operations with far better precision using end mills as actuators [8, 9, 10]. A robot also has the ability to easily machine freeform surfaces, which eliminates the previous design restrictions on implant components.

The articulating surfaces of a knee implant have a generic shape that might change the gait for many patients. These have been well-known problems for a long time, and in the '70s, several attempts were made to develop custom-sized implants that would fit better. However, the fabrication technologies available at that time made it prohibitively expensive to produce custom parts. The custom sized implants were based on radiographs, which was a fairly inaccurate method due to the 2-dimensional limitations. Most modern orthopedic implants are manufactured through investment casting, which is an excellent fabrication technology that provides high precision parts with good surface finish. Unfortunately it is expensive in small quantities. Solid freeform fabrication (SFF) technologies have enabled manufacturers to produce small quantities through investment casting at a reasonable price, opening up new possibilities for custom design and fabrication of orthopedic implants.

Recent advancements in medical imaging and image processing have enabled custom design of biomedical implants based on patient specific Computed Tomography (CT) data [11,12]. The CT data is edited, and an accurate 3D-model of the joint is created and exported as an stl-file. A different software is used to convert the stl-file into a CAD-model that can be used as the base for the custom designed implant components. Several SFF-technologies can be used to produce a master pattern for investment casting, but producing a finished implant component is still time consuming and labor intensive. With the introduction of the Electron Beam Melting (EBM) machine by Arcam (Sweden), a new possibility for fabrication of custom implant components has become available. Initially, the EBM technology was only available with tool steel, which is not a biocompatible material. In theory, the EBM machine can process most

materials that are electrically conductive, and a collaborative effort between North Carolina State University and Arcam AB was initiated to develop titanium for the EBM process.

To enable clinical testing of the custom designed implants, an animal study is the first step, and collaboration between the Industrial Engineering Department and the Veterinary School at NCSU was initiated [13]. Surgeons at the veterinary school have developed generic hip implants for canines that are currently being implanted on a weekly basis. At this time, no commercial knee implants for canines are available due to the number of sizes that would be needed to accommodate most patients. However, the demand is present. The idea of custom designing and fabricating knee implant components for canines became an interesting solution for the veterinary surgeons at the same time as it would serve as a clinical trial for humans. A CT-scan of a potential patient was acquired, and a custom femoral component was designed in collaboration with the orthopedic surgeons. Both the articulating surface and the bone-implant interface surface were custom designed based on the CT-data.

This paper describes the development of the titanium powder for the EBM process as well as the initial fabrication of the first custom implant components. The traditional investment casting process of implant components is compared to the EBM fabrication.

Figure 2. Computer models of a custom designed implant component for a canine stifle joint.

Material and Methods

As a first step to enable direct fabrication of custom designed orthopedic implants using the Electron Beam Melting technology, the process parameters for titanium (Ti6Al4V) were developed. North Carolina State University partnered with Arcam AB in the development, which took place at Arcam's facility in Mölndal, Sweden. Both Ti6Al4V and pure titanium are commonly used for biomedical implants. Pure Ti is softer and less suitable for high impact applications. The first challenge was to find a supplier that offers a Ti powder with the right composition and particle size, which cannot be disclosed at this time. The particle size is very important for the final result and affects the flow of the powder and the melt pool behavior. For each new material, a long list of processing parameters must be developed through experimentation. The initial parameters are calculated based on material dependent factors such as melting temperature and flow characteristics. Each parameter is optimized through an iterative process based on testing and evaluation. To further complicate matters, the process parameters are geometry dependent as well and require a vast amount of testing to fully develop. At the

present time, parameters for many types of geometries have been developed and successfully fabricated, however no custom designed implant component has been fabricated in titanium. The processing parameters and the powder composition for the Ti6Al4V is proprietary and cannot be disclosed at this moment but the processed material properties are reported in the next section.

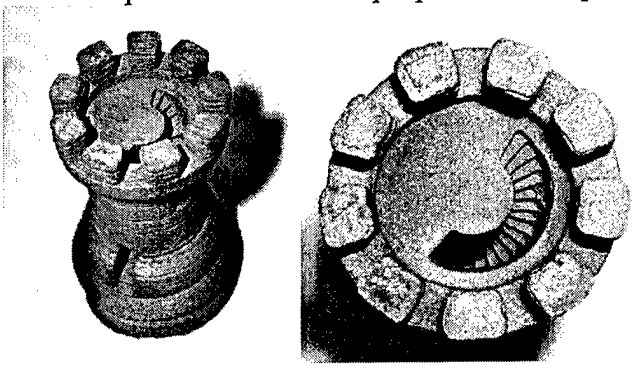

Figure 3. Chess piece built of Ti6Al4V in the EBM S12

The Electron Beam Melting process is powder based, and the excess powder supports the structure during the build phase. It does not eliminate the need for support structure, however. The parts are built on a substrate, and the part and start plate are kept at an elevated temperature throughout the build to minimize residual stresses. When the build is completed, the part and substrate will cool down and a shrinkage of 1.4 % for tool steel will take place that has been compensated for through the software prior to the build. The part tends to shrink towards the center causing a curling or bending motion of the edges. To prevent distortion, support structure is used to secure the part to the substrate and to secure overhanging structures to the underlying structure. The orientation of a part is very important considering the amount of support structure needed and the surface finish of the final part. On thin features with down facing surfaces, "icicles" can form that will affect the surface finish and complicate the finishing of the part. At the present time, no automatic support generation for the EBM process is available. If Magics from Materialize is used to generate support, substantial editing is needed since excessive support is generated. For this project, the implant component was oriented on its side, and support structure was manually created directly in SolidWorks. When building parts with very thin cross sections, it is difficult to effectively transmit enough heat through the part to keep the elevated temperature without over melting the powder. To solve this problem, a "dummy" structure was added as an artificial means to impart more heat to each. In this case, a large diameter cylinder was added to increase the total melting area for each layer.

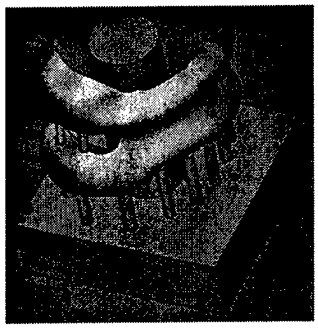

Figure 4. Computer model showing the implant with support and heat sink

As a time and cost comparison, a canine stifle joint component was fabricated using the Electron Beam Melting machine and was compared with traditional investment casting using an RP-pattern as a master. It was decided to use an SLA-190 to fabricate the master pattern to be used for the investment casting process and a QuickCast model of the implant was produced. Due to the small and thin geometry of the canine femoral component, it was difficult to drain the resin from the model leaving an almost solid RP-pattern. Several attempts of reorienting the component and creating drain and vent holes still did not deliver a hollow structure sufficient for the QuickCast process. To complete the investment casting process, an RTV-mold was created using the SLA-pattern and a wax pattern was cast.

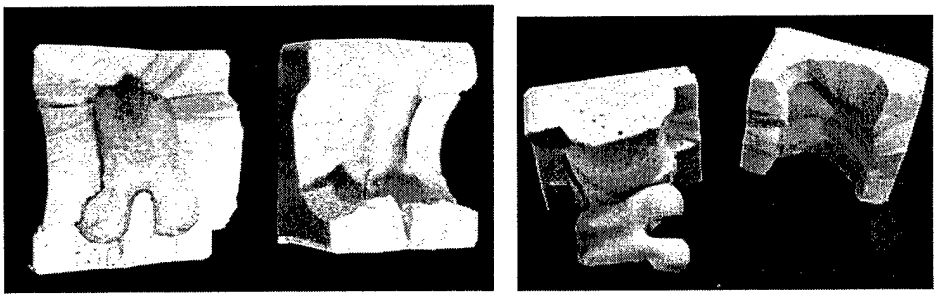

Figure 5. RTV mold with SLA RP-master (L) and resulting wax pattern (R)

The wax pattern was attached to a wax sprue and placed in an investment-casting flask. Quikvest was used as the ceramic media and poured around the wax pattern. The flask was placed in a convection oven to remove moisture and later fired in a high temperature furnace according to the manufacturer's recommendation. For this comparison, aluminum was used for the casting.

Results

The material properties of the EBM processed titanium powder are very similar to conventionally processed titanium. The processed titanium is fully dense and is biocompatible in accordance with FDA regulations. The Ti6Al4V parts fabricated in the EBM process feature good machinability and can be machined as stock Ti6Al4V parts. Pure titanium is under development but the material properties are not publishable at this time. The chemical composition of the EBM processed Ti6Al4V is as follows:

Element	Weight- %
Nitrogen (N)	0.01
Oxygen (O)	0.19
Aluminum (Al)	**6.2**
Vanadium (V)	**4.5**
Iron (Fe)	0.45
Nickel (Ni)	0.037
Chromium (Cr)	0.03
Sulphur (S)	< 0.01
Manganese (Mn)	0.04
Tin (Sn)	1.3
Zirconium (Zr)	< 0.02

Table 1. Typical chemical composition of EBM processed Ti6Al4V (Source: Arcam Ti6Al4V Data Sheet)

The mechanical properties of the EBM processed Ti6Al4V are as follows:

Property	
Hardness HRc	30-35 HRc
Tensile Strength, R_m	930 MPa 135 000 psi
Yield Strength, $R_{p0.2}$	880 MPa 120 000 psi
Elongation	10%

Table 2. Mechanical properties of Ti6Al4V (Source: Arcam Ti6Al4V Data Sheet)

At the time of writing this paper, the processing parameters for the Ti6Al4V were not fully developed for thin walled structures like the stifle joint component. As a proof of concept, the custom designed stifle joint implant was fabricated on the EBM machine using the commercially available tool steel H13. The total building time for the implant was 5 hours. After the part had cooled down to room temperature, the support structure was removed using a rotary cutting tool and the articulating surface was polished to a mirror finish. The total finishing time was approximately 2 hours, which would be similar if it had been fabricated out of titanium. The total setup time for the EBM machine was approximately 2 hours and the implant was left to cool down over night.

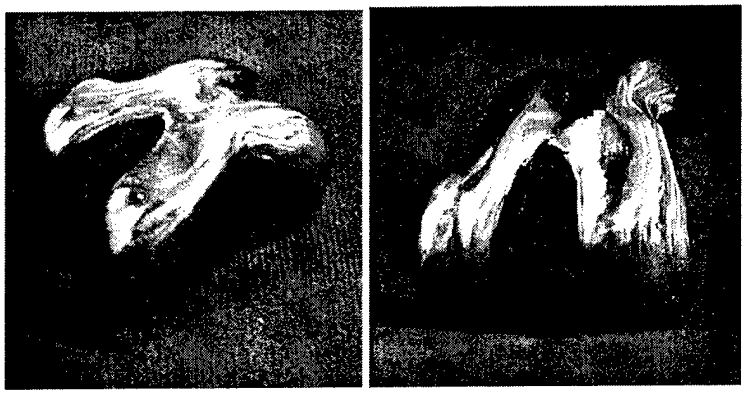

Figure 6. Custom designed knee implant processed on EBM S12

The investment-cast implant took considerably longer time to complete with many more steps. The total time for the investment cast implant from stl-file to finished product was 78 hours compared to 25 hours for the EBM process. A considerable amount of time was spent waiting for the RTV mold to cure as well as drying the investment. A total time of 11 hours of labor was spent on the investment cast version compared to 7.25 hours for the EBM version. The total machine time for the EBM machine is 8.25 hours as compared to 8.5 for the SLA machine. The hourly rate for an EBM machine is slightly higher than a modern SLA machine, but the investment cast version requires additional equipment such as a convection oven, a furnace for firing the investment, as well as melting the metal, and additional tools needed for the mixing of investment and RTV rubber.

Investment Casting	Hours	EBM	Hours
Start with STL		Start with STL	
Prepare SLA Build File	1	Prepare EBM Build File	1.5
Startup SLA	0.5	Startup EBM Machine	2
SLA build time	8	Draw Vacuum	0.75
Clean and postcure	3.5	Heat Start Plate	0.5
Sand SLA pattern	0.5	EBM Build Time	5
Prepare to Pour Silicone	1	Cool down	12
Silicone Cure time	24	Remove sintered powder	0.25
Finish silicone mold	0.5		
Wax casting	1		
Build wax tree	0.5		
Mix and pour investment	0.5		
Dry investment	24		
Fire investment	10		
Pour metal	0.25		
Cool down	1		
Cut off tree	0.25	Cut supports/ remove start plate	1
Clean/Polish	1.5	Clean/Polish	2
Total	**78**	**Total**	**25**

Table 3. Time comparison between investment casting and EBM processing of custom designed implant

Discussion and Conclusions

It is the authors' opinion that the EBM technology can successfully be used to fabricate custom designed implants for knees, hips, elbows, shoulders, fingers, and bone plates in titanium. Even though the initial results appear promising, additional material development will be necessary to optimize the processing parameters for Ti6Al4V and Ti. There are differences between processing steel and titanium using the EBM technology. The build time for titanium is approximately half of that for steel, however the cool down must take place under vacuum inside the build chamber. There are other potential advantages with using the EBM technology to fabricate custom designed orthopedic implants that can not be achieved through traditional processes such as investment casting. In the case of a knee implant component, it is desired to have a very hard and smooth surface finish on all articulating surfaces and a soft and porous bone-implant interface. To achieve this through investment casting, a porous coating is applied to the bone-implant interface surface through a sintering process. Similar coatings are applied to hip, elbow, and shoulder implants to promote the bone ingrowth in selected areas. The Electron Beam Melting technology has the prospect of fabricating parts with functional gradient microstructures, which would be very useful for orthopedic implants. This would allow for the porous surfaces to be directly designed into the components. Further, the EBM technology lends itself to deposit multiple materials that is of highest interest to the orthopedic implant industry as well. Often orthopedic implant components are made out of several materials to achieve the desired properties. Modular hip implant systems are often combined out of both titanium and cobalt-chromium components.

References

1. Taylor J, Rorabeck C H, Bourne R B , et al: Total Knee Arthroplasty in Patients 50 Years or Younger: Long-Term Follow-Up. American Academy of Orthopedic Surgeons 2000, Paper No 185, Orlando, AAOS.

2. Knutson, K., S. Lewold, et al. (1994). "The Swedish knee arthroplasty register. A nation-wide study of 30,003 knees 1976-1992." Acta Orthop Scand 65(4): 375-86.

3. Robertsson, O., K. Knutson, et al. (1999). Knee Arthroplasty for Osteoarthrosis and Reumatoid Arthritis 1986-1995. 1999 American Academy of Orthopaedic Surgeons, Anaheim.

4. Chaffin, D. B., G. B. J. Andersson, et al. (1999). Occupational Biomechanics. New York, John Wiley & Sons, Inc.

5. Krackow, K. A. (1990). The Technique of Total Knee Arthroplasty. St. Louis, The C. V. Mosby Company.

6. Lotke, P. A. (1995). Knee Arthroplasty. New York, Raven Press Ltd.

7. Ho, S. C., H. R.D., et al. (1995). "Robot Assisted Knee Surgery." IEEE Engineering in MEdicine and Biology(May/June): 292-300.

8. Pokrandt, P., A. Both, et al. (1999). Computer Assisted Surgery Planning And Robotics By orto MAQUET. 4th International Workshop on Rapid Prototyping in Medicine & Computer-Assisted Surgery, Erlangen, Germany.

9. Pransky, J. (1997). "Robodoc - surgical robot success story." Industrial Robot 24(3): 231-233.

10. Vander Sloten, R., V. A. G., et al. (1998). Robot Assisted Total Knee Arthroplasty Enhances the Total Quality of the Bone Cuts. 11th Conference of the ESB, Toulouse, France.

11. Ola L.A. Harrysson, Customization of Knee Implants and Optimization of Bone-Implant Interface, Ph.D. dissertation, December 2001, Copyright registered in 2003

12. Yasser A. Hosni, Ola L.A. Harrysson, Design and Manufacturing of Customized Implants, IERC 2002, Orlando, Florida, USA, May 19-21, 2002.

13. Ola L.A. Harrysson, Denis R. Cormier, Ketan Jajal, Custom Design and Manufacturing of Canine Knee Implant, IERC 2003, Portland, Oregon, USA, May 18-20, 2003

DIRECT LASER SINTERING OF CERAMICS

F. Klocke, C. Ader
Fraunhofer Institute for Production Technology IPT, Aachen, Germany

Abstract

For more than one decade layer manufacturing technologies assist the development of new products. Due to a layer-wise build-up of a three-dimensional geometry, nearly every complex design is producible in a short period of time. Selective Laser Sintering is a powder-based technique to produce plastic prototypes (Rapid Prototyping) or metal mould inserts (Rapid Tooling). The laser sintering of ceramic powder is not yet commercialized but applications could be both Rapid Prototyping and Rapid Tooling. The former involves the laser sintering of investment casting shells and cores to cast metal prototypes and the latter the laser sintering of ceramic master patterns for metal spray forming of steel mould inserts. The advantage compared to actual processes are a faster availability of the final product. To facilitate these applications, special ceramic powders as well as new process parameter combinations were investigated. This paper will present achieved results within the above-described applications.

Introduction

Steadily decreasing product life cycles make it ever more important to reduce the development time for new products. Time-to-market instead of development costs has become the key factor for a products success. New methods from the organizational (Simultaneous Engineering) and the operative point of view have been developed [1].

At the end of a product development, technical prototypes which closely resemble the final product are demanded. Viable solutions for plastic components have been around for years, but the prototyping of metal components has often thought to be too time-consuming, and has been unable to meet comparable specifications. The fast production of metal prototypes still remains a central concern in the area of layer manufacturing technologies [2].

Within the sphere of **direct manufacture of metal prototypes**, a few technologies such as 3D Printing or laser sintering are already commercialized. Since laser sintered or 3D printed metal prototypes contain low melting alloys, the mechanical properties are limited.

The **indirect manufacture of metal prototypes** provides two different approaches either the direct Rapid Tooling where mould inserts instead of prototypes are layer-manufactured or the combination of Rapid Prototyping techniques and casting processes (indirect Rapid Tooling). The direct Rapid Tooling is utilized if higher quantities of prototypes are necessary. To date, this application achieves good results for plastic injection molding. Examinations and case studies of Magnesium and Aluminum die casting or thixo casting are carried out at several research institutes [2, 3, 4].

If smaller amounts of metallic prototypes are required the combination of rapid techniques and casting processes such as investment casting is used. Virtually, all metals may be cast and thin walls or small details are readily reproduced because the metal is poured into a closed hot shell. With actual Rapid Prototyping techniques the manufacturing time for the necessary master pattern is minimized but the time-consuming slurrying, sanding and drying of the samples is not eliminated.

Ceramic Laser Sintering

The laser sintering of ceramic materials is comparable to plastic or metal laser sintering whereas ceramic laser sintering is a transient liquid-phase sintering. With regard to the process, the combination of layer thickness, laser power, scan velocity, hatch spacing and scanning vector length has to be adjusted to the ceramic powder, **Fig. 1**.

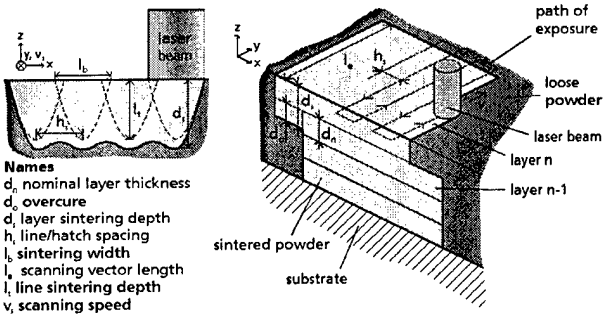

Fig. 1: Process parameters of ceramic laser sintering

The investigations on ceramic laser sintering at Fraunhofer IPT started on a laser sintering system with up to 100 W of laser power (CO_2). From initial tests with different ceramic powders such as aluminum oxide, aluminum silicate or zirconium silicate, the zirconium silicate powder ($ZrSiO_4$) was found the most suitable to process [5]. Today, a 200 W laser sintering system is used.

The basic research with **zirconium silicate** was carried out with ground powder. Several grain size distributions like 125 mesh, DIN 70 and 325 mesh and mixtures of these powders were tested. The result was that a high portion of small grains not only improves the surface quality but also improves the sintering itself since smaller particles need less energy to melt than larger particles. In contrast, an increased amount of small grains increases agglomeration so that an automatic recoating with a uniform surface was not possible. Dedusting and fractionating of the powder solved these problems. Today, the use of granular powder is preferred: due to the spherical surfaces a recoating with small granules is possible.

To determine the influence of process parameters on laser sintering each parameter has to be varied on its own. An increase in **laser power P_L** leads to an increase in the density of the specimen, since more energy is delivered into the powder and larger melt pools fill up the porous structures of previous layers. However, surface roughness also increases because the

molten particles tend to form larger spherical structures due to their effort to reduce the free enthalpy by optimizing the ratio between the area of free surfaces and the related volume.

Increasing the **scan speed v_S** has the opposite effect: due to higher velocity of the laser focus, less energy is delivered into the powder bed and less material is sintered. The result is that the density decreases but the surface finish improves.

A variation of **hatch spacing h_S** leads to different effects: if hatch spacings are too small, the molten powder particles form larger beads of high density leading to an overall high density of the part, yet the surface roughness also increases. For a hatch spacing larger than the focal diameter, the molten beads of material from line to line are not connected to each other and the gaps are filled with unsintered powder, resulting in a rough surface and low density respectively low strength.

A reduction of **layer thickness d_n** allows a faster scan velocity because the necessary sintering depth to ensure a fusion to the previous layer is reduced. Additionally, a smaller layer thickness increases the dimensional accuracy of the laser sintered part since the step effect is minimized. The thickness is limited by the grain size of the powder. Actually, the smallest layer is 50 µm.

Of all the parameter combinations that lead to a stable sintering process, the maximum density achieved was approx. 50 % of theoretical density so that two direct applications arise: the laser sintering of casting components and the laser sintering of master patterns for metal spraying.

Investment Casting Application

The conventional investment casting process begins with the fabrication of wax patterns with the same basic geometrical shape as the finished cast part. These master patterns are normally made by injection molding. Once a wax pattern is produced, it is assembled with other wax components to form a metal delivery system, called the gate and runner system. The entire wax assembly is then dipped in a ceramic slurry, covered with sand and allowed to dry. The dipping, sanding and drying process is repeated until a shell of approx. 6 mm to 8 mm is applied. These process steps generally require several days. Once the ceramic shell is finished, the entire assembly is placed in a steam autoclave to remove the wax. Finally, the mould is preheated to a specific temperature and filled with molten metal, creating the metal casting [6].

The major impact Rapid Prototyping processes have had on investment casting is their ability to make master patterns without the cost and lead times associated with fabricating injection molds, **Fig. 2.**

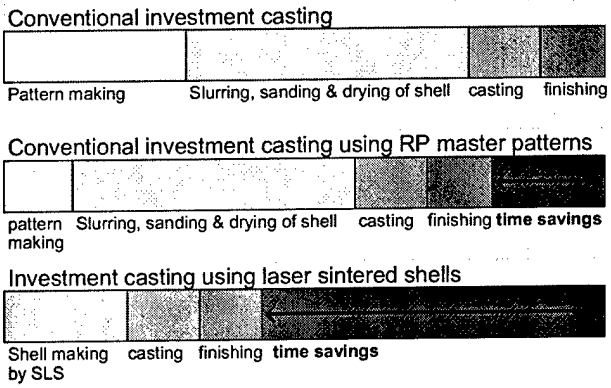

Fig. 2: Comparison of investment casting processes

A direct generation of casting shells without the need of master patterns could have the highest time savings because the iterative process steps of slurrying, sanding and drying of master patterns are eliminated. But since complete shells are generated the running systems and risers have to be designed and incorporated within the part geometry. A cavity is generated within the complete system with an external off-set of 6 mm to 8 mm (corresponding to the wall thickness of the shell).

Before casting, the loose powder in the shell has to be removed and the shell cleaned. As usual, the laser sintered shell is preheated in an oven directly before casting. **Fig. 3** and **Fig. 4** show some examples of metal prototypes cast in laser sintered shells:

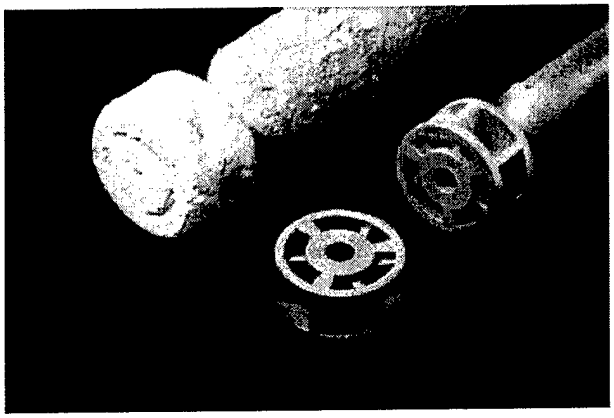

Fig. 3: Impeller wheel cast in AlSi7

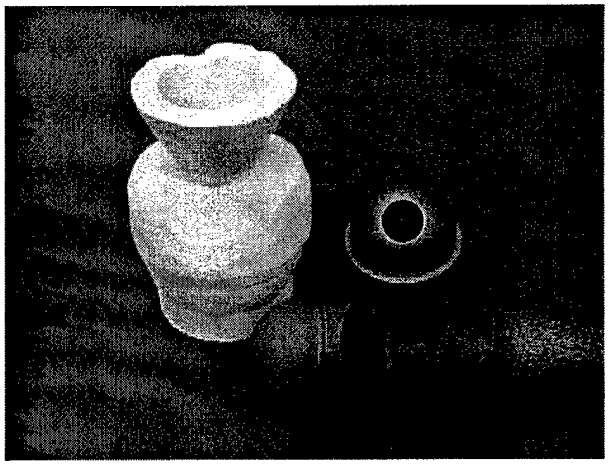

Fig. 4: Whirl chamber of a diesel engine cast in X15CrNiSi25 20

The processing time for three casting shells of the impeller wheel respectively four shells of the whirl chamber in parallel was only 10 hours, each. The dimensional accuracy of the cast prototypes is approx. +/- 0.6 % which is typical for investment casting. The surface roughness of cast prototypes is worse (R_a ~ 12 µm) compared to conventional investment casting (R_a < 6.3 µm) so that a mechanical finishing/polishing may be necessary.

Another problem of laser sintered shells is the lacking possibility to examine the quality of inner surfaces and contours before casting with the exception of Computer Tomography (CT) or endoscopy.

A comparable application of ceramic laser sintering is the use for investment casting cores. They are necessary for conventional investment casting if the metal part has complex inner geometries. Today, the core production is expensive and/or time-consuming since a metal pressing die or a mold for slip casting is needed. Thus, they are mostly used for mass production runs and not for prototyping. The production by laser sintering could be a fast and favorable way especially for prototypes, single part productions or small batches. A typical core geometry is shown in **Fig. 5**:

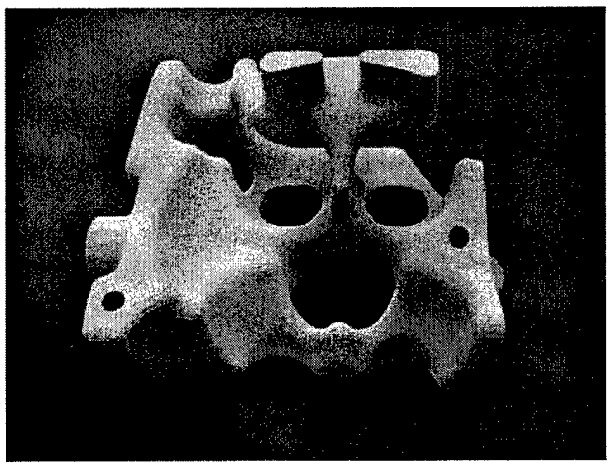

Fig. 5: Laser sintered water jacket core of a single cylinder ($ZrSiO_4$)

Since the laser sintering parameters are not changeable to ensure the tightness of cores, the surface quality is still bad. But a dipping of the laser sintered core into a ceramic slurry increases the surface quality (R_a ~ 4.0 µm) so that laser sintered cores are also usable for production runs, **Fig. 6**.

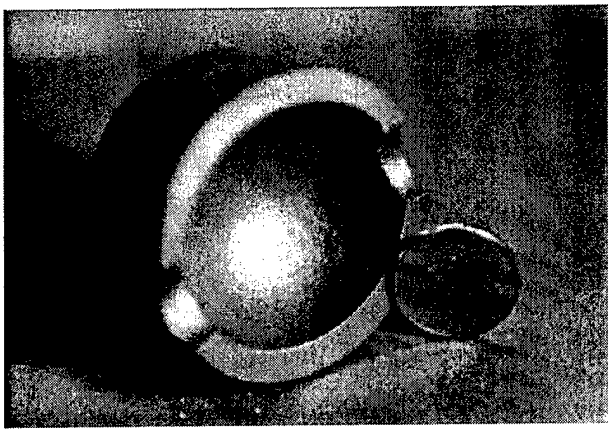

Fig. 6: Cast part split in two with an inner contour made by a laser sintered core

Spray Metal Tooling Application

Metal spraying belongs to the indirect Rapid Tooling where a master pattern is produced by Rapid Prototyping techniques. Afterwards, a metal alloy is sprayed onto the surface. Finally, the master pattern is destroyed, the mold insert is trimmed to the desired dimension and attached to the mother mold.

This process is well-known for low-melting alloys (e.g. Kirksite or Zamac) which are sprayed onto a plastic master pattern. Compared to conventional mould making, prototype moulds could be available in better time. In 1999, Ford Motor Company licensed this technology for carbon steel [3, 7].

Due to the high temperatures involved, ceramic master patterns are necessary in order to be able to spray steel. The requirements on ceramic materials for steel spraying are [7, 8]:

1. A low coefficient of thermal expansion,
2. A high thermal shock resistance,
3. A good compatibility to sprayed carbon steel and
4. A fast processing with laser sintering.

Ceramic powders like silicon oxide, silicon carbide, aluminum titanate and zirconium silicate are compatible with these four requirements, **Fig. 7**.

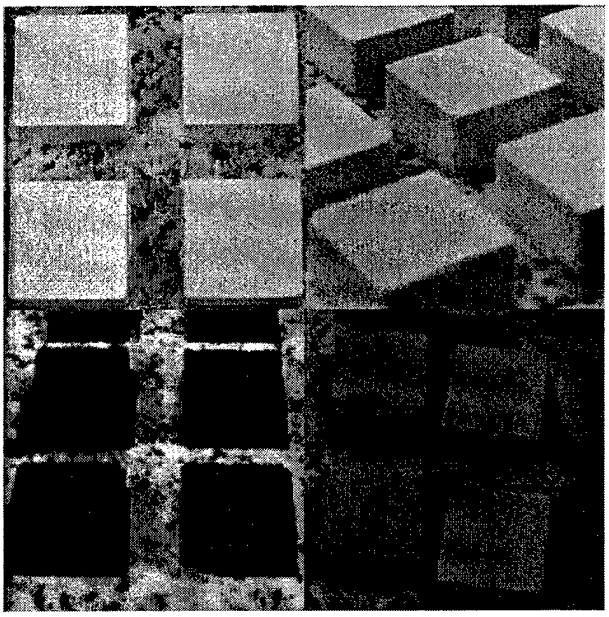

Fig. 7: Sample parts (from upper left to lower right: SiO_2, $ZrSiO_4$, Al_2TiO_5 and SiC)

While the laser sintering of silicon oxide led to an inaccuracy of the master pattern due to sporadic delamination the silicon carbide respectively aluminum titanate patterns were to fragile to handle. An infiltration with epoxy increased the strength but then the ceramic pattern were not removable by sand blasting so that zirconium silicate was used for practical tests [8].

The following picture shows four laser sintered master patterns of a sheet metal forming die, **Fig. 8**. The segments were produced on a laser sintering system with a maximum laser power of 200 W and a maximum work area of 250 mm by 250 mm (~ 9.8" by 9.8").

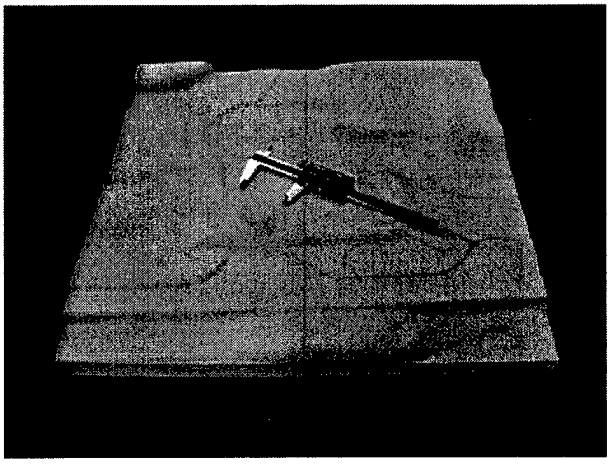

Fig. 8: Laser sintered ceramic master patterns

To prevent a relative movement of the segments during spraying, tongues and grooves were designed. The base of each segment was approx. 245 mm by 245 mm. The average manufacturing time for each segment was approx. 30 hours. Without tongues and grooves the manufacture would be reduced by 50 %. After laser sintering the segments were compared with the 3D-CAD data. The average dimensional accuracy was better than 0.2 mm, a very good result and acceptable for sheet metal forming.

Figure 9 illustrates the sprayed steel mold. The average surface roughness (R_a) was approx. 17 µm which is high compared to milled surfaces. In addition, cross lines due to the fitting of the four segments were visible so that a post-machining and polishing would be necessary.

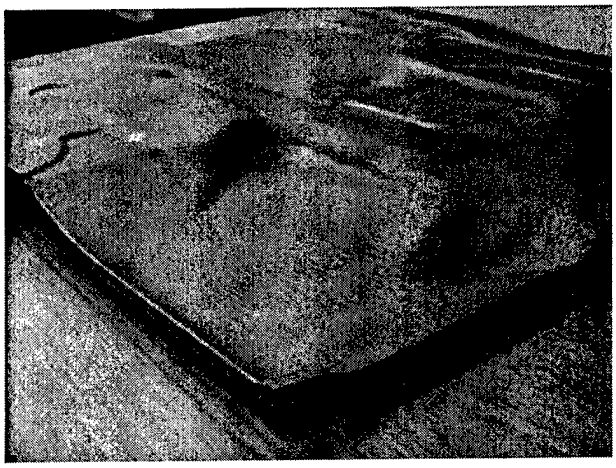

Fig.8: Sprayed carbon steel mold

The surface quality could be improved by painting the surface with a ceramic slurry similar to the one used to produce investment casting cores. The post processing would be minimized thereby. This could form the subject of the next investigation leading to a faster production of steel molds.

Conclusion and Outlook

It has been shown that ceramic laser sintering is a promising method of producing metal prototypes or moulds very rapidly. The examples shown illustrate that both ferrous and non-ferrous alloys can be successfully cast using laser sintered shells. The dimensional accuracy of the metal prototypes compare favorably with conventional cast parts.

The advantages of laser sintered investment casting cores are that they are usable for complex prototypes as well as for single part productions since a slurrying increases the surface quality. A quality analysis could be done directly after laser sintering and not after casting. Finally, laser sintered cores are easier to remove after casting than conventional cores.

The use for spray metal tooling of stamping dies or sheet metal forming moulds is only limited by the present work area of laser sintering systems. A segmentation of large moulds is possible but the dimensional accuracy could be affected.

Future research on laser sintering will focus on the investigation and assessment of further ceramic powders including aluminum oxide, zirconium oxide or silicon nitride with particular reference to medical and technical applications.

Acknowledgement

The authors are grateful for the assistance of John Bennett, Lost Wax Development Ltd., Stourport-on-Severn, UK and Richard Allor, Ford Research Laboratory, Dearborn, USA.

Bibliography

[1] Gebhardt, A.: "Rapid Prototyping: Werkzeuge fuer die schnelle Produktentstehung", Carl Hanser Verlag, Munich/Vienna (2000)

[2] Klocke, F., Ader, C.: "SFB 361 – Modelle und Methoden zur integrierten Produkt- und Prozessgestaltung: Arbeits- und Ergebnisbericht 1999 – 2001", RWTH Aachen (2001)

[3] Wohlers, T.: "Wohlers Report 2002", Wohlers Associates, Fort Collins (2002)

[4] Dickens, P.: "The Introduction and Take-up of Rapid Prototyping and Tooling into companies", Proceedings of EOS International User Meeting 2000, Castle Elmau (2000)

[5] Wirtz, H.: "Selektives Lasersintern von Keramikformschalen für Giessanwendungen", Dissertation, RWTH Aachen (2000)

[6] Sprunk, J. et all: "Feinguß für alle Industriebereiche", Castings Application Center (ZGV), Duesseldorf (1987)

[7] Chalmers, R. E.: "Rapid Tooling Technology from Ford Country", Manufacturing Engineering Magazine, Vol. 127, No. 5, p. 36 – 41 (2001)

[8] Klingenburg, D.: "Investigations on Rapid Manufacturing of Ceramic Patterns for Metal Spray Forming", Study thesis, RWTH Aachen (2001)

ON CERAMIC PARTS FABRICATED RAPID PROTOTYPING MACHINE BASED ON CERAMIC LASER FUSION

H. H. Tang*, H. C. Yen*, and W. H. Lin**
*Department of Mechanical Engineering, National Taipei University of Technology,
**Institute of Manufacturing Technology
Taipei 106, Taiwan

Reviewed, accepted August 29, 2003

Abstract

Conventional ceramic manufacture processes are not feasible to make ceramic parts with complex shape because of restrictions such as high tooling cost, time consuming and skillful workmanship. A new facility taking advantage of patented Ceramic Laser Fusion (CLF) technology to fabricate complex ceramic parts automatically is developed. According to the samples made by CLF machine, they are verified that hollow and over hung structures can be supported by solid green portion and complex ceramic parts can be fabricated. Apparently, this facility could promote the applications of ceramic materials, such as direct fabrication of ceramic shell mold.

Keywords: Ceramic Laser Fusion, Rapid Prototyping, Green Parts, Ceramic Shell Mold

1. Introduction

There are many restrictions on conventional ceramic manufacture processes, which are not feasible to make ceramic parts with complex shape such as turbine propeller and fan blade. Most of manufacture process are inevitable to use tooling which needs rather high cost and time for R&D. Traditionally, ceramic parts are sintered from green parts. Most of green parts are formed by powder pressing which is difficult to make complex parts.

Rapid prototyping technology makes use of layer manufacturing process. The most important advantages are there is no dead zone in working area and almost no any restrictions on shapes. No doubt, it provides a considerably satisfied method for ceramic parts manufacture. Using welding technology, complex polymer or metal parts can be fabricated by connecting some simple parts. In addition, they also can be made by NC machining. For the time being, ceramic is still difficult to be welded or machined. For the point view of shape making, the features of rapid prototyping are more sensible on ceramic than polymer and metal.

Over decades, there are some ceramic processes and systems available in different applications such as direct shell production casting (DSPC) and selective laser sintering (SLS) which had applied to mixture of polymer and ceramic powder. Recently, ceramic without binder using selective laser sintering to fabricate shell mold was developed by Wirtz [1]. To prevent from agglomeration, the layer thickness should not be thinner than 50 μ m (Wirtz, 2000). Instead of powder, Tang employed ceramic slurry to develop ceramic laser fusion (CLF) process[2,3]. This process not only eliminates agglomeration, but also reduces the layer thickness. Slurry behaves as a highly viscous liquid so that the porosity can be reduced and some mechanical properties of ceramic parts can be improved (Ian Gibson, 1997)[4]. Further studying on control of shrinkage and accuracy is on the way, developing a reliable automatic machine is indispensable.

2. Intention and Method

Based on Ceramic Laser Fusion, an intention of this study is designing and setting up an automatic facility to make ceramic parts in order to raise the processing speed and extends its applications. For the purpose of reaching the ends as mentioned, we have to implement material selection, facility automation, parts making and feasibility study of direct fabrication of ceramic shell mold. All subjects will be illustrated as following.

3. The process of Ceramic Laser Fusion

The technology of Ceramic Laser Fusion (CLF) was developed by Dr. H. H. Tang, professor of Manufacture Institute of Technology, Taipei University of Technology. It can fabricate ceramic parts with very complex shape. Owing to high heat-resist, the application of the parts made by this process will be extensive.

3.1 Process Description

Fig. 1 illustrates the process details. Special made ceramic slurry (1) supplied from feeding device paves a membrane (2) on platform and is heated by drying device to produce a green part (3). Platform descends a layer thickness (4), then laser scans selectively right away (5) to directly fuses membrane from green material to ceramic. Process will repeat steps from (2) to (5) until the 3D part (6) completed. The final stages are to remove the portion (7) which is not fused by laser and takes out the ceramic part (8).

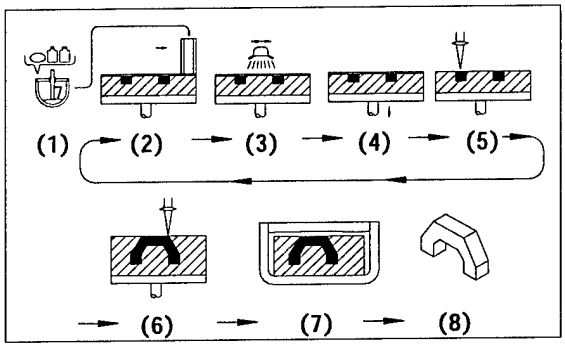

Fig. 1 CLF process

3.2 Material Selection

Raw materials used in this process are SiO_2 powder and inorganic binder. They are diluted by water uniformly.

The pores among ceramic particles can be filled by inorganic binder which is also helpful to get rid of air in pores. Even under high temperature of fusing, the movement of ceramic particles will be prevented because of little amount of expanded air and binding effect of the binder. Under the phenomenon mentioned above, this process can use high energy leaser beam to fuse the green parts, ceramic particles will not be moved upon heating. After melting and solidification, particles will not congregate [2]. For the purpose of getting well mixed slurry in order to make green parts, raw materials will be blent by a blender.

4. Design and Manufacture of an Automatic CLF Prototyping Machine

An automatic CLF rapid prototyping machine includes a mechanical system and a control system. Mechanical system is comprised of a laser scanning device and a layer making device. The function of the control system is to direct the processing sequence and monitor the whole process. We will discuss each system as following.

4.1 Mechanical system

In this study, the function of the laser scanning device is provided by an existing engraving machine, the key components, the layer making device and the control system are designed by our group. The function of laser scanning device is to make 2D cross-sectional hatching scanning. The layer making device has to execute slurry feeding, layer paving and drying, residual slurry clearing, and platform descending.

4.1.1 Laser scanning device

The existing engraving machine is shown in Fig. 2. Owing to laser absorption rate of ceramic green parts is over 90%, we select CO_2 laser as heating source. Vector scanning is implemented because of an easily creating of scanning path. Scanning speed can not be pretty high because of a relatively low laser power, 50W.

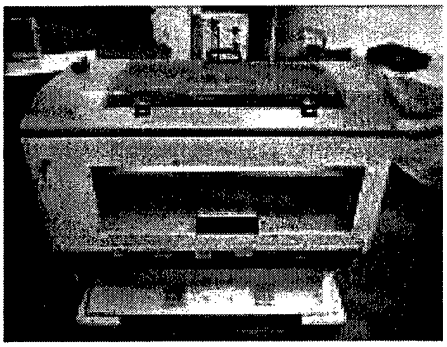

Fig. 2 Engraving machine

4.1.2 Layer making device

Layer making device is a key technique in CLF process. It is similar to Doctor Blade in Tape Casting [5], paves slurry evenly on a plate and then let it dry. Fig. 3 illustrates the CLF layer making device which includes slurry feeding unit, layer paving unit, drying unit, clearing unit for residual slurry, and platform elevating unit.

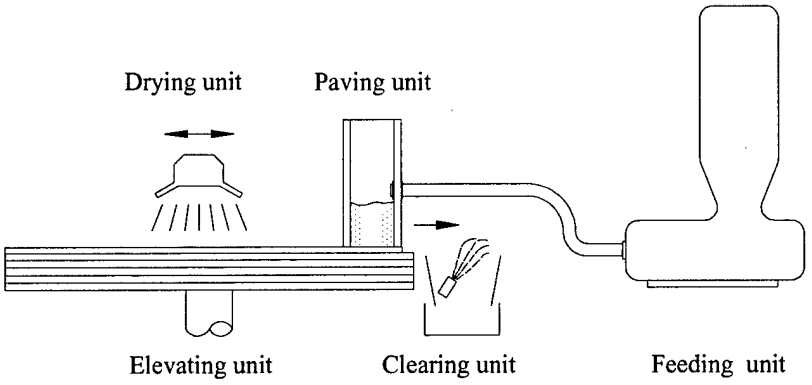

Fig. 3 CLF layer making device

4.2 Control System

The purpose of the control system is to develop highly intelligent process equipment and to

achieve an automation of CLF process to reduce manufacturing time and promote the stability of process. Just after setting some basic process parameters by an operator and pushing the start button, the system will run fully automatically. Less experience and technique are required for the machine operator.

Design of control system focuses on integrating all of the individual devices and writing man-machine interface software. For the time being, an automatic CLF rapid prototyping machine has been constructed and tested as well by this group. We will discuss control hardware and control software so-called man-machine interface.

4.2.1 Control Hardware of CLF Rapid Prototyping Machine

The control system of CLF rapid prototyping machine integrates the laser scanning device and layer making device. Using process computer and programmable logic controller (PLC) conducts the sequence control. Fig. 4 is the structure of control system. Process computer and PLC together control the activity of each device in the laser making device to manufacture green layer. Process computer transfers HPGL files to laser controller and path controller that control CO_2 laser and X-Y plotter respectively.

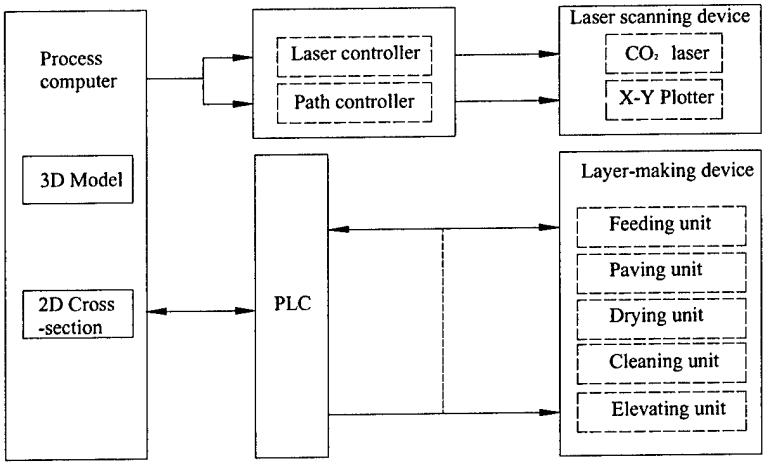

Fig. 4 Structure of control system

4.2.2 Man-Machine interface Programming

Application software for CLF machine named CLF man-machine interface is developed in Visual Basic language. This program, which comprises of two sections – monitor and control, can communicate with PLC and laser scanning device.

Monitor section traces the state of each process and indicates it in terms of color lamps.

"Red" represents system is under operation, "green" represents stop. Control section includes "Manual" and "Auto". System's default is "Manual". Under "Manual" mode, individual devices can be operated manually. This mode can be used for checking the functionality of the CLF machine. If you choice "Auto" mode, system will follow the parameters set by operator and program to complete all steps.

In "Manual" mode, if one of the devices is running, other control buttons cannot be activated at all. If plotter is still, the laser scanning head has to be in origin and light sensor will be activated. The state of light sensor will indicate that plotter has left from origin or not. For the safety reason, whole system cannot be operated when plotter isn't in origin.

In "Auto" mode, software will open a recording file to record information such as finished steps and time consuming of each layer. In case of power failure or extraordinary system stops during operation, operator can get details of finished steps from this file, and then operate manually to complete the unfinished procedures and return to "Auto" mode to continue the operation of following layers.

On the right bottom of monitor displays time consuming of last layer and total time consumption for all layers. Some useful information, such as current paving layer number and 2D file name of scanning, are shown on monitor. This information will help operator to handle the layer manufacturing process easily.

5. Parts Making

Drawing a 3D model by PRO/ENGINEER is the first step of CLF, then using slicing software which is developed by our laboratory to create hatching files, they will be transferred to control program to drive laser scanning device in order to scan the 2D hatching selectively. Using the high temperature induced by focusing the laser beam fuses ceramic green part. By means of elevating the platform, process will repeat layer by layer. Finally, it will pile up a 3D solid ceramic prototype as our designing.

After paving and scanning, work piece should be cleansed to remove un-fused material in hollow. High pressure water spouts out from faucet or nozzle to remove most of un-fused materials. However, it has to be placed into a supersonic cleaner to remove all small green portions which weren't cleansed by water.

According to the experiments of feasibility, we can get better fusing result under the

condition of laser power 50W, scanning space 0.2mm, scanning speed 20 mm/s and layer thickness 0.15 mm. In this study, all parts and direct casting shell mold are based on these parameters.

5.1 Hollow parts, fan blades and turbine propellers making

Fig. 5 shows ceramic pump blades made by CLF process. They are 30 mm diameter/ 8 mm height and 15 mm diameter/ 4 mm height respectively. One of the most important features is there are solid supports in hollow portion so that this process can make complex ceramic parts with internal cavity. Un-fused materials in hollow portion can be removed easily by putting parts into a supersonic cleaner which fills with NaOH solution.

Fig. 6 shows fan blade and turbine propeller made of ceramic. They certify that CLF can make 3D complex parts. Blade thickness is 1 mm and propeller thickness is 0.8 mm. respectively.

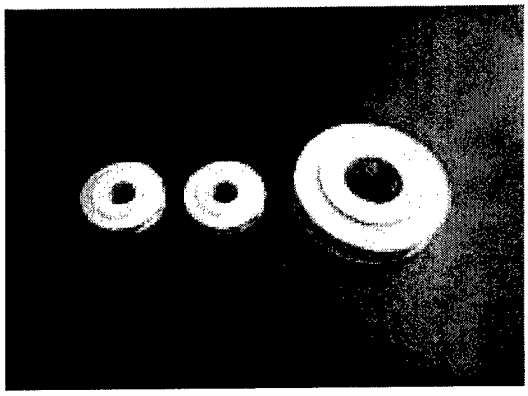

Fig. 5 Pump blades made of ceramic

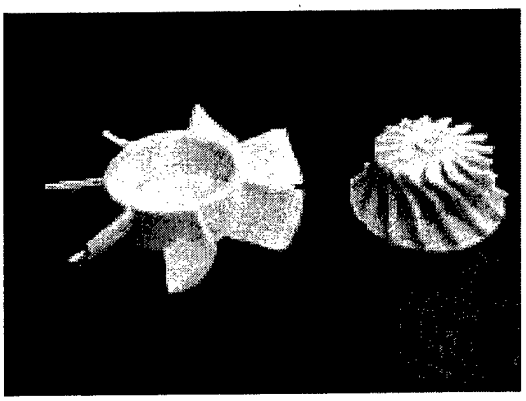

Fig. 6 Fan blade and turbine propeller made of ceramic

5.2 A study of ceramic shell mold making feasibility

Owing to high temperature resistance and small deformation, CLF process might apply to direct casting mold making. In sand casting, model is used to make cavity, then the cavity is cast to get metal work piece. Conventionally, it has to make model in advance, sand core must be made for a production of internal features in hollow. This process is very complicated. Using CLF process, ceramic shell mold with 2 mm thickness can be made. It can be used for casting aluminum alloy and copper alloy to get metal work piece in a short period.

According to the accuracy requirement, 3D model with features of gating system, which is designed by PRO/E, is sliced by CLF software to build hatching information for each layer, the

working procedures afterwards are similar to general part making method.

Fig. 7 represents a direct casting shell mold made by CLF process. Before casting, we can use ceramic slurry to bond upper and bottom molds. Fig. 8 shows a bonded CLF direct casting shell mold.

Bonded CLF direct casting shell mold have to be preheated to a temperature over 400℃ to vaporize water in ceramic shell mold and to enhance the filling of liquid metal in mold cavity. Following the regular process, a metal work piece is done. The finished pure aluminum casting work piece is shown on Fig. 9.

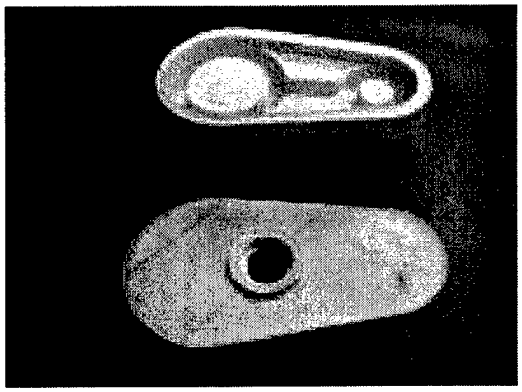

Fig. 7 A direct casting mold made by CLF

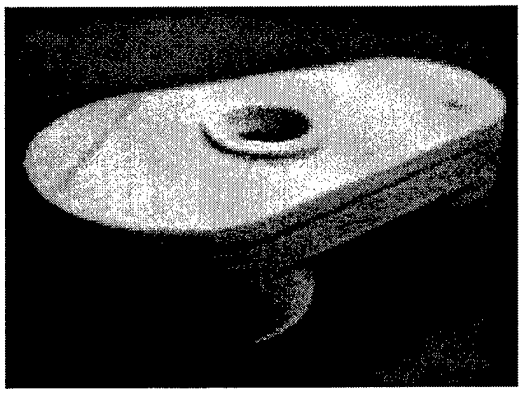

Fig. 8 A bonded CLF direct casting mold

Using CLF facility can make complex ceramic parts. Paving and control system can fulfill the requirements of 3D layering. Layering process can be accomplished automatically without any manpower involved.

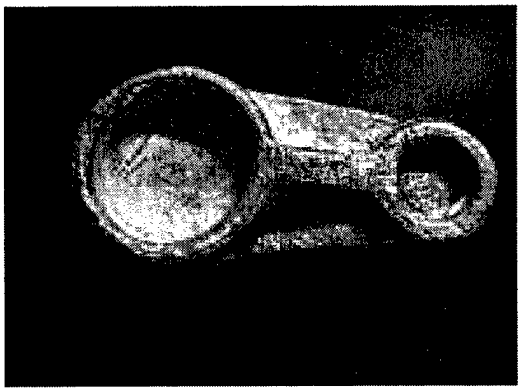

Fig. 9 A pure aluminum casting work piece

6. Conclusion

Using CLF facility can make complex ceramic parts. The mechanical and control system can fulfill the requirements of 3D layer manufacturing. Layer manufacturing process can be accomplished automatically without any manpower involved.

It also verifies this process can provide solid supports in hollow or over hang structures. Complex ceramic part as turbine propeller can be made. Furthermore, CLF process is also feasible for making a high strength direct casting shell mold in a short period. For some small features and high accuracy requirements, except a proper after finishing for a smoother mold surface we can pave thinner layer to improve the internal surface of the mold. In this study, paving a green layer under 25μm is possible. Comparing to other powder ceramic processes which also can make direct casting molds, it is really a thinner layer. Therefore CLF process has an opportunity to make smoother and accurate work pieces. There are some basic requirements for rapid tooling process, such as smooth surface for easy part ejection and limited finishing operations[6]. No doubt, CLF meets those requirements and has great potential to compete with another ceramic processes in service of CAD to metal.

Reference

1. Wirtz, H.: "Selektives Lasersintern von Keramikformschalen für Gies anwendungen", Dissertation, RWTH Aachen (2000).
2. H. H. Tang. "Method for rapid forming of a ceramic work piece" U.S. patent no. 6217816B1, (2001)
3. H. H. Tang, Direct laser fusing to form ceramic parts, Rapid Prototyping Journal, Vol. 8, No. 5, pp.284-289, 2002.
4. Ian Gibson and Dongping Shi, "Material properties and fabrication parameters in selective laser sintering process", Rapid Prototyping Journal, Vol. 3, No. 4, 1997, pp.129 – 136.
5. James S. Reed, Principles of ceramics processing, New York: John Wiley & Sons.1994, pp.25, pp.509, pp.514 and pp.525.
6. Karapatis, N.P., Griethuysen, J.-P.S. and Glardon, R., "Direct rapid tooling: a review of current research", Rapid prototyping Journal, Vol. 4, No. 2, 1998, pp. 77 - 89

Recycling of RP Models by Solution – Casting Technique

K. Siva Prasad*, E.Rathakrishnan+, Sanjay. G. Dhande*

*Department of Mechanical engineering, IIT-Kanpur, India
+Department of Aerospace Engineering, IIT-Kanpur, India

Abstract

Most of the Rapid Prototyping systems process polymeric materials for model making. Increased environmental concerns and waste minimization demands the recycle of these polymeric models. One way is to melt the models and cast it. However, in this method polymer degradation may occur leading to diminished functionality. In the present work a preliminary attempt has been made to reuse the polymer components by dissolving in a suitable solvent and casting the same into the required shape using soft tooling. Acrylonitrile Butadiene Styrene (ABS) polymer components, made by Fused Deposition Modeling (FDM) process were taken for the present study

1. Introduction

Rapid Prototyping is key prototyping technology for producing accurate parts directly from CAD models with little need for human intervention. With the introduction of RP, designers have the freedom of realizing all the instances of the conceptual design. Further, this allows unlimited checking as required of form, fit and assembly of the design [1]. In the total product development cycle, there will be a lot of design iterations before the design is freezed. During each cycle, prototypes will be made for checking. The end products of the most of the RP systems are polymeric models. Plastics are so versatile in use that their impact on the environment is extremely wide ranging. However, they are difficult to destroy and are classified as non-biodegradable materials. The each design iteration will produce a prototype which will accumulate to significant solid waste. With increased environmental concerns, strict legislations with further emphasis on material recovery there is a requirement for recycle of RP solid waste. One way is to reuse these polymers by melting and casting the same to required shape through proper tooling. Polymeric materials are mostly thermo – dynamically incompatible. Often during recycling, a decline in the quality of the material properties is observed. The properties of secondary products may be worse than the properties of products made from virgin plastics.

In the present work, a preliminary attempt has been made to recycle the RP polymeric materials. A solid based RP method FDM (Fused Deposition Modeling) was chosen for the present study. The basic material for the FDM is ABS (Acrylonitrile Butadiene Styrene). ABS is copolymer composed of two copolymers and is one of the most common polymer materials. Styrene and Acrylonitrile form a linear copolymer (SAN) that serves as a matrix. Butadiene and styrene also form a linear copolymer (BS rubber) which acts as the filler material. The combination of the two copolymers gives ABS an excellent combination of strength, rigidity and toughness. The main objective of the present work is to get a component from a solid waste. For this purpose ABS polymer, a used FDM (Fused Deposition Method) component was taken and dissolved in suitable solvent and casted through proper tooling.

2. Methodology

The procedure of solution-casting technique for recycle of RP polymeric waste is depicted in Fig. 1 and described subsequently.

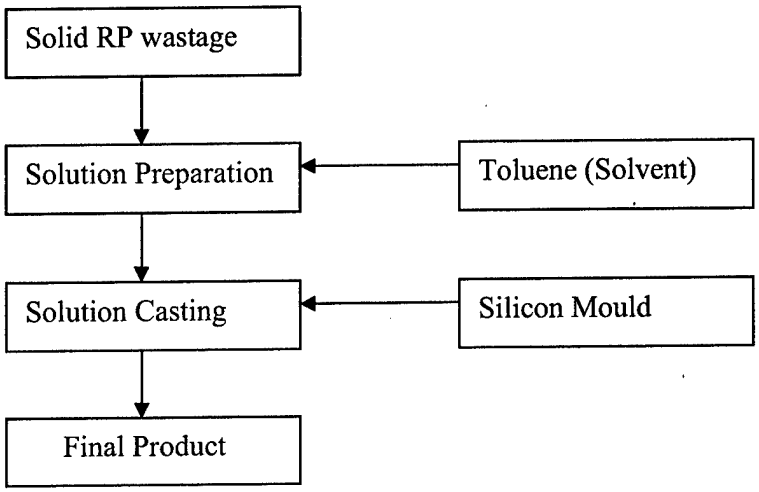

Fig. 1. Sequential Steps of the Proposed Methodology

2.1 Materials

Acrylonitrile Butadiene Styrene (Stratasys & Co, USA), Analytical grade toluene (Ranbaxy, India), Silicone (HEK, Germany), release agents (HEK, Germany) were used for the work.

2.2 Polymer Solution Preparation

The solubility of a given polymer in a solvent depends on the chemical structure. One way to measure the solubility is by finding the difference between solubility parameters of the polymer and solvent [2]. If the difference between these two is small, then the polymer is completely soluble in solvent. Solubility parameter is defined as the square root of cohesive energy density. The cohesive energy density is defined as the cohesive force (heat of vaporization) to the molar volume. The cohesive energy density as well as solubility parameters of various polymers and solvents are listed in the Van Krevelen [3]. For unknown polymers group contribution method is used.

The first step in estimating the solubility parameter for the present specification of ABS is to measure the butadiene content. Butadiene is estimated by dispersed fixed quantity of ABS in acetone solvent and centrifuged. The supernatant contains copolymer of Acrylonitrile and Styrene and is decanted from the grafted phase of Butadiene. The butadiene content is 14% and further, it is assumed that Acrylonitrile and Styrene are present in equal molar ratio. Therefore, solubility parameter of ABS estimated is 17 $J^{0.5}/m^{1.5}$. This value is

compared to solubility parameters of various solvents given in the Van Kreyelen [3] and toluene is selected (solubility parameter 18-18.5 $J^{0.5}/m^{1.5}$) as solvent.

ABS polymer in 1:4 was added to toluene in a conical flask. The mixture was kept on magnetic shaker for two days to get homogenous solution. The obtained solution was centrifuged (REMI model -R 24) at 10000 rpm for 30 minutes for the removal of un-dissolved polymer and dust particles. The supernatant homogeneous solution was transferred to a conical flask (air tight) and kept for overnight for the removal of entrapped air bubbles.

2.3 Silicon Mould Preparation

The Master model is examined thoroughly for its dimensions and cleanliness. Further, parting line and position of the gate are decided. Clear taping along the parting line and coloring the edge of the tape is done to assist in cutting the mould along parting line. The master model is hanged in a casting frame (laminated chip board/ wooden board) whose dimensions allow for sufficient clearance from the model. Degasified silicon resin and catalyst (HEK, Germany) are mixed in proper ratio (10:1). This semi solid mixture is poured slowly and steadily into the casting frame. For secondary degasification, the casting frame is kept in vacuum chamber (10 – 25 minutes). The actual time of degasification depends on volume of the rubber. To get extreme dimensional accuracy in the castings, the resin mixture is cured in oven (40^0C for 6-8 hours). The cured mould is then cut along the parting line with a help of sharp scalpel and mould openers. Cutting is made along undulating path to allow for perfect alignment of male and female halves.

2.4 Casting Models

Figure 2. Silicon Mould for Cube

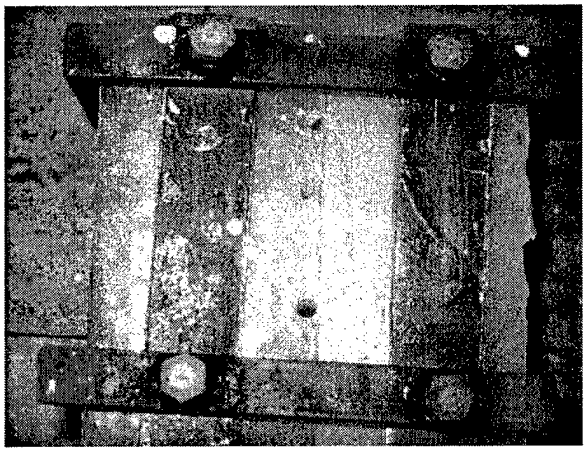

Fig. 3 Silicon Mould for Aerofoil wing

The prepared silicon mould is ready for casting is shown in Figure 2 & 3 for aerofoil wing and cube subsequently. Release agents are applied on the cavity of the silicon mould for easy detachment of cast component. The mould parts are held together by proper fixturing so as to prevent deformation in silicon mould due to excessive swelling as toluene diffuses during evaporation. The solution is poured into the mould and left to cure by exposing the same to atmosphere 10 to 12 hours. The mould is further kept in vacuum oven for removal of residual solvent.

3. RESULTS AND DISCUSSION

Aerofoil wing model is chosen to demonstrate the applicability of the proposed methodology. Aerofoil wing is a typical shape which has variation in thickness from head to tail. The obtained aerofoil wing model is satisfactory from the shape and smoothness point of view which is shown in Figure 4. However, the strength is varying from the head to tail because part of head is strong and part of it is hollow. This is because of improper casting and it can be rectified by pouring the polymer solution in regular time intervals. The main objective of the present work is to answer the following questions

- How many steps it will take for complete casting?
- Exactly, how many days it will take to complete the model?
- What is the dimensionality of the end product?
- What more conditions are required for the present process?

Aerofoil model is too ambitious to answer the above questions because of its complex shape. So, a simple cube 5 x 5 x 5 (cm^3) has been taken for experimentation. Approximately 25 steps and 15 full days were taken to complete the component. The dimensionality is satisfactory and is shown Fig. 5. The present casting is carried out in atmospheric conditions. The silicon mould after detaching the model is thoroughly checked and there is no surface damage. It indicates that there will not be any severe destructive chemical reaction between silicon, toluene and ABS.

4. CONCLUSIONS

The present work is an attempt to prepare the prototype/products from the solid wastage of FDM (ABS) components using solution-casting method. Aerofoil wing and cube are chosen to demonstrate the present work. The obtained shape (dimensions) and smoothness is satisfactory for chosen model. However, more studies are required to understand the role of various properties and/or conditions required to get the final product. This preliminary study underlines the potential of application solution-casting technique to recycle of FDM (ABS) components.

5. REFERENCES

[1] Kai and Fai, Rapid Prototyping: Principles and applications in Manufacturing, 1997, John Wiley & Sons, Singapore.

[2] J.H. Hildebrande, Demonstration of the rational character of the new solubility formula, J. Am. Chem. Soc., 38, 1916, 1452-1473.

[3] D.W. Van Krevelen, Properties of polymers, Elsevier Publishers, Amsterdam, 1990, New Age International (P) Limited, Publishers.

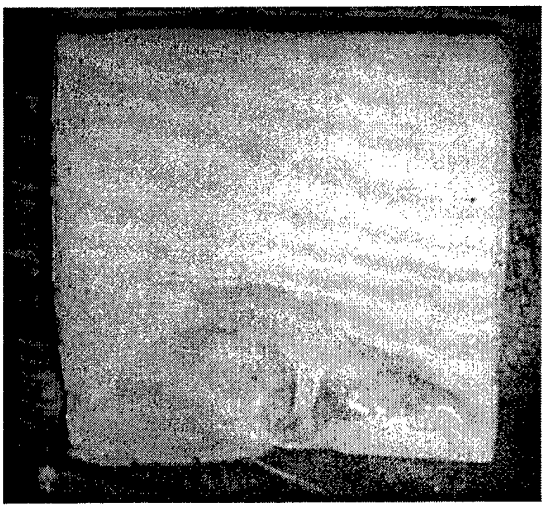

Fig. 4. Final Aerofoil wing model

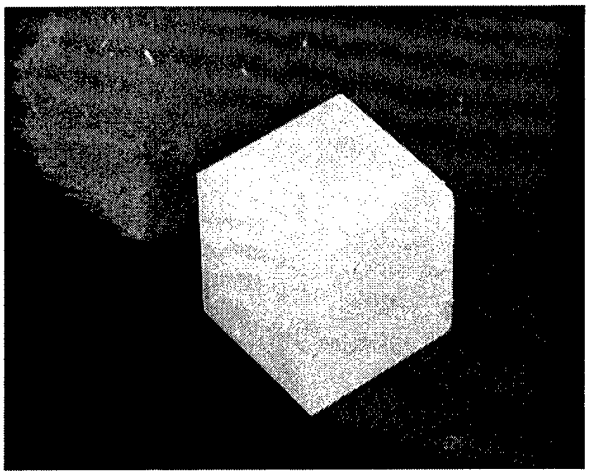

Fig. 5. Final Aerofoil wing model

A Study on the Manufacturing of Large Size Hollow Shape Parts for Prototype-Car using Rapid Prototyping Technology and Vacuum Molding

Hwa-Joon Yang, Tae-Sik Jang, Choong-Ryeol Ryu, Il-Yup Lee
(Pilot & Proto vehicle Assembly Team, Hyundai Motor Company)

ABSTRACT

Rapid Prototyping(RP) techniques have revolutionized traditional manufacturing methods. These techniques allow the user to fabricate a part directly from a conceptual model before investing in production tooling and help develop new models with significant short time. This paper suggests the new process to manufacture large size hollow shape parts for prototype-car using Rapid Prototyping technology and Vacuum Molding with the reduction of delivery time. In addition, this paper introduces the dividing and combining method to make large size RP master model in spite of the limit of the build chamber dimensions of commercialized RP systems and post-processing method to achieve sufficient surface quality.

1. INTRODUCTION

In the development stage of new cars, prototype-cars manufactured for an aim to inspect a shape of design, performance, and stability generally adopt the same process of manufacturing parts as mass production in order to get the reliability of test results, but the modified manufacture methods which are different from mass production are used considering urgency of manufactured parts and quantity in case of manufacturing cars having unique specifications like RHD(Right Hand Drive) cars, shapes of parts, and needs for the early stage-test of functions due to the urgent change of design. In this case, it is necessary for parts manufactured by the changed manufacture process to have mechanical function for the whole external appearance and the performance of assembly such as dimensional accuracy and a reliable result.

This paper suggests the new process to rapidly manufacture half molds for vacuum molding using a master model of a large size hollow shape part for prototype-car made by Rapid Prototyping machine, SLS(Selective Laser Sintering)[1][2][3] , and to adhere two parts made by vacuum molding. In addition, this paper introduces the dividing and combining method to make large size RP master model despite of the limit of the build chamber dimensions of commercialized RP systems and post-processing method to achieve sufficient surface quality.

2. MAIN PROCESS

The general method to make hollow shape parts for prototype-car is blow molding. There are two blow moldings which are Resin-based blow molding[4] and ZAS(Zinc Alloy for Stamping) blow molding. ZAS blow molding is used in large size mass production due to the requirement of the same size of mold equipment and specification. Fig. 1 shows the comparison between suggested method and conventional method for manufacturing of large size hollow shape parts using ZAS blow mold.

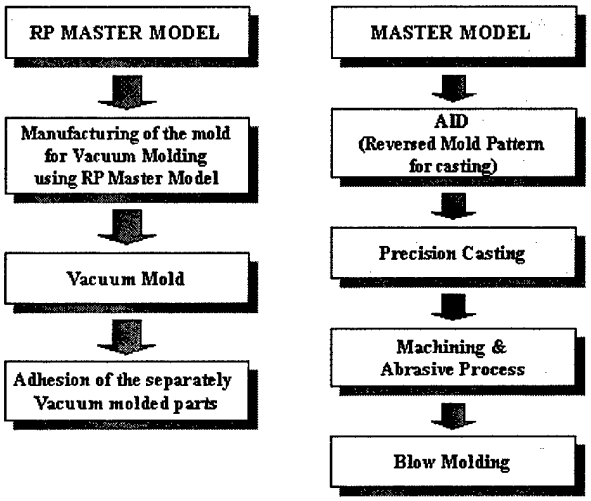

Fig. 1 Comparison between suggested method (a) and conventional method for manufacturing of large size hollow shape parts using ZAS blow mold(b)

2.1 Manufacture of Mater Model

2.1.1 Special features of molding parts

A part manufactured in this paper is a Heater to Air Ventilation Duct Connector to control temperature and humidity of the inside car using heat and energy from an engine. It is installed inside an instrument panel and has a shape to avoid interference with electric wires and outer parts controlling equipment of sound and temperature. Fig. 2 shows a feature of heater to air ventilation duct connector

2.1.2 Parting and molding of master model

The part to mold is modeled by CATIA. The part is 1200mm long. So, it is impossible to mold the whole part at one time due to the chamber size of SLS machine, Sinterstation 2000. Therefore the method to divide the modeled shape into seven parts and adhere them is applied as shown in Fig. 3.

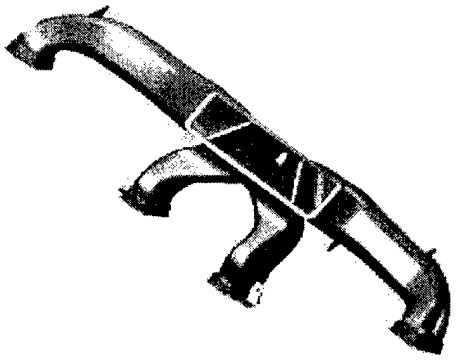

Fig. 2 Feature of heater to air ventilation duct connector

Fig. 3 Feature of divided CATIA data

The ladder-shaped structure at each divided parts is adopted to get an exact position and keep the adhesion strength during the process of adhering a master model. After the two mold inverted from the master model are manufactured, the process of removing the master model from the mold should be performed to make the complete mold for vacuum molding. The thickness of the master model is about 2mm because the method to crush the master model in the mold is used. The complete molded parts are adhered along the ladder-shaped structure. If the surface of this area is rough, it is difficult to adhere 7 parts. In case there are rough surfaces, post-processing is required for adhesion. Fig. 4 shows the process of adhering those parts.

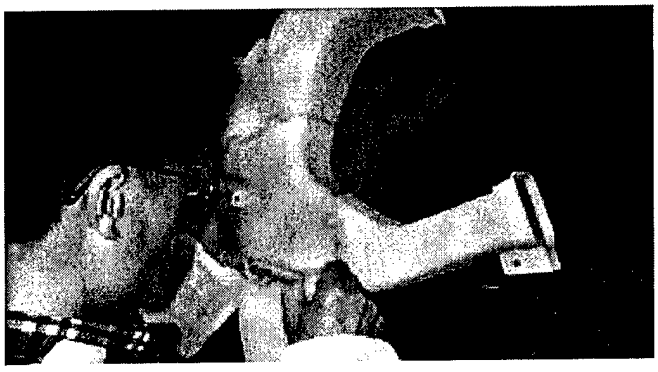

Fig. 4 Adhesion of separately built SLS subparts

2.1.3 Post-process of combined SLS master model

There are two methods to improve the surface roughness of parts made by RP machine. One is to control building orientation and laser scan path and the other is to post-process built parts. The improvement of the surface roughness using building orientation and laser scan path has limitations and increases building time. Therefore this paper uses the method of post-processing parts.

There are two post-processing methods that are abrasion and coating. It depends on mechanical strength. It is difficult to use an abrasive method because the master models manufactured by SLS process have sufficient mechanical strength. This paper adopts a coating method to improve the surface roughness using resin. The used coating method has three steps. Three steps are demonstrated as follows;

First, undercoat is sprayed on the master model to improve the surface roughness in short time. Undercoat uses urethane material, PUTTY(P000-C4125). After spraying, hardened undercoat material needs to sandpaper.

Second, fine air bubbles exist due to property of spraying PUTTY and it is not easy to remove all the fine air bubbles. Rapidly dried RED PUTTY is covered on the area of air bubbles using brush and needs to sandpaper.

Third, the surface of the master model is coated with SANDING SEALER to get sufficient surface roughness for tooling. Table 1 shows materials used to enhance the surface roughness

Table 1 Materials used to enhance the surface roughness

	Materials
First step	PUTTY(P000-C4125)
Second step	RED PUTTY(051144-05972)
Third step	SANDING SEALER

2.2 Manufacture of Mold

2.2.1 Selection of parting line and works

The selection of parting line is an initial process of manufacturing mold and an important work for the whole mold structure, cost, delivery time, and qualities of molded parts. In this paper, the parting line is determined by the following rules.

First, additional combining structures designed to assemble surrounding parts is included in the parting line.

Second, a space between a sheet and a vacuum mold in order to absorb the sheet into the vacuum mold using suction pressure generated from the pump of vacuum molding machine should be sealed up. In case of having air-leakage shape, it is necessary to have a dam for protecting air-leakage in outer area of a product.

Third, trivial undercut is negligible in selection of partin g line.

2.2.2 Manufacturing process of half mold

A work of accumulating heat-resisting resin is carried out above a master model fixed on a base plate after work of parting line. The heat-resisting resin plays a role in preventing the damage of the mold surface at high temperature of about 150°C. Then frames for reinforcement are built and outer frames are installed to prevent the damage of the mold under strong suction pressure generated from the process of vacuum molding in Fig. 5. Resin is accumulated to support the strength of mold between the reinforcement frame and the outer frame. Fig. 6 shows a completely built mold structure and a feature.

In order to make the second half mold, the work is carried out on base plate without separating the master model from already finished first half mold. The work process to manufacture the second half mold is equal to the process of the first half mold. When the manufacture of the second half mold is completed, two molds are separated and the master model stuck to the second half mold is crushed.

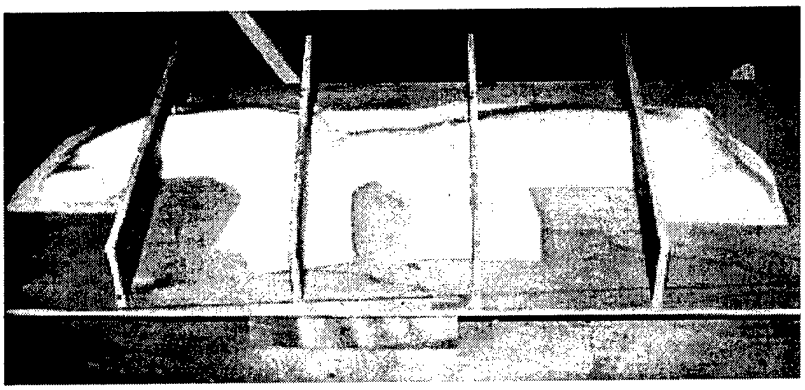

Fig. 5 Feature of mold reinforcement structure

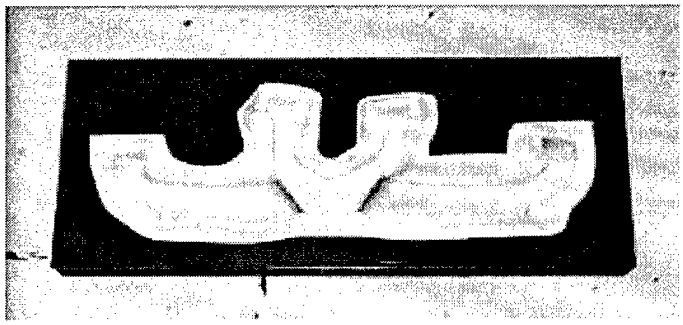

(a)

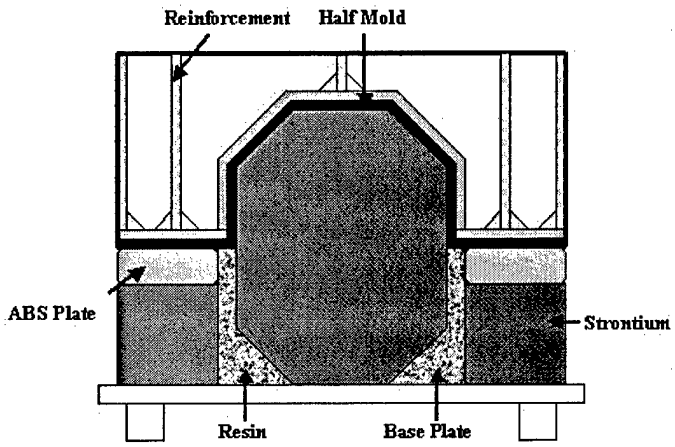

(b)

Fig. 6 Schematic diagram of half mold for vacuum molding(a) and feature of the first half mold.(b)

2.3 Process and condition of vacuum molding

The first step for vacuum molding is that the mold is loaded into the vacuum mold machine. The contact surface between the mold and the vacuum mold machine should be completely airtight when the mold should be loaded into the vacuum molding. After loading the mold, a sheet for vacuum molding is set up into the clamp. Then the sheet is heated to get enough flexibility. Table 2 shows the operating conditions applied to this paper. ABS sheets are used for the suggested process.

Table 2 Operating conditions of vacuum molding with respect to materials

	ABS	PP
Standard Condition (Thickness : t, Temperature : °C)	2.5t/23°C	2.5t/23°C
Shrinkage	8/1000	16/1000
Heating Temperature (°C)	250	300
Heating Time (sec)	155	180
Transfer Time (sec)	4 ~ 5	4 ~ 5
Mold Uploading Velocity (mm/sec)	100	100
Cooling (with fan) Time (sec)	80	150

The heated sheet is then transferred to molding area. After sheet transferred to molding area is fixed on clamp, the elevator uploads and the surface of mold lifts up the surface of sheet. Then the pumps loaded into vacuum mold machine inhale the air between the mold and the sheet. The sheet is cooled using a fan after inhaling the air. The completely cooled sheet is separated from the mold. Fig. 7 shows the whole process of vacuum molding.

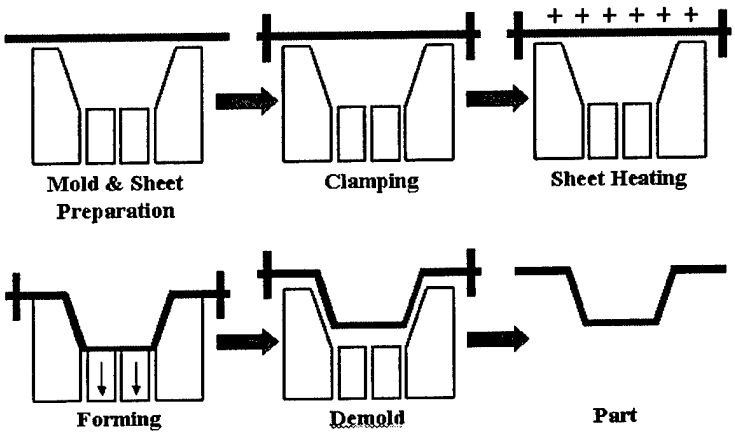

Fig. 7 Schematic diagram of vacuum molding

The sheet is then cut along the boundary of product-shape area and surrounding area is removed. The first half part and the second half part molded from vacuum molding are adhered

together along the parting line. Finally, a complete part is obtained. Fig. 8 shows the feature of manufactured part from vacuum molding.

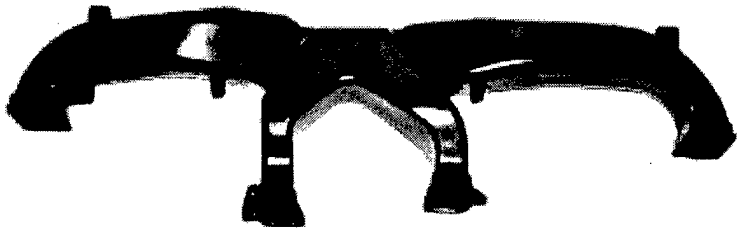

Fig. 8 Photo of manufactured part

3. EXPERIMENTAL RESULTS

3.1 Measuring error

Fig. 9 shows the main dimensional sections to get measuring error of manufactured parts between the design dimensions and the molded part dimensions. Table 3 shows the design dimensions and the average value of sampling dimensions of vacuum molded parts. SLS parts were manufactured considering shrinkage 0.8% of vacuum molded parts.

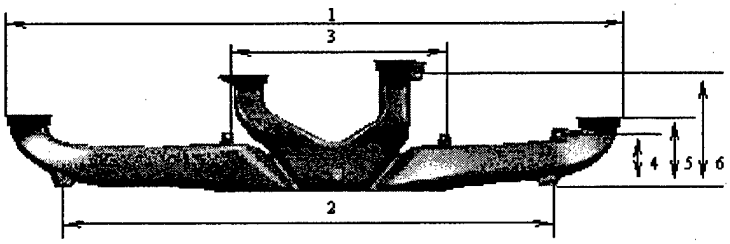

Fig. 9 Sample dimensions of a model

Table 3 Design Dimension and Molded Part Dimension

	Design Dimension (mm)	Molded Part Dimension (mm)	Shrinkage (mm)
1	1298.16	1297.68	-0.48
2	1033.88	1033.52	-0.36
3	452.99	452.78	-0.21
4	110.80	110.68	-0.12
5	159.40	159.25	-0.15
6	265.32	265.08	-0.24

4. CONCLUSIONS

This paper suggests the new process to manufacture large size hollow shape parts for prototype-car using Rapid Prototyping technology and Vacuum Molding. In addition, this paper introduces the dividing and combining method to make large size RP master model despite the limit of the build chamber dimensions of commercialized RP systems and post-processing method to achieve sufficient surface quality. In order to know if the suggested process is used in industrial fields, the suggested process is compared with the existing process, ZAS blow molding. From experiment results, the suggested vacuum molding process shows that products have sufficient quality considering that the tolerance of large size blow molding is 1 mm approximately.

REFERENCES

1. F. Prioleau, "Selective Laser Sintering – The Process and Its Materials," Proceedings of the ANTEC '93, Vol. 3, pp. 3231-3234, 1993.
2. T.S. JANG, "Development and Technology of Prototype-Car using Rapid Prototyping," PKATEC Workshop and RP Exhibition", pp. 34-38, 1998.
3. P.F. Jacobs, "Streolithography Accuracy, QuickCast™ & Rapid Tooling," ICALEO, p. 194, 1995.
4. H.J. YANG, B.J. HWANG, S.H. LEE, "A Study on Manufacturing Resin-based Blow Mold using SLS Parts and Forming Prototype-Car Parts," Journal of the Korean Society of Precision Engineering, Vol. 17, pp. 124-131, 2000.

Instrumented Prototypes

M. Shimek, K. Lappo, K. Wood, D. Bourell, and R. Crawford
Department of Mechanical Engineering
Laboratory for Freeform Fabrication
The University of Texas at Austin, Austin, TX 78712

Abstract

Full scale prototyping can be expensive and time consuming. Virtual prototypes reduce costs and time but often cannot be relied on for full scale production. Instrumented SFF prototypes update virtual prototypes, reducing cycle times and costs for full scale production. Both single and multi-layer access, two different methods for embedding sensors, are investigated at the University of Texas at Austin. Sensors are first embedded in a simulated SLS process to determine if embedding off the shelf sensors is feasible. Foil strain gages are then embedded into cantilever beams using multi-layer techniques. Both foil strain gages and bead type thermocouples are also embedded using single layer techniques. The results of the single layer tests will be used to construct a proof-of-concept prototype for single layer embedding.

Introduction

The field of prototyping is under scrutiny at the present time. Making a full scale prototype is very expensive and often too time consuming to justify. Many engineers are turning to virtual prototyping with the recent increase in computing power. A problem arises because virtual prototyping methods often do not provide engineers with sufficient data to proceed with full scale production. The goal of this research is to develop methods of creating instrumented prototypes, using Solid Freeform Fabrication techniques, which can update the virtual prototypes. Sensor arrays within instrumented prototypes measure the raw data necessary to update virtual prototypes. Empirical similitude techniques are then used to transform the data for application. Accurate and updated virtual prototypes will allow engineers to proceed to full scale production, reducing cycle times and costs.

The goal of this research is to develop a method for embedding sensors while a part is being built. Accomplishing this goal requires no human intervention. However, developing an automated system requires human intervention in order to work around the existing Sinterstation™ procedures. The end result will be a proof of concept prototype for embedding sensors within a single layer, without human intervention.

There are two primary concerns when creating instrumented prototypes. The data collected must be transformed into usable data for the full scale part. This data must first be collected from sensors at the locations of interest however. Methods for embedding sensors at these locations of interest are being investigated at The University of Texas at Austin.

General Embedding

Sensors suitable for the embedding process must be identified before proceeding. This research focuses on the Selective Laser Sintering process. Sensors must therefore meet temperature and size constraints or work around them somehow. The environment inside the SLS chamber is heated to just below the melting temperature (T_m) of the material being used. A laser then provides the energy required to locally melt the powder, solidifying the two dimensional computer model cross-section and fusing it to the previous layer. Resolution is maximized by minimizing layer thickness within thermal property allowances. The size of layers can also be a condition for sensor selection.

Operating temperature is the primary constraint for selecting an appropriate sensor. Duraform GF (glass filled) is a composite, used in the SLS process, with the highest T_m of all the polymer based materials used. It has a melting temperature of 185°C [1]. Sensors are selected which can withstand the temperatures for all the polymers with Duraform GF being the upper bound. Sensors are exposed to these temperatures for extended periods of time. A sensor that can merely survive these temperatures will possibly degrade with prolonged exposure. Therefore, sensors with operating temperature ranges encompassing these high temperatures are chosen.

Sensor size is the next concern for embedding sensors. Sensor size will determine the method for embedding sensors. There are two possibilities for embedding off the shelf sensors; single and multi-layer access. Single layer access refers to embedding sensors inside one layer of a Solid Freeform Fabrication process. Multi-layer access means embedding sensors which are thicker than one layer of the process being used. Both methods have advantages and disadvantages. Smaller sensors will be more fragile and expensive but will be less intrusive to the SLS process. Larger sensors will be more robust but require significant alteration of the SLS process. Both methods are investigated but it must first be determined if the concept of embedded sensors is feasible.

A simulated SLS process is used to test the feasibility of embedding off the shelf sensors into SLS parts. A survey of available sensors shows bead type thermocouples to be the preferred sensor for the feasibility study. Time constraints require the use of a mold instead of a layer based process. Using a kitchen oven heats all the powder at the same time, fusing the entire part as opposed to layer by layer. The mold is made of aluminum, which can withstand the heat of the process. Aluminum is also chosen for its machinability. The shape of the final product is chosen as a cylinder to facilitate ease of sensor placement and recording temperature data. [2]

Using a simple cylinder allows the temperature data to be used for a one dimensional, steady state heat conduction analysis. The temperature distribution profile for extended surfaces can follow one of four analytical models, depending on conditions at the end (tip). The first case involves convection heat transfer at the tip. The second assumes adiabatic conditions at the tip. Case three keeps the tip at a constant temperature. Case four assumes infinite length. Infinite fin length assumptions become valid for this material and shape (polycarbonate cylinder) at lengths over $28.3mm$ ($1.11in$). The test

samples were 72mm (2.83in), validating this assumption. The infinite length assumption provides an exponential temperature distribution.

$$T(x) - T_\infty = (T_s - T_\infty)e^{-mx} \quad [4]$$

where

$$m = \sqrt{\frac{hP}{kA_c}}$$

Variable h is coefficient of convection; P is perimeter; k is conduction coefficient; and A_c is cross-sectional area. The curve fitted results from testing were compared to the analytical curve.

The analytical model is constructed using data from the testing procedure. The variables used are:

$T_s = 165^0 C$
$T_\infty = 45^0 C$
$k = 0.18 W/mK$
$h = 5 W/m^2 K$
$P = 0.0345m$
$A_c = 0.000095m^2$

As mentioned earlier, the analytical model is created with the infinite fin length assumption. Figure 1 shows the experimental results with the theoretical plotted as a solid line. This plot summarizes the data from nine test samples.

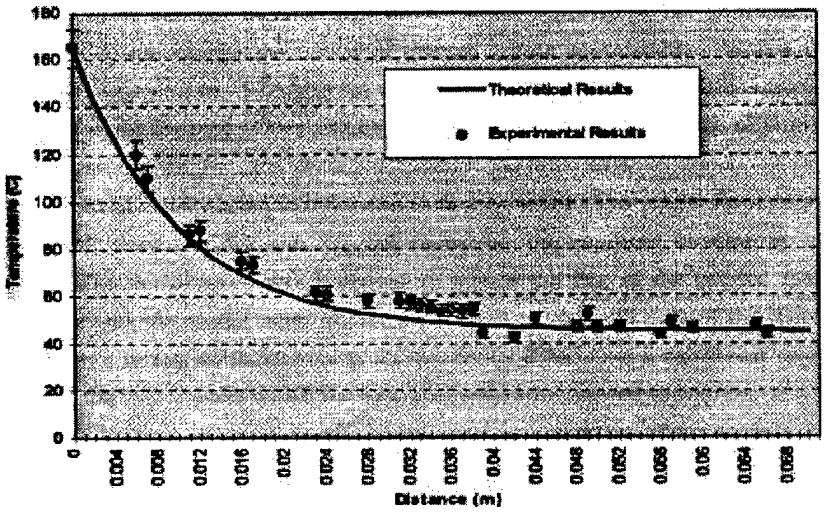

Figure 1. Theoretical and experimental data for 1-D heating [2]

These experiments show general embedding to be valid. Embedding sensors in actual SLS parts is the next step. Two methods for accomplishing this are being investigated, multi-layer access and single layer access. Each method has advantages and disadvantages. The larger sensors used in multi-layer access are typically more durable and robust. However, their larger size does not allow collection of accurate point data. Smaller sensors are able to provide more accurate point data but are typically more fragile. Single layer access also requires sensors to be embedded during the build cycle. This places an additional constraint on sensors due to temperature requirements. Sensors must be able to survive the elevated temperatures experienced during the SLS build cycle.

Multi-Layer Access

Strain gages are embedded into SLS prototypes using multi-layer methods. Cantilever beams are made with cavities inside them for embedding strain gages post build. Strain gages are embedded into the cavity which is then filled with epoxy. Experiments are conducted to determine appropriate cavities and epoxies for embedding multi-layer sensors [3].

The first experiment uses a cantilever beam with a large cavity, illustrated in figure 2, accessible from the top of the beam. This possibility allows easy access for the installation of the sensor, adhesive, and epoxy. The cantilever beam is placed in a setup with a static load of 2.2 pounds [3]. Results from the embedded strain gage are compared to data from a finite element model. Data from the strain gage, when compared to the stress contours from the FEM, show this method to be feasible. However, better ways of filling the cavity to more accurately simulate a fully dense structure are investigated.

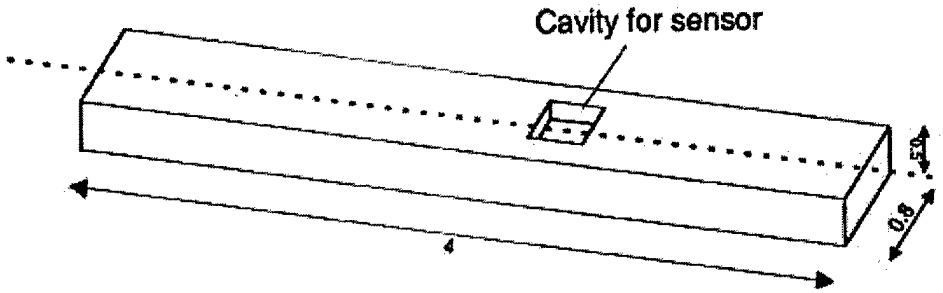

Figure 2. method #1 for multi-layer access [3]

The second test uses a similar concept to the first one. However, the size of the cavity is reduced in order to reduce its influence on the stiffness of the beam. The beam for the second test is dimensionally very close to method #1, the only difference being the cavity size. Figure 3 shows an illustration of this beam. The reduced cavity size makes gage placement more difficult due to reduced access. Prototype 2 is also compared to a finite element model with promising results. The FEM shows the measured value of

33psi to be very close to a beam with no cavity [3]. This shows prototype 2 to give better data than the first method but sensor placement is far more difficult.

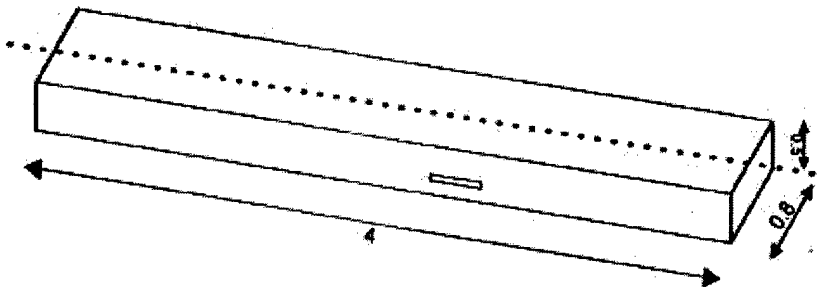

Figure 3. Method #2 for multi-layer access [3]

Prototype 3 uses the same concept as prototype 2 but adds one key feature. Accurate mounting of the sensor is difficult with method #2 due to the small clearance of the cavity. A mold or base is made for the sensor as shown in Figure 4. The sensor is mounted on the mold and both are inserted into the cavity. The results of testing this method show 27 psi, similar to results for prototype 2. This method provides good results and is much easier than method #2.

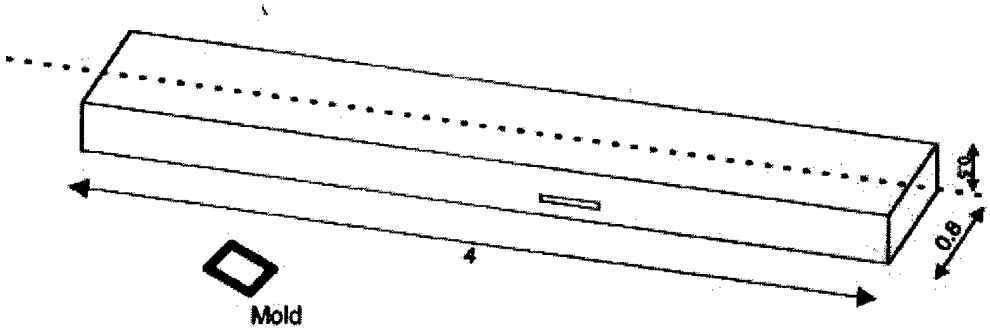

Figure 4. Method #3 for multi-layer access

Experimental Set Up

Single layer access is pursued with two off-the-shelf sensors in mind, bead thermocouples and foil strain gages. Embedded thermocouples are to be evaluated using a 1-D heating model as in previous tests. Strain gages embedded with single layer access are to be tested on an instron, tension testing machine. Results from the strain gages will be compared to extensometer results.

Thermocouples

K type thermocouples with bead diameters of 0.003 inches are used based on recommendations from previous work and investigation [2]. These thermocouples are chosen for their temperature characteristics as well as there size. Operating temperatures of these gages are well above the temperature of the process chamber during a build. The

sensors might be directly exposed to the laser but it only raises the temperature of the powder a few degrees and the powder has higher absorbtivity than the sensors. Therefore detailed tests are not conducted to verify the temperature of the thermocouples is not raised above the operating temperature.

Embedding tests are conducted to verify the validity of data collected from embedded thermocouples and to uncover issues in the embedding process itself. Three small cylinders are created in a prototype SLS machine using Duraform™, a nylon based powder. This machine is often used for research purposes due to its simplicity. Initially, the surface of a freshly sintered part is presumed tacky enough for the sensor to adhere to the part directly after laser scanning. The surface of the freshly sintered cylinder is found to be solidified. Next, the sensor is put in place after a layer of fresh powder is deposited but before the laser begins scanning. Sensor and plastic powder are both scanned by the laser, making the plastic temporarily molten. The sensor is fused to the part, effectively gluing it in place.

Strain Gages

Embedding strain gages is an important goal of this research. Foil strain gages are chosen because of cost reasons. They are cheaper than other strain gage options, fiber optic strain gages for example. However, embedding strain gages into SLS parts is more challenging than embedding thermocouples. Strain gages are physically larger than thermocouples. Accuracy of strain gages relies on good axial alignment, adding a third degree of freedom to sensor placement; X and Y placement plus rotation in the XY plane. They are also more sensitive to the high temperatures of the SLS process, due in large part to their backing material. These gages are generally adhered to the surface of a structure to measure the strain. An embedded sensor will provide data that is more point specific and will possibly eliminate the need for adhesive.

Experimental Procedure

Thermocouples

A couple of unforeseen problems are observed while placing the thermocouples. Lead wire management presents a large problem. Long wires become tangled in the roller of the SLS machine, requiring short lead wires. Shortened lead wires prevent tangling but new issues arise. Roller movement over the part bends the wires back and forth raising concerns of fatigue. Placing the sensor and lead wires flat on the surface of the part also presents major concerns. Two sensors are placed adequately on the part surfaces. A third placement results in one lead wire protruding above the layer with solid plastic, linking it to the part below. This results in part shift, an unsuccessful build. The remaining two cylinders are completed successfully and tests are performed to check the data from the thermocouple.

Having completed the first step of the feasibility study, successfully embedding thermocouples, data must be collected and compared to expected results. Figure 5 shows the setup for obtaining the necessary data.

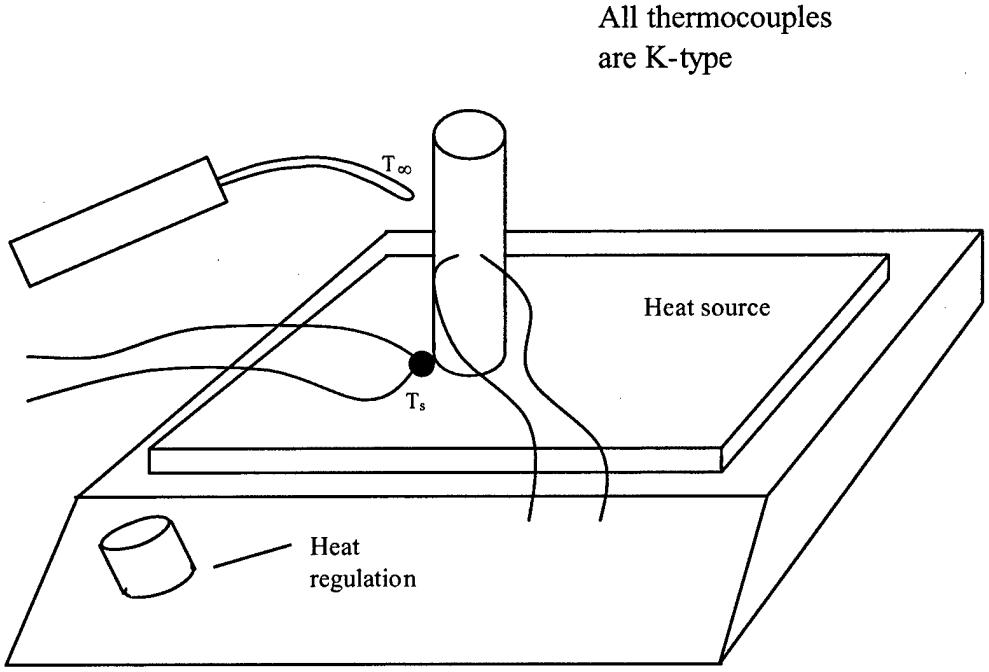

Figure 5. Set up for heating verification

A reading of the temperature is taken at the heating surface by a thermocouple secured to the heating surface. A wand type thermocouple measures the T_∞ for the cylinder. The embedded thermocouple then measures the temperature inside the cylinder during steady state conditions. An expected temperature is calculated analytically using a 1D heating model, similar to the one used for testing general embedding:

$$T(x) - T_\infty = (T_s - T_\infty)e^{-mx}$$

where [4]

$$m = \sqrt{\frac{hP}{kA_c}}$$

Variable h represents convection coefficient; P is perimeter; k is conduction; and A_c is cross sectional area. The values for this model match the physical characteristics of the specimen tested.

Strain Gages

Initial experiments are conducted with demo sensors in order to develop the technique for embedment. These demo sensors consist of brass rectangles matching the dimensions of the gages to be used. Wires are soldered to the base of the rectangle in order to simulate the lead wires of the sensor. The solder beads are made as small as possible to minimize the thickness of the simulated sensor. Figure 6 is an illustration of the demo sensors.

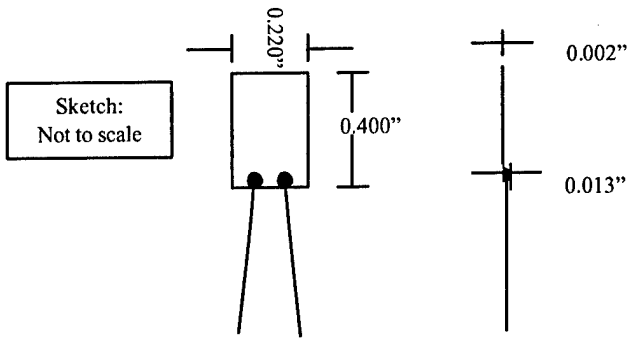

Figure 6. Sketch of demo sensors

Two experiments are conducted to hone the technique for embedding strain gages. The strain gages will be used in dog-bone structures so strain can be measured with an extensometer and compared to data from the strain gage. The dog-bones are built as two separate pieces. The bottom half contains a small cavity so the powder roller does not affect sensor placement. The top half is a solid dog-bone shape. Figure 7 is an exploded view of this technique. These tests are given a rating from 1-10 to indicate how well the method works. 10 meaning the method works perfectly; 1 meaning the method does not work at all.

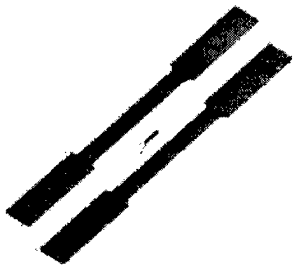

Figure 7. Exploded view of build technique

The first test involves embedding one demo sensor. The goal of this experiment is to identify any major problems with the embedding technique. The bottom half was constructed using general practices for CastForm™. However, the Sinterstation™ is not allowed to perform the cool down cycle typically performed with CastForm™. The machine is stopped and opened after the bottom half is finished but before a new layer of powder can be deposited. Excess powder needs to be removed from the cavity before sensor placement. A vacuum cleaner is used to suck away the excess powder.

Unfortunately, the vacuum sucks the entire part away from the part-bed. The part is replaced and the experiment continues. Lead wires from the "sensor" are gently pushed into the powder to prevent shifting caused by "sensor" and/or lead wires. Voids in the powder caused by "sensor" placement and vacuum shifting are filled by powder needed to cover part. The first few layers are not covered by needed powder. However, "sensor" and lead wires did not cause shifting. This build is stopped before completion. Inspection of part shows weak bonding but bonding is achieved. This is important because the use of adhesive is undesirable. The voids caused by the vacuum mishap and the disassembled dog-bone sample are shown in figures 8 and 9. This test is given an overall rating of five. Problems are exhibited but embedding does seem possible based on this test. The "sensor" shows some adhesion to the part and problems such as shifting and incomplete layer deposition are attributable to embedding technique.

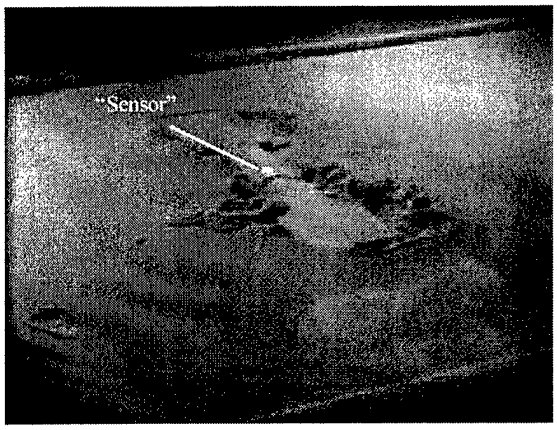

Figure 8. Vacuum mishap

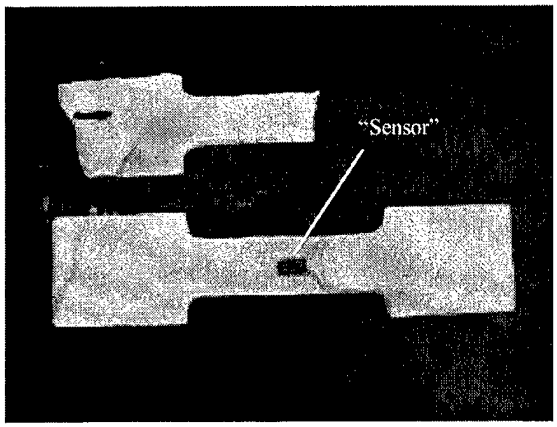

Figure 9. Disassembled sample 1

Valuable lessons are learned from the initial test and implemented on the second test. Two samples are constructed in order to identify the effect of part/sensor orientation on embedding. Figure 10 is a photograph of the part orientation. Both parts protrude beyond the recommended build circle so warping and/or delamination is expected. Solder faces up on both samples. A soft bristled paint brush is used to sweep away excess powder once the bottom is completed. Lead wires are bent downward at the part' s edge and the "sensors" are angled for the roller to encounter the downward edge first. Both methods are employed to prevent part shifting. The "sensors" are placed without incident but voids in the powder caused during placement result in incomplete layer deposition. The build is paused and the powder feed distance is briefly increased. The remainder of the build occurs uneventfully.

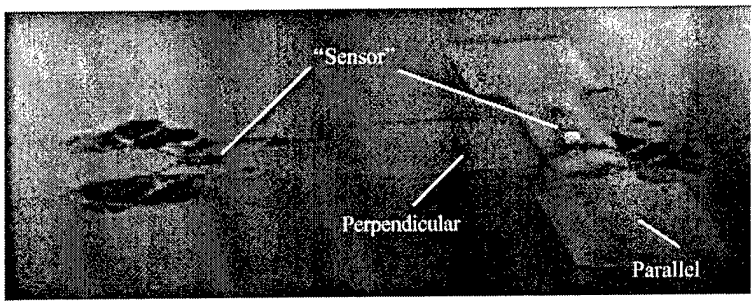

Figure 10. Part orientation

Post-build inspection reveals the appearance of proper embedding. The parallel part exhibits some shifting which is largely attributed to warping. Both parts also exhibit minor delamination due to extension beyond the recommended build circle, see figure 11. Although shifting in the parallel part is largely attributed to warping, the perpendicular part does not exhibit any shifting. This build is given an overall rating of eight. Results are promising to the point where real sensors are attempted next. The next experiment uses the actual sensors in two perpendicular parts. The strain gages are embedded with both; solder up and solder down.

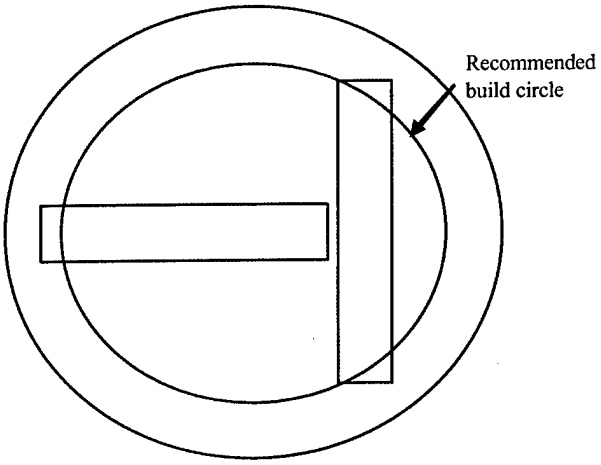

Figure 11. Build two layout

Results

Thermocouples

Following the procedure listed above, samples are placed in the illustrated set up to collect data for a steady state 1-D heating model. The variables used for the model are listed below:

$T_s = 89^0 C$	Using these values
$T_\infty = 31^0 C$	$m = 251.3$
$h = 5 W/m^2 K$	The infinite fin length assumption is
$k = 0.025 W/mK$	valid for $mL >> 1$
$P = 0.040m$	$mL = 251.3(0.075m) = 18.8$
$A_c = 1.267 \times 10^{-4} m$	Infinite fin length assumption is used

The model predicts a temperature of 31°C. 30°C is recorded during the experiment. The error is less than three percent which validates embedding thermocouples during the build process. A sample is machined to show the embedded thermocouple. Figure 12 shows both a photograph and x-ray of the sample. One wire seems to kink and cross the other in the x-ray but the second wire can barely be seen in the photograph. This indicates that the second wire is at a different Z height. Duraform™ is an insulator so a short circuit is avoided. However, this reemphasizes the importance of keeping the lead wires separate.

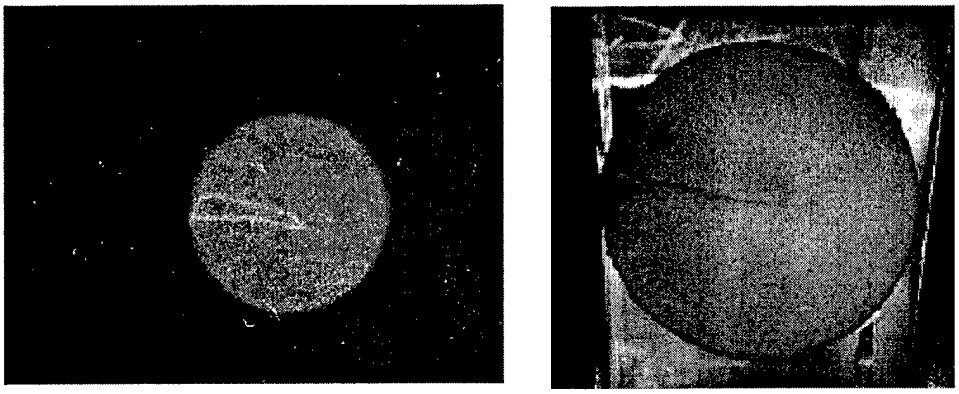

Figure 12. X-ray and photograph of embedding sample

Strain Gages

Build three is very different due the use of actual strain gages. This build uses no adhesive as do the other experiments. Using no adhesive simplifies the design of an embedding system. The absence of adhesive allows an automated system to omit the process of applying it, thus reducing and simplifying the operations required from an

automated system. The sensors are placed with the solder facing up and down. This is done in order to evaluate the effect of solder orientation.

Observations are made as the experiment is conducted. One sensor breaks during handling and prior to embedment. This occurrence illustrates the fragility encountered with smaller sensors. The sensor lead wires prove to be very difficult to shape before embedding. The material and thickness of the lead wires make their stiffness such that the wires are resistant to shaping for embedding. A lead wire fixture is used in pre-shaping the lead wires. The sensors are difficult to fit into the fixtures and do not stay in the shape dictated by the fixture. The powder feed distance is increased for the first layers of the second half build. Voids created during sensor placement are filled by the increased feed distance. Sensors are also angled toward the roller so it encounters the downward side of the sensor as it spreads a new layer. The strain gages are not rolled flat after the first layer of powder deposition due to the stiffness of the lead wires. Several layers of powder are needed to fully cover the strain gages. The strain gages are not embedded within a single layer. This build is given an overall rating of two. Single layer access proves unmanageable with foil strain gages. The geometry of the demo sensors matches the actual strain gages but the lead wires prove to be very different. Foil strain gage embedding is no longer pursued with this research at present due to the stiffness encountered with the real lead wires.

Future work

A proof of concept prototype is under construction that embeds bead type thermocouples during the build process. The prototype embeds the thermocouple without human intervention into the build chamber. It is able to withstand the environment inside the Sinterstation™. It is able to separate and lay flat the sensor lead wires and interact with the existing systems of the Sinterstation™. It can be retrofitted to a current device and is removable to facilitate easy powder addition/removal. This is an initial step towards realizing instrumented prototypes.

References

[1] 3D Systems website: http://www.3dsystems.com

[2] Gregory Falkner, Design of a Method to Embed Sensors In a Solid Freeform Fabrication Process, Masters Thesis 1997.

[3] Nachiket Patwardhan, Instrumented Prototyping, Masters Thesis 2002.

[4] Frank P. Incopera & David P. DeWitt. *Fundamentals of Heat and Mass Transfer.* John Wiley & Sons.

Laser Direct-Write of Nanoporous Optical Coatings: Preliminary Results

R. Ruizpalacios[1], H. Kyogoku[2], V. Sriram[1], K.L. Wood[1], and J.J. Beaman[1]

[1]Department of Mechanical Engineering, The University of Texas at Austin, Austin TX

[2]Department of Mechanical Engineering, Kinki University, Hiroshima, Japan

Reviewed, accepted August 13, 2003

Abstract

The combination of nanoporous optical thin films prepared by the sol-gel process with direct-write capabilities has been an area of interest over the past decade. Recent advancements in both fields suggest the possibility of fabricating novel components for rapid prototyping purposes. This paper presents the work in progress done over the past year, initially aimed at process characterization. Standard silicate sol-gels were synthesized and deposited by spin coating on silicon wafers. Further post processing was done prior to laser densification with a CO_2 laser.

1. Introduction

The recent increase in demand for information bandwidth has created the need for improving current technologies for data, voice and video transmission. New technologies have emerged addressing different aspects of networking, such as transmission protocols, communication devices, and manufacturing methods of these devices. Transmission through optical fibers plays a fundamental role in the current and future infrastructure [1].

The current bottleneck in transmitting data optically does not lie in the long lengths of cabling required over large distances, but rather in delivering higher bandwidths to the end users in what has recently been named as ultra-high capacity optical networks. Two areas that address these needs include function integration in optoelectronic components and advanced materials, respectively. The combination of advanced materials derived from sol-gels with direct-write technologies, has the potential of addressing these initiatives. As documented in recent NSF and DARPA workshops, a critical area of research is the "Direct Writing" of components for industries such as telecommunications. Direct-write technologies are manufacturing processes characterized by the use of computer-generated patterns and shapes for direct fabrication without part-specific tooling. They represent a set of emerging technologies, competing with more conventional fabrication techniques primarily in the microelectronics field and lie at the forefront in research and development as alternatives of current photoresist technologies [2,3,4].

Sol-gel processing allows the creation of high optical-quality films and monoliths through the strict control of processing parameters (concentration, pH, temperature, humidity) in combination with high-purity sol-gel precursors [5]. This approach has received great attention because of the possibility of low processing temperatures and standard atmospheric conditions, and its ability to produce highly pure materials directly from their synthesis. Likewise, laser scanning has the ability to selectively achieve high-density levels of sol-gels comparable to vapor deposition and melting [6,7]. A direct relation exists between a sol-gel's density and index of refraction [8], hence the ability to control the index of refraction through density changes based on laser power control is an area of keen interest.

In this paper we report the work in progress done over the past year towards the development of a novel manufacturing process for the direct write of optical components, combining the advantages of controlled laser densification with sol-gel coating. The paper is organized as follows. First we present a description of the experimental procedures that were followed for preparation of the sol-gels, their deposition and heat treatment, followed by laser scanning. The following section presents the results and discussion in each of these areas.

2. Experimental Procedure

In this section we outline the experimental procedures that were followed, starting from the preparation of the sol-gel solution, the deposition of the solution by spin coating, the process for heat-treating the film, and the final laser densification step. Figure 1 illustrates in general the experimental procedure that was followed.

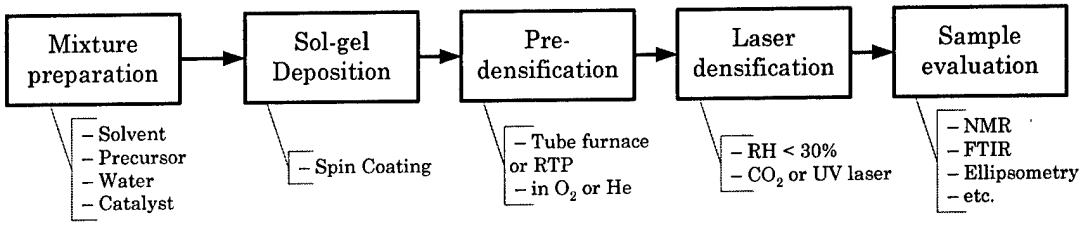

Figure 1. Outline of the experimental process

2.1 Sol-Gel Preparation

The sol-gel process consists, in general, in the hydrolysis of a precursor, in this case an alkoxide, in the presence of a catalyst (acid or base), and followed by condensation and poly-condensation reactions to form particulate or polymeric structures [5]. The solutions synthesized were based on well know purely inorganic silica-based systems [5,9,10,11].

For the preparation of the purely inorganic Si-based sol we used tetraethyl orthosilicate (TEOS) as the sol-gel precursor, ethanol as a solvent, de-ionized water, and hydrochloric acid as catalyst. A number of mixtures were prepared and are indicated in the ternary diagram of Figure 2(a), which is based on [5]. The preparation procedure, based on [9,10], consisted of a two-step hydrolysis process, followed by refluxing of the solution for 60 minutes at 60-65°C.

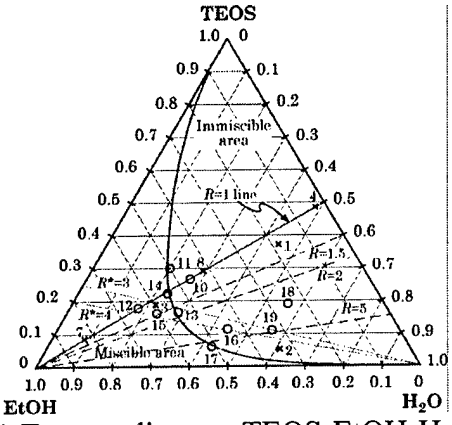

(a) Ternary diagram TEOS-EtOH-H_2O

Mixt.	Molar fraction (%) TEOS	H_2O	EtOH	R	R*	Density (g/cm^3)	Viscosity Kinematic (cSt)	Dynamic (cP)
7	19.60	21.00	59.40	1.07	3.03	0.928	2.826	2.622
15	18.00	18.00	64.00	1.00	3.56	0.931	2.082	1.939
16	18.00	22.00	60.00	1.22	3.33	0.951	2.250	2.140
17	22.00	22.00	54.00	1.00	2.45	0.937	2.028	1.900
18	18.00	28.00	54.00	1.56	3.00	0.956	3.107	2.970
19	10.90	55.70	32.80	5.11	3.01	0.980	4.921	4.821

(b) Composition of mixtures

Figure 2. Molar ratios of various experiments

2.2 Deposition of Thin Films by Spin Coating

The films were spin coated on two types of substrates: Si (100) wafers, and borosilicate glass slides. Surface preparation is critical for successful deposition of the films. To achieve this, the substrates were cleaned with trichloroethylene, then rinsed with acetone, isopropyl alcohol, and de-ionized water using an ultrasonic bath. After this, the substrates were dried and stored in a drying cabinet, prior to deposition by spin coating.

The spin coating was carried out at various spinning velocities for various duration times under N_2 and standard air using a single-wafer spin processor. The spin-coating profiles consisted in an acceleration step, deposition of 20 μl of filtered solution, acceleration to desired speed, and finally a dwell period for solvent evaporation. Typical deposition velocities ranged from 2000 up to 5000 rpm, while the complete process time ranged from 40-60 sec.

2.3 Heat Treatment

Following the deposition step a consolidation or sintering step is required because of the highly porous nature of the as-spinned films. During sintering, an increase in density occurs due to further solvent and water evaporation (chemisorbed and physisorbed). So the initial chemistry and the desired final physical properties dictate the sintering or heat treatment temperature. The design of an appropriate heat treatment process represents a crucial step and a common roadblock for the achievement of films with thickness compatible with standard single-mode fiber optics. For this reason we devoted a substantial amount of time experimenting with various heating profiles, atmospheres, and processing equipment. A good understanding of the evolution of the psychochemical properties after the heat treatment step is required to characterize and ultimately control the process. With this in mind, we performed a series of experiments that involved the drying and densification of the films that would provide evidence and insight. The main issues explored were the relationship between heating temperature and thickness or index of refraction, and the effects of the drying step on the final structural composition of the film.

The films were heat-treated using a hot plate (120–200°C), a horizontal tube furnace (200–880°C), and an experimental vertical furnace (400–900°C) developed in our lab for rapid thermal annealing; all of them having controlled environment capabilities. Various dwell times and heating rates under He or O_2 gas flow were implemented.

2.4 Film Characterization: Techniques

For sample evaluation, process characterization, and process optimization, we used a number of standard techniques, which are described below.

For the analysis of the sol-gel solutions we used Nuclear Magnetic Resonance (NMR) spectroscopy for structure analysis. The viscosity was measured 24 hrs after preparation, with a Cannon-Frenske kinematic viscometer. Multiple-Angle Ellipsometry carried out in air was used for measurement of thickness and index of refraction. Fourier Transform Infrared Spectroscopy (FTIR) was used for evaluation of the molecular structure of the deposited films for various concentrations and heat treatment procedures. Atomic force microscopy (AFM) was employed to measure surface roughness and observe film morphology.

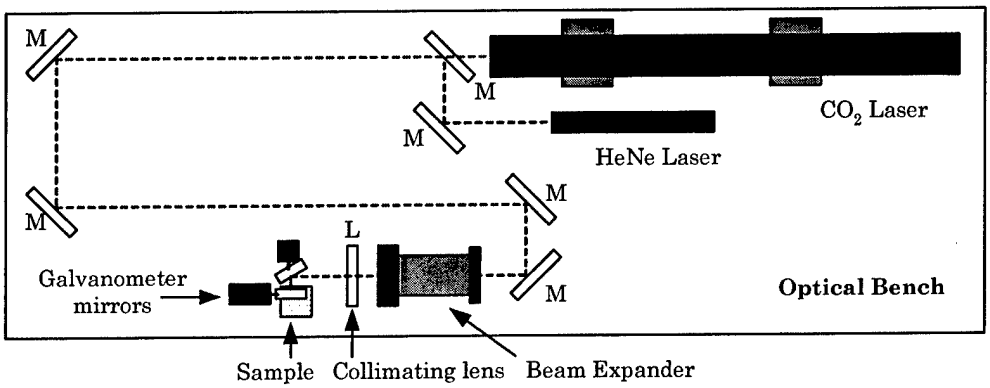

Figure 3. Schematic of optical setup for laser densification.

2.5 Laser Densification

Laser densification was performed with a CO_2 laser (λ=10.6μm), with maximum power of 50 W, beam diameter at exit of cavity of 3.5mm, and a spot size at the working surface of ~80μm. The control of laser power is performed by a pulse-width modulation (PWM) scheme. Both software and hardware versions were implemented, being the latest the most consistent one. Figure 3 shows a schematic of the optical assembly. A galvanometer-mirror assembly, which was controlled by a PC, deflected the beam onto the working surface, following the desired geometry. The position of the beam and the laser power were controlled simultaneously by a single graphical interface programmed in LabVIEW. The laser power was varied from 0.5–4.0 W, while scanning speeds from 0.486–2.429 cm/s, with a spot size of ~80μm ($1/e^2$). The purpose of the initial experimentation was to find an appropriate operating window for laser power and scan speed that would produce smooth tracks in a controllable manner.

3. Results and Discussion

3.1 Effects of Composition on Structure, Physicochemical Properties and Morphology

Optical waveguides require a high degree of purity (typically <1 ppb of metallic compounds) and property uniformity, in combination with the desired index of refraction. For this reason, the election of both the sol-gel type and the synthesis procedure will dictate how well these requirements can be fulfilled. As mentioned before, we began by synthesizing a purely inorganic silicate sol-gel, which has been well documented in the literature [5, 9,10,11,12]. For this study, we made a number of sol-gel solutions, exploring various regions in the ternary diagram TEOS-H_2O-EtOH (Figure 2a). The compositions and properties of typical sol-gel solutions are given in the table of Fig. 2(b). The molar ratios between water to alkoxide, R, and solvent to alkoxide, R^*; are defined as: R=[H_2O]/[TEOS] and R^*=[EtOH]/[TEOS]. Different lines of constant R and R^* are indicated in the ternary diagram of Figure 2(a).

Si-NMR spectroscopy has been extensively employed to investigate the polymerization kinetics in the sol-gel process [5,13]. The NMR results of the typical sol-gel solutions are shown in Fig. 4. Fig. 4(a) shows a broad profile with no detectable peaks, which can be associated to a high degree of polymerization, as in a three-dimensional network structure. On the other hand, the spectrum from Fig. 4(b) with sharp peaks can be interpreted as a structure poorly branched., where the solutions presented low viscosity, and resulting in films prone to cracking.

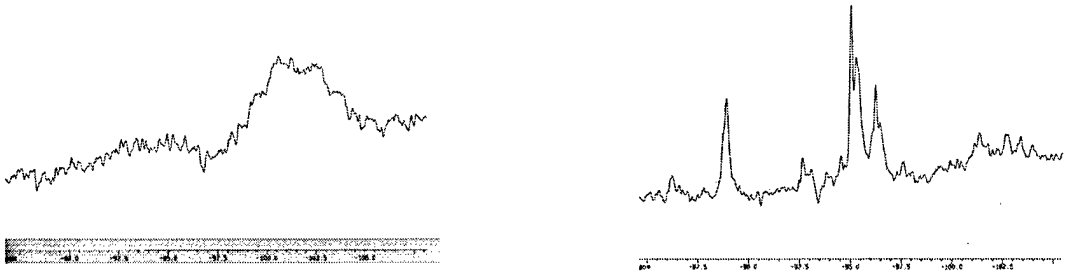

(a) NMR spectra for mixture #7 (b) NMR spectra for mixture #16

Figure 4. Typical plots from NMR and FTIR spectroscopy.

The water content on the sol affects greatly the structure and optical characteristics of the spin-coated films [15]. In particular, the index of refraction depends strongly on the water content remaining in the films. Therefore, we also evaluated the effects of the molar ratio R on the thickness and index of refraction. The combination of $R = 2$ and $R^* = 4$, produced $t_f = 652$ nm and $n = 1.4134$; while for $R = 5$ and $R^* = 4$, we observed a substantial increase of both properties to $t_f = 905$ nm and $n = 1.4401$. Although this is in agreement with the work done by Fardad [15], films with high R values cracked during sintering at temperatures above 400°C.

The morphology of the spin-coated films is influenced by both the composition of the solution and the spin-coating conditions. Solutions with high branching and mid- to high viscosity (~2.4 cP), produced smooth surfaces with an R_a on the order of 10 nm. On the other hand, less branched solutions produced cloudy and inhomogeneous films, with a higher tendency to crack.

3.2 Deposition of Single Layer Films

After studying the effects of the mixture composition, we explored the various processing parameters involved in the deposition of films, in this case by spin coating. Our goal was to characterize the process in order to control it and achieve repeatability. The homogeneity and thickness uniformity of spin-coated films strongly depend on the spin-coating speed and time, and also on the viscosity of the sol-gel solution, as observed from the following equation [16]:

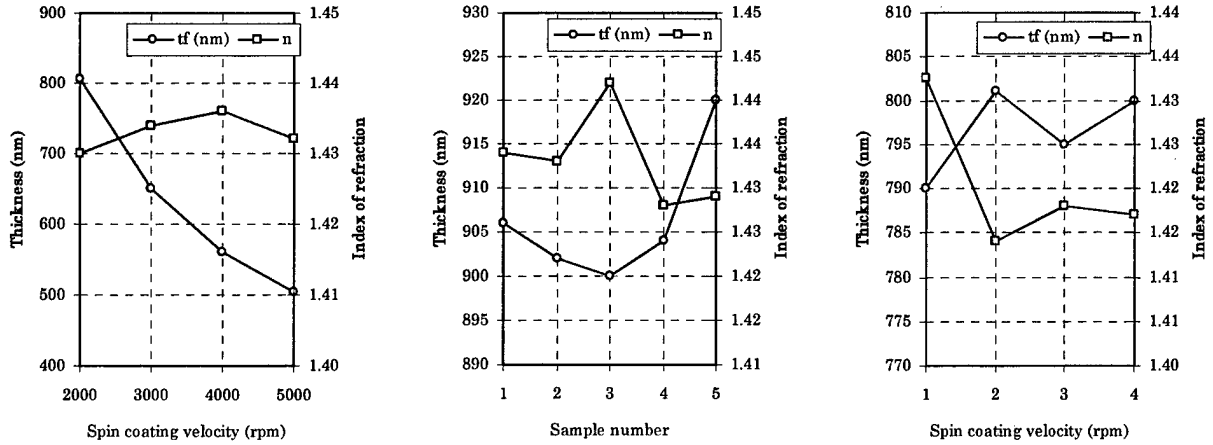

(a) effect of spinning velocity (b) variability between samples (c) variability within a sample

Figure 5. Various factors that affect the spin coating of films.

$$t_{final} = c_o \left(\frac{3\eta e}{2(1-c_o)\rho\omega^2} \right)^{\frac{1}{3}} \quad (1)$$

where c_o is the solids concentration, η the dynamic viscosity, e the evaporation rate (assumed constant), ω the angular velocity, and ρ the initial density.

Viscosity plays a fundamental role for proper deposition by spin coating. In our study we were able to verify this (see Fig. 2b). For viscosities greater than 2.5 cP we found good spinnability and repeatability. Although for a viscosity of 4.8 cP, cracking of the film took place during the heat treatment process, induced mainly by thermal stress effects. Viscosity in a sol-gel solution depends on many factors, and changes over time, reaching a maximum during gelation [5]. In our study we found that increasing the water content, for example at R values greater than 4, caused the viscosity of the sol-gel solutions to increase (see Fig. 2b). On the other hand, we found that too great of a water content was detrimental for further post processing, during heat treatment or subsequent layer deposition. We found that a spinning velocity of 4000 rpm, in combination with R=3 or 4 and R^*=2 produced consistent results. Further control of film thickness and index of refraction can be done by addition of solvent, in this case EtOH.

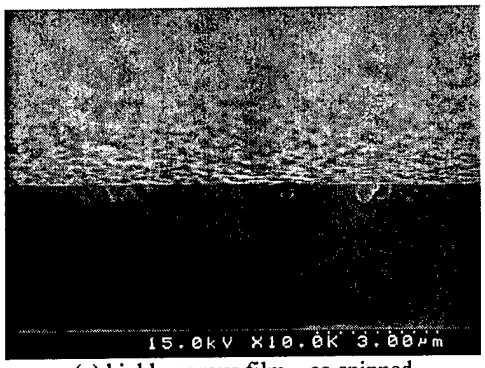

(a) highly porous film – as-spinned

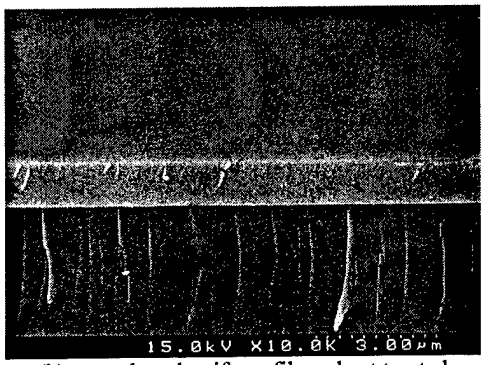

(b) smooth and uniform film – heat treated

Figure 6. SEM pictures of porous and sintered films.

For process design, we were interested in studying the effects of spinning velocity, together with variability between samples and within a single sample. Figure 5(a) shows the effect of spinning velocity on the thickness and index of refraction of the as-spin-coated film. The thickness decreases with increasing spinning velocity. On the other hand, the index of refraction slightly increases with a spinning velocity of 4000 rpm. This result was in accordance to the equation proposed by Syms and Holmes [17], which states: $t_f = k\omega^{-\gamma}$; where k and γ are constants. Figure 5(b) shows an example of variability in thickness and index of refraction of samples coated with the same solution. The differences in thickness and index of refraction among the samples are about 20µm and 0.02, respectively, although the index of refraction is affected by the thickness. Figure 5(b) shows an example of unevenness in thickness and index of refraction in the same sample. The differences in thickness and index of refraction were observed to be in the order of 10 µm and 0.013, respectively.

3.3 Heat Treatment of Films

As mentioned above, the design of an appropriate heat treatment process is crucial for the fabrication of uniform crack-free films. This can be observed by comparing Figures 6(a) and (b),

where the highly porous nature of the as-spinned films is evident, while almost completely disappearing at high processing temperatures (~800°C). To determine the heat treatment profile, the TGA analysis was carried out (plot not shown). The change in weight took place at two stages: below 500 K and over 500 K. During the first stage, the rapid decrease in weight is mainly attributed to the evaporation of water and the volatilization of remaining ethanol. In the second stage, the gradual weight reduction is attributed to the combustion of organic compounds [14]. This result suggests sintering followed by viscous flow of the SiO_2 structure.

Further more, we studied the influence of a drying step at low temperature prior to baking at higher temperatures. This drying step was performed in a hot plate under He or O_2, with a temperature of 150°C for 15 minutes. After this, the samples were heated at a rate of 4°C/min until a certain temperature T_{max}, and held there for 20 min under O_2. Table 1 shows the various conditions, together with the values for thickness and index of refraction. FTIR transmission spectroscopy was employed to compare these samples, and the results are presented in Figure 7. From these plots we can make the following observations. The drying in O_2 results in no C-H bonds (ethyl group), which are found in the range of 1400-800 cm^{-1}, while on the rest of the samples they are still present. In samples heated at 400°C there is a broad band around 3400 cm^{-1} corresponding to O-H stretching in H_2O, which is evidence of remaining H_2O in the film. This shoulder almost completely disappears for samples heated at 880°C. This is desired for optical communications, since hydroxyl groups are generally associated with attenuation loss. In sample 4, it is also observed that there is no presence of SiC_6H_5, appearing around 667 cm^{-1}. Si-OH bonds are absent in samples heated to 880°C, irrespective of whether the sample was dried in O_2 or He. Peaks for the Si-O-Si bending mode appear at higher wavenumbers for samples heated at higher temperatures, which has been correlated to stress relief phenomena [18].

Table 1. Experimental conditions for studying the effects of a drying step.

Sample	T_{drying} (°C)	Drying Atmosphere	T_{max} (°C)	Baking Atmosphere	Thickness (nm)	Index of refraction
1	150	He	400	O_2	646.82	1.3920
2	150	He	880	O_2	495.34	1.4013
3	150	O_2	400	O_2	482.15	1.3899
4	150	O_2	880	O_2	495.09	1.4064
5	None	None	400	O_2	522.90	1.3933
6	None	None	880	O_2	500.00	1.4000

3.4 Laser Densification

In the case of sol-gel SiO_2 thin films on Si wafers, CO_2 laser is not absorbed well because of the small thickness of the films and the low absorption of Si at this wavelength. For this reason we changed the substrate to borosilicate glass slides. A continuous wave (CW) mode was used for the laser densification of the sol-gel films. We observed that it is critical to maintain a constant power within <5% in oder to obtain a continuous track at low energy densities. In many cases we observed a high degrees of cracking, perhaps caused by the uneven heating and cooling experienced by the film.

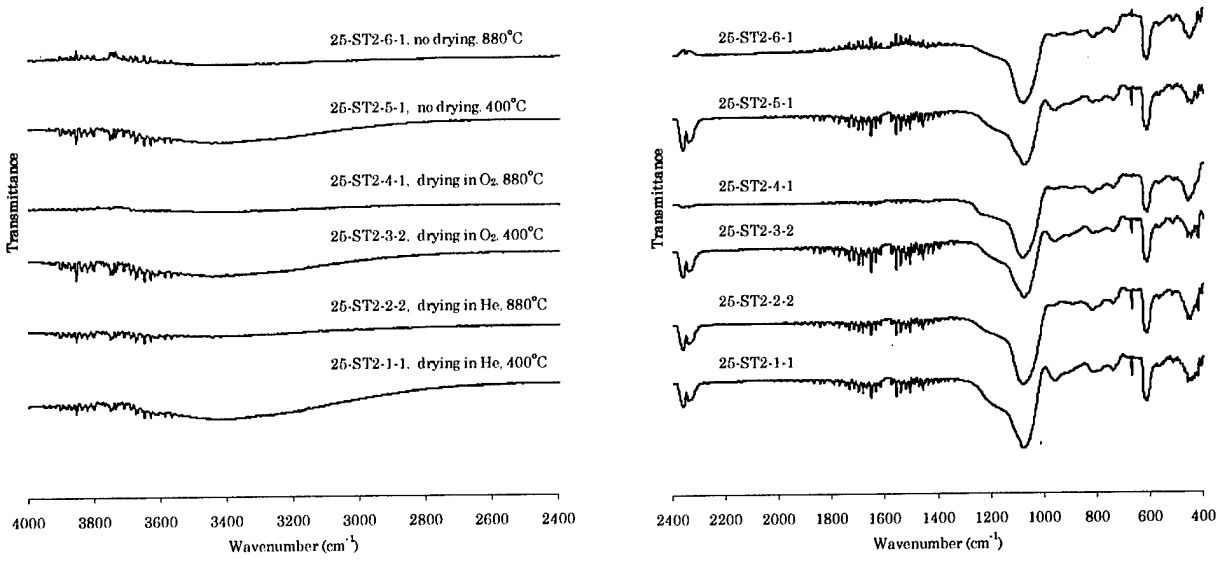

Figure 7. FTIR transmittance plot: influence of drying step.

Figures 8(a) and (b) show the changes in shape of the tracks with continuous laser power at the process time of 1.40 s and 0.65 s, respectively. In both cases, continuous tracks were obtained, but the track is smooth only at 0.93 W. Thus the morphology of the surface of the tracks is greatly affected by the laser power. In the case of the SiO_2 thin films on borosilicate glass, it is important for the laser power to keep less than 0.93 W to fabricate the continuous smooth tracks. For the CW mode, we observed a linear increase in the track width with increased laser power. Different scanning speeds produced a change in these slopes. As described above, since the range of laser power, in which the smooth tracks can be fabricated, is less than 0.93 W, it is necessary to examine the relation between the width and the laser power to control the width of waveguides accurately.

Figure 8(c) and (d) show SEM images of laser-densified tracks. Higher power and slower scanning speeds produced many defects, such as holes and bumps on the track. This phenomenon suggests that a closer examination of the heat-treatment process of deposited films is required to fabricate smooth convex-type tracks. For the energy density levels in our experiments, we observed concave tracks. This was the case for 0.93 W and a scanning speed of 1.458 cm/s. Defects such as bumps were still observed on both sides of the track, while the depth of the track was in the order of 10 nm. For these tracks the surface was very smooth, although the presence of cracks was observed at the boundary between the matrix and the heat-affected zone.

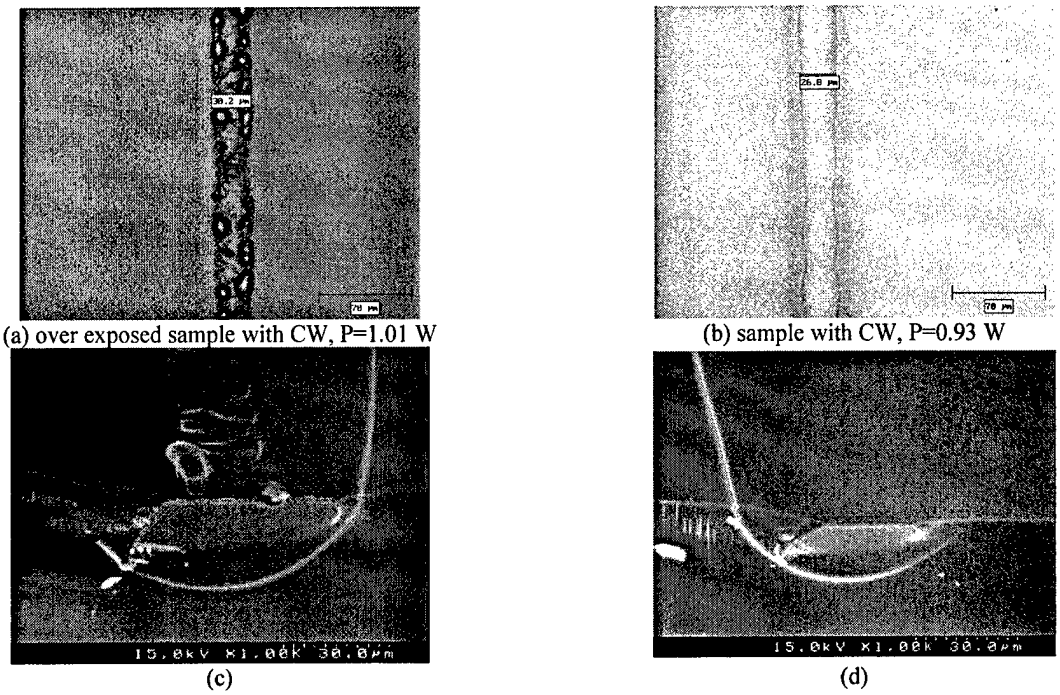

(a) over exposed sample with CW, P=1.01 W (b) sample with CW, P=0.93 W

(c) (d)

Figure 8. Images of laser densified sol-gel films.

4. Conclusions and Future Work

In this study we systematically investigated the materials design of sol-gel silica solutions, the fabrication conditions for the deposition of homogeneous thin films, and some initial experimentation with laser densification by a CO_2 laser. From our studies we concluded the following:

(1) For the successful deposition of purely inorganic silicate sol-gel by spin coating, the molar concentration of compounds plays a fundamental role since only a narrow combination of them can be applied. Specifically, the molar ratio of water to alkoxide precursor, R, has a strong effect in viscosity and structure.

(2) It was found that the uniformity of the spin-coated film strongly depends on the viscosity of the sol-gel solutions. The suitable film can be fabricated at the viscosity of more than 2.5 cP, but in the case of 4.8 cP, the cracking of the film took place by heating because of thermal stress. Viscosity also greatly affects the final thickness of the films.

(3) The heat treatment temperature strongly affects not only the thickness of the films but also their morphology and characteristics. The thickness of the films decreases with increasing heat treatment temperature, on the other hand, the index of refraction increases.

(4) The sol-gel films with high index of refraction could be fabricated by examining the contents of sol-gel solutions, the spin-coating conditions and the heat-treatment conditions in detail.

(5) The drying of the film at low temperature under oxygen, prior to sintering or laser densification, helps reduce undesired chemisorbed and physisorbed water and solvent from the film. Further analysis of this hypothesis is required, by measuring the attenuation loss in the films.

(6) We found that a small operating window between laser power and scanning speed exists for the fabrication of uniform and smooth tracks with a CW CO_2 laser. Further investigation is still required. A laser with smaller wavelength might help produce better results.

Acknowledgements

The authors wish to thank Joseph Pham, Sean Burns, and Michael Stewart, graduate students from the Materials Science and Chemical Engineering programs, for their support in the measurements of materials properties. We also thank Dr. Jose Lozano, Dr. Manthiram, and Mr. Jim Wallin for their technical assistance, and Mr. Robert Lewandowski for his help with the glasswork. We kindly thank the guidance provided by Dr. Heim, Dr. Norman, Dr Wood, and Dr Fray from 3M.

This work has been partially sponsored by the Texas Higher Education Coordinating Board, together with the National Science Foundation and 3M Co.

References

[1] Hecht, J. (1999). *Understanding Fiber Optics*, 3rd edition, Prentice Hall, NJ.

[2] Church, K. H., Fore, C., et al. (2000). "Commercial applications and review for direct write technologies." *Materials Development for Direct Write Technologies*, San Fco., CA, Materials Research Society.

[3] Pique, A. and Chrisey, D.B. (ed), (2002), *Direct-Write Technologies for Rapid Prototyping Applications*, Academic Press, San Diego, CA.

[4] Miura, K., J. Qiu, et al. (1997). "Photowritten optical waveguides in various glasses with ultrashort pulse laser." *Applied Physics Letters*, 71(23): 3329-3331.

[5] Brinker, C.J., Scherer, G.W. (1990). *Sol-Gel Science*. San Diego, CA, Academic Press, Inc.

[6] Shaw, D.J., King, T.A. (1990), "Densification of sol-gel silica glass by laser irradiation", SPIE 1328, *Sol-Gel Optics*, p 474-479.

[7] Chia, T. (1992). "Laser Densification of Gel-Silica Glasses and Optical Application", Ph.D. Diss., University of Florida.

[8] Hench, L. L. (1998). *Sol-Gel Silica*. Westwood, NJ, Noyes Publications.

[9] Sakka, S., Kamiya, K., (1982), "The Sol-Gel Transition in The Hydrolysis of Metal Alkoxides in Relation to The Formation of Glass Fibers and Films", *Journal of Non-Crystalline Solids*, Vol.48, pp.31-46.

[10] Sakka, S., Kamiya, K., Makita, K., Yamamoto, Y., (1984), "Formation of Sheets and Coating Films from Alkoxide Solutions", *ibid.*, Vol.63, pp. 223-235.

[11] Righini, G., Pelli, S. (1997), "Sol-Gel Waveguides", *Journal of Sol-Gel Science and Technology*, 8, pp. 991-997.

[12] Parrill, T.M. (1994), "Heat treatment of spun-on acid-catalyzed sol-gel silica films", *Journal of Materials Research*, Vol.9, No.3, pp.723-730

[13] Brinker, C.J., et al (1984), "Sol-Gel transition in simple silicates II", *Journal of Non-Crystalline Solids*, Vol.63, (1984), pp.45-59.

[14] Primeau, N., et al (1997) "The effect of thermal annealing on aerosol-gel deposited SiO_2 films: a FTIR deconvolution study", *Thin Solid Films*, 310, pp.47-56.

[15] Fardad, M.A. et al (1995), "Effects of H_2O on Structure of Acid-Catalysed SiO2 Sol-Gel Films", *Journal of Non-Crystalline Solids*, Vol.183, pp.260-267.

[16] Meyerhofer, D. (1978). "Characteristics of Resist Films Produced by Spinning." Journal of Applied Physics, 49(7), p 3993-3997.

[17] Syms, R.R.A., Holmes, A.S., (1994), "Deposition of thick silica-titania sol-gel films on Si substrates", *Journal of Non-Crystalline Solids*, Vol.170, pp.223-233.

[18] Ramkumar, K., Saxena, A.N. (1992) "Stress in SiO2 films deposited by plasma and ozone tetraethylorthosilicate chemical vapor deposition processes", *Journal of the Electrochemical Society*, Vol.139, pp.1437-1442.

MODELING AND CHARACTERIZATION OF A NOVEL, LOW-COST, DIRECT-WRITE WAVEGUIDE

M.A. Mignatti, M.I. Campbell, R. Ruizpalacios, K.L. Wood, J.J. Beaman
Department of Mechanical Engineering, University of Texas at Austin, Austin, TX 78712

Reviewed, accepted August 29, 2003

Abstract

Both the current long-term telecommunication trends toward optical networking and the recent growth in information bandwidth have pushed the necessity for improved optical communications. Our fabrication approach, which leverages our expertise in solid freeform fabrication in conjunction with sol-gel technology, has advantages over these other methods because of the inherent benefits of using a direct-write philosophy, such as design flexibility and minimal post-processing. However, fabrication of such novel optical components requires extensive knowledge of their light guidance capabilities. This paper will show the technical issues involved in both modeling and characterizing small optical components fabricated by locally densifying sol-gels in a modified direct-write process.

I. Introduction

The use of sol-gel technology with direct-write manufacturing techniques facilitates the construction of integrated optical devices, including three-dimensional communication devices with low-losses and increased functionality. Sol-gels are created in a low-temperature process that utilizes a colloidal silica suspension to create a porous silicate gel of high purity. The introduction of dopants in the sol-gel alters the resulting silica structure and thus be used to produce glasses with novel optical properties (Pierre, 1998). The sol-gel process has inherent advantages over other small-scale fabrication methods since it is a low temperature process and the resulting materials are both homogenous and of high purity.

Direct-write manufacturing techniques for fabrication of micro-scale optical components involves focusing of a laser onto the desired workpiece and writing a desired pattern or shape by moving either the beam itself or by moving the workpiece via a high-precision multi-dimensional stage (Hansen, 2002). The chief advantages of this process over traditional lithographic techniques such as CVD are that the direct write process does not require the use of masks or caustic etchants. Additionally, in the direct write process parts are made directly from CAD files, eliminating the needed for tooling changes and thus increasing the flexibility of the process.

Using these direct-write techniques with sol-gel technology enables the fabrication of novel optical waveguides. Laser interaction with porous silica structures results in a localized change in the refractive index of the sol-gel, which can then be used to guide light. Additionally, the use of lasers in the process allows for the creation of waveguides with novel shapes such as unique curves and bends, and even, the creation of a truly three-dimensional waveguide. The main benefits with sol-gel are its inherent low-cost, flexibility to design and material changes (e.g. use of dopants), and unlimited geometry.

Fabrication of such a device requires extensive knowledge of both manufacturing techniques and light guidance capabilities. Extensive modeling and testing is therefore necessary

in order to fully realize and utilize the properties and benefits from the direct-write manufacturing technique. This paper discusses efforts completed in the last year at both the modeling and experimental characterization of a sol-gel waveguide manufactured using direct-write techniques. The organization of the paper is as follows. First, we present an overview of the manufacturing process. Next, we discuss applicable thin-film characterization techniques and associated efforts to realize characterization. This is followed by a section presenting a description of the modeling efforts to date. The final section presents preliminary results and is concluded with a discussion including future work.

II. Process Overview

The manufacturing process is comprised of four main steps: the sol-gel is first prepared; the sol is deposited onto a substrate using standard spin-coating techniques; the wafer and sol-gel is heat treated; and finally a path is locally densified with a laser. In general, sol-gel processes take advantage of the hydrolysis of a precursor (in the presence of a catalyst), followed by condensation and poly-condensation reactions to form particulate and polymeric structures (Ruizpalacios, 2003).

As mentioned above, the second step in the process is the deposition of the sol-gel onto a substrate – either silicon wafers[1] or borosilicate glass slides. This is accomplished using standard spin-coating techniques. Spin coating allows for quick depositions in a controlled environment with layer thickness and uniformity controlled by process variables, such as differential velocity profiles and deposition times. Deposition film thicknesses are typically between 300 and 600 nm. After successful deposition has occurred, the wafer is pre-sintered. Appropriate heat treatment represents one of most crucial steps in the process. Heat treatment reduces film stresses which lead to cracking and it increases the global index of refraction, as sol-gel density and index of refraction are directly related (Hench, 1998).

The final step in the process is laser densification using direct-write techniques. The sample is first mounted on a two-dimensional stage with a resolution of 0.5 microns. A 50W CO_2 laser with an operating wavelength of 10.6 microns and a spot size of approximately 80 microns is used for densification. Using a moving test bed allows us to systematically characterize both the laser power and scan speed, both of which are crucial in locally increasing the index of refraction without ablating the sol-gel film. Additionally, precise control of the laser's power and duty cycle allows for specific geometries and patterns to be written onto the film. Once laser densification has been completed, the sample is then tested for its light guidance properties.

III. Waveguide Characterization

To determine the exact properties of the individual waveguides created, and thus evaluate their future potential as light guidance devices, the waveguides must be fully characterized. Specifically, characterization refers to measurements of both the index of refraction and the index profile in the guided region, film thickness and attenuation of the laser-densified sol-gel films. All global index of refraction measurements, such as index of the film (before laser-densification), are measured with ellipsometry techniques. A two-prism coupler method is used

---

[1] To guide light with pure silicon wafers, an oxide buffer layer must exit between the film and the wafer. This is primarily because pure silicon has an index of refraction much greater than the film.

to determine the index of refraction and film thickness characteristics. Both a three-prism coupler technique and an end-fire method are used to study the attenuation of the waveguide.

Multiple-angle ellipsometry techniques are capable of measuring the global film index and initial film thickness, assuming the film is less than a few microns thick. In ellipsometry, collimated, coherent and polarized light is incident on the surface of a thin-film; both the change in polarization and the phase shift of the reflected light are then measured (Azzam, 1995). From these measurements, the index of refraction and film thickness are calculated. Unfortunately, ellipsometry can not be used to measure the index of refraction in the densified region due to the large spot size of the ellipsometer.

The technique used to characterize the guided region of the waveguide is the two-prism coupler method. Implementation of this method requires two millimeter scale prisms with high index of refraction, such that $n_{prism} >> n_{film}$. Figure 1 below shows a schematic of the three-prism coupler; implementation of the two-prism method is identical but uses only prisms one and three. Prism one is clamped onto the waveguide in the region where light is coupled into the guide. When light is incident on the face of the prism at a particular angle, as measured from the normal to the prism face, a specific mode becomes excited within the film (Chen, 1991). This coupling occurs because the phase matching condition is satisfied at the prism/waveguide boundary: as the horizontal portion of the incident wave approaches the propagation constant[2] of the waveguide, light will begin to tunnel into the guide. Maximum coupling occurs when the propagation constant is equal to the horizontal portion of the incident wave (Chen, 1991). The second prism is typically at the far end of the waveguide with a photodetector attached. Coupling of specific modes corresponds to peaks in the power output as measured by the photodetector. When more then three modes are present, a root mean square approach is necessary to determine the precise index of refraction and film thickness.

For attenuation measurements, the two-prism method is modified by the introduction of a third prism. A schematic of this setup can be seen in Figure 1. The additional prism, labeled as Prism 2 in this figure, is free to move laterally along the length of the waveguide, and has a photodetector mounted to it. The mobile prism is used to find power readings at various points along the guide, a technique which yields improved loss measurements, as the attenuation is measured as a function of the waveguide length (Tien, 1971).

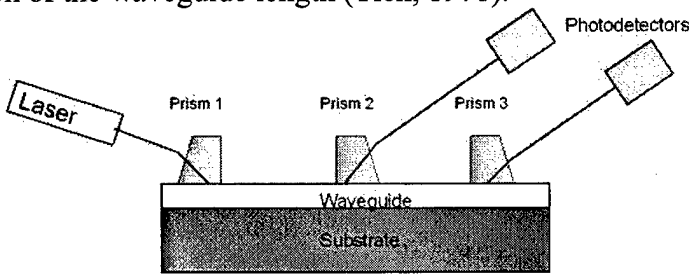

Figure 1: Three-Prism Coupler Schematic.

[2] The propagation constant is the magnitude of the wave vector, decomposed into its x- and y-components. The wave vector describes the propagation of light waves in distinct media. Each wavelength has a unique wave vector.

The advantages of using the two-prism coupler method for index and thickness characterization lie in the accuracy of the results. If more then two modes are excited, the accuracy of the measurements becomes self-checking (Ulrich, 1973). While this method will yield very accurate results, implementation is remarkably difficult. The size of the prisms makes handling difficult, and as they need to be optically smooth during use, any imperfections will alter the results. Clamping of the prisms to the waveguide is also challenging. The prisms can not be clamped too tightly, else the integrity of the film will be disturbed and the waveguide itself will be warped, altering the light propagation. If the clamping is too loose, scattering will occur due to the air gap between the prism and waveguide. Additionally, the method demands accurate measurements of incident light on the prism relative to the face normal. Ulrich recommends using a rotation stage with accuracy better than one arc minute (1973). Locating the center of the prism face at the normal angle is also a significant challenge.

Another method, known as the end-fire method, is also used to characterize the attenuation of the waveguide. In this method, light is coupled into the waveguide through a microscope objective lens which focuses a laser beam into the film and, after the light propagates through the film, the light is detected at the other end in the same manner. Coupling of light in this fashion requires that the ends of the waveguide are cut and highly polished, else the coupling losses would be substantially high and no light would be effectively coupled into or out of the waveguide. The output power is measured by a photodetector mounted at the exit. The end-fire method does not require measurements as precise as the three-prism coupler method, but it does require the ends to be optically polished so that surface roughness is less then 0.5 microns. Polishing must be done after both the film deposition and laser densification steps and, because the polishing process is destructive, there is potential for film damage. Additionally, polishing the end of a wafer (approximate thickness of 0.5 mm) is extremely challenging and requires special polishing jigs to hold the sample without damage. The other drawback to this method is that, in order to characterize the attenuation losses as a function of waveguide length, several samples of different lengths will first need to be prepared, cleaved, and polished. Thus, the method is performed iteratively over a number of assorted sample lengths.

Figure 2 shows a current implementation of the three-prism coupler method. The exciting laser is a HeNe with an operating wavelength of 632.8 nm. The prisms have a 5mm square base, are made from lithium tantalate ($LiTaO_3$), and have an index greater than 2.1. In this configuration, the waveguide is mounted vertically on a rotation stage with a resolution of one arc minute. Additionally, the mounting platform must be optically flat in both the horizontal and vertical directions as any slight deviation can produce erroneous results.

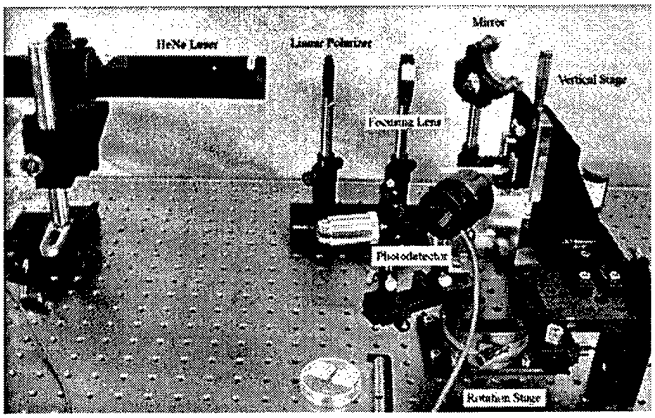

Figure 2: Current implementation of the 3-Prism Coupler method.

IV. Modeling

This section focuses on a computational model we created to study light propagation through waveguides manufactured via the aforementioned direct-write process. The development of the model centered on the chief attributes associated with this process, namely localized refractive index change.

The model was conceived as a design tool to assist the waveguide designer in determining the utility of a novel waveguide. Figure 3 shows the changes in the index of refraction over a sol-gel component. The designer is free to choose all aspects of this profile, including the extent and locations of local index changes and the nature of these changes (graded or defined step). Once the designer has created the waveguide profile, it is then fed into the propagation model along with initial state information such as location and trajectory of the light. After the propagation has been calculated, the designer will receive output in the form of a graphical representation of the path of light through the waveguide.

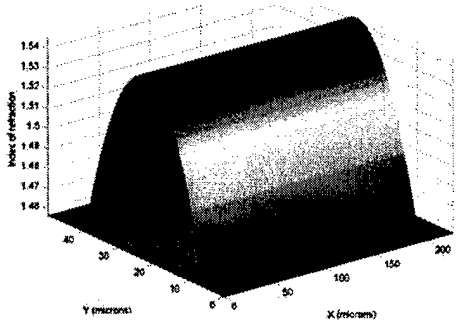

Figure 3: Waveguide modeled as refractive index profile.

The type of refractive index profile used by the designer is largely governed by the beam profile of the incident laser. The beam profile for the CO_2 laser used for densification is a Gaussian, as shown in Figure 4a. Gaussian profiles are typically measured by the beam half-width, which is the point where the average power drops to approximately 14% (Hecht, 1998). With a given spot-size, most of the power will therefore be at the center of the spot, decaying exponentially outward. As the densification process is thermally driven, it follows that the largest change in refractive index will occur at the center of the beam/film interface. The scan speed and

laser power also play a large role in shaping of the refractive profile, as slow scan speeds allow for significant thermal diffusion from the beam center, and therefore the resulting refractive profile is wider then the spot size (see Figure 4b). Additionally, as the densification process is physical in nature, there will likewise be a physical change to the film in the form of localized shrinkage, as shown in Figure 4c.

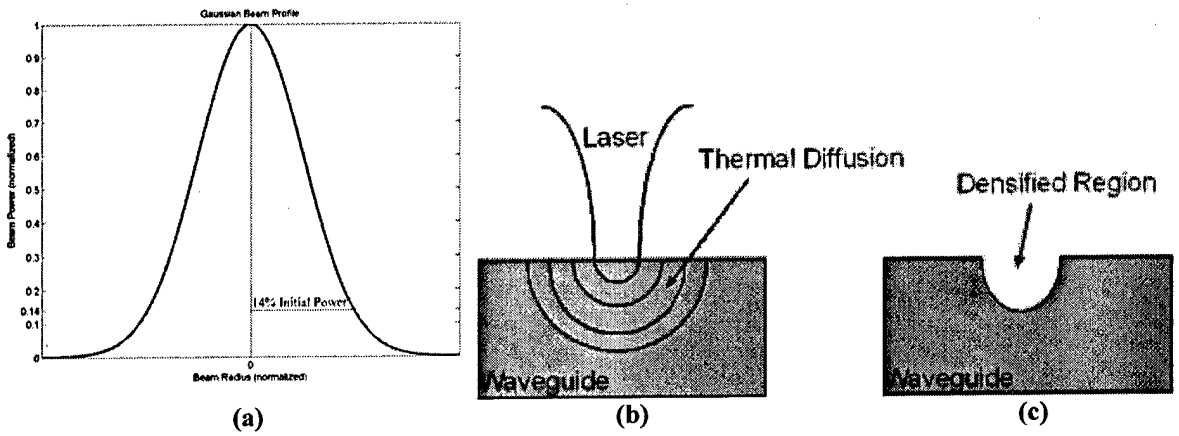

Figure 4: Gaussian Profile and Thermal/Physical Effects

Conceptually, the algorithm that drives the model is based on Huygens's Principle. Huygens was the first physicist to suggest that light traveled in a series of propagating wavefronts as shown in Figure 5. This principle is used to model light propagation through distinct media with planar point sources. Each of these point sources will propagate a new wavefront with a trajectory based on both the current index of refraction and a discrete time step. This instantiation of Huygens's Principle allows for propagations of various light phenomena, particularly reflections and refractions. It should be noted that, while based on the wave nature of light suggested by Huygens's Principle, this algorithm lies in the physical or geometrical optics domain. The ray is used to map the path of the wave so that it can be represented graphically.

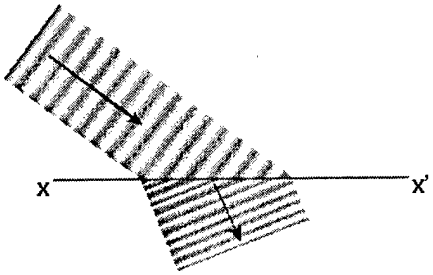

Figure 5: Huygens's Principle of propagating wavefronts (Hecht, 1998)

Huygens's Principle has been employed in the model using a finite-difference approach. While the algorithm has a geometrical foundation, finite-difference approaches are, strictly speaking, based on discretization of derivatives, generally differential equations. Our approach discretizes the light into a series of positions at discrete time intervals. The first step in the problem is to discretize the waveguide into a grid or mesh of nodes, with equal spacing in each direction of the grid (Note: the spacing need not be the same in all directions, but each distinct

direction needs to have uniform spacing) (Greenberg, 1998). The discretization occurs in two spatial dimensions with respect to the refractive index profile and in the temporal dimension with respect to overall propagation. Thus, the model uses the same basic framework as a finite difference approach, but a geometrical interpretation is substituted for the differential equation.

V. Results and Discussion

Figure 6a and Figure 6c show two refractive index profiles and the subsequent light propagation through each profile is shown in Figure 6b and Figure 6d, respectively. The step down profile (Figure 6a) is representative of the interface between core and cladding of a step-index fiber and its propagation is a simple reflection. The step up profile (Figure 6c) is representative of the interface between air and glass and its propagation is a simple refraction. As these figures demonstrate, the model predicts both reflections and refractions with less then 1% error relative to Snell's Law. These results verify the model is producing accurate results and is useful as a tool to study propagation through a waveguide.

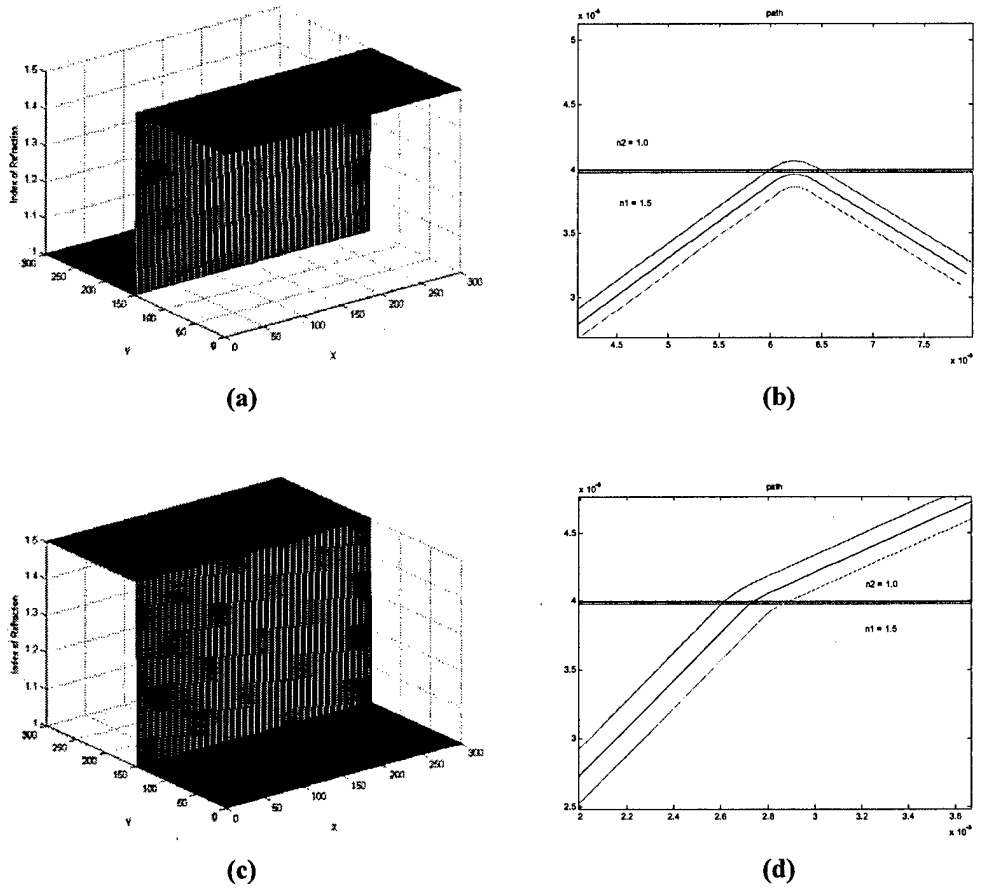

Figure 6: Step profiles and associated propagation. Figure 6a shows a step-down profile and associated reflection, while Figure 6b shows a step-up profile and associated refraction.

Figure 7a and Figure 7b show plots of a unique refractive index profile and subsequent light propagation through this profile. The refractive index profile is conceptualized as an array of refractive index hills. The index of refraction is the highest at the center of each hill, and the

hill size corresponds with the spot size of the incident laser, approximately 5 – 10 microns. Notice that as the light travels through the waveguide, its path is sinusoidal in nature, and similar to that of a graded index waveguide. Strategic placement of these hills can significantly alter the trajectory of the path of the light, as shown in Figure 7b. Conceivably, this sort of profile could be tailored to guide only particular wavelengths or trajectories of incoming light. Additionally, as this profile is only 80 microns in length, it remains a viable option for integrated optics applications.

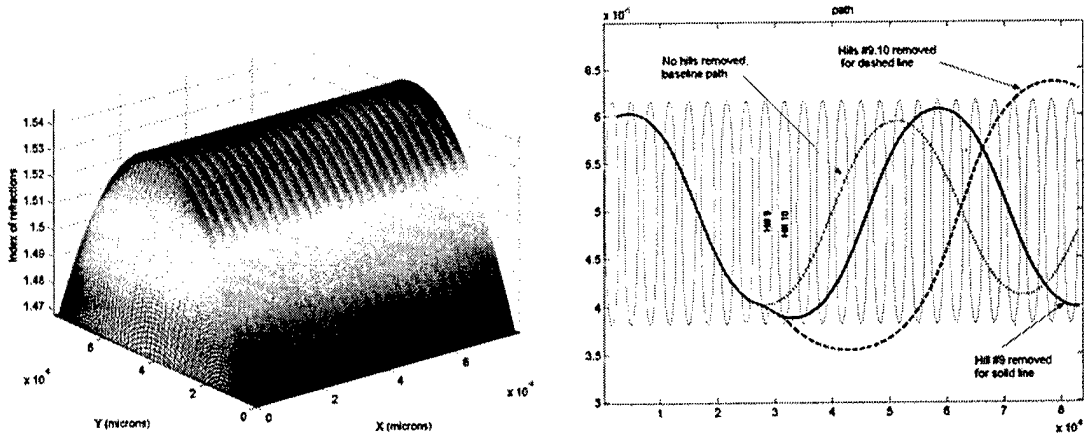

(a) (b)

Figure 7: Refractive index profile and associated propagation path. Note that in Figure 7b, the aspect ratio is not one-to-one. Also in Figure 7b, ovals represent the refractive index hills.

Characterization efforts to date have yielded results only from the ellipsometry method as shown in Table 1. Listed in the table are index of refraction and thickness results. Other characterization efforts have yet to be completed. These results are preliminary, but show a significant index difference between the film and substrate. The maximum index difference, Δn, is crucial to containing light within the film. Without local densification the light will not be confined to a specific region of the waveguide and significant scattering losses will occur. Typically, current optical fibers achieve a Δn on the order of 1% (Agrawal, 1996) which is half of the change in refractive index that we have been able to achieve. However, while we have been able to couple light only, we have not yet coupled light into the guided region of the film.

Sample	Substrate Index	Film Index	Film Thickness	Δn
10% Ti – SiO_2	1.4537	1.4837	372 nm	2.05 %
10% Ti – SiO_2	1.4537	1.4933	307.4 nm	2.65 %

Table 1: Representative Ellipsometry Results

VI. Conclusions and Future Work

This paper describes research efforts to model and characterize a novel sol-gel based waveguide manufactured with direct-write techniques. The computational model is built on the idea of localized change in refractive index and allows the designer to create an arbitrary refractive index profile. While the designer is free to choose any refractive index, the profile should be realistic, thus the typical fully dense index range is between 1.47 and 1.49.

Additionally, there are geometric and process limitations that restrict the shape of the refractive index profile. Furthermore, as characterization efforts come to fruition, real index data, including index profiles of the guided region, will be incorporated into the model thus increasing its accuracy.

Efforts to further validate the model are currently underway. These involve determining the actual index profile created from the laser densification and creating an experimental setup to verify model predictions. Efforts are also underway to complete the characterization of the waveguides, and preliminary results are promising.

VII. References

Agrawal, G.P. (1996) *Fiber Optic Communication Systems*. John Wiley and Sons. NY.

Azzam, R.M.A. (1995). *Handbook of Optics, Volume II. Chapter 27, Ellipsometry.* McGraw-Hill, Inc. NY.

Chen, D.G. (1991). "Synthesis and Characterization of Germanium Dioxide – Silicon Dioxide Waveguides." DAI-B 52/10. p. 5472.

Greenberg, M.D. (1998). *Advanced Engineering Mathematics*. Prentice Hall, NJ.

Hansen, W., Fuqua, P., et al. (2002). "Laser Fabrication of Glass Microstructure." *Industrial Physicist*. v8(3):18.

Hecht, E. (1998) *Optics, 3rd Edition*. Addison Wesley. NY.

Hench, L.L. (1998). *Sol-Gel Silica.* Noyes Publications. NJ.

Pierre, A.C. (1998). *Introduction to Sol-Gel Processing*, Kluwer Press. MA.

Ruizpalacios, R., Kyogoku, H., Beaman, J.J., Wood, K.L., Sriram, V. (2003). "Laser Direct-Write of Nanoporous Optical Coatings: Preliminary Work." *Proceedings from the 14th Annual SFF Symposium.* Austin, TX. 4-6 August 2003.

Tien, P.K. (1971). "Light Waves in Thin Film and Integrated Optics." *Appl. Opt.* v.10(11): 2395.

Ulrich, R., Torge, R. (1973). "Measurement of Thin Film Parameters with a Prism Coupler." *Appl. Opt.* v.12(12): 2901.

Silicon Carbide Growth using Laser Chemical Vapor Deposition

Jian Mi, Josh Gillespie, Ryan W. Johnson, Scott N. Bondi, and W. Jack Lackey
Rapid Prototyping and Manufacturing Institute
Woodruff School of Mechanical Engineering
Georgia Institute of Technology
Atlanta, GA 30332-0405
Reviewed, accepted August 13, 2003

Abstract

Silicon Carbide (SiC) has been grown from methyltrichlorosilane (MTS) and hydrogen using the Georgia Tech Laser Chemical Vapor Deposition (LCVD) system. A morphology study of LCVD-SiC fibers and lines was completed. Graphite and single crystal silicon were used as the substrates. In order to provide guidance to future growth of SiC, thermodynamic calculations for the C-H-Si-Cl system were performed using the SOLGASMIX-PV program.

Introduction

Silicon carbide (SiC) has outstanding material properties, including extreme hardness, high electrical breakdown field, wide band gap energy, good thermal conductivity, and excellent resistance to corrosion and thermal shock. It is either presently being used or considered primarily for use in critical parts for uncooled gas turbine and adiabatic diesel engines and high temperature bearings. It is also currently being considered for use in semiconductor devices, especially for high temperature, high frequency, and high power electronic applications.

Laser Chemical Vapor Deposition (LCVD) is a process that uses a laser to initiate a chemical reaction of gaseous reactants, which results in solid deposits on selectively heated areas of the substrate. The LCVD technique has the potential to make small and complex shaped metal and ceramic parts. Due to the nature of the LCVD process, deposited materials have desirable properties, such as purity and little porosity. There are very few papers on making SiC using LCVD. T. Noda *et al.*[1] reported the formation of polycrystalline SiC by excimer-laser chemical vapor deposition. Chin *et al.*[2] explored the relationship between the morphology and experimental parameters of CVD-SiC prepared from CH_3SiCl_3 and H_2. Choi *et al.*[3] reported the CVD-SiC microstructure obtained from different chlorosilanes, such as DDS ($(CH_3)_2SiCl_2$), TCS ($(CH_3)_3SiCl_2$), and TS ($(CH_3)_4Si$). Tsui *et al.*[4] tried to explain the observed morphology of CVD-SiC with chemical kinetics and mass transport arguments. In our research, SiC lines and fibers have been grown using the Georgia Tech LCVD system for the pyrolysis of CH_3SiCl_3 (MTS, methyltrichlorosilane) and H_2. A morphological study of the SiC lines and fibers was performed, which gave indications of the LCVD-SiC growth mechanism.

Thermodynamic calculations are extremely useful for analyzing the combination of condensed phases that will be most stably deposited during the LCVD process.

Thermodynamic calculations based on making SiC from the C-H-Si-Cl system, which represents the experimental mixture of CH_3SiCl_3 and H_2, were explored using the SOLGASMIX-PV computer program. The calculations are based on minimization of the Gibb's free energy of the system, which has been explained in detail by Eriksson.[5] Volcano effects[6] have been observed in the SiC fibers & lines produced by the Georgia Tech LCVD apparatus. Volcano effects are undesirable because of detrimental results for surface quality and component fabrication. Hopefully, the thermodynamic calculations will help to explain the cause of the volcano effects and offer direction how to avoid them.

Experimental

Duty et al.[7] described the Georgia Tech LCVD system in detail. For the deposition of SiC, a vaporizer (bubbler) was used. A simple schematic drawing of vaporizing the liquid MTS and transporting the vapor MTS to the reaction chamber is shown in Figure 1. Normally, MTS is assumed saturated under room temperature. The amount of MTS flowing into the reaction chamber was controlled by the amount of input hydrogen at given temperature and pressure. In order to meet the desired dilution ratio of MTS to H_2, more H_2 was introduced downstream of the vaporizer. For all the experiments, the pressure of the reaction chamber was maintained at 500 Torr. The growth temperature was measured and controlled by a thermal imager.[7] Process variables that were investigated were deposition temperature, reagent flow rate, and the MTS to H_2 ratio.

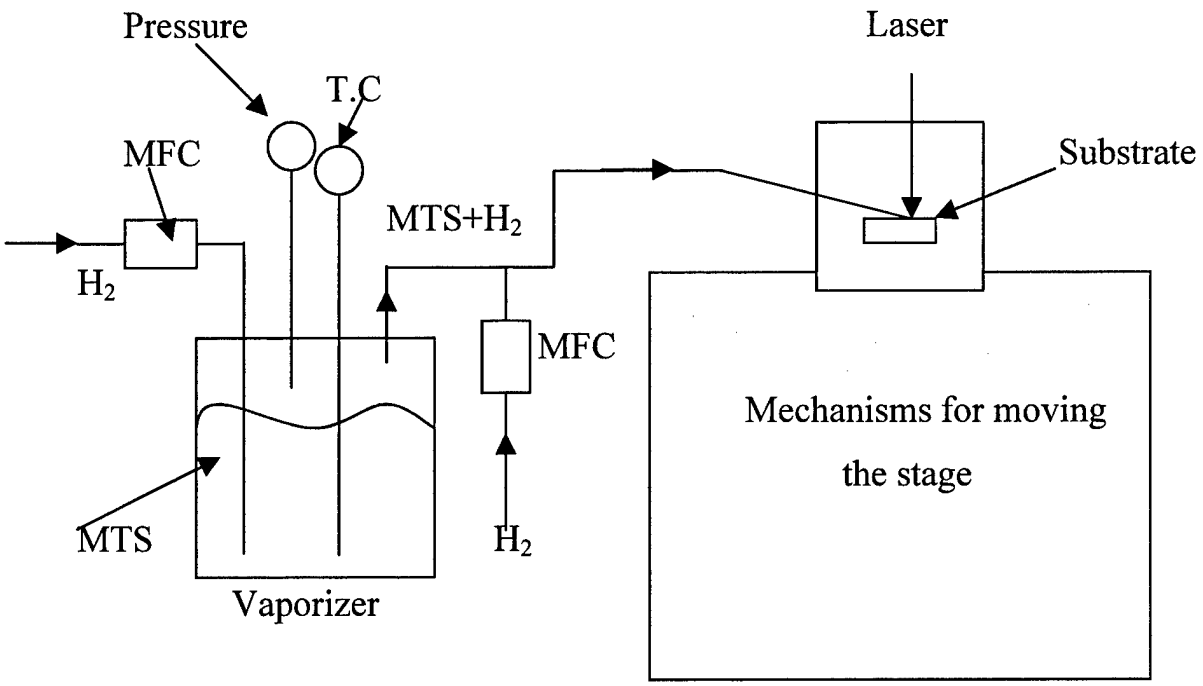

Figure 1 Reagent supply system

LCVD-SiC

Fibers and lines of SiC were grown using the Georgia Tech LCVD system. The experimental variables for the SiC fibers and lines are shown in Tables 1 and 2. The SEM micrographs in Figures 2 - 6 show the deposit microstructure and permitted correlating the processing conditions with the microstructure. Many morphologies were observed. These include nodular, rounded columnar, strongly faceted, and needle like structures.

For the fibers of the L176 series of experiments (Figure 2), as temperature decreased, the surface morphology changed from strongly faceted to nodular. This may be explained by the fact that temperature often influences nucleation.[8] For the fibers with faceted surface structures, the outer regions of the fibers, which have lower growth temperatures than the middle region, nodular structures were commonly observed for almost all the LCVD-SiC fibers. Surprisingly, the grains in the center of the deposit were often smaller than at the outer region.

As the ratio of MTS to H_2 increased, the crystallite sizes were increased in the indicated deposition temperature range as can be seen in Figure 3. For CVD of SiC Tsui et al.[4] found that the change in concentration of MTS affected the surface structures to a lesser extent than the growth temperature. As shown in Figures 2 and 3, the fibers typically had larger crystallites at the outer regions than in the middle areas.

Except for L265-7 and L265-8 shown in Figure 4, all of the SiC fibers showed depressions in the middle. This is known as the volcano effects.[6] Depressions were present because of either high temperatures or the lack of reactants in the effected region. Future work is needed to understand the reasons and to determine how to grow SiC fibers without these defects.

The observed LCVD-SiC fiber morphologies did not correlate well with the relationships of CVD SiC morphology vs. process parameters described by Chin.[2] The reasons are, probably, that for the LCVD process, the temperatures within the reaction zone are not constant while during the CVD process the whole reaction region has the same temperature. As for the SiC fibers grown on single crystal Si, shown in Figure 5, they show similar morphology and bad volcano effects, but different from those grown on the graphite substrate.

Figure 6 shows LCVD-SiC lines grown on graphite and single crystal Si. The lines on graphite have nodular surface structures. Fine crystallites were obtained in the middle region and coarse crystallites were observed at the outer areas. This is consistent with the observation for fibers. The lines on single crystal Si show different morphologies from those on graphite. For the line on the smooth surface of the single crystal Si, there is more material in the middle. For the line on the rough surface of single crystal Si, the line is very flat.

The laser used to deposit SiC has a laser spot of 200 μm in diameter on the substrate. But all the fibers grown are at least twice as big in diameter, which are shown in Table 3.

This indicates that the laser used to initiate the chemical reaction introduced a reaction zone much bigger then the spot size of the laser. For the processing conditions investigated, the spatial resolution for making SiC parts using the LCVD system is bigger than the laser spot size, which will require special attention for process and component modeling.

Table 1. Experimental variables of LCVD-SiC fibers

Sample No.	Substrate	Gas-jet	[a]Growth temp (°C)	Growth pressure (Torr)	H_2 flow (cm^3/min)	MTS flow (cm^3/min)	Volume ratio MTS: H_2
L176-3	Graphite	Off	[b]N/A	500	500	25	1:20
L176-4	Graphite	Off	1600	500	500	25	1:20
L176-5	Graphite	Off	1600-1550	500	500	25	1:20
L176-6	Graphite	Off	[c]1600	500	500	25	1:20
L265-1	Graphite	On	1300	500	500	5	1:100
L265-5	Graphite	On	1350	500	500	8.4	1:60
L265-7	Graphite	On	1300	500	500	25	1:20
L265-8	Graphite	On	1400	500	500	25	1:20
L252-2	[d]Single Si	On	977	500	500	5	1:100
L253-2	[e]Single Si	On	980-1011	500	500	5	1:100

[a] Temperature averaged over a given region
[b] Laser power higher than for other L176 experiments
[c] Temperature averaged over a smaller region than the one most commonly used, therefore, the actual temperature was lower than for L176-3 through L176-5
[d] Polished surface of Si wafer
[e] Rough surface of Si wafer

Table 2. Experimental variables of LCVD-SiC lines

Sample No.	Substrate	Gas-jet	[a]Growth temp (°C)	Growth pressure (Torr)	H_2 flow (cm^3/min)	MTS flow (cm^3/min)	Volume ratio MTS: H_2
L251-1	Graphite	On	1265	500	500	25	1:20
L252-3	[b]Single Si	On	900-1000	500	500	5	1:100
L253-1	[c]Single Si	On	970	500	500	5	1:100

[a] Temperature averaged over a given region
[b] Polished surface of Si wafer
[c] Rough surface of Si wafer

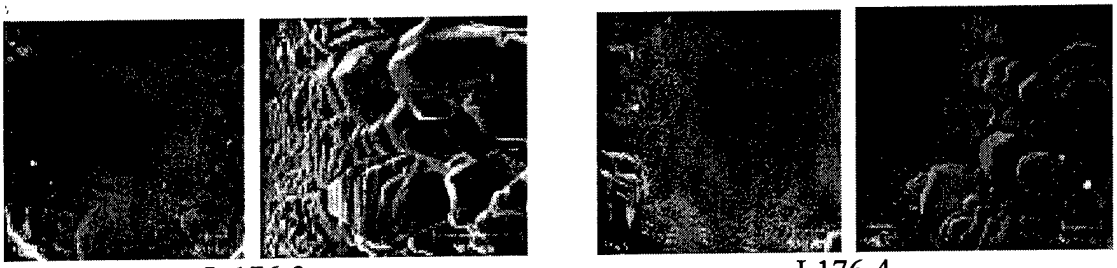

L 176-3 L176-4

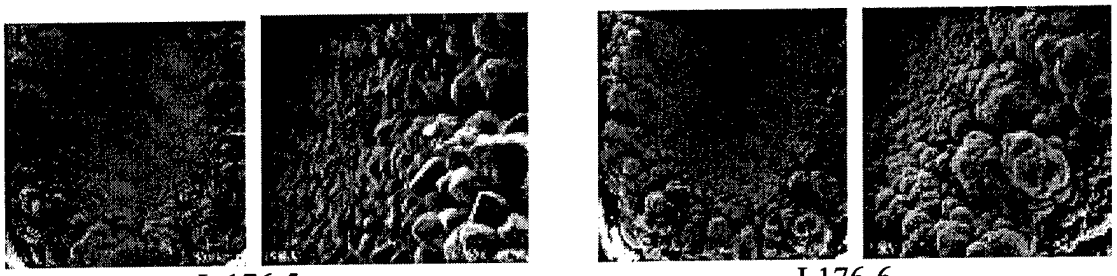

L 176-5 L176-6

Figure 2 Microstructure of fibers in L176 series of experiments

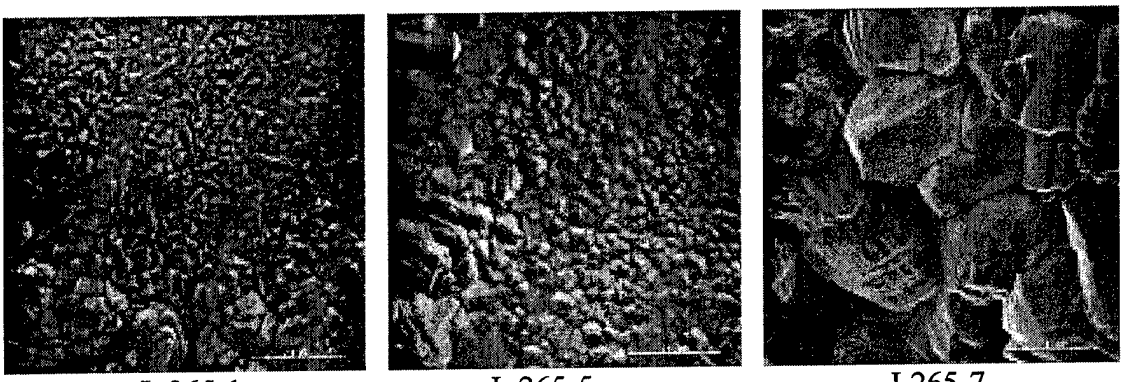

L 265-1 L 265-5 L265-7

Figure 3 Influence of MTS to H2 ration on crystallite size

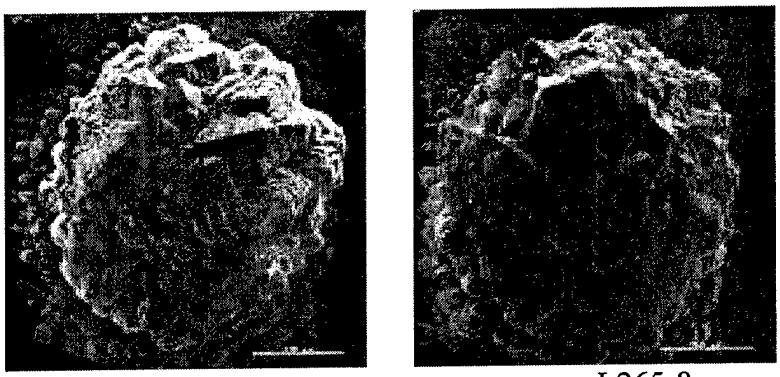

L 265-7 L265-8

Figure 4 SiC fibers without volcano effects

L252-2

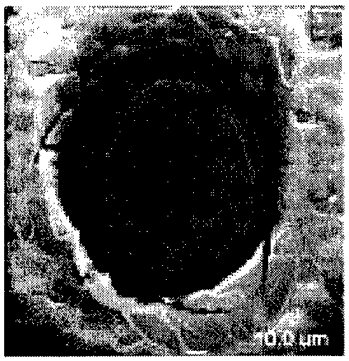

L253-2

Figure 5 SiC fibers grown on single crystal Si

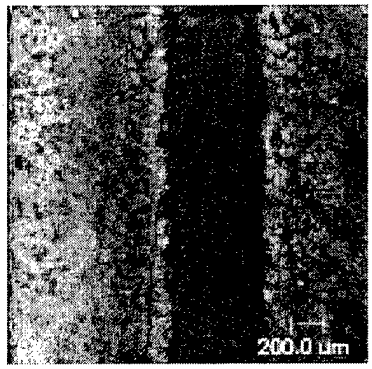

L251-1

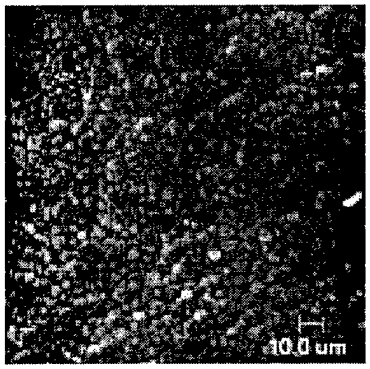

L251-1-middle

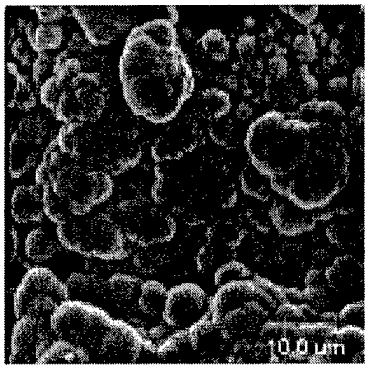

L251-1-outer

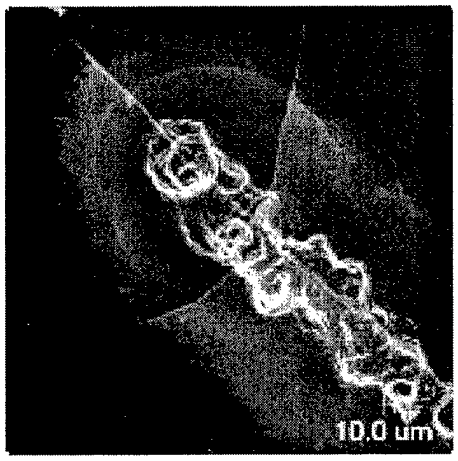

L252-3

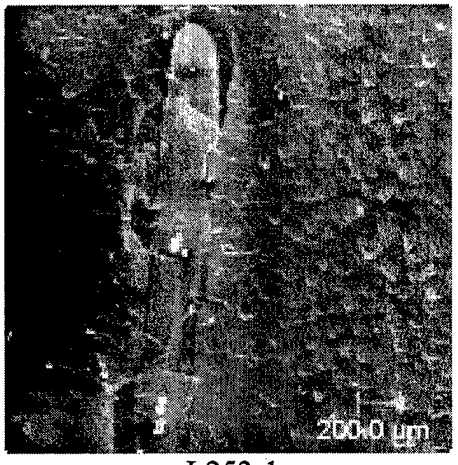

L253-1

Figure 6 SiC lines on grown by LCVD

Table 3. Diameters of LCVD-SiC fibers

Sample No.	T_{avg} (°C)	MTS: H_2	[a]D_{inner} (μm)	[b]D_{outer} (μm)
L265-1	1300	1: 100	423.0	838.4
L265-2	1400	1: 100	510.1	947.2
L265-3	1250	1: 60	366.1	801.8
L265-5	1350	1: 60	479.8	841.9
L265-6	1450	1: 60	616.5	924.0
L265-7	1300	1: 20	621.4	788.3
L265-8	1400	1: 20	781.9	958.5

[a] Actual fiber size

[b] The whole region that has SiC deposited

Thermodynamic Calculations

The C-H-Si-Cl system used to simulate the deposition of SiC was defined by specifying pressure, temperature, and the amount of each element present. By holding the pressure and temperature constant, the volume of the system can expand and contract during reaction depending on the given pressure and temperature. Because the calculations are based upon equilibrium thermodynamics, the final results are independent of the initial form of the elements. Therefore, while inputting the element mole value, the concern is the molecular ratios of each element to satisfy the initial gas reactants used. Also, it is assumed that the reactions in the gas phase come to equilibrium quickly, and the molecules formed represent the most stable distribution.

Two sets of thermodynamic calculations were performed; one was based on MTS and H_2, which were used for growing SiC. The other set was based on the mixture of CCl_4, $SiCl_4$, and H_2, which were used to check our calculations with those of Kingon et al..[9] The MTS set included 44 gas species and 5 condensed phases (graphite, liquid silicon, solid silicon, α-SiC, and β-SiC). Those species are listed in Table 4. For the calculations including CCl_4 and $SiCl_4$, the species considered by Kingon were used[8], which are shown in Table 5. The enthalpies of formation and entropies of formation were taken from the JANAF Thermodynamical Tables.[10]

Table 4. Species considered in the C-H-Si-Cl (MTS) system

Equilibrium gas phases				
C(g)	Si_2(g)	C_2Cl_2(g)	C_4(g)	$SiCl_3$(g)
CCl(g)	CH_2Cl_2(g)	C_2Cl_4(g)	C_5(g)	$SiHCl_3$(g
CCl_2(g)	CH_3(g)	C_2Cl_6(g)	Cl(g)	$SiCl_4$(g)
CCl_3(g)	CH_3Cl(g)	C_2H(g)	HCl(g)	H(g)
CCl_4(g)	CH_3SiCl_3(g)	C_2HCl(g)	SiH_3Cl(g)	SiH(g)
CH(g)	CH_4(g)	C_2H_2(g)	SiCl(g)	H_2(g)
CHCl(g)	SiC(g)	C_2H_4(g)	$SiCl_2$(g)	SiH_4(g)
$CHCl_3$(g)	Si_2C(g)	SiC_2(g)	Cl_2(g)	Si(g)
CH_2(g)	C_2(g)	C_3(g)	SiH_2Cl_2(g)	
Equilibrium condensed phases				
C[s]	Si[l]	Si[s]	α-SiC[s]	β-SiC[s]

Table 5. Species considered in the C-H-Si-Cl (CCl_4, $SiCl_4$) system

Equilibrium gas phases				
CCl(g)	$C_2H(g)$	SiH_3Cl(g	$SiCl_3(g)$	$H_2(g)$
$CCl_4(g)$	$C_2H_2(g)$	SiCl(g)	$SiHCl_3(g)$	$SiH_4(g)$
$CH_3(g)$	$C_2H_4(g)$	$SiCl_2(g)$	$SiCl_4(g)$	Si(g)
$CH_3Cl(g)$	Cl(g)	$Cl_2(g)$	H(g)	
$CH_4(g)$	HCl(g)	$SiH_2Cl_2(g)$	SiH(g)	
Equilibrium condensed phases				
C[s]	Si[l]	Si[s]	α-SiC[s]	β-SiC[s]

(1) MTS/H_2

For the series of calculations based on MTS and hydrogen, the system was consistently defined with our experimental conditions. The moles of each element input were the values of actual moles in the reaction chamber multiplied by 1000. This adjustment was made because for some cases, the mole values were too small to get reasonable answers due to a quirk of the software. The pressure was kept as 500 Torr and the temperature ranged from 300 K to 2900 K. Three different ratios of hydrogen to MTS were used, which were 20, 60, and 100. The moles used to perform the calculations are listed in Table 6.

Table 6. Element input mole values

MTS: H_2	C (mole)	H (mole)	Si (mole)	Cl (mole)
1:20	4.672	200.896	4.672	14.016
1:60	4.672	574.565	4.672	14.016
1:100	4.672	948.416	4.672	14.016

The calculated results of the condensed phases are shown in Figures 7(a) to 7(c). Because only β-SiC and liquid Si existed according to our calculations, the other condensed phases were not plotted here. In fact, according to the data of the JANAF Tables,[10] β-SiC is more stable than α-SiC. Therefore, no α-SiC was expected. From the Figures 7(a) to 7(c), it can be seen that under the indicated conditions, most of the time, β-SiC was the only condensed phase predicted to exist. The amount of β-SiC increased with temperature, reaching a maximum value, and then less β-SiC was predicted to form with increasing temperature. At higher temperatures, around 2400 K, the amount of β-SiC decreased dramatically and co-existed with liquid Si. The curves for β-SiC are similar in shape. Figure 8 shows the β-SiC curves for different MTS to H_2 ratios. Although it is not that pronounced, it is noted that at temperature less than 2300 K, more hydrogen helps to produce β-SiC; at temperatures greater than 2300 K, more hydrogen leads to less β-SiC. The curves show what would happen when the system is in equilibrium. There may be some deviations between the real SiC growth process and the predicted curves. However, these curves provide the tendency for producing β-SiC under different process conditions.

As mentioned before, the SiC fibers and lines grown using the Georgia Tech LVCD system had undesirable volcano effects.[6] From the previous calculations, in the temperature range of 1000 K to 2000 K, the amount of β-SiC increased with temperature and met the maximum value, then decreased with temperature (Figures 7 and 8). It is possible that these thermodynamic influences of the growth process are the reason for the volcano effects. To confirm this, further experiments and more modeling are required.

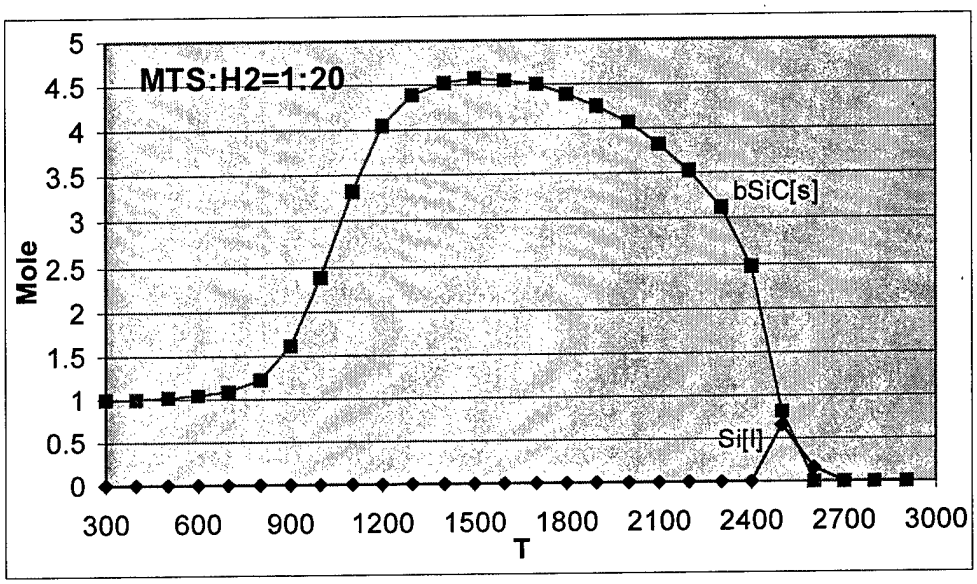

(a)

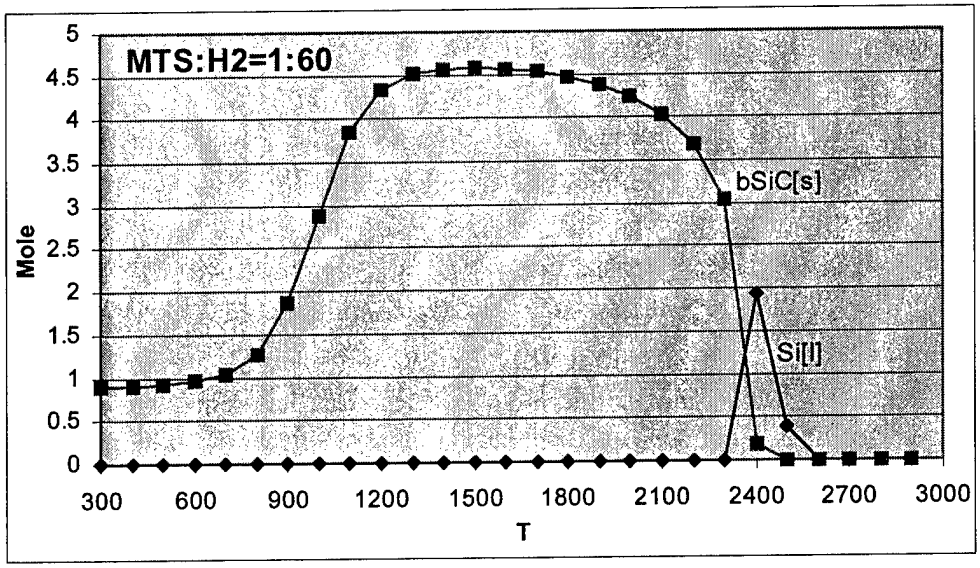

(b)

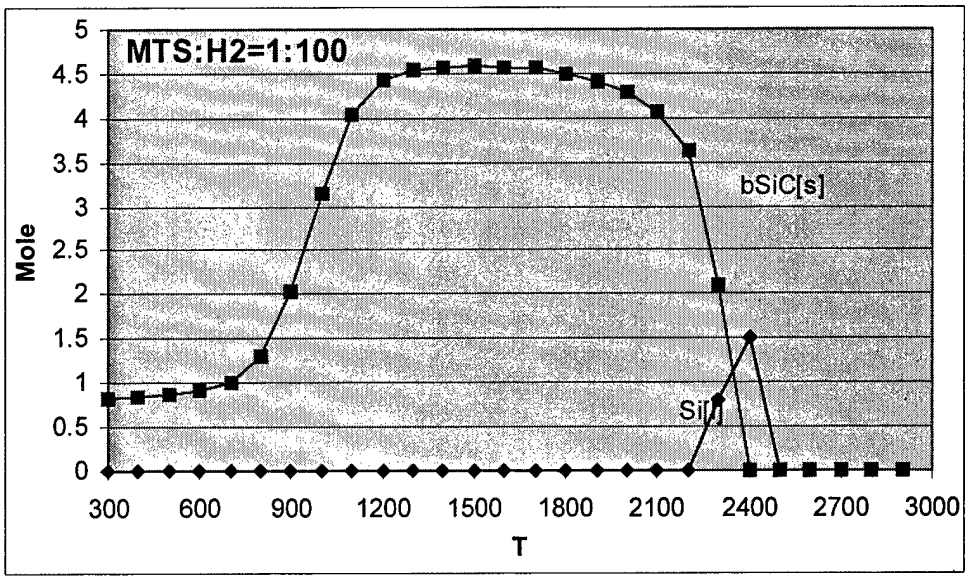

(c)

Figure 7 The condensed phases of system MTS/H_2 at pressure 500 Torr and MTS to H_2 ratios indicated

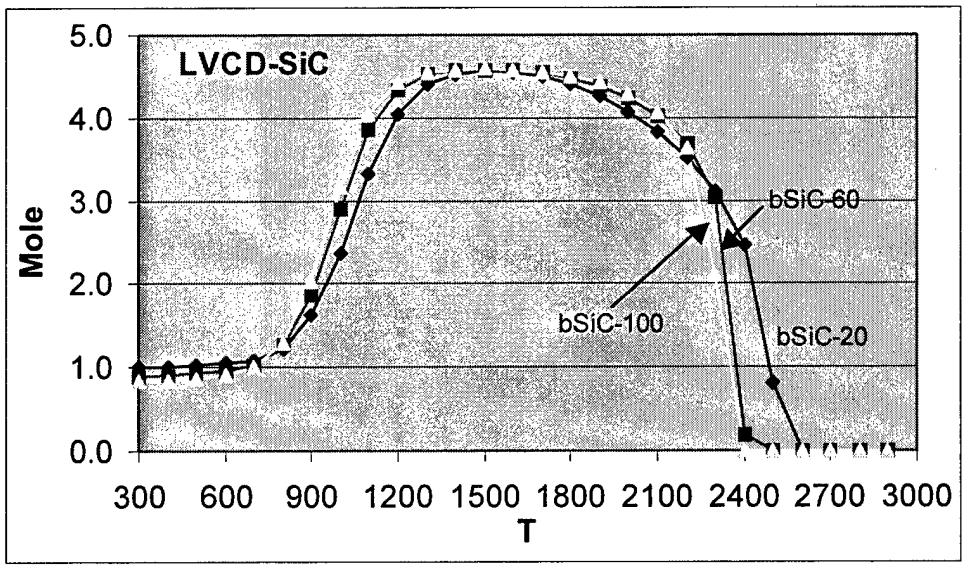

Figure 8 β-SiC mole value curves at pressure of 500 Torr and MTS to H_2 ratios indicated

(2) $SiCl_4/CCl_4/H_2$

As previously mentioned, this series of calculations was performed as a check of the method by comparing with Kingon's results.[9] For a system of $CCl_4/SiCl_4/H_2$, the total amount of Si and C was fixed as 10 moles, the ratio of H_2 to (Si+C) was 10, and the amount of Cl was40 moles. The detailed information used to specify the calculations is shown in Table 7. For each set of calculations having a specific pressure and Si/ (Si+C)

ratio, the temperature ranged from 1000 K to 2000 K. The calculated results are shown in Figure 9.

Table 7. Conditions used to specify the system of $CCl_4/SiCl_4/H_2$

Pressure (Pa)	Si/(Si+C)				
10^2	0.1	0.3	0.5	0.7	0.9
10^4	0.1	0.3	0.5	0.7	0.9
10^5	0.1	0.3	0.5	0.7	0.9
10^6	0.1	0.3	0.5	0.7	0.9

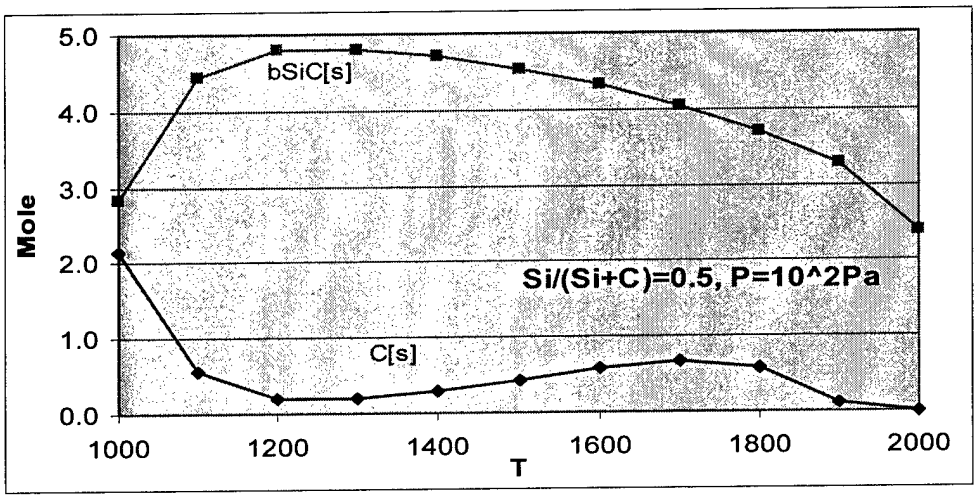

(a)

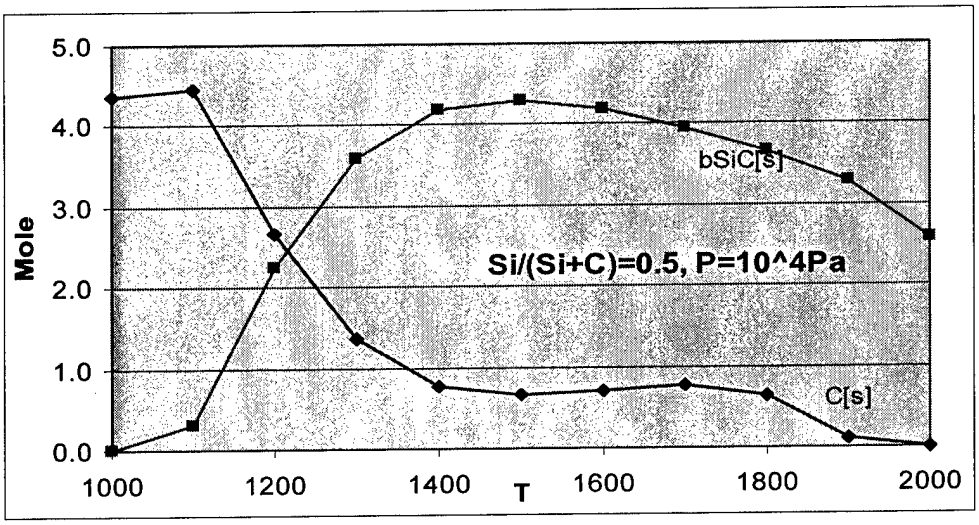

(b)

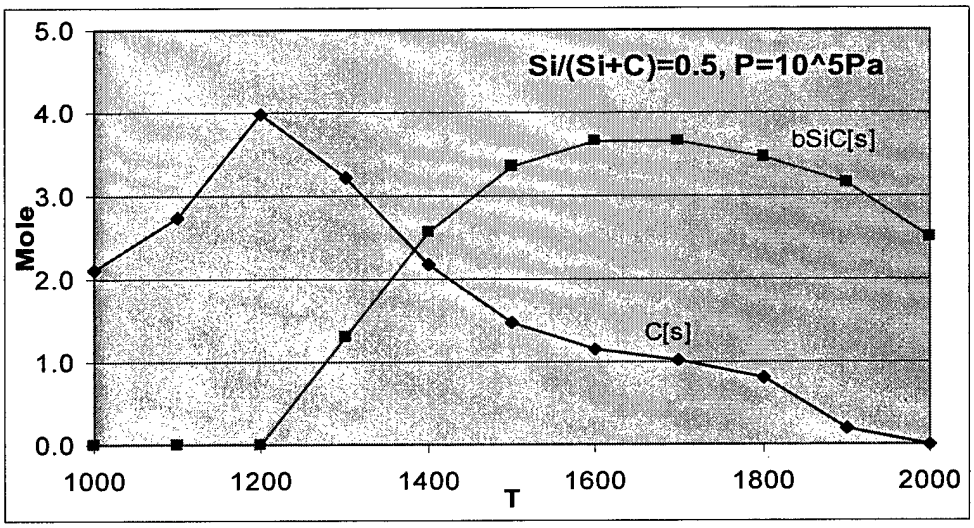

(c)

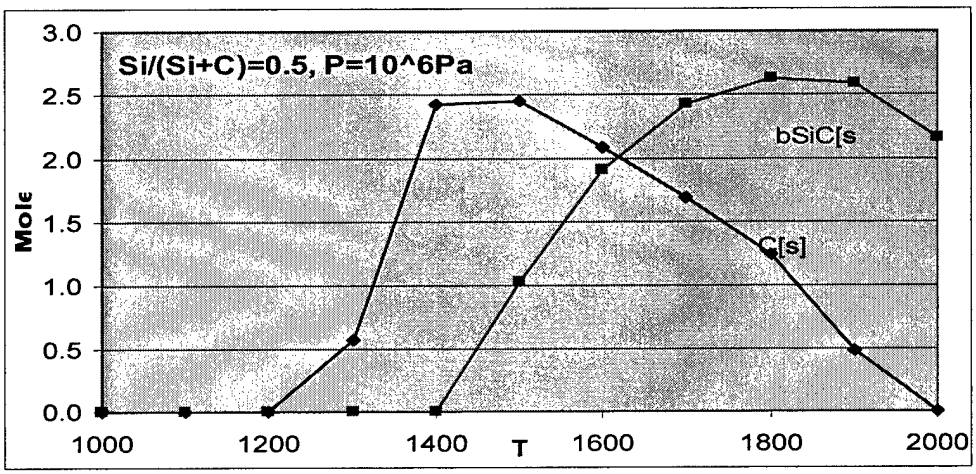

(d)

Figure 9 $CCl_4/SiCl_4/H_2$ system at Si/(Si+C)=0.5

In each case the calculations were in good agreement with Kingon's[9] results, which provide confidence for the MTS/H_2 calculations. Also, observing the relationship between the pressure and the amount of β-SiC, it seems that higher pressure inhibits the deposition of β-SiC. But there are no experimental data showing this relationship.

Summary and Conclusions

LCVD-SiC fibers grown using the Georgia Tech LCVD system have surface structures that ranged from nodular, rounded columnar, strongly faceted, and needle like depending on the growth parameters. LCVD-SiC lines did not show any faceted surface structures. From our experiments, it can be concluded that the growth temperature, reactant concentration, and the substrate type play an important role in determining the morphology of LCVD-SiC.

Thermodynamic calculations on the system C-H-Si-Cl system using SOLGASMIX-PV software provide the basis for getting the most stable combination of condensed phases, especially to make β-SiC. The calculations suggest that the deposition rate increased with increasing temperature, reached a maximum, and then decreased. This information should be useful in establishing processing condition that permit the growth of uniform SiC fibers and lines that do not exhibit the volcano effect.

Reference:

1. T. Noda, H. Suzuki, H. Araki, F. Abe, M. Okada, "Formation of polycrystalline SiC film by excimer-laser chemical vapour deposition", Journal of Materials Science Letters 11 p. 477-478,1992.

2. J. Chin, P. K. Gantzel and R. G. Hudson, " The Structure of Chemical Vapor Deposition Silicon Carbide", Thin Solid Films, 40 p.57-72, 1977.

3. Byung Jin Choi, Dong Won Park, Dai Ryong Kim, "Chemical Vapour Deposition of Silicon Carbide by pyrolysis of methylchlorosilanes", Journal of Materials Science Letters, 16 p.33-36, 1997.

4. P. Tsui and K. E. Spear, "A Morphological Study of Silicon Carbide Prepared by Chemical Vapor Deposition", Materials Science Research 17 p. 371-80, 1984.

5. G. Eriksson, "Thermodynamic Studies of High temperature Equilibria," Acta Chem. Scand., 25 [7] p. 2651-58, 1971.

6. D. Jean, C. Duty, R. Johnson, S. Bondi, and W. J. Lackey, "Carbon Fiber Growth Kinetics and Thermodynamics Using Temperature Controlled LCVD", Carbon, 40 (9) p. 1435-1445, 2002.

7. C. Duty, D. Jean, W. J. Lackey, "Design of a laser CVD rapid prototyping system", Ceram. Eng. Sci. Proc. 20 (4), p. 347-54, 1999.

8. K. A. Appiah, Z. L. Wang, W. J. Lackey, "Effects of deposition temperature on microstructure of laminated (SiC-C) matrix composites", Journal of Materials Science 35, p 1979-1984, 2000.

9. A. I. Kingon, L. J. Lutz, P. Liaw, and R. F. Davis, "Thermodynamic Calculation for the Chemical Vapor Deposition of Silicon Carbide," J. Am. Ceram. Soc., 66 [8] p. 558-66, 1983.

10. JANAF Thermochemical Tables, 2nd ed., Natl. Stand. Ref. Data. Ser. (U. S. Natil. Bur. Stand.), No. 37, 1971

Fabrication of Laser Deposited TiC/Steel Matrix Composite Coatings

W.H. Jiang, R. Kovacevic

Research Center for Advanced Manufacturing,
School of Engineering, Southern Methodist University,
1500 International Parkway, Suite #100, Richardson, TX 75081, USA

Reviewed, accepted August 25, 2003

Abstract

The present work investigates the effect of laser scanning beam speeds and the content of TiC in injected powder on morphologies and microstructures of laser deposited beads of a TiC/H13 tool steel composite. The results show that the beam scanning speeds affect the size and morphology of the beads. During laser processing, TiC melts, decomposes, and subsequently, a number of fine TiC precipitates form during cooling that are uniformly distributed in the tool steel matrix. The beam scanning speeds and the amount of injected TiC exert a strong influence on the morphology and size of the fine TiC precipitates. It is believed that the precipitated TiC is the primary phase in hypereutectic Fe-TiC. Rapid cooling develops martensite with retained austenite in a steel matrix. The precipitated TiC can refine grains of the steel matrix as a solidified nucleus. TiC/H13 tool steel composite coatings with various contents of TiC were produced using the laser deposition processing technique.

Introduction

Laser cladding is widely used for creating various surface coatings of a significant thickness that can effectively protect substrates from harsh service conditions. Various coating materials, such as carbides, oxides, nitrides, borides and their composites, have been developed [1-4]. These coatings display high hardness, wear, erosion and corrosion resistance, heat insulation.

Metal matrix composites (MMCs) as coatings have recently attracted much interest, for they combine excellent ductility and toughness of metallic matrices with high strength and hardness of ceramic reinforcements. Due to its high hardness, melting point, and thermodynamic stability as well as availability, TiC is extensively used as a reinforcing phase in MMCs' coatings, such as Ni based [5-8] and steel based composites [8-10]. Due to a relatively low cost, iron and steels as a coating matrix have a potential application prospect. Utilizing laser surface alloying, Ariely et al. [8] produced TiC reinforced steel coatings on the surfaces of Armco iron, AlSl 1045 and 1095 steels, exhibiting a higher hardness. Tassin et al. [9] incorporated TiC into the surface of AlSl 316 L stainless steel by laser processing, which substantially improved sliding wear resistance. Jiang and Molian [10] increased life of die-casting dies by laser surface processing with micrometer- and nanometer-sized TiC powder.

Slurry erosion happens extensively in the industries of mining, metallurgy, and crude-oil drilling, etc. Materials with improved wear resistance to slurry erosion are in increasing demand in the industries. It is well known that hard materials have a high erosion resistance at a low impact angle, while ductile materials have a high erosion resistance at a high impact angle.

However, in some service conditions, components suffer slurry erosion at varying impact angles. Therefore, it is of practical significance to develop coatings with an overall excellent erosion resistance, no mater what the impact angles are. Considering their good combination of hardness and ductility, steel matrix composites may be potential erosion resistant materials at various impact angles. Utilizing laser surface processing, the present work tries to develop TiC/H13 tool steel composite coatings as a new erosion resistant material.

Laser processing is characterized by its high energy density, low heat input, and consequently, high heating and cooling rates that minimizes its effect on a substrate. However, laser processing parameters such as beam power and beam scanning speed affect metallurgical quality, microstructures, and furthermore, mechanical properties of coatings [10]. In this work, laser deposition is used to synthesize TiC/H13 tool steel coatings with different concentrations of TiC. The effect of beam scanning speeds on the microstructures of coatings is investigated for a given laser beam power and powder feeding rate. Their erosion resistance is being investigated and will be reported.

Experimental procedure

Fig. 1 shows the schematic diagram of the 3D laser cladding system setup used in this investigation. A 1 kW continuous wave Nd: YAG laser with a 200-mm focusing optics is used to deposit the powders. The laser beam guided by the optical fiber is reflected from the partial reflective mirror, and is focused on the substrate by the set of lens arranged in the laser head. The computer-controlled powder feeders are used for dosing and feeding the powder mixture into the desired composition, and allow for an exact setting and continuous change of the powder mixture during the cladding process [11]. The alignment of the laser beam, powder nozzles, and their positioning in relation to the substrate must be accurate for the process to be reproducible. The feeding rate of each of the powders and laser processing parameters are controlled automatically.

AISI 4140 steel plate was used as a substrate, whose composition is shown in Table 1. H13 tool steel powder was used as a matrix of composite coatings. The original size of the H13 tool steel powder is around 50-100 μm. Its composition is also shown in Table 1. The original TiC particles are 50-100 μm.

Table 1 Nominal chemical composition of steels used, wt.%

Element	C	Cr	Mo	Mn	Si	V	Fe
4140	0.4	1.0	0.2	0.9	0.2	-	Balance
H13	0.4	5.0	1.0	0.4	1.1	1.1	Balance

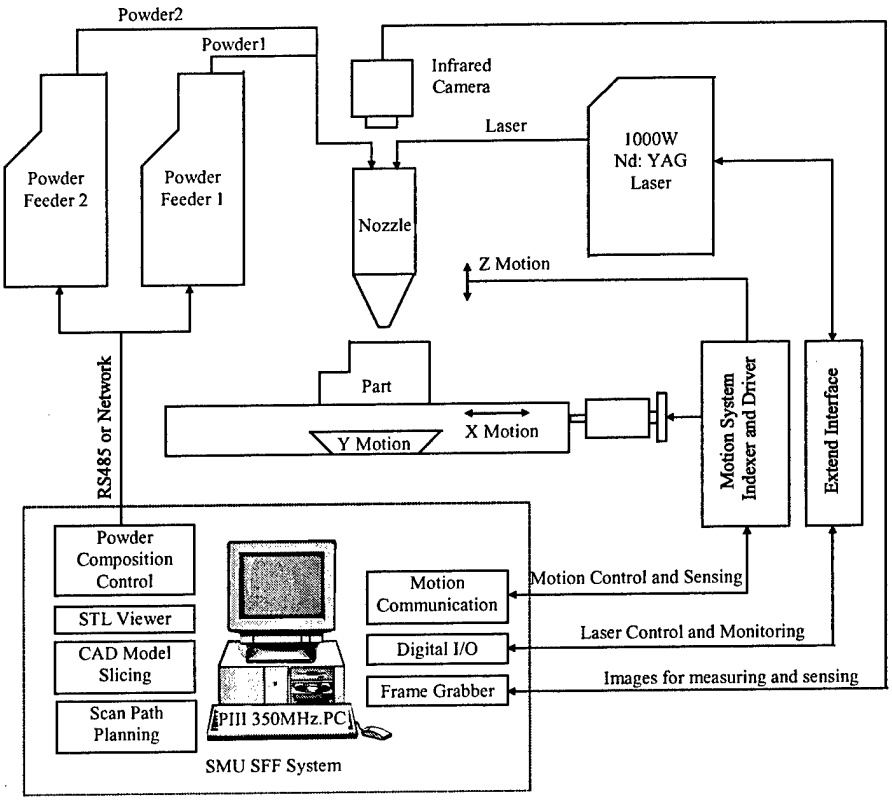

Fig. 1 Schematic diagram of 3D laser cladding system setup.

The laser beam power used in the experiments was 380 W, with a spot diameter of 1 mm. The beam scanning speeds were set to 5.08, 7.62, 10.16, and 12.7 mm s^{-1}. A feeding system was used for direct injection of powders with argon flow as a powder carrier. The TiC and H13 tool steel powder was injected by a powder feeder through four nozzles of 1 mm in diameter. The feeding rates of TiC and H13 tool steel are dependent on designed constitutions of coatings. They are (3 × TiC vol.%) g min^{-1} and (4.65×H13 vol.%) g min^{-1} for TiC and H13 tool steel, respectively. Single and double layer beads were deposited at various beam scanning speeds. In case of overall coating, substrate samples (25.4 mm × 25.4 mm) were coated uniformly with double layers of about 1 mm in thickness. The beam scanning speed is 10.16 mm s^{-1}. A 40% overlap of a successive melting track was selected to produce a uniform coating on a substrate.

The transverse cross sections of the deposited beads were cut for microstructural examination. The optical microscopy and electron microprobe with energy dispersive analysis of X-ray (EDAX) were used for microstructural observation and microanalysis of composition. X-ray diffraction with Cu Kα was performed to identify the phases in coatings.

Results

Laser beam scanning speeds affect the sizes and morphologies of deposited beads. However, their effect is independent of the constitutions of the deposited powder, that is, the proportion of H13 tool steel to TiC. The typical morphologies of the cross sections of the beads

produced at various beam scanning speeds are shown in Fig. 2. It is well known that a laser clad layer can be divided into three zones, i.e., coating, melting and heat-affected zones in a substrate. From Fig. 2, it can be seen that coating and melting zones are influenced severely by the beam scanning speeds. The faster the beam moves, the smaller the volume and the mass of the coatings. Yet, the melting zone of the substrate decreases with decreasing beam scanning speed, and disappears completely at the minimal speed, i.e. 5.08 mm s^{-1}. It can be seen that only two intermediate beam scanning speeds can develop well geometric and symmetric beads. At the maximum beam scanning speed, 12.7 mm s^{-1}, the coating fails to coincide with the melting zone; while at the minimal speed, the coating tends to lean. It is noted that the maximum beam scanning speed leads to involvement of the substrate material into the coating, but fails to homogenize them, as shown in Fig. 2d. This may result from both the larger melting zone in the substrate and higher solidification rate, which mixed much substrate material with deposited materials. Double layer depositions have the same melting and heat affected zones as the single ones. Undoubtedly, a double layer deposition increases the sizes of deposited coatings. Worthy to mention, the beads of the double layer depositions at the minimal beam scanning speed completely lose geometrical symmetry.

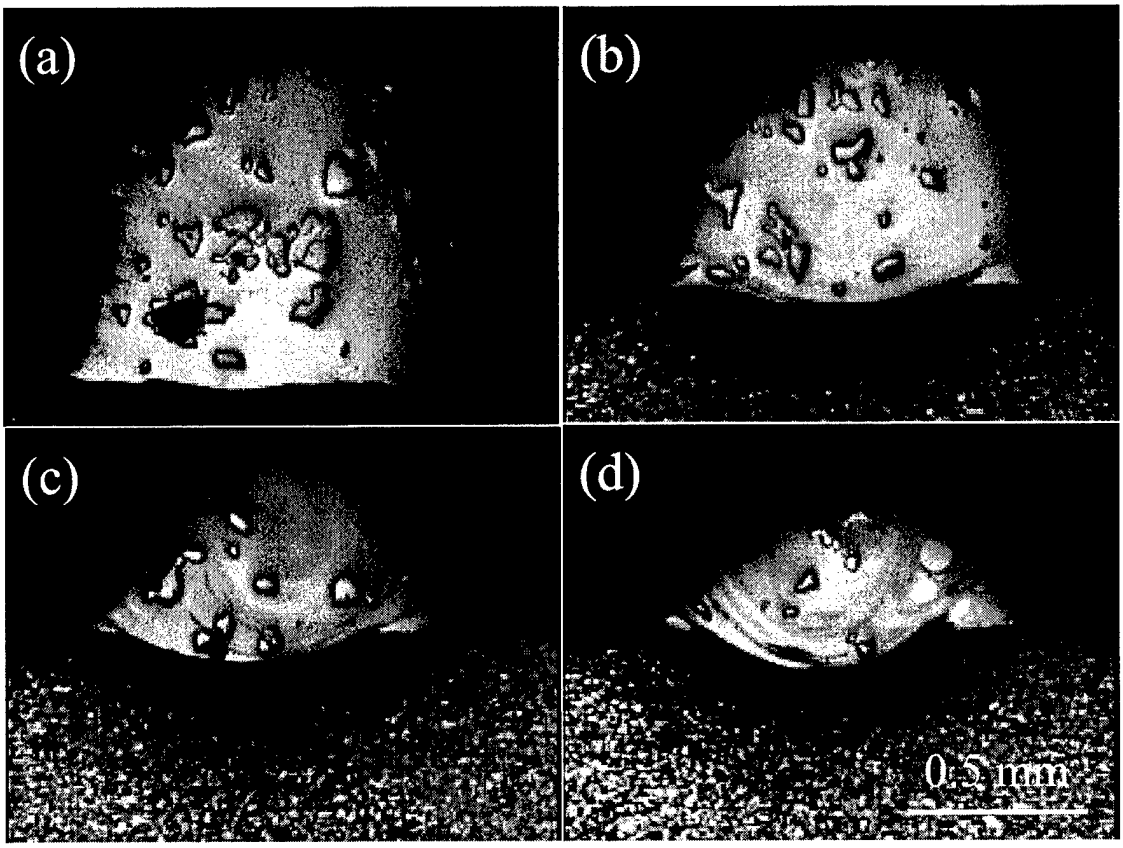

Fig. 2 Morphologies of beads of 60 vol.% TiC/H13 steel formed by single layer scanning at speeds of (a) 5.08, (b) 7.62, (c) 10.16 and (d) 12.7 mm s^{-1}.

From Fig. 2, it can be seen that the interface morphologies between a melting zone and a heat-affected zone change with the beam scanning speeds. By decreasing the beam scanning speeds, their curvatures decrease. In the example of the minimal beam scanning speed, a melting zone disappears and the interface becomes planar. Fig. 3 shows the typical high magnification micrographs of planar (at a speed of 5.08 mm s^{-1}) and curved (at a speed of 12.7 mm s^{-1}) interfaces. Evidently, the curved interface has a better melting bond than the planar.

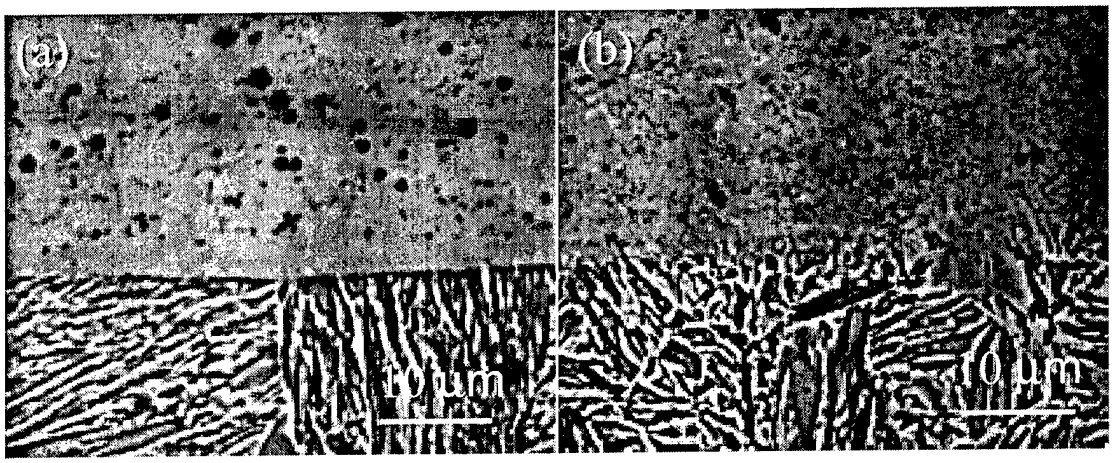

Fig. 3 High magnification micrographs of interfaces in 60 vol.% TiC/H13 steel formed by single layer scanning at speeds of (a) 5.08 and (b) 12.7 mm s^{-1}.

High magnification observation indicates that TiC particles decompose, and a great number of fine precipitates formed during laser processing. For this reason, the injected coarse TiC particles in beads appear fewer in the low magnification micrographs (Fig. 2). By increasing the beam scanning speeds, the fine precipitates decrease. Fig. 4 shows the typical microstructures of the beads produced at various beam scanning speeds.

For all the coatings, the fine precipitates are well distributed in steel matrices. Fig. 5 shows the backscattered electron images of the beads with 40, 60, and 80 vol.% TiC formed at a beam scanning speed of 10.16 mm s^{-1}. In these images, both the coarse TiC and the fine precipitates appear dark, indicating that their constituting elements are lighter than the iron matrix. EDAX demonstrated that fine precipitates are rich in Ti. Furthermore, it can be seen that by increasing the contents of the injected TiC, the fine precipitates increase both in quantity and size. The injected TiC particles exhibit clear, smooth edges and no reaction layer, indicating that they melt and dissolve rather than react with the melt during laser processing.

The morphologies and sizes of the fine precipitates are related to the contents of the injected TiC. Fig. 6 shows the fine precipitates in the beads with various contents of injected TiC produced at a beam scanning speed of 10.16 mm/s. In 40 vol.% TiC, they assume substantially spherical and cubic shapes. In 60 vol.% TiC, some precipitates evolve into small flower-petal shapes, while the majority are still spherical. But, in 80 vol.% TiC, the precipitates are rather large and take spherical, cross, rod, and dendrite forms.

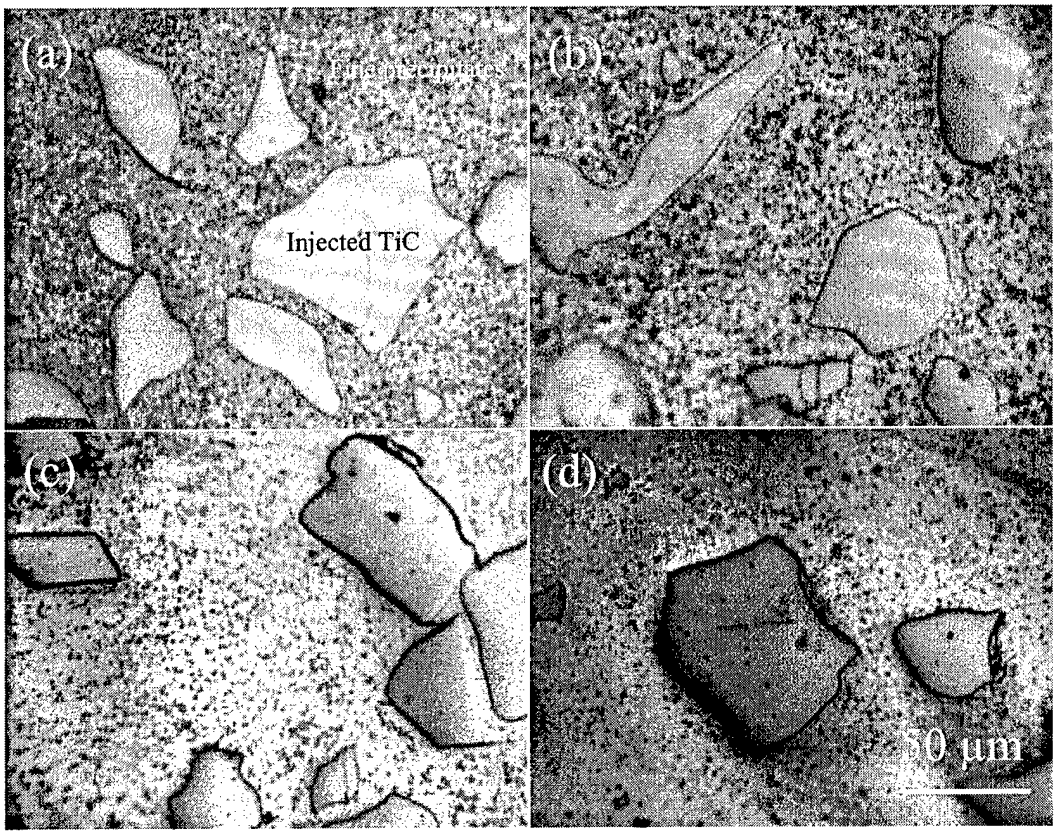

Fig. 4 Microstructures of 60 vol.% TiC/H13 steel formed by single layer scanning at speeds of (a) 5.08, (b) 7.62, (c) 10.16 and (d) 12.7 mm s^{-1}.

By a careful examination of Fig. 6b, it can be found that numerous fine precipitates are located at the center of the matrix grains. This indicates that they acted as a heterogeneous site for solidified nucleus of steel matrix grains to nucleate.

X-ray diffraction analysis was performed on the coatings with 40, 60, and 80 vol.% TiC produced at the beam scanning speed of 10.16 mm s^{-1}, respectively. The resulting diffraction patterns are shown in Fig. 7. It can be seen that the diffraction patterns of all the coatings are similar, and there are only diffraction peaks of steel matrix and TiC, indicating that TiC is only the secondary phase. These results mean that the fine precipitates are also TiC. The steel matrices are martensite and retained austenite.

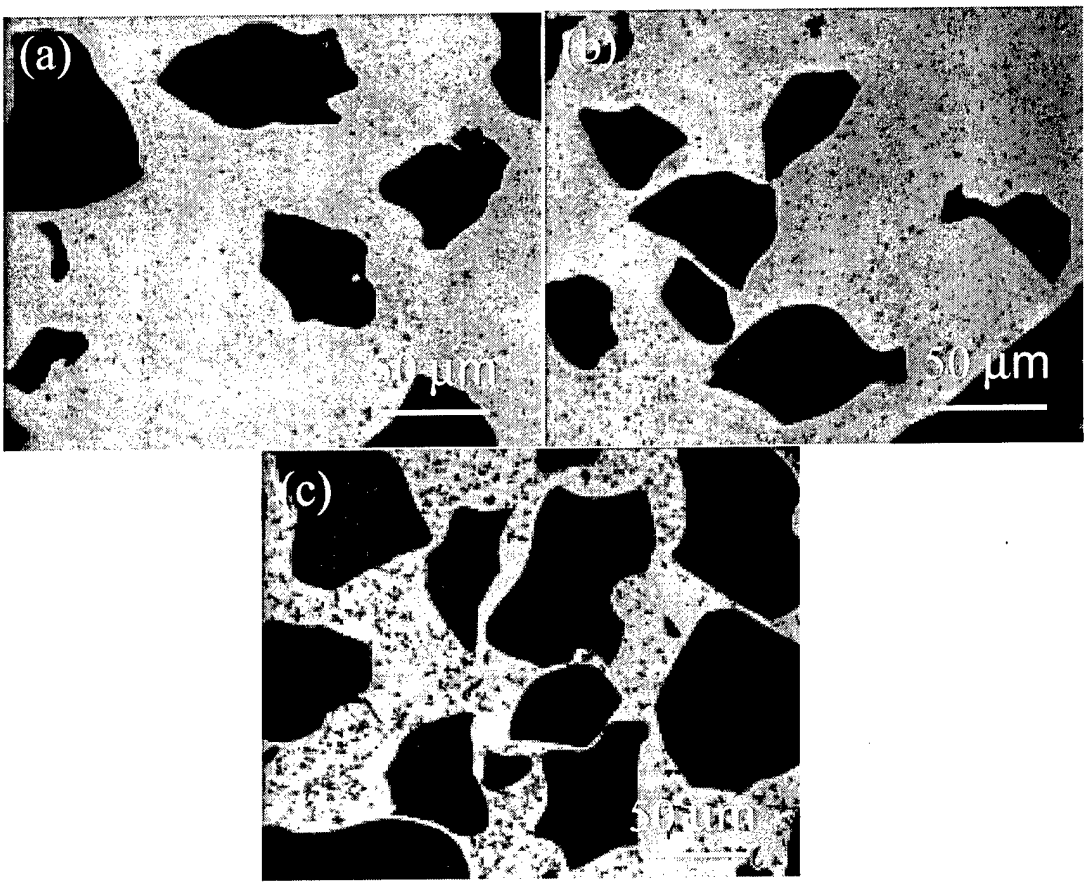

Fig. 5 Backscattered electron images (BEI) of (a) 40, (b) 60 and (c) 80 vol.% TiC/H13 steel formed at a beam scanning speed of 10.16 mm s^{-1}.

Discussion

The present results demonstrate that sizes and morphologies of the deposited beads are closely related to a beam scanning speed. In fact, they are dependent on the proportion of a powder feeding rate to a beam speed for a given powder constituent. During laser processing, laser energy is absorbed by both fed powder and substrate. Undoubtedly, their proportion decides the morphologies of the beads. Changing a beam speed is equal to inversely modifying a powder feeding rate. In the case of a smaller powder feeding rate, or a larger beam scanning speed, the amount of powder injected per unit time is small. Consequently, the energy that the powder absorbs is smaller, and the more energy may be spent to melt a substrate, resulting in a larger melting zone and a smaller bead. That is obvious for the maximum beam scanning speed (12.7 mm s^{-1}) used in the work (Fig. 2d). In the case of a larger powder feeding rate, or a lower beam scanning speed, more powder is injected. Therefore, more energy is absorbed by the injecting powder than the substrate. That results in a larger bead and a smaller melting zone. The situation of the minimal beam scanning speed (5.08 mm s^{-1}) is typical (Fig. 2a). Furthermore, no obvious

melting bond at the interface (at a speed of 5.08 mm s^{-1}) (Fig. 3a) can be explained in this viewpoint.

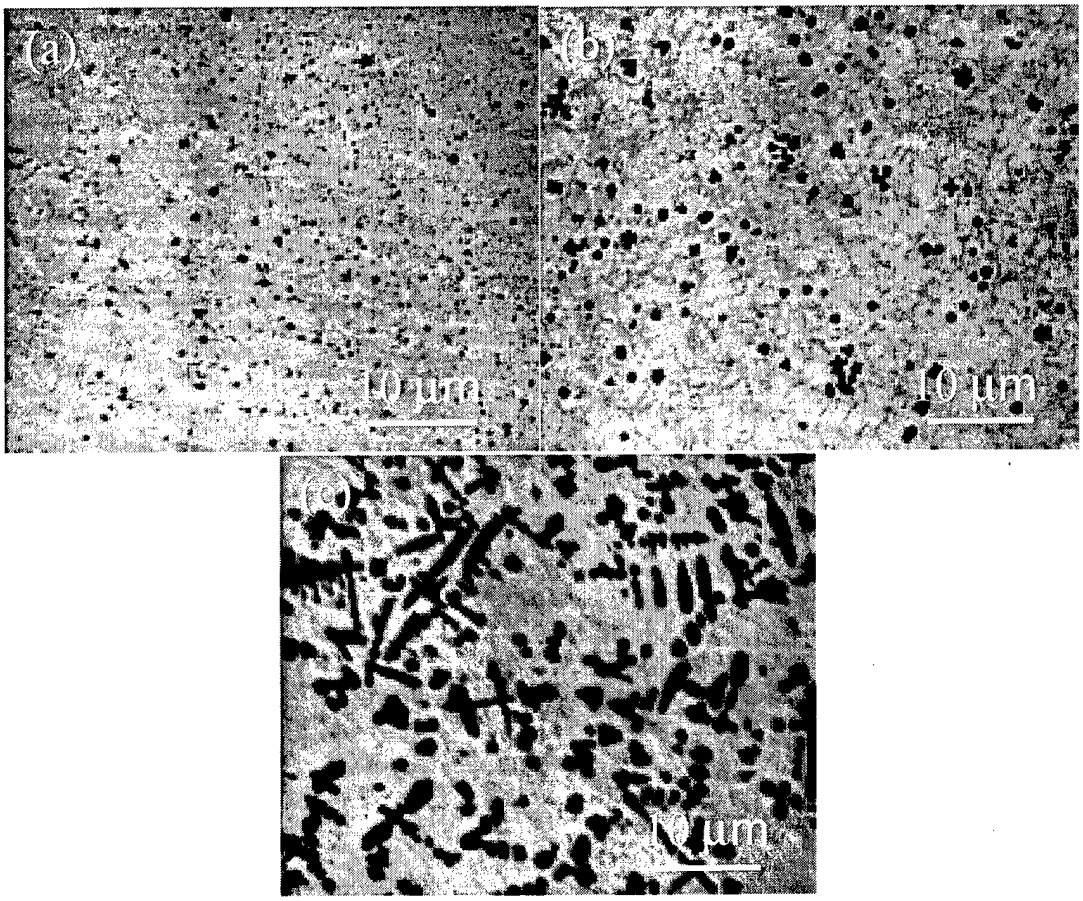

Fig. 6 High magnification BEI of (a) 40, (b) 60 and (c) 80 vol.% TiC/H13 steel formed at a beam scanning speed of 10.16 mm s^{-1}.

At the minimal beam scanning speed, the lack of a melting zone in a substrate results in a weak interface bond between the coating and substrate, as shown in Fig. 3a. Evidently, this speed is not suitable for producing a coating, not to mention the asymmetrical bead it produced (Fig. 2a and Fig. 3), that may accommodate gas and cause formation of pores during overlapping in coating production. However, the maximum beam scanning speed fails to make the upper coating coincide properly with the lower melting zone. More severely, some substrate material in the melting zone does not mix well with the deposited materials (Fig. 2d). These disadvantages make it unsuitable for producing a coating. In view of the morphology of beads, both the maximum and minimal beam scanning speeds are not ideal for coating production, while the intermediate beam scanning speeds, 7.62 and 10.16 mm s^{-1} seem to be appropriate.

The smooth edges of the coarse TiC particles indicate that the injected TiC melts and dissolves rather than reacts with the melt. As it is well known, the laser beam is characterized by a high energy density. The degree of absorption of the laser beam on metal and ceramic is very different. Ceramics have a much higher capability to absorb laser energy than metals [12].

Therefore, in spite of its extremely high melting point (3140°C) [13], melting of TiC occurs during processing. As the laser processing time is extremely short, its melting is incomplete and unmelted TiC remains.

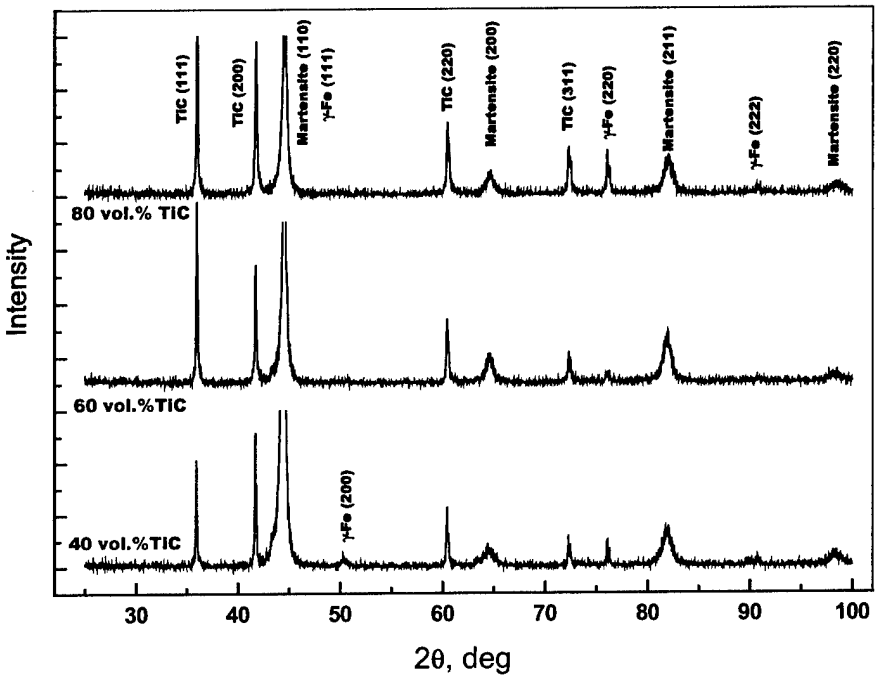

Fig. 7 X-ray diffractogram of 40, 60, 80 vol.%TiC/H13 tool steel formed at a beam scanning speed of 10.16 mm s^{-1}.

As melted TiC has a high tendency to dissociate into Ti and C, melting of a large amount of TiC results in a substantial increase in the concentration of Ti and C in the melt. Undoubtedly, TiC reprecipitate in the melt during cooling. EDAX and X-ray diffraction analysis confirms that fine TiC reprecipitated during subsequent cooling may contain less amount of other carbide forming elements, such as Mo and Cr. As the melt cools at a relatively high rate, solidified structures must be in a thermodynamic nonequilibium. That results in the development of various morphologies of TiC. At a higher beam speed and a lower content of injected TiC, the TiC precipitated in globular and cubic shapes. By lowering the beam scanning speed and increasing the amount of injected TiC, they tend to assume hexagonal and flower-petal shapes and finally the form of dendrites. This shows that the morphologies of TiC are closely related to the processing parameter and composition of melts. Considering the high contents of injected TiC, other alloying elements in the melt are neglected. The melt is approximately taken as the binary components of Fe and TiC. Refer to the binary Fe-TiC phase diagram (Fig. 8) [14], we explain qualitatively the morphologies of TiC. It can be seen that all the present constitutions of the coatings are hypereutectic. Therefore, TiC precipitates as a primary phase during cooling. Their morphologies depend on growth, as their nuclei are globular. Various morphologies of TiC can be developed during growth [15]. At a lower beam speed, solidification lasts a longer time and

primary TiC has time to grow a bit. For a higher content of injected TiC, the melt has a higher concentration of Ti and C, that is, a higher supersaturation. Therefore, their growth rate is higher, as a high solute concentration speeds up growth. Observed morphologies of TiC, spherical, faceted, rod, flower-petal shapes, and dendrites are from various growth stages. Due to rapid solidification, it is believed that the deposited beads are far from equilibrium and precipitated TiC is only primary phase during solidification.

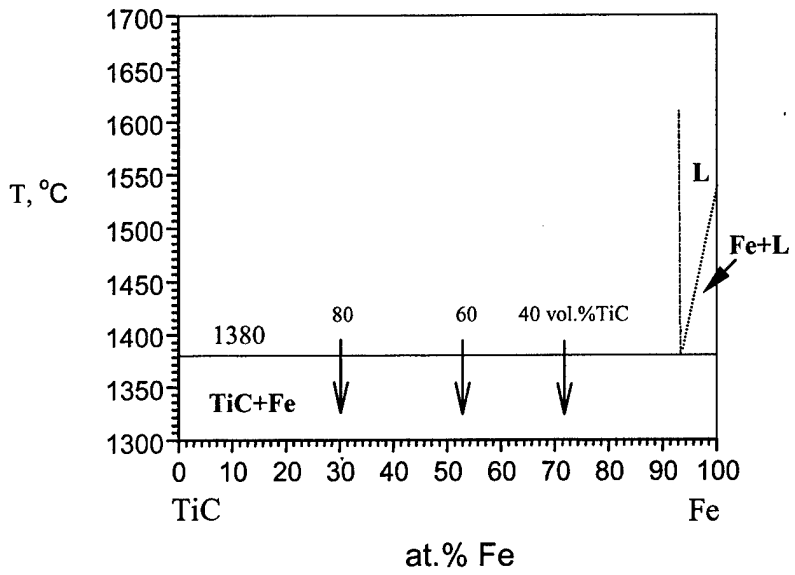

Fig. 8 Fe-TiC phase diagram [14].

In all the coatings, fine TiC precipitates are uniformly distributed in the matrix. They do not segregate around coarse TiC particles. This indicates that titanium and carbon atoms released by injected TiC are well distributed in melts. Their homogeneous distribution must be attributed to vigorous convection caused by rapid heating of the laser beam. A convective trace is evidenced in Fig. 2. It seems that the larger the beam scanning speed, the more obvious the convection.

Rapid cooling leads to the transformation of steel matrices into martensite (Fig. 7) that hardens a steel matrix. The fine precipitated TiC was observed to be a solidified nucleus for the steel matrix (Fig. 6b). They refined the grain structures of the matrix. In fact, it is well known that TiC is a good refiner for steels. Undoubtedly, this favors to modify solidified structures and furthermore, to improve both the strength and toughness of the steel matrix.

The present work indicates that microstructures of deposited beads are closely related to processing parameters. The beads with microstructures of coarse injected and fine precipitated TiC are developed. It is believed that tailored microstructures of TiC/H13 steel composite coatings can be achieved by choosing appropriate laser processing parameters.

As well known, fine particles would improve the mechanical properties of composites. It is expected that melting of coarse TiC and subsequent reprecipitation of fine TiC would impart better overall mechanical properties to coatings than the mechanical insertion of coarse TiC particles. Both the coarse remaining and the fine precipitated TiC particles are believed to have a clean interface with the steel matrix, as the original surface of injected TiC melts, a fresh surface is developed, and fine TiC precipitates are formed in-situ within the melts. Therefore, a stronger interface bond between TiC and the matrix may be achieved. As well known, the interface is a crucial location affecting the mechanical properties of composites. Impurity atoms usually tend to adhere to the surfaces of particles that disfavor an interface bond. In-situ formed composites can circumvent such disadvantages and therefore, have received much attention recently [16]. It is believed that the interface quality between TiC and the matrix in the present coatings is the same as that in in-situ formed composites. It is expected that the coating composites possess better overall mechanical properties.

Conclusions

1. The beam scanning speed affects the size and morphology of the deposited beads. The faster the beam moves, the larger the melting zone at the substrate, and the smaller the deposited zone. But, the size of heat-affected zones is independent on beam scanning speed.
2. The higher beam scanning speed fails to mix the deposited material properly with a substrate.
3. During laser processing, TiC melts, decomposes, and subsequently, a number of fine TiC precipitates form. They are uniformly distributed in the steel matrix, which is attributed to vigorous convection caused by rapid heating.
4. The beam scanning speeds and the amount of injected TiC have a remarkable impact on the morphology and size of the precipitated TiC. The lower the beam scanning speeds and the more the injected TiC, the larger the precipitated TiC. The larger TiC assumes spherical, rod, flower-petal, and dendrite shapes, while the smaller TiC is spherical and faceted.
5. It is believed that precipitated TiC is the primary phase in hypereutectic Fe-TiC.
6. Steel matrices in coatings are martensite with retained austenite. Precipitated TiC can refine grains of the steel matrix as a solidified nucleus.

Acknowledgements

The authors would like to express gratitude to Dr. H. H. Mei, Mr. Z.G. Liu and Mr. M. Valant for their helps during the experimental work.

References

1. T.C. Lei, J.H. Ouyang, Y.T. Pei and Y. Zhou, Surface Engineering, 12, 1996, 55.
2. B.J. Kooi, Y.T. Pei and J.Th.M. De Hosson, Acta Mater., 51, 2003, 831.
3. A. Agardwal, Surface Engineering, 17, 2001, 66.
4. Y.T. Pei, J.H. Ouyang and T.C. Lei, Surface and Coating Technology, 81, 1996, 131.
5. Y. T. Pei and T.C. Zou, Mater. Sci. Eng. A, A241, 1998, 259.
6. Q. Li, T.C. Lei and W.Z. Chen, Surface and Coating Technology, 114, 1999, 278.
7. J.H. Ouyang, Y.T. Pei, T.C. Lei and Y. Zhou, Wear, 185, 1995, 167.

8. S. Ariely, M. Bamberger, H. Hugel and M. Geller, SPIE Vol. 1972, 8th Meeting on Optical Engineering in Israel, 1992, 284-292.
9. C. Tassin, F. Laroudie, M. Pons and L. Lelait, Surface and Coating Technology, 76-77, 1995, 450-455.
10. M. Riabkina-Fishman, E. Rabkin, P. Levin, N. Frage, M. P. Dariel, A. Weisheit, R. Galun and B.L. Mordike, Mater. Sci. Eng. A, A302, 2001, 106.
11. R. Kovacevic, D. Hu, and M. Valant, "Apparatus and Method for Controlling the multiple Metal/Ceramic powder Feeding Systems", (Invention Disclosure, submitted to Southern Methodist University), May 2002.
12. To Hoon Kim, Section A-ICALEO (the International Congress on Applications of Lasers and Electro-Optics), Laser Institute of America: 1997, 21.
13. Wenping Jiang and Pal Molian, Surface and Coating Technology, 135, 2001, 139.
14. P. Villars, A. Pronce and H. Okamoto, in "Handbook of Ternary Alloy Phase Diagrams" (ASM International, 1995) p. 6850.
15. W.H. Jiang, W.D. Pan, G.H. Song and X.L. Han, J. Mater. Sci. Lett., 16, 1997, 1830.
16. H. Berns and B. Wewers, Wear, 250-251, 2001, 1386.

Particle Size Influence Upon Sintered Induced Strains Within 3DP™ Stainless Steel Components

Scott Johnston,[1,2] Rhonda Anderson[1,2] and Duane Storti[1,*]

[1] Dept. of Mechanical Engineering, University of Washington, Seattle, WA 98195-2600
[2] Concurrent Technologies Corporation, Bremerton, WA 98312
*Author to whom correspondence should be addressed.
Reviewed, accepted August 19, 2003

Abstract

Three-dimensional printing (3DP™[1]) is a layer-by-layer manufacturing process whereby a three-dimensional (3D) component is created by the distribution of a liquid binder onto a powder media. A 3DP™ process using stainless steel powder as its printing media requires post-printing thermal processing for debinding and sintering of the printed green component. To minimize dimensional distortion while increasing structural integrity of the green component, 3DP™ thermal post-processing is designed to produce only neck growth between particles, defined as initial stage sintering.

The accepted theoretical model governing initial stage sintering strain for spherical powder particles provides a qualitative account of strain development with respect to time and temperature variance; however, the model does not produce an accurate quantitative account for the magnitude of the strain when compared to dimensional experimental results. The theoretical model indicates that powder particle size is the dominant parameter governing sintering strain.

The purpose of this study is to introduce an effective particle size into the theoretical model, thus enabling the application of the theoretical model to estimate dimensional change for components produced by 3DP™. Dimensional sintering experimentation has been performed using 3DP™ test specimens with spherical powder particles having mean diameters of 20 μm, 80 μm, and 200 μm. Experimental results and progress on the theoretical model are discussed.

Introduction

It is extremely difficult to accurately predict the effects of sintering for dimensional, structural, and compositional changes due to the phenomenological aspects involved in sintering. Modeling efforts often result in inadequate approximations or inconclusive results. These approximations can be attributed to inaccurate material properties at sintering temperatures and non-rigorous understanding of basic relationships [1]. Most analytical sintering models provide qualitative illustrations of dimensional change (strain), but cannot quantitatively represent the magnitudes of these strains when applied to 3DP™ sintering process.

The widely accepted analytical formulation of initial stage sintering exhibiting an appropriate development of strain has been presented by German [2,3]. These equations are valid for isothermal conditions and provide a solid foundation for analysis of strain development of

[1] 3DP is a registered trademark of the Massachusetts Institute of Technology.

components manufactured by 3DP™. An expansion of these equations to allow for non-isothermal conditions is required in order to quantify some of the phenomenological aspects of initial stage sintering theory when applied to 3DP™ sintering practices.

This study emphasizes the analysis of strains produced from sintering stainless steel 3DP™ components. 3DP™ components are manufactured in a layer-by-layer construction using liquid binder applied to powdered materials [4]. This study is limited to analysis of components comprising a polymeric binder and 316L stainless steel (316L SS) powder with individual test specimens consisting of distinctively different particle diameters.

Initial Stage Sintering Mechanisms

Sintering occurs in three stages: initial, intermediate, and final. In the 3DP™ process, sintering involves only initial stage sintering, which can be characterized by neck formation between adjacent particles [2,3], as illustrated in Figure 1. Neck formation can be reduced to surface transport mechanisms and bulk transport mechanisms; both of these contribute to the mass deposited within the neck. Only bulk mechanisms produce any shrinkage between particles, thereby producing strain. This analysis is concentrated solely on dimensional changes, so only bulk mechanisms are considered.

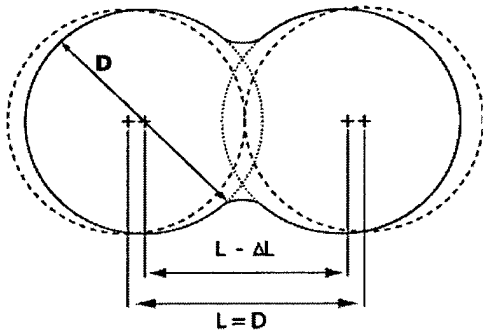

Figure 1. Dimensional representation of sintering neck growth and strain of two ideal spherical powder particles.

Initial stage sintering bulk mechanisms are comprised of plastic flow (PF), grain boundary diffusion (GB), and volume diffusion (VD) [2,3]. These three mechanisms affect the overall shrinkage of powder particles occurring from sintering. The relation of the associated parameters and their effective sintering strain, as produced between two spherical particles for each mechanism follows the basic kinetic law:

$$\left(\frac{\Delta L}{L}\right)^{n/2} = \varepsilon(t)^{n/2} = \frac{B \cdot t}{2^n D^m} \tag{1}$$

where t is time, D is the powder particle diameter, and L is the original length between the centers of the spherical particles (i.e., particle diameter).

Each mechanism is dependent on different material and physical parameters. The constant B depends on the specific sintering mechanism being considered and is exponentially related to temperature by the relationship:

$$B = B_o \exp\left(-\frac{Q_{mech}}{kT}\right) \tag{2}$$

where Q_{mech} is the activation energy for the corresponding mechanism, and the variables B_o, m, and n are defined in Table 1.

Table 1. Summary of initial-stage sintering equations and parameters for spheres [2,3].

Mechanism	n	m	B_o
Volume diffusion (VD)	5	3	$\frac{80\gamma D_v \Omega}{kT}$
Grain boundary diffusion (GB)	6	4	$\frac{20\delta\gamma D_b \Omega}{kT}$
Plastic flow (PF)	2	1	$\frac{9\pi\gamma b D_v}{kT}$

Symbols

γ = surface energy	D_v = volume diffusivity
δ = grain boundary width	D_b = grain boundary diffusivity
Ω = atomic volume	b = Burgers vector
k = Boltzmann's constant	T = Absolute temperature

The total strain produced is the superposition of all three bulk mechanisms, VD, GB, and PF. The bulk mechanisms will be the analytical basis used for a predictive analysis of sintering strains produced in 3DP™ components. An illustration of the qualitative strain development for VD is shown in Figure 2.

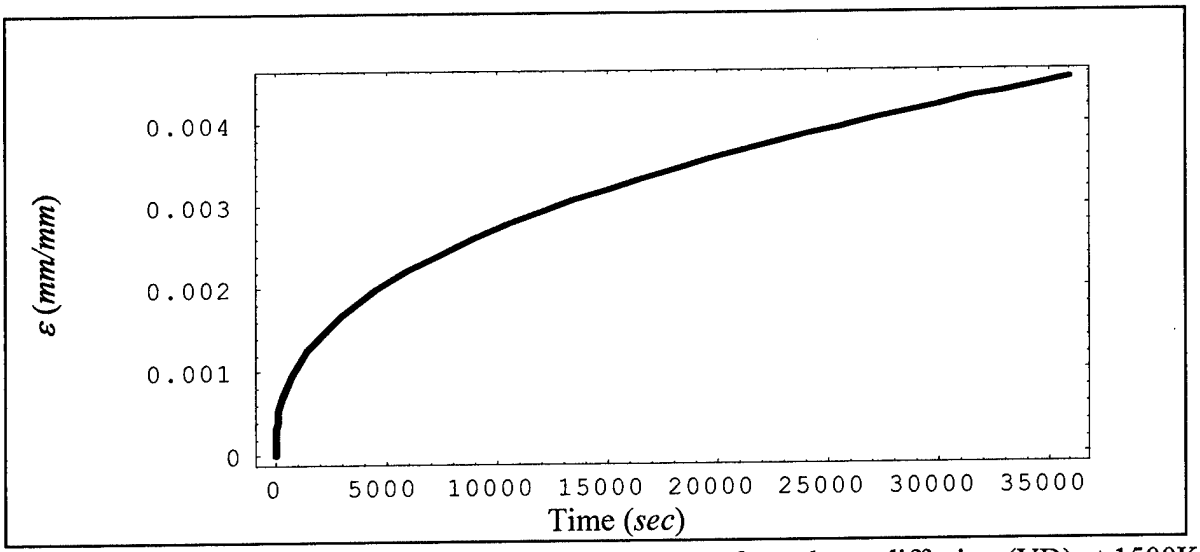

Figure 2. Isothermal sintering strain rate development for volume diffusion (VD) at 1500K for 10 hours.

The bulk mechanism equations presented in Equation 1 are valid for isothermal conditions; therefore, additional computational work must be developed in order to apply these equations to actual sintering temperature profiles. Hence, Equation 1 is more accurately represented as:

$$\varepsilon(t)_T = \left(\frac{B \cdot t}{2^n D^m}\right)^{2/n} \tag{1'}$$

As mentioned previously, the total strain is the sum of the bulk mechanisms, VD, GB, and PF; since each mechanism depends upon different material properties, their contribution to the total strain is unequal. Volume diffusion has been identified as the dominating bulk mechanism by Thümmler [5]. It can be observed from Table 2 that the strain produced from VD is the dominating bulk mechanism, while GB diffusion contributes less than 0.01% of the total strain, and PF's contribution is negligible. Therefore, only VD will be considered during strain calculations for this analysis.

Table 2. Strain values for 316L SS bulk mechanisms with varying particle diameter, isothermal temperature of 1500K, and 10-hour sintering time.

Powder Particle Diameter (μm)	Strain due to Volume Diffusion	Strain due to Plastic Flow	Strain due to Grain Boundary Diffusion
20	0.02393	2.528×10^{-20}	2.248×10^{-5}
80	0.00453	6.319×10^{-21}	3.540×10^{-6}
200	0.00151	2.528×10^{-21}	1.043×10^{-6}

Analytical Calculation of Strain

Equation 1' represents initial stage sintering strain formulation under isothermal conditions. Consequently, Equation 1' is only valid once a temperature has been selected. This is an idealistic model because it assumes that a component instantly achieves a sintering temperature; but, for practical applications, a component begins at room temperature and heat is applied until a desired sintering temperature is reached. As a result, the component is traversing through a series of isothermal strain curves described by Equation 1'. Once a desired temperature is constantly sustained, then strain can be computed by the isothermal strain curve represented by Equation 1'.

Strain is not only produced at the sintering temperature, but at temperatures below the sintering temperature [6]. Strain has already started to form before the maximum temperature of the thermal cycle is reached and the calculation of strain must consider the current level of strain as well as the current temperature. Since a 3DP™ sintering profile involves a temperature decrease as well as increase (i.e., the component must be cooled in order to be handled), knowledge of whether the temperature is increasing or decreasing is essential. The reason for incorporating a relationship between previously produced strain and the corresponding temperature gradient allows for correct transition between higher and lower level isothermal strain curves, thereby including any additional strain that may be produced prior to and after reaching the desired sintering temperature.

Strain rate surface, $\dot{\varepsilon}(t_i)|_{T_j}$

In order to perform a calculation of strain produced from a sintering temperature profile using isothermal strain curves required the introduction of a strain rate surface. It can be observed from Figure 2 that amount of strain produced at any time is dependant upon the temperature and the current level of strain. Namely, strain increases at greater rates at the beginning of isothermal time-strain curves produced from Equation 1'. It is reasonable to postulate that sintering strain can be calculated by summing the area under a strain rate surface over a defined temperature profile.

The creation of a strain rate surface that is dependant upon strain level and temperature is formulated using Equation 1' and *Mathematica* [7]. The premise is to choose specified strain increments and temperature increments that span the range of the temperature profile, $T_{profile}(t)$. The strain rates are then algebraically calculated at each of these strains and temperatures using Equation 1'.

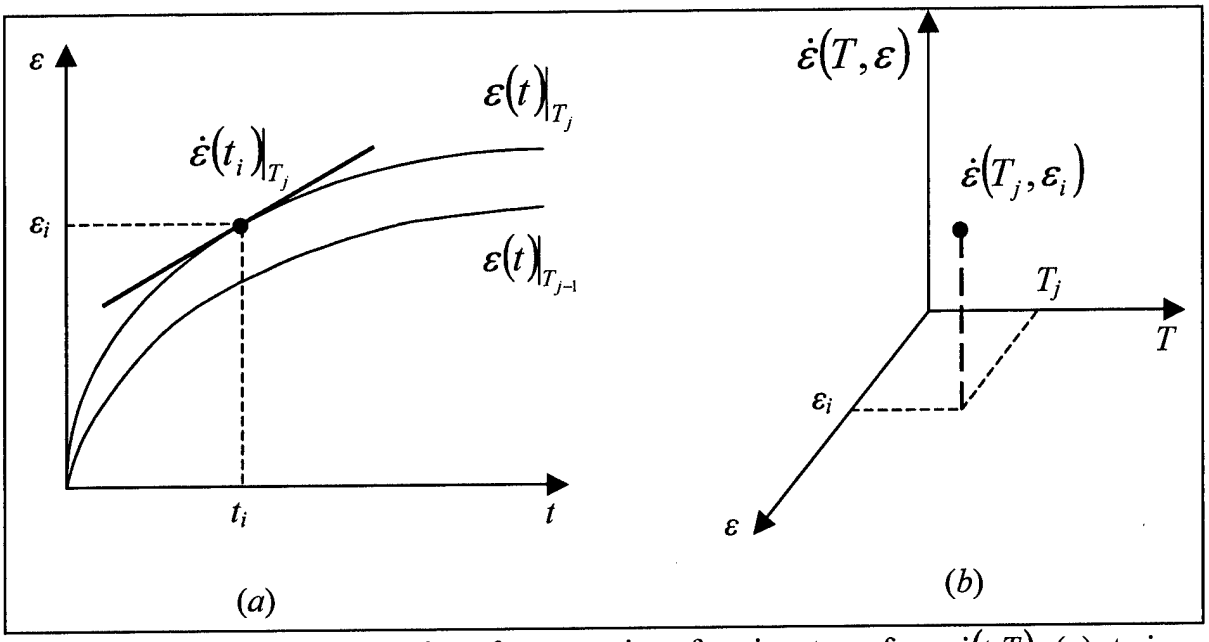

Figure 3. Graphical representation of construction of strain rate surface, $\dot{\varepsilon}(t,T)$; (*a*) strain development for a mechanism, (*b*) strain rate plotted according to value of strain and time.

To create the strain rate surface, the temperature domain is divided into *n* discrete temperatures T_j. Since temperature has an important role in sintering activity, a coarse ΔT is used at lower temperatures where the sintering activity is almost non-existent, and a finer ΔT is used at elevated temperatures where sintering activity is high. The primary reason for performing this varied ΔT is to reduce computation time. To ensure that the strain rate surface will contain every possible strain-temperature combination for the defined temperature profile, the maximum strain is computed at a temperature that exceeds the highest temperature achieved in the profile for a time period equal to the length of the profile.

One difficulty in creating the strain rate surface, $\dot{\varepsilon}(t_i)\big|_{T_j}$, involves how strain is defined. Strain is dependent upon time, t, and defined in terms of temperature, T. For each ε_i and T_j it is necessary to find an associated time, t_{ij}, where $t_{ij} \equiv$ time required to reach strain ε_i at temperature, T_j. Finally, the strain rate may be calculated using Equation 3, and is represented graphically in Figure 3.

$$\dot{\varepsilon}(t_i)\big|_{T_j} = \dot{\varepsilon}(t_{ij}) = \dot{\varepsilon}(T_j, \varepsilon_i) \tag{3}$$

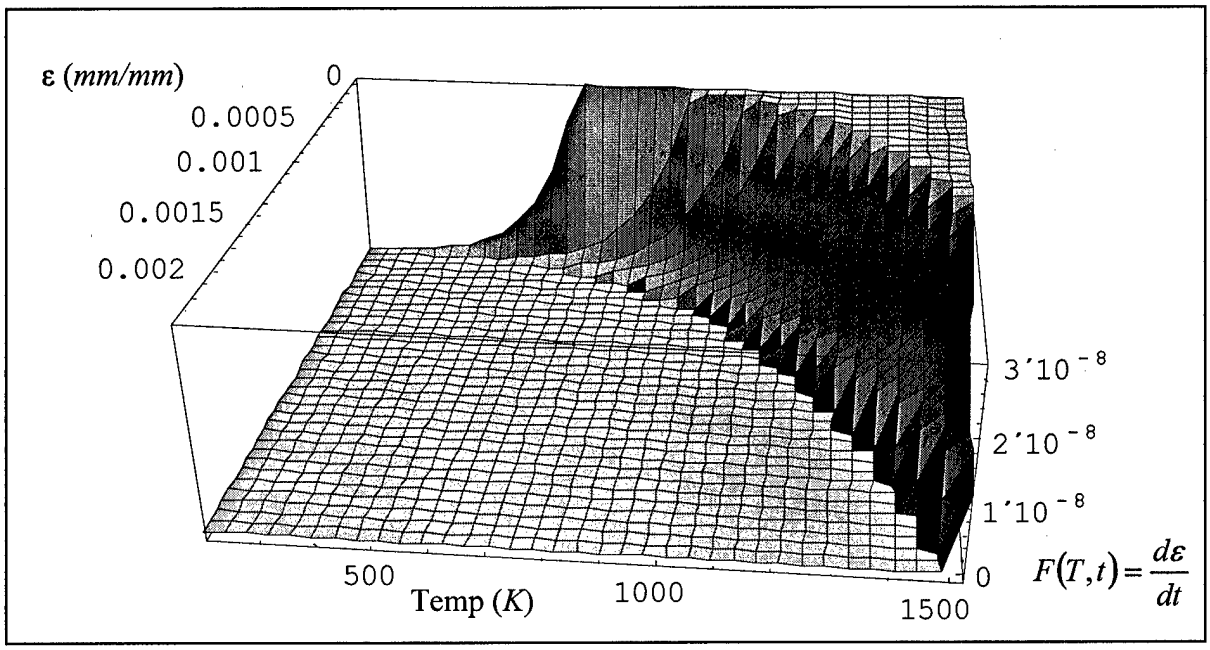

Figure 4. Strain rate surface for volume diffusion (VD).

The resulting strain rate surface (Figure 4) illustrates that at small values of existing strain, the strain rate is large and increases as the temperature increases, whereas at large values of current strain, the sintering strain rate is negligible. Both of these behaviors correspond to defining the strain rate as the tangential value to the curve shown in Figure 2.

Strain calculation using strain rate surface, $\dot{\varepsilon}(t_i)\big|_{T_j}$ for a defined temperature profile

The goal of creating the strain rate surface is to predict dimensional changes occurring during initial stage sintering of 3DP™ components using a defined temperature profile. Calculating the strain involves solving an ordinary differential equation (ODE) that incorporates the temperature profile. Representing the strain rate surface as $F(T, \varepsilon)$, it is possible to solve for a time-strain curve that is the result of a specified temperature profile, $T_{profile}$. A formal mathematical expression of this expression can be written as:

$$\frac{d\varepsilon}{dt} = F(T_{profile}(t), \varepsilon(t)) \tag{4}$$

where $\varepsilon(t)$ is the strain at the corresponding time and temperature of $T_{profile}$ (defined by Equation 1') and the initial condition $\varepsilon(0) = 0$. The solution to this ODE is a time-strain curve representing the amount of strain (shrinkage) produced between two equally sized spherical powder particles.

Experimental Results Compared to Analytical Calculations

To validate the analytical formulation presented herein, theoretical results were compared to experimental measurements using 316L SS samples. Components were manufactured on a ProMetal RTS-300, a solid freeform fabrication machine capable of creating metal components as large as 12x12x10 *in.* Typical process speed is 10-20 in^3/hr, depending on resolution. Components were thermally processed in a non-vacuum atmosphere furnace. Metal powders and binder were used as obtained from commercial vendor (Extrude Hone Corporation, Irwin, PA). Experimental strain measurements were measured pre- and post-sintering using a Smart Scope non-contact video measuring device (Optical Gaging Products, Inc.). The Smart Scope measuring method selects several points along each edge of the sample at a magnification of 53x. A least squares linear fit is used for the edges of the samples. Dimensional measurements are calculated from the linear fit lines with an accuracy of $\pm 40\mu m$ (0.00015 *in.*). Experimental results for 3DP™ samples printed using 20-, 80-, and 200-μm-diameter diameter spherical powder particles are shown in Table 3.

The analytical calculation of the strain requires that the material properties of the sintering media, namely 316L SS, be known. Material properties for 316L SS used for the analytical calculations are presented in Table 4. The magnitudes of the analytically calculated strain are shown in Table 4 where the values can be readily compared to the measured values for 20, 80, and 200 μm diameter particles. The calculated analytical strain is approximately one order of magnitude less than the experimentally obtained strain measurements. A graphical representation of the analytical strain development for a defined sintering temperature profile is presented in Figure 5.

Table 3. Comparison of experimental measured and calculated strains for X-print direction, ($\mu m/\mu m$).

Powder Particle Diameter (μm)	Experimental Strain Measurements	Calculated Analytical Strain
20	0.1314	0.012850
80	0.0166	0.002860
200	0.0098	0.000812

Table 4. Material properties of 316L SS powder particles.

$Q_v = 280\ kJ/mol$
$\gamma = 2\ J/m^2$
$\Omega = 6.9565\ mol/cm^3$
$D_v = 40{,}000\ m^2/s$

The strain curve shown in Figure 5 is indicative of the intuitive progression of neck growth and strain. Comparing the temperature profile and the corresponding analytically computed strain, it is observed that strain does not readily increase until the temperature reaches approximately 825 °C, which conforms with [6]. It should also be noted that after the sintering temperature has been reached and the samples begin to decrease in temperature, sintering activity becomes negligible, which corresponds to no additional strain (neck growth).

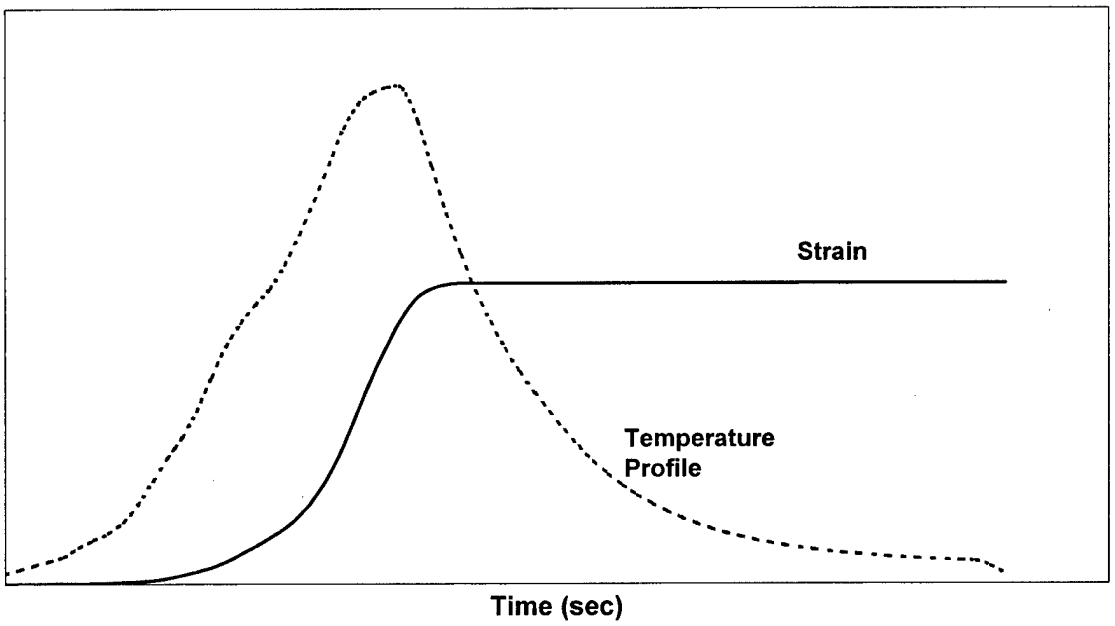

Figure 5. Typical sintering temperature profile displayed with the corresponding strain calculated using the strain rate surface.

It has been noted by German [1,2], that the equations describing initial stage sintering are only approximations and should be considered as such. The authors propose that a modification of these equations will lead to relatively accurate prediction of sintering strains which can be applied to the 3DP™ sintering processes. All of the contributing factors of Equations 1 and 2 have accepted values except for powder particle diameter, D. The only option for any type of modification to Equation 1 would be to alter the particle diameter influence.

Effective Particle Size, D_{eff}, Formulation

The discrepancy between the analytical formulation and experimental results can be accounted for by creating an effective particle size parameter to use in the analytical formulation. To formulate the new parameter, experimental study involving sintering strains produced within components comprised of particles with different diameters was performed. Since 3DP™ predominantly creates components using particle diameters in the range of 20-100 μm, experimentation was performed using samples that were comprised of 20-, 80-, and 200-μm spherical powder to allow for a range of experimental values to be obtained. It should be noted that the powder particle diameter is not constant throughout the component; however the particle diameters are highly concentrated about their respective mean diameter (20, 80, and 200 μm).

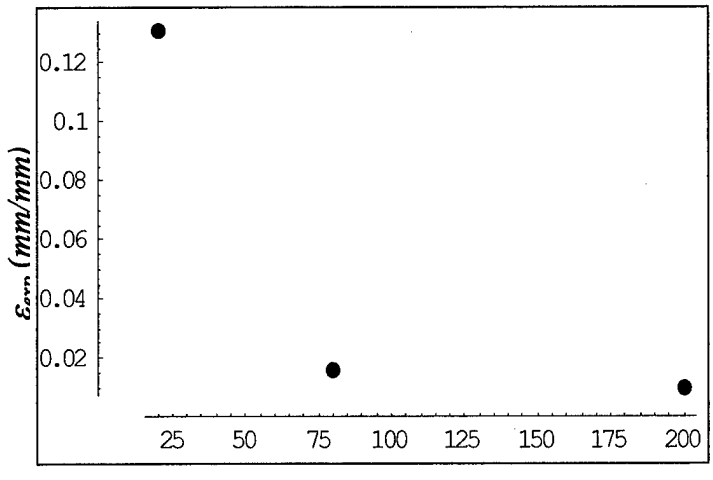

Figure 6. Powder particle diameter compared to experimentally measured sintering strain.

Table 3 indicates that the magnitude of the strain calculated using the strain rate surface has values less than the experimentally measured strain. It is also observed in Equation 1 that the strain does not possess a simple linear relationship with particle diameter. Figure 6 displays a graphical representation of the data displayed in Table 3; note the non-linear relationship between the strain and the powder particle diameter. Therefore, a constant correction factor will not suffice as an effective particle diameter. The strain increases as the particle size decreases, which is consistent with the algebraic relation of strain and particle diameter defined in Equation 1.

It is proposed to introduce an effective particle diameter to use in the analytical calculation as a parameter indicative to 3DP™ sintering. The effective particle diameter is determined by calculating what effective particle diameter is required to produce the experimentally measured strain, while using the strain rate analysis calculation method. The effective diameter, D_{eff}, would then be dependant upon the sintering temperature profile that was used during the experimental work as well as the actual diameter of the powder particles, D_{act}, namely:

$$D_{eff} \equiv D_{eff}(D_{act}, t, T) \tag{5}$$

The sintering temperature profile must be accounted for while formulating the analytical form of $D_{eff}(D_{act}, t, T)$. Examination of Equation 1 (for VD) reveals that the isothermal strain curve, $\varepsilon \equiv \varepsilon(t)$, can be thought of as:

$$\varepsilon \equiv \varepsilon(t, T, D) = \left(\frac{B \cdot t}{2^5 D^3}\right)^{2/5} \tag{6}$$

Using Equation 6, a fixed time, t, and fixed temperature, T (isothermal temperature profile), and with the experimentally obtained strain values, it is possible to solve for an effective particle diameter, D_{eff}, for each of the 20-, 80-, and 200-μm samples. The effective diameter, D_{eff}, would then be dependant upon the chosen isothermal temperature profile.

The only known values for actual strain production are obtained from the experimental temperature profile, $T_{exp}(t)$. To find the effective particle diameters for T_{exp}, successive strain rate analyses were performed to obtain a relationship between the particle diameter and produced strain. Next the strain values were back-solved to find the effective particle diameter for T_{exp}. Those results are shown in Figure 7. The relationship of the effective particle diameter, D_{eff}, to the actual diameter, D_{act}, can be defined by a logarithmic relationship, and the effective data points were fitted to the generic equation:

$$D_{eff}(D_{act}) = A \cdot [\ln(D_{act}) + B] \tag{7}$$

resulting in

$$D_{eff}(D_{act}) = 11.0 \cdot [\ln(D_{act}) - 2.7]. \tag{7'}$$

Again, it should be noted that Equation 7' represents a D_{eff}, which is dependant upon T_{exp}.

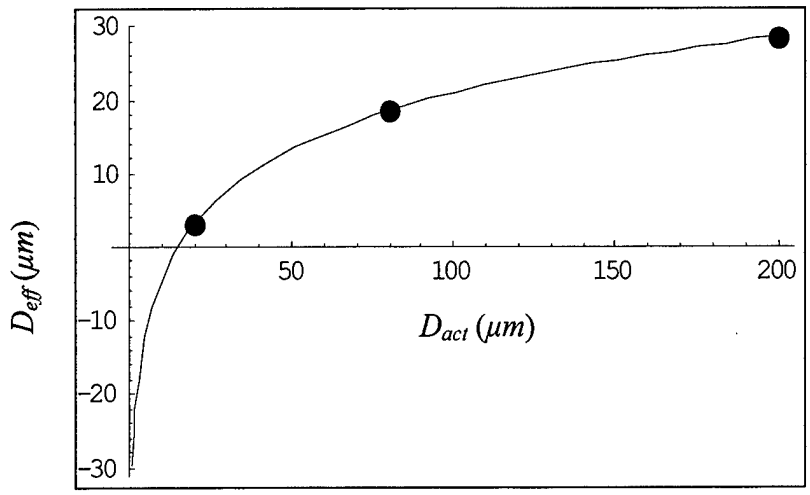

Figure 7. Actual particle diameter compared to the effective particle diameter.

The fitted curve for D_{eff} represented by Equation 7' can be expanded to be used for any temperature profile. Introduction of a temperature profile factor (*TPF*) whose value will be dependent upon the active sintering area of the temperature profile. The active sintering area for a material can be defined as the time where the temperature exceeds a threshold temperature where strain begins to form. Strain begins to form before the sintering temperature is reached, which is observed in Figure 5 and for 316L SS, temperatures above 825 °C (or 1100*K*) are the most active temperatures for sintering [3,6]. For sintering of 316L SS, it is possible to relate the active area for any sintering profile to $T_{\exp}$, creating a D_{eff} for that particular profile. Therefore Equation 7' can be modified such that:

$$D_{eff}(D_{act}) = TPF \cdot 11.0 \cdot [\ln(D_{act}) - 2.7] \tag{8}$$

where *TPF* is the sintering temperature profile factor.

A possible definition of the *TPF* is defined as the ratio of the integral of $T_{\exp}$, to the integral of $T_{profile}$, where their respective temperatures exceed 1100*K*, namely:

$$TPF = \frac{\int_{T \geq 1100} T_{\exp}(t)dt}{\int_{T \geq 1100} T_{profile}(t)dt} \tag{9}$$

Equation 9 displays an intuitive relationship between any $T_{profile}$ when compared to results for $T_{\exp}$. The longer a component is exposed to temperatures within its active sintering area, the more strain is produced. This relationship between the temperature profile and the effective particle diameter, D_{eff}, creates an initial foundation from which to produce quantitative results for sintering of 316L SS 3DP™ components.

Conclusions

This study expands upon the qualitative initial stage isothermal sintering strain equations presented by German [2] by creating a strain rate surface. Using the strain rate surface, it is possible to analyze and qualitatively predict dimensional change of initial stage sintering

subjected to any sintering temperature profile by solving the corresponding ODE. The result is a time strain relation for the applied temperature profile

Comparing experimentally obtained strain values and analytically calculated strain values using different diameter particles demonstrates the influence of powder particle diameter upon sintering strain in 3DP™ components. The experimental results are consistent with the theory that powder particle diameter is a dominating influence upon initial stage sintering strain. The relationship between the powder particle diameter and corresponding sintering strain introduces a method to create quantitative results for sintering analysis of 3DP™ components in the form of an effective particle diameter.

The strain rate surface, when combined with experimental strain measurements, provides an analytical form for an effective particle diameter. The effective particle diameter has been formulated such that it is dependant upon the corresponding sintering temperature profile to be applied. Using the effective particle diameter within the analytical strain calculation (strain rate surface) yields quantitative results of sintering strain for 316L SS 3DP™ components.

Future Endeavors

Additional experimentation is required to formulate a rigorous relationship between the *TPF* and the experimental temperature profile. Several sintering runs must be performed using temperature profiles that possess drastically different sintering activity areas. This experimental study would allow for a more concrete definition of the *TPF*.

The analytical method developed herein can be expanded upon by incorporating dimensional strain computations into a Finite Element Analysis. Including isotropic strain formulation characterized by Johnston [8], a three-dimensional strain analysis can be performed for 3DP™ components. By combining strength values and fracture or failure modes, it becomes possible to predict problematic sintering profiles for component geometry.

Further development of this theory is possible to include components that are comprised of powder particles of different diameters, thereby creating components with increased green and sintered densities.

Acknowledgements

Financial support for this work is provided by the Office of Naval Research, Contract #N00014-C-00-0378. The authors are grateful to the Physics Department at University of Washington for equipment use.

References

[1] R. German, *Computer Modeling of Sintering Processes*, The International Journal of Powder Metallurgy, Vol. 38, No. 2, 2002, p. 48-66.

[2] R. M. German, *Sintering Theory and Practice*, Wiley & Sons, New York, 1996.

[3] ASM International, *Powder Metal Technologies and Applications*, ASM Handbook, Volume 7, 1998, pp.448-452.

[4] E. Sachs, P. Williams, M. Brancazio, Cima, and K. Kremmin, *Three Dimensional Printing: Rapid Tooling and Prototypes Directly From a CAD Model*, Proceedings of Manufacturing International, ASME, 4, 1990, pp. 131-136.

[5] F. Thümmler and R. Oberacker, *An Introduction to Powder Metallurgy*, The University Press, Cambridge, 1993.

[6] R. German, *Powder Metallurgy Science*, 2nd ed., Metal Powder Industries Federation, Princeton, NJ, Chapters 7 and 9, 1997.

[7] *Mathematica* 4.2, A product of Wolfram Research, Inc.

[8] S. Johnston and R. Anderson, *Finite Thermal Analysis of Three Dimensionally (3DP™) Printed Metal Matrix Composites*, Proceedings of the 13th Annual Solid Freeform Fabrication Symposium, Austin, TX, August 2002.

CHARACTERIZATION OF HIGH ALLOY STEEL PRODUCED VIA ELECTRON BEAM MELTING

Denis Cormier[+], Ola Harrysson[+], and Harvey West[+,++]
[+]Industrial Engineering [++]Materials Science and Engineering
North Carolina State University
Raleigh, NC 27695-7906
Reviewed, accepted August 19, 2003

Abstract

Electron Beam Melting (EBM) is a direct-to-metal freeform fabrication technique in which a 4 kW electron beam is used to melt metal powder in a layer-wise fashion. As this process is relatively new, there have not yet been any independently published studies of the high alloy steel microstructural properties. This paper describes the EBM process and presents results of microstructural analyses on H13 tool steel processed via EBM.

Introduction

Electron Beam Melting (EBM) is a relatively new direct-metal freeform fabrication process that has been commercialized by Arcam (www.arcam.com). Figure 1 illustrates the basic elements of an Arcam S12 EBM machine. Typically, a 0.1 mm thick layer of metal powder is first spread across the build platform. A 4 kW electron beam gun then preheats the layer using a relatively low beam current and a relatively high scan speed. This preheating step serves two purposes. First, it lightly sinters the metal powder in order to hold it in place during subsequent melting at higher beam powers. Second, it imparts heat to the part that helps reduce the thermal gradient between the melted layer and the rest of the part. By maintaining a more consistent overall part temperature, built-in residual stresses are reduced. Following this preheating step, the layer is melted by increasing the beam power and/or decreasing the scan speed. The build platform is lowered by an amount equal to one layer thickness, a new layer of metal powder is spread, and the process is repeated until the part is complete. Upon completion of the build process, the part is removed from the build chamber. The loose powder supporting the part is removed, and the part is air cooled to room temperature. Bead blasting with silicon carbide, aluminum oxide or other appropriate blast media removes any powder clinging to the part surface. At this point, the as-processed part has a textured surface that resembles a sand casting. If necessary, finish machining of critical part features can be performed.

One advantageous feature of the EBM process is that the loose powder supports all downward-facing surfaces, thus highly complex geometric shapes such as conformal cooling channels are easily built without any need for complex 5-axis programming for collision avoidance. Taminger [1] observed that electron beam melting of metals is very energy efficient and is particularly well suited for processing highly reflective metals such as aluminum that can be difficult to melt with lasers. Lastly, as the entire process takes place in a vacuum, a certain amount of material purification takes place due to the removal of gasses such as those that cause porosity in metal castings.

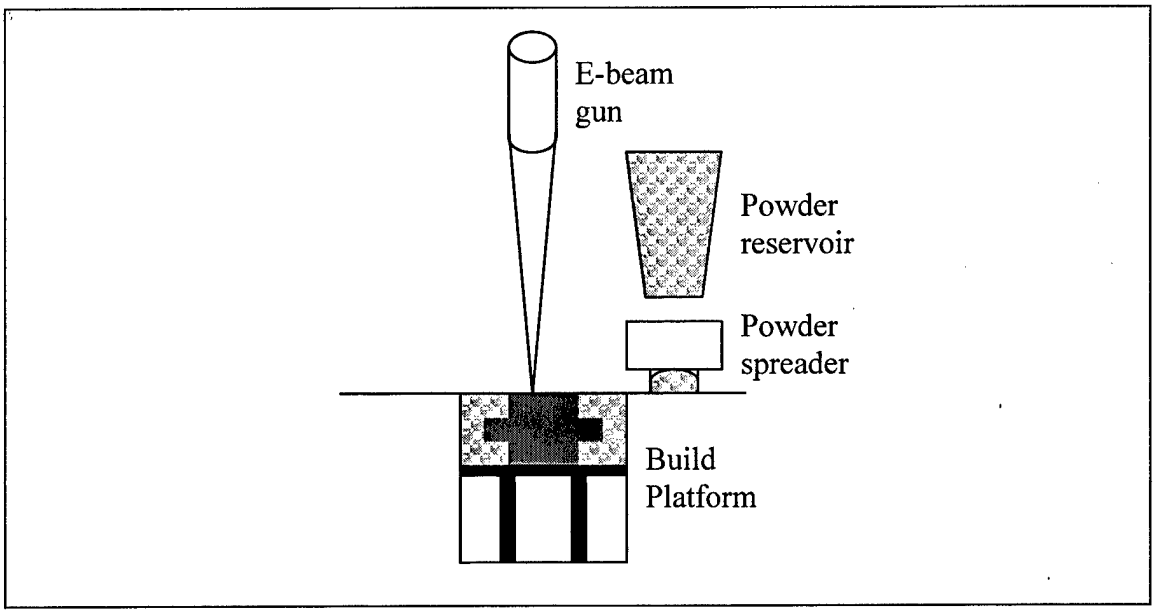

Figure 1 - Layout of Arcam EBM S-12 Machine

During the EBM build process, each slice is divided into two regions – contours and squares. The example in Figure 2 only shows a single contour, however, the user can specify that multiple offset contours be built. The area within a layer that remains after the area of the contours is melted is the bulk area to be melted. Rather than melting all of this area in a left-to-right or spiral scanning pattern, the slicing software subdivides this area into a series of sub-regions called "squares". In order to evenly distribute heat and to prevent thermal distortions, these squares are melted in a random order that changes from one layer to the next. As is illustrated in Figure 2, squares that are adjacent to a contour are cropped to the shape of the contour. The size of the squares is typically 10 - 15 mm.

At present, there do not appear to have been any independently published studies of the Arcam EBM process. The company states that a wide variety of metal powders can be processed with the process, although Arcam initially chose to concentrate on the use of H13 tool steel alloys for tooling applications. A titanium alloy (Ti6Al4V) has also been developed, and the company is now working on developing parameters for other high-performance alloys. Taminger [1] describes encouraging experiments involving e-beam freeform fabrication of 2219 aluminum alloy in wire form, and Matz [2] also describes unique material properties of a 718 nickel-based superalloy that was fabricated using a similar wire-feed e-beam freeform fabrication process. These studies provide strong evidence that e-beam freeform fabrication is well suited for a wide variety of metal and metal composite materials. The remainder of this paper discusses preliminary results of tests conducted using Arcam's EBM S12 machine to process H13 tool steel powder.

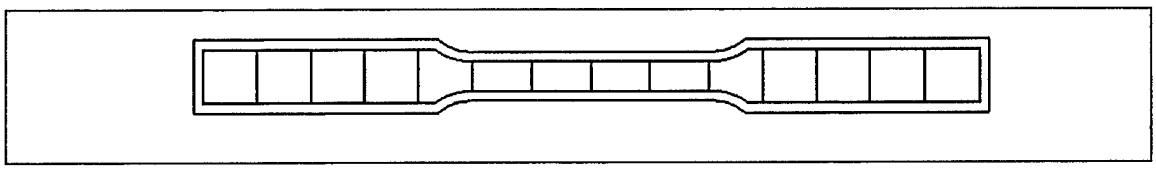

Figure 2 – Illustration of Contours and Squares for a Tensile Test Specimen

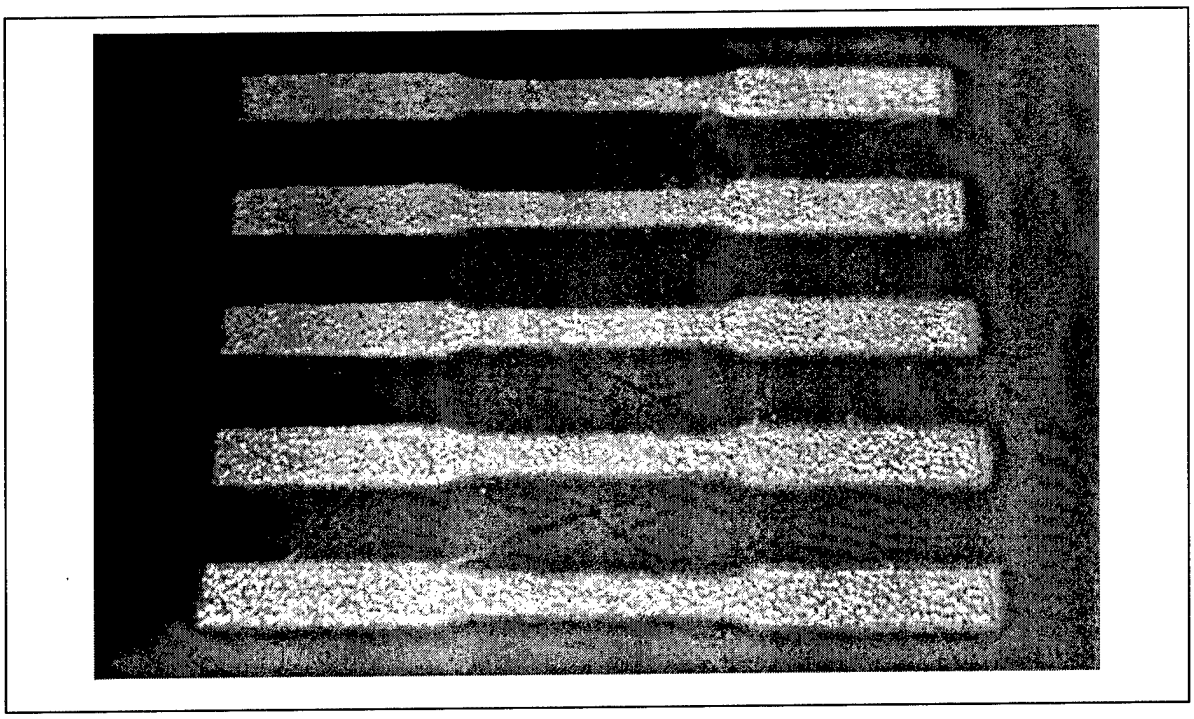

Figure 3 – A Set of Five Subsize Tensile Test Specimens Prior To Powder Removal

Experimental Procedure

In order to begin studying the microstructure and properties of H13 steel produced via EBM, several sets of standard 4-inch sub-size tensile test specimens were fabricated in accordance with ASTM E8 [3] (see Figure 3). Parts were built using the default layer thickness of 0.1 mm. Each layer was preheated 10 times with a scan speed of 10,000 mm/sec and a beam current that was progressively increased from 2 mA on the first scan to 20 mA on the 10^{th} scan. Note that at a scan speed of 10,000 mm/sec, the entire preheating cycle takes a matter of seconds. Following preheating, each layer was melted. A total of two contours were first melted using a beam speed of 100 mm/sec and a beam current up to 20 mA. The squares were then melted at a speed of 500 mm/sec and a beam current up to 20 mA. All processing parameters such as scan speed and beam current can be specified by the user. As is to be expected, the choice of parameter values considerably influences build time and material properties.

In total, three jobs consisting of five specimens each were fabricated using identical build parameters as described above. The first two sets of specimens were removed from the S12 machine immediately upon completion of the job and were rapidly air-cooled. As this is an air-hardening steel, it was hypothesized that rapid air cooling would result in the formation of martensite. The second of these two sets was then annealed in a furnace by heating it to a temperature of 900°C and then allowing it to cool to room temperature at a rate of 22°C/hr. The third set of specimens was allowed to slowly cool to room temperature in the build chamber under vacuum in order to determine whether or not the properties would be affected by the slower cooling rate (without a subsequent anneal).

Prior to preparation of the specimens for microstructural examination, the hardness of the slowly cooled set of specimens was tested. A set of measurements from different samples produced a range of hardness values from 46.0 to 47.3 HRC. This suggested that cooling in the build chamber under vacuum was not slow enough to prevent the formation of martensite. Consequently, samples from this group were not considered for microstructural examination.

One specimen from each remaining group was prepared for microstructural examination. Transverse and longitudinal sections of solid bars were obtained using a water-cooled cutoff wheel and mounted in Bakelite. The surfaces to be viewed were ground on progressively finer grits of silicon carbide paper, rough polished using 6-micron diamond paste, and fine polished with 1 micron and 0.3 micron alumina suspensions. The samples were etched with a 4% solution of nitric acid in methanol. An Olympus inverted stage metallurgical microscope equipped with digital camera was used for optical examination. The microstructure was also viewed using a Hitachi S-3200N Environmental Scanning Electron Microscope (SEM) equipped with an Oxford energy dispersive X-ray spectrometer capable of light element detection.

For the chemical analysis, samples of the H13 powder as well as a section from a fabricated bar were submitted to NSL Analytical Services for chemical analysis. X-ray fluorescence spectroscopy was used to determine the levels of cobalt, chromium, manganese, molybdenum, nickel, silicon, vanadium, and tungsten. The amount of phosphorus present was measured with optical emission spectroscopy, and the amounts of carbon and sulfur were determined via LECO furnace.

Results and Discussion

Chemical Analysis

The results of the chemical composition analysis for the as-processed H13 steel are presented in Table 1. ASTM A681 upper and lower limits [4] for H13 steel are included in the table for reference. Arcam considers its powders to be proprietary at this time, hence composition of the raw powder cannot be included in the table.

Table 1- Chemical Composition of as-processed H13 Steel Versus ASTM A681 Specifications

Element	Minimum Allowable %	Measured %	Maximum Allowable %
Carbon	0.32	0.37	0.45
Manganese	0.20	<0.1	0.60
Phosphorus	0.000	0.011	0.030
Sulfur	0.000	0.005	0.030
Silicon	0.80	1.02	1.25
Chromium	4.75	4.99	5.50
Vanadium	0.80	1.05	1.20
Molybdenum	1.10	1.65	1.75

With the exception of manganese, all alloying elements fall within ASTM limits for H13 steel. One of the interesting challenges with e-beam melting of metal alloys lies in the fact that the process typically takes place in vacuum. Ordinarily, the vaporization of lower melting point alloying elements would be a significant concern. With EBM and similar processes, however, solidification of the melt pool takes place so rapidly that the magnitude of vaporization is quite limited. The degree of vaporization is obviously a function of the processing parameters, and future experiments are planned to help obtain a better understanding of how rapidly the metal solidifies under a given set of conditions.

Hardness

The hardness of both air-cooled and annealed specimens was measured. The air-cooled specimens had hardness values ranging from 48.0 to 50.0 HRC. This provided initial confirmation of the hypothesis that the as-processed material would consist of martensite. As expected, the specimens that were subsequently annealed had HRC values under 20.

Microstructural Analysis

As described previously, samples of both air-hardened and annealed specimens were prepared for inspection via optical microscopy and SEM. Figure 4 shows a micrograph of air-cooled steel produced via the EBM process. For reference, a 500 μm scale is shown. Recall that a layer thickness of 100 μm was used to fabricate this part. As expected, the structure is 100% martensite. It is apparent that the part is virtually 100% dense. Interlayer fusion also appears to be complete.

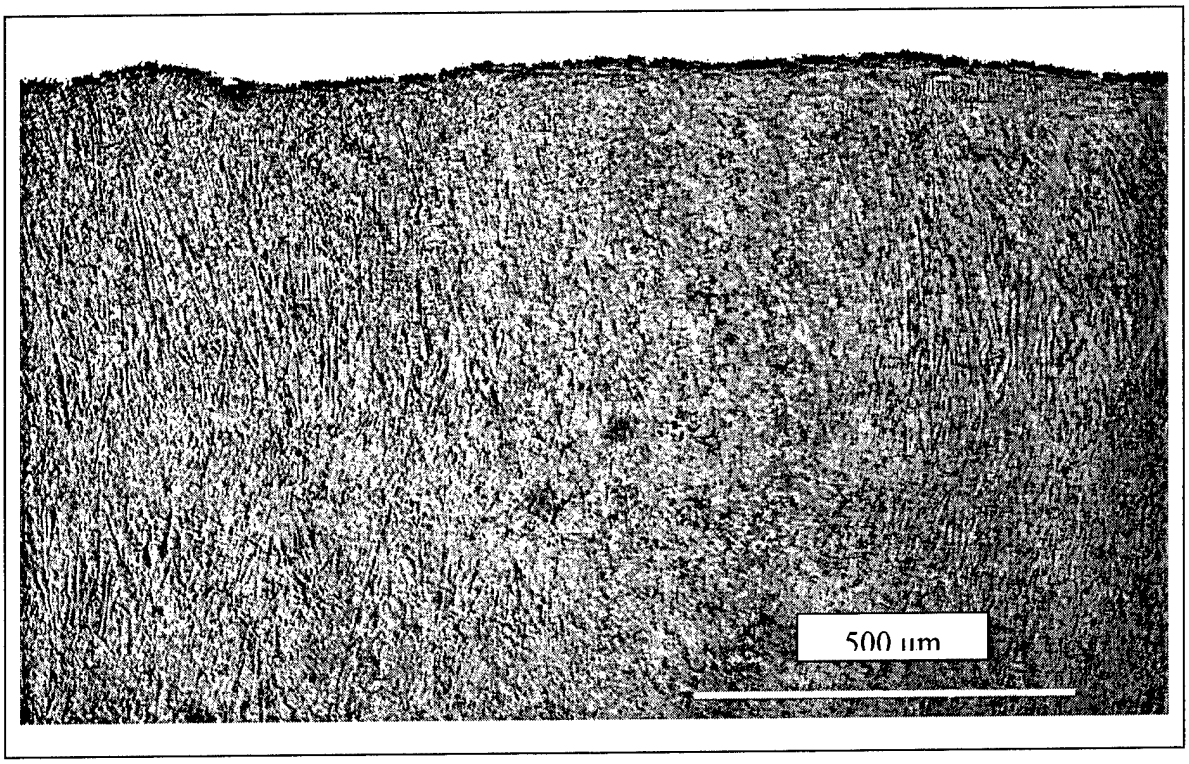

Figure 4 - Microstructure of Air-Cooled H13 Specimen

Figure 5 - Optical Micrograph Showing Local Inhomogeneities

From a metallurgical perspective, a set of interesting localized non-homogeneities were observed at the boundary between the melted contours and interior square regions (see Figure 5). These non-homogenous regions are not visible prior to etching. In an attempt to characterize this non-homogeneity, an X-ray line scan across the region shown in Figure 6 was performed to detect variations in the amounts of C, Si, Mo, V, Cr, and Fe present. As indicated in the spectra to the right of the figure, the chemical composition within the non-homogeneity is essentially identical to what is found in the surrounding matrix. The specimen was immersed in liquid nitrogen to determine if the non-homogeneity might be retained austenite. Unfortunately, this treatment had no effect on the non-homogeneity. Lastly, a Micromet microhardness tester was used to measure hardness within the non-homogeneity. Microhardness testing indicated that the hardness within the non-homogeneity is identical to that of the surrounding martensite. Work is continuing on the characterization of these localized non-homogeneities that are only observed after etching.

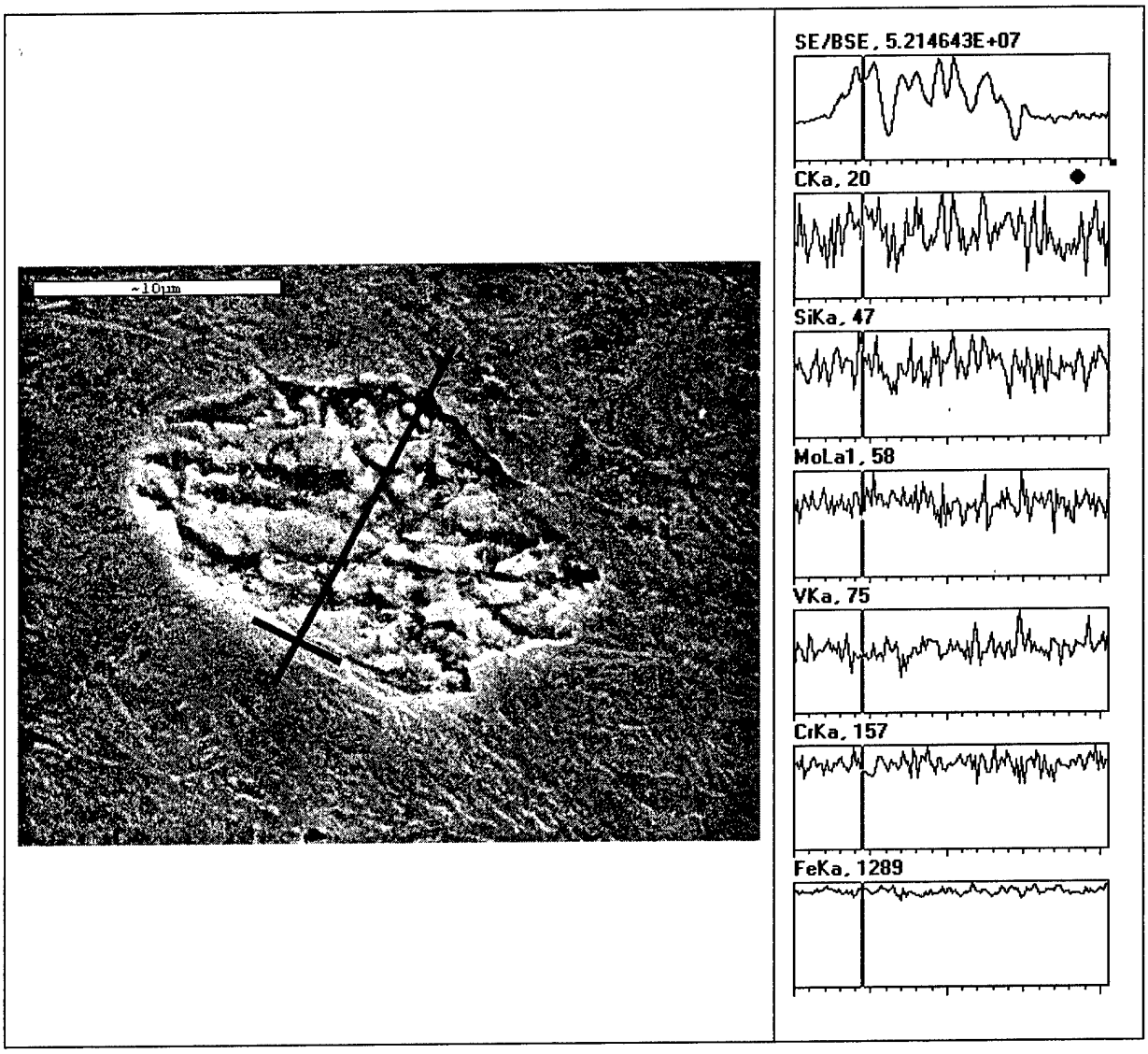

Figure 6 – SEM Photograph Showing Line Scan and Spectra Analysis Across Inhomogeneity

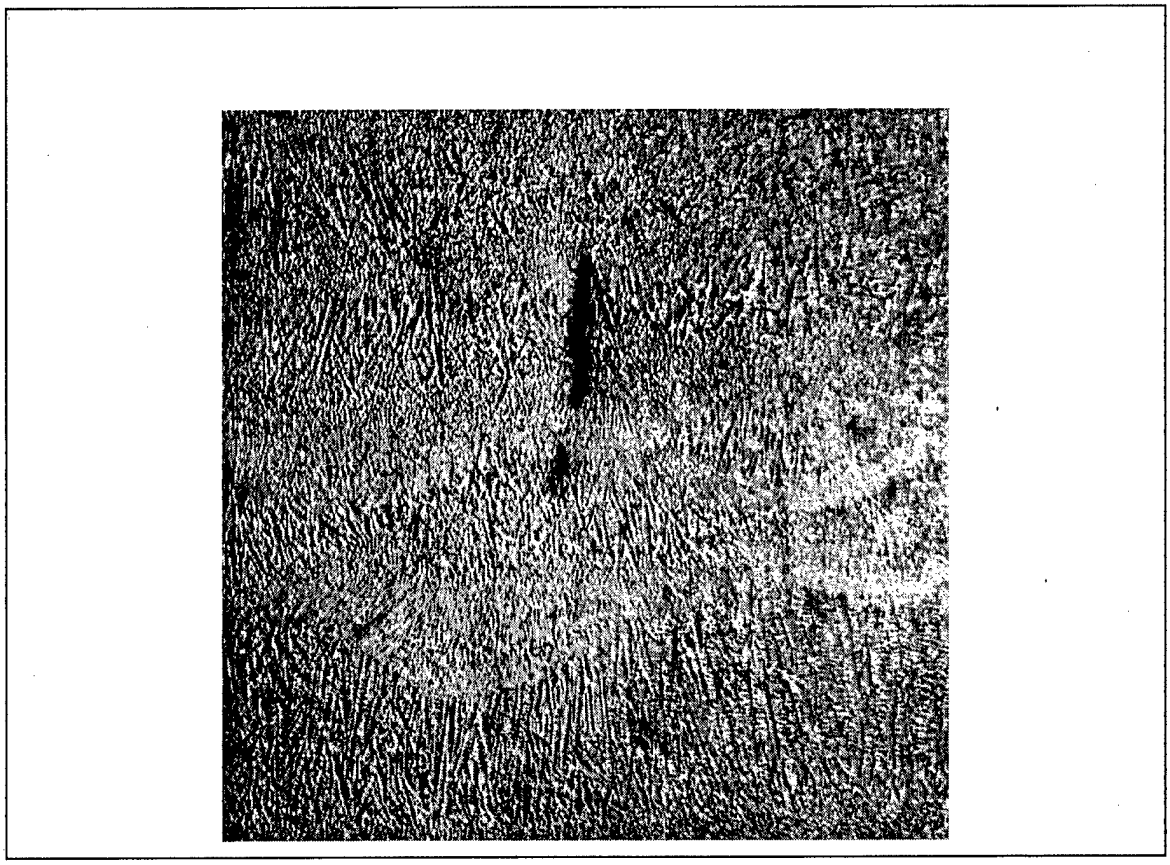

Figure 7 - Optical Micrograph of Intralayer Shrinkage Crack

Although the metallurgical properties were generally quite good under the processing parameters that were used, a small number of isolated shrinkage cracks that were contained within specific layers could be observed. One such crack is shown in Figure 7. As the data presented in this paper is specific to one single set of processing parameters, future experiments will be necessary to determine the effect of processing parameters on microstructure and defects.

Figure 8 shows a micrograph of an annealed specimen taken at 1000X magnification. The microstructure is characteristic of spheroidize-annealed steel. The carbides are distributed both along the grain boundaries and within the grains.

Figure 9 shows an SEM photomicrograph taken at 30,000X magnification that shows the carbide morphology. As shown in Figure 10, an X-ray spot scan of an individual carbide particle (red) was obtained and compared to the X-ray spectrum of the bulk material (black line). Note the increased amounts of C, Mo, Cr, and V and decreased amount of iron present in the red spectrum.

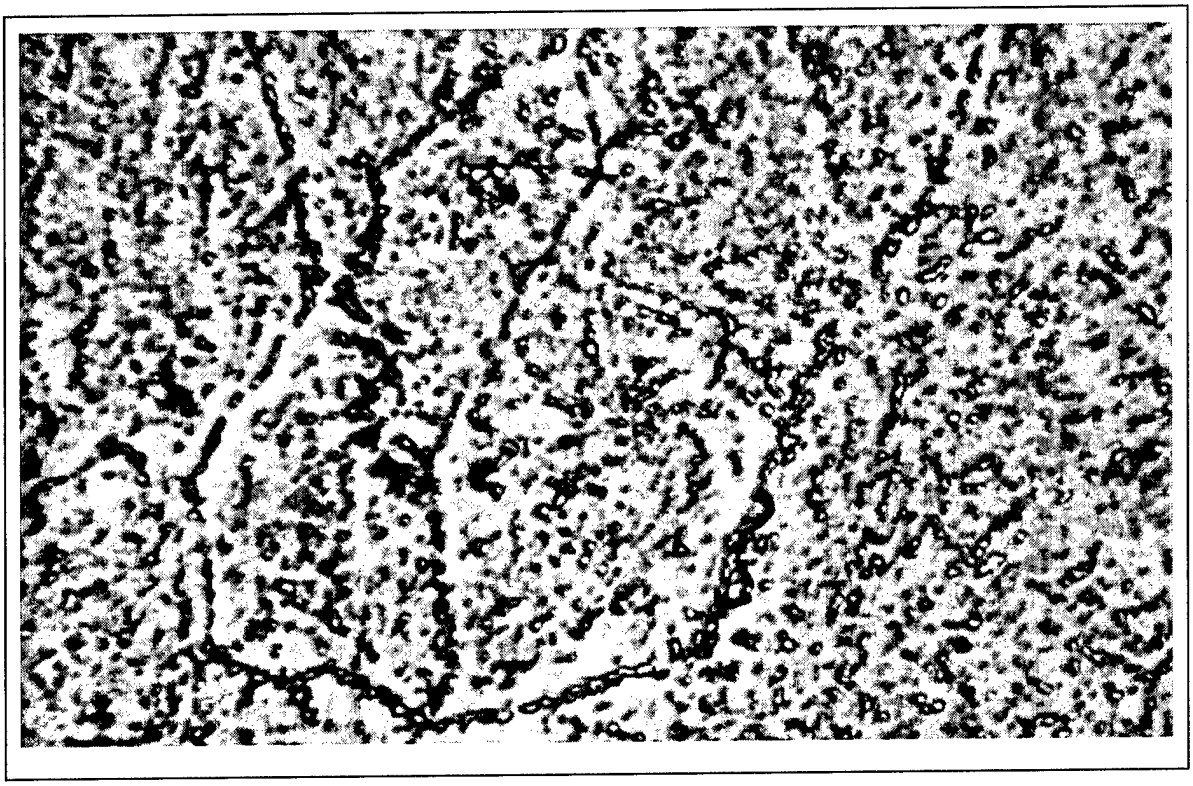

Figure 8 – Optical Micrograph of Spheroidize-Annealed Microstructure (1000X)

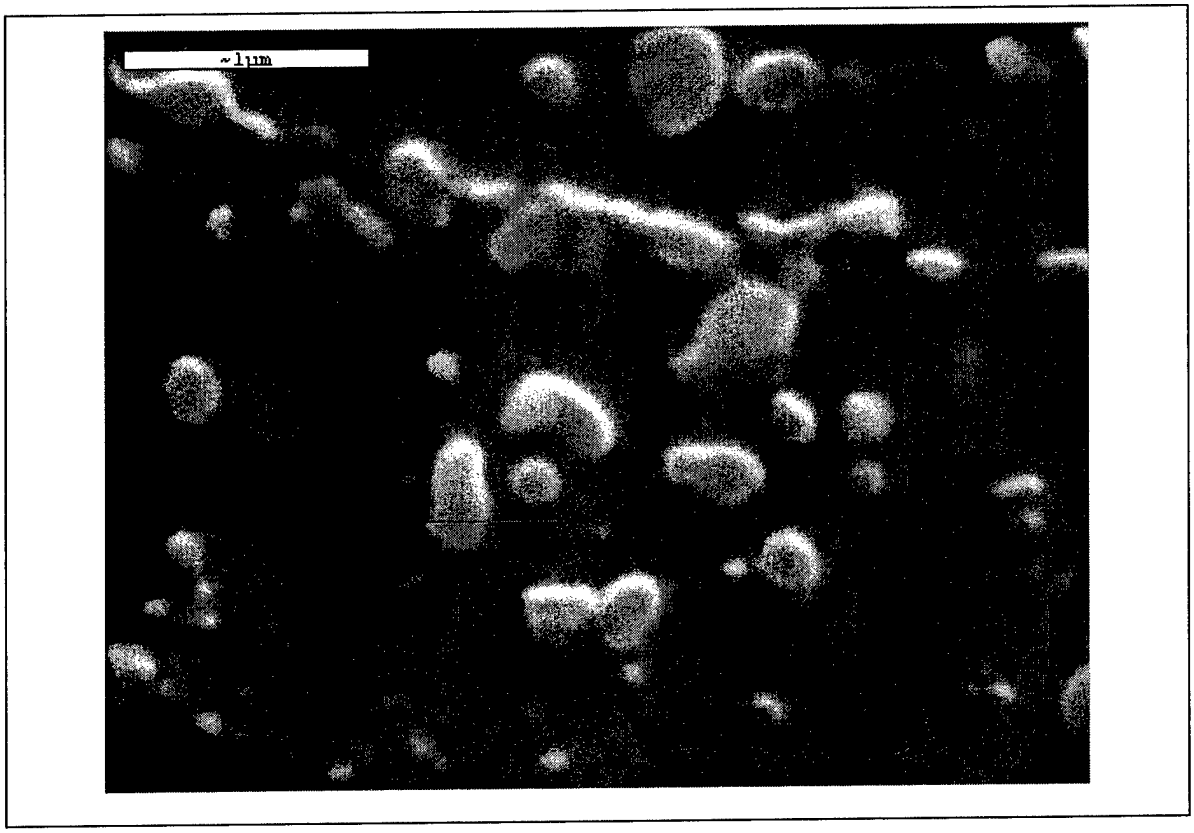

Figure 9 - SEM Photograph of Free Carbides In Annealed Specimen (30,000X)

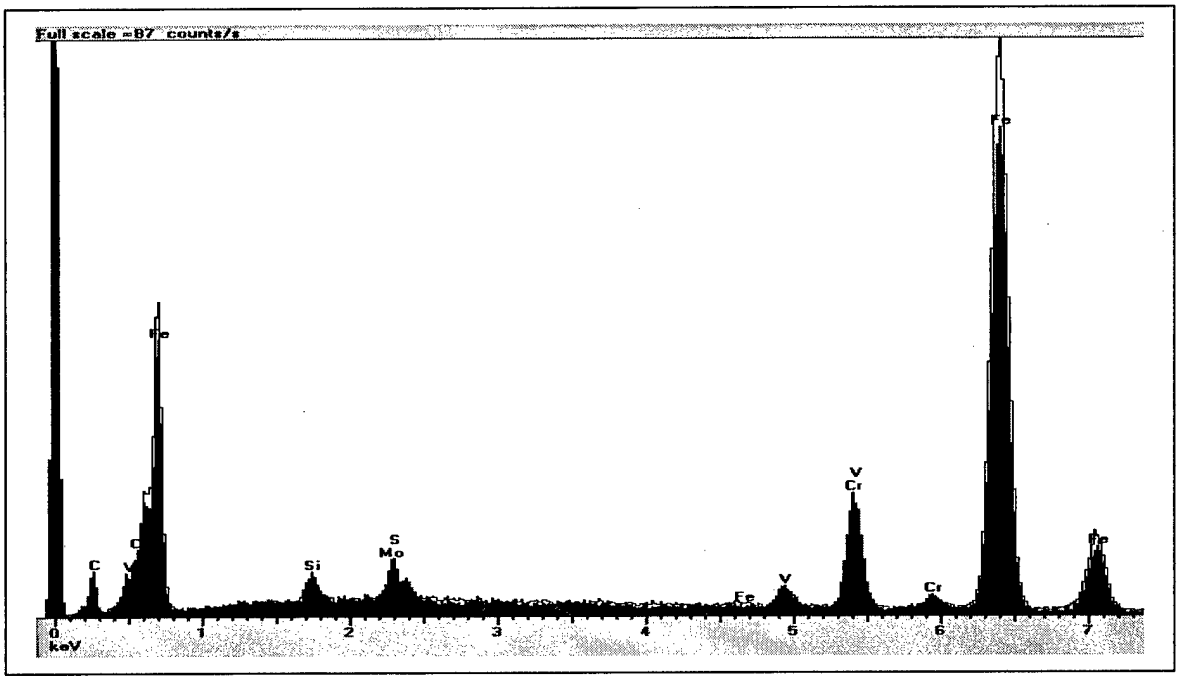

Figure 10 – X-ray Spectra of Bulk Material and Carbide In Annealed Specimen

Conclusions

This paper has presented a microstructural analysis of H13 tool steel produced via the EBM process. As the processing conditions will significantly affect metallurgical properties, the decision was made to conduct this initial study using default processing conditions. Although parameters can be "tuned" for each build according to the part's geometry, the metallurgical properties obtained using the default parameter values were quite good. The parts exhibited full interlayer bonding with virtually no porosity. The as-processed material was martensite having a hardness of 48-50 HRC. The spheroidize-annealed material also appeared much as expected, with carbides dispersed along the grain boundaries and within the grains themselves.

An interesting observation was the presence of localized non-homogeneities along the boundary between the part's exterior contours and interior squares. The chemical composition and hardness of these regions is virtually identical to that of the surrounding martensite. Work continues to further characterize these regions.

As one would expect, the selection of processing conditions has a significant influence on build speed as well as mechanical properties. Generally speaking, an increase in build speed is accompanied by a decrease in mechanical properties. The next phase of experimentation (just underway) is to begin studying the relationships between mechanical properties and parameters such as the number of contours, the square sizes, the beam currents (for contours and squares), the beam speed (for contours and squares), the layer thickness, etc. These experiments will help map out the tradeoffs between build speed and metallurgical properties so that the processing parameters can be selected that best meet the needs of the application.

References

[1] Taminger, K. and Hafley, R. (2002) "Characterization of 2219 Aluminum Produced by Electron Beam Freeform Fabrication" 2002 Solid Freeform Fabrication Symposium Proceedings, pp. 482 - 489

[2] Matz, J. and Eagar, T. (2002) "Carbide Formation in Alloy 718 during Electron Beam Solid Freeform Fabrication" *Metallurgical and Materials Transactions A*, vol. 33A, pp. 2559 – 2567.

[3] Standard Test Methods for Tension Testing of Metallic Materials, ASTM E8-01.

[4] Standard Specification for Tool Steels Alloy, ASTM A681-94.

Mechanics of the Selective Laser Raster-Scanning Surface Interaction

J.A. Ramos[1], D.L. Bourell[2]

(1) Department of Mechanical and Metallurgical Engineering, Pontificia Universidad Católica de Chile, Vicuña Mackenna 4860, Santiago, Chile
(2) Department of Mechanical Engineering, Laboratory for Freeform Fabrication The University of Texas at Austin, Austin, Texas, 78712

Reviewed, accepted August 19, 2003

ABSTRACT

In recent years, the use of a high power laser beam actuated by fast speed scanning mirrors has opened up novel selective laser raster-scan processing venues as extremely rapid motion and high overlapping of the beam can be attained. This permits distribution of laser energy precisely over geometric patterns such as rectangles, circles, triangles etc. The surface thermal history at any given point under such processing was estimated using an analytical solution for the 1D, semi-infinite, surface flux boundary condition heat conduction problem together with linear superposition theory. Presented here is the comparison of the thermal histories of different selective laser surface processes previously implemented, namely: laser surface polishing of flat surfaces, laser induced cementation of cylindrical surfaces and direct laser single layer masked deposition. It was possible to verify that in laser induced cementation, long-width and short-length scanned regions provided low average temperature and low heating rate with spaced out temperature peaks, whereas for direct laser single layer deposition in which a narrow-width – long-length region is scanned, the heating rate and peak temperature are higher and the peaks are squeezed. The analysis also provided ways to estimate the Andrew's number associated with a raster-scan process for the sake of comparison with single-beam processes having a given number value. Understanding the influence of scan geometry and overlapping on the selective raster-scan processing provides a method to tailor the surface peak temperature as well as the heating and cooling rates, affecting the solidification or sintering conditions and therefore the mechanical properties of the parts obtained.

Introduction

It was in the mid 80s when the need to deposit low power infrared laser energy selectively in space over the surface of materials became a necessity for the development of certain rapid prototyping technologies that were evolving at that time. One particular case, was the development of the Selective Laser Sintering (SLS) process created at the University of Texas at Austin [1]. Energy deposition in 2D space was achieved by modulating laser energy using galvanometer driven mirrors. The main advantage of the "galvo-mirrors" was the fact the laser beam could be raster-scanned at much higher

speeds, along any planar trajectory, than any conventional positioning mechanism available then such as CNC x-y tables.

By raster-scanning a focused laser beam along a zig-zag pattern, galvanometer driven mirrors allowed the creation of a "pseudo-energy-line" source capable of sustaining an homogenous melting front of certain width. The traveling speed, V_t, (slow-direction) of this front is a function of the scan speed, V_s, (fast direction) and the density of scanning lines. The latter in turn, determined the percent of scanning-line overlap, ϕ, for a given beam spot diameter size. However, it was not until early 90s that high-laser-power handling galvo-mirror delivery systems became available to investigators. By 1998 Das *et al.* at the University of Texas at Austin had built two such SLS stations capable of harnessing up to 1.4 kW from a CO_2 laser and 500 W from a Nd:YAG for research purposes [2].

In this work the thermal history at any surface point under laser raster-scan processing was estimated numerically using the analytical solution to the 1D, semi-infinite, surface flux boundary condition heat conduction problem together with linear superposition theory. Results were obtained for the thermal histories of different laser surface processes, namely: laser surface polishing of a planar surface, laser induced cementation of a cylindrical surfaces and direct laser single layer masked deposition. Common variables to all these processes are: width and length of the scanned rectangular region, number of scanning lines, scan speed along the width and laser power.

Laser Surface Polishing of Indirect-SLS Parts

Laser surface processing is emerging as a suitable technique for reducing surface roughness in metals, ceramics and polymer materials as it offers several modification regimes depending on the laser processing parameters. [3-5]. The schematic drawing of the laser polishing process utilized to reduce the surface roughness of indirect SLS parts is illustrated in Figure 1 [7].

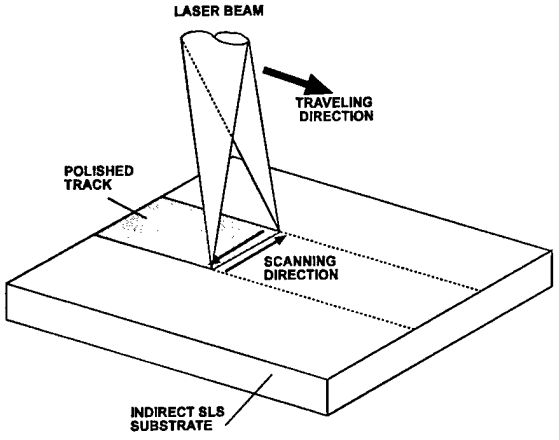

Figure 1. Schematic diagram of the laser polishing process.

A focused laser beam of sufficient power to shallowly melt the surface of the object was raster-scanned at high speed a long a rectangular track. The length to width aspect ratio of the scan track in this case ranged from 5 to 12.5; a geometric file with 2000 scanning lines/inch was used.

Laser Induced Cementation of Cylindrical Substrates

The purpose is to develop a laser fusion methodology to deposit coatings over cylindrical ceramic substrates. The scanning trajectory of the focused laser beam is programmed so that the beam scans back and forth along the major axis of the cylinder a narrow fringe with a small length to width aspect ratio of 0.05 using up to 4000 scanning lines/inch. The laser beam was scanned over the specimen the same amount of time the cylindrical specimen was rotated. Figure 2 illustrates the set up developed to carry out the laser induced cementation process [7]. The cylindrical specimen rotates suspended from a narrow stem while the focused laser beam raster-scans back and forth a long the longitudinal length of the cylinder.

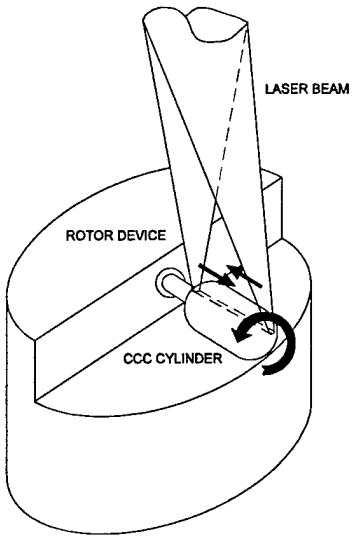

Figure 2. Schematic drawing of the "Laser Induced Cementation" process.

Direct Laser Single Layer Masked Deposition

Finally, in this research the objective is to restore superalloy single crystal components (e.g. aircraft combustion engine turbine blades) to near original properties and dimensions. It is crucial to develop the ability to tailor the microstructure of the deposited material as it is being laid. A schematic diagram of the laser melting process used in this work is illustrated in Figure 3 [7]. The laser beam raster-scans back and forth laterally and travels along the mask trough, melting the entire powder depth and a small fraction of the substrate. As the melt pool advances its tail solidifies forming a sound metallurgical bonding with the substrate. The length to width aspect ratio of the scan

track in this case corresponds to 12.5 and a total of 7000 scanning lines/inch is considered.

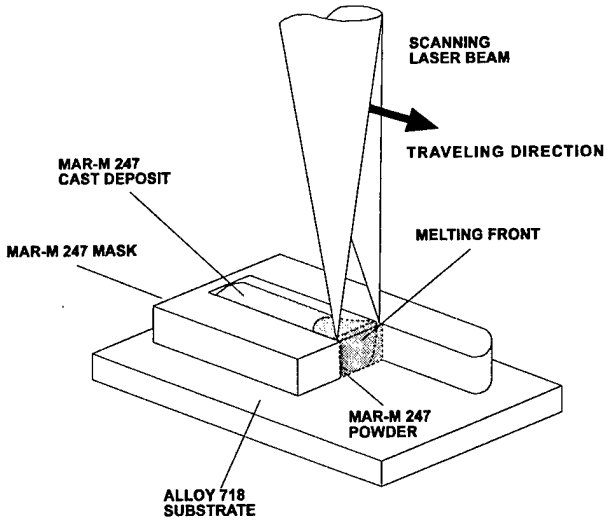

Figure 3. Overall schematic of the mask-powder-substrate arrangement during selective laser melting.

Mechanics of a Raster-Scanned Laser Beam

In recent years, the use of high-power laser beams actuated by high-speed scanning mirrors has opened up novel surface raster-scan processing venues as extremely rapid motion of the beam (> 0.5 m/s in the scan direction) and high percentage overlap (> 99.9%) can be attained. This permits distribution precisely of laser energy along specific geometric patterns such rectangles, circles, triangles or almost any complex closed regions. Because of this processing scheme, each point at the surface of the material experiences multiple high-frequency heating-cooling (HC) cycles during the overall laser scanning time. The HC cycle period is a function of position along the scanning direction and overall geometry of the scanning pattern.

Energy Density Relationship: Raster-Scan and Line Sources

The Andrew's number (Eq. 1) is a measure of the energy deposited per unit area over the surface of a material by a moving energy source. It can also be expressed as the power deposited over an area that is being continuously displaced per unit time; thus for a given laser power, P, focused at a spot of diameter, D, which moves with a traveling speed, V_t, the Andrew's number becomes,

$$A_{SPOT} = \frac{P}{D \cdot V_t} \tag{1}$$

If the energy source were no longer circular but of rectangular shape, with dimensions D and W, where W corresponds to the width of the source and D the thickness; in the case of W>>D, the source can be considered a line source having its speed, V_L, perpendicular to its width, W. The Andrew's number then becomes

$$A_{LINE} = \frac{P}{W \cdot V_L} \tag{2}$$

If such linear source moved a length L, then the overall rastered area would be L*W. The average time taken to cover that area is, $\Delta t = \frac{L}{V_L}$, and the total energy density deposited corresponds to, $\frac{P \cdot \Delta t}{L \cdot W}$. Therefore, Eq. 2 is verified, when Δt is substituted in. Now let us consider what happens when the area, L*W, is rastered not by a line source of width W, but by a spot source of diameter, D, that scans parallel to the width W of the area. Figure 4 shows a schematic illustration of this laser raster scan process.

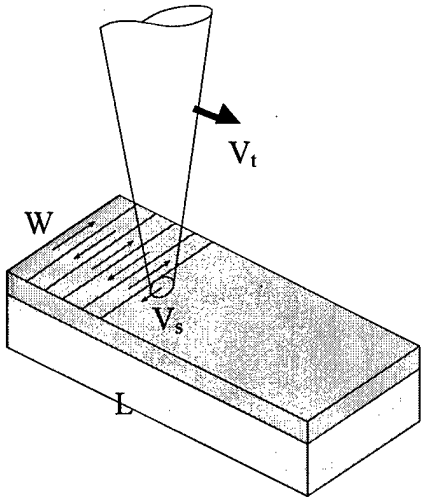

Figure 4. Schematic of a typical laser raster-scan fusion coating process.

Moreover, it is assumed that there is not overlap of the spot source as it travels back and forth the width W at a speed V_s (generally faster than the traveling speed V_t), so that at each edge, its perpendicular position is offset a distance D. Then, the number of scan-lines required to cover the area L*W becomes,

$$N = \frac{L}{D} \tag{3}$$

In this situation the average time taken to cover the raster-scanned area, L*W, can be expressed as,

$$\Delta t_{R\text{-}S} = \frac{N \cdot W}{V_S} = \frac{L \cdot W}{D \cdot V_S} \tag{4}$$

and the total energy deposited over the area, L*W, by the raster-scanned source now becomes,

$$\frac{P \cdot \Delta t_{R\text{-}S}}{L \cdot W} = A_{R\text{-}S} = \frac{P}{D \cdot V_S} \tag{5}$$

We can then conclude that in order to obtain the same Andrew's number associated with the area, L*W, and a fixed laser power, P, the following equivalence relation (from Eq. 2 and 5) must hold:

$$\frac{V_L}{V_S} = \frac{D}{W} \tag{6}$$

That is, the equivalence between the traveling speed, V_L, of a line source of width W, relates to the raster-scan speed, V_s, of a spot source of diameter D, by the quotient, D/W, which is generally less than 1.

If we now allow a certain amount of overlapping between successive scanned lines, we may define the percentage of overlap, ϕ, as,

$$\phi = 1 - \frac{\Delta x}{D} \tag{7}$$

Where, Δx, is the distance between the corresponding edges of two successive scanned tracks as illustrated in Figure 5 .

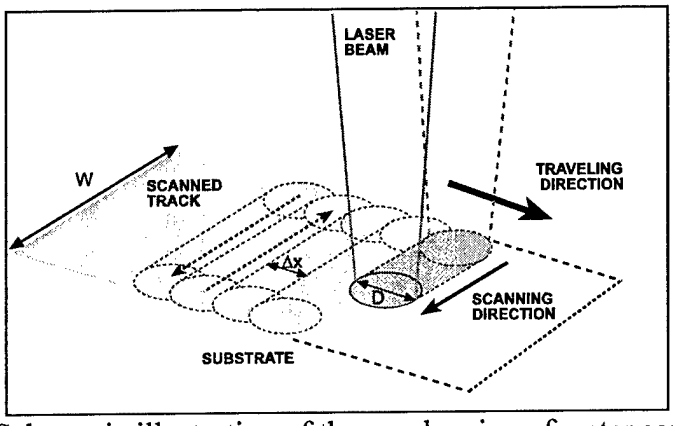

Figure 5. Schematic illustration of the overlapping of raster scans tracks.

Then, the number of scan lines, N_{OL}, when overlap exists, needed to cover the area, L*W, becomes,

$$N_{OL} = \frac{L}{(1-\phi)\cdot D} \tag{8}$$

The average time taken to cover such an area is,

$$\Delta t_{R\text{-}S/OL} = \frac{L\cdot W}{(1-\phi)\cdot D\cdot V_S} \tag{9}$$

and the total energy deposited over L*W by the raster-scanned and overlapped source is,

$$\frac{P\cdot \Delta t_{R\text{-}S/OL}}{L\cdot W} = A_{R\text{-}S/OL} = \frac{P}{(1-\phi)\cdot D\cdot V_S} \tag{10}$$

The equivalence relationship then becomes,

$$\frac{V_L}{V_S} = \frac{D}{W}\cdot(1-\phi) \tag{11}$$

This relationship verifies Eq. 5 when $\phi = 0$, i.e., when no overlap exists. Simultaneously, when ϕ is non-zero, the average traveling speed, V_t, of the raster-scanned source becomes,

$$V_t = \frac{L}{\Delta t_{R\text{-}S/OL}} = (1-\phi)\cdot\frac{D}{W}\cdot V_s \tag{12}$$

It can be observed that Eq.12 is equivalent to Eq. 11. This means that when Eq. 11 holds, the traveling speed of the line source, V_L, corresponds to the average traveling speed of the raster-scanned source.

Surface Temperature Evolution During Laser Raster-Scanning

At a given point on the surface, the temperature increase due to the heating portion of the heating-cooling cycle can be modeled through the analytical solution to the 1-D, semi-infinite, flux boundary heat conduction problem. The core of the heat conduction problem is the known parabolic differential equation in one-dimensional space,

$$\frac{\partial^2 T}{\partial z^2} = \frac{1}{\alpha} \cdot \frac{\partial T}{\partial t} \tag{13}$$

with initial temperature, T_o, over all the domain, and at the surface of the specimen, the flux boundary condition is,

$$K \cdot \left. \frac{dT}{dz} \right|_{z=0} = I \tag{14}$$

where, I, is the power density of the laser beam,

$$I = \frac{(1-\Re) \cdot P}{A} \tag{15}$$

$\Re$ incorporates the effect of surface reflectivity, which is a strong function of the laser wavelength, as well as radiative and convective surface heat losses. The area illuminated by the beam, A, can be circular as in the case of a raster-scanned-source (i.e., $\pi \cdot D^2/4$) or rectangular as for a line-source (i.e., $W \cdot D$).

The analytical solution to this problem provides a uniaxial temperature distribution in closed-form, which is a function of position and time in the semi-infinite solid [3,6],

$$T(z,t) = \frac{2 \cdot I}{K} \cdot \left(e^{\frac{z^2}{4 \cdot \alpha \cdot t}} \left(\frac{\alpha \cdot t}{\pi} \right)^{0.5} - \frac{z}{2} \cdot \mathrm{erfc}\left(\frac{z}{(4 \cdot \alpha \cdot t)^{0.5}} \right) \right) \tag{16}$$

Here, α and K correspond to the thermal diffusivity and heat conductivity of the solid respectively, and erfc( ) is the complementary error function. When evaluated at $z = 0$, Eq. 16 then simplifies down to

$$T(z,t)\big|_{z=0} = T(t) = \frac{I}{K} \cdot \left(\frac{4 \cdot \alpha \cdot t}{\pi} \right)^{0.5} \tag{17}$$

Linear superposition theory can then be applied to obtain both the heating and the cooling portion of the HC cycle [3,6]. The latter, after the heat source has stopped interacting for a given time interval, D/V_s, is approximately equivalent of being turned off. This corresponds to the following surface boundary condition,

$$K \cdot \left.\frac{dT}{dz}\right|_{z=0} = \begin{cases} I \text{ for } 0 < t \le \dfrac{D}{V_S} \\ 0 \text{ for } t > \dfrac{D}{V_S} \end{cases} \tag{18}$$

The resulting expression for the complete temperature evolution has the form,

$$T_{HC}(t, \tau_0) = T(t) \cdot H(t) - T(t-\tau_0) \cdot H(t-\tau_0) \tag{19}$$

where H(t), corresponds to the Heaviside step function and τ_0 is half the laser interaction time interval or heating time, $D/2V_s$. This is the time one half the laser spot spends traveling over a specific surface coordinate. This time interval causes increase in local surface temperature and corresponds to the first term on the right hand side of Eq. 19. The heating cycle is immediately followed by a cooling cycle that corresponds to the second term on the right hand side of Eq. 19. The complete HC cycle is illustrated in Figure 6.

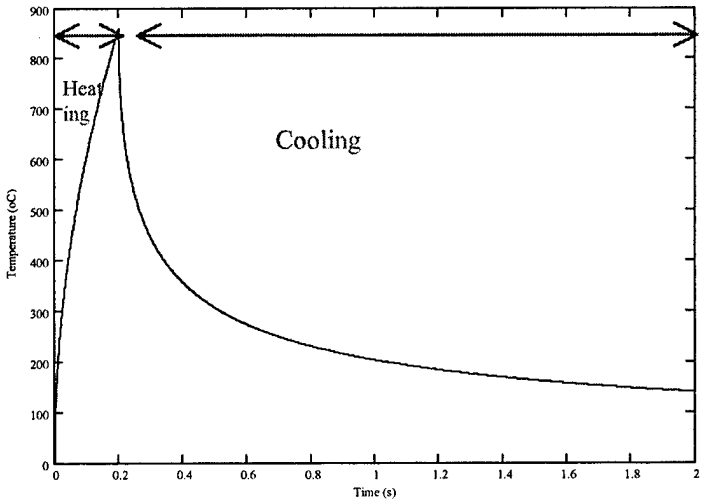

Figure 6. Typical heating cycle followed by the corresponding cooling cycle after the source is turned off or displaced.

Linear superposition theory can be further applied to determine the superposition of temperature histories due to multiple overlaps. An arbitrary x position, along the scan-width W is considered, measured from the left edge. The temperature evolution at this location during the initial heating interval at each complete raster scan cycle, is determined then by,

$$f_{\text{Initial}}(t, \tau_1, \tau_2) = \sum_{i=0}^{\frac{1}{1-\phi}} \left(1-(1-\phi)\cdot i\right) \cdot \left[T(t-\tau_1) \cdot H(t-\tau_1) - T(t-\tau_2) \cdot H(t-\tau_2)\right] \tag{20}$$

Where the summation limit, $1/1-\phi$, refers to the number of times the laser has to scan over its spot area in order to raster it completely. After every scan, the beam is offset a percentage, $1-\phi$, of the total spot width, so the intensity of the heat flux experienced by the space coordinate, x, is assumed to decay as $1-(1-\phi)*i$, where, i, is the summation index corresponding to the raster-scan number count. Here, τ_1, corresponds to one full raster scan time interval in which the source travels from the x coordinate and back to it, and, τ_2, corresponds to the same interval plus a heating cycle of length D/2.

Additionally, the temperature evolution during first cooling interval (the time it takes the source to travel from the x coordinate to the right edge of the width and then back to the former) is given by a similar relationship,

$$f_{\text{Right}}(t,\tau_3,\tau_4) = \sum_{i=0}^{\frac{1}{1-\phi}} \left(1-(1-\phi)\cdot i\right)\cdot\left[T(t-\tau_3)\cdot H(t-\tau_3) - T(t-\tau_4)\cdot H(t-\tau_4)\right] \qquad (21)$$

However, here the function τ_3, corresponds to the cooling interval as the beam moves away from x to W and from W to back x, and the function τ_4, corresponds to the same cooling interval plus one heating cycle of length: D when $0 < x < W$, D/2 when $x = 0$, and zero heating interval when $x = W$. Similarly, the temperature evolution during the second cooling interval (this is time it takes the source to travel from x to the left edge of the width, and then back to the former) is given once again by,

$$f_{\text{Left}}(t,\tau_5,\tau_6) = \sum_{i=0}^{\frac{1}{1-\phi}} \left(1-(1-\phi)\cdot i\right)\cdot\left[T(t-\tau_5)\cdot H(t-\tau_5) - T(t-\tau_6)\cdot H(t-\tau_6)\right] \qquad (22)$$

This differs only in the form of the cooling intervals, τ_5 and τ_6. Thus, the temperature profile at a given position, x, for a raster scan processing, as a function of time is, given by the sum of the latter three expressions:

$$T(t,x)_{\text{Raster-Scan}} = f(t,\tau_1,\tau_2)_{\text{Initial}} + f(t,\tau_3,\tau_4)_{\text{Right}} + f(t,\tau_5,\tau_6)_{\text{Left}} \qquad (23)$$

More details on this model can be found in Ref. 7.

To illustrate the use of Eq. 23, a plot of a typical sequence of heating and cooling cycles when two complete back and forth raster scans are performed is presented in Figure 7. The continuous line corresponds to the temperature measured at the center of the width while the dotted line corresponds to the temperature as measured at either one of the edges. In the both cases, the first and last peaks are narrower as it corresponds to half the total heating interval, $D/2V_s$, whereas the other peaks correspond to a full heating interval.

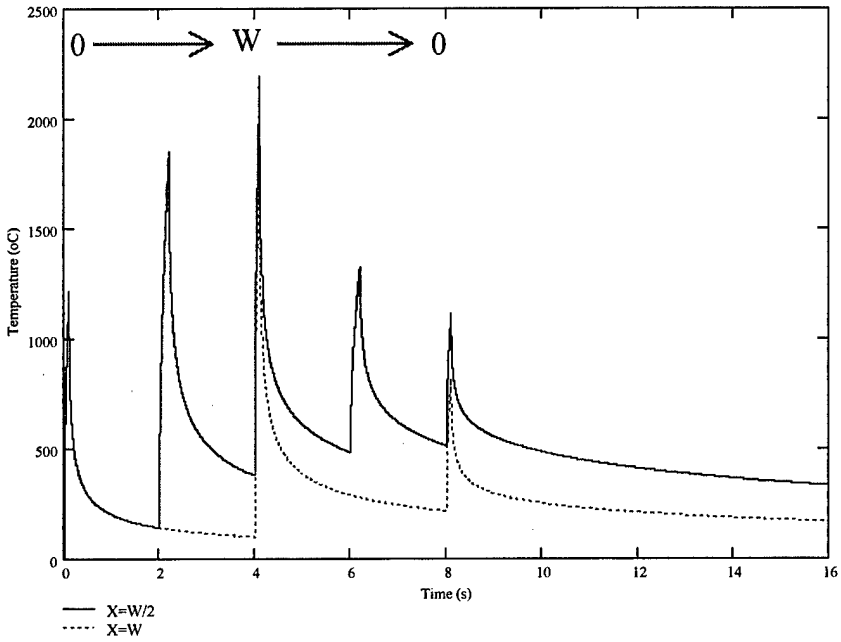

Figure 7. Typical sequence of heating and cooling cycle when a complete back and forth raster scan is performed.

Simulation Results and Discussion

Numerical implementation of Eq. 23 was done and the temperature profile results are plotted in Figure 8. These temperature profiles were evaluated at half the width of the scan pattern. These results were used to compare the thermal histories of three different laser surface processes, namely: (a) laser surface polishing of flat surfaces, (b) laser induced cementation of cylindrical surfaces and (c) direct laser single layer masked deposition. However, to compare the different temperature profiles, the material properties, the laser power and spot diameter on all three processes were equally assigned. Temperature independent materials properties for 420 stainless steel-40wt.% bronze alloy were considered, the laser power was set equal to 250 W, and the spot size was 0.4 mm. Variables common to all these processes were: width, W, and length, L, of the scanned rectangular region, number of scanning lines, N, and the overall scanning time, Δt, These variables were assigned different values for each of the three processes as illustrated in Table 1. The percent overlap, f, the scan speed, the Andrew's number and the traveling speed were calculated from Eq. 8,9,10 and 11, respectively.

Table 1. Processing variables for three difference laser raster-scan process.

Process	L (mm)	W (mm)	Δt (s)	N (line/inch)	ϕ (%)	V_s (mm/s)	$A_{R\text{-}S/OL}=A_L$ (J/mm^2)	$V_t = V_L$ (mm/s)
a	25.4	4	20	2000	96.825	400	49.21	1.27
b	1.3	25.4	180	4000	99.919	564.4	1367.1	0.0072
c	25.4	2	20	7000	99.093	700	98.44	1.27

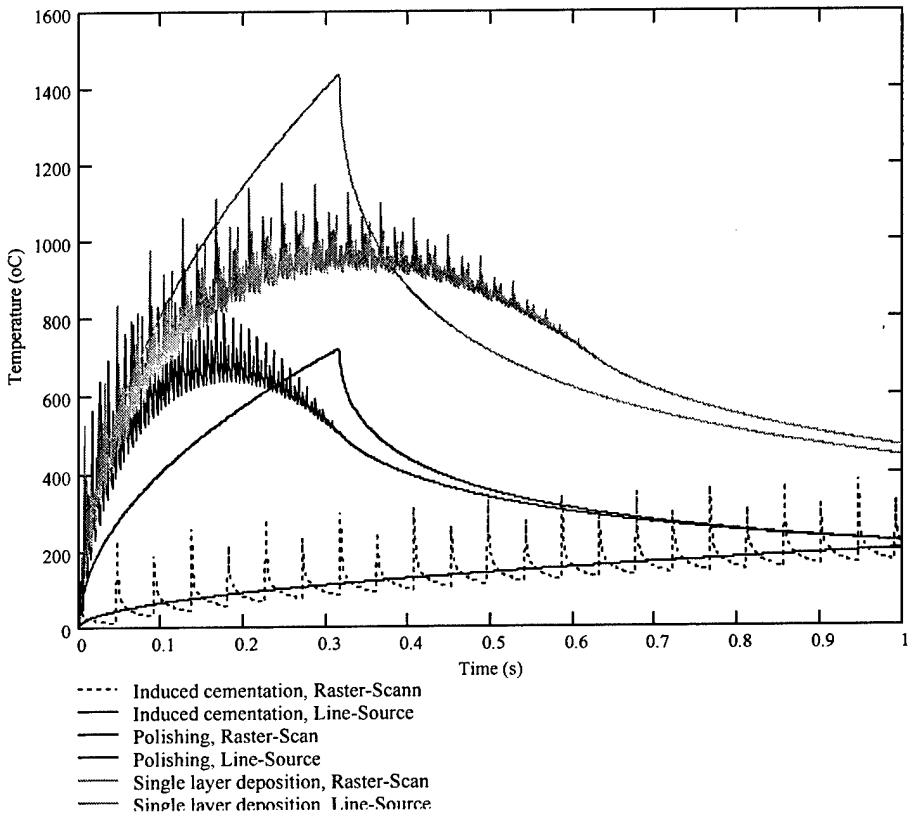

Figure 8. Surface temperatures at a fixed position versus interaction time for raster-scan processing and line-source processing for 3 different processes.

From Figure 8 it can be observed that for a diffusion-driven process like the laser induced cementation, long-width short-length scanned regions (L/W = 0.32) with intermediate number of scan lines (N=4000), provide a low average temperature with spaced out sharp temperature peaks, whereas for narrow-width long-length scanned regions (L/W = 6.35) with lower number of scan lines (N=2000) as in the case of laser polishing, the average temperature is higher but short lived, and the temperature peaks are shorter and much closer together. When increasing the number of scan lines (N=7000) and doubling the length to width ratio (L/W= 12.7) as in direct laser single layer masked deposition, the average temperature is higher than in the previous case and it also lasts longer and the peak temperatures are less spaced out than in the first case.

The temperature history obtained for a line source of equal power and traveling speed, along the length direction, is also plotted in Figure 8 for comparison purposes from a single heating-cooling cycle as given by Eq. 19. In the case of processes (a) and (c), the temperature profile shows the same heating interval length because of the same traveling speed (1.27 mm/s), but for the former the peak temperature is lower as the associated Andrew's number (44.22 J/mm^2) is half that of the latter (98.44 J/mm^2). This

is because of the twofold difference in number of scan lines (2000 versus 4000 lines/inch). In the case of the laser polishing process, the peak average temperature obtained by the raster-scan and the line sources are very close in magnitude. However, the heating interval for the raster-scan is almost half that of the line source due to the lower percent overlap (96.83%). The heating rate is also steeper for the raster-scan source than for the line source, while the cooling rate is steeper for the line source only at the beginning of the cooling cycle. In the case of process (c), a much higher peak temperature is obtained with the line-source as well as steeper heating and cooling rates. Moreover, the peak average temperature of the raster-scan source occurs at almost the same heating interval as the peak temperature of the line source due to the high percentage overlap (99.09%). In the case of process (b), the corresponding Andrew's number is the highest of the three processes (1367 J/mm^2). However, it can be observed that the line source temperature is not much higher than the mean temperature obtained for a raster-scan source, and the peak temperatures from the latter source are higher in this particular case. The maximum average temperature is achieved for the longest heating interval of the three processes due to the largest percentage overlap used (99.92%).

It is worth noting that for all three processes, the Andrew's numbers of the line and raster-scan sources are the same as imposed by the equivalence relationship given by Eq. 11.

Conclusions

Equation 11 is a general and useful relationship that allows to comparison of surfaces that have been laser processed and thus modified by line or raster scanned sources, keeping constant in both cases the Andrew's number by varying ϕ and Vs, when W, L, D and V_t are kept constant.

Increasing the number of scan lines (N) while keeping constant the traveling speed (V_L=V_t) and laser power (P) produces higher peak temperatures after heating intervals that approach the limiting value given by a (D/V_L) for a line source traveling at the same speed. This is because the percent overlap, ϕ, is increased towards 1.

For a fixed traveling speed, increasing the number of scan lines increases the scan speed provided the length to width aspect ratio is kept constant as determined by Equation 11.

If the number of scan lines is now reduced, not only the peak temperature is reduced but also the heating interval is shorter than the limiting value as the percentage overlap is decreased.

Understanding the influence of scan geometry (L-W aspect ratio), percent overlapping (ϕ) and number of scan lines (N), on the raster-scan surface processing provides a method to tailor the surface peak temperature and heating interval as well as

the heating and cooling rates. This in turns affects the solidification or sintering conditions of the process and therefore the mechanical properties of the parts obtained.

References

[1] C.R. Deckard, "Method and apparatus for producing part by selective sintering", US Patent 4863538 (September 1989)

[2] S. Das, "Direct selective laser sintering of high performance metals : machine design, process development and process control", Ph.D. Dissertation Thesis, The University of Texas at Austin, December 1998

[3] W.M. Steen, Laser Material Processing, 2nd edition, (Springer Verlag 1993)

[4] J. Powell, P.S. Henry and W.M. Steen, "Laser Cladding with Preplaced powder: Analysis of thermal cycling and dilution effects", Surface Engineering, 4 1988, 141-149.

[5] Conde, R. Colaco, R. Vilar, J. de Damborenea, "Corrosion behavior of steels after laser surface melting", Materials & Design 21 (2000) 441-445

[6] H.S. Carls and J.C. Jaegger, Conduction of Heat in Solids, (Oxford 1996)

[7] J. A. Ramos Grez, "Surface modification of ceramic and metallic alloy substrates by laser raster-scanning", Ph.D. Dissertation Thesis, The University of Texas at Austin, August 2003

PRECISION EXTRUDING DEPOSITION AND CHARACTERIZATION OF CELLULAR POLY-ε-CAPROLACTONE TISSUE SCAFFOLDS

F. Wang, L. Shor, A. Darling, S. Khalil, W. Sun*, S. Güçeri, A. Lau

Laboratory for Computer-Aided Tissue Engineering
Department of Mechanical Engineering and Mechanics
College of Engineering
Drexel University
Philadelphia, PA 19104

Reviewed, accepted August 13, 2003

Abstract

Successes in scaffold guided tissue engineering require scaffolds to have specific macroscopic geometries and internal architectures in order to provide the needed biological and biophysical functions. Freeform fabrication provides an effective process tool to manufacture many advanced scaffolds with designed properties. This paper reports our recent study on using a novel Precision Extruding Deposition (PED) process technique to directly fabricate cellular Poly-ε-Caprolactone (PCL) scaffolds. Scaffolds with a controlled pore size of 250 μm and designed structural orientations were fabricated. The scaffold morphology, internal micro-architecture and mechanical properties were evaluated using SEM, Micro-Computed Tomography (μ-CT) and the mechanical testing. Preliminary biological study was also conducted to investigate the cell responses to the as-fabricated tissue scaffolds. The results and the characterizations demonstrate the viability of the PED process to the scaffold fabrication as well as a good mechanical property, structural integrity, controlled pore size, pore interconnectivity, and the anticipated biological compatibility of the as-fabricated PCL scaffolds.

Keywords - Tissue Engineering, Tissue scaffold, Solid Freeform Fabrication, Micro-CT characterization, Scaffold fabrication

1. Introduction

Three-dimensional scaffolds play important roles in scaffold guided tissue engineering because they provide critical functions as extra-cellular matrices onto which cells can attach, grow, and form new tissues. Design and fabrication of tissue scaffolds is always a challenged subject in regenerative medicine, particularly, for load bearing scaffolds in bone and cartilage tissue engineering application. To design this type of tissue scaffold often needs to address multiple biological, mechanical and geometrical design constraint in terms of scaffold external and internal geometry, porosity, pore size and interconnectivity in order to provide the needed structural integrity, strength, transport property, and an ideal micro-environment for cell and tissue ingrowth and healing [1-3]. Advances in computer-aided tissue engineering and the use of biomimetic design approach enable to introduce biological and biophysical requirement into the scaffold design [4, 5]. However, thus designed scaffolds often have intricate architectures that can only be fabricated through advanced manufacturing techniques. Most available scaffold

* Corresponding author: Dr. W. Sun, Associate Professor, 215-895-5810; sunwei@drexel.edu

fabrication methods, such as solvent casting, fiber bonding, phase separation, gas induced foaming, and salt leaching, are either limited to producing scaffolds with simple geometry, or to depending on in-direct casting method for scaffold fabrication [6, 7], so they are impractical for being used to manufacture scaffolds with complex structural architectures. To overcome this hurdle, solid freeform fabrication techniques, such as 3D Printing, Multi-phase Jet Solidification, and Fused Deposition Modeling (FDM) have been widely adopted for scaffold fabrication [8-10]. Among the reported techniques, FDM-based extruding deposition seems to be one of the most promising processes because of its versatility of using different scaffolding materials, possibility of manufacturing scaffolds in a cell-friendly environment, and feasibility of controlled drop-on-demand high precision deposition [11, 12].

On the other hand, the ability of quantification of the scaffold fabrication-microstructure relationships, such as the effect of the process on the morphologies and the functional properties of the scaffolds, is as important as the scaffold fabrication itself because the biological and mechanical functions of the scaffold are in part dominated by the fabricated local micro-architecture of the scaffold. Micro-Computed Tomographic imaging technology (micro-CT) enables the characterization of the salient features of the scaffolds for tissue engineering applications. Recent reports have shown that micro-CT techniques are capable of characterizing micro-architectural and mechanical properties of tissue scaffolds [13], evaluating porous biomaterials [14], quantifying the bone tissue morphologies and internal stress-strain behavior [15] and conducting nondestructive evaluation for tissue properties [16].

The objective of this paper is to present our recent study on using a Precision Extruding Deposition (PED) process to fabricate Poly e-Caprolactone (PCL) tissue scaffolds with designed micro-architecture, and to present the study of using micro-CT technique for evaluation and characterization of the morphologies and microstructures of the PED fabricated scaffolds. In contrast to the conventional FDM process that requires use pre-cursor filaments, the presented PED process directly extrudes scaffolding materials in its granulated or pellet form without the filament preparation and freeform deposits according to the designed micro-scale features. A brief outline of the fabrication procedure, including the description of the PED system major components, the PED process and the scaffold architecture, and the use of the PED process to freeform fabricate cellular Poly-ε-Caprolactone (PCL) scaffolds is introduced in Section 2. Section presents the material and the process. Section 4 reports a summary of the study on using SEM, micro-CT and the experimental testing to characterize the morphology, internal geometry, mechanical property and biological compatibility of the as-fabricated scaffolds, followed by a conclusion and discussion in Section 5.

2. System Configuration for Precision Extruding Deposition

2.1 Precision extruding deposition (PED) system

A Precision Extruding Deposition system developed at Drexel University [17] was used for this study. A schematic configuration of the PED system is described in Fig. 1. The hardware component consists of an XYZ position system, a material extruder system, and a temperature control system. The software component consists of a data processing software and a system control software. The data processing software slices the STL files and generates the process

toolpath. The system control software controls the material deposition according to the process toolpath to form a layered 3D object.

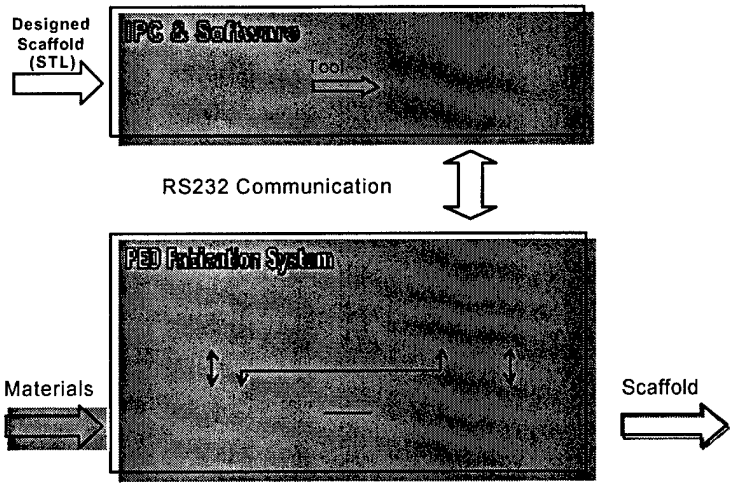

Fig.1: Configuration of the PED fabrication system

The material mini-extruder system deliveries the PCL in a fused form through the deposition nozzle. The major difference of the PED process with the conventional FDM process lies in that the scaffolding material can be directly deposited through PED process without involving filament preparation. The pellet-formed PCL is fused by a liquefier temperature provided by two heating bands and respective thermal couples and then extrudes by a pressure created by a turning precision screw. A schematic of the material mini-extruder system is shown in Fig. 2.

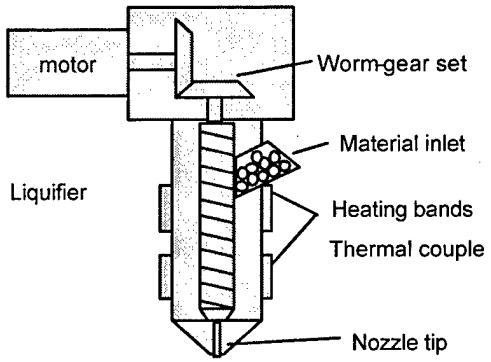

Fig.2: Schematic of Material Mini Extruder

To achieve deposition accuracy, the positioning system and the material mini extruder are synchronized as depicted in Fig. 3. The material deposition roads (of both contouring and raster filing) consist of series of line segments, so the extruder movement is composed of a series of 2-D linear interpolations upon which a simultaneous proportional signal to the XY position is extracted. The signal is used to drive the rotating motor of the material extruder. The

proportional ratio can be adjusted to coordinate the positioning system and material dispensing system according to its controlled movement, speed, and material extrusion flow rate.

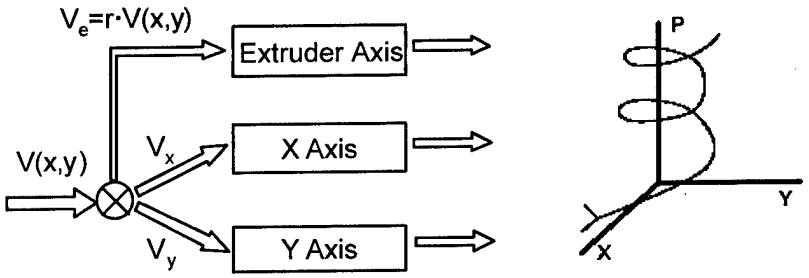

Fig. 3 Synchronization of positioning and material dispensing system

Fig. 4 shows the information pipeline during the fabrication process. The designed scaffold CAD model is first converted into STL format, and then sliced with each slice patterned stored in the pattern library for toolpath generation. Initialized by a parameters file, the in-house developed system control software provides functions for 3D part visualization, machine and process setup, testing and monitoring during the real-time fabrication process.

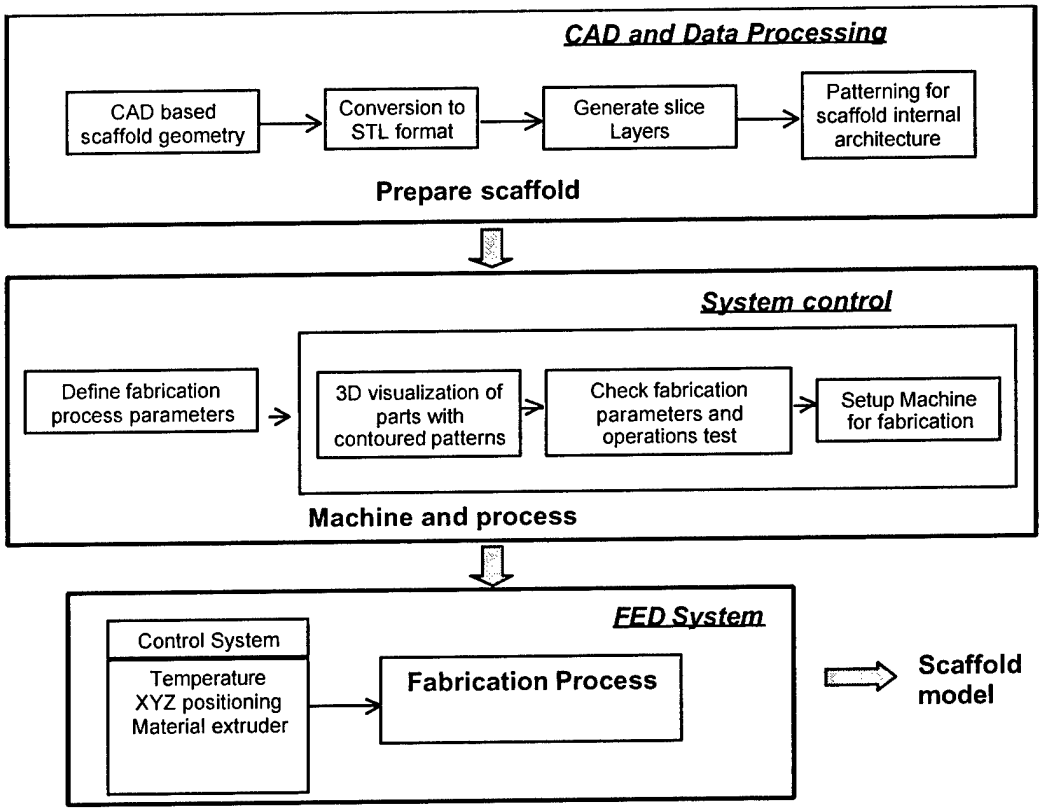

Fig. 4: Information process of the manufacturing system

3. Materials and Process

Poly e-Caprolactone (PCL, Sigma Aldrich Inc, Milwaukee, Wisconsin) in the form of pellets was used as the scaffolding material. PCL is a semi-crystalline aliphatic polymer that has a slower degradation rate than most biopolymers in its homo-polymeric form. It has a low glass transition temperature at -60°C, a melting temperature at about 58°C - 60°C, and a high thermal stability. It has a high decomposition temperature Td of 350°C. The mechanical properties of PCL (Mw = 44,000) with a tensile strength of 16MPa, tensile modulus of 400MPa, flexural modulus of 500MPa, elongation at yield of 7.0%, and elongation at break of 80% have been reported.

A designed scaffold cylinder model, measuring 20mm in diameter and 10mm in height, was first created in a CAD format. This cylinder CAD model was converted to a STL format then sliced into layers. Each layer was then filled with the designed scaffold pattern to generate toolpath file. The strands of PCL were extruded in four distinct layer patterns: 0^0, 90^0, 60^0, and 120^0 (designated P1, P2, P3 and P4, respectively), or alternating layers of $60^0/120^0$ with different gap lengths between the strands. The definition of scaffold layout pattern is shown in Fig. 5.

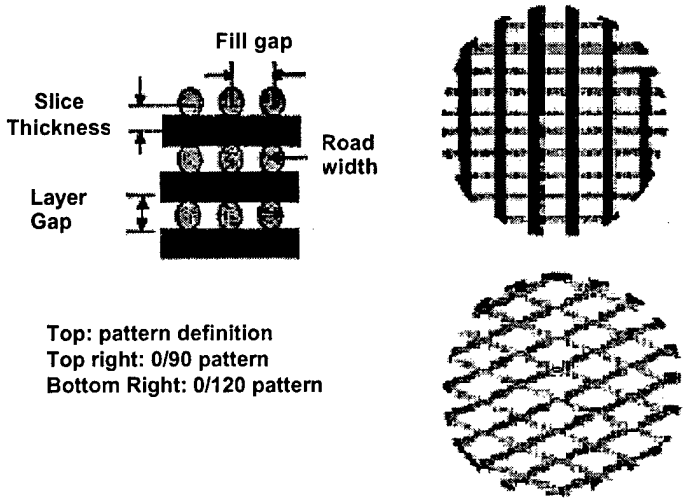

Fig. 5: Definition of scaffold Layout pattern

4. Evaluation of morphology, mechanical and biological properties

4.1 Results of scaffold fabrication

A set of PCL scaffolds was fabricated using the PED system. The following processing parameters were used for all scaffold fabrication: the processing liquefier temperature 90°C, the orifice diameter of the tip 0.25 mm, and deposition velocity at 20mm/s. The filling gaps of 0.42 mm and 0.51 mm were applied for two different sets of scaffolds. For each scaffold, there are a total of 39 layers with each layer thickness at 0.254 mm. The scaffold patterns were either 0°/90° (3 samples), or 0°/120° (3 samples), or combined 0°/120° (for top 19 layers) and 0°/90° (for bottom 20 layers) pattern.

4.2 Evaluation of morphology, mechanical and biological properties

The effect of the PED process on the morphology and structure of the as-fabricated scaffolds were evaluated using SEM and Mirco-CT. The compression tests were also conducted to evaluate the mechanical strength of the as-fabricated scaffold. Preliminary biological experiments were also conducted to evaluate the biocompatibility of the scaffold. Descriptions of the evaluations, results and experimental procedures are presented as follows.

SEM imaging characterization

FEI/Phillips XL-30 Field Emission Environmental Scanning Electron Microscope (ESEM) was used to evaluate the micro-structural formability and internal morphologies of as-fabricated scaffolds. The SEM images were taken by using a beam intensity at 20.0 keV and the Gaseous Secondary electron detectors at 1.3 Torr. The SEM images of scaffolds are shown in Fig. 6(a) (for 0°/90° deposition pattern) and Fig. 6(b) (for 0°/120° deposition pattern), along with the images of the as-fabricated scaffolds. Both SEM images clearly present that the fabricated micro-architecture of the scaffolds could be achieved at about 250 μm scale level. The good uniformity of the fill gaps and the depositing struts shown in Fig. 6, and the internal pore connectivity shown in Fig. 7 demonstrate the applicability of using the PED process to fabricate PCL scaffolds at micro-scale level.

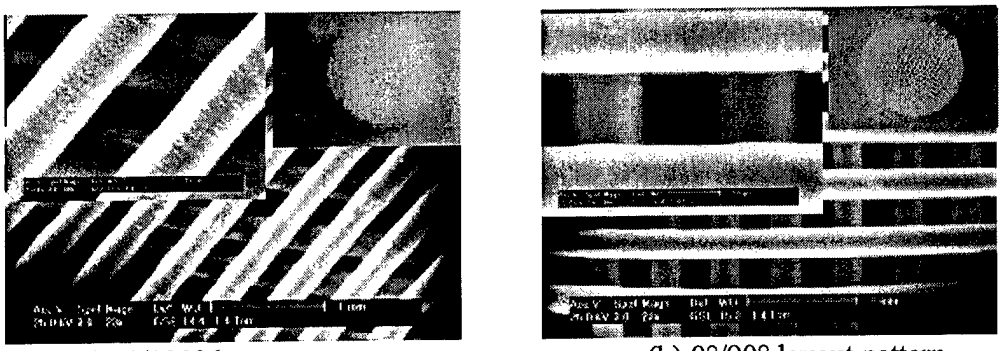

(a) 0°/120° layout pattern (b) 0°/90° layout pattern

Fig. 6: SEM image scaffold with different layout pattern

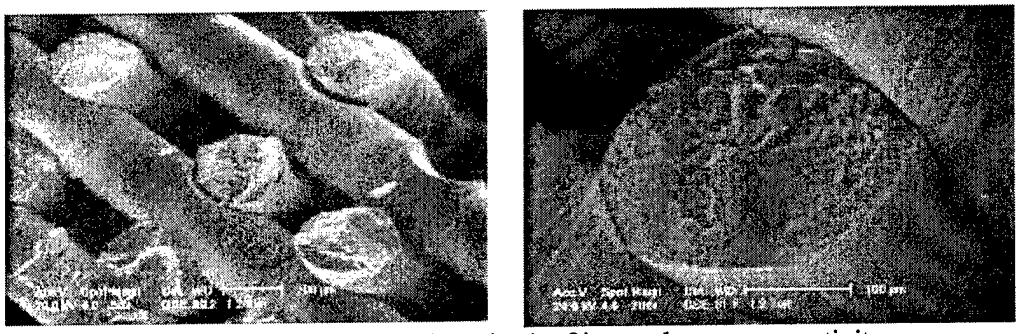

Fig. 7: SEM image (section view) of internal pore connectivity

Micro-CT imaging based 3D morphological characterization

Micro-CT enables 3D characterization of the salient features, the structural formability and the morphologies of the as-fabricated PCL scaffolds. The micro-CT was set at 19.1 micron resolution. 2D analyses and 3D reconstructions of core regions of the sample scaffolds were performed. These results illustrate that qualitative and quantitative analysis of polymer scaffolds is possible through micro-CT and 3D reconstruction techniques.

Micro-CT imaging acquisition: SkyScan 1072 micro-CT desktop scanner (Skyscan, Belgium) was used to scan the internal architecture of the scaffold. The output format for each sample was approximately 500 serial 1024x1024 bitmap images. These slice images were analyzed in SkyScan's Tview software. Initially, length measurements were taken around the sample to determine the degree to which the sample conformed to the cylindrical template. Volume analyses were performed on the center of each sample. Volume fraction and surface per unit volume were determined in 3D analysis, and relative area was measured in 10 randomly selected slice images in 2D analysis. 10 strut and pore widths were measured in 2D images from each sample.

3D reconstruction: 3D reconstruction was performed using Mimics software (Materialise, Belgium) with pre-processing using ImageJ. 62 sequential 200x200 pixel images were cropped from the serial images from the center of each sample. Imported into Mimics, these serial core images were reconstructed into 3D volumetric models. Thresholds were inverted to allow measurement of the volume of all pore spaces within the model. Subsequently, a region-growing operation was performed, creating a mask consisting only of interconnected pore spaces. Volume for this region-grown mask was determined and the ratio of region-grown volume to the total volume was calculated. The percentage of this ratio is defined as the degree of interconnectivity.

A summary of data retrieved from the analysis through Tview is displayed in Table 1. The results also include the measurements of individual strut and pore widths based on the 2D serial slice imaging. 10 measurements were taken for each sample in this analysis. 3D reconstructed models by using Mimics are displayed in Table 1 with a sample of corresponding 2D images and the characterized porosity and interconnectivity of each sample. Results of micro-CT imaging based 3D reconstruction, porosity and interconnectivity analyses are shown in Fig. 8.

Table 1: Summary of the micro-CT morphological analyses

Sample	SP-1	SP-2	SP-3	SP-4
Max./Min. Diameter (mm)	19.74/ 18.79	19.62/18.59	19.44/ 18.51	19.56/ 18.57
Surface (mm^2) Rel. Area	9219 60.89%	20854 55.8%	18936 47.28%	10036 44.24%
Total Volume (mm^3) Vol. Fraction	490 60.8%	1004 53.1%	957 47.4%	458 45.1%
Strut width (n=10, mm)	0.264 ± .023	0.264 ± .023	0.270 ± .019	0.250 ± .034
Pore width (n=10, mm)	0.196 ± .054	0.210 ± .089	0.254 ± .034	0.292 ± .04

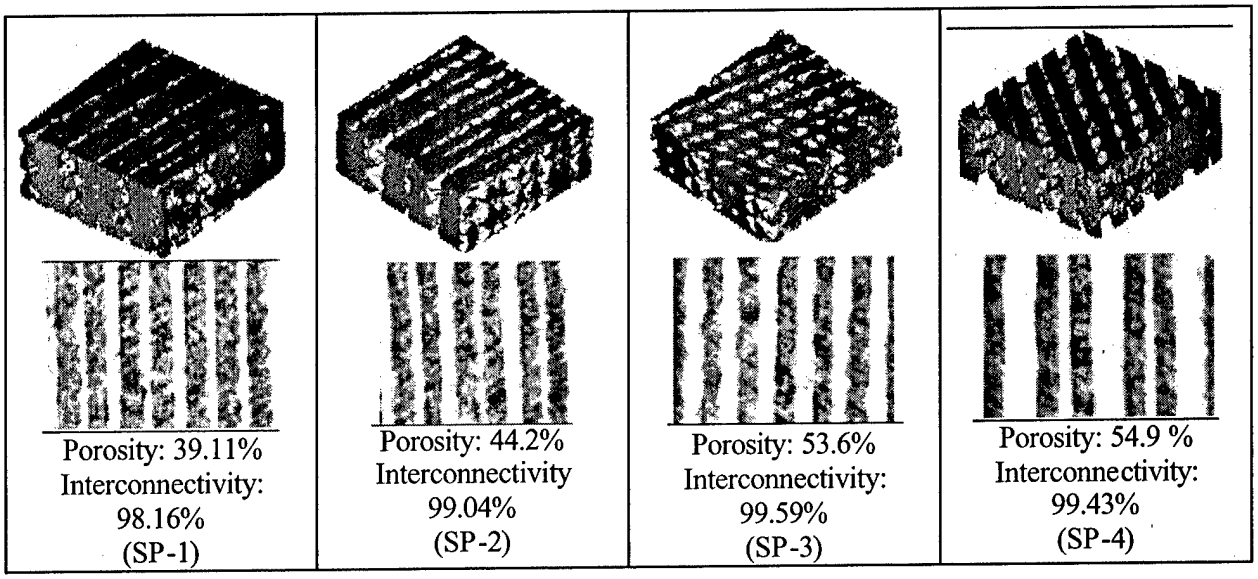

Fig. 8: Micro-CT imaging based 3D reconstruction, porosity and interconnectivity analyses

Compression Experiment

The Instron 5800R machine was used for the test of as-fabricated scaffold. The initial strain rate of the tests was adjusted to 10% per minute at the beginning of the test and no preload was applied before initiating compression testing. Standard solid compression platens were used for testing. Stress-Strain data were computed from Load-Displacement measurements. Compressive modulus was determined based on the slope of the Stress-Stain curve in the elastic region. The data was corrected on the Strain axis to a value approximately 0.025 for calculating the compressive elastic modulus of the scaffold. The stiffness of the machine was also put into the calculations to decrease machine error.

Three SP-2 specimens were tested under compression to a limit of specific compressive displacements. The PCL specimens were measures for their dimensions for accurate area calculations. The scaffolds were cylindrically shaped with minute irregularities on the circumference wall due to specimen processing. The samples were tested at a speed of 0.1 mm/minute at a room temperature of 24 C^{o} with a relative humidity of 15%. The average data of the test results is plotted in Fig. 9.

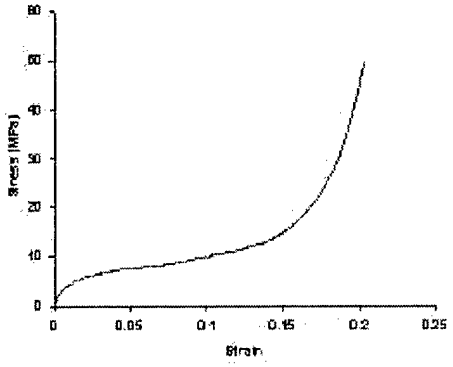

Fig. 9: PED as-fabricated scaffold stress-strain curve under compression test

Preliminary Biological Experiments

Preliminary biological experiments have been conducted to study the basic scaffold biocompatibility. These experiments were intended to address the issue of free radicals caused by heating of the polymer and whether these radicals would be detrimental to cell growth. Another question was whether the pore size of approximately 250 microns would be conducive to cell growth alone or would require a filler material.

Cardiomyoblasts (H9C2) were seeded onto three sets of 90° scaffolds, one set with no filler material, one with collagen filling the pores, and one with fibrin gel filling the pores. Initial seeding size was approximately 10^5. All samples showed cell attachment to the scaffold at five days, and a monolayer of cells atop the scaffold sample. Displayed in Fig. 10 are (from left to right), a scaffold without filler material, a scaffold with fbrin gel filler, and a close-up of a single fibrin filled pore. The confluence of the monolayer atop the scaffold at 5 days indicates uninterrupted cell growth. We feel this illustrates a proof of concept and that the PCL scaffold post-heating is not immediately detrimental to seeded cells.

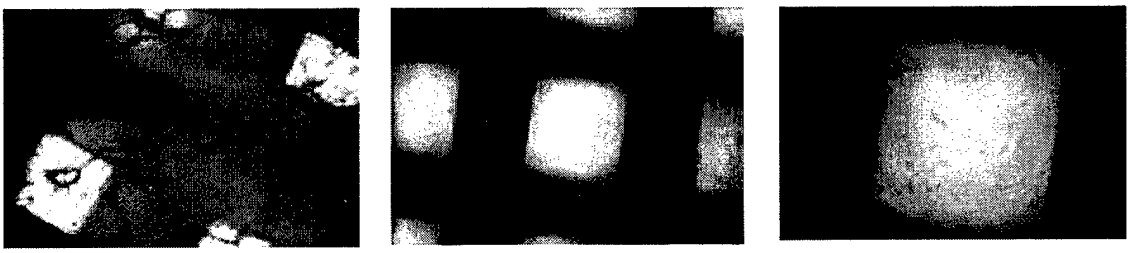

Fig. 10: Results of preliminary biological experiments

The presence of a material greatly enhanced proliferation and differentiation of cells, as indicated by the visible cellular processes in the figure. This would indicate a 250 micron pore size may be too large alone to optimally enhance cardiomyoblast growth. While 250 microns is ideally suited for the free diffusion of oxygen, the cells were unable to cross the pore spaces without the presence of a fibrin gel filler material. Currently, quantitative proliferation and attachment studies are being performed for three cell types with cytofluorimetry, fluorescence microscopy, and immunofluorescence as methods of analysis.

For the comparative proliferation study, 10^4 cardiomyoblasts, fibroblasts, and smooth muscle cells were seeded upon 90° PCL scaffolds of 1 mm thickness without filler material. Cell numbers were measured using Alamar blue staining and cytofluorimetry. Initial results showed that anchorage-dependent cells such as fibroblasts are better able to take advantage of the scaffold microarchitecture without a filler material. The fibroblasts attach to the surfaces preferentially compared to polystyrene and progressively grow into the porespace, narrowing the channel. Qualititatively, the ingrowth of the fibroblasts is such that it may close off pores completely. While the sample scaffolds for this proliferation study were thin (1mm), the fibroblast ingrowth may reduce nutrient flow in thicker scaffolds. Followup studies are underway focusing on fibroblasts, examining long-term growth, the occurrence of pore closure, and the effects of scaffold thickness on proliferation.

5. Conclusions

A study on using Precision Extruding Deposition (PED) process to freeform fabricate cellular Poly-ε-Caprolactone (PCL) scaffolds and on using SEM, micro-CT and the experimental testing to characterize the morphology, internal geometry, mechanical property and biological compatibility of the as-fabricated scaffolds were conducted. Both hardware and software configuration of the PED process system was described and the PCL scaffolds with controlled internal architectures were produced. Results of the characterization demonstrated the capability of the PED fabrication process in manufacturing the PCL scaffolds with microstructure and pore size at about 250μm scale. This process directly fabricates tissue scaffolds by converting designed architecture into layered deposition pattern without involving the material preparation and in-direct casting, thus opens opportunities for complex scaffold fabrication.

Results of the characterization also shown that micro-CT is a capable tool for nondestructive evaluation of PCL scaffolds. The use of 2D analysis and 3D reconstruction software allows the examination of morphologies, internal architecture, the interconnectivity of as-fabricated tissue scaffolds, and provides a quantitative measurement of porosity and micro-architecture. As shown in the analysis, a typical pore size of the fabricated scaffold range from 200-300 microns, near the optimal size suggested for bone tissue scaffold application. In addition, Strut width is consistent between samples, all samples showed greater than 98% interconnectivity. The scaffold compression modulus obtained from the test is in the ranging between 150 ~ 200 MPa. The preliminary result of biological experiments demonstrated the biocompatibility of the process and material, and also suggested larger spaces for further investigation and improvement. All these suggest the viability of the fabrication and the characterization process, as well as its potential applications in tissue engineering.

5. Acknowledgement

The authors acknowledge the NSF-0219176 project funding support to graduate students Andrew Darling and Saif Khalil, and the ONR research funding support to graduate student Lauren Shor. The authors also would like to thank for Dr. P. Lelkes at Drexel University for allowing to use the Cellular Biological and Tissue Engineering Laboratory for the biological study.

References

1. D.W. Hutmacher, "Scaffolds in tissue engineering bone and cartilage," Biomaterials, 21, 2529-2543, 2000.
2. Hollister, S.J., Maddox, R.D. and Taboas, J.M., 'Optimal design and fabrication of scaffolds to mimic tissue properties and satisfy biological constraints," Biomaterials 23, 4095-4103, 2002.
3. Sun, W and Lal, P., "Recent development on computer aided tissue engineering – a review," Computer Methods and Programs in Biomedicine, 67, 85-103, 2002.
4. Sun, W., Darling, A., Starly, B. and Nam, J., "Computer aided tissue engineering: Part I – Overview, Scope and Challenges" J. of Biotechnology and Applied Chemistry, in review.
5. Sun, W., Starly, B., Darling, A. and Gomez, C., "Computer aided tissue engineering: Part II – Application in biomimetic modeling and design of tissue scaffold," J. of Biotechnology and Applied Chemistry, in review.
6. Yang, S., Leong, K., Du, Z. and Chua, C., "The design of scaffolds for use in tissue engineering. Part 2. Rapid prototyping techniques," Tissue Engineering, 8 (1), 1-11, (2002).
7. Taboas, J.M., Maddox, R.D., Krebsbach, P.H. and Hollister, S.J. "Indirect solid free form fabrication of local and global porous, biomimetic and composite 3D polymer-ceramic scaffolds," Biomaterials 24, 181-194, 2003.
8. Wu, B.M., Borland, SW., Giordano, R.A., Cima, L.G., Sachs, E.M. and Cima, M.J., "Solid free-form fabrication of drug delivery devices", Journal of Controlled Release, 40:77-87, 1996.
9. Koch, K.U., Biesinger, B., Arnholz, C. and Jansson, V, "Creating of bio-compatible, high stress resistant and resorbable implants using multiphase jet solidification technology", Rapid News Publication, 209-214, 1998.
10. Zein, I.W., Hutmacher, D.W., Tan, K.C. and Toch, S.H., "Fused deposition modeling of novel scaffold architecture for tissue engineering application", Biomaterials, 23, 1169-1185, 2002.
11. Xiong, Z., Yan, Y., Zhang, R. and Sun, L., "Fabrication of porous poly(L-lactic acid) scaffolds for bone tissue engineering via precise extrusion," Scripta Materialia, 45, 773-779, 2001.
12. Vozzi, G., Previti, A., Rossi, D. and Ahluwalia, A., "Microsyringe-Based Deposition of Two-Dimensional and Three-Dimensional Polymer Scaffolds with a Well-Defined Geometry for Application to Tissue Engineering", Tissue Engineering, 8, 1089-1098, 2002.
13. Lin, A.S.P., Barrows, T.H. Cartmell, S.H. and Guldberg, R.E., "Micro-architectural and mechanical characterization of oriented porous polymer scaffolds", Biomaterials, 24, 481-489, 2003.
14. Müller, R., Matter, S., Neuenschwander, P., Suter, U.W. and Rüegsegger, P., "3D Micro Tomographic Imaging and Quantitative Morphometry for the Nondestructive Evaluation of Porous Biomaterials", In: R. Briber, D.G. Pfeiffer, C.C. Han, editors, Morphological Control in Multiphase Polymer Mixtures. Mat. Res. Soc. Proc. 461, 217-222, 1996.
15. Van Rietbergen, Müller, R., Ulrich, D., Rüegsegger, P. Huiskes, R., "Tissue stresses and strain in trabeculae of canine proximal femur can be quantified from computer reconstructions", J. Biomech., 32, 165-174, 1999.

16. Müller, R. and Rüegsegger, P., "Micro-tomographic imaging for the nondestructive evaluation of trabecular bone architecture", In: Bone Research in Biomechanics. Ed.: G. Lowet et. al. IOS Press Amsterdam, 61-80, 1997.
17. Bellini, A., "Fused deposition of ceramics: a comprehensive experimental, analytical and computational study of material behavior, fabrication process and equipment design", Ph.D. Dissertation, Department of Mechanical Engineering and Mechanics, Drexel University, 2002.

Selective Laser Sintering of Duraform™ Polyamide with Small-Scale Features

Vinay Sriram, Kristin Wood, David Bourell and Joseph J Beaman
Department of Mechanical Engineering
Laboratory of Freeform Fabrication
The University of Texas at Austin, Austin, TX 78712
Reviewed, accepted August 25, 2003

Abstract

Selective Laser Sintering (SLS) has been used to make a fiber management module having very small feature size and ratios. Currently these modules are made out of Stereolithography using standard epoxy acrylate materials. SLS has been chosen to make these modules by the virtue of the material system it offers. The material system was chosen based on the flame retardant properties. The material used for this study is a Duraform™ Polyamide and Alumina-Ammonium Phosphate system. Ammonium Phosphate served as the binder in the Alumina-Ammonium Phosphate system. Experiments were done in order to find out the minimum feature size possible with the two material systems. Minimum hole diameters and maximum possible l/d ratios are determined by particle size, shape and processing conditions. Builds were made in different directions to understand the effect of the various processing parameters on the system. One particularly noteworthy observation was that part growth as a proportion of hole diameter became increasingly significant as hole size decreased. Optical microscopy was performed to measure the hole diameters and also to reveal the surface roughness. Results indicate material system determines the minimum diameter of micro-sized holes that can be effectively manufactured using Selective Laser Sintering.

Introduction

Selective Laser Sintering is a layer based manufacturing process. Successive layers of powder are deposited one above the other and the powder surface is raster scanned with a high power laser to achieve the desired geometry. The ability to manufacture any shape and geometry using Selective Laser Sintering has been well discussed in books and literature [1]. The current study focuses on manufacturing small sized features using three different material systems having flame retardant properties.

Initially Stereolithography was used to manufacture the desired geometry. Layers of photo-curable polymer are deposited from a vat and selective solidification is carried out by scanning with a laser beam. At a later stage the parts are flood exposed to UV light for 90 minutes to complete UV curing and is subjected to post thermal curing steps to achieve desirable properties of the material. The primary problem associated with Stereolithography

is using flame retardant polymers. In order to overcome this problem Selective Laser Sintering was selective as a viable technology based on the wide variety of material choices offered.

Objectives

1. The primary objective is to achieve hole diameter compatible with standard optical fibres.
2. Usage of flame retardant materials meeting UL 94 V0 standards.

The geometry of the Optical connector is as shown.

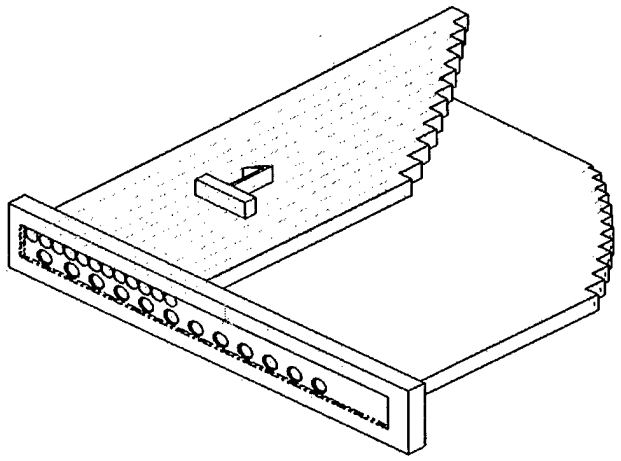

Material Requirements

The following are the material properties required in the manufacture of optical connectors.

Property	Requirement	Test Method
Glass Transition Temperature	120-130C	DMA
Moisture Absorption	< 1%	ASTM D570 95 % RH @ 600C for 14 days
Tensile Elongation at Break	3-4 %	ASTM D638
Tensile Modulus	350-450 Kpsi	ASTM D638
Tensile Strength	7-8 Kpsi	ASTM D638

Impact Resistance	0.4-0.6 ft-lb/in	ASTM D256
Heat Deflection Temperature	> 1200C at 256 psi	ASTM D648
Vibration Resistance	No cracks	10 to 55Hz per ETA/TIA FOTP

Table 1. Material Requirements

UL 94 VO flammability standards

This covers tests for flammability of plastic materials used for parts in devices and appliances. The standard consists of two tests which are Horizontal burning test (Ref 2) and the Vertical burning test. Table 2.0 shows the classification of materials as V0, V1 and V2 based on the afterflame and afterglow times.

Criteria Conditions	**V-0**	**V-1**	**V-2**
Afterflame time for each individual specimen	<= 10s	<= 30s	<= 30s
Total afterflame time for any condition set	<= 50s	<= 250s	<= 250s
Afterflame plus Afterglow time after second flame	<= 30s	<= 60s	<= 60s
Afterflame or afterglow up to holding clamp	No	No	No

Table 2. Flammabiltiy Criteria

Afterflame time is defined as the length of the time for which a material continues to flame under specified conditions, after the ignition source has been removed. Afterglow time has been defined as the length of time for which a material continues to glow under specified test conditions after the ignition source has been removed and or cessation of flaming.

Materials Chosen

Based on the above material properties needed the following 3 material systems were chosen

1. Duraform ™ Polyamide
2. Alumina and Ammonium Phosphate
3. Alumina and Duraform ™ Polyamide

Duraform ™ Polyamide is a nylon based material and copyright of 3d Systems. It is one of the most widely used materials in Selective Laser Sintering Duraform ™ and is used to build rugged durable thermoplastic parts and withstand aggressive functional testing. The table below gives a comparison of the properties of Duraform ™ and the required properties.

Property	Requirement	Duraform™
Glass Transition Temperature	120-130C	185C
Moisture Absorption	< 1%	< 0.41%
Tensile Elongation at Break	3-4 %	9%
Tensile Modulus	350-450 Kpsi	220 Kpsi
Tensile Strength	7-8 Kpsi	6.2Kpsi
Impact Resistance Heat Deflection Temperature	0.4-0.6 ft-lb/in > 1200C at 256 psi	4 ft-lb/inch
Vibration Resistance	No cracks	168C at 66psi, 64C at 264psi
Flammabilty	UL 94 V0 standards	UL 94 V2 standards

Table 3. Duraform Properties

Duraform ™ Polyamide satisfies all the requirements except for flammability. The tensile strength and tensile modulus as seen from the graph are slightly less than the required.

In the alumina-ammonium phosphate system, the ammonium-phosphate acts as the binder. This system is primarily chosen because of its ability to withstand high temperature, high density attainable, low shrinkage and good surface finish.

The optimum binder weight lies at 20% where shrinkage attained is minimal [3]. The melting point of Ammonium phosphate is around 190C and that of Alumina is around 2045C.

Based on the experiments done by Lakshminarayan and et al. the composition of the blend was 50 % by wt Alumina having a particle size of 70 μm, 25% by wt Alumina having a particle size of 10 μm and Ammonium phosphate having a particle size of 50 μm. The above blend provides the least shrinkage as compared to other particle sizes used.

The third material system used was alumina and Duraform system. Here the Duraform acts as the binder and Alumina as the base material. The optimum weight percentage of the binder is found to be between 20% and 30% by weight [1].

Initial Experiments

Experiments were done in order to find out the minimum hole diameter that is possible with the Duraform powder. A number of process parameters affect the Selective laser sintering process. The black box model of Otto and Wood [5.] is applied to the SLS process and all the parameters are classified as Performance variables, tuning variables, design variables and noise variables. The black box model is applied to the selective laser sintering process as shown in Fig 1.

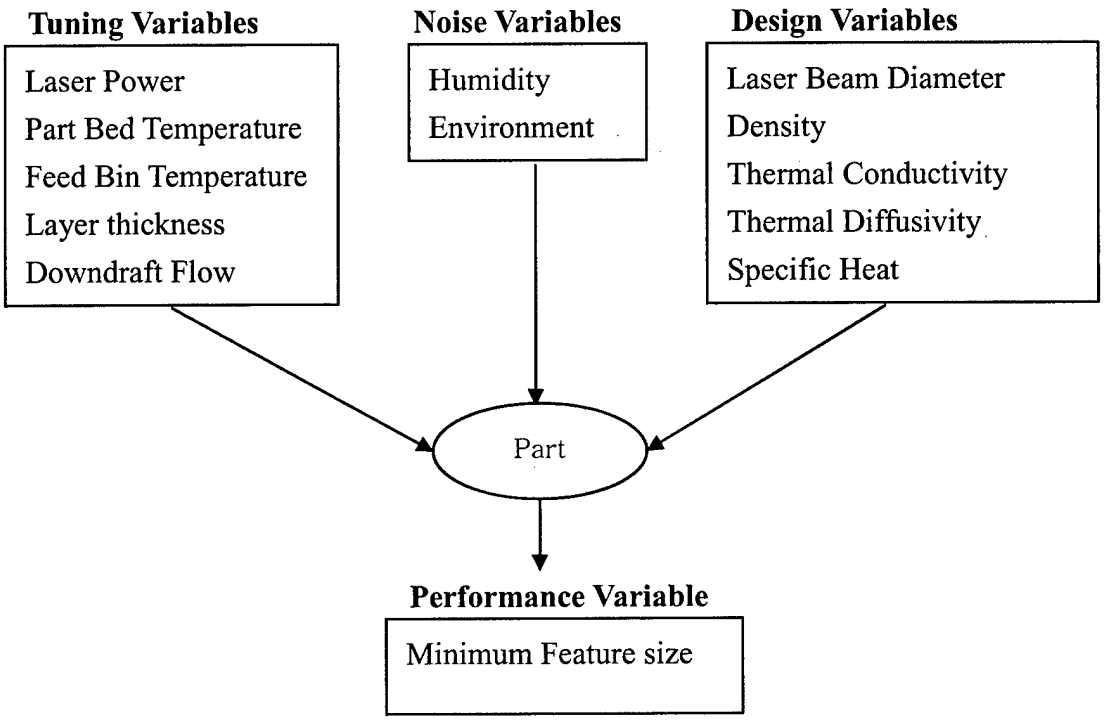

Fig1. Black Box Model of SLS

Based on all the above parameters standard values were chosen for a simple geometry to find out the minimum hole diameter possible. The process parameters are given below

Process Parameters	Value
Laser Power	5.5W
Fill Scan Speed	49.5 in/s
Bed Temperature	160 C
Layer Thickness	0.004 in
Outline Scan Speed	11.0 in/s

Table 4.

Results & Discussion

A simple geometry having holes of varying diameter and length is fabricated. The following graph shows the intended hole diameter and the actual measured diameter.

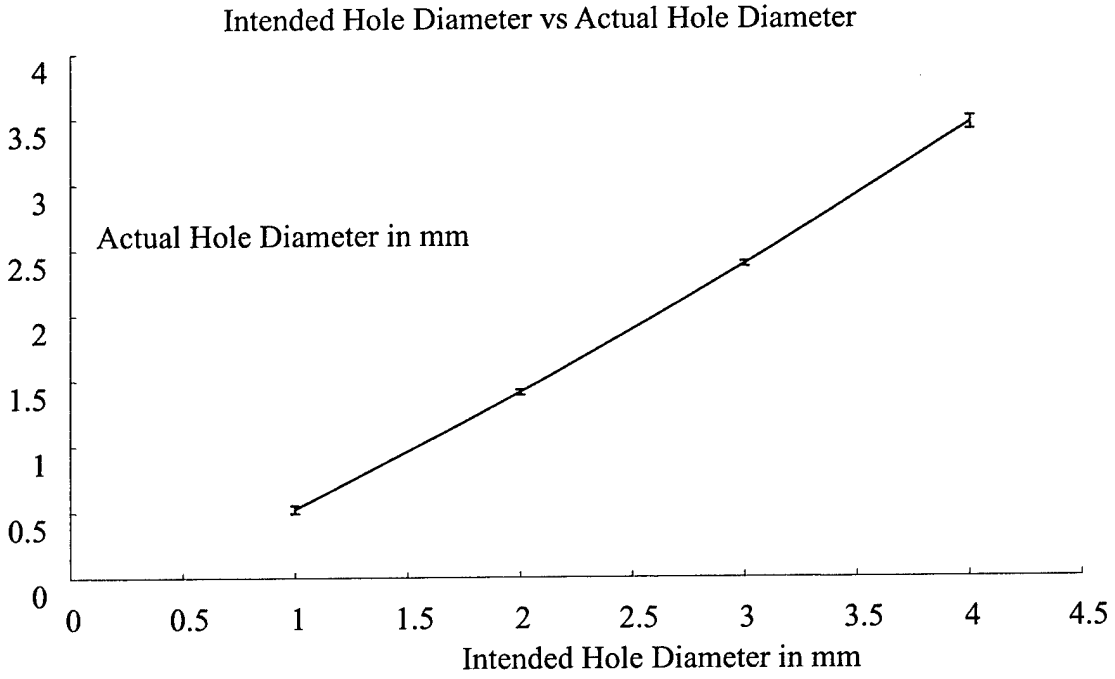

Fig 2. Graph of Intended Hole Diameter vs Actual Hole Diameter

The hole diameters were measured using Optical microscopy. From inspection of the graph, it is evident that shrinkage increases as the hole diameter decreases. The minimum hole diameter possible with the Duraform system was 0.52 ± 0.02 mm. The shrinkage for a intended hole diameter of 1.0mm was 48 %. Holes below 0.5mm are fully infiltrated with

powder. As a result it is not possible to measure the diameter. All the holes tested are straight and built in the vertical direction. Incorporating shrinkage pattern in the hole diameter it is possible to manufacture the required hole size.

The diameter of the hole with respect to l/d ratio is shown below. A set of 3 measurements were taken at the bottom, middle and top part of the cross-section of the pipe for all the material-systems and is shown in Figures 2, 4 and 7. The standard deviation indicates the overall variation of the diameter. It is seen that as l/d ratio increases there is lesser variation in the hole diameter. The significance of this is that it is possible to maintain concentricity of hole for long straight pipes. The minimum hole diameters possible is different for different material systems. The following photographs show hole diameter as measured by an optical microscope.

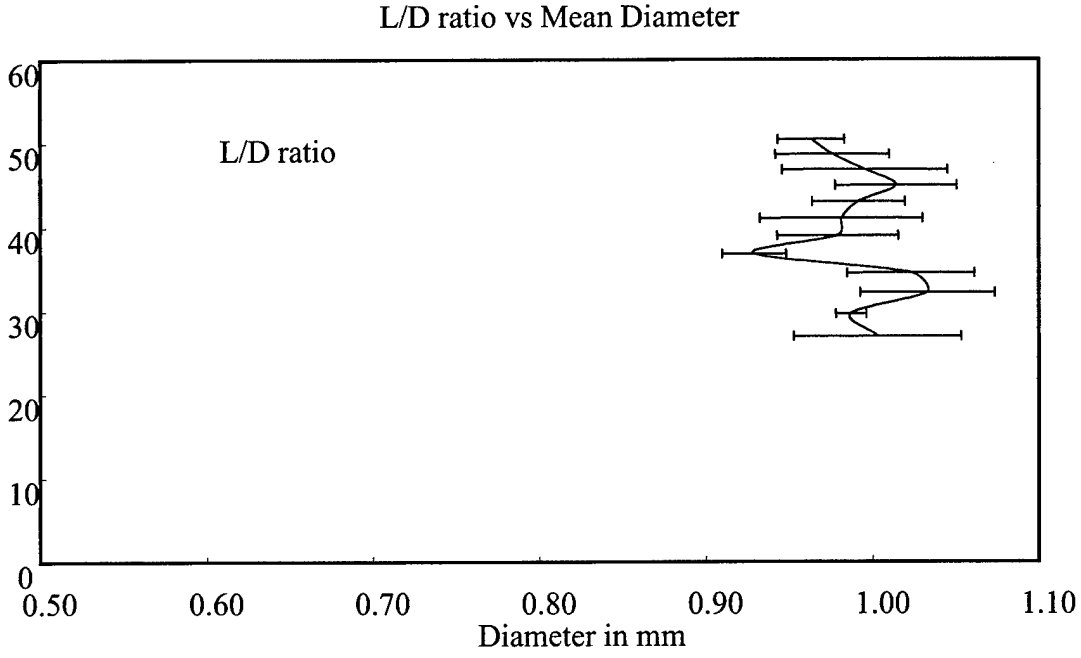

Fig 3. Feature size

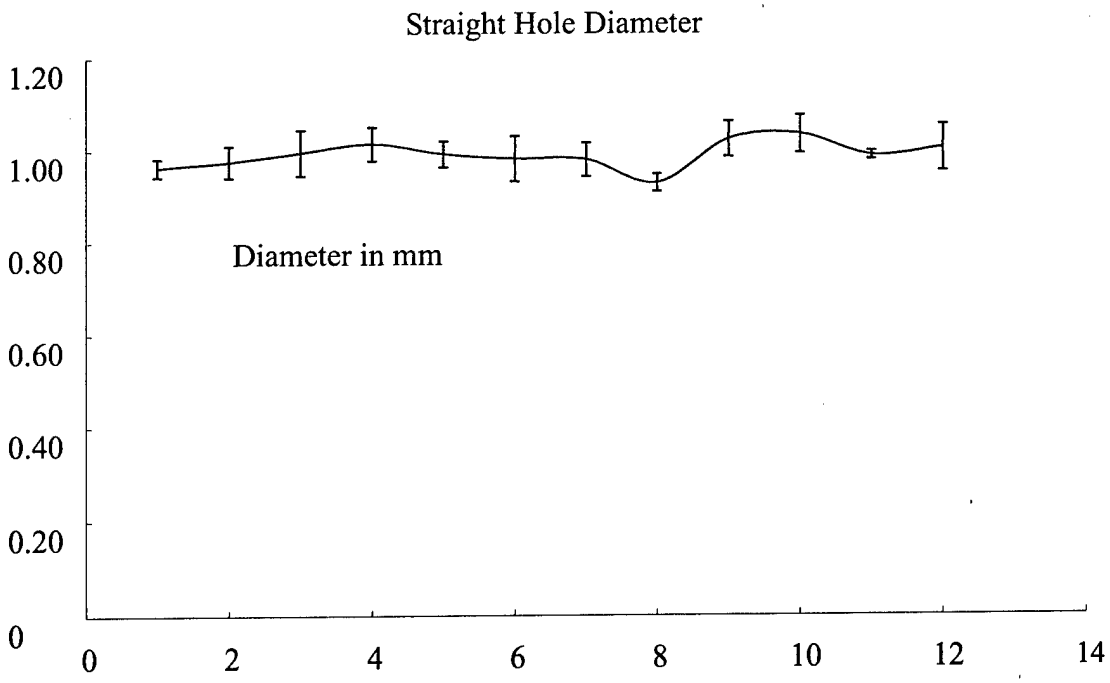

Fig 4. Hole Diameter with Error Bars

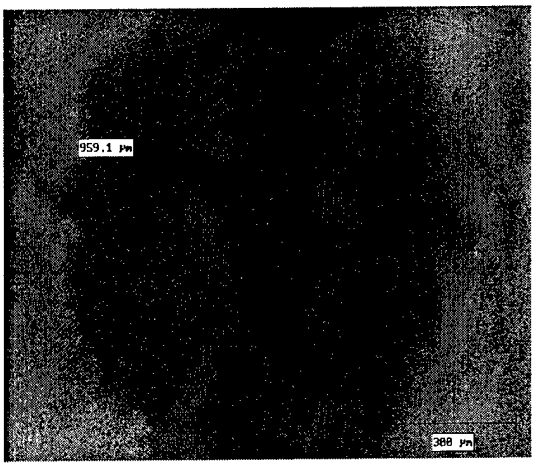

Photo 1

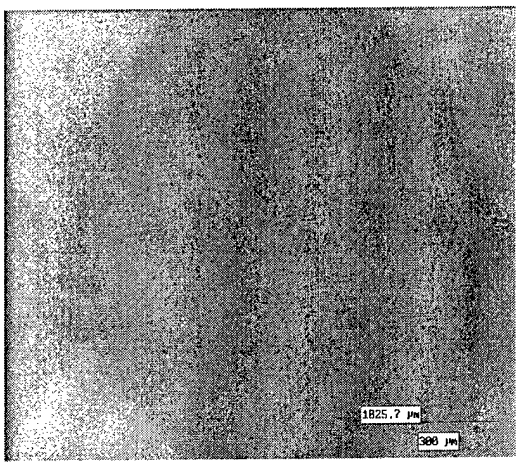

Photo 2

Fig 5. Photographs of Straight Pipes

Hole Diameter for curved pipes

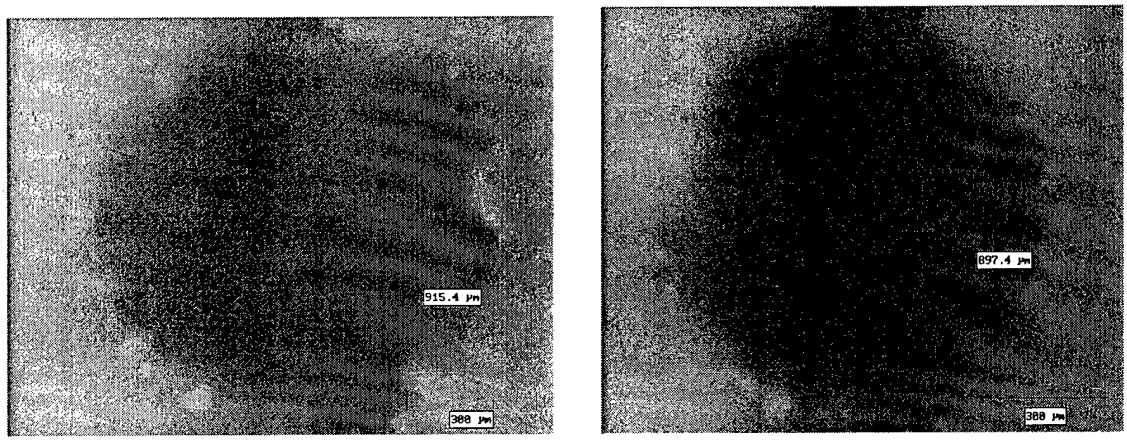

Photo 1 Photo 2

Fig 6. Photographs of Curved Pipes

The same amount of growth effect was incorporated for curved pipes. The results are shown below.

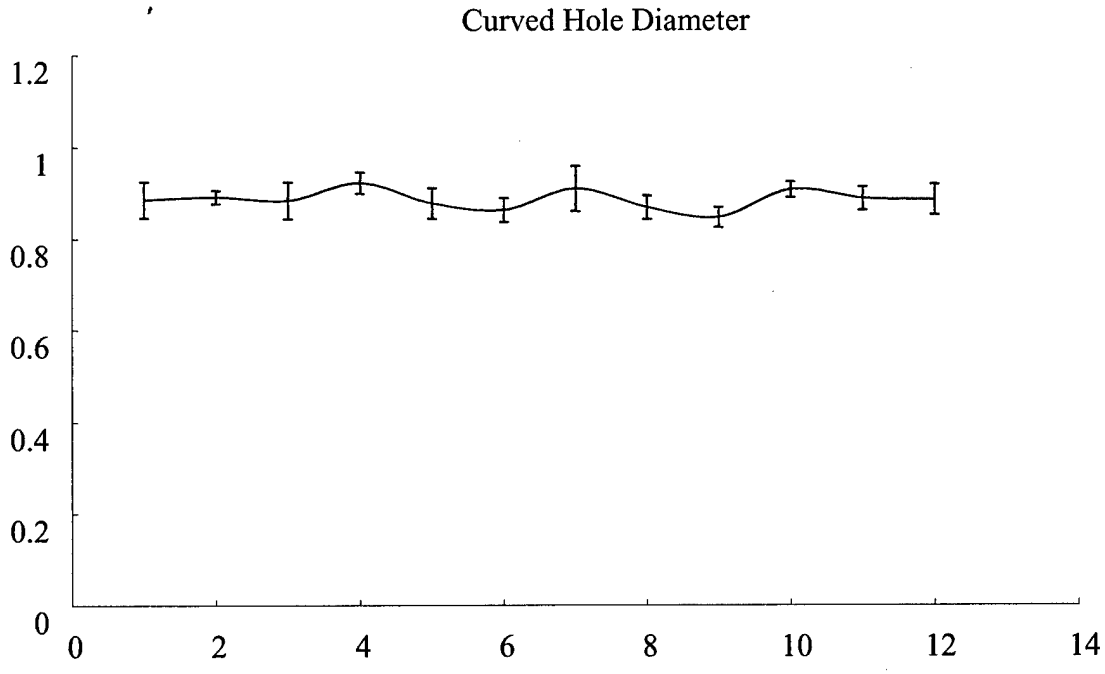

Fig 7. Curved Hole Diameter with Error bars

The most common problems encountered were growth effect, surface finish and powder removal. Growth occurs as powder sinters along the part, blurring features altering part dimensions and visibly apparent on small features such as holes. Growth effects can be taken into account by the above discussed method. Surface finish is affected by the particle

size of the powder, build direction and packing density of the powder. The best surface finish is achievable when virgin powder is used. Surface finish tends to degrade on repeated use of the old powder. Streak lines are noticeable on the part when it is built in the horizontal direction. Streaking primarily occurs because the Duraform powder is too hot and tends to stick to the roller. One approach to avoid streaking is to reduce the feed bin temperature by 3 or 4 degree centigrade. Powder can be removed either by vacuuming or blowing it using a sand blaster. For holes smaller than 1mm diameter the friction coefficient is rather high between the loose powder particles and the inner surface of the hole. This creates difficulty in removing the powder. The powder is basically removed by using steel wires of varying diameters. Smaller wire diameters loosen the powder and the bigger wires are used to remove the powder. The hole diameter is then verified by passing an optical fibre through the connector.

The second material system tried was Alumina-Ammonium phosphate system. In this system the binder is Ammonium phosphate. The parameters chosen are as follows.

Parameter	Value
Laser Power	20 W
Scan Speed	4 cm/s
Bed Temperature	21 0C
Layer Thickness	0.2mm
Scan Distance	0.5mm

Table 5. Parameters for Alumina-Ammonium Phosphate System

The major problems associated were crumbling of the part, achieving right particle size and blending of powder. The weak porosity of the part resulted in crumbling of the optical connector as a result no dimensions of the parts could be obtained. The reason behind the weak porosity is incorrect binder particle size. The binder particles were slightly greater than those that were given in the literature and resulted in incomplete bonding of the alumina to Ammonium phosphate.

The third material system that is tried out is the Duraform – Alumina system. Here Duraform acts as the binder for the alumina particles. A mixture consisting of 78 % by weight of Alumina and 22 % by weight of Duraform is prepared. The processing parameters are the same as that of Duraform alone apart from lowering the feed bin temperature to prevent glazing effect. One of the primary concerns in this material system is also powder removal. The diameter measured for this material system is 1.02 ± 0.02 mm.

Conclusion

It is possible to achieve small scale features using Duraform to manufacture optical connectors. The shrinkage measurements were done only for straight pipes. Curved pipes exhibit considerably more growth and further study needs to be done to understand them. Incorporating growth effect of straight pipes to that of the curved pipes works only to certain extent. Understanding the phenomenon of growth for different material systems it is possible to make virtually any complicated hole structure without sacrificing accuracy and hole tolerances.

References

1. Beaman, Joseph, et al. Solid FreeForm Fabrication. Austin: Kluwer, 1997.

2. Lakshminarayan, Uday. Selective Laser Sintering of Ceramic Materials. Diss. Univ of Texas at Austin, 1993, Austin.

3. Wood, Kirstin and Otto Kevin. Product Design. New Jersey: Prentice Hall, 2001.

4. Lee, William, et al. Ceramic Microstructures. Sheffield: Chapman, 1994.

5. Epel, Joseph, et al. Engineering Plastics. Vol. 2 Cleveland: ASTM, 1988.

POST-PROCESSING OF DURAFORM™ PARTS FOR RAPID MANUFACTURE

H. Zarringhalam and N. Hopkinson
Wolfson School of Mechanical and Manufacturing Engineering, Loughborough University, UK

Abstract

In recent years layer manufacturing processes have evolved from Rapid Prototyping (the production of pre-production prototypes) to Rapid Manufacture (the production of end use parts) where limitations of the processes do not affect end use. There is no doubt that applications for Rapid Manufacture will grow in coming years, however there are a number of current limitations that will need to be addressed so as to maximise the scope for Rapid Manufacturing applications.

One of the main limitations for the adoption of Rapid Manufacturing is material properties of the parts produced. This research has looked at the possibility of increasing the range of material properties that may be achieved from parts made using current commercial Laser Sintering systems.

A series of tensile and impact test parts were built using Duraform™ powder on a 3DSystems Vanguard machine. These parts were then subjected to various form of post-processing including thermal treatment and infiltration with polymer infiltrants. The parts were subjected to tensile and impact tests with results showing that thermal post-processing achieved preferable results when compared with infiltration. Heating above the glass transition temperature yielded superior results though as the melt temperature was approached issues of deformation arose. These initial results have formed the basis for further work to consider how material properties for Rapid Manufacture by Laser Sintering may be improved.

Keywords

Rapid Prototyping, Rapid Manufacture, Selective Laser Sintering, Post-processing, Material properties.

Introduction

Rapid Prototyping (RP) is a relatively new family of technologies which emerged in the late 1980's. *Wohlers Report 2000*, defines it as: "A special class of machine technology that quickly produces models and prototype parts from 3-D data using an additive approach to form the physical models." [1]

Currently all commercially available RP processes build parts layer by layer. Thin, essentially 2D, cross sections of the part are built one on top of the other enabling parts to be built with geometries often impossible to achieve by machining and other methods. Such geometries include intricate internal structures, parts within parts, and very thin-wall features which are just as easy as building a simple geometry such as a cube.

Another important characteristic of RP processes is that they need no part specific tooling to produce parts. The manufacture of tooling for conventional manufacturing processes is expensive and time consuming. The lack of tooling therefore means RP processes can offer advantages from both time and direct cost points of view.

As the technology evolves production of parts for end use is becoming possible, rather than just for prototypes. Where RP technology is used to build parts for end use, the term 'Rapid Manufacturing' (RM) arises. RM has already found numerous uses for production of parts in relatively small quantities and where production of certain geometries is not feasible with conventional methods. Examples include Hearing-aid bodies [2], air handling systems [3] and electronics housings for Formula One cars [4].

The use of RP technology for RM is currently limited by a number of issues, and many of these relate to the physical properties of the parts. Parts tend to be weaker than parts made by conventional methods such as injection moulding, even when using the same materials. Also, repeatability of material properties is a serious issue with values varying throughout individual parts and between different parts according to the position within the build volume.

In order for RM to become more widely used the parts will ideally have at least the strength of parts made by conventional methods. This project looks at methods of post-processing to improve the mechanical properties (tensile and impact) of parts built from Duraform™ Nylon using the Selective Laser Sintering (SLS) process with the aim of facilitating the use of the material more widely in RM. The SLS process has been selected due to the versatility of the system and the wide range of materials available. Also important was the fact that many companies hoping to implement RM methods have already expressed particular interest in the SLS process and that it is already used in various industries to create end use products.

Theory & Analysis

Powder metallurgy (PM) has fundamental similarities with the SLS process. Both involve creating solid objects from compacted powder material using sintering/heating processes for bonding of the particles. Considering the similarity between the two, a logical progression can be made by applying basic PM principals to SLS: Parts made by such processes will usually contain voids or porosity and as such will be less dense than if there were no voids or porosity. A part with zero voids or porosity can be expressed as having 100% theoretical maximum density. The higher the density, the greater the part's tensile strength, elastic modulus and toughness. As such, the denser the part, the higher the 'strength'.

There are two main factors that cause decreased strength with lower densities. At densities less than 80% of maximum density, the size of inter particle bonds is the main factor and at densities of over 80% it is the pore size, shape and spacing which becomes the predominant factor [5]. This relates to the fact that porosity may consist either of a network of interconnected pores or of sealed holes, and that interconnected pores are generally found with densities less than 80% of maximum density [6]. This has major implications for infiltration since the material must be less than 80% dense otherwise infiltration will be unlikely to occur much further beyond the surface.

By accurately measuring and weighing a cube sintered on the same SLS machine as the other parts and with the same build parameters, the density was found to be 87%. This was based on measured density of 0.96 g/cm^3 compared with a quoted maximum density for Duraform™ of 1.10 g/cm^3 [7].

Most materials generally contain structural imperfections and small cracks or voids. The presence of such voids causes high local concentrations of stress. It is mentioned above that, with parts made by SLS or PM, at different densities the voids will either be a network of interconnected pores or of sealed holes. It can be shown theoretically and practically that voids in the shape of circles (sealed holes) cause significantly less stress concentration than voids consisting of long 'cracks' [8]. This suggests why increased density would result in a tougher material.

Figure 1 shows a representation of particles of Duraform™ nylon modelled as contiguous spheres. They are drawn within cubes to indicate how they would be arranged cubically. This model was chosen for simplicity and would not represent the true packing characteristics, however it is sufficient for this explanation. The inter particle area of contact is shaded and it is shown that as the spheres become compressed, hence denser, the particles press against each other and deform and hence the area of contact increases (right). Also, it shows that as density increases, the free space, hence pore size, also decreases. It can be seen that in the loosely packed state the porosity is interconnected while in the tightly packed state the porosity takes the form of sealed holes. The arrows represent equal tensile forces being applied

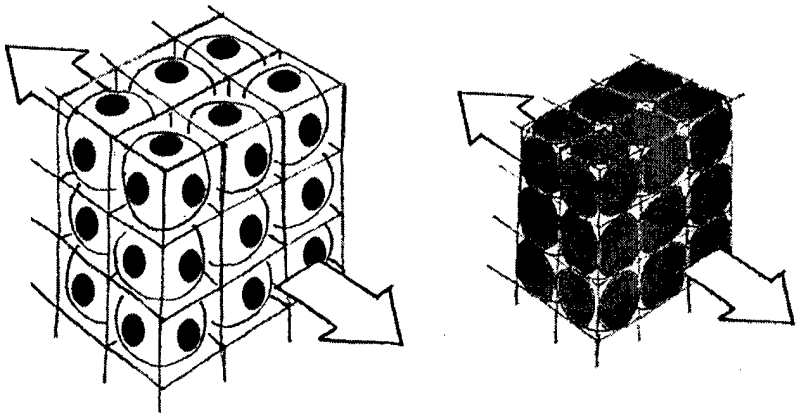

Figure 1. Inter particle contact area of loosely packed (left) and tightly packed nylon (right)

Under tensile loading the stress can be calculated simplistically by:

Stress (σ) = Force applied (F)/ Cross sectional area (A)

This shows that the higher the density is, the higher the total cross sectional area will be and hence the lower the stress within the material will be under the same applied load. Therefore the tensile strength of the material will be higher. Sheer strength and toughness would be affected in the same way.

When a semi-crystalline polymer such as Duraform™ is heated beyond its melting point (T_m = 184°C) it behaves like a highly viscous liquid

It is currently common practice to infiltrate the surface of SLS parts with 'Superglue' which allows a higher quality surface after finishing. Since this is a widely used method of post processing, this and other common infiltrants were investigated to assess their impact on physical strength properties of parts.

Methodology

The project consisted of the following practical stages:

1. Production of parts
2. Initial post processing and tensile/impact testing
3. Simple analysis of initial results
4. Further post processing and testing
5. Analysis of further results

The SLS Build process is outlined below:

1. Thin layer of heat-fusible powder deposited in part-build cylinder
2. Laser 'traces' cross-section matching corresponding layer in STL file, bonding particles to each other and adjacent layers
3. Roller mechanism deposits another powder layer
4. Platform in part-build cylinder moves part downwards a layer and process repeats.
5. Part removed and loose particles shaken off
6. Post-processing if required, such as infiltrating with superglue for improved surface finish.

The SLS machine used in this project was a 3DSystems Vanguard and the material was Duraform™ powder. Duraform™ is based on Nylon 12, a commonly used thermoplastic used in injection moulding and other plastics forming methods.

As mentioned above (step 5), the parts were removed from the SLS machine as a 'powder cake' containing the sintered parts held in the compacted but unsintered powder. While the parts were being removed from this 'cake' they were carefully numbered and photographed to record their position and orientation within the build volume.

As mentioned earlier, part properties vary throughout the build volume but using data generated by other research [9] compensation factors where generated which theoretically eliminate the effects of property variation as a factor of part bed distribution. The data available was for positions across the 'face' of the build but not for different depths. However, the build of parts (3 horizontal layers) and selection for each variation of PP meant that for each variation there were 6 parts used, from 2 locations across the face of the build, each with 3 parts, one from each height. Because of this, effects of property variation due to different build heights were practically eliminated. In addition, although compensation factors were used, the selection of the 2 locations on the face of the build for each variation was carried out to ensure an even 'distribution' as much as possible, so that, for example, if the first location was central then the

second would be near the edge. These steps were essential to stop factors relating to build position interfering with the results of the post processing.

It is common practice for unsintered powder from the 'powder cake' to be mixed with virgin powder for further use to minimise waste. However, since this is a potential source of variation only virgin powder was used in this project.

Conventional heating was carried out in a Zwick temperature chamber using a controlled heating and cooling cycle to avoid potential issues of thermal shock. Thermocouples placed in the oven were used to measure temperatures rather than having them attached to parts. This was done primarily due to the need to maximise the use of the limited parts from a single build and that a significant number of parts would be un-testable if they had thermocouples attached. It was considered acceptable since all parts were heated in the same positions hence for the purpose of an 'initial' relative comparison' there should be no problems. In addition the small internal volume of the oven and high rate of air circulation should theoretically result in a relatively even temperature distribution compared with other conventional ovens.

Initial testing suggested further processing by varying heating times beyond 1 hour with temperatures in the approximate range of just below the glass transition temperature to as close to the melt temperature as possible. Table 1 shows the temperatures and times that parts were subject to after building on the SLS machine. The temperatures selected for the 3 hour heating were based on initial results from 1 hour heating.

Time (Hours)	Temperature (°C)				
	155	165	175	180	183
1	✓	✓	✓	✓	✓
3			✓	✓	✓

Table 1. Heating parameters employed for post-processing

Infiltration was performed using 'Superglue' (Loctite 406), 'Thomsons Water Seal' (for sealing bricks/mortar against moisture ingress), and 'MDF sealer' (for protecting MDF wood). These are all polymer based. Due to the Superglue's high cost per volume and low viscosity the method used was to place the parts on a rack and place drops of the liquid along the faces which spread evenly on its own. This took place in an extraction bay because of irritant fumes. For the 'Thomsons' and MDF sealer the parts were submerged in the liquids for durations of 2mins, 1 hour and 24 hours.

Initial testing suggested further processing by infiltrating with Superglue and Thomsons, but not MDF sealer.

Testing was carried out as per ISO standards as follows.

Impact testing: BS EN ISO 180:2001
Tensile testing: BSI EN ISO 527-1:1996

The impact tests were notched Izod and the notches were 'built in' to the STL file.

Results & Discussion

Methods of post processing are compared with 'original' un-post-processed parts from the same build and textbook values for Nylon 12 (equivalent to Duraform™) and Nylon 6 (another very widely used Nylon). Mean values for each set of 6 samples are shown on the graphs as well as the max/min range.

Figure 2 shows the effects of post-processing on the impact strength of parts. Conventional heating yielded significant improvement especially with higher temperatures and longer times. Improvements from 180°C to 183°C were significant given the small increase in temperature. Heating at 183°C for 3 hours resulted in an improvement in impact strength of 60% over standard Duraform™ parts and at a value over that for Nylon 6. However the melt temperature is 184°C and hence at 183°C the parts deformed considerably (see Figure 3). All methods of infiltration resulted in slight increases in impact strength over standard Duraform™ parts. Shorter soak times for Thomsons resulted in marginally higher values than the longer soak times though the relatively high spread compared with this increase means this finding is not conclusive.

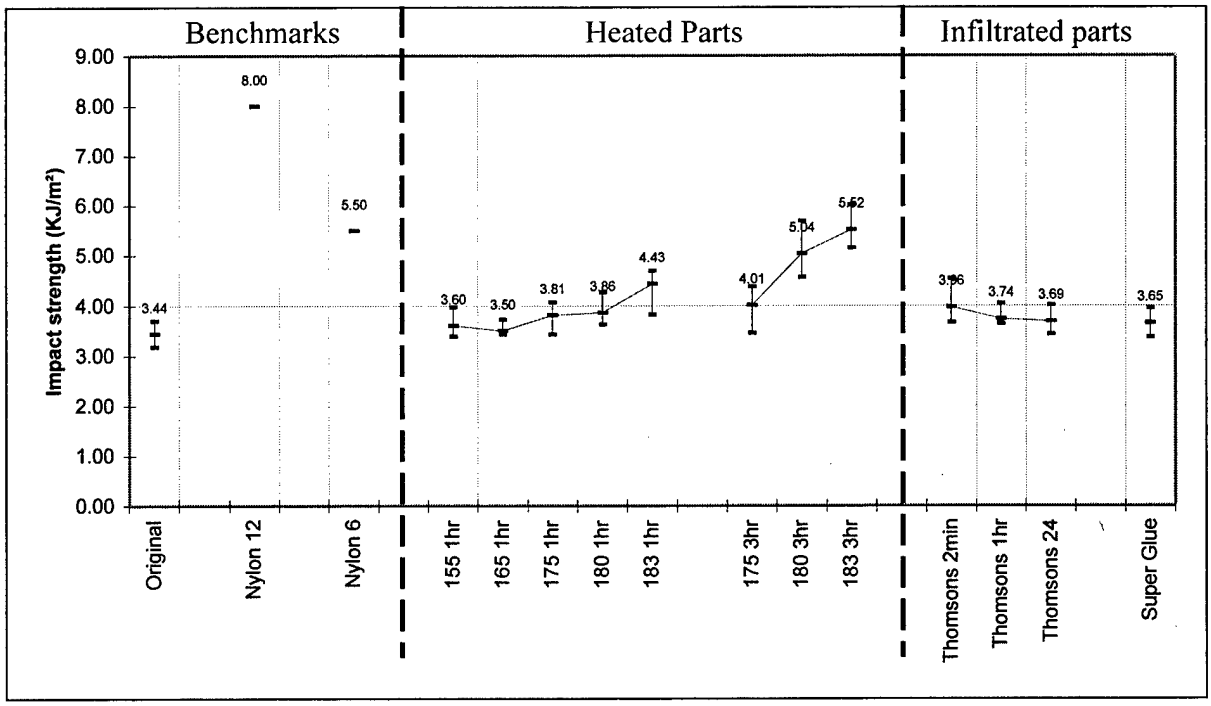

Figure 2. Impact strength results

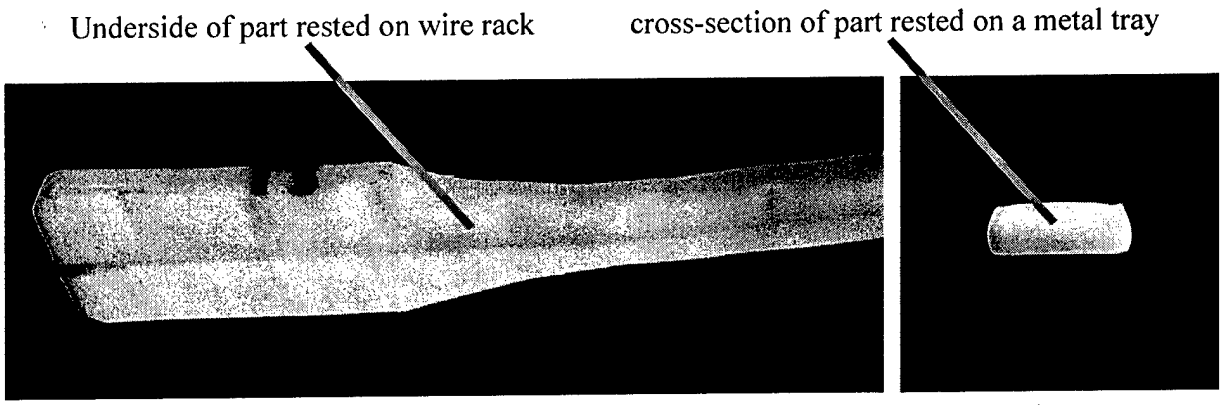

Figure 3. Deformation of parts heated to 183°C for 3 hours

Figure 4 shows that Young's Modulus for standard Duraform™ parts is higher than those for moulded Nylon 12 parts and that heating increased the stiffness further. Higher temperatures resulted in higher stiffness though prolonged heating for 3 hours yielded no improvements on the 1 hour heating indicating an optimum heating time (to achieve maximum stiffness) is under 1 hour. The effects of infiltration on stiffness appeared to be negligible, probably due to the minimal depth of infiltration.

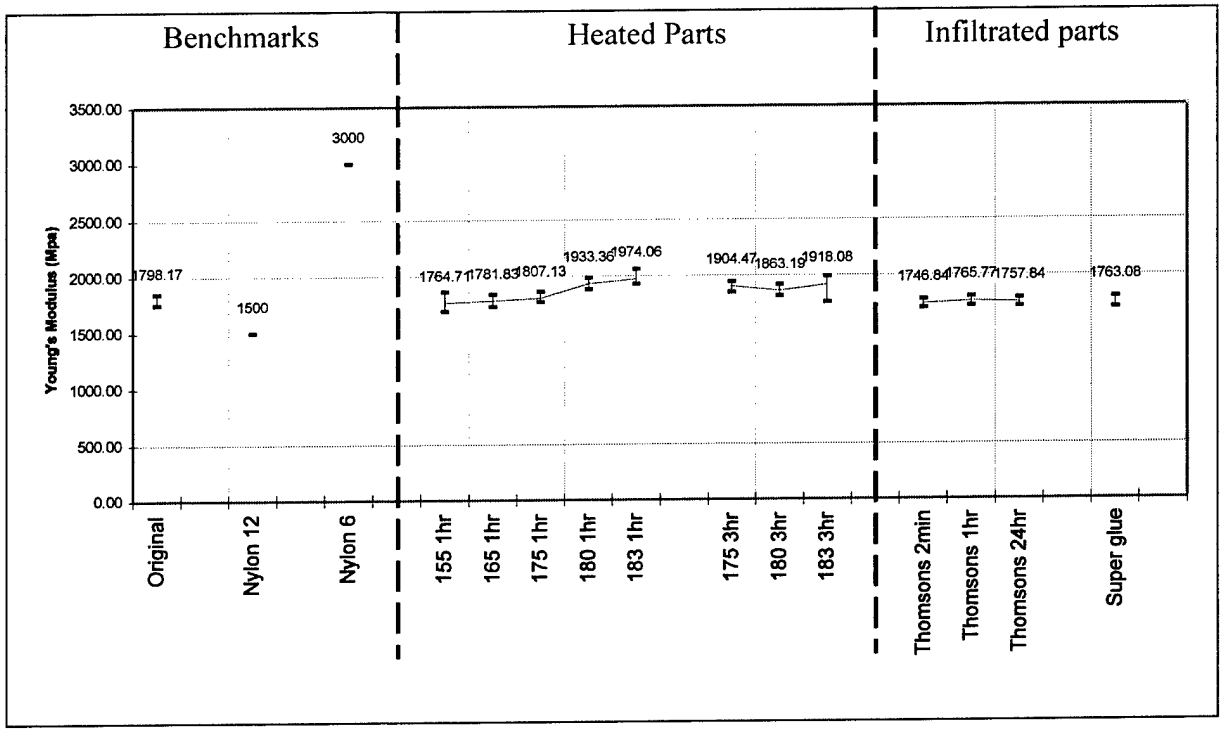

Figure 4. Young's Modulus Results

Figure 5 shows that standard Duraform™ parts have a slightly lower UTS than moulded Nylon 12 although heating close to the melt temperature increases the UTS so that it just surpasses that of Nylon 12. As with Young's modulus, the optimum heating time would appear to be less than an hour, again this is of particular significance for RM. Infiltration appears to have a slightly detrimental effect on the UTS of Duraform™ parts, although it is not clear why this occurs.

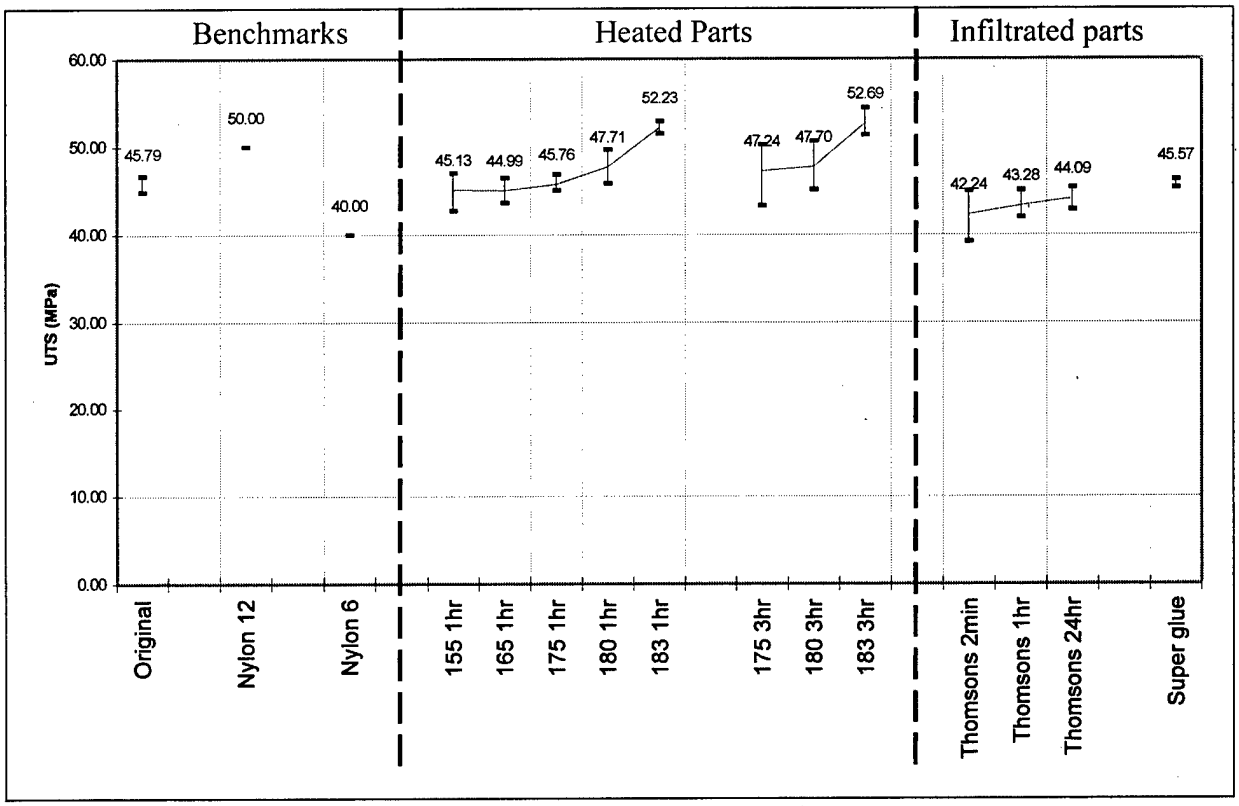

Figure 5. UTS Results

Figure 6 shows that standard Duraform™ parts are considerably less ductile than moulded nylon parts and that elongation at break decreased marginally when parts were heated to temperatures below 180°C. Marked increases at 183°C are shown however it was observed by visual inspection that these parts did neck before failing where as other parts did not. Figure 7 shows a tensile sample that had been heated to 183°C for 3 hours. There is some necking, however moulded nylon would show considerably more elongation. The responsible mechanism may be related to re-solidification and that the lower the viscosity reached when heating then the greater the degree of parallel chains/lamellae formation and hence increased crystallinity and thus increased ability for polymer chains to align under stress. However, it is interesting to note the extremely high elongation since it suggests that Duraform™ necks far less than Nylon 12 which in many cases is a desirable property. It suggests the true yield stress for Duraform™ is significantly higher than that of Nylon 12. As with the other tensile results, infiltration had a negligible effect on elongation at break.

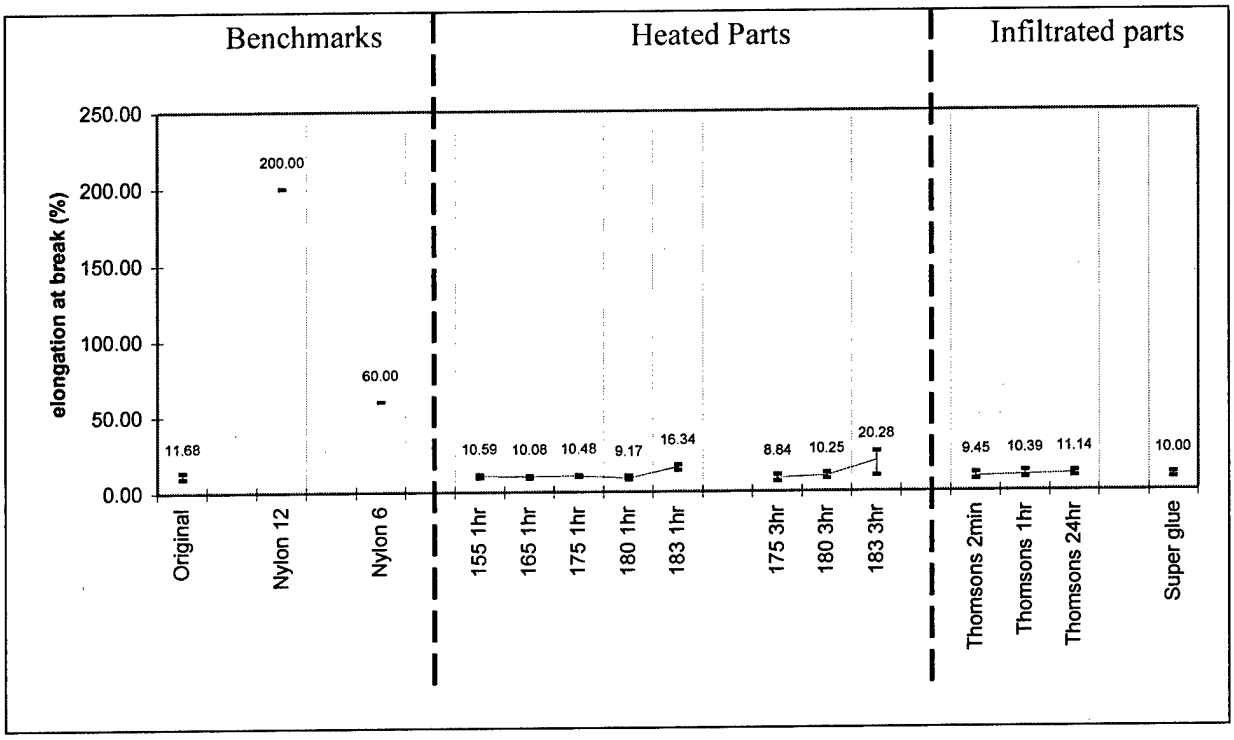

Figure 6. Elongation at break results

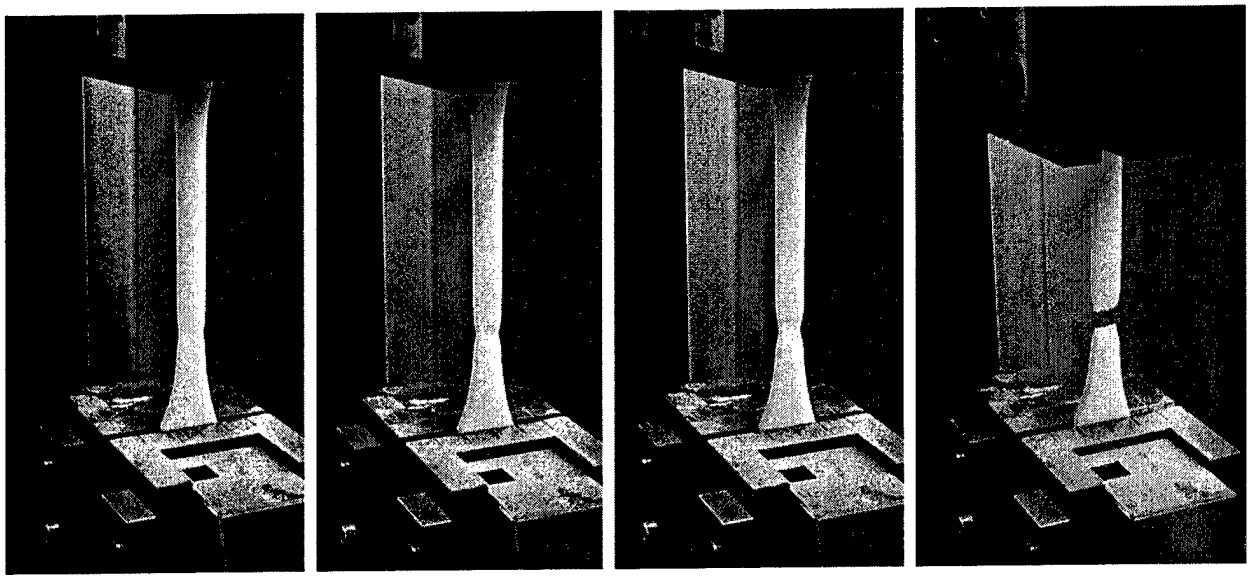

Figure 7. Necking observed in tensile test part heated to 183°C for 3 hours

Conclusions & Recommendations

The objective of this project was to investigate post-processing methods to improve tensile and impact properties of SLS Nylon parts for further investigation. The investigation suggested methods of increasing inter particle contact area would result in improvements and heating of the parts yielded significant increases in both impact and tensile 'strength'. Heating just below the melt temperature resulted in significant improvements compared with lower temperatures. The higher the temperature the better the results though close to the melt temperature issues of part distortion and necking of samples arose. Surface infiltration, commonly used to improve surface properties, was shown to have little effect on bulk properties even though the ratio of surface area to volume was quite high.

This initial research demonstrates that it is possible to modify certain properties of SLS parts to match and in some cases exceed those of comparable polymers, processed by conventional means which is very important in relation to the objective of developing RP for RM.

The two major physical attributes of parts are strength and accuracy/surface finish. When altering SLS build parameters, improvements in one will often result in detriment to the other, so that, for example, the strongest parts tend to have low accuracy and poor surface finish [10]. Therefore, a compromise set of build parameters is usually selected. However, since accuracy/surface finish appear less affected by build position a logical approach would be to bias build parameters towards maximising accuracy/surface finish and then use separate post processing to improve the part strength. This may result in parts that are accurate, strong with constant strength characteristics throughout the build. It is recommended that this is investigated by applying parts from identical build locations to different forms of post processing. A separate build would therefore be required for each PP method and spread of results could then be compared.

Some other recommendations for further investigations can be made:

- Microwaving was investigated briefly but due to difficulties encountered was not investigated further and the results not presented. Problems encountered related to lack of heating followed by extreme localised heating of parts resulting in rapid melting. However, based on microwave theory and initial findings, it is predicted that effort focussed on this could overcome the problems that arose.
- Pressing was not investigated though it could be, and is predicted would yield improvements.
- Coloured infiltrants could be used to determine accurately the degree of part penetration. Build parameters could be modified to produce parts with densities considerably below 80% to enable complete infiltration.
- Methods to compensate results for variations due to build position are vital so further research in this field would be useful.
- Combining methods of post processing such as heating and pressing could also be investigated.
- Deformation observed at high temperatures could be addressed by supporting parts in glass balls which is standard when post-processing laser sintered polymer coated ceramics.

References

1. Wohlers, T., 2000, **'Wohlers report 2000'**, *Colorado Wohler associates*
2. Caloud, H., Pietrafitta, M., Masters, M., 2002 **'Use of SLS technology in direct manufacture of Hearing aids'**, *2002 SLS users group conference*
3. Palumbo, B., 2002. **'Use of Duraform™ GF in customized Manufacturing of Air Handling Systems'**, *2002 SLS users group conference*
4. Stocker, M., 2002, **'From Rapid Prototyping to Rapid Manufacturing'**, *Auto Technology,* vol. 2 2002, pp38-40
5. Agarwala, M., Bourell, D., Beaman, J., Marcus, H., & Barlow, J., 1995, **'Post-processing of selective laser sintered metal parts'**, *Rapid Prototyping Journal*, vol. 1, number 2, pp36-44.
6. Kalpakjian, S., 2001, **'Manufacturing Engineering and Technology'**, *Prentice-Hall*
7. Bugeda, G., Cervera, M., Lombera, G. 1999 **'Numerical prediction of temperature and density distributions in selective laser sintering processes'** *Rapid Prototyping Journal*, vol. 5, number 1, pp21-26
8. John, V.B., 1992, **'Introduction to engineering materials'**, *Macmillan Press Ltd*
9. Saleh, N., 2003, **'Duraform™ heat zones'**, *Loughborough University*
10. Gibson, I., Dongping, S. 1997, **'Material properties and fabrication parameters in selective laser sintering process'** *Rapid Prototyping Journal*, vol. 3, number 4, pp129-136

EFFECTS OF CRYOGENIC PROCESSING ON RAPID PROTOTYPING MATERIALS (DSM SOMOS-8110 AND DURAFORM PA)

J.Jackson[1], G. Chapple[1], J. Do[1], X. Zhuang[1], J. Bulman[1], J. Foyos[1],
M. Mendelson[1], R. Noorani[1], B. Fritz[2]
[1]NSF Research Experiences for the Undergraduates (REU)
Loyola Marymount University, Los Angeles, CA - 90045

[2]Northrop Grumman , El Segundo, CA - 91355

ABSTRACT

This research investigates the effects of cryogenic processing on the properties of rapid prototyped materials. Not much research has been done on the post-processing (aging) of rapid prototyped (RP) polymers at temperatures below 159K (–173°F). Test specimens of RP thermoplastic resin DSM-Somos 8110 and DuraformPA Nylon were fabricated and cryogenically aged from 5-30 hours. The tensile strength and impact toughness were measured. The goal of this work was to study the effect of cryogenic aging on yield strength and ductility. This research investigated (1) the cryogenic aging of DSM-Somos 8110 and DuraformPA Nylon, (2) the effects of controlled ramp-downs/ups on the ultimate and tensile strengths of samples, (3) the experimental methods, and (4) the analysis and interpretation of the data.

INTRODUCTION

The primary objective of this research project is to apply cryogenic processing to Rapid Prototyped materials. Cryogenics is the science and art of producing cold. It started in 1877 when two scientists, Cailletet in Paris and Picet in Geneva, developed a procedure to liquefy oxygen in a laboratory [1-2]. Nowadays, nitrogen and helium are the most common cooling media. Since the normal boiling points of nitrogen and other permanent gases such as helium, oxygen and argon are about 120 K (approx. –244 °F), the cryogenic temperature is generally considered 120 K or below [3-4].

Cryogenic processing is one of the most important fields in industry today [4]. It helps to reduce costs for industry and increase industrial efficiency. For example, industrial application has reported 195% to 817% increase of wear resistance for standard steel that was cryogenically treated [2]. The cryogenic process consists of three stages based on time and temperature variables. This process starts with gradual ramping down of temperature to a specific point, the temperature is held at that point for a period of time, then the temperature is brought up to room temperature. As a result of this deep cooling and heating cycle, molecular changes occur, binding the atoms in the metal together [4].

Over the last 10-20 years, relatively little research has been conducted on cryogenic processing. Most research in cryogenics has been preformed on metals. Rapid Prototyping (RP) is a new technology the takes information from a computer-aided design file and makes a 3D part by building it one layer at a time [5]. When RP was first introduced in the late 80's, the

materials used to produce the parts had low yield strength. This experiment attempts to show that the strengths of RP materials can be increased by cryogenically processing these parts before industrial application. As mentioned before, in all the cryogenic work the scientists and engineers lowered the temperature of the sample to cryogenic condition very fast, held it to the temperature for a few hours and then ramped up the temperature as fast as possible [4]. Two years ago, the authors did research on the cryogenic processing of both ABS plastic using Fused Deposition Modeling (FDM) and DSM SOMOS 8110 from Stereolithography Apparatus (SLA)-250 machines. While the cryogenic processing did not have much effect on ABS plastic, the yield strength of DSM SOMOS was increased between 25-50% [6]. The authors believe the ramp-down and ramp–up conditions might make a significant contribution to the increase in strength of the polymer samples.

The authors have recently developed a Data Acquisition System (DAS) using LabVIEW from National Instruments that provided the programming power for the ramp-down and ramp-up conditions. The conventional and proposed cryogenic processes are shown in **Figures 1** and **2**.

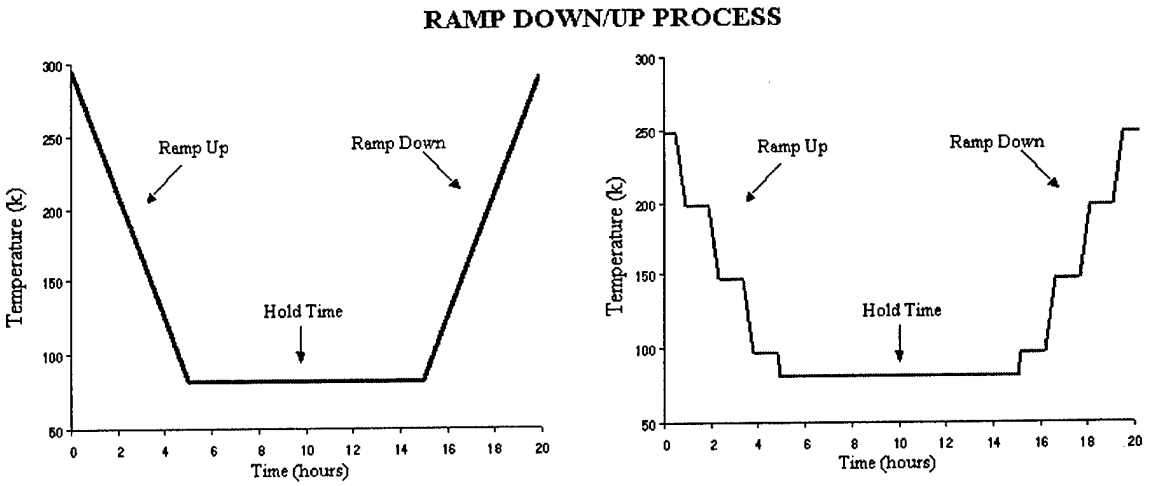

Figure 1. Original Procedure

Figure 2. Proposed Procedure

EXPERIMENTAL PROCEDURE

Equipment and Process

The following major components were used in this experiment:

1. Northrop Grumman SLA-250 RP Machine
2. Cryogenic Treatment Equipment, **Figure 3**
3. Instron Tensile Testing Machine
4. Izod Impact Tester
5. Scanning Electron Microscope (SEM)

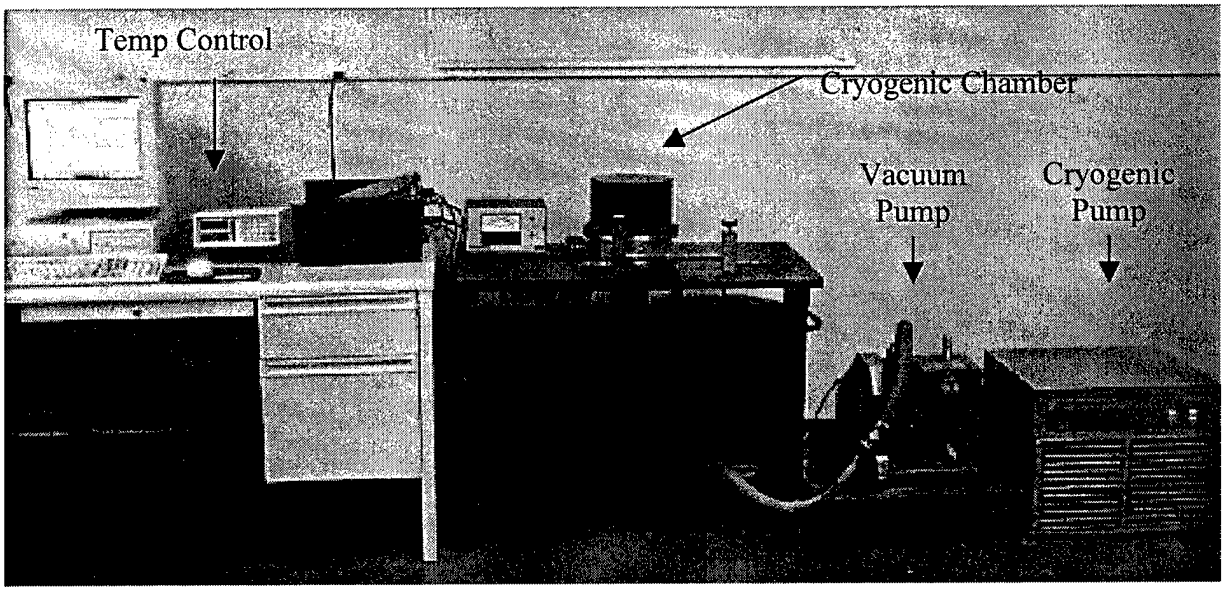

Figure 3. Cryogenic Equipment

The following **Figure 4** outlines the experimental process that was used to design, fabricate, test, and analyze the samples.

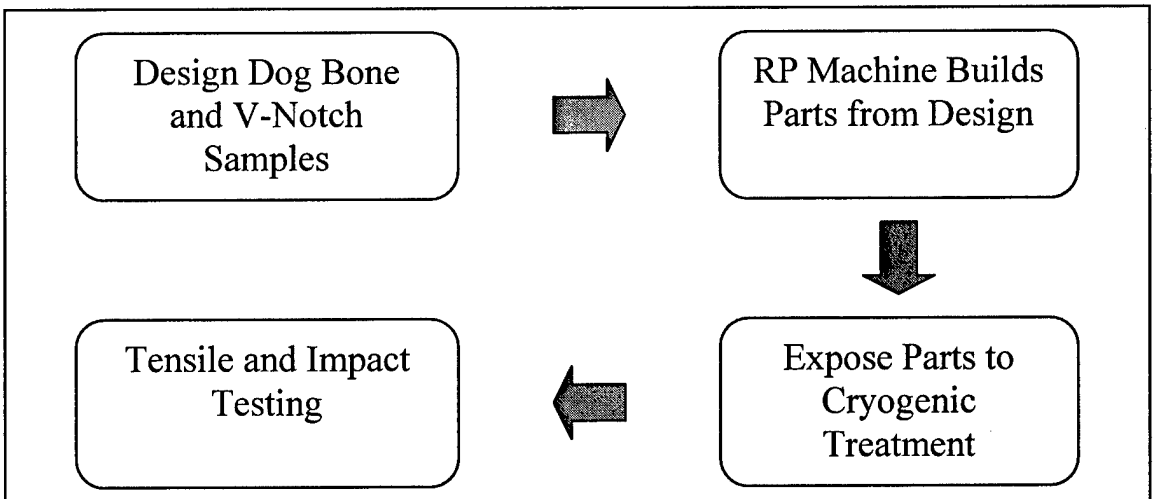

Figure 4. Outlines of Steps for the Experiment

Designing and Prototyping the Samples

Drawings of the dog bone and v-notch shaped samples were created using AutoCAD (**Figs. 5A and 5B**) and then were saved as separate .DWG files. These files were then converted into .STL format for use with QuickSlice software. The SLA-250 (Northrop Grumman) RP machine was then used to rapid prototype the parts.

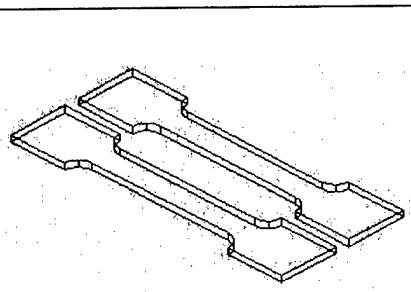

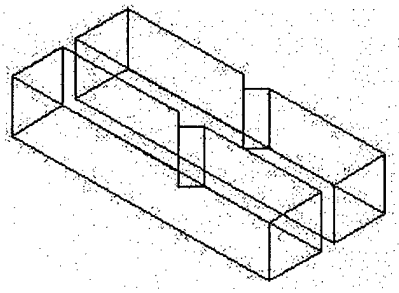

Figure 5A. Two dog bone-shaped samples. **Figure 5B.** Two v-notch-shaped samples.

Cryogenic Treatment

The following procedure was used to cryogenically treat each sample.

1. All samples except the baseline went through cryogenic treatment before testing. The samples were prepared at Northrop Grumman and processed at Loyola Marymount University.
2. The cryogenic process is characterized by three parameters: ramping down time from room temperature to 82K (–312°F), holding time at 82K, and ramping up time from 82K to room temperature.
3. Preliminary experiments are then performed on the samples with the ramping cryogenic treatment process. Ramp-down times of 5 hours are used. Holding times of 5, 8, 10, 12 and 20 hours, and ramp up times of 5 hours are used.
4. Samples are labeled as follows: XX-XX-XX. The numbers represent the ramp-down time, holding time and ramp-up time, respectively, in hours. (e.g: 05-10-05 means that the samples were ramped-down in 5 hours, held in a cryogenic state for 10 hours, and then ramped-up in 5 hours.)

Tensile Testing

The tensile strength of the samples was measured using the Instron Universal Testing Instrument 4500. The cross-head speed of the test machine was 0.0212 mm/s. The machine was interfaced using its front panel and a software program running on a desktop computer. The test specimens were created in the shape of dog-bones, as shown in **Figure 5A**. The dog-bone shaped samples were held in place by the two opposing grips of the testing platform. A computerized load cell located inside the frame unit measured the force applied to the dog-bone shaped samples. Strain was measured with an extensometer, and the stress vs. strain curves were plotted while the specimen was gradually loaded. The yield stress was measured at 0.2% offset strain, and the ultimate strength was measured at the maximum stress the material could withstand.

Four to six samples were tested for each cryogenic aging treatment (0-20 hours). The tensile strength data was statistically analyzed to determine the effects of aging treatment on yield and ultimate strength.

Izod Impact Testing

Izod impact testing was performed to determine the toughness of the treated material. The samples were made with a centered v-shaped notch. During the impact testing, the samples were subjected to an impulsive blow by a hammer pendulum. The impact test evaluates the material's resistance to crack propagation.

RESULTS AND DISCUSSION

Tensile and Impact Testing

The results of the yield strength, ultimate strength and impact energy per unit area vs. cryogenic treatment time (0-30 hours) are shown in **Figures 6A, 6B, 6C, 6D, 6E and 6F.** For the yield strength of the Somos 8110, it appears to peak at a hold time of 10 hours, which is consistent with the results of the previous year, though the results show too much variance to determine a definite trend. Three of the four points of the 10 hour hold time are above the base line, so an increase is inferred, **Figure 6A**. On the other hand, the 10 hour hold time appears to be a low point of the ultimate tensile strength graph for the Somos 8110. Again, the scatter of data points makes it difficult to discern a trend, **Figure 6B**.

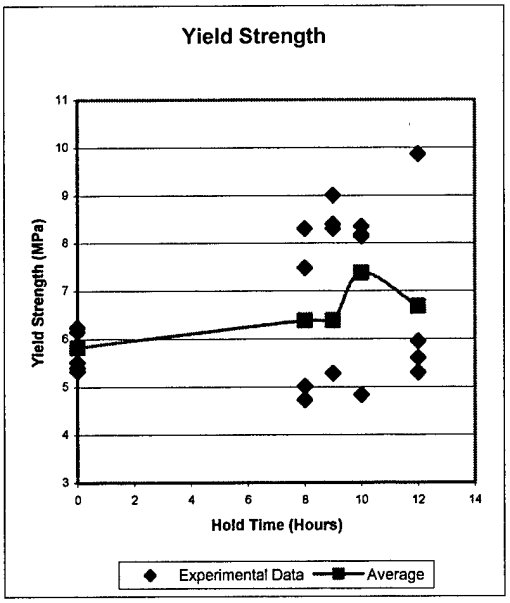

Figure 6A. Somos 8110 Yield Strength.

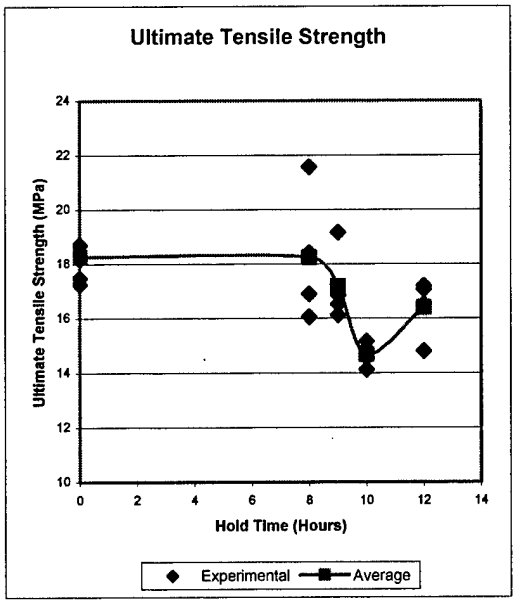

Figure 6B. Somos 8110 Ultimate Strength.

The impact energy of the Somos 8110 appears to decrease as the holding time increases. The trend, again, is complicated to find because of the erratic nature of the data -- even the baseline samples have a large degree of scatter, **Figure 6C**. As for the yield strength of the DuraformPA nylon, there is a significant drop for the hold time of 12 hours, **Figure 6D**. Further testing will need to be done to determine a reason for this effect.

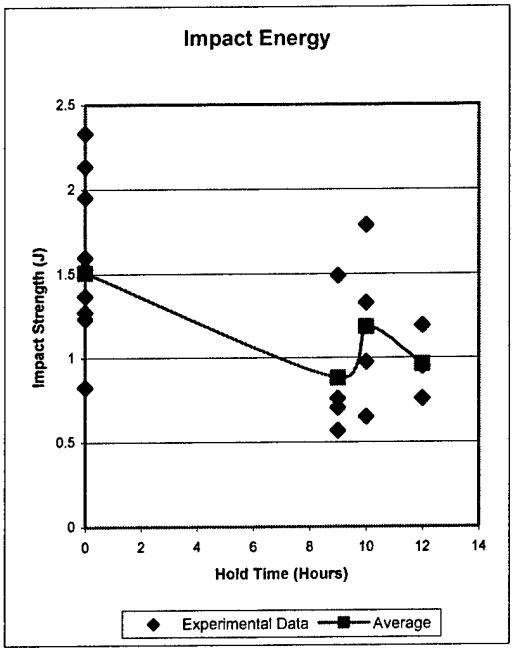

Figure 6C. Somos 8110 Impact Energy.

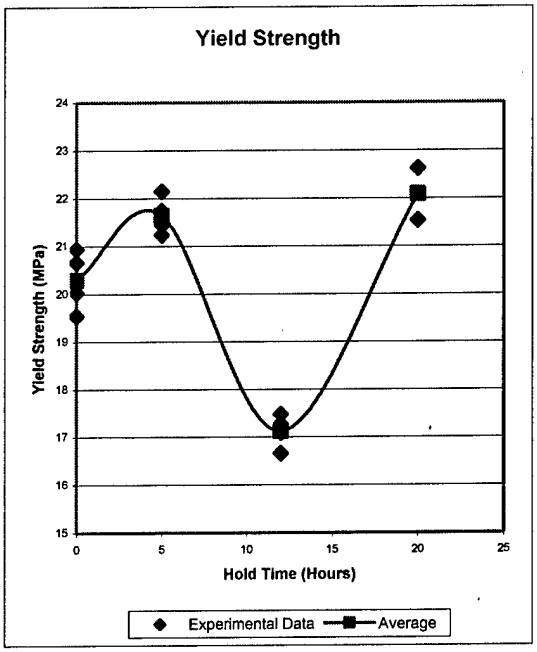

Figure 6D. DuraformPA Yield Strength.

The ultimate strength appears to increase with the increase in hold time, **Figure 6E.** Once again there is a significant scatter of data and the true trend is unclear. There is a significant increase in the impact energy at the 5 hour hold time, **Figure 6F**, with a variance of the data points as in the previous samples. The v-notch samples varied based on their position in the copper carrier. The v-notch samples were arranged four in a row. The middle samples had lower impact energies than the outside samples.

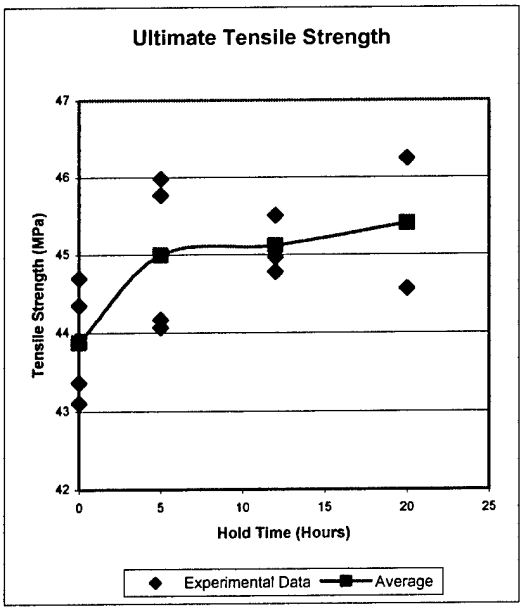

Figure 6E. Duraform Ultimate Strength.

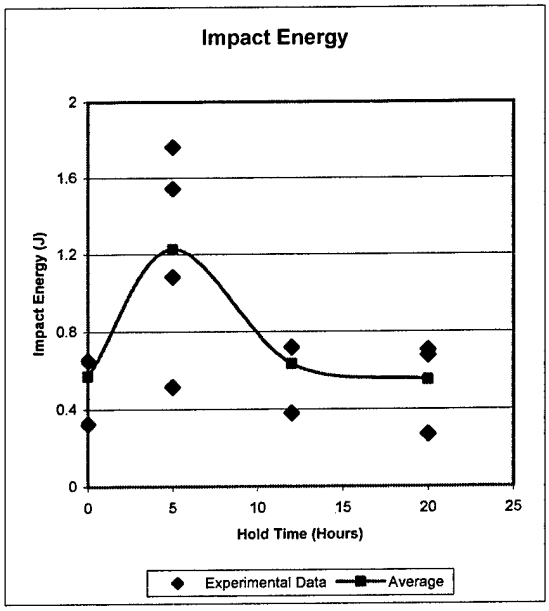

Figure 6F. Duraform Impact Energy.

The effects of ramp-down times on the yield strength and ultimate strength are shown in **Figures 7A and 7B.** In both cases, the strengths appear to be negatively affected.

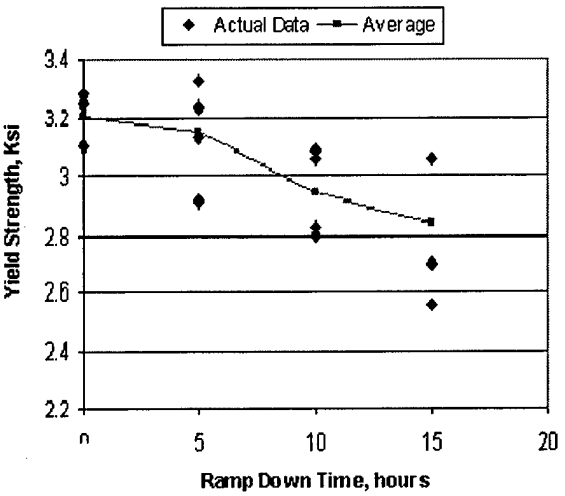

Figure 7A. Yield Strength vs. Ramp-up Time

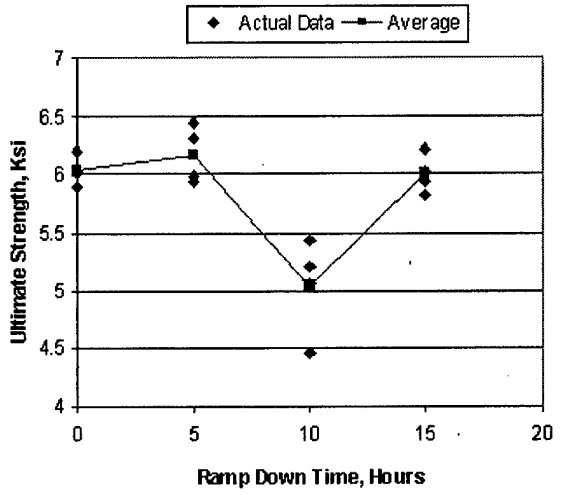

Figure 7B. Ultimate Strength vs. Ramp-up Time

Fractography

The DuraformPA Nylon samples were too ductile to produce a flat fracture surface. The plasticity was demonstrated by the necking of the sample as shown in **Figure 8A,** which also illustrates the rough surface of the break.

The Somos 8110 samples broke cleanly, producing a clear mirror which can be seen in **Figure 8B.** All Somos 8110 samples contained an array of dimples along one side, which were a byproduct of the rapid prototyping process. The dimples introduced weak points and can be seen in **Figure 8C**. The parts always broke along the dimples and this can be seen in **Figure 8D**.

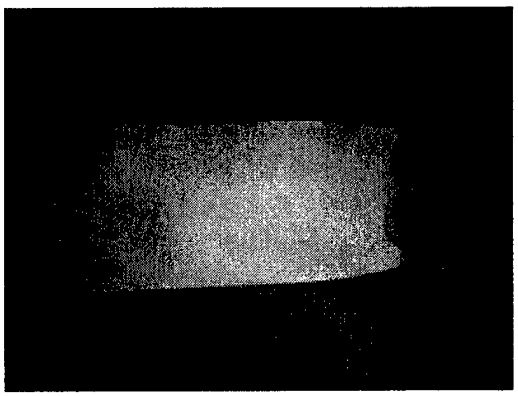

Figure 8A. Duraform PA Nylon Necking

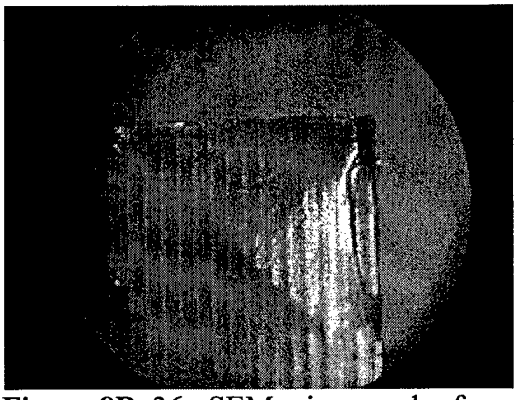

Figure 8B. 36x SEM micrograph of DSM-Somos 8110

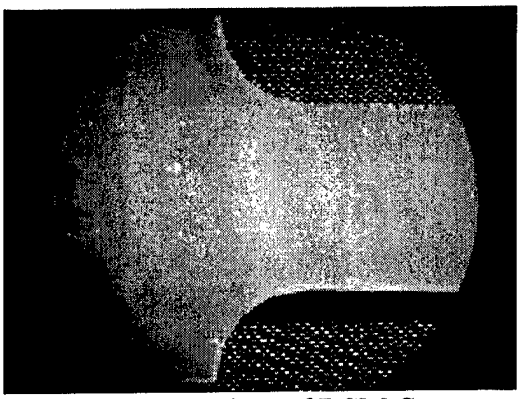

Figure 8C. Top view of DSM-Somos

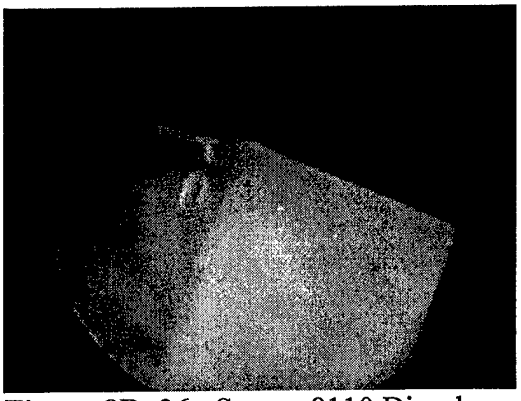

Figure 8D. 36x Somos 8110 Dimples and fracture surface

CONCLUSIONS AND RECOMMENDATIONS

Based on the findings from this experiment, the following conclusions and recommendations can be made:

1. Due to large data scatter it is difficult to determine the trend of the data.
2. The defects in the Somos 8110 samples from the previous year were corrected resulting in improved data, but the Somos 8110 contained an array of dimples that created weak points. If these dimples could be removed from the sample the results may improve.
3. The v-notch parts of both the Somos 8110 and the Duraform 8110 should be arranged around the perimeter of the copper carrier of the cryogenic chamber to ensure a uniform heat distribution to each sample during the ramp-up phase.
4. Cryogenic processing of prototypes samples has not significantly and consistently impacted the strengths of the samples. As the strengths of the rapid prototyping materials are increased through research and development, cryogenic processing of rapid prototyped samples may not be necessary.

ACKNOWLEDGEMENTS

Part of this work was funded by a NSF Grant under Research Experiences for Undergraduates. The authors also appreciate the support provided by the Northrop Grumman Corporation, as well as Dr. Bulman and Joe Foyos for their support in testing the materials.

REFERENCES

1. Scurlock, R.G., 1992, "History and Origins of Cryogenics," Institute of Cryogenics, University of Southampton, UK. Oxford: Clarendon Press.

2. Chhabra, V., July 1994, "Ingenious Cryogenics: Gainsville inventor Frank Masyada Brings the future to Our Fingertips," Business.

3. Hartwig, G., "Polymer Properties at Room and Cryogenic Temperatures," Plenum Press, New York and London.

4. Askeland, D.R., 1995, "The Science and Engineering of Materials," Third Edition, Boston: PWS Publishing Company.

5. Noorani, R. Gerencher, P. Mendelson, M. Es-Said, O and Dorman, S. "Impact of Rapid Prototyping on Product Development". Proceedings of the International Conference on Manufacturing Automation, Hong Kong, April 28-30, 1997.

6. Fritz, B., Noorani, R., 2000, "Effect of Cryogenics on Rapid Prototyping Materials (SLA and FDM 1650)", North American Stereolithography Users Group Conference, Los Angeles, CA.

Three Dimensional Printing of Tungsten Carbide-Cobalt using a Cobalt Oxide Precursor [†]

Brian D. Kernan, Emanuel M. Sachs
Department of Mechanical Engineering
Mark A Oliveira, Michael J. Cima
Department of Materials Science & Engineering
Massachusetts Institute of Technology
Cambridge, MA 02139

Reviewed, accepted August 13, 2003

Abstract

Tungsten Carbide 10 wt% Cobalt parts were formed by Slurry-based Three Dimensional Printing (3DP™). The slurry contained a mixture of Tungsten Carbide and Cobalt Oxide powders, as well as dispersing and redispersing agents. The cobalt oxide is fully reduced to cobalt metal during the early stages of the sintering process. A new binder system, polyethylenimine, is described for use with powders with acidic surfaces, such as WC. Sintered densities approach the theoretical values for WC-10% Co, and the microstructures produced are similar to those of conventionally processed (press and sinter) materials. Up to four parts were produced in a single print run using a layer thickness of 25 μm, with good dimensional agreement between them, and within the range of target dimensions after sintering.

I. Introduction

Tungsten Carbide - Cobalt is widely used due to its high strength, hardness and stiffness at high temperature, particularly in metal working and mining industries and wear coating applications. Fabricating WC-Co parts is usually done by die compaction with high associated tooling costs.[1] Following compaction, liquid phase sintering is used to achieve high density.[2] The ability to quickly fabricate small batches of prototype parts for design iterations, testing or small-scale production runs has been an impetus for the development of various layer-based manufacturing or Solid Freeform Fabrication (SFF) techniques.[3-9]

SFF of WC-9wt% Co has been previously explored by selective laser sintering of both mixed and mechanically alloyed <25 to 50 μm WC and 2-4 μm Co powders to form thick 2-D layers, but not 3 dimensional parts.[10] In metal cutting applications, small (1 micron) WC grains are needed for adequate toughness; while in wear applications, larger WC grains are tolerable. Our primary aim was applications involving metal cutting inserts (milling, turning, etc.), so micron or sub-micron powders delivered via a slurry were necessary.

Slurry-based Three Dimensional Printing [11-13] (3DP™) is another SFF technique. In 3DP™, a ceramic powderbed is formed by jetting a slurry through a small diameter nozzle

[†] Supported in part by Kennametal, Inc. Latrobe, PA.

which is raster-scanned over a porous substrate, forming a thin slip cast layer of material. After drying, a binder material is ink-jet printed into the powder bed to form the layer geometry; followed by a second drying step. This process is repeated, building each layer on top of the previous one, until the part is completed. Sufficient binder must be printed to not only form the layer geometry, but to also penetrate through the thickness of the top slip cast layer to the layer below and knit the layers together. The regions of unprinted material serve as support for the printed regions, enabling formation of complex geometries, such as internal cavities, passages or negative draft angles. After printing is complete, the binder is cured and the parts are then retrieved from the powderbed in a process called redispersion. During redispersion, water is slowly wicked into the powder bed until the pore space is saturated. Those areas where binder is printed remain held together, while those areas without binder swell and break up by osmotic pressure and can be washed away, revealing the printed part. A low power ultrasonic bath aides in removing powder from deep crevasses.

There are several aspects that make a slurry useable in 3DP™. It must produce a body with a green density of 45% or greater for good sinterability. The slurry should slip cast slow enough so that the inter-arrival time of slurry lines during deposition is about $1/10^{th}$ the time to slip cast a single line. This allows for a process called line merging, where the flatness of the bed is improved greatly when the slurry from several successive lines merge in a "wet region" before slip casting completely, as described by Polito.[14] (Bed flatness is quite important for good surface finish; a rough powderbed can cause migration of the binder along the powderbed surface in the direction of the slurry lines by capillary induced effects.) Further, the slurry must be able to be jetted through a small diameter nozzle for many hours without clogging or changing flow rate. Lastly, the unprinted regions of the powder bed must easily redisperse in water or other liquid after binder curing to enable part retrieval.

Although we did pursue both cobalt metal[15] and cobalt oxide material systems, this article will show results from the cobalt oxide route. The challenges faced in 3DP™ of Tungsten Carbide-Cobalt Oxide include reducing the cobalt oxide to cobalt metal in typically sized WC-Co cutting inserts, making a suitable slurry of mixed WC and cobalt oxide powders, and development of a suitable binder material. Each of these subjects will be explained in one of the following sections; section II on oxide reduction, section IIIA on slurry, section IIIB on binder. Section IIIC will deal with 3DP™ processing and show several green parts, and finally section IV will show some sintered properties and microstructures.

II. Cobalt Oxide Reduction - Thermodynamics and Kinetics

The primary reasons for pursuing the use of cobalt oxide was to avoid concerns about the chemical reactivity or corrosion of cobalt metal at various stages of the process (i.e. slurry milling, printing aqueous binder, and redispersing in water),[16] and to avoid the magnetic properties of cobalt metal powder in the slurry media. Since the oxide is already formed, there is no concern about reactions occurring during processing that would change the nature of the slurry. Cobalt oxide exists in two forms, CoO, which has the NaCl structure, and Co_3O_4, a normal spinel. The spinel powder was used in this work because it was available in

an appropriate size and purity. Quite recently, CoO has been used to form nano-grained WC-Co particles, which were converted to dense coatings via thermal spray.[17]

Because cobalt oxide was used rather than cobalt metal, there is a modest penalty in the green density after the cobalt oxide has been reduced to cobalt metal. The densities of cobalt and Co_3O_4 are 8.90 gm/cc and 6.11 gm/cc respectively. Thus, one cc of Co_3O_4 , which is 73% Co by weight, will be 6.11*0.73/8.9 = 0.5 cc of Co after complete reduction. For the final mixture of WC-10 wt% Co, a mixture of WC-13.2 wt% Co_3O_4 or 28 vol% Co_3O_4 was used. For this mixture, the powder volume after oxide reduction will be (1-0.28 * 0.5) = 0.86 that of the green volume. Thus, a slip cast density of 52% or greater is desired to achieve good sintered density.

Reduction of the cobalt oxide phase to cobalt metal is a critical step in the post-processing of printed parts. Thermodynamically, reduction is quite easy to achieve, as can be seen by comparison of the Gibbs free energy of cobalt oxide and water at 400 °C, table 1. The data for Fe_3O_4 is also shown for reference. The oxidation reaction of cobalt to cobalt oxide has the least negative free energy, so it is the least favorable reaction, or conversely, the reduction of the oxide to metal is most favored.

Table1. Thermodynamic data for Co_3O_4, H_2O and Fe_3O_4.

Reaction	ΔH_o^{298} (kJ/mol O_2)	ΔS_o (J/mol O_2)	ΔG at 400°C
3/2 Co + $O_2 \Rightarrow$ 1/2 Co_3O_4	-452.8	-192.95	-323
2 H_2 + $O_2 \Rightarrow$ 2 H_2O	-484	-89.4	-423
3/2 Fe + $O_2 \Rightarrow$ 1/2 Fe_3O_4	-558.8	-170.5	-444

The main concern is therefore the kinetics of reducing small particles of the oxide to metal, particularly in modestly thick bodies, at time scales amenable to sintering cycles. Figure 1 shows a TGA curve of as received Co_3O_4 powder reduced in Ar -5%H_2. The sample (~70 mg) was heated from room temperature to 600 °C at 3 °C/min. Oxide reduction begins at around 280 °C and is essentially completed by 420 °C. The weight remaining after reduction is 73.7%, indicating near complete reduction of the oxide to metal. Oxide reduction in the presence of WC was confirmed by mixing 86.8 wt% WC and 13.2 wt% cobalt oxide. The powders were milled in DIW for ~20 hrs and slip cast onto a porous plaster block. After slip casting, the sample was put in a desiccator overnight. A piece of the slip casting was then subject to the same TGA cycle as the Co_3O_4 powder, shown in Figure 2. The weight remaining is 96.5%, whereas theoretically 96.8% should remain. The extra mass loss can be attributed to water loss during the early part of the burnout (0.02 wt%) and perhaps partial reduction of cobalt hydroxide that might be formed on surfaces during the milling process in water. In the presence of WC, the temperature range for oxide reduction begins at about the same temperature (280 °C) as the case without WC present, but slight weight loss continues above 420 °C. The increase in temperature for complete reduction may be because of the higher packing fraction in the slip cast piece of WC-cobalt oxide vs. the loose packing of dry cobalt oxide powder, in which case gas flow is easier in the larger pores of the loose packed powder.

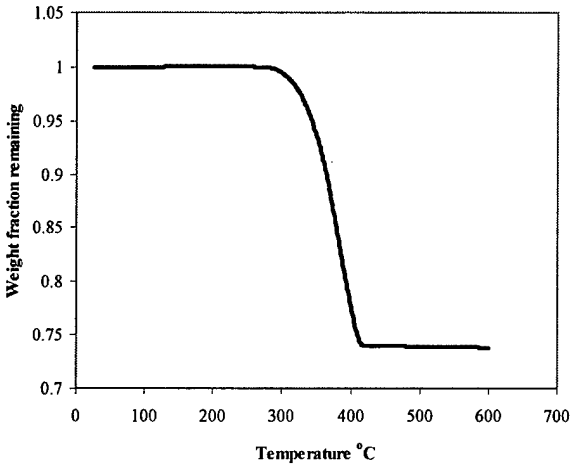

Figure 1. TGA of Co_3O_4 in Ar-5%H_2.

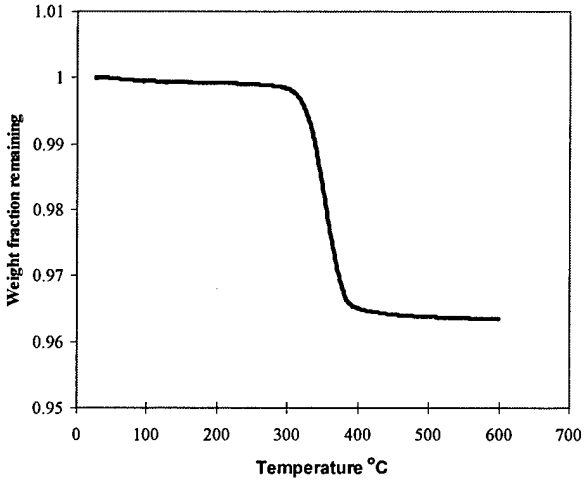

Figure 2. TGA of WC-13.2w% Co_3O_4 in Ar-5%H_2.

The kinetics of the reduction process can be viewed in the following analysis. We assume that the diffusion of gas in the powderbed is the rate-limiting step in calculating the time required for reducing the printed part. For reduction of a half-thickness, t, we first calculate the diffusivity of an H_2 - H_2O mixture according to;

$$D_{H2,H2O} = \frac{\left(1x10^{-3}\right)T^{1.75}}{P\left(V_{H2}^{1/3} + V_{H2O}^{1/3}\right)^2}\sqrt{\frac{1}{M_{H2}} + \frac{1}{M_{H2O}}} \qquad \text{eq 1}$$

where V is the atomic volume and M is the molecular weight of a gas molecule (g/mol), T is temperature (K) and P is total pressure (atm).[19] Using T = 673K, P = 1 atm, V_{H2} = 7.07, V_{H2O} = 12.7, M_{H2}=2 g/mol and M_{H2O}=18 g/mol, then $D_{H2,H2O}$ = 3.69 cm^2/sec.

Next, calculate the flux of gas across a half-thickness of powder bed with a linear concentration gradient of 1 atm at 673K assuming ideal gas behavior. For this model, assume that the powder bed is unreactive, and on one side there is a pure hydrogen atmosphere and on the other side a pure water vapor atmosphere each maintained at 1 atm. Across the bed at steady state, there will be a flux of gas

$$J = -D_{eff}\frac{dc}{dx}\frac{1}{\tau} = -D_{eff}\frac{\Delta c}{\Delta x}\frac{1}{\tau} \qquad \text{eq 2}$$

where Δc = 1.81e-5 mol/cm^3 , Δx = t = 0.3 cm, and τ is the tortuosity, which is assumed to be 3. Then J = -7.42e-5 mol/cm^2·sec.

Next, calculate the mass of cobalt oxide and hydrogen gas that are reacted in the half-thickness of powderbed. The mass of cobalt oxide in a 1 x 1 x 0.3 cm volume of WC-13.2 wt% cobalt oxide powderbed at 53% density is 0.271g, which is 1.14e-3 moles. The reduction reaction is

$$Co_3O_4 + 4H_2 \Rightarrow 3\,Co + 4\,H_2O$$

so by mass balance 4.56e-3 moles of H_2 are needed to reduce the oxide. Assuming the limiting case that all the hydrogen gas diffuses through the half thickness of powderbed,

$$-J = n/A \bullet t \qquad \text{eq 3}$$

where n is the number of moles of diffusing gas (4.56e-3), A is the cross sectional area (1 cm^2) and t is the time for diffusion (sec). Rearranging eq 3 and solving for t, we find that t = 61.5 seconds. Assuming a hydrogen gas pressure of 48 torr (5% of 1 atm), rather than 1 atm, the time is approximately 20.5 minutes, which is within the time range allowable in an industrial setting.

While this model is not exact, as it does not account for the reduced tortuosity of the reacted powderbed, or the reactivity of the powderbed; it does provide us with an upper limit of the reaction time, assuming that gas diffusion in the powderbed is the rate limiting step.

III 3DP Processing: A. Slurry Development

Two different slurries were used; a water-based slurry achieved some initial success, however better results were found with an isopropyl alcohol (IPA) based slurry, which will be shown here. The slurry formulation is shown in Table 2. Two levels of solids loading are shown for the IPA slurry, 25% and 18% of solids by volume. The WC used was Valenite 1399 powder with an average size of 0.8 μm. The cobalt oxide powder used was Umicore 73 (73.5% Co with 0.036 wt% Ni and 0.014 wt% Fe impurities, 95% Co_3O_4/5%CoO) with an average size of ~1-2 μm. Polyethylene glycol (mw 200) was used as the redispersion aid to increase the osmotic pressure in the unprinted regions of the powderbed.[20] The slurries were

balled milled in a polypropylene container using magnesia stabilized zirconia milling media. Milling times were typically 18-22 hrs. After milling, the slurry was passed through a 30 μm nylon screen to remove any gross agglomerates.

Table 2. Slurry Formulations.

	Alcohol system	Alcohol system
Powder loading, vol%	25%	18%
Weight %:		
WC	72.80	67.34
Co_3O_4	11.08	10.25
Dispersant	0.42 Polyvinylpyrolidone	0.39 Polyvinylpyrolidone
PEG 200	0.67	0.62
Liquid	IPA	IPA
Slurry density (g/cc)	3.85	3.00

The viscosity of the 25 vol% IPA slurry was measured on a parallel plate viscometer over shear rates ranging from 1 to 3000 sec^{-1} at 22 °C, shown in Figure 3. Initially, the slurry is slightly shear thinning but the viscosity becomes constant at 5 cP above a shear rate of 20 sec^{-1}. However, the viscosity at low shear rates is still quite low and the slurry is fairly well behaved.

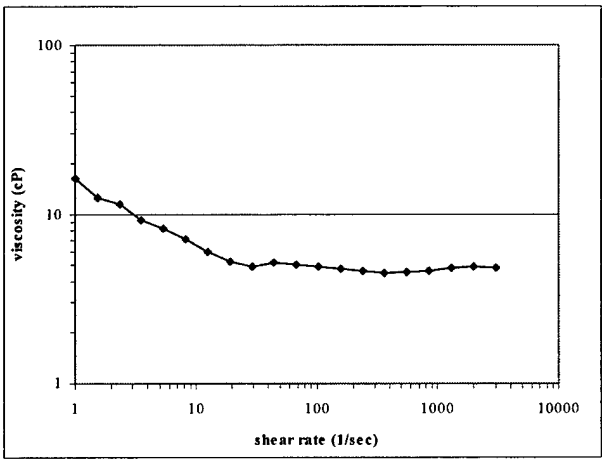

Figure 3. Viscosity of 25 vol% WC-Co3O4 slurry in IPA

The slurry was jetted through a 127 μm diameter alumina nozzle (Gaiser Tool Co., Ventura, CA) onto porous alumina substrates to form powderbeds. In our slurry jetting station, a linear nozzle speed of up to 2.0 m/sec can be obtained with a frequency of 5.8 lines per second deposited over a powder bed 100 mm wide. The fast turn-around time aides in obtaining a "wet region" and smooth powderbed.

To observe the layer roughness of the powder bed surface and find the density of the powder bed, jetted beds were formed using the 18 vol% IPA slurry at carriage velocities of 2

m/sec and slurry line spacings of 300 μm. A mass flow rate of 7.93 g/min yielded a layer thickness of 25 μm. Density measurements were by Archimedes' method in water after infiltrating the powderbed sample with a paraffin wax. Layer roughness was measured by examining successive layer height profiles taken (after slurry drying) with a laser profilometer over a 3 mm wide section of the bed with readings taken every 10 μm.

The density of the IPA slurry powder bed was 53%, resulting in theoretical post-oxide reduction density of 45.6%, which met our minimum density requirement. Typical height profiles of the powder bed are shown in Figure 4. Ten consecutive layers are shown. The average surface roughness (standard deviation of layer height) of the 10 layers is 3.7 μm, and the average layer thickness was 24.3 μm. Although the surface is not completely flat, there is little periodicity to the surface that reveals the 300 μm line spacing. The wet region visible during layer formation was about 3-5 slurry lines, only one-third to half the number (10) that Polito *et al.* describe as necessary for good smoothness. [14] (In fact, the reason for using the 18 vol% slurry over the 25 vol% slurry when making powder beds was to increase the wet region). A low-angle-light optical micrograph of a typical area of the bed, Figure 5, shows that there are still some remnants of the slurry lines in the top surface, running vertically in the photo, although these are not discernable in the profilometry data.

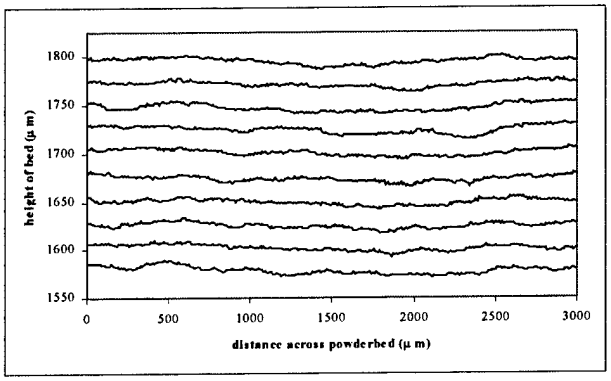

Figure 4. Laser height profiles of 10 consecutive layers formed from the 18 vol% IPA slurry. Each line is the profile of a 3 mm section of one layer scanned perpendicular to the slurry rastering direction.

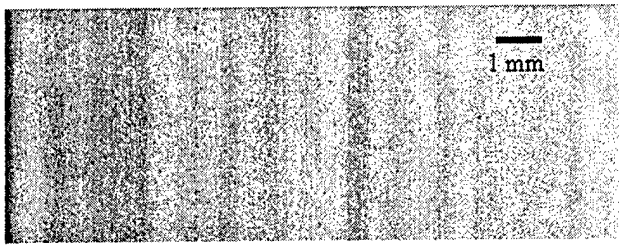

Figure 5. Top surface of jetted bed, typical region. 18 vol % slurry.

In their studies of line merging in alumina slurries, Polito *et al.* were able to form a wet zone up to 6 mm wide encompassing 30 lines with a line spacing of 200 μm. While the

3-5 line wet zone of the IPA slurry is not nearly as large, they used a layer thickness of 50 μm, versus our 25 μm. Since the time to slip cast a line is dependant on the square of the layer thickness, our results would give a wet zone of 12-20 lines at 50 μm layer thickness.

III B Binder Development

Previously in 3DP™, an aqueous solution of polyacrylic acid (PAA) and glycerol has been used as the binder, the glycerol serving as a cross linking agent during curing.[21] Holman *et al*,[22] showed that the basic surface of many ceramic powders adsorbs PAA. In the WC-Co_3O_4 system, the WC surface is acidic, while the Co_3O_4 surface is basic, isoelectric point pH=10.4.[23] Given that there is several times more surface area of WC powder as there is Co_3O_4 powder in the powder bed, it is more reasonable to have a binder that is strongly attracted to the WC, than one that is strongly attracted to the cobalt oxide.

Polyethylenimine (PEI, $H[NHCH_2CH_2]_n NH_2$), mw = 10K (Polysciences) was chosen as a new binder because of it's high pH in aqueous systems. Laarz and Bergstrom[24] previously found that PEI is a good dispersant for WC-Co in water based systems, and theorized that the dispersion was due to a combination of steric and electrostatic forces, so we theorized that it might make it a suitable binder. Following the method of Holman, a series of five 20 vol% WC slurries were made containing differing amounts of PEI, (5, 2.25, 0.75, 0.3 and 0 vol% PEI). The slurries were mixed for 19 hrs then centrifuged at 1150 gees for 30 minutes and the supernatant decanted and centrifuged again at 12000 gees for 60 minutes, and decanted again. The residual PEI concentration in the supernatant was measured by nitrogen analysis, and the remaining PEI was assumed to be adsorbed onto the WC surface. The adsorption profile of PEI onto WC powder is shown in Figure 6, along with the data pertaining to alumina from Hollman, *et al*. The y-intercept value shows the amount of binder (mg/m^2) adsorbed onto the powder surface at the point were there is no binder left in solution. The plot shows the continued increase in adsorption vs. the residual solution concentration. There is a strong tendency for the PEI to bind to the WC surface, nearly as strong as for PAA to bond to alumina, however, in the WC case, PEI continues to adsorb onto the WC as the solution concentration is increased.

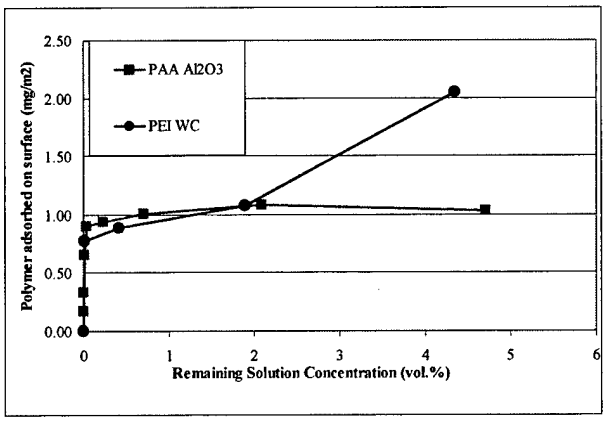

Figure 6. Binder adsorption onto ceramic surfaces. PEI adsorbs strongly to WC and PAA adsorbs strongly to Al_2O_3. PAA data from Holman et al.[22]

The binder solution used in printing is 2.5 wt% PEI (2.4 vol%) in deionized water with 0.25 wt% glycerol added as a cross linking agent. The binder solution has a pH = 9.5, and it's viscosity is 1.1 cP, making it easily printable in our drop-on-demand printhead.[25] The binder is cured in a flowing argon atmosphere at 1 atm. in an oven held at 150 °C for 1 hour. While we have no direct chemical evidence of cross linking, freshly retrieved (still wet) 0.3 μl cured binder droplets in WC-Co_3O_4 powder beds were flexible without the presence of glycerol, but stiff with the presence of glycerol. Further, cured binder droplets with glycerol were much stronger than uncured binder droplets with glycerol.

III C Processing Parameters

Typical slurry deposition parameters for the printed parts were similar to those given in section IIIA. Between layer jetting cycles, the flow of slurry was interrupted to conserve slurry. Twenty foundation layers were deposited before printing the first part layer, and five top layers were made after the last printed part layer. The slurry and binder were both dried for 25 seconds at 60 °C in a convection oven after deposition. The binder was applied in two steps, the first is the traced (or vector) outline of the layer, the second is a raster fill of the interior. Up to four separate nozzles, each producing one part, were used for several builds. The initial binder dosage after drying was 3.9% of the pore space in the slip cast bed, achieved during raster printing by using a 55 μm drop spacing at a frequency of 1272 Hz, a printhead traverse speed of 7 cm/sec, a 40 μm raster line spacing and a flow rate of 3.2 mg/min. A similar dosage was applied in the vector pass. The vector printed lines were offset 50 μm to the inside of the actual part geometry to account for the thickness of printed line.

III D Green Parts

Several geometries of green parts were printed. One was a simple square shaped insert, 16.21 mm on a side and 6.20 mm thick (252 layers), was made using the 18 vol% slurry. Previous sintering experiments on smaller printed parts had shown that the scaling factor for shrinkage in the thickness was 1.3 and in the width and length was 1.27. Thus the simple square insert would be 12.7 mm (1/2") square and 4.77 mm (3/16") thick when sintered, typical of the size of many common indexable cutting inserts. (The total volumetric reduction assuming 100% final density and the 1.27 x 1.27 x 1.3 shrinkage factors yields a starting density of 47.6%, slightly greater than the 45.6% measured by Archimedes' method on the jetted bed.) A tapered groove 0.65 mm deep extends along the perimeter of both the top and bottom of the part, simulating a chip breaking groove in a double sided cutting insert. The goal of printing this part was primarily to confirm that the cobalt oxide could be completely reduced, good microstructures developed in objects the size of cutting inserts, and to make some geometrical measurements in the green and fired state.

One of the green square inserts is shown in Figure 7. Close up views of the top and bottom surfaces of the part are shown in Figure 8 (a&b). The top surface, Figure 8a, is discernable by the relatively smooth surface, with evidence of slurry line rastering in the vertical direction. The bottom surface, Figure 8b, is discernable by the bleed through of the array of binder droplets, each binder droplet forming a spheroid on the bottom surface. Table 3 shows the average dimensions of the green parts, they are just slightly larger than the target

size. (Measurements were taken using a stereo-microscope with a stage micrometer accurate to 0.01 mm). The locations of the dimensions are shown in Figure 9. The difference between the actual and target dimensions are mostly less than one binder droplet diameter, so good dimensional control has been demonstrated in this simple part. There are some delaminations, or partial chipping, in the parts in the area of the cutting edge, indicating that a higher binder dosage was needed.

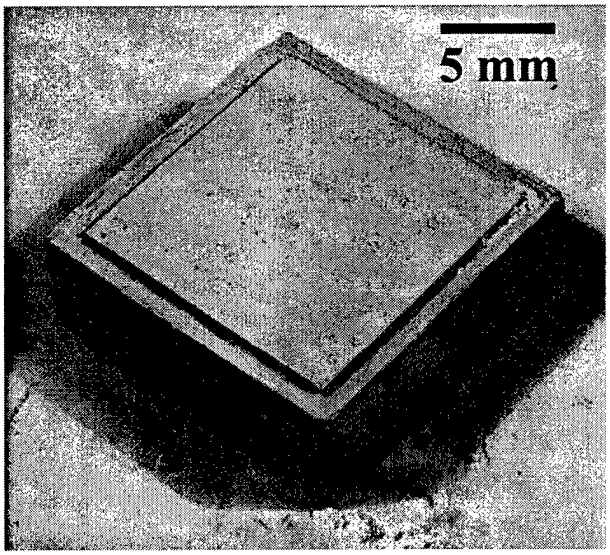

Figure 7. Square 16.2 mm x 6.2 thick insert. Shown after part retrieval.

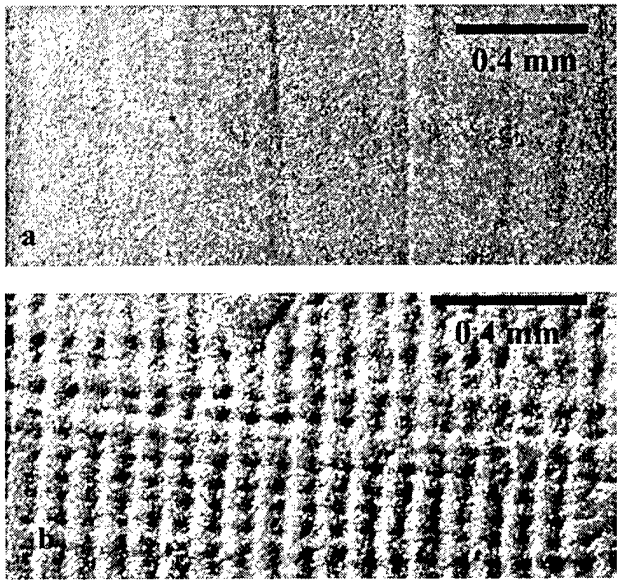

Figure 8. a) Top surface of square insert. Slurry rastering direction is vertical. No binder deposition is visible. b) Bottom surface of square insert. Slurry rastering direction is horizontal. Binder bleed through is evident by array of droplets.

Table 3. Measured dimensions of green square inserts.

Dimension	A (mm)	B (mm)	C (mm)	D (mm)
Average	16.24	16.23	13.68	13.67
Range	0.09	0.17	0.07	0.06
Target	16.21	16.21	13.61	13.61
Deviation	0.03	0.02	0.07	0.06

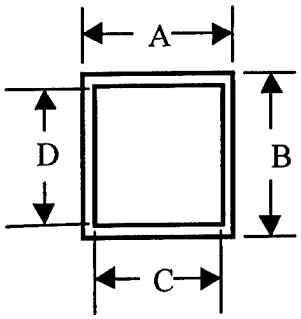

Figure 9. Location of dimensions shown in Table 3 for square insert.

A second set of four parts was the top 80 layers (2mm thick green part) of a CNMG style cutting insert. The perimeter of the part is a diamond with rounded corners and a through hole for mounting and there is much more surface detail present in the top layers than in the simple square insert. The diamond sides are 16.27 mm apart with an acute angle of 80°, and the center through hole has a diameter of 6.61 mm. The slurry parameters were the same as for the simple square insert, however a higher binder dosage was used, 4.4 % of the pore space, in order to get better knitting of the layers.

The four green printed parts are shown together in Figure 10. Figure 11 shows a top view of one of the inserts. Shown in Figure 12 are: the area around the sharper radiused corner (12a), one of the edges showing the chip breaking groove (12b), one quadrant of the countersunk through hole (12c), and the side edge of the part (12d). Printed and target dimensions are shown in Table 4. Locations of measured dimensions are shown schematically in Figure 13. Dimensions A and B are exterior dimensions, while the other dimensions are interior dimensions. Exterior dimensions will become larger than target with insufficient offset, while interior dimensions become smaller with insufficient offset. It is clear from the measurements in Table 4 that a larger offset value should have been used for printing this geometry. Since more binder was used in printing the CNMG insert than in printing the square insert, this accounts for some of the difference in part size. Further indication of insufficient offset is that the recessed text (which should read '80', '2' and 'MP') within the 3 recessed areas is mostly unreadable. The range of actual values for the four parts is quite good, a maximum of 0.07 mm, with most dimensions 0.04 mm or less, demonstrating good reproducibility in a highly complex part.

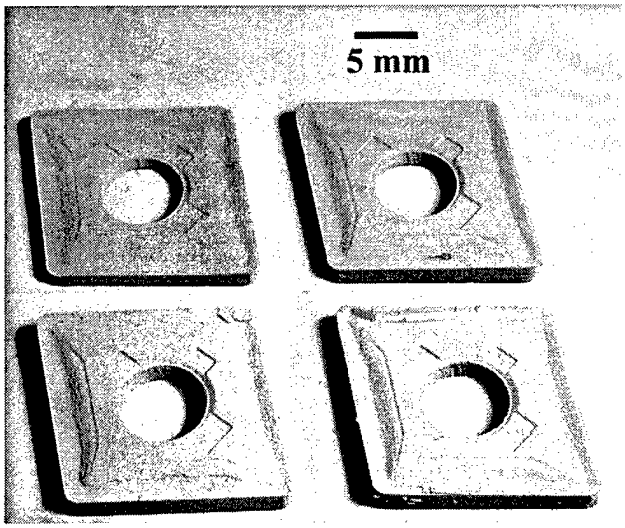

Figure 10. Four printed CNMG style inserts.

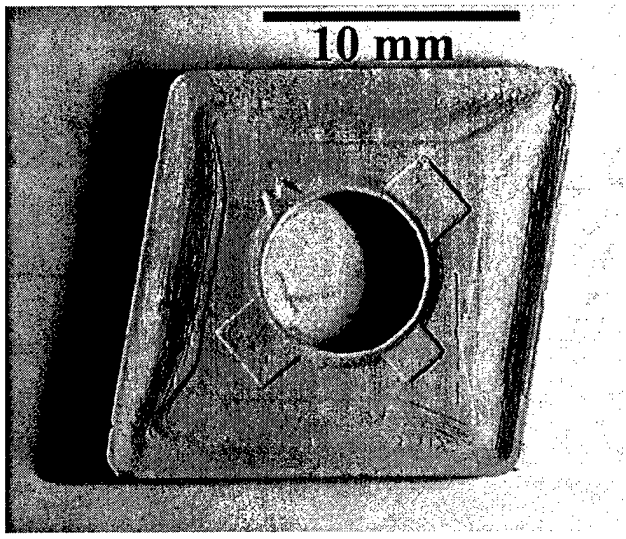

Figure 11. Top view of one CNMG style insert.

Comparing the quality of the printed regions in Figure 12, it is evident that some regions are expressed better than others. The countersunk area of the through hole (figure 12c) is among the best produced geometry on the part. The consecutively larger circles are well defined, producing a uniform stair step. The area to it right of the through hole, which slopes back down toward the chip-breaking groove, is not as clean. Several layers appear to have areas that have been washed away, as evidenced by the wavy stair step, particularly the top most layer (along the line marked "A"). The critical difference between the two areas may be the size of the horizontal step. In the countersunk region, the horizontal step is 45 μm, which is less than the thickness of one printed vector line, ~70 μm. In the sloped region the horizontal step is 80 μm for most of the steps, but 356 μm for the long step where significant washing out occurred, as noted by points A and B in the figure. The central region

of Figure 12b is similar to the right side of Figure 12c. It is possible that a higher binder dosage will preserve these geometries more precisely.

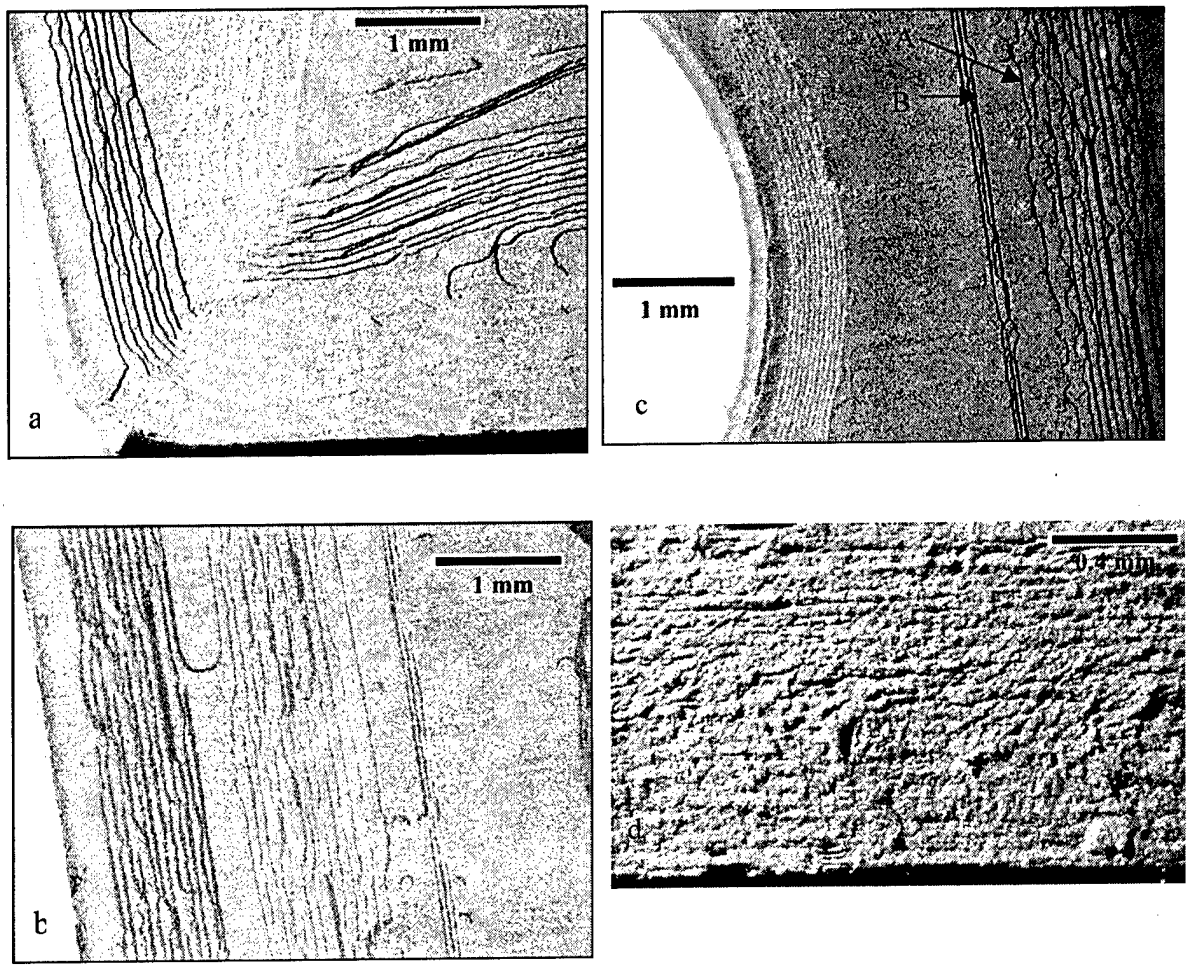

Figure 12 (a-c). Images of printed CNMG style insert. a) 110° corner. b) edge, chip breaking groove top land. c) through-hole with counter sink, top land and slope back to chip breaker. d) edge (side view), slurry rastering direction is out of the page.

Table 4. Measured dimensions of CNMG style insert (all dims in mm).

Dimension	A	B	C1	C2	D	E	F
Average	16.16	16.15	6.47	6.45	2.99	2.00	2.98
Range	0.02	0.02	0.07	0.05	0.03	0.04	0.04
Target	16.08	16.08	6.61	6.61	3.10	2.13	3.10
Deviation	0.08	0.07	-0.14	-0.16	-0.13	-0.13	-0.12

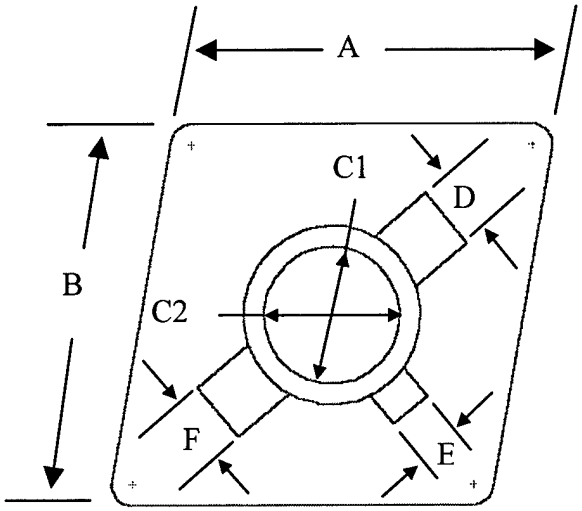

Figure 13. Schematic showing location of measured dimension given in table 4.

The side of the part, Figure 12d, is relatively flat, although there is evidence of layering in this view where all of the layers line up directly (layers run horizontally). Certainly, the side is not as flat as the top or bottom, however, the low angle lighting exaggerates the surface roughness. Shown is the side of the part that is perpendicular to the slurry forming raster direction (also parallel to the binder rastering direction). In this view, the effects of a rough powder bed surface would be maximized, because the slurry lines are running out of the page.

IV Sintered structures

The large double sided insert was reduced in a series of slow ramps, with 1 hour holds every 56 °C (100 °F) between 93 °C (200 °F) and 371 °C (700 °F) and another hold at 510 °C (950 °F) in a flowing partial pressure of 30 milliTorr of H_2., which was somewhat more aggressive than either the TGA or numerical model suggested was necessary. This reduction schedule is similar to the burnout process used with heavily lubed WC-Co press-and-sinter articles.[26] The part was then sinter-HIPed according to normal industrial practice for WC-10 Co articles, the HIP pressure being 800 PSI. Dimensionally, the sintered part is within 80 μm of the target square dimension (12.70 mm) after sintering, however the height is a bit low 4.52 mm actual vs. 4.77 mm target. The ASTM porosity rating is A04B00C00; so there are a small number of pores all smaller than 10 μm. The density of smaller similarly processed parts was 14.42 g/cc, which compares fairly well with conventionally processed WC-10 Co which has a density of 14.5 g/cc. Figure 14 shows the typical etched microstructure. The WC grain size is 1-4 μm, and some cobalt rich areas up to 15 μm are present. The number and size of pores, WC grain size and amount of cobalt pooling are within the range of acceptable WC-10 Co microstructures. There is some *eta* phase (W_2C) present in the microstructure (not visible in Fig 14), indicating that the part was partially decarburized during the oxide reduction process. Less aggressive oxide reduction would result in no *eta* phase.

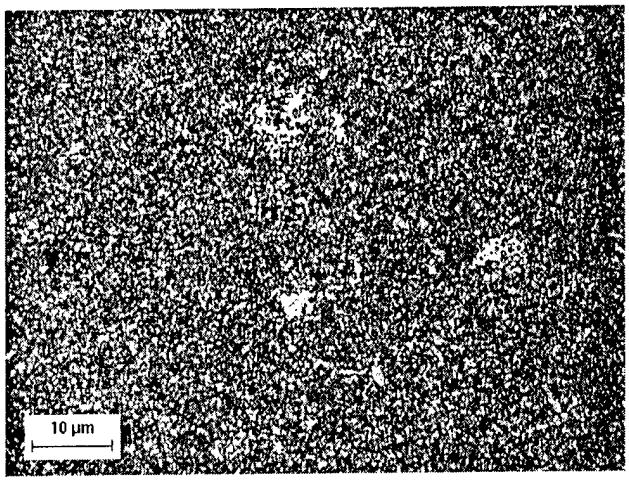

Figure 14. Etched microstructure of reduced and sintered square insert showing typical WC grain size and occasional cobalt pooling. (Micrograph courtesy of Kennametal, Inc.)

V Summary

The 3DP process has been shown to be able to produce a multitude (up to four) of both simple and complex geometry parts from a WC-cobalt oxide - IPA slurry using a polyethylenimine binder. It has been demonstrated that complete reduction of the oxide and high sintered densities and acceptable WC grain size and cobalt distribution can be achieved from the mixed WC-cobalt oxide materials in part sizes that are typical of WC-Co cutting inserts. Dimensional repeatability from part to part is excellent, and target dimensions have been met in sintered parts with simple geometries although further work is needed concerning offsetting dimensions to meet target values in complex geometries printed with higher binder dosing. Surface roughness of printed parts is good, although some wash-out of printed regions is found, indicating higher binder dosing (more than 4.4% of the pore space) may be needed. The direct manufacture of custom metal cutting tools and inserts via 3DP^{TM} is distinctly possible. Further, this route to forming fine grained WC-Co items may have implications outside of the realm of 3DP^{TM}, for instance in spray drying, slip casting or other liquid aided forming processes.

Acknowledgements

We would like to thank Mr. Chris Stratton for his programming help, Mr. James Serdy for his assistance in the lab, and also Mr. David Siddle of Kennemetal for sintering samples and analysis, printing files and materials, and the TDK Corp for assistance in developing the 3DP machine used in this work.

---

[1] K. Rodiger, H. Van Der Berg, K. Dreyer, D. Kassel, S. Orths, " Near-net-shaping in the hard metal industry," , European Conference on Advances in Hard Materials Production Proceedings (UK), 91-102 (1999).
[2] R.M. German , *Sintering Theory and Practice*, John Wiley & Sons, New York 1996.

[3] H. L. Marcus and D. L. Bourell, "Solid Freeform Fabrication Finds New Applications," *Adv. Mater. Processes*, **9**, 28-35 (1993).
[4] J. D. Cawley, A. H. Heuer, W. S. Newman, and B. B. Mathewson, "Computer-Aided Manufacturing of Laminated Engineering Materials," *Am. Ceram. Soc. Bull.*, **75** [5] 75-79 (1996).
[5] M. K. Agarwala, A. Bandyopadhyay, R. van Weeren, A. Safari, S. C. Danforth, N. Langrana, V. R. Jamalabad, and R. J. Whalen, "FDC, Rapid Fabrication of Structural Components," *Am. Ceram. Soc. Bull.*, **75** [11] 60-65 (1996).
[6] E. M. Sachs, M. J. Cima, P. Williams, D. Brancazio, and J. Cornie, "Three-Dimensional Printing: Rapid Tooling and Prototypes Directly from a CAD Model," *J. Eng. Ind.*, **114**, 481-88 (1992).
[7] D. L. Bourell, H. L. Marcus, J. W. Barlow, and J. J. Beaman, "Selective Laser Sintering of Metals and Ceramics," *Int. J. Powder Metall.*, **28**, 369-81 (1992).
[8] M. L. Griffith and J. W. Halloran, "Solid Freeform Fabrication of Ceramics via Stereolithography," *Am. Ceram. Soc. Bull.*, **79**, 2601-608 (1996).
[9] W.M. Sigmund, N.S. Bell, L. Bergstrom, "Novel powder-processing methods for advanced ceramics," J Am. Ceram Soc. 83 [7] 1557-1574 (2000).
[10] T. Laoui, L. Froyen, and J-P. Kruth, " Effect of Mechanical Alloying on Selective Laser Sintering of WC-9Co Powder," Powder Met., **42** [3] 203-205 (1999).
[11] J. E. Grau, S. A. Uhland, J. Moon, M. J. Cima, and E. M. Sachs, "Controlling Cracking of Multilayer Ceramic Bodies," *J. Am. Ceram. Soc.*, **82** [8] 2080-86 (1999).
[12] J. E. Grau, J. Moon, S. Uhland, M. J. Cima, and E. M. Sachs, "High Green Density Ceramic Components Fabricated by the Slurry-Based 3DP Process"; pp. 371-79 in Proceedings of the Solid Freeform Fabrication Symposium (Aug. 11-13, 1997). Edited by J. J. Beaman, H. L. Marcus, D. L. Bourell, J. W. Barlow, and T. Crawford. University of Texas, Austin, TX, 1997.
[13] S. A. Uhland, R.K. Holman, S. Morissette, M.J. Cima, E.M. Sachs, "Strength of Green Ceramics With Low Binder Content." *J. Amer. Ceram. Soc.* **84** [12] 2809-2818 (2001).
[14] B.F. Polito, B.N. DeBear, P.C. Saxton, E.M. Sachs, M.J. Cima "Line Merging: A Layer Deposition Technique for Fine Ceramic Powders." submitted to J. Amer. Ceram. Soc.
[15] Mark A. Oliveira "Slurry Based Three Dimensional Printing (S-3DP^{TM}) of Tungsten Carbide Cobalt," SM Thesis, Massachusetts Institute of Technology, June 2002.
[16] K.M. Andersson, L. Bergstrom " Oxidation and dissolution of tungsten carbide powder in water," *Int J. Ref. Met Hard Mat.*, **18** [2-3] 121-129 (2000).
[17] Z-G Ban, and L.L. Shaw, " Synthesis and processing of nanostructured WC-Co materials," *J. Mat Sci.*, 37 [16] 3397-3403, (2002).
[18] J.W.Evans, L.C De Jonghe, *The Production of Inorganic Materials*, New York, Maxwell Macmillan International Pub. Group, 1991.
[19] D.H. Geiger, D.R. Poirier, "Transport Phenomena in Metallurgy," Addison-Wesley Publishing Co., Reading, MA, 1973. p 467.
[20] J. Moon, J. E. Grau, M. J. Cima, and E. Sachs, "Slurry Chemical Control to Produce Easily Respersible Ceramic Powder Compacts," *J. Am. Ceram. Soc.*, **83**[10] 2401-08 (2000).
[21] J. Moon, J.E. Grau, V. Knezevic, M.J. Cima, E.M. Sachs, "Ink-Jet Printing of Binders for Ceramic Components," *J. Am. Ceram. Soc.* **85** [4] 755-762 (2002).
[22] R.K. Holman, S.A. Uhland, M.J. Cima, E. Sachs, "Surface Adsorption Effects in the Inkjet Printing of an Aqueous Polymer Solution on a Porous Oxide Ceramic Substrate. *J. of Colloid and Interface Sci,* **247**, 266-274 (2002).
[23] P.H. Tewari, A.B. Campbell, "Temperture Dependence of Point of Zero Charge of Cobalt and Nickel Oxides and Hydroxides," J. Coll Inter Sci. **55** [3] 531-539 (1976).
[24] Laarz, E., Bergstrom, L., "Dispersing WC-Co powders in aqueous media with polyethylenimine." *Int J. Ref Met & Hard Mat.* **18** (6) 281-286 (2000).
[25] Blake W. Gleason, "Positive Pressure Drop-on Demand Printhead for Three Dimensional Printing," SM Thesis, Massachusetts Institute of Technology, September, 2002.
[26] Personal communication, Dave Siddle, Kennametal, Inc., Latrobe, PA.

A GENERIC SYSTEM FOR HOMOGENOUS SLS STEEL MATERIALS

Klas Boivie
Woxéncentrum, KTH, The Royal Institute of Technology
Sweden

Abstract

A generic approach to a variety if different steel materials for SLS based application has been examined. This approach is based on a base steel alloy powder mixed with a powder blend of much smaller particles. The powder blend is designed to both provide the highest possible density in the powder mass and melting material components for liquid phase sintering to full density. Furthermore, the liquid phase components in the powder blend are composed to both serve as a metallic binder for the green bodies and maintain the possibility to completely dissolve into the base material, forming a homogenous alloy. A powder blend with stainless steel base material was composed and tested and taken through the different process steps. While the formation of green bodies had limited success, to a large extent due to limitations in the process equipment, the sintering and diffusion behaviour showed promising results, both in respect to acquired densities, and homogeneity of the material.

1. Introduction

While conventional polymer based SFF has established a position as an important strategic tool for the manufacturing of prototypes, and is gaining momentum as a competitive direct manufacturing process for parts with complex or unique shapes, a similar development for the metallic applications still seems distant. The most important reasons for this may be found in the combination of the inherent constrains within the different approaches to metallic SFF processes, and the limitations in the selections of materials, available for SFF applications [1]. Therefore, developments in theses areas could significantly improve the capacity for new applications of SFF technology. Since steel materials are established for a very wide set of applications, with a long tradition as the engineering materials of choice, most potential users are likely to have steel materials as a major point of reference. Homogenous, SFF applicable steel materials, with similar properties as conventional steels, would therefore not only improve the capacity for SFF manufactured parts, they would also bring the technology closer to the users' point of reference and thereby make it appear less alien to the potential user.

However, for such a material development to have any significant impact, it should preferably by applicable to a SFF system with a wide distribution on the market. This is possible with a procedure beginning with the formation of porous steel powder green bodies by the use of SLS, followed by metallic consolidation and homogenisation by liquid phase sintering in a subsequent furnace process. A generic approach to this procedure, where most variables can be kept constant, -except for those characteristic for the desired outcome, would not only offer SFF products of a homogenous steel material to a wider market, it would also facilitate the development of a much larger number of steel materials for a wide set of applications.
(The term "homogenous" is in this text referring to solid non-porous steel alloy, with phase structure corresponding to as-cast material of the specific alloy composition, with respect to heat

treatments. This term is used to mark the difference from the composite or highly segregated materials used in some commercial application of metals SFF.)

The whole procedure, from powder composition, application and processing in the SLS equipment, to the sintering and consolidation during the furnace treatment, is a vast area with a large number of variables, which could be used in many possible different combinations. Considering the endless possible variations, it is hardly possible to scientifically prove that such a material system and procedure is impossible. However, since this hypothesis is concerning technical matters, any successful attempt on any part of the procedure, would indicate that the whole procedure is possible, which is one principal object of this research, Another object is to find witch variables are critical to control, and how they affect the outcome of the process. In respect of this, the style of this work will be investigative and argumentative.

2. Background

The formation of parts made of homogenous steel alloy, from SLS, with a subsequent furnace procedure, is a very complex project were a number of variables may be of significant importance. This has been the subject for a series of investigations in the past [2], [3], [4], and [5]. This present work is based on conclusions and acquired knowledge from the preceding investigations as well as the application of established knowledge in conventional powder metallurgy. The approach can be separated into three distinct steps: powder composition, formation of green bodies, and the furnace process, were the limitations and results of each step, affects the conditions for the others.

2.1. Powder composition

If one step should be singled out as being the most critical, it should be the powder composition. Obviously, the powder composition determines the alloy composition of the finished material, but it is also fundamental for every part of each process step, from spreading and application of powder in thin layers, to the sintering into full density and homogenisation of the finished product.

The principal idea of the present process approach, is to combine a base material powder, which's alloy composition will dominate the finished material, with lower melting temperature components, that will serve as a liquid phase during sintering and ideally completely dissolve into the base material, forming the desired homogenous steel alloy. As a most demanding example, a stainless steel, Anval 2205, has been selected as base material for this present investigation, however the principle as such, is generic and could be applied to a vast number of different steel materials.

For liquid phase, previous work has exclusively used copper, [2], [4] and [5], partly for being established in conventional powder metallurgy, as a liquid phase with good sintering properties for iron based alloys, but also because it does improve some desirable properties, such as corrosion resistance, strength and toughness, [6].

However, the amount of copper that can dissolve into the base material is limited, and for successful liquid phase sintering into full density, with a limited amount of liquid phase, it is important to have the powder mass as dense as possible. This has been experienced and

addressed in the past [2], [4] and [5]. It was found that using a suitable combination of size ranges and particle shapes in the correct proportions, will improve the density of the powder layers applied in the SLS equipment, [3]. Since the base material is expected to remain stable, and maintain the geometrical shape of the part during the furnace process, the base material should obviously be the largest fraction and also largest sized particles in the powder blend. Additional components, such as the melting material, should, if possible be kept at particle sizes that will fit into the voids between the larger particles.

This approach has been tried with -44μm Anval 2205 powder, copper powder of the smallest particle size available, and with an additional amount of small particle size carbonyl iron powder for further densification, [5]. However the high inner friction, and the unexpected unfavourable size range relation between base powder and copper in the powder mass gave the powder blend poor particle packing properties. This, in combination with the low fraction of melting material for the liquid phase sintering (8%), made it impossible to achieve full density in the material. Therefore has this present investigation changed the size range for the base material to 44μm - 75μm, and added a second melting material: ferrophosphorus. ***Fig.1. & Tab.1, Fig.2. Fig.3. & Tab.2, Fig.4. & Tab.3.***

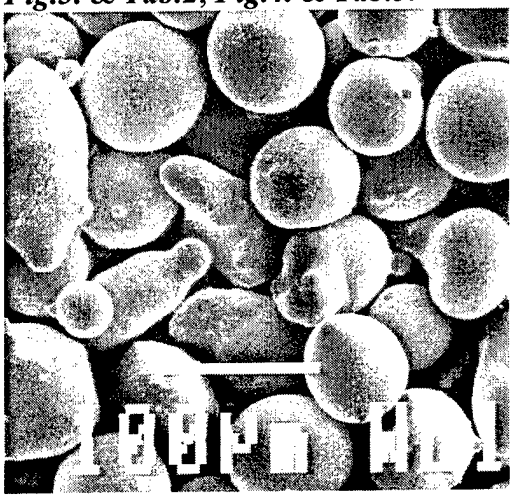

Fig.1. Anval2205. A stainless steel material, with the characteristic smooth shape of gas atomised metal powder. This alloy has been selected as a challenging material with interesting properties. Size analysis: ASTM-E11 sieve, 99 %< -75μm, 9 %<-45μm.

C	Si	Mn	P	S	Cr	Ni	
0.019	0.70	1.17	0.017	0.002	22.3	5.17	

Mo	Nb	Cu	Co	V	W	N	O
3.02	0.00	0.16	0.03	0.07	0.02	0.19	165

Table 1. *The chemical composition of the stainless steel base material, Anval 2205, O in ppm.*

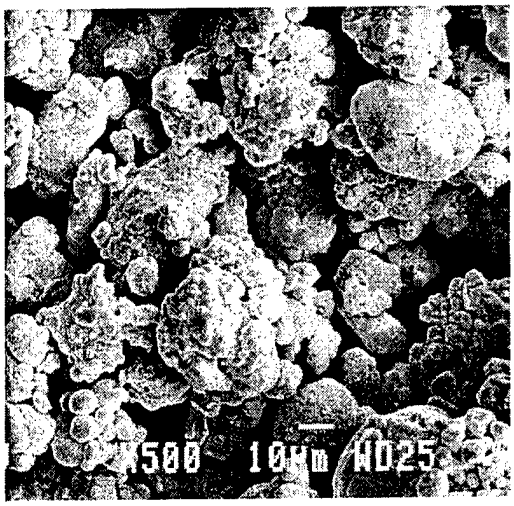

Fig.2. Copper powder, 99.9% Cu. According to vendor1-5 μm spherical shape, which in reality obviously is not the case. This discrepancy is however most likely due to the method of measuring and calculating size. In many cases are such small sized particle's sized estimated by a measured value for particle surface that is recalculated to volume and diameter assuming spherical shape. For a sponge like powder such as this, this method would indicate a much smaller particles size than really is the case. For this investigation this defect will not disturb the size range composition, however, it will limit the density improvement.

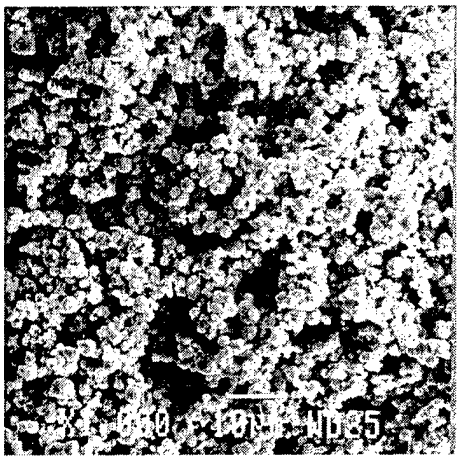

Fig3. Carbonyl Iron SM: almost pure iron, with the spherical shape typical of carbonyl metal powder. In this size range (2-8 μm), the interparticle friction is associated with van der Waal's and electrostatic forces, and is thus increasingly independent of particle shape. Nevertheless, the spherical shape still is the best possible considering the achievable packing properties.

Fe	C	O	N
Min. 99.0	Max. 0.2	Max. 0.8	Max. 0.1

***Table 2.** The chemical composition of the filler material, Carbonyl SM*

Fig.4. Ferrophosphorus powder, coarse and uneven. Particles. This has normally a negative effect on powder packing properties. However at this size range are these properties dominated by the powder mass' internal friction, associated with van der Waal's and electrostatic forces. For this investigation, surface smoothness of ferrophosphorus particles will be of minor importance.

Fe	C	Si	Cr	Mn	P	Ti
Base	0.78	Max. 0.50	Max. 0.50	Max 0.50	15.6	Max 1.50

***Table 3.** The chemical composition of ferrophosphorus powder. Physical properties (Sympatec): 10% below 2.61 μm, 50% below 8.25 μm, 90% below 15.23 μ*

Phosphorus, P, is a well-known additive to powder compositions to improve sintering properties by liquid phase sintering, though other positive side effects, such as improved tensile strength, elongation and hardness, with small additions of P, has been reported from conventional powder metallurgy, [7]. The best results were acquired with additions of 0.75 % - 0.80% P, and the added amount of ferrophosphorus will therefore be adjusted to yield this content of P to the finished material.

2.2. Formation of green bodies

This process is expected to be capable to deliver hollow parts and geometries with deep cavities, and since the part in all cases will be subjected to a significant shrinkage during liquid phase sintering, a supportive powder during the furnace process is not desirable. Therefore, organic binders, requiring a supportive powder during the binder burn out and the early stages of sintering, should be avoided. This issue has been addressed in previous work, [4] and [5], and it has been found that despite the low absorbance of energy from a carbon dioxide laser, copper can be melted during SLS processing and thus work as a metallic binder. The green bodies formed are however quite brittle, with especially weak bonds between the layers. On the other hand, in this present investigation, there is possibility that the second melting phase, ferrophosphorus, also could melt at process conditions and improve this situation.

Since copper has such low absorbance for energy transmitted by carbon dioxide lasers [8], it is more likely that it is secondary heating that melts the copper. The laser energy is absorbed by the iron-based particles, which in turn heats the adjoining copper particles until melting and bonding occurs. If so, the increased particle size will require more energy to raise the temperature of the base material particles to the melting point of copper (1084.5 C) and even more for ferrophosphorus, (melting point 1168.0 C), if the same heating mechanism is active as in copper. Since the equipment available for this investigation is a rather old Sinterstation 2000, 50 W CO_2 laser, with a measured maximum output of 41.5 W, this may be a crucial limiting factor for the formation of green bodies. However, the formation of perfect green bodies is not the primary object of this investigation, but the establishment of a generic principle for a series of homogenous steel materials that could be achieved from a procedure consisting of SLS and a subsequent furnace process. For this object, sintering and homogenisation behaviour is more vital, and it is sufficient to show that green bodies *can* be formed by SLS, while quality is of less importance at this stage.

2.3. Furnace process conditions

The feasibility, as well as process time and temperatures for the furnace procedure, in order to achieve a homogenous, liquid phase sintered steel material, are determined by some important boundary conditions. First of all, the process parameters must allow the liquid components (here: copper and ferrophosphorus) in the powder composition to melt and sinter the material to full density. Second, the process time and temperature must be sufficient for the liquid material to completely dissolve into the base material, as well as allowing the alloy components from the base steel to homogenously be distributed within whole part, -both by means of diffusion. Third, since the risk of evaporation of alloy components from the material during the vacuum process is controlled by the combined effect of temperature and pressure, there is an upper limit on the acceptable temperatures, -or a lower limit for pressures, at process conditions. Meanwhile the pressure in the process chamber must be kept low enough to allow desoxidation of the material during the process. Fourth, the processing time must be as short as possible, partly to avoid unnecessary grain growth, but also to keep the process times at a competitive level.

However, this complex situation can be simplified by applying standard settings for vacuum pressure, and thus leave time and temperatures as the process controlling variables. Further simplifications can be made by application of conclusions from previous work. It has been found that at standard vacuum settings, temperatures above 1200 C will cause evaporation of chromium from stainless steel powder, (1233.6 C for 22.4% Cr) [5]. Therefore 1200 C can be considered a maximum process temperature, which, in combination with vacuum, will allow the desoxidation reaction between carbon present in the powder blend, and oxide on the particles' surfaces. This leaves process time as the critical variable to control.

Since the copper's only means for dissolving into the steel material under these process conditions is by self-diffusion, and the longest predictable diffusion distance for any material under these circumstances is from the surface to the centre of the largest particles, the diffusion of copper through the base material will be the determining factor of the process times. This simplification may overlook the closure of large pores, but the occurrence of those, as well as their size and distribution, is not entirely predictable, and must be experienced experimentally.

The previously mentioned investigation, [5], also found that 4 h would be sufficient process time for 8 % copper to completely dissolve into -44μm base material steel powder. However, in this present investigation has the size range for the base material been changed the to 44μm - 75μm, and ferrophosphorus has been added as a second melting material. The increased particle diameter gives an increased maximum diffusion distance, which, reasonably, would increase the required process times beyond practical and competitive limits. However, that investigation and the following estimation of process time are based on the assumption of the atomic configuration of γ-iron, which would normally be the phase present for most steels at process temperatures, especially since the added copper is γ-stabilising. But, in this case, ferrophosphorus is added as a second melting material, and this could vitally change the conditions for the diffusion of copper and other alloying components.

Phosphorus is known to have a powerful stabilising effect for α-phase and, compared to for example copper, a rapid diffusion behaviour in both α-, and γ-phase. Therefore, the hypothesis is, that the phosphorus will diffuse into the base material of γ-phase configuration, ahead of copper and other significant alloying components, and thus cause a phase transformation to α-phase. Since the atomic configuration of α-phase steel allows much higher rates of diffusion for copper than γ-phase, this would probably make it possible to achieve homogeneous distribution of alloying- and former liquid components in the finished steel material within reasonable process times. This, in combination with the additional amount of liquid phase and increased powder packing densities could make it possible to achieve a homogenous steel material with no, or very low porosity, by SLS and a subsequent furnace processing.

2.4. Calculations

The time to dissolve the copper into the base material is controlled by the fractional saturation of copper in the base material particles. Darken & Gurry [9] gives us the relationship:
For diffusion into spherical shape: $Dt/L^2 = -0.05043 - 0.2333\log(1-F)$, **[Eq. 1]**

Diffusion constant, $D = D\gamma_{Cu}^{Fe} = 1.8\exp\left(-295kJmol^{-1}/RT\right)m^2/s$, **[Eq. 2]**, [10].

Fractional saturation, $F = \frac{C_m - C_0}{C_s - C_0}$, **[Eq. 3]**, and L is the diffusion distance, here the radius of the base material particles. From previous work [5], we know that at 1200 C, 8% copper can theoretically be completely dissolved in spherical -44μm steel powder, in 3.85 hours. For reasons previously mentioned, a particle size range of 44μm - 75μm has been used for this present investigation. With 75μm powder particles, the diffusion distance is 0.00375 cm. Added copper, $C_m = 8\%$, at 1200 C saturation of copper is $C_s = 9\%$, which gives $F = 0.889$. Applied to **[Eq. 1]**, $Dt/L^2 = 0.17$. At 1200 C is $D\gamma_{Cu}^{Fe} = 6.21\cdot10^{-11} \Rightarrow t = 369.42$ h, which is too long. However, with phosphorous induced phase transformation, diffusion is expected to take place in α-phase where,

$D = D\alpha_{Cu}^{Fe} = 8.6\exp\left(-250kJmol^{-1}/RT\right)m^2/s$ **[Eq. 4]**, [10]. Under these conditions $D\alpha_{Cu}^{Fe} = 1.17\cdot10^{-8} \Rightarrow t = 204.32$ s (!), which is much more reasonable.

However, these ideal conditions cannot be fully expected under real process conditions. For example, if the material has sintered to full density, the particles will not be spherical during the whole dissolving process. Complete homogeneity concerning pore size and orientation, or particle distribution within the green body can neither be expected. Furthermore, the liquid phase will be a solution melted copper and ferrophosphorus, which means that the concentration of the different elements will vary during the process, and during the diffusion of copper, the balance between α-, and γ-phase in the outer perimeter of each particle is difficult to predict, and therefore also the real diffusion rate. Considerable longer process times will therefore be used for this investigation, however the calculations above demonstrates that complete dissolving and diffusion to homogeneity is not unreasonable to expect with this material composition and process conditions.

3. Experimental

The experimental part of this investigation follows the principles outlined in the background section. The powder blend is composed to yield maximum applied powder density using the selected powders. Green bodies are formed using SLS equipment, and processed to full density in a vacuum furnace. Samples examined regarding porosity and have been further analysed regarding alloy composition and distribution using SEM equipment at the Department of Materials and Engineering, KTH.

3.1. Powder composition

The different selected powder materials have to be combined in the correct proportions to yield the expected results. The amounts of the different liquid components is determined by their respective solubility in the base material, and possible desirable effects on the material properties of the final alloy. Copper has a good solubility in iron-based alloys up to around 8 %, at process conditions, which settles the share of copper. Phosphorus has been reported to have most positive effect on material properties at 0.8 % P. The added ferrophosphorus contains 15.6 % P, which makes an addition of 5.12 % yield the desirable amount of P in the final material. This combination would give a liquid share of 13.12 %, which is slightly less than conventional, [11]. However if the experiment should indicate that the liquid share is too small for pore closure, it is possible to increase the addition of ferrophosphorus.

Besides getting the right amount of liquid phase, it is also important have the highest density possible in the powder mass. Since the amount of small sized particles for the liquid phase has been determined by other boundary conditions, the remaining means to control this issue is the combination of large particle base material, Anval 2205, and a fill material powder with much smaller particle size, in this case Carbonyl Iron SM.

The suitable proportions was found experimentally using the procedure described in [3], with the amounts of copper and ferrophosphorus kept constant at 8 % respective 5.12 %. The final powder composition can be seen in ***Tab.4. Fig.5,*** showing the powder blend gives an impression of particle size proportions and packing behaviour. The density of the applied powder layers in the SLS equipment was measured by the procedure described in [3], and was found to range between 65.8 % and 67.4, which seems promising for the following process steps.

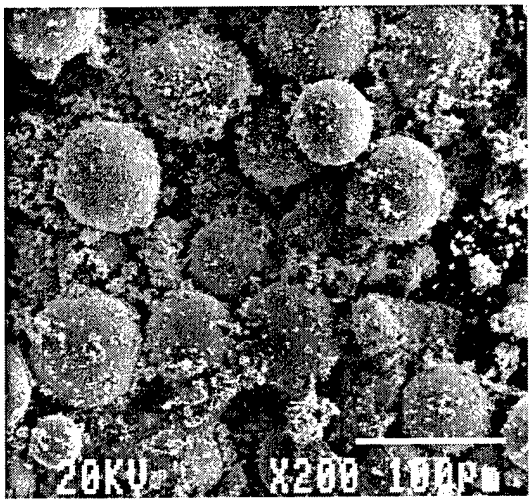

Anval 2205	*Carbonyl SM*	*Cu*	*Fe_3P*
75.88 %	11.00 %	8.00 %	5.12 %

Table 4. *The composition of the powder blend.*

Fig.5. *The powder composition after mixing.*

3.2. Formation of green bodies

The determined powder composition was exposed to SLS processing for several attempts with successively increased laser power and decreased scanning speeds before any usable green bodies could be formed. This occurred at the very limit of machine capacity. Apparently, the assumption concerning the need for increased energy due to the increase in base material particle size was correct. Still, green bodies were formed, however of poor strength, with very weak bonds and high porosity between the layers, and with a strong tendency for curling of the layers. It is a likely assumption that only copper melted to serve as a binder, and that this situation could improve, -in terms of improving green strength by melting the of ferrophosphorus, with the use of a more powerful laser, such as the 100 W laser common in more modern versions of SLS equipment from DTM/3Dsystems, or the even stronger lasers used by EOS.

3.3. Furnace processing

Samples were sintered in a conventional vacuum furnace, in accordance with conditions described in the calculations section, and the principles described in [12]. The parts were placed on an alumina bed, in a graphite crucible, with no supportive powder and loaded into the furnace. The temperature was raised to 1200 C at a rate of 200 C/h. held at that temperature for 4 h, when the temperature was lowered at the same rate.

4. Results and analysis

The samples had sintered to solid objects and undergone some shrinkage, ***Fig.6,*** notable is the fact that the samples with less successful layer adhesion have had less shrinkage in X –Y –direction, instead, the more separated layers have had a predominant shrinkage in Z –direction, whereas the samples with more successful adhesion between the layers have shrunk more equally in all three dimensions. Furthermore, some sagging of large overhangs can be noted. Looking deeper into the material we find that there are some remaining pores, predominantly oriented in between powder layers, ***Fig.7.*** However none of these imperfections are unexpected, and could probably be traced to the less than perfect conditions during the formation of green bodies.

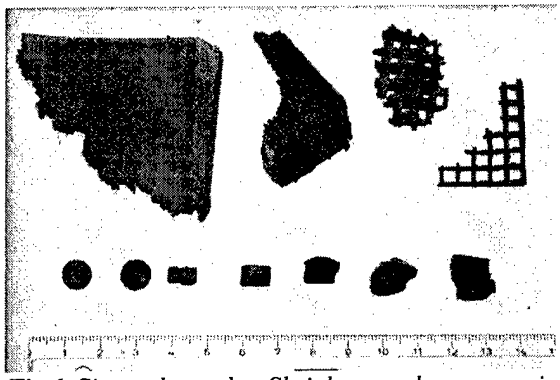

Fig.6. Sintered samples. Shrinkage and some sagging of overhangs are evident. Especially notable is the shrinkage of the cylindrical samples in the bottom line. The same STL file and laser power was used for all of them, however with different scanning speeds.

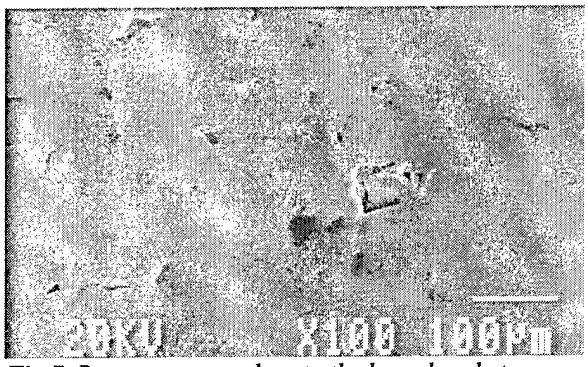

Fig.7. Pore structure, close to the boundary between two layers. The porosity increases with decreasing layer adhesion due to increased curling of the layers at lower laser scanning speed

More interesting, still, is the analysis of material alloy and distribution of alloy elements in the material. It shows that complete homogeneity has not been reached, which is quite reasonable, complete homogeneity hardly exist even in conventional steels. Certain elements naturally concentrate into certain phases, and nothing else could be expected under these circumstances. But the distribution analysis as shown in ***Fig.8*** and ***Fig.9***, displays encouraging tendencies.

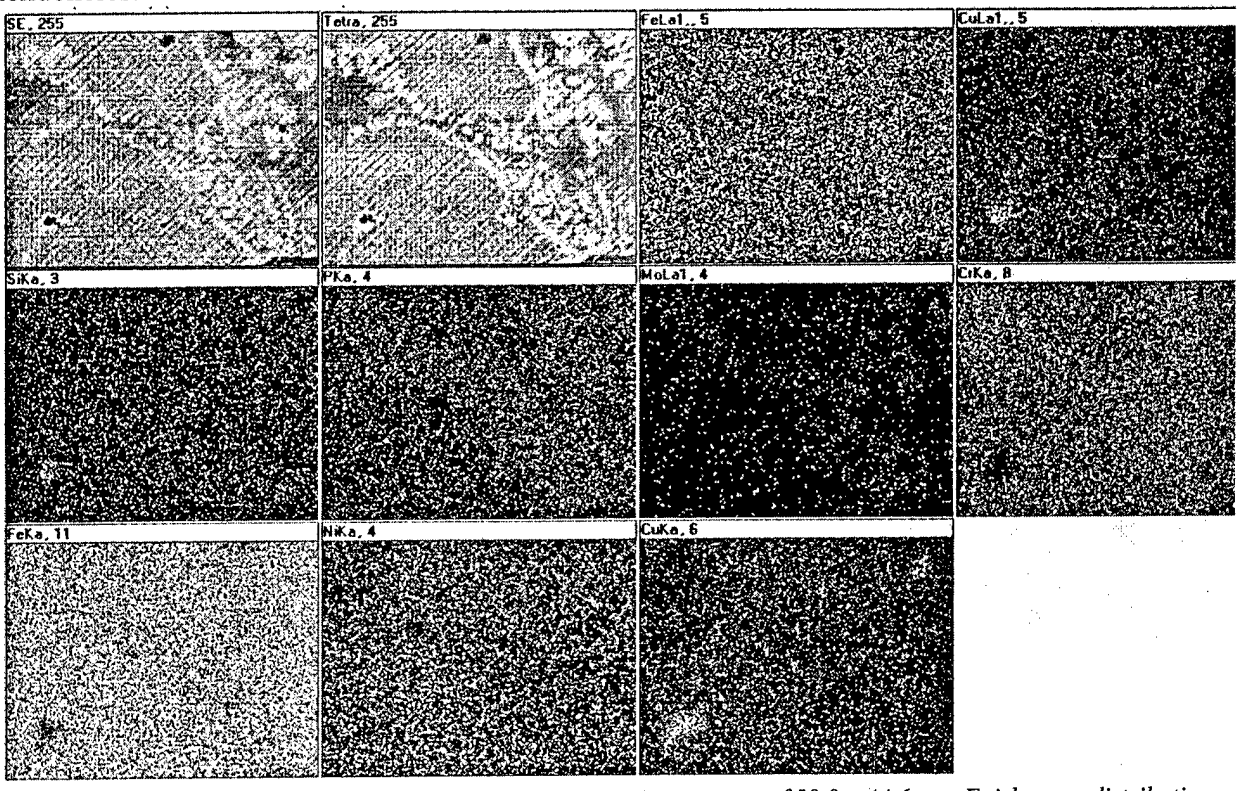

Fig.8. First distribution analysis of important elements covering an area of 58.9 x 44.6 µm. Fairly even distribution throughout the part, however complete homogeneity has not been reached. As could be expected have some elements, such as Mo, had the tendency to concentrate to certain phases as is normal in conventional steels. Also interesting is the area of Cu and Si concentration in the lower left side corner. Apparently has this been an area where larger amounts of liquid phase has been gathered than could be dissolved in the surrounding base material.

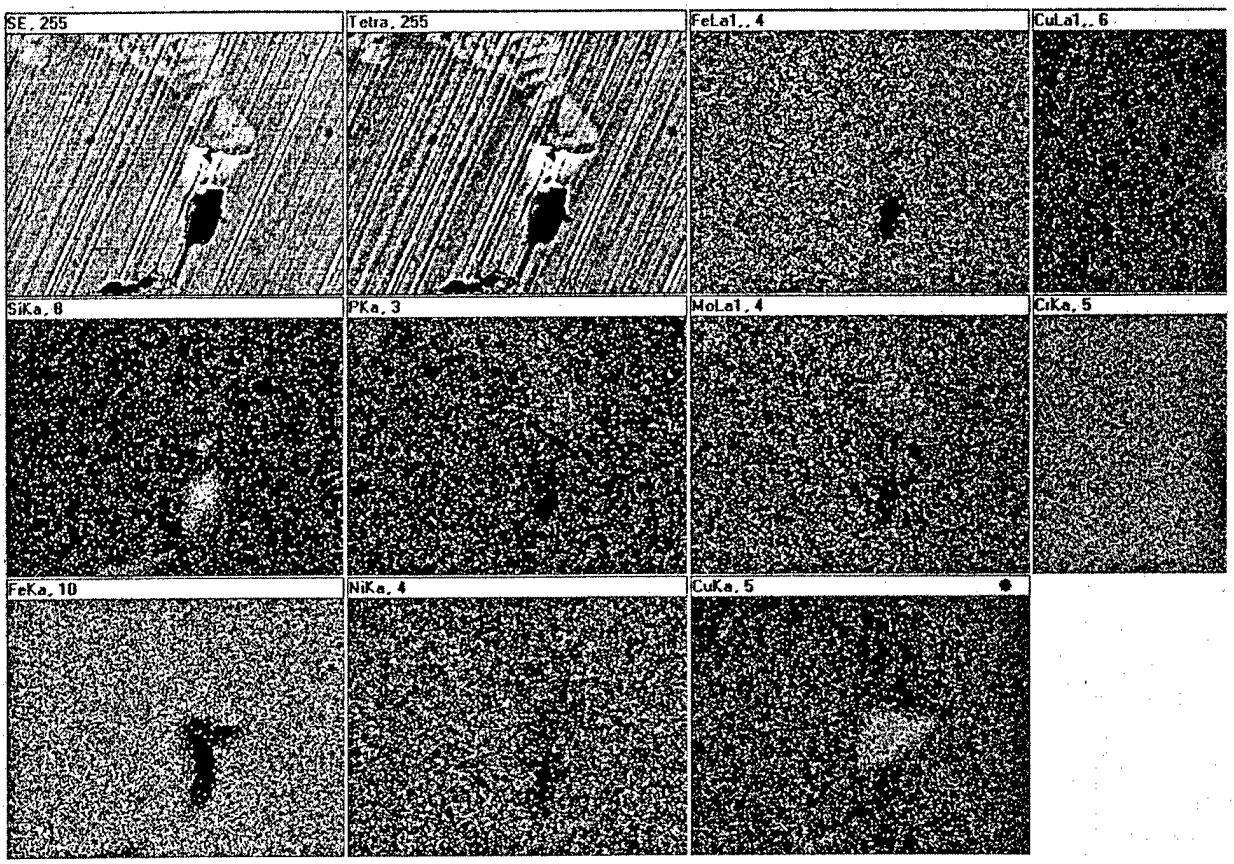

Fig.9. *The second distribution analysis of important elements covering an area of 51.0 x 42.5 μm. The tendencies from previous analysis appear to be confirmed. There are some areas where Cu and Si have been enriched, while P and Mo have been concentrated to certain phases.*

From an overall view, all elements are fairly even distributed over both areas analysed. There are however some points were certain elements (for example Cu & Si) are especially concentrated, and other elements, for example iron, is sparse. This could probably be traced back to the liquid phase during sintering. Silicon is highly soluble in both liquid copper and iron (such as in ferrophosphorus), and since phosphorus has the higher diffusion rate, iron will leave the liquid phase ahead of copper, thus the dissolved silicon will concentrate to the liquid copper. As pores are closing during the sintering process, remaining liquid material, in this case copper, will concentrate to the remaining larger pores. With the larger amounts of copper amassed in a small region, it is hardly surprising that all copper will not dissolve into the surrounding material within the limited process time.

5. Discussion and conclusions

The primary aim for this investigation was to explore a possible generic principle to build parts of homogenous steel, using SLS equipment in combination with a subsequent furnace procedure. Despite the obvious shortcomings of the parts manufactured, it is not unreasonable to say that this possibility has been confirmed. Solid pieces of steel were formed from green parts made in the SLS machine, and the analysis of the distribution of the principal alloy elements shows, with some exceptions, a reasonable even dispersion.

However the material selected for this investigation was a stainless steel, and apart from the most general material properties, such as tensile strength, hardness, and others, the corrosion resistance of the new alloy still has to be determined. This could be problematic, however, since there still are some areas with significant porosity or with excess concentration of, for example, copper. How much this would influence the corrosion resistance by crevice- or galvanic corrosion is unclear, but any measurements on the available pieces would not be conclusive either. As mentioned earlier, the areas with excess copper concentration probably originates in large pores, and since the porosity is primarily oriented between the applied powder layers, these could thus in many cases be deduced to poor adhesion of powder layers. Small pores could be addressed by increasing the fraction of liquid phase in the powder blend, but the large pores, which could end up filled with remaining copper, are more difficult and the best would be if they could be avoided altogether. One likely way to at least decrease their frequency could be to improve the adhesion between the layers.

The most obvious method to improve layer adhesion would be to increase the laser power. A more powerful laser, such as those installed in more modern SLS machines on the market by DTM/3D Systems and EOS would penetrate deeper into the powder layer and thereby increase the melting of material in between the layers. Furthermore, the higher laser effect would enable the melting of the ferrophosphorus during SLS, thus increasing the metal bonding and thereby further improve the quality of the green bodies. On the other hand more extensive metallic bonding will also increase the temperature induced tensions in the green bodies, though these tensions will be relieved during the furnace process. If needed for complete pore closure, the fraction of liquid phase (here the ferrophosphorus) could be increased. However, a less desirable effect, of increased fraction liquid phase would most likely be an increase of the small sagging observed on the sintered parts, and thus loss of part geometry. On the other hand this behaviour could probably be moderated by stronger metallic bonds in the green bodies that comes with an increase in laser power.

The full process of making solid homogenous steel objects from an SLS approach could not be verified by this investigation. However, the acquired results concerning sintering and diffusion are encouraging, and while the observations of the SLS behaviour are challenging, they do not contradict this possibility.

References

1. Boivie, K, "Systematic view of SFF Metal Tooling Approaches" Proceedings of the 3rd Annual International Conference on Rapid Product Development, 2002, Bloemfontein, South Africa, 2002.
2. Boivie, K, "SLS Application of the Fe-Cu-C System for Liquid Phase Sintering" Bourell, D.L., et al., editors, Proceedings of the Solid Freeform Fabrication Symposium 2000, The University of Texas at Austin 2000.
3. Boivie, K, "Limits of Loose Metal Powder Density in the Sinterstation" Bourell, D.L., et al., editors, Proceedings of the Solid Freeform Fabrication Symposium 2001, The University of Texas at Austin 2001.
4. Boivie, K, "Investigation of Size Range Composed Powder For SLS Based Liquid Phase Sintered Tooling" Dimitrov, D., editor, Proceedings of the 2nd Annual Conference on Rapid Technologies 2001, The University of Stellenbosch 2001.
5. Boivie, K, "Investigation of the Liquid Phase Sintering of Size Range Composed Powder for SLS Application" Bourell, D.L., et al., editors, Proceedings of the Solid Freeform Fabrication Symposium 2002, The University of Texas at Austin 2002.
6. Runfors, U. "Powder metallurgy", Dep. of Physical Metallurgy, KTH, Sweden 1987. (Swedish)
7. Jones, W. D. "Fundamental Principles of Powder Metallurgy" Edward Arnold LTD, 1960.
8. Bonse, J. "Selective Laser Sintering of Metal Powders" Ph.D. Thesis, Jan. 2001. Katholieke Universiteit Leuven, 2001.
9. Darken, L.S. and Gurry, R.W. "Physical Chemistry of Metals" McGraw-Hill 1953.
10. Le May, I. et al. "Copper in Iron and Steel" John Wiley & Sons, 1982.
11. German R.M. " Powder Metallurgy Science", MPIF 1994.
12. Boivie, K, "A Vacuum Furnace Process for DTM's RapidSteel 2.0 Material" Bourell, D.L., et al., editors, Proceedings of the Solid Freeform Fabrication Symposium 1999 The University of Texas at Austin 1999.

DIRECT SELECTIVE LASER SINTERING OF TOOL STEEL POWDERS TO HIGH DENSITY. PART A: EFFECTS OF LASER BEAM WIDTH AND SCAN STRATEGY

C. Hauser, T.H.C. Childs, C.M. Taylor and M. Badrossamay
School Of Mechanical Engineering, University of Leeds, UK

S. Akhtar, C.S. Wright and M. Youseffi
Engineering Materials Research Group, University of Bradford, Bradford, UK

J. Xie, P. Fox and W. O'Neill
Department of Engineering, University of Liverpool, UK

ABSTRACT

This paper describes progress on the Direct Selective Laser Sintering of M2 and H13 tool steel powders, comparing this with previous and further observations on stainless steel powders. The distinguishing feature is the melting of single tracks and layers in deep powder beds. The paper focuses on changing characteristics of the melt pool (mass, volume, aspect ratio, stability) and laser-powder interactivity as the laser beam width, power and scan speed change. It also compares the melt pool of neighbouring tracks during single layer construction. Simulations from a computer model to predict melt pool shape and dimension show reasonable agreement with experimental results at low scan speeds (0.5mm/s). But unexpected increases in melt depth above 1.0mm/s have been observed, suggesting higher values and more variability in laser absorptivity than expected, even approaching 1.0 for the CO_2 laser radiation used in this work.

INTRODUCTION

Selective melting of a metal alloy powder bed, aimed at direct production of one-off components and series tooling, is currently at the forefront of Selective Laser Sintering (SLS) research activities. Recent advances have used specially blended alloys [1] and commercially available powders, including stainless steels [2-4] and tools steels [5,6]. However, reported part densities produced from these powders varies considerably, from just above the tap density of the virgin powder [4,6] to densities exceeding 99% of theoretical density [2,3]. Research in [4] has highlighted that understanding the behavioural differences and dimensional variations of the melt pool and rastering melt front as laser powers and scan speeds change allows for process refinement leading to improvements in the quality of melted layers. This paper extends [4] by also investigating the effects of laser beam width and powder material and how this information might be used to improve the quality of multiple layer components. The microstructure and density of tracks, layers and multiple layers produced in this work are examined in Part B [7].

Running in parallel with the experimental activity is the continual development of a thermally-based finite element model which simulates the SLS process, being the subject of previous papers [8-10]. In this work the model has been used to generate plots of melt track cross-sections which are compared, geometrically, with similar images obtained from the experimental results. It is this comparison between simulation and experiment which leads to conclusions of highly variable absorptivity in the powder beds.

THE FINITE ELEMENT MODEL AND ITS MATERIAL ASSUMPTIONS

The finite element thermal, powder melting and densification model has been described before, both in its 2-D [8,9] and 3-D [10] versions. It has been well-validated experimentally and quantitatively for the SLS of polymers [8,9]. For metals there are more severe issues of selecting correct material data than there are for polymers, when it comes to comparing simulations with experimental data, because of the larger temperature range to which the powder is exposed during processing, the larger difference between the powder bed and solid metal thermal conductivity and, particularly with the use of CO_2 laser radiation, the lower and possibly more variable absorption of the radiation into the bed. In this paper handbook sources have been used for a metal solid's variation of thermal conductivity K and specific heat C with temperature, over the range 20°C to 800°C. A linear variation has been fitted and assumed to apply up to the melting temperature of the metal. With T as absolute temperature

$$K = K_o + K_v T; \quad C = C_o + C_v T \tag{1}$$

Latent heats of melting, L, have been obtained by a rule of mixtures from the latent heats of the alloys' constituent elements. The conductivity K_p and absorptivity α of powder beds at room temperature have been calculated from experiments in which the surface of a bed was exposed to incident non-scanning radiation for a short period of time and the subsequent sub-surface temperature variation in the bed measured by thermocouples. The variation with depth of time for maximum temperature to occur was used to calculate the bed's thermal diffusivity - and K_p obtained from knowledge of the bed's density and material specific heat, and α was obtained from the variation of maximum temperature rise with depth, both in the same theoretical way as described and used in [11]. K_p is assumed to vary with temperature in the same way as K.

Estimates of track size, based on α measured as just described, in many conditions grossly underestimate experimental observations, as will be seen later. Measured track mass per unit length, m_L, has been used to obtain an alternative estimate of absorptivity, α^*. Equation 2 as an equality is an expression for the minimum value of α^*, based on a heat balance. $\alpha^*(P/U)$ is the absorbed energy per unit track length, with P the laser power and U the scan speed while $m_L[C_{av.}(Tm - To) + L]$ is the energy to melt unit track length, where $C_{av.}$ is the average specific heat from ambient bed temperature T_o to the metal's melting temperature Tm.

$$\alpha^* \geq [m_L/(P/U)][C_{av.}(T_M - T_o) + L] \tag{2}$$

EXPERIMENTATION

Materials. Three types of gas atomised powder have been used in this investigation: M2 (1C-4.15Cr-6.4W-5Mo-2V-bal.Fe) and H13 (0.4C-5Cr-1.3Mo-1.05V-bal.Fe) tool steels and 314S HC stainless steel (0.4C-20Ni-25Cr-1Si-bal.Fe). All powders were obtained from Osprey Metals Ltd, UK and were supplied with a particle size distribution of -150 + 75μm. No heat treatments, additives or fluxes or powder pre-heating was used in this work. A particle size distribution of -75 + 38μm was also investigated for examination in Part B [7] of this paper.

Equipment. SLS was performed in a research machine (Figure 1). A 250W continuous wave CO_2 laser beam with a spot diameter adjustable between 0.55mm and 1.1mm at the focal length was scanned by galvanometer controlled mirrors on to the powder surface inside a controlled environment process chamber. A window in the chamber roof allowed the beam to enter. In the sealed chamber there were two build areas. For multiple layer experiments the build area (70mm in diameter) was at the base of the chamber and on top of the piston assembly which could be moved up and down to control layer depth (accurate to 0.001mm). For single track and layer experiments the build tray (120mm x 150mm x 5mm deep) was used to maximise productivity. A hopper, driven by a stepper motor, deposited and spread fresh powder layers in one operation.

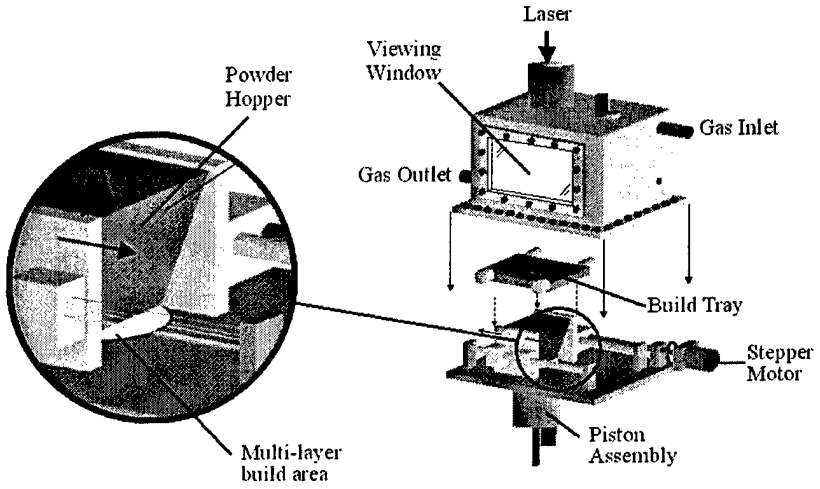

Figure 1. Controlled environment process chamber.

Melting Experiments. All experiments were carried out in an argon environment (obtained from 99.9% purity bottled argon). The chamber was evacuated to a rough vacuum followed by a one minute purge back to atmospheric pressure. This procedure was repeated twice before being followed by a 15 minute pre-sinter purge. During processing the flow rate of argon through the chamber was 3 litres/min and the net pressure was kept at 30mbar above current atmospheric pressure to ensure no air leakage into the chamber. Melting of all powder was carried out in a deep powder layer with a minimum first layer depth of 5.0mm. All scanning conditions for single tracks, layers and multiple layers are reported in Table 1. The experimental conditions were the same for all three powders and two beam widths of 0.55 and 1.1mm were used. The length of the single tracks was nominally 30mm, the size of the layers was nominally 15mm x 12mm and the multiple layers consisted of 12 and 25 layers. The multi-layer results will be reported elsewhere, some in Part B [7].

Table 1: Experimental Conditions.

Experiment	Laser Power (W)	Scan Speed (mm/s)	Scan Spacing (% of beam width)	Layer Thickness (mm)
Single tracks	32, 58, 77, 110, 143, 170	0.5, 1 - 12	n/a	n/a
Single Layer	58, 77, 110, 143	0.5, 1, 3, 5, 8, 10	25, 50, 100	n/a
Multiple layers	143	5, 8, 10	25, 50	0.4

Simulations. Simulations of the single track experiments were carried out for all three powder materials. Results for a power of 77W, a beam diameter of 1.1 mm and for scan speeds (mm/s) of 0.5, 1, 2, 4 and 8 are presented here. Material properties used are given in the results section. GSharp V3.1 (AVS Inc) was used to produce 2D sectional views of modelled tracks, with a superimposed grid for dimensional analysis. Image-Pro Plus V4 (Media Cybernetics) was used to evaluate the cross sectional solid area and take measurements from the images.

Further Experiments. Measurements of powder bed diffusivity and absorptivity in the manner of [11] were carried out in air, with a CO_2 laser beam of power up to 10W, defocused to a diameter of 4 mm at the powder bed surface. For these experiments, powder to a depth of 30 mm was placed in a cylindrical container of diameter 60 mm, with a thermocouple placed 10 mm beneath the surface coaxially with the laser beam.

Video and series of still photographs were taken of single tracks as they formed, to gain insight into powder movement during processing. These were taken through the viewing window (Figure 1) using a hand-held digital camera behind a MIG welding glass viewing filter.

RESULTS

Process Maps. Single track process maps that detail heating and melting behaviour of the metal powders as scan speed and laser power change were produced first to highlight areas where the melt pool remained continuous i.e. did not fragment or ball. A fragmented melt pool has been shown in [4] to reduce the surface quality and density of layers. Process maps for M2 and H13 are given in Part B [7]. Figure 2 is for the 314S powder processed using a spot size of 1.1mm. The map is a refinement of the same process map originally presented in [12]. It shows several different qualitative regimes, common to all maps including those from different laser beam diameters. These are regions of continuous flattened tracks, continuous rounded tracks, melted and balled tracks, not fully melted and unmelted regions. Continuous tracks were removed from the bed and sectioned. Observations from all three powders, from P = 50 to 150 W and scan speeds up to 10 mm/s are considered in more detail next.

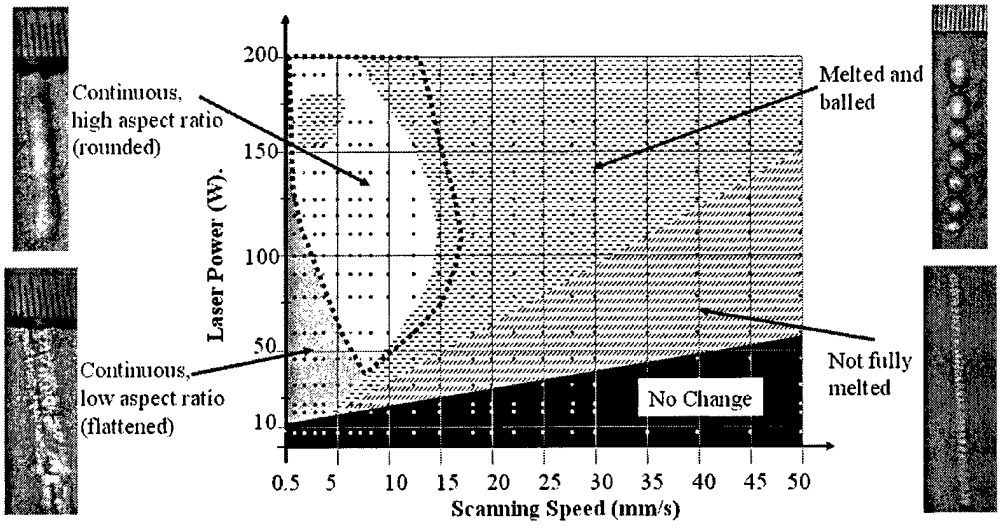

Figure 2. 314S single track process map produced using a laser spot size of 1.1mm.

Track cross-section observations. Figure 3 shows track cross-sections for all three powders at powers of 77, 110 and 143 W. The boundary between the flattened and rounded tracks is added as the solid line. It is noticeable that track cross-section area increases with increasing scan speed as that boundary is crossed. The rounded tracks all have a much larger area than expected from the level of power absorption deduced from the embedded thermocouple tests to measure that (see later). Some qualitative observations may be relevant to this. In the rounded track regime (the whole of the region enclosed by the dashed line in Figure 2), the tracks sink well into the powder bed. Powder to either side of a track collapses into it, leaving a trench surrounding the track. At low scan speeds (~1-2mm/s - Figure 3) track profiles are quite rounded, with only a few groups of satellite particles visible around the lower fringe of the solidified track. However, at higher speeds there are large clusters of sintered bonded particles at the lower surface, giving rise to 'bell' shaped track cross sections. Perhaps these differences arise from the time available for metal in the melt to flow - longer at low than higher scan speeds.

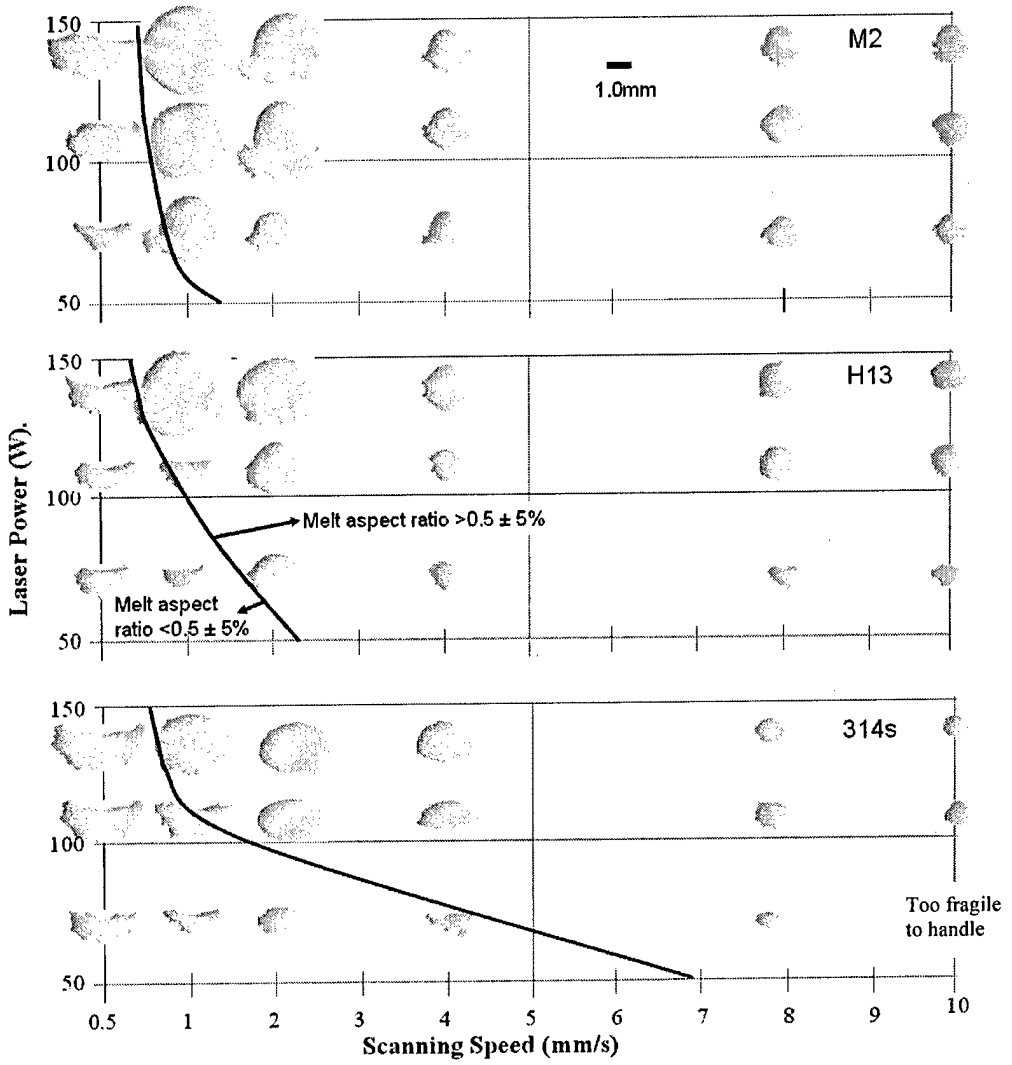

Figure 3. Track cross-sections for M2, H13 and 314S powders, beam diameter 1.1 mm.

Track masses per unit length. Figure 3 clearly shows increase of track cross-section with increase of scan speed at the boundary between flattened and rounded tracks. But the exact areas vary from place to place along a track. To obtain an average measure of size, tracks were removed from their powder beds and weighed. Figure 4 plots mass per unit length against speed for all three powders, for P = 77W. The two regimes, low speed (LS) and high speed (HS), are clear.

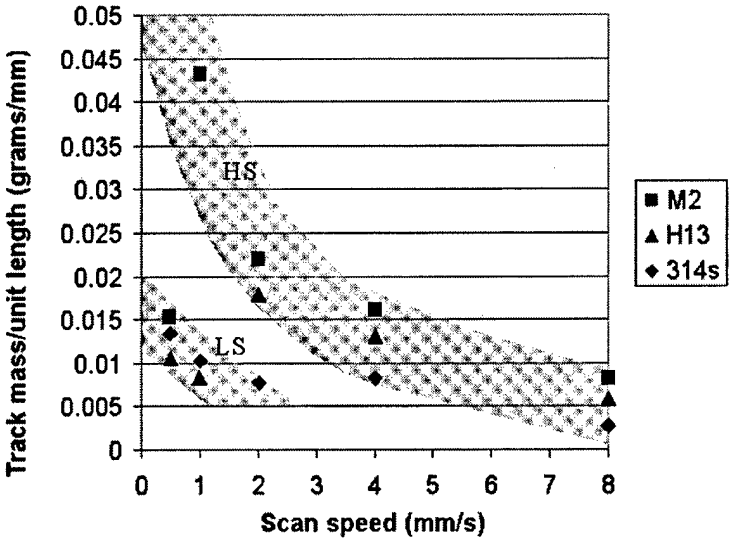

Figure 4. Mass per unit length dependence on scan speed, P = 77W, beam diameter 1.1 mm.

Figure 5 presents an alternative view, plotting mass per unit length against energy density (P/U), for two of the powders (as examples), but for all powers and speeds. In each case, data fall between upper and lower limits. All data for U > 4 mm/s fall on the upper limit, labelled HS. The lower limit labelled LS corresponds to U = 0.5 mm/s. The HS and LS slopes for all materials, and experiments with both laser beam widths, are collected in Table 2, in units of milligram/J. According to equation 2, a constant slope $m_L/(P/U)$ corresponds to a constant 'effective' absorptivity, α^*, obtained from the equality of equation 2. Table 3 gives approximate values of α^* derived from Table 2 on the basis that $C_{av.}$ = 700 J/kg and L = 280 kJ/kg - but see the next section for a more detailed consideration of absorptivity. The HS limits vary with beam diameter.

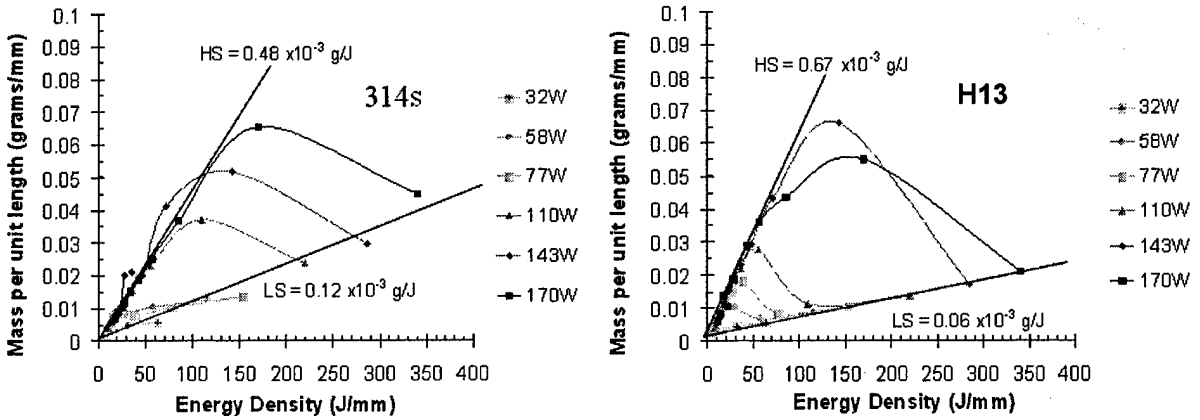

Figure 5: Mass per unit length of 314S and H13 single tracks plotted against energy density for a 1.1mm beam width for 32 < P(W) < 170 and 0.5 < U(mm/s) < 12.

Table 2: Boundary gradients calculated from mass/length vs. P/U figures.

Beam Diameter (mm)	M2 (mg/J)		H13 (mg/J)		314S (mg/J)	
	HS	LS	HS	LS	HS	LS
1.1	0.76	0.10	0.67	0.06	0.48	0.11
0.6	0.84	0.43	-	-	0.59	0.07

Table 3: Values of α^* (Equation 2) calculated from data in Table 2.

Beam Diameter (mm)	M2		H13		314S	
	HS	LS	HS	LS	HS	LS
1.1	0.92	0.12	0.8	0.07	0.58	0.13
0.6	1.0	0.52	-	-	0.79	0.09

Simulations. The main material data used in the simulations is given in Table 4. T_S and T_L are the solidus and liquidus temperatures. Two values of α were used: α_1 from the powder bed temperature distribution thermocouple measurements and α_2 from the HS limit, Table 3, except that for M2 and H13, α_2 was rounded up to 1.0.

Table 4. Material property data used in the simulations.

Mat-erial	K_o (W/mK)	K_v (W/mK^2)	C_o (J/kg)	C_v (J/kgK)	L (kJ/kg)	T_S (°C)	T_L (°C)	ρ_{bed} (kg/m^3)	K_p (W.mK)	α_1	α_2
M2	18.1	0.0106	313	0.5	270	1246	1437	4300	0.26	0.38	1.0
H13	28.6	0.0	313	0.5	270	1361	1471	4500	0.32	0.25	1.0
314S	7.83	0.0183	437	0.275	280	1280	1380	4500	0.26	0.24	0.58

Figure 6 shows a typical simulation result, a boat-shaped track with a crescent cross-section, the consequence of the model allowing only movement of powder material normal to the bed surface on solidification.

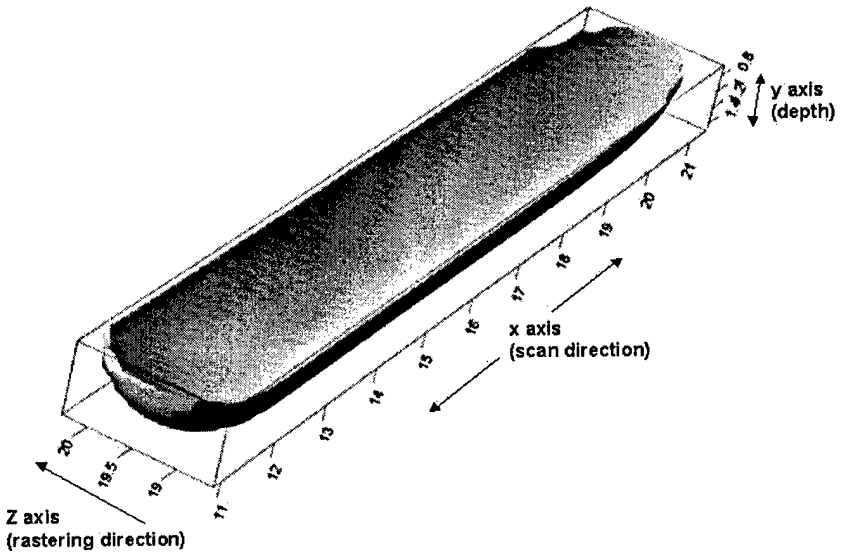

Figure 6. Simulated melt track: P = 100W, U = 6 mm/s, α = 1; dimensions in mm.

Cross-section areas from the simulations were converted to track mass per unit length by multiplying by a solid density of 7,850 kg/m^3. For this purpose, track area was defined as that within the simulated density boundary contour of 7,500 kg/m^3. Table 5 summarises results for P = 77 W in the form of $m_L/(P/U)$, for comparison with the observations of Figure 5 / Table 2. The italic and bold entries are data obtained respectively by use of α_1 and α_2 in the simulations, to be compared with the LS and HS boundary values in Table 2. The simulations follow the same qualitative characteristic as the experiments. However, in the LS range, the data (with the exception of that for M2) range from 0.06 to 0.08, compared to 0.07 to 0.13 in Table 2: for H13, the simulation values are 6% higher than experiments; for 314S they are 36% lower. In the HS range, the data are approximately constant for each material, in line with experiment: comparing Tables 5 and 2, the simulation data are 63 ± 5 % of the experimental ones, for all three materials.

Table 5. $m_{L,simulated}$ / (P/U) (mg/J) - P = 77W, beam diameter = 1.1 mm.

Material	U (mm/s)				
	0.5	1.0	2.0	4.0	8.0
M2	*0.15*	**0.47**	**0.51**	**0.48**	**0.48**
H13	*0.07*	*0.08*	**0.48**	**0.46**	**0.41**
314S	*0.06*	*0.07*	*0.08*	**0.28**	**0.27**

Alternatively, simulated results may be compared to the equivalent point experimental data in Figure 4. Table 6 records the ratio of the simulated to experimental values of mass per unit length. The italicised and bold scripts are obtained with α_1 and α_2, as in Table 5.

Table 6. ($m_{L,simulated}$ / $m_{L,experiment}$), P = 77W, beam diameter = 1.1 mm.

Material	U (mm/s)				
	0.5	1.0	2.0	4.0	8.0
M2	*1.54*	**0.83**	**0.89**	**0.58**	**0.57**
H13	*1.03*	*0.71*	**1.03**	**0.68**	**0.66**
314S	*0.66*	*0.53*	*0.37*	**0.64**	**0.89**

The simulations and experiments differ from each other at both the LS and HS extremes, but in different ways. In the LS conditions, some simulations under- and others over-estimate the experimental observations, although on average they underestimate, and the more so the higher the scan speed. It is probable that the main issue here is uncertainty in what are correct material data to enter into the simulation, particularly the value of α_1. In HS conditions, however, the simulations consistently predict track mass per unit length of around 65% of the observed values. This is despite, for the tool steels, absorptivity of 1.0 being assumed.

There are two possible explanation. The tracks may contain a substantial amount (about one third of their mass) of unmelted powder, e.g. attached round their perimeters. Evidence to support this possibility comes from two directions: a) the simulated track masses reported here on the basis of the track boundary being the 7,500 kg/m^3 boundary contour may be increased by c. 35% by expanding that boundary to include everywhere where any densification at all occurs; b) the experimental observations (Figure 3) frequently show irregular 'skirts' at the track bases (e.g. P = 77W, U = 2 to 10 mm/s for M2). Figure 7 is an enlarged view of the 4 mm/s track section. It shows the skirt occupying c. 30% of the track area. This is typical.

Or the model's assumption of heat transfer normal to the surface only by conduction is wrong. Associated with movements in the bed leading to cylindrical tracks, there may be powder motions that lead to more rapid movement of the melt front into the bed than by conduction. Powder movements are considered more next. Whether an absorption of 1.0 is realistic for CO_2 laser radiation incident on to a steel powder bed is also addressed.

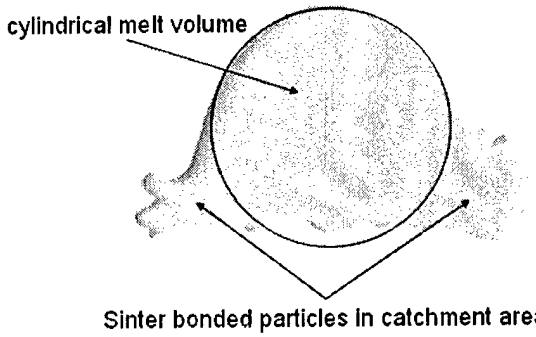

Figure 7. M2 track cross-section enlarged from Figure 3, P = 77W, U = 4 mm/s.

Track photography. Viewing rounded track formation by eye, through the viewing window (Figure 1), revealed periodic melting of powder ahead of the main track. This has been recorded by video-filming through a MIG welding glass filter (actual tracks were bright orange, almost white, directly under the laser beam; without a filter clear images could not be obtained). Figure 8 is an example from filming a M2 track (P = 100 W, U = 1 mm/s).

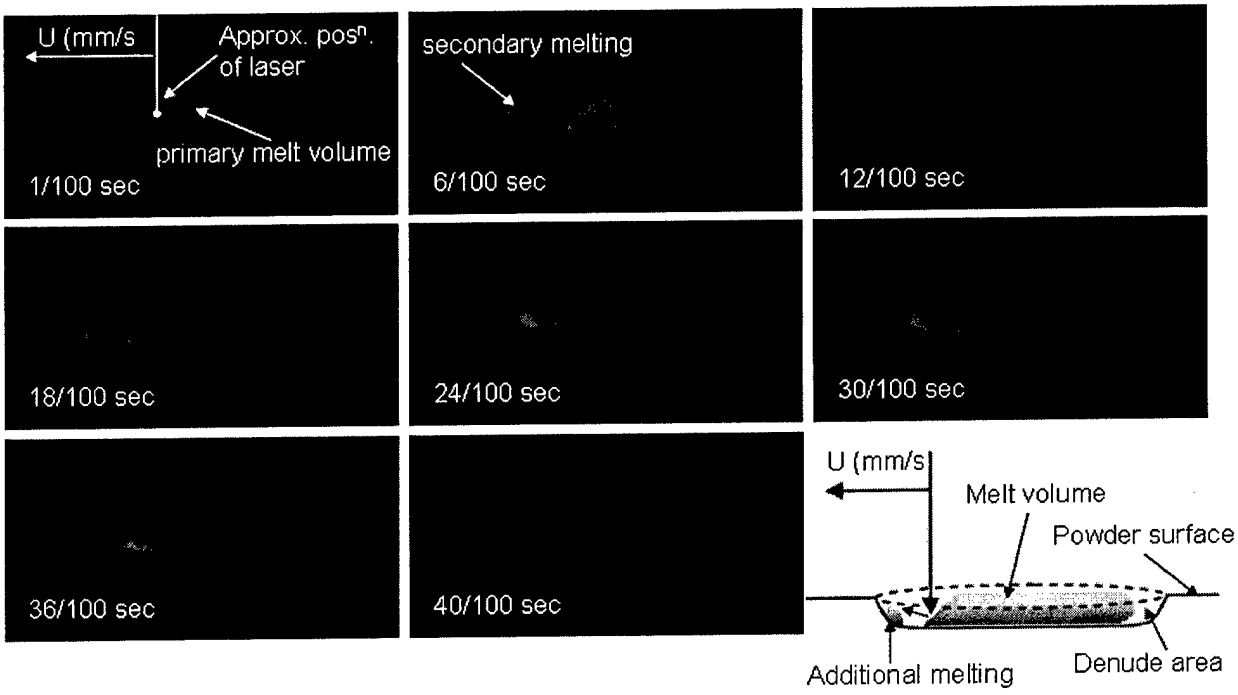

Figure 8. Video stills from track filming for M2: P = 110W, U = 1 mm/s, beam diameter 1.1 mm.

The first frame, at 0.01s, has marked on it the position of the axis of the incident laser beam, judged by where the melted track was brightest. 0.05s later, melting (marked 'secondary melting') is seen ahead of the track. This grows over the next 0.3s and finally flips (too fast to catch on film) into contact with the main track. The process starts again. In summary, tracks do not grow in length steadily but as a series of steps. In this example, the periodic time is about 0.4s. This behaviour is seen qualitatively with all rounded tracks up to a scan speed of 4 mm/s, though filming has been only at 1 mm/s. As speed increases it becomes more difficult to resolve what is happening. A possible explanation of what is happening is illustrated by the sketch in the bottom right corner of Figure 8. Because the melt track is below the powder bed surface and has a steeply sloping nose, it is possible for the incident laser beam to be partly reflected from it on to the end wall of the powder trench in which the track sits. This double absorption opportunity will certainly lead to an increased α, but whether up to 1.0 is not clear.

Single layer formation. Single layers have been created, based on understanding from the single track experiments. Two examples are discussed here (Figure 9), of M2 with P = 110W and U from 0.5 to 8 mm/s, at various scan spacings; and of H13 at P = 110W and U = 4 mm/s. First,

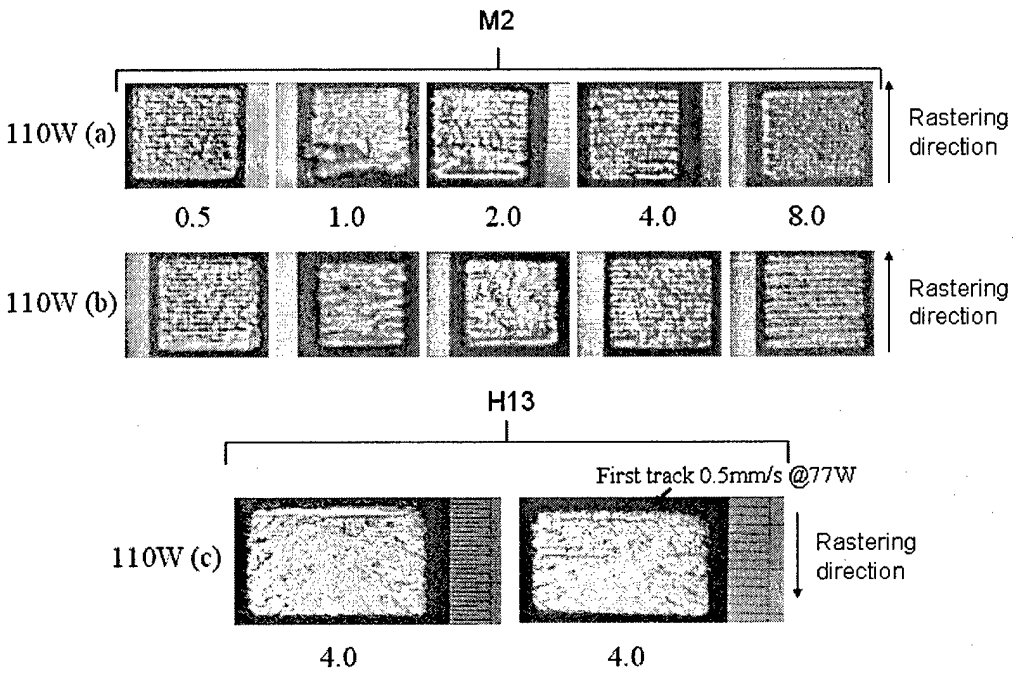

Figure 9. Single layers, with scan spacing as a % of beam diameter; (a) 50%, (b) 100%, (c) 25%.

the surface morphology of layers produced using M2 powder changed from flat to undulating and globular at the (P, U) condition where single tracks changed from flattened to rounded (Figure 3). Improvements in layer quality occurred with a scan spacing of 25% at higher speeds (8.0mm/s), but at lower speeds (1.0-2.0mm/s) the first two/three scan tracks within the layer were often globular and irregular. At a scan spacing of 100%, layers produced at 8mm/s had an undulating surface morphology and the fusion bond between tracks was usually weak, causing areas of porosity. If a scan spacing, as a percentage of single track width is considered instead of as a % of beam diameter, globular layers occur at values lower that ~30% (as in the case for Figure 9a; 1-4mm/s and b, 2mm/s) and undulating and low porosity layers occur at values greater

than ~60%. Layers with improved surface quality shown in Figure 9a, 8mm/s and b, 4mm/s have a scan spacing relative to the melt track width of 40% and 36% respectively. The only exception to this rule occurred in layers produced from flattened tracks (0.5mm/s) where surface quality had less dependence on scan spacing.

Figure 9c makes a different point. Its general condition (P = 110W, U = 4 mm/s) is in the rounded single track regime (Figure 3). The left panel shows the first track indeed to be rounded, but subsequent ones are not. Rounding of tracks is suppressed in layer formation with H13 powder more so than with M2 powder. How pre-existing tracks modify the absorptivity and heat capacity / conductivity environment of a currently melted track is currently under investigation. As a practical point, modifying the first scan power and speed (right panel of Figure 9c) to produce a flattened track at the start of each layer can improve the overall layer morphology.

SUMMARY AND CONCLUSION

Observations of the formation mainly of single tracks, but also layers, of three different steels (M2, H13, 314S) in deep powder beds are reported. In the absence of a constraining solid substrate, tracks may form with a flattened section, a rounded section that sinks into the bed or as broken or balled segments. The different laser power / scan speed conditions in which these occur are mapped and are similar for all three steels. A common observation is that there exists a scan speed range where melted mass increases with increased scan speed. This is not expected from constant power heating models. The speed range is the same as that in which single tracks change from a flattened to a rounded section with increasing speed. Track masses per unit length predicted by a thermal finite element model are in good agreement with experiment when flattened tracks are formed, using thermal absorption coefficients obtained independently, from measurements of temperature / time variations beneath a powder bed surface. To gain agreement when rounded tracks are formed, absorption coefficients close to 1.0 are required. This has led to the video-filming of track formation that has revealed that rounded tracks do not form in a steady manner, but in a way that can enhance laser power absorption, whether up to 100% is another question. Another factor that leads to more track mass than is calculated - from the assumption that all of a track is melted matter - is the possible inclusion of unmelted or partially melted material round the bottom of a track.

A remaining question to be answered is what causes the change from a flattened to a rounded track cross-section. Even without answering it, observations of single track quality can be used to plan the processing conditions for single layers. Here differences of detail occur between one tool steel and another (M2 and H13) with respect to the influence of laser power and scan speed on whether flattened or rounded multi-tracks are formed.

ACKNOWLEDGEMENT

This work was carried out at the University of Leeds as part of a UK EPSRC funded project, ref. no. GR/R32239, linked to two other projects at the Universities of Bradford and Liverpool.

REFERENCES

[1] M. Wohlert, S. Das, J. J. Beaman, D. L. Bourell (1999). Direct laser fabrication of high performance metal components via SLS/HIP. *Proc.10th Solid Freeform Fabrication Symposium*, University of Texas, Austin, pp. 281-288.

[2] W. Meiners, C. Over, K. Wissenbach, R. Poprawe (1999). Direct generation of metal parts and tools by Selective Laser Powder Remelting (SLPR). *Proc.10th Solid Freeform Fabrication Symposium*, University of Texas, Austin, pp. 655-661.

[3] R. H. Morgan, A. J. Papworth, C. Sutcliffe, P. Fox, W. O'Neill (2000). *J Materials Science*, No. 37, pp. 3093-3100.

[4] C. Hauser (2003). Selective laser Sintering of a Stainless Steel Powder, PhD Thesis, University of Leeds.

[5] H. J. Niu, I.T. H. Chang (2000). Selective laser sintering of gas atomised M2 high speed steel powder. *J Materials Science*, No. 35, pp. 31-38.

[6] M. M. A. Dewider, (2002). Direct and Indirect Laser Sintering of Metals, PhD Thesis, University of Leeds.

[7] S. Akhtar, C. S. Wright, M. Youseffi et. al. (2003). Direct Selective Laser Sintering of Tool Steel Powders to High Density. Part B: The Effect on Microstructural Evolution. *Proc.14th Solid Freeform Fabrication Symposium*, University of Texas, Austin.

[8] T. H. C. Childs, M. Berzins, G. R. Ryder, A. Tontowi (1999). Selective laser sintering of an amorphous polymer - simulations and experiments. *Proc. I. Mech. E.* 213B, 333-349.

[9] T. H. C. Childs, A. E. Tontowi (2001). Selective laser sintering of a crystalline and a glass-filled crystalline polymer: experiments and simulations. *Proc. I.Mech.E.* 215B, 1481-1495.

[10] C. M. Taylor, T. H. C. Childs (2002). Morphology of Direct SLS-processed stainless steel layers. *Proc.13th Solid Freeform Fabrication Symposium*, University of Texas, Austin.

[11] S. S. Sih, J. W. Barlow (1992). The measurement of the thermal properties and absorbtances of powders near their melting temperatures. *Proc.3rd Solid Freeform Fabrication Symposium*, University of Texas, Austin, pp. 131-140.

[12] C. Hauser, T. H. C. Childs, K. W. Dalgarno, R. B. Eane (1999). Atmospheric control during direct selective laser sintering of stainless steel 314S powder. *Proc.10th Solid Freeform Fabrication Symposium*, University of Texas, Austin.

DIRECT SELECTIVE LASER SINTERING OF TOOL STEEL POWDERS TO HIGH DENSITY: PART B – THE EFFECT ON MICROSTRUCTURAL EVOLUTION

S Akhtar*, CS Wright* and M Youseffi*
*Engineering Materials Research Group, University of Bradford, Bradford, UK

C Hauser#, THC Childs#, CM Taylor# and M Baddrossamay#
#School Of Mechanical Engineering, University of Leeds, UK

J Xie+ and P Fox+ and W O'Neill+
+Department of Engineering, University of Liverpool, UK

Abstract

This paper describes recent progress on the Direct Selective Laser Sintering of M2 [Fe-6W-5Mo-4Cr-2V-0.8C] high speed steel (HSS) and H13 [Fe-5Cr-1V-1Si-1.5Mo-0.4C] tool steel powders. Part B will focus on the microstructural evolution of laser scanned powder beds. It has been found that H13 powders are more amenable to Direct Selective Laser Sintering than M2 powders. Densities up to 90% are possible with H13 powder compared with 70% for M2. The relationship between alloy composition, microstructure, post-scanned density and scan conditions will be discussed for single track, single layer and multi-layer constructions.

Introduction

Selective laser sintering (SLS) is one of the more important solid freeform manufacturing processes developed in the last 10-15 years [1]. One of the main applications of SLS is for the manufacture of prototype or low volume production tooling using steel powders. Commercial systems are available which generate parts from either polymer coated steel powders [DTM RapidTool 2.0™] or by processing a mixture of metal powders that contains a low melting point component [EOS DirectTool™]. The need to post process, i.e. infiltrate with bronze, or the reliance on a low melting point liquid, leads to components with poor mechanical and tribolological properties. This has led to a number of studies aimed to investigating Direct Selective Laser Sintering (DSLS) pre-alloyed metal powders with the aim of eliminating the above disadvantages. These studies generally made use of commercially available powder stainless steel [2, 3], and tool steels [4, 5]. Recently Dewidar [6] has reported studies on an experimental Mo-based High Speed Steel, a composition developed by Wright *et .al.*[7], specifically as a "process-friendly" grade for processing by conventional die pressing and vacuum sintering. Whilst it is possible to process Stainless Steel powders to densities of +99% [3], less success has so far been achieved with tool steels. This paper presents results of investigations into the melting / densification behaviour of tool steel powders during DSLS which has the aim of identifying the factors which control the ability to fabricate fully dense, multi-layer components.

Experimental Techniques

Three types of powder were used in this investigation. Annealed water atomised M2 (WA-M2), gas atomised M2 (GA-M2) and gas atomised H13 (GA-H13). The water atomised M2 was sourced from Powdrex, UK and the gas-atomised powders were obtained from Osprey Metals Ltd, UK. The various size fractions used, along with Apparent Density and flowability (Hall Flowmeter) data are given in Table 1.

Powder Type	Size Fraction (μm)	Apparent Density (gcm^{-3})	Flowability (s/50g)
WA-M2	<150/+75	2.14	55.4
	<75/+38	2.18	59.8
	<38	2.60	No flow
GA-M2	150/+75	3.97	23.7
	<75/+38	ND	ND
	<38<	4.31	No flow
GA-H13	<150/+75	4.17	20.2
	<22	3.41	no flow

Table 1. Powder Properties of materials investigated

Selective laser sintering was performed on specially constructed machines at the Universities of Leeds and Liverpool. The Leeds machine includes a 250W continuous wave (CW) CO_2 laser. Preliminary studies were conducted at a Beam size of 1.1mm diameter. This was subsequently reduced to 0.55mm diameter. Galvanometer controlled mirrors direct the laser beam within a 70.0mm diameter build area which is housed in a 300 cm^3 (L = 460mm, H = 260mm, and D = 250mm) chamber capable of sustaining a variety of atmosphere conditions including an absolute pressure of 10mbar. Details of this machine are given in Reference 2. In this study, the atmosphere inside the chamber was high purity argon (bottled argon at 99.9% purity). The chamber was evacuated to 30 mbar followed by a 15 min pre-sinter purge with argon at atmospheric pressure. During sintering the gas pressure inside the chamber was 30mbar above atmospheric. The Liverpool system, described by Morgan, et. al. [3], consists of a Rofin Sinar 90W, flash lamp pumped Q-Swiched Nd : YAG laser. An analogue galvanometer-scanning head attains beam position over an area of 80 x 80 mm2. Pulse repletion rates are in the range 0 – 60kHz and minimum beam diameter is 80μm. The shroud gas was nitrogen

The two systems employed different approaches to placing layers of powder. In the Leeds machine, the initial powder layer comprised loose powder to a depth of 5 mm contained in a mild steel tray. This layer was levelled with a blade to ensure a flat powder surface. Subsequent layers were deposited using a hopper system. The layer depth was 0.4 mm. In the Liverpool machine mild steel sheet was used as a substrate. In this system, the powder delivery system, which employs a counter rotating roller system [3], was optimised for an even 100μm coating of powder to be layered for every build layer. Whilst all size fractions studied could be processed on the Leeds machine, the Liverpool machine was restricted to processing just the <38μm and <22μm fractions.

After sintering samples were prepared for metallographic examination by mounting and grinding on SiC paper to 1200 grit, then polished on cloths impregnated with 6 and 1μm diamond. Polishing was completed using 0.05μm γ-alumina. Samples were studied in the etched and un-etched conditions. M2 samples were etched in 5% Nital whilst 10% Nital was used for the H13 specimens. Samples were examined using both optical and scanning electron microscopy techniques.

Isopleths were calculated for the M2 and H13 systems using ThermoCalc™ [www.thermocalc.se] software and the SGTE SSOL database in order aid with both the selection of post-processing conditions and interpretation of microstructures, Figure 1.

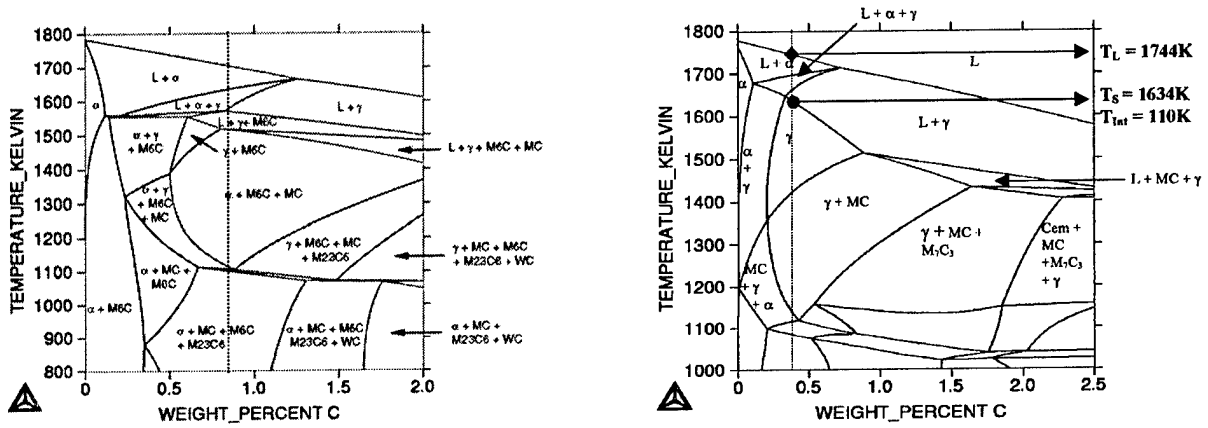

(a) (b)

Figure 1. Calculated Isopleths for (a) Fe-6W-5Mo-4Cr-2V-C, and (b) Fe-5Cr-1V-1Si-1.5Mo-C systems

Results and Discussion

M2 Powders

Typical SEM micrographs of the "as-received" powders are given in Figure 2.

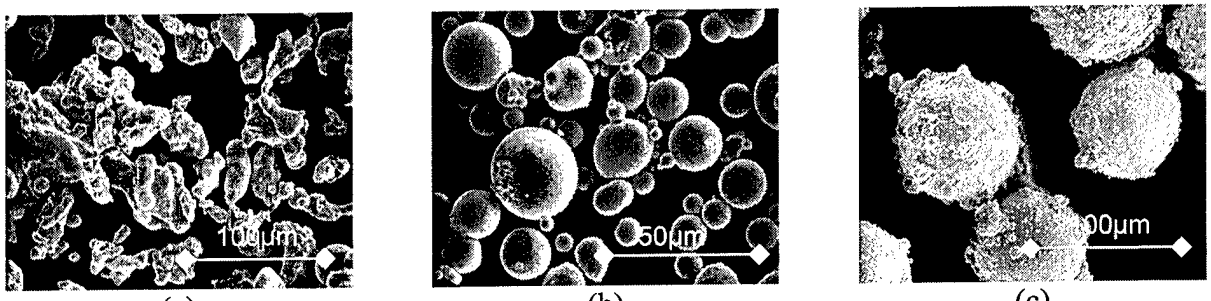

(a) (b) (c)

Figure 2. SEM micrographs of M2 powders. (a) WA-M2 <150μm, (b) GA-M2 <38μm, (c) GA-M2 <150/+75μm size fractions.

The water-atomised powder was composed of highly irregular particles and, as such, is typical of this method of powder production. As expected the gas-atomised powders were composed of spherical particles. However, whilst the >38μm GA-M2 size fraction consisted of

spherical particles with smooth surfaces [Figure 2(b)] the particle surfaces of the coarser fractions were much rougher due to the presence of many smaller satellites formed as a result of collisions during atomisation, Figure 2(c).

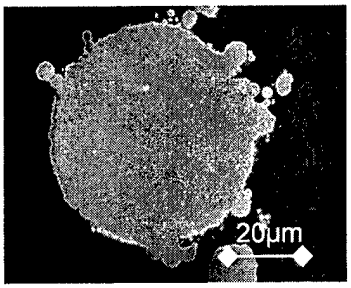

(a)

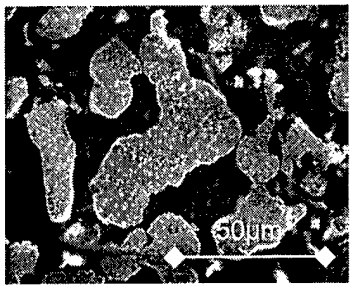

(b)

Figure 3 Microstructures of M2 powders. (a) Gas atomised <150/+75. Note the fine carbide network. (b) Water atomised <38µm fraction. Note fine discrete carbides.

At the outset of this work two strategies were envisaged for the manufacture of high density, multi-layer components;

(a) Partial melting of successive powder layers forming sufficient liquid to bond both powders and layers together, followed by a post processing sintering step. High Speed steels are one of the few alloys systems that are commercially sintered to full density (i.e. +99% relative density) via a supersolidus liquid phase sintering mechanism [7]. The aim of the post processing step would be to vacuum sinter the laser sintered performs at a temperature of ~1260°C, the optimum sintering temperature for conventional die-pressed M2 powders [10], initiate controlled re-melting, inducing densification through particle rearrangement and solution – re-precipitation mechanisms [7]. The challenge was to produce intact laser sintered performs which, in order to avoid distortion during post-processing sintering, contained uniform distributions of porosity

(b) Complete re-melting of powder layers.

The heating and melting behaviour of each batch of M2 powder was systematically studied using the CO_2 laser SLS machine at Leeds in order to identify appropriate processing conditions to achieve the two processing strategies. Single tracks were produced for a wide range of Laser power and scanning conditions. In common with previous investigations [2, 6] the results for M2 are presented as process maps, Figure 4.

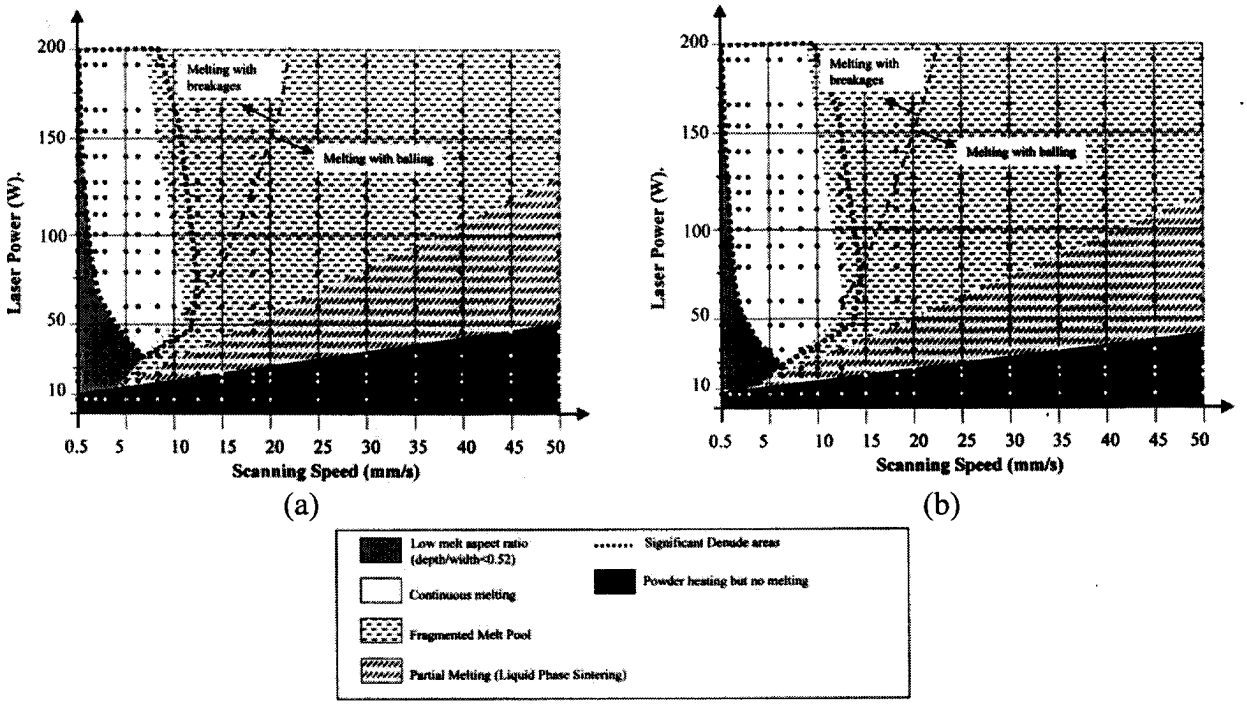

Figure 4. CW CO_2 laser process maps for gas-atomised M2 <150/+75μm fraction (a) 1.1mm and (b) 0.55mm spot size.

A feature of the process maps was that the size of the regimes and the positions of the boundaries defining each regime were comparable, irrespective of whether the powder was gas or water atomised and size fraction. Reducing spot size had a only small effect on increasing the size of the continuous melting regime, e.g. Figures 4(a) and 4(b). Attempts were made to fabricate single and multi-layer blocks (12 x 12 x 12 mm^3) using conditions located within the partial melting and continuous melting regimes using the CO_2 laser SLS machine, Table 2.

Size Fraction (μm)	Beam Overlap (%)	Power (W)	Scan Speed (mms^{-1})	Spot Size (mm)	Comments
$<38_{water\ atomised}$	25	60	60, 100	1.1	Single Layer
$<38_{gas\ atomised}$	25	50,100	70,130	1.1	Single Layer
$<75/+38_{water\ atomised}$	25	50,100	70, 130	1.1	Single Layer
$<150/+75_{gas\ atomised}$	25	50, 60	100,130	1.1	Single Layer
$<150/+75_{gas\ atomised}$	25	130, 135	8	0.55	Multiple Layer
$<75/+38_{gas\ atomised}$	25,75	130	5,8	0.55	Multiple Layer
$<75/+38_{water\ atomised}$	25,50,75	130	5,8,10	0.55	Multiple Layer

Table 2. Conditions used to process M2 powders using CW CO_2 Laser

Irrespective of powder type or particle size fraction, attempts to produce multi-layer blocks were unsuccessful using conditions located within the partial melting regime were unsuccessful. The sub 38μm water and gas atomised size fractions were difficult to spread, layers tended to form

furrows. However the major issue with processing within the partial melting regime was that at the conditions studied, insufficient melting took place to bond the next layer on to the previous layer, making it impossible to build intact blocks. Thus it was not possible to pursue fabrication of multi-layer components for M2 via strategy (a). Multi-layer blocks made from 25 individual layers were fabricated using conditions within the continuous melting regime. Unfortunately, the resultant blocks were very porous.

Using the Liverpool SLS system, it was possible to scan at up to 500 mms^{-1} and operate either in pulsed or continuous modes. Initial experiments were performed using water atomised M2 at scan speeds of 10 –500mms^{-1}, laser current 16-20A, Spot size = 0.1 mm, Beam overlap of 25-80%, pulse repetition frequency of 0kHz. The layer thickness was 100μm. Both single and 3 layer samples were produced. A feature of the scanned areas, though, was that they contained large amounts of un-melted powder. Removal of this by ultrasonic cleaning revealed that the beds were very porous, Figure 5(a). The porosity levels were unaffected by scanning conditions. This high level of porosity was attributed to the low apparent density of the water atomised powder arising from its highly irregular shape, Table 1, and the layer thickness. In previous studies with 316L stainless steel, operating in pulsing mode blocks with 100% relative density being obtained [4]. Consequently, additional experiments with M2 powders were carried out at layer thickness of 100 and 50μm, pulse repetition frequencies of 40 and 50kHz, scan speed = 500 mms^{-1}, current = 20A, spot size = 100μm, beam overlap = 50%. Blocks 5 x 15 x 15mm^3 were produced. Operating in pulse repetition mode resulted in an increase in density compared to continuous mode. However densities were only 5.5 gcm^{-3}, i.e. ~70% relative, and were independent of processing conditions, Figure 5(b).

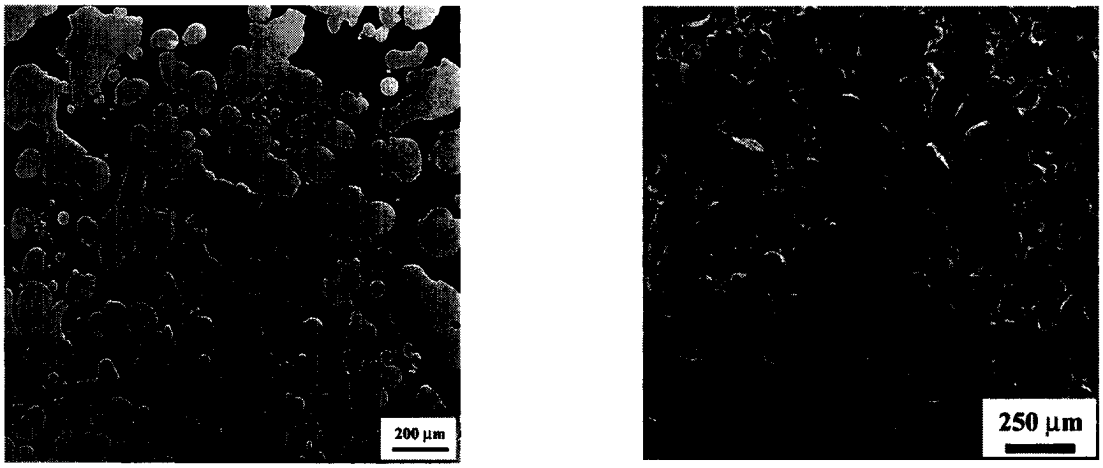

(a) (b)

Figure 5. Micrographs of Nd : YAG laser scanned multi-layer M2 (a) <38μmWA-M2, 400 mms^{-1}scan speed, 50% beam overlap, current 20A, spot size 0.1mm, (b) 500 mms^{-1}scan speed, 50% beam overlap, current 20A, spot size 0.1mm, pulse rate 40kHz. (100μm layer thickness).

Despite the higher apparent density of the <38μm gas atomised powder, Table 1, use of this powder had no beneficial effects on the density of laser scanned blocks, densities were similar to those obtained for <38μm water atomised M2 powder.

The microstructures of samples produced on the two systems were comparable and independent of starting powder. Single layers produced using the CO_2 laser operating within the partial melting regime contained regions of un-melted powder, Figure 6(a). The melted regions had a very fine cellular - dendritic structure (grain size <10μm) with fine eutectic networks at grain boundaries, Figure 6(b). Partially melted regions were also visible [Figure 6(c)].

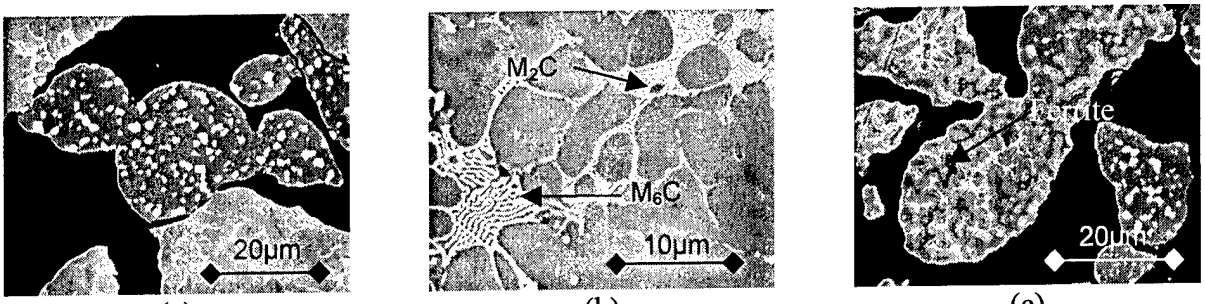

(a) (b) (c)

Figure 6 CW CO_2 M2 single layers at 1.1mm spot size. (a) <38μm, 60W, 25% beam overlap, 100mms^{-1} Scan speed, (b) <38μm, 60W, beam overlap 25%, scan speed 70mms^{-1}, (c) <38μm, 60W, beam overlap 25%, scan speed 100mms^{-1}.

The dark areas [Figure 6(c)] are believed to be ferrite, suggesting that these regions been reheated to within the L + γ+ α or L +γ region of Figure 1(a). Two types of eutectic were observed. Given the small size of the eutectics it was not possible to identify them using X-ray microanalysis. However based on both grey levels in Back Scattered Electron imaging (Atomic Number contrast) and eutectic morphology, it is possible to identify the carbide components as M_6C (Fe-W-Mo rich) and M_2C (Mo-W-Fe –V rich) [8]. Irrespective of composition or cooling rate, M_6C adopts a characteristic "herringbone" structure. The presence of M_2C is not expected from Figure 1(a), instead V rich MC would be expected to form under equilibrium cooling. High cooling rates, such as those of laser processing techniques, favour M_2C formation over MC [8]. M_2C eutectic can adopt one of three morphologies, feathery, cellular or lamellar [8]. High cooling rate also favours the formation the cellular morphology observed in the SLS samples [8]. Microstructures of single layer samples processed in the continuous melting regime were comparable, the only difference being a reduction in the amount of un-melted powder present.

Examination of the multi –layer samples revealed that re-melting was taking place to a depth of 2-3 layers. For example in the blocks produced from 25 powder layers on the CO_2 laser system only 13 layers were visible afterwards. In terms of eutectic type and morphology, presence of partially melted regions, the microstructures were identical to the single layer samples. However an important additional microstructural feature was the presence of coarse eutectic layers within the blocks, e.g. Figure 7(a), believed to be formed by epitaxial solidification at solid-liquid interfaces.

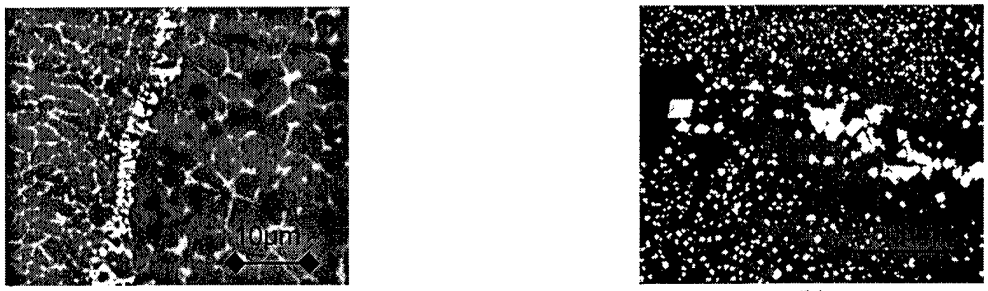

(a) (b)

Figure 7 Micrographs of M2 CW CO_2 laser multi-layer specimens (a) GA-M2 <150μm<38μm, 60W, 25% beam overlap, 70mms^{-1} Scan speed, 0.55 mm spot size (b) Post processed sample – 1260°C for 60 min.

Eutectic structures in High Speed Steels are considered to be detrimental to mechanical properties. Hoyle [9] demonstrated for conventional cast HSS that it was possible to refine the "as cast" eutectic structures by reheating to just above the solidus followed by slow cooling. In a similar manner, the multi-layer blocks were subjected to a post processing step which involved heating in vacuum at 10°Cmin^{-1} to 1260°C, the optimum Supersolidus Liquid Phase Sintering temperature for M2 powders [10], holding for 60min then furnace cooling at an average rate of ~2°Cmin^{-1} to room temperature. Whilst this treatment did not produce any further densification, it resulted in the breakdown of the eutectic structures; networks being replaced by fine, discrete carbides with regions such has those of Figure 7(a) being replaced by coarser carbide clusters, Figure 7(b). This is considered significant because even if M2 powders could be processed to ~100% density by DSLS, such regions would be potential points of weakness since it is known that in cast wrought and powder metallurgy processed HSS that carbide clusters are preferred sites for crack nucleation at low applied stresses under static and dynamic loading [11].

H13 Powders

The Gas atomised H13 powders were spherical with minimal satellites. The microstructure of "as-received" powders comprised cellular-dendritic grain structure with continuous grain boundary carbide films, Figure 8. The grain size decreased with particle size.

(a) (b)

Figure 8. Microstructure of gas atomised H13 <150/+75μm size fraction

Figure 9 shows the Process Map for <150/+75μm powder processed using a 0.55mm spot size on the CWCO_2 system.

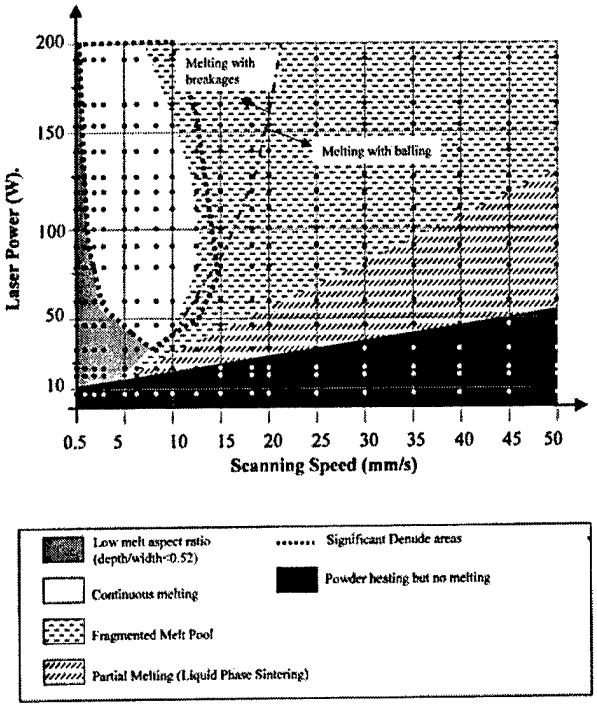

Figure 9. CW CO_2 laser process maps for gas-atomised H13 <150/+75 μm fraction, 0.55mm spot size

Comparing Figure 9 with Figure 4(b), it can be seen that the process map for H13 is comparable to those for M2 powders. Interestingly, processing H13 powders within the partial melting regime of Figure 9 was slightly more successful than with M2 in that it was possible to produce multi-layer blocks. The individual layers were ~1/3 thinner than for M2 processed in the same regime but these multi-layer blocks were very porous and fragile, Figure 10(a).

Much more promising results were obtained with H13 compared to M2 in the Nd : YAG SLS. Processing at condition of Pulse repetition frequency of 30kHz, scan speed 500mms^{-1}, current 20A, spot size 100μm, beam overlap 50% give well-bonded, multi-layer blocks with a density of 90%, cf. Figure 10(b) and Figure 5(b).

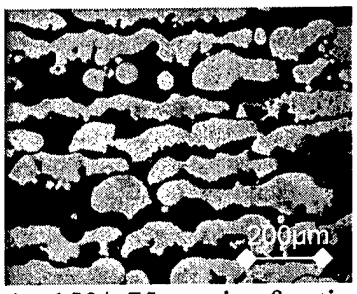

(a) <150/+75μm size fraction

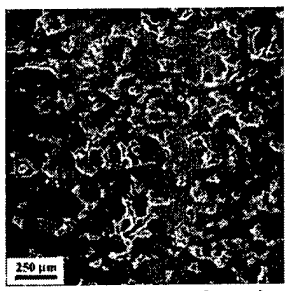

(b) <22μm size fraction

Figure 10. H13 multi-layer samples (a) CW $C0_2$ laser at 0.55mm Spot size size, 5mms^{-1} scan speed, 50% Scan spacing, 32W Power. (b) Nd : YAG laser at 500 mms^{-1} scan speed, 50% beam overlap, current 20A, spot size 0.1mm, pulse rate 30kHz. (100μm layer thickness)

Figure 11 shows typical microstructures produced for continuous melting using the Nd: YAG system and partial melting using the CO_2 system.

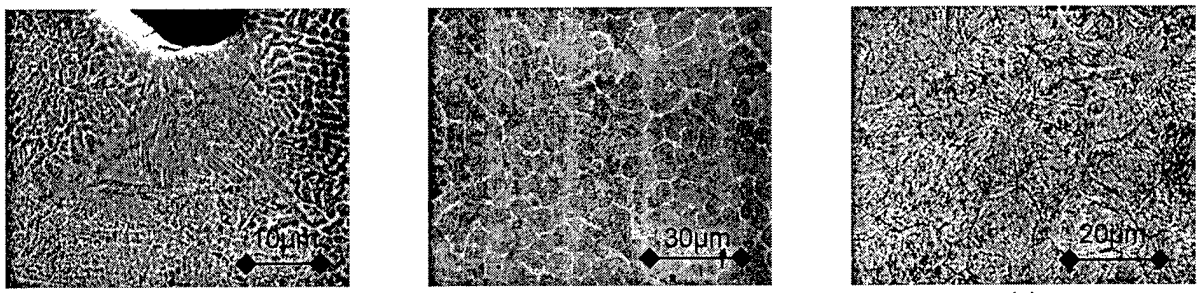

(a) (b) (c)

Figure 11. Micrographs of H13 powders scanned at same conditions as Figure 10. (a) Nd : YAG laser [Pulsed Mode], (b) and (c) CW CO_2 laser

Processing using the Nd : YAG laser produced a fine, grained cellular – dendritic size with continuous grain boundary carbide films, Figure 11(a). The matrix was martensitic. Carbide depleted zones were observed [Figure 11(a)] and in some areas there was no bonding between layers. Due to the fineness of the microstructure, this carbide phase could not be identified using X-ray microanalysis. However, unlike M2, coarse carbide clusters were not observed at interfaces. Superficially the microstructures of the samples produced by processing in the partial melting regime of the CO_2 laser were similar to those produced by Nd : YAG laser scanning. They appeared to consist of a cellular – dendritic grain structure, a martensitic matrix and continuous grain boundary carbide films, Figure 11(b) and (c). Detailed observation using SEM revealed a more complex situation in that the network features were simply regions of differential contrast, they were crossed by austenite grain boundaries and by individual martensite laths, Figure 11(c). X-ray microanalysis indicated that these regions were slightly richer in Chromium than the grain interiors. This type of structure could arise due to reheating of a previous solidified layer during subsequent scanning of the top layer of powder. The carbides present in laser scanned H13 materials have yet to be positively identified but it can be inferred from Figure 1(b) that non-equilibrium solidification will result in the formation of Cr rich M_7C_3 carbide in preference to vanadium-rich MC predicted for equilibrium solidification. M_7C_3 carbides readily dissolve in austenite at temperatures above ~950°C. Reheating for a short time, at a temperature below the solidus sufficient to dissolve the carbides, yet high enough to form austenite, followed by rapid cooling could, in principal, produce the microstructure seen in Figure 11(c). Carbon diffusion rates are much high in γ-Fe than Chromium diffusion rates and, if the time at temperature is insufficient for homogenisation, a coring effect will result, as indicated by X-ray microanalysis. Once the carbides have dissolved there will be no pinning effect and an austenite grain structure will form with grain boundaries cutting across the cored regions. The austenite will transform to martensite on cooling with individual laths passing through cored regions. It is not yet understood why this structure was not observed in the Nd : YAG processed powders.

The results presented here indicate, as with the previous studies of Nui and Chang [4, 5], that gas-atomised powders are more suited to the DSLS approach than water-atomised powders. Whether this is due to the higher oxygen content of water-atomised powders, as suggested by them or particle morphology have still to be established. For example, are the differences in

behaviour due to lower apparent density of water atomised producing less dense powder beds or is due to the bed powder flowability and how the powder interacts and flows into the moving melt pool. More interestingly, the current studies have shown that H13 powders are more amenable to DSLS than M2 powders. Given that powder properties for the two compositions are comparable this would suggest that alloy composition has an important role to play, particularly since similar sized stainless steel powders can be processed to 100% density [3]. The reasons for this are the subject of ongoing investigations.

Conclusions

[1] M2 high speed steel powders are not amenable to processing to full density by a DSLS processing. The maximum density achieved in multi-layer samples, using pulsed Nd : YAG processing was only 70% relative. Much lower densities were obtained using CW CO_2 and CW Nd : YAG processing operating in the same continuous melting regimes.

[2] Gas-atomised H13 powders are amenable DSLS with densities of 90% relative being achieved using pulsed Nd : YAG processing operating in a regime of continuous melting

[3] The reasons for the differences in processing behaviours of M2 and H13 powders of similar powders properties are, as yet, unclear.

Acknowledgements

The research reported in this paper is a joint project between the Universities of Bradford, Leeds and Liverpool, funded by the UK Engineering and Physical Sciences Research Council under Grant Number GR/R32222.

References

[1] KW Dalgarno and CS Wright; "Approaches to Processing Metal and Ceramics through the Laser Scanning of Powder Beds", *Society of Manufacturing Engineers,* Technical Paper PE03-143, 2003.

[2] C Hauser, THC Childs & KW Dalgarno, "Selective Laser Sintering of Stainless Steel 314HC Processed Using Room Temperature Powder Beds", proc. *Solid Freeform Fabrication Symposium* Austin, Texas August 9 – 11, 1999, pp273-280.

[3] RH Morgan AJ Papworth, C Sutcliffe, P Fox & W O'Neill, "High Density Net Shape Components by Direct Laser Re-melting of Single Phase Powders", *J Materials Science*, 2002, **37**, 3093-3100.

[4] NJ Niu and ITH Chang, "Selective Laser Sintering of Gas and Water Atomised High Speed Steel Powders", *Scripta Materialia,* 1999, **41**, pp 25 – 30.

[5] NJ Niu and ITH Chang, "Instability of Scan Tracks of Selective Laser Sintering of High Speed Steel Powder", *Scripta Materialia,* 1999, **41**, pp 1229 – 1234.

[6] MM Dewidar, "Direct and Indirect Laser Sintering of Metals" *PhD Thesis*, University of Leeds, 2002.

[7] CS Wright et. al., "Supersolidus Liquid Phase Sintering of High Speed Steels – Part 3 the Computer Aided Design of Sinterable Alloys", *Powder Metallurgy*, 1999, **42**(2), pp 131-145.

[8] M Boccalini and H Goldenstein, "Solidification of High Speed Steel", *International Materials Reviews*, 2001, **46**(2) pp 92 –115.

[9] G Hoyle, "Modification of the Cast Structure of High Speed Steel", *J.Iron Steel Institute,* 1959, November, pp254-269.

[10] CS Wright and B Ogël, "Supersolidus sintering of high speed steels. Part I-supersolidus sintering of molybdenum based alloys", *Powder Metallurgy*, 1993, **33**(3), pp 213-219.

[11] MA Gomes, AS Wronski and CS Wright, "Fracture behaviour of a highly alloyed high speed steel", *Fracture and Fatigue of Engineering Materials and Structures*, 1995, **18**, pp 1 -18

LASER MELTING OF Ti-Ni SHAPE MEMORY ALLOY

H. Kyogoku*, J.A. Ramos** and D.L. Bourell***
*Department of Mechanical Engineering, Kinki University,
Higashihiroshima, Hiroshima 739-2116 Japan
**Department of Mechanical Engineering and Metallurgy, Pontificia Universidad Católica de Chile, Av. Vicuña Mackenna 4860, Santiago, Chile
***Department of Mechanical Engineering, The University of Texas at Austin, Austin, TX 78712
Reviewed, accepted August 28, 2003

Abstract

The applicability of laser melting in fabrication of Ti-Ni shape memory alloy was investigated experimentally. Elemental powders of Ti and Ni and mechanically alloyed (MA) TiNi powder were used to fabricate specimens. The effects of powder characteristics on the microstructure and shape memory characteristics of the alloy were examined. The morphology and microstructure of the laser-melted specimens were varied with fabrication conditions. Parts fabricated from elemental powders exhibited a shape memory effect, but those from MA powder did not exhibit it, although the latter showed more homogeneous microstructure than the former.

Introduction

Laser sintering or melting is one of the rapid prototyping processes which can produce complex-shape parts directly from metals and ceramics powders, and this process has been applied to fabricate various parts, molds and so on[1-3]. Shape memory alloys, especially Ti-Ni alloys, are widely applied as joints, springs, actuators in the field of industry as well as functional elements in the filed of medical, energy industry and so on because they have not only excellent shape memory characteristics but also superior erosion and corrosion resistances. One of the authors has been reported that shape memory alloys fabricated by a pulse-current pressure sintering method have superior thermo-mechanical characteristics[4-6] and high erosion and corrosion resistances[7,8]. However, since the sintering of elementally blended powders resulted in inhomogeneous microstructure in the sintered compacts, it was found that the alloys obtained have some problems in fatigue properties and temperature-response. Also, since it is difficult for the pulse-current pressure sintering technique to fabricate complicated-shape parts, the application of laser sintering or melting to fabrication of shape memory parts is significant. But there have been no reports on the application of this technique to shape memory alloys.

In this study, we attempt to fabricate Ti-Ni shape memory alloys by CO_2 laser melting. The laser melting conditions are investigated experimentally, and the microstructure and shape memory characteristics of the laser-melted specimens are also examined.

Experimental Method

Experimental procedure

In this study, we used a gas-atomized Ti powder and a carbonyl Ni powder. The mean particle diameter and chemical compositions are shown in Table 1. We prepared two types of powders: (1) Ti-50.2at%Ni elementally blended powder and (2) Ti-50.2at%Ni mechanically alloyed (MA) powder. The blended powder of Ti and Ni was prepared by a V-blender at the composition of Ti-50.2at%Ni. The MA powder was fabricated by means of a planetary ball mill. The ball to powder weight ratio was 5:1. The powder mixture of Ti and Ni powders milled together with stainless steel balls in an atmosphere of argon gas at various rotational speed for various milling time between 3.6 ks and 360 ks. In this study, we used the MA powder milled at 500 rpm for 36 ks. The MA powder obtained was in amorphous state judging from the result of

X-ray diffraction patterns as shown in Fig.1. The oxygen and carbon contents of this powder were 0.28 mass% and 0.075 mass%, respectively. These powders were filled into an aluminum die coated with carbon spray and then laser-melted by means of a CO_2 laser equipment.

Table 1 Mean particle diameters and chemical compositions of Ti and Ni powders

	Powder	Mean particle diameter (μm)	Chemical compositions (mass%)				
			Fe	O	N	H	C
Ti	Gas-atomized powder	24	0.053	0.13	0.005	0.007	0.009
Ni	Carbonyl powder	6.2	0.003	0.069	—	—	0.078

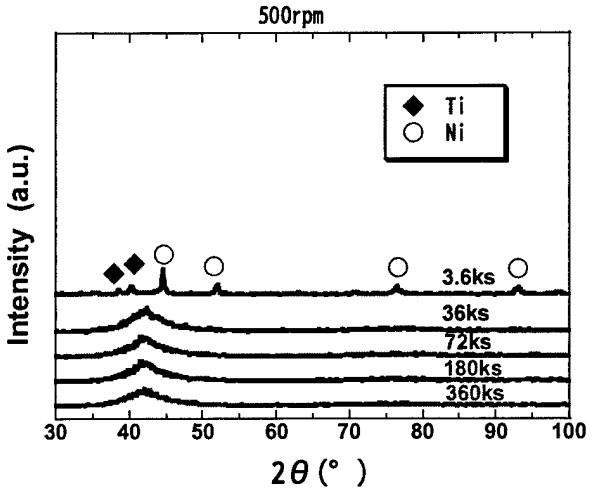

Fig.1 X-ray diffraction patterns of MA powders

The laser melting process scheme consisted of a CO_2 laser beam raster-scanned along a rectangular area, so that a pseudo-energy line source was traversed over a pre-placed powder. The laser beam was focused down a spot of diameter 0.35 mm +/-0.05mm. By altering the density of scan lines per inch, the width and length of the scan pattern, the scan step and scan period, multiple combinations of scan speed (V_s 508-816 mm/s) and traveling speed (V_t 0.41-3.05 mm/s) were achieved. The laser power delivered at the free surface corresponded to 152-334 W. Fig. 2 shows a schematic diagram of this setup. The powder was compacted manually inside a rectangular trough of dimensions 25.4 mm x 12.7 mm x 6.35 mm carved out in an aluminum holder of dimensions 50.8 mm x 76.2 mm x 25.4 mm and placed inside of the right piston in the CO_2 laser processing chamber. The trough was previously spray-coated with graphite to prevent melting of the aluminum and ease the removal of the cast material. The powder surface was then leveled so that it matched the focal position of the laser beam. The chamber was initially brought to a rough vacuum of approximately 250 mmTorr; the powder was then allowed to degas for 24 hours under a vacuum of 60 mmTorr. During the laser melting, argon gas was purged directly to the processing zone from an annular ring located above the powder bed.

The microstructures of the specimens were examined by optical microscope, scanning electron microscope with EDX and X-ray diffractometer. The shape memory characteristics were examined by DSC equipment.

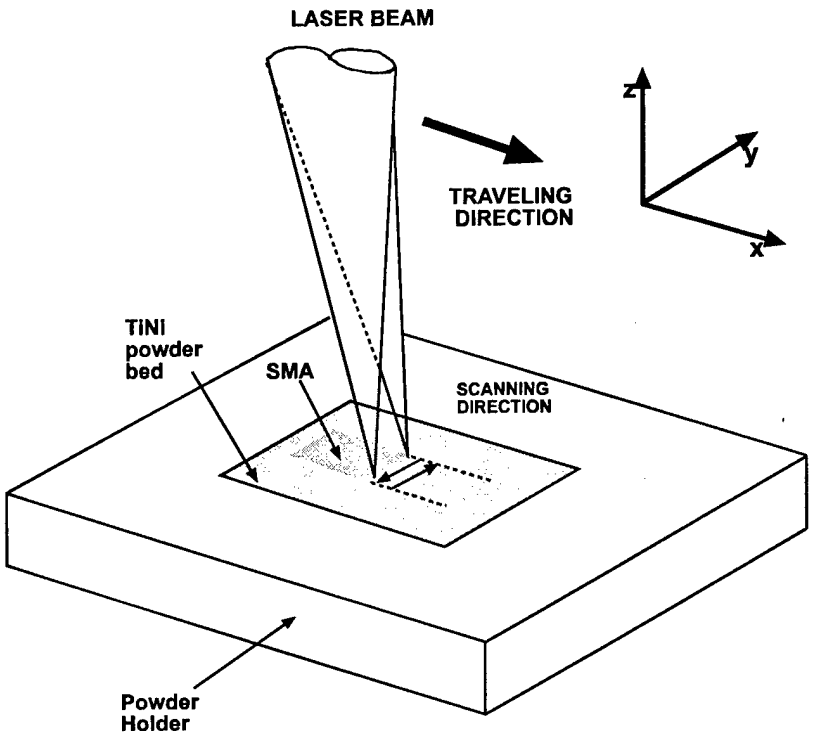

Fig. 2 Schematic diagram of the laser melting of a shape memory alloy powder.

Results and Discussions

Effects of laser melting conditions on the shape and surface conditions of scan tracks

It is significant to investigate the laser melting conditions, such as laser powder, scan speed, traveling speed and so on, in order to fabricate superior laser-melted bodies. Therefore, we investigated the effects of laser power, scan speed and traveling speed on the shape and surface conditions of scan tracks. Figure 3 shows the change in shape of scan track of blended powder with scan speed and traveling speed. In the case of higher power (334 W on the surface), higher scan speed (816 mm/s) and lower traveling speed (0.41 mm/s) as shown in Fig.3(a), the continuity in shape of the laser-melted body is lost and the laser-melted body becomes round in shape during the melting-solidification process. This may be because the powder absorbed too much amount of energy due to higher laser power and lower traveling speed. These conditions create a large and deep melt pool having a surface thermal gradient along both the traveling and scanning directions. This in turn induces a surface tension gradient in the liquid, that favors the formation of surface ripples behind the laser moving front [9]. When the traveling speed is slow, low frequency high amplitude ripples tend to develop which become frozen after solidification. Moreover, a large size melt pool will take longer to solidify and so its surface is exposed to oxygen contamination for longer periods. This surface adsorbed oxygen could also be responsible for the "balling" effect observed by further increasing the surface tension of the liquid.

On the other hand, in the case of lower power (169 W on the surface), lower scan speed (508 mm/s) and higher traveling speed (3.05 mm/s) as shown in Fig.3(b), although fewer "balling" of the surface is observed, the continuity in shape of the body can be obtained and the surface shows to be fairly smooth. In this case, the melt pool is less deep and narrower; a thermal

gradient mainly develops parallel to the traveling speed. The surface tension gradient will now cause ripples to have high frequency and low amplitude, providing a smoother surface. Additionally, solidification occurs at a faster rate on the melt pool and less time is available for surface ripples to fully develop. These ripples are of a high frequency due to the faster traveling speed.

Figure 4 shows the shape of scan track of the MA powder. Comparing with the shape of scan track of the blended powders, although some large pores exist in the body, the surface is smooth and few "balling" are observed. This existence of some large pores may be caused by higher oxygen and carbon contents in the MA powder.

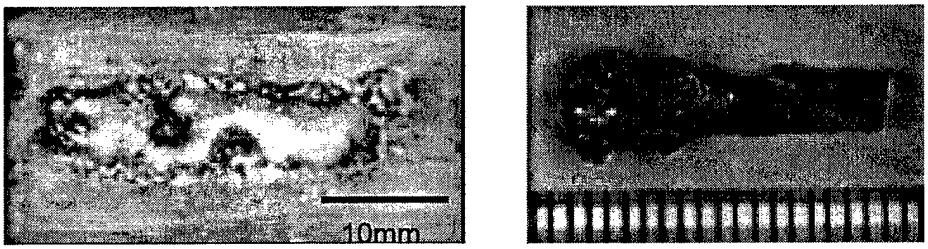

(a) V_s=816 mm/s, V_t=0.41 mm/s (b) V_s=508 mm/s, V_t=3.05 mm/s

Fig.3 Change in shape of scan tracks of the blended powder with scan speed and traveling speed

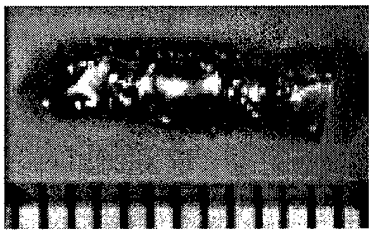

Fig.4 Shape of scan track of the MA powder

Effects of powder characteristics on the microstructure

Figure 5 shows the microstructure of laser-melted body of the blended powder. The microstructure appears to be that of a liquid sintered particles and the size of sintered clusters is different depending on the position in the body. This indicates that partial melting of the blended powder took place. However, at the center the structure is more homogenous, dense and has a cellular structure appearance. This figure corresponds to the microstructure along a vertical direction to the laser traveling speed, that in the horizontal direction to the laser traveling speed was also similar. This fact suggests that the solidification took place rapidly and the concentration gradient of oxygen in liquid state existed in the body as already reported[10]. Figure 6 shows comparison in microstructure of the laser-melted body between the blended powder and the MA powder. The microstructure of the blended powder shows to be that of a liquid sintered particles, while that of the MA powder is a very fine cellular structure. This is caused by difference of powder characteristics between both powders. In Fig.6(a) and Fig.7, the liquid sintered particles of symbol A is primary TiNi and the lamellar structure of symbol B is a eutectic mixture of TiNi and Ti_4Ni_2O as reported by Shugo et al.[10]. Comparing with the microstructure in this reference and Fig.6(a), the oxygen content is estimated at about 0.3 mass%.

In the case of blended powder, the concentration gradient in the liquid alloy results in existence of the lamellar area. The distributions of Ti, Ni, O and C elements were examined by means of a SEM with EDX. Scanning electron micrographs and EDX analyses of the laser-melted bodies of the blended powder and the MA powder are shown in Fig.7 and 8, respectively. In the case of blended powder, the liquid sintered particles and the lamellar structure exist as shown Fig.7(a). The distributions of Ti and Ni elements of the lamellar area (B) are little

different from those of the liquid sintered particles (A) as shown in Fig.7(b) and (c).

On the other hand, in the case of the MA powder, the lamellar area is not observed probably because the MA powder is not only alloy but also amorphous state. In this case, since very small particles were observed in optical microstructure as shown in Fig.6(b), the EDX analysis was carried out. The results of SEM observation and EDX analyses in Fig.8 do not suggest existence of precipitates such as oxides or carbides except the generation of very small pores due to higher oxygen and carbon of the MA powder.

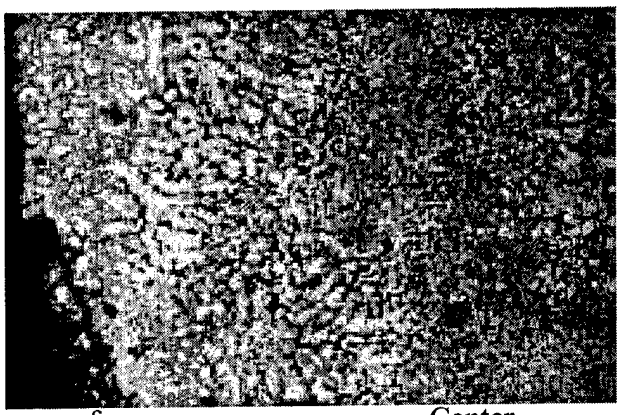

Fig.5 Microstructure of laser-melted body of the blended powder.

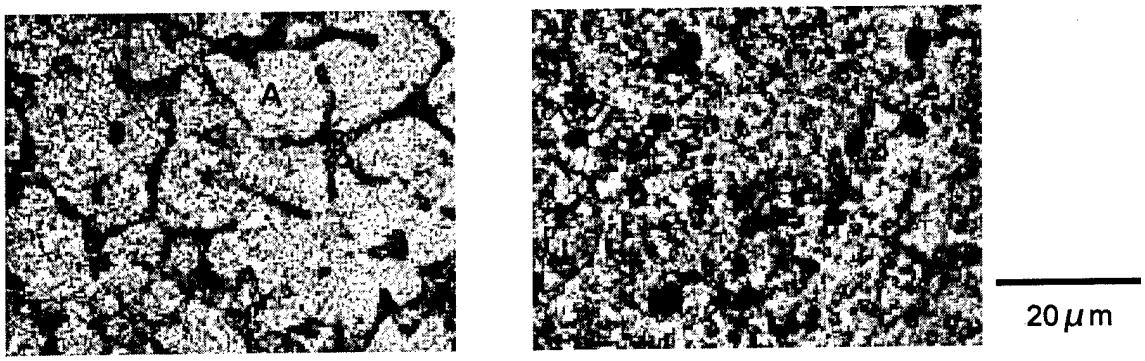

(a) Blended powder (b) MA powder

Fig.6 Comparison in microstructure of laser-melted bodies between the blended powder and the MA powder

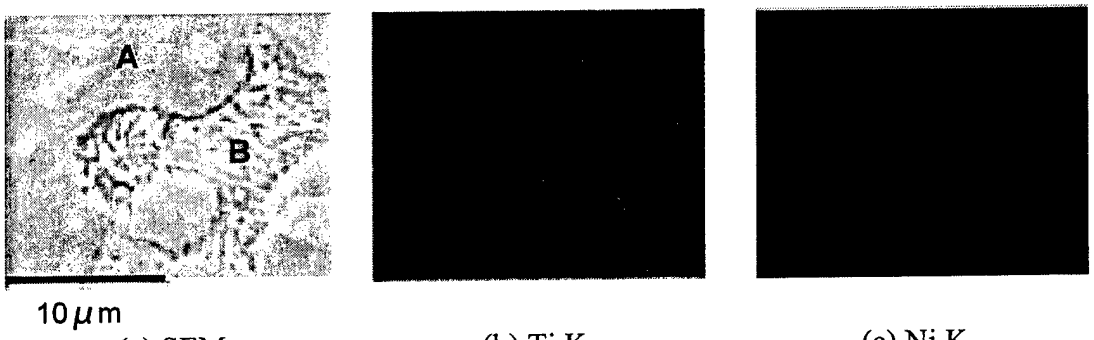

(a) SEM (b) Ti K_{α} (c) Ni K_{α}

Fig.7 SEM and EDX analyses of laser-melted bodies of the blended powder

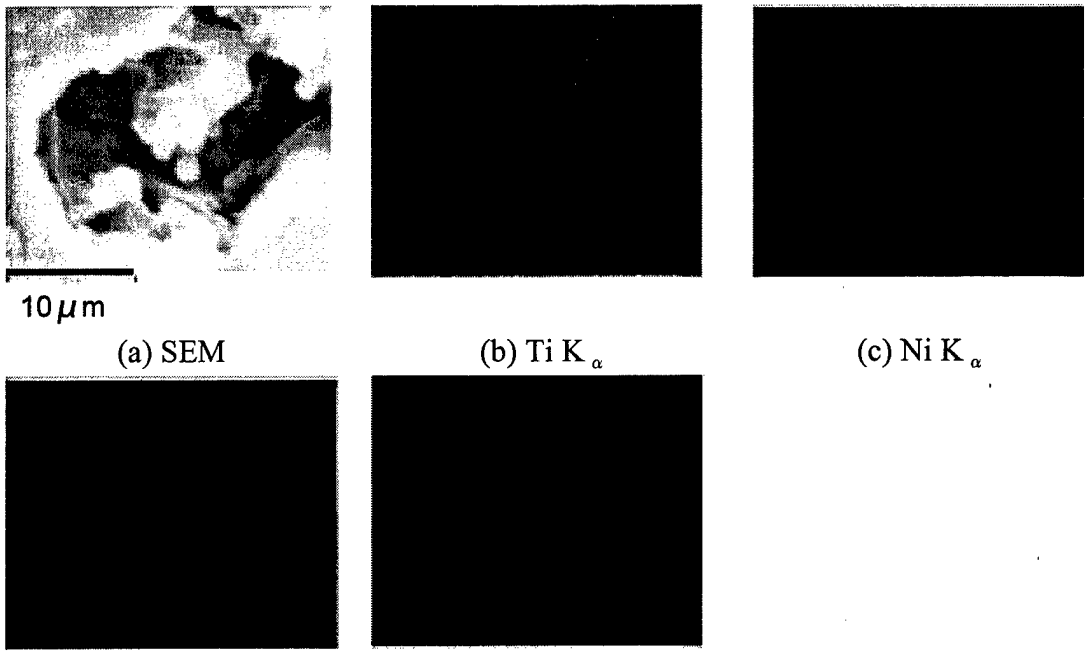

(a) SEM (b) Ti K_α (c) Ni K_α

(d) O K_α (e) C K_α

Fig.8 SEM and EDX analyses of laser-melted bodies of the blended powder

Comparing with the microstructure of sintered body by a pulse-current pressure sintering, the microstructure of the laser-melted body is greatly different from that of the sintered body. In the case of the as-sintered body of the blended powder, the microstructure is very inhomogeneous. Therefore, the solid-solution treatment is needed to homogenize the structure for a long time[4-6]. The results of X-ray diffraction patterns of the laser-melted body of the blended powder and the MA powder are given in Fig.9. It is found from this figure that the microstructure of laser-melted body is consisted of homogeneous TiNi phase in every laser-melted conditions. This suggests that the laser-melted body may show the shape memory effect. Since the peak of TiNi phase in the MA powder is higher than that in the blended powder, the microstructure of the former is more homogeneous and dense than that of the latter as shown in Fig.6. In the case of the sintered body, similar results were obtained. Thus, the MA powder results in more homogeneous and dense structure of the laser-melted body.

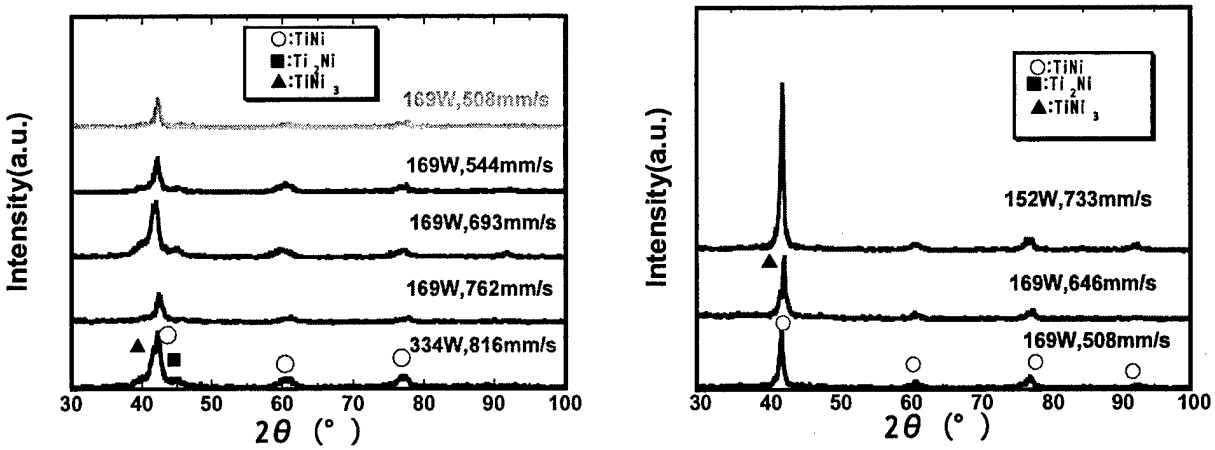

(a) Blended powder (b) MA powder

Fig.9 X-ray diffraction patterns of laser-melted bodies of the blended powder and the MA powder

Shape Memory Characteristics

In this study, the existence of the shape memory effect was examined by DSC measurements. The results of laser-melted body of the blended powder and the MA powder are shown in Fig.10. In the case of the blended powder, since the peaks of exothermic and endothermic reactions are observed clearly, this body has the shape memory effect. The martensite peak temperature and the reverse transformation peak temperature are 294 K and 333 K, respectively. The latter is nearly equal to the peak temperature of the wrought material of the same composition, but the former is lower than the peak temperature of the wrought material. On the other hand, in the case of the MA powder, since the peak of both reactions is not clearly observed regardless of homogeneous TiNi phase as described above, the body does not show the shape memory effect. This is because the MA powder contains high oxygen and carbon as already reported in the case of sintered materials [11]. The lower oxygen and carbon of the MA powder resulted in the shape memory effect of the sintered body. Therefore, it is important to use lower oxygen and carbon powder in order to fabricate superior shape memory alloys.

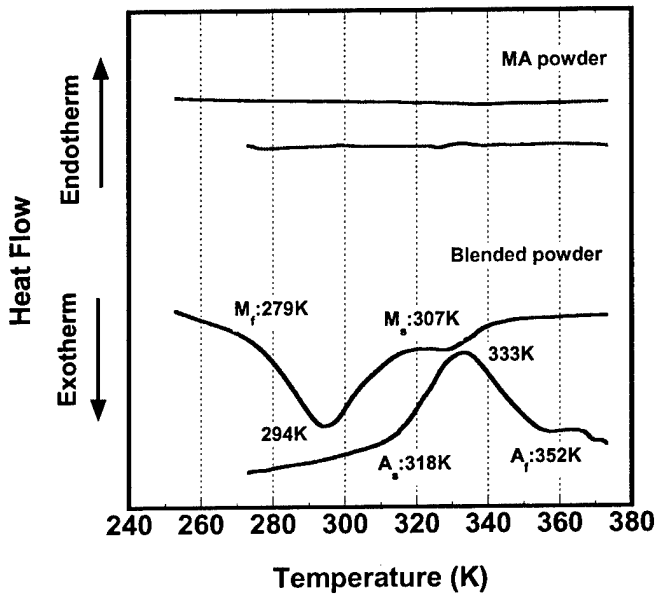

Fig.10 DSC results of laser-melted alloys of the blended powder and the MA powder

Conclusions

In this study, we attempted to fabricate Ti-Ni shape memory alloys by CO_2 laser melting. The laser melting conditions were investigated experimentally, and the microstructure and shape memory characteristics of the laser-melted specimens were also examined. The results obtained are as follows:

(1) The laser-melted specimens having continuous columnar (i.e., rod-like appearance) shape and smooth surface can be fabricated in both cases of the blended powder and the MA powder at the power of 169 W on the surface, the scan speed of 508 mm/s and the traveling speed of 3.05 mm/s.

(2) The microstructure of the blended powder resembles that of liquid sintered particles, while that of the MA powder consists of very fine cells. The MA powder results in more homogeneous structure of the laser-melted body than the blended powder. The laser melting blended powder is

less dense than the MA powder.
(3) The laser-melted specimen fabricated from elemental powders exhibited clearly a shape memory effect, but that from MA powder did not exhibit it, although the latter showed more homogeneous and dense microstructure than the former.

References

[1] J.J. Beaman, J.W. Barlow, D.L. Bourell, R.H. Crawford, H.L. Marcus and K.P. McAlea, *Solid Freeform Fabrication:A New Direction in Manufacturing*, Kluwer Academic Publishers, Massachusetts, 1997.
[2] D.L. Bourell, H.L. Marcus, J.W. Barlow and J.J. Beaman, "Selective laser sintering of metals and ceramics", *International Journal of Powder Metallurgy*, Vol.28, No.4, 1992, pp.369-381.
[3] M.K.Agarwala, D.L. Bourell, J.J. Beaman, H.L. Marcus and J.W. Barlow, "Direct selective laser sintering of metals", *Rapid Prototyping Journal*, Vol.1, No.1, 1995, pp.26-36.
[4] H. Kyogoku, T. Tanbo, M. Yokota, S. Komatsu, F. Yoshida, T. Sakuma and U. Iwata, "Influence of composition on thermo-mechanical properties of TiNi shape memory alloy fabricated by spark-plasma sintering", *Advances in Powder Metallurgy & Particulate Materials-2001*, Part7, Compiled by W.B. Eisen and S. Kassam, MPIF, New Jersey, 2001, pp.1-9.
[5] T. Watanabe, H. Kyogoku, F. Yoshida and T. Sakuma, "Fabrication of TiNi shape memory alloy by spark-plasma sintering and its thermo-mechanical properties", *Transactions of the Materials Research Society of Japan*, Vol.26, No.1, 2001, pp.149-152.
[6] H. Kyogoku, F. Yoshida and S. Komatsu, "Shape memory properties of Ti-Ni alloy fabricated by spark-plasma sintering method", *International Journal of Materials Processing Technology* (CD-ROM), Vol.117, Issue 3, 2001, pp.1-6.
[7] L.B. Niu, T. Sakuma, H. Takaku, H. Kyogoku, and Y. Sakai, "Erosion resistance of Ti-Ni shape memory alloy to hot water jet", *Materials Science Forum*, Vol.394-395, 2002, pp.353-356.
[8] L.B. Niu, T. Sakuma, Y. Sakai, H. Kyogoku, and H. Takaku, "Hot water jet erosion characteristics of Ti-Ni shape memory alloys", *Materials Transactions*, Vol.43, No.5, 2002, pp.840-845.
[9] T.R. Anthony and H.E. Cline, *J. Applied Physics*, Vol. 48, No 9, 3888-3894 (1977).
[10] Y. Shugo, S. Hanada and T. Honma, "Effect of oxygen content on the martensite transformation and determination of defect structure in Ti-Ni alloys", *Bulletin of research Inst. Mineral Dressing and Metallurgy (Tohoku University)*, Vol.41, 1985, pp.23-34.
[11] H. Kyogoku, A. Terayama, M. Sakamura and S. Komatsu, "Fabrication of shape memory alloy powder by mechanical alloying", *Proceedings of JSME/ASME International Conference on Materials and Processing 2002*, Vol.1, 2002, pp.136-141.

Christoph Ader (447)
Fraunhofer IPT
Steinbachstrasse 17
Aachen 52074
DE
ader@ipt.fhg.de
T: +49-241-8904-403
F: +49-241-8904-6403

Seokyoung Ahn
University of Texas at Austin
Mechanical Engineering
1 University Station C2200
Austin, TX 78712-0292
syahn@mail.utexas.edu
T: 512-471-5838
F:

Safina Akhtar (644, 656)
University of Bradford
School of Eng, Design & Technology
Richmond Bldg., Richmond Road
Bradford BD7 4DP
GB
s.akhtar18@brad.ac.uk
T: 01274-232323 x 4553
F: 01274-234507

Joe Allison
Solid Concepts Inc.
28231 Avenue Crocker Bldg. 10
Valencia, CA 91355
USA
jallison@solidconcepts.com
T: 661-257-9300
F: 661-2557-9311

Bahram Asiabanpour (25)
Texas State University at San Marcos
Department of Technology
601 University Dr.
San Marcos, TX 78666
USA
asiabanp@yahoo.com
T: 512-665-4617
F:

Joe Beaman (93, 109, 414, 491, 501, 585)
University of Texas at Austin
Mechanical Engineering
1 University Station C2200
Austin, TX 78712-0292
USA
jbeaman@mail.utexas.edu
T: 512-471-3058
F: 512-471-8727

Jack Beuth (196, 328)
Carnegie Mellon University
Dept. of Mechanical Engineering
5000 Forbes Avenue
Pittsburgh, PA 15213-3890
USA
beuth@andrew.cmu.edu
T: 412-268-3873
F: 412-268-3348

Shweta Bhandari
University of Texas at Austin
Mechanical Engineering
1 University Station C2200
Austin, TX 78712-0292
Shwets8uf@mail.utexas.edu
T: 512-659-1495
F:

Klas Boivie (632)
Woxéncentrum, KTH
The Royal Institute of Technology
Brinellvagen 68
10044 Stockholm
Sweden
kbv@iip.kth.se
T: +46-8-7906371
F: +46-8-210851

Richard B. Booth
3D Systems
26081 Avenue Hall
Valencia, CA 91355
USA
boothr@3dsystems.com
T: 661-295-5600 x 2546
F: 661-295-7181

Dave Bourell (93, 109, 414, 479, 559, 585, 668)
University of Texas at Austin
Mechanical Engineering
1 University Station C2200
Austin, TX 78712-0292
USA
dbourell@mail.utexas.edu
T: 512-471-3170
F: 512-471-7681

Ian Campbell (126)
Loughborough University
Dept. of Design & Technology
Loughborough LEI LE11 3TU
UK
r.i.Campbell@lboro.ac.uk
T: 44-1509-228312
F:

Matt Campbell (414, 501)
University of Texas at Austin
Mechanical Engineering
1 University Station C2200
Austin, TX 78712-0292
Mc1@mail.utexas.edu
T: 512-232-9122
F: 512-471-7682

Larry Casner
University of California-Irvine
Irvine, CA
USA
lacasner@pacbell.net
T: 310-831-8392
F:

Richard Chartoff (385)
University of Arizona
Arizona Materials Laboratory
4715 E. Fort Lowell Rd.
Tucson, AZ 85712
USA
chartoff@email.arizona.edu
T: 520-322-2979
F: 520-322-2993

Shaochen Chen
University of Texas at Austin
Mechanical Engineering
1 University Station C2200
Austin, TX 78712-0292
USA
scchen@mail.utexas.edu
T: 512-232-6094
F: 512-471-1045

Thomas H.C. Childs (644, 656)
University of Leeds
School of Mechanical Engineering
Leeds LS2 9JT
EN
t.h.c.childs@leeds.ac.uk
T: +44-113-34-2165
F: +44-113-34-2150

Denis Cormier (439, 548)
North Carolina State University
Dept. of Industrial Engineering
Raleigh, NC 27695-7906
USA
cormier@eos.ncsu.edu
T: 919-515-1549
F: 919-515-1543

Nathan Crane
Massachusetts Institute of Technology
77 Massachusetts Avenue
Cambridge, MA 02142
USA
ncrane@mit.edu
T: 617-253-7274
F: 617-253-0209

Terry S. Creasy
Texas A&M University
M.S. 3123
100 ENPA
College Station, TX 77843-3123
USA
tcreasy@mengr.tamu.edu
T: 979-458-0118
F:

Suman Das (82, 227)
University of Michigan
2250 GG Brown
2350 Hayward St.
Ann Arbor, MI 48109-2125
USA
sumandas@umich.edu
T: 734-615-6646
F: 734-647-3170

Carl Deckard
6618 Hergotz Lane
Austin, TX 78742
USA
carldeckard@hotmail.com
T: 512-389-0455
F;

Ron DeFonce
Boeing
8900 Frost Avenue
Mail Code S245-1003
Berkeley, MO 63134
USA
Ron.c.defonce@boeing.com
T: 314-232-3716
F:

Phill Dickens
Loughborough University
Wolfson School of MME
Loughborough Leics LE11 3TU
UK
p.dickens@lboro.ac.uk
T: +44-1509-227530
F: +44-1509-227549

Rajeev Dwivedi (1)
Research Center for Advanced Manufacturing
Southern Methodist University
1500 International Parkway, Suite 100
Richardson, TX 75081
USA
rdwivedi@engr.smu.edu
T: 214-768-4873
F: 214-768-0812

Angelos Economou
DeMontfort University
Innovation Centre
The Gateway
Leicester LE1 9BH
GB
economou@dmu.ac.uk
T: +44-116-2506466
F: +44-116-2577064

Alair Emory
Javelin 3D
533 S 700 E
Salt Lake City, UT 84102
USA
alaire@javelin3D.com
T: 801-466-5518
F: 801-363-6376

Poonjolai Erasenthiran
Loughborough University
Wolfson School of MME
Loughborough Leics LE11 3TU
UK
p.erasenthiran@lboro.ac.uk
T: +44-1509-227568
F: +44-1509-227549

Michael Ervin
University of Texas
SFF Center
1 University Station C2200
Austin, TX 78712-0292
USA
maervinassoc@austin.rr.com
T: 512-431-2954
F: 512-329-6085

Scott Evans (414)
University of Texas at Austin
Mechanical Engineering
1 University Station C2200
Austin, TX 78712-0292
rsevans@mail.utexas.edu
T:
F:

Mario Faustini (400)
University of Texas at Austin
Mechanical Engineering
1 University Station C2200
Austin, TX 78712-0292
USA
faustini@mail.utexas.edu
T: 512-471-5838
F:

Kent Firestone
University of Texas
SFF Center
1 University Station C2200
Austin, TX 78712-0292
USA
kentf@austin.rr.com
T: 512-695-4073
F:

Vito Gervasi
Milwaukee School of Engineering
1025 N. Broadway
Milwaukee, WI 53202
USA
gervasi@msoe.edu
T: 414-277-4550
F: 414-277-4550

Amol Ghanekar (348)
University of Texas at Austin
Mechanical Engineering
1 University Station C2200
Austin, TX 78712-0292
amolsg@mail.utexas.edu
T: 512-471-5838
F:

David Gill (324)
Sandia National Laboratories
PO Box 5800, MS 0958
Albuquerque, NM 87185-0958
USA
ddgill@sandia.gov
T: 505-844-1524
F: 505-844-2894

Josh Gillespie (510)
Georgia Institute of Technology
Mechanical Engineering Dept, MARC 457
813 Ferst Drive, NW
Atlanta, GA 30332-0405
USA
513@gttx.org
T: 404-894-1836
F: 404-894-9342

Connie Gomez
Drexel University
3802 Lancaster Avenue
Philadelphia, PA 19104
USA
Cg24@drexel.edu
T: 267-230-9686
F: 215-895-1478

George Hadipoespito (13)
University of Wisconsin-Madison
2130 University Avenue #39
Madison, WI 53726
USA
hadipoespito@wisc.edu
T: 608-358-4206
F: 608-265-2316

Masashi Hagiwara
Aspect Inc.
3104-1-101
Higashi-Naganuma
Inagi-city, Tokyo 206-0802
Japan
hagiwara@aspect.rp.co.jp
T: +81-42-370-7900
F: +81-42-370-7901

Richard Hague
Loughborough University
Wolfson School of MME
Loughborough Leics LE11 3TU
UK
r.hague@lboro.ac.uk
T: +44-1509-227619
F: +44-1509-227549

Ola Harrysson (433, 439, 548)
North Carolina State University
Dept. of Ind. Engr. Campus Box 7906
100 Current Drive, Park Shops 119
Raleigh, NC 27695-7906
USA
harrysson@nc.rr.com
T: 919-513-0220
F: 919-515-1543

Carl Hauser (640, 656)
The University of Leeds
The School of Mechanical Engineering
Woodhouse Lane
Leeds BD10 8XD
GB
c.hauser@leeds.ac.uk
T: 0113-2332197

George Hazelrigg
National Science Foundation
4201 Wilson Blvd, Rm 550
Arlington, VA 22230
USA
ghazelri@nsf.gov
T: 703-292-8330
F: 703-292-9056

Cheung Hoi Hoi (138)
University of Hong Kong
Room 824, Haking Wong Building
Pokfulam Road
Hong Kong
HK
H9941603@hkusua.hku.hk
T: 852-2859-7967
F: 852-2858-6535

Neil Hopkinson (596)
Loughborough University
Wolfson School of MME
Loughborough Leics LE11 3TU
UK
n.Hopkinson@lboro.ac.uk
T: +44-1509-22752
F: +44-1509-227549

Hoiyin Ip (340)
University of California-Irvine
5511 Verano Place
Irvine, CA 92612
USA
hoiyinip@uci.edu
T: 310-920-5896
F:

John Jensen
University of Texas at Austin
Mechanical Engineering
1 University Station C2200
Austin, TX 78712-0292
John.Jensen@mail.utexas.edu
T: 512-293-2671
F:

Wenhui Jiang (301, 524)
Research Center for Advanced Manufacturing
1500 International Parkway, Suite 100
Richardson, TX 75081
USA
wjiang@engr.smu.edu
T: 214-768-4873
F: 214-768-0812

Scott Johnston (536)
University of Washington
916 NE 72nd, Apt. 201
Seattle, WA 98115
USA
Scott524@u.washington.edu
T: 206-250-4968
F:

Lalit Karlapalem
University of Texas at Austin
Mechanical Engineering
1 University Station C2200
Austin, TX 78712-0292
USA
ckl@mail.utexas.edu
T: 512-232-4331
F:

Brian Kernan (616)
Massachusetts Institute of Technology
Room 35-011
77 Massachusetts Avenue
Cambridge, MA 02139
USA
bkernan@mit.edu
T: 617-253-2230
F: 617-253-0209

Nathan W. Klingbeil (219)
Wright State University
209 Russ Engineering
3640 Colonel Glenn Hwy.
Dayton, OH 45435
USA
Nathan.klingbeil@wright.edu
T: 937-775-5088
F: 937-775-5009

Martin Koch
IME Dept.
Cal Poly
1 Grand Ave.
San Luis Obispo, CA 93407
mkoch@calpoly.edu
T: 805-756-1114
F: 805-756-5439

Ashok V. Kumar (39)
University of Florida
PO Box 116300
237 MAE-B
Gainesville, FL 32611-6300
USA
akumar@ufl.edu
T: 352-392-0816
F: 352-392-1071

Hideki Kyogoku (491, 668)
Kinki University
1 Takayaumenobe
Higashihiroshima 739-2116
JP
kyogoku@hiro.kindai.ac.jp
T: +81-824-34-7000
F: +81-824-34-7011

Robert G. Landers (186, 246)
University of Missouri-Rolla
205A Mechanical Engineering Bldg.
1870 Miner Circle
Rolla, MO 65409-0050
USA
landersr@umr.edu
T: 573-341-4586
F: 573-341-6899

Karmen Lappo (93, 109, 479)
University of Texas at Austin
Mechanical Engineering
1 University Station C2200
Austin, TX 78712-0292
lappokn@mail.utexas.edu
T:
F:

Morgan Larsson (433)
Arcam AB
Krockslattsfabriker 30
Molndal SE-431 37
SE
Morgan.larsson@arcam.com
T: +46708183807
F: +46708183877

Wing K. Lau (162)
Therics Inc.
115 Campus Drive
Princeton, NJ 08540
USA
wlau@therics.com
T: 609-514-7200
F: 609-514-7219

Andrew C. Layton (289)
Rapid Prototyping and Manufacturing Institute
Georgia Institute of Technology
813 Ferst Dr NW, MS 0560
Atlanta, GA 30332
USA
Andrew.Layton@marc.gatech.edu
T: 404-385-1053
F:

Lydia Lee
Drexel University
7255 Ridge Avenue
Philadelphia, PA 19128
USA
variant8@yahoo.com
T: 215-508-4925
F:

Loh Han Tong (174, 423)
Design Technology Institute
National University of Singapore
10 Kent Ridge Crescent
Singapore 119260
SG
mpelht@nus.edu.sg
T: +65-6874-1226
F: +65-6773-6098

Evan Malone (363)
Cornell University
B60 Rhodes Hall
Ithaca, NY 14853
USA
Em224@cornell.edu
T: 607-254-8940
F: 607-255-1222

Harris L. Marcus (392)
University of Connecticut
Institute of Materials Science, U-3136
97 North Eagleville Road
Storrs, CT 06269-3136
USA
hmarcus@mail.ims.uconn.edu
T: 860-486-4623
F: 860-486-4745

Ausenda Luis Avelar Mendes (60)
ESTG
Q to S. Bartolomeu Lote 4 R/e
2410 Leiria
Morro do Lena, Aldovieiro
Leiria 2401-951
Portugal
amendes@estg.iplei.pt
T: +351-244820389
F: +351-244820310

Jian Mi (510)
Georgia Institute of Technology
Mechanical Engineering Dept., MARC 457
813 Ferst Drive, NW
Atlanta, GA 30332-0405
USA
Gte445y@prism.gatech.edu
T: 404-894-8411
F: 404-894-9342

Michael Mignatti (501)
University of Texas at Austin
Mechanical Engineering
1 University Station C2200
Austin, TX 78712-0292
mmignatti@mail.utexas.edu
T: 512-471-7347
F:

Jeremy Murphy
University of Texas at Austin
Mechanical Engineering
1 University Station C2200
Austin, TX 78712-0292
Jmurphy101@hotmail.com
T:
F:

Rick Neptune (400)
University of Texas at Austin
Mechanical Engineering
1 University Station C2200
Austin, TX 78712-0292
rneptune@mail.utexas.edu
T: 512-471-0848
F:

Toshiki Niino
The University of Tokyo
Institute of Industrial Science
4-6-1 Komaba Meguro
Tokyo 153-8505
Japan
niino@ieee.org
T: 81-354526216
F: 81-354526214

Olli Nyrhila
EOS Finland
Aholantie 17
Rusko 21290
FI
Olli.nyrhila@eos-finland.com
T: +358-2-4365611
F:

Jeremy A. Palmer
Sandia National Laboratories
PO Box 5800, MS 0958
Albuquerque, NM 87185-0958
USA
japalme@sandia.gov
T: 505-284-9623
F: 505-844-2894

Sashikanth Prakash (254)
University of Missouri-Rolla
1300 North Oak Street Apt. 20
Rolla, MO 65401
USA
Sp3m4@umr.edu
T: 573-426-4137
F:

K. Siva Prasad (375, 465)
I.I.T. Kanpur, India
Kanpur UT 208016
IN
ksp@iitk.ac.in
T: 91-512-2597838
F: 91-512-2597302

Aparajit Pratap (150)
University of Texas at Austin
Mechanical Engineering
1 University Station C2200
Austin, TX 78712-0292
aparajit@mail.utexas.edu
T:
F:

Jorge Ramos (559, 668)
University of Texas at Austin
Mechanical Engineering
1 University Station C2200
Austin, TX 78712-0292
jaramos@mail.utexas.edu
T: 512-471-6709
F:

Kian Rasa (363)
Cornell University
B60 Rhodes Hall
Ithaca, NY 14853
USA
Kr85@cornell.edu
T: 607-254-8940
F: 607-255-1222

David Rosen (70, 289)
Georgia Tech
School of Mechanical Engineering
813 Ferst Drive
Atlanta, GA 30332-0405
USA
David.rosen@me.gatech.edu
T: 404-894-9668
F: 404-894-9342

Rodrigo Ruizpalacios (491, 501)
University of Texas at Austin
Mechanical Engineering
1 University Station C2200
Austin, TX 78712-0292
rruizpal@mail.utexas.edu
T: 512-471-7731
F:

Benay Sager (70)
Georgia Institute of Technology
School of Mechanical Engineering
813 Ferst Drive, Marc Rm. 251
Atlanta, GA 30332-0405
USA
Gte646w@prism.gatech.edu
T: 404-894-8528
F: 404-894-9342

Scott Schermer
S.C. Johnson & Son
1525 Howe Street MS090
Racine, WI 53403-2236
USA
scscherm@scj.com
T: 262-260-6023
F: 262-260-2537

Leon Shaw (233, 392)
University of Connecticut
97 North Eagleville Road, U-3136
Storrs, CT 06269
USA
lshaw@mail.ims.uconn.edu
T: 860-486-2592
F:

Meghan Shilling (70)
Georgia Tech
324433 Georgia Tech Station
Atlanta, GA 30332
USA
Gte642w@mail.gatech.edu
T: 404-372-6798
F:

Moss Shimek (479)
University of Texas at Austin
Mechanical Engineering
1 University Station C2200
Austin, TX 78712-0292
Orig.mossimo@mail.utexas.edu
T: 512-471-5838
F:

Lauren Shor (573)
Drexel University
Dept. of Mech. Engg.
3141 Chestnut Street
Philadelphia, PA 19104
USA
Lauren@drexel.edu
T:
F:

Prabhjot Singh (266, 279)
University of Michigan
1647 Beal Avenue, Apt. 1
Ann Arbor, MI 48105
USA
psinghz@engin.umich.edu
T: 734-763-4056
F:

Vinay Sriram (491, 585)
University of Texas at Austin
Mechanical Engineering
1 University Station C2200
Austin, TX 78712-0292
karkehalli@mail.utexas.edu
T: 512-471-5838
F:

Binil Starly (162)
Drexel University
Department of Mechanical Engineering
3141 Chestnut Street
Philadelphia, PA 19104
USA
Bs49@drexel.edu
T: 215-895-6688
F:

Brent Stucker (120)
Utah State University
Mechanical & Aerospace Engineering
Logan, UT 84322-4130
USA
Brent.stucker@usu.edu
T: 435-797-8173
F:

Qian Sun (313)
University of Calgary
Chemical & Petroleum Department
205 Jackson Place NW
Calgary, Alberta T3B 2V3
Canada
sunq@ucalgary.ca
T: 403-284-1697
F: 403-284-4852

Wei Sun (162, 573)
Drexel University
Dept. of Mechanical Engineering
3141 Chestnut Street
Philadelphia, PA 19104
USA
sunwei@drexel.edu
T: 215-895-5810
F: 215-895-2094

Sharath Suryanarayan
Texas A&M University
4302 College Main #302
Bryan, TX 77801
USA
Sharath1878@tamu.edu
T: 979-268-0469
F:

Feng Wang (573)
Drexel University, MEM Dept.
3141 Chestnut Street
Philadelphia, PA 19104
USA
Feng.wang@drexel.edu
T: 215-895-6688
F:

Huijun Wang (301)
RCAM at SMU
1500 International Parkway, Suite 100
Richardson, TX 75081
USA
huijun@engr.smu.edu
T: 214-768-4873
F: 214-768-0812

Harovel G. Wheat
University of Texas at Austin
Mechanical Engineering
1 University Station C2200
Austin, TX 78712-0292
USA
hwheat@mail.utexas.edu
T: 512-471-1451
F: 512-471-7681

Hwa-Joon Yang (470)
Hyundai Motor Company
Jang Duk dong
Hwa Sung, Kyoung Gi Do
South Korea
rpproto@hyundai-motor.com
T: 82-31-369-4172
F: 82-31-369-6239

Pin Yang (50)
Sandia National Laboratories
Org. 14192; MS0959
Albuquerque, NM 87185-0959
USA
pyang@sandia.gov
T: 505-844-3386
F: 505-844-0276

Hsiao-Chuan Yen (456)
National Taipei University of Technology
Fl. 4, No. 11, Lane 39, Tai Shun Street
Taipei 106
TW
hcyen@ms14.hinet.net
T: 886-2-23634075
F: 886-2-23632961

Wong Yoke-San (423)
National University of Singapore
Faculty of Engineering
Department of Mechanical Engineering
9 Engineering Drive 1
Singapore 117576
Singapore
mpewys@nus.edu.sg
T: 65-6874-2221
F: 65-6779-1459

Yuwen Zhang (208)
New Mexico State University
PO Box 30001, MSC 3450
Las Cruces, NM 88003
USA
Zhangy12@asme.org
T: 505-646-6546
F: 505-646-6111